I.C.E.F.M. 94

Proceedings of the 2nd International Conference on Experimental Fluid Mechanics

July 4-8, 1994 - Torino, Italy

Edited by
M. ONORATO

LEVROTTO & BELLA
TORINO

I.C.E.F.M. 94

Proceedings of the 2nd International Conference
on Experimental Fluid Mechanics
July 4-8, 1994 - Torino, Italy

Edited by
M. Onorato

LEVROTTO e BELLA

DISCLAIMER NOTICE

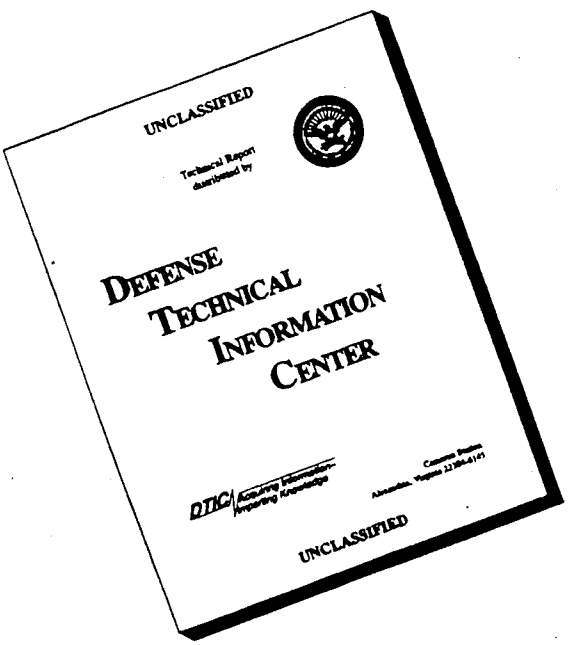

THIS DOCUMENT IS BEST QUALITY AVAILABLE. THE COPY FURNISHED TO DTIC CONTAINED A SIGNIFICANT NUMBER OF PAGES WHICH DO NOT REPRODUCE LEGIBLY.

I.C.E.F.M. 94

Proceedings of the 2nd International Conference
on Experimental Fluid Mechanics
July 4-8, 1994 - Torino, Italy

Edited by
M. Onorato

LEVROTTO e BELLA

Finito di stampare nel mese di settembre 1994

Stampato da Stampatre, Torino
per conto della Levrotto & Bella Editrice S.a.s.
Corso Vittorio Emanuele, 26/F - Torino

ORGANIZED BY

Dipartimento di Ingegneria Aeronautica e Spaziale - Politecnico di Torino
Centro Studi Dinamica Fluidi del CNR

SPONSORED BY

Politecnico di Torino
Consiglio Nazionale delle Ricerche (CNR)
Cassa di Risparmio di Torino (CRT)
European Research Office of the U.S. Army

CONFERENCE CHAIRMAN

M.Onorato (Politecnico di Torino, Italy)

SCIENTIFIC COMMITTEE

R.J. Adrian (USA), G. Brown (Australia), G. Carlomagno (Italy), A. Cenedese (Italy), G.Chernyi (Russia), G.Comte-Bellot (France), J.P.Crowder (USA), A.Elseenar (N.L.), W. Fiszdon (Poland), S. S. Grigorian (Russia), R.K. Hanson (USA), C.M .Ho (USA), H.G. Hornung (USA), V.V.Kozlov (Russia), J.L.Le (China), V.Y.Levchenko (Russia), M.J.Leynaert (France), S.X.Li (China), A. Libchaber (USA), G.E.A.Meier (Germany), W.Merzkirch(Germany),R.Narasimha(India),V.M.Neyland(Russia), M.Nishioka(Japan), M. Onorato (Italy), A. E. Perry (Australia), J. Rom (Israel), A. Roshko (USA), W.Saric(USA), H. Sato (Japan), R.J. Stalker (Australia), K. Takayama (Japan), J.F.Wendt (Belgium), J.H. Whitelaw (UK), F.G. Zhuang (China)

LOCAL ORGANIZING COMMITTEE

G. Chiocchia, G. Iuso, M.S. Oggiano, F. Quagliotti, D. Tordella

PREFACE

This volume contains 7 invited papers and 85 contributed papers presented at the Second International Conference on Experimental Fluid Mechanics, ICEFM 94, which was hold in Torino, Italy, from July 4 to 8, 1994.

The ICEFM 91 was organized by prof. F.G. Zhuang in Chengdu, China.

The purpose of the Conference is to provide an opportunity for scientists and engineers, active in different areas of Experimental Fluid Mechanics, to exchange their ideas, to present the state of the art and to discuss new developments.

The response from the experimental fluid mechanics community, as in the previous Conference was quite encouraging: more than 130 partecipants, from 22 countries, were present.

The success of the meeting was such that the members of the Scientific Committee decided to organize a third Conference. The ICEFM 97 will be held in Moscow.

To conclude and to stress the importance of these conferences, I would like to quote part of the Opening Remarks made by prof. Hans W. Liepmann at the first ICEFM:

'In this time of theoretical abstractions and ever increasing computing power, it is most important, I think, to recall the empirical foundation of all physical sciences and to remember the fact that experiments are primarly important for the discovery of new facts, with code verification an often necessary but no means sufficient reason for an interest in experimentation.

The extraordinarily rapid development of digital electronics, solid state sensors and modern optics has opened a host of new avenues for intelligent and incisive experiments into the many facets of fluid dynamics which are still puzzling today. The experimenter today has to become not only familiar with these new tools but with new theoretical concepts like chaos and fractals and the accompanying often wildly exaggerated claims for their significance. Without some familiarity and understanding, new concepts or techniques can be dismissed as unimportant or useless. Consequently, the often heard need for more specialization is in my opinion plainly wrong. Like in any field of applied physics, meaningful experimentation in fluid mechanics requires a much broader background in the sciences than ever before, and the difference between programmable tests and analytical experimentation grows continously."

Michele Onorato

CONTENTS

THE FLOW PHYSICS OF LEADING-EDGE VORTICES BEFORE AND AFTER VORTEX BREAKDOWN

Dr. Robert C. Nelson
Department of Aerospace and Mechanical Engineering
Hessert Center for Aerospace Research
University of Notre Dame
Notre Dame, IN 46556
United States of America

The aerodynamic characteristics of wing planforms with large, leading-edge sweep are governed by the vortices that form above the upper wing surface. As the angle of attack of a highly swept wing is increased the boundary layer on the lower surface flows outboard and separates at the sharp leading edge to form a free shear layer. The shear layers roll up to form two counter-rotating vortices above the leeward surface of the wing. When the angle of attack reaches some critical value, the leading-edge vortices undergo a dramatic and sudden transition from a tightly wound spiraling vortical flow to a larger swirling turbulent flow called vortex breakdown.

The leading-edge vortices of highly swept wings have been the subject of numerous experimental and theoretical studies since the mid-1950s. This paper presents a review of the underlying flow physics of the leading-edge vortex structure and its contribution to the aerodynamic characteristics of highly swept wings. The paper includes a discussion of the flow topology over a delta wing by way of surface and off-surface flow visualization data. The flowfield structure of the leading-edge vortices is also examined through presentation of detailed flow surveys before and after breakdown. After summarizing the current state of understanding of leading-edge vortex flows and breakdown for stationary wings, the paper concludes with a brief review of the influence of unsteady wing motions on vortex breakdown and the aerodynamic loads.

Introduction

Vortices and vortex breakdown are important features of many industrial and aeronautical flows. The phenomena known as vortex breakdown is the process whereby a vortex undergoes a sudden and rapid change in its flow state. Prior to breakdown the vortex core is small relative to the overall length of the vortex, however , when breakdown occurs the core appears to burst or increase in size in a distance of the order of the initial core size. Vortex breakdown can be either an advantageous or detrimental consequence depending on the flow of interest. In an industrial flow where fuel is introduced by way of a vortex generator, vortex breakdown is desirable so the proper fuel/air mixing occurs. On the other hand, breakdown of the leading-edge vortices generated by the wings of slender winged aircraft lead to detrimental effects such as limits on maneuverability and the possibility of severe tail buffeting due to flow interaction with the vertical tail surface.

In this paper I will attempt to review the basic flow physics associated with leading-edge vortices for both static and dynamic model motions. The first part will examine the flow structure of the leading-edge vortices before and after breakdown and the influence of the vortices on the aerodynamic performance of slender delta wings. The second part will present a brief review of the influence of unsteady large amplitude motion on the vortex dynamics and unsteady loads.

Leading-edge Vortical Flows

The leading-edge vortices generated by slender wings have been the subject of numerous experimental studies starting in the mid-1950s and continuing to today. References 1-9 are some of the more frequently cited references of the earlier research efforts.

The flow structure on the upper side of a delta wing at angle of attack is extremely complex. At moderate angles of attack the leeward flow field for these planforms is dominated by

a highly organized vortical flow structure emanating from the sharp leading edge. A sketch of the classic leading-edge flowfield above a delta wing is shown in Fig. 1a. The vortex sheet shed from the leading edge rolls up into a pair of leading-edge or primary vortices. The leading-edge vortices induce a flow in the spanwise direction on the upper surface. This outward flow separates from the surface forming a smaller secondary vortex outboard and below the leading-edge vortex. It is possible that there are additional vortices near the surface in this region. The surface flow patterns can be equally complex as illustrated in the sketch in Fig. 1b. The surface patterns reveal the attachment and separation lines of the primary and secondary vortices. The interpretation of surface and off-surface visualization patterns can be, at times, very difficult. However, recently flow topology methods have been used by Perry and Chong\s\up3((10)), Peake and Tobak[11], and Delery[12] to explain the flow structure around various aerodynamic shapes. The flow topology rules provide a fundamentally sound basis for constructing detailed flow topology images.

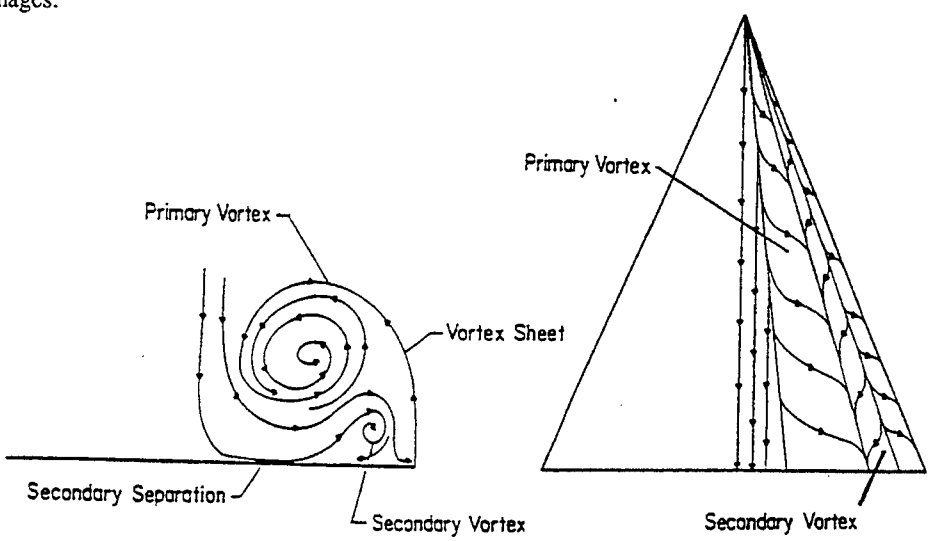

a) Off-surface flow

b) Surface flow

Figure 1. Sketch of the leading-edge flow structure above a sharp-edge delta wing.

Earnshaw[9] proposed that the leading-edge vortex on a delta wing could be divided into three regions; the shear layer, rotational core and viscous subcore. The shear layer or vortex sheet, is generated at the wing's leading edge and feeds vorticity into the vortex core. The thickness of the shear layer increases with increasing distance from the leading edge. The rotational core is approximately 30 percent of the local semispan in diameter, wherein the traces of the vortex sheet produce only minor perturbations on the circumferential or longitudinal velocity distribution. The vorticity inside the core is assumed to be distributed continuously. The viscous subcore, approximately 5 percent local semispan in diameter, is a region in which the gradients of local head, static pressure and velocity are very high. The subcore rotates as a solid body and axial velocity can exceed three times the freestream value. Figure 2 is a sketch illustrating the various regions of the vortex as described by Earnshaw.

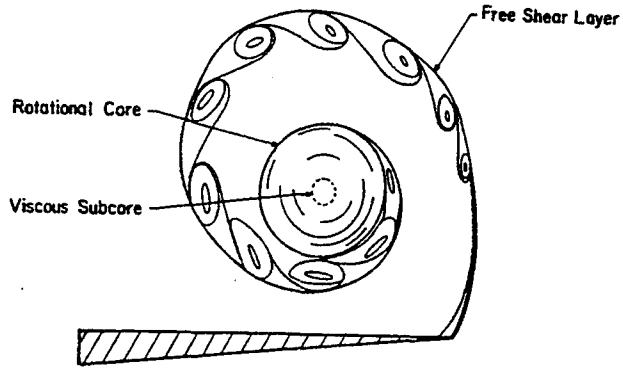

Figure 2. Three regions within a leading-edge vortex.

The leading-edge vortices above a slender, flat-plate, delta wing can be visualized by means of smoke introduced into the flow. The vortices are marked by the entrainment of smoke particles, and can be illuminated at locations along the wing by a laser light sheet that is normal to the wing surface.[13, 14] Figure 3 is a photograph of the laser light sheet illumination of the crossflow sections through the leading-edge vortices. The smoke patterns clearly show the vortical nature of the flow field. The vortical flow field on the leeward side of the delta wing is characterized by large velocity variations. As the angle of attack of a delta wing is increased, the leading-edge vortices will grow in strength and at some point along the vortex breakdown will occur. The change in the flow structure after breakdown is shown in Fig. 4. In this photograph the vortex is breaking down at approximately fifty percent of the root chord.[13] For very large sweep angles, vortex breakdown has been found to occur asymmetrically. When the sweep angle is less than 80°, breakdown is symmetric. Notice how rapidly the core region expands. It should also be noted that the position of the vortex breakdown is not stationary. The breakdown position is unsteady and typically oscillates about some mean position.

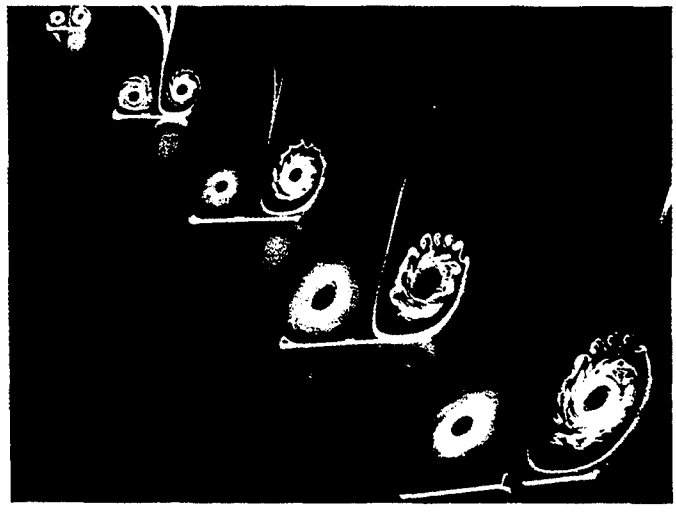

Figure 3. Laser light sheet illumination of the crossflow of the leading-edge vortices above an 85° sweep delta wing. (α = 10° without vortex breakdown) (Payne, 1987)

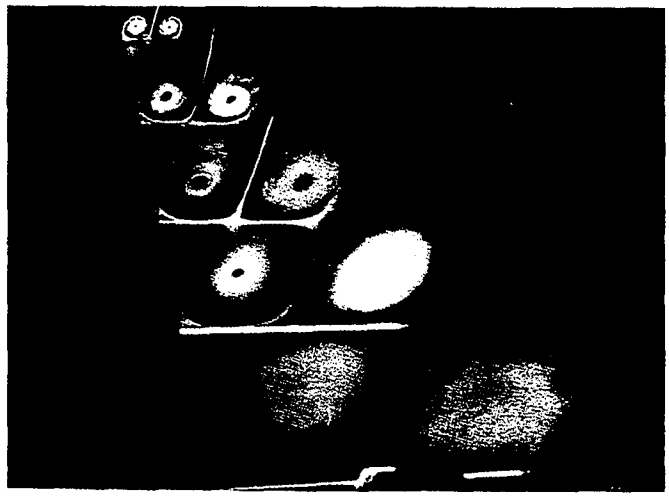

Figure 4. Laser light sheet illumination of the crossflow and longitudinal axis of the leading-edge vortices above an 85° swept delta wing ($\alpha = 40$, vortex breakdown). (Payne, 1987)

Flow Features of Leading-Edge Vortices

The velocity field associated with the leading-edge vortices of simple delta wing planforms has been studied using pressure probes, hot-wire and Laser Doppler Anemometry. Non intrusive measurements of the velocity distribution through a leading-edge vortex above a slender, delta wing is presented in Figure 5. These measurements were made by Pagan and Solignac.[15] The flow surveys were obtained using laser anemometry in the wake of a 75° swept delta wing. The measurements were made just aft of the wing trailing edge ($x/c \simeq 0.27$) in the wake.

Prior to breakdown, the leading-edge vortex can best be described as a swirling jet flow as illustrated in Fig. 5. These measurements show the variation of the velocity distribution through the leading-edge vortex as a function of angle of attack. As the angle of attack is increased, both the maximum axial velocity at the vortex center and the maximum tangential velocity increase. The jetting along the vortex center line can be up to three or more times the freestream velocity depending upon the wing sweep angle. Erickson[16] explains the large axial velocity within the leading-edge vortex by means of a spiraling vortex sheet. The vortex sheet, originating at the wing leading-edge, spirals around the vortex axis as it convects downstream. The spiraling vortex lines are inclined to the vortex axis and induce an axial flow in the downstream direction. For this particular wing the maximum axial velocity is over two and one-half times the freestream velocity. The other noticeable feature is the relative size of the jet core versus the core associated with the maximum tangential velocity. The jet core increases with angle of attack and for the largest angle of attack shown in Fig. 5 the jet core is approximately 50% of the wing semi-span whereas the core based upon the distance between the maximum and minimum tangential velocities is approximately 5-10% of the semi-span. The smaller core region remains essentially the same size as the angle of attack is increased. These two core structures are similar to those proposed by Earnshaw.[9]

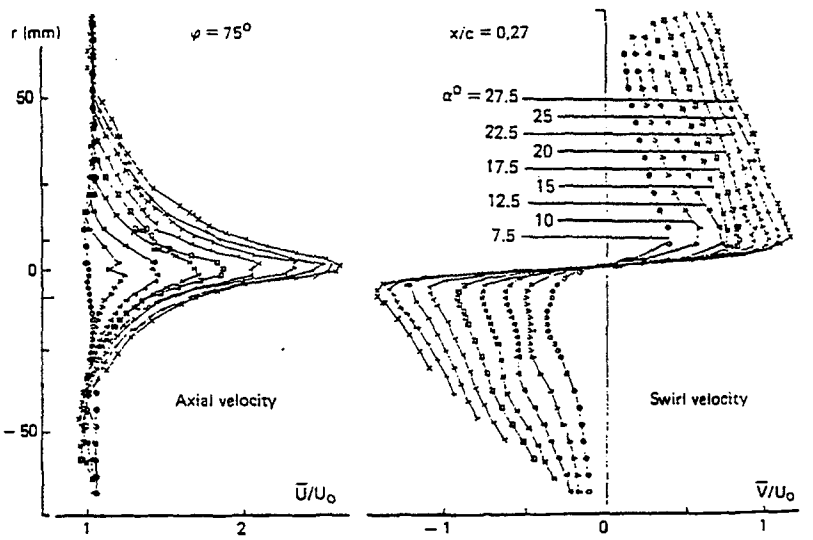

Figure 5. Velocity distribution through a vortex prior to breakdown.
(Pagan and Solignac, Ref. 15)

Vorticity and Circulation

The vorticity distribution and circulation provide additional understanding of the overall structure of the leading-edge vortices. Several investigators have put forth ideas specifically concerned with aspects of vorticity and circulation. Lee and Ho[17] state that "a stationary leading-edge vortex is achieved only when the convection of vorticity along the core axis balances the vorticity generation from the boundary layer of the leading edge" and the swirl angle is an indicator of this balance. A reduction in the axial convection, via the adverse pressure gradient at the trailing edge of the planform, is concluded to cause vortex breakdown.

The argument of a critical vorticity distribution can be substantiated in light of the work by Pagan and Solignac[15] and Delery, Pagan and Solignac[18] They examined the effects of an adverse pressure gradient on a vortex generated by a 75-degree sweep delta wing at $\alpha = 27.5$ deg. The vortex was allowed to enter a two-dimensional duct with movable flaps at the aft end enabling various pressure distributions to be created in the duct. Their results indicate that a maximum vortex strength, as given by the maximum swirl velocity ratio, is strongly dependent on the local freestream pressure gradient. This can also be interpreted that the maximum amount of vorticity or circulation at a given station is limited by the ability of the flow to move downstream, which in turn is regulated by the pressure gradient.

A hypothesis by Brown and Lopez[19] based on physics governing a stagnant recirculating flow region in confined cylindrical flows, argues that breakdown mechanisms rely on the production of negative azimuthal vorticity. This results from a tilting and stretching of the predominantly axial vorticity vector, Ω_x. Vorticity diffusion leads to a radial redistribution of the circulation and a stretching and tilting of vortex lines due to a local increase of the tangential

velocity, V_θ. A reduction in the initially positive azimuthal component of vorticity occurs with axial distance and the subsequent "inviscid breakdown" process develops.

Unfortunately the information on the vorticity distribution within the leading-edge vortices is quite limited. In a recent study by Visser and Nelson reported in references 20-22, hot-wire anemometry was used to examine the vorticity and circulation distributions above a 75° swept delta wing. The axial, radial, and azimuthal vorticity components were measured. The majority of the axial vorticity component are found to be confined to 10% of the span on either side of the vortex core center location. The azimuthal vorticity was smaller in magnitude. Figure 6 is a plot of the axial vorticity at numerous stations along the wing. The axial vorticity has been nondimensionalized and are overlaid for each of the measured x/c locations; similar profiles are seen to exist at each station.

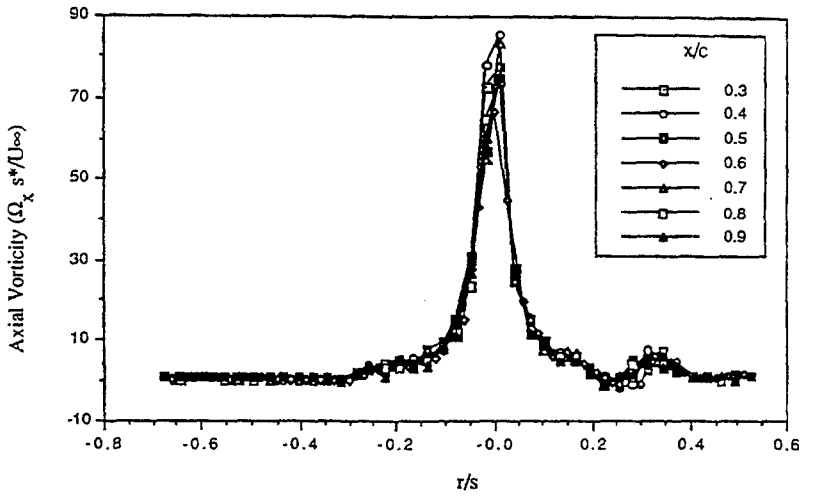

Figure 6. Axial vorticity distribution.

The circulation, Γ, was also calculated using either of the definitions given below.

$$\Gamma = \int_c V \bullet dr = \int_A (\nabla x V) \bullet dA = \int_A \Omega x dA \qquad (1)$$

The circulation is shown in Fig. 7, the values are plotted outward from the core center (r = 0) where the radial distance has been nondimensionalized by the local semispan. Each curve represents a chordwise location and the circulation is seen to grow in a chordwise manner. This is what one would expect, as the feeding sheet is continually being wrapped into the vortex. The circulation increases at a decreasing rate from the vortex center and reaches a maximum near the wing leading edge.

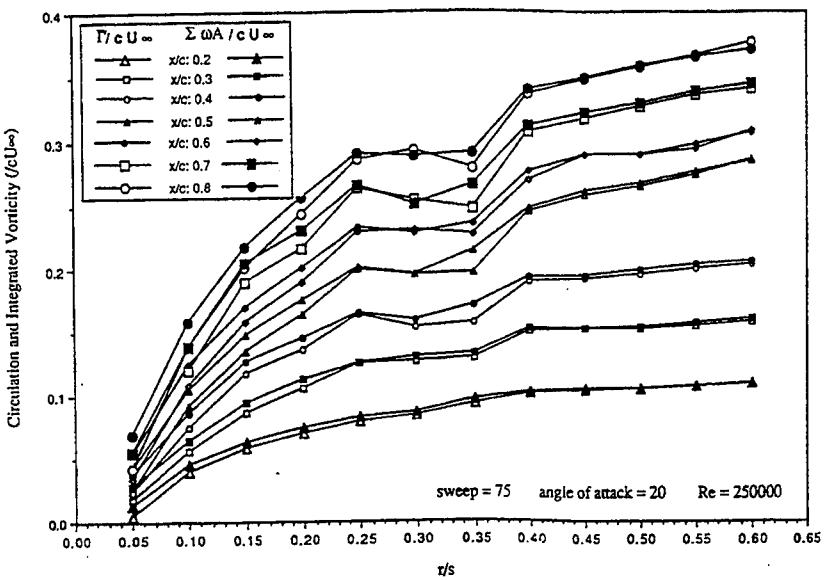

Figure 7. Radial distribution of circulation and integrated vorticity.

Vortex Strength Correlation

Parameters can be defined to incorporate external conditions, such the sweep angle and angle of attack, along with the measured flowfield properties in an effort to determine what, if any, interaction occurs as breakdown is approached. This approach has already been utilized, to a certain extent, by scaling the field properties by the local semispan. A more direct line of reasoning was incorporated by Hemsch and Luckring[23] in a correlation for the measured vortex circulation. Their relation utilized a parameter derived by Sychev[24] in his Euler analysis of flow about an arbitrary slender body. Sychev assumed

$$\delta = s/c << 1 \tag{2}$$

and obtained an approximate set of equations for the inner region of the flow involving only the parameter $k_1 = \delta \cot \alpha$. Hemsch and Luckring[23] used this Sychev parameter to correlate the strength of a delta wing vortex at the trailing edge in the form of

$$g = \frac{\Gamma}{U_\infty c \tan^2\varepsilon \cos \alpha} = AK^n \tag{3}$$

where

$$K = \tan \alpha / \tan \varepsilon = 1/k_1 \tag{4}$$

for some constant values of n and A. By plotting g and K in a log-log format, they demonstrated that a fit of the form $g = AK^{1.2}$ was seen for data obtained from Wentz and MacMahon,[25] and that of Delery, et al.[18] Values of g and K ranged from 0.5 to 10.0 and 0.2 to 2.0, respectively. A value of n = 1.2 was seen to accurately fit the numerical conical slender body theory of Smith.[26]

Since the present tests were conducted at locations above the wing surface, a further scaling of g by the local chord ratio x/c was found to bring the data into line with theory for A = 4.63 as shown in Fig. 8. The seven-hole probe data of Payne[13] were also scaled by x/c and are presented in Fig. 8 along with that of Wentz and MacMahon.[25] Payne's data represent sweep angles of 70, 75, 80, and 85 degrees at various chord locations. It is seen to extend the theoretical line of Smith[26] to a g of 100 and a K of 10. Thus, it would appear that this relation strongly correlates the vortex strength with the angle of attack and the wing geometry.

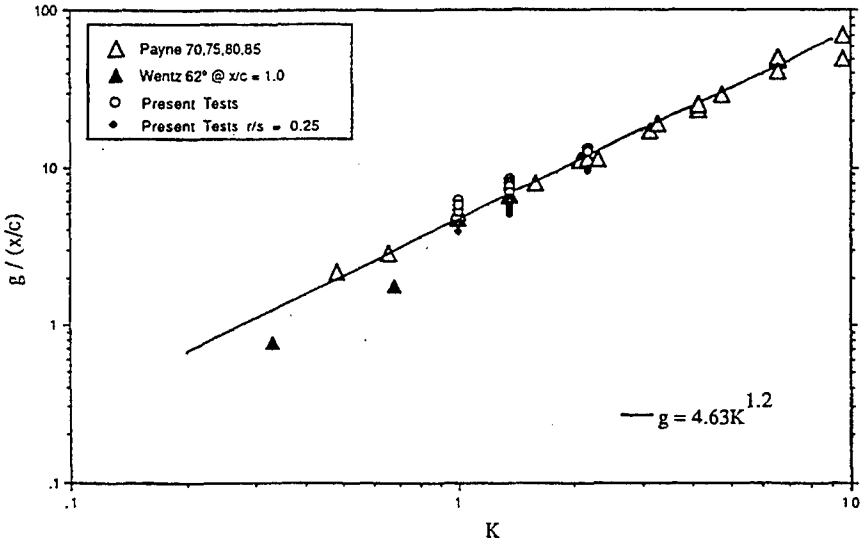

Figure 8. Sychev parameter based correlation of Hemsch and Luckring.

Vortex Breakdown

Vortex breakdown represents a limiting condition for slender wings. Once vortex breakdown reaches the wing, the surface pressure field begins to be altered and the lift curve slope is reduced. As the breakdown progresses toward the apex of the wing the maximum lift coefficient is reached. Stall occurs when the leeward flow completely separates from the wing. There are a number of theories for vortex breakdown, however, at this time no one theory has been widely accepted. A detailed discussion of vortex breakdown theories can be found in the references by Leibovich,[27-29] Wedemeyer[30], Benjamin[31], Hall[32-33] and Delery[34].

Much of what we know about vortex breakdown comes to us from experiments conducted on an isolated vortex created inside a tube.[35-32] Many different types of breakdown have been identified in vortex tube experiments. For slender wings at angle of attack only two types of breakdown are generally identified: the bubble and the spiral types, although in reality they may just represent the extremes in a continuum of breakdown forms. Examples of either a bubble or spiral breakdown are shown in the following photographs. In Fig. 9 the core flow seems to expand around an oval-shaped recirculation zone. At the exit of this recirculation zone the core flow appears to shed in the form of vortex rings which are then convected downstream. The cross section of these doughnut shaped vortex rings appears as a pair of holes in the smoke.

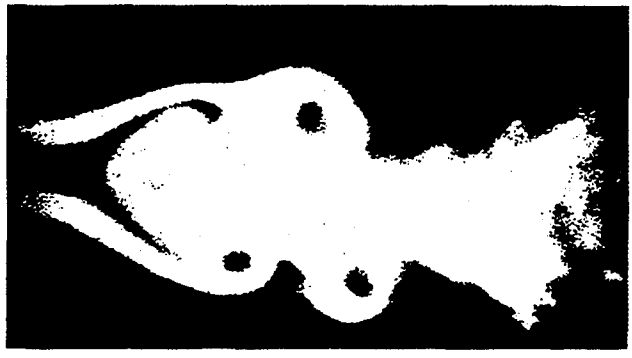

BUBBLE TYPE BREAKDOWN

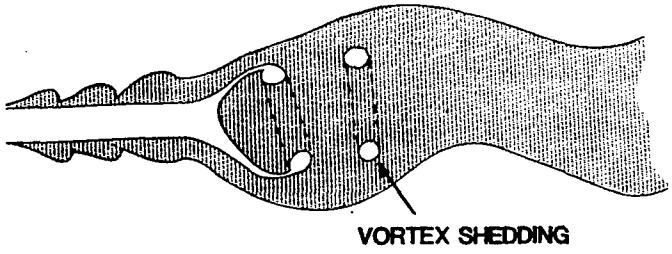

Figure 9. Enlargement from 16mm movie frame and schematic of bubble type breakdown (longitudinal cross section) (Payne, Ref. 13)

Figure 10 shows a lateral cross section of the recirculation zone which is surrounded by a ring of core flow. The breakdown process occurring above was occasionally observed to change into what might be interpreted as a spiral mode. When this occurred the mean location of the breakdown moved downstream and took the form depicted in Fig. 11. The large recirculation zone has disappeared and the core flow now appears to corkscrew downstream. In this case, the holes in the flow are assumed to be the cross sections of the spiraling core flow. This type of result was also obtained in wind tunnel tests at ONERA using the laser light sheet technique.[15, 18] In that study "holes" appearing in the wake of a breakdown were also observed and interpreted to be cross

sections of the spiraling vortex core. Figure 12 shows a lateral cross section which appears to show a rotating core. After a short time this spiral mode would transform back into the "bubble" form and move upstream.

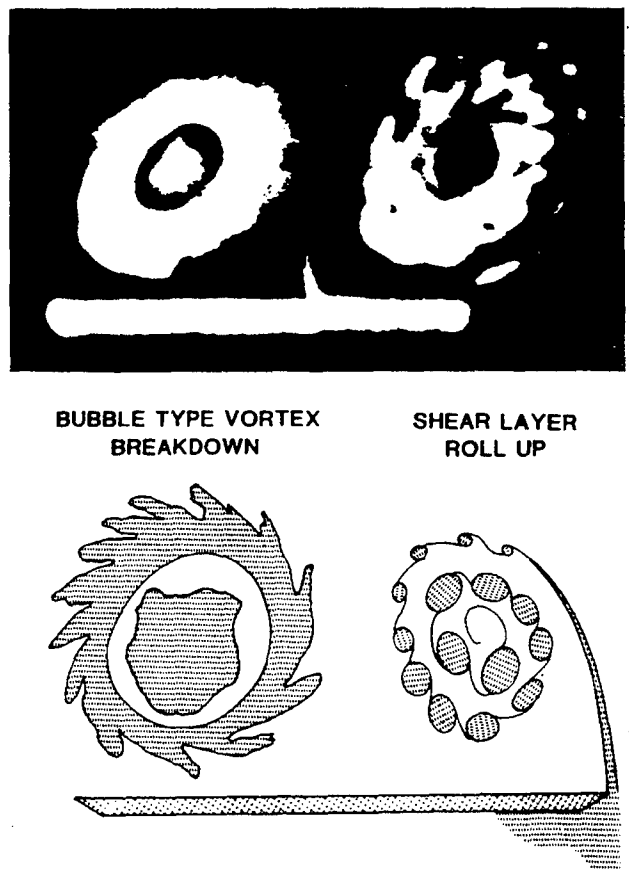

Figure 10. Enlargement from 16mm movie frame and schematic of bubble type breakdown (lateral cross section). (Payne, Ref. 13)

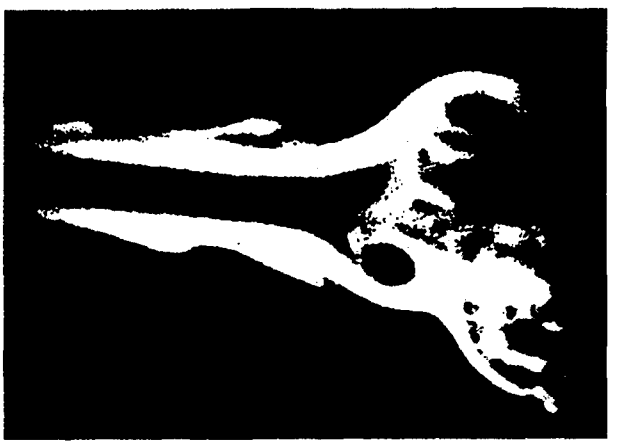

SPIRAL TYPE VORTEX BREAKDOWN

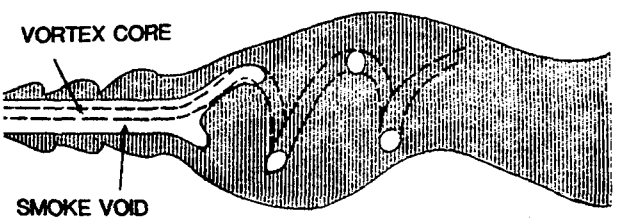

Figure 11. Enlargement from 16mm movie frame and schematic of spiral type breakdown (longitudinal cross section) (Payne, Ref. 13).

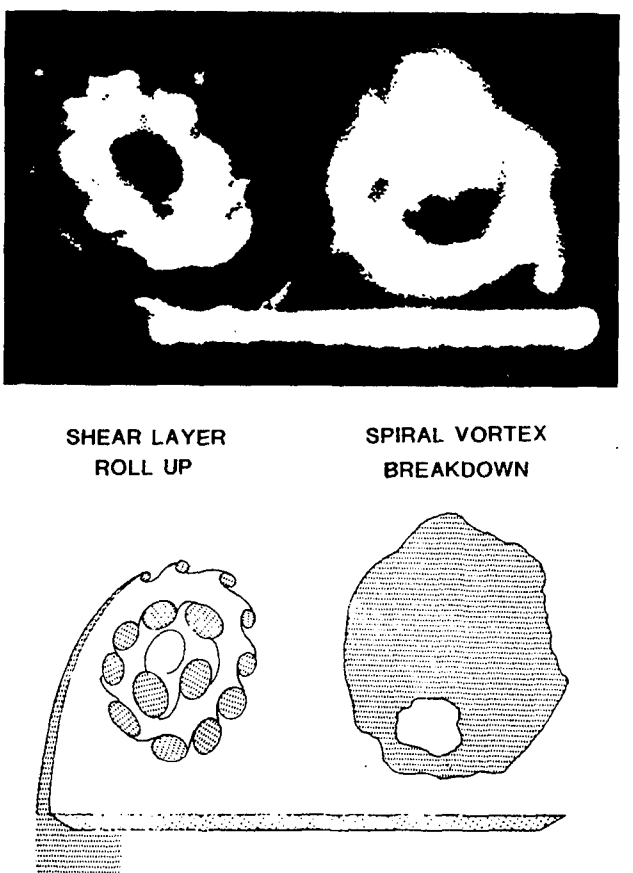

Figure 12. Enlargement from 16mm movie frame and schematic of spiral type breakdown (lateral cross section) (Payne, Ref. 13).

The position of breakdown has been measured by numerous investigators. Figure 13 shows the effect of sweep angle and angle of attack on vortex position.(43) For a given sweep angle, the breakdown position moves from the wake onto the wing toward the wing apex with increasing angle of attack. Sweep angle affects the onset angle of vortex breakdown. The higher the leading-edge sweep angle the higher the onset angle. Figure 14 shows the effect of sideslip angle on the position of breakdown.(43) When a slender wing at angle of attack is given a sideslip angle the leading-edge vortex on the windward side (with respect to the sideslip angle) breaks down closer to the apex while the other vortex breaks down farther away for the apex. This is consistent with the effective change in sweep created by the sideslip. The windward side of the wing has an effective decrease in sweep angle while the leeward side has an effective increase in sweep. Because increasing sweep favors a delay in vortex breakdown, the influence of sideslip on vortex breakdown is as expected.

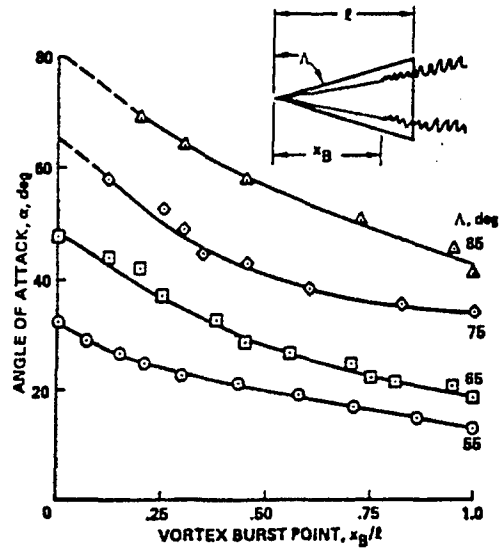

Figure 13. Vortex breakdown position on delta wing models (Malcolm, Ref. 43).

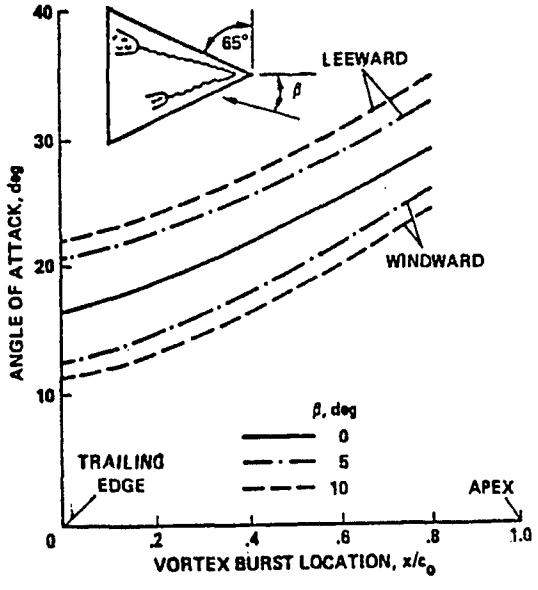

Figure 14. Vortex breakdown for varying side slip angles (Malcolm, Ref. 43).

As discussed earlier, once vortex breakdown has occurred, the flow structure of the leading-edge vortices changes dramatically. Details of the flow before and after vortex breakdown were studied by Iwanski[44] and Ng, Nelson and Payne[45] on a sharp-edge delta wing having a leading-edge sweep of 70° for 30° angle of attack. Figure 15 is a sketch showing the approximate positions of the survey planes relative to the vortex breakdown. In interpreting these data one should keep in mind the breakdown position is not stationary. The spanwise variation of the axial and tangential velocity components through the leading-edge vortex above a sharp-edge delta wing having a leading-edge sweep of 70° is shown in Fig. 16 for various chordwise positions along the wing. In Fig. 16a upstream of the breakdown (x/c = 0.412 and 0.448), the axial velocity component within the vortex is similar to a jet-like flow discussed earlier. The peak axial velocity occurs at the center of the vortex and is approximately three times the freestream velocity. The jet-like region is approximately 0.5 semispan wide. The first indication that vortex breakdown is about to occur is the deceleration of the core flow at (x/c = 0.484). After breakdown (x/c > 0.521) a wake-like velocity defect appears in the axial velocity profile. The wake defect region is approximately 0.3 of a semispan wide at x/c = 0.521 and broadens with increasing distance downstream.

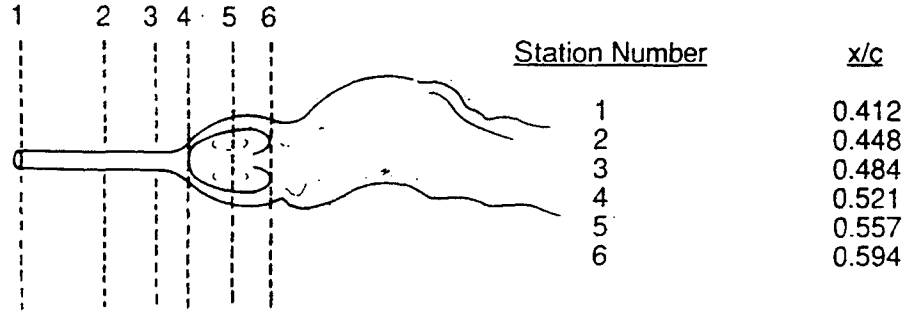

Figure 15. Relative position of wake surveys to vortex breakdown position (Iwanski, Ref. 44; Ng, Nelson, and Payne, Ref. 45).

The tangential velocity component is shown in Fig. 16b. The peak tangential velocity prior to breakdown is approximately 1.5 times the freestream velocity and after breakdown it is approximately equal to the freestream. Before breakdown the subcore region is small as indicated by the steep velocity gradient. However, after breakdown there is a reduction in the tangential velocity component and a rapid diffusion of the subcore. The subcore region expands from approximately 10% of the local semispan before breakdown to nearly 50% of the local semispan after breakdown (x/c = 0.594).

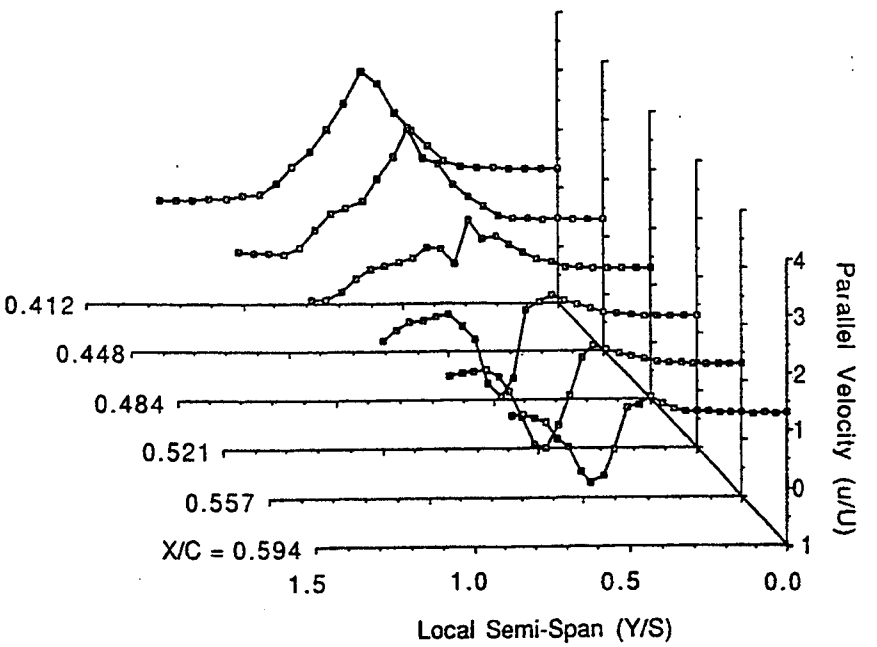

a) Axial velocity

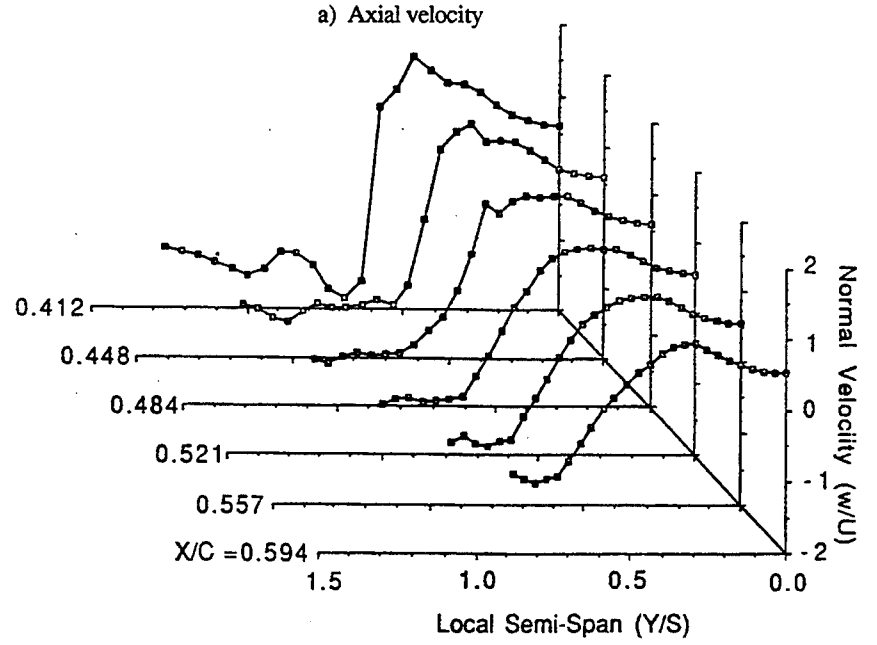

b) Normal velocity

Figure 16 (a & b). Velocity field of the leading-edge vortices above a 70 degree swept delta wing (Iwanski, Ref. 44; Ng, Nelson, and Payne, Ref. 45).

The axial vorticity was estimated from the velocity data presented above and is shown in Fig. 17 for the different chordwise locations. The axial vorticity profile distribution is seen to increase in magnitude and narrow in width in the downstream direction, up to x/c = .411 (just prior to breakdown). The peak then broadens and a reduction in the maximum axial vorticity value is seen as the breakdown region is entered. This is consistent with the breakdown model proposed by Brown and Lopez.[19] From their analysis they concluded that breakdown occurred due to the production of a negative azimuthal vorticity which is due to a tilting and stretching of the axial vorticity vector.

Jumper, Nelson, and Cheung[46] proposed a simple model to explain spiral vortex breakdown. Using an isolated line vortex that deforms into a spiral, they showed that the sense of the spiral had to be opposite that of the circulation in order to produce an induced flow in the upstream sense to sustain the breakdown. This simple model is consistent with experimental findings and the more comprehensive theory proposed by Brown and Lopez.[19]

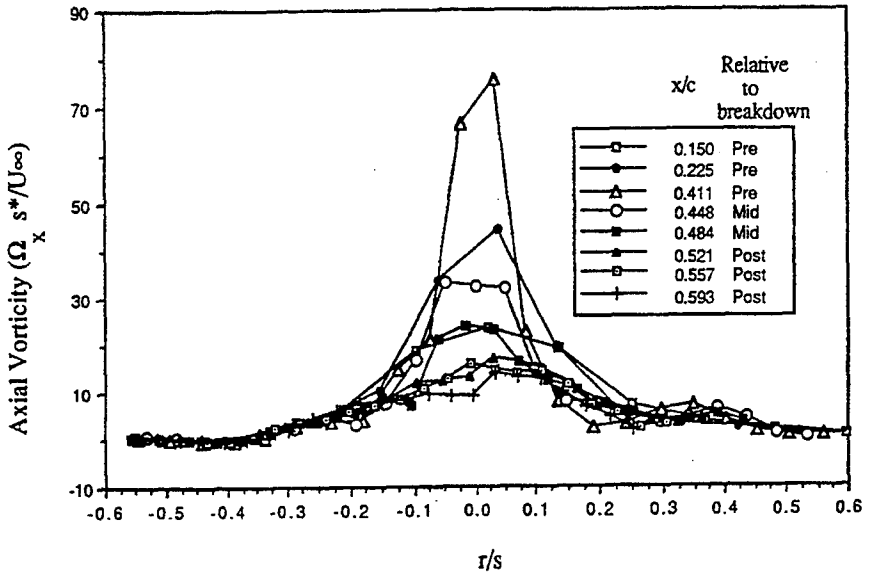

Figure 17. Axial vorticity distribution (Nelson and Visser, Ref. 22).

Pressure Gradient

The pressure gradient acting along the vortex axis is an essential factor in the promotion or delay of vortex breakdown. An adverse or positive pressure gradient tends to promote breakdown whereas the opposite effect occurs for a favorable pressure gradient. The pressure gradient imposed on the vortex core can come from a variety of sources. For example, the pressure rise over the rear portion of the delta wing or pressure gradients caused by the wind tunnel walls or obstacles (support systems) located downstream of the generating model but near the vortex wake.

To examine the influence of the pressure gradient on a vortex, various investigators have developed simple analytical expressions relating the pressure gradient to vortex parameters. The reader is referred to the paper by Raat,[47] Krause and Althaus,[48] and Hall.[33]

The pressure gradient acting along the vortex axis can be derived from the radial momentum equation which after the appropriate simplification reduces to

$$\rho\frac{v_\theta^2}{r}=\frac{\partial P}{\partial r} \tag{5}$$

This equation represents the balance between the fluid particles centripetual acceleration and the restraining radial pressure force. If we differentiate this expression with respect to the axial distance, x, and integrate with respect to the radial distance, r, then the following expression for the axial pressure gradient is obtained.

$$\frac{\partial P}{\partial z}\Big|_o=\frac{\partial P}{\partial z}\Big|_{r_c}+\frac{\partial}{\partial z}\rho\int_o^\infty\frac{v_\theta^2}{r}dr \tag{6}$$

This expression shows us that the pressure gradient at large distances from the core center is imposed along the core axis.

The pressure gradient across the core can be shown to be as follows,

$$\frac{\partial P}{\partial z}\Big|_o-\frac{\partial P}{\partial z}\Big|_{r_c}\sim\rho\alpha\Gamma^2/r_c^3 \tag{7}$$

where Γ is the magnitude of the circulation of the vortex, r_c is the core radius and α is the angle of divergence of the vortex core.[18] This expression shows that the pressure gradient along the vortex axis is greater than at the vortex core boundary. The vortex strength being a controlling parameter.

The importance of vortex strength on breakdown can be seen in Fig. 13. As this figure shows, the angle of attack, when breakdown reaches the trailing edge, increases as the sweep angle increases. However, as was shown earlier, the circulation on a delta wing at a given angle of attack decreases as the sweep angle is increased. Therefore, from equation 7 one would expect that as the wing sweep is increased vortex breakdown would be delayed to a higher angle of attack. This is exactly what is observed experimentally.

Experiments conducted by Delery, Pagan and Solignac[18] confirm the importance of both vortex strength and adverse pressure gradient on vortex breakdown. Their experimental setup consisted of a 75° delta wing and a two-dimensional air intake located downstream of the delta wing. The exit area of the intake could be varied to change the magnitude of the adverse pressure gradient. Figure 18 is a sketch of their experimental setup. They measured flow characteristics at approximately 1/4 chord length downstream of the wing trailing edge. Figure 19 shows the axial and circumferential velocity distribution along the centerline of the vortex. These data illustrate several key features of leading-edge vortices. Notice the large drop in the axial velocity and vorticity as the measurements are made after breakdown.

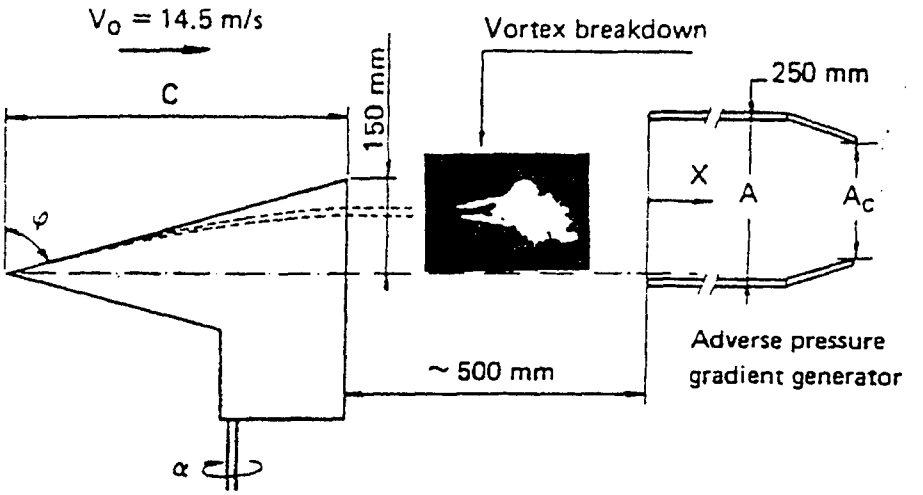

Figure 18. Experimental set up used to study adverse pressure gradient on vortex breakdown (Pagan and Solignac, Ref. 15).

The influence of the pressure gradient on vortex breakdown was examined by varying the two-dimensional duct area. Figure 20 shows the relationship between the pressure gradient and vortex strength as given by the local swirl velocity ratio. A limit to vortex strength was found, beyond which breakdown occurred even in the absence of an adverse pressure gradient.

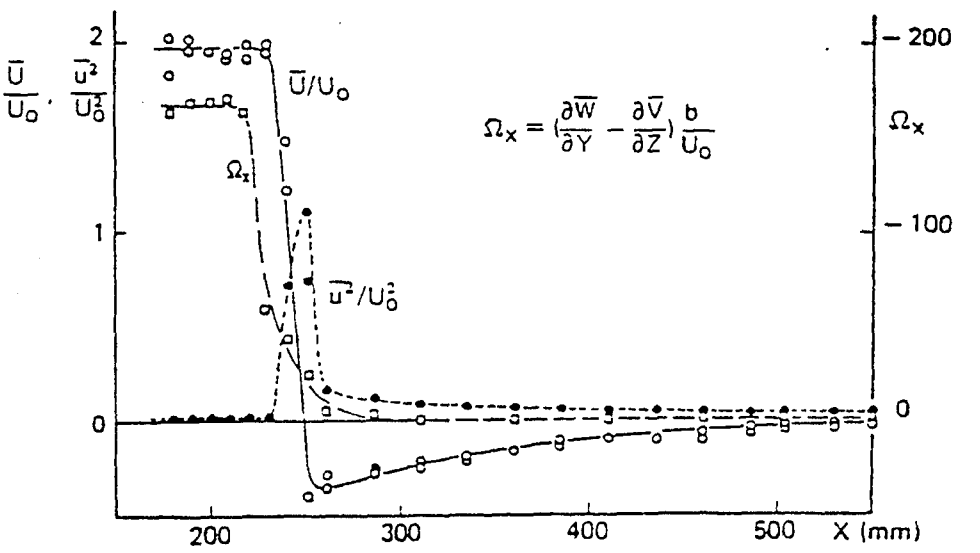

Figure 19. Axial variation of vortex properties (Pagan and Solignac, Ref. 15).

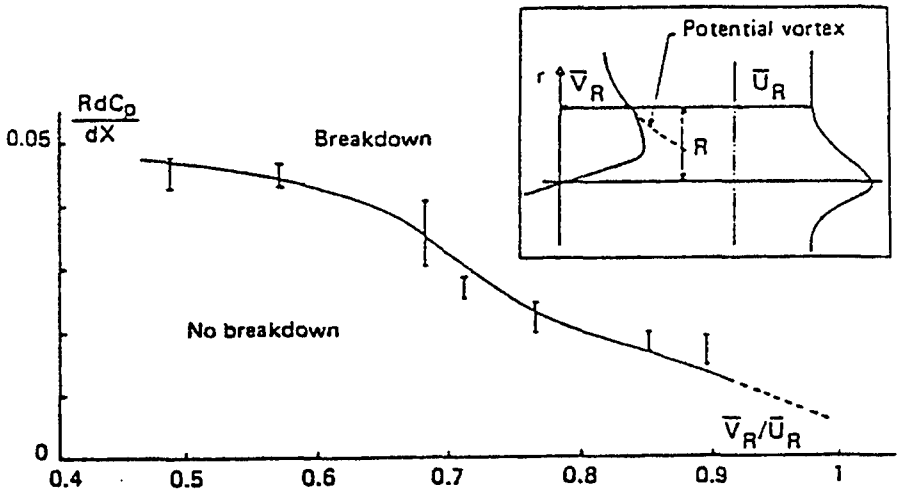

Figure 20. Influence of adverse pressure gradient on breakdown limit Pagan and Solignac, Ref. 15).

Aerodynamic Characteristics

The aerodynamic characteristics of slender, sharp-edge wings are nonlinear as illustrated in Fig. 21. A significant portion of the lift generated by a slender wing is attributable to a low pressure region created on the wing surface by the leading-edge vortices. This region of low pressure is due to the flowfield created by the vortices. As the wing sweep is increased, there is a reduction of the lift curve slope. The circulation increases with angle of attack, but for a given angle of attack the circulation decreases with increasing sweep angle. Therefore the reduction in the lift curve slope with sweep angle is to be expected. When vortex breakdown reaches the wing the low pressure region created by the vortices is reduced. The reduction in the suction pressure results in a lowering in the lift curve slope. Although the lift may still continue to increase, the lift curve is starting to bend over. As the breakdown progresses forward on the wing, the maximum lift coefficient is reached and the wing stalls. Figure 22 shows the lift and pitching moment coefficient for delta wings of varying aspect ratio at low speeds. These data were obtained by Wentz and Kohlman[49]. At low-angles-of-attack the lift and pitching moment coefficients are linear. However, as the angle of attack is increased further the lift produced by the leading-edge vortices produces the nonlinearity in the force and moment curves. Increasing the aspect ratio (lowering the sweep angle) results in higher normal force coefficients. This can be explained in the following manner. For a given angle of attack the strength of the leading-edge vortices increases with increasing aspect ratio or lower leading-edge sweep. Therefore one would expect higher vortex lift at a given angle of attack for the higher aspect ratio delta wings.

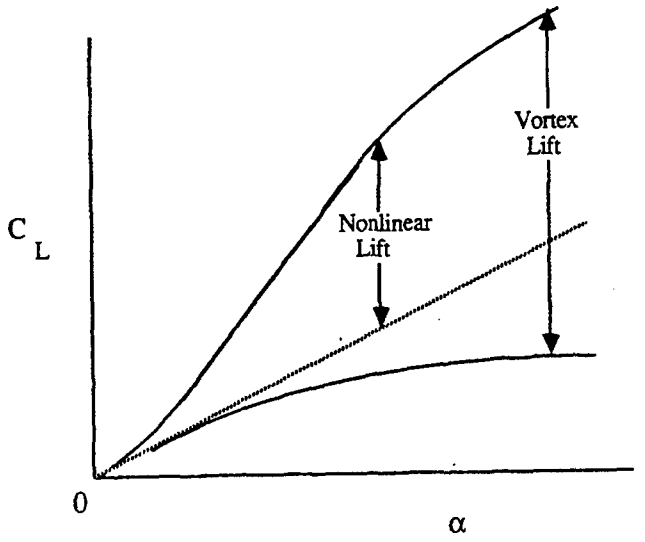

Figure 21. Sketch of nonlinear lift.

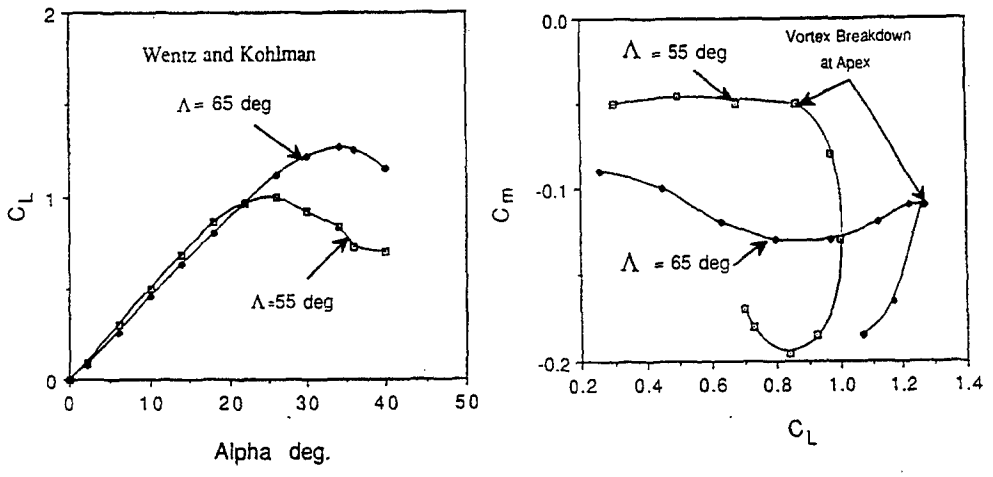

Figure 22. Lift and pitching moment characteristics for two delta wings, $\Lambda = 55°$ and $\Lambda = 65°$ (Wentz and Kohlman, Ref. 49).

Pressure Fields

The pressure distribution on the surface of a slender wing at angle of attack is as shown in Fig. 23. This data is for an angle of attack where breakdown has not reached the wing. The large suction peaks or low pressures occur directly beneath the primary vortices. This conclusion was reached by correlating the pressure data with above surface flow visualization data. It should be

noted that in some experiments evidence of secondary suction peaks have been observed. The maximum suction peaks decrease in the downstream direction, however, the region of low pressure acts over a larger area. When vortex breakdown occurs, the pressure distribution is changed markedly. When breakdown occurs the suction peak is reduced significantly but the footprint of the vortex acts over a wider region.

As noted earlier, the sideslip angle affects the position of the vortex breakdown. Vortex breakdown becomes asymmetric with sideslip angle. The vortex on the windward side of the wing (with respect to the sideslip) moves closer to the apex, the reverse is true of the leeward side vortex. The effect of sideslip on the surface pressure distribution is shown in Fig. 24 based on data from Hummel.(50)

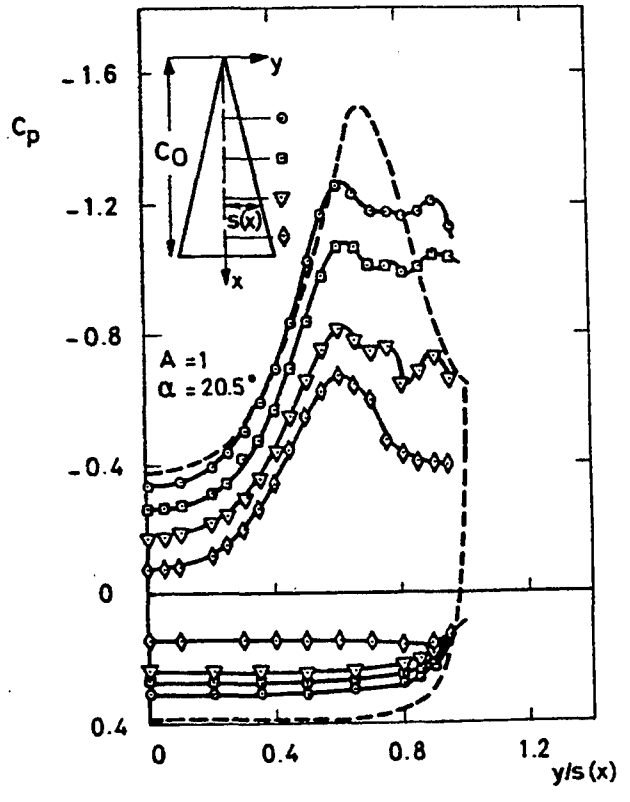

Figure 23. Upper surface pressure distributions (Hummel, Ref. 4).

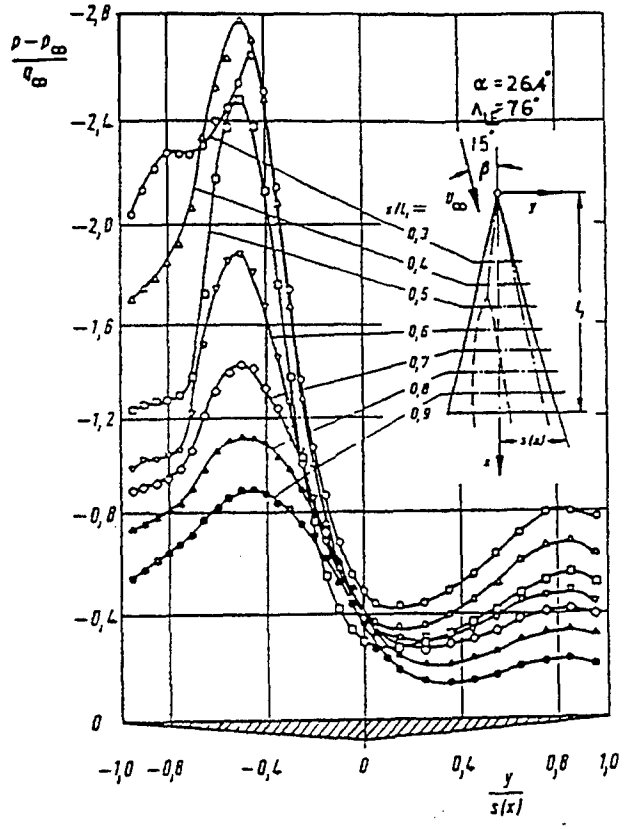

Figure 24. Influence of side slip angle on upper surface pressure distribution (Hummel, Ref. 50).

Reynolds Number Effects

Most researchers agree that many of the qualitative features of the flow are independent of Reynolds number. This is particularly true for wings with sharp leading edges. For example, the position of vortex breakdown does not appear to have any strong Reynolds number sensitivity. Erickson has compared experimental measurements of vortex breakdown over a wide range of Reynolds numbers. The lack of Reynolds number sensitivity is due to the fact that the models have sharp leading edges, thereby fixing the point of separation. There are, however, differences in the flow structure that are attributable to Reynolds numbers. The position of the vortices is affected by the Reynolds number. The pressure distributions show the relative positions of the primary and secondary vortices by way of the suction peaks. The suction peak is higher for the turbulent flow case. As the Reynolds number increases, the primary vortex moves outboard due to the Reynolds number influence on the secondary vortical flow. The influence of Reynolds number on the other properties of the flow field such as circulation or vorticity is unknown.

Mach Number Effects

The flow above a delta wing at supersonic speeds can be very similar to that discussed so far provided that the flow at the leading edges is subsonic. When the leading edges are supersonic, shock waves can occur on the leeward surface. Figure 25 is a sketch based upon the observations of Stanbrook and Squire[51] of two types of flow fields that may occur at supersonic speeds. When the flow normal to the leading edge is subsonic, the leeward flow pattern is identical to the flow patterns described earlier. At low-angles-of-attack the flow is completely attached on the leeward side, however, at higher-angles-of-attack the flow again separates at the leading edge to form the leading-edge vortices observed at low speeds. As the freestream Mach number is increased, the component of the flow normal to the leading edge may become supersonic. In this case, the leeward wake patterns are quite different as shown in Fig. 25b. At low-angles-of-attack, after the supersonic flow expands over the leading edge, it is turned downstream resulting in shock waves between the leading edges and the wing centerline. These shock waves run from the apex to the trailing edge. Because the shocks are weak, the boundary layer flow remains attached. At higher-angles-of-attack the shock waves are strong enough to cause the boundary layer flow to separate. A more detailed classification of the leeside flow fields above thick delta wings at supersonic speeds is presented by Miller and Wood[52].

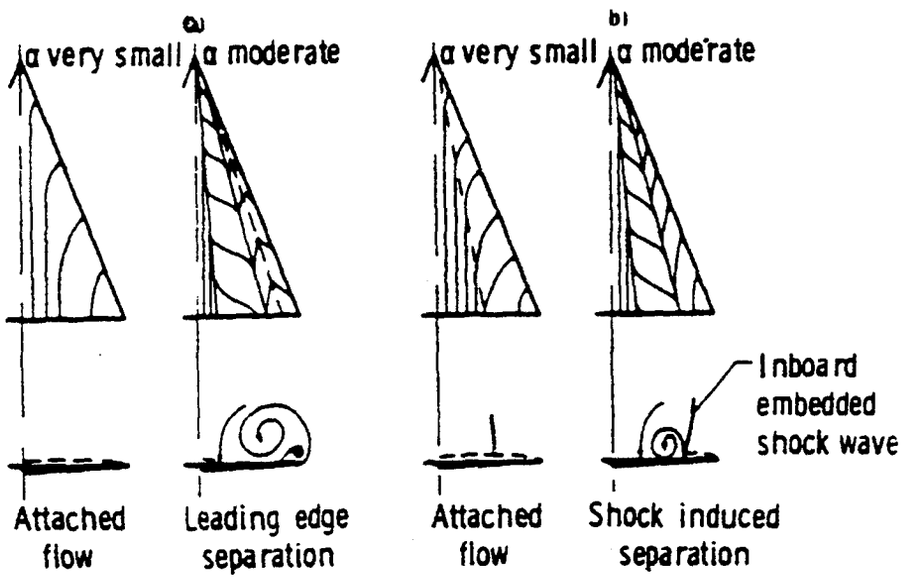

Figure 25. Leeward flow models as defined (Stanbrook and Squire, Ref. 51)

a) Subsonic leading edge, and

b) Supersonic leading edge.

The aerodynamic coefficients are affected by Mach number as shown in Fig. 26. As the Mach number increases, the normal force coefficient decreases. The reason for the decrease in normal force coefficient is explained by Stallings[53] by examining the pressure data from which the force coefficients were obtained. The contribution to the normal force coefficient of the leeward and windward sides were obtained separately and are included in Fig. 26. The subscripts,

w and L, refer to the windward and leeward contributions respectively. As the Mach number is increased, the leeward side contribution to the normal force coefficient decreases, whereas the windward side contribution increases with Mach number for the higher-angles-of-attack.

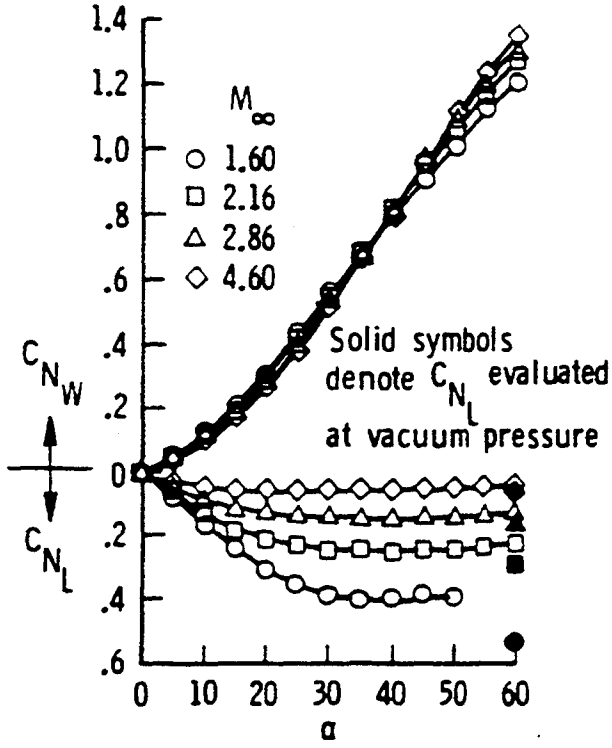

Figure 26. Normal force coefficient, AR = 1.0 (Stallings, Ref. 53).

Unsteady Slender Wing Aerodynamics

An unsteady motion of a delta wing results in a modification of the flow field in response to the maneuver. This can result in delays of flow separation and vortex formation at low angles of attack, and changes in vortex location and the onset of breakdown at higher angles of attack. During oscillatory or periodic motions, a hysteresis develops in the positions of the vortex core and the vortex breakdown relative to the static locations. Due to this hysteresis in the flow field, there is a corresponding modification of the aerodynamic loads on the delta wing. The results presented in the following section are used to show the importance of flow field hysteresis in either vortex position or breakdown on the unsteady loads and surface pressure distributions of simple delta wing planforms. A detailed review of the flow physics of pitching delta wings is given by Rockwell.[54]

Ashley, Katz, Jarrah, and Vaneck[55] have recently published a paper summarizing the current state of unsteady swept wing aerodynamics research. Theoretical, computational, and experimental research involving both flow field behavior and aerodynamic forces and moments are described and representative data are presented. Ashley, et al., concluded that for unsteady maneuvers where vortex breakdown is not present, quasi-static behavior results. However, for ranges of motion where breakdown is present over the wing, hysteretic behavior is seen.

For a dynamically pitching wing it is possible to delay the detrimental effects of breakdown. A substantial overshoot in the aerodynamic forces is typically seen for oscillatory or transient pitching maneuvers.

This section will present a brief review the current understanding of large angle of attack unsteady motions on the aerodynamic and vortical wake characteristics. The discussion will emphasize the fluid mechanic mechanisms governing the nonlinear aerodynamic loads. Emphasis will be given to showing the relationship between the force and moment coefficients, surface pressures and the flow field structure.

Pitching Delta Wing

Unsteady force measurement is a relatively new area of research, but the limited number of studies that are available have documented the hysteretic nature of the forces and moments. Bragg and Soltani[56] conducted an experiment using a 70° sweep wing oscillating in pitch. Hysteretic behavior was noted in the dynamic loads; the amount of which was a function of the pitch rate. This was also seen by both Brandon and Shah[57] and Jarrah.[58] Brandon and Shah examined the effects of both sinusoidal and ramp pitching motions. They reported a large overshoot of the forces relative to the steady state values. Brandon and Shah[57] suggested that this may be due to a lag in the separation and reattachment of the leading-edge vortices during the dynamic maneuver. Jarrah[58] utilized delta wings with aspect ratios of 1, 1.5, and 2, and angle of attack ranges of 0-30° and 0-60°. He saw a large overshoot in the aerodynamic coefficients for the 0-60° motion, and noted that this overshoot was a function of the aspect ratio as well as the pitch rate. Figure 27 is an example of Jarrah's data that clearly shows the large aerodynamic hysteresis.

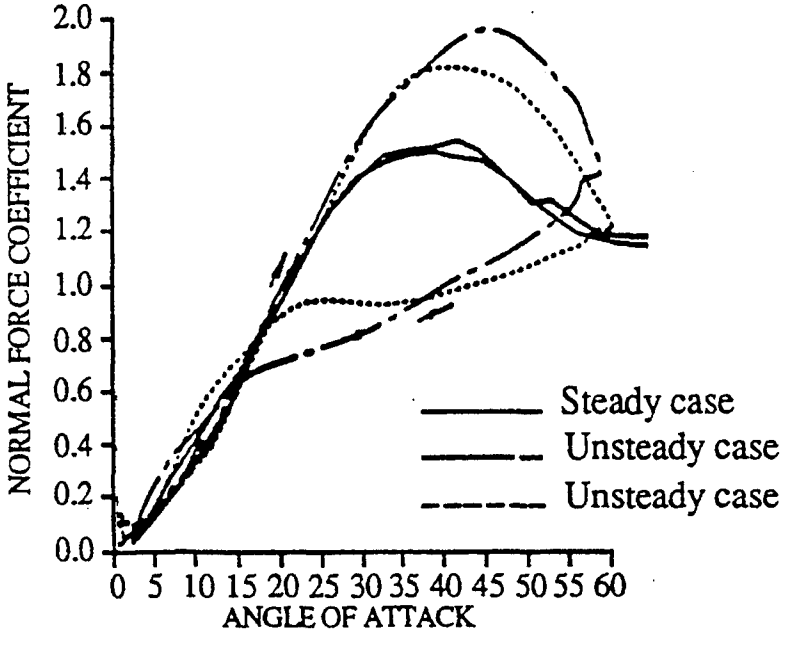

Figure 27. Unsteady aerodynamic coefficients for a slender delta wing. Aspect ratio = 1.0. k = 0.03, Re = 635,000. Pitch amplitude = 0-60° (Jarrah, Ref. 58).

Unsteady delta wing research has shown the force and moment coefficients to overshoot or undershoot the static values depending on both the type of unsteady maneuver and the motion history. For example, if the model pitches from 0-45°, the peak overshoot in C_L will be higher than if the model pitches from 25-45°[57]. An example of the dynamic normal force coefficient for a pitching delta wing is shown in Fig. 28 along with the static curve. This data was obtained by Brandon and Shah[57] using a force and moment balance to measure the dynamic loads on a pitching delta wing.

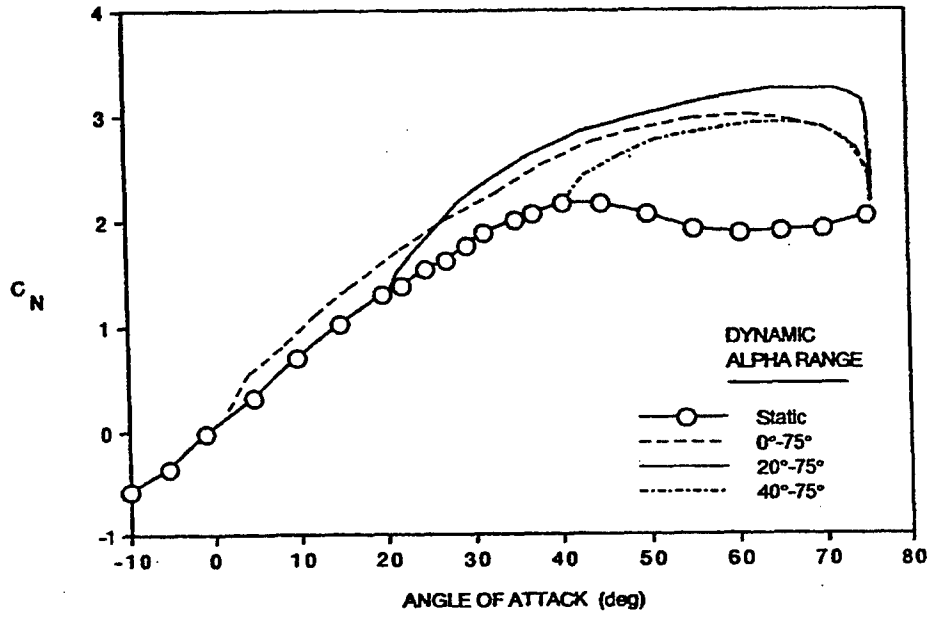

Figure 28. Dynamic lift overshoot of a slender delta wing. Leading-edge sweep angle = 70° (Brandon and Shah, Ref. 57).

Additional insight into the mechanisms causing the dynamic loads can be obtained by examining the dynamic characteristics of vortex breakdown and the unsteady pressure acting on the wing in a dynamic motion.[59-64] Thompson[63] studied the unsteady aerodynamics of a delta wing undergoing a large amplitude motion. Figure 29 shows unsteady breakdown location data obtained from a flow visualization experiment of a 70 degree swept delta wing undergoing large amplitude pitching motions. The wing was pitched from 0 to 60 degrees angle of attack in a sinusoidal manner. The breakdown location is shown as a function of instantaneous angle of attack for four, nondimensional, pitching frequencies, where $k = 2\pi fc/U$ (where c is the root chord length, f the pitch frequency, and U the freestream velocity). The arrows in Fig. 29 indicate the direction of motion (angle of attack increasing or decreasing). The steady breakdown location data has not been shown in order to maintain clarity. However, it should be noted that the unsteady data bracketed the steady state breakdown location.

The hysteresis which is characteristic of unsteady high angle of attack delta wing aerodynamics can be seen in Fig. 29. At a given instantaneous angle of attack, the difference in

breakdown location is as much as 0.45c, depending on the direction of motion. The size of the hysteresis loop increases with increasing reduced frequency. At very high angles of attack,

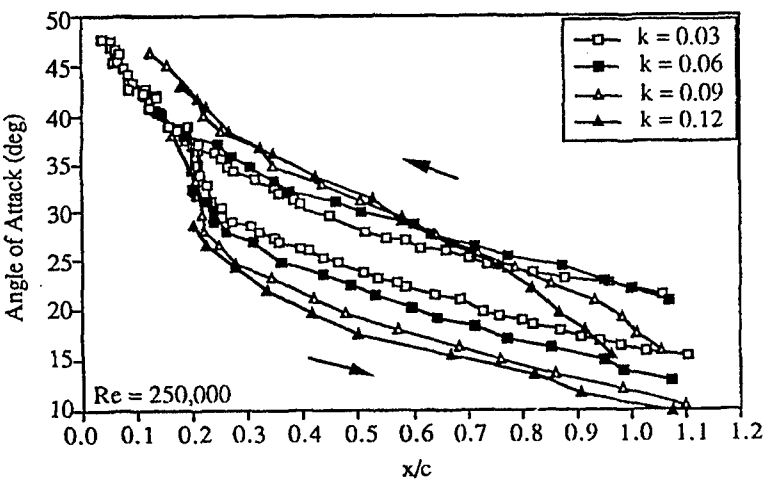

Figure 29. Breakdown location for 2-60° oscillation. Four pitch frequencies shown

(Nelson and Thompson, Ref. 64).

over 50°, the flow over the wing becomes fully separated, similar to a bluff-body flow. Thus breakdown does not exist. As the wing pitches down, the leading-edge vortex system reforms with breakdown near the apex. Breakdown then moves aft as the angle of attack continues to decrease.

These data illustrate the lags that develop for the unsteady case. For the upward motion, there is a lag in the development of the vortex core and the upstream progression of vortex breakdown. For the downward motion there is a lag in reformation of the vortex system (from fully separated flow conditions) and thus in the downstream progression of vortex breakdown. These lags give rise to the large unsteady effects seen in the aerodynamic loads on the wing.

Figure 30 shows an example of the unsteady pressure data as a function of instantaneous angle of attack, along with the steady data. This data is for a single surface pressure tap located at x/c = 25% and located beneath the primary vortex. The location of vortex breakdown has been noted at specific points along the curve.

As the angle of attack increases, the pressures uniformly decrease. With the occurrence of breakdown on the wing the pressure gradient begins to decrease. Further increase in angle of attack moves the breakdown to the apex. This precedes the total separation of the leeward side,

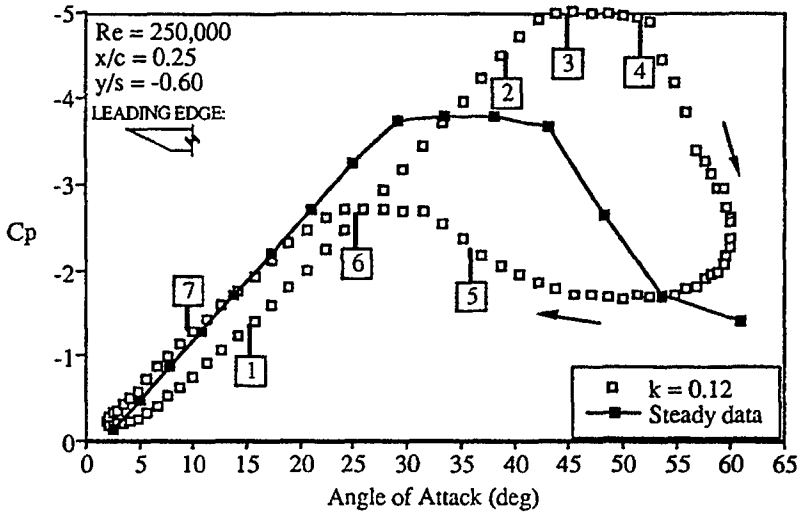

UPSTROKE:	DOWNSTROKE:
1 Breakdown first occurs over wing	5 Reformation of vortex system
2 Breakdown reaches pressure tap	6 Breakdown reaches pressure tap
3 Breakdown reaches apex	7 Breakdown moves off of wing
4 Full scale separation	

Figure 30. Unsteady surface pressure data for 2-60° oscillation. Chordwise progress of vortex breakdown (from flow visualization tests) also noted (Nelson and Thompson, Ref. 64).

and, as a result, the pressures begin increasing due to the lack of an organized flow structure over the wing. However, before the pressure field can become relatively uniform (as for the steady high angles of attack case), the wing pitches down again, until the point is reached at which the leading-edge vortex structure reforms (with breakdown near the apex). Thus a pressure recovery begins and the pressures begin decreasing. Breakdown then moves down the length of the wing and into the wake. Concurrent with this behavior of the vortex is a partical recovery of the suction pressures. Further decrease in angle of attack results in a collapse of the vortex system and the vortex-induced pressure field.

Summary

In this paper I have attempted to review the flow structure above slender delta wings and its influence on delta wing aerodynamics. A brief summary of the current understanding of leading-edge vortices and breakdown is presented below.

The strength of the leading-edge vortices depends upon the angle of attack and the wing leading-edge sweep angle. For a given angle of attack the strength decreases with increasing sweep angle. The circulation of slender delta wings can be scaled with the Hemsch and Luckring correlation parameter developed from slender body theory.

The velocity field associated with a leading-edge vortex can be characterized as the super position of a jet flow and vortical flow. The maximum axial velocity occurs at the vortex center and can be as much as two or more times the freestream velocity. The extent of the jet-like flow (i.e., velocity greater than the freestream) can be as much as 30% of the local semi span. The

maximum tangential velocity can reach approximately 1.5 times the freestream. The core (viscous subcore) defined by the distance between the peak tangential velocities is smaller than the jet core. The jet core increases in size with angle of attack while the subcore remains nearly constant in size over the wing.

The vorticity distribution through the leading-edge vortex is primarily in the axial direction prior to breakdown. Most of the axial vorticity is found within the viscous subcore. The radial and azimuthal vorticity components are small before breakdown. When spiral breakdown occurs, the core flow is deflected into a spiral geometry having the opposite sense of that of the circulation. The axial vorticity is reduced substantially and a large negative azimuthal vorticity is present after breakdown. The large negative azimuthal vorticity is consistent with the requirement to sustain the vortex breakdown.

The pressure gradient along the vortex axis is a major factor in causing breakdown. The pressure gradient can be thought of as being created by the external flow and by a self-imposed component that is a function of the vortex strength.

The leading-edge vortices contribute a substantial portion of the lift generated by slender delta wings. The primary vortices produce large suction peaks on the upper surface pressure distribution prior to breakdown. After breakdown reaches the wing, the suction pressure peaks are reduced aft of the breakdown location. The modification of the pressure field affects the lift and moment characteristics of slender delta wings.

The aerodynamic characteristics of slender wings are modified during oscillatory or transient motions. For the large amplitude unsteady motions the aerodynamic forces and moments exhibit large over and undershoots with respect to the static load measurements. The dynamic load measurements are functions of the reduced frequency and model motion. As the reduced frequency is increased, the aerodynamic hysteresis increases. The hysteric behavior of the unsteady loads is a result of the lag in vortex breakdown due to the models motion.

Although we have made much progress in understanding the flow structure of leading-edge vortices before and after breakdown, a comprehensive theory for breakdown still is unavailable. On the other hand, the experimental studies conducted during the past decade have provided details of the flow that may allow for the development of a new theoretical model or an improvement of one of the existing theories.

Acknowledgment

The author wishes to acknowledge Frank Payne, Ken Visser, Scott Thompson, Andrew Arena, Ken Iwanski, Ken Cheung, Eric Jumper, and Terry Ng for their collaboration on research dealing with leading-edge vortex flows and breakdown. Their research and many lively discussions dealing with the subject of this paper are reflected in this article.

References

[1]Peckham, D. H. and Atkinson, S. A., "Preliminary Results of Low Speed Wind Tunnel Tests on a Gothic Wing of Aspect Ratio 1.0," A.R.C. CP-508, April 1957.

[2]Peckham, D. H., "Low speed Wind Tunnel Tests on a Series of Uncambered Slender Pointed Wings with Sharp Edges," A.R.C., R. & M. No. 3186, Dec. 1958.

[3]Earnshaw, P.B. and Lawford, J.A., "Low-Speed Wind Tunnel Experiments on a Series of Sharp-Edged Delta Wings," A.R.C., R.& M. No. 3424, March 1964.

[4]Hummel, D., "Untersuchungen über das Aufplatzen der Wübel an Schlanken Deltaflügeln, Z. Flugwiss 13, 1965.

[5]Elle, B.J., "On the Breakdown at High Incidences of the Leading Edge Vortices on Delta Wings," *J. of the Royal Aero. Soc., Vol.* 64, Aug. 1960.

[6]Harvey, J. K., "Some Observations of the Vortex Breakdown Phenomena," *J. Fluid Mech.*, Vol. 14, 1962.

[7]Lowson, M. V., "Some Experiments with Vortex Breakdown," Journal of the Royal Aeronautical Society, Vol. 68, May 1964.

[8]Lambourne, N. C., and Bryer, D. W., "The Bursting of Leading Edge Vortices - Some Observations and Discussion of the Phenomena," Aeronautical Research Council, Reports and Memoranda, No. 3282, April 1961.

[9]Earnshaw, P.B., "An Experimental Investigation of the Structure of a Leading Edge Vortex," R.A.E. Tech. Note No. Aero. 2740, March 1961.

[10]Perry, A. and Chong, M., "A Description of Eddying Motions and Flow Patterns Using Critical-Point Concepts," *Annual Review of Fluid Mechanics*, Vol. 19, 1987, pp. 125-155.

[11]Peake, D. J. and Tobak, M. "Three Dimensional Interactions and Vortical Flows with Emphasis on High Speeds," NASA TM-81169, March 1980, AGARDograph No. 252.

[12]Delery, J. "Physique des Ecoulements Tourbillonnaires," AGARD Symposium on Vortex Flow Aerodynamics, Oct. 1990, Scheveningen, The Netherlands.

[13]Payne, F. M., "The Structure of Leading Edge Vortex Flows Including Vortex Breakdown," Ph.D. Dissertation, University of Notre Dame, May 1987.

[14]Payne, F.M., Ng, T. T., Nelson, R.C., and Schiff, L.B., "Visualization and Wake Surveys of Vortical Flow Over a Delta Wing," *AIAA Journal*, Vol. 26, No. 2, Feb. 1988, pp. 137-143.

[15]Pagan, D. and Solignac, J.L., "Experimental Study of the Breakdown of a Vortex Generated By a Delta Wing," *La Recherche Aérospatiale*, No 3, May-June 1986.

[16] Erickson, G. E., "Vortex Flow Correlation," Tech. Report AFWAL-TR-80-3143, 1980.

[17]Lee, M. J. and Ho, C. M., "Vortex Dynamics of Delta Wings," in *Lecture Notes in Engineering 46, Frontiers in Experimental Fluid Mechanics*, Springer-Verlag, pp. 365-427.

[18]Delery, J., Pagan, D. and Solignac, J.L., "On the Breakdown of the Vortex Induced by a Delta Wing," Colloquium on Vortex Control and Breakdown Behavior, Baden, Switzerland, ONERA TP 1987-105, April 6-7, 1987.

[19]Brown, G.L. and Lopez, J.M., "Axisymmetric Vortex Breakdown Part II: Physical Mechanisms," *Journal of Fluid Mechanics*, Vol. 221, 1990.

[20]Visser, K. D., "An Experimental Analysis of Critical Factors Involved in the Breakdown Process of Leading Edge Vortex Flows," Ph.D. dissertation, University of Notre Dame, May 1991.

[21]Visser, K. D. and Nelson, R. C., "Measurements of Circulation and Vorticity in the Leading Edge Vortex of a Delta Wing," *AIAA Journal*, Vol. 31, No. 1, 1993.

[22]Nelson, R. C. and Visser, K. D., "Breaking Down the Delta Wing Vortex: The Role of Vorticity in the Breakdown Process," AGARD Symposium on Vortex Flow Aerodynamics, Scheveningen, The Netherlands, Oct. 1-4, 1990.

[23]Hemsch, M. and Luckring, J., "Connection Between Leading-Edge Sweep, Vortex Lift, and Vortex Strength for Delta Wings," *J. of Aircraft*, Engineering Notes, May 1990.

[24]Sychev, V. V., "Three Dimensional Hypersonic Gas Flow Past Slender Bodies at High Angles of Attack," Prikladnaia Matematika i Mechanikal, Vol. 24, 1960, pp. 205-212.

[25]Wentz, W. H. and MacMahon, M. C., "Further Experimental Investigations of Delta and Double Delta Flowfields at Low Speeds," NASA CR-714, Feb. 1967.

[26]Smith, J. H. B., "Calculations of the Flow Over Thick, Conical, Slender Wings with Leading Edge Separation," Aeronautical Research Council R & M 3694, London, March 1971.

[27]Leibovich, S., "The Structure of Vortex Breakdown," *Ann. Rev. Fluid Mech.*, Vol. 10, 1978.

[28]Leibovich, S., "Vortex Stability and Breakdown," AGARD-CP-342, No. 23, April 1983.

[29]Leibovich, S., "Vortex Stability and Breakdown: Survey and Extension," *AIAA Journal*, Vol. 22, No. 9, Sept. 1984.

[30]Wedemeyer, E., "Vortex Breakdown," No.9, AGARD-LS-121, Dec. 1982.

[31]Benjamin, T. B., "Some Developments in the Theory of Vortex Breakdown," *Journal of Fluid Mechanics*, Vol. 28, 1967.

[32]Hall, M.G., "A Theory for the Core of a Leading-Edge Vortex", *J. Fluid Mech.*, Vol. 11, 1961.

[33]Hall, M.G., "The Structure of Concentrated Vortex Cores," *Prog. in Aeronautical Science* (Ed. D. Kucheman), Vol. 7, 1966.

[34]Delery, J. M., "Aspects of Vortex Breakdown," Prog. Aerospace Sciences, Vol. 30, pp. 1-59, 1994.

[35]Escudier, M.P. and Keller J.J., "Vortex Breakdown: A Two Stage Transition," AGARD-CP-342, No. 25, April 1983.

[36]Sarpkaya, T., "On Stationary and Travelling Vortex Breakdowns," *J. Fluid Mech.*, Vol. 45, Part 3, 1971(a).

[37]Sarpkaya, T., "Vortex Breakdown in Swirling Conical Flows," *AIAA Journal*, Vol. 9, Sept. 1971(b).

[38]Sarpkaya, T., "Effect of Adverse Pressure Gradient on Vortex Breakdown," *AIAA Journal*, Vol. 12., May 1974.

[39]Escudier, M.P. and Zehnder, N., "Vortex Flow Regimes," *J. Fluid Mech.*, Vol. 115, 1982a.

[40]Escudier, M.P., Bornstein, J., and Maxworthy, T., "The Dynamics of Confined Vortices," Proc. R, Soc. London, A382, 1982b.

[41]Faler, J.H., and Leibovich, S., "Disrupted States of Vortex Flow and Vortex Breakdown," *Phys. Fluids*, Vol. 20, No. 9, Sept. 1977.

[42]Faler, J.H., and Leibovich, S., "An Experimental Map of the Internal Structure of a Vortex Breakdown," *J. Fluid Mech.*, Vol. 86, Part 2, 1977.

[43]Malcolm, G. N., "Impact of High-α Aerodynamics of Dynamic Stability Parameters of Aircraft and Missiles," AGARD Lecture Series No. 114, Dynamic Stability Parameters, 1981.

[44]Iwanski, Kenneth P., "An Investigation of the Vortex Flow Over a Delta Wing With and Without External Jet Blowing," Masters Thesis, University of Notre Dame, April 1988.

[45]Ng, T. T., Nelson, R. C. and Payne F.M., " Flow Field Surveys of Leading Edge Vortex Flows," AGARD Symposium on Validation of Computational Fluid Dynamics, Lisbon, Portugal, May 2-5, 1988.

[46]Jumper, E. J., Nelson, R. C., and Cheung, K., "A Simple Criterion for Vortex Breakdown," AIAA paper 93-0866, Jan. 1993.

[47]Raat, J., "Vortex Development and Breakdown," Technical Report AFFDL-TR-75-69, Wright-Patterson AFB, OH, 1975.

[48]Krause, E. and Althaus, W., "Vortex Breakdown: Mechanism of Initiation and Change of Mode," IUTAM Symposium on Fluid Dynamics of High Angle of Attack," Sept. 1992.

[49]Wentz, W.H. and Kohlman D.L., "Vortex Breakdown on Slender Sharp Edged Wings," *J. of Aircraft*, Vol.8, #3, March 1971 (AIAA Paper 69-778 July 14-16, 1969).

[50]Hummel, D., "On the Vortex Formation Over a Slender Wing At Large Angles of Incidence," AGARD-CP-247, Oct. 1978.

[51]Stanbrook, A. and Squire, L. C., "Possible Types of Flow at Swept Leading Edges," *Aeronautical Quarterly*, Vol. 15, 1964.

[52]Miller, D. S., and Wood, R. M., "An Investigation of Wing Leading Edge Vortices at Supersonic Speeds," AIAA Paper 83-1816, July, 1983.

[53]Stallings,R. L., "Low Aspect Ratio Wings at High Angles of Attack," Chapter 3, Tactical Missile Aerodynamics, Vol. 104, Progress in Astronautics and Aeronautics, AIAA, 1987.

[54]Rockwell, D., "Three Dimensional Flow Structure on Delta Wings at High Angle-of-Attack: Experimental Concepts and Issues," AIAA Paper 93-0550, Jan. 1993.

[55]Ashley, H., Katz, J., Jarrah, M. A. M., and Vaneck, T., "Unsteady Aerodynamic Loading of Delta Wings for Low and High Angles of Attack," Proc. from International Symposium on Nonsteady Fluid Dynamics, June 1990.

[56]Bragg, M. B., and Soltani, M. R., "An Experimental Study of the Effect of Asymmetrical Vortex Bursting on a Pitching Delta Wing", AIAA-88-4334, August, 1988.

[57]Brandon, J. M., and Shah, G. H., "Effect of Large Amplitude Pitching Motions on the Unsteady Aerodynamic Characteristics of Flat-Plate Wings", AIAA-88-4331, August, 1988.

[58]Brandon, J. M., and Shah, G. H., "Unsteady Aerodynamic Characteristics of a Fighter Model Undergoing Large-Amplitude Pitching Motions at High Angles of Attack", AIAA-90-0309, January, 1990.

[59]LeMay, S. P., Batill, S. M., and Nelson, R. C., "Dynamics of Leading Edge Vortices on Pitching Delta Wing," *AIAA J.of Aircraft*, Vol. 27, No. 2, pp. 131-138, Feb. 1990.

[60]Thompson, S. A., Batill, S. M., and Nelson, R. C., "The Separated Flow Field on a Slender Wing Undergoing Transient Pitching Motions," *AIAA J.of Aircraft*, Vol. 28, No. 8, pp. 489-495, Aug. 1991.

[61]Thompson, S. A., Batill, S. M., and Nelson, R. C., "Unsteady Surface Pressure Distributions on a Delta Wing Undergoing Large Amplitude Oscillations," AIAA Paper 90-0311, Jan. 1990.

[62]Thompson, S. A., Nelson, R. C., and Batill, S. M., "Delta Wing Surface Pressures for High Angle of Attack Maneuvers," AIAA Paper No. 90-2813, Aug. 1990.

[63]Thompson, S. A., "The Unsteady Aerodynamics of a Delta Wing Undergoing Large Amplitude Motions," Ph.D. Dissertation, University of Notre Dame, May 1992.

[64]Nelson, R. C. and Thompson, S. A., "Flow Visualization of the Leading Edge Vortices on Slender Wings Undergoing Large Amplitude Unsteady Motions," 6th International Symposium on Flow Visualization, Yokohama, Japan, Oct. 1992.

PULSATILE HEART FLOW: A UNIVERSAL TIME SCALE

M. GHARIB, E. RAMBOD, D. DABIRI AND M. HAMMACHE
California Institute of Technology, Pasadena, California

T. SHIOTA, D. SAHN
Oregon Health Science University, Portland, Oregon

Introduction

The maximum efficiency of cardiac filling requires that blood entering the left ventricle decelerate and mix evenly before energy is spent deforming the cardiac apex or forming localized high stress regions. From various ultrasound studies of the left ventricle, by our group and others, it appears that this deceleration is achieved through a rapid roll-up of the flowing blood into the vortical structures within the left ventricular body. This vortex formation occurs during the diastolic period. Lee and Talbot [1], tried to apply the concept of Strouhal number $St=fd/u$, where f is the heart rate, d is the mitral valve diameter, and u is the maximum velocity during diastole, in order to characterize the dynamics of the filling process of the left ventricle. Based on their report, they found that the Strouhal number did not indicate any useful trend in characterizing the mitral flow. The concept of the Strouhal number has been used successfully by Crow and Champagne [2] to characterize the maximum efficiency of pulsed jets and by Triantafyllou, et al., [3] to characterize the maximum efficiency of swimming fish. In our opinion, to apply a Strouhal frequency approach to the flow in the left ventricle is not appropriate because, in reality, cardiac pulsating filling flow resembles a single transient vortex puff more than a continuous jet. This is due to the more than 90% variation in the velocity amplitude during the left ventricle filling process. Therefore, a more proper non-dimensional parameter that can demonstrate the dynamics of this vortex roll-up process is the Formation number which we define as:

$$F = \frac{T\bar{U}}{D}$$

where T is the filling period, $\bar{U}$ is the average velocity for the filling period and D is the mitral valve annulus. This number is different in its nature from the "Strouhal number" where the time scale is the frequency of occurrence rather than the period of the event.

To test whether the Formation number could characterize the flow process in the left ventricle, we conducted a series of in vivo tests on 73 normal, healthy subjects ranging in age from 5 days to 84 years. In addition, 8 patients with dilated cardiomyopathy were selected to be examined by the echocardiography described below.

Echocardiography

Two-dimensional, pulsed Doppler echocardiography was performed using commercially available ultrasound machines (Toshiba 140A and Hitachi EUB-165 with 2.5, 3.75, or 5 MHz transducers). We recorded transmitral flows with the ultrasound transducer paced at the cardiac apex and guided by two-dimensional echocardiographic imaging in a four chamber view. A pulsed Doppler sample volume was placed in the center of the atrio-ventricular junction at the level of the mitral annulus. Once adequate transmitral blood flow velocities had been recorded, velocity time integrals for early diastolic transmitral flow (VTI cm) were measured using the track ball systems on the echo systems. The mitral annular diameter (D cm) was also measured at end-diastole using the calibrated track ball measurements from the frozen images. Doppler measurements were averaged over three cardiac beats. Then, the Formation number was calculated as the ratio of D/VTI (non-dimensional number).

Results

A power law curve presents the general behavior of the Formation number with age. This curve shows a steady decrease of the Formation number in the early stages until it reaches a base line value of 4.5 for ages over 30. The mean Formation number for the whole data set is about 4.795.A marked decrease in the formation number can be seen for all of the DCM patients ranging from 2.88 to .27 (mean 1.89$\pm$.7).

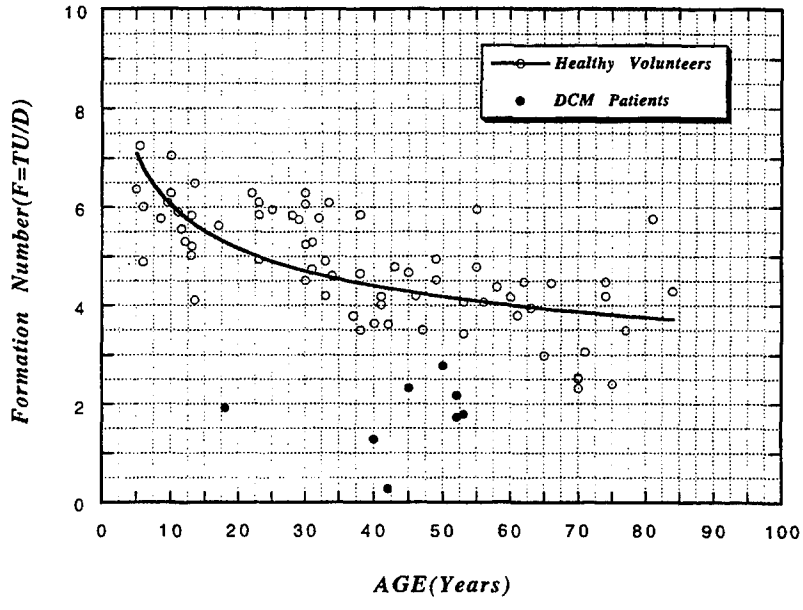

Figure 1. Variation of Formation number with age (o → normal patients, • → DCM)

The mean value of 4 for the formation number appears to indicated the existence of a universal time scale that describes left ventricle flows during diastole. The statistical significance and importance of the narrow range of the formation number becomes obvious when one considers the broad spectrum of the ages and backgrounds of the test subjects. A low formation number might indicate a poor volume efficiency due to low average velocity or a short diastolic period. A typical example can be found for dilated cardiomyopathy where decreased systolic function and increased cardiac chamber size is accompanied by reduced left ventricular wall motion, increased filling pressures and abnormal relaxation of heart muscle. A high value of Formation numbers can be indicative of a high heart rate which results in excessive mean velocities through the mitral valve. At this time, we cannot identify a high value of Formation number with any known cardiac problem.

The results presented in Figure 1 indicate that the normal heart as a responsive system operates around a Formation number of 4. Whether this base line has a significant fluid mechanical value is an important issue that needed to be addressed through an understanding of the vortex formation process. We need to be aware of the fact that the vortex formation process in the left ventricle is not a clean process and might depend on the geometry and motion of the compliant surfaces that form the LV chamber. But the fact that the Formation number shows a strong trend toward the

base line of 4 over a variety of chambers and mitral valve geometries, heart rates and ages is an encouraging sign that fluid mechanics of the initial formation process might be a very robust process and a help to the understanding of LV flows. The critical issue here is the role of the accumulation of vorticity in the vortex which in fact characterizes the deceleration process through the vortex roll up mechanism. In this we decided to conduct a series of experiments on the vortex formation process to investigate the importance of the Formation number. In this paper, we report some of the preliminary results obtained through the experiments.

Experimental Set-Up

The main experiment was designed to generate a vortex ring through the action of a light piston in a long cylindrical tube. The forward motion of the piston pushed the fluid in the cylinder out of an orifice which resulted in the formation of a vortex ring. The piston motion was obtained by a programmable pump. The vortex generator was situated in a Plexiglas tank (30.5 cm x 30.5 cm x 91 cm). The visualization was done by using a laser sheet made of an Argon-ion laser beam and fluorescent dye (Figure 2). Silver-coated glass particles of less than 10 microns in diameter were used to visualize and quantify the velocity and vorticity fields through the method of Digital Particle Image Velocimetry (DPIV) (Willert and Gharib, 1991).

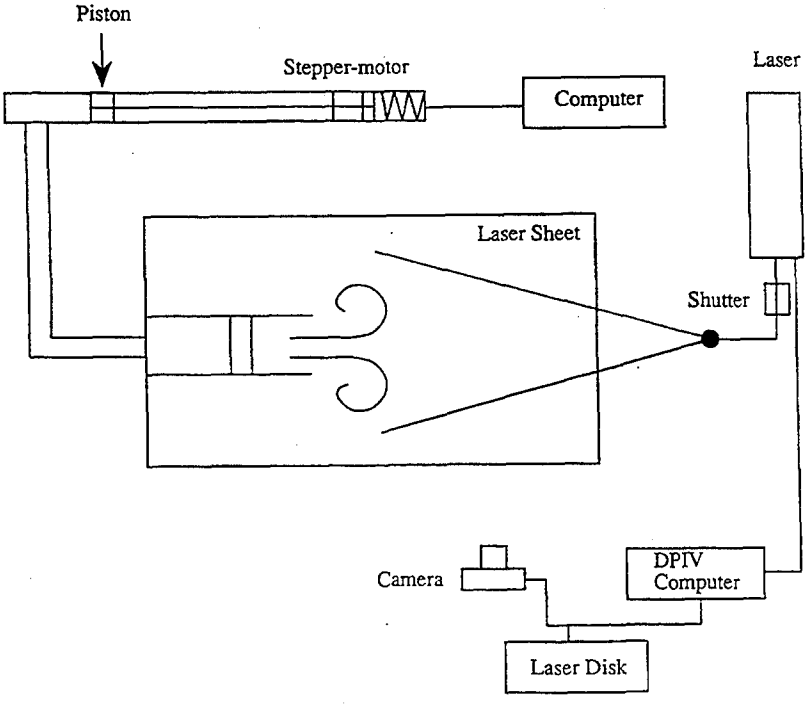

Figure 2: DPIV experimental set-up.

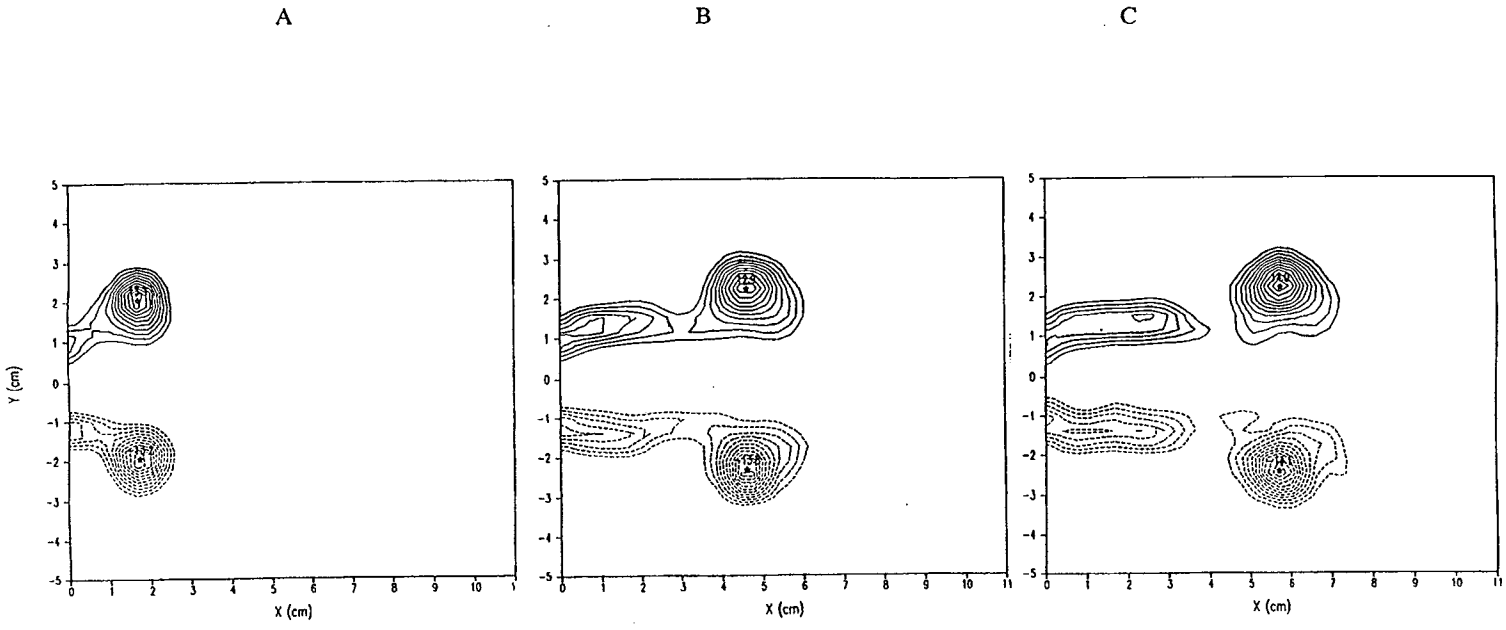

Figure 3: Different stages of the vorticity field of a forming vortex.

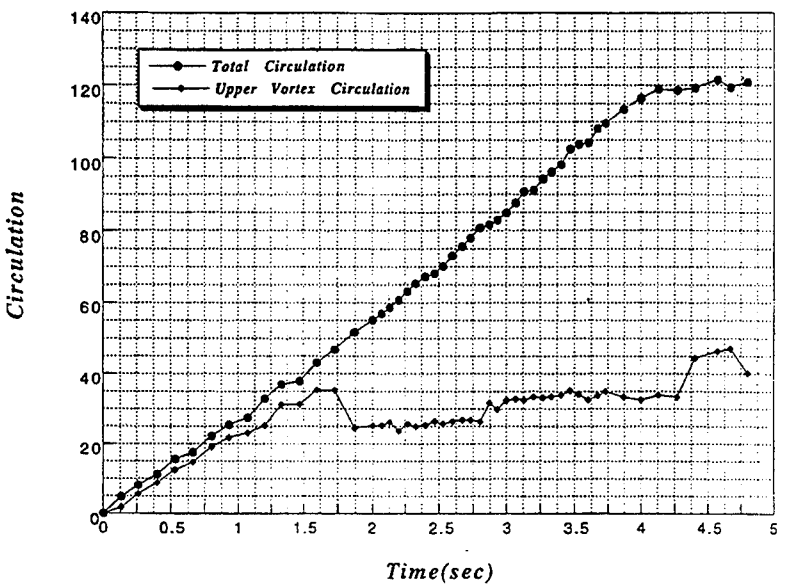

Figure 4: Total (Re ~ 3000) and vortex ring circulation as a function of time.

Temporal behavior of vortex circulation

Figures 3a, b and c show the vorticity field of a forming vortex. The main feature to notice is the fact that the vorticity field of the starting vortex detaches itself from the preceding jet flow. This event occurs while the piston still moves and fluid is being pushed out of the cylinder. Therefore, this disconnection process is independent of piston motion and must be inherent to the motion of vortex formation. Figure 4 shows the total circulation and circulation of the starting vortex as a function of time. It is interesting to note the disconnection process as an asymptotic process of saturating the circulation of the starting vortex. This can easily be seen in the branching of the starting vortex circulation from the total circulation produced by the vortex ring generator. The time of this branching process in conjunction with the average piston velocity and piston diameter can be used to produce a Formation number.

Our preliminary results indicate that for various piston motion profiles, the Formation number based on the disconnection time is between 3.5 and 4.5. This variation is due to the history of piston velocity and needs further investigation. The experimental Formation number of 3.5 - 4.5 is well within the Formation range found in our ultrasound tests for healthy cases, indicating that the cardiac discharge process benefits from the natural instability of the unsteady flow. The stability characteristics of the starting jet which results in the disconnection of the vorticity field of the starting vortex is a natural part of an efficient cardiac cycle.

Acknowledgment

The work was conducted under a grant from the National Institute of Health (R01 HL 43287).

References

1. Lee, C. S. F, and L. Talbot, *JFM* (1979), vol. 91.
2. Crow, S. C., and F. H. Champagne, *JFM* (1971), vol. 48.
3. Triantafyllou, G. S. et al., *JFS* (1993), vol. 7.\
4. Willert, C. E., and M. Gharib, *Exp. in Fluids* (1991), vol. 10.

THE WAVELET ANALYSIS : A NEW TOOL FOR THE EXPERIMENTAL INVESTIGATION OF THE STRUCTURE OF TURBULENT FLOWS

ANSELMET Fabien

I.M.S.T. 12, Avenue Général Leclerc, 13003 Marseille (France)

Abstract

Analyzing the complex mechanisms involved in the dynamics of turbulent flows is still an important challenge for experimental research, even in basic configurations. Indeed, a large range of scales are involved in these flows, and it is important to investigate their characteristics and their interactions. Thus, the time-frequency decomposition provided by the rather recently worked out wavelet analysis appears as an efficient new tool that complements the classical statistical approach and Fourier transform. This paper reviews applications such as for the eduction and analysis of coherent motions in various shear flows or the investigation of the properties of the intermittent small scales in large Reynolds number turbulence. Emphasis is given on the new available information in terms of localized spectral distributions or the investigation of local scaling laws. The pitfalls of this analysis as well as the need for a wider use of it in order to better define its domains of application are also discussed.

I. INTRODUCTION.

Our understanding of the properties of turbulent flows has considerably improved since Reynolds' pioneering work[1] which resulted, one century ago, in the decomposition of any physical variable such as the three components of the velocity vector or pressure into its mean value and fluctuations about this mean value. These ideas were important since they allowed quantitative experimental exploration of turbulent flows together with the development of various modelling procedures. In particular, fluctuations can then be analyzed either in terms of moments of second, third, or higher order[2], or in terms of the probability density function of the considered variable[3].

However, this statistical information is not sufficient since it is well established that the balance of energy within turbulent flows is also associated with the presence of structures of very different scales which are in strong interaction. Thus, in order to precisely understand and represent the properties of the energy tranfer, it is also important to characterize the behaviour of these scales. Indeed, Kolmogorov[4] has proposed the first theory of turbulence that quantifies the energy transfer characteristics when the flow Reynolds number is sufficiently large for an inertial range of scales - i.e. independent from both the way energy is injected at large scales and the way it is dissipated by molecular effects at small scales - to exist. This anlysis is most often performed in the so-called Fourier space since the Fourier tranform is a very efficient and low-cost tool to study these problems either through experimental temporal

records of velocity or vorticity fluctuations[5] or by studying and modelling the Fourier-transformed Navier-Stokes equations[6].

But turbulence phenomena are even so complex that none of the previously described global approaches is sufficient. Indeed, in particular, turbulence involves space localized events commonly referred to as coherent structures which require more sophisticated investigation. The major role played by these organized coherent structures in the dynamics of various turbulent shear flows has now been widely documented[7], [8]. These motions are particularly important for the development of turbulent boundary layers but, in spite of numerous experimental and numerical studies devoted to the subject, the classification of various types of structures inferred from different data analyses, and the precise understanding of their mutual interactions and of their spanwise characteristics are still requiring efforts. Another aspect of turbulence that is still poorly understood is the intermittent nature of small scales. Indeed, when energy is transferred from the larger scales to the smaller ones through the so-called energy cascade, it is found that energy is concentrating in some places whereas it is almost zero in other places, resulting in specific anormal behaviour of the high order moments of velocity increments[5], [9] (or differences $\Delta U(r)=U(x+r)-U(x)$ between two points separated by a distance r). This feature may be associated with the presence of localized singularities in the Navier-Stokes equations[10] and refined analysis is required in order to quantitatively study the organization of these singularities in both the physical and scales spaces.

Thus, it is obvious that using a statistical tool which allows one to get local information about the distributions of scales is important for improving our present knowledge of various turbulence aspects. This tool has been existing for a few years and its use is now getting generalized : it is the wavelet decomposition. The present paper will first recall (section 2) the main properties of the wavelet analysis before displaying a few typical applications for the experimental investigation of turbulent flows. Section 3 will report results concerning the scaling properties of turbulence energy transfer whereas section 4 will present data associated with the properties of large-scale coherent motion.

Note that more detailed information can be found in the review paper of Farge[11] or in proceedings of conferences specifically devoted to wavelets[12], [13]. The wavelet decomposition is also an efficient tool for improving the performance of numerical modelling of turbulence. In particular, several studies[14], [15] have been devoted to investigate their ability to obtain better estimates of derivatives by refining the mesh resolution in regions where gradients are strong. The properties and problems associated with these multiresolution schemes will not be addressed here.

II. THE WAVELET DECOMPOSITION.

II.1) Definition and basic properties.

Mathematical properties and constraints associated with wavelets will be only briefly recalled hereafter. More detail can be found in specialized presentations[16], [17].

The geometrical formalism of the continuous wavelet transform was first developed by Grossmann and Morlet[18] in order to improve the available scale decompositions. Indeed, figure 1 shows that, with the classical Fourier transform (1.a) or with the windowed Fourier transform of Gabor (1.b), the localizations in space and scales are not very efficient because the number of oscillations within the analyzed portion of the signal S(t) is not varying enough. The classical Fourier transform is well localized in scale but it is not at all in space whereas the windowed Gabor transform efficiency is limited by the fixed window size. On the other hand, the wavelet transform is based on dilation and translation of the analyzing windows along the scale direction and the space (or time) evolution respectively. Thus, as the number of oscillations of the analyzing function is constant in any window, wavelets provide very good spatial resolution in the small scales and very good scale resolution in the large scales. This feature is one of the main characteristics of the wavelet analysis, which is generally named as the "similarity property".

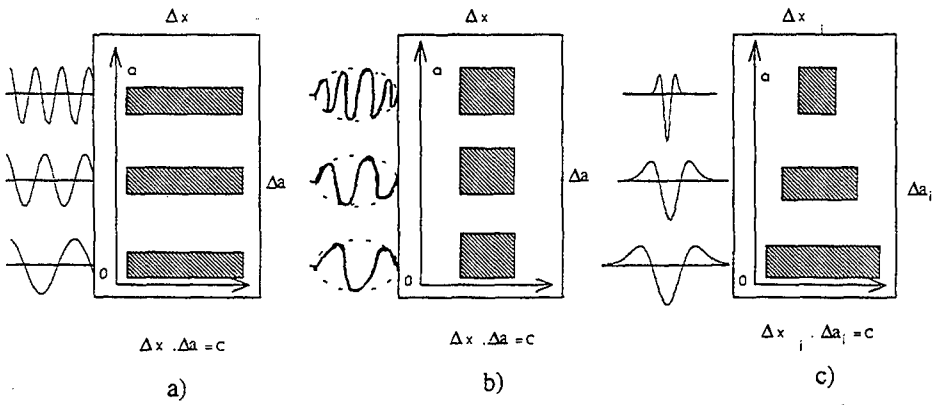

Figure 1. Examples of analyzing functions for scale decomposition of a signal together with their associated scale and space (or time) localization properties. a) Fourier transform; b) Gabor transform; c) Wavelet decomposition (figure adapted from Farge[11]).

More specifically, the wavelet transform $T_S(b,a)$ of S(t) is computed from its scalar product with the family of analyzing wavelets $\psi_{ab}(t)$ by :

$$T_S(b,a) = \frac{1}{\sqrt{a}} \int_{-\infty}^{+\infty} S(t)\psi^*_{ab}(t)dt$$

or (1)

$$T_S(b,a) = \sqrt{a} \int_{-\infty}^{+\infty} \hat{S}(\omega)\hat{\psi}^*(a\omega)e^{ib\omega}d\omega$$

where $\hat{\psi}$ denotes the Fourier transform of ψ and $\psi^*(\omega)$ its complex conjugate. The family of functions $\psi_{ab}(t)$ is generated from the mother function $\psi(t)$ by continuous dilation (factor a) and translation (factor b) :

$$\psi_{ab}(t) = \psi\left(\frac{t-b}{a}\right) \quad (2)$$

The wavelet decomposition of S(t) is thus made of the coefficients $T_S(b,a)$. It is required that the mother function should be admissible, which means that its average should be zero :

$$\int_{-\infty}^{+\infty} \left| \frac{\hat{\psi}(\omega)}{\omega} \right|^2 d\omega = A < +\infty,$$

$$\int_{-\infty}^{+\infty} \psi(t)dt = 0 \text{ or } \hat{\psi}(\omega=0)=0 \tag{3}$$

There should also be one reconstruction formula for recovering the signal exactly from its wavelet coefficients and for allowing the computation of energy from them :

$$S(t) = \frac{1}{A} \iint_{\Re^2} T_S(b,a)\psi_{ab}(t)\frac{dadb}{a^2},$$

$$\frac{1}{A}\iint_{\Re^2}|T_S(b,a)|^2 \frac{dadb}{a^2} = \int_{-\infty}^{+\infty}|S(t)|^2 dt \tag{4}$$

In fact, one may also be interested in studying the derivatives of S(t), which requires additional constraints on the mother wavelet $\psi(t)$. For instance, if one wants to study the nth order derivative of S(t), then the moments of $\psi(t)$ up to the nth order should also vanish. This is often known as the regularity property :

$$\int_{-\infty}^{+\infty} t^n \psi(t)dt = 0 \text{ or } \frac{d^n}{d\omega^n}\hat{\psi}(\omega=0)=0 \tag{5}$$

II.2) Examples of commonly used wavelets and their implementation.

The Morlet wavelet.

This is the wavelet most commonly used. It is a modulated gaussian function :

$$\psi(t) = e^{i\lambda t}.e^{-t^2/2} \tag{6}$$

The term $e^{i\lambda t}$, with λ about 6, makes the correction terms necessary to ensure the function satisfies the condition of zero average negligible. Its Fourier transform is then given by :

$$\hat{\psi}(\omega) = (2\pi)^{-\frac{1}{2}} e^{-(\omega-\lambda)^2/2} \tag{7}$$

Figure 2 presents the Morlet mother function together with its Fourier transform. You will note that due to its gaussian envelope this wavelet achieves the optimum of localization in time and scale spaces.

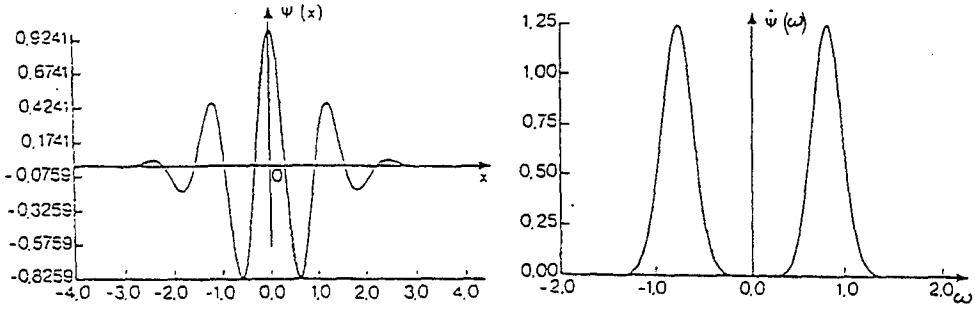

a) b)

Figure 2. The Morlet wavelet function (a) together with its Fourier transform (b).

The Mexican hat wavelet.

This wavelet is obtained from the second derivative of the gaussian function. It is also widely used because high wavelet coefficients then correspond to a strong curvature of the signal at the scale, a, of the wavelet and can then be used for detection of local increase or decrease of the signal.

The Haar wavelet.

As these wavelet generating functions present quite a few oscillations, a lot of points are necessary to represent them on a discrete basis as is the case when analyzing sampled signals. Thus, it is often interesting to use sharp edged functions, such as the Haar wavelet ($\psi(t)=-1$ for $t<t_0$ and $=1$ for $t>t_0$ where t_0 denotes the mid-position of the analyzed portion of signal) or a ramp-like function, which require much fewer points to define them. Even though such wavelets are admissible (zero average), they generate oscillations associated with the discontinuities in the Fourier space, so that they are poorly localized in that space.

Implementation.

Most commonly, for turbulence analysis, sampled signals are used. Then, the dilation, a, and translation, b, factors will be defined on a discrete basis :

$a_i=a_0A^i$, $b_j=jb_0$ where a_0 and b_0 are expressed in terms of numbers of points of the signal. These relations first show that quite a large number of operations is required if one wants to study quite long portions of signal using a sufficiently large range of scales : this problem is important since it makes the wavelet analysis rather expensive in terms of computing time. However, considering the scale resolution, two interesting properties are easily evidenced : first, one can precisely choose the lowest and the largest analyzed scales through the free parameters defining the range of a_i; secondly, the computed coeffients $T_S(b_j,a_i)$ are distributed on a geometrical progression corresponding to logarithmically spaced scales, which is much more convenient for turbulence analysis than the linearly distributed Fourier coefficients.

In fact, in order to reduce the number of operations, these coefficients are often evaluated on a coarse mesh[17], such that b_j varies with the scale a_i : b_j is doubled once every fourth scale, starting with b_0 corresponding to one point for a_0. Then, an interpolation procedure is used to compute the missing coefficients of the complete grid and this is generally sufficiently precise since large scale variations do not need to be computed for each of the points.

Figure 3 gives an example of the wavelet decompositions of synthesized portions of signals, one with a strong discontinuity and the other one with periodic oscillations including one period doubling. The contours of iso-values of the real parts of the coefficients T(b,a) are reported, together with their modulus and their phase. One of the main features of these plots is that, especially for the phase, strong coefficients are located within a cone that points (at small scales) towards the discontinuities. Indeed, if ψ is well localized in the time (or space) interval τ for a=1, then the wavelet coefficients corresponding to the position t_0 will all be contained in the influence cone defined by $t \in [t_0-(1\tau)/2 , t_0+(1\tau)/2]$. This cone corresponds to the spatial support of all dilated wavelets at the position t_0. The corresponding property is also valid if $\hat{\psi}$ is well localized in the Fourier space. These properties will be more thoroughly examined in the examples reported in the two following sections.

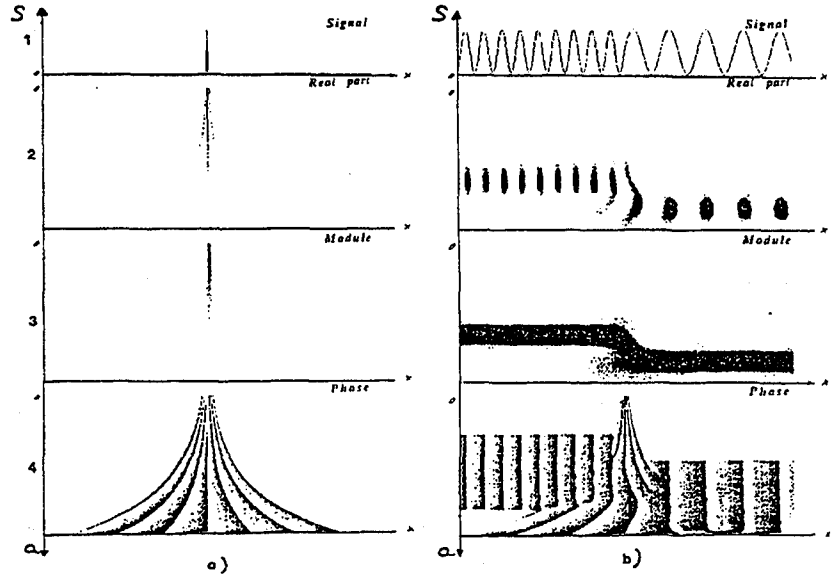

Figure 3. Wavelet coefficients associated with two types of signals (From Farge[11]).
a) Dirac signal; b) Periodic signal.
(scales are decreased from bottom to top of each plot).

III. APPLICATION OF WAVELETS FOR INVESTIGATING THE SCALING PROPERTIES OF TURBULENCE ENERGY TRANSFER.

In order to take into account the intermittent nature of energy transfer towards the small scales, quite a few models refining Kolmogorov's[4] original ideas have been proposed. The most recent ones are based on the concepts of fractality or multi-fractality and they tend to

interpret the existence of violent rare fluctuations of the energy transfer as associated with the presence of localized singularities of the Navier-Stokes equations[10]. Thus, the wavelet analysis appears as a very attractive tool to study this phenomenon in more detail since it can provide local scale decompositions.

These singularities result in a wide admissible range of scaling exponents h for the velocity field. Indeed, according to Kolmogorov's original ideas, there was no fluctuation of the energy transfer so that there was only one possible scaling exponent, h=1/3, such that :

$$\Delta U(r) = r^h \qquad (8)$$

This scaling exponent is directly related to the famous -5/3 law for the kinetic energy spectrum. From experiments performed in an industrial wind tunnel at a very large Reynolds number (R_λ=2700, based on the Taylor micro-scale), Bacry et al.[19] showed that there actually exists a wide range of singularity exponents for the velocity field. Indeed, if the analyzed signal has the scaling exponent $h(x_0)$ at the position x_0, then, $\Delta U_{x0}(r)$ will scale as $r^{h(x0)}$ at this point and the wavelet transformed velocity signal will also scale as $T(a,t_0) \approx a^{h(x0)}$ for scales a lying within the inertial range. Figure 4 reports examples of scaling laws experimentally determined for different time (or space) positions. If there is one case (Fig. 4.a) where h is equal to 0.4, i.e. not very far from the value 1/3, there are other cases (Fig. 4.b) where h can reach values very different from 1/3. These latter values are associated with portions of signals presenting a violent event with very sharp velocity gradients and very large signal excursions (Fig. 4.c). In fact, figure 4.d presents the histogram of the obtained values for h : they can range in the domain -0.3<h<1. It is that variability of the scaling exponents h, together with the associated probabi-

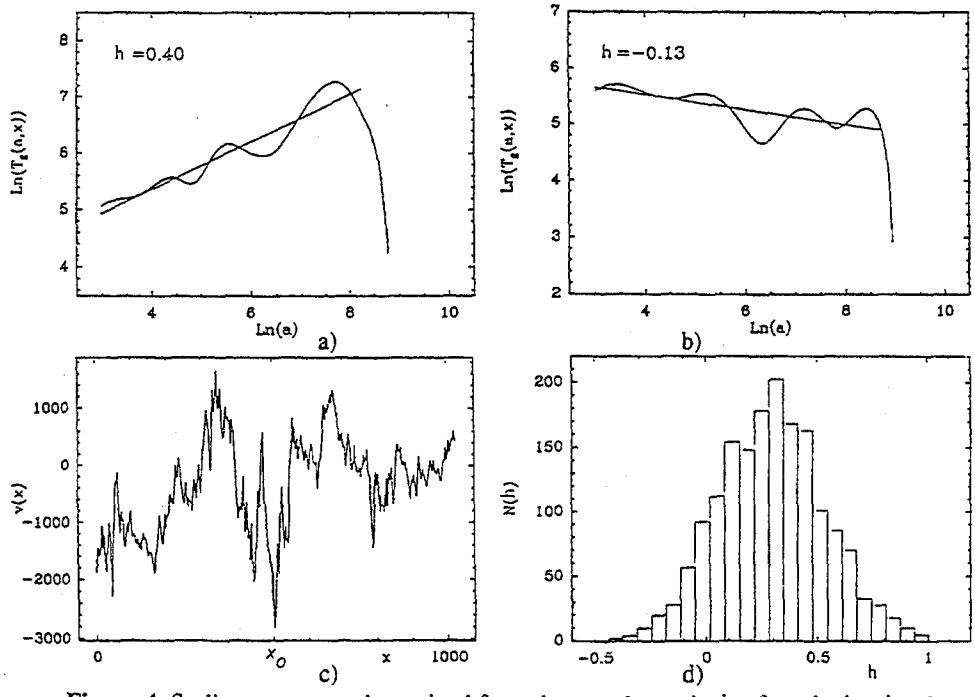

Figure 4. Scaling exponents determined from the wavelet analysis of a velocity signal (From Bacry et al.[19]). a) Example giving h=0.4; b) Example giving h=-0.13; c) Associated signal for h=-0.13; d) Histogram of scaling exponents.

lity of finding them within the flow - which is often characterized by the Hausdorff dimension D(h) of the fractal set for which velocity increments behave as r^h - which induces the anormal behaviour of the high order moments of velocity increments[5], [9]. Similar trends were obtained by more classical investigations[20] based on measurements of a simplified version of the dissipation rate ε and statistical tools used in studies of dynamical systems.

Another analysis related to turbulent energy transfer mechanisms was performed by Meneveau[21] using wavelets. From the wavelet-transformed Navier-Stokes equations, new quantities such as e(r,x), t(r,x) and π(r,x), respectively the kinetic energy, the transfer of kinetic energy and the flux of kinetic energy through the scale r at position x were defined. This permits to study fluctuations of these quantities for which only the mean values are generally considered in spectral modelling of turbulence[5, 6]. Analyzing data, obtained from laboratory experiments in a wake flow behind a circular cylinder as well as three-dimensional velocity fields computed from numerical simulations, showed that e(r,x), t(r,x) and π(r,x) actually fluctuate greatly in physical space for scales between the energy containing scales and the dissipative ones. Through the detailed study of the non-linear advection terms, it was also evidenced that backscatter energy transfer can occur quite frequently, i.e. corresponding to energy transferred backward from the smaller scales to the larger ones, even though, of course, the mean value of π is corresponding to usual forward transfer of energy. Typical results are reported on figure 5 for data associated with the scale r such that r/η=5.6 and obtained with different wavelet functions. For the transfer of kinetic energy (Fig. 5.a), the variability is very important as exponential tails are obtained in the pdf. These tails spread more and more widely for decreasing scales. However, this feature is not unexpected since t(r,x) is directly related to velocity increments $\Delta U(r)$[5], but, to our knowledge, this is the first reported data of this nature. The probability density function of the local kinetic energy is reported on figure 5.b, clearly evidencing the strongly intermittent nature of e at that scale. In addition, it is worth noting that these results only marginally depend on the analyzing wavelet function.

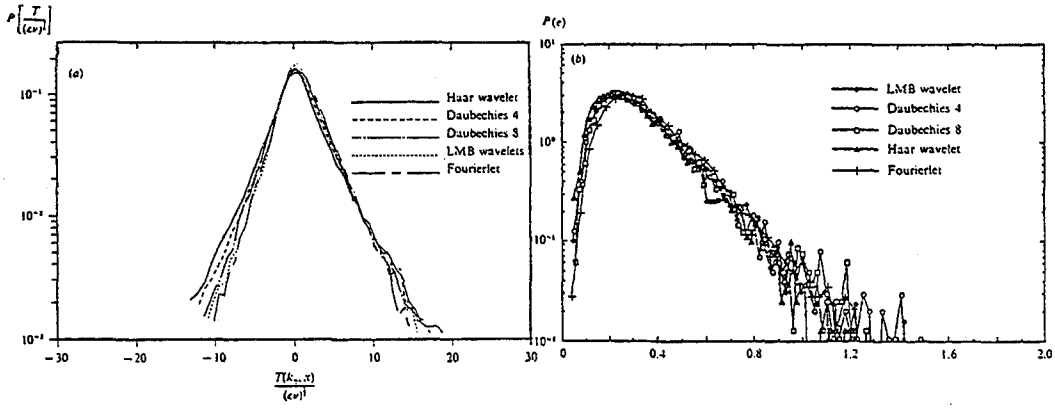

Figure 5. Direct evidence of the intermittent nature of energy transfer at scale r/η=5.6 (η is the Kolmogorov length scale. From Meneveau[21]). a) Probability density distribution of transfer of kinetic energy π; b) Probability density distribution of kinetic energy e.

IV. APPLICATION OF WAVELETS FOR INVESTIGATING THE LARGE SCALE ORGANIZATION OF TURBULENT FLOWS.

The localized information provided by the wavelet analysis is also very well suited for studying the large scale organization of turbulent flows as local scale decompositions may be used, for instance, to characterize various properties of coherent structures.

Indeed, Liandrat and Moret-Bailly[22] displayed several interesting applications of the wavelet analysis for the experimental investigation of turbulent flows. In particular, a velocity signal recorded in a shock-wave/free turbulence interaction was examined from the point of view of intermittency. In this supersonic flow, jumps or discontinuities corresponding to the crossing of the shock-wave through the measurement position were efficiently detected using a Mexican-hat function. At very small scales, the intricate scale decomposition is resulting from both free turbulence and shock-wave interaction scales. On the contrary, at large scales, the wavelet decomposition is simpler and exhibits cone-like structures retaining a great part of the energy of the signal. They characterize the presence of the jumps. A quantitative analysis of these distributions then permits to determine the intermittency factor as a function of the downstream position in the flow. The wavelet decomposition was also used[23] to detect transition from the laminar to the turbulent regime in a flow over a rotating disc. Azimuthal velocity measurements were performed at different radial distances from the centre of the disc, the Reynolds number then increasing progressively from the centre to the outer region of the disc. From the wavelet coefficients T(b,a), the local energy distributions E(b,a) were then estimated by :

$$E(b,a)=\int \frac{T(b,a)^2}{a^2}\frac{1}{a}\chi((b'-b)/a)db' \qquad (9)$$

where the gaussian smoothing function χ accounts for the fact that the neighboring points b' are involved in the computation of the wavelet coefficients at the position b. These energy distributions are finally used to define, for each position of the signal, the scales $a^+(b)$ and $a^-(b)$ between which 80% of the energy at this position b is distributed. Studying the scale expansion of the energy partition at each position was shown to be a very efficient way to define the intermittency function since, obviously, for the oscillating regime, energy is concentrated over quite a narrow range of scales whereas, for the turbulent regime, it is spreading over a much wider range.

Direct investigations of the organized large-scale motions were performed in turbulent boundary layer flows by Collineau[24] and Benaïssa[25]. These coherent structures are known to be particularly important for the development and the dynamics of such flows[8]. However, in spite of numerous experimental and numerical studies devoted to the subject, the classification of various types of structures inferred from different data analyses, and the precise understanding of their mutual interactions and of their spanwise characteristics are still requiring efforts. These two experimental studies aimed at determining new procedures for the eduction of these structures in order to investigate their contributions to various properties of the flow. Criteria based on the wavelet decomposition were worked out[24] to detect the positions in temporal velocity signals of the strong gradients associated with the occurence of coherent structures at the measurement point. In particular, it was shown that a zero-crossing method is well suited when using the Mexican hat function : this prevents one from applying a

threshold criterion as is usually the case with the classical eduction algorithms such as Vita and Wag. This new eduction criterion is based on the zero-crossing positions of the wavelet coefficients $T(b,a_0)$, where a_0 is the scale for which the wavelet spectrum - estimated from $\int|T(b,a)|^2 db$ - attains its peak value, which were demonstrated to coincide with the strong signal jumps. Conditional averages then allowed a representative pattern to be extracted for each turbulent variable, and for the cross-products representing vertical turbulent transfer within the boundary layer. Thus, it was possible to determine the relative importance of the small-scale and coherent structure mixings, both on average and on an instantaneous basis.

Temperature signals obtained with a rake of 8 wires extending along the normal to the wall direction were studied by Benaïssa[25] in order to detect the so-called heating and cooling events. These events are associated respectively with fluid coming regions close to the heated wall and engulfment of cold fluid originating from the outer regions of the boundary layer. Figure 6 presents an example of local scale decomposition obtained by the Haar (6.b) and Morlet (6.c) wavelets for a 1200 point portion of temperature signal obtained in the wall vicinity. The range of analyzed scales extends from 23 to 7400 points (this range of scales includes 40 wavelets) so that, when computing the largest scale coefficients, signal portions not visible on the graph are taken into account. Since these two wavelets are quite different in terms of lateral oscillations, in order to provide more meaningful comparisons, figure 6.b is truncated for the largest scales whereas figure 6.c is truncated towards the smallest ones. However, both sketches show an almost regular succession of zones of large positive and negative positions extending over quite large ranges of scales. The former ones are generally coincident with the cooling events and the latter ones extend over smaller scales as heating events are associated with large velocities. However, the regions of "most intense activity" have characteristic scales of about the same amplitude. The positions of detected coolings (Fig. 6.d) using Wag and two different thresholds (0.65 and 0.80 times the temperature standard deviation at that distance from the wall) together with two window sizes (45, a_1, and 75, a_2, points) are pointed with arrows. Comparison is also provided with the corresponding energy distributions $E(b,a_1)$ and $E(b,a_2)$ defined from equation (9). For both scales presented here, a quite good correspondence is found between the positions of the Wag detected events and those associated with large values of the energy. In addition, innovative results were reported for the local spectral distributions which were found to be quite different from the mean ones when conditioned by heating or cooling events. In particular, cross-wavelet characteristics were defined in order to analyze in detail the linkage between two signals such as the temperature and its squared gradient (or dissipation) fluctuations, which is important for both a basic understanding of turbulence small-scale properties and various aspects of modelling. The possibility to investigate cross-spectral correlations, at the same scale or at different scales, and with or without a time lag, between these two quantities appeared as very promising even though only preliminary trends could be displayed.

V. CONCLUSION.

This paper has briefly reviewed some interesting applications of the wavelet analysis for the experimental investigation of the structure of turbulent flows. Even though innovative results have already been obtained, we must also confess that there is still a great

need to go further ahead and define new quantitative parameters that will allow one to take advantage of its promising capacities. Indeed, one of the main pitfalls is associated with the large number of coefficients one obtains. It is then tempting to reduce this amount of information by averaging integrations along either the scale or the space direction, but the result is not very different from what can be obtained using more classical tools. So, we hope that these preliminary results will promote new developments that will allow to fully take advantage of all the information that wavelets provide.

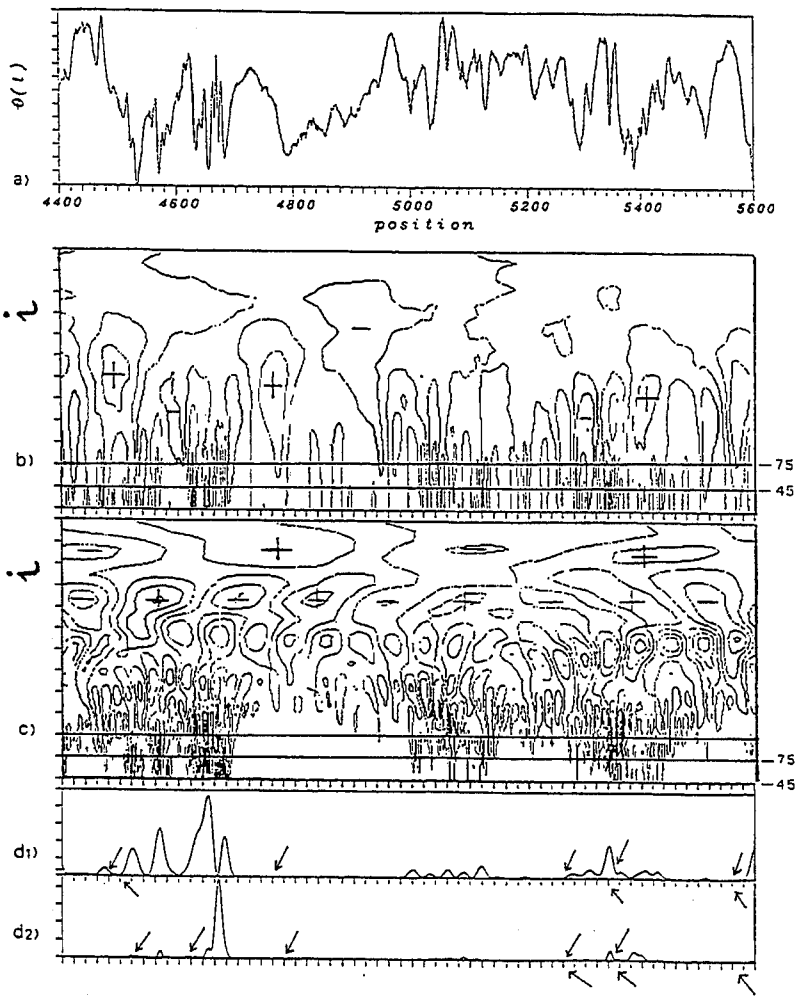

Figure 6. Distribution of wavelet coefficients for a typical temperature signal obtained in the wall vicinity of a boundary layer (from Benaïssa et al.[25]).
a) Temperature trace; b) Haar function; c) Morlet function; d) Associated energy distribution for one particular scale together with positions of Wag detected coolings using that window size : 1- Scale corresponding to 45 points; 2- 75 points.

Fruitful collaboration with A. Benaïssa, J. Liandrat and L. Fulachier for various aspects of the work reported herein is gratefully acknowledged.

REFERENCES

(1) REYNOLDS, O., Phil. Trans. Roy. Soc. A, vol. 186, p 123, 1895.

(2) LAUNDER, B.E., REECE, G.J. and RODI, W., Journal Fluid Mech., vol. 68, p 537, 1975.
LAUNDER, B.E., Int. J. Heat and Fluid Flows, vol. 10, p 282, 1989.

(3) POPE, S.B., Annual Rev. Fluid Mech., vol. 26, p 23, 1994.

(4) KOLMOGOROV, A.N., C. R. Acad. Sci. S.S.S.R., vol. 30, p 301, 1941.

(5) MONIN, A.S. and YAGLOM, A.M., *Statistical Fluid Mechanics*, MIT Press, 1975.

(6) LESIEUR, M., *Turbulence in Fluids*, Kluwer Acad. Publ., 1990.

(7) HUSSAIN, A.K.M.F., Journal Fluid Mech., vol. 173, p 303, 1986.

(8) ROBINSON, S.K., Annual Rev. Fluid Mech., vol. 23, p 601, 1991.

(9) ANSELMET, F., GAGNE, Y., HOPFINGER, E. and ANTONIA, R.A., Journal Fluid Mech., vol. 140, p 63, 1984.

(10) PARISI, G. and FRISCH, U., *In Turb. and Predict. in Geoph. Fluid Dynamics*, North-Holland, p 94, 1984.

(11) FARGE, M., Annual Rev. Fluid Mech., vol. 24, p395, 1992.

(12) RUSKAI, M.B., BEYLKIN, G., COIFMAN, R., DAUBECHIES, I., MALLAT, S., MEYER, Y. and RAPHAEL, L., *Wavelets and their applications*, Jones and Barlett Publ., 1992.

(13) MEYER, Y. and ROQUES, S., *Progress in Wavelet Analysis and Applications*, Fontières Edit., 1993.

(14) PERRIER, V., *Ondelettes et simulation numérique*, Ph. D. Thesis, Univ. Paris VI, 1991.

(15) LIANDRAT, J. and TCHIAMITCHIAN, Ph., To appear in SIAM J. Num. Anal., 1994.

(16) MEYER, Y., *Ondelettes et opérateurs*, Herman Edit., 1990

(17) DAUBECHIES, I., IEEE Tansf. Inf. Theory, vol. 36, p 961, 1990. See also *Ten lectures on wavelets*, CBMS Lecture Notes Series, SIAM, 1991.

(18) GROSSMANN, A. and MORLET, J., SIAM J. Num. Anal., vol. 15, p 723, 1984.

(19) BACRY, E., ARNEODO, A., FRISCH, U., GAGNE, Y. and HOPFINGER, E., *In Turbulence and Coherent Structures*, Kluwer Acad. Publ., p 203, 1991.

(20) MENEVEAU, C. and SREENIVASAN, K.R., Journal Fluid Mech., vol. 224, p 429, 1991.

(21) MENEVEAU, C., Journal Fluid Mech., vol. 232, p 469, 1991.

(22) LIANDRAT, J and MORET-BAILLY, F., Eur. Journal Mech. B/Fluids, vol. 9, p 1, 1990.

(23) MORET-BAILLY, F., CHAUVE, M.P., LIANDRAT, J. and TCHAMITCHIAN, Ph., C.R.A.S., vol. 313, Série II, p 591, 1991.

(24) COLLINEAU, S., *Etude expérimentale des mouvements cohérents turbulents au voisinage des couverts végétaux*, Ph. D. Thesis, Ecole Centrale de Paris, 1993.
COLLINEAU, S. and BRUNET, Y., Bound. Layer Meteor., vol. 56, p 125, 1993.

(25) BENAISSA, A., *Interaction entre les mouvements organisés et les structures à petite échelle en couche limite turbulente*, Ph. D. Thesis, IMST, Univ. Aix-Marseille II, 1993.
BENAISSA, A., ANSELMET, F., MORET-BAILLY, F. and LIANDRAT, J., *In Eddy Structure Identification in Free Turbulent Shear Flows*, Kluwer Acad. Publ., 1993.

TRANSITION IN A SWEPT-WING BOUNDARY LAYER

RADEZTSKY, R.H., REIBERT, M.S. and SARIC, W.S.
Mechanical and Aerospace Engineering
Arizona State University, Tempe, AZ 85287-6106, USA

ABSTRACT

Following the traditional role, we begin transition studies by trying to understand the instabilities that are harbingers of transition. Stability experiments are conducted in the Arizona State University Unsteady Wind Tunnel on a 45° swept airfoil. The pressure gradient is designed so that both crossflow and Tollmien-Schlichting disturbances are weakly amplified. The surface of the airfoil is hand polished to a 0.25 μm rms finish. Under these conditions, natural stationary crossflow amplitudes are not measurable. This provides an ideal environment for measuring roughness-induced stationary crossflow. Spanwise arrays of 70–150 μm roughness elements are introduced near the attachment line. These elements induce clearly defined stationary crossflow vortices downstream. Detailed hot-wire measurements are taken to document the growth and development of these vortices. Roughness spacing and Reynolds number are varied in order to examine the behavior of all amplified wavelengths. The measurements clearly show that traditional linear stability theory does not accurately predict the growth rates of stationary crossflow waves under these conditions.

NOMENCLATURE

A	disturbance amplitude
C_p	pressure coefficient
c	airfoil chord
k	roughness height
N	$=\ln(A/A_o)$, amplification factor
Re_c	$=U_\infty c/\nu$, chord Reynolds number
Re_k	$=k\sqrt{u^2+w^2(k)}/\nu$, roughness Reynolds number
U_e	boundary-layer edge velocity
U_∞	freestream velocity
u,v,w	velocity field in (x,y,z) coordinates
u',v',w'	disturbance velocity field in (x,y,z) coordinates
x,y,z	global test-section coordinates: x is along flow axis, y is wall-normal, z is unswept spanwise coordinate (positive down)
λ_{cf}	crossflow disturbance wavelength measured normal to vortex axis
λ_s	crossflow disturbance wavelength measured in swept spanwise direction

1. BACKGROUND AND MOTIVATION

Transition to turbulence continues to be an important link for Laminar Flow Control and energy-efficient aircraft. The objective of the present swept-wing research program is to examine the fundamental nature of the crossflow instability which leads to transition in three-dimensional boundary layers. Reviews of the current literature and problems are given by Reed & Saric [1], Arnal [2,3], and Saric [4,5]. The DLR efforts in Germany on a swept flat plate are summarized by Bippes & co-workers [6–11]. Another swept-flat-plate experiment is reported by Kachanov & Tararykin [12]. The CERT/ONERA experiments on swept wings are given by Arnal & co-workers [13,14,15,16,17,18]. The IFS work in Sendai on cones and spheres is contained in Kobayashi & co-workers [19,20] and Kohama [21,22]. The swept-cylinder experiments are described by Poll [23,24]. The ASU swept-wing experiments are summarized by Dagenhart & co-workers [25–27,44], Kohama et al. [28], and Radeztsky et al. [29]. These papers established the existence of both traveling and stationary crossflow vortices, saturation of the stationary crossflow vortex, the nonlinear secondary instability leading to transition, and the sensitivity to freestream disturbances and surface roughness. The theoretical basis for the crossflow instability comes from Gregory et al. [30]. It results in an Orr-Sommerfeld type solution that can be implemented in a variety of ways (Arnal [31,2,3]; Balakumar & Reed [32]; Cebeci & Stewartson [33]; Chen & Cebeci [34]; Collier & Malik [35]; Dagenhart [36]; Malik [37]; Nayfeh [38,39]; Parikh et al. [40]; Poll [23], Srokowski & Orszag [41]). See Mack [42] for the development of the details of the instability and Saric [4] and Arnal [2,3] for current reviews. In contrast to T-S type instabilities, the crossflow problem is characterized by having stationary as well as traveling disturbances that are amplified.

1.1 Fundamental Issues. Whereas linear stability theory predicts that the traveling crossflow waves are more amplified than the stationary crossflow waves, many experiments observe stationary waves. The question of whether one observes stationary or traveling crossflow waves is cast inside the receptivity problem. Müller & Bippes [9], Bippes & Müller [10], and Bippes [7] describe a series of comparative experiments in a low-turbulence tunnel and a high-turbulence tunnel. Their results show that traveling crossflow waves are observed in the high-turbulence tunnel rich in unsteady freestream disturbances and the dominant structure in a low-turbulence tunnel is a stationary crossflow vortex. Since the flight environment is more benign than the wind tunnel, one expects the low-turbulence results to be more important. However, one of the important results to come out of the DLR group is the set of data that show early saturation of the disturbance amplitude and the failure of linear theory to predict the growth of the instability.

The saturation phenomena of crossflow vortices and the measurements of phase velocity and group velocity directions by Bippes and co-workers [6–11] is important work. They report distorted mean profiles similar to those of Dagenhart et al. [27] and Kohama et al. [28]. The saturation phenomena are predicted by DNS calculations in the DLR group. This may be part of the Arnal [3] conjecture that e^N methods do not work in crossflow-dominated flows.

A similarity between the DLR and ASU experiments is the high *N-factors* and high amplitude of the u' distortion. Measurements were taken under conditions of 10%–20% mean-flow distortion. Perhaps then it is not surprising that linear theory fails. This motivated our recent work, which is an attempt to measure the development of crossflow vortices under conditions of very weak growth.

Another major shortcoming of traditional linear stability theory is the treatment of initial amplitudes. Radeztsky et al.[29] show that the receptivity process for stationary waves is strongly influenced by surface roughness near the attachment line. A successful transition-prediction scheme must account for initial conditions.

1.2 Objectives. This experiment uses the same NLF(2)-0415 airfoil (Somers and Horstmann[43]) swept at 45° as the previous work. This model has a pressure minimum at approximately $x/c = 0.71$, and is an ideal platform for the study of crossflow (Fig. 1). Previous work used a small negative angle of attack to produce considerable crossflow amplification while suppressing Tollmien-Schlichting (T-S) modes. For the present experiment, the angle of attack is changed to 0°, significantly reducing crossflow amplification. Under this more realistic pressure gradient, T-S waves are also weakly amplified. A new set of contoured wall liners modeled after Saric et al.[44] produce an infinite swept-wing flow. Carefully prepared arrays of roughness near the leading edge introduce controlled initial conditions. This provides a database for receptivity calculations, and produces well-defined stationary crossflow waves. Specific stationary modes can be identified and followed as they develop over the airfoil. This provides direct comparisons with single-wavelength linear stability calculations.

2. EXPERIMENTAL METHODS

A number of major changes have been made in the experimental operations since our previous work[25,26,27,28,29,44]. A new high-resolution, computer-controlled three-dimensional traverse mechanism allows extremely accurate probe placement. The minimum step size is 1 μm in the wall-normal and spanwise directions and 10 μm in the streamwise direction. Computer-controlled scans allow detailed observation of disturbance contours over long span intervals. Software-corrected scanning techniques produce self-consistent arrays of boundary-layer profiles over a span of 240 mm even in boundary layers less than 1 mm thick. Spanwise scans at constant u/U_e can be maintained over the same spanwise distance.

The long measurement times for this experiment require careful attention to hot-wire calibration issues. For the low-speed conditions of the Unsteady Wind Tunnel, the temperature response of the hot-wires is modeled very well by a linear correction term (Radeztsky et al.[45]). This correction scheme is integrated into all acquisition software for automated processing. Temperature-drift coefficients are measured before calibration, during preheating of the tunnel. Flow conditions are also monitored by a computer in order to maintain a constant unit Reynolds number throughout the experiment.

Many experiments which report the variation of total crossflow disturbance amplitude are inaccurate because all stationary modes which are present in the flow are lumped together. Interpretation of experimental results is simplified if the measurements are extensive enough to allow the application of spectral methods. If individual crossflow modes can be extracted from the total signal, comparisons with linear theory will be much more meaningful. For the detailed spanwise scans presented here, a span of 240 mm is covered in 256 steps, yielding a wavelength spacing of 0.6 mm at the most-important crossflow wavelength of 12 mm. The lowest resolvable wavelength is 1.9 mm. Eight averages are used in all spectral transformations in order to reduce variance.

The Fast Fourier Transform (FFT) is by far the most common method used for analyzing data, but is particularly prone to error when analyzing the small data sets found in

these difficult spatial measurements. Strong peaks associated with a distinct crossflow mode are often spread out so that the peaks are no longer clearly identified. The Maximum-Entropy Method (MEM) is an alternative transformation technique which is well-suited for identifying strong spectral features under limited sampling conditions. The chief drawback of this method is that the user must specify the value of a key parameter in the transformation. Fortunately, in this experiment the results are relatively insensitive to this parameter over a large range, and the correct spectral peaks are easily identified with sufficient precision for amplitude comparisons. Therefore, the MEM is used for all quantitative work, and the FFT is used only for qualitative verification of the results.

This experiment uses the same highly polished surface as in the previous work (Radeztsky et al.[29]). The rms roughness amplitude is measured to be 0.25 μm near the attachment line. This extremely low roughness level was large enough to produce significant stationary crossflow amplitudes in the previous experiment. For the present configuration, there is no evidence of stationary crossflow with this polished surface, and transition occurs well beyond the pressure minimum. This provides an extremely clean baseline condition.

Stationary crossflow is introduced by attaching arrays of artificial roughness elements at $x/c = 0.005$. Two new roughness types are used. The first type are circular plastic that have a very uniform height of 73 μm, very clean edges, and are easy to apply and remove. They can be stacked to produce a height of 146 μm. The second type is a paper dot with a height of 112 μm. Both dots have a diameter of 6.2 mm. The dots are applied as single elements and as spanwise arrays. The single elements are useful for tracking vortex paths. The full arrays produce crossflow wave patterns with well-defined spectral content.

Roughness Reynolds numbers, Re_k, vary between 42 and 195, depending on the flow parameters. For the higher Reynolds numbers, care must be taken to avoid the direct-tripping mechanism associated with three-dimensional roughness elements[17,46]. This mechanism occurs at high Re_k values, and is easily identified by the presence of a transition wedge beginning immediately behind the roughness element. For this experiment, the goal is to directly influence the *linear* modes of the boundary layer.

3 RESULTS

3.1 Basic State. The freestream turbulence level is an important parameter in crossflow experiments. Bippes & Müller[7,9,10] show that traveling crossflow disturbances dominate the flow in a high-turbulence wind tunnel, and stationary modes are more important in a low-disturbance environment. The ASU Unsteady Wind Tunnel has very low turbulence levels[47]. Most of the disturbance energy is concentrated in the lowest frequencies. With a filter pass band of 1–1000 Hz, the fluctuation level u'/U_∞ is measured to be 0.038%. With a pass band of 10–1000 Hz, the value for u'/U_∞ is 0.015%. Measurements of the pressure coefficient show that the experimental flow field is very close to that predicted by the theoretical codes. The data show very good agreement at all chord positions.

Previous experiments with this model in a crossflow-dominated configuration use naphthalene flow visualization as the standard vortex-location method[26,29]. For the present configuration with a clean surface, the naphthalene measurements show no trace of any stationary vortices. There is no jagged transition front like that found in the high-amplitude

crossflow experiments. This indicates a nearly disturbance-free baseline condition for comparison with the roughness configurations.

Figure 2 shows a set of 25 boundary-layer profiles obtained without roughness. These measurements are for direct comparison with later profiles with roughness installed. The profiles cover a span of 24 mm, or two wavelengths of the most-amplified stationary disturbance. The profiles appear as a single line in the plot, indicating a very clean basic state with no measurable stationary crossflow and no spanwise nonuniformities. Extensive spanwise scans verify this.

3.2 Boundary-Layer Scans With Roughness. A spanwise array of 6.2 mm-diameter, 117 μm roughness elements is installed at $x/c = 0.005$, with a spanwise spacing of 12 mm. Figure 3 shows a spanwise array of 25 boundary-layer scans for the same flow conditions as in Fig. 2. With the roughness in place, significant boundary-layer distortions are present, indicating substantial stationary crossflow disturbances. Disturbance contours obtained by subtracting the mean profile are shown in Fig. 4. These shapes clearly indicate a stationary crossflow structure. Velocity contour plots corresponding to Fig. 3 and 4 are shown in Fig. 5 and 6. These plots show the entire velocity field in the (y,z) plane for the u component of velocity. The flow is toward the reader, and the stationary vortices are turning in the right-handed sense. The crossflow disturbances are clearly visible, producing alternating regions of velocity surplus and deficit. A slight asymmetry gives a hint of the "rolling over" motion observed by Kohama et al.[28] at higher amplitudes.

Measurements at $x/c = 0.05$. show successful disturbance measurements in a boundary layer only 1 mm thick. The pattern here is more complex due to the presence of shorter-wavelength components, in agreement with linear theory. As the vortices develop, the shorter wavelengths decay, and the 12 mm mode corresponding to the roughness spacing begins to dominate. However, in contrast with linear theory, the overall amplitude does not increase, but instead decays.

Figure 7 shows a comparison of linear PSE computations (Arnal et al.[18]) and experimental crossflow modes. In this case, the PSE profiles have been scaled to match the experimental amplitudes, so that the shapes may be compared directly. The remarkable agreement verifies that the experimentally observed disturbances are indeed the same stationary crossflow modes predicted by linear theory. It is important to note that even though linear theory is predicting the correct mode shapes, the growth rates are incorrect. This result will be made quantitative through the spanwise hot-wire scans. Boundary-layer measurements and mode-shape calculations are performed for many different roughness configurations and flow conditions. The results are similar in all cases, with linear theory severely over-predicting the growth rate.

3.3 Spanwise Scans With Roughness. A more careful comparison with linear theory is possible through the use of spanwise hot-wire scans at constant height in the boundary layer. These scans are easier to perform, have better alignment than the profiles, and allow spectral analysis for single-mode measurements. For the conditions of this experiment, scans at $u/U_e = 0.75$ are close to the maximum of the crossflow disturbance modes.

Figure 8 shows a spanwise scan at $x/c = 0.6$ with a full array of roughness installed at $x/c = 0.005$. The dominant 12 mm crossflow mode is clearly visible as a regular variation in the streamwise velocity. At $x/c = 0.3$, as with the boundary-layer scans,

shorter wavelengths are present, while the dominant longer-wavelength mode dominates at larger x/c.

Spanwise arrays of roughness elements are applied with a range of spacings in order to produce uniform stationary crossflow waves. Long spanwise scans (240 mm) are used to produce accurate average amplitudes, and also to provide enough resolution for wavelength discrimination. With spanwise wavelengths in the 10–12 mm range, at least 20 wavelengths are covered in a typical scan. The power spectrum is computed for each scan, using both MEM and FFT methods. Figure 9 shows a MEM spectrum for a scan taken with a roughness spacing of 36 mm. Dominant peaks can be observed at 36 mm, 18 mm, 12 mm, and 9 mm. The scans typically show peaks at the roughness spacing and the first few terms in the Fourier spectrum of the roughness, provided these smaller wavelengths lie in the unstable range. No significant peaks are observed at multiples of the roughness spacing. The spectral peaks are roughly fixed for all chord positions, and do not indicate any significant evolution of the dominant frequency. This indicates that initial amplitudes are as important as growth rates in determining which components will dominate the transition process.

Amplitudes can be obtained in several ways. For configurations with one dominant wavelength, amplitudes can be accurately estimated by simply taking the rms of the disturbance component of the scan. For more complex situations, the high resolution provided by the long scans allows a separate integration of each significant peak. Individual modes can be followed throughout their development, allowing meaningful comparisons with single-mode predictions from stability computations. Amplitude data are obtained for wavelengths in the 5–36 mm range.

The amplitude information extracted from the spanwise scans can be processed to obtain growth rates and N-factors, for direct comparison with linear stability predictions. Figure 10 shows a direct comparison of experimental and linear-theory N-factors for a pure stationary mode with a spanwise wavelength of 12 mm. The Orr-Sommerfeld and linear PSE calculations are performed by Arnal, et al.[18]. The SALLY results are based on Srokowski and Orszag[41]. The MARIA results are based on Dagenhart[36]. The experimental curve shows a behavior similar to that found in the boundary-layer scans. The amplitude decays at first, and then grows very slowly. All of the linear stability calculations show very large growth rates. In order to correct for curvature effects, the corrected version of COSCUR (Collier and Malik[35]) is used. These results are also shown in Fig. 10. COSCUR does not show growing modes before $x/c = 0.2$, so the growth is started at the experimental point at that location. The growth is not as large in this case but the sign is still wrong. Clearly, these linear calculations do not capture the behavior of realistic stationary crossflow waves. A nonlinear calculation is needed to account for the changes of the basic state due to the stationary vortices.

N-factor comparisons at other wavelengths show similar results. The discrepancy between theory and experiment seems to be largest for the shorter wavelengths, and smaller for the longer wavelengths. Figure 11 shows N-factors for a spanwise wavelength of 9 mm.

A direct comparison of wavelength dependence of growth rates is difficult without a receptivity calculation to account for the different initial amplitudes. An approximate evaluation can be made by comparing final amplitudes at $x/c = 0.6$ with total linear-

stability N-factors. Figure 12 shows that linear theory correctly predicts a maximum near $\lambda = 10$ mm.

3.4 Other Measurements. An extensive set of additional measurements creates a large database of detailed data for stability and receptivity code development. A total of 18 distinct run conditions and 24 data groups cover a wide variety of roughness configurations, including height and spacing variations, single and multiple roughness elements, and Reynolds number variations. Data sets include long-span arrays of boundary-layer scans containing over 5000 points, and extensive sets of spanwise scans with spectral information. These data are contained in Radeztsky [49].

4. CONCLUSIONS

Linear stability theory correctly predicts the expected mode shapes for stationary crossflow. When the computed and measured profiles are scaled and compared, the agreement is excellent. Moreover, linear theory correctly predicts the expected wavelengths for the crossflow modes. Short wavelengths dominate the flow early, and longer wavelengths dominate at larger chord locations. The most-amplified wavelength is correctly predicted.

Linear theory does not correctly predict the growth rates for stationary crossflow waves. The growth curves do not even have the correct sign. Linear theory often predicts strong growth where the amplitude is actually decaying. Previous experiments (Bippes [6,7]; Dagenhart [25]) showed the failure of linear theory for extremely large crossflow vortices. This experiment extends these results to include low-amplitude crossflow waves. The inclusion of curvature and nonparallel effects improve the predictions only marginally, and it is conjectured that a nonlinear calculation is required to obtain complete agreement.

ACKNOWLEDGMENTS

The experimental work was supported by NASA-Langley Research Center Grants NAG1-937 & 1111 and the Office of Naval Research Fellowship Program. Dr. H. Reed, Dr. J.R. Dagenhart, and Dr. D. Arnal provided theoretical and computational support.

REFERENCES

1. Reed, H.L., Saric, W.S. 1989. Stability of Three-Dimensional Boundary Layers. *Ann. Rev. Fluid Mech.* vol. 21, 235.
2. Arnal, D. 1992. Boundary-layer transition: Prediction, application to drag reduction. *Special Course on Skin Friction Drag Reduction, AGARD Report 786*, March 1992.
3. Arnal, D. 1993. Predictions based on linear theory. *Progress in Transition Modelling, AGARD Report 793*, March 1993.
4. Saric, W.S. 1992a. Laminar-Turbulent Transition: Fundamentals. *AGARD Report 786* (Special course on skin friction drag reduction) VKI, Brussels, March 1992.
5. Saric, W.S. 1994. Low-speed boundary-layer transition experiments. *Transition: Experiments, Theory & Computations*. Eds. T.C. Corke, G. Erlebacher, M.Y. Hussaini, Oxford.
6. Bippes, H. 1990. Instability feature appearing on swept wing configurations. *Laminar-Turbulent Transition, Vol III*, eds. D. Arnal and R. Michel, Springer-Verlag.
7. Bippes, H. 1991. Experiments on transition in three-dimensional accelerated boundary-layer flows. In *Proc. R.A.S. Boundary-Layer Transition and Control*, Cambridge, U.K.

8. Bippes, H., Nitschke-Kowsky, P. 1987. Experimental Study of Instability Modes in a Three-Dimensional Boundary Layer. *AIAA Paper No. 87-1336.*
9. Müller, B., Bippes, H. 1988. Experimental Study of Instability Modes in a Three-Dimensional Boundary Layer. In *Fluid Dynamics of Three-Dimensional Turbulent Shear Flows and Transition. AGARD C-P 438.*
10. Bippes, H., Müller, B. 1990. Disturbance growth in an unstable three-dimensional boundary layer. In *Numerical and Physical Aspects of Aerodynamic Flows IV* (ed. T. Cebeci). Springer.
11. Deyhle, H. Höhler, G., Bippes, H. 1993. Experimental investigation of instability wave-propagation in a 3-D boundary-layer flow. *AIAA J., vol. 31,* 637–45.
12. Kachanov, Yu.S., Tararykin, O.I. 1990. The experimental investigation of the travelling waves in a three-dimensional boundary layer. *Laminar-Turbulent Transition, Vol III,* eds. D. Arnal and R. Michel, Springer-Verlag.
13. Arnal, D. and Juillen, J.C. 1987. Three-dimensional transition studies at ONERA/CERT. *AIAA Paper No. 87-1335.*
14. Arnal, D., Juillen, J.C. 1988. Etude de la transition et de la contamination de bord d'attaque sur ailes en fleche. In *Fluid Dynamics of Three-Dimensional Turbulent Shear Flows and Transition. AGARD C-P 438,* October 1988.
15. Arnal, D., Casalis, G., Juillen, J.C. 1990. Experimental and theoretical analysis of natural transition on infinite swept wing. *Laminar-Turbulent Transition, Vol. III,* eds. D. Arnal and R. Michel, Springer-Verlag.
16. Arnal, D., Juillen, J.C., Casalis, G. 1991. The effects of wall suction on laminar-turbulent transition in three-dimensional flow. *Boundary Layer Stability and Transition to Turbulence, FED-Vol. 114,* Eds: D.C. Reda, H.L. Reed, R. Kobayashi, ASME.,
17. Juillen, J.C., Arnal, D. 1990. Etude expérimentale du déclencement de la transition par rugosités et par ranier sur de bord d'attaque d'une aile en flèche en ènçoulement incompressible. *CERT/ONERA Rapport Final 51/5018.35.*
18. Arnal, D., Casalis, G., Copie, M. 1994. *Personal Communication.*
19. Kobayashi, R., Kohama, Y., Kurosawa, M. 1983. Boundary-layer transition on a rotating cone in axial flow. *J. Fluid Mech. 127,* 341.
20. Kobayashi, R., Kohama, Y., Arai, T., Ukaku, M. 1987. The boundary-layer transition on rotating cones in axial flow with freestream turbulence. *JSME Int. J.* **30**(261), 423.
21. Kohama, Y. 1985. Flow structures formed by axisymmetric spinning bodies. *AIAA J., 23,* 1445.
22. Kohama, Y. 1987a. Some expectation on the mechanism of crossflow instability in a swept-wing flow. *Acta Mech. 66*:21–38.
23. Poll, D.I.A. 1984. Transition description and prediction in three-dimensional flows. *Special Course on Stability and Transition of Laminar Flows, AGARD Report 709,* March 1984.
24. Poll, D.I.A. 1985. Some observations of the transition process on the windward face of a long yawed cylinder. *J. Fluid Mech. 150,* 329
25. Dagenhart, J.R. 1992. Crossflow Disturbance Measurements on a 45 Degree Swept Wing. *PhD Thesis,* Virginia Polytechnic Institute and State University, July 1992. Also *NASA-TM-108650,* December 1992.
26. Dagenhart, J.R., Saric, W.S., Mousseux, M.C., Stack, J.P. 1989. Crossflow Vortex Instability and Transition on a 45-Degree Swept Wing. *AIAA Paper No. 89-1892.*
27. Dagenhart, J.R., Saric, W.S., Mousseux, M.C. 1990. Experiments on swept-wing boundary layers. *Laminar-Turbulent Transition, Vol III,* Ed. D. Arnal, Springer.
28. Kohama, Y., Saric, W.S., Hoos, J.A. 1991. A High-Frequency Secondary Instability of Crossflow Vortices that leads to Transition. *Proc. R.A.S. Boundary Layer Transition and Control,* Cambridge UK.

29. Radeztsky, R.H. Jr., Reibert, M.S., Saric, W.S. 1993a. Effect of Micron-Sized Roughness on Transition in Swept-Wing Flows. *AIAA Paper No. 93-0076.*
30. Gregory, N., Stuart, J.T., Walker, W.S. 1955. On the stability of three-dimensional boundary layers with applications to the flow due to a rotating disk. *Phil. Trans. Roy. Soc. Lon., A248,* 155.
31. Arnal D. 1984. Description and prediction of transition in two-dimensional incompressible flow. *Special Course on Stability and Transition of Laminar Flows, AGARD Report 709*, March 1984.
32. Balakumar, P., Reed, H.L. 1991. Stability of three-dimensional supersonic boundary layers. *Phys. Fluids A, 3,* 617.
33. Cebeci, T., Stewartson, K. 1980. Stability and transition in three-dimensional flows. *AIAA J., vol. 18,* 398.
34. Chen, H.H., Cebeci, T. 1990. An evaluation of stability-based methods for transition of three-dimensional flows. *Laminar-Turbulent Transition, Vol III,* eds. D. Arnal and R. Michel, Springer-Verlag.
35. Collier, F.S., Malik, M.R. 1988. Curvature effects on stability of three-dimensional laminar boundary layers. *AGARD C-P 438.*
36. Dagenhart, J.R. 1981. Amplified Crossflow Disturbances in the Laminar Boundary Layer on Swept Wings with Suction. *NASA TP-1902.*
37. Malik, M. R. 1982. COSAL—A black box compressible stability analysis code for transition prediction in three-dimensional boundary layers. *NASA CR-165952.*
38. Nayfeh, A.H. 1980a. Stability of three-dimensional boundary layers. *AIAA J., vol. 18,* 406.
39. Nayfeh, A.H. 1980b. Three-dimensional stability of growing boundary layers. *Laminar-Turbulent Transition,* ed: R. Eppler and H. Fasel, Springer-Verlag.
40. Parikh, P.G., Sullivan, P.P., Bermingham, E., Nagel, A.L. 1989. Stability of a 3-D wing boundary layer on a SST configuration. *AIAA Paper No. 89-0036.*
41. Srokowski, A.J., Orszag, S.A. 1977. Mass Flow Requirements for LFC Wing Design. *AIAA Paper No. 77-1222.*
42. Mack, L.M. 1984. Boundary-layer linear stability theory. Special Course on Stability and Transition of Laminar Flows, *AGARD Report 709*, March 1984.
43. Somers, D.M., Horstmann, K.H. 1985. Design of a Medium-Speed Natural-Laminar-Flow Airfoil for Commuter Aircraft Applications. *DFVLR-IB/29-85/26.*
44. Saric, W.S., Dagenhart, J.R., Mousseux, M.C. 1989. Experiments in Swept-Wing Transition. *Numerical and Physical Aspects of Aerodynamic Flows, Vol. IV,* Ed. T. Cebeci, Springer-Verlag, 1990, 359 (first appeared Jan. 1989).
45. Radeztsky, R.H. Jr., Reibert, M.S., Takagi, S. 1993b. A software solution to temperature-induced hot-wire voltage drift. In *Proc. Third International Symp. on Thermal Anemometry*, ASME-FED, Washington, DC.
46. von Doenhoff, A.E., Braslow, A.L. 1961. The Effect of Distributed Surface Roughness on Laminar Flow. *Boundary Layer Control, Vol.II.* Ed. Lachmann, Pergamon.
47. Saric W.S. 1992b. The ASU Transition Research Facility. *AIAA Paper No. 92-3910.*
48. Kaups, K., Cebeci, T. 1977. Compressible laminar boundary layers with suction on swept and tapered wings. *Journal of Aircraft* **14**, 7.
49. Radeztsky, R.H. Jr. 1994. Growth and development of roughness-induced stationary crossflow vortices. *PhD Thesis*, Arizona State University, March 1994.

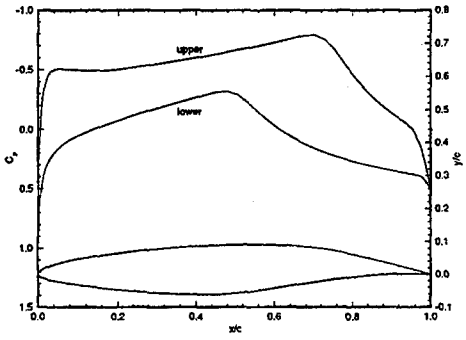

Fig. 1. Unswept NLF(2)-0415 airfoil coordinates and design C_p at $\alpha = 0°$

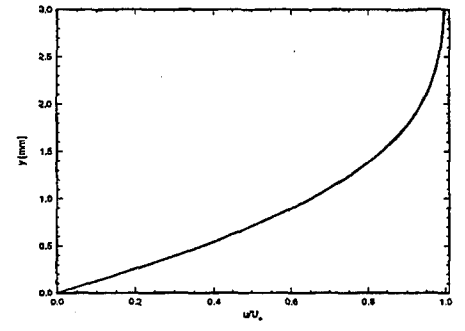

Fig. 2. Spanwise array of boundary-layer scans at $x/c = 0.60$. No roughness. $Re_c = 3.2 \times 10^6$.

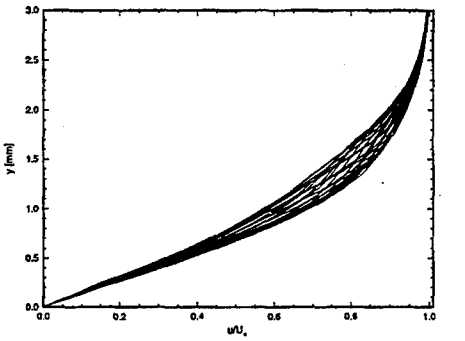

Fig. 3. Spanwise array of boundary-layer scans at $x/c = 0.60$. A 10-element array of 117 mm roughness with a spacing of 12 mm is at $x/c = 0.005$. $Re_c = 3.2 \times 10^6$.

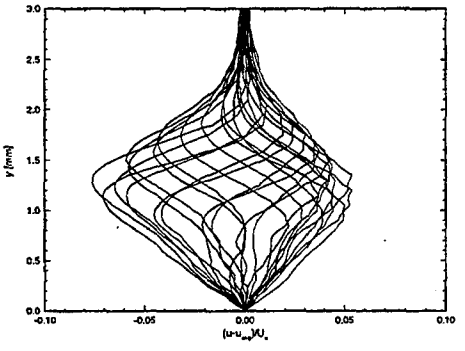

Fig. 4. Disturbance profiles for boundary-layer scans at $x/c = 0.60$. A 10-element array of 117 mm roughness with a spacing of 12 mm is at $x/c = 0.005$. $Re_c = 3.2 \times 10^6$.

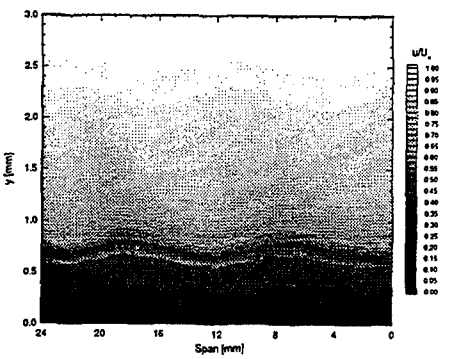

Fig. 5. Velocity contours at $x/c = 0.60$, showing total u component. A 10-element array of 117 mm roughness with a spacing of 12 mm is at $x/c = 0.005$. $Re_c = 3.2 \times 10^6$.

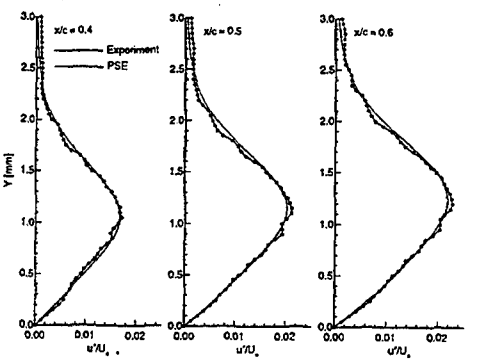

Fig. 7. Comparison of measured and theoretical stationary crossflow mode shapes. Spanwise array of 146 mm roughness at $x/c = 0.005$, 12 mm spacing. $Re_c = 3.0 \times 10^6$.

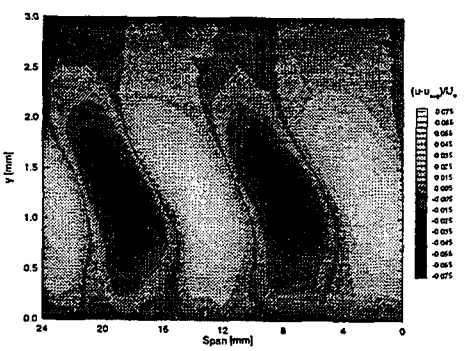

Fig. 6. Disturbance contours for boundary-layer scans at $x/c = 0.60$. A 10-element array of 117 mm roughness with a spacing of 12 mm is at $x/c = 0.005$. $Re_c = 3.2 \times 10^6$.

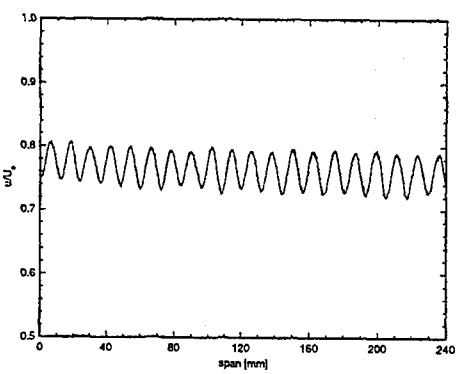

Fig. 8. Spanwise hot-wire scan at $x/c = 0.60$. Spanwise array of 146 mm roughness at $x/c = 0.005$, 12 mm spacing. $Re_c = 3.0 \times 10^6$.

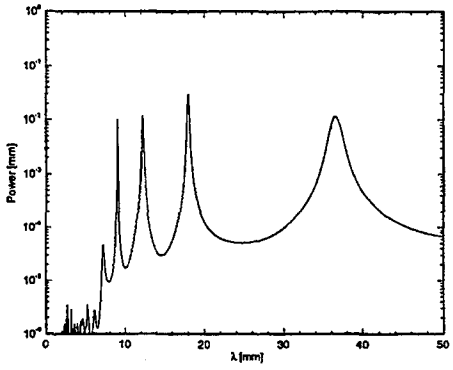

Fig. 9. Maximum-entropy power spectrum of spanwise hot-wire scan. Spanwise array of 146 mm roughness at $x/c = 0.005$, 36mm spacing. $Re_c = 3.0 \times 10^6$.

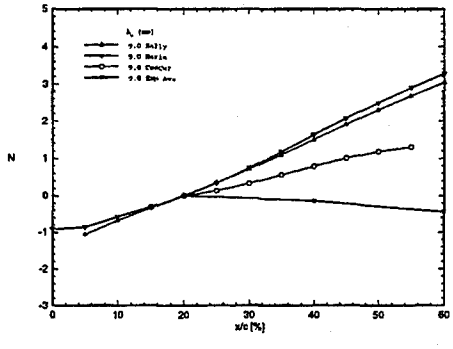

Fig. 11. Measured and theoretical relative N-factors for $\lambda_s = 9$ mm. Reference point is $x/c = 0.20$. $Re_c = 3.0 \times 10^6$.

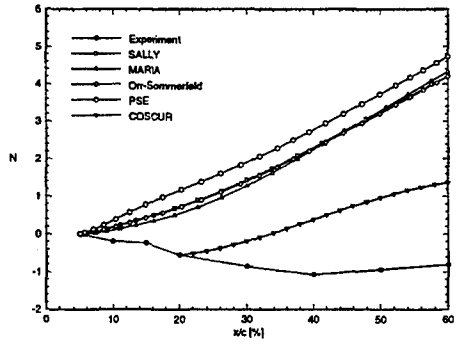

Fig. 10. Measured and theoretical N-factors for $\lambda_s = 12$ mm. Reference point is $x/c = 0.05$. Growing solutions from COSCUR begin at $x/c = 0.20$. $Re_c = 3.0 \times 10^6$.

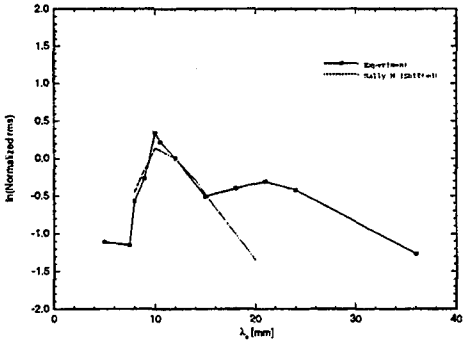

Fig. 12. Comparison of measured roughness sensitivity and SALLY N-factors. $Re_c = 3.0 \times 10^6$, $\alpha = 0°$.

EXPERIMENTAL, COMPUTATIONAL and THEORETICAL TECHNIQUES OF THE SIMULATION of HYPERSONIC FLOWS in TsAGI WIND TUNNELS

V.Ya.Neiland, Deputy Director of TsAGI, Zhukovsky, Russia

Abstract

Different experimental,computational and theoretical techniques to simulate the flow near a hypersonic vehicle streamline have been developed at TsAGI first to investigate a capsule flight (first-generation of HV), then Bor-4, the Buran-type orbiters (second-generation). It has been shown that only a combination of these three methods and comparison of the results with the data of the corresponding flight tests (on flying models) make it possible to obtain reliable data and minimize the expenditures on the program to develop a vehicle as a whole.

1. Introduction

Requirements to the aerodynamic test at hypersonic velocities are specified by the peculiarities of hypersonic vehicles, their shape, flight regimes, requirements to operational characteristics.

The evolution of flight vehicle shapes at hypersonic velocities has already passed two phases. The first phase is the most simple shapes of descending vehicles, the capsule -type. The second phase is orbiters of complex aircraft shapes of the Space Shuttle space stage-type, Buran-type and also vehicles with a lifting body, e.x., Bor-4. In the future we may expect the development of hypersonic aircraft or orbiters with air-breathing engines.

Hypersonic vehicles have an extremely wide range of flight regimes: from a free-molecular flight at hypersonic velocities in the regime of strong to weak viscous and non-viscous interaction to the flight at moderate and low velocities. (Flight regimes at mean and low velocities will not be considered in the report though they make a great influence on the selection of a hypersonic vehicle configuration (1)).

Besides a very wide range of Mach and Reynolds numbers (and Kn

as well), a hypersonic flight differ in a considerable effect of a number of physical effects that do not appear at lower velocities (dissociation, ionization, etc.).

The investigations have shown that a full simulation of a hypersonic flow over a hypersonic vehicle is impossible in ground installations; and it is also difficult to perform the simulation that is enough for practical purposes and a reliable simulation by CFD methods and/or it is very expensive.

Therefore to study hypersonic vehicle characteristics reliably and completely, a complex method "philosophy" has been developed that is based on theoretical methods, a corresponding test in hypersonic wind tunnels and CFD methods (computational aerodynamics).

The use of such a complex approach changes considerably an attitude to the estimation of hypersonic wind tunnels and test beds. As this takes place, some traditional estimations, that base simply on the use of a diagram (M,Re) or evaluate the usefulness of the installation from the stagnation enthalpy value, appeared to be either deficient or, in a number of cases, erroneous.

For example, high-enthalpy wind tunnels are inconvenient for the investigation of an air dissociation effect on aerodynamic characteristics due to the fact that it is impossible to simulate thermodynamics of a real streamline on one side and data on the distribution of internal energy between the degrees of freedom of molecules are not accurate enough to be used as a standard for the development of a mathematical model when we solve a problem by CFD methods.

Before presenting the correctness of the mentioned-above heads of the report on a number of examples in the main part of the report, I shall name one more notice of a general character.

An important feature of hypersonic wind tunnels is specialization of installations according to problems which is much more deep than at mean flow velocities.

In the following parts of the report, I shall consider examples of the utilization of TsAGI laboratory installations to solve the problems of aerodynamic heating and thermal protection and physical gas dynamics of the hypersonic vehicle flight. To solve

the problem of the hypersonic flight, we have used TsAGI's hypersonic wind tunnels that are presented in Tables 1, 2, 3. [2]

2. Hypersonic Aerodynamics Problems Study

Up to the present main studies in hypersonic aerodynamics have been performed for descending vehicles.

On the first portion of the atmospheric entry aerodynamic characteristics are usually obtained by computational methods (the Monte-Carlo methods). In this case, the reliable initial data on molecular accommodation coefficients, when interacting with the flight vehicle surface, are necessary. Since a direct interaction has a local character, it is enough to test small specimens. Characteristics of the installations of VAT-102, VAT-103, AT-2-type, etc. are presented in Table 3. Such an approach makes it possible to obtain the results that agree satisfactory with the flight test data (Fig.1).

The investigations of aerodynamic characteristics in the regimes of a "continuum" flight (usually H$\leqslant$70km) also are not provided by ground installations directly. The reason is that it is not possible to simulate even an equilibrium air dissociation in wind tunnels as the gas thermodynamic state "freezes" when the gas accelerates in the nozzle close to behind the critical section at full-scale temperature values (stagnation enthalpy in the classical-type wind tunnel). Therefore the gas superheat up to the temperatures that exceed the level that excludes condensation during the cooling, gives nothing to the solution of aerodynamic problems. Besides this effects unfavorably the most important problem to ensure a steady incoming flow. The comparison of the results also becomes difficult.

However the problem has been solved for hypersonic vehicles of the first- and second-generation by another method. Theoretical estimations have shown that aerodynamic forces and moments are determined with a high degree of accuracy by the streamline on the windward side for the vehicles that are characterized by a low and mean hypersonic L/D ratio and fly at large angles of attack (Fig.1^a). In the regimes when dissociation influences considerably aerodynamic moments and control efficiency, the tempera-

ture and gas pressure in this portion of the flow are high and dissociation is equilibrium. Therefore a developed approach consists of the utilization of the hypersonic wind tunnel T-117 (Table 1), the wind tunnel that operates on gases and has a specific heat capacity relation γ=Cp/Cv close to a full-scale one (IT-2, UT-1, Table 1) and solutions of Euler equations for equilibrium dissociated air. A detailed presentation of these results is given in the work [3]. In this report I shall give a total presentation of the test data in T-117, T-116 and also flight test data together with the computational data for the longitudinal moment and corrections for the air dissociation effect in Fig.2. I should note that this effect is important only for the determination of aerodynamic moments that should be equal to zero in the state of equilibrium. Therefore their distinguishing feature requires an additional control deflection that is not desirable. For example, during the first flight of "Colombia" the control deflection by 16^0 instead of 8^0 according to preflight estimations increased heat fluxes to the control surface approximately two-fold. The air dissociation influence on aerodynamic forces is not so important (e.x., Fig.3) and should be taken into account when generating the data bank of a hypersonic vehicle with the automatic control system as the scatter of characteristics is possible. The flight test plays a considerable role in verifying a reliability of the complex technique. The comparison of the preflight prediction data, based on the wind tunnel tests and computational data, with the flight test results rather good.

When we come back to the data in Fig.1^a, we can notice that if it is necessary to use a hypersonic vehicle with a high hypersonic L/D ratio, a number of new problems occurs. (The utilization of such vehicles can be a result of the necessity to obtain a longer side range during the recovery from the orbit, e.x., for landing in Europa from the near-equator orbit).

To obtain a maximum L/D ratio, it is necessary to perform flight at low angles of attack at which a vehicle leeward side begins to influence aerodynamic characteristics considerably. In this case, the utilization of simple mathematical models even for main regimes becomes impossible. It will be necessary to solve parabolized Navier-Stokes equations taking into account the final

rate of chemical reactions. Also the necessity to use hypersonic wind tunnels with higher pressure values in the prechamber (maybe, IT-2-type (Table 1) or new TsAGI wind tunnels even with higher stagnation pressure values which use for this the so-called pressure intensifiers for adiabatic compression of the operating gas appears.

3. Aerodynamic Heating and Heat Protection

The problems associated with aerodynamic heating of the orbiter and an improvement of its heat protection are more complex in their nature than those of determining aerodynamic characteristics. The reason for it is a stronger response of a slow flow in streamlines of the boundary-layer to various disturbances, e.x., effects of pressure gradients that may lead to flow separation and reattachment, to the formation of attachment lines at the vehicle surface, the influence of various even tiny variations of the streamlined body contour. These factors can result in narrow zones ("peaks") with local increase of heat fluxes. The surface quality, the values of Mach and Reynolds numbers, of the temperature factor, catalytic properties of the surface do influence significantly the level of heat fluxes over large portions of the vehicle surface. If the necessity of reproducing the laminar-turbulent transition and thermodynamic nonequilibrium is taken into account, it becomes obvious that a full simulation of the heat transfer to the orbiter surface is impossible. Therefore, when methods of determining the heat transfer are developed, it is extremely important to combine the methods of experimental studies with theoretical and computational ones. Figure 4 gives typical data on heat transfer rate distribution in the symmetry plane of the orbiter with deflected body flap (here q_0 is the heat transfer rate at a forward critical point). To obtain these results, Tempilaq is used that makes it possible to acquire rather accurate data on a continuous distribution of the heat flux and not to "miss" local peaks q. At most critical places special discrete-type transducers are used, some of them are shown in Fig.5.

However, these data are not always applicable to define the

temperature scheme for a real flight. Since there are no simultaneous simulations in Mach and Reynolds numbers, it is often necessary to resort to various correlation relationships. As an example of this approach, Fig.6 presents a correlation of test data for a heat transfer rate "peak" on the cockpit canopy at the point where there takes place the attachment of the boundary layer separated upstream of it. There exist formulae for corresponding entropy effects. When correlation formulae are chosen, it is important to visualize well enough the flow pattern near the surface (Fig.7-8). In this respect, much information on the flow field is contained in photos made using the "laser knife" technique (see, e.g., photos in Fig.9-11).

For the case of the application of insulation tiles numerous investigations were dealt with the problem of heating process in slots, an increase of heat fluxes when tiles fell out or protruded. Local characteristics of the boundary layer were simulated in the wind tunnel on a large-scale structural element with insulation tiles; typical results are shown in Fig.5.

The most complex phenomena requiring investigations are the effect of catalytic properties of surface insulation on heat transfer under the conditions of a thermodynamic nonequilibrium.

The influence of this effect on heat transfer and thermal protection surface temperature can be considerable. In Fig.12 are shown the experimental data obtained in a special plazmatron for catalytic and noncatalytic coatings and for dissociating gas (nitrogen) and one-atomic gas (argon). In the latter the effect is naturally absent. The amplitude differs considerably.

Figure 13 gives calculated temperature distributions over the vehicle surface in the symmetry plane of a large-scale (1:6) flying model for which the calculation techniques used for the "Buran" orbiter were evaluated. It is seen that when the catalytic activity measured in a WT using a special means of electrodeless gas heating (no impurities) is equal to 2 m/s the calculated results are verified well by flight test results. Figure 14 gives data temperatures distribution in equilibrium dissociated air and for real flight condition with noncatalytic surface.

4. Some Problems of Physical Gas Dynamics

Since a number of problems in this field have been considered above due to the effect on aerodynamics, I shall give only one example. This is the investigation of ionization near the vehicle. The problem is of interest as it has an effect on radio communication that, in its place, due to a possible disconnection in the radio communication makes the control system more complex and the requirement to determine aerodynamic characteristics, etc. to be more accurate.

In this case, also theoretical and computational studies, a test bed experiment in the IT-2 installation (hot-shot type, see Table 1) as well as the results of measurements on the Bor-4c model during the flight have been used. The mathematical model of the nonequilibrium ionization took into account for the mixture N_2 - O_2 an oscillating relaxation of the molecules N_2, O_2, NO, dissociation, ionization, possible chemical reactions between atoms, ions N_2^+, O_2^+, NO^+, molecules and electrons. The investigations have shown that the effect of impurities, that appear due to evaporation of the material of electrodes and the nozzle throat, is considerable for $T \leqslant 4000$ K. At higher temperatures the associative ionization NO^+ dominates as this occurs under the conditions of atmospheric flight. The developed theory has shown that for some regimes it is possible to obtain similar distributions of absolute values of the concentrations of electrons n_e in the wind tunnel and during the flight. In Fig 15. is given a comparison of the results of measurements in flight and in IT-2 experiment; the agreement of data is fully satisfactory.

References

1. V,Ya.Neiland. Aerothermodynamic configuration of the first generation orbiters (Buran-type) and the results of the first flight. The report at "The First European Symposium on the Orbiter Aerothermodynamics", the Netherlands, 28-30.05.1991.

2. V.Ya.Neiland. "Overview of TsAGI wind tunnels". The conference "Wind tunnels and test technique". Great Britain, September 14-17, 1992.

3. V.Ya.Neiland. "The effect of the air dissociation on the orbiter aerodynamic characteristics". Journal of Aircraft, v.30, N4, 1993.

1. Aerodynamic characteristics and heat transfer

Facility	Type	M range velocity	Max P_t Atmos	Max T_t K	Max Re · 10^{-6}	Mean Exit Diam D cm	Test time sec	Parameter F,p,T	Comment
1	2	3	4	5	6	7	8	9	10
T-33	B	3; 4; 5	8	750	9 at M=3 2.4 at M=5	30	300	p,T	Air
T-116	B	1.8-5; 6; 7; 9; 10	80	1075	16.8 at M=4 5.1 at M=5	100	300	F,p,T	Air
T-117	B	10; 12; 14; 18; 20.5	160	2600	2 at M=10	100	120	F,p,T	Air
T-120	C	4; 6; 8; 9; 10	140	1100	5.1 at M=4	15	>60	F,p,T	Air
T-121	C	4; 5; 6; 7; 8; 9	90	960	4.7 at M=5	20	>60	F,p	Air
ИТ-2	Hot shot	16.3-17.9 10-22	1500	5000	1.2 at M=16.33 10 at M=10	44 20; 53; 90	0.1	F,p,T	N_2 CO_2 Air
УТ-1	Ludwig HST	5; 6; 8; 10; 15.5 8-He; 6; 8-CF_4	150	2200	23 at M=6 Air	30; 40; 50	<<1	F,p,t	Air Ludwig He 5; 6; 8; 10 CF4 Shock 10; 15.5
ГТ-1	B	17-25	40	300		15	≈1	F,p	He
ГТ-2	B	8-Air,He, CF_4 16-22 He	40	800	1.3 at M=8 Air	30	1	F,p,T	Air He CF_4
ВАТ-3	B	12 20	60	2000	0.12 at M=12 H=75-100km	15:30	0.07-5	F,p,T	N_2 CO_2

2. Thermal protection

Facility	Type	M range velocity	Max P_t Atmos	Max T_t K	Max Re · 10^{-6}	Mean Exit Diam D cm	Test time sec	Parameter F,p,T	Comment
1	2	3	4	5	6	7	8	9	10
T-34	B	1-9	100	4000	2.9 at M=5	35	300	p,T	Air Tests Heatprotection Materials
T-122	B	4; 8	10	5000		3 x 18	1800	p,T	Tests Heatprotection Materials
BAT-104	Vacuum T.	4-8 V=4.2 km/sec	0.4	8000 Induction-heated	0.001 at l=0.05m H=70-80 km	Core of Flow ≤5 cm	3600	p,T	Determination of Air Catalytic Properties N_2 and Emissivity Ar
BTC	Vacuum T.	4-6	0.8	8000 Induction-heated	0.003 at L=0.05m H=60-80 km	4 cm	3600	p,T	Material life testing Air
T-123	B	7-20; 1-7	200 50	5000 4000	4.6 at M=7	30 2.2; 3; 5; 8	180	F,p,T	Aerodynamics and Heatprotection, Materials testing

3. Physical gas dynamics and rarefield gas dynamics

1	2	3	4	5	6	7	8	9	10
ИТ-1	B	12.2; 15	120	950	0.49 at M=12.2	34 cm	0.3	F,p,T	N_2,; CO_2
	Hot shot	12.5-18.3	1200	2700	1.2 at M=13	24	0.1	F,p,T	N_2,; CO_2
BAT-102	Vacuum T.	5; 8 0.2-1.3 km/sec	0.1	1800	0.01 at L=0.05m H=85-105 km	20; 30 Core of Flow <10cm	>60	F,p,T	N_2 Electron beam gas heater
BAT-103	Vacuum T.	7 V=4-8 km/sec	0.4	6000 Induction-heated	0.3 at L=0.05m H=150-500 km	Core of Flow ≤10cm	>60	F,p,T	Air; N_2; He; Ar; Ar+O_2; He+O_2+Air
BAT-105	Vacuum T.	V=10-40 km/sec			10 at L=0.05m	Core of Flow ≤2 cm	>60	F,p,T	N_2,, Air, Ar
ТЭР		V=4-14 km/sec		4000-14000		5x12	10 msec		Air
JAT-2	C	Neutral flow M=6	Neutral flow V=6-15 km/sek		H=250-300 km	Core of Flow 6 cm		Accomodation coefficient estimation. Measuring device characteristics investigation.	
			Ionized flow V=4-10 km/sec		H=250-500 km				

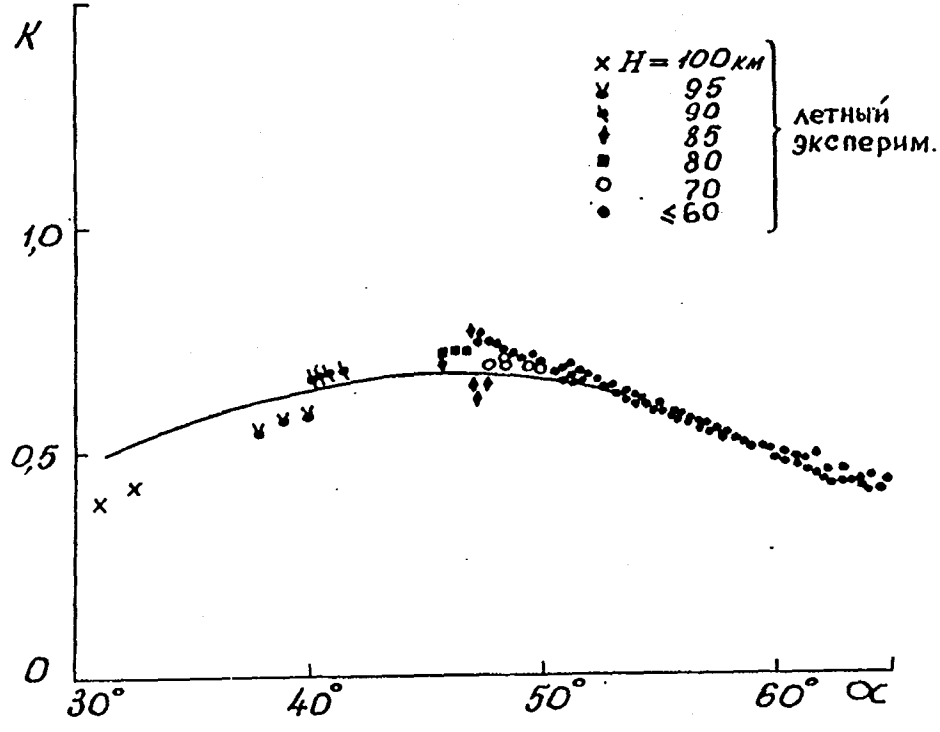

Fig. 1

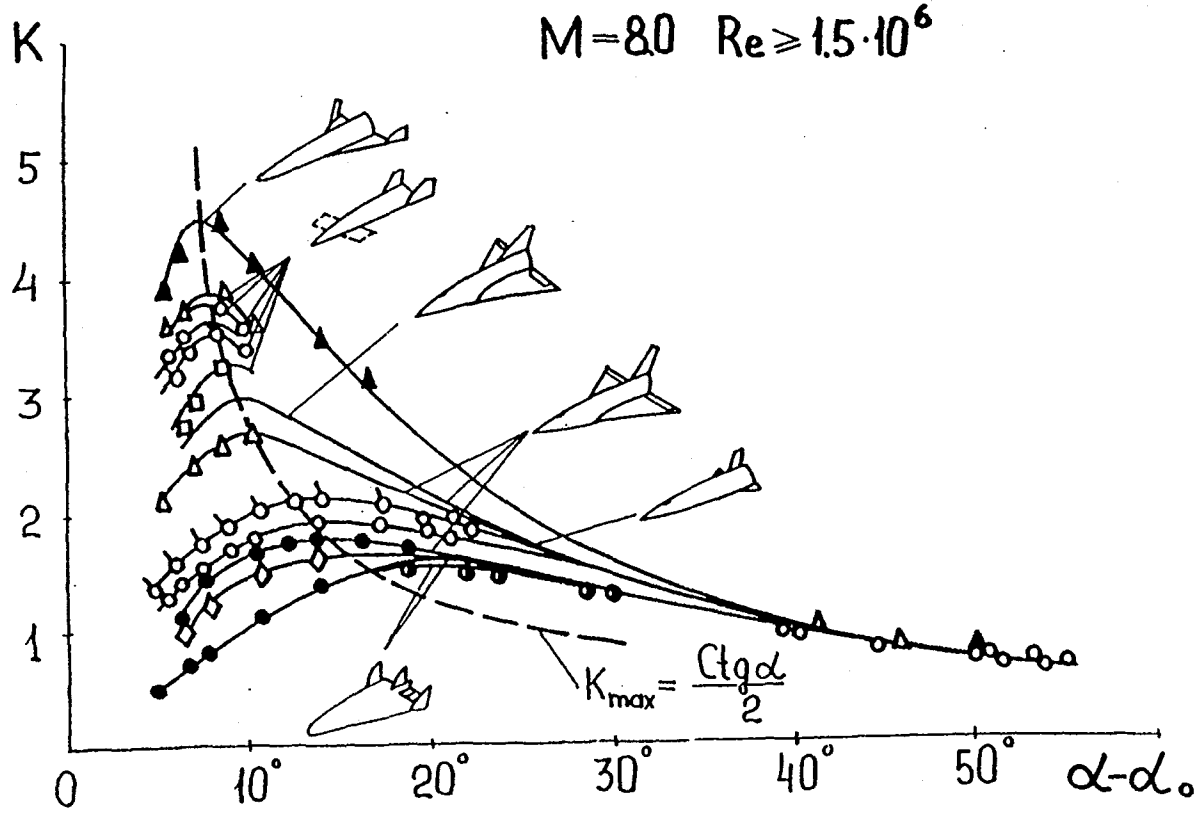

Fig. 1a

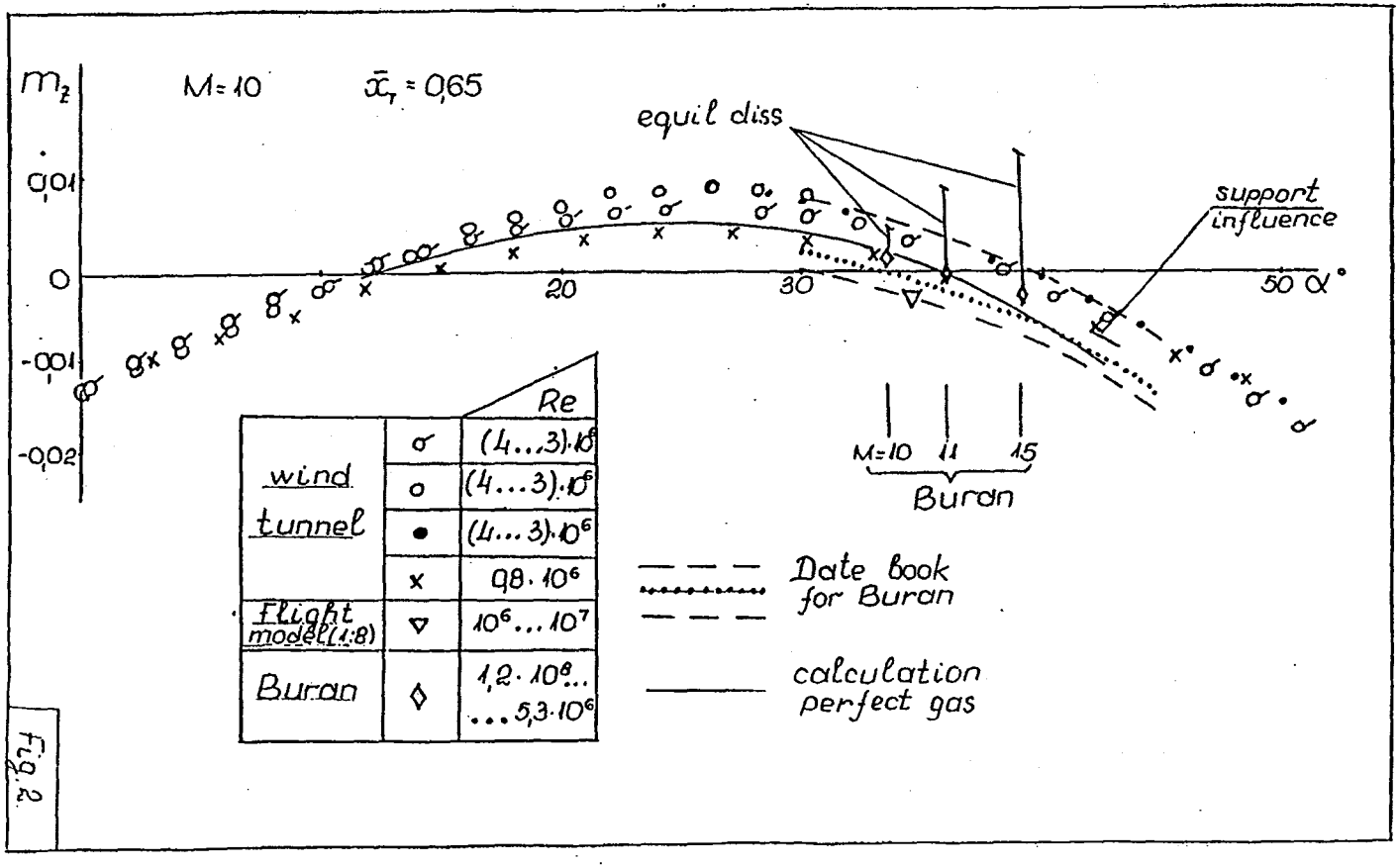
m_z
M=10
$\bar{x}_T$ = 0,65
equil diss
support influence
0,01
0
-001
-0,02
20
30
50 α°
M=10 11 15
Buran
Re
wind tunnel
σ (4...3)·10⁶
o (4...3)·10⁶
• (4...3)·10⁶
x 98·10⁶
Flight model(1:8)
▽ 10⁶...10⁷
Buran
◊ 1,2·10⁸...
...5,3·10⁶
Date book for Buran
calculation perfect gas

Fig. 2

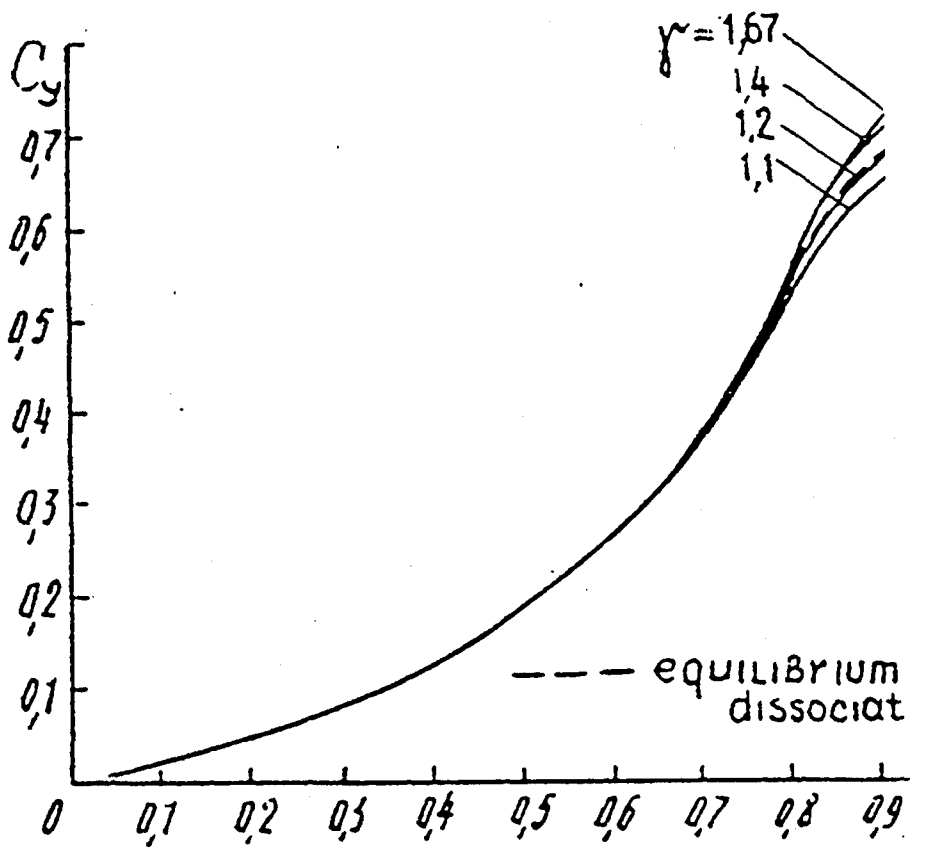
Cy
0,7
0,6
0,5
0,4
0,3
0,2
0,1
0
0,1
0,2
0,3
0,4
0,5
0,6
0,7
0,8
0,9
γ = 1,67
1,4
1,2
1,1
equilibrium
dissociat

Fig. 3

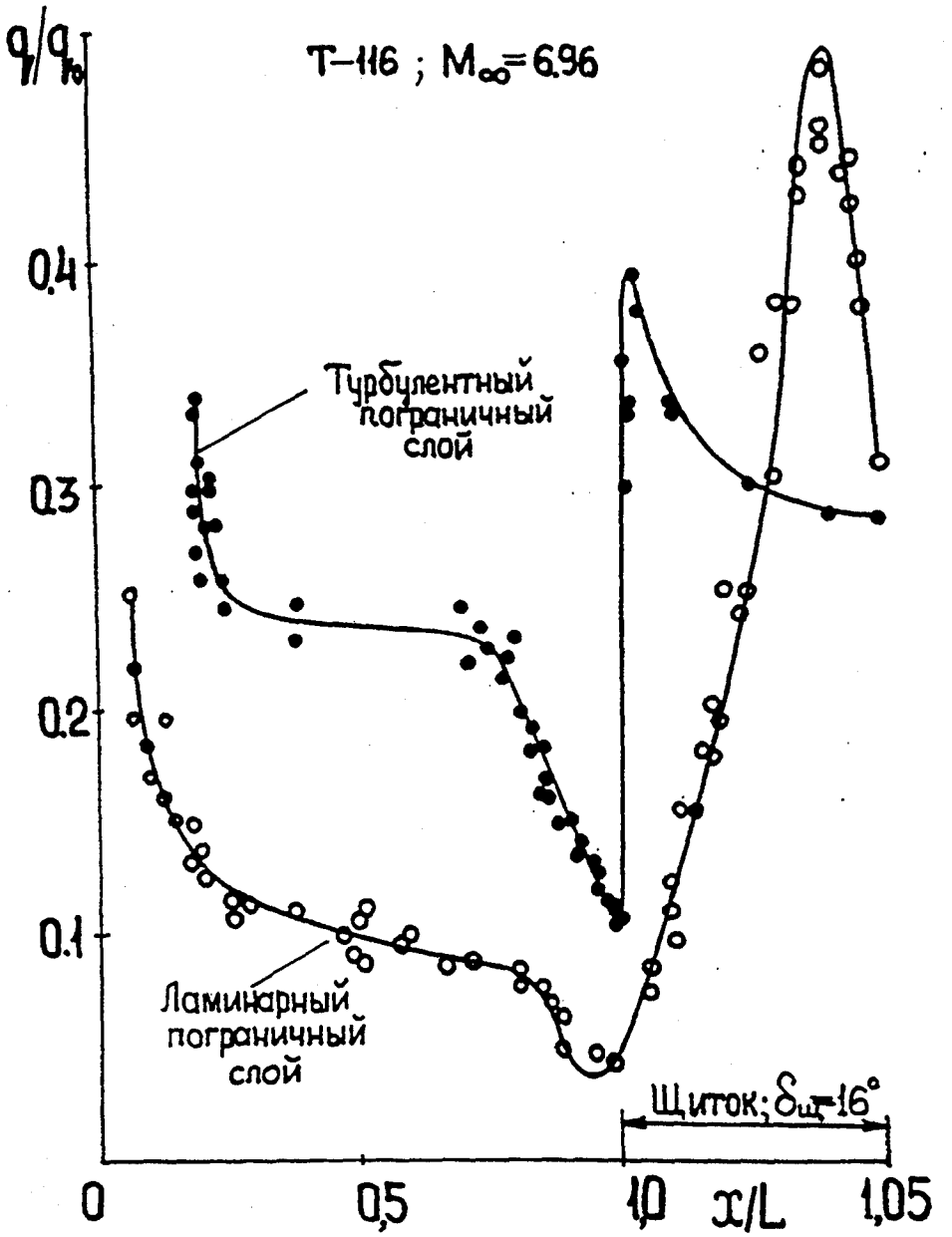
q/q∞
T-116 ; M∞=6.96
8
0.4
0.3
0.2
0.1
Турбулентный пограничный слой
Ламинарный пограничный слой
Щиток; δщ=16°
0
0,5
1,0
x/L
1,05

Fig. 4

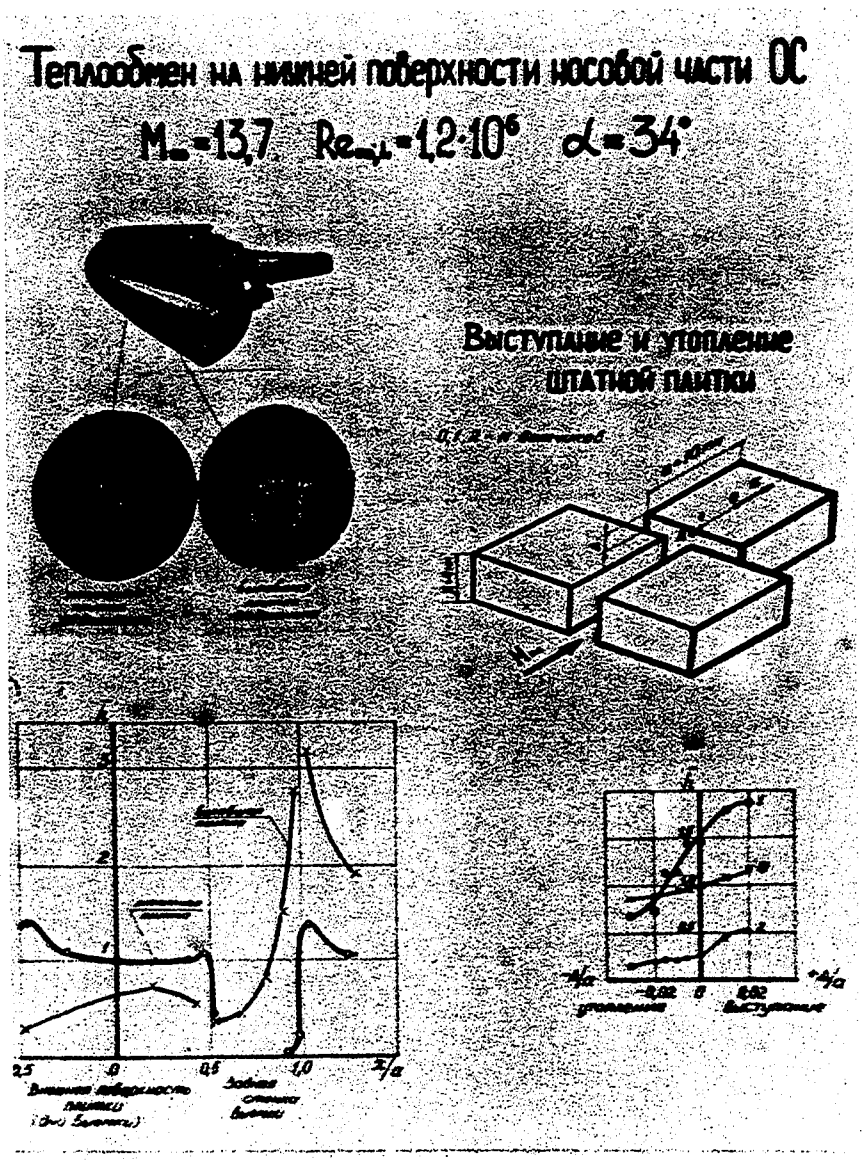
Теплообмен на нижней поверхности носовой части ОС
M∞=13,7 Re∞1=1,2·10⁶ α=34°
Выступание и утопление
штатной панели
-0,02
0
0,02
0,5
1,0

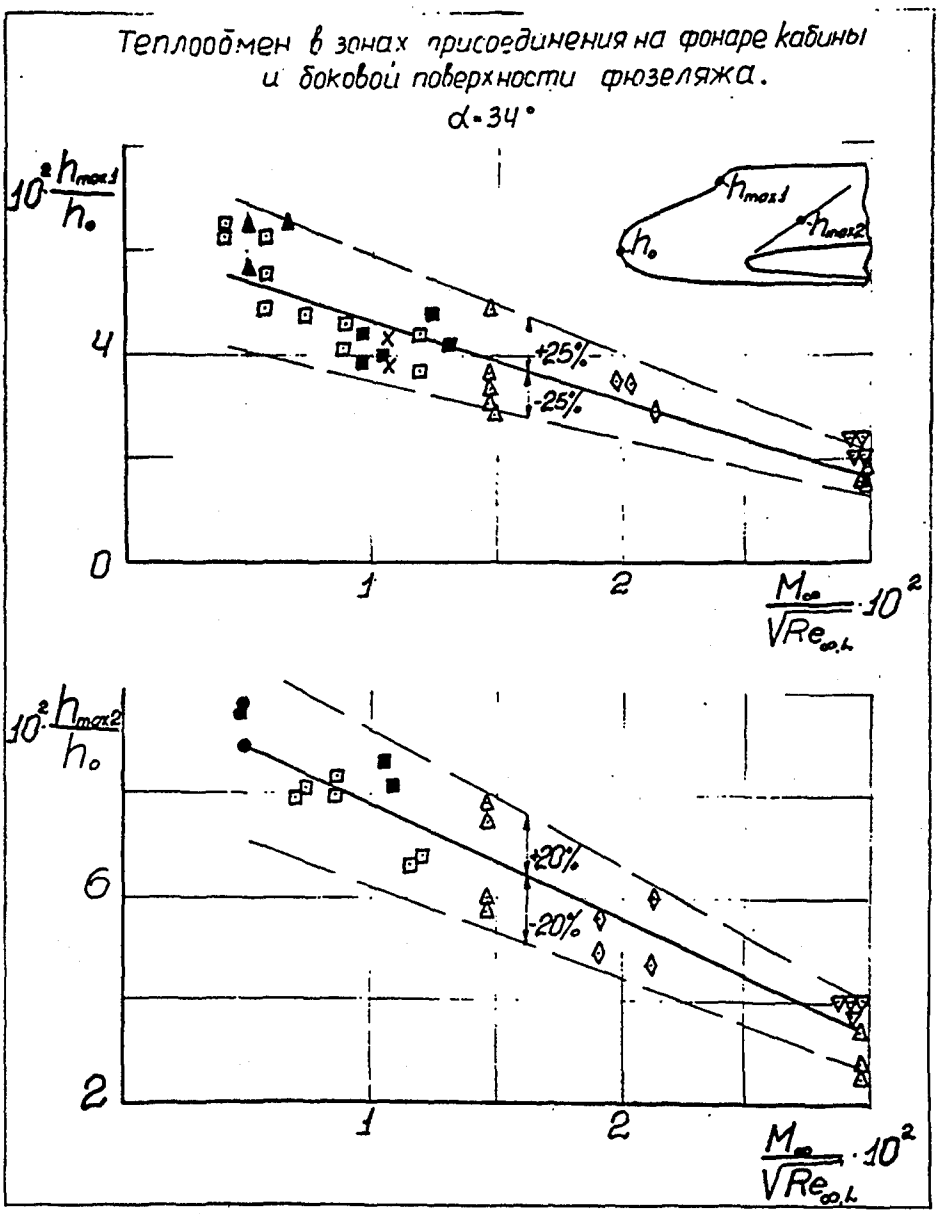
Теплообмен в зонах присоединения на фонаре кабины и боковой поверхности фюзеляжа.
α=34°
$10^2 \frac{h_{max1}}{h_0}$
h_{max1}
h_{max2}
h_0
4
0
+25%
-25%
1
2
$\frac{M_\infty}{\sqrt{Re_{\infty L}}} \cdot 10^2$
$10^2 \frac{h_{max2}}{h_0}$
6
2
+20%
-20%
1
2
$\frac{M_\infty}{\sqrt{Re_{\infty L}}} \cdot 10^2$

Fig. 6.

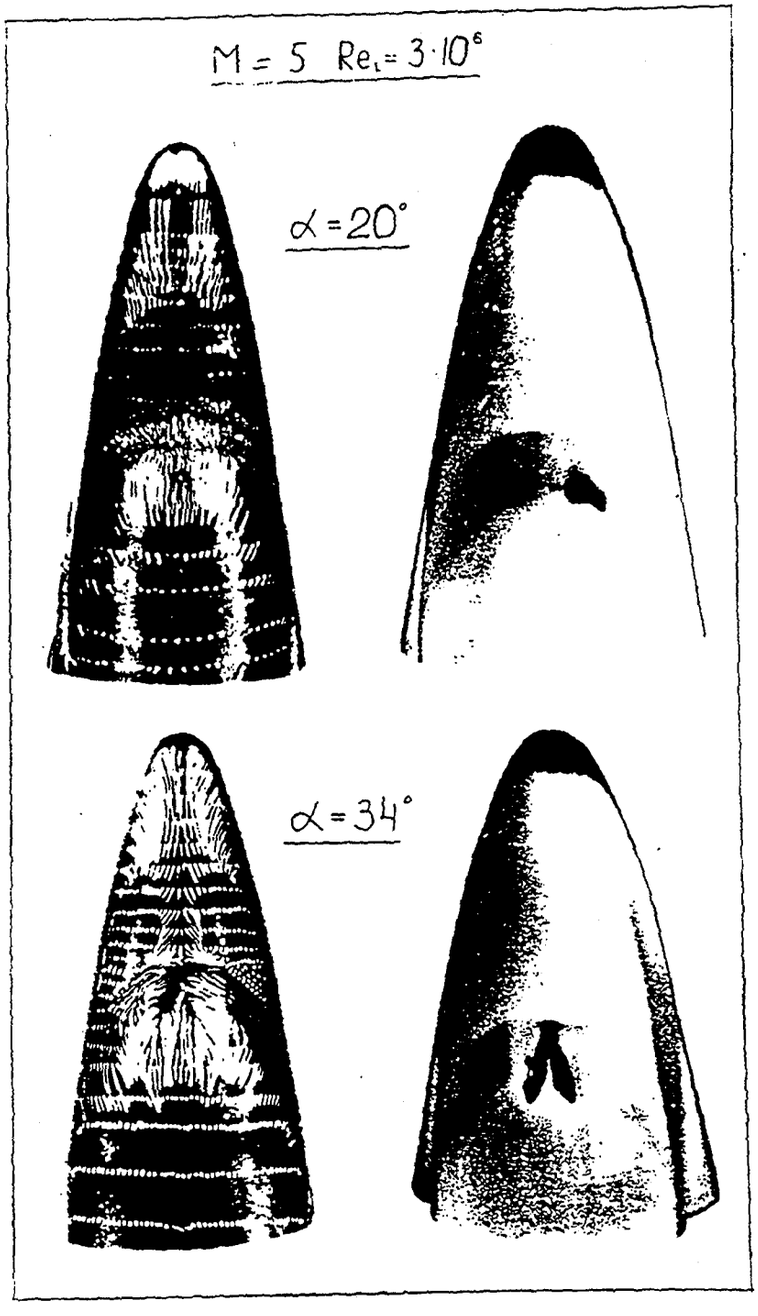

Fig. 7.

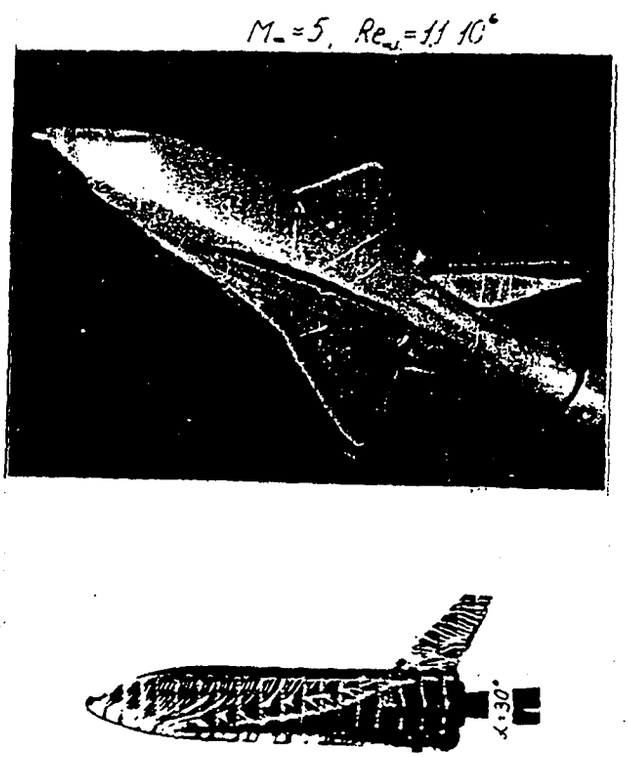

Fig. 8.

$M_\infty = 3 \quad \chi = 80° \quad \alpha = 2{,}5° \quad Re_{\infty} x = 4 \cdot 10^6$

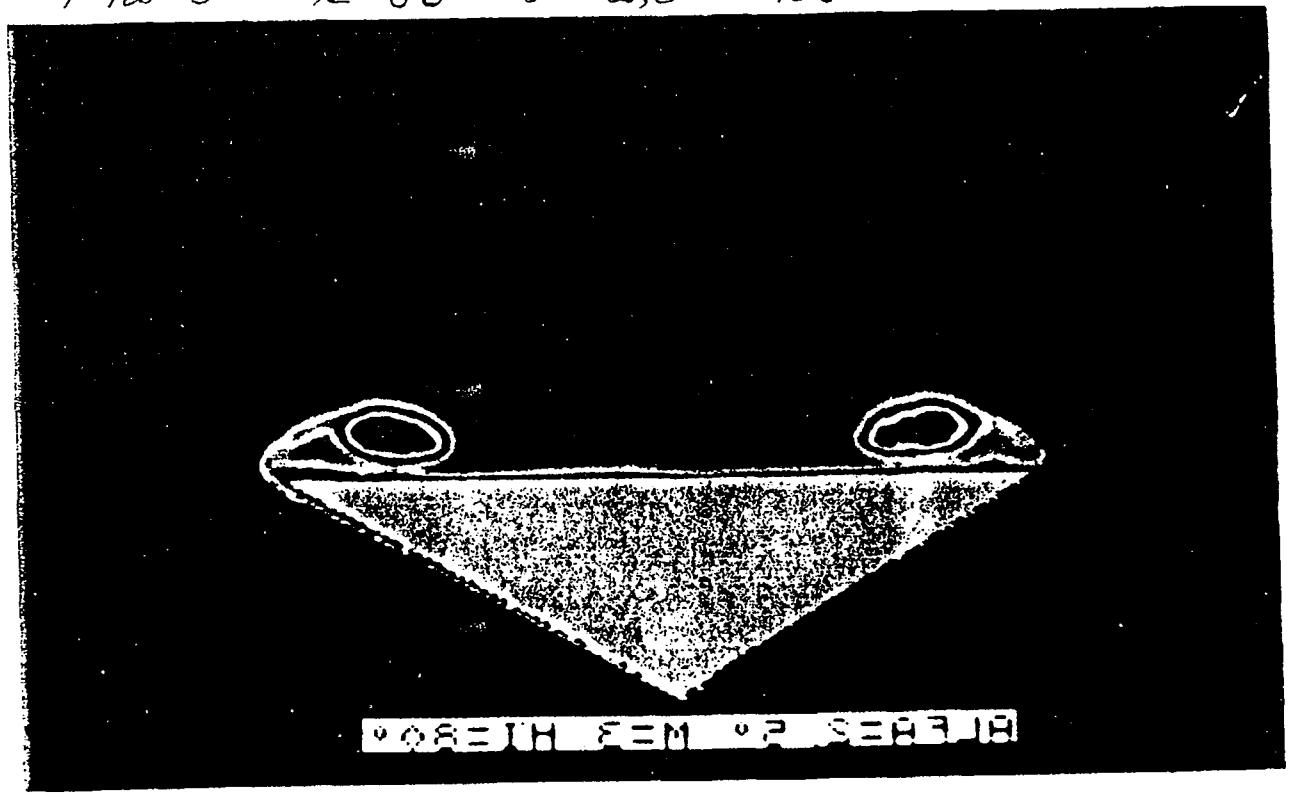

Fig. 9

$M_\infty = 3$ $\chi = 80°$ $\alpha = 10°$ $Re_{\infty x} = 4 \cdot 10^6$

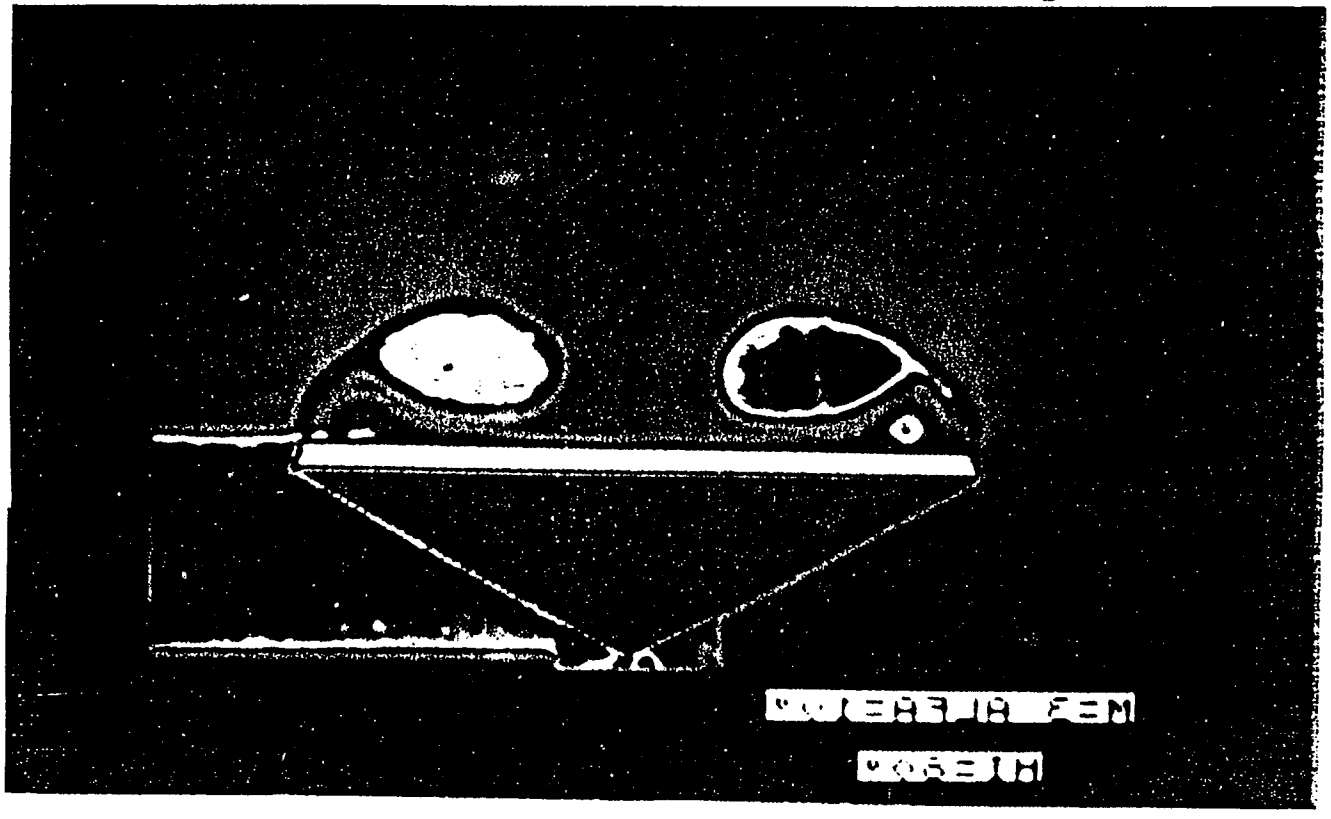

Fig. 10

$M\infty = 3 \quad \chi = 80° \quad \alpha = 25° \quad Re_{\infty x} = 4 \cdot 10^6$

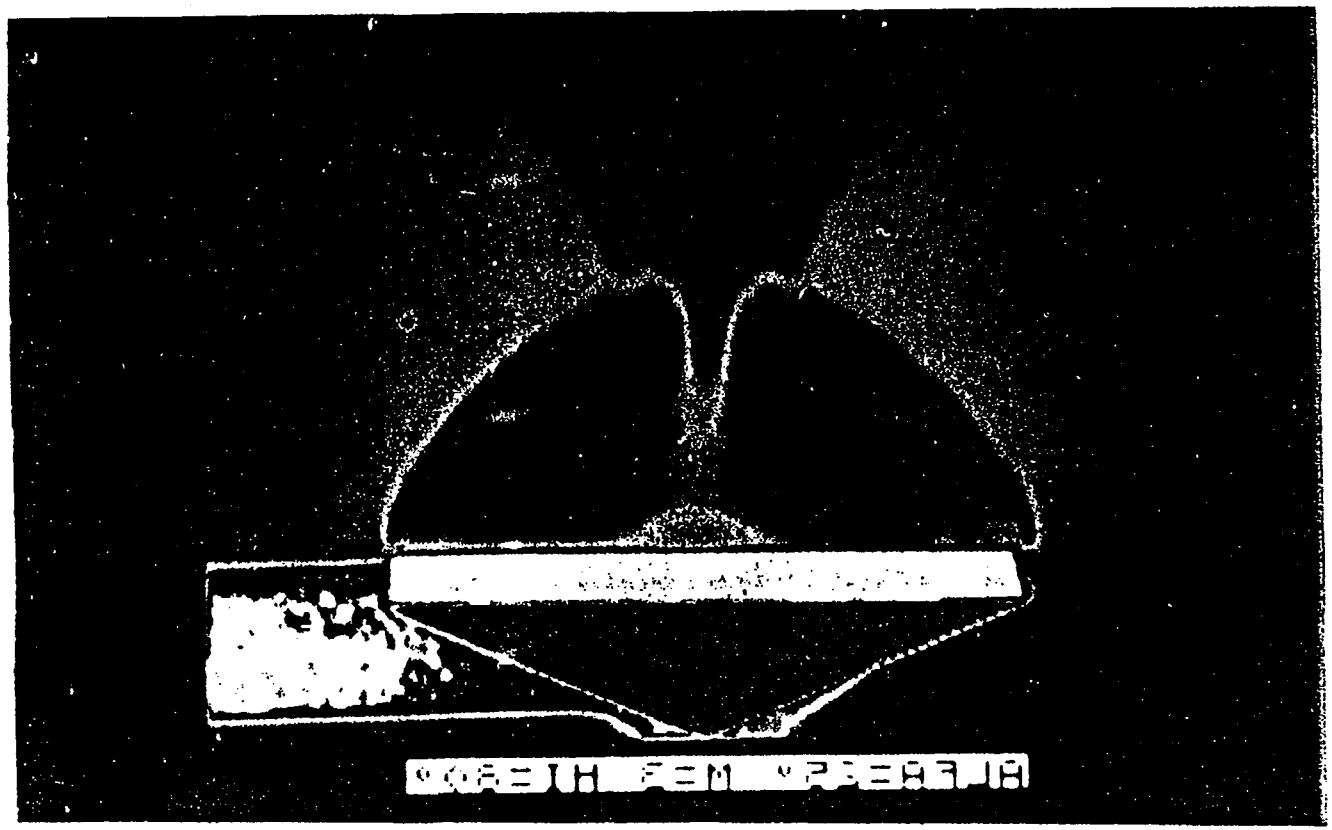

Fig 11

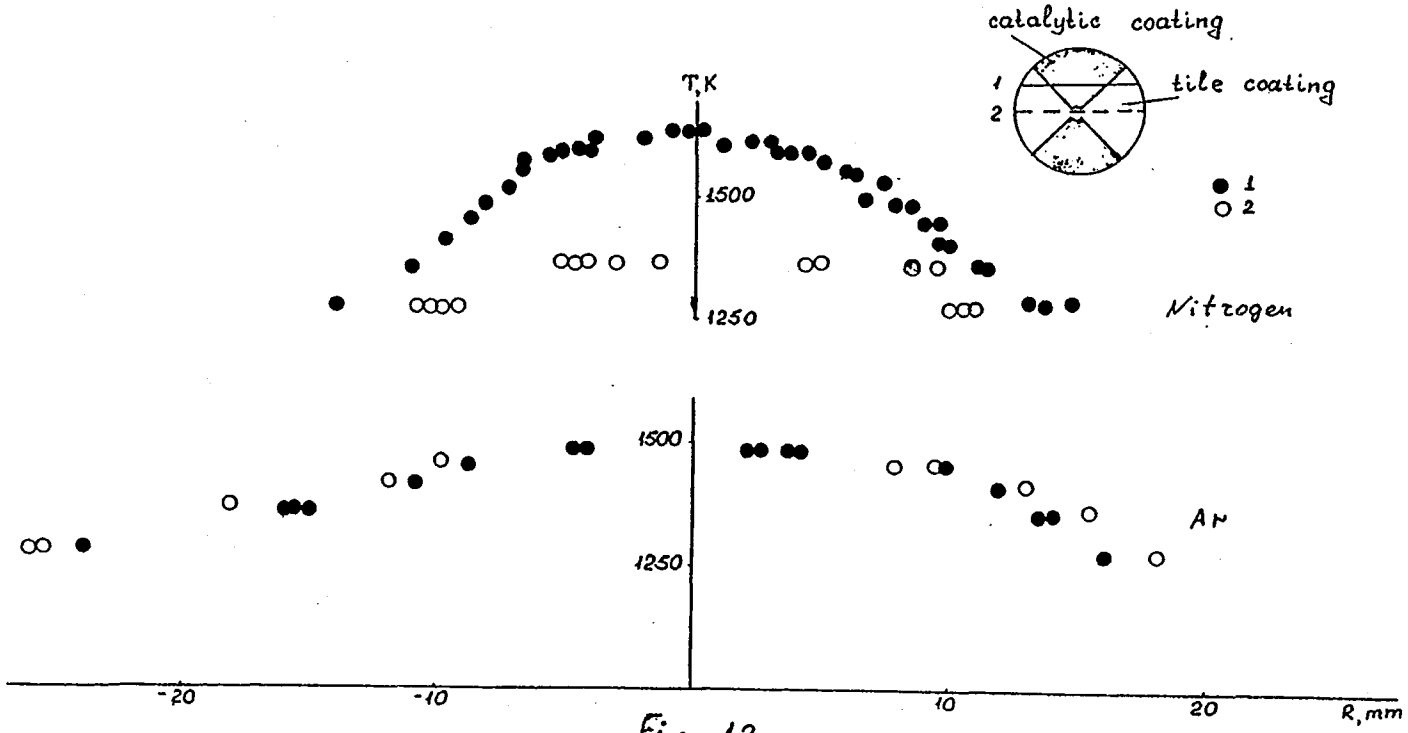
catalytic coating
tile coating
1
2
T, K
1500
1250
1 2
Nitrogen
1500
1250
Ar
-20
-10
10
20
R, mm

Fig. 12

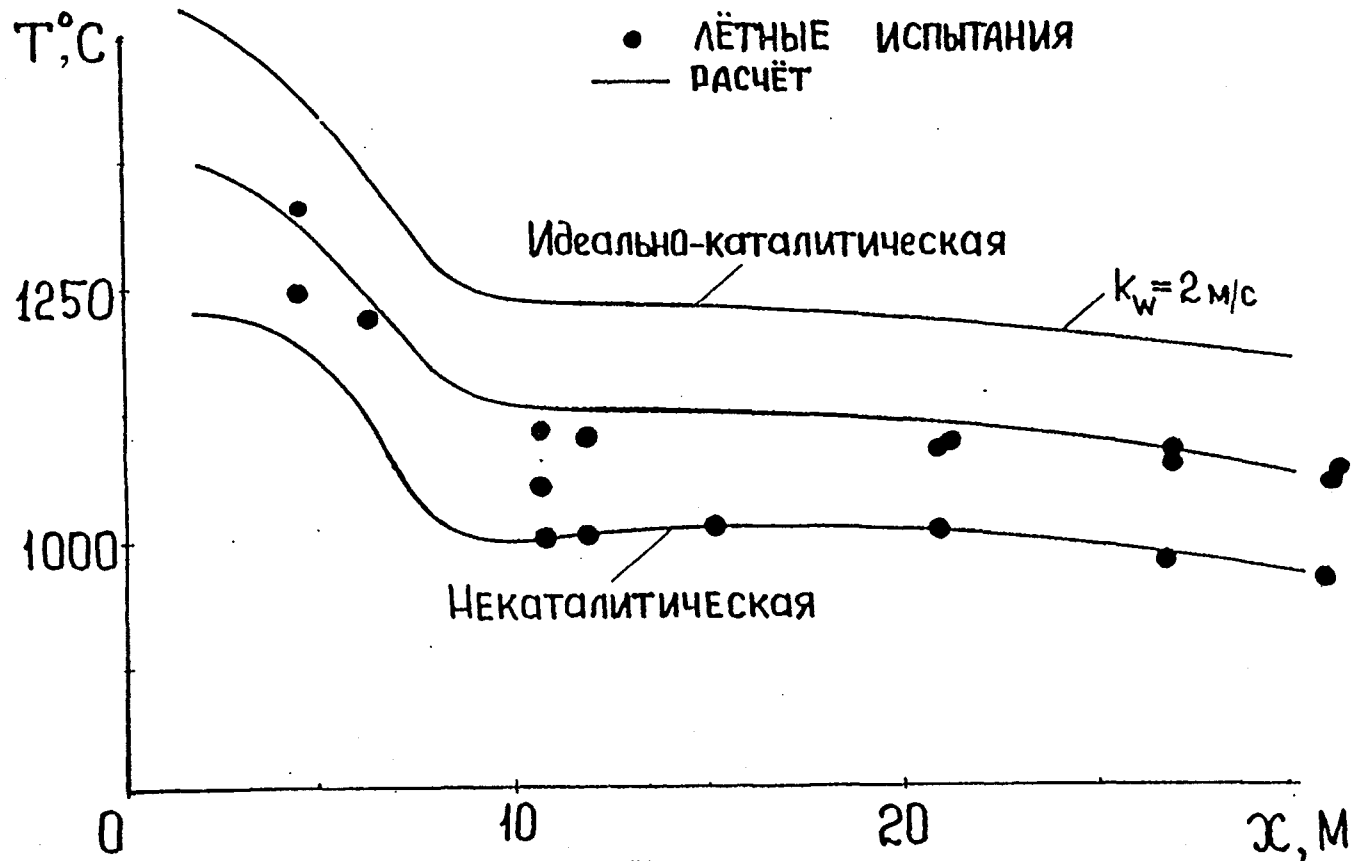
T°C
ЛЁТНЫЕ ИСПЫТАНИЯ
РАСЧЁТ
Идеально-каталитическая
k_w=2 м/с
1250
1000
Некаталитическая
0
10
20
x, м

Fig. 13.

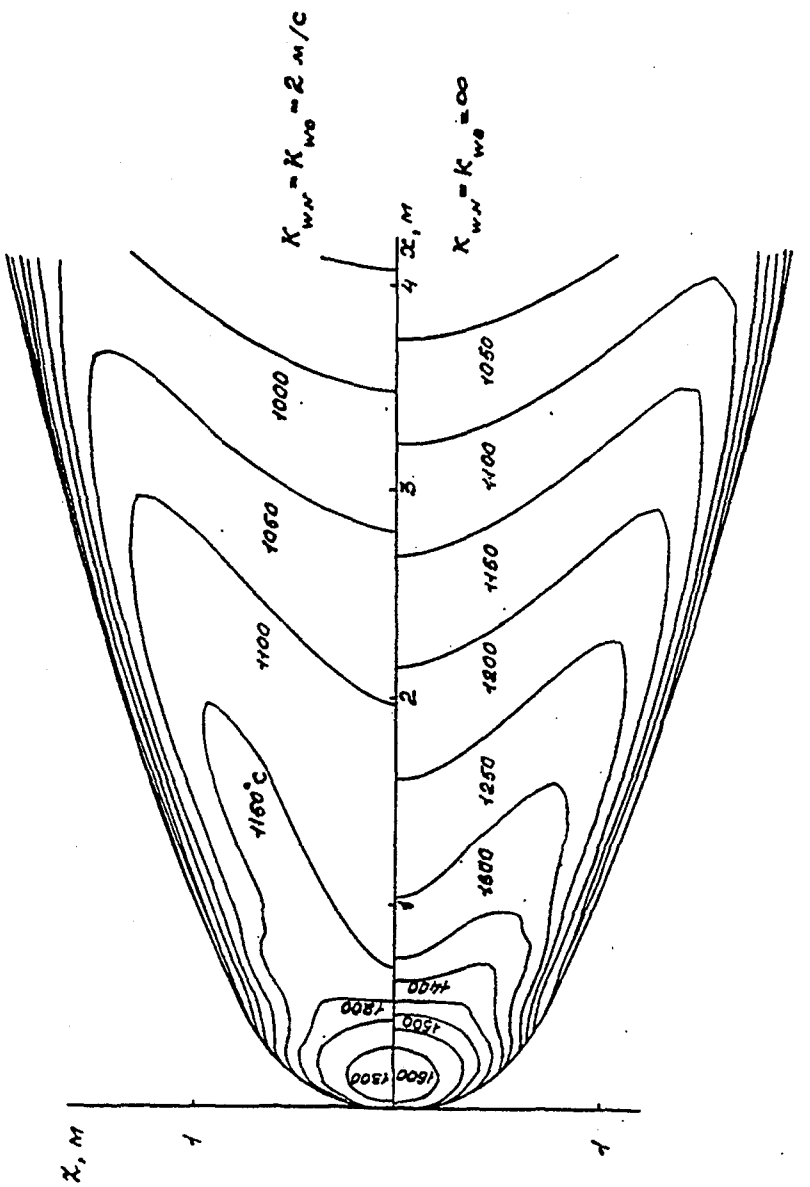
$K_{wx} = K_{wo} = 2$ м/с
$K_{wx} = K_{wo} = \infty$
x, м
4
3
2
1
1000
1050
1100
1150
1200
1250
1300
1350
1400
1450
1500
1550
1600
1650
1700
1750
1800
1850
1900
1950
2000
2050
2100
2150
1160°C
x, м
1
1

Fig. 14

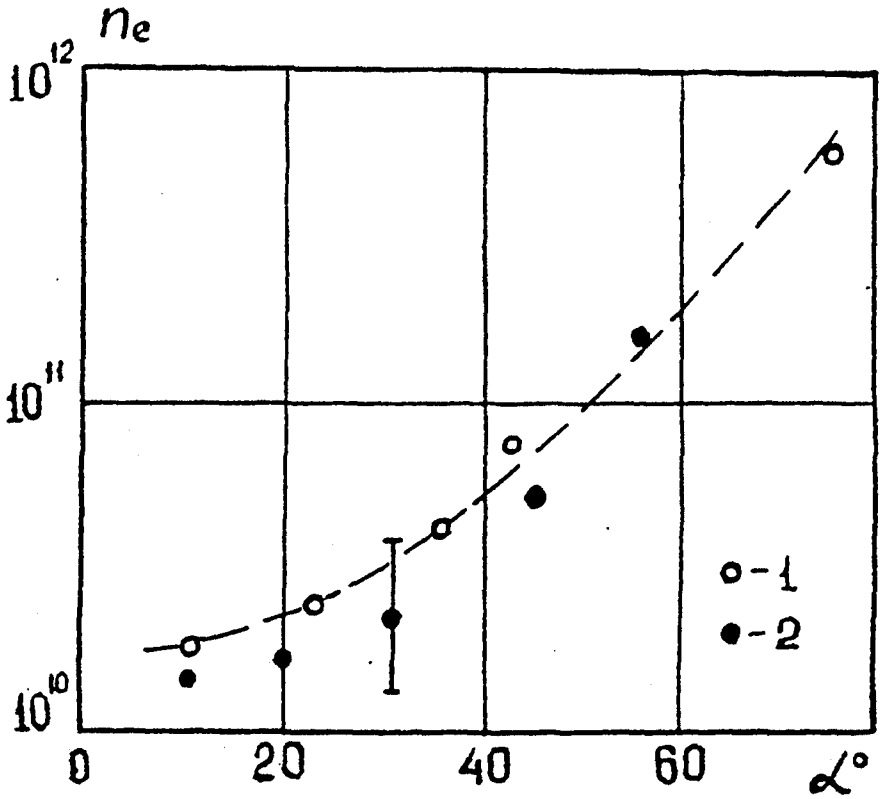

Fig.15 . Comparison of flight (HV Bor- 4c) and laboratory measured $\bar{n}_e$, α - angle of attack, 1- flight measured n_e, 2- "HOT-SHOT" measured n_e .

INVESTIGATION OF UNSTEADY FLOW FIELDS IN WIND TUNNELS AT HIGH FLOW VELOCITIES BY MEANS OF PARTICLE IMAGE VELOCIMETRY

J. KOMPENHANS, M. RAFFEL, A. VOGT, M. FISCHER, B. BRETTHAUER,
H. VOLLMERS, B. STASICKI

Deutsche Forschungsanstalt für Luft- und Raumfahrt (DLR)
Institut für Strömungsmechanik, Göttingen, Germany

Particle Image Velocimetry (PIV) is increasingly used to investigate unsteady velocity fields instantaneously. For the first time the PIV technique allows the recording of a complete velocity field in a plane of the flow within microseconds. This does not only give information about unsteady flow fields otherwise not obtainable but also helps to save operational time in the wind tunnel. At DLR a set up for PIV has been developed which can be operated under the rough environmental conditions (noise, vibrations) of a large wind tunnel. This system has been successfully applied to low speed as well as to high speed flows (U = 5 ... 500 m/s). The evaluation and post processing of the PIV recordings run fully automatical on a workstation.

INTRODUCTION

Today PIV is applied to the investigation of flow fields in many different areas. This means that also a number of special implementations of the PIV technique had to be developed for such different applications as e.g. in biology or in turbomachinery. One important application of PIV at industrial research is in aerodynamics. A PIV system for the investigation of air flows in wind tunnels must be be operated as well in low speed flows (e.g. flow velocities of $\approx$ 5 m/s in boundary layers) as in high speed flows (flow velocities up to 500 m/s in transonic flows with shocks). Flow fields above solid, moving, or deforming models have to be investigated. Special problems appearing at the application of the PIV technique in large, industrial wind tunnels are: large observation area, long distances from observation area to the light source and the camera for recording, only limited time available for the measurement, and high operational costs.

In spite of all these severe problems, the use of the PIV technique is very attractive in modern aerodynamics, because it helps to understand unsteady flow phenomena as e.g. in separated flows above models at high angle of incidence. PIV enables spatially resolved measurements of the instantaneous flow velocity field within a very short time and allows to detect large and small scale spatial structures in the flow velocity field, which is not possible by means of other measuring techniques. Another problem of modern aerodynamics is that the increasing number and increasing quality of numerical calculations of flow fields require adequate experimental data for validation of the numerical codes in order to decide whether the physics of the problem has been modelled correctly. Carefully designed experiments have to be performed in close cooperation with those scientists doing the numerical calculations. The experimental data of the flow field must possess high resolution concerning time and space in order to be able to compare them with high density numerical data fields. The PIV technique is such an appropriate experimental tool, if information about the instantaneous velocity field is required.

The description of the problems as given above leads to the definition of boundary conditions which should be fulfilled for application of PIV in aerodynamics. First of all a high spatial resolution of the data field is required in order to resolve large scale as well as small scale structures in the flow. This boundary condition directly influences the choice of the recording medium. Photographic film (24 × 36 mm² format) can have a resolution of more than 100 line pairs per mm (lp/mm) whereas a CCD chip for video recording with e.g. 2048 × 2048 pixels and 25 × 25 mm² sensor size achieves only 40 lp/mm. Therefore, at present the photographic recording technique is used by us due to its higher spatial resolution, though the video technique would have higher flexibility and easier handling by avoiding the wet photographic process - features, which are also very important for the application of PIV in wind tunnels. A second important boundary condition is that a high density of experimental data is required for a meaningful comparison with the results of numerical calculations. Thus, the image density (i.e. number of particle images per interrogation spot) must be high. This requires a powerful seeding generator (high concentration of tracer particles in the measuring volume in the flow even at high flow velocities). As the flow velocity is measured indirectly by means of the measurement of the velocity of tracer particles added to the flow, the tracer particles must follow the flow faithfully. This means that very small tracer particles are required. However, small particles scatter little light. This fact results in a third important boundary condition for the application of PIV in aerodynamics: A powerful (and expensive) pulse laser is required for the illumination of the flow field.

EXPERIMENTAL SET UP FOR PIV

A summary of the theoretical and experimental aspects of the PIV technique is given by Adrian[1]. Our experimental set up of a PIV system for application in aerodynamics consists of several subsystems. First of all tracer particles, generated by an aerosolgenerator, have to be added to the flow. These particles have to be illuminated in a plane of the flow two times within a short time interval. The light scattered by the particles has to be recorded. The displacement of the particle images between the two light pulses has to be determined at the evaluation of the PIV recordings. In order to be able to handle the great amount of data, which are collected by employing the PIV technique, a sophisticated post processing system is required. The general concept for the development of our PIV system for application in wind tunnels was to have a system with the following features: robust and reliable; easy installation and adjustment; fast, but accurate evaluation; fully automatic evaluation (because of the large amount of data); automatic validation of data; easy adaptation of PIV system to different wind tunnels and different aerodynamic problems.

Fig. 1 briefly explains the set up for recording. Small tracer particles are added to the flow (olive oil droplets, diameter ≈ 1 µm). A plane (light sheet) within the flow is illuminated two times by means of a Nd:YAG pulse laser (wavelength $\lambda = 532$ nm, energy 70 mJ per pulse, pulse length 20 ns, time delay between pulses ≈ 20 µs - depending on the flow velocity and the magnification at imaging). It is assumed that the tracer particles move with flow velocity between the two illuminations. The light scattered from the tracer particles is recorded photographically via a high quality lens on a single photographical negative (KODAK TMAX film). This means we are employing the 'dual illumination - single frame' recording technique.

For evaluation the PIV recording (24 × 36 mm² format in our case) is interrogated in small sub areas (interrogation spots; diameter 0.7 mm, step size 0.5 mm). The local displacement vector for the images of the tracer particles is determined for each interrogation spot by means of statistical methods (autocorrelation). It is assumed that ali particles within one interrogation spot have moved homogeneously between the two illuminations. The projection of the vector of the

flow velocity into the plane of the light sheet (2d velocity vector) is calculated taking into account the time delay between the two illuminations and the magnification at imaging. The process of interrogation is repeated for all interrogation spots of the PIV recording (i.e. 70 × 48 interrogation spots for 35 mm film = 3500 velocity vectors/recording).

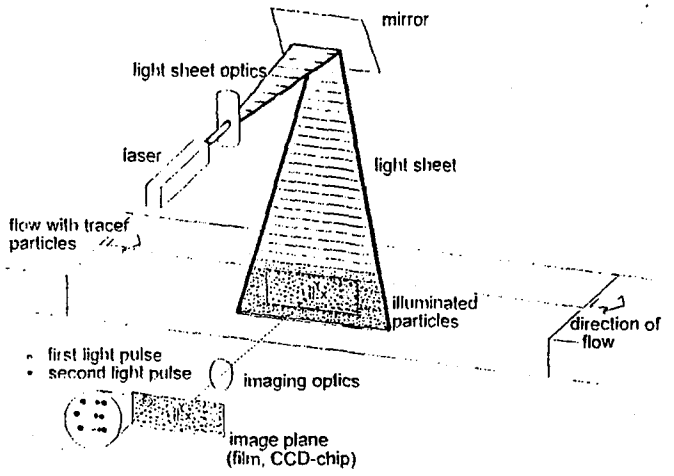

Fig. 1 Experimental set up for PIV recording in the wind tunnel.

After automatic evaluation of a PIV recording a certain number of obviously incorrectly determined velocity vectors can usually be found by visual inspection of the raw data. In order to get rid of these incorrect data the raw flow field data have to be validated. For this purpose special algorithms have to be developed, which must also work automatically [2]. These algorithms shall ensure with high level of confidence that no questionable data are stored in the PIV data set. Questionable data will be rejected, if it cannot be decided by application of the validation algorithm whether data are valid or not. It should be emphasized that for all PIV results presented in this paper only this validation algorithm has been applied after automatic evaluation.

A PIV system for application in wind tunnels also requires some special developments, which are not commercially available. One major problem is associated with the limited amount of light scattered by the small tracer particles. Typically, the depth of focus at recording is of the order of 1 mm in our experiments, which means that the intensity of the light as scattered by out-of-focus particles is not high enough to expose the photographic material. Already first PIV experiments in large wind tunnels have shown that a high quality and reliable fast focusing device is absolutely necessary, in order to save time at the alignment of the system. For this purpose our photographic 35 mm camera is equipped with a device for fast focusing [3]. We have mounted a CCD sensor in the viewfinder of a SLR camera. The position of the CCD sensor is carefully aligned in such a way that the distance between lens and CCD sensor via the mirror is exactly the same as from the lens to the the film plane. The distance between light sheet and film plane can be changed by moving the complete camera system by means of a traversing table, thereby observing for minimum diameter of the particle images on a TV monitor.

A second problem becomes obvious from the description of the recording and evaluation process as given above, i.e. the sign of the direction of the motion of the particles within each

interrogation spot cannot be determined if employing the 'dual illumination - single frame' recording technique since there is no way to decide which image is due to the first and which is due to the second exposure of a particle. Although, for many applications the sign of the velocity vector can be derived from a priori knowledge of the flow, in reverse flows, for example in areas of detached flow and in wakes behind models, steps have to be taken to determine the sign of the displacement and hence the velocity vector correctly. The great interest in PIV measurements in many different fields of research requires a flexible technique for ambiguity removal which can be applied to a variety of experimental situations. Especially for aerodynamic investigations it is very important to be able to apply this technique at high speed flows, i.e. with short time intervals of a few microseconds between both illuminations. Such a method is the image shifting technique as described by Adrian [4], which enforces a constant additional displacement, which must be greater than the maximum displacement due to the reverse flow, on the images of all tracer particles at the time of their second illumination. Only minor modifications of the evaluation technique by means of the autocorrelation method are required when applying the image shifting method for recording at PIV. At present the most widely used experimental technique for image shifting is to utilize a rotating mirror system. The observation area in the flow is imaged onto the recording area in the camera via a rotating mirror. The magnitude of the additional displacement of the images of the tracer particles depends on the number of revolutions of the mirror per time, the distance between light sheet plane and mirror, the magnification of the imaging system and the time delay between the two illuminations, see Landreth et al [5]. In order to achieve very high shift velocities electro-optical methods employing differently polarized light for illumination have been proposed and applied by Landreth and Adrian [6] and Lourenço [7]. The constant shift of the particle images is obtained e.g. by means of birefringent crystals of appropriate thickness. Problems as e.g 'depolarization effects' for bigger particles are associated with this technique.

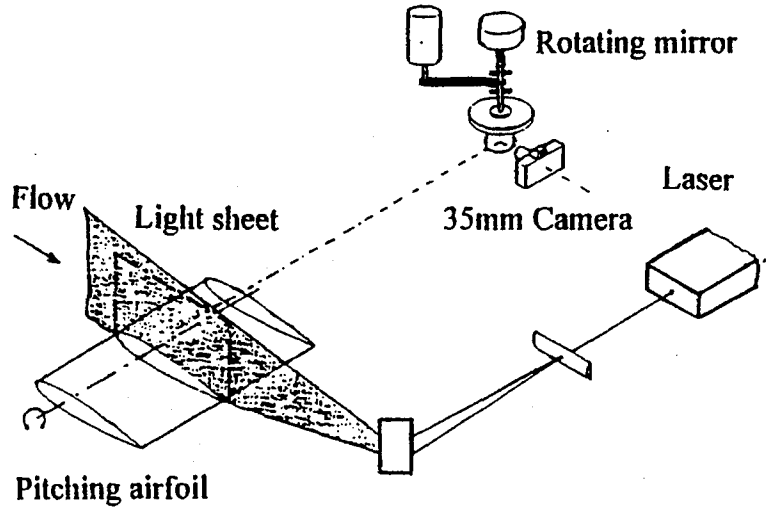

Fig. 2 Experimental set up for the recording of the instantaneous flow field above a pitching airfoil by means of a pulse laser, a rotating mirror system and a 35 mm photographic camera.

Due to our experience we see most practical advantages at aerodynamic investigations if applying a rotating mirror system for image shifting. A high speed rotating mirror system as described by Raffel [8] has been developed at DLR in order to be able to carry out measurements even in transonic flows. The frequency of rotation ranges from 1 Hz to 100 Hz, thus covering a range of shift velocities from 5 m/s to 500 m/s (at a ratio of reduction of 1:4 between observation plane in the flow to the recording plane). This system has been successfully applied to different aerodynamic investigations in wind tunnels. Fig. 2 shows the experimental set up for the recording of the instantaneous flow field above a pitching airfoil by means of a rotating mirror. A detailed analysis of the errors involved with image shifting by means of a rotating mirror has also been given by Raffel [8].

A third major problem at the application of PIV in wind tunnels is the short time available for the PIV recording, which requires a computer controlled automatic measurement with simultaneous acquisition of such data as pressure and temperature in the test section, or the actual angle of incidence of the model during the wind tunnel run. The whole measuring sequence, including the laser pulse (Pockels cell), the angular position of the rotating mirror, the film transport and shutter release of the camera must be synchronized.

Flow fields with the following parameters have been investigated by means of our PIV system as described above: velocity range: U = 0 ... 550 m/s, observation area: up to 300 × 200 mm^2, spatial resolution: ≈ 1-2 mm in the flow field (depends on magnification), dynamic range of velocity (without image shifting): 1 : 10, accuracy of velocity measurement: < 1 % of mean flow velocity. One statement should be made concerning the accuracy of the PIV technique. The absolute over-all accuracy of the PIV system depends on many different parameters and has to be checked separately for each experiment. It is no simple means available to check the accuracy of PIV against another measuring technique. Thus, usually it is tried to determine the accuracy of each individual component of the PIV system to derive a statement about the over-all accuracy, as has been done e.g. by Vogt [9]. One has to distinguish between three different error sources: the first one influences all velocity vectors of a PIV recording in the same manner (e.g. the magnification factor at imaging, scale factor of the evaluation system), the second one influences each velocity vector in a different, but steady way (e.g. velocity lag of tracer particles, optical distortion of the lens system, out-of-plane velocity component, errors due to image shifting) - however, neighbouring vectors are affected in a similar way, and the third one would be random errors associated with e.g. the evaluation process. The first two error sources would affect the appearance of spatial structures in the flow field only in a minor way. This means, we can demonstrate the relative accuracy of our system by successfully resolving very weak spatial structures in flow fields.

AERODYNAMIC APPLICATIONS

GRID TURBULENCE. Laminar and turbulent flow fields have been studied in order to obtain information on the accuracy attainable with the PIV technique. The experiments were carried out in a low turbulence wind tunnel (TUG), which is of an Eiffel type. Screens in the settling chamber and a high contraction ratio of 15:1 lead to a low turbulence level in the test section (cross section 0.3 × 1.5 m^2). The experiments were performed on the center line of the wind tunnel. Different grids can be installed near the end of the nozzle of the wind tunnel in order to generate turbulence. The basic turbulence level in the test section of the TUG of Tu ≈ 0.06 % (measured by means of a hot wire) can be increased by this modification. The flow was seeded in the settling chamber upstream of the screens used to reduce the turbulence of the wind tunnel flow.

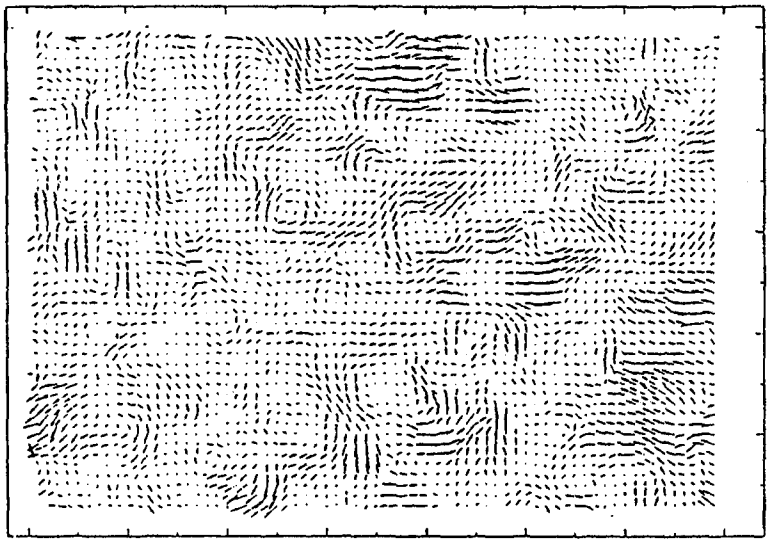

Fig. 3 Instantaneous flow field of the fluctuating velocity component (u-$\overline{U}$,v) behind a grid at $\overline{U}$ = 10 m/s.

As an example the instantaneous flow field behind a grid with a mesh size of 19 mm and a rod diameter of 1.5 mm is presented in Fig. 3. The degree of turbulence was Tu ≈ 0.46 %, measured with a hot wire located downstream of the observation area. The distance between grid and observation area was ≈ 1.3 m (i.e. > 850 rod diameters, slowly decaying grid turbulence). The observation area is 15 × 10 cm² and is subdivided into 70 × 48 interrogation spots. The mean flow velocity was $\overline{U}$ = 10 m/s. In order to enhance the visual impression of the spatial structures in the flow field, the mean flow velocity $\overline{U}$ is subtracted from the u-component of each local vector. Thus, the instantaneous field of the fluctuating velocity component (u-$\overline{U}$,v) is obtained. Fig. 3 clearly shows that it is possible to resolve spatial structures in a flow field with a degree of turbulence of Tu ≈ 0.46 % by means of the PIV technique.

BOUNDARY LAYER INSTABILITIES. The transitional process in a boundary layer is determined by a mechanism of generation and decomposition of various instabilities. Small oscillations may cause primary instability (two-dimensional waves, the so-called Tollmien-Schlichting (TS) waves). The growth of such TS waves leads to a streamwise periodic modulation of the basic flow, which gets sensitive to three-dimensional, spanwise periodic disturbances. These disturbances are amplified and lead to a three-dimensional distortion of the TS waves and farther downstream to the generation of three-dimensional Λ-vortices.

The extension of the knowledge about this mechanism enables the prediction and control of transition as required for applications in fluid mechanical engineering. In order to study these phenomena quantitative data of velocity fields of artificially forced instabilities have been acquired in a flat plate boundary layer also in the TUG. In order to get reproducible and constant conditions for the development of the instabilities it is necesssary to know the initial amplitude at the beginning of the observation area. In our experiment [10] this is achieved by introducing artificial disturbances by means of acoustic excitation through a narrow slot close to the leading edge of the plate. The velocity at the outer edge of the boundary layer was U = 11 m/s. The average free stream turbulence level was Tu = 0.065 %. The light sheet (thickness 0.5 mm in the

observation area) was orientated parallel to the plate. Its distance from the plate was 0.5 mm in this experiment. The observation area was 18 x 12 cm^2.

With the arrangement for acoustic excitation of instabilities it was possible to produce different transition types. A single-frequency excitation by a sine-wave with f = 154 Hz was used to generate the so called 'Fundamental Type'. The amplitude of the excitation has been carefully controlled as 'Sound Pressure Level' (SPL) in the acoustic chamber. Fig. 4 shows the field of the instantaneous velocity fluctuations (u-$\overline{U}$, v-$\overline{V}$). The mean flow velocity has been subtracted from all velocity vectors in order to show the fluctuating components of the velocity. From left to right the beginning of the distortion of the TS waves and the development of the Λ-vortices can be clearly seen. It has to be realized that the PIV recording represents a cut through the three-dimensional structures in the boundary layer. The circular structures at the right side of the velocity field can be identified as the 'footprints' of the Λ-vortices. For the 'Fundamental Type' the Λ-vortices exhibit in an aligned pattern. For the first time, the PIV technique allowed us the recording of a complete instantaneous velocity field in a plane of the boundary layer within microseconds.

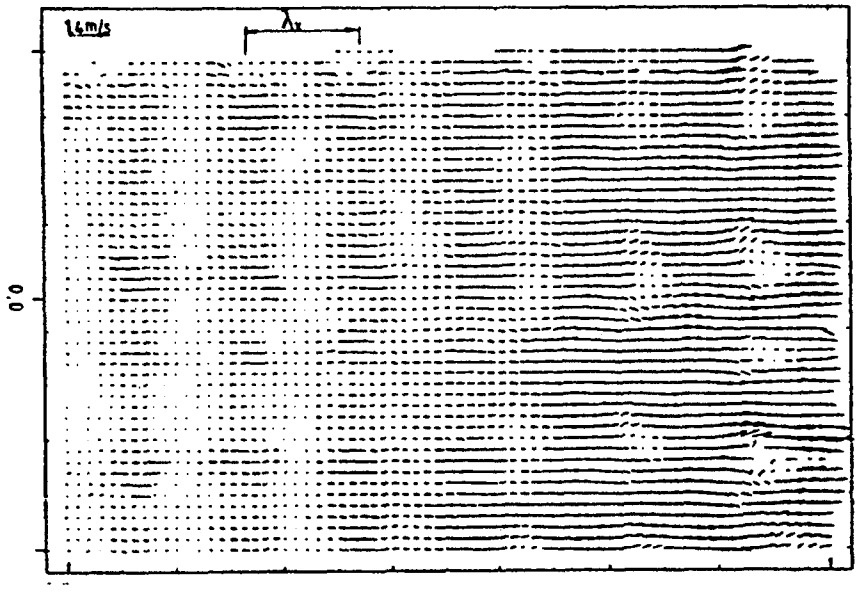

Fig. 4 Field of instantaneous velocity fluctuations (u-$\overline{U}$, v-$\overline{V}$), input signal: sin(2πft), SPL=108 dB.

DYNAMIC STALL. If an airfoil undergoes a pitching motion, the flow separation starts at higher angles of incidence as compared with the steady case (i.e. it is delayed with respect to the motion of the airfoil). This process is called 'Dynamic Stall'. With increasing pitching rate the flow separation and the reattachment during the downward motion appear at higher phase angles. The delayed flow separation is accompanied by a remarkable increase of lift, followed by a sharp drop at further increasing angles of incidence. The experimental set up has already been shown in Fig. 2. In our experiment [11] the angle of incidence of the NACA 0012 airfoil (chord length c_L =

20 cm, span 56 cm) was varied between $\alpha = 5°$ and $\alpha = 25°$ in a sinusoidally pitching motion with a frequency of $f = 6.66$ Hz. The free stream velocity was $U = 28$ m/s. The Reynolds number, based on the chord length, is $Re = 373.000$, the reduced frequency $\omega^* = 0.3$, ($\omega^* = 2\pi f c_L/U$). The airfoil is mounted between two circular end plates of perspex (diameter 40 cm) in order to provide two-dimensional flow in the vertical center plane of the test section (i.e. plane of illumination for PIV). When inspecting the flow field map, it has to be taken into account that the photographic camera was mounted at an angle of 15° (normal position of the airfoil) against the direction of the undisturbed flow.

For the case of the steady airfoil the flow has fully separated from the airfoil at an angle of incidence of $\alpha = 24°$. The flow field changes drastically, if the airfoil oscillates. The flow stays attached to the model during the upstroke motion of the airfoil up to an angle of incidence of $\alpha = 17°\uparrow$. The dynamic stall vortex, which is responsible for the strong increase of lift, appears at $\alpha \approx 20°$. With further increasing angle of incidence the vortex starts growing, beginning from the leading edge of the airfoil. The temporal variation of the flow field (from PIV recording to PIV recording) is small. A fully developed dynamic stall vortex, which rotates clockwise, can be observed at $\alpha = 24°\uparrow$ (Fig. 5). Now the vortex extends over 75% of the upper surface of the airfoil. The spatial resolution of the velocity data is even high enough to be able to detect small scale structures within the dynamic stall vortex.

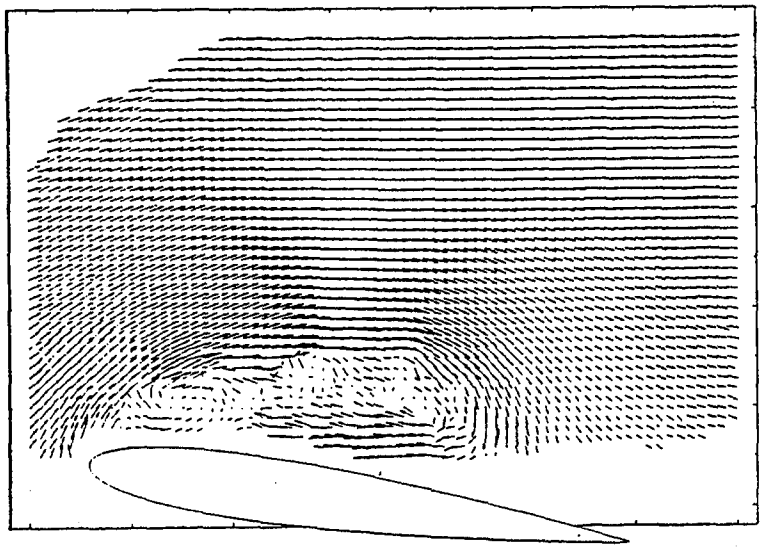

Fig. 5 Velocity vector map of instantaneous flow field above NACA 0012 airfoil at U=28m/s and $\alpha=24°\uparrow$ (pitching airfoil, upstroke motion).

The experimental results obtained by means of the PIV technique are a good basis for a comparison with the results of numerical computations [12]. As an example Fig. 6 shows a comparison of numerical and experimental flow field data also above a pitching NACA 0012 airfoil at $\alpha=24°\uparrow$. It can be seen that the general shape of the instantaneous streamlines is similar for numerical and experimental data. However, especially close to the dynamic stall vortex significant differences appear. More experimental and numerical work has to be carried out to clarify these differences. As the PIV technique is concerned, the high data density, which could

be obtained in this experiment, is remarkable. Such a high data density is absolutely necessary to be able to carry out a comparison with numerical data. Also very important for the comparison of numerical and experimental data is the availability of sophisticated software tools for the graphical presentation and analysis of flow field data [13].

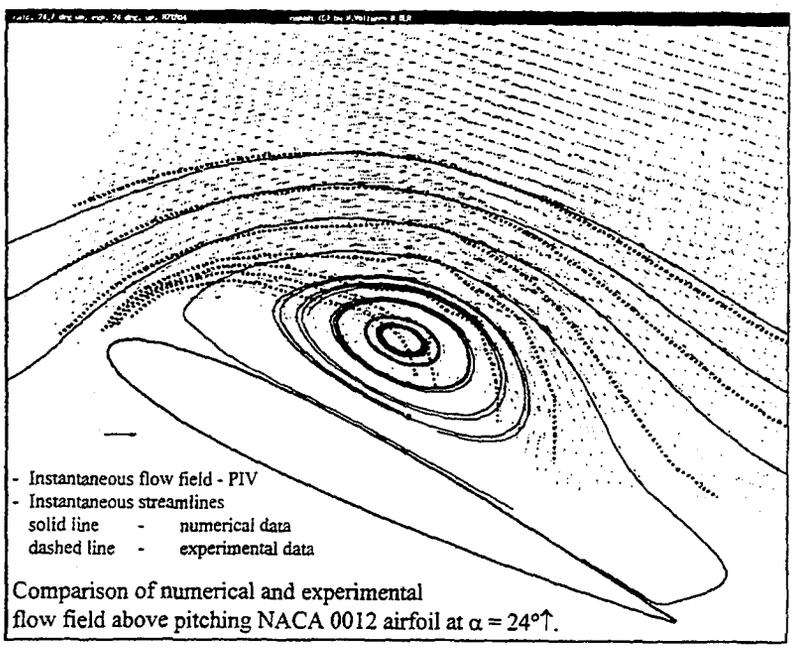

Fig. 6 Comparison of numerical and experimental flow field data above a pitching NACA 0012 airfoil at α=24°↑.

TRANSONIC FLOW. The instantaneous flow field above a NACA 0012 airfoil has also been investigated at transonic flow velocities by means of the PIV technique. The experiments were carried out in the high-speed blow-down wind tunnel (HKG) of DLR-WT-WK. Transonic flow velocities are obtained by sucking air from an atmospheric intake into a big vacuum tank. A quick-acting valve, located downstream of the test section, is quickly opened to start the flow. Ambient air, which is dried before entering the test chamber, flows for max. 20 seconds through a nozzle with a cross section of 0.75 × 0.75 m^2. Grids in the settling chamber and a high contraction ratio of 10:1 lead to a low turbulence level in the test section.

Fig. 7 presents the flow field above the airfoil at $Ma_\infty = 0.75$ and $\alpha = 5°$. The flow velocity ranges from 280 to 520 m/s. Due to the strong velocity gradients, image shifting was required in this experiment. A shift velocity of 174 m/s was selected. The Reynolds number, based on the chord length and the freestream flow velocity is $Re = 3.4 \times 10^6$. The time delay between the two laser pulses was 4 μs. The NACA 0012 airfoil had a chord length of 20 cm. The size of the observation field is 23 × 16 cm^2. The distance between light sheet and mirror axis was 70 cm, resulting in a magnification of 1 : 6.6. A reference velocity of $U_{ref} = 311$ m/s has been subtracted from all local velocity vectors in order to enhance details of the flow field shown in Fig. 7. All velocity vectors pointing to the right indicate supersonic flow, those pointing to the left subsonic flow. The supersonic flow regime above the leading edge of the airfoil, which is terminated by a strong shock, can be seen clearly.

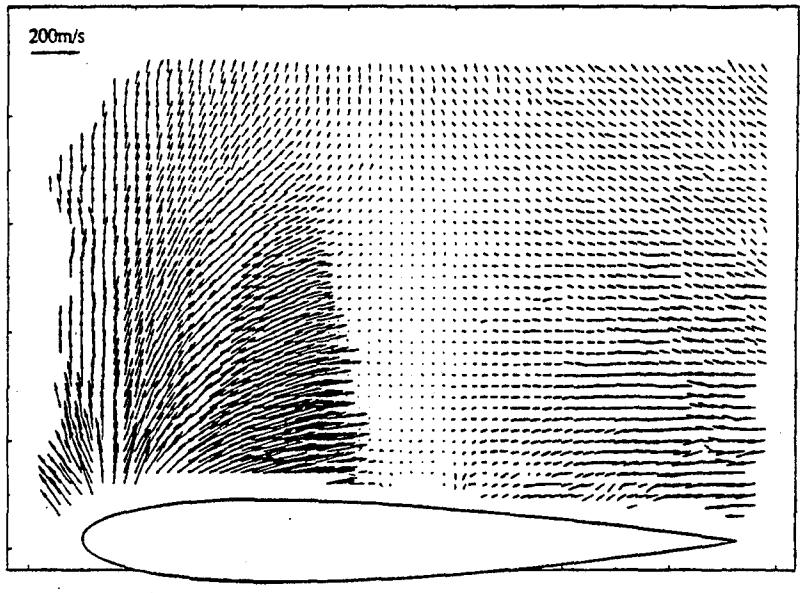

Fig. 7 Velocity vector map of instantaneous flow field (u - U_{ref}, v) above NACA 0012 airfoil at $Ma_\infty = 0.75$ and $\alpha = 5°$, $U_{ref} = 311$ m/s.

FUTURE DEVELOPMENTS OF PIV TECHNIQUE: VIDEO RECORDING

The problem of ambiguity removal at the application of PIV in aerodynamics has already been discussed. In principle the cross correlation technique instead of autocorrelation methods can also be employed for ambiguity removal. However, for this purpose it must be possible to store the images of the tracer particles due to the first and due to the second exposure on two separate recordings ('dual illumination - dual frame' recording technique). The temporal sequence of the recordings is known. Thus, it is no problem to decide which image was first and which was second. The cross correlation technique has been realized in connection with the development of Digital Video PIV by Willert and Gharib [14]. In the case of video PIV two subseqent video frames can be utilized to store the images of the particles at two subsequent illuminations. For video as well as for high speed photographic recording there remains the problem that there exists a minimum time which is necessary to change between two subsequent recordings (video frame rate, transport speed of film). This means that at the present state of the development of PIV the cross correlation technique for ambiguity removal is restricted to applications in low speed flows.

However, progress has been made recently with specially developed video cameras. Until now these cameras are only available for CCD chips with standard resolution. That means that the spatial resolution is lower as for photographic recording. However, these cameras as the Ultra high-speed video camera UHSV-288 can already be utilized for PIV, if a high temporal resolution is required. The ultra high-speed video camera UHSV-288 was developed by Stasicki and Meier [15] at DLR Göttingen primarily for the purposes of making video recordings of very fast processes, especially of unsteady flows. The UHSV-288 is a PC-supported system allowing manual selection of exposure times going down to 0.6 µs and exposure intervals with a resolution of 50 ns, resulting in a theoretical framing rate of over one million images per second.

The system delivers a sequence of up to 8 pictures with an image resolution of 512 x 256 pixels with 256 grey levels. The object to be registered is projected onto 8 CCD sensors (two of them are shown in Figure 8) by means of a beam-splitting mirror located directly behind the camera lens. Due to the high responsivity of the used CCD sensors the sensitivity of the UHSV-288 camera is that of a photographic camera using a fast film, even if each CCD sensor is only illuminated by 1/8th of the incident light intensity. The series of time-staggered images is created by the sequential release of freely triggerable electronic shutters. The images are stored on 8 frame grabber cards located in an industrial standard PC, and are accessed as bitmap files. An enhanced system with an image resolution of 752 x 291 pixels is manufactured under licence by the Cordin Company/U.S.A. The UHSV-288 camera system has already been applied to the investigation of the flow field above a pitching airfoil in compressible flow [16]. The evaluation was performed employing the crosscorrelation technique between subsequent images as obtained from the different CCD sensors.

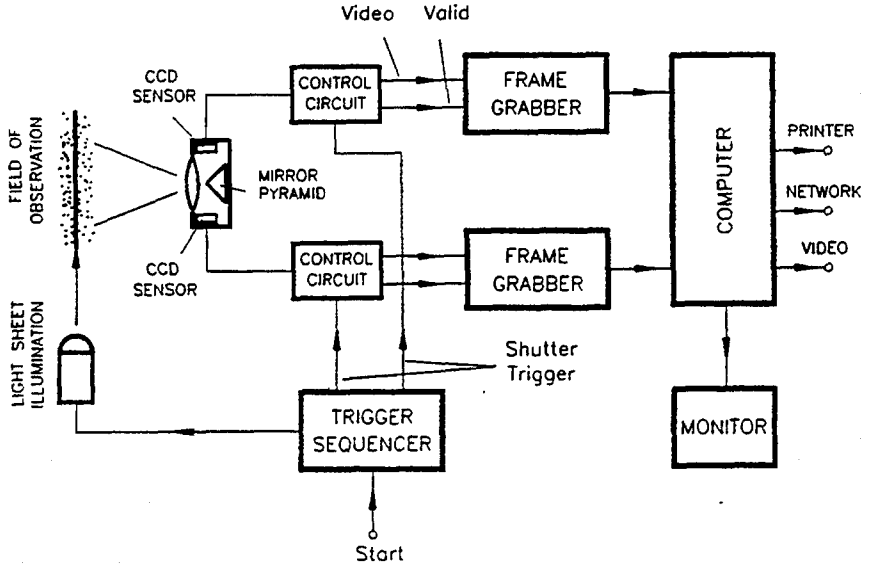

Fig. 8. Block diagram of the UHSV-288 (only two channels shown).

CONCLUSION

It has been demonstrated that investigations of the instantaneous flow field for different aerodynamic problems in different wind tunnels are possible by means of the PIV technique - in low speed flows as well as in transonic flows. It appears to us, that all major problems due to particles, optics, electronics and software have been solved in principle. However, there are still some refinements of the PIV technique necessary in order to be able to handle the special operational conditions in large wind tunnels. The results, presented in this paper, already show, that the PIV technique is a useful tool for aerodynamic investigations in the field of grid turbulence, boundary layer instabilities, Dynamic Stall effect on pitching airfoils, and for the investigation of transonic flows above airfoils. The quality of the instantaneous flow velocity data as measured by means of PIV is already adequate for comparison with the results of numerical calculations.

REFERENCES

[1] Adrian R. J., "Particle-Imaging Techniques for Experimental Fluid Mechanics", Annual Rev. Fluid Mechanics, Vol. 23, pp. 261 - 304, 1991.

[2] Raffel M., Leitl B., Kompenhans J., "Data Validation for Particle Image Velocimetry", in 'Laser Techniques and Applications in Fluid Mechanics', Eds. R.J. Adrian et al, Springer-Verlag, pp. 210 - 226, 1993.

[3] Kompenhans J., Raffel M., "Application of PIV technique to transonic flows in a blow-down wind tunnel", Proc. SPIE 2005, pp. 425 - 436, 1993.

[4] Adrian R. J., "Image shifting technique to resolve directional ambiguity in double-pulsed velocimetry", Appl. Optics 25, pp. 3855 - 3858, 1986.

[5] Landreth C. C., Adrian R. J., Yao C. S., "Double pulsed particle image velocimeter with directional resolution for complex flows", Exp. Fluids 6, pp. 119 - 128, 1988.

[6] Landreth C. C., Adrian R. J., "Electrooptical image shifting for particle image velocimetry", Appl. Optics 27, pp. 4216 - 4220, 1988.

[7] Lourenço L. M., "Velocity bias technique for particle image velocimetry measurements of high speed flows", Appl. Optics 32, pp. 2159 - 2162, 1993.

[8] Raffel M., "PIV Messungen instationärer Geschwindigkeitsfelder an einem schwingenden Rotorprofil", DLR Forschungsbericht, DLR-FB 93-50, 1993.

[9] Vogt A., "Optische Auswertung von Particle-Image-Velocimetry-Messungen im Nachlauf eines quer angeströmten Kreiszylinders", DLR Forschungsbericht, DLR-FB 93-49, 1993.

[10] Fischer M., "Untersuchung künstlich angeregter Instabilitäten in einer zweidimensionalen laminaren Grenzschichtströmung mit Hilfe der Particle Image Velocimetry", DLR Forschungsbericht, DLR-FB 93-58, 1993.

[11] Kompenhans J., Raffel M., Wernert P., Schäfer H.J, "Instantaneous flow field measurements on pitching airfoils by means of Particle Image Velocimetry", Proc. 'Optical Methods and Data Processing in Heat and Fluid Flow', April 14-15, London, pp. 117 - 121, 1994.

[12] Geissler W., Vollmers H., "Unsteady separated flows on rotor-airfoils", 18th European Rotorcraft Forum, Avignon, France, paper 79, 1992.

[13] Vollmers H., "Diagnostic and visualization tools for flow fields", Proc. 26th Int. Symposium on Automotive Technology and Automation (ISATA), 13. - 17.9.1993, Aachen, Germany, paper 93EM076, 1993.

[14] Willert C. E., Gharib M., "Digital particle image velocimetry", Exp. Fluids 10, pp. 181 - 193, 1991.

[15] Stasicki B., Meier G. E. A., "Elektronische Hochgeschwindigkeitskamera", Patent # 42 12271, 1992.

[16] Raffel M., Kompenhans J., Stasicki B., Bretthauer B., Meier G.E.A., "Velocity measurement of compressible air flows utilizing a high-speed video camera", to be published.

INFRARED THERMOGRAPHY IN THERMO-FLUID-DYNAMICS

Giovanni Maria Carlomagno
University of Naples, D.E.T.E.C. Italy

1. INTRODUCTION

The good results obtained in the last decade by the widespread use of the infrared scanning radiometer (IRSR) in experimental studies of convective heat transfer problems have proved the IRSR to be an effective tool in overcoming several limitations of the standard sensors originating both from the measurement and the visualization techniques.

The exploitation of quantitative infrared (IR) thermography needs the solution of several problems. These are mainly concerned with: an accurate characterization of the IR system performance and a precise calibration of the radiometrer; the use of external additional optics and/or mirrors, e.g. to increase the spatial resolution; the choice of the most appropriate heat flux sensor and its characterization especially with regard to lateral thermal conduction effects and to radiation losses; the determination of the body surface emissivity; the correct geometrical identification of the measured points; the design of the optical access window including the choice of the most appropriate IR material. Herein, the use of the IR imaging system in three different termo-fluid-dynamic problems is discussed. The chosen examples are selected so as to emphasize some relevant issues that arise in the application of the IR technique.

2. VISUALIZING FLOW FIELDS AND MEASURING CONVECTIVE HEAT FLUXES

When using the IRSR, a temperature difference is required between the flow stream and the tested body; it is therefore useful to make some remarks about the different experimental procedures to be followed, depending on the flow Mach number (M) range.

In the case of iposonic flow regime (M«1), the aerodynamic heating is not adequate to the sensitivity of IRSR; it is thus necessary to artificially produce a temperature difference between the model surface and the flow (*active* mode). This may be achieved either by varying the flow temperature or by heating the model in steady state or transient ways.

A very convenient method to steadily heat models, with a cylindrical geometry of their surface, is the so-called *heated-thin-foil* technique. This consists of realizing (or coating) the model surface with a very thin metallic foil and heating it by the Joule effect. By measuring the surface temperature, it is possible to compute the heat transfer coefficient from the foil to the flowing stream. Carlomagno et al. apply this technique to study the heat transfer from a plate to impinging jets[1] and to characterize the boundary layer development over a model wing, so as to detect transition and separation regions[2]. Another active technique consist of heating the model, at least for short periods of time, e.g. by means of a radiative source whose effects are superimposed on the convective ones.

At high Mach numbers, because of the stream high kinetic energy content, the detection of the thermal image by IR thermography may be relatively simpler. In fact, the strong aerodynamic heating makes possible the use of the so-called *passive* mode. In general, the model, which is initially at uniform ambient temperature, is suddenly exposed to the flowing steam. The *thin-skin*[3] or the *thin-film*[4] heat flux sensors are generally used to obtain the convective heat transfer coefficients and/or to make diagnostics of the boundary layer. Obviously, by properly creating an initial temperature difference between body and flow, these sensors may also be used, in a transient way, for the case of iposonic flow regimes[3].

In the following two applications of the *heated-thin-foil* tecnique and one of the thin-film sensor will be presented. The first two refer to the *active* mode while the last one to the *passive* mode.

3. ROTATING DISK

The laminar flow due to an infinite flat disk rotating in still air is one of the few exact solutions to the three-dimensional Navier-Stokes equations. This type of flow was first theoretically investigated with an approximate method by von Kàrmàn[5] who found that it resembles a boundary layer flow but with a boundary layer thickness independent of the radial distance.

Wagner[6] first evaluated the convective heat transfer coefficient by finding an approximate solution in the laminar regime based on the von Kàrmàn velocity distribution. The Wagner relation between the local Nusselt and Reynolds numbers is:

$$Nu = a \cdot \sqrt{Re} \qquad (1)$$

where a is a constant which is equal to 0.335 for $Pr = 0.74$. The local Nusselt and Reynolds numbers are respectively defined as:

$$Nu = \frac{hr}{k} \quad ; \quad Re = \frac{\omega r^2}{\nu} \qquad (2)$$

where h is the local convective heat transfer coefficient, r is the local radius, ω is the angular speed, k and ν are the fluid thermal conductivity and kinematic viscosity coefficients, respectively.

Millsaps and Pohlhausen[7] solved, always in the laminar regime, the exact equation of the thermal field by including viscous dissipation effects and found the coefficient a to be equal to 0.334 when viscous dissipation is neglected and $Pr = 0.74$.

Cobb and Saunders[8] performed an experimental investigation on the mean heat transfer coefficient for a range of conditions from entirely laminar to mixed laminar-turbulent flow. The lowest tested Reynolds number based on the disk radius is about 100,000. Although their data show a dependence of Nu from Re with an exponent which seems lower than 0.5, they affirmed that, in the laminar range, experimental results fit eq. (1) with a coefficient a equal to 0.36. Moreover at the lowest tested Re, probably due to the importance of natural convection effects, their results are much higher than what predicted by eq. (1). Cobb and Saunders detected the onset of transition to turbulent flow at about $Re = 240{,}000$.

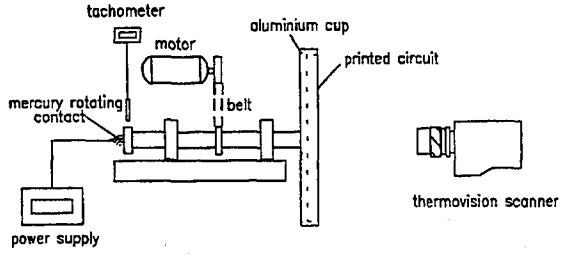

Fig. 1 - Experimental apparatus for the rotating disk.

Popiel and Boguslawski[9] measured the local heat transfer coefficient at a certain location over a disk rotating at different angular speeds and found the coefficient a to be equal to 0.33 for laminar conditions. Nu seems to depend on Re with an exponent much lower than 0.5 for their results too. In fact, at the lowest tested Reynolds number (≈7000), Popiel and Boguslawski, who took into account also the effects of natural convection, measured a Nusselt number which is about 35% larger than the theoretical predictions. They found the onset of transition at about Re = 195,000. In the transitional and turbulent regimes their experimental data fit respectively the relationships: $Nu = 10^{-19} Re^4$ for Re ranging from 195,000 to 250,000 and: $Nu = 0.0188 \cdot Re^{0.8}$ for Re greater than 250,000.

The sketch of the experimental apparatus used in the present tests is shown in Fig 1. The disk section consists of a 300*mm* (or 450*mm*) diameter cup filled with a 20*mm* thick polyurethane foam on which a printed circuit board, 0.2 *mm* thick, is glued. The circuit, which represents the *heated-thin foil*, is used to generate, by Joule effect, an uniform heat flux over the disk surface. Electric power is supplied to the printed circuit by means of a mercury rotating contact.

A pulley, which is connected by a transmission belt to an electric motor, is fixed on the transmission shaft supporting the disk. The rotating speed of the disk, can be varied in a continuos way within the range 100-4500*rpm* and is monitored by a tachometer.

The infrared thermographic system is based on AGEMA Thermovision 880 LW. Nominal sensitivity, expressed in terms of noise equivalent temperature difference (NETD) is 0.1°C when the scanned object is at ambient temperature. The scanning spatial resolution is 175 instantaneous fields of view per line at 50% slit response function. A 20°x20° lens is used during the tests. The thermal image is digitized in a frame of 140x140 pixels x 8 bits.

An application software is developed to correlate measured temperatures to heat transfer coefficients by means of the *heated-thin-foil* technique:

$$h = \frac{q_j - q_r}{T_w - T_{aw}} \qquad (3)$$

where q_j is the Joule heating, q_r is the radiative heat flux to ambient, T_w is the measured wall temperature and T_{aw} the adiabatic wall temperature of the flow. The radiative thermal losses q_r are computed by using the measured T_w, while the conductive ones toward the inner polyurethane foam, are neglected.The adiabatic wall temperature T_{aw} is measured by means of the same thermographic technique under the assumption that it coincides with the disk surface temperature when the Joule heating is suppressed.

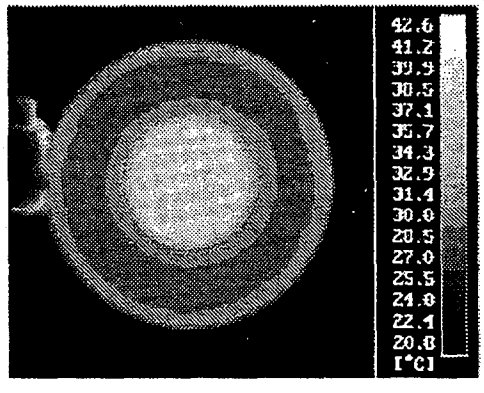

Fig. 2 - Map of T_w

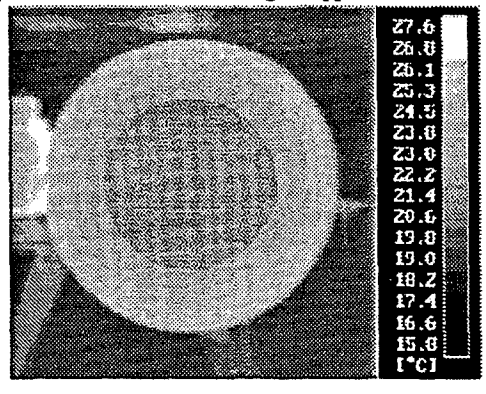

Fig. 3 - Map of T_{aw}

Fig. 2 is a thermal picture of the disk (450*mm*) recorded while it is rotating at 4390*rpm* and is subject to a heat flux of 871W/m^2. A relatively small (about 16% of the total surface) region around the disk center, where temperature is constant and the flow is laminar, is clearly evident. In the outer zone the temperature decreases, first quickly in the transitional regime and then slowly in the turbulent one; near the disk edge the temperature trend is reversed as it begins to rise slowly.

In order to explain the temperature behavior in the turbulent regime, first consider that due to the turbulent correlation law the heat transfer coefficient is expected to increase as the local radius increases. Consequently, as long as the adiabatic wall temperature distribution is uniform, eq. (3) shows that the wall temperature must decrease along the radial direction. Indeed, by examining the *cold* thermogram of Fig. 3, relative to the adiabatic wall temperature recorded at the same disk angular speed as Fig. 2, it should be noted that T_{aw} is practically constant (and equal to T_a) within the circumference whose radius is about 60%

of the disk one. The T_w trend in this region is thus confirmed. Instead, close to the disk limb, T_{aw} experiences a significant increase (about 3°C over T_a at the disk edge); therefore, for the present experimental conditions ($T_{w\text{-}Ta}$ is of the same order of magnitude as $T_{aw\text{-}Ta}$), the increasing trend of the wall temperature is accordingly explained. It has to be explicitly pointed out that in the case of relatively high boundary heat fluxes q_j, or high temperatures differences $\Delta T = T_w - T_{aw}$, the effect of the adiabatic wall temperature is negligible and the expected T_w trend is monotonically decreasing.

Results of performed tests, with both the 300*mm* and 450*mm* in diameter disks are shown in Fig. 4 in terms of local *Nu* and *Re* numbers. The theoretical prediction of Millsaps and Pohlhausen is also reported. The rise of *Nu* around *Re* = 250,000 is to be attributed to the onset of transition from laminar to turbulent flow. In the laminar zone, all the points before transition fall around a straight line in the log-log plane down to very low Reynolds numbers. Following the Wagner theory, a correlation of all the data in terms of equation (1) is made and the value of the constant is found to be $a = 0.33$. This value looks in good agreement with previous theoretical findings and the agreement seems even better due to the low data scatter over more than four decades of *Re*.

The results relative to the 450*mm* diameter disk for *Re* ranging from 40,000 to 1,400,000, are shown in Fig. 5. While the almost sudden rise of *Nu* around *Re* = 250,000 is to be attributed (as in the previous figure) to the beginning of transition, the second slope change, which appears at the right end of figure, may be to attributed to the onset of fully turbulent flow.

A linear regression of the data in the transitional range of *Re* from 260,000 to 320,000 yields: $Nu=8.0 \cdot 10^{-14} \cdot Re^{2.8}$. Present transitional results do not agree at all with those of Ref. [9] as far as both the transitional *Re* range and the regression slope are concerned. Apart from the remark that measurements in transitional flow regimes may be in general strongly affected by the environmental conditions of the actual experimental apparatus, it should be stressed that the results of Ref. [9] are obtained by using a calorimetric device too large to achieve the fine spatial resolution exhibited by the data reported in the cited paper.

In the fully turbulent regime present data fit the relation: $Nu=.16 \cdot Re^{0.8}$ which is in relatively good agreement with the theoretical and experimental findings of the literature.

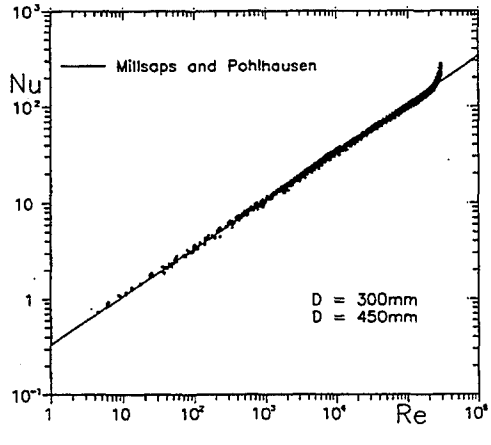

Fig. 4- *Nu* at low local *Re*

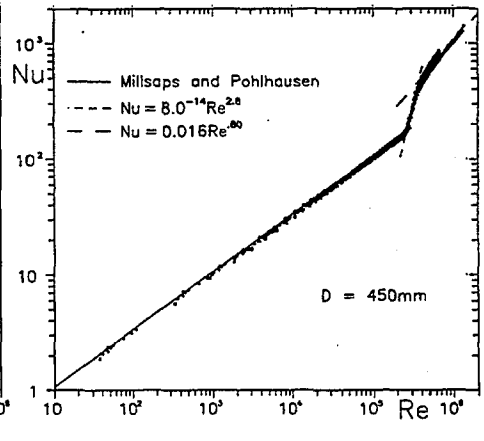

Fig.- 5 - *Nu* versus *Re*

4. BACKWARD-FACING STEP FLOW

When a duct flow encounters an abruptly enlarged area change, it separates from the wall and, depending on the downstream conditions, the separated flow will eventually reattach and undergo a redevelopment. Separated flows which reattach may cause large variation of the local heat transfer

coefficient values. The non-symmetric abrupt enlargement in a parallel-plate channel, generally referred to as backward-facing step, has been perhaps investigated more than any other separated flow situation.

A comprehensive experimental investigation (in the laminar, transitional and early turbulent flow regimes) on the backward-facing step flow has been probabily carried on by Armaly et al. [10]. Beyond the expected primary zone of recirculational flow attached to the step corner, they found that additional regions of flow separation, downstream of the step and on both side of the channel, are present in the transitional regime. Furthermore they showed that the flow downstream of the step only remains two-dimensional at low and high Reynolds numbers.

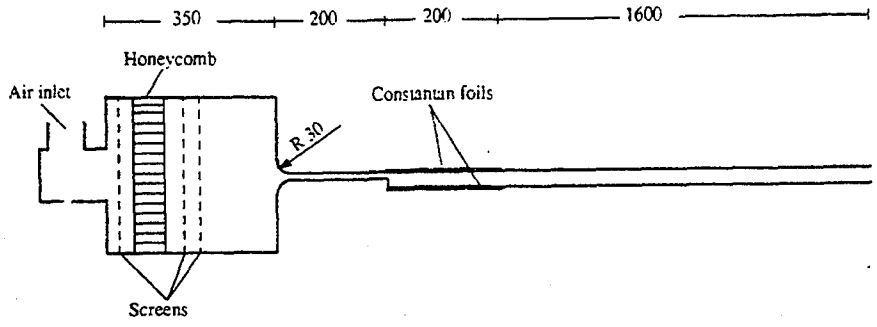

Fig. 6- Experimental apparatus for the backward-facing step

Heat transfer experimental investigations can be separed into three groups: laminar (Aung,[11] ; Sparrow et al[12]., Cardone et al. [13]), transitional (Aung and Goldstein[14], ; Kottke[15], ; Cardone et al. [13]), and turbulent (Seban[16],; Vogel and Eaton[17], Scherer et al. [18],Cardone et al.[19]). The streamwise distribution of the convective heat transfer coefficient, downstream of the step and on the step side, is generally characterized by an initial increase that leads to the attainment of a maximum which is followed by a subsequent decrease. Further downstream the distribution recovers the typical behaviour of the redeveloped flow.

The open air driven flow channel, used for this study, is shown schematically in Fig.6. The two-dimensional backward-facing step provides an expansion ratio 1:2. The larger channel, downstream of this step, has a height of 10mm and an aspect ratio 17:1. The air flow originates from a large settling chamber, having flow straighteners and screens, and is afterwards guided into a converging nozzle whose walls have a 30*mm* radius of curvature. The nozzle outlet is connected to the inlet channel, which is 5*mm* in height and 200*mm* in length up to the step. These dimensions ensure a two-dimensional, almost fully developed, flow at the cross section where the step is located. The two wide walls of the channel after the step, for a length of 200*mm*, are made with a very thin costantan foil (50$m\mu$ in thickness) that is heated by Joule effect; the foil is embedded in a 50$m\mu$ groove cut in a bakelite frame which in turn is flush mounted with the aluminium walls so not to have a step on these latters. Each foil is kept well taut by means of springs which act on two couples of copper clamps; a thin indium wire is inserted in between foil and clamps so as to realize a good electric contact. In order to rise the surface emissivity coefficient e of the viewed surface, the foil is coated there with a thin layer of a black paint which gives $\varepsilon = 0.95$.

IR camera takes, alternatively, temperature maps of both sides of the channel downstream of the step; these maps are correlated to the heat transfer coefficient by means of the heated-thin-foil technique. In particular, for each pixel, the convective heat transfer coefficient h is calculated as in equation (3) but with the quantity Taw replaced by the bulk temperature of the flow. The bulk temperature is evaluated by measuring the stagnation temperature just before the step and by making an energy balance along the channel. To insure relatively high temperature differences, test are performed with q_j values ranging from 450 to 4400W/m^2 according to the air flow rate. Heat transfer coefficients are presented in non-dimensional form by means of the local Nusselt number: $Nu = h\,D\,/\,\lambda$ where D is the equivalent diameter of the inlet channel and λ the thermal conductivity coefficient of air evaluated at film temperature. Tests are carried

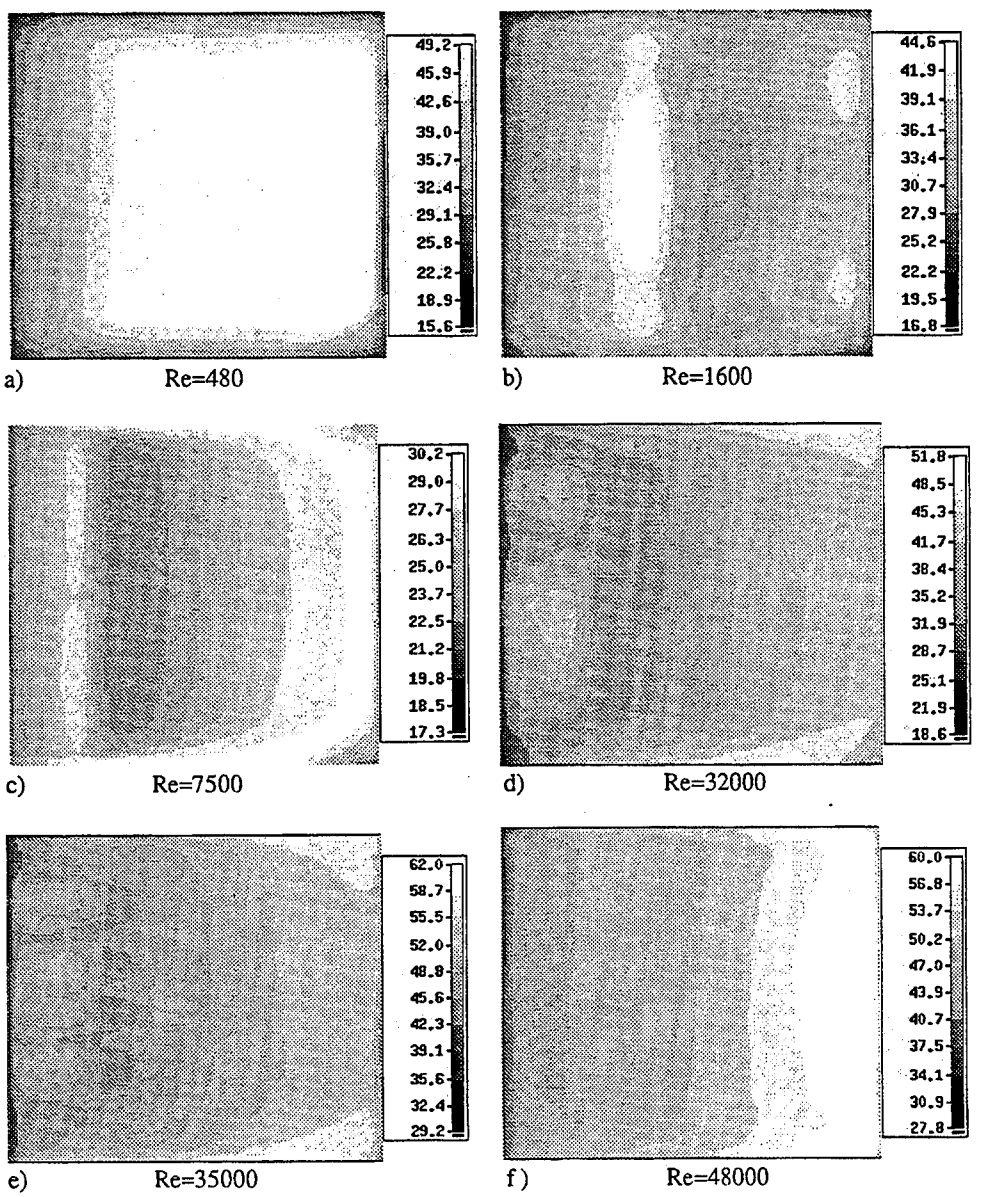

Fig.7 - Temperature maps at different Reynolds numbers.

out for Reynolds number *Re* ranging from 260 to 50400. *Re* is defined in the conventional way: $Re = VD/\nu$ where V and ν are the average velocity in the inlet channel before the step and the kinematic viscosity coefficient of air.

The regions of separation strongly influence the value of the convective heat transfer coefficient h; in particular the streamwise distribution of the heat transfer coefficient within and downstream of the separated region on the step side is typically characterized by an initial increase of h which leads to the attainment of a maximum and a subsequent decrease. In the following, the aforementioned heat transfer maximum, which occurs at a streamwise location x_{max}, is assumed to coincide with the location x_r at which the flow reattaches. There is, however, considerable evidence that the assumed equality of xmax and x_r is by no means universal as shown by Sparrow et al.[12].

The employed IR thermographic system is based on AGEMA THV 900 LW characterized by a NETD of 0.08 °C. A 5°x 10° lens is used during the tests at two viewing distances of about 1.2*m* and 2*m* which give a field of view of 0.2x0.1m^2 and 0.34x0.17 m^2 respectively. The thermal image is digitized in a frame of 272x136 pixels x 12 bits.

Fig. 7 shows a sequence of thermograms for increasing Reynolds numbers. Each thermogram refer to the upper wall, i.e. to the wall opposite to the step side. Flow is from left to right.

As shown by the thermogram of Fig. 7a; in the laminar range $260 < Re < 500$ the flow appears essentially two-dimensional; in this regime the reattachment length increases for increasing Reynolds number. However, regardless of the high aspect ratio of the channel, temperature maps show a three-dimensionality of the flow downstream of the step in the Reynolds number range $500 < Re < 5000$(see Fig.7b) ; in any case the flow practically maintains its symmetry to the centerplane of the test section. Within this regime, and in particular for $1400 < Re < 3400$, the presence of two peaks in the Nusselt number distribution on the step side wall, across the channel centerline, indicates the existence of an additional recirculating-flow region, besides the primary one that is attached to the step corner, which has also been found by Armaly et al.[10]. Armaly et al. however report that the additional recirculating flow region disappears for $Re > 2300$. The latter discrepancy may be attributed to both the different ways of detecting the separation region in the two investigations and, to a lesser extent, to the different nozzle configuration being used.

In the range $5000 < Re < 20000$ a two-dimensional flow is completely re-established. This behaviour is shown by the thermogram of Fig. 7c, which is relative to *Re*=7500 and by the relief map of the Nusselt number distribution at the step side, relative to the same Re and reported in Fig. 8. As it may be seen especially from the map a certain degree of regular waviness is present spanwise; this may be due to a pattern of vortices which are superimposed to the main flow and produce the periodic variation of the heat transfer coefficient The heat transfer maxmum is located at xmax/s≅8 where s is the step height.

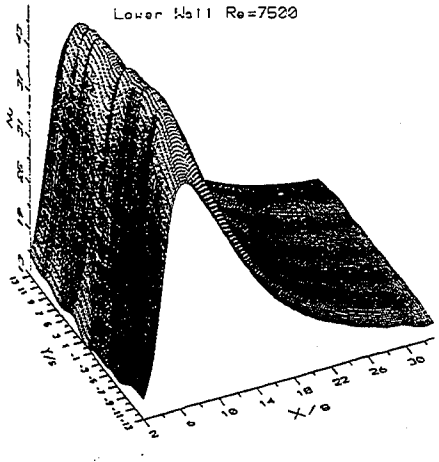

Fig 8 - Nusselt distribution for *Re*=7500

For further increasing Reynolds number, again a three-dimensional zone of separation is found expecially in the proximity of the upper wall, across and just downstream of the step location (see Fig. 7d and 7e). In particular, for $20000 < Re < 39000$ the thermograms seem to indicate, there, the presence of one or more vortices, which seem to rotate about an axis normal to the two wide walls of the channel, of a type similar to the one already described by Abbott and Kline[20]. It has to be stressed, however, that, while Abbott and Kline find always these vortices on the step side and of small size, in this case there is strong evidence of much larger size vortices only on the flat wall of the channel at the indicated Reynolds number range. The number and the position of such vortices (see Fig. 7d) appears generally random; the

symmetry to the centerplane of the test section is generally lost; however, as shown by the thermogram of Fig. 7e, only for about Re = 35000 these vortices seem to assume a regular symmetric pattern. In any case no evidence of such vortices is found on the lower wall except for disturbances, most probably caused from them, which manifest after reattachment of the flow.

The relief maps of Fig. 9 show the Nusselt number distributions on both sides of the channel for Re = 35000). The right map of Fig. 9, which is relative to the regular pattern of vortices shown in the thermogram of Fig. 7e looks quite impressive; it is hard to believe that such a high variation of the Nusselt number may occur spanwise on a flat wall even if in the vicinity of a step. Similar variations, althought not showing a regular pattern such as the one of Fig. 9, have been found in all the range 20000 < Re < 39000.

For further increasing Reynolds number the regular pattern of vortices indicated by Fig. 7 tends rapidly to disappear and also any recirculating-flow region on the wall opposite to the step vanishes.

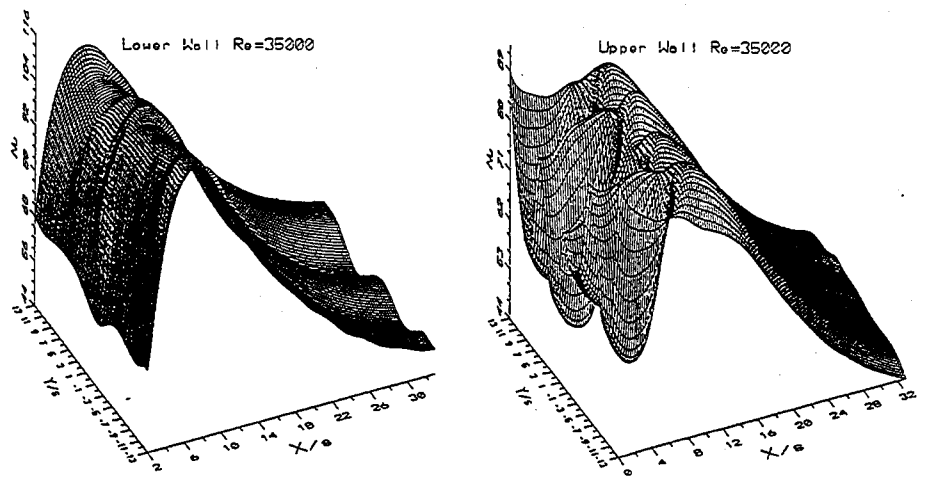

Fig. 9 - Nusselt distributions for Re=35000

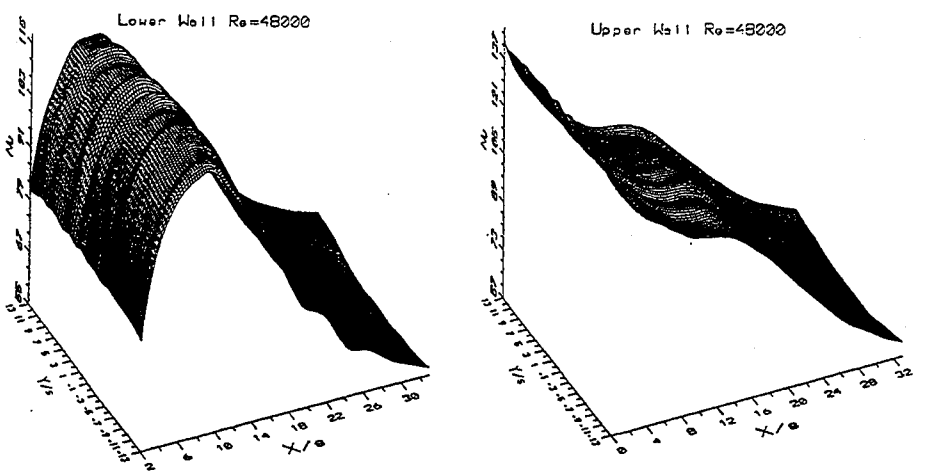

Fig. 10 - Nusselt distributions for Re=48000

Finally, in the range 42000 < *Re* < 50400, a two-dimensional turbulent flow is completely recovered; this behaviour is evident in the relief maps of Nusselt number distribution on both sides of the channel for Re=48000 which are reported in Fig.10. By comparing the left maps of Fig. 9 and 10 it is possible to see that the thermal reattachment zone has moved slightly downstream for the highest Reynolds number($x_{max}/s \cong 10$) and that, at this latter *Re*, the *Nu* peak looks wider. The right map of Fig. 10 shows a continuous decrease of the Nusselt number with an inflexion zone located slightly downstream of the thermal reattachment zone which is present on the opposite side of the channel.

5. GOERTLER INSTABILITY OF A HYPERSONIC BOUNDARY LAYER

In the recent past, within the European Community space program Hermes devoted to the development of the first European Space Shuttle, the University of Naples and CEAT of Poitiers carried out a joint experimental investigation to measure the aerodynamic heating and to analyse the related flow field over a delta wing/flap configuration in order to study a 3D transitional shock/boundary layer interaction in hypersonic flow[21]. Attention was paid, in particular, on visualizing a spanwise periodic variation of the wall heat transfer coefficient over the flap that is to be ascribed to the formation of Goertler counter-rotating vortices in the reattaching flow region. To the aim of obtaining a more basic knowledge about the formation of such vortices and of comparing experimental data with numerical results, a particular study has been carried out on ad hoc designed models, consisting of concave walls (producing a weak interaction regime) having a constant longitudinal curvature radius. Present heat transfer measurements and surface flow visualizations have been performed by means of the computerized infrared imaging system, AGEMA thermovision 880 LW[22].

Experimental tests have been carried out in the hypersonic blowdown tunnel H210 of CEAT, Poitiers, having a test section diameter of 210mm. The operating fluid is dry air which has a stagnation temperature T = 800°K and a stagnation pressure 4.5MPa < p0 < 10MPa. Unit free stream Reynolds number Re is changed mainly by varying the stagnation pressure and ranges from .89 x 10^7/m to 1.91 x 10^7/m. The nominal free stream Mach number is M = 7; in effect Mach number slightly depends on the stagnation pressure (due to the interaction of the nozzle boundary layer thickness) and ranges from 6.9 to 7.1. Optical access windows are made of germanium.

At the beginning of each test run the model (which is initially in a remote position at room temperature) is vertically injected into the stream. The time rise of its surface temperature is measured by viewing the model with an IR camera. Injection time is about 0.15s and testing duration of a few seconds.

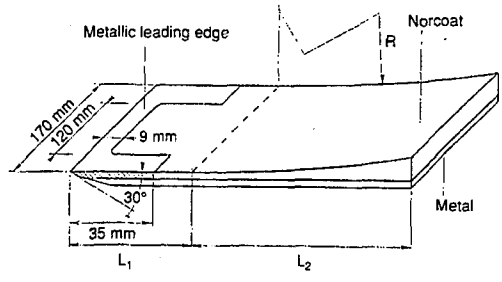

Fig.11 - Model configuration

In the present problem the spanwise periodic variation of the convective heat transfer coefficient produces an analogous spanwise periodic variation of the model surface temperature which allows the detection of the vortices by means of the IR technique. The Goertler wavelength is assumed to be the distance between two subsequent peaks of the convective heat transfer. Thermograms may also be used to visualize the surface flow. The dimensionless heat transfer coefficient is expressed in terms of Stanton number:

$$St = q_c/\rho c_p V(T_{aw}-T_w) \qquad (4)$$

where ρ, V, and c_p are respectively the mass density, the velocity and the specific heat at constant pressure of the free stream. The history of the measured wall temperature T_w is related to the net convective wall heat flux q_c using the thermal model of the *thin-film* sensor (or semi-infinite wall). To this end a time sequence of thermograms (average time step is 0.24s) is recorded during the test runs.

In order to quantitatively estimate the effect of the presence of Goertler vortices on the surface heat transfer distribution, it has been also necessary to include an image restoration algorithm into the data post-processing software, to correct data from both electro-optical (de Luca and Cardone[22])and lateral thermal conduction (de Luca[23])degradations.

Models consist of two parts: a 2D flat plate placed at zero angle of attack, which is followed by a concave wall having a constant curvature radius (Fig. 11). Both the flate plate and the concave wall are made of melted NORCOAT 4000, which is jointed to a stainless steel leading edge.

In order to achieve a small field of view, i.e. the highest possible spatial resolution of the IR system (the expected vortices wavelength is of a few millimeters), proper extension rings have been used in conjunction with the standard 7° IR lens. A measurement frame of either 35x35mm or 47x47mm has been thus obtained with a spatial resolution of 4 pixels/mm or 3 pixels/mm, respectively.

The relief surface temperature distribution presented in Fig. 12 refers to a measurement frame recorded on the concave wall of a model having $L_1 = 0.05m$ and $R = 1m$ and centered $125mm$ from the leading edge. Data have been taken 1.12s from the injection instant and are relative to $M = 7.0$, $Re = .89x10^7/m$ and zero angle of attack (the arrow indicates the stream direction). The presence of the vortices produces the temperature periodic variation whose amplitude increases downstream (the average wavelength is about $8mm$). Testing conditions correspond to a spatial frequency for which a limited data correction is needed to account for imaging and sampling as well as lateral conduction degradations. The plot of Fig. 12, however, has no such corrections but only a weak smoothing of the recorded data.

Fig. 13 shows the comparison between the Stanton number spanwise profiles (relative to a distance from the leading edge $x = 135mm$) for coarse (dotted line) and restored data referring to the same model and testing flow conditions of previous Fig. 12. For the restored data the broken line represents the values corrected from imaging and sampling degradation effects due to the limited spatial resolution of IRSR. The continuous line gives the fully restored values, which take into account also the lateral thermal conduction. The maximum corrections performed by the image restoration algorithm are in present case of the order of 5%but may be much higher for shorter wavelengths. As is evident, the amplitude of the fluctuations of the heat transfer coefficient ranges from about 20% to about 30% of the mean value.

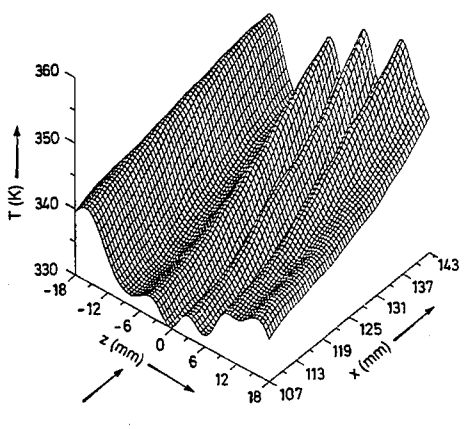

Fig 12 - Relif surface temperature map

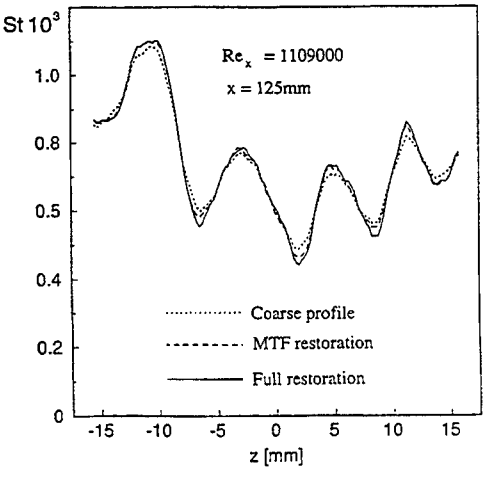

Fig 13 -Coarse and restored *St* spanwise profile

Experimental observations generally show that the measured vortices wavelength is unchanged along the flow directors. All dimensionless wavelength data has been correlated to a particular Goerther number based on the vortex wavelength and found to fall into the instability region numerically predicted. The experimental value of this Goertler number is, however, almost double of the numerical one because the physical selection mechanism of the disturbances strongly depends on the particular apparatus being used for the experimental tests.

6. CONCLUSION

The use of quantitative infrared thermography in the field of thermo-fluid-dynamics has been addressed. The different experimental procedures, to be followed according to the free stream Mach number value, have been analyzed.

The infrared technique has been applied to three different thermo-fluid-dinamic problems so as to put in evidence its capability and some relevant questions: a disk rotating in still air, a backward-facing step flow, the Goerther instability of a hypersonic boundary layer. The first two applications refer to the use of the steady-state *heated thin-foil* technique while far the last one the transient *thin-film* technique (*semi-infinite* wall) is employed.

As far as the rotating disk is concerned, an excellent argument has been found, in the laminar region, between experimental findings and theoretical predictions. Also the data relative to full turbulent flow seem in good concordance with previous findings. Instead transitional result do not agree with preceding experimental outcomes. In the present study, no attempt has been mode to detect azimuthal instabilities.

The Infrared technique looks quite powerful in studying the backward-facing step flow is essentially two-dimensional while, far higher Reynolds number up to 5000, temperature maps show a three-dimensional behavior. Far $1400 < Re < 3500$, the presence of two peaks in the Nu distribution on the step side, across the channel centerline, indicates the existence of an additional recirculation region besides the primary one attached to the step corner. In the range $5000 < Re < 20000$ a two-dimensional flow is reestablished, while far $20000 < Re < 39000$ a three-dimensional flow is found especially in the vicinity of the upper wall across and just downstream of the step location. Far further increasing Reynolds number a two-dimensional turbulent flow is completely recovered.

With regard to the Goertler instability of a hypersonic boundary layer, the IRSR is capable of bath measuring the vortices wavelength as wall as to quantify the Stanton number fluctuations. A proper data correction (image restoration) is however need to take into account both the limited spatial resolution of IRSR as well as degradation effects due to lateral thermal conduction

7. REFERENCES

[1] Carlomagno G.M. and de Luca L., Heat Transfer to Impinging Jets Measured by Infrared Termography, Proc. COBEM 89 (Eds. Hirata, M.H. et al.), pp.209-212, Rio de Janeiro, 1989

[2] de Luca L., Carlomagno G.M. and Buresti G., Boundary Layer Diagnostics by Means of an Infrared Scanning Radiometer, *Experiments in Fluids*, **9**, pp. 121-128, 1990

[3] Carlomagno G.M. and de Luca L., Infrared Thermography in Heat Transfer, in Handbook of flow Visualization (Ed. Yang W.J.), Ch. 32, pp. 531-533, Hemisphere, 1989.

[4] de Luca L. , Cardone G., Carlomagno G.M., Aymer de la Chevalerie D. and Alziary de Roquefort T., Flow Visualization and Heat Transfer Measurement in Hypersonic Wind Tunnel, *Experimental Heat Transfer*, **5**, pp. 65-79, 1992

[5] Von Kàrmàn Th., Laminare und Turbulente Reibung, *ZAMM*, **1**, pp. 233-252, 1921.

[6] Wagner C, Heat Transfer from a Rotating Disk to Ambient Air, *J. Applied Physics*, **19**, pp. 837-839, 1948.

[7] Millsaps K. and Pohlhausen K., Heat Transfer by Laminar Flow from a Rotating Plate, *J. Aeronautical Science*, **19**, pp. 120-126, 1952.

[8] Cobb E. C. and Saunders O. A., Heat Transfer from a Rotating Disk, *Proc. Royal Society*, **236**, pp. 343-351, 1956.

[9] Popiel Cz. O. and Boguslawski L., Local Heat-Transfer Coefficients on the Rotating Disk in Still Air, *Int. J. Heat Mass Transfer*, **18**, pp. 167-170, 1975.

[10] Armaly B.F., Durst F., Perreira J.C.F. and Schonung B., Experimental and theoretical investigation of backward- facing step flow, *J. Fluid Mech.*, **127**, pp.473-496, 1983.

[11] Aung, W., An experimental study of laminar heat transfer downstream of backsteps, *J. Heat Transfer*, **105**, pp. 823-829, 1983

[12] Sparrow, E.M., Kang, S.S. and Chuck, W., Relation between the points of flow reattachment and maximum heat transfer for region of flow separation, *Int. J. Heat Mass Transfer*, **30**, pp. 1237-1245, 1987

[13] Cardone, G., Di Leva, O.M. and Carlomagno, G.M., Heat transfer in a backward-facing step flow, *Proc. II Int. Conf. Fluid Mechanics*, pp. 970-975, Peking Univ. Press.,1993

[14] Aung, W. and Goldstein, R.J., Temperature distribution and heat transfer in a transitional separated shear layer, in *Heat Transfer* (*Grigull, U. and Hahne, F., eds.*), Vol. **2**, pp. 1-11, Elsevier, 1970

[15] Kottke, V., Strömung, Stoff-, Wärme- und Impulsübertragung in lokalen Ablösegebieten, *Fortschr. Ber. VDI Z*, Reihe 7, Nr.77, 1993

[16] Seban, R.A., Heat transfer to the turbulent separated flow of air downstream of a step in the surface of a plate, *Trans. ASME, J. Heat Transfer*, **86**, pp. 259-270, 1964

[17] Vogel, J.C. and Eaton, J.K., Combined heat transfer and fluid dynamic measuments downstream of a backward-facing step, *J. Heat Transfer*, **107**, pp. 923-929, 1985

[18] Scherer, V., Wittig, S., Bittlinger, G. and Pfeiffer, A., Thermographic heat transfer measurements in separated flows, *Experiments in Fluids*, **14**, pp. 17-24, 1993

[19] Cardone G., Di Leva G.M. and Carlomagno G.M., Heat Transfer Measurements and Surface Flow Visualization of a Backward - Facing Step Turbolent Flow, in Experimental and Numerical Flow Visualization, Eds. B. Khaligi et al. , FED- Vol. **172**, pp. 35-42, ASME, 1993

[20] Abbot D.E. and Kline, S.J., Experimental investigation of subsonic flow over single and duble backward facing steps, *Trans. ASME, J. Basic Eng.* , **84**, pp. 317-340, 1962

[21] de Luca L., Cardone G., Carlomagno G.M., Alziary de Roquefort T., Aymer de la Chevalerie, D., Infrared measurements of aerodynamic heating in hypersonic wind tunnel. in: Aerothermodynamic for space vehicles Ed., (Battrick, B.) ESA SP-**318**, pp. 229-234, 1991

[22] de Luca L., Cardone G, MTF cascade model for a sampled Ir imaging system,. *Appl. Opt.*, **30**, 1659-1664, 1991

[23] de Luca L., Computerized IR Thermography for convective heat transfer measurement. in: Computational Methods and Experimental Measurements V (Eds. Sousa, A., Brebbia, C. A. and Carlomagno, G.M.), CMP/ Elsevier, New York, pp. 347-358, 1991

SINGLE DROP IMPINGEMENT ON THIN LIQUID FILM

A. Coghe*, G.E. Cossali**, M. Marengo*

* Politecnico di Milano, Milan -Italy
** Università di Bergamo, Bergamo-Italy

Abstract

The impact of a drop on thin liquid film is studied to understand the mechanism of secondary drop formation from the corona and to measure the secondary drop size and velocity. Weber number range from 25 to 2500 and the non-dimensional film thickness δ varies from 0.038 to 0.095 (Laplace = 380000). Weber was found to have the main role in splash characteristics. δ number has a little influence, at least at the thin film regime. The number of jets and the secondary drop diameter evolution are investigated for a combination of We and δ numbers. Photographic report is annexed.

Introduction

The spray impingement has a raising importance for his industrial application. A number of good experimental works investigated the spray characteristics in a wide range of dynamical conditions[1-2-3-4-5]. The splash is one of the main phases of the impingement phenomenon. Determination of splash limit, of secondary drop characteristics are some of the aims of the investigations in this field. The dynamics of the impact of a single liquid drop on a wall covered by a film (made by the same liquid) is depending on the dynamic characteristics of the impinging drops (ϕ = diameter, v = final drop velocity), on the physical characteristics of the liquid (μ = viscosity, ρ = density, σ = surface tension) and on the film thickness (h). The evolution of the liquid film flow field after the impact is driven by the opposite action of surface and inertial forces, and damped by the viscous forces, but also gravity may play a role in a way similar to that of the surface forces, acting to reduce the film thickness uniformity. By applying the Buckingham theorem, four non-dimensional groups can be defined, and the characteristics of the phenomenon are expected to be completely determined by those groups. A possible choice is: Weber number ($We = \rho v^2\phi/\sigma$), Laplace number ($La = \phi\rho\sigma/\mu^2$), non dimensional film thickness ($\delta = h/\phi$) and Bond number ($Bo = \rho g h^2/\sigma$), although in the literature, other non dimensional groups have been used: Reynolds number ($Re = \rho v\phi/\mu = (La\ We)^{1/2}$), Ohnesorge number ($Oh = \mu/(\phi\sigma\rho)^{1/2} = La^{-1/2}$), Froude number ($Fr = v^2/gh = \delta We/Bo$). The choice of any combination of the above mentioned groups is arbitrary and in the present work We, La, Bo and δ will be used.

Some previous investigations on single drop impingement

The first general study of impingement is the Worthington's investigation of 1896[6]. Photographs of splashes were taken by very complex techniques for the times. Worthington investigated in a qualitative manner the phenomenon, describing the formation of the crown and the jets, noting main perturbations along the corona and the droplets break-up.

Engel (1966-1967) proposed a theoretical analysis of splashing on a deep film[7-8]. By energy consideration, an explicit expression for the velocity potential of the flow after the impingement is obtained. The author considered the cavity of splash as a cylindrical wave. The energy is written in three terms: the gravity potential energy of the crater, the gravity potential energy of the

wave swell, the potential energy of the new surface generated by splash. Using cylindrical and spherical coordinates, fixing the boundary conditions, Engel determined the kinetic energy in the liquid around the cavity, the kinetic energy in the cylindrical wave and the dissipated energy. A numerical solution of equations was obtained for We = 19360, Laplace = 330260 (Re = 80000, Oh = 0.002).

Macklin and Metaxas (1976) studied the first period of splash phase in detail[9]. Using different fluids (methanol, water and glycerin), they correlated the crown characteristics to the impinging drop Weber number. Following Engel's theoretical approach, with the simplification to take into account only the liquid mass in the corona, neglecting the mass in the jets and in the secondary droplets, they found the role of the viscous term in the energy balance (always less than 7% respect the total kinetic energy) and of secondary drops energy (with high impact energy, the total volume of secondary drops reaches 2-4 times the volume of the primary drop). The main conclusions are: the 5% of kinetic energy goes to atomization process; greater is Weber, thinner is the corona thickness, greater the liquid volume in the corona. The authors also determine a shallow-deep splash threshold: depending on the presence of *swells*, there is a deep film splash condition when $\delta>5$, shallow film splash when $\delta<2$.

Walzel (1980) investigated the splash limit with different mixtures of water and glycerol, to vary the Weber number and Laplace number in an independent way[10]. The analysis was performed both with a dry surface and with a surface covered by a film ($\delta = 0.1$). The kinetic energy for splashing is greater with a dry surface than with a film. An increasing of Laplace number improves the splash for a constant Weber. Walzel found two correlation for the limit curves: a) dry surface, $We = 7.9\ 10^{10}\ La^{-1.4}$, with a minimum splashing velocity $v = 2.8\ 10^{5}\ \phi^{-1.2}\ \rho^{-1.2}\ \mu^{1.4}\ \sigma^{-0.2}$; wet surface, $We = 2.5\ 10^{3}\ La^{-0.2}$, $v = 50\ \phi^{-0.6}\ \rho^{-0.6}\mu^{0.2}\ \sigma^{0.4}$. The explored region in We-La-δ space is limited by $90 < We < 8000$, $10^4 < La < 4.0\ 10^6$, $\delta = 0.1$.

Rodriguez and Mesler (1985) investigated the drop impingement on a deep pool[11]. They characterized the phenomenon with the Froude and Reynolds number. Drops with a diameter smaller than 2 mm were obtained with the aid of a puff of nitrogen gas. A solenoid valve delivers flow for 5 msec to blow off the droplet from a hypodermic needle. Water drops were dyed with a colored liquid to make vortexes and flow motion visible in the pool water. A threshold curve for the splash region was obtained in a Fr, Re region. The We number was very low, La was comprised in the range $3.4\ 10^4$ - $3.4\ 10^5$. This curve has a slight similarity with the limit curve in We, La space showed by Walzel with a different δ.

Allen (1988) proposed a method to determine the distribution of the velocity and direction of secondary droplets[12]. The mechanism of splashing can be divided, with the author, in two defined areas: the creation of independent splash droplets, their subsequent motion and final configuration. The first area is ruled by a lot of parameters, as the sphericity of incident drop, the inclination of impingement surface, the presence of a film, the thickness of this liquid film, the fluid properties. In a former study[13], Allen (1975) investigated the role of surface tension in the case of a drop incident on a dry surface, found Rayleigh-Taylor instability to be significant in spike formation. The angle at which the droplets are ejected depends on the depth of the standing liquid. Considering the effect of air-friction, gravity and in-flight evaporation, Allen writes two parametric equation for the secondary droplets trajectory originating from the splash center at velocity V and inclination θ (in-flight evaporation is neglected, because it causes only a 0.5% reduction in droplets diameter). The author performed a series of experiments where some photos of splash was obtained with a laser sheet illumination technique. Allen obtained a (V,θ) distribution for splashes caused by incident water drop of diameter 4 mm falling at 6 m/sec into

water of depth 1 mm (We = 1950, La = 252000, Bo = 0.13, δ = 0.25): the emission angle lies in the range 50-70° while the emission velocity is the range 1-5 m/sec.

Mundo & al (1994) investigate the correlation of the deposition/splashing limit using Reynolds and Ohnesorge numbers to characterise the splash on a solid and dry surface[14]. Using a monodisperse droplets generator, they observe the impingement on a rotated disk with a synchronised illumination. Varying the velocity of the disk, the impact angle changes from 4° to 65°. To obtain different values for viscosity, surface tension and density, ethanol, water and a mixture of water-saccherose-ethanol are used. A two-component phase Doppler anemometer measures the secondary droplet size and velocity. The deformation and splashing depend on the ratio of the surface roughness of the disk. So the results are divided in two different situation. With a smooth surface, an instability develops from the corona and leads to a ring propagating upward. This ring break-up into secondary droplets (high Reynolds number: Re = 711). In the case of low Reynolds number (Re = 49), no corona is formed. With a rough surface, the deformation of the droplet is more irregular: the high roughness S_t leads to a faster disintegration and to the presence of more secondary droplets behind the impingement point (high Reynolds number). For low Reynolds number, no splashing is formed. A strong correlation for the deposition limit is found both for the smooth surface and the rough surface: $K = Oh\, Re^{1.25}$. For $K > 57.7$, splashing happens. The normal velocity to the surface is a more influencing factor on the splashing limit than the total momentum. Using PDA techniques, the diameter distribution with some values of K is found: the size distribution of the secondary droplets gets narrower and the mean size smaller with a greater K. For a smooth surface, the analysis of velocity distribution shows that the impingement angle strongly determines the flight direction of the secondary droplets. The fluid properties seems not to be influent for the velocity and direction of spray motion. A rough surface has the effect of decreasing the reflection angle and of increasing the mean normal velocity.

Figure 1 shows the ranges of Weber, Laplace and δ that could be obtained by the present set up. It is noteworthy that a large region characteristic of diesel spray can be covered in this way.

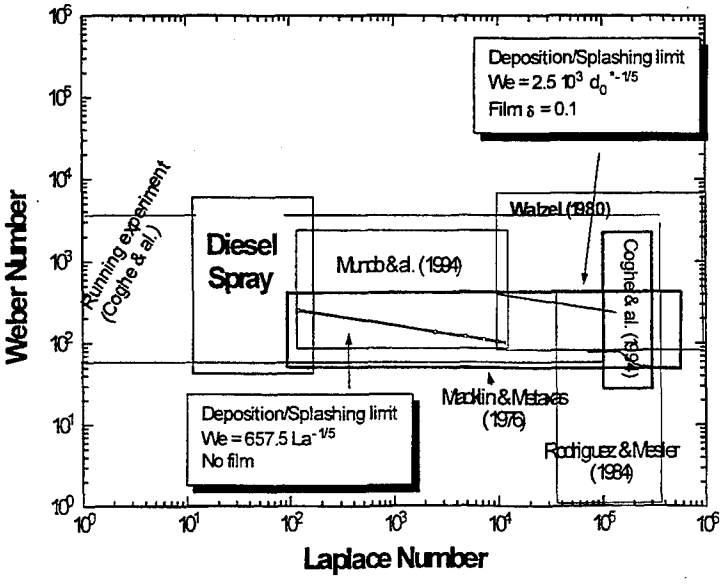

Figure 1 shows the ranges of Weber, Laplace and δ that could be obtained by the present set up. It is noteworthy that a large region characteristic of diesel spray can be covered in this way.

Experimental setup

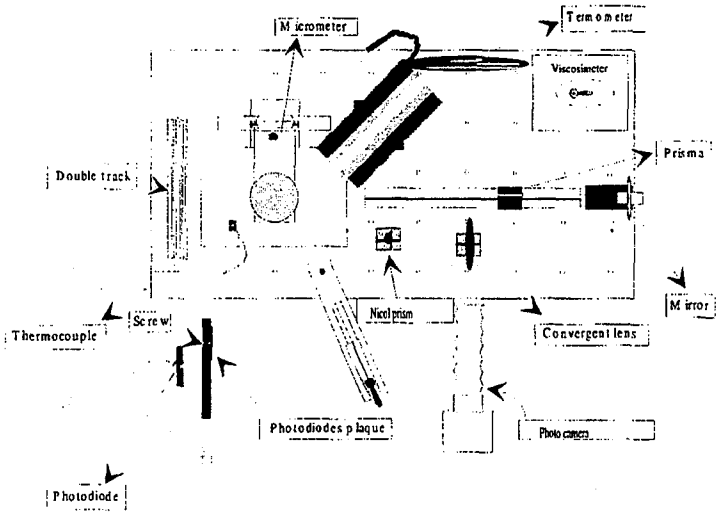

Fig. 2 Experimental setup

The experimental set-up is shown in figure 2. The drop generator produces drops of diameter between 2.5 and 5.5 mm. The liquid film was generated by submerging into a small tank an aluminum disk whose position relative to the free liquid surface could be varied with a 10 μm precision. The liquid film thickness could be measured by mechanical means with accuracy better than 30 μm and the parallelism between the upper aluminum disc surface and the free liquid surface was controlled by a toric level which allowed a parallelism better than 10 μm over the 10 cm diameter of the disk; to avoid big errors, film thickness bigger than 100 μm was used. The splash was observed and recorded by a still camera. The illumination was obtained by a lamp whose flash duration was 10 μs. The lamp was controlled trough a delayed generator that was triggered by the obscuration of a laser beam, detected by a photodiode, caused by the passage of the falling drop. By varying the delay between the trigger and the flash the whole phenomenon could be recorded. The splash velocity of the drop was varied by varying the drop generator high and velocities from 1.5 to 5 m/sec could be obtained.

Results and Discussion

In the experiment discussed below, the height of the drop generator relative to the impacting surface determines the primary drop velocity and varies the Weber number. Aerodynamic drag C_d was taken into account. Drop velocity was determined at a distance of 15 cm from the film by measuring the flying time between two laser beams imaged onto two photodiode. The agreement with a numerical simulation for falling velocity was better than 5% (acceptable, taking into account that the measurement uncertainty is not better than 10%). Weber was calculated using the calculated velocity rather than the measured one, because the relative values of the velocity are then affected only by the error in measuring the drop generator distance from the impacting surface, that is estimated to be 0.5%. Drop size was measured by photographing a falling drop together with object of known size. The estimated accuracy of this method (size was measured on

a digitised image by pixel counting) was better than 85 μm, that for the smallest droplets (2 mm) gives an error lower than 4%. Thus, absolute values of We are known with 15% accuracy, and relative value with accuracy better than 4.5%. Laplace number accuracy depends only on drop diameter measurement and is then better than 4%. Film thickness could be measured with 50 μm or lower accuracy that gives a maximum error on δ of 22.5% (but usually much lower). Finally, Bond number, which depends on the square of the film thickness, could be evaluated with a maximum error of 40% (but again much lower for h higher than 200 μm).

Fig. 3a $\Delta t = 0.1$ *msec*

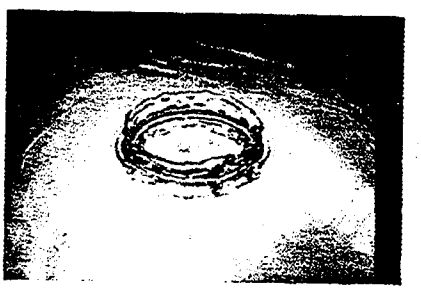

Fig. 3a $\Delta t = 1.1$ *msec*

Fig. 3a $\Delta t = 6.3$ *msec*

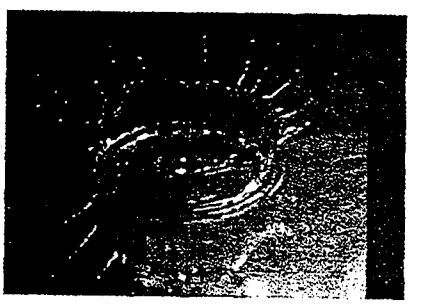

Fig. 3a $\Delta t = 11.3$ *msec*

Fig. 3a $\Delta t = 20.3$ *msec*

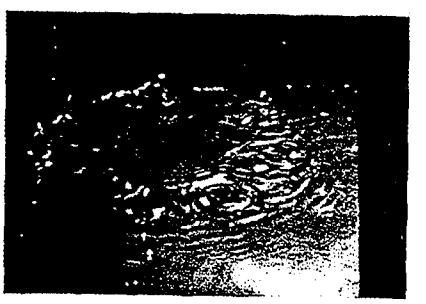

Fig. 3a $\Delta t = 25.3$ *msec*

Fig. 3 Evolution of splash process (We = 325, La = 384500, δ = 0.1)

The evolution of the splash can be conveniently subdivided into four periods, whose characteristics can be observed through the picture of fig. 3.

1) crown formation period (fig. 3 a-b): the liquid drop impacts on the film and, as a consequence, an annular perturbation (crown) begin to grow; 2) the jet formation period: liquid jets caused by azimuth perturbation on the crown grow, protruding from the crown (fig. 3 c); 3) the jet break-up period: the jets begin to break-up following the Rayleigh break-up mechanism (the jets velocity is low); drops with size comparable to the jet diameter and smaller (satellite droplets) are formed (fig. 3 d); 4) collapsing period: the crown collapses partially reabsorbed by the film and partially by the jets (fig. 3 e-f).

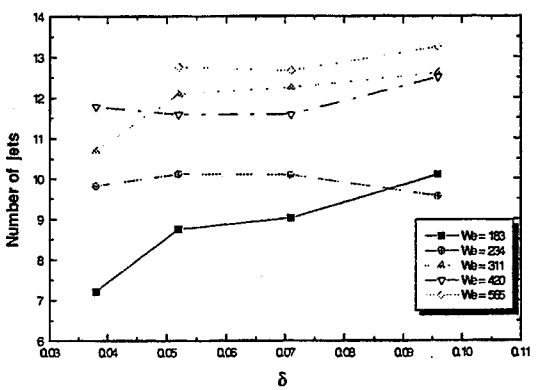

Fig. 4 Number of jets vs non dimensional film thickness

The influence of the non-dimensional film thickness and Weber number on the jets formation and break-up was analysed in a range of δ comprised between 0.038 and 0.096, and We ranging from 25 to 2500. From pictures the number of jets protruding from the crown after impact was counted; twelve is the minimum number of pictures taken for each condition that assures the rms of the measured number of jets be always lower than 10%. Figure 4 shows the number of jet as a function of δ, for different values of We. Apparently δ does not have a strong influence on the measured parameter, and no evident trends can be observed. Figure 5 shows instead the same data but plotted versus the Weber number. It can easily be appreciated that the number of jet is influenced by the impinging drop Weber number: over all the investigated range of δ, the number of jet increases with We. The diameter of the drop produced by the jet break-up could also be measured from the pictures, but some problem arises.

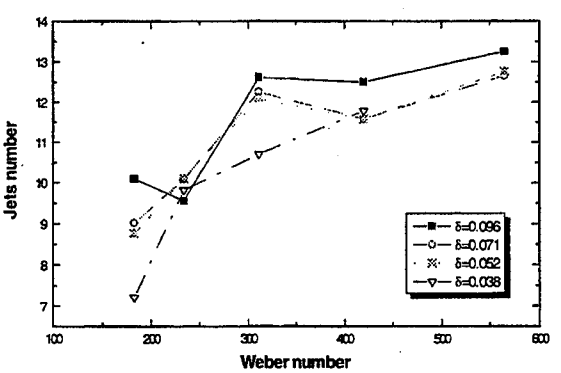

Fig. 5 Number of jets vs Weber number

1) Not all the drops produced by Rayleigh break-up of a liquid jet have the same diameter: satellite droplets can be formed due to second wave instability and in the present experiment this phenomenon was frequently observed (see fig. 6)

2) A picture taken at a defined time after impact may not give a statistically representative view of the secondary drop diameter distribution, due to the fact that diameter PDF may depend on time and that many drops may not be seen because they moved outside the illuminated region.

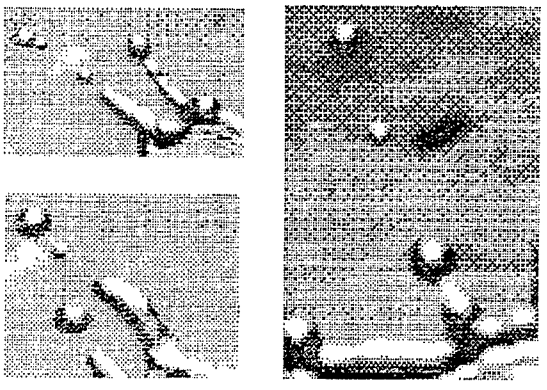

Fig 6 Some satellite second order droplets

It was then chosen to measure only those droplets that are detaching from the jet, excluding satellite droplets; in this way the measured droplet diameter gives also information about the jet diameter (in Rayleigh break-up detaching drop diameter is proportional to the jet diameter[15]) which cannot be easily measured from the pictures due to the fact that the liquid column does not usually have a uniform diameter. The non-dimensional film thickness on the drop diameter has small effects on the detaching drop diameter showing that for shallow splashing ($\delta<1$) the influence of the film thickness can be neglectful. The most influencing parameter is the impinging drop Weber number, fig. 7 shows that an increase of the drop We produces smaller droplets over all the investigated range of δ.

At different times after impact and with different drop Weber number, the crown growth was observed and figure after impact shows the crown diameter versus time. The crown continues to grow during all the splash although the radial velocity decreases with time (non-dimensional time $t^*=tv/\delta$, is used, following Macklin and Metaxas).

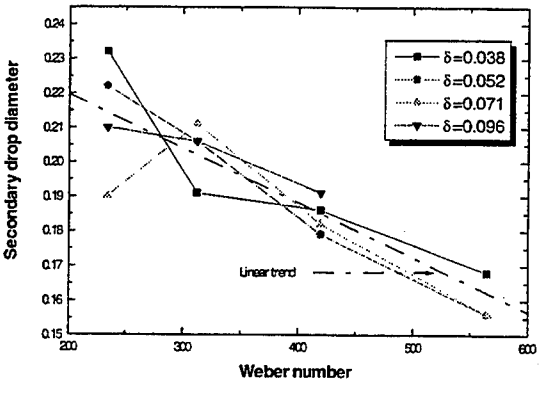

Fig. 7 Secondary drop diameter vs Weber number at different δ

These findings show that the whole phenomenon is controlled mainly by the impinging drop dynamic characteristics rather than the film structure, at least for the shallow splashing regime here investigated. Secondary drop diameter increases with time and a possible explanation is that when the crown begins to collapse, part of the liquid is reabsorbed by the jets, which then increases their diameter producing bigger drops; this effect is quite important because is partially responsible of the secondary drop diameter PDF widening.

Conclusions

The investigation revealed :

⇒ The splash can be subdivided into four periods: 1) crown formation, 2) jet formation, 3) jet break-up, 4) crown collapse.

⇒ The crown formed by the splash continues to grow but the crown diameter increasing rate diminishes with time.

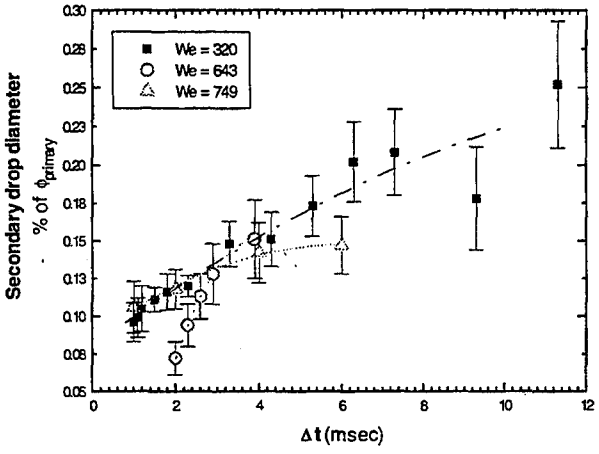

Fig. 8 Evolution of secondary drop diameter

⇒ The non dimensional film thickness does not have a strong influence on the splash dynamics: the number of jet and the detaching drop diameter are almost independent of δ

⇒ The increase of the impinging drop Weber number produces an increase of the number of jets, and a decrease of the secondary drop mean size.

⇒ The secondary drop diameter increases with time, probably due to the increase of the jet diameter produced by a reabsorbtion of the liquid forming the crown.

Acknowledgments

The experiments were performed at CNPM CNR laboratories in Milan. The authors would like to thank Mr. Valentino Michelotti for his work during the experiments.

References

[1]Araki K., Moriyama A., 1982, Deformation Behavior of a Liquid Droplet Impinging on a Hot Metal Surface, ICLASS '82

[2]Choi K.J., Yao S.C., 1987,Mechanism of film boiling heat transfer of normally impacting spray, Int. J. Heat Mass Transfer, 30, 2

[3]Fujimoto H., Saito M. , Minoura A. & oth., 1988, Characteristics of a diesel spray impinging on a flat wall, ICLASS '88

[4]Harlow H.F., Shannon J.P., 1967, The splash of a liquid drop, J. of Applied Phys, 38

[5]Makino K., Michiyoshi I., 1984, The behavior of a water droplet on heated surfaces, Int. J. Heat Mass Transfer, 27

[6]Worthington A.M., 1896, Impact with a liquid surface studied by the aid of instantaneous photography, Proc. Roy. Soc.,25

[7]Engel O.G., 1966, Crater depth in fluid impacts, J. of Applied Physics, 37, 4

[8]Engel O.G., 1967, Initial pressure, Initial flow velocity and the time dependence of crater depth in fluid impact, J. of Applied Physics, 38, 10

[9]Macklin W.C., Metaxas G.J., 1976, Splashing of drops on liquid layers, J. of Appl. Phys, 47

[10]Walzel P., 1980,Zerteilgrenze beim Tropfenprall, Chem. Ing. Tech., 52

[11]Rodriguez F., Mesler R., 1985, Some drops don't splash, J. Colloid Interface Sc., 106, 2

[12]Allen R.F., 1988, The mechanics of splashing, J. Colloid Interface Sc., 124, 1

[13]Allen R.F., 1975, J. Colloid Interface Sc., 51, 351

[14]Mundo Chr., Sommerfeld M., Tropea C., 1994, Droplet-Wall Collisions: Experimental Studies of the Deformation and Break-up Process, to be published

[15]Lafrance P., 1975, Nonlinear breakup of a laminar jet, The Physics of Fluids, 18, 4

MEASUREMENTS IN LAMINAR SPRAYS

LEVY, Y., GOLOVANEVSKY, B. and TIMNAT, Y.M.
Faculty of Aerospace Engineering, Technion - Israel Institute of Technology Haifa (Israel)

ABSTRACT

In spray combustors with low velocities in the laminar range, a unique operating mode with large amplitude self-induced oscillations of the flame shape is observed. Several coupled aero-thermodynamics mechanisms are responsible for the triggering of the flame oscillation. The phenomenon, previously described by the first author was only qualitatively analyzed. A parametric study is described, directed to investigate the various coupled mechanisms. Two main parameters were changed during the present work, namely the fuel flow rate and the momentum of the coflowing streams. The flow was monitored using a PDA system together with a computerized video camera. The results show an increase in the frequency of the flame oscillations with fuel flow rate and a decrease in oscillation frequencies with an increase in the momentum of the coflowing jets. Both effects indicated the significance of gravity. Finally we mention briefly methods required for measuring temperature, pressure density and species concentration.

INTRODUCTION

A Burke-Schumann type flame, using liquid fuel in the form of droplets, was studied recently both theoretically by Greenberg and coworkers[1-4] and experimentally[5]. The last work indicated that gravity, which was neglected in the above theoretical studies, can have a significant effect in the behavior of a laminar spray flame, causing under most operating conditions an oscillatory motion of the flame. It practically oscillates from very low flow velocities until relatively high flow rates are obtained, when it can no longer be considered as a laminar flow. It was assumed that gravity causes the heavier central fuel stream to loose its momentum and collapse into a mushroom shape. Thereafter it is accelerated vertically by the buoyancy force generated through heat transfer from the flame. This cycle, which is explained in more detail in Ref. (5) is repeated periodically. It was not predicted by any of the theoretical work, probably due to the fact that gravity was neglected.

Flame oscillations in a gaseous flame were reported in the literature. However, they are much smaller in amplitude and have higher frequency. Various observations of a Burke-Schumann type flame revealed the phenomenon of the flame tip flickering at frequencies of about 10-20 Hz. This effect, which was observed experimentally[6-10] and also predicted numerically[11,12], is the direct result of gravity induced buoyant forces on the flow of the reaction products, of aerodynamic instabilities in the jet itself and of heat release effects. Ellzey et al.[12] presented predictions both considering and neglecting gravity. They showed that neglecting gravity gave a steady flow field but including it caused large structures to form and to be convected downstream at frequencies of the order of 15-20 Hz.

An interesting experimental configuration is that of a combustor operating in a horizontal direction as if it is unaffected by gravity. This case is explained in more detail in the paper. In the present study we investigate the governing parameters that affect the oscillatory motion, mainly the amplitude and frequency. The fact that the oscillatory motion is affected by a relatively large number of aerothermodynamic phenomena has led to a parametric study, where each time only one parameter is changed. In the present work the equivalence ratio and the momentum of the co-flowing streams were changed between the maximum possible limits. Future work will include geometrical configurations as well.

THE EXPERIMENT

A schematic drawing of the combustor is illustrated in Fig. 1. The combustor consisted of two coaxial quartz tubes. The outer tube had an I.D. of 71 mm with a wall thickness of 2 mm and the inner one had an I.D. of 12.9 mm and an O.D. of 14.8 mm. The length (height) of the outer tube was 30 cm. Tests with different length tubes or even without the outer tube, were performed to eliminate the possibility that the dominant phenomena originate from acoustic coupling, and it has shown negligible differences in behavior. As illustrated in Fig. 1, the combustion air entered through four radial entrance holes and passed through a series of fine-mesh screens and flow straighteners. The upstream length from the screens to the combustor (the tip of the center tube) was about 25 cm and the total length of the center tube (from the atomizer to the tip) was about 50 cm.

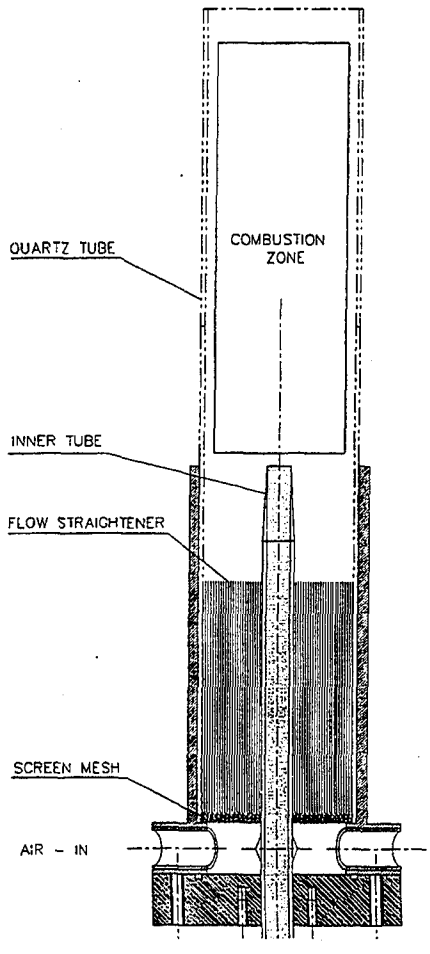

Fig. 1 - Schematic drawing of the combustor.

Heptane fuel was introduced into the combustor through the center tube in the form of fine droplets. A slightly modified Sonotek ultrasonic nozzle # 8700-60 MS was used to generate the droplets. As shown in Fig. 2, the droplets were injected as a narrow conical spray. The droplets were then carried upwards by a nitrogen gas stream. The nitrogen was injected through a tube

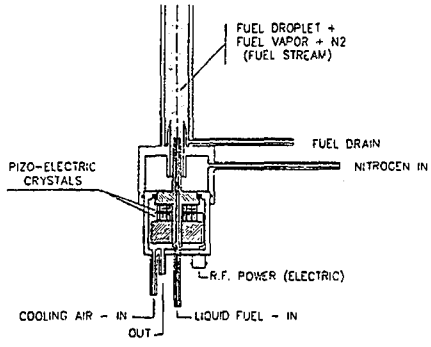

Fig. 2 - Schematic drawing of the ultrasonic atomizer.

which surrounds the "horn" of the ultrasonic atomizer. As the droplets traveled upwards through the 50 cm tube, they partially vaporized and interacted with each other, causing a subsequent change in their size and momentum. The flow of nitrogen was always adjusted to have an average velocity value equal to that of the air. The properties of the droplets were measured at the exit of the central tube. Typical size distribution on the center line just at the exit of the inner tube is shown in Fig. 3a. Figure 3b shows the total velocity histogram and Fig 3c demonstrates the size velocity correlation. It can be seen that the velocity histogram has a nearly Gaussian distribution which extends to near zero negative values. As can be seen from Fig 3c, that part of the histogram originates mainly from the large droplets which are too heavy to continue to be carried upwards by the sudden expanded nitrogen. The small droplets (less than about 10 microns) can be used to represent the carrier gas velocity. Experimental uncertainty in measurements for drop size is estimated at ±6.5% and at ±0.5% for velocity[5]. The relatively low velocity of the carrier gas near the wall of the inner tube was not sufficient to carry the larger drops. This caused them to descend and come into contact with the tube wall forming a liquid film that flowed downward. The number of droplets that hit the wall and the resulting fuel flow in the downward direction was significant, especially in the lower parts of the center tube. A drain was incorporated in the combustor configuration at the bottom of the center tube (see Fig. 2) for continuous removal of the liquid film. The measurement of the actual fuel flow rate to the combustion zone always considered the drained amount. Due to the high turbulence within the inner tube, caused by the interaction between ascending droplets and the descending heavier droplets, fluctuations in the drained amount were detected and hence also in the net fuel flow, see Fig. 4.

Experimental measurements were obtained using two techniques: Phase Doppler Anemometry (PDA), which simultaneously measured the size and velocity of individual droplets, and a CCD camera alternatively coupled with laser light-sheet illumination for large scale observations of the two-phase flow and the flame. The frequency of the flame oscillation was measured using the FFT routine over the instantaneous gas velocity (PDA) results in the combustion zone during several flame cycles. A special case where the combustor was mounted horizontally was also investigated. This test was performed in an attempt to isolate the effect of gravity on the flame. However, due to accumulation of droplets on the inner tube walls and the necessity for drainage, a small inclination angle (2°) was allowed. The special alignment of the combustor in this case did not allow for PDA measurements and only video photography was employed.

RESULTS AND DISCUSSION

The oscillatory motion analyzed in the present study is different from the conventional flame flickering commonly reported in the literature. In the present study the entire volume of the flame is affected in an expansion-contraction type modulation whereas the reported gaseous flame

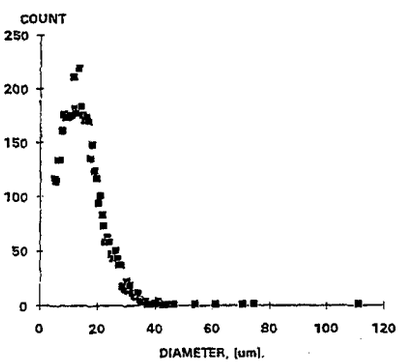

a. size distribution

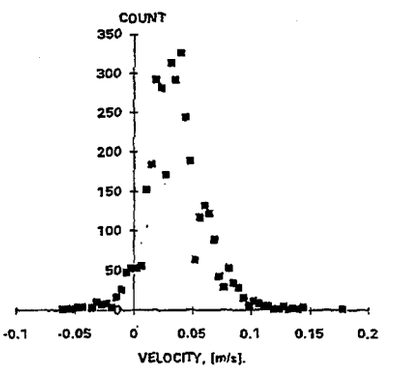

b. velocity histogram

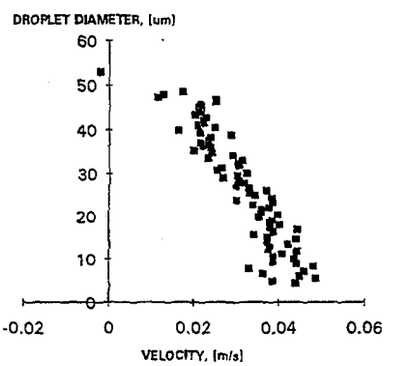

c. size - velocity correlation

Fig. 3 - Droplets characteristics at the exit of the center tube, h=0 mm (entrance to the combustor).

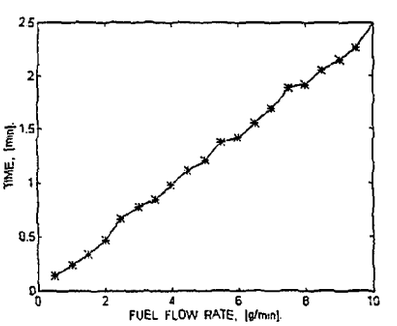

Fig. 4 - Variation of net fuel flow with time.

flickering affected the flow of reaction products only at a distance downstream of the nozzle. Operating the combustor in a horizontal orientation changed the behavior of the flame significantly. The primary goal, which was to eliminate or minimize the effect of gravity, was only partially achieved. The initial part of the flame showed a constant behavior with a steady flame. However further downstream the flame, which was horizontal at the beginning, exhibited a vertical direction (due to buoyancy). In conditions, where fuel evaporation was completed before the vertical part of the flame, the flame remained almost stable. In cases where droplets existed even in the region where the flame obtained a vertical direction (higher flow momentum), periodic oscillations were observed only in the vertical portion of the flame. As indicated, this part of the experiment was only recorded by a CCD camera and therefore no quantitative data are given in the paper. It seems that this experiment strengthens the hypothesis that oscillations are induced by gravity (as only the vertical portion oscillates). However, it cannot yet be considered as conclusive.

A major part of the experimental effort was directed to study the influence of fuel to air ratio on the flame behavior. The combustor was operated during constant air and nitrogen flow rates while altering only the liquid fuel flow rate to the ultrasonic nozzle. This arrangement enables one to maintain constant velocity of the fuel stream while changing the mass flow rate of the fuel. Hence it allows to isolate the effect of fuel flow and heat release on the flame behavior. Several similar sets of tests were performed, while each set was carried out with different air (and nitrogen) velocity. Results are given in Figs. 5-10.

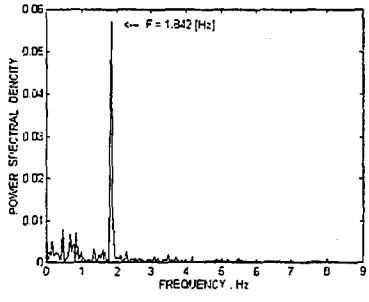

Fig. 5 - A typical frequency spectral density of the velocity oscillations.

Figure 5 shows a typical result of an FFT performed on the instantaneous velocity fluctuations. A dominant amplitude in the frequency spectra is clearly observed at the value of the oscillation. Figure 6 shows size and velocity histograms of the flow at 3 mm above the nozzle. A double peak is seen, typical of oscillating flows. The histogram is distributed around the zero value with relative large negative velocity values. This could indicate that the measurements were performed within the core of the vortex that is responsible for the descent of the flame within the oscillation cycle (Ref. 5). Figure 7 illustrates the variation of oscillating frequency with height for typical operating conditions. It shows that the frequency remains almost constant along the flame. This indicates that the whole of the flame is oscillating as a common element and that the effect is of macro-scale type. The figure also shows that the frequency is reduced to zero, hence no oscillations, close to the fuel nozzle tip. This indicates that the oscillations are not driven by the fuel or air supply lines but rather are self induced at some distance downstream of the combustor (the zero frequency value at higher levels, above 12 mm, are due to insufficient measurement data). Even though the flame oscillates, the average velocity along the center line increases rapidly with height (a factor of 10 within 15 mm). This is mainly due to the heat addition from the chemical reaction, the associated expansion of reaction products and entrainment from the

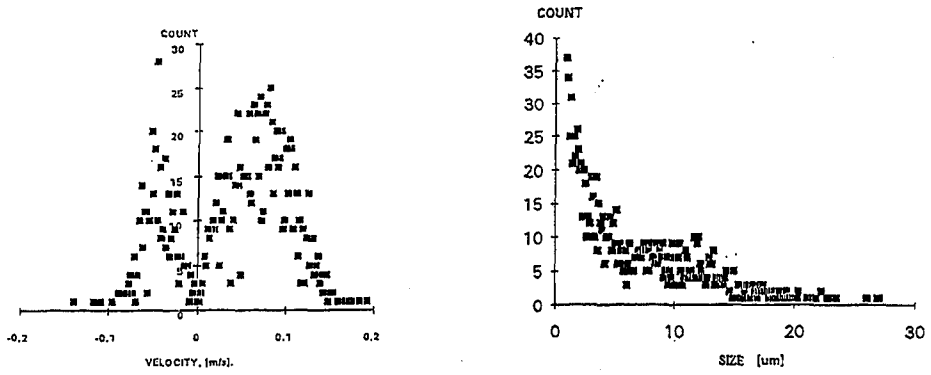

Fig. 6 - Velocity and size histogram at 3 mm downstream of the fuel nozzle.

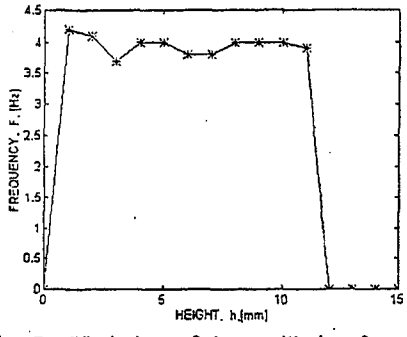

Fig. 7 - Variation of the oscillation frequency with height along the combustor center line.

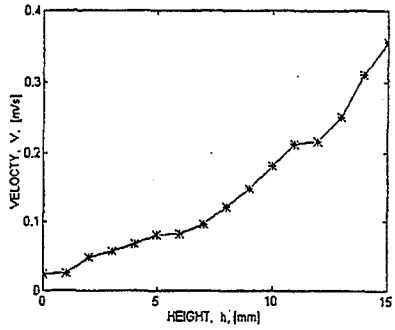

Fig. 8 - Variation of average velocity along the centerline of the combustor.

surrounding air. Meanwhile the average diameter of the fuel droplets is decreased by a factor of 4 (from 22 microns to about 5 microns over a distance of about 7 mm), see Fig. 9. An apparent bias effect on the measurements of the mean size of the droplets indicated that the size of the droplets increases after a certain distance. This effect is typically caused by the fact that most of the small droplets evaporate and disappear, leaving only the big ones, hence mathematically indicating an increase in the mean size.

Figure 10 summarizes numerous experimental results during which a parametric study of two major parameters was performed. The combustor was operated from the lowest possible air flow to the maximum practical one. The nitrogen flow in the central tube was always adjusted to maintain an average velocity equal to that of the air. It is clearly seen from Fig. 10 that increasing the fuel flow rate (and the fuel to air ratio) increases monotonically and significantly the frequency of oscillations. This phenomenon occurs independently of the air and fuel stream velocities. The changes in frequency are sometimes by more than a factor of 2 in the investigated range. The reason for the latter is probably the higher associated heat release, which increases buoyancy that accelerate faster the elevation of the flame and its separation from the fuel stream. The fuel stream which is even heavier, due to the higher portion of fuel, collapses faster and disengages itself earlier from the heat source. The flame is consequently reduced in size and pulled downwards by the center part of the vortex generated at the wake of the central fuel stream(5). Hence all the process occurs faster.

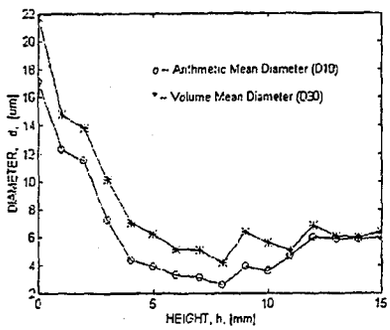

Fig. 9 - The change in average fuel droplet diameter along the centerline of the combustor.

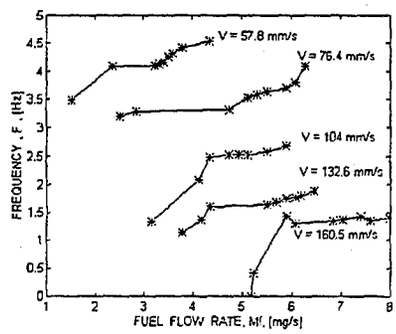

Fig. 10 - Variation of flame oscillation frequency with fuel flow rate and average velocity (air and nitrogen).

The momentum of the flow seems to have an opposite and more significant effect. The higher the air (and fuel stream) velocities, the slower the oscillation frequency. This phenomenon was investigated over a large range of velocities and was found to exist monotonically over the whole operating range. The reason for the latter is probably the fact that higher surrounding air flows reduce and delay the collapse of the fuel stream into the mushroom shape, hence it maintains a higher vertical level. Consequently, it separates less from the flame, reducing the driving force for the oscillations.

ADDITIONAL MEASUREMENTS

Other important data that must be obtained for a more complete understanding of laminar sprays are temperature, pressure, density and major species concentration. The measurement of these quantities is discussed in detail in a paper by Timnat[13]. Here we shall mention briefly the various options. We shall treat only non-intrusive methods, which do not introduce disturbances into the flow.

Temperature measurements can be performed by a modified line reversal technique, by spontaneous Raman scattering, by Rayleigh thermometry, by coherent anti-Stokes Raman scattering (CARS) and by spectroscopic techniques.

Simultaneous measurement of temperature and density can be obtained by using laser induced fluorescence (LIF). This method allows also to obtain major species concentration. These variables can also be measured by a microwave resonance lamp absorption technique, by CARS and by photo-deflection spectroscopy. Due to their relatively large associated cost, the choice of the appropriate technique will depend on the experimental conditions and the availability.

CONCLUSIONS

The recent experimental results strengthen the hypothesis that the naturally occurring oscillations are primarily induced by gravity. The horizontal combustion experiment indicated that the initial (small) zone, where the flame was still horizontal and uninfluenced by gravity, did not oscillate. In the vertical (normal) configuration, the increase of heat release has led to speeding the frequency of oscillations where as increasing the momentum of the flows decreased the speed of oscillations. Both effects are directly linked to gravity further highlighting the necessity to incorporate gravity effects in the numerical modeling.

REFERENCES

1. Greenberg, J.B. *Combust. Sci. Technol.* 75:13-30 (1991).
2. Greenberg, J.B. *Combust. Flame* 77:229-240 (1989).
3. Greenberg, J.B., and Cohen, R. *Atomiz. Sprays* 2:275-293 (1192).
4. Greenberg, J.B., and Cohen, R., Winter Annual Meeting of ASME on Heat and Mass Transfer in Spray Systems, Atlanta, Georgia, HTD - Vol. 187, 1991, p. 11.
5. Levy, Y. and Bulzan, D., "On the Oscillation of Combustion of a Laminar Spray", accepted for publication in *Combust. Flame* (1994)
6. Durao, D.F.G., and Whitelaw, J.H. *Proc. R. Soc. A.* 338:479-501 (1974).
7. Toong, T.Y., Salant, R.F., Stopford, J.M., and Anderson, G.Y. *Tenth Symposium (International) on Combustion*, The Combustion Institute, Pittsburgh, 1965, p. 1301.
8. Kimura, I. *Tenth Symposium (International) on Combustion*, The Combustion Institute, Pittsburgh, 1965, p. 1295.
9. Ballantyne, A., and Bray, K.N.C. *Sixteenth Symposium (International) on Combustion*, The Combustion Institute Pittsburgh, 1976, p. 777.
10. Chen, L.D., Seaba, J.P., Roqumore, W.M., and Goss, L.P. *Twenty-Second Symposium (International) on Combustion*, The Combustion Institute, Pittsburgh, 1988, p. 677.
11. Davis, R.W., Moore, E.F., Roqumore, W.M., and Chen, L.D. *Combust. Flame* 83:263-270 (1991).
12. Ellzey, J.L., Laskey, K.J., and Oran, E.S. *Combust. Flame* 84:249-264 (1991).
13. Timnat, Y.M., *Progress in Aerospace Sciences* 26:153-186, 1994.

NATURAL CONVECTION ON INCLINED STEPWISE SURFACES

U.M. Fomin, A.V. Lebedev, S.V. Haidarov
Institute of Theoretical and Applied Mechanics,
Siberian Branch of Russian Academy of Science, Novosibirsk, Russia.

Free convective flows near an inclined surface are well studied at present both theoretically and experimentally. The present study is aimed at investigation of gasdynamic and thermal peculiarities of the flow arising at natural convection on inclined stepwise surfaces in the air.

The experimental facility consisted of two inclined heated plates and connecting unheated horizontal ledge. The temperature was measured by means of thermopairs both on the surface and in the boundary layer. The distribution of the flow velocity in the boundary layer was studied by kinematic method. The measurements were taken for various values of the heat flux on the surface. The flow visualization was realized by Schlieren-method and by fume method.

The simulated Rayleigh numbers Ra are varied in the range from 10^2 to 10^{11} ($Ra=Gr \cdot Pr$) where Gr is the Grashof's number, Pr is the Prandtl number. The studies proved that this range corresponds to laminar and transitional flow regimes. The Nusselt number dependence $Nu=f(Gr \cdot Pr)$ for the flow near inclined stepwise surfaces has a discontinuity at natural convection, unlike the flow near a separate inclined plate. The discontinuity is stipulated by the presence of a ledge. The experiments showed a separated nature of the flow about the ledge and formation of vortices there. The turbulent jet originating at the lower plate joins the boundary layer of the upper plate. The heat flux density increasing, the point of joining shifts downwards to the ledge. This turbulent jet changes the boundary conditions on the outer border of the boundary layer of the upper plate: velocity is not equal to zero, temperature is not equal to the temperature of the environment. Besides, the velocity and temperature profiles in the boundary layer are changed. The parameters of the temperature pulsation were studied in the thermal boundary layer of the heated plates. The characteristic pulsation frequencies and dependencies of the pulsation values on the coordinates were determined. The dependence of the pulsation intensity on the coordinate normal to the surface has an explicit maximum. The results of measurements and visualization allowed us to discern two parts in the boundary layer: the internal part adjacent to the surface where the flow remains laminar when the Grashof's numbers are large enough and the external part with considerable perturbations even at small Grashof's numbers. It was found that flow turbulization starts at the external border of the boundary layer.

Free-convection flows near inclined surfaces are quite well studied [1-9]. The conducted studies resulted in theoretical and empirical dependencies allowing one to determine parameters of such flows with acceptable accuracy. But no data are found is references concerning the flows arising near inclined stepwise surfaces under the condition of natural convection in the air. The present study is aimed at experimental investigation of gasdynamic and thermal peculiarities on inclined stepwise surfaces under the condition of natural convection. Such problems arise at ventilation of various open casts for mining mineral resources.

EXPERIMENTAL FACILING

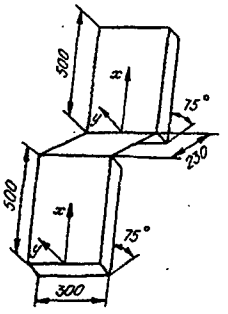

The device scheme.

Fig.1.

To carry out experiments an experimental facility was created (Fig.1). It is a construction consisting of two electrically heated plates and unheated horizontal ledge connecting the lower plate top with the upper plate bottom. Both heated plates have multilayered construction comprising the test surface, electric heater and heat insulator limiting the heat flux in the direction from the test surface. The plates length is 500mm. In the symmetry plane of the facility, on its test surfaces, 29 Ni-Cr-constantan thermocouples with the junction diameter 0.4mm are located to measure the local surface temperature. The power to the heaters was applied through two-channel voltage regulator (laboratory autotransformer) and was controlled by an ammeter and voltmeter placed on each channel. To examine the boundary layer with a probe we designed and manufactured a coordinate device consisting of U-shaped frame with a microscrew attached to it, where various measurement equipment was mounted to find the flow parameters. The coordinate device resolution over the Y axis is better than 0.1mm, over the X axis - better than 1mm (see the coordinate system in Fig.1).

The influence of unheated horizontal ledge on the flow character near the stepwise surfaces was investigated. The study was carried out in two-dimensional statement so all measurements were taken in the symmetry plane. The facility allowed the simulation of the Rayleigh number range $10^2 < Ra < 10^{11}$, where $Ra_* = Gr_* * Pr$, $Gr_* = Gr * Nu$. Here Gr is the Grashoff number, Nu is the Nusselt number calculated by the current coordinate x, Pr is the Prandtl number. All measurements were taken for various values of the heat flux density on the plate surfaces (132.8; 247.4; 401.6; 514.9; 612.7 Wt/m^2). The facility had constant geometric parameters: the inclination angle of the plates to horizontal line $\alpha = 75^\circ$, the ledge length/plate length ratio k=0.46 and k=0.16 (Fig.1).

MEASUREMENT METHODS

To measure the temperature in the boundary layer we used a Ni-Cr-constantan probing thermocouple with the junction diameter $d = 0.05$mm. The thermocouple thread was placed at the U-shaped holder and was located perpendicular to the symmetry plane of the facility, along isotherms. The mean temperature was measured with a digital voltmeter connected with the thermocouple through a ripple filter.

Pulsation temperature characteristics were found as follows: thermal electromotive force was applied via a linear amplifier to an oscillograph where it was recorded during 10 sec. The recorded signal was photographed and the obtained data helped to determine the root-mean-square values of pulsations σ and their characteristic frequencies.

The problem of velocity measurement in the boundary layer turned out to be the most complicated. The difficulty lies in a small velocity value and in the presence of the thermal boundary layer beside the dynamic one. To take the measurements we elaborated and realized a new kinematic method. The scheme of

this measurement device is shown in Fig.2a. The essence of the method is as follows: a thin Ni-Cr thread (d=0.05mm) tightened perpendicular to the symmetry plane of the plates performs harmonic oscillations along the normal to the surface with a prescribed frequency . In the thread center a small glycerin droplet is placed, it evaporates when the thread is electrically heated. The external flow carries off the smoke trace and a running sinusoid of microscopic glycerin droplets appears for a motionless observer. This sinusoid is fixed on a film by the optic system (Fig.2b). To "freeze" the pattern for the instant when it is photographed we used an impulse light source with the impulse length not exceeding 0.001 sec. Having found, after the film development, the distance L between one-phase points on the curve image, one can calculate the flow velocity by the formula: U=f*L. The construction of the measurement device allowed the change in the amplitude and frequency of the thread oscillations. These parameters were chosen in such a way that the flow over the thread was continuous, and sufficient number of oscillation periods was fixed at the still. According to H.Schlichting [6], the first signs of the flow separation from the cylinder at its transverse flow around are observed at the Reynolds number Re=5. In the present paper this requirement was made even more strict by imposing the constraint Re<1. Here is found from the thread diameter. The frequency f=50Hz and amplitude 1mm satisfy all above mentioned conditions. Nevertheless, the influence of the heat jet from the heated oscillating thread stipulates a systematic error in velocity profiles. To eliminate this error we considered the solution of the problem of a pointwise linear heat source [2] and made the correction [10].

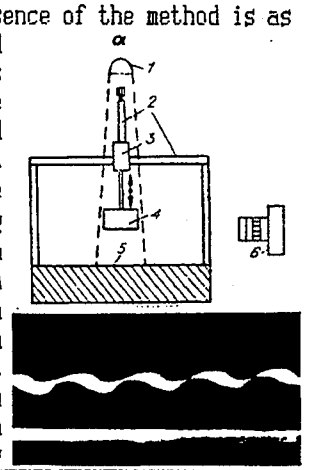

Fig. 2. Velocity measurement method.
a — measurement device scheme (*1* — impulse light source, *2* — coordinate device, *3* — oscillator, *4* — thread, *5* — heated plate, *6* — optic system); *b* — a characteristic curve for determining velocity.

The visualization was carried out by the shadow method and with the help of glycerin smoke.

MEASUREMENT RESULTS AND ANALYSIS

The dependence $Nu=f(Ra_*)$ was found from the results of the temperature measurement on the plate surfaces. The data processing was conducted as follows. For each of the five values of the heat flux density at which the measurements were taken, 5-7 temperature measurements were chosen. With the help of the data obtained the arithmetical mean temperature values in every point were calculated depending on the heat flux density, and these values were used to find the values of Ra_* and Nu numbers. The experimental points were marked on the graph in coordinates $\lg(Ra_*)$-$\lg(Nu)$ and were approximated by the least squares method by separate straight lines for the upper and lower plates. But since very close dependencies were obtained, one generalized graph was built (Fig.3) which is described by an approximation dependence of the form

$$Nu = 0{,}492\ (Ra_*)^{0{,}233} \qquad (1)$$

The boundary layer probing resulted in the mean temperature distribution there both for the upper and lower (Fig.4) plates (x =0.005m; 0.025m; 0.065m; 0.249m; 0.462m). The dependencies are plotted in the axes $\bar{T} = \frac{T - T_\infty}{T_w - T_\infty}$

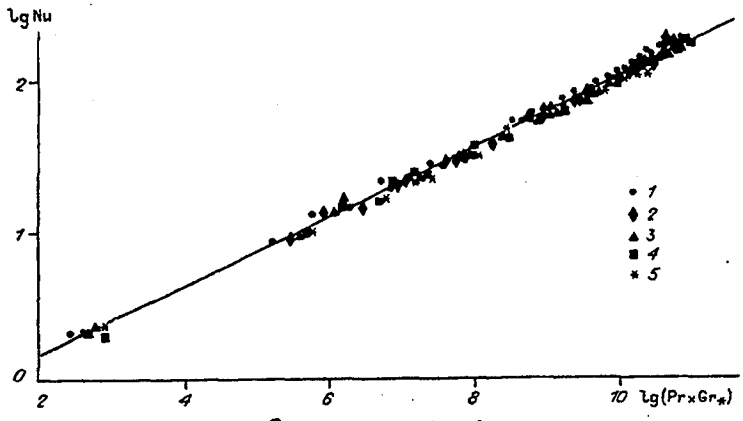

Fig. 3. Heat exchange on the surfaces.
1–5 – q = 132.8; 247.4; 401.6; 514.9; 612.7 Wt/m².

$\bar{y} = y/y_{1/2}$, where $y_{1/2}$ is the coordinate where the condition $\bar{T}(y_{1/2})=0.5$ is satisfied; T_w is the plate surface temperature. For the lower plate the experimental points are well approximated by the equation of the form $\bar{T}=(1-\bar{y}/3.41)^2$

Figure 5 shows some results of the measurements of temperature pulsation parameters in the lower plate boundary layer in the axes $\bar{\sigma}(y)=\sigma/(T_w-T_\infty)$ (Fig.5a) and $\bar{\sigma}_A=\bar{\sigma}/\bar{T}$ (Fig.5b). The characteristic pulsation frequencies were qualitatively estimated and lay in the range 0.5...3 (Hz).

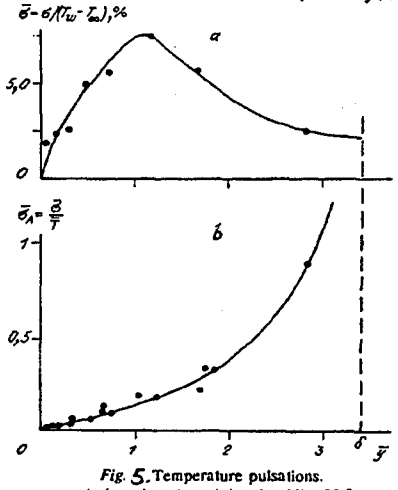

Fig. 5. Temperature pulsations.
a – absolute values; b – relative values (X = 0.207 m, q = 132.8 Wt/m²).

The velocity distribution was studied for $x=0.5$m both on the upper and lower surfaces for various heat flux densities. The velocity profiles obtained after the experimental data processing with due account of the influence of the heat jet from the heated thread are given in Fig.6a,b. Figure 6d shows the maximum velocity u_{max} in the boundary layer as a function of the heat flux density. Vliet and Liu [3] introduced the notion of "displacement width" of the boundary layer for the natural convection near the heated surface by the formula $\delta^*=\int_0^\infty \frac{u}{u_{max}}dy$ and made the Y coordinate dimensionless for this parameter. In the present paper a similar transformation was made. Figure 6c shows the dimensionless velocity profile near the lower surface generalized for four heat fluxes. Such a generalized pattern cannot be obtained for the velocity profiles on the upper plate. The dependence of δ^* on the heat flux density for the lower surface is shown in Fig.6f.

To have more complete knowledge about the flow pattern, various visualization methods were used, their results were correlated with each other and with measurement results. To reveal the boundary layer state on the plate surfaces we used visualization by the smoking wire method and with Tappler device. Even at small heat flux density, disturbances occur both in dynamic and thermal boundary layer on both plates. Judging from the shadow photographs of the thermal boundary layer, the disturbances development starts from its

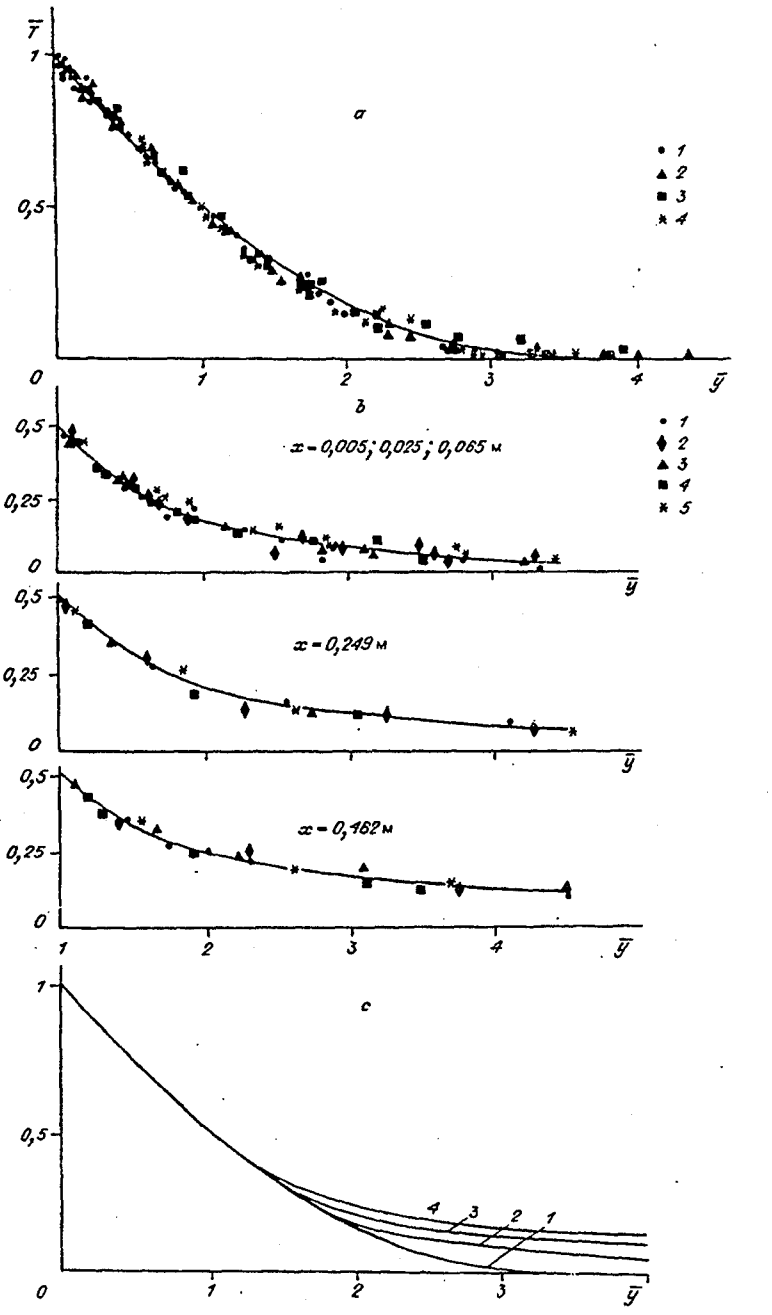

Fig. 4. Temperature profiles.

a — at the lower surface ($1-4-q$ = 132.8; 247.4; 401.6; 612.7 Wt/m^2); *b* — at the upper surface ($1-5-q$ = 132.8; 247.4; 401.6; 514.9; 612.7 Wt/m^2); *c* — generalized temperature profiles (*1* — for the lower surface; for the upper surface; 2 — X = 0.005; 0.025; 0.065 m; *3* — X = 0.249 m; *4* — X = 0.462 m).

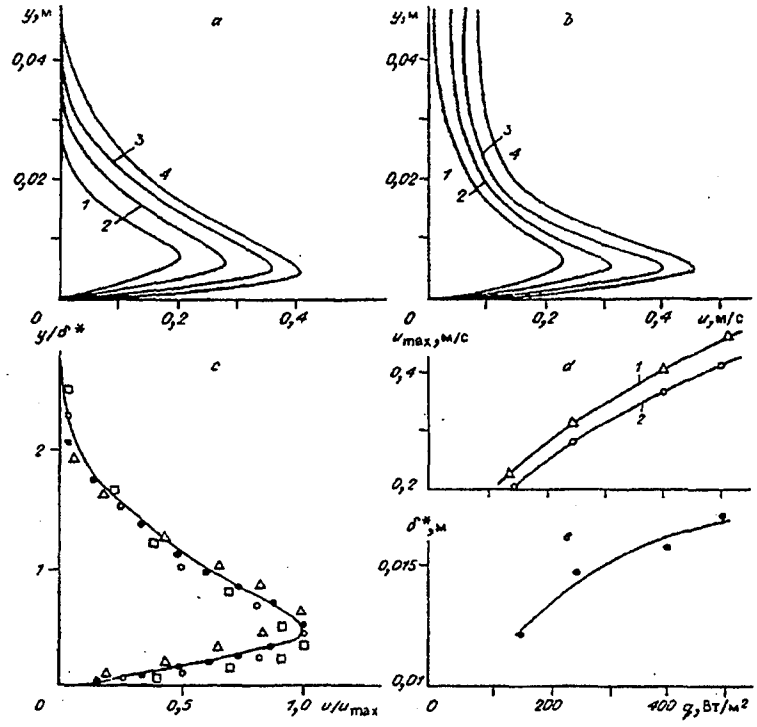

Fig. 6. Dynamic boundary layer characteristics.

a — velocity profiles at the lower surface; *b* — velocity profiles at the upper surface; *c* — dimensionless velocity profile at the lower plate (*1*, Δ — q = 132.8; 2, ● — 247.4; 3, ○ — 401.6; 4, □ — 514.9 Wt/m^2); *d* — dependence of the maximum velocity on the heat flux density (*1* — the upper plate, *2* — the lower plate); *e* — dependence of the boundary layer displacement width on the heat flux density at the lower surface.

external border, the flow in the inner region remaining laminar. This is proved by the measurement results (Fig.5b): the temperature pulsation temperature related to the mean local temperature in a definite point increases with the y coordinate.

The flow organization near the ledge was of greatest interest. Figure 7a shows the streamlines passing from the upper part of the lower plate. The closer to the plate surface they were located, the more they are deflected towards the ledge. Most distant streamlines are practically straight, keeping up the inclination angle of the plate. The deflection is associated with the air inflow by the upper heated plate. Some regularity was found: the inclination angle of the streamline adjacent to the lower plate surface increases with the heat flux density increasing. The shadow flow pattern (fig.7b) taken near the upper part of the lower plate does not reveal noticeable deflection of the boundary layer towards the upper plate. This allows one to draw the following conclusion: flowing over the unheated ledge, the air deflected due to the upper plate inflow is cooled more intensely than the air rising in the undeflected jet. From the lower plate edge vortices broke away periodically (Fig.8a) and moved towards the upper plate nearly horizontally. This is a probable mechanism of mass transfer over the ledge surface. This testifies to the separation nature of the flow around the ledge. The flow visualization at less sloping location of the plates and the geometric parameter k=0.16 made it possible to state the absence of continuous flow around the ledge, which is well seen at the photograph in Fig.8b where the

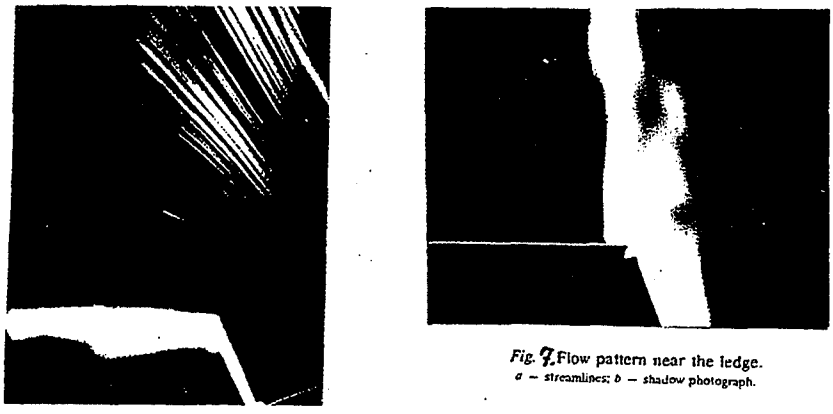

Fig. 7. Flow pattern near the ledge.
a — streamlines; *b* — shadow photograph.

transfer from the lower to the upper plate is realized by the system of two attached vortices located at the ledge. The visualization of complete flow pattern at k=0.46 allowed us to find that the jet passing from the lower plate is deflected towards the upper plate and is attached to the flow in its boundary layer. The point of attachment shifts downwards to the ledge with the heat flux density increasing.

The same conclusion may be drawn from the analysis of the mean temperature and velocity profiles. Let us take the distance from the upper plate surface to the point where the condition $\frac{\partial T}{\partial y}=0$ is satisfied as the boundary layer width at the upper plate. At the external border of the introduced thermal boundary layer the temperature is not equal to the temperature of the surrounding medium, but is somewhat higher. This is caused by the impact of the heated jet passing from the lower plate. If, similarly, we introduce to the above the dynamic boundary layer width (the distance from the surface to the point where the condition $\frac{\partial u}{\partial y}=0$ is satisfied) one may note that the velocity is not equal to zero at its external border (influence of the jet from the lower plate). At the upper plate the dynamic boundary layer width is practically constant with the heat flux density increasing, and the point of the velocity maximum shifts slightly to the surface. For the lower plate the dynamic boundary layer width increases slightly with the heat flux density and the point of the velocity maximum shifts to the surface. The general fact for both plate is the increase of the flow velocity with the heat flux density increasing. Note that for nearly equal conditions at the wall the velocity is higher at the upper plate.

Fig. 8. Vortex systems on the ledge.
a — k = 0.46; *b* — k = 0.16.

Self-similarity of the temperature profiles was found at the lower plate (Fig.4a) and their similitude for various heat flux densities in the fixed

sections - at the upper plate.

As was mentioned above the heat exchange between the plates is described by a criterion equation (1) similar to theoretical one describing the heat exchange for the laminar flow near an inclined surface under the condition of natural convection [4] $Nu=0.519(Ra_*)^{0.2}$. The difference in the power indices may be explained by the fact that experimental points for all heat fluxes and coordinates of the both plates (Fig.3) were generalized though the points corresponding to the Rayleigh number range $6.5\cdot10^9 - 9\cdot10^{11}$ may be approximated by one curve corresponding to the dependence with the larger power index approaching the power index for the dependence for turbulent flow [5]: $Nu=0.241(Ra_*)^{0.25}$, which testifies to the presence of transition region. The visualization results proves the same.

In conclusion, let us summarise the main results of the work: 1.The heat exchange processes at the upper and lower plates are characterized by close criterion dependencies and are similar to the heat exchange process at a single plate of the same dimensions.

2.Separation flow near the ledge was found. Depending on the ledge length/plate length ratio two flow forms were observed: a) a system of two attached vortices on the ledge surface; b) vortices separation from the lower plate edge and their motion along the ledge.

3.The jet passing from the lower surface is attached to the boundary layer of the upper surface and changes the velocity and temperature profiles there. The point of attachment shift downwards to the ledge with the an increase in the heat flux density at the surfaces.

4.Two regions may be classified in the boundary layer: the internal region where the flow remains laminar for large Ra_* and the external one where disturbances are observed even at small Ra_* numbers.

REFERENCES

1.T.Cebeci and P.Bradshaw. Physical and Computational Aspects of Convective Heat Transfer. Moscow, Mir, 1987, p.330.
2.B.Gerhart, Y.Jaluria, R.Mahajan and B.Sammakia. Buyoancy-induced flows and transport. Moscow, Mir, 1991, p.104.
3.G.Vliet and C.Liu. An experimental study of turbulent natural convection boundary layers. Translations of the ASME, series C, 1969, vol.91, No.4, p.73.
4.O.G.Martynenko and Yu.A.Sokovishin. Free convection heat exchange at a vertical surface. Minsk: Nauka i Tekhnika, 1977, p.61.
5.E.Eckert and R.Drake. Heat and mass transfer. Moscow, Gosenergoizdat, 1961, p.400.
6.H.Schlichting. Boundary layer theory. Moscow, Nauka, 1969, p.74.
7.S.S.Kutateladze, A.G.Kirdyashkin and V.P.Ivakin. Doklady AN SSSR, 1974, vol.217, no.6, p.1270.
8.R.Cheesewright. Translations of the ASME, series C, 1968, vol.90, no.1, p.1.
9.R.Eichhorn. Int. J. of Heat and Mass Transfer, 5 (1962) 915-928.
10.Lebedev A.V., Fomin V.M., Khaidarov S.V. Thermophysics and Aeromechanics, Vol. 1, No. 1, 1994.

MEASUREMENT OF LOCAL FLUID DYNAMICS IN 2D- AND 3D-BUBBLING FLUIDIZED BEDS

GROEN J.S., DE HASETH D.C., MUDDE R.F., VAN DEN AKKER H.E.A.
Kramers Laboratorium voor Fysische Technologie
Delft University of Technology, Prins Bernhardlaan 6, 2628 BW Delft, The Netherlands

Abstract-In this paper we report on the development of an intrusive technique for measuring local bubble dynamics in heterogeneously fluidized beds using light transmission in synthetic (poly-ethylene) fibres. The technique was tested by measuring bubble dynamics with the probe in a 2D fluidized bed (dimensions 50 × 3 cm, ungassed powder height up to 121 cm) and simultaneously making video recordings of the bed. The agreement of the probe measurement results with the video images is good. The probe was used for determining local bubble dynamics in the 2D bed and in a 3D bed (23 cm dia, ungassed powder height up to 75 cm). A transformation to calculate the bubble diameter distribution from the bubble chord length distribution was used. The obtained results are in good agreement with literature.

1 Introduction

Fluidized beds are used extensively in process industry as gas-solid, liquid-solid or gas-liquid-solid contactors. Their lack of moving parts and excellent mixing properties are the most important reasons for their popularity. These good mixing characteristics are mainly caused by bubbles. These occur for most types of powder above a certain value of the superficial gas velocity u (at a value of u above the minimum fluidization velocity u_{mf} of the powder). The 'stirring' effects of individual bubbles cause mixing of the powder at a local scale. Furthermore, bubbles tend to form 'bubble streets' (like those known in bubble columns), carrying powder upwards in between them, resulting in large overall circulation of the powder phase[1]. In order to fully understand the behaviour of a fluidized bed (or, in fact, of *any* multiphase reactor), it is of paramount importance to know the local values of its fluid dynamic parameters. Furthermore, it is believed that detailed knowledge of local multiphase fluid dynamics will be of considerable assistance in developing scaling rules. Regarding the significance of the bubbles, in the case of fluidized beds important parameters are those describing bubble dynamics. This illustrates the need for local measuring techniques for multiphase reactors. However, in the case of fluidized beds, determining local values of bubble dynamics is particularly difficult, since the bed material generally is non-transparent. In this paper we report on the development and testing of a technique for determining local bubble dynamics in heterogeneously fluidized beds.

2 Concise bubble dynamics in fluidized beds

Small bubbles (a few centimetres dia) in fluidized beds can be considered to be spherical. Isolated larger bubbles (larger than ~3 cm dia) usually have the typical *'spherical cap'*-shape as depicted in figure 1. An ideal spherical cap bubble is fully characterized by its radius R and the wake angle θ (assuming the bubble envelope is a perfect sphere). Other parameters used frequently in describing a bubble are its bubble volume V_b, and wake volume V_w. The so-called

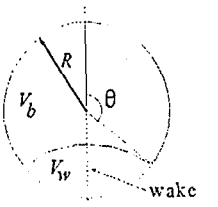

Figure 1. Spherical cap bubble.

equivalent bubble diameter d_{eq}, defined as $\sqrt[3]{(6V_b/\pi)}$, is commonly used to describe the bubble size. The single bubble rise velocity u_{bs} is dependent on this bubble diameter. Generally this dependence is taken as:

$$u_{bs} = k \cdot \sqrt{g d_{eq}} \tag{1}$$

This relation was drawn up on the anology of spherical cap bubbles in bubble columns[2]. From theoretical considerations, a value for k of 0.711 is obtained[3]. However, this value is known to give overestimations of the rise velocity. A value of 0.5 to 0.66 gives better results[4]. The bubble rise velocity u_b in a heterogeneously fluidized bed can be estimated as the sum of the superficial gas velocity in excess of the minimum fluidization velocity and of the single bubble rise velocity[5]:

$$u_b = (u - u_{mf}) + u_{bs} \tag{2}$$

Several other relations predicting the bubble rise velocity have been presented. Based on measurements performed by Werther, Kunii & Levenspiel presented the following empirical correlation (in S.I. units) for the bubble rise velocity, which is valid for column diameters D up to 1 meter[1,6]:

$$u_b = 1.6\left[(u - u_{mf}) + 1.13\sqrt{d_{eq}}\right] \cdot D^{1.35} + u_{bs} \tag{3}$$

A two-phase fluid dynamic description of a bubbling fluidized bed is usually given by distinguishing a dense or particulate phase (the powder with intermittent gas) from a lean (bubble) phase. The fraction the bubble phase occupies in the bed is referred to as bubble *hold-up*.

3 The optical 'Double Horseshoe' probe

Several techniques for obtaining local values of bubble dynamics have been presented. They are generally subdivided into two types of techniques: intrusive and non-intrusive. The non-intrusive techniques invoke e.g. capacitance measurements or the application of γ-ray absorption. These are however particularly complex and expensive techniques, not to mention the severe safety measures that have to be invoked when using γ-ray equipment.

Intrusive techniques comprise conductive, inductive and optical probes. These techniques basically distinguish the particulate from the bubble phase using their differences in physical properties. Because of rapid development of glass and synthetic fibres, optical methods have gained a lot of attention in the last few years. These techniques can be subdivided into reflection and transmission techniques. Their principle of operation is simple. Light is sent into one end of a glass or synthetic fibre, the other end (tip) of which is submerged in the fluidized bed. In the case of reflection techniques, (frequently used in bubble columns[7,8]), light leaves the fibre when a bubble is present at the tip, but is reflected back into the fibre when the probe tip is surrounded by particles and can thus be detected by a light-sensitive cell. In this way a distinction between the bubble and the particulate phase is made.

The transmission technique, developed and tested in this paper and summarized in figure 2, is even more straightforward. The 'Double Horseshoe

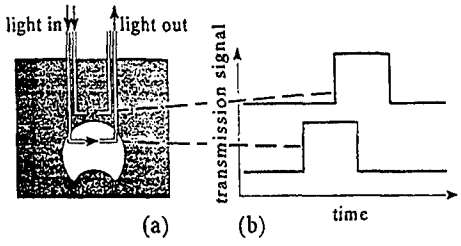

Figure 2. Overview of the light transmission technique.

(*DHS*)'-probe is shown schematically in figure 2(a). Light is sent into the fibres in the two 'emitter' legs and is detected via fibres in the other two 'detector' legs only when a bubble passes the probe. Idealized bubble passing signals are given in figure 2(b). By evaluating the time difference between the lower and upper pair of probe legs the rise velocity of the bubbles can be determined; the bubble fraction can be calculated in a straightforward way as the fraction of the measuring time that a bubble is present at either fibre pair. The calculation of the bubble diameter (distribution) is somewhat more complicated. See chapter 6 for a more extensive treatise on this procedure.

4 Experimental setup

The probe was tested in a so-called two-dimensional (2D) fluidized bed. The term 2D refers to the fact that one of the dimensions of the bed is considerably smaller than both the others. The 2D bed consisted of two vertical 200 × 50 cm perspex plates that were 3 cm apart. Thus, bubbles larger than 3 cm .dia can be observed visually. The bed was fluidized with air with a perforated plate sparger (39 holes of 1 mm dia). Fluidization phenomena in a 2D bed can be described using the same models as mentioned in section 2, be it that due to increased wall effects the bubble rise velocity is smaller than in a 3D bed. The influence of these wall effects is dependent on the distance between the plates. Equation (1) may in this case be used when the parameter k is taken to be 0.41 for sand-like powders[9]. In this case, d_{eq} should be calculated using the bubble cross sectional area, $d_{eq}= \sqrt{(4A_b /\pi)}$.
The bed material was spherical polystyrene particles of diameter 560 μm and partcle density 1102 kg/m³ (type B particles[10]). This type of powder is characterized by easy bubble formation: the incipient bubbling velocity is close to the minimum fluidization velocity. The minimum fluidization velocity for this powder is 14 cm/s (that is in a 3D bed, in the 2D bed u_{mf} equals 18 cm/s). The ungassed bed height was varied up to 121 cm, the super-ficial gas velocity was varied up to 26.7 cm/s (u-u_{mf}=8.7 cm/s).

The *DHS*-probe is shown in figure 3. The fibre material was 1.1 mm diameter polyethylene, which is appropriate enough for the transmission technique and which is considerably less vulnerable than glass. The probe was hung in the 2D bed via a support rod from above and one from the side (to prevent the probe from swinging). The probe could thus be traversed throughout the bed. The four fibres were connected to a sender-detector interface. A HP workstation was used for data acquisition.
The probe was tested in the following way: probe measurements were performed simultaneously with making video recordings of the bed. The video recordings were made with a CCD camera (256 × 256 pixels at 50 pictures per second). A trigger provided that both processes started at exactly the same instant. By placing a light box behind the bed the contrast between the bubbles and the particulate phase was maximized. The pictures were analyzed using the SCIL-IMAGE processing package, the probe signals were processed with the VEE-Test signal analysis program. Comparing the video pictures with the probe transmission signals, the characteristics of the latter were determined. Several criteria for determining bubble boundaries from the signals and from the pictures were tested, in order to gain the correct bubble properties and velocities. The determination of the beginning and the end of the bubble

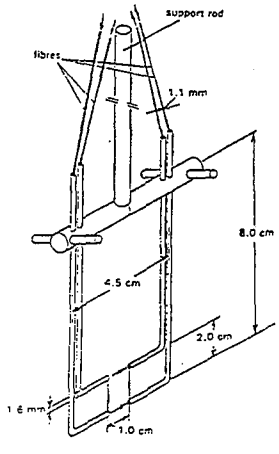

Figure 3. The 'Double Horseshoe' probe.

signal is essential for obtaining accurate results. As can be seen in figure 4, the signals aren't quite so clear as the ideal ones in figure 2. Simple thresholding techniques in determining the beginning and ending of the bubble signal will therefore not work. Different algorithms were developed and tested by comparing the results with those given by image analysis. Eventually, the following procedure was found to be most accurate: The bubble signals were first smoothed using a five point moving-average algorithm, then the derivative of this smoothed signal was calculated. Thresholding this derivative signal gave satisfactory values for the bubble begin and end points. The determination of the bubble boundaries from the video pictures could be done accurate enough by direct segmentation of the pictures. By applying multiple segmentation, it was possible to obtain pictures that showed the gradient of powder content in the region directly surrounding a bubble.

The probe was then used to measure profiles of bubble hold-up, size and velocity in the same 2D and a 3D fluidized bed. The 3D bed was of 23 cm inner diameter and had an ungassed bed height of up to 75 cm. This bed was fluidized with a perforated plate sparger consisting of 61 holes of 1 mm. The same bed material was used as in the 2D bed. The superficial gas velocity was 19 cm/s, so $u\text{-}u_{mf} = 5$ cm/s.

5 Results of the probe calibration

The results of the simultaneous measurements and video recordings are summarized in figure 4. The four frames in the top half of the figure are taken from a series processed with SCIL-IMAGE (the position of the probe was known; it was explicitly drawn into the picture), the lower picture shows the corresponding bubble passing signals of the lower (dashed line) and the upper (solid line) fibre pair. It is seen that the transmission signal of the lower fibre pair starts rising at t_1 when the bubble hits the probe, at t_2 the bubble reaches the upper fibre pair, at t_3 the bottom of the bubble passes the lower pair and at t_4 the bubble leaves the upper pair behind. As can be seen, the bubble passing signal is somewhat more disturbed than the ideal signal of figure 2(b); this is due to particles that are 'raining' through the bubbles (this could be made visible in the video pictures by applying multiple segmentation). The downfall of the signals is seen to be much sharper than the rise at the beginning. It could thus be anticipated that evaluating the times of downfall of both fibre pairs might be the most accurate way of determining the bubble rise velocity. This proved to be the case; only when it was doubted whether this end point evaluation gave realistic values, the rise velocity was determined by calculating the cross correlation of the fibre signals. This was necessary for about 3% of the bubbles. The chord length was calculated by multiplying the rise velocity by the duration of the bubble passing signal registered with the lower fibre pair, since it could be expected that the bubble will be more distorted when it reaches the upper fibre pair.

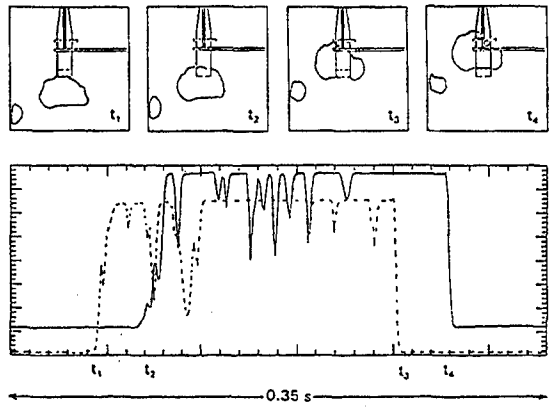

Figure 4. Overview of the probe testing measurements: simultaneous measurements and video recordings.

Typical results of the comparison between the image analysis and the probe measurements are given in figures 5 and 6. Figure 5 shows the results as to the rise velocity. As can be seen, both techniques

give the same results, the maximum difference being about 7%. This difference becomes larger (up to 15%) when coalescing or splitting bubbles are encountered. In figure 6, the chord lengths as

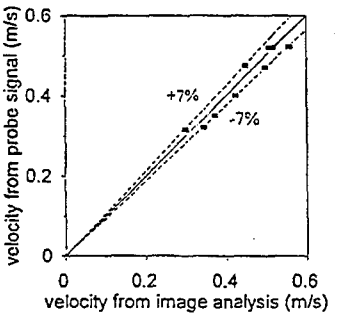

Figure 5. Comparison of the bubble rise velocities obtained from the image analysis and the probe measurements.

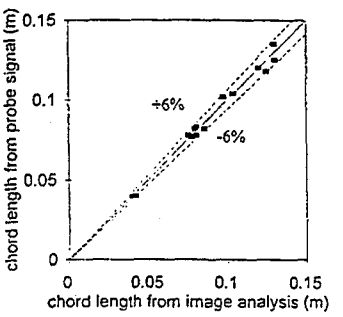

Figure 6. Comparison of the bubble chord lengths obtained from the image analysis and the probe measurements.

obtained with both techniques are compared. In this case, the maximum difference is about 6% (14% for coalescing and splitting bubbles). It can thus be concluded that the probe measurements give accurate results.

By comparing video pictures that were made with and without the probe present in the bed an estimation could be made of the disturbance of the probe on the bubble flow field. This comparison showed that evidently the probe has its influence (mainly *down*stream, that is), but the interactions between the bubbles themselves dominate over these disturbances. The influence the probe has on the bubbles diminishes with increasing bubble size.

6 Results of the probe measurements

In the 2D bed, measurements were carried out at five different heights (h) above the distributor plate and at each height at five different lateral positions (with respect to the bed centre plane). These positions were all on one half of the bed: it was expected that the bubble flow field was symmetric; measurements performed to check this assumption supported it. At all positions, between 100 and 200 bubbles were registered.

Typical results are shown in figures 7 and 8. Figure 7 shows the measured bubble hold-up at various

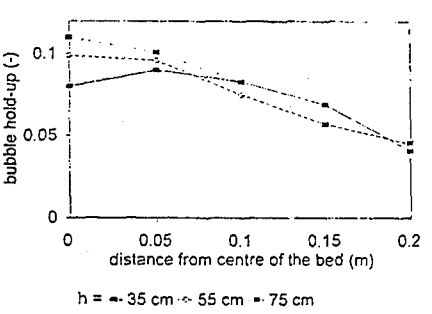

Figure 7. Measured bubble hold-up profiles.

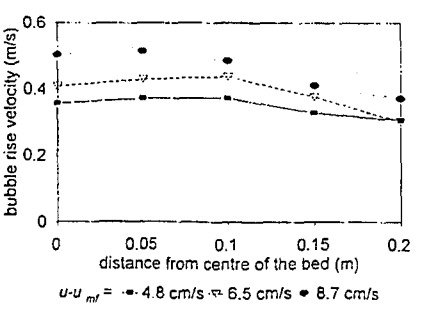

Figure 8. Measured bubble rise velocity profiles.

heights as a function of the lateral position (u-u_{mf} = 6.5 cm/s). It is seen that the bubble fraction profiles become somewhat steeper with increasing height above the distributor, and that the bubble fraction is considerably higher in the centre of the column than it is near the wall. This is what was expected. In figure 8, the mea-sured bubble rise velocity is given at h = 55 cm and at three different values of u-u_{mf}. It is seen that the bubble rise velocity increases with increasing gas velocity. This is in accordance with literature.

As mentioned in section 3, the determination of the bubble fraction and rise velocity from the probe signals is straightforward, but determining the bubble size is more complicated. What is measured is the ***bubble chord length*** λ (see figure 9), which is determined by multiplying the measured bubble rise velocity with the duration of the bubble signal of either (preferably the lower) probe pair. Since bubbles of different size hit the probe and are 'pierced' at different positions r, what is obtained is the chord length ***distribution***. Assuming all bubbles rise vertically, an estimation of the bubble diameter distribution can be derived from the chord length distribution in the following way[11]: the probability density distribution for the measured chord length, $P(\lambda)$, is given by:

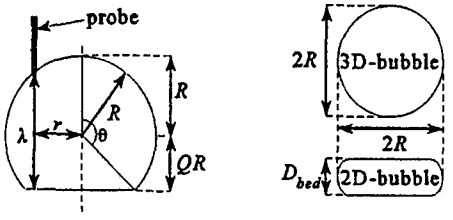

Figure 9. Bubble model used.

$$P(\lambda) = \int_0^{\infty} P(R)P(\lambda \mid R)dR \qquad (4)$$

in which $P(R)$ is the probability density function that a bubble of radius R hits the probe, and $P(\lambda \mid R)$ is the probability density function that a value λ is found at a bubble of radius R. Assuming axisymmetry (or planisymmetry in the 2D case) for all bubbles the latter distribution is given by:

$$P(\lambda \mid R) = P(r \mid R)\left|\frac{dr}{d\lambda}\right| \qquad (5)$$

$P(r \mid R)$ is the probability density function that the bubble hits the probe at a distance r from its centreline. What is measured is $P(\lambda)$, $P(R)$ is the size distribution wanted. By assuming a given bubble form (irrespective of its size) expressions for $P(r \mid R)$ and $\mid dr/d\lambda \mid$ can be obtained. The bubble shape used in this project is shown in figure 9. The parameter Q was taken to be 0.77 (θ=140° [12]) in the 2D case and 0.5 in the 3D case (θ=120° [13]) .
For both 2D and 3D bubbles the following equations hold:

$$\left|\frac{dr}{d\lambda}\right| = \frac{\lambda}{4r},\ 0 \le \lambda \le 2QR\ ;\ \left|\frac{dr}{d\lambda}\right| = \frac{\lambda - QR}{r},\ 2QR \le \lambda \le r(1+Q) \qquad (6)$$

In the 2D case, $P(r \mid R) = 1/R$, in the 3D case it is $2r/R^2$. Combining these equations and eliminating r using $r = \sqrt{[R^2 - (\lambda/2)^2]}$ for $0 \le \lambda \le 2QR$ and $r = \sqrt{[R^2 - (\lambda - QR)^2]}$ for $2QR \le \lambda \le R(1+Q)$ gives the wanted expressions for $P(\lambda \mid R)$. Now the measured chord length distributions can be converted to

bubble radius distributions. From the mean (m) bubble radius the mean equivalent bubble diameter can be calculated, using the bubble model as given in figure 9. For the above 2D case, basic goniometry shows that $d_{eq,m} = 1.93\sqrt{((R^2)_m)}$, in the 3D-case $\sqrt{(d_{eq,m})} = 1.37\sqrt[3]{((R^{3/2})_m)}$. These values for the equivalent bubble diameter were used in comparing diameter and velocity measurement results to the models given in section 2.

In figure 10, a typical transformation from bubble chord length distribution to bubble diameter

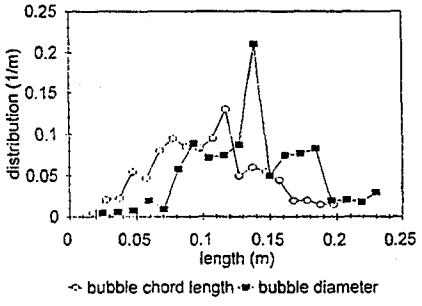

Figure 10. Bubble chord length and bubble diameter distribution.

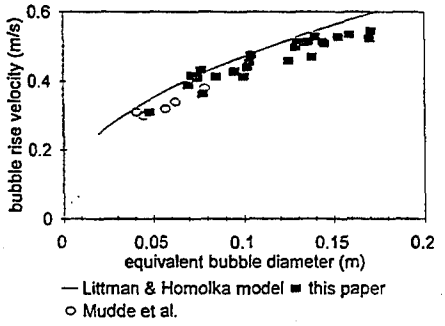

Figure 11. Comparison of the 2D measurements with the model of Littman & Homolka.

distribution is shown. All differences between these two distributions can be easily explained qualitatively. Figure 11 shows the measured velocity-equivalent bubble diameter data, compared with the Littman & Homolka model and with earlier measurements in the same bed[12]. The agreement is good.

The 3D bed operated under rather poor conditions, so only a few operating con-ditions were investigated. Given these facts, the measurements in this bed can only be regarded as rather preliminary. However, it could be observed that the bubbles gradually were moving towards the centre of the column. In figure 12, measured velocity-diameter data are presented and compared to the model given in equation (3) with k=0.6. It can be seen clearly that the measurements coincide neatly with this model.

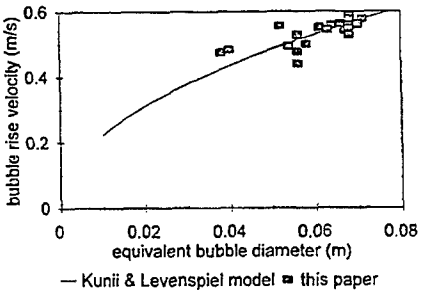

Figure 12. Comparison of the 3D measurements with the model of Kunii & Levenspiel.

7 Conclusions

The results of the probe testing measurements in comparison with the analysis of the video images, show that the probe gives accurate values for bubble fraction, bubble rise velocity and bubble chord length. The influence of the probe on the bubble flow is considerably smaller than the interaction between the bubbles themselves. Both in the 2D and in the 3D case, the measured profiles of bubble hold-up and rise velocity are in agreement with literature values. The calculation of the bubble diameter distribution from bubble chord length distribution gives good results.

The above leads to the conclusion that the Double Horseshoe probe is a reliable instrument that will be helpful in determining local bubble dynamics in fluidized beds.

Nomenclature

symbol	description	unit	symbol	description	unit
A_b	cross sectional area	m^2	u_b	bubble r	
D	column diameter	m	u_{bs}	single bubble rise velocity	m s^{-1}
d_{eq}	equivalent bubble diameter	m	u_{mf}	minimum fluidization velocity	m s^{-1}
g	gravity acceleration	m s^{-2}			
h	height above distributor	m	V_b	bubble volume	m^3
k	proportionally constant	-	V_w	wake volume	m^3
P	probability density	m^{-1}			
Q	shape factor	-	θ	wake angle	°
R	bubble radius	m	λ	bubble chord length	m
r	distance from centreline	m			
u	superficial gas velocity	m s^{-1}	m (subscript)	mean	

References

(1) Kunii, D., Levenspiel, O. (1991), Fluidization Engineering, 2nd Ed., Butterworth-Heinemann, Boston.
(2) Davies, R.M., Taylor, G.I., Proc. Roy. Soc., **A200**, 375.
(3) Geldart, D., (1986), Gas fluidization Technology, Wiley, New York.
(4) Clift, R., Grace, J.R., Weber, M.E., (1978), Bubbles, drops and particles, Academic Press, London.
(5) Davidson, J.F., Harrison, D., (1963), Fluidized particles, Cambridge University Press, New York.
(6) Werther, J., (1983), in Fluidization IV (D. Kunii and R. Toei Eds.), Engineering Foundation, New York.
(7) Frijlink, J.J., (1987), Physical aspects of gassed suspension reactors, Ph.D.-thesis, Delft University of Technology.
(8) Groen, J.S., Mudde, R.F., Van den Akker, H.E.A., (1994), Flow structures in bubble columns as obtained from glass fibre measurements and pressure fluctuations, Proc. 7th Workshop on two-phase flow predictions (M. Sommerfeld, Ed.), Erlangen.
(9) Littman, H., Homolka, G.A.J., (1970), Bubble rise velocities in two-dimensional gas fluidized beds from pressure measurements, Chem. Engng Proc. Symp. Ser., **66**, 37-46.
(10) Geldart, D., (1973), Types of gas fluidization, Powder Technol., 7, 285.
(11) Clark, N.N., Turton, R., (1988), Chord length distributions related to bubble size distributions in multiphase flow, Int. J. Multiphase Flow, **4**, 413-422.
(12) Mudde, R.F., Schulte, H.B.M., Van den Akker, H.E.A., (1994), Analysis of a bubbling 2D gas-fluidized bed using image processing, submitted to Powder Technol.
(13) Grace, J.R., (1970), The viscosity of fluidized beds, Can. J. Chem. Engng, **38**, 30-33.

Identification of Multiphase Flows Regimes by means of Diffusional Analysis of Density Fluctuations

MASSIMILIANO GIONA
Dipartimento di Ingegneria Chimica, Universitá di Cagliari
Piazza d'Armi, 09123 Cagliari, ITALY

ALESSANDRO PAGLIANTI
Dipartimento di Ingegneria Chimica, Universitá di Pisa
Via Diotisalvi 2, 56100 Pisa, ITALY

ALFREDO SOLDATI
Dipartimento di Scienze e Tecnologie Chimiche, Universitá di Udine
Via Cotonificio 108, 33100 Udine, ITALY

ABSTRACT

The problem of the identification of two-phase flow regimes is addressed. Different two-phase signals (void fraction from γ-densitometer and conductance probes and pressure drop) from an oil-air rig are analyzed with Diffusional analysis, which proves to be an objective and clear method to identify different flow regimes. The quality of the information carried by different signal is discussed.

1. Introduction

In multiphase systems the hydrodynamic features of the flow depend upon the particular flow pattern at which the flowing mixture suit itself. Therefore, the accurate determination of the flow regime is understandably a key issue in multiphase flow characterization. Considering for simplicity air and water flowing cocurrently into an horizontal pipe, the two phases may flow separated (stratified and annular flow), intermittently (plug and slug flow) or dispersed (mist flow). The flow regime identification is customary performed by visual inspection. The development of a more reliable technique would greatly improve the flow characterization.

In order to achieve a more objective characterization of multiphase regimes, research in the last years focused on the definition of analytical methods which, starting from an experimental time series associated with a charateristic fluid-dynamic quantity (pressure drop, density) were capable to predict the nature of the flow (Stratified, Intermittent, Bubble, etc.), and to obtain quantitative information on flow properties (i. e. slug length statistics, main frequency of oscillation in Intermittent regime etc.). The fundamental underlying concept in this analysis is that the fluctuations in characteristic physical quantities measured istantaneously along the duct may carry information about the flow conditions, i.e. *fluctuations bring the signature of the flow regime.*

Generally speaking, two main approaches may be followed: chaotic time series analysis and stochastic methods. The analysis of chaotic time series is based on the

assumption that fluctuations have a deterministic low-dimensional explanation* and attempts the characterization of flow conditions by means of the classical methods of chaotic data analysis [1,2,3]. Even though chaotic methods look very appealing, since they could give a low-dimensional reconstruction of the flow dynamics, they were not fully successfull in supplying conclusive results about flow regime identification. Stochastic methods, on the other hand, allow the quantitative characterization of the correlation properties of the time series. Since no hypothesis on the character of the phenomenon is required, these methods can be applied to both deterministic and stochastic signals†

2. Experimental

2.1. Experimental Setup

The experiments used to analyze the different flow regimes were performed with the facility‡depicted in Figure 1. The loop consists of acrylic pipes of 31.7 mm I.D. supported by an inclinable bench 13 meters long. Data have been obtained in the horizontal set-up at atmospheric conditions, using air and light oil. The superficial velocities were varied in order to span all the different flow patterns: Stratified, Intermittent, Dispersed Bubbles and Annular flow. For each experiment, the apparatus could record three different signals from four measuring stations. A DP cell recorded the pressure drop, while two conductance probes recorded the void fraction, and one γ-densitometer recorded the liquid holdup[4]. The test section, gathering the measuring devices, was located 8 meters far from the inlet to reduce entrance disturbances. The differential pressure transducer used allows to measure pressure drops in the range of 0-0.1 bar, and the pressure taps were settled such that the γ-densitometer was centered in between. Capacitance probes measure the capacitance of the flowing mixture between two conducting rings 0.1 diameters far apart: since air capacity is very low if compared to the oil capacity, the capacitance probe output is directly related to the liquid fraction in the pipe. The gamma densitometer is a one-shot collimator ray densitometer developed at IFE.

2.2. On the choice of the experimental signal

Different observables were measured in the experiments, and, in principle, the same results should derive from processing any of them. However, due to the measuring technique, different level of information can be retrieved from different observables. The great majority of the analyses of experimental time series features was performed using pressure drop fluctuations[2,6]. In the present work, the three differ-

*This ultimately implies that flow dynamics can be described by means of a deterministic chaotic system of differential equations.

†Chaotic time series may possess very complex statistical properties depending on the structure of the invariant measure (if it exists) associated with the dynamical system generating the time series. See, e. g. Lasota and Mackey[5].

‡The experimental facility is assembled at the Institute for Energy Technology (IFE), Kjeller, Norway.

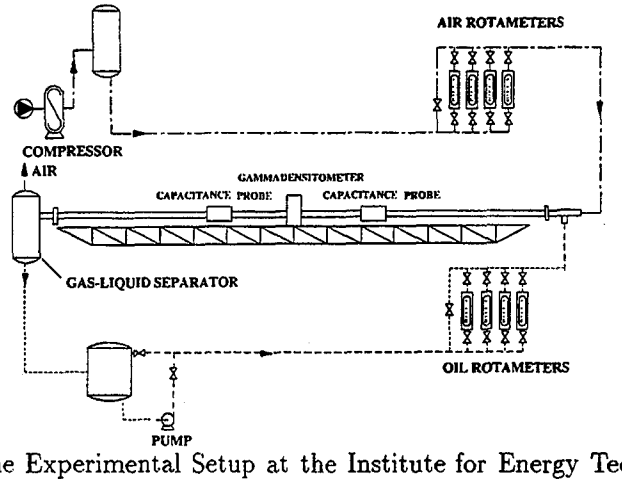

Figure 1: The Experimental Setup at the Institute for Energy Technology, Kjeller, Norway

ent signals available allowed a comparison on the quality of the information carried by the different observables. The information carried by the pressure drop signal is intrinsically *non-local*: since the two probes are far apart, the signal is volume averaged. On the other hand, both capacitance probes and γ-densitometer give a section averaged density signal of higher quality if compared to the pressure drop. However, the γ-densitometer output allows the detection of small fluctuations characteristic of Dispersed Bubble Flow that may not be detected from capacitance probes signals. In this work, to present a consistent analysis of the different flow regimes, γ-densitometric signals were used. Nevertheless, diffusional analysis can be definitely applied to any fluid dynamic time series, provided it is an observable characteristic of the flow conditions.

3. Analysis of Fluctuations by Diffusional Methods

Usually, multiphase flow analyses of the properties of observable time series have been performed by Rescaled Range approach (R/S)[2,6,7] or by estimating the correlation dimension. Here, an alternative, although classical approach to the estimation of correlation properties of fluctuating time series is presented. The diffusional analysis, in connection with multiphase flow characterization, allows a more precise and complete estimation of the time series features[8]. Diffusional analysis is basically a method capable of quantitatively ascertaining the way in which the information is lost (or conserved) in the time evolution of the signal.

To analyze the time series $\{\xi_i\}$, a random walk $\{z_i\}$ on the real line linearly driven by the signal $\{\xi_i\}$ was considered[§] If z_i is the position at time i of the walk,

[§]Here, only linearly driven diffusion processes are considered. Multiplicative processes[9] or relative diffusion analysis[10] may also be applied[11].

Flow Regime	β_1	β_2
Stratified	$\simeq 2$	$>> 1$
Intermittent	$>> 1$	$<< 1$ ($\simeq 0$)
Bubble	$\simeq 1$	$\simeq 1$
Annular	$>> 1$	< 1

Table 1: Behavior of β_1 and β_2 in typical two-phase flow regimes

the dynamics of the process is described by the equations

$$z_{i+1} = z_i + \xi_{i+1} \ , \tag{1}$$

with the initial condition $z_0 = 0$ (the random walk starts from the origin). Information about the correlation properties of the random walk is provided by the mean square displacement $R_z^2(n)$, defined as:

$$R_z^2(n) = < (z_{k+n} - z_k)^2 > = \frac{1}{N_{av}} \sum_{k=1}^{N_{av}} (z_{k+n} - z_k)^2 \ , \tag{2}$$

where N_{av} is the number of averaging points. The mean square displacement may be written as:

$$R_z^2(n) \sim n^{\beta} \ . \tag{3}$$

If the driving signal (i. e. the experimental time series, is a *regular Brownian motion process*, totally random), $\beta = 1$. On the other hand, deterministic oscillating signals present a twofold behavior: at short time scales $n \leq n_c$ then $R_z^2(n) \sim n^2$; at long time scales $R_z^2(n)$ oscillates with an average slope equal to zero. Experimental time series may present behavior that is intermediate between these two extreme cases. This behavior may be characterized by the analysis of the short time scale exponent, β_1, the long time scale exponent, β_2, and the crossover instant, n_c, related to the fundamental period of oscillations, T_c by the relation $T_c = 4n_c\Delta t$, where Δt is the sampling time. These parameters can be related to the superficial gas and liquid velocity j_g, j_l for the flow regime characterization.

4. Identification of multiphase flows

The diffusional analysis was applied to data for different two-phase flow regimes characterized by different gas and liquid superficial velocities. The flow patterns were identified examining the correlation exponent and the crossover time. A comprehensive review of the results is reported in Table I, obtained from the analysis of a significant number of experimental time series from the γ-densitometer, for a wide range of gas and liquid superficial velocities: $0.5 < j_g < 15$ [m/s], $0.07 < j_l < 10$ [m/s].

The interpretation of the values of the exponents for the different flow regime is rather straitforward. Bubble flow is characterized by a random distribution of the gas

bubbles flowing in the main liquid stream. It is natural to hypothesize that the motion of a generic gas bubble is not correlated to the motion of other bubbles. Therefore, the density signal exhibits a linear scaling with time, $\beta_1 = \beta_2 = 1$, as in the case of purely Brownian motion.

In Stratified flow, a clearcut separation between the two phases exists. However, fluctuations of stochastic nature at the interface separating the two phases occur. Therefore, the void fraction signal has a strongly persistent character and $\beta_1 \simeq 2$, $\beta_2 > 1$. Their exact values, definitely larger than unity, are tightly dependent on the intensity of the interface fluctuations.

The interpretation of Intermittent flow is sort of cumbersome, being characterized by a superposition of almost periodic propagation of gas slugs followed by aerated liquid pistons. According to the *mixed* nature of this flow, the resulting signal exhibits a typical crossover behavior, with a value of β_1 in the range (1.5,2) - the greater β_1 the more coherent the signal is - and a value of β_2 close to zero, with asymptotic oscillations in $R_z^2(n)$ (see e.g. figure 3).

A preliminary analysis of Annular flow indicates that $R^2(n)$ presents a crossover behavior between a value of $\beta_1 > 1$ and a value of β_2, $0 < \beta_2 < 1$. A possible physical interpretation of this behavior is related to the biasing effect of liquid oscillations at the liquid boundary layer near the walls ($\beta_1 > 1$) and of complex (non Brownian) liquid bubble fluctuations in the main gas stream ($\beta_2 < 1$). However, the identification of Annular regime can be further improved by analyzing the temporal behavior of the relative mean square displacement[¶]

Table I can be used as a predictive tool to identify the regime directly from the behavior of the mean square displacement of the processed time-series. The exponents β_1, β_2 depend continuously on the superficial gas and liquid velocities. It is just this dependence that allows the identification of the various regimes and to localize in the j_g-j_l plane (this is the representative plane in the macroscopic analysis of multiphase flow; the Mandhane map [12] is defined in this plane) the boundary associated with regime transitions.

It is important to stress that the prediction of the scaling behavior of $R_z^2(n)$ (resumed by Table I) is directly related to the physical interpretation of the nature of the density signal fluctuations. This phenomenological connection with the physics of multiphase evolution makes diffusional analysis a simple but powerful tool to understand macroscopically the dynamics of the flow.

In other works[2] a calculation of the fractal dimension of the signal is presented. In cases like the one treated here, the fractal dimension of the signal may not be easily related to the complex shape of the interface between the two phases[13] in any regime but in Stratified (or annular) Flow. Indeed, in this regime the density in the measuring section can be directly related to the structure of the interface. With Diffusional analysis, the fractal dimension of the signal can be calculated from

[¶]The scaling the the relative mean square displacement $< (x_1(t) - x_2(t))^2 >$ was considered by Suzuki[10] in connection with chaotic maps. It has been applied to multiphase flow problems by Giona et. al. [11]

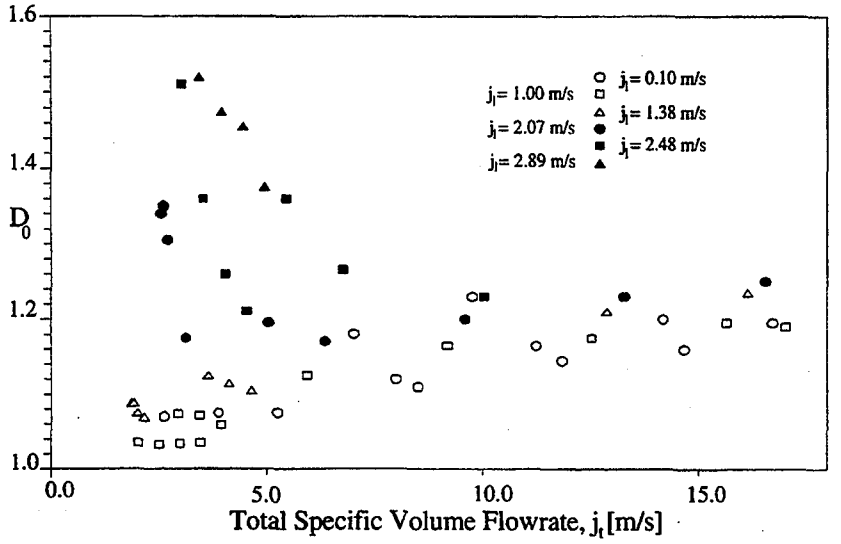

Figure 2: Fractal dimension of the density signals, Eq. (4) vs. $j_T = j_g + j_l$ for different values of the superficial liquid velocity j_l.

the exponent β_1, if the time series is regarded as the discretized representation of the graph of a function which is continuous but almost nowhere differentiable. The fractal dimension D_0 of the graph is given by

$$D_0 = 2 - \frac{\beta_1}{2} . \tag{4}$$

Figure 2 shows the behavior of the fractal dimension D_0 versus the total specific flowrate $j_t = j_l + j_g$, for different values of j_l. In the Annular Flow region, the fractal dimension increases with j_t. This may be easily explained considering any increase of j_t causes larger disturbances of the interface.

5. Concluding Remarks and Further Developments

It is clear now how the nature of the flow regime is ascertainable from the scaling behavior of the mean square displacement. However, other results can be obtained within the framework of diffusional analysis. For instance, considering the case of Intermittent Flow, the crossover instant n_c is related to the main period of oscillations ($T_c = 4n_c\Delta t$). From the analysis of $R_z^2(n)$ the slug frequency may be obtained as $f_c = 1/T_c$. Values of f_c obtained from diffusional analysis are in good agreement with spectral analysis based on the properties of the autocorrelation function. This is a first important confirmation of the validity of these methods to quantitatively predict the features of the flow.

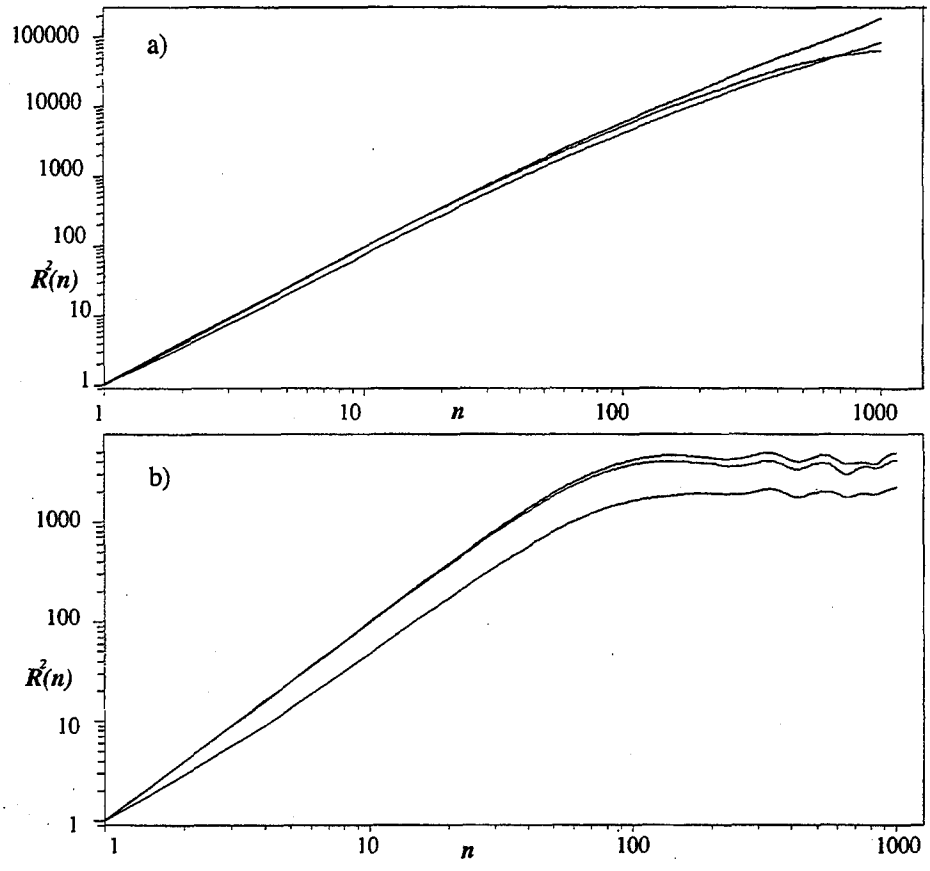

Figure 3: Mean square displacement $R_z^2(n)$ of signals from i) γ-densitometer; ii) pressure-drop cells; iii) capacitance probe, for a) Stratified flow ($j_g = 2.525$ [m/s], $j_l = 0.10$ [m/s]); b) Intermittent flow ($j_g = 2.07$ [m/s], $j_l = 2.07$ [m/s]).

The importance of the method developed lays in the possibility of using it as a predictive tool for the identification of fluid dynamic regimes. For example, diffusional analysis may be a practical method to achieve the *on-line* characterization of multiphase flow, applicable in monitoring and control units of industrial plant involving two and three phase systems. Within the limitations discussed in section 2.2, this method can be applied to experimental time series coming from arbitrary probes.

This note was limited to the presentation of results deriving from the analysis of linearly driven diffusion processes. However, diffusional analysis encompasses many other methods that can capture other statistical properties of the processed signal (for a review see ref.[8]). In particular, by considering relative diffusion it is possible to estimate the fraction of the power spectrum associated with stochastic fluctuations (and correspondingly the fraction relative to deterministic modes). This aspect is of

some interest from the theoretical point of view in order to attempt a macroscopic modelling of the flow dynamics. and from the experimental point of view for the development of filtering methods in order to extract the deterministic part of the signal and filter out noisy and stochastic components.

References

1. B. L. Hao, *Elementary Symbolic Dynamics and Chaos in Dissipative Systems*, World Scientific, Singapore (1989).
2. C. S. Daw, W. F. Lawkins, D. J. Downing and N. E. Clapp Jr., *Phys. Rev.* **A 41** (1990) 1179; D. P. Skrycke, K. Nguyen and C. S. Daw, *Fluidized Bed Combustion* **1** (1993) 155; F. Franca, R. Acikgoz, R. T. Lahey and A. Clausse, *Int. J. Multiphase Flow* **17** (1991) 545; G. Sæther, K. Bendiksen, J. Müller and E. Frøland *Int. J. Multiphase Flow*, **16** (1990) 1106.
3. C. M. van den Bleek and J. C. Schouten, *Chem. Engng. J.* **53** (1993) 75; M. L. M. van der Stappen, J. C. Schouten and C. M. van den Bleek, *Fluidized Bed Combustion* **1** (1993) 129; P. Grassberger and I. Procaccia, *Physica* **D 9** (1983) 189; P. Grassberger and I. Procaccia, *Phys. Rev.* **A 28** (1983) 2591.
4. P. Andreussi, A. Di Donfrancesco and M. Messia, *Int. J. Multiphase Flow*, **14** (1988) 777; R.P. Gardner, R.H. Bean and J.K. Ferrell, *Nucl. Appl. Technol.* **8** (1970) 88.
5. A. Lasota and M. C. Mackey, *Chaos, Fractals and Noise - Stochastic Aspects of Dynamics*, Springer Verlag, New York (1994).
6. L.T. Fan, D. Neogi, M. Yashima and R. Nassar, *AIChE J.* **36** (1990) 1529; L.T. Fan, Y. Kang, D. Neogi and Yashima, *AIChE J.* **39** (1993) 513; J. Drahos, F. Bradka and M. Puncochar, *Chem. Engng. Sci.* **47** (1992) 4069.
7. J. Feder, *Fractals*, Plenum Press, New York (1988).
8. M. Giona, A. Paglianti and A. Soldati, *Fractals* **2** (1994) 265; ibidem, in press (1994).
9. H. Fujisaka, in *Chaos and Statistical Methods*, ed. Y. Kuramoto, Springer Verlag, Berlin (1984) 254.
10. M. Suzuki, *Physica* **A 117** (1983) 103; M. Suzuki, in *Chaos and Statistical Methods*, ed. Y. Kuramoto, Springer Verlag, Berlin (1984) 260.
11. M. Giona, A. Paglianti and A. Soldati, in *Chaos and Fractals in Chemical Engineering - I Italian Conference*, eds. G. Biardi and M. Giona, World Scientific, Singapore, in press (1994).
12. Mandhane, J. M., G. A. Gregory and K. Aziz, *Int. J. Multiphase Flow*, **1**, 537 (1974).
13. G. Sæther, K. Bendiksen, J. Müller and E. Frøland, in *Wavelets, Fractals, and Fourier Transforms*, eds. M. Farge and J. C. R. Hunt, Clarendon Press, Oxford (1993).

EXPERIMENTAL INVESTIGATIONS OF HIGH-SPEED FLUID FRICTION

SHUGAI A.

Institute of Mechanics, Moscow University (Russia)

The behaviour of different continuous media in conditions of high velocity gradients (velocities of deformations) always causes great interest on the part of investigators since exactly in these conditions one can expect the appearance of new qualitative effects. Such conditions are realized in case of the high-speed friction of a solid surface against the medium which is being tested. However, experiments based on rectilinear motion with friction are associated with difficulties because it is necessary to ensure sufficiently large ways of sliding in an experimental set-up. The results presented have been obtained on a set-up based on the observation of the braking process of a flat ring rotating with high velocity during friction against the medium which is under study. Such approach makes it feasible to study the friction process in a compact way. As it will be shown below, the braking process can be regarded as quasi-stationary and, consequently, the dependencies of required parameters are obtained in the whole range of motion velocities or Reynolds numbers during a single experiment. Therefore, the used scheme of the set-up is optimal for obtaining in laboratory conditions new qualitative and quantitative data on continuum media in case of considerable shear stresses. Comparing experimental data with corresponding theoretical models, it is possible to get the values of needed rheological constants for such complex continuum media as pastes, emulsions and suspensions. In this report the results of investigations of the high-speed friction on water, ice and weak aqueous solutions of polymers are presented.

To study viscous interaction between the moving flat solid surface and different continuous media a computerized set-up was worked out[1]. The process of braking of a rotating flat ring ~15cm in radius due to a friction with the medium under test is recorded in the storage of a personal computer by means of CAMAC equipment and special tracking system. The dependence of the moment coefficient on Reynolds number and other parameters is determined by numerical differentiation with the use of regularizing algorithms. The experimental complex makes it possible to carry out the measurements of the viscous friction at speeds up to 150 m/s and with the load and at external pressure (from atmospheric pressure to the 0.04atm) which vary within wide limits.

The experimental set-up incorporates a mechanical part, a tracking system and units of a measuring-computational complex (fig.1).

The mechanical part serves for accelerating the ring up to the prescribed angular velocity and fixing the axis of rotating during the experiments. After the accelerating the ring is smoothly lowered to the surface of the medium. A protective screen is envisaged for reducing disturbances from the ring which is being accelerated on the medium under test (at the moment of lowering of the ring the screen is removed, in experiments with reduced external pressure the screen is not needed). The sketch of mechanical part shows a motor; a disk with revolution counter (a special shape of the disk as a turned over dish secures contact with medium only for the lower surface - the ring); a pool filled with the medium the friction against which is under study; a device for dropping the rotating disk and a protective screen.

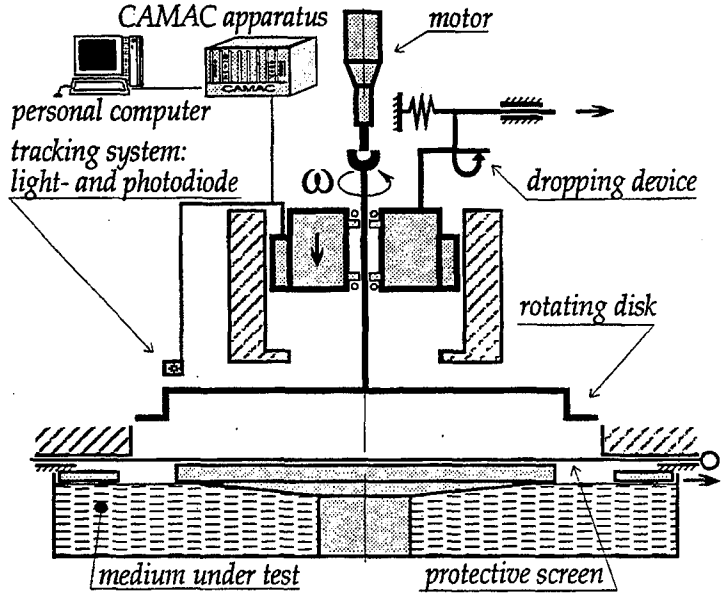

Fig.1 Schematic diagram of the experimental set-up

The tracking system is used for measuring the angular velocity of rotation. Several polished equidistant marks are placed on the blackened external surface of the ring. During the rotation of the ring the mark, passing under the lightdiode-photodiode system, causes a pulse in the photodiode circuit. The calculation of the number of pulses of the reference timer between those pulses enables one to determine the angular velocity of rotation. After numerical differentiation the angular acceleration and the moment coefficient are determined. The relative error of this system does not exceed 0.1%. In experiments with ice to measure the melting rate a television system of measuring the vertical displacement of the ring was worked out. A light rectangle the height of which is linked with the position of the ring is shaped

on the TV screen with the aid of a videocamera and a system of shutters. The number of lines in the image of this rectangle is calculated. The dependence of melting rate on time is determined by numerical differentiation using the results of preliminary graduation. This scheme is linear and the relative error does not exceed 1%.

The measuring-computational complex ensures a fixing of dependencies of angular velocity and vertical coordinate on time in computer memory, a numerical differentiation of these dependencies and a storage of experimental results in a database.

During the experiments the rotating ring is braked due to a friction. The braking process can be regarded as quasi-stationary and, consequently, the moment coefficient depends only on a instantaneous value of angular velocity. Actually, the dimensionless parameter which characterize the relative change of angular velocity during characteristic time t_c (time of one turn) is:

$$\xi = \frac{d \ln \omega}{dt} t_c = \frac{2\pi}{\omega^2} \frac{d\omega}{dt}.$$

In experiments on ice, when the braking is most intensive: $\xi < 0.1$ till $\omega = 90$rad/s. For higher speeds it is smaller: $\xi < 0.02$ from $\omega = 200$rad/s (linear velocity ~30m/s).

The experimental set-up and the measuring complex were tested in experiments on water. Theoretical data obtained by the integral method of the boundary layer theory were compared with the experimental results. The integral method was used in a similar manner that it was used by Karman in his original paper[1], which concerned the friction of a rotating disk against viscous liquid in turbulent and laminar regimes. The only difference is that the friction of rotating ring was studied, therefore the integration of ordinary equations system was started from the point of singularity at the inner radius of the ring. The dependencies derived is going onto the Karman's ones for the large values of outer radius of the ring. The formula for moment coefficient obtained has the next structure:

$$c_m = \frac{2M}{\rho\omega^2 R^5} = \frac{C(r_1)}{Re^p}, \quad r_1 = \frac{R}{R_0}, \quad Re = \frac{\omega R^2}{\nu}$$

where R is outer radius of the ring and R_0 is the inner one, C is the function of dimensionless width of the ring r_1 only. The power index p is equal to 1/2 for laminar and to 1/5 for turbulent regimes. The friction of two rings were investigated (R_0=13.5cm; R=15, 16.5cm) in the region of Reynolds number from $3 \cdot 10^6$ till $2 \cdot 10^7$ (linear velocity 20÷120m/s), when the flow regime is turbulent.

On the fig.2 the experimental and theoretical data for the ring with outer radius of 15cm are shown in logarithmic coordinates. The experimental points evidently correspond to linear dependence with the coefficient which is very close to 1/5. The agreement of coefficient C is worse, so the experimental line

is displaced from the theoretical one (C_{exp}= 0.039, C_{th}= 0.032). It may due to the special features of the flow in the experimental set-up (the area of the contact with water may be larger than the area of the ring). Other probable reasons are the integral method based on conception of finite thickness of the boundary layer and velocities profiles used. Moreover, for the narrow ring the influence of outer edge may be significant, whereas the Karman's approach corresponds rather to the ring of infinite width. For the wider ring the agreement is better: relative error ~13% (C_{exp}= 0.054, C_{th}= 0.047).

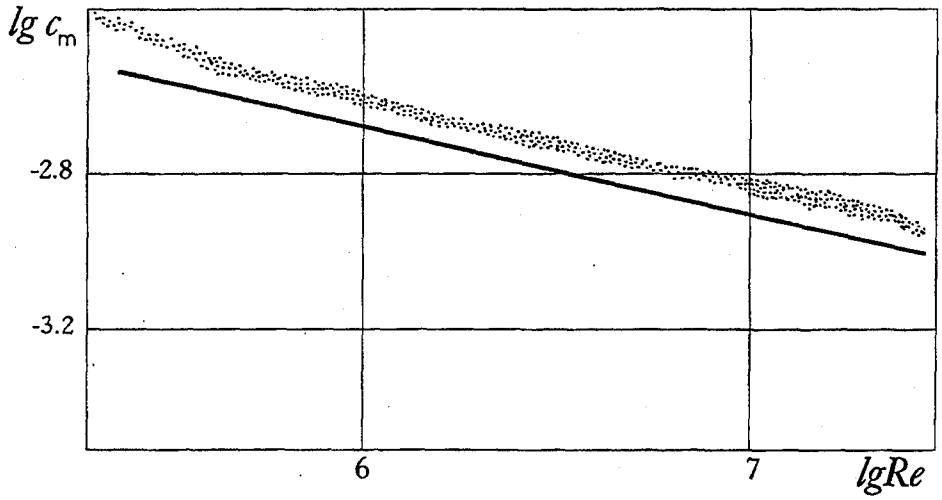

Fig.2 The moment coefficient as a function of Reynolds number (friction on water in turbulent regime, linear velocity: 20-120m/s)

A series of experiments on ice was performed. The dry friction of solid bodies at high relative speeds may be accompanied by a transition to plastic and liquid state in the friction contact zone. For the quite high speeds of motion the developed molten layer regime takes place, when the liquid layer thickness is greater than 10^{-4}cm and plastic effects in surface layers of bodies may be neglected. The problems of heat and mass transfer with phase change are very complicated for direct numerical and analytic investigations. The integral method which is widely used needs to be approved. Thus, besides the obtaining of experimental data for the friction in developed molten layer regime the experiments allow to check the applicability of the integral method to problems of this kind.

The ice sample was the hollow cylinder of ice ($R_0 = 13.5$, $R = 16.5$cm, height $h = 4$cm) made from settled tap water. The results of typical experiment: dependencies of moment coefficient $c_i = M/\rho\omega^2 R_0^5$ and melting rate $v_0 = -dh/dt$ on the angular velocity are shown on the fig.3,4.

The theoretical curves, which are shown also, were obtained by the integral method. The model problem of ice melting by the rotating heated ring was investigated[3]. The problem was treated as quasi-stationary in the coordinate system lowering with the ring. Using of quadratic profiles of velocities and temperature across the layer makes it possible to take into account main effects in the molten layer: induced pressure gradient and viscous dissipation and to use only the balance correlations of mass, impulse and energy. The dependencies of moment coefficient and melting rate on angular velocity and temperature of the ring were obtained by numerical integration of the ordinary equations system.

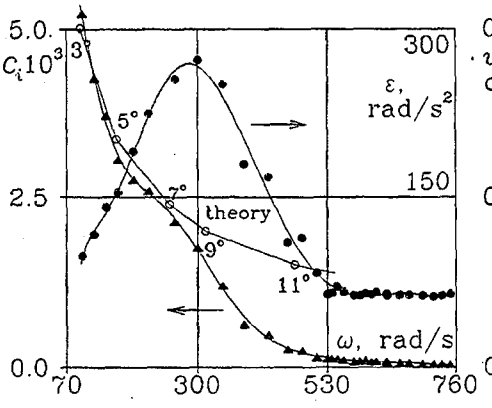

Fig.3 The moment coefficient c_i and angular acceleration ε as functions of angular velocity ω.

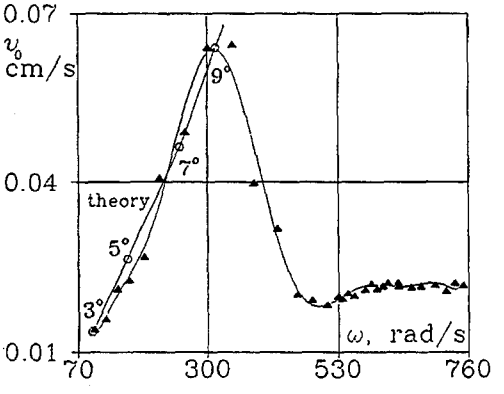

Fig.4 The melting rate v_0 as a function of angular velocity ω.

The points on the theoretical curves correspond to the temperature 3,5,7,9,11°C. The values of the temperature for calculating of these points were chosen from the condition of closeness of both c_i and v_0 to the experimental ones. Thus, despite the fact that the temperature of the undersurface of the ring was not measured during the experiments, the joint measuring of the two independent parameters c_i and v_0 made it possible to compare them with the theoretical data and to determine the agreement and dependence of the temperature on angular velocity. The temperature falls during the experiment.

A comparison of experimental and theoretical results reveals good qualitative and quantitative agreement when angular velocity is below 300rad/s (linear velocity till 50m/s). In the region 300-400rad/s a transition to new friction regime takes place, when the angular acceleration and the melting rate reach its peak values. The new friction regime from 600rad/s is characterized by approximately constant values of angular acceleration and melting rate,

which are significantly below the theoretical data for developed molten layer regime.

At the high rotating speed the friction regime with peeling off and throwing out of surface layers of the ice is possible. It is possible also the unstationary regime, in which the melting and ejection of the molten layer alternate with tearing off surface layers of ice. The television system, in which the frequency of measuring is decreased to 10Hz by the regularizing algorithm, does not secure the investigation of these high-frequency processes and measures only the mean values. Obviously the friction regime discovered is associated with the qualitative effects in surface layers of ice, on the contrary of the model of developed molten layer regime, wherein the effects of plastic deformations at low speeds and cracks expansions at high speeds are neglected. The investigations of mechanical properties of ice in high-speed conditions are absent. From the quasi-stationary experiments the characteristic time of macrocrack expansion in ice sample of such size is known: $\tau \sim 5 \cdot 10^{-4}$s. If the surface layer of ice is peeled off and velocity of the ice particles is about the linear velocity of the ring then the time of the layer flight out of the friction contact zone would be equal to τ just when angular velocity is ~600rad/s and corresponds to the beginning of the new friction regime. From theoretical estimation the component e_{rz} of the velocities of deformations tensor in the molten film becomes equal to τ^{-1} when angular velocity corresponds to the peak values of angular acceleration and melting rate. This equality is usually interpreted as a criterion of the beginning of brittle destruction mechanism in a radius direction. Therefore, at high rotating speeds the friction regime with surface layers splitting of may take place. At the lower values of the rotating speed the time of flight of the layer out the contact zone is longer and some portion may be melted. From $\omega \sim 300$rad/s the all layer is melted and developed molten layer regime of friction is realized.

A series of experiments of high-speed friction on weak aqueous solutions of polymers and other substances was conducted to study the effectiveness of using of these additions to reduce the turbulent friction. The solutions of polyactylamide, polyethilenoxide, asbestos fibres, surface-active substances were investigated[3,4]. It was found that there is a limited region of turbulent friction reduction for a given concentration of solute. The friction reduction increases with increasing of Reynolds number. Then for some Reynolds number Re_* the reduction is highest and after that it falls down to zero at Re_{**}. The dependencies of Re_* and Re_{**} on the concentration are monotonously increasing. Thus, for arbitrary concentration of addition there is a gain-optimum region of Reynolds number. This fact is evidently seen on the fig.5 when the dependencies of the gain parameter L:

$$L(Re,c) = (c_m(Re,0) - c_m(Re,c)) / c_m(Re,0)$$

on Re are presented for weak solutions of polyacrylamide with different weight concentrations c (R_0=13.5, R=16.5cm). The X-axis corresponds to pure water.

The approaching of experimental curves to dependence for pure water at high Reynolds numbers is connected with reorganization of polymer molecules, probably with irreversible mechanical degradation of polymer due to the large shear stresses in the boundary layer near the rotating ring.

It was observed that the set of the moment coefficient dependencies for different weight concentrations of polymer is rounded by the curve which fixes the maximum of friction reduction in weak solutions for a given Reynolds number.

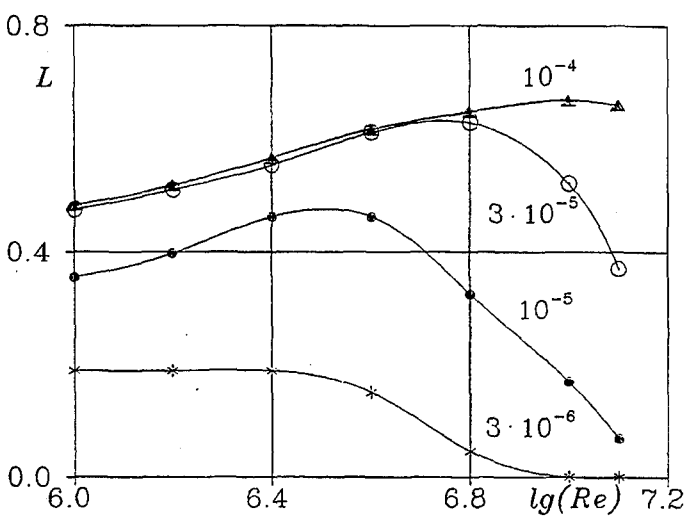

Fig.5 The gain parameter L as a function of Reynolds number for weak aqueous solutions of polyacrylamide with different weight concentrations.

REFERENCES

1. I.I. Kozlov, A.A. Shugai, Ju.L. Yakimov "Experimental Investigations of High-Speed Liquid Friction", Fluid Dynamics, 1994, Vol.29, N.3. Translated from Izv. Akad. Nauk Russia, Mekh. Zhidk. Gaza, 1994, N.3, p.74-82.

2. Th.v.Karman "Über Laminare und Turbulente Reibung", ZAMM, 1921, Bd1, H.4, p.233-252.

3. A.A. Shugai "Problem of a Solid Half-Space Melted by a Hot Rotating Disk or Ring", Fluid Dynamics, 1990, Vol.25, N.3, p.352-355. Translated from Izv. Akad. Nauk SSSR, Mekh. Zhidk. Gaza, 1990, N.3, p.30-34.

4. I.I. Kozlov, N.M. Kalinichenko, V.N. Pilipenko "Effect of Different Additions on Reduction of the Turbulent Friction of Rotating Ring", Report of the Institute of Mechanics, Moscow University, 1987, N.3537 [in Russian].

THREE-DIMENSIONAL HEAVIER THAN AIR GAS RELEASES RECONSTRUCTION.

S. SIMOENS*, M. AYRAULT*.

*LMFA, E.C.L.,
C.N.R.S. URA 263, BP 163, 69131 Ecully Cédex.

ABSTRACT

We present a general solution for an automatic three-dimensional reconstruction of non-static, non-reproductible and complex strutures in turbulent flows. The experiment is based on a plane laser sheet sweeping the flow fast enough to consider the flow frozen. In order to solve the problems related to experimental and physical difficulties, we use two-dimensional spectral analysis. Finally we reconstruct three-dimensional surface composed of triangular tiles. This method is an heuristic one, criterion based on Fourier descriptors coefficients (Fdc) allow to determine which of the contours are to link together, and if necessary, which of them need intermediary contour interpolation to give more acceptable surface. This gives a new method easy to implement which enables us to take into account all problems that we can encounter in lots of realistic analysis of fluid mechanics.

I INTRODUCTION

Industrial installations may provide accidental releases of dense gases. Previous work on this subject was presented by Ayrault and al.[1] for planar concentration measurements in the same case, with turbulent external conditions. It was interesting after this quantitative two-dimensional analysis to provide instantaneous three-dimensional data information for a better understanding. Previous works[2,3,19] have used Taylor hypothesis to achieve three-dimensional rendering of structures in turbulent flows. Successive time exposures of the same plane were recorded to perform such reconstruction converting the time dimension to space. More recently such representations were provided[4] avoiding Taylor's hypothesis, with hight performance experimental set-up, using scanning mirror to sweep a laser sheet through a volume of a flow field. In both cases simple volume rendering algorithm was used but generally due to sharp or jagged surfaces (thus complex morphologies) coupled with weak samples such one is not suitable.

To the best of our knowledge no publications exist on specific algorithms avoiding clearly these problems underlying to three-dimensional reconstruction of such complex structures. Local deformations, due to turbulent flows (complex morphology) movement and statistical phenomena do not allow good samples nor reproducibility and thus do not permit the use of global solutions like Delaunay triangulation[5], cubic-spline interpolation or minimal area surface approximation[6]. Global

optimal solutions (time consuming) or works based on local heuristic criterion[7] have been proposed. Unfortunately great differences between successive planes prohibited them because of interpolation necessities.
Thus a specific local and heuristic algorithm based on 2D (Fdc) analysis is proposed to solve all these problems. The analysis was applied to the two-dimensional contour lines extracted from successive parallel cross-sectional planes intersecting the real surface in the flow studied. For an homogeneous solution, without loss of time, the different criteria and interpolation, based on spectral analysis[8], are well defined. We take also into account the problems like multiple-branching or terminal connections. This paper presents an heuristic algorithm which enables to solve : weak samples, complexity morphology, multiple-branching, ... ; and which operate automatically[9]. An instantaneous three-dimensional iso-concentration reconstruction of releases of heavier gas than air is presented.

II THREE-DIMENSIONAL RECONSTRUCTION TECHNIQUE

Contrary to medical area for example, fluid mechanics need to reconstruct complex, nonstatic and nonreproductible forms. This require special algorithms to take into account some experimental problems underlying, as few samples and complex morphology due to turbulence. To solve it we do not use classical methods like global ones but a local heureustic method, based on 2D Fdc applied to 2D contour lines extracted from successive parallel cross sections which scan quasi-instantaneously the flow studied.

The first part presents all definitions, properties associated with spectral analysis and necessary in the second part where we describe the algorithm.

1. HARMONIC ANALYSIS

Lot of works treat of bidimensional harmonic analysis of plane contour[8,10,11,12].

To define a distance between two contour lines we use the definition in the spectral space given by Persoon[8]. It is easier to define a spectral distance than an Euclidian one.

Cartesian axis $\left(O, \vec{x}, \vec{y}, \vec{z}\right)$ are used. Let T be the number of parallel planes, perpendicular to the z axis and named $S_1,...S_T$, in ascending order (fig. 1). For a better explanation of the method let us consider two consecutive planes S_k and S_{k+1}. From S_k (resp. S_{k+1}) a contour line C_k (resp. C_{k+1}) or some contour lines $C_{k,i}$ ($i \in \{1,..., p\}$) (resp. $C_{k+1,j}$ ($j \in \{1,..., q\}$))

are extracted by digital image treatment whose process is not developped here. These contour lines correspond to an isoconcentration from the studied pattern on S_k (resp. S_{k+1}) and are coded in the Freemann code (direct sense). The points P_s ($s \in \{1,...,m_i\}$) of coordinates $(x_{s,P} ; y_{s,P})$ describe C_k and $P_{s,i}$ describe $C_{k,i}$ with the coordinates $(x_{s,iP} ; y_{s,iP})$. Note that

$\sum_{i=1}^{p} m_i = M$ and that $C_k = C_{k,i}$ if $i = 1$.

From the point sequence, which describe C_k, a discrete Fourier decomposition is perfomed. When the inverse discrete Fourier transform is applied to the ℓ first harmonics, the reconstitued associated contour line is named C_k^{ℓ} with P_k^{ℓ} and $\left(x^{\ell}_{s,P} ; y^{\ell}_{s,P}\right)$ the points and coordinates associated.

a General definitions

A complex formulation of the closed contour line C_k is :

$$z_{s,P} = x_{s,P} + i\, y_{s,P} \text{ with } u \in \left\{\frac{-M}{2}, \ldots, \frac{M}{2} - 1\right\} \qquad \text{(D 1)}$$

We consider[10] the finite serie of points $z_{s,P}$ as M-periodic. We supposed M equal to 2^m and if it is not the case (in general $2^m \le M < 2^{(m+1)}$, $m \in N$) we resample it to obtain a new number of points M' (equal to 2^m). This allow to use discrete fast Fourier transform[10] and use the notation 'quote' along the text.

The Discrete Fourier Transform (D.T.F) is defined as :

$$F(u) = \sum_{s=\frac{-M'}{2}}^{\frac{M'}{2}-1} z'_{s,P} \exp\left(-\frac{2i\pi}{M'} s u\right) = X(u) + j\, Y(u) \qquad \text{(D2)}$$

where $u \in \left\{\frac{-M'}{2}, \ldots, \frac{M'}{2} - 1\right\}$ and we use $\tilde{F}(k) = \tilde{X}(k) + j\,\tilde{Y}(k)$ for the inverse Fourier transform. The Fourier Descriptors $(z'_{s,P})$ and the Fdc $(A_{r,P})$ of a contour C_k are defined from the DFT by $A_{r,P} = \sum_{s=-M'/2}^{M'/2-1} z'_{s,P} \exp\left(-\frac{2i\pi}{M'} sr\right)$ and $z'_{s,P} = \frac{1}{M'} \sum_{r=-M'/2}^{M'/2-1} A_{r,P} \exp\left(\frac{2i\pi}{M'} sr\right)$

The sum of the Fdc $A_{s,P}$ and $A_{-s,P}$ define the s harmonic order $H_{s,P}$ of C_k :

$$H_{s,P} = A_{s,P} + A_{-s,P} \qquad \text{(D 3)}$$

Note that is you preserve the fundamental and the ℓ^{th} harmonic the reconstitued contour line is an ellipse[13] E^{ℓ} of order ℓ (Fig.2.a)

b. Distance

If two contours lines are described with a different number of points or are morphologicaly different, we have to define a distance (Euclidean or other) between two contour lines in frequency space which eliminate this problem. Let us consider two contours lines C_k and C_{k+1}, with their associated Fourier descriptors $A_{s,P}$ and $A_{s,Q}$. The distance expressed as :

$$d_1(C_k,C_{k+1}) = \sum_{s=\frac{-O'}{2}}^{\frac{O'}{2}-1} \left[(A_{s,P} - A_{s,Q})^2 \right]^{\frac{1}{2}} \qquad \text{(D4)}$$

with $O' = \min(M', N')$ is independant of the numbers of points $(z'_{s,P})$ et $(z'_{s,Q})$. The scale orientation and position must be keep fixed to take the physic reality of experimental data into account (but this can be modified[8]).

c. Interpolation

It is a way to obtain the interpolation $C_{k,k+1}$ between different contours lines C_k et C_{k+1} in case of few samples. Let $(A_{r,P})$ and $(A_{r,Q})$be the Fdc of C_k and C_{k+1}. If we want need n interpolated contour lines, the ponderate Fdc $(A_{r,(P,Q)}{}^{\lambda i})$ $\left(r \in \left\{\frac{-O'}{2}, \ldots, \frac{O'}{2} - 1\right\}\right)$ associated to $C_{k,k+1}{}^{\lambda i}$ are defined by :

$$A_{r,(P,Q)}{}^{\lambda i} = (\lambda_i A_{r,P} + (1-\lambda_i) A_{r,Q}) \qquad \text{(D5)}$$

with , $\lambda_i = \frac{i}{(n+1)}$, i varying from 1 to n. Using inverse Fourier transform of the Fdc, we obtain the n interpolated contours (Fig. 2.b) (Wallace[10] gives the errors related to this kind of interpolation).

d. Area

The area[15] A_k of the contour line C_k is expressed as:

$$A_k = -\frac{1}{M'} \sum_{s=\frac{-M'}{2}}^{\frac{M'}{2}-1} |A_{s,P}|^2 M' \pi \qquad \text{(D7)}$$

e. Reconstruction error

A reconstruction error between the original and the p order contour is given by $a(p) = \frac{E(p)}{E(1)}$ with $E(p) = \frac{1}{M'} \sum_{k=-M'/2}^{M'/2-1} \sqrt{\left(x_k - \tilde{X}_k^p\right)^2 + \left(y_k - \tilde{Y}_k^p\right)^2}$. Note that : $0 \le \alpha(p) \le 1$ and $\forall$ p $E(p) \le E(1)$ (Fig. 3)

2. TRIANGULAR PATCHES RECONTRUCTION

After detection of all closed contour lines $C_{k,i}$ on a same plane S_k we establish the correspondance criterion between contour lines of two successive parallel planes S_k and S_{k+1}. This criterion is defined in the sense of position and morphological continuity of $C_{k,i}$. This is function of geometrical position of the points describing $C_{k,i}$.; the morphological continuity being deduced from the error $\alpha(p)$). A sub-contour $C_{k,i}$ of S_k is linked, or not, to another one $C_{k+1,j}$ of S_{k+1}.

Finally new contour lines may be interpolated between S_k and S_{k+1} for intermediary z-level.

a. Correspondance criterion

The first step is to detect all sub-contour lines $C_{k,i}$ of S_k which continue on the plane S_{k+1}, those which are not the extension of another contour line of S_{k-1} or do not have extension in the following plane, S_{k+1}.

Once obtained the number p and q of sub-contour lines of S_k and S_{k+1}, let two sub-contour lines be projected on the same plane $\left(0, \vec{x}, \vec{y}\right)$. In case of high surface curvature along oz, the oxy position of $C_{k+1,j}$ move a lot compared to the oxy position of $C_{k,i}$.

Let us calculate elliptic sub-contour lines $C^1_{k,i}$ et $C^1_{k+1,j}$ (Fig.2.a) which are a convex caracterisation (convex hull is too much time consumer[15]).

Consider $i_0 \in \{1, \ldots, p\}$ et $j_0 \in \{1, \ldots, q\}$ and C^1_{k,i_0} et C^1_{k+1,j_0} the orthogonal projection on the same plane $\left(O, \vec{x}, \vec{y}\right)$. Let $x^1_{\min s,i_0}$ and $x^1_{\max s,i_0}$ (resp. $y^1_{\min s,i_0}$ and $y^1_{\max s,i_0}$) be the smaller and the bigger abscissa (resp. ordinate) of points describing C^1_{k,i_0} (as for C^1_{k+1,j_0}) and which allow to define the minimum out-rectangle R_1 containing C^1_{k,i_0} (R_2 for C^1_{k+1,j_0}). By this this way we take into account the complexity of the contours lines (Fig. 4, 6)
The intersection area of R_1 and R_2 and the mean area intersection normalized by A_k and A_{k+1} are expressed as :

$$\text{Aire}(k,k+1)_{i_0,j_0} = \max\Big(\big(\sup(x^1_{\min s,i_0} - x^1_{\max s,i_0}, x^1_{\min s,j_0} - x^1_{\max s,j_0}) \cdot \sup(y^1_{\min s,i_0} - y^1_{\max s,i_0}, y^1_{\min s,j_0} - y^1_{\max s,j_0})\big), 0\Big)$$

$$\text{and } A_{i_0,j_0} = \frac{1}{2}\left(\frac{\text{Aire}(k,k+1)_{i_0,j_0}}{A_k} + \frac{\text{Aire}(k,k+1)_{i_0,j_0}}{A_{k+1}}\right) \qquad \text{(D 7)}$$

Consider a threshold S_{e1} related to A_{i_0,j_0} ($0 \le A_{i_0,j_0} \le 1$). If

$A_{io,jo}$ is lower than S_{e1} we link $C_{k,i0}$ and $C_{k+1,j0}$. This threshold, a function of the sample and of the pattern complexity, is choosen according two criteria :

(1) p is equal to 5% of harmonics. In order to take into account the pattern complexity, if $\alpha(p)$ is greater than 95 we choose $C^1_{k,i}$ otherwise we choose $C^2_{k,i}$ (Fig.2.a).

(2) The threshold S_{e1} is now the area calculated by (D7) between the two extremas contour lines (S_1 and S_T), divided by the plane number T and ponderate by an error of 10 %.

b. Deformation criterion

Because of great deformation in case of complex patterns, the continuity between C_{k,i_0} and its correspondant contour line C_{k+1,j_0} can be unsufficient. Therfore we calculate $d_1(C_{k,i_0},C_{k+1,j_0})$ with the definition (D 4). A general threshold S_{e2} is defined to judge if contour line deformations between the two splanes S_k and S_{k+1} are too important. S_{e2} is choosen in the same way as S_{e1}.

If deformation is too important, links are unsignificant. We must have another phase to analyse it and if it is necessary to create new planes to compensate : the few samples and the great pattern complexity effects.

c. Intermediary planes

Let us consider p sub-contour lines $C_{k,i}$ of S_k and q sub-contour lines $C_{k+1,j}$ of S_{k+1}. In order to class the sub-contour lines detected C_{k,i_0} and C_{k+1,j_0} three cases have to be considered :

1. $A_{io,jo} \geq S_{e1}$ (Fig.5.b).

We calculate the distance $d_1(C_{k,i_0},C_{k+1,jo})$ and the following

1.a. $d_1(C_{k,i_0}, C_{k+1,j_0}) > S_{e2}$ the deformation is important and may create links of bad quality. We create one intermediary plane $S_{k,k+1}$ at the level $z_{k,k+1} = (z_k + z_{k+1})/2$. This is made using frequential mean interpolation between C_{k,i_0} et C_{k+1,j_0} (2.b.) with λ_i equal to 0,5. We obtain in the physic space a mean contour line $C_{k,k+1,io,jo}$.

1.b. $d_1(C_{k,i_0},C_{k+1,j_0}) >> S_{e2}$. We create n plane interpolations (2.b.) $z_{k,k+1}{}^{\lambda i}$ with λ_i equal to i/ (n+1).

1.c. Otherwise we link directly.

2. $0 < A_{io,jo} \leq S_{e1}$ (Fig.5.b).

We have to verify :

$$\forall\ i_0 \in \{1, \ldots, p\} \text{ fixed } \exists\ j \neq jo\ /\ 0 \leq A_{io,j} \leq S_{e1}$$

In order to see which contour lines of S_k and S_{k+1} verified this property. Various cases could appear. Suppose two contour lines $C_{k,i0}$ and $C_{k,i1}$ of S_k and one contour line $C_{k+1,j0}$ of S_{k+1} veriying $0<A_{io,jo}<S_{e1}$ and $0<A_{i1,jo}<S_{e1}$. We search for two points P_1 and P_2 of $C_{k,io}$ and $C_{k,i1}$ which correspond to :

$$d_2(P_1,P_2) = \min_{i,j} \{d_e(P_i,Q_j),\ P_i \in C_{k,io}\ ,\ Q_j \in C_{k,jo}\}$$

where $d_e(.,.)$ represents the Euclidean distance in $\left(O, \vec{x}, \vec{y}, \vec{z}\right)$. We connect the two sub-contour lines $C_{k,io}$ and $C_{k,jo}$ by segment $[P_1,P_2]$. Therefore a new contour line $C_{k,io,jo}$ is composed by the all points of $C_{k,i0}$, $C_{k+1,j0}$ and segment $[P_1,P_2]$. With the precedent method, we interpolate $C_{k,io,jo}$ on intermediary plane $S_{k,k+1}$.

When the links are constructed, all the points of this connection are ajusted to P_1 or P_2 in function of a minimum distance criterion.

3. $A_{io,jo} = 0$ (Fig. 5.a)

This is the case of extreme contour lines of the three-dimensional pattern and we close the three-dimensional reconstruction by classical filling.

3. LINKS

We connect the contour lines, points by points, in function of the minimum distance criterion.

Let P_s be the points of C_k and Q_t those of C_{k+1}. For C_k (resp.C_{k+1}) we calculate C_k^2 (resp. C_{k+1}^2) which is close to the convex hull of C_k (resp. C_{k+1}). It is necessary to use the second order reconstructed contour lines in the case of many convexities to avoid deformed links or noncentered links. If the pattern is relatively simple we choose C_k^1 in place of C_k^2.

First for each point $P_{i_0}^2$ we search $Q_{j_0}^2$ defined by the minimum distance :

$d_3(P_{i_0}^2, Q_{j_0}^2) = \min\{d_e(P_{i_0}^2, Q_j^2)),\ j \in \{1, ..., q\}\}$.

All the points P_k of C_k are linked. Generally some points $Q_{j_1}^2$ of C_{k+1}, are unlinked (a single point Q_j can have lot of links $(P_{j_1}^2, Q_j^2), ..., (P_{i_n}^2, Q_j^2)$).

Secondly we search, for these points, the points P_j realizing the minimum distance. To avoid errors we search between the 2 points P_{jo-1} and P_{jo+1} wich are the points of C_k linked in the first step to the first precedent point Q_{j1} of C_{k+1} and to the first next point Q_{j1} of C_{k+1}.

These two steps are realized for C_k^2 and C_{k+1}^2 and we have the same number of points for these contour lines than for C_k and C_{k+1}. Then we conserve the links constructed for P_{io}^2 and to transpose directly to P_{io}. The original contour lines C_k and C_{k+1} and the point list of connexion are used to realize triangular patches and a Z-buffer algorithm.

III EXPERIMENTAL SET-UP

This new technique was applied to heavy gas dispersion purpose. A finite volume of dense gas was released in a simulated neutral atmospheric boundary layer on a flat floor[17]. The gas of density 2.1 and seeded with incense particles was contained in a cylindrical box whose characteristics are : d= 10 cm (diameter), H= 10 cm (higth) and V_o = 402 cm^3 (volume).

The visualisation technique was achieved using an Argon ion laser beam deflected by 12 rotating mirrors creating a 1 mm thin plane ligth sheet (Fig. 1). Another12 rotating mirrors system provides the sweep of the plane on the area where the fixed volume was released. The images were recorded using a 512x512 CCD camera with a 50 mm focal lens and acquired on a video recorder.

The frequency rotation of the mirrors was set to (50 + ΔF) Hz in order to record one plane at different z-level per frame. The relative low spread velocity allows such recording.

To test the algorithm we have reconstructed turbulent releases without external turbulent conditions. The main difficulty of this technique is to synchronised the first plane position with the diameter of the box at the initial time t_0. This was solved by using an optical cell.

Different release times were choosen to observe the different phases of the phenomenom.

IV RESULTS

The successive planes were digitized and corrected for geometrical distorsions if necessary (in fact the use of the center of the objective avoid geometrical distortions).

The following step was the images enhancement in order to obtain contour lines of the release on each plane. The algorithm was then applied. This gives approximately 50000 connexion points with one interpolation between each plane. A number of 25 planes were recorded for each

reconstruction. Recording begin on a diameter.

Results concern the two successive phases of the dense gas releases : the gravity phase and the inertial phase[16]. It is possible to see in Fig. 6.a that the release is affected by the top of the box. Furthermore we can observe that no lateral phenomenom disturb the spreading during this phase. The second reconstruction concerns the inertial phase (Fig. 7.b). We can compare horizontal visualisation of the release with an upview of our reconstruction. No difference appear in the general form. Our reconstruction is obtained by vertical visualisation thus we can say that physically the results agree fairly well.

V.CONCLUSIONS

In this paper we have presented a new automatic method to reconstruct three-dimensional complex, nonstatic and nonreproductible forms. Reconstruction is based on interpolation and linkage between a set of parallel slices. The experimental difficulties and the complex morphology of the forms imply to use local and adaptative criteria. Furthermore, classical problems like multiple-branching, are solved. On the other hand, the frequent discontinuities between two successive slices are taking into account. The advantage of this method lies in the adaptative criteria based on the resolution in spectral space of the specific problems underlying in fluid mechanics.

The method is not time consumer in spite of Fourier Transform use. The application of the algorithm to three-dimensional dispersion problems provides good results. This method have been also employed in water for coherent structures study in boundary layer[18,9].

The next step of this work will be the reconstruction of mean, variance of concentration of such releases in external turbulent conditions[1] and to compare with numerical simulations.

REFERENCES

1. AYRAULT, M.; SIMOENS, S.; MEJEAN, P. 1993: "Effects to two-dimensional obstacle on the dispersion of dense gas releases", 3rd Symposium on experimental and numerical flow visualisation", New-Orlean, Dec..

2. JIMENEZ, J.; COGOLLOS, M.; BERNAL, L.P. 1985: "A perspective view of the plane mixing layer ", J.F.M., 152, pp 125-143.

3. YODA, M. and HESSELINK, L., "A three-dimensional visualisation technique applied to flow around a delta wing", Experiments in fluids 10, pp.102-108, 1990

4. YIP, B.; SCHMITT, R.L.; LONG, M.L. 1988: "Instantaneous three-dimensional concentration measurements in turbulent jets and flames", Optics Letters, Vol. 13, N° 2, pp 96-98.

5. BOISSONAT, J.D. 1986: "Shape reconstruction from planar cross-section", Rapport de recherche, INRA, 07/86.

6. KEPPEL, E. 1975: "Approximating complex surfaces by triangulations of contour lines", IBM journal of research and developpment, Vol. 19.

7. EKOULE, A.; PEYRIN, F.; ODET, C. 1987: "Description d'une procédure de triangulation entièrement automatique", Cognitiva 87.
8. PERSOON, E.; FU, K.S. 1986: "Shape discrimination using Fourier Descriptors" IEEE trans. on pattern analysis and machine intelligence vol Pami 8 N°3 May 86.
9. SIMOENS, S. 1992: "Applications de l'analyse d'images à des phénomènes de dispersion et de mélangeage turbulents", Thèse de Doctorat, E.C.L., 27 Avril 1992.
10. WALLACE, T. and WINTZ, P.A. 1980:"An efficient three-dimensional aircraft recognition using normalised Fourier descriptors", Computer Graphics and Image Processing, Vol 13, pp. 99-126.
11. TESAMI, F.E. and VICKER Jr., J.J. 1985:"Automatic inspection of machine ... cross-sections using Fourier Descriptors." Computer vision, graphics and image processing, Vol 29, pp216-246.
12. MITCHELL, O.R. and GROGAN, T.A. "Global and partial shapes discrimination for computer vision, " Optical engineering, Vol. 23, sept-oct., N°5, pp. 484-491.
13. CHEN, Z. and HO, S.Y. 1991:"Computer vision for robust 3D aircraft recognition with fast library search", Pattern recognition, vol. 24, n° 5, pp 375-390.
14. GIARDINA, C.R. and KHUL, F.P. 1983:"Elliptic Fourier features of a closed contour ", Computer graphics and image processing,Vol 18, pp. 236-258.
15. GRAHAM, R.L. 1972:"An efficient algorithm for determining the convex hull of a finite planar set", Information processing letters 1, pp 132-133.
16. HUPPERT, H.E. and SIMPSON, J.E. 1980:"The slumping of gravity currents", J.F.M., vol. 99, part. 4, pp 785-799.
17. AYRAULT, M. and MEJEAN, P. 1990:"Etude comparative en soufflerie de la dispersion d'un rejet instantané de gaz passif et de gaz plus lourd que l'air," IV^{e} Colloque national de visualisation et traitement d'images en Mécanique des Fluides, pp. 55-61, Mai-Juin 1990.
18. LADAHRI, F., GAGNARD, M. and MOREL, R. 1991:"Visualisation des structures turbulentes dans une couche limite ", Congrès A.U.M., Paris.
19. MUNGAL, M.G.; LOZANO, A.; VAN CRUYNINGEN, I. 1992: "Large-scale dynamics in high Reynolds number jets and jet flames", Exp. in Fluids, 12, pp 141-150.

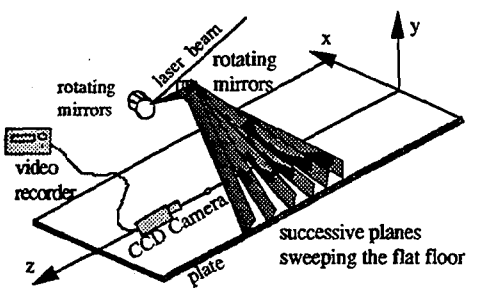

Figure 1
Experimental set-up. Two rotating mirrors allow to sweep the area of interest.

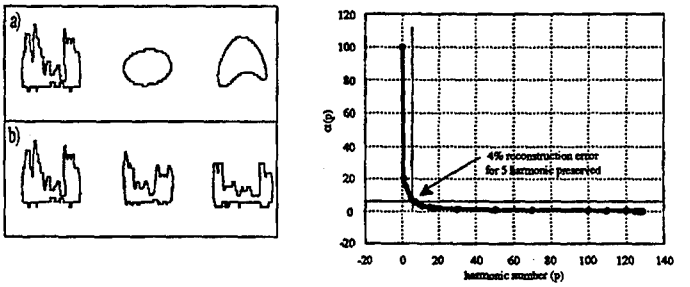

Figure 2
a) original, 1st order and 2nd order reconstructed contours.
b) Interpolated contour between two original contours

Figure 3
Reconstruction error

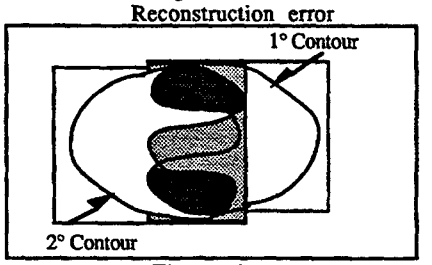

Figure 4
intersection giving erroneous area information

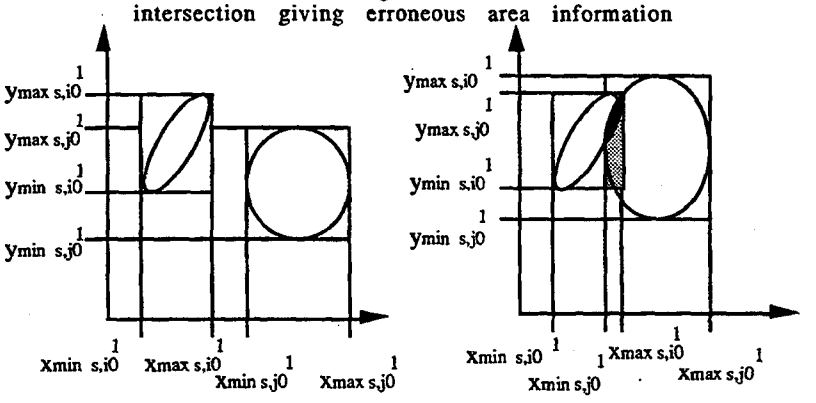

Figure 5
Superimposition of the minimal out-squares the first order Fourier Descriptors
a) No intersection thus no linkage; b) Intersection thus area calculus.

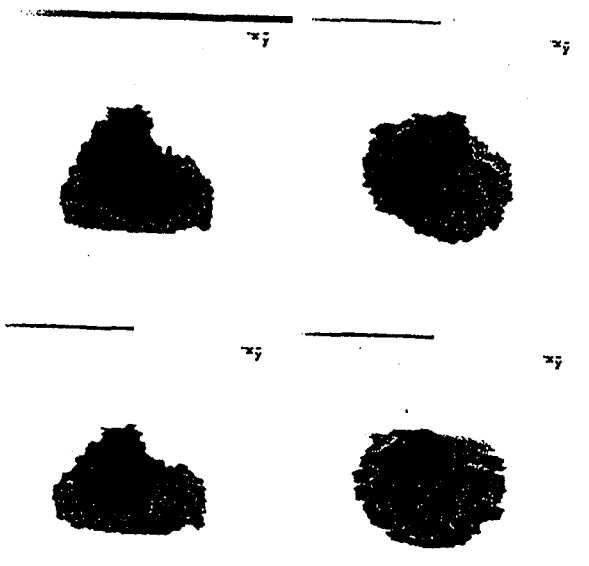

Figure 4 - [illegible]

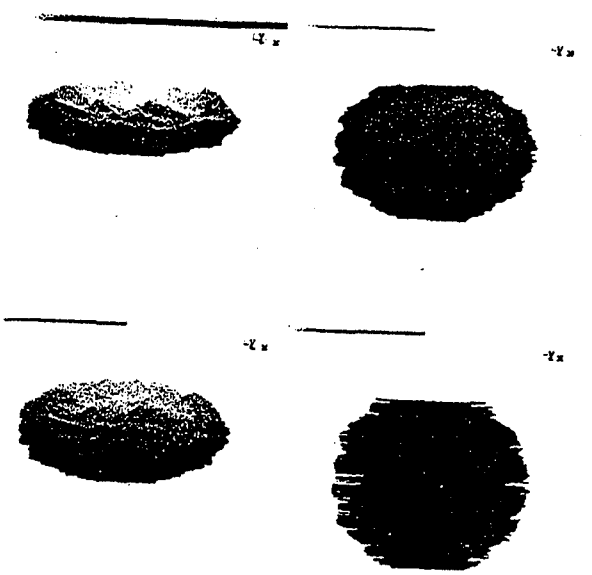

Figure 4b - [illegible]

LABORATORY SIMULATIONS OF INTERACTION BETWEEN BAROTROPIC FLOWS AND SCHEMATIC 3-D OBSTACLES

S.Alessio[+], L.Briatore[+], E.Ferrero[*], C.Giraud[Δ], A.Longhetto[+], O.Morra[Δ]

[+] Institute of General Physics, University of TORINO

[*] Faculty of Sciences, University of ALESSANDRIA

[Δ] Institute of Cosmo-geophysics of CNR of TORINO

Abstract

Simulations of interactions between barotropic flows and 3D obstacles, performed in the "Rotating Laboratory" of the ICGF-CNR Torino, are presented.

The phenomenon has been reproduced towing the obstacles throughout the water channel (4.5x1.5x0.6 m^3) in a non-stratified homogeneous fluid (fresh water). Streamlines were visualised by dye tracers injected in the fluid and continuously recorded on a magnetic videotape. The films were analysed following the trajectories described by the dye and recording their coordinates at different times. Then, using a software post processor, the velocity field was calculated and interpolated on a two-dimensional regular grid. Finally, mean flow streamlines and vorticity field, in a horizontal plane above the obstacle, were obtained.

The experiments have been carried out with different values of the mean flow velocities in order to simulate different atmospheric or oceanic situations characterised by Rossby numbers lower than unity.

The results show the presence of a Taylor Column on the topography (when the Rossby number is small) and of two instabilities (anticyclonic above the obstacle and cyclonic in the lee) due to potential vorticity conservation and boundary layer effects.

Experimental techniques and apparatus

The experiments have been performed in the rotating hydraulic channel of CNR. The tank, mounted along a diameter of the rotating platform[(1),(2),(3),(4)], is 4.5 m long, 1.5 m wide and 0.6 m deep. It contains, at full load, about 3500 kg of water. The maximum rotation speed attainable with the present arrangement correspond to a period of about 15 s.

In a series of preliminary tests, the flow in the channel proved to be quite irregular, in spite of the presence of several devices aimed at regularising it. This observation led to the choice of towing the obstacle along the channel, filled with still water, rather than working with a static obstacle immersed in a flow, in order to reduce the elevated background noise revealed by analyses of previous experiments.

The hemispheric obstacle, of radius r=6.3 cm, used in the experiments, was towed by a trolley placed over the tank upon which was mounted the video-camera. The trolley was put into operation after a delay of at least one hour after the platform was set in to rotation, in order to obtain the condition of rigid rotation of the fluid.

The trolley is operated by a step by step engine and enabled the movement of the obstacle at a constant speed, in the range 0.5-2.5 cm/s.

The dye was sprayed in front of the moving obstacle, so as to form stripes transversally to the flow, that ran across the field of view of the video camera.

After covering the entire length of the tank, there was a 20 minutes delay before activating the trolley in the opposite direction, in order to eliminate residual wave motions in the fluid. The video camera attached to the trolley was a solid block with the obstacle. The image of the flow

filmed by the camera resulted, therefore, from the relative motion of the obstacle with respect to the tracer, which was added to the water that was at rest in the rotating frame of reference.
From a theoretical point of view, towing the obstacle could not be perfectly equivalent to fluxing water with respect to a still obstacle. In the second case, the dynamics of the phenomenon must be interpreted as an interaction of a barotropic geostrophic flow, where an equilibrium is established between the forces due to the rotation and the pressure gradient perpendicular to the direction of the flow (as it happens in undisturbed real geophysical flows where friction forces are neglected).
The longitudinal pressure gradient imposed by the pump of the tank partly turns into a cross-wind gradient, because of the rotation, and partly compensates for the energy losses due to friction with the channel bottom, the walls and the air above.
The cross-wind pressure gradient and the Coriolis forces are in geostrophical equilibrium above the obstacle. The moving fluid, interacting with the channel bottom, creates a Ekman layer (due to the rotation) both on the flat bottom and on the obstacle surface. This Ekman layer dominates the dynamical behaviour of the lower layers of the flow.

The towing technique, extensively used both in the past (Taylor([9]), in the twenties; Davies later([5])) and recently, implies a relative motion that is, in principle, equivalent to the previous description; however, due to the rotation of the fluid, some differences arise, that are in no way trivial, though they are often negligible. As a matter of fact, the fluid is static in the reference frame of the hydraulic channel. Therefore no dynamical equilibrium is established between Coriolis force and pressure gradient, which are both zero. The dynamics of the phenomenon can be interpreted thinking that the moving obstacle tends to be deviated from its inertial rectilinear trajectory by Coriolis force. The vincular reaction due to the towing device (metallic thread taut along the channel) opposes to the Coriolis force.
Forces due to the rotation therefore do not act on the fluid particles, that are everywhere at rest, except that on those particles belonging to the layers close to the towed obstacle, that acquire a velocity component due to friction.
The dye used as a tracer was a mixture of ink and water (about 1:5), properly chosen in order to obtain a density close to that of the surrounding liquid, thus minimising buoyancy effects; the streamlines of the flow that were evidenced in that way, were filmed from above.
The films obtained have been analysed by means of a personal computer and of a system for storing space-time co-ordinates of the points of the trajectories. Subsequently, with a software post-processor, the velocity field has been calculated and interpolated on a two-dimensional grid. Finally, the vorticity field has been deduced from the velocities.
This method introduces an error, due to both the distortion of images captured by the video camera and to the uncertainty in locating the points forming the trajectories.
The maximum error evaluated is of the order of 0.1 cm/s for mean velocities of 2.5 cm/s (percentual error less than 4%). This error, propagated on to vorticities, gives absolute errors on vorticities of the order of 0.08 s^{-1}, corresponding to relative errors of 27%.

Similarity criteria
When operating with a barotropic, incompressible, non stratified fluid, the adimensional parameters peculiar to the phenomenon are Rossby and horizontal and vertical Ekman numbers,

$$Ro = \frac{U}{2\Omega L} \qquad E_H = \frac{\nu}{2\Omega L^2} \qquad E_v = \frac{\nu}{2\Omega H^2}$$

where $\Omega = 2\pi / T$ (T is the channel rotation period), U and L are velocity and length scales, ν is water molecular viscosity and H is height of the obstacle. In table 1 the values of the quantities, characterising the experiments that were performed, are listed.

TABLE 1

- T=20 s
- $\nu = 0.01\, cm^2 / s$
- $L \approx 12$ cm
- $H = 6$ cm
- $H_0 = 40\, cm$
- $U = 2.5 - 0.5\, cm / s$

The length scale is given by the diameter of the hemispheric obstacle and the velocity scale is given by the towing speed. H_0 is the fluid height.
The shape and dimension of the obstacle have been chosen in order to satisfy, with this height of fluid, the rigid-lid hypothesis (the presence of orography does not affect the fluid free surface).
From the values of the quantities listed in table 1, one can estimate the range of Rossby number values covered by the experiments and the values of the Ekman numbers:

$$Ro \approx 0.32 - 0.06 \quad E_H \approx 1 \cdot 10^{-4} \quad E_v \approx 4 \cdot 10^{-4}.$$

The above values denote that our laboratory experiments can simulate naturally occuring atmospheric processes at synoptic and sub-synoptic scale.

Experimental results
The experiments were performed in stationary conditions, that is, over an interval of times much larger than the duration of the initial phase of the process, which show a transient behaviour while the relative motion field establishes itself.
Table 2 show the values of the flow velocity and the corresponding values of Rossby number with a rotation period of 20 s used in our experiments.

TABLE 2

U cm/s	Ro
2.5	0.32
2.0	0.25
1.6	0.20
1.2	0.15
1.0	0.13
0.8	0.10
0.5	0.06

A preliminary analysis of the films concerning these tests allowed singling out a number of episodes, each one having a duration corresponding to the time necessary for a dye cloud to run across the whole image field. For all these episodes, streamlines, velocity field and isolines of relative vorticity were then drawn (Figures 1 a,b,c). Their inspection led to some interesting observations.

Evaluation of velocities in the various parts of the spatial domain evidentiates a moderate slowing down of the flow at right, near the obstacle, in agreement with the observations of Davies[5].
The most evident phenomena induced by the obstacle are an anticyclonic curvature of the streamlines over the obstacle and a subsequent cyclonic curvature downstream, when the fluid particles' trajectories re-align along the channel axis.
In some cases (figure 2) a slow-down region is well visible over the obstacle, associated with an anticyclonic circulation, that indicates the presence of a Taylor column, generated by processes different from those of vorticity induction.
In the neighbouring region of the obstacle, relative vorticity is about zero. The extremal values of vorticity, that are sometimes found in the undisturbed flow in regions scarcely influenced by the obstacle presence, are connected to local accelerations and decelerations (shear vorticity) and are not due to the curvature of streamlines. In fact, from the definition of relative vorticity ς, one sees that ς may be produced when one of the two gradients of horizontal velocity components prevails over the other, although trajectories are locally parallel to one an other.
Close to the obstacle, on the contrary, a pair cyclone-anticyclone is observed, with the two components having more or less the same intensity.
A minimum of vorticity is associated with anticyclonic curvature of trajectories, caused by compression of vortex tubes overcoming the obstacle. Observed minima of relative vorticity are in good agreement with theoretical value, predicted by the law of conservation of potential vorticity in a barotropic fluid without friction[6]:

$$\varsigma = 2\Omega\left(\frac{H}{H_0} - 1\right)$$

where letters indicate the quantities as above. For these particular experiments, characterised by the parameter shown in table 1, $\varsigma = -0.099\ s^{-1}$.
Table 3 show the minimum values of relative vorticity we found in five different tests.

TABLE 3

1	$\varsigma = -0.100\ s^{-1}$
2	$\varsigma = -0.150\ s^{-1}$
3	$\varsigma = -0.125\ s^{-1}$
4	$\varsigma = -0.099\ s^{-1}$
5	$\varsigma = -0.143\ s^{-1}$

The minima, on average, do not differ too much from the theoretical expectation, but show a certain variability that could be due to the error introduced by the method of image analysis adopted. This error, already mentioned before, is of the order of $0.08\ s^{-1}$. However, the fact that they overstimated, on average, the theoretical value by about 25% led us to inspect the possibility of a systematic variability superimposed on the experimental error.
For this reason. average values of maximum and minimum vorticity of different tests performed in the same conditions have been evaluated.
The results are shown in figure 3, as functions of Rossby number. Standard deviations of the two series of data of positive and negative vorticity are both $0.04\ s^{-1}$. This value coincides with what is found calculating the error affecting average values relative to each run, on the basis of the error affecting a single measurement ($0.08\ s^{-1}$).

Looking at the figure 3, a separation between maxima and minima may be noted. That becomes greater and greater as the velocity increases.
Therefore it can be stated that the method employed allows distinguishing effects due to vorticity induction by the obstacle from fluctuations. Moreover, a dependence of vorticity maximum and minimum values on Rossby number seems to appear, even if the length of errors bars is such that caution must be used in drawing definitive conclusions concerning this subject.
A variation of Rossby number, therefore, causes a change in measured values of vorticity, even if the qualitative trends of the streamlines for the different runs seem to be similar.
It may be interesting to notice the constant presence, in all runs and with all velocities, of an area of cyclonic vorticity that is not predicted by the theory in the stationary case[7].
The theory developed by Hupper and Bryan accounts for the evolution of the structures that are formed in time-dependent transient interactions between the flow and three-dimensional obstacle, on the basis of the values of two parameters: the *stagnation parameter:*

$$s = h_0 R_0^{-1}$$

where $h_0 = \frac{H}{H_0}$ is the obstacle height, normalised to fluid depth, and R_0 is the Rossby number, and the *advection parameter:*

$$\gamma = \frac{4H_0}{HfL} \begin{cases} U_0 & \text{per } U_0 \geq U_c \\ \dfrac{U_c}{1 - \ln(U_0 / U_c)} & \text{per } U_0 \leq U_c \end{cases}$$

where L is the horizontal scale length (horizontal dimension of the obstacle), U_c is a threshold velocity below which stagnation occurs over the obstacle, f the Coriolis parameter and U_0 indicates mean flow velocity.
Both these parameters have a critical value that discriminates the dynamical evolution of the phenomenon, according to the values of fundamental variables.
The essential problem here is to understand what conditions are needed for a cyclonic vorticity, that is formed in the initial transient phase by stretching of vortex tubes in the fluid that moves down the obstacle, to be advected by mean flow.
Starting from the conditions given by Huppert and Bryan, we derived the following general formula:

$$\frac{h_0 L}{\left(h_0 Ro^{-1}\right)_c} \frac{f}{U_0} \geq e^{\left(\frac{4}{\left(h_0 Ro^{-1}\right)_c \gamma_c} - 1 \right)}$$

where the subscript "c" means "critical".
It represents a sufficient condition for the cyclone not to be advected by the flow but rather a sort of vortex-vortex interaction to occur near the obstacle.
In the case of the present experiment, if one substitutes for the critical values quoted above and the dimensions of the obstacle, the previous expression reduces to simple formula:

$$\frac{f}{U_0} \geq 2.96e^{0.85}$$

Fulfilling this condition would imply flow and rotation conditions that are not attainable yet in the channel employed in this experiment. For example, one would need fluxes of the order of 1 cm/s with associated rotation periods less than or equal to 1.4s, or alternatively, fluxes of 0.1 cm/s coupled with period of about 14 s. While the last condition is achievable (t=14 s is presently possible with our apparatus), fluxes of 0.1 cm/s are still impossible.

In all the runs we worked with values of velocity flow and rotation period that do not satisfy the above condition.

The presence of permanent cyclonic vorticity, evidenced by the laboratory experiments, must therefore be interpreted, probably, outside the quasi-geostrophical theory of the Huppert and Bryan model, that holds for Rossby and Ekman numbers much lower than unity, that is in the case of friction and inertial forces negligible in comparison with those due to rotation.

As a matter of fact, this theory is based upon potential vorticity conservation and does not take into account friction effects in the Ekman layer.

A possible interpretation of our experimental evidence may be provided in terms of shear vorticity.

In stationary conditions, as in the present experiment, the stretching of vortex tubes that, from the top of the obstacle, descend in the obstacle's lee, cannot generate a cyclonic structure (a phenomenon that, on the contrary, does take place during the initial transient phase) but only can balance the effect due to the compression of the same tubes during upward motion.

The maximum of positive vorticity that was found experimentally is therefore explainable in terms of horizontal shear of velocities, whose absolute values turn out to be small over the obstacle, due to anticyclonic circulation induced by the obstacle, that combines with mean flow.

The presence of vorticity maxima in the lee of the obstacle is not due to the curvature of the streamlines, that turns out to be very small, but is due to velocity changes of the flow in different positions, that would result in a spatial variation of velocity field components and, consequently, would produce relative vorticity.

In the real process, that takes place in the rotating tank, in fact, a Ekman layer is created, that is not present in the theoretical model. Therefore, the velocity vector varies in direction and intensity with height, and Rossby and Ekman numbers are not any more negligible[8].

The phenomenon, associated with vertical displacement of fluid particles overcoming the obstacle, generates a vertical transport of linear momentum that can cause velocity variations, even at relatively big heights from the bottom. These variations are important enough to generate cyclonic and anticyclonic shear vorticity.

It must be noted that if conditions were such to have a well-developed Taylor column over the obstacle (Rossby and Ekman numbers much less than one), accompanied by corresponding stagnation zone, and a perfectly two-dimensional flow, no vertical motion would be present and no momentum exchange would occur.

Conclusions

In the present paper, experiments have been described, that were performed in a rotating hydrodynamic laboratory, concerning the interaction of barotropic non stratified fluid with schematic three-dimensional obstacles.

Many runs were performed, with different values of characteristic fluid dynamical adimensional parameters (Rossby and Ekman numbers).

The results are presented in terms of velocity fields, streamlines and relative vorticity fields, obtained by means of a image analysis technique developed specifically for these experiments.

The experiments have been carried out in the frame of the quasi-geostrophyc theory, that predicts, in conditions of Rossby and Ekman numbers much less than one, the evolution of the phenomenon and specifies the conditions of flow velocity and rotation period necessary for advection of the cyclonic vortex or, instead, for vortex-vortex interaction.
The analysis of the experimental results has put into evidence the generation of cyclonic and anticyclonic structures induced by topography, that are well separated, at least for what concern their maximum values.
Positive and negative vorticity maxima, relative to different flows, show average variations with respect to theoretical values that seem to depend on Rossby number, even when the relatively large experimental error is considered.
Because of the interaction between flow and obstacle, regions of cyclonic vorticity are generated, that are not advected by the mean flow, even if the values of simulation parameters would lead to expect it.
This phenomenon may be interpreted as a consequence of the friction between fluid and obstacle, that though is not taken into account by theoretical models, does not seem to be negligible.

Aknowledgments
The Authors are grateful to Dr. Roberto Purini for the helpful discussion on theoretical aspects of this research work.

References
1) S.Alessio, L.Briatore, E.Ferrero, C.Giraud, A.Longhetto, O.Morra ***Experimental results on atmospheric dynamical and thermal structures modeled in a rotating hydraulic channel*** Il Nuovo Cimento, Vol. 12 C, N. 4, pp. 427-438, 1989.
2) S.Alessio, L.Briatore, E.Ferrero, C.Giraud, A.Longhetto, O.Morra ***Interaction between atmospheric flows an obstacles: experiments in a rotating channel*** Boundary Layer Meteorology 60, pp. 235-241, 1992.
3) S.Alessio, L.Briatore, G.Elisei, E.Ferrero, C.Giraud, A.Longhetto, O.Morra ***Laboratory simulation of Coriolis effects on atmospheric dispersion of airborne tracers over a complex terrain*** Il Nuovo Cimento , vol 15C, N. 4, p. 461, 1992
4) S.Alessio, L.Briatore, E.Ferrero, C.Giraud, A.Longhetto, O.Morra ***Experimental study in rotating channel on similarity law of tracer concentration distribution in the turbulent Ekman boundary layer of atmosphere*** Atmospheric Environment, vol 27A, No 13, pp. 2075-2083, 1993
5) P.A.Davies ***Experiments on Taylor columns in rotating stratified fluids.*** Journal of Fluid Mechanics, 54, pp 691-718, 1972
6) J.P. Pedlosky ***Geophysical Fluid Dynamics*** Springer-Verlag, 2nd Edition, 1987
7) H.E.Huppert and K.Bryan ***Topographically generated eddies*** Deep See Research, 23, 665-679, 1976
8) A.Buzzi and S.Tibaldi ***Inertial and frictional effects on rotating and stratified flow over topography*** Quar. Jour. R. Met. Soc., 103, 1977
9) Taylor G.I. ***Experiments on the motion of solid bodies in rotating fluids*** Proc. Roy. Soc. A 104, 213-218, 1923

Fig 1: Examples of the image analysis results. a) streamlines; b) velocity field; c) vorticity isolines

Fig 2: Velocity field above the obstacle with stagnation zone

Fig.3: Maxima and Minima of vorticy as function of Rossby number

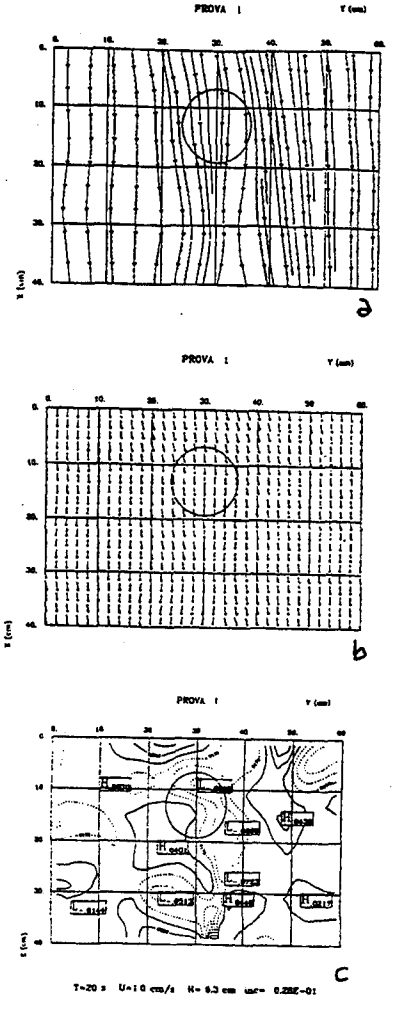

Fig. 1

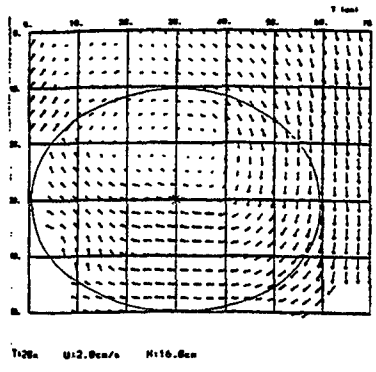

Fig. 2

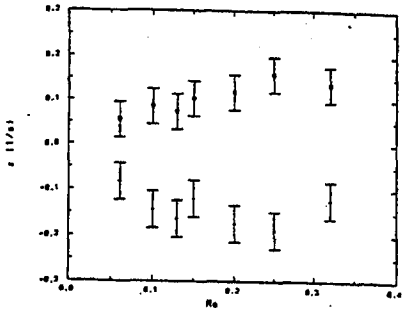

Fig. 3

PHYSICAL SIMULATIONS IN ROTATING TANK OF LEE CYCLOGENESIS

L.Briatore[+], E.Ferrero[*], C.Giraud[Δ], A.Longhetto[+], G.Chabert d'Hieres[°], H.Didelle[°]

[+] Institute of General Physics, University of TORINO
[*] Faculty of Sciences, University of ALESSANDRIA
[Δ] Institute of Cosmo-geophysics of CNR of TORINO
[°] IMG - University of GRENOBLE

Abstract

Some results of physical simulations of baroclinic flows, carried out in a rotating tank, are presented. In particular, the interaction between flow and a tridimensional mountain is investigated.

Complex dynamic and thermodynamic processes occur when the so called lee cyclogenesis can develop; in this case, potential energy of the basic flow is converted into kinetic energy of its perturbation field, giving rise to strengthening and deepening of its pressure troughs. The presence of an obstacle can exert a blocking on the colder lower layers of the impinging stably stratified airflow, forcing it to deflect horizontally round its borders. In this way, these layers get the lee region with a delay. These two effects, of blocking and delay, are the responsible for the initial pressure decrease downwind of the mountain and for the subsequent proper baroclinic development.

Following this rather simple scheme, the lee cyclogenesis has been simulated in the rotating tank of the IMG of GRENOBLE.

The experiments were observed by three TV cameras continuously recording the trajectories of dye tracers at three levels of the stratified fluid. In order to measure the vertical density profiles, a rectangular mesh of samplers was rapidly moved up and down in the tank.

The results of the simulations, both from a qualitative and quantitative point of view, are here shown. They demonstrate the possibility of reproducing the main features of the lee cyclogenesis and encourage to go on with this kind of experimental approach in order to better understand the atmospheric processes occurring downwind actual mountain chains, like the Alps and the Pyrenees

General outline of lee cyclogenesis

Cyclogenesis is generally referred to as a development of synoptic scale weather disturbances ([1,2,3]). The process of cyclogenesis can be regarded as an infinitesimal perturbation superposed on an unstable zonal current. For this infinitesimal perturbation to amplify, the basic flow must provide potential and kinetic energy to the perturbation([4]).

Where the westerlies increase with height (as is normal in mid-latitudes), cyclones form, develop thermal asymmetries, and intensify. This is why in middle latitudes baroclinic instability is the most important cyclogenetic process. In fact, in baroclinic instability, the potential energy of the basic state flow is converted to potential and kinetic energy of the perturbation.

In a sufficiently strong wave-shaped westerly flow, horizontal divergence and convergence occur in such a distribution as to cause eastward movement of the troughs and crests (figure 1). The superimposed wave pattern in the upper layers of westerlies produces overcompensating accumulation of air where the low levels show depletion, and depletion of air where the low levels show accumulation.

When the unstable zonal current interacts with topographical features, like the Alps or Pyrenees, it has been suggested that the obstacle can act as a trigger for the cyclogenetic development([1,5]).

In this case, lee cyclogenesis can occur, which means that the mountain can induce a cyclogenetic process, which couldn't have appeared otherwise (if the mountain had been absent) and which is intensified and locked in the region downwind of the obstacle.
Most theories of lee cyclogenesis consider this phenomenon as the modification induced by the mountain on a perturbation of a time independent mean state. Other theories, instead, identify the lee cyclone as the standing downwind cyclone induced by the interaction of the mean flow with the mountain.
Lee cyclogenesis should not be confused with high-low pressure perturbations, with the associated anticyclonic vorticity over the mountain and cyclonic vorticity in the lee ([6]) (vorticity induction and Ekman pumping at the lower boundary) but should be restricted only to those cases in which *baroclinic development*, leading to a deep cyclone, is evident ([1]).
Alpine lee cyclogenesis is induced by the interaction with the mountain of a primary growing baroclinic wave embedded in a mean westerly shear flow. The shape and the location of the Alps are necessary conditions ([2]) for the strong cyclogenetic activity on the Mediterranean (*boundary condition*), from the Gulf of Genoa to the Po Valley and thence to the north of the Adriatic Sea.
Cold outbreaks into the Mediterranean Basin from the north or the Northwest are very favourable for the formation of cyclones (*initial condition*)([2]).
The Alps can be considered as a wall blocking the normal flow in the lowest layers: the following two processes seem to be responsible for the initial pressure fall in the lee ([1]).
1) Horizontal advection, which varies in the vertical because of the blocking effect of the mountain.
2) Horizontal deformation of the thermal field, which is induced by differential advection in the horizontal.
This process can be summarised as an **advection-retardation** effect, which simulates the orographic influence by a retarding term of advection in the basic forecast equation:

$$\left(\nabla^2+\frac{f_0^2}{\sigma}\frac{\partial^2}{\partial p^2}\right)\chi=-f_0 V_g\bullet\nabla\left(\frac{1}{f_0}\nabla^2\Phi+f\right)+\frac{f_0^2}{\sigma}\frac{\partial}{\partial p}\left(-V_g\bullet\nabla\frac{\partial\Phi}{\partial p}\right)$$

$$\left(\nabla^2+\frac{f_0^2}{\sigma}\frac{\partial^2}{\partial p^2}\right)\omega=-\frac{f_0^2}{\sigma}\frac{\partial}{\partial p}\left[V_g\bullet\nabla\left(\frac{1}{f_0}\nabla^2\Phi+f\right)\right]+\frac{1}{\sigma}\nabla^2\left[V_g\bullet\nabla\left(-\frac{\partial\Phi}{\partial p}\right)\right]$$

where Φ is the geopotential, χ its time derivative and ω the atmospheric pressure change following the motion ($\omega=\frac{dp}{dt}$).
A very simplified theory of the lee cyclogenesis can be given in terms of primary and secondary pressure waves. The primary wave of pressure fall, caused by processes in higher levels, crosses the Alps without hindrance. The secondary "thermal" wave, which is connected with the cold front and which should cause pressure rise after the front is passed, is prevented by the Alps from penetrating into the cyclogenetic area ([2]).
Therefore, the effect of the primary wave is isolated in the lee of the Alps and cyclogenesis has to be expected.
The sequence of cyclogenetic processes upwind and downwind of the Alps can then be summarised as follows (see figure 2).
1- The approach of the cold front is connected with divergence in higher levels.

2- The compensating flow from the cold to the warm region in lower layers is hampered by the mountains.
3- This leads to cyclogenesis in the lee of the Alps.
Then, a proper baroclinic development, triggered at low level by the frontal readjustment process and sustained aloft by the deepening of the large-scale trough, takes place accounting for the subsequent stage of the cyclone life.
Finally, the cyclone increases its horizontal scale to about 500 km and takes the typical feature of a cut-off cyclone of mid-latitudes.

The rotating tank and the current generator

The experiments were carried out on the rotating platform of the Institute of Mechanics, Grenoble University. This platform ([7]) consist of a 14 meters diameter, flat reinforced concrete table, with a rotation period which can adjusted continuously from about 500 to about 10 seconds (kept constant to within 0.01%), which can be loaded with fresh and salted water up to about 150 tons. In these conditions, the total weight of the facility is order of 300 tons. The error from the vertical is 5 10^{-6} rad.
Ten large tanks, placed 3 meters underground, can supply fresh and salt water whose temperature and salinity become very stable and can be controlled at a very high degree (also thanks to the thermal inertia of such a big water mass). The refilling time is order of 4-5 hours, when accurate density stratification is required, and other 2-3 hours are necessary for suppressing entirely any spurious vorticity and drive water in solid rotation conditions.
The platform is supported centrally by a spherical thrust bearing and peripherically on 23 rollers, equally spaced around the circumference of the table.

The laboratory experiment

In the present laboratory experiment we aimed at simulating a baroclinic flow, representing a zonal frontal current unstable vis-a-vis non infinitesimal perturbations produced by an obstacle modelling the shape and the horizontal extent of the Alps. In other words, we were interested in studying the behaviour of a baroclinic zonal flow which should not have given rise to baroclinic development in absence of the mountain, so as to ascertain in manifest way to effective role played by this last in the cyclogenetic process.
The baroclinic frontal flow has been created in the laboratory experiment by using the technique of intermediate density currents ([7]). The background atmosphere was represented by a two-layers fluid, whose densities were respectively ρ_1 and ρ_2 with a sharp separating interface, in equilibrium with the rotating frame of a cylindrical tank.
An intermediate density fluid, generated by a system which mixes waters from the two layers, is introduced at the separating interface, and this gives rise to a density driven current, parallel to the tank wall, which attains almost immediately an equilibrium speed, relative to the two layers and the tank, given by the geostrophic balance condition, which is favoured also by the particular triangular shape of the outlet-mouth of the generator.
When the intermediate density stream leaves the outlet mouth of the front generator and penetrates between the two fluid layers, a typical meandering due to adjustment processes (bringing about compression and stirring of vortex tubes) occurs, which simulates the relevant features of a cyclone-anticyclone dipole structure (see figure 3), closely corresponding to the synoptic natural situation which is most favourable to lee cyclogenesis development south of the Alps (see figure 4).
The development of the intermediate density current, simulating our synoptic front, and its interaction with the obstacle simulating the Alps, were observed both by three TV cameras and by a rectangular mesh of 15 ultrasonic density samplers. Each TV camera recorded, in its own field of

view, the tracks of dye tracers emitted at three different levels in the layer simulating the front, so giving a synoptic representation of the baroclinic development occurring near and downstream of the obstacle.
The density sampler network provided, at each time it was operated, continuous vertical density profiles simultaneously recorded at 15 points upstream and downstream of the obstacle. This measurements allowed us to reconstruct the density field at many levels in the region where the intermediate water took the shape of the synoptic cyclone-anticyclone dipole and in the region (around and downwind of the obstacle) where the baroclinic interaction and the lee cyclogenesis occurred.
The analysis of these density patterns was then used to evaluate the corresponding atmospheric fields of pressure and potential temperature, which represent the most important diagnostic factors for testing the occurrence of the physical conditions characterising the natural phenomenon we wanted to simulate.

Analysis of the results

The density field was used to calculate both the atmospheric potential temperature (or entropy) field, through the equation $\frac{\Delta\rho_\vartheta}{\rho_\vartheta} = -\frac{\Delta\theta}{\theta}$, corresponding to the assumption of incompressible fluid ([8]), and the pressure field, through the hydrostatic equilibrium law; for each density profile, the pressure at each level can be calculated by the summation, starting from the top, of the quantities $\rho_a(z)g\Delta z$, where $\rho_a(z)$ is the value of atmospheric density at level z, calculated from the potential atmospheric density $\rho_\vartheta(z)$, which corresponds to the actual water density $\rho_w(z)$, and Δz is the displacement of the samplers between two subsequent measurements in the vertical profile (g is the acceleration of gravity).
These two fields can be represented both as cut-a-way diagrams of isobars and isentropes (figure 5, representing the initial situation when the cyclone-anticyclone dipole structure is still north-west of the Alps) and as horizontal projections over constant-z planes of isobaric and isentropic surfaces (figure 6).
The analysis of the above diagrams allows one to get an immediate perception of the baroclinicity of the background flow (the front before the interaction) and of the cyclogenetic region, which can be compared to the prototype situation, i.e. the synoptic baroclinic front impinging the Alps from north-west (figure 7 to be compared to fig 5).
Figure 7 shows the vertical distribution of isentropes (constant potential temperature surfaces) where the front is passing over and around the Alps. The deformation of isentropes with respect to the isobares reveals a baroclinic situation, which is amplified by the mountains.
We recall here that an atmospheric flow is said to be baroclinic, when the horizontal gradients of potential temperature at constant pressure (i. e., calculated over isobaric surfaces) are different from zero. This is the case of figure 7, whose vertical axis is substituted by the pressure co-ordinate, so that the constant pressure surfaces are horizontal straight lines.
The features of isentropes in figure 7 seem to be quite well reproduced by the isentropic analysis of one of our experiments (figure 5), for which the TV camera records showed a well developed cyclogenesis South of the Alps. In fact, the isoentropes of our laboratory simulation exhibit the characteristic downward bending in the flow which impinges on the obstacle, and a deformation pattern, over and around it, which resemble the one shown in figure 7.
Other cut-a-way isoentrope-isobar diagrams, not shown here, referring to different stages of the development, from the initial situation corresponding to figure 5 to the final situation where the cyclone in the Tyrrenian sea is completely developed(figure 8), confirm the agreement (at least qualitative) between processes occurring in the prototype and in the model.

The flow appears to be almost barotropic at the first beginning, then it becomes slightly baroclinic when the cyclone-anticyclone structure starts appearing, and exhibits afterwards large distortion features, bringing about the highest degree of baroclinicity, when it interacts with the obstacle. In this last phase, there is the maximum conversion of potential energy (due to the fluid density stratification) to kinetic energy of the perturbation (the downwind lee cyclone).
Figures 9 and 10 show the trends, from the initial to the final stage of the experiment, of the isobaric horizontal gradient of the potential temperature, giving an other representation of the development of the process.

Conclusions

The analysis of a laboratory experiment in rotating hydraulic tank of a lee cyclone development produced very interesting and promising results, which have shown that this modelling technique is able to simulate, at reduced scale, subsynoptic complex atmospheric processes of interaction between airflows and mountains, whose prediction by numerical models is still a not fully resolved problem.
The interest of experiments like the one here discussed is represented by the possibility, they offer, to inspect physical processes occurring at sub-grid scale of synoptic numerical circulation models of atmosphere, so giving a better and more reliable parametrization to be introduced in the above models, in the regions where there are large mountains, in order to include important information which is unresolved by them.

Acknowledgements

The Authors wish to thank Mr. R.Carcel, Mr. R.Forza and Mr. D.Bertoni for their skilful technical assistance before and during the experimental runs. This work has been supported by ENEL S.p.A.-Roma, under the research contract "Interazione dei sistemi energetici con la salute dell'uomo e l'ambiente"-Sub Project 3, Line 2.4

References

1) Buzzi A. and Tibaldi S. (1977) Cyclogenesis in the lee of the Alps: a case study *Quart. J. R. Met. Soc.*, 104, 271-280

2) Egger J. (1972) Numerical experiments on the cyclogenesis in the Gulf of Genoa *Beitr. Physi. Atmos.*, 45, 320-346

3) Radinovic D. (1965) On forecasting of cyclogenesis in the West Mediterranean and other areas bounded by mountain range by baroclinic model *Archiv. Met. Geoph. Bioklim.*, A 14, 279-299

4)Atkinson B.W. Dynamical meteorology: some milestones *in Dynamical Meteorology - B.W.Atkinson Ed.- Methuen* - 124-127 (1981)

5) Boyer D.L., Chen R. and Davies P.A. (1987) Some laboratory models of flow past the Alpine/Pyrenee mountain complex *Meteorol. Atmosf Phys.*, 36,187-200

6) Huppert H.E. and Bryan K. (1976) Topographically generated eddies *Deep Sea Res.*, 23, 655-679

7) Chabert d'Hieres G., Didelle H. and Obaton D. (1991) A laboratory study of surface boundary currents: application to the Algerian current *J. Geophys. Res.*, C-7, 12539-12548

8) Turner J.S. Buoyancy effects in fluid - *Cambridge University Press,* 4-5, (1973)

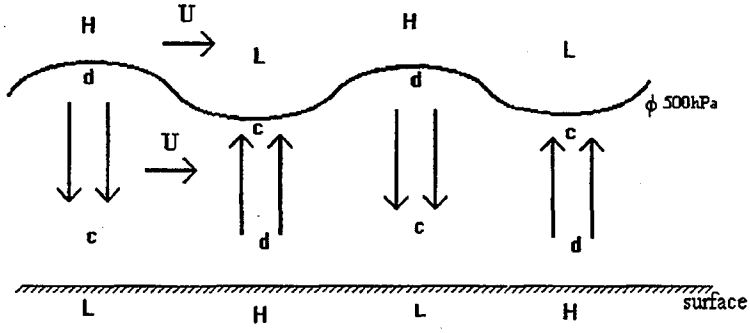

Fig 1: In a westerly flow horizontal divergence and convergence occur in such a distribution as to cause eastward movement of troughs and crests.

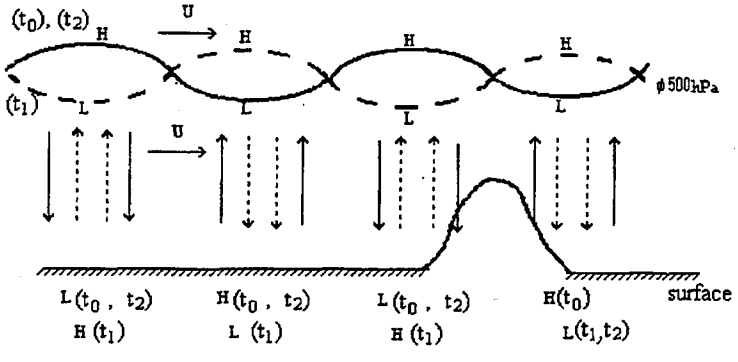

Fig 2: The obstacle inhibits the restoring of divergence (pressure increase) at surface downwind of it.

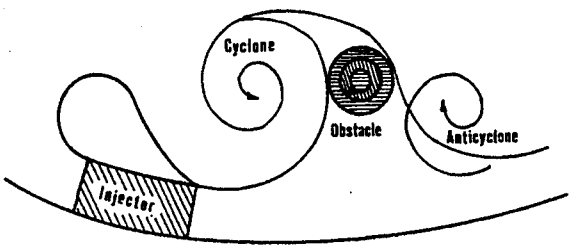

FIG. 3

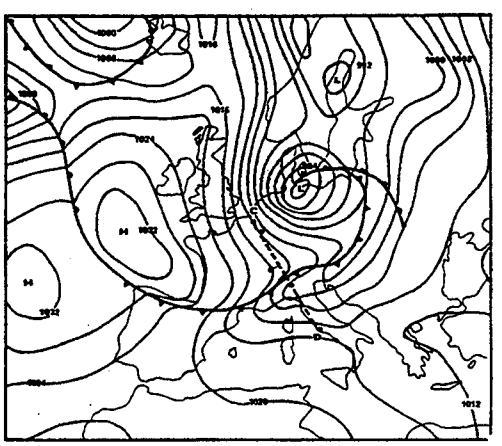

Fig. 4.

Fig. 1(b). 3 April 1973, 00GMT

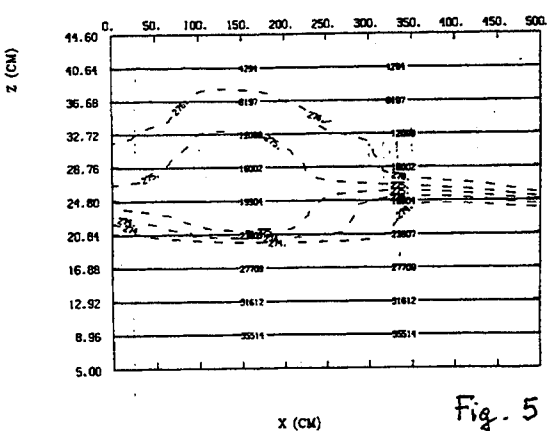

Fig. 5

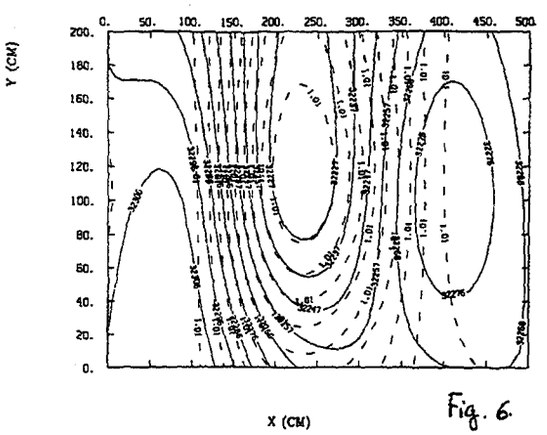

Fig. 6.

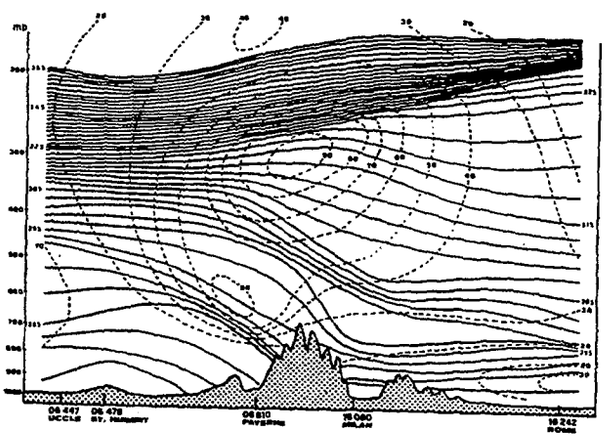

Fig. 7

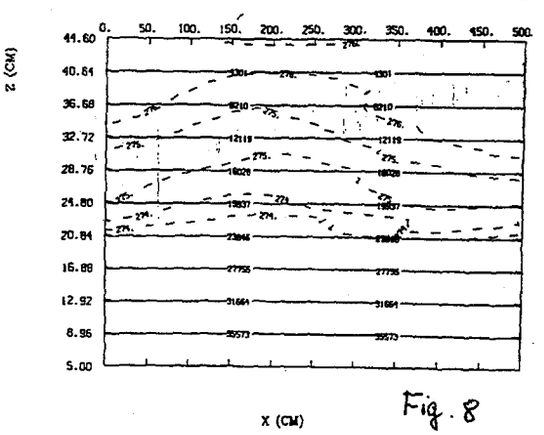

Fig. 8

CORRELATION OF DRAG COEFFICIENT VERSUS FROUDE NUMBER FOR VARIOUSLY STRATIFIED FLUIDS

SHISHKINA O.D.
Institute of Applied Physics, Russian Academy of Sciences,
Nizhny Novgorod (Russia) [1]

Abstract

The comparative analysis results of drag coefficient versus Froude number based on drag measurements of uniformly and horizontally driven models both for two–layered and continuously stratified liquid (exponential stratification and thermocline) in the range of small Froude numbers ($Fi \sim 1$) are presented.
Comparison of the experimental data, obtained by the author for a thermocline, with those for the two – layered and exponentially stratified liquid, presented in literature is fulfilled. Linear dependence for Froude numbers Fi versus the same values of the drag coefficient increment ΔCx for continuously stratified fluids and square dependence between Fi for exponential stratification and two–layered liquid were obtained.

1 Introduction

There are few experimental works conserning study of drag on uniformly driven solid bodies in a stratified fluid. In the work by Nikitina (1959)(1) experiments on drag value measurements of a ship model mowing at a free surface of a two–layered fluid with various layers thickness has been fulfilled. The drag coefficient values were not estimated in this paper.

Both drag force and drag coefficient versus Reynolds and Froude numbers in rotating and nonrotating exponentially stratified fluid were obtained by Mason (1977)(2).

Experiments by Lofquist and Purtell (1984)(3) also conserned drag parameters study in a linearly stratified liquid. The increment in drag coefficient due to the stratification was obtained as a function of inverce Froude and Reynolds numbers. All of investiations were provided in the range of relativelly small "internal" Froude numbers ($Fi \leq 10$).

A limit of exerimental data is the reason of any correlation analysis absence for the drag coefficient as a function of Fi for different stratification cases. Nevertheless it seems to be useful to have such results as an inquiry information for various experimental and theoretical estimations.

2 Experiments

[1]E-mail: ols@appl.nnov.su

As a towed body for continuously stratified liquid a sphere was used. In the exponentially stratified fluid [3] the sphere of diameter $D = H/8$ was towed at the depth $H/2$ (H is the fluid depth). In the case of two - layered fluid [1] the ship model with the draught $R = (0.54 \div 3.0)H_1$ (H_1 is the upper layer thickness) has been used.

Drag measurements in homogeneous fluid have been fulfilled previously. The stratification presence caused respective variations in drag force values for each stratification profile. Drag coefficient values increase in comparison with those for homogeneous fluid in the range of Froude numbers $Fi \sim 1$ was explained by intensive internal waves generation.

Froude numbers were calculated in accordance with following eqations:

— for the two - layered model

$$Fi = U/Co \tag{1}$$

— for the continuous stratification

$$Fi = U/(N * 2R) \tag{2}$$

where

U	body's velocity;
Co	internal wave speed in the two - layered liquid of finite depth;
R	characteristic vertical body dimension ($= D/2$ for bodies of revolution);
N	the Brunt–Vaisala frequency ($N = N_{max}(z)$ for the thermocline).

$$N(z)_{max} = (-\frac{g}{\rho_o}\frac{d\rho}{dz})^{1/2}_{max} \tag{3}$$

where

g	acceleration due to gravity;
ρ_o	water density at the center of the thermocline;
$d\rho/dz$	density variation due to the temperature variation at the horizon.

3 Quantitative estimations of experimental results

Experimental results matching method was based on the dividing - streamline concept (Snyder et al. 1985[4]; Hanazaki 1988[5]) that all the kinetic energy of the stationary and potential (for $Fi \leq 0.5$) flow passing around submerged body in the hydrostatic limit is converted into potential energy of the vertically displaced fluid parcel.

It is necessary to point out that in the mentioned Froude number range the stratification influence on the flow regime is considerable. In particular, it manifests in prevalence of the plane motion in the fluid particles flow:

— vertical for fluid with the enough kinetic energy for overcoming of vertical forces caused by the vertical fluid density inhomogeneity, and

— horizontal for the fluid volume with the small energy resource.

Taking into account all above, the displacement of the interface in the two - layered fluid and the position of the streamline dividing pointed flow areas will be determined by respective energy ballace equations[4]:

— for the two – layered fluid

$$\frac{1}{2}\rho_1 U^2(z_s) = g\,\Delta\rho\,(z_s - H_1) \tag{4}$$

where

g	acceleration due to gravity;
U	velocity of the flow (in the inverse movement);
R	characteristic vertical body's dimension;
z_s	dividing streamline vertical coordinate;
H_1	the upper–layer thickness:
ρ_1	the upper–layer fluid density;
$\Delta\rho$	the fluid layers density difference.

— for continuously stratified fluids

$$\frac{1}{2}\rho(z_s)U^2(z_s) = g\int_{z_s}^{R}(R-z)(-\frac{d\rho}{dz})dz \tag{5}$$

where $d\rho/dz$ is a density gradient at the horizon.

Respective resulting dependences for the displacement amplitude $\Delta = R - z_s$ of the layers interface (two–layered fluid) and dividing streamline (continuous stratification) versus Froude number for flows of uniform velocity are:

— for the two – layered fluid

$$\Delta = 1/2 * H_1 * Fi^2 \tag{6}$$

— for the fluid with constant density gradient and for the thermocline, presented by an exponentially stratified layer placed between two homogeneous layers

$$\Delta = R * 2Fi \tag{7}$$

For wave – drag coefficients versus Froude number following dependences were obtained:

$$\Delta C_{exp}(Fi) = K * \Delta C_{double}(Fi) \tag{8}$$

$$\Delta C_{exp}(Fi) = \Delta C_{therm}(Fi) \tag{9}$$

With

$$Fi^2_{double} = K_1 * Fi_{exp} \tag{10}$$

$$Fi_{therm} = K_2 * Fi_{exp} \tag{11}$$

where K, K_1, K_2 are coefficients depended on the body's geometry and stratification parameters in the certain experiment.

Explanation of the dependence (10) and the value of coefficient K_1 follows from the comparison of Eqs. (6), (7) and the condition of relative displacements Δ/R and Δ/H_1 equality:

$$\frac{\Delta}{R} = \frac{\Delta}{H_1} = 2\,Fi_{exp} = 1/2\,Fi^2_{double} \tag{12}$$

$$K_1 = Fi^2_{double}/\,Fi_{exp} = 4 \tag{13}$$

K_1 values obtained from an experimental data comparison are in the range $3.88 \div 4.16$.

Results of adaptation of initial curves $\Delta Cx\,(Fi)$ for the two – layered fluid in accordance with Eqs. (9), (11) are presented in Figs. 1 *a*, *b* (cases when the ship model's draught is more and less than the upper layer thickness respectively).

The coefficient K_2 value in Eq. (11) has been defined taking into account the fact of similarity of *IW* propagation in continuously stratified fluids and equality of equations describing wave processes in one – waveguide systems. In particular, dispersion dependence for fluid with N = const and for the thermocline, modelling by the exponentially stratified layer contained between two homogeneous layers,

$$\omega^2 = N^2 \frac{k_n^2}{k_n^2 + k_{z\,n}^2} \tag{14}$$

where

ω	*IW* frequency;
N	the Brunt – Vaisala frequency;
k_n	n-mode horizontal wave-number;
$k_{z\,n} = \pi n/h'$	n-mode vertical wave–number;
h'	characteristic vertical waveguide dimension.

From Eq. (14) it follows an equation for dimensionless k_n.

$$(k_n\,h')^2 = \frac{1}{Fi^2{}_h} + (\pi\,n)^2 \tag{15}$$

where $Fi_h = Cp_n\,/\,N\,h'$.

As Froude numbers $Fi_h = Fi * 2R/h'$ are of order 10^{-2} for $Fi \leq 0.5$ it follows from Eq. (15) that $k_1 >> k_{z\,1}$. Eqs. (14) and (15) may be rewritten now

$$Cp_{1\,exp} = \frac{\omega}{k_1} \cong \frac{N}{k_1} \tag{16}$$

$$k_1 = \frac{1}{Fi_h * h'} = \frac{1}{Fi * 2R} \tag{17}$$

It seems to be natural to assume *the phase speed equality* to be the similarity condition for continuously stratified fluids $Cp_{1\,exp} = Cp_{1\,therm}$. Under this condition the Brunt – Vaisala frequency provided the similarity of $\Delta Cx(Fi)$ for continuously stratified fluids will be defined from Eqs. (16), (17) as follows

$$N_{exp} = Cp_{1\,therm}/(Fi_{exp} * 2R_{exp}) \tag{18}$$

In the comparison of experimentally obtained dependences $\Delta Cx(Fi)$ the particular value of N has been defined from Eq. (18) for the maximum values $\Delta Cx_{\max}(Fi)$. The obtained value of $N_{exp} = 2.73\ \ s^{-1}$ allowed to count the similarity coefficient of Fi for two stratification profiles

$$K_{Fi} = \frac{K_{Cp}}{K_N * K_R} \tag{19}$$

where

K_{Fi}	proportionality coefficient for Froude numbers;
$K_{Cp} = 1$	similarity coefficient for phase velocities;
K_N	similarity coefficient for Brunt–Vaisala frequencies;
K_R	geometric similarity coefficient.

The theoretically obtained value of $K_{Fi} = Fi_{therm}/Fi_{exp} = 3.73$ equals to the result of experimental data adaptation. Curves of $\Delta Cx(\,Fi\,)_{exp}$ and $\Delta Cx(\,Fi\,)_{therm}$ where Fi_{therm} is transformed in accordance with Eq. (18), are presented in Fig. 2.

To explain the presence and relative position of nonmonotonicity regions in both curves ($Fi_{exp} = 0.5, Fi_{therm} = 0.4$) we can use the diagram of wake regimes past a sphere moving in the exponentially stratified fluid (Lin et al. [6]) (Fig. 3) .

It's obvious that the region of lee IW existence is limited from above by the Froude number $Fi = 0.4$ (with the transitional zone at $Fi = 0.4 \div 0.5$) in the Reynolds number range $Re = 200 \div 2000$. This is the reason of the wave–drag coefficient insensitivity from Re for $Fi \leq 0.5$ ($Fi \leq 1.0$ in their definition) noted by Lofquist & Purtell[3] (corresponding characteristics are shown in Fig. 3 by dashed lines).

Characteristic line for the Brunt–Vaisala frequency $N = 2.73\ s^{-1}$ obtained under the condition of similarity of $\Delta Cx(\,Fi\,)$ is shifted to the diagram region where position of lee waves upper boundary becomes sensitive to Re. Comparing the nonmonotonicity regions position (points no. $4 \div 6$ in Fig. 3) we can find that their presence and relative position are connected with the change of IW generation regime by attached vortex production.

4 Conclusions

Summarizing experimental results we can conclude that a phenomenon of the drag coefficient increase for Froude numbers $Fi \leq 0.5$ obviously has wave nature.

The *similarity* of wave processes accompanying the sphere movement in stratified flows with one – wavequide profiles as well as characterictics describing those processes

was observed. It was also found out that values of drag coefficient increment due to stratification (named wave-drag coefficient) ΔCx are the same for continuously stratified liquids.

The values of ΔCx for exponential and two – layered stratifications are proportional.

Comparison of $\Delta Cx(Fi)$ dependences for variously stratified fluids showed also an existence of linear dependence of Froude numbers Fi for continuously stratified one–waveguide fluids and square dependence between Fi for the two – layered liquid and an exponential stratification.

Appendix

Eq. (7) allows to explain the phenomenon observed by Chashechkin & Sysoeva (1988)[6] and by Chomas et al. (1992)[7] – a square shape of the wake just behind the sphere in the linearly stratified flow when $Fi_R = 2Fi \cong 0.3$.

The vertical coordinate z_s of the dividing streamline provides also the position of horisontal separation line on the sphere (as the fluid particle returns to its equilibrium level after flowing over the sphere). In this case the vertical coordinate of the horizontal separation line

$$z_s = R - \Delta = R(1 - Fi_R) = 0.7R = R * sin\,45^0$$

Thus, two horizontal separation lines and vertical lines with the separation angle close to 90^0 form almost square shape of the separation curve which provides, in its turn, the shape of the nearest wake.

The latter expression is also valid for horizontal separation line coordinate for flow regimes with $Fi_R \leq 1$ $(\Delta \leq R)$.

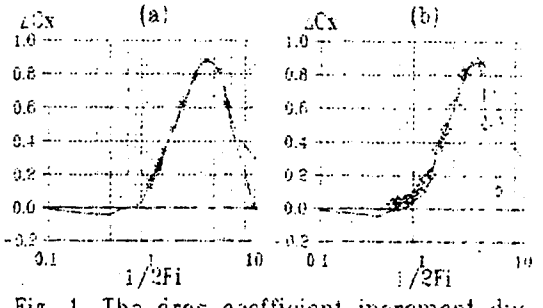

Fig. 1. The drag coefficient increment due to stratification versus inverse Froude number:
—— linear stratification Lofquist & Purtell (1984).
two-layered fluid Nikitina (1959):
***** (a) H1/R = 0.79.
○○○○○ (b) H1/R = 1.32.

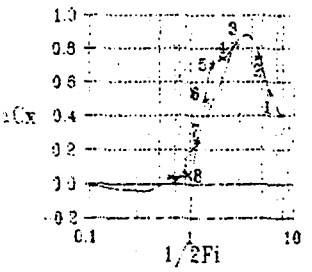

Fig. 2. The drag coefficient increment due to stratification versus inverse Froude number: ——— linear stratification Lofquist & Purtell (1984), ***** thermocline Bogatyrjov & Shishkina (1990).

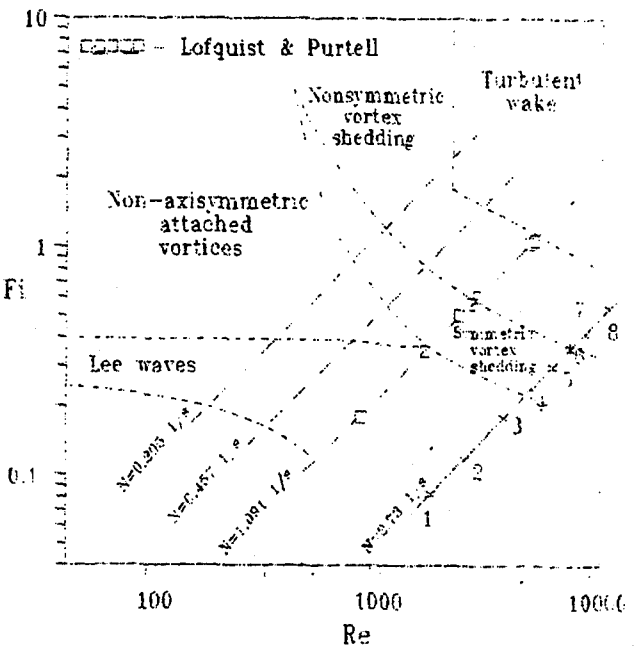

Fig. 3
The diagram of wake processes past a sphere in an exponentially stratified fluid [6].

References

1. Nikitina, H. A. 1959: Drag of the ships in a "dead water". *Izvestiya akademii nauk, OTN, Mechanika i machinostroyeniye*. 1, 188-192 (in Russian).

2. Mason, P.J. 1977: Forces on spheres moving horizontally in rotating stratified fluid. *Geophys. Astrophys. Fluid Dyn.* 8, 137-154.

3. Lofquist, K. E. B.; Purtell, L. P. 1984: Drag on a sphere moving horizontally through a stratified liquid. *J. Fluid Mech.* 148, 271-284.

4. Snyder, W.H.; Thompson, R.S.; Eskridge, R.E. 1985: The structure of strongly stratified flow over hills: dividing-streamline concept. *J. Fluid Mech.* 152, 249-288.

5. Hanazaki, H. 1988: A numerical study of three-dimensional stratified flow past a sphere. *J. Fluid Mech.* 192, 393-419.

6. Lin Q.; Lindberg W.; Boyer D. L.; Fernando H. J. S. 1992: Stratified flow past a sphere. *J. Fluid Mech.* 240, 315-354.

7. Sysoeva E. Y.; Chashechkin Yu. D. 1988: The space structure of the wake past a sphere in a stratified liquid. *J. Appl. Mech. Techn. Phys.* 5, 59-65.

8. Chomas J. M.; Bonneton P.; Butet A.; Perrier M.; Hopfinger E.J. 1992: Froude number dependence of the flow separation line on a sphere towed in a stratified fluid. *Phys. Fluids A*, 4 (2), 254-258.

RESONANT GENERATION OF SOLITARY WAVE IN THE THERMOCLINE

SHISHKINA O.D.
Institute of Applied Physics, Russian Academy of Sciences
Nizhny Novgorod, Russia [1]

Abstract

Process of resonant generation of second mode internal solitary waves as a result of ship internal waves system damping in the thermocline is studied experimentally. As a source of the stationary internal waves an oblong ellipsoid of revolution towed horizontally and uniformly at the depth of the thermocline center was used. The Reynolds and the Froude numbers range provided were $5000 \leq Re \leq 15000$ and $0.3 \leq Fi \leq 1.0$ respectively. In the case of the body's speed and the linear long-wave second mode phase speed equality the internal second mode solitary wave was observed. The wave's profile shape satisfied the Korteweg–de Vries (KdV) equation solution. The speed of the wave increased slightly linear long – wave second mode phase speed. Urcell parameter was equal to 9.2.

List of symbols

L, B, H	the towing tank length, breadth and height respectively
z	vertical coordinate
D	characteristic vertical dimension of the body (maximum ellipsoid diameter $D = 2a$)
a	minor semiaxis of ellipsoid
b	major semiaxis of ellipsoid
l	length of the body $(= 2b)$
U	velocity of the body
ν	kinematic viscosity
t	temperature
g	acceleration due to gravity
ρ_i	fresh water density for temperature at i-th horizon
$\rho_4 o$	fresh water density for temperature $t = 4°C$
ρ_o	water density at the center of the thermocline
$\Delta\rho_i$	density variation due to the temperature variation at the i-th horizon
N	Brunt-Vaisala frequency
$N_{\max}$	maximum value of Brunt-Vaisala frequency
Re	Reynolds number $(= U * l/\nu)$

[1]E-mail: ols@appl.nnov.su

Fi	"internal" Froude number $(= U/N_{\max}D)$
σ	conventional density
f_n	n–th mode boundary-value problem eigenfunction
ω_n	n–th mode frequency
k_n	n–th mode horizontal wavenumber
λ_n	n–th mode wavelength $(= 2\pi/k_n)$
C_n	limiting speed of a linear n–th mode internal wave $(= \omega_n/k_n;\ k_n \to 0)$
Ur	Urcell parameter
Δ	half-length of the solitary wave
η_0	solitary wave amplitude

1 Introduction

Experimental investigation of long internal waves of finite amplitude formation from initial disturbances of different nature in variously stratified fluids have been studying earlier.

One of the first papers dealing with mentioned problem was the work by Davis & Acrivos (1967)[1]. One of the most interesting phenomenon they observed is so called "*algebraic*" second–mode soliton resulting various initial disturbances. The results of an experimental investigation dealing with finite–amplitude internal solitary waves in a two– fluid system are presented in papers by Koop & Butler (1981)[2], Segur and Hammack (1982)[3]. Interfacial disturbances were generated using a displacement-type wavemaker. A study of the internal KdV solitary wave on the pycnocline of a continuously stratified fluid with the initial disturbance condition as a step-like pool of light water was fulfilled by Kao, Pan & Renouard (1985)[4]. Nonlinear dispersive waves produced by the region of mixed fluid in continuously stratified liquid with a pycnocline (Kao & Pao 1980[5], Maxworthy 1980[6]). Observation of experimental study of internal gravity, in particular, solitary waves produced by motion of a self-propelled model in stratified fluid was presented by Gilreath & Brandt (1985)[7].

Theoretical models of nonlinear internal wave propagation including the model evolution equations and their soliton solutions were discussed by Ostrovsky & Stepanyants (1987)[8]. Grimshaw & Smyth (1986)[9], Grimshaw & Zengxin (1991)[10] considered the flow of uniformly stratified fluid over topography in the long-wavelength weakly nonlinear limit for the case when the flow speed is close to a linear long-wave phase speed for one of the long-wave modes (flow is near resonance). The amplitude of this mode was governed by a forced KdV equation.

Observations of nonlinear transformations of internal waves trains shapes observed at the sea shelf were discussed by Serebryanyi (1990)[11].

In the present paper an intermediate case of mentioned above experimental and theoretical conditions is presented: dispersive wave train propagation and resonant generation of internal waves by a solid body. After the ship internal waves system formation the body was stopped and further waves propagation depended on stratification parameters only. The body's speed is close to a linear long–wave phase speed of the second mode (resonance case). This way helps to find out the presence of nonlinearity in the ship internal waves system, from one side, and to test nonlinear parameters of stratification, from the other side.

2 Experimental apparatus and procedures

Experiments have been fulfilled in a thermostratified laboratory tank 1.6 m wide, 1.2 m deep and 5 m long. Horizontally homogeneous thermocline–type stratification, provided in the fresh water, presented a scale model of the ocean thermocline. The thermocline of a thickness $d = 0.17\,H$ has its center's depth $h = 0.33\,H$.

For measurements of a stable temperature profile $t = t(z)$ and for indication of temperature variations in the point of the water volume a number of thermistors are applicated as the input data source. For the space temperature field investigations 16 similar thermistors can be applicated simultaneously. Each of them can be installed in any point of the basin's volume. The induced internal waves field has been studing with two vertical garlands of thermistors (four thermistors in each garland) placed at the depths of sufficient temperature gradients (in the thermocline zone). Experimentally obtained temperature variations in the point has been counted over to internal waves amplitude characteristics in accordance with the tempertature gradient at the corresponding horizon.

A temperature t, a conventional density σ and a Brunt– Vaisala frequency N versus vertical coordinate z are represented in Fig.1 (the body's position is shown by a shaded hemicircle). The temperature profile is obtained by temperature scanning in the undisturbed liquid. Conventional density and Brunt–Vaisala frequency are counted numerically:

$$\sigma_i = ((\rho_i/\rho_4 o) - 1) * 10^3 \tag{1}$$

$$N_i = (-\frac{g}{\rho_o}\frac{\Delta\rho_i}{\Delta z})^{1/2} \tag{2}$$

where

i is a counting level number,

Δz is a counting step (0.005 m).

During all the experiments the Brunt-Vaisala maximum value (in the center of the thermocline) varied in the range $N_{max}(z) = 0.30 \pm 0.02\ sec^{-1}$ for $z = 0.31 \pm 0.01\ m$ while the thermocline thickness being determined by the basin's design remained constant.

Bodies towing is provided by monorail system which consists of driving variable-speed electric motor, double-reduction gear, driving drum, rail installed in the middle plane of the tank, towing carriage and infinite rope connected the carriage with the drum. A linear velocity value is calculated according to the measured frequency, gear ratio and diameter of the drum. Velocity range provided is $U = 0.01 \div 0.50\ m/s$.

As a source of internal waves an oblong ellipsoid of revolution with the axial ratio a : $b = 1 : 3$ ($D = 2a = 0.15\ m$) was chosen to eliminate the wake turbulence influence for covered Reynolds number range. An ellipsoid was moved at a depth h with different constant velocities provided the Reynolds number range $5000 \leq Re = U * l/\nu \leq 15000$ and internal Froude number range $0.3 \leq Fi = U/D\,N_{max} \leq 1.0$. The body's dimensions and stratification parameters provided induced internal waves slope of about $\eta_0/\lambda \cong 0.01$. After

the ship internal waves system became stationary the body was stopped and further waves propagation depended on stratification parameters only.

3 Experimental results

The mode structure of internal waves field has been calculated as the solution of Shturm–Liouvill boundary-value problem in the long-wave limit ($kH << 1$) according to Brunt-Vaisala frequency profile $N = N(z)$:

$$\frac{d}{dz}\left(\rho(z)\frac{df_n}{dz}\right) + \rho(z)\frac{N^2(z)}{C_n^2}f_n = 0 \tag{3}$$

$$f_n(0) = f_n(H) = 0$$

These data were used to obtain the modes phase speed values and coefficients of nonlinearity α and dispersion β for KdV equation for plane long waves propagation in the nonlinear and dispersive medium

$$\frac{\partial\eta}{\partial t} + C_n\frac{\partial\eta}{\partial x} + \alpha_n * \eta\frac{\partial\eta}{\partial x} + \beta_n\frac{\partial^3\eta}{\partial x^3} = 0 \tag{4}$$

where

$\eta(x,t)$ wave profile coordinate
α_n n–th mode nonlinearity coefficient
β_n n–th mode dispersion coefficient

$$\alpha_n = \frac{3}{2}C_n\frac{\int_{-H}^{0}\rho(z)(f_n')^3dz}{\int_{-H}^{0}\rho(z)(f_n')^2dz} \tag{5}$$

$$\beta_n = \frac{3}{2}C_n\frac{\int_{-H}^{0}\rho(z)f_n{}^2dz}{\int_{-H}^{0}\rho(z)(f_n')^2dz} \tag{6}$$

Quantitative estimations showed that $\alpha : \beta$ ratio being an indicator of soliton solution existence of the KdV equation for the specific wave shape for the II$-nd$ mode was two order greater than for the I$-st$ mode and one order greater than for the III$-rd$ mode.

Experimetal fact was that when the body's speed was equal to the maximum second mode phase speed the first nondispersive wave of the ship internal waves system has been propagating further without its profile variation while the dispersive wave trane inside damped (see Fig.2).

The speed of this wave increased slightly maximum linear II$-nd$ mode phase speed. The presence of the second mode (bulge-type) fluid motion is confirmed by temperature variation oscillograms made by the vertical garland of four thermistors placed in the thermocline in the far end of the tank (see Fig.3).

Urcell parameter

$$Ur = \alpha_{II} * \eta_0 * \Delta^2/\beta_{II} \tag{7}$$

(where Δ is half-length of the solitary wave, η_0 is the solitary wave amplitude) in this case has the value of 9.2. The solitary wave profile satisfied the KdV equation solution (see Fig.4). Dispersive waves shape was rather similar to this for internal waves propagating at the shelf (Serebryanyi 1990).

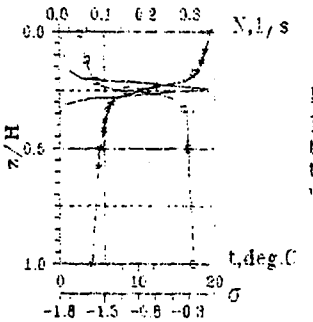

Fig. 1.
The Brunt-Vaisala frequency (——), the water temperature and (—·—·—) the conventional density (– – – –) versus basin's depth.

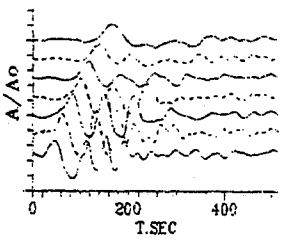

Fig. 2.
Internal wave train evolution (oscillograms of the temperature variations in eight points along the tank at a depth 0.22H (lower curve corresponds to the body's stop moment).

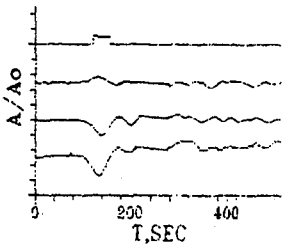

Fig. 3.
Oscillograms of the isotherms displacement at the depths 0.18H, 0.22H, 0.26H, 0.30H (from upper to lower).

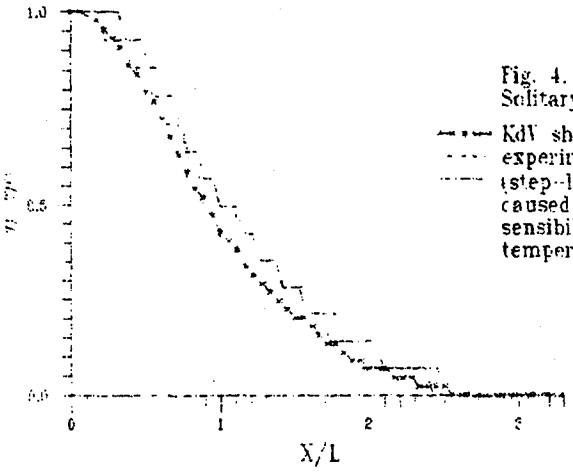

Fig. 4.
Solitary wave shape:
KdV shape;
experimental samples
(step-like curves are
caused by the finite
sensibility of the
temperature sensors).

References

1. Davis, R. E.; Acrivos, A. 1967: Solitary internal waves in fluid flows. *J. Fluid Mech.* 29, 593-607.

2. Koop, C. G.; Butler, G. 1981: An investigation of internal solitary waves in a two-fluid system. *J. Fluid Mech.* 112, 225-2512.

3. Segur, H.; Hammack, J. L. 1982:Soliton models of long internal waves. *J. Fluid Mech.* 118, 285-304.

4. Kao, T. W.; Pan, F.-S.; Renouard, D. 1985: Internal solitons on the pycnocline. *J. Fluid Mech.* 159, 19-53.

5. Kao, T. W.; Pao, H.-P. 1980: Wake collapse in the thermocline and internal solitary waves. *J. Fluid Mech.* 97, 115-127.

6. Maxworthy, T. 1980: On the formation of nonlinear internal waves from the gravitational collapse of mixed regions in two and three dimensions. *J. Fluid Mech.* 96, 47-64.

7. Gilreath, H. E.; Brandt, A. 1985: Experiments on the generation of internal waves in a stratified fluid. *AIAA J.*, 23 , 693-700.

8. Ostrovsky, L.; Stepanyants, Yu. 1987: Internal solitary waves in the ocean: theory and observations. In: *Methods of hydrophysical research. Waves and vortices.* Gorky. Inst. Appl. Phys. USSR Acad. Sci., 18-47 (in Russian).

9. Grimshaw, R. H. J.; Smyth, N. 1986: Resonant flow of a stratified fluid over topography. *J. Fluid Mech.* 169, 429-464.

10. Grimshaw, R.H.J.; Zengxin, Yi. 1991: Resonant generation of finite – amplitude waves by the flow of a uniformly stratified fluid over topography. *J. Fluid Mech.* 229, 603-628.

11. Serebryanyi, A. N. 1990: Internal waves effects of nonlinearity at the shelf. *Izvestiya Academii Nauk. Phyzika atmosphery i okeana.* 26, 285-293 (in Russian).

EXPERIMENTAL STUDY OF DRAG ON A SUBMERGED SPHERE MOVING HORIZONTALLY IN THE THERMOCLINE

SHISHKINA O.D.
Institute of Applied Physics, Russian Academy of Sciences
Nizhny Novgorod, (Russia) [1]

Abstract

Results of experimental study of the thermocline stratification influence on drag parameters of horizontally and uniformly driven sphere are represented. The sphere of a diameter D of about thermocline thickness was towed at a depth of the thermocline center. The Reynolds and the Froude number ranges were respectively $1.6 * 10^3 \leq Re = U * D/\nu \leq 1.1 * 10^4$ and $0.3 \leq Fi = U/D * N_{max} \leq 2.0$. The mode structure of the lee - wave field analysis showed that the number of internal waves modes induced by the sphere increased while the sphere's speed has increase and became equal to the maximum phase velocity of each of the three lowest modes. Maximum increase of the drag coefficient value (of about three times compared to this for a homogeneous fluid) was obtained for regimes of the first mode effective generation.

1 Introduction

The effect of fluid stratification on dynamics, in particular, on drag coefficient Cx , of a submerged sphere moving uniformly and horizontally in the linearly stratified fluid has been investigated both theoretically and experimentally.

Research of Hanazaki (1988)[(1)] is devoted to numerical studies of the relationship between Cx and the parameters of three-dimensional flow of viscous incompressible exponentially stratified fluid. Calculations were performed for the constant Reynolds number $Re = 200$ and yielded the results close to the experimental ones for mentioned conditions.

Two papers are available now (Mason 1977[(2)]; Lofquist and Purtell 1984[(3)]) dealing with experimental dependences of the coefficient Cx on the Froude number for a sphere moving in an exponentially stratified fluid, as well as of its variations ΔCx relatively to the value Cx_0 corresponding to a uniform fluid.

Fluids with more complicated stratification profiles were not treated experimentally from this viewpoint.

2 Experimental equipment

The aim of this experiment was to confirm and evaluate the influence of thermocline–wise stratification on the drag force and the drag coefficient of a submerged solid sphere.

All the experiments have been fulfilled in a thermostratified laboratory tank 1.6 m wide, 1.2 m deep and 5 m long. Horizontally homogeneous thermocline–type thermal

[1]E-mail: ols@appl.nnov.su

stratification, provided in the fresh water, presented a scale model of the ocean thermocline. To prevent heat transfer through the tank walls and bottom made of carbon steel 3 mm thick, all the tank surface is thermally insulated with raised dusted foam polyurethane 25 mm thick (inside the tank) and with plate foam plastic 60 mm thick (outer surface).

Stratification making system consists of a refrigerating machine connected with heat exchangers made of duraluminium finned tubes arranged horizontally along the tank walls inside the tank. Lower heat exchangers with the height $2/3\,H$ (H is the tank's depth) and the refrigerating machine evaporator form the cooling contour. It provides the lower water layers temperature of about $4 \div 6°C$. Refrigerator's condenser, washed by water from upper heat exchangers with the height $1/3\,H$ forms with them an another contour, heating upper layers to the temperature of $18 \div 20°C$. Thus, all the installation acts as a heat pump. As a result of the system's action and due to natural convection in heated and cooled water layers a scale model of natural ocean thermocline is provided in the tank. The thermocline of a thickness $D = 0.17\,H$ has its center's depth $h = 0.33\,H$.

Usually it takes about $8 \div 9$ hours to "boil" a stratification in the homogeneous liquid with the temperature $t = 10°C$ and $3 \div 4$ hours to restore it night later.

We investigated a body with hydrodynamic characteristics thoroughly studied before. A sphere of diameter $D = 150\ mm$ was towed with constant velocities $U = 0.014 \div 0.09\ m/s$ at the depth of about the thermocline centre $h = 0.32\ m \cong 2D$, which excluded free surface effect. The Reynolds and Froude numbers varied in the ranges $1.6 * 10^3 \leq Re = U * D/\nu \leq 1.1 * 10^4$ and $0.3 \leq Fi = U/D * N_{max} \leq 2.0$. respectively.

$$Re = U * D/\nu \tag{1}$$

where ν is fresh water kinematic viscosity coefficient for the temperature $12°C$(water temperature in the center of the thermocline).

$$Fi = U/D * N_{max} \tag{2}$$

where $N = N_{max}(z)$ - maximum value of the Brunt-Vaisala frequency.

$$N_i = (-\frac{g}{\rho_o}\frac{\Delta\rho_i}{\Delta z_i})^{1/2} \tag{3}$$

where

g acceleration due to gravity;

ρ_o water density at the center of the thermocline;

$d\rho_i/dz_i$ density variation due to the temperature variation at the i-th horizon.

During the experiment the maximum buoyancy frequency $N_{max}(z)$ was kept equal to $0.30 \pm 0.02\ rad/s$ at the depth $z = 0.31 \pm 0.01\ m$.

The body was towed by means of a monorail d.c. motor–operated towing system provided with double–reduction gear, driving drum and infinite rope which connects towing carriage to the drum. The motor rotation frequency was measured with a tachometer.

The drag force was measured using a towing dynamometer shown schematically in Fig. 1. The dynamometer is a two–armed lever with arms ratio $L_1 : L_2 = 20.9$. The

longer arm is formed by towing knife (1) having a cross-section in the form of the wing profile. The rotation axis of the lever is attached fixedly to the towing carriage normally to the trajectory of the towed body motion. The drag force was transferred from the towed body to elastic element (2), which deformation caused variations of electric signal value. A differential inductive sensor (3) with fixed coils and a core connected to the elastic element, was used as an energy transducer.

The range of measured forces was not limited from above. The lower limit depended on threshold sensitivity of the dynamometer. In our case it was $0.05\,g(f)$ for sensitivity of the dynamometer equal to $19\,\mu A/g(f)$.

It is clear from the above description of the towing device that the dynamometer with a sphere fixed on it is a pendulum system with natural frequency of oscillations initiated at the onset of the towing carriage motion.

A damping system consisted of a vessel filled with machine oil, mounted on the towing carriage, and a damper made of vertical plates with staggered holes, submerged in oil. The damper was attached fixedly to the towing knife . Deviation of the knife from vertical causes displacements of damper plates in the vessel and slow leakage of oil through a labyrinth of holes. Thus, oscillations of the towing knife were changed by smooth deviation from vertical at an angle proportional to the drag force of sphere motion. After the sphere motion becomes stationary, the damping system does not affect the dynamometer operation.

After the sphere was moved, the designed velocity was achieved following tachometer indications. In the case of stationary motion indications of microammeter connected to the electric circuit of an inductive sensor were read.

Induced internal waves damping was measured by a temperature sensor placed at the thermocline centre horizon.

The vertical temperature profile has been recorded before every towing motion and the Brunt-Vaisala frequency $N = f(z)$ was calculated according to Eq. (3).

3 Experimental results

In accordance with experiments, fluid stratification results in change of the drag force and the drag coefficient of a submerged body compared to the corresponding values for a uniform fluid.

The drag force versus the sphere motion velocity $Rx = f(U)$ (is plotted in Fig. 2) in the presence of sharp thermocline stratification, which yields appropriate values of the drag coefficient

$$Cx = \frac{2Rx}{\rho_o * U^2 * S} \tag{4}$$

where

Rx the measured drag force;
ρ_o the water density at the thermocline centre horizon;
U the towing velocity;
$S = \pi D^2/4$ the body's cross–section.

$$\Delta Cx = Cx - Cx_o, \tag{5}$$

where Cx_o is the drag coefficient of a sphere in the homogeneous liquid.

Maximum (threefold) increase of the towing drag coefficient is observed at values of the Froude number $Fi = 0.58$ ($U = 0.026\ m/s$) (see Fig. 3). Investigations of body generated internal waves (IW) have demonstrated that this increase is caused by their intense generation ($U \div Cp_i$, where Cp_i is the phase velocity of the first three *IW* modes, $i = 1,3$).

Parameters of these *IW* analyzed simultaneously with drag measurements evidence that while velocities of body motion increase in the range mentioned above, the number of modes excited by the body increases. The drag coefficient increases with the number of modes and has a maximum value for Cp_1. Therefore, of appreciable importance is the first mode which is also confirmed by comparing data of mode *IW* analysis with the dependence of ΔCx versus Fi (see Fig. 4).

4 Conclusions

Summarizing experimental results we can conclude that a phenomenon of the drag coefficient increase for the Froude numbers $Fi \sim 1$ obviously has wave nature. The structure of the induced *IW* system produced by the uniformly driven sphere is a superposition of certain modes according to the correlation of the body's and *IW* mode maximum phase velosities. The first mode *IW* provides decisive effect on the drag parameters of the sphere.

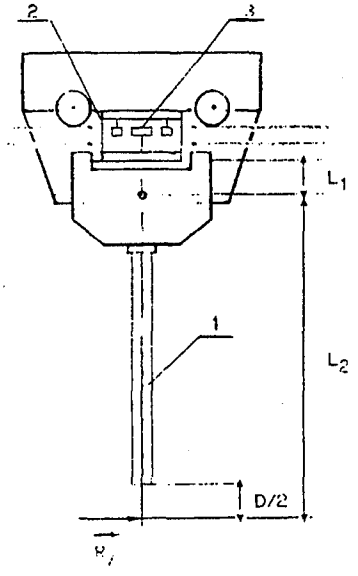

Fig. 1.
A towing system.

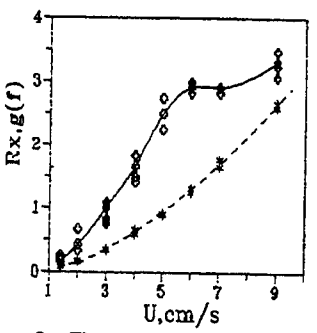

Fig. 2. The drag force value versus body's speed:
***** homogeneous fluid,
◇◇◇◇◇ stratified fluid.

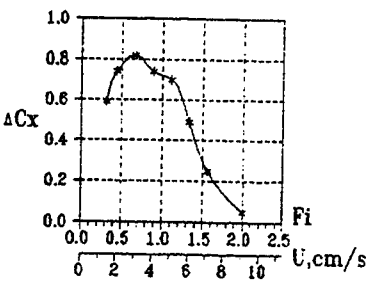

Fig. 3. The drag coefficient increment versus internal Froude number and the sphere's velocity.

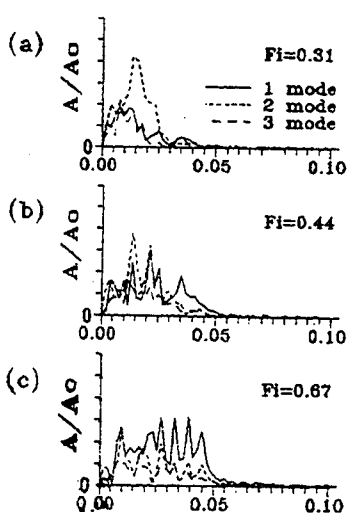

Fig. 4. FW modes spectra (sphere in the thermocline).

References

1. Hanazaki, H. 1988: A numerical study of three-dimensional stratified flow past a sphere. J. Fluid Mech. 192, 393-419

2. Mason, P.J. 1977: Forces on spheres moving horizontally in rotating stratified fluid. Geophys. Astrophys. Fluid Dyn. 8, 137-154

3. Lofquist, K. E. B.; Purtell, L. P. 1984: Drag on a sphere moving horizontally through a stratified liquid. J. Fluid Mech. 148, 271-284

NON-LOCALIZED ACOUSTIC RECEPTIVITY OF LAMINAR BOUNDARY LAYERS

Illinois Institute of Technology
Chicago, IL
USA

M. WIEGEL
DLR Göttingen, Bunsenstraße 10, 37073 Göttingen (Germany)
R. W. WLEZIEN
High Technology Corporation, NASA Langley Research Center, Mail Stop 163
Hampton, VA 23665-5225 (USA)

ABSTRACT

Acoustic receptivity of laminar boundary layers over surfaces with non-localized low-amplitude (40 μm) periodic waviness is experimentally investigated. An array of two-dimensional strips is used to simulate continuous wall waviness. Particular attention to measurement techniques is required to minimize facility-dependent flow and acoustic field anomalies. Balanced arrays of acoustic sources upstream and downstream of the test section are used to generate a travelling acoustic mode, effectively eliminating the standing modes that would distort the results of continuous receptivity measurements. Hot-wire measurements of Tollmien-Schlichting (T-S) mode shapes are shown to be in excellent agreement with theory. By increasing the number of wall wavelengths, it is demonstrated that an effectively infinite wavy wall can be produced by a small wavy-wall region near lower branch. It is also shown that the ratio between receptivity at distributed waviness and at localized surface inhomogeneities is of O(10). The effect of mismatching the T-S wavelength with the geometric wall wavelength is investigated by changing the free stream velocity at a constant forcing frequency. Strong receptivity occurs only over a narrow band where the wall wavelength and the T-S wavelength are matched. The results of this experiment are shown to match trends as well as absolute amplitudes predicted by receptivity theory.

1. INTRODUCTION

The process of transition in boundary layers can roughly be divided into three stages: receptivity to external disturbances followed by exponential growth (typically predicted by linear theory) and finally (if a sufficient amplitude is achieved) nonlinear breakdown through secondary instabilities. A conventional approach to predicting boundary-layer transition is the determination of the location at which the boundary layer becomes linearly unstable to spatially and/or temporally growing instabilities. When the total amplification of a range of disturbance frequencies exceeds a threshold level (typically e^N) transition is said to occur. Inaccuracies in these methods can be attributed to the inability to predict initial disturbance amplitudes, secondary instabilities, three dimensional modes, and interaction among modes. More recent numerical approaches (such as the parabolized stability equations, PSE) can account for the linear and nonlinear growth of disturbances in boundary layers, but the initial disturbance levels must still be known. Receptivity thus plays a crucial role in the refinement of transition prediction techniques.

In their classic experiments, Schubauer and Skramstad[1] determined that propagating T-S waves can be excited by external oscillating fields, and that transition is strongly influenced by the freestream disturbance environment. Receptivity (a concept first introduced by Morkovin[2]) is the process by which external disturbances couple with the boundary layer and create the initial amplitude of an instability mode. Receptivity experiments are usually much more difficult to configure and control than stability experiments, and can produce ambiguous results that are inconclusive and confusing (see Nishioka and Morkovin[3] for a discussion of these issues). Extreme care must therefore be exercised in performing experiments, preferably with theoretical guidance to properly focus the experimental effort.

Localized coupling with sound at a surface inhomogeneity was demonstrated by Aizin and Polyakov[4] using a 34-μm-thick Mylar strip. Their experiment (summarized in Nishioka and Morkovin[3]) showed convincing evidence of acoustic receptivity at low-amplitude two-dimensional roughness. Their results were first explained by the theory developed by Goldstein[5] and Ruban[6], which described the rescaling

process from the acoustic field to the two-orders-of-magnitude smaller T-S instability wavelength. The unsteady field produced by acoustic scattering at a local surface inhomogeneity, inherits its temporal scale from the freestream disturbance and its spatial scale from the sum and difference wave-number interaction between the acoustic field and the surface inhomogeneities. Thus the acoustic disturbance field acquires a Fourier spectrum that overlaps with that of the boundary-layer instabilities. Localized receptivity theory is addressed extensively in References 7 – 9.

Experimental measurement of acoustic receptivity is complicated by the high sensitivity to external conditions and the low T-S amplitudes in the vicinity of receptivity sites. Experiments by Wlezien et al.[10] addressed acoustic receptivity at the leading edge and at a porous strip. These results illustrate the difficulty inherent in distinguishing among various receptivity paths. It is therefore of critical importance to minimize (or fully characterize) extraneous receptivity paths. The two-dimensional roughness receptivity measurements of Saric et al.[11] take advantage of T-S amplification in the boundary layer to produce greater response at the upper-branch measurement location. These results show excellent agreement with those of Crouch[8] and the finite Reynolds number extension of the Goldstein-Ruban theory of Choudhari and Streett[9].

In general, the receptivity mechanism at distributed inhomogeneities is similar to that for localized roughness if one considers the total receptivity to be the sum of contributions from a series of infinitesimal subdomains. The general approach to an arbitrary nonlocalized roughness distribution is provided by Choudhari[12]. Receptivity over periodic two-dimensional wall roughness is addressed by Choudhari[13] and Crouch[14]. Crouch and Bertolotti[15] extend these results using parabolized stability equations that include the effects of boundary-layer non-parallelism and show that the non-parallel effects are only significant for three-dimensional disturbances. Bertolotti and Crouch[16] also found the transition location to be highly sensitive to the amplitudes of both the acoustic disturbance and the surface waviness.

The objective of this study is to provide experimental data on acoustic receptivity over two-dimensional periodic surfaces to validate the theory of Choudhari[13] and Crouch[14]. Acoustic receptivity is directly measured, and the influence of the streamwise extent of roughness and wavelength detuning are verified. The experiment is specifically designed to generate data that can be directly related to theory, both in terms of trends and absolute amplitudes.

2. EXPERIMENTAL CONFIGURATION

2.1 Facility and Apparatus

The experimental measurements were conducted in the 5.9 m long test section of the Mark V. Morkovin Wind Tunnel at IIT. The wind tunnel is closed-return with a turbulence intensity (u'/U_∞) of less than 0.1% in the test-section freestream for flow speeds up to 35 m/s.

The boundary layer plate was a 12.7-mm thick by 2.9 m long and 0.61 m wide aluminum jig plate with polished surface. Schematics of the test section and the flat plate model are shown in Figures 1 and 2, respectively. The leading edge had an elliptic profile with a ratio of major to minor axes of 24:1, which is sufficient to reduce leading-edge receptivity when plane wave acoustic excitation is used (Wlezien et al.[10]). The stagnation line on the leading edge was adjusted using a variable-angle flap at the trailing edge of the plate. Smoke visualization verified that attachment always occurred on the upper surface of the leading edge. Mean velocity measurements established the transition Reynolds number (Re_{tr}) (an important parameter in the assessment of flow quality) to be near 2.7×10^6.

The low-amplitude wall waviness was produced using 40-μm-thick polyester tape. The initial strip was attached across the span of the plate near lower branch of the neutral stability curve. This is a critical location because the greatest effective receptivity is predicted to be at this location. Additional strips were attached alternately upstream and downstream of the first strip, up to a total of 13 strips (see Figure 2). All strips were equally spaced by the tape width of 25.4 mm. This arrangement nominally produces a square-wave on the plate surface, the first Fourier component of which has a wavelength of 50.8 mm. If the wall-wavelength is tuned to the T-S wavelength, theory shows that higher harmonics introduced by the square shape of the strips are strongly detuned from the range of the growing T-S waves. This detuning of higher harmonics made it possible to simulate a sinusoidal surface waviness with discrete strips.

The range of parameters for a receptivity experiment is bounded by several limits which must be considered in the design of the experiment. The optimal acoustic forcing frequency (f) (limited to those below which transverse tunnel modes are cut off) was 80 Hz.

Several issues must be considered in the choice of strip height. First the height of the strips must be below the critical roughness height for hydraulically smooth surfaces, which is roughly 190 μm for U_∞=12 m/s. The height must also be sufficiently small to preclude flow separation, which would introduce other receptivity mechanisms. A nonlinear triple-deck analysis sets the limiting height to 120 μm for the present experiment, which is substantially greater than the tape height of 40 μm.

The acoustic field was generated by two sets of speakers driven by phase-locked function generators. The upstream set consisted of four speakers arranged in a square pattern (Figure 1). The speakers were mounted flush with the inside tunnel surface through holes. The speaker array was located in the outer wall of the tunnel leg upstream of the last turn before the test section. This arrangement allowed the speakers to be aligned in a single plane normal to the test-section flow direction while producing negligible flow disturbance. The second source was a single speaker mounted in the outer wall of the leg downstream of the diffuser. Two function generators were phase-locked to drive both sets of speakers at the same frequency with a specified phase shift.

2.2 Measurement Techniques

Mean and fluctuating velocities were measured by a single hot-wire sensor on a two-axis traversing system and converted to velocity using a fourth-order polynomial and temperature compensation. The two-dimensional computer-controlled traversing mechanism allowed precise positioning and movement of the probes in streamwise (x) and normal (y) directions with a vertical resolution of 0.013 mm. Freestream velocity was measured using a pitot probe and pressure transducer. The zero offset of the pressure transducer was regularly measured to maximize measurement accuracy. Velocity, temperature, and pressure data were directly digitized through a 12-bit A/D converter. The hot-wire was also band-pass filtered about the acoustic excitation frequency, amplified, digitized on a second channel, and linearized based on the mean-flow measurements. This technique provided high-precision measurements of the fluctuation velocity components. The forcing signal from the function generator was digitized on a separate channel. The cross-spectral density function between the function generator and the hot-wire was computed to provided accurate phase information (ϕ).

In acoustic receptivity experiments the acquired hot-wire signal is generally a superposition of two components, the T-S wave and the Stokes wave, which both occur at the same frequency. A Stokes layer will exist near the plate when the acoustic field is a two-dimensional travelling wave. In order to determine the T-S mode shapes, the Stokes wave must be removed. This decomposition can be achieved by relying on differences in the spatial structure of the two components. For example, the profile of a Stokes wave asymptotically approaches constant phase and amplitude far from the wall for fixed x. In general the acquired streamwise fluctuating velocity at the forcing frequency (u'_t) and the Stokes wave and T-S wave components of u'_t (u'_{ts}) can be represented as complex vectors having amplitude and phase which depend on y . The Stokes wave component is approximated by u'_t far outside the boundary layer ($\hat{u}'_{ac}$) and by theoretical phase and amplitude distributions as the wall is approached. The T-S component (u'_{ts}) is the vector difference between u'_t and $\hat{u}'_{ac}$. This decomposition scheme has been documented in the literature (Nishioka and Morkovin[3]). A further refinement is the removal of leading edge effects (which was weak but measurable) by first measuring the T-S response with no strips and vectorially subtracting these values from the total T-S response.

3. REFERENCE CONDITIONS

Great care must be exercised in conducting any receptivity experiment and the mean flow must be thoroughly characterized using the four criteria established by Nishioka and Morkovin[3].

3.1 Boundary-Layer Characteristics

A nominal zero-pressure gradient boundary layer (desirable as a test case because streamwise pressure gradients have a strong influence on the stability characteristics) was achieved by adjusting the plate angle

of attack and the test-section ceiling. Mean-velocity profiles were acquired normal to the plate at several streamwise locations to obtain the integral quantities of displacement thickness (δ^*), momentum thickness (θ), and shape factor H_{12}, which was 2.59 +/− 0.02 over the entire streamwise-range of the experiment. A new reference location (at x = -70 mm relative to the physical leading edge), commonly called the virtual leading edge (x_V), is introduced to account for the recovery region downstream of the leading edge. Normalized mean velocity profiles are plotted in Figure 3 and show excellent agreement with theoretical Blasius profiles.

3.2 Acoustic-Field Characteristics

When a closed-loop wind tunnel is acoustically driven below the frequency at which higher-order modes are cut off, the acoustic field is generally a combination of one-dimensional standing and travelling acoustic modes. If distributed receptivity is viewed as a continuous array of localized receptivity sites, then (in contrast to localized receptivity) the relative phase and magnitude of the acoustic field must be measured at each site. Theoretical treatment of continuous receptivity assumes infinite sound speed, i.e., that the acoustic phase and amplitude are constant in x. The nearest approximation that can be achieved in the laboratory is a purely travelling acoustic field, which can be produced in a wind tunnel with an appropriate sound source. Reference data was taken far outside the boundary layer at various freestream velocities to document the acoustic field. Measurements were performed using various speaker combinations. In each case data were taken over an axial range which covered at least half of an acoustic wavelength.

Figure 4 shows the measured variation of amplitude when only the upstream set of speakers is used at 80 Hz (shown as squares, λ_{ac} = 4.28 m). The acoustic amplitude shows a sinusoidal variation in x, indicating a combination of a standing and travelling wave. Decomposition of the data in Figure 4 produces an amplitude ratio of downstream- to upstream-travelling waves (A_S) of 1.7. Amplitude ratios (A_S) obtained at four different frequencies in the range of 72 to 225 Hz are also in the range of 1 to 2, which indicates a strong standing-wave component in each case. Data from Saric et al.[14] were similarly decomposed and produce an amplitude ratio of A_S = 1.25. Thus strong standing waves are not a characteristic of our particular wind tunnel.

To solve the problem the second acoustic source was installed downstream of the test plate and its phase and amplitude were adjusted to effectively cancel the upstream travelling wave (and thus minimize the standing wave component) inside the test section.

The amplitude distribution for the final configuration is represented by the circles in Figure 4. This configuration produced an amplitude ratio A_S near 12. The phase distribution for the final configuration (not plotted here) shows only a small scatter of the data from the theoretically-predicted slope of 84 degrees/m. As a final check, the amplitude and phase variation normal to the plate were measured at three different streamwise locations. The results (not shown here) have nearly constant amplitude and phase, verifying that the acoustic field consists of plane waves with fronts normal to the test plate.

Spectra of velocity fluctuations in the freestream (U_∞) with and without an acoustic source are shown in Figures 5. A well-defined peak of $\hat{u}'_{ac}$ = 0.0014 m/s can be identified at the forcing frequency of 80 Hz. Other peaks at 60 and 180 Hz correspond to power-line harmonics and do not influence the experiment. Thus the low-level acoustic forcing can be easily distinguished from background disturbances.

4. RESULTS

4.1 Tollmien-Schlichting Mode Shapes

Using the complex plane decomposition scheme we can determine the T-S mode shapes which result from T-S receptivity. Figure 6 shows the results at x_V = 1350 mm and U_∞ = 12.5 m/s with thirteen strips comprising the wavy wall. The mode shape is determined by removing the Stokes wave and the leading-edge T-S contribution. The measured normalized mode shape shows excellent agreement with numerical calculations using stability analysis, demonstrating the adequacy of the decomposition scheme. Mode shapes acquired in a localized receptivity experiment (Saric et al.[11]) show significant discrepancies with theory, particularly for y-positions above zero crossing. This excellent match in the present data can be

ascribed to the precise control of the acoustic field. The phase variation of the measured T-S wave shows a 180 degree phase shift at $y/\delta^* \approx 2$, matching the position of the zero crossing of the mode shape.

4.2 Influence of Number of Strips

To date, experiments have focused on localized receptivity at leading edges and at localized roughness using a single two-dimensional roughness element (Aizin and Polyakov[4] and Saric et al.[11]). The theory of receptivity at a continuously wavy surface considers an infinitely long wavy wall. As an intermediate step, the effect of increasing the number of surface wavelengths is considered. Continuous receptivity theory can be applied to this intermediate problem by considering the waviness to be non-periodic.

Mode shapes were acquired at a fixed streamwise location x_v = 1350 mm and the freestream velocity was set to 12.5 m/s in order to tune the excited T-S wavelength to the wavelength of the surface. Figure 7 shows the T-S amplitude due to wall receptivity ($\hat{u}'_{ts}$) as a function of the number of wall wavelengths (show as circles). There is generally an asymptotic behaviour with increasing number of strips. Beyond nine strips (which covers the range of R_v = 482 to 749), the T-S wave amplitude does not increase significantly with additional strips. Thus there is only a narrow region around lower branch that produces the same acoustic receptivity as an infinite wavy wall. The relative narrowness of this region is shown in Figure 8, in which the region from R_v = 482 to 749 is represented as a horizontal solid line. This sensitive region is also symmetric about lower branch. This symmetry is expected because the roughness element at lower branch produces the greatest effective receptivity. Elements upstream of lower branch have diminishing effectiveness because the T-S mode is damped until lower branch is reached. Elements downstream of lower branch have diminishing effectiveness because the total amplification decreases. The decreasing effectiveness is observed in Figure 7 as a decreasing slope as n increases.

Figure 7 also shows a direct comparison of absolute magnitudes made with calculations by Choudhari (shown as triangles) and Bertolotti (shown as stars). Bertolotti utilised parabolized stability equations to simulate the experiment while Choudhari uses a perturbation analysis and Green's functions. These results were computed using the physical parameters of the experiment to facilitate direct comparison. The theoretical prediction and the experimental results show the same asymptotic behaviour as the number of strips increases. More significantly, the quantitative agreement in terms of absolute T-S amplitude is very good. For the first three strips the difference between experiment and theory is less than 8%, and this error increases to only 20% at thirteen strips. The reduced response observed in the experiment can be attributed to an inherent detuning between the wall and the T-S waves. Small variations in velocity and viscosity (due to temperature changes) can effectively detune the T-S waves. Even more important are the small variations in strip location, which will spread the peak in the wall wave-number spectrum and decrease its magnitude. In this case, the deviation between theory and experiment should be expected to grow with an increasing number of wall wavelengths. It should also be noted that Choudhari was only provided with the physical parameters of the experiment (tape height, flow field characteristics, and forcing level) to compute the numerical predictions, which makes such agreement even more impressive. While Choudhari utilised a constant acoustic forcing amplitude in streamwise direction, Bertolotti utilized the measured distribution shown in Figure 4.

The ratio of the receptivity at one strip (localized receptivity) can be compared to that at an infinite wavy wall (non-localized receptivity). The results for thirteen strips is taken to represent an infinite wavy wall. In this experiment the response ratio between thirteen strips and one strip is 4.7, while the inherent errors discussed above will tend to reduce this ratio. Furthermore, the fixed errors in the decomposition scheme manifest themselves to the greatest degree in the single-strip measurements. This compares with a ratio of 7.6 between continuous and localized receptivity predicted by Choudhari[13] and the O(10) difference predicted by Crouch[14].

4.3 Background Forcing

After each additional strip was added, mode shapes were also obtained without acoustic forcing and showed also T-S like mode shapes. A potential mechanism for this background T-S response is the ambient acoustic forcing at 80 Hz due to fan noise and boundary layer noise from other parts of the tunnel circuit. For the present experiment, the 80 Hz component measured by a hot wire in the freestream has been shown to be dominated by the acoustic sources when excitation is used (the forced case). When the external

sources are not used (referred to as the unforced case), the measured amplitudes are a combination of the ambient noise plus contributions from freestream turbulence. The acoustic component of this signal constitutes the environmental acoustic forcing that can influence the laminar boundary layer through the same receptivity mechanisms as the forced case. The freestream power spectra in Figure 5 show that the amplitude ratio at 80 Hz between the forced and unforced cases is 8.9. Thus the ratio between the forced ($\hat{u}'_{ac}$) and unforced ($\hat{u}'_{t}$) acoustic levels is at least 8.9, and can potentially be greater if the unforced amplitude contains significant contributions from freestream turbulence. Figure 9 compares the forced and unforced response in the boundary layer as a function of number of strips. For comparison, a line corresponding to the ratio of forced to unforced freestream disturbance level is provided. If the unforced freestream component is purely acoustic, and if the boundary layer response is through linear receptivity mechanisms, then the receptivity results should fall near this line. The data of Figure 9 verify this receptivity response. Thus it may be concluded that: a) the freestream unforced velocity perturbations are primarily acoustic, and b) the amplitudes measured within the boundary layer in the unforced case are essentially due to background acoustic forcing of T-S waves.

4.4 Detuning

Detuning is defined as the mismatch between the excited T-S wavelength (λ_{ts}) and the wavelength of the surface roughness (λ_w) . Detuning can be achieved by varying the wall wavelength, the acoustic forcing frequency, or the freestream velocity. The wall geometry was kept fixed to minimize errors introduced by irregularities in strip spacing. Wlezien et al.[10] as well as Saric et al.[11] report a change in freestream acoustic amplitude with frequency. This variation would add an additional physical parameter to the experiment. Furthermore, a complex forcing configuration (discussed above) was used to minimize the standing wave component. Since the phase and amplitude ratios between the speaker systems would have to be changed for different forcing frequencies, it is preferable to run the experiment at a fixed frequency. The freestream velocity was therefore chosen as the appropriate parameter. A detuning parameter, σ, is defined as $(\lambda_{ts}-\lambda_w)/\lambda_w$. On the basis of theory (Choudhari[13] and Crouch[14]) we chose a detuning range $\sigma = \pm$ 10%, which is achieved by varying the freestream velocity from 10.5 m/s to 14.5 m/s. Detuning was measured by obtaining mode shape profiles at a constant streamwise position (x_v = 1350 mm) at fifteen different freestream velocities with thirteen strip configuration (see Figure 2).

In Figure 10 the normalized receptivity coefficient C is plotted as a function of the detuning parameter, σ. The receptivity coefficient, C, is defined to be the ratio between the effective $\hat{u}'_{ts}$ at lower branch, designated $\hat{u}'_{ts,o}$, and the acoustic amplitude, $\hat{u}'_{ac}$. The T-S amplitudes are measured sufficiently far downstream so that the amplification inherent in the boundary layer increases the amplitude of the measured mode. This measurement is brought back to lower branch using the total amplification calculated from linear stability theory. Thus $\hat{u}'_{ts,o}$ is the effective T-S amplitude at lower branch as if all receptivity occurred at that single location.

The results shown in Figure 10 are normalized with the maximum receptivity, which occurs at zero detuning. The theoretical curves of Choudhari[13] and Crouch[14] are virtually indistinguishable when normalized with their respective maxima. Analytical theory (Choudhari[13]) indicates that the dropoff in the coupling coefficient behaves in a Gaussian manner away from the resonant wave number. When the raw experimental data is compared with theory, there appears to be a 1% detuning mismatch between the experiment and theory. However, the incompressible flow assumption used in the theory effectively produces a detuning of -1.2% when compared with the downstream-travelling acoustic wave, because of the finite sound speed in the experiment. In the nonlinear sum and difference wave-number interaction through which receptivity occurs, theory predicts the interaction between the wall wave number and a zero-wave-number acoustic field. This interaction transfers energy to a T-S mode having the same wave number as the wall waviness. In the experiment, the nonlinear interaction between the finite wave number of the downstream-travelling acoustic wave and that of the wall waviness produces a higher effective wave number for the interaction mode (i.e., the wall waviness is effectively shortened by 1.2%). The experimental data in Figure 10 have been corrected for this effective detuning.

Profiles were acquired two to three times at the same freestream velocity but at different temperatures and atmospheric pressures to verify repeatability of the measurements. Although the peak magnitude is lower,

the measured receptivity closely follows the detuning response predicted by theory. The receptivity coefficient decreases symmetrically with increasing and decreasing σ to nearly zero response for $\sigma = \pm 10\%$. This strong detuning effect implies that a mismatch between wall wave number and excited T-S wave number of more than ten percent will produce negligible receptivity.

Similar results would be expected for an upstream travelling wave, although the detuning (due to the incompressible flow assumption) in this case would effectively be +1.2%. However a strong standing wave (which contains both downstream and upstream travelling components) would effectively detune the interaction to both positive and negative σ. The net effect would be a broadening of the experimental curve and poorer agreement between experiment and theory. Thus it is of critical importance to have negligible standing wave components in continuous receptivity experiments.

Four measurements are involved in computing the detuning parameter: the kinematic viscosity, ν, the freestream velocity, U_∞, the spacing of the strips on the plate, and the location of lower branch. The error in U_∞ is less that 0.5%. The calculated viscosity results in an error of less than 1% due to temperature measurement errors. A strip spacing error of one mm results in a corresponding error in σ of 1%, however this spacing error is most likely manifested as a broadening of the wall wave number spectrum. Thus the uncertainty in σ is estimated to be $\pm$ 1%, which is shown in Figure 10.

There are several complications that arise when using velocity changes to effect detuning. The wavy-wall region is fixed, and when changing the freestream velocity the position of lower branch will change approximately two wall wavelengths for a change in σ of 10%. Because the receptivity occurs in a narrow region around lower branch, the region covered with strips extends sufficiently far to effectively simulate an infinite wavy wall. Choudhari[13] predicts the length of the sensitive region to go as $R_o^{3/8}$ times the neutral wavelength (R_0 is Reynolds number at lower branch). This indicates a small change in the sensitive region in the range F = 35 to 65 over which the detuning experiment was conducted. Thus thirteen strips was sufficient to cover the sensitive region for all detuning measurements.

The best way to conduct the detuning measurements would have been to change the wavelength of the wall and keep the frequency and velocity constant, as in the calculation of Choudhari and Crouch. Figure 5 in Choudhari[13] shows the normalized receptivity coefficient as a function of the detuning parameter for F = 25 and 55. The results do not have a strong dependence on F. In order to more directly compare our results with theory, the present experiment was computed by Choudhari and Bertolotti using the same parameters as in the experimental configuration. The T-S amplitude $\hat{u}'_{ts}$ was computed at the physical probe position x_v = 1350 mm, and the detuning parameter was varied by changing the freestream velocity. Figure 11 shows the excellent match between theory and experiment, not only in trends but also in absolute amplitude. As before, the measured amplitudes are lower than theory, but the details of changes in the T-S response with the detuning parameter follow closely with those predicted by theory.

5. CONCLUSIONS

The purpose of this investigation was to directly validate the theory of acoustic boundary-layer receptivity at periodic distributed waviness. Continuous waviness was simulated by discrete tape strips arranged in a periodic array. Plane-wave acoustic forcing was used to excite a T-S response in the boundary layer, and the resulting mode shapes were measured and analyzed. It was established that a plane travelling wave is the requisite forcing field for distributed receptivity experiments, but it does not occur naturally in a closed-return wind tunnel. When the acoustic frequency was below transverse-mode cut off, a purely travelling plane wave could be established using the appropriate source configuration. A primary source was located upstream of the test section, and a secondary source downstream of the test section was used to actively cancel upstream-travelling acoustic components. It was possible to generate a forcing field that nearly approximates waves travelling downstream at zero incidence to the test plate.

After proper decomposition of the excited T-S mode from the total fluctuating velocity, a good match between the measured T-S mode shape and the theoretical T-S mode shape was observed. Other receptivity mechanisms were shown to be small compared to that due to wavy-wall receptivity, and contributions from these extraneous components were removed from the net response. By increasing the number of wavelengths comprising the receptivity site it was shown that only a small symmetric region in the vicinity

of lower branch can produce the same receptivity as an infinite wavy surface. It was also shown that the ratio between wavy-wall receptivity and the receptivity due to one strip (equivalent to the ratio between distributed and localized receptivity) is of O(10), as predicted by theory.

Strong detuning was verified by measuring the effect of mismatching the excited T-S wavelength with the wall wavelength. A mismatch of ± 10% produces negligible T-S response in the boundary layer, which is in agreement with theoretical predictions by Choudhari[13] and Crouch[14]. Numerical calculations by Choudhari that directly simulate the freestream velocity detuning used in the present experiment show good agreement in the shapes of the curves as well as in absolute amplitude. It is thus possible to conclude that the theory captures the physics of the acoustic receptivity mechanism.

ACKNOWLEDGEMENT

The authors thank Drs. M. Choudhari, J. D. Crouch and F. P. Bertolotti for their suggestions and calculations which were crucial to the success of these experiments. This research was supported by the Air Force Office of Scientific Research under Contract AFOSR-90-0173. The first author was also supported by a stipend from Flughafen Frankfurt Main Stiftung.

REFERENCES

[1] Schubauer, G. B. and Skramstad H. K., "Laminar Boundary-Layer Oscillations and Transition on a Flat Plate," Research Paper RP1772, **38**, 1947

[2] Morkovin, M. V., "Critical Evaluation of Transition from Laminar to Turbulent Shear Layer with Emphasis on Hypersonically Traveling Bodies," Air Force Flight Dyn. Lab. Rep. AFFDL-TR-68-149, NTIS AD-686178, 1969.

[3] Nishioka, M. and Morkovin, M. V., "Boundary-Layer Receptivity to Unsteady Pressure Gradients: Experiments and Overview," J. Fluid Mech., **121**, pp. 219-261, 1986.

[4] Aizin, L. B. and Polyakov, M. F., "Acoustic Generation of Tollmien-Schlichting Waves over Local Unevenness of Surfaces Immersed in Streams," Preprint 17, Akad, Nauk USSR, Liberien Div., Inst. Theor. Appl. Mech., Novosibirsk (in Russian), 1979.

[5] Goldstein, M. E., "The Evolution of Tollmien-Schlichting Waves Near a Leading Edge," J. Fluid Mech., **127**, pp. 59-81, 1983.

[6] Ruban, A. I., "On the Generation of Tollmien-Schlichting Waves by Sound," Transl. in Fluid Dyn., **19**, pp. 709-716, 1985.

[7] Goldstein, M. E. and Hultgren, L. S., "Boundary-Layer Receptivity to Long-Wave Free-Stream Disturbances," Ann. Rev. Fluid Mech., **21**, pp. 137-166, 1989.

[8] Crouch, J. D., "Localized Receptivity of Boundary Layers," Phys. Fluids A., **4**, No. 7., 1992.

[9] Choudhari, M. and Streett, C. L., "A Finite Reynolds-Number Approach for the Prediction of Boundary-Layer Receptivity in Localized Regions," Phys. Fluids A, **4**, No. 11., 1992.

[10] Wlezien, R. W., Parekh, D. E., and Island, T.C., "Measurement of Acoustic Receptivity at Leading Edges and Porous Strips," Appl. Mech. Rev., **43**, No. 5, part 2, 1990.

[11] Saric, W. S., Hoos, J. A., and Kohama, Y., "Boundary Layer Receptivity: Part 1. Freestream Sound and 2-D Roughness Strips," College of Engineering and Applied Sciences Report CEAS-CR-90191, Arizona State University, 1990.

[12] Choudhari, M., "Boundary-Layer Receptivity due to Distributed Surface Imperfections of a Deterministic or Random Nature," Theoret. Comput. Fluid Dynamics, **4**, 101-118, 1992.

[13] Choudhari, M., "Distributed Acoustic Receptivity in Laminar Flow Control Configurations," Contract Report NASA-CR-4438, 1992.

[14] Crouch, J. D., "Nonlocalized Receptivity of Boundary Layers," J. Fluid Mech., **244**, pp. 567-581, 1992.

[15] Crouch, J. D. and Bertolotti, F. P., "Nonlocalized Receptivity of Boundary Layers to Three-Dimensional Disturbances," AIAA 92-0740, 1992.

[16] Bertolotti, F.B. and Crouch, J.D., "Simulation of Boundary-Layer Transition: Receptivity to Spike Stage," Comput. Fluid Dynamics '92, vol. **1**, 183-190, ed. Ch. Hirsch et al., 1992.

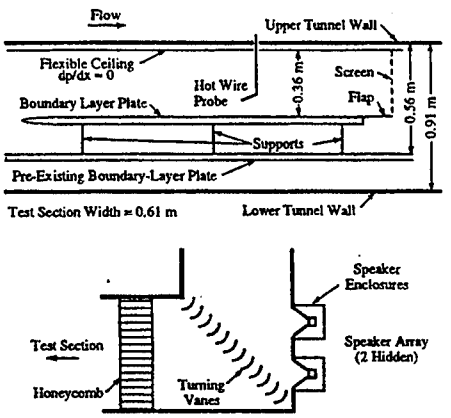

Fig. 1 Schematic of test section, boundary-layer plate, and upstream speaker installation.

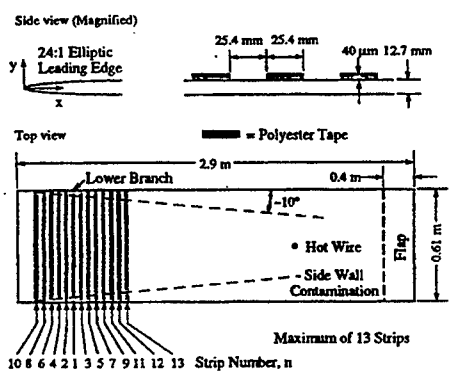

Fig. 2 Top and side view schematic of boundary-layer plate

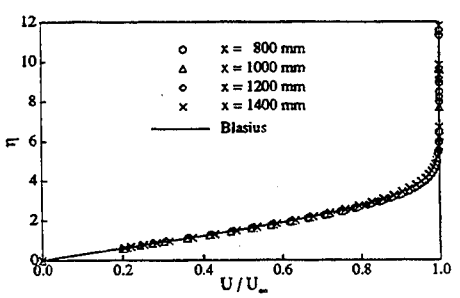

Fig. 3 Comparison of theoretical and measured mean velocity profiles; U_∞ = 12 m/s

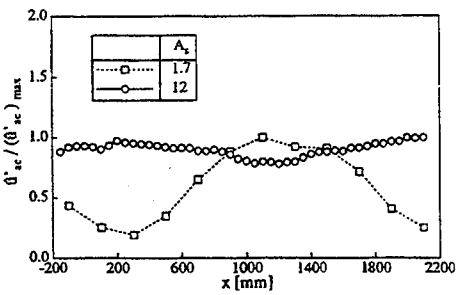

Fig. 4 Normalized freestream acoustic amplitude versus streamwise distance from leading edge for two source configurations ; f = 80 Hz, $\hat{u}'_{ac}$ = 0.0014 m/s, λ_{ac} = 4280 mm

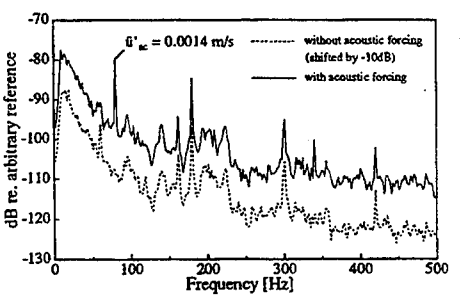

Fig. 5 Power spectral density of freestream velocity fluctuations; U_∞ = 13 m/s; with and without acoustic forcing at 80 Hz

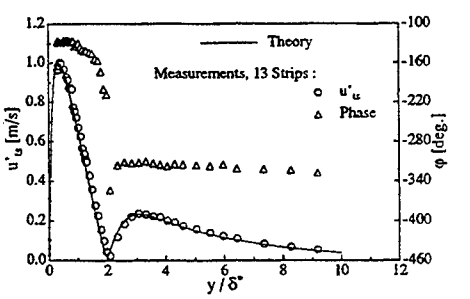

Fig. 6 Theoretical and measured mode shape and phase distribution of T-S wave due to wavy-wall receptivity ; thirteen strips, f = 80 Hz, $\hat{u}'_{TS}$ = 0.023 m/s, $\hat{u}'_{ac}$ = 0.0014 m/s, U_∞ = 12.5 m/s, x_V = 1350 mm

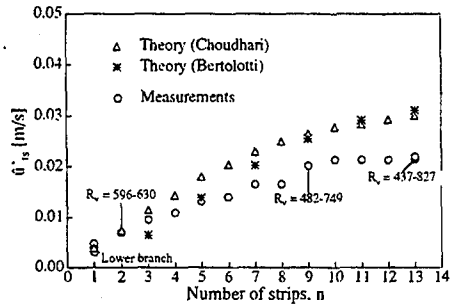

Fig. 7 Magnitude of T-S mode due to wavy-wall receptivity versus number of wall wavelengths; comparison of theory and experiment; f = 80 Hz, $\hat{u}'_{ac}$ = 0.0014 m/s, U_∞ = 12.5 m/s, x_V = 1350 mm

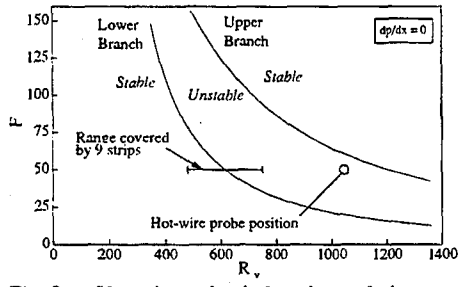

Fig. 8 Hot-wire and strip locations relative to neutral stability curve

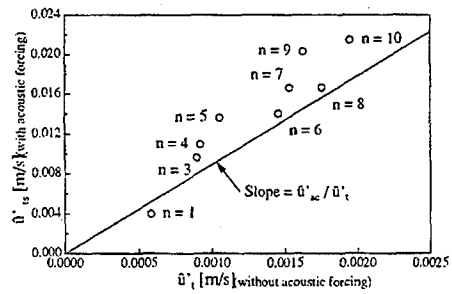

Fig. 9 Comparison of T-S amplitude with acoustic forcing versus disturbance amplitude without acoustic forcing for various numbers of strips

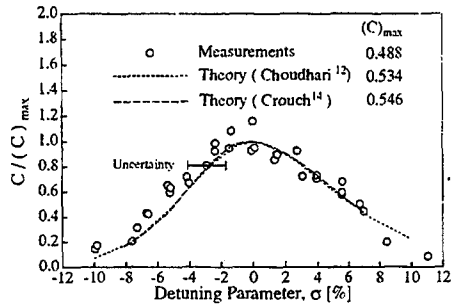

Fig. 10 Receptivity coefficient versus detuning parameter; f = 80 Hz, $\hat{u}'_{ac}$ = 0.0014 m/s

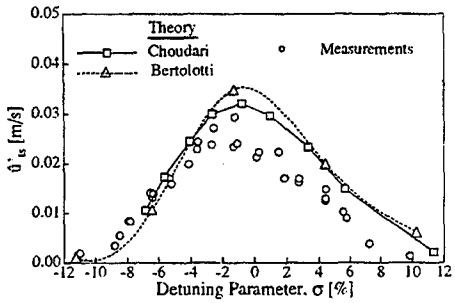

Fig. 11 Magnitude of T-S response to wavy-wall receptivity versus detuning parameter; f = 80 Hz, $\hat{u}'_{ac}$ = 0.0014 m/s

VISUALIZATION OF BOUNDARY LAYER TRANSITION IN INDUSTRIAL WIND TUNNELS

J. P. CROWDER
Technical Fellow
R. L. WATZLAVICK
Senior Engineer
Boeing Aerodynamics Laboratory, Seattle, USA

ABSTRACT

Rationale for, and experience in applications of transition visualization in industrial wind tunnel testing is discussed. Most recent applications have relied on IR camera visualization in combination with various schemes for inducing surface temperature patterns.

INTRODUCTION

Knowledge of the state of the boundary layer on airplane wind tunnel models and visualization of the transition location is important to the wind tunnel testing programs conducted by the Boeing Aerodynamics Laboratory. Consequently, methods of detecting and observing this condition are frequently used and are under continuous pressure for improvement.

This paper is an account of recent activities in the development of improved transition visualization methods, especially in high productivity industrial wind tunnels. Transition visualization using infrared (IR) cameras has been the greatest focus of this activity, although alternative methods are still under active development. Examples are presented of recent transition visualization experiments with this method in several industrial wind tunnels.

INFRARED CAMERA TRANSITION VISUALIZATION

The IR camera is proving to be the most effective tool for transition visualization. Several very successful applications in routine testing have demonstrated the value of the method. The utility of this technique, however, is dependent on having the ability to control the temperature of the wind tunnel airstream, which is difficult to provide in some facilities.

IR Camera Basic Requirements

IR cameras are devices that respond to the infrared radiance from a surface. Under the right conditions, that radiance is related to the surface temperature. Such cameras are readily available on the industrial equipment market, although the costs ($50,000) are high. The images they produce are fundamentally monochrome, although they are frequently presented in a false color format.

IR cameras typically respond to optical radiation in the 5 to 13 μm wavelength range. This part of the spectrum is far removed from the visual spectrum of 0.4 to 0.7 μm, which leads to several unusual aspects of IR camera utilization.

The most important aspect is the optical condition of the model surface. Most organic materials have a high emissivity (close to 1.0) and low reflectivity while metallic surfaces usually have the opposite effect condition, with low emissivity (near 0.1) and high reflectivity. The practical result of this behavior is that it is nearly impossible to observe a temperature pattern on a bare metal wind tunnel model. The surface appears like a mirror and the IR camera sees the temperature of the surrounding environment reflected from the surface. Therefore, a fundamental requirement is that any metallic model surface must be painted.

Another important factor in the visibility of IR camera transition images is the thermal conductivity of the model surface. Low thermal conductivity at the model surface greatly enhances the transition visibility. Unfortunately, most wind tunnel models used in Boeing programs have very stringent strength and stiffness requirements that dictate the use of steel primary structures with some aluminum parts. It is sometimes possible to make local pockets filled with epoxy as a thermal insulating material, but that is a nuisance to be avoided if possible.

Ordinary windows such as glass and acrylic are opaque at the IR wavelengths. Therefore, any viewing ports must be made from special materials like germanium.

Current technology IR cameras produce a low resolution video image that makes it hard to recognize small features and may be unsuitable for observing the necessary detail. In our applications, we make up for this by providing the camera with a narrow field of view lens and use a computer-controlled traversing camera mount.

Mechanisms for Inducing Temperature Patterns

Given that an IR camera shows images corresponding to the model surface temperature, the most obvious question is "What mechanism is responsible for producing a surface temperature difference between the laminar and turbulent state?" The three most prominent processes are: (1) Differential Aerodynamic Heating, (2) Global Temperature Perturbation, (3) External Radiant Heating.

Many other possible temperature control reactions have been identified, and in some cases studied in a small laboratory wind tunnel, but not yet applied to large industrial wind tunnel settings. Some of these are discussed in a subsequent section.

Differential Aerodynamic Heating

The first of these mechanisms, Differential Aerodynamic Heating, has been recognized for a long time and served as the basis for early suggestions for IR camera transition visualization. It is known that there is a slight difference in the temperature recovery factor between the two boundary layer states. At transonic mach numbers this effect should lead to the turbulent boundary layer appearing warmer than the laminar boundary layer by a difference of between 1-4°C.

Modern IR camera equipment is easily capable of resolving temperature differences of this magnitude. In our experience however, this Differential Aerodynamic Heating effect seldom produces a useful transition indication.

Global Temperature Perturbation

The Global Temperature Perturbation technique has been the most successful process in the application of IR cameras for transition visualization. This process, as first proposed in [1], and subsequently described in [2] relies on producing a rapid change in the temperature of the entire wind tunnel air mass. This induces a momentary temperature pattern on the model surface due to the different heat transfer rates of the two boundary layer states. For example, if the wind tunnel airstream temperature is increased rapidly from an equilibrium condition, the model surface temperature will increase more rapidly in the turbulent boundary layer than in the laminar boundary layer. Conversely, if the temperature is rapidly decreased, the opposite effect is observed.

A non-rigorous consideration of the factors controlling the visibility of the temperature pattern leads to the hypothesis that, for a given type of model construction, and starting from a thermal equilibrium condition, the time gradient of airstream temperature is the parameter that best dictates the development of the surface temperature pattern. Empirical evidence from various wind tunnel demonstrations suggests that on a painted steel model, the transition pattern may become faintly visible at a time gradient of about 2°C/min, and strongly visible at 6°C/min.

Figure 1 shows typical results from the 8-by-12-foot Boeing Transonic Wind Tunnel (BTWT). This wind tunnel runs at a total pressure of one atmosphere. It employs a temperature control system that diverts about 10 percent of the airflow to the atmosphere and takes in an equal amount of fresh outside air. By changing the cooling bypass door settings, a rapid time gradient of airstream temperature of better than ±15°C/min can be repeatedly produced for short periods. Since the field of view of the IR camera is relatively narrow (15-by-25-degrees) and can only observe about one-third of the model semi-span at a time, a computer-controlled traversing mirror system is used for viewing different regions of the wing in sequence. The flow direction is from top to bottom.

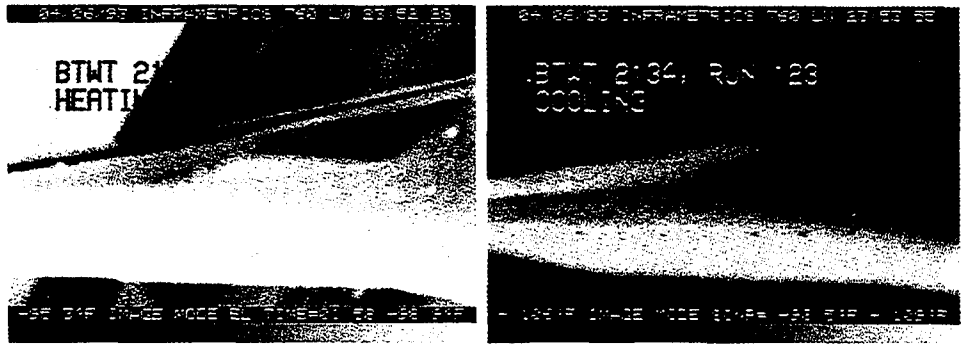

Fig. 1a Airstream Temperature Increasing at 15°C/min

Fig. 1b Airstream Temperature Decreasing at 15°C/min

Figure 1 Transition Image from BTWT

The image in Figure 1a shows the model at a mach number of 0.85 while the airstream temperature is increasing at 15°C/min. The transition pattern is strongly visible with the turbulent boundary layer appearing warmer (brighter) than the laminar region. In Figure 1b, the opposite effect is visible as the airstream temperature is decreasing at a similar rate.

The model in this example is made from solid steel with a thin (about 50μm) layer of paint. The wing leading edge is bare steel, and irregular patches in the paint have been scraped away with sandpaper during the course of changing parts of the model.

A similar set of IR camera transition images are shown in Figure 2 from the NASA Ames Research Center 11-by-11-foot transonic wind tunnel. The same trends for airstream heating and cooling are visible in the images. The model has a bare steel leading edge and is coated with a thin layer of paint over the rest of the upper surface. The flow direction is from left to right.

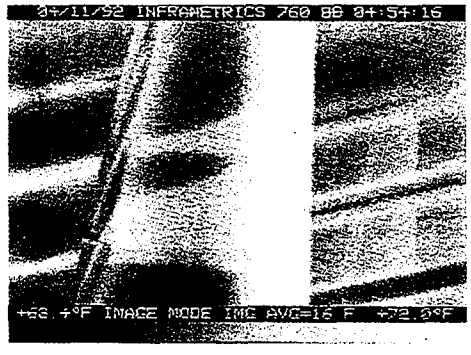

Fig. 2a Airstream Temperature Increasing at 8°C/min

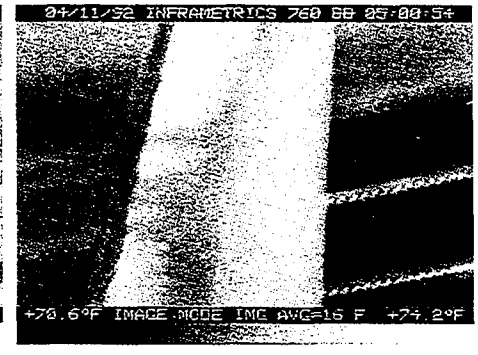

Fig. 2b Airstream Temperature Decreasing at 8°C/min

Figure 2 Transition Image from NASA 11 foot Transonic Wind Tunnel

This wind tunnel employs a high capacity chilled-water heat exchanger in the circuit to control temperature. In this demonstration, temperature gradients of up to 10°C/min were induced by alternately closing and opening the water control valves to the heat exchanger.

External Radiant Heating

The use of External Radiant Heating for IR camera transition visualization was first observed during the NASA/Boeing 757 Hybrid Laminar Flow Control flight test program in 1991. In this process, the hypothesis is made that the solar radiant energy acts to heat the surface uniformly but the greater heat transfer rate of the turbulent boundary acts to cool that region more effectively than the laminar region.

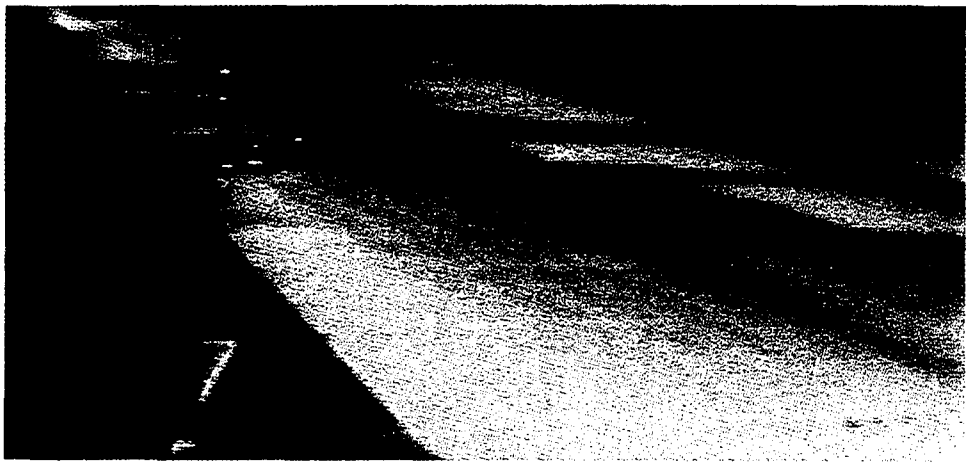

Figure 3 Transition Image from NASA/Boeing 757/HLFC

Figure 3 shows a typical image from that program. The airplane is flying at a mach number of 0.8, an altitude of 40,000 feet, and a constant heading angle. The IR camera images show strongly visible transition patterns over a wide range of flight conditions. The leading edge is at the upper right of the image. The wing skin forward of the front spar is made of bare titanium, perforated with small suction holes. It appears dark in the image. The region of the wing surface between the front and rear spar is made of conventional aluminum construction and coated with black paint.

The laminar boundary layer is depicted by the bright region extending aft of the front spar, interspersed with dark turbulent wedges (caused by surface defects on the wing leading edge). The turbulent boundary layer appears cooler than the laminar region by about 5°C. This effect is in competition with the Differential Aerodynamic Heating process, which tends to increase the turbulent boundary layer temperature by several degrees.

PRELIMINARY EVALUATION WIND TUNNEL FACILITY

Preliminary evaluation of various transition visualization reactions is carried out in a small wind tunnel at the Boeing Aero Lab. This facility employs a conventional single-return circuit, operates at a static pressure of one atmosphere, has a test section size of 14.4-by-18-inches and is able to run at up to 0.4 mach number. Figure 4 shows the test section with the IR camera mounted on the computer-controlled traversing mount which is arranged to view the model through a small port.

The IR camera is an Inframetrics model 760. This camera has a single detector made of mercury-cadmium-teluride with a scanning mirror system. The minimum detectable temperature difference is 0.1°C. A convenient feature of most IR cameras is the ability to independently control the gain and offset of the video signal. In this model camera the most sensitive setting is usually employed. This corresponds to a temperature span of 2°C over the brightness range of black to white. Frame averaging is used to reduce noise in the image.

This wind tunnel has been fitted with heating and cooling provisions to produce a global temperature perturbation of ±8°C/min. This facility is used on a regular basis for comparisons of different IR camera commercial products and alternative concepts.

Figure 4 Transition Evaluation Wind Tunnel Facility

The model used in the evaluations is a two-dimensional airfoil with a 178 mm chord length installed between the floor and ceiling and is mounted on a manually operated turntable. It is made of solid steel and coated with a relatively thick layer (100 μm) of epoxy paint. In an attempt to observe the effect of even thicker paint layers, 6 small recessed pockets are located along the wing span near the leading edge extending from 5% to 20% chord. These are filled with epoxy resin under the paint layer to simulate a paint thickness over a graduated range of 150, 200, 250, 300, 350 and 600μm, respectively. In addition to these graduated depth pockets, a large area epoxy filled pocket of more than 4mm depth is located near the leading edge. An isolated roughness spot is located at a chordwise position of 14% chord to produce a distinctive turbulent wedge.

The behavior of this model is illustrated in Figure 5 at two different global temperature perturbation rates. In Figure 5a, the temperature gradient is about 1°C/min and in Figure 5b, 6°C/min. The transition visibility at the higher rate is noticeably greater. Also, the graduated thickness resin patches strongly show a effect of thicker thermal insulation in improving the transition visibility. The turbulent wedge emanating from the roughness spot is distinctly visible. The wind tunnel is running at a mach number of 0.24 and a chord reynolds number of 0.9 million. The flow in all these images is from bottom to top.

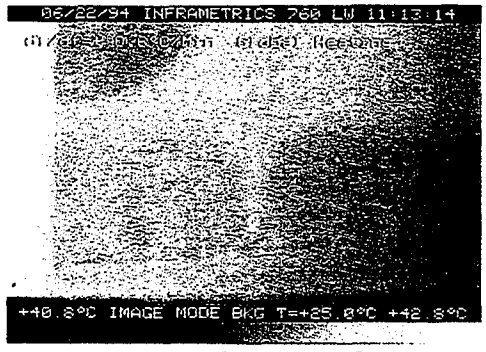

Fig. 5a Airstream Temperature Increasing at 1°C/min

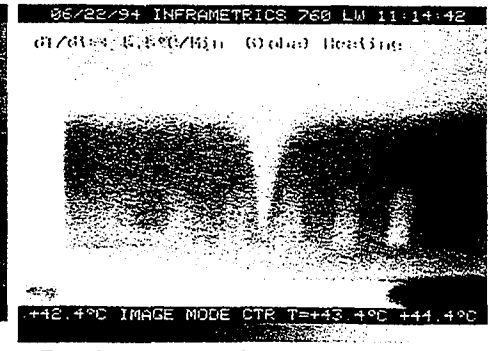

Fig. 5b Airstream Temperature Increasing at 6°C/min

Figure 5 Transition Image on Evaluation Model with Global Temperature Perturbation

OTHER IR CAMERA TRANSITION VISUALIZATION REACTIONS

Implementing the global temperature perturbation process in various industrial wind tunnels is sometimes hampered by an inability of the facility to produce a sufficiently rapid temperature change. In these cases, there is a need for alternative reactions. Several possible reactions have been identified but so far only two of them have been demonstrated as being effective. These are discussed further below.

Local Electric Heating.
Local electric heating of the model surface was evaluated in two different configurations. In the first, a thin film electric heater was bonded to the lower surface of the steel wind tunnel model opposite the region where the graduated thickness pockets are located in the upper surface. It is powered with an alternating current of 135 volts and draws 60 watts.

Figure 6a shows the resulting IR camera image. The elevated temperature from the heater soaks through the approximately 1-inch-thick steel model and results in a diffuse warm patch on the upper surface of rather limited extent. The visibility of the transition, when located within the heated area, is strongly evident. The presence of the graduated thickness pockets is increasingly visible as the thickness of the resin increases.

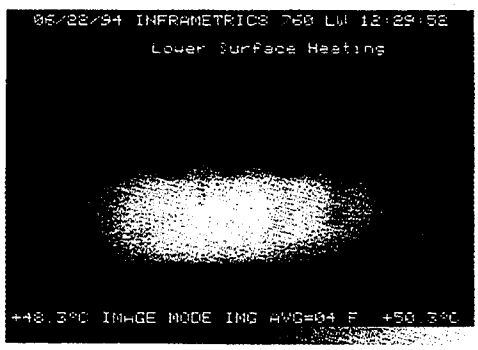

Fig. 6a Lower Surface Electric Heating

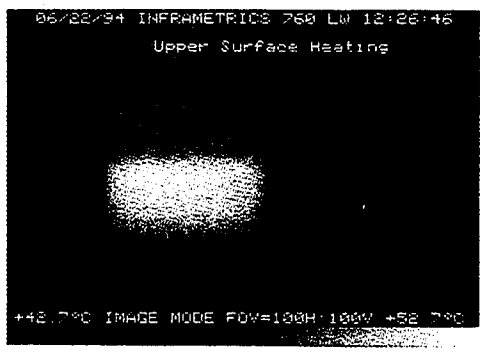

Fig. 6b Upper Surface Electric Heating

Figure 6 Transition Image on Evaluation Model with Electric Heating

Another configuration of electric heating involved installing the heater in a 4mm deep pocket milled in the model upper surface and filled with epoxy resin. This provided a much larger temperature perturbation on the model surface and a somewhat more distinct transition pattern, as shown in Figure 6b. However, it is more difficult to integrate the heater into the model without interfering with other model features.

This process of electric heating can produce a strongly visible IR camera transition image but is relatively awkward to implement, not only because of the additional model fabrication time and effort, but it is often difficult to find a region of the model that is not occupied with pressure instrumentation tubing.

Local Airstream Temperature Perturbation

Instead of controlling the temperature of the entire wind tunnel airstream mass, it may be possible to produce a local temperature perturbation in a small region of the airstream that impinges on the model. Figure 7 shows the IR camera transition image when a local plume of cooled wind tunnel air is generated by injecting liquid nitrogen into the airstream far upstream of the model. The image shows strong cooling in the turbulent boundary layer.

Figure 7 Transition Image with Local Airstream Cooling

Even though the evaporation and mixing of the liquid nitrogen at the upstream injection site involves a vigorous thermodynamic reaction and drastic increase in airstream turbulence, by the time the cooled plume of air reaches the model surface it appears to have damped out with little adverse effect on the boundary layer behavior.

Of course, the injection site must be positioned in the interior of the wind tunnel flow at some point where the cooled plume will eventually intersect the model surface. Also, the liquid nitrogen must be conducted over what may be a long distance and onto a traversing system.

CONCLUSIONS

Boundary layer transition is an extremely important component of airplane fluid mechanics, and methods of visualizing this behavior will continue to be important in routine industrial wind tunnel testing. Based on work accomplished to date, the use of IR camera transition visualization remains one of the most successful and productive methods for these results.

Many IR camera shortcomings, i.e. high cost, poor spatial resolution, limited temperature sensitivity, are soon to experience dramatic improvement due to continuing evolution of commercial IR camera equipment.

Providing the necessary temperature perturbations will continue to be the major limitation for the process. As various wind tunnel facilities invest in improving their control capability, this method will become more widely applicable. Alternative reactions will continue to be examined, however.

REFERENCES

1. Quast, A., Detection of Transition by Infrared Image Technique, ICIASF '87 Record, IEEE Publication CH 2449-7/87/0000-0125, pp.125-134.

2. Crowder, J.P., Infrared Cameras for Detection of Boundary Layer Transition in Transonic and Subsonic Wind Tunnels, AIAA Paper 90-1450, June, 1990.

BOUNDARY LAYER TRANSITION INDUCED BY ROUGHNESS IN HYPERSONICS

J.-M. Charbonnier*, H.L. Boerrigter†, S. Braem‡
von Karman Institute for Fluid Dynamics
Rhode-Saint-Genèse (Belgium)

Abstract

The transition induced by a roughness due to the misalignment of the tiles of the thermal protection system of a re-entry vehicle is studied in a hypersonic Mach 6 wind tunnel using flat plates with sharp leading edges. Experiments are conducted with perturbations composed of a transverse gap with a forward facing step and of an elevated tile model. The critical values of the perturbation height above which transition starts to be affected by the roughness are ranging between 1.5 and 2 when normalized by the boundary layer displacement thickness. The van Driest and Blumer criterion is found to underpredict the effective normalized perturbation height whereas data are successfully compared with the experiments made on an Orbiter model at 30° incidence in a Mach 8 wind tunnel. Correlation parameters are proposed to unify the roughened transition data obtained with sharp leading edge models and with blunt bodies.

Nomenclature

Re_u	Unit Reynolds number [1/m]
St	Stanton number [-]
Pr	Prandtl number [-]
δ^*	Laminar boundary layer displacement thickness [m]
θ	Laminar boundary layer momentum thickness [m]
h	Step or tile height or sphere diameter [m]
SLE	Sharp leading edge
FP	Flat plate

Subscripts

w	wall value
e	boundary layer edge value
r	recovery value
tr	evaluated at the beginning of transition
effect.	relative to the effective perturbation height
lam.	laminar value
smooth	evaluated for the smooth model
rough	evaluated for the rough model
max.	maximum value on the model

Introduction

During the hypersonic re-entry phase of a spacecraft, the very high surface heating occurring requires the use of a thermal protection system. Usually it is achieved by covering the surfaces which are subject to high temperatures by ceramic tiles. Junctions between the tiles or vertical misalignment of consecutive tiles are likely to promote the transition of the boundary layer otherwise laminar. Consequently, it modifies the specifications for the thermal protection design and it can change the payload of the craft. Therefore quantitative information on the effect of such perturbations on boundary layer transition are required during the design phase of the vehicle.
A study of the boundary layer transition induced by this kind of roughness in the hypersonic regime was undertaken at the VKI several years ago. This paper presents quantitative data on the

* Assistant Professor
† Doctoral Candidate
‡ Research Assistant

modification of the transition location due to the presence of a transverse gap with a forward facing step and of several three-dimensional perturbations simulating the vertical misalignment of a tile. A comparison with existing predictions is given and the results are discussed.

Experimental details

Measurements are conducted in a hypersonic blowdown wind tunnel[1] at Mach 6 with the unit Reynolds number ranging between 8 million and 22 million per meter and a ratio of model wall to stagnation temperature of 0.5-0.6. Infrared thermography is used to provide a quantification of the heat transfer from the flow to the model surface[2,3,4]. The basis of all models used is a flat plate on which the roughness elements are placed. Experimental distributions of Stanton number are compared with theoretical predictions for the smooth flat plate. The laminar skin friction coefficient is deduced from the Blasius theory corrected for compressibility effects using the reference temperature method[5]. The Reynolds analogy is applied to compute the theoretical Stanton number from the skin friction coefficient using a recovery factor equal to $Pr^{2/3}$.

The data presented hereafter are obtained using models with leading edge thicknesses between 26 µm and 47 µm which will from now on be characterized as sharp leading edges (SLE). An analysis of the smooth flat plate transition for these sharp leading edges is given in (4,5), where it can be seen that the Reynolds number based on the position of the beginning of transition is a function of both the unit Reynolds number and the leading thickness. Therefore for each flow condition and leading edge thickness, the corresponding Reynolds number based on the position of smooth transition has to be used as a reference to compare with the roughened test results. Three methods are used to define the beginning of the boundary layer transition depending on the perturbation studied[4]. In the case of both the smooth flat plate and the transverse gap/step perturbation, the beginning of transition is found using the distribution of the heat transfer coefficient. It is defined as the intersection of the straight line fairing through the transition region with the laminar theory[6] (see fig. 1). For the elevated tile model and the spheres, the transition is defined as the location where the vortices formed around the obstacle start to spread[5].

Transverse gap-step model

A basic perturbation composed of a transverse gap with a forward facing step is analysed. The gap width and depth are equal to 4 mm and the step height varies between 0 and 3.2 mm. An analysis of more complex gap-step configurations is given in (5). In the presence of a gap with step, the approaching boundary layer separates before the gap and reattaches at the step producing a locally high heat transfer level. Figure 1 displays a streamwise profile of the Stanton number on the model centerline which shows that after the perturbation the heat transfer level can recover to the laminar level before transition takes place.

The change in Reynolds number based on the beginning of transition between the smooth and the roughened flat plates is correlated with the step height normalized by the boundary layer displacement thickness computed at the location of the perturbation. Figure 2 gives the correlation obtained using tests conducted with three different sharp leading edges. The perturbation starts to influence the boundary layer transition location only when the normalized step height is higher than a critical value equal to about 2. As seen in figure 2, the critical normalized step height is not depending on the leading edge thickness for sharp leading edges.

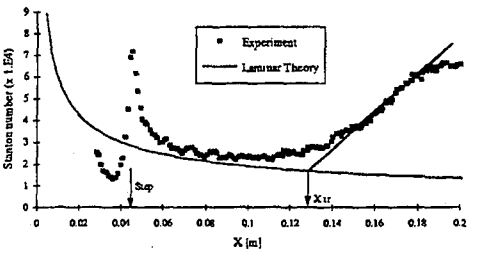

Fig. 1 : Streamwise profile of Stanton number for a transverse gap model

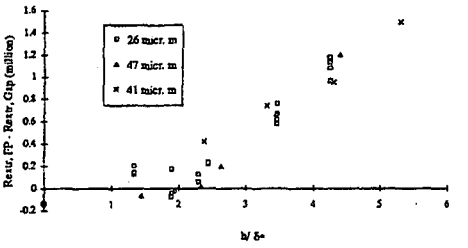

Fig. 2 : Change in Reynolds number of beginning of transition

Elevated tile perturbation

A second kind of perturbation is studied to simulate a vertical misalignment of the tiles. An elevated square tile (19.7 x 19.7 mm) is mounted on a smooth plate. The possible configurations include variation of the tile height (0 - 2.2 mm), the tile orientation with respect to the incoming flow and the slant of the tile. In the case of the flat tile oriented at 45°, a gap of 1.5 mm width and 4 mm depth can be added around the tile.

In a first step, the influence of the tile height is investigated using flat tiles oriented at 45° mounted on a sharp leading edge (41 μm) flat plate. In figure 3 are plotted the changes in Reynolds number based on the location of the beginning of transition between the smooth case and the configurations with and without a gap around the tile. Clearly these results show that the presence of the gap around the tile does not affect the transition. Comparison with the transverse gap step perturbation shows a similar evolution of the transition in both cases, although the critical normalized tile height value ($h/\delta^* \approx 1.5$) is somewhat smaller than the critical normalized step height ($h/\delta^* \approx 2$). This is not surprising since it has already been found by several researchers that a two dimensional roughness is less efficient to promote transition than a three dimensional roughness[7,8,9,10].

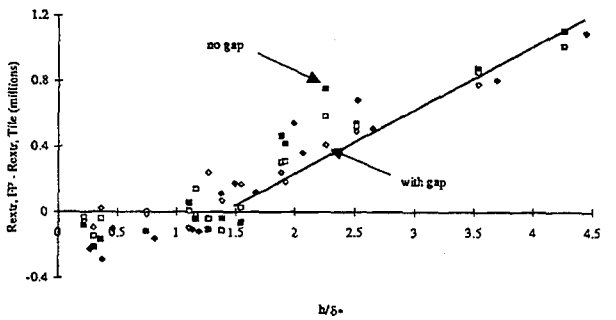

Fig. 3 : Change in Reynolds number of beginning of transition for the elevated tile model

The influence of the tile orientation on the transition is shown in figure 4. Although the critical normalized tile height is not strongly dependent on the tile orientation, it shows that the tile oriented at 45° is the most efficient to promote transition.

On the contrary, the critical normalized height is significantly affected by the tile slant. Figure 5 displays the results obtained for flat tiles and for positively and negatively slanted tiles only for the

45° orientation. For the positive slant, the upstream corner of the tile is mounted flush to the flat plate surface whereas the downstream corner is elevated by the value h (1.2 or 2.2 mm). The opposite geometry is used for the negative slant. The negatively slanted tile produces the same effect as the flat tile for a given height, whereas the positively slanted tile has almost no effect on transition.

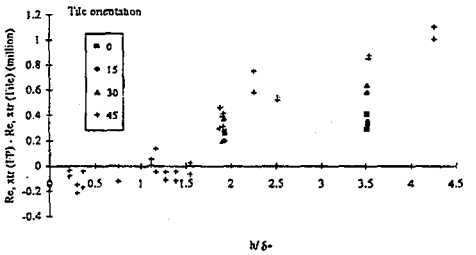

Fig. 4 : Effect of the elevated tile orientation on transition

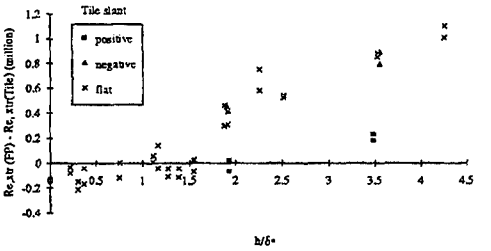

Fig. 5 : Effect of the tile slant on transition

As a result of the investigation of the influence of the tile geometry, it can be considered that the case of the flat tile oriented at 45° with respect to the upstream flow direction is the most relevant to study. Of course in the real case of a re-entry vehicle, it is likely to observe that several tiles are subject to a vertical misalignment. Therefore the influence of the combination of several elevated tiles on the boundary layer transition is also currently being studied.

Comparison with classical roughness induced transition results

The results are compared with tests performed using spheres placed on a flat plate in the same wind tunnel. For most of the tests, two spheres are placed along the model span at 30 mm apart. The distance between the spheres is much larger than is considered by Mc Cauley et al[7] as the minimum distance to avoid interaction (2 diameters) and therefore it can be assumed that there is no interaction between the two spheres. Varying both the unit Reynolds number and the sphere diameter, the Reynolds number based on the beginning of transition is correlated with the sphere diameter normalized by the local laminar boundary layer displacement thickness (fig. 6). The critical normalized heights for the sphere and the tile are of the same order of magnitude. Nevertheless the tile configuration is more efficient to bring back the beginning of transition close to the obstacle.

There is a minimum distance after the sphere which can not be decreased even by increasing the sphere diameter[8,9,11]. For given flow conditions, the smallest sphere diameter which leads to this minimum distance is called the effective sphere diameter. Consequently, it is expected that the effective perturbation height is larger than the critical height. In the case of the tile, the transition location can move back to the side corners of the tile as opposed to the observation made using spheres. This difference may be linked to the fact that in the case of the sphere, the vortices formed around the obstacle which are likely to promote transition are very close to each other in the sphere wake and it may lead to some kind of stabilization of the vortices. For the tile, the distance between the two branches of the vortices is linked to the tile size and is much larger than the vortex size. Therefore the interaction between the two vortices is reduced and it may explain that they burst almost immediately after the tile when the tile height is sufficient.

The transition induced by spheres of the boundary layer on a cone was studied in details in the supersonic regime by several researchers[7,8,9,10]. Van Driest and Blumer proposed a correlation to predict the Reynolds number based on the value of the effective perturbation height[10]. It is used to compute the effective perturbation height for the experiments conducted in this study where the perturbations are placed at 0.04 m from the leading edge. The Reynolds number based on the effective perturbation height is given by van Driest and Blumer :

$$R_{e,heffect.} = 44.0 \cdot \left(1 + 0.9 \cdot (T_w/T_e - 1) + 0.28 \cdot (T_r/T_e - 1)\right) \cdot R_{e,Xheffect.}^{1/4}$$

The effective step heights computed for the conditions of the experiments are ranging between 0.4 mm and 0.75 mm. Using the laminar boundary layer displacement thickness to normalize the perturbation height, it leads to an effective normalized perturbation height around 0.75 which is about 3 times less than the value of the critical normalized perturbation height found in these experiments. This discrepancy is not surprising since, although the van Driest and Blumer prediction accounts for both the heat transfer and the compressibility effects, it was established for Mach numbers lower than 4. Consequently, the difference between the van Driest and Blumer prediction and the present results may be a Mach number effect.

In order to assess the influence of the Mach number on the validity of the van Driest and Blumer criterion, tests were conducted at negative angle of attack. Experiments were made with the transverse gap/step model at -5° and -8° incidence to provide an inviscid local Mach number of 5.3 and 4.9. As a result of the model incidence, the smooth transition moves closer to the leading edge and it is observed that a very small step height can change the position of the beginning of transition. Variations of the Reynolds number based on the beginning of transition with respect to the smooth case are plotted in figure 7. Clearly, the main effect of reducing the Mach number under these conditions is to decrease the critical normalized step height.
The application of the van Driest and Blumer criterion for these tests gives a value of the effective normalized perturbation height of about 0.7 for both incidences. The results obtained (fig. 7) show that the critical normalized step height is larger than 1 for the -5° incidence and of the order of 0.7 for the -8° incidence. Therefore in this case the prediction of the effective normalized perturbation height is in closer agreement compared to the results of the tests conducted at Mach 6. It gives an indication that there is a Mach number effect which is not properly accounted for in the van Driest and Blumer transition criterion.

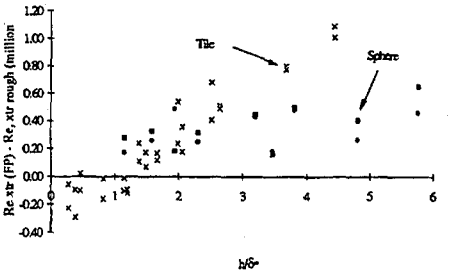

Fig. 6 : Comparison between sphere and tile disturbances

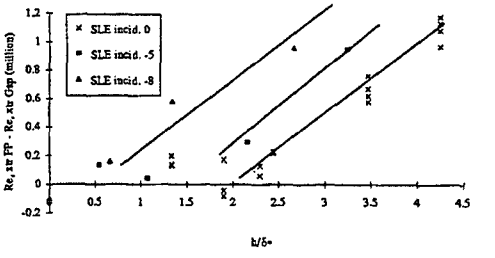

Fig. 7 : Effect of model incidence on roughened transition

As in the real problem the craft leading edge is always blunt and since it is well known that leading edge bluntness stabilizes the boundary layer in the case of smooth transition[4,11], the influence of the bluntness on the transition criteria has to be taken into account. Two effects are observed for blunt cases: a decrease in Mach number compared to the free stream, and the presence of the entropy layer which leads to continuously changing boundary layer edge conditions until the entropy swallowing distance is reached.

In order to estimate the relevance of the present set of data with respect to the induced boundary layer transition for a re-entry vehicle, the results of Bertin et al[12] are presented. They studied the transition induced by randomly distributed elevated tiles on the windward side of a model of the Orbiter at 30° angle of attack. Experiments were conducted in a wind tunnel with a Mach number equal to 8 using a 0.57 m length model. The transition locations were determined on the centerline of the model and data are reduced using the local conditions for the Mach and Reynolds numbers. The ratio of the Reynolds numbers based on the boundary layer momentum thickness at the transition location for the roughened and the smooth cases is used to correlate the data. Figure 8 shows this ratio as a function of the Reynolds number based on the perturbation height for Bertin et al experiments and figure 9 shows the same quantity for VKI experiments. The two figures are rather similar but the values of the Reynolds number based on h for Bertin et al experiments are two orders of magnitude lower than VKI values. This is linked to the observation that although the upstream unit Reynolds numbers are similar in both studies, the roughness heights are two orders of magnitude smaller in the case of the Orbiter than in the case of the flat plate. However, figure 9 shows that data obtained for different perturbations are in good agreement, and the distribution of the data points suggests that there may exist a critical value of Re,h around 5 000 and an effective value around 40 000.

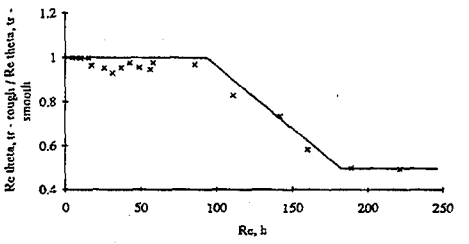

Fig. 8 : Transition data from the Orbiter by Bertin et al[12].

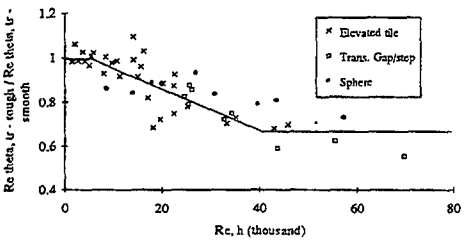

Fig. 9 : Transition data for the different perturbations studied.

Using the set of data given in Bertin et al[12], the change in the Reynolds number based on the location of the beginning of transition between the smooth and the roughened cases is plotted in figure 10 as a function of the normalized height in comparison with the data obtained in this study. This representation of the results shows that the two sets of data are in good agreement although the test conditions are rather different. Actually, the free stream Mach numbers are different (8 and 6) but moreover the flow field itself is different. For the Orbiter, there is a significant entropy layer which hardly exits in the case of the VKI experiments with a sharp leading edge plate. This difference probably explains the fact that the dimensions of the roughness are smaller in the case of the Orbiter. Moreover, the comparison of these two sets of data indicates that the correlation parameter is not the Reynolds number based on the perturbation height but the perturbation height normalized by the local laminar boundary layer displacement thickness.

The normalized perturbation height is used to correlate the ratio of the Reynolds numbers based on the boundary layer momentum thickness in figure 11. The two sets of data are in good agreement and they both show that there exists a critical normalized perturbation height equal to about 1.5 and an effective normalized perturbation height equal to about 3.5.

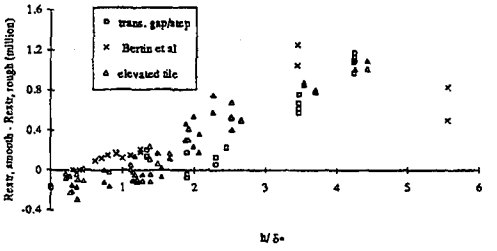

Fig. 10 : Change in Reynolds based on the location of the beginning of transition. Comparison with data from Bertin et al[12]

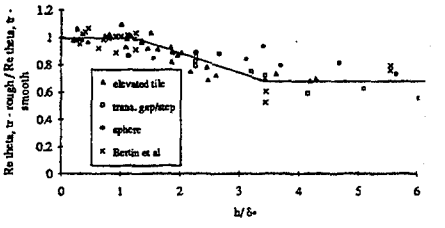

Fig. 11 : Correlation between the ratio of Reynolds numbers based on the boundary layer momentum thickness and the normalized perturbation height

Based on this last comparison, it is believed that the results obtained in the VKI wind tunnel on flat plates at Mach 6 are relevant for the application to the configuration of a re-entry vehicle. The comparison of the two sets of data also gives a good indication that the parameters that should be used to study the roughened induced transition are presumably the normalized perturbation height, the change in Reynolds number based on the beginning of transition and the ratio of the Reynolds numbers for the smooth and roughened cases based on the boundary layer momentum thickness computed at the transition location.

Concluding remarks

Several models simulating the roughness induced by a misalignment of the thermal protection system tiles of a re-entry vehicle were tested in a hypersonic Mach 6 wind tunnel using flat plates with sharp leading edges. For the transverse gap/step perturbation, a value of 2 is found for the critical step height normalized by the laminar boundary layer displacement thickness of the smooth plate computed at the perturbation position.
Experiments were also conducted on an elevated tile model with several configurations including variations of the height, the orientation and the slant of the tile as well as the presence of a gap around the tile. The experiments show that the most relevant case to study is the flat tile oriented at 45° with respect to the upstream flow direction. In this case, the presence of a gap around the tile does not modify the transition location and a value of about 1.5 is found for the critical normalized tile height.

Comparison with the van Driest and Blumer criterion shows that the predicted effective normalized perturbation height is too small. Experiments made with the transverse gap/step model at negative incidence give an indication that the Mach number effects are not properly accounted for in the van Driest and Blumer criterion.
Data are successfully compared with the experiments made by Bertin et al on an Orbiter model at 30° incidence in a Mach 8 wind tunnel. The comparison indicates that the parameters that should be considered are the perturbation height normalized by the boundary layer displacement

thickness, the change in transition Reynolds number or the ratio of the roughened to the smooth Reynolds numbers based on the boundary layer momentum thickness.
When these parameters are computed using the actual conditions at the boundary layer edge, it appears that the results obtained at VKI with sharp leading edge models are in very good agreement with data obtained with blunt bodies.

Acknowledgements

Dassault Aviation, the Centre National d'Etudes Spatiales and the European Space Agency are acknowledged for the financial support of this work which has been carried out within the Hermes R&D, R&Q programmes.
The authors are grateful to the research assistants R. Cajina, R. Klaput and M. Lucas, and to the Aeronautics/Aerospace technical staff for their contribution in the experiments.

References

1 G.A. Simeonides : "The VKI hypersonic facilities and associated measurement techniques." *Von Karman Institute TM* 46, November 1990.
2 J.F. Wendt : "Infrared thermography." *Proceedings of the 2nd Joint Europe/US Short Course on Hypersonics*, Colorado Springs, CO, Jan. 1989.
3 G.A. Simeonides, J.-P. Vermeulen, H.L. Boerrigter, J.F. Wendt : "Quantitative heat transfer measurements in hypersonic wind tunnels by means of infrared thermography." *IEEE Transactions on Aerospace and Electronic Systems*, Vol. 29, 3, July 1993, pp.878-893.
4 H.L. Boerrigter, J.-M. Charbonnier, M.K. Elbay : "Application of quantitative infrared thermography to the study of boundary layer transition in hypersonic flow." *Workshop'93 on Advanced Infrared Technology and Applications*, Capri, Italy, Sept. 20, 1993, pp. 113-141.
5 J.-M. Charbonnier, H.L. Boerrigter : "Contribution to the study of gap induced boundary layer transition in hypersonic flow." *AIAA Paper* 93-5111, 5th Int. Aerospace Planes and Hypersonics Technologies Conference, Munich Germany, Dec. 1993.
6 B. E. Richards : "Transitional and turbulent boundary layers on a cold flat plate in hypersonic flow." *The Aeronautical Quarterly*, Vol. XVIII part 3, August 1967, pp. 237-258.
7 W. D. Mc Cauley, A.R. Saydah, J.F. Bueche : "Effect of spherical roughness on hypersonic boundary layer transition". *AIAA J.*, Vol. 4, 12, Dec. 1966, pp. 2142-2148.
8 E. R. Van Driest, W. D. Mc Cauley : "The effect of controlled three dimensional roughness on boundary layer transition at supersonic speeds." *J. of the Aerospace Sciences*, April 1960, pp. 261-271.
9 E. R. Van Driest, C. B. Blumer : "Boundary layer transition at supersonic speeds. Three dimensional roughness effects (spheres)." *J. of the Aerospace Sciences*, August 1962, pp. 909-916.
10 E. R. Van Driest, C. B. Blumer : "Boundary layer transition at supersonic speeds. Roughness effects with heat transfer". *AIAA J.* Vol. 6, 4, April 1968, pp.603-607.
11 D. Arnal. "Laminar-turbulent transition problems in supersonic and hypersonic flows." *in AGARD Report* 761, June 1989.
12 J. J. Bertin, T. E. Hayden, W. D. Goodrich : "Shuttle boundary layer transition due to distributed roughness and surface cooling." *J. Spacecraft* Vol. 19, 5, Sept. Oct. 1982, pp. 389-396.

EXPERIMENTAL STUDY OF A TURBULENT FREE JET ISSUING FROM A SMALL-ASPECT-RATIO SHARP-EDGED RECTANGULAR SLOT

W. R. Quinn
Department of Engineering
St. Francis Xavier University
P. O. Box 5000
Antigonish, Nova Scotia
Canada B2G 2W5

ABSTRACT

The flow field of a turbulent free jet issuing from a sharp-edged rectangular slot of aspect ratio 2 has been studied experimentally. Hot-wire anemometry was used to measure all the three components of the mean velocity vector, the three Reynolds normal stresses, and the two Reynolds primary shear stresses. The mean flow field changed from a rectangular to an elliptical and finally to a circular shape at about thirty equivalent slot diameters downstream of the slot exit plane. This change in the shape of the mean flow field was brought about by spanwise and lateral gradients in the Reynolds normal and shearing stresses which were present in the region of interaction between the shear layers emanating from the long and short sides of the rectangular slot. Unlike that in a small-aspect-ratio elliptic jet, mass entrainment in this small-aspect-ratio rectangular jet was not found to be higher than that in a round turbulent free jet in the very near flow field, the region up to about three equivalent diameters downstream of the slot exit plane.

LIST OF SYMBOLS

A,B	=	constants in the hot-wire exponent power-law
Bhlf	=	general half-velocity width
D_e	=	equivalent diameter
E	=	hot-wire output voltage
Q	=	mass flow at a streamwise location
Q_o	=	mass flow at the slot exit plane
Q_s	=	secondary flow velocity vector
U	=	mean streamwise velocity
U_{Cl}	=	mean streamwise velocity on the jet centreline
U_{eff}	=	effective hot-wire cooling velocity
U_{exit}	=	mean streamwise velocity at the centre of the slot exit plane
$\overline{u'^2}$	=	streamwise Reynolds normal stress
$\sqrt{\overline{u'^2}}$	=	rms streamwise fluctuating velocity
$\overline{u'v'}$	=	spanwise Reynolds primary shear stress
$\overline{u'w'}$	=	lateral Reynolds primary shear stress
V	=	mean spanwise velocity
$\overline{v'^2}$	=	spanwise Reynolds normal stress
$\sqrt{\overline{v'^2}}$	=	rms spanwise fluctuating velocity
W	=	mean lateral velocity
$\overline{w'^2}$	=	lateral Reynolds normal stress

$\sqrt{\overline{w'^2}}$ = rms lateral fluctuating velocity
X = streamwise coordinate
Y = spanwise coordinate
Yhlf = half-velocity width of the jet in the Y-direction
Z = lateral coordinate
Zhlf = half-velocity width of the jet in the Z-direction

INTRODUCTION

The usefulness of rectangular jets in industrial applications cannot be overemphasized. Indeed these jets feature prominently in the aerospace and other industrial areas. It is difficult, for reasons of installation, to use nozzles with smoothly contoured upstream shaping in some applications. The jets in such cases then have to issue from slots, with sharp edges, cut in flat surfaces. Rectangular jets issuing from sharp-edged slots have, therefore, been the subject of a number of experimental studies[1]-[11]. The study of Quinn[10] has shown that the rate at which these jets mix with the surrounding fluid increases with increase in the slot aspect ratio provided that the jets remain three-dimensional. Apparently, mass entrainment in the near flow field of a small-aspect-ratio elliptic jet[12] is significantly higher than that found in a circular jet. One of the two objectives of the present study is to evaluate mass entrainment into a small-aspect ratio rectangular jet and to compare the results to those for a large-aspect-ratio rectangular jet and to those for a circular jet. The second objective is to show the evolution of the mean flow and turbulence fields of the present jet.

The previously mentioned objectives are realized with detailed mean flow and turbulence data obtained with hot-wire anemometry. These detailed data can, in addition, be used to facilitate the turbulence modelling of three-dimensional flows. The slot exit plane Reynolds number, based upon the slot equivalent diameter (D_e = 0.0453 m), was about 2 x 10^5. The mean streamwise velocity and the streamwise turbulence intensity ($\sqrt{\overline{u'^2}}/U_{exit}$) at the centre of the slot exit plane were 60 m/s and 0.5%, respectively.

EXPERIMENTAL DETAILS

A sketch of the jet flow facility, which is an open-loop, blower type and which has been described in detail elsewhere[10], is shown in Fig. 1a. It consists of a centrifugal fan, a settling chamber, a three-dimensional contraction and the sharp-edged rectangular slot. The rectangular slot, which is used to cap the downstream end of the three-dimensional contraction, consists of four mitred pieces of aluminium which are assembled in a 0.305m x 0.305m retaining plate. Two of the mitred aluminium pieces are shown in Fig. 1b.

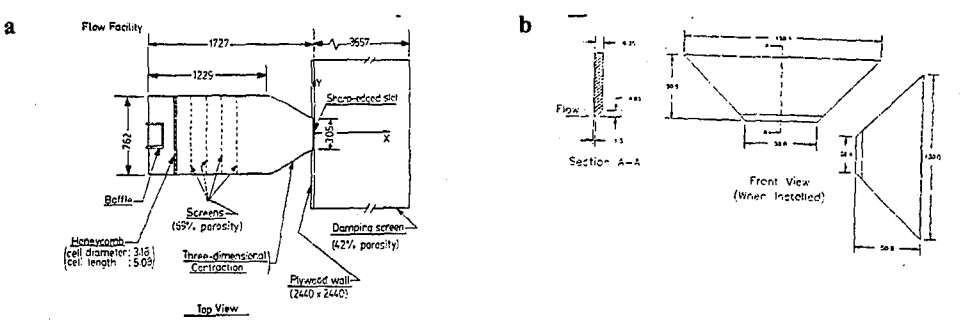

Fig. 1a,b Flow facility. **a** Top view; **b** Slot detail.

The hot-wire probe was moved in the flow field by means of a three-dimensional, microcomputer-controlled traversing system. The traversing system used a rack and pinion system in the streamwise direction and lead screws in the spanwise and lateral directions. The hot-wire probe could be positioned to within 0.3mm in the streamwise direction and to within 0.01mm in the spanwise and lateral directions.

DANTEC x-array hot-wire probes (55P51) were used for the measurement of the mean and fluctuating velocities. The hot-wire probes, operated by constant temperature anemometers at a resistance ratio of 1.8, were calibrated on-line on the jet centreline in the very near flow field against the output of a pitot-static tube connected to a pressure transducer and a Barocel electronic manometer. The calibration data were fitted to the exponent power law: $E^2 = A + BU_{eff}^n$ and A, B, and n were optimized with a linear least-squares goodness-of-fit procedure. A cosine law response to yaw was assumed and the effective angle was found from a yaw calibration following Bradshaw[13]. The hot-wire signals were linearized by the laboratory microcomputer and digitized, at about 1 KHz, by a 12-bit successive approximation A/D converter. A two-channel sample-and-hold unit with very low droop rate, two low-pass analog, antialiasing filters and amplifiers were used for signal processing and signal conditioning. Temperature variations from the calibration temperature were monitored with a thermocouple placed in close proximity to the hot-wire probe and corrections for such variations were made, using the procedure in Bearman[14] in the data-reduction software. The correction formulae derived by Champagne and Sleicher[15], for the effect of tangential cooling of x-array hot-wire probes, were also incorporated in the data-reduction software.

RESULTS AND DISCUSSION

The mean streamwise velocity contours are shown in Fig. 2. The dimensions on the plot boundaries in this figure and in all subsequent figures showing contour maps and velocity vectors are inches. The data for all contour maps and velocity vector plots were acquired on a grid at each streamwise measurement station. The grid spacing, which was kept constant at a given streamwise measurement station, was varied from 1.27mm at $X/D_e = 0$ to 12.5mm at $X/D_e = 30$. At the slot exit plane ($X/D_e = 0$), the mean streamwise velocity overshoots its local centreline value, due to the vena contracta effect, by as much as 15%. Slightly downstream of the exit plane, at $X/D_e = 0.25$, the mean streamwise velocity contours have the rectangular shape prescribed by the slot and remnants of the velocity overshoots from the slot exit plane are still evident. At $X/D_e = 0.8$, the mean streamwise velocity contours take on a diamond shape which persists at $X/D_e = 2.5$. The sides of the jet at $X/D_e = 0.25$ are inverted at $X/D_e = 4.2$ and this inverted shape is maintained at $X/D_e = 20$. The mean streamwise velocity contours are fully axisymmetric at $X/D_e = 30$. The change in shape of the mean streamwise velocity contours from rectangular to diamond to elliptical and finally to circular is attributable to turbulence-generated secondary flows (Prandtl's secondary flows of the second kind)[16]. Similar to the interaction of two boundary layers in the corner of a non-circular duct, the shear layers emanating from the long and short sides of the rectangular slot also interact and spanwise and lateral gradients of the Reynolds normal and shearing stresses in the interacting flow region will generate vortices which then trigger secondary circulatory flow in the YZ plane. Figure 3 shows contours of the turbulence anisotropy gradients ($(\partial^2(\overline{v'^2}-\overline{w'^2})/\partial Y\partial Z)\, D_e^2/U_{Ct}^2$) and the contours of the Reynolds primary shear stress gradients. It is clear that the shapes of the mean streamwise velocity contours are intimately linked to those of the Reynolds stress gradients shown in Fig. 3.

The secondary flow velocity vector plots are shown in Fig. 4. The vectors at $X/D_e = 0$ are, consistent with the vena contracta effect, directed towards the centre of the jet. The

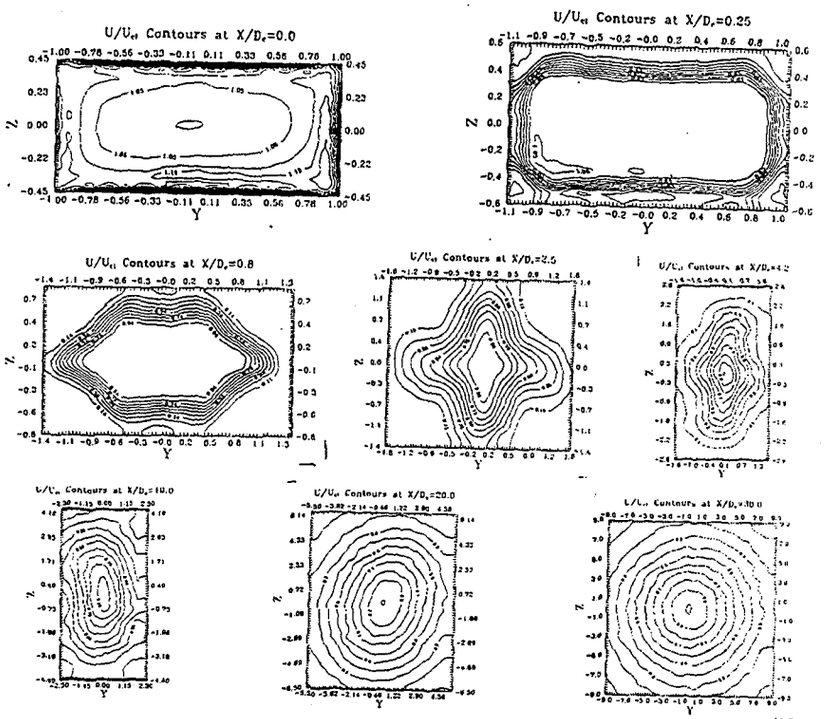

Fig. 2 Mean streamwise velocity contours.

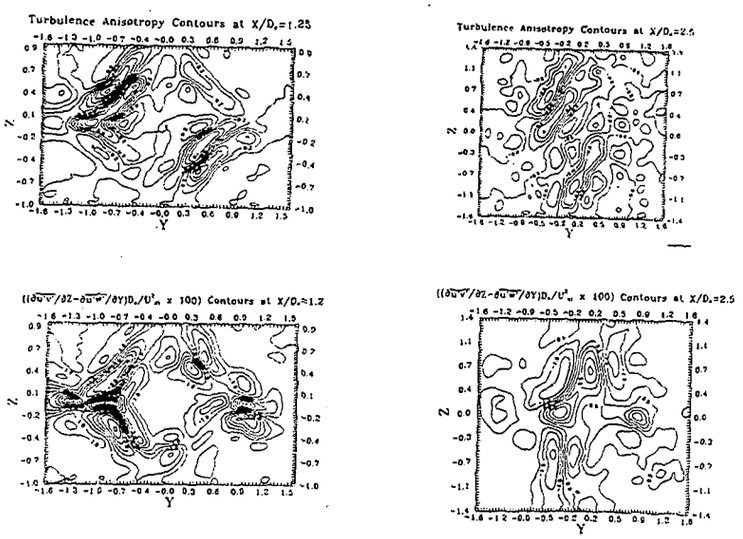

Fig. 3 Turbulence anisotropy gradient and Reynolds primary shear stress gradient contours.

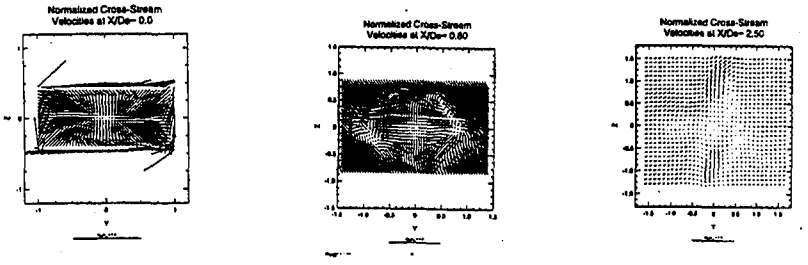

Fig. 4 Secondary flow velocity vector plots.

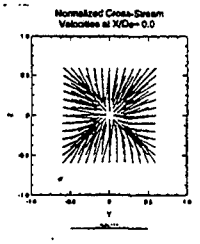

Fig. 5 Secondary flow velocity vectors at the exit plane of a square jet issuing from a sharp-edged slot.

vectors also reveal a strong peripheral clockwise rotational motion. The existence of such a swirling-type motion at the exit plane of a rectangular jet issuing from a sharp-edged slot has been known for some time now[17]; it is due to variations in the pressure field, brought about by differences in the curvature of the streamlines as a result of the difference in length between the long and short sides of the slot, in the upstream flow closest to the slot exit plane. This means then that such a swirling-type motion must be absent in jets issuing from a sharp-edged square slot as indeed Fig. 5 shows. It should be noted that the data for Figs. 4 and 5 were obtained in the same flow facility; the swirling-type motion shown in Fig. 4 at $X/D_e = 0$ can, therefore,not be considered to be a facility-dependent phenomenon. One aspect of the observed swirling-type motion, namely, the preferred (clockwise) direction, remains a puzzle. The secondary flow velocity vectors at $X/D_e = 0.8$ and at $X/D_e = 2.5$ (Fig. 4) help to illustrate the complex nature of this apparently simple flow.

The mass entrainment into the jet has been calculated by numerical quadrature (Simpson's rule) and the results are shown in Fig. 6 along with the results for a rectangular jet of aspect ratio 20, the data of Ho & Gutmark[12] for an elliptic jet of aspect ratio 2 and the data of Hill[18] for a circular turbulent free jet. It is clear that for rectangular jets, mass entrainment into the jet increases with increase in the slot aspect ratio. This is consistent with the finding, made in the study of Quinn[10], that mixing in rectangular jets increases with increase in the slot aspect ratio. The results shown in Fig. 6 also indicate that mass entrainment into an elliptic jet of aspect ratio 2 in the near flow field is significantly larger than that into a rectangular jet of the same aspect ratio.

The development of the jet half-velocity widths in the two central planes of symmetry (X-Y and X-Z) is shown in Fig. 7. The jet half-velocity width is the distance from the streamwise axis of a point in the flow field at which the mean streamwise velocity is half its value on the streamwise axis. The results of Tsuchiya et al.[7] are included for comparison.

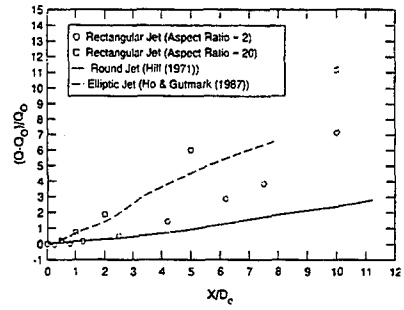

Fig. 6 Mass entrainment into turbulent free jets.

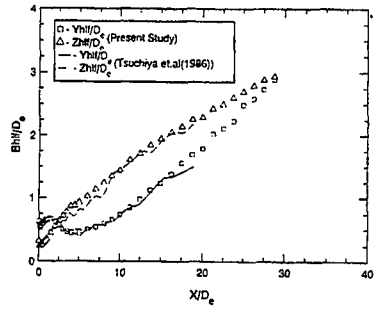

Fig. 7 Development of the jet half-velocity widths.

The agreement between the two sets of data is very good. The reader interested in the spreading rates (dYhlf/dX and dZhlf/dX) of the rectangular jet of the present study is referred to the study of Quinn[10]. Zhlf grows monotonically with downstream distance while Yhlf, which is initially larger than Zhlf, increases up to about $X/D_e = 2$ and then decreases up to about $X/D_e = 5$ before it finally increases monotonically with downstream distance. Zhlf and Yhlf cross-over at about $X/D_e = 2.5$ after which Zhlf becomes larger than Yhlf. It should be recalled that the mean streamwise velocity contours already had an inverted rectangular shape at $X/D_e = 4.2$. Zhlf and Yhlf are approximately the same at $X/D_e = 30$ where the mean streamwise velocity contours become axisymmetric. The initial increase in Yhlf in the present small-aspect-ratio rectangular jet is unlike the behaviour of Yhlf in larger-aspect-ratio rectangular jets[10] in which Yhlf decreases initially. Abramovich[19] has shown that the behaviour of Yhlf and Zhlf in the mixing region of rectangular jets is governed by the pressure field induced by the shear-layer vortices. A rectangular vortex ring generated from these vortices will have higher pressure on its shorter sides since these sides are farther away from the centre of the ring than the longer sides. The resulting pressure imbalance will drive flow from the shorter sides to the longer sides in the plane of the ring cross-section and thus account for the increase in Zhlf and the decrease in Yhlf in the mixing region. When the shear layers emanating from the short sides of the slot merge on the jet centreline, the shear-layer vortices would have diffused and the behaviour of Zhlf and Yhlf will be governed purely by mass entrainment into the jet and hence the monotonic growth of both Zhlf and Yhlf with downstream distance beyond the mixing region. The initial growth of Yhlf in lower-aspect-ratio rectangular jets[10] must be due to the fact that these jets have longer potential cores[10]

which inherently delay the formation of the shear-layer vortices and thus leave mass entrainment as the means by which Yhlf grows in such jets initially.

The variation of the streamwise ($\sqrt{\overline{u'^2}}/U_{exit}$), spanwise ($\sqrt{\overline{v'^2}}/U_{exit}$), and lateral ($\sqrt{\overline{w'^2}}/U_{exit}$) turbulence intensities along the jet centreline is shown in Fig. 8. The steep increase in all the turbulence intensities in the very near flow field is brought about by the growth and interaction of the shear layers on all four sides of the jet. All Three turbulence intensities peak at about $X/D_e = 6$. It is clear that the turbulence intensities, which are produced in the shear layers, are transported by diffusion and convection to the jet centreline; hence the peak in the turbulence intensities indicates the arrival of the shear-layer structures at the jet centreline. The turbulence intensities seem to have reached a self-preserving state at $X/D_e = 55$.

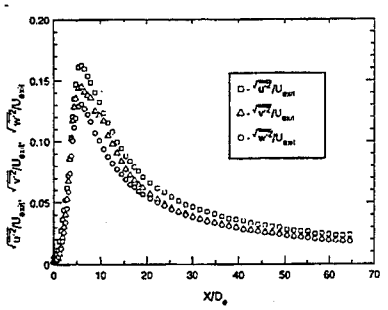

Fig. 8 Variation of the turbulence intensities along the jet centreline.

Contour maps of the Reynolds normal and primary shear stresses are available but are, for space reasons, not presented here. The shapes of these contours are similar to those of the mean streamwise velocity at the corresponding streamwise locations.

CONCLUSIONS

Detailed time-averaged data for the mean streamwise velocity, the secondary flow velocity, the Reynolds normal stresses, and the Reynolds primary shear stresses have been provided by this experimental study of a turbulent free jet issuing from a small-aspect-ratio sharp-edged rectangular slot. Mass entrainment into the jet, Reynolds stress gradients, and the jet half-velocity widths have been calculated from the appropriate data.

The following conclusions, from the available data, can be drawn:

1. A swirling-type of secondary flow is present at the exit plane of rectangular jets issuing from sharp-edged slots; this secondary flow, which has a preferred clockwise rotation, is not a facility-dependent phenomenon and it is not found in jet flows issuing from sharp-edged square slots.
2. The very near flow field of a rectangular jet issuing from a sharp-edged rectangular slot of aspect ratio 2, is dominated by a complex pattern of secondary flows.
3. The mean streamwise velocity field changes shape from rectangular to diamond to elliptic before becoming axisymmetric at $X/D_e = 30$. The change in shape is brought about by spanwise and lateral gradients of the Reynolds normal and shearing stresses. Such Reynolds stress gradients generate vortices which are referred to turbulence-generated secondary flows (Prandtl's secondary flow of the second kind).
4. Mass entrainment into turbulent free rectangular jets, issuing from sharp-edged slots, increases with increase in the slot aspect ratio.
5. The initial increase in the jet half-velocity width in the central plane of the slot major

axis is due to mass entrainment into jet while the subsequent decrease in this quantity is due to the pressure imbalance generated by the shear-layer vortices.

6. The turbulence field reaches a self-preserving state at about $X/D_e = 55$.

ACKNOWLEDGEMENT

This study was supported by a grant from the Natural Sciences and Engineering Research Council of Canada.

REFERENCES

1. Sfeir, A. A. 1976: The velocity and temperature fields of rectangular jets. Int. J. Heat Mass Transfer **19**, 1289-1297.
2. Sfeir, A. A. 1979: Investigation of three-dimensional rectangular jets. AIAA J. **17**, 1055-1060.
3. Marsters, G. F. 1979: The effects of upstream nozzle shaping on incompressible turbulent flows from rectangular nozzles. Trans. CSME **5**, 197-203.
4. Marsters, G. F.; Fotheringham, J. 1980: The influence of aspect ratio on incompressible, turbulent flows from rectangular slots. Aeron. Q. **31**, 285-305.
5. Marsters, G. F. 1981: Spanwise velocity distributions in jets from rectangular slots. AIAA J. **19**, 148-152.
6. Quinn, W. R.; Pollard, A.; Marsters, G. F. 1983: Measurements in a turbulent rectangular free jet. Proc. 4th Sym. Turbulent Shear Flows, Karlsruhe, Germany, 7.1-7.6.
7. Tsuchiya, Y.; Horikoshi, C.; Sato, T. 1986: On the spread of rectangular jets. Exp. Fluids **4**, 197-204.
8. Pollard, A.; Schwab, R. R. 1988: The near-field behavior of rectangular free jets: An experimental and numerical study. Proc. 1st World Conf. on Exp. Heat Transfer, Fluid Mech. and Thermodyn., Elsevier, New York, 1510-1517.
9. Quinn, W. R. 1991: Passive near-field mixing enhancement in rectangular jet flows. AIAA J. **29**, 515-519.
10. Quinn, W. R. 1992: Turbulent free jet flows issuing from sharp-edged rectangular slots: The influence of slot aspect ratio. Exp. Thermal Fluid Sci. **5**, 203-215.
11. Quinn, W. R. 1994: Development of a large-aspect-ratio rectangular turbulent free jet. AIAA J. **32**, 547-554.
12. Ho, C.-M.; Gutmark, E. 1987: Vortex induction and mass entrainment in a small-aspect-ratio elliptic jet. J. Fluid Mech. **179**, 383-405.
13. Bradshaw, P. 1975: An introduction to turbulence and its measurement, Pergamon Press, Oxford.
14. Bearman, P. W. 1971: Corrections for the effect of ambient temperature drift on hot-wire measurements in incompressible flow. DISA Info. **11**, 25-30.
15. Champagne, F. H.; Sleicher, C. A. 1967: Turbulence measurements with inclined hot-wire probes - Pt. 2: Hot-wire response equations. J. Fluid Mech. **28**, 177-182.
16. Bradshaw, P. 1987: Turbulent secondary flows. Ann. Rev. Fluid Mech. **19**, 53-74.
17. Owczarek, J. A.; Rockwell, D. O. 1972: An experimental study of flows in planar nozzles. ASME J. Basic Eng. **94**, 682-688.
18. Hill, B. J. 1971: Measurement of local entrainment rate in the initial region of axisymmetric turbulent air jets. J. Fluid Mech. **51**, 773-779.
19. Abramovich, G. N. 1982: On the deformation of the rectangular turbulent jet cross-section. Int. J. Heat Mass Transfer **25**, 1885-1894.

CONTROL OF TWO PARALLEL PLANE JETS WITH ACOUSTIC EXCITATION

J. C. S. Lai and A. Nasr

Department of Aerospace and Mechanical Engineering, University College
The University of New South Wales, Canberra, ACT 2600, AUSTRALIA

ABSTRACT

The flow field of unventilated two parallel plane jets under controlled acoustic excitation introduced at the outer shear layer mode has been studied using LDA. The effect of excitation on the distributions of mean velocity components, turbulence intensities and Reynolds shear stress is presented. Overall, excitation reduces the merging length and combined length of the parallel jets and the size of the potential core of individual jets.

1. INTRODUCTION

Unventilated parallel plane jets have been studied in the past primarily because of their potential technological applications such as in entrainment and mixing processes. The classification of the flow field of parallel plane jets into converging, merging and combined regions (Fig.1) is quite well known. However, few measurements were reported for the converging region because of measurement difficulties experienced in the recirculation zone. LDA measurements of the velocity field for two parallel plane jets with nozzle aspect ratio of 24 and nondimensional nozzle spacing (s/w) of 4.25 were presented for the first time in (1). For technological applications and for providing further understanding of the dynamics of parallel jets, it is interesting to investigate how parallel plane jets can be controlled by acoustic excitation.

The evolution of large-scale quasi-periodic turbulent motions, known as coherent structures, can be considered as a combination of interacting instability waves. The evolution, development and merging processes of coherent structures play an important role in the energy and momentum transport phenomena. Various methods of instability control have been studied by many investigators to manipulate the instability characteristics of shear layers [(2)-(8)].

In their studies of parallel interacting jets, Ko & Lau[(9)] found respective trains of coherent structures in the merging and combined regions. They stated that besides the pairing of successive initial vortices which involves deceleration and outward movement of the leading vortex and acceleration and inward movement of the trailing vortex, there is an amalgamation or combination of successive vortices without rotation. Nasr & Lai[(1)] has shown that, in their studies of two parallel plane jets, the fundamental vortex roll up frequency in the outer and inner shear layer is essentially the same and its associated subharmonic development can be identified.

The primary objective of this paper is, therefore, to document how the spatial development of parallel plane jets can be controlled by exciting the flow at the fundamental vortex roll up frequency in the outer shear layer. Comparisons of the mean velocity, turbulence intensity and Reynolds shear stress are made between the excited and unexcited jets.

2. APPARATUS AND INSTRUMENTATION

The unventilated parallel plane jet facility, shown schematically in Fig.1, has been described in ref.(1). Briefly, the two plane nozzles, each of width (w) 10 mm and length (l) 240 mm, have a nozzle aspect ratio of 24 and are separated by 42.5 mm (s/w=4.25). The nozzle exit Reynolds number is 11,000 with a streamwise turbulence intensity u'/U_o of 0.01 on the jet axis at the exit of each nozzle. Except for the streamwise fluctuation spectra, u'(f), which were obtained using a single hot-wire, all measurements reported here were obtained using a DANTEC two colour laser Doppler anemometer. Both the hot-wire and LDA systems have been described in ref. (1) and will not be repeated here.

As reported in ref. (1), the fundamental instability frequency (f_o) for the parallel plane jets has been found to be 2400 Hz at a nozzle exit Reynolds number of 11,000. Controlled excitation was introduced by two Realistic Minimus 7W loudspeakers located symmetrically in the settling chamber upstream of the nozzles. The loudspeakers were driven by a Bruel &Kjaer 2706 power amplifier with a sinusoidal signal at 2400 Hz supplied by a Feed Instrument function generator FG 601. As the acoustic wavelength is relatively large compared with the nozzle width, the acoustic wave field in the settling chamber is uniform. The excitation level, defined as v'_{ex}/U_o by Gutmark & Schadow[10], was 0.019. Here v'_{ex} is transverse velocity fluctuation measured at x/w=0.8 on the jet axis. In this study, experiments were conducted in a relatively large and quiet basement in order to reduce the effect of surrounding noise. The spectra of turbulence intensity obtained at the nozzle exit on the jet axis indicate no spatial disturbances associated with the jet rig.

3. RESULTS

3.1 Spectral measurements

Fig. 2 shows the spectra of x-component fluctuation obtained at x/w=0.7 in the inner and outer edges of the potential core under excited and unexcited conditions. In both inner and outer layers, the fundamental vortex rolls up at 2400 Hz. However, the development of the fundamental vortex appears to be faster and stronger in the outer shear layer than in the inner shear layer whose development is constrained by the recirculation zone. As seen in Fig.2, under excitation, the second subharmonic ($f_o/4$) has already appeared by x/w=0.7 while only the first subharmonic ($f_o/2$) has just started to develop in the inner shear layer. Fig. 3 shows the instability behaviour of the jet in time domain at x/w=1 at the inner edge of the potential core. It is clear that the instability wave is more organised and periodic in the excited jet than in the unexcited jet. Subharmonics and higher order harmonics are also present in the excited jet.

3.2 Variation of static pressure on x-axis

The variation of static pressure, $(P_c - P_{atm})/0.5\rho U_o^2$, on the axis of symmetry (x-axis) is shown in

Fig. 4 for unexcited and excited conditions. The static pressure first decreases to a minimum value in the recirculation zone, around x/w=3 and 2.5 for unexcited and excited jets respectively, and then increases to a maximum in the vicinity of the merging point. The location of maximum pressure on the x-axis has been found to be 4.7w and 4w for the unexcited and excited jets respectively. The pressure increase in the merging region is due to the merging of the individual jets on either side of the axis of symmetry. Downstream of the merging point, the static pressure on the x-axis decreases to below atmospheric as the two jets combine to spread as a single jet.

3.3 Mean velocities

Fig. 5 shows the spatial distribution of nondimensional mean x-component velocity (U/U_o) under excited and unexcited conditions. For x/w<3.5, reversed flow is detected in both the unexcited and excited jets; however, the stronger reversed flow (larger negative U) under excitation indicates higher deflection of the individual jet axis towards the axis of symmetry, which is evident in Fig. 5. Fig. 6 displays the spatial distribution of the nondimensional y-component velocity (V/U_o) for both the unexcited and excited jets. In the vicinity of the nozzle plate out to the vortex centre (x/w=3.5 and 2.5 for unexcited and excited jets respectively), V is positive and larger under excitation than that without excitation, thus indicating stronger upward motion of the recirculating flow for the excited jet. This is primarily due to the higher spreading rate of the excited inner shear layer (sections 3.4 and 3.5), resulting in a smaller recirculation zone. Downstream of the vortex centre within the recirculation zone, V turns negative and is larger in magnitude for the excited jet than for the unexcited jet, thus indicating stronger downward motion of the flow for the excited jet. Hence both the U and V results suggest stronger recirculating motion for the excited jet than for the unexcited jet. As the flow proceeds further downstream, the magnitude of V decreases for both the unexcited and excited jets until at around x/w=4.5 (the location of maximum pressure for the unexcited jet), it is less than that for the unexcited jet, thus indicating the merging process for the excited jet is at a more advanced stage than that for the excited jet. As the flow proceeds downstream of the combined point (x/w=7 and 8 for excited and unexcited jets respectively), V is positive everywhere when the two jets have combined to form a single jet .

It can be seen from Figs. 5 and 6 that the merging length and combined length of the two parallel jets have been reduced respectively from 4w to 3.5w and from 8w to 7w by controlled excitation.

3.4 Potential core

The effect of excitation on the spatial development of the two parallel jets can be illustrated by the size of the potential core. Fig. 7 shows the locations of the potential core in both the excited and unexcited jets. In a single free jet issuing from an identical nozzle, the potential core length has been determined to be 6w; by comparisons, the size of the potential core in interacting parallel jets has been reduced considerably. This is attributed to the deflection of the individual jets towards the axis of symmetry as a result of the formation of the recirculation zone with lower static pressrue (Fig. 4). The potential core length for the individual jet has been reduced by excitation from 4w to 2.5w. Furthermore, its extent in the y direction has also been significantly reduced, thus indicating that excitation introduced at the fundamental vortex roll up frequency enables the jet to spread faster in both the inner and outer shear layers.

3.5 Jet spreading

In order to illustrate the spreading of the jet, the variation of half-widths (b) in the inner and outer shear layers with downstream distances has been determined and plotted in Fig. 8 for both the unexcited and excited jets. Here half-width refers to the distance between the position of the local maximum x-component velocity (U_{max}) and the location where the local x-component velocity (U) is $0.5U_{max}$. It can be seen that both the inner and outer shear layers spread considerably faster through excitation. The effect of excitation on the initial spreading is more pronounced in the inner shear layer than in the outer shear layer. This could be attributed to the stronger deflection of the jet towards the axis of symmetry as a result of lower pressure in the recirculation zone under excitation. As shown in Fig. 9 which displays the location of the half-width ($y_{0.5}$) in the outer shear layer, the outer shear layer spreads faster in the converging and merging regions but slower once it has proceeded past the combined point.

3.6 Decay of maximum velocity

Fig. 10 shows the decay of nondimensional maximum x-component velocity (U_{max}/U_o)of the parallel jets under excited and unexcited conditions. It is clear that excitation has caused the maximum velocity to decay faster, and the velocity decay rate is faster in the converging region than in the merging region for both excited and unexcited conditions. This is due to the deflection of the jet towards the axis of symmetry and perhaps the interaction between the inner shear layer and the recirculation zone. Faster decay in the maximum velocity implies higher jet spreading, which is supported by Figs. 8 and 9. For comparisons, the decay of the maximum velocity for a single free jet with and without excitation is also shown in Fig. 10. It can be seen that excitation has caused the maximum velocity of a single free jet to decay faster. While the maximum velocity of a single free jet is higher than that of the parallel jets for $x/w<7$, it is considerably lower for $x/w>7$, indicating that the development of a single free jet is far more advanced than the two parallel jets combined as a single jet.

3.7 Entrainment

Fig. 11 shows the effect of the excitation on the jet volume entrainment $(Q- Q_o)/Q_o$. Here Q is the volume flow rate obtained by integrating the x-component velocity (U) from the axis of symmetry to the point where U is $0.95\ U_{max}$ and Q_o is the volume flow rate at the nozzle exit. Compared with the experimental values of volume entrainment for a single free jet[10] also shown in Fig. 11, the volume entrainment for parallel jets is higher in the converging region and is lower downstream of the merging point. This is consistent with the jet spreading and decay of maximum velocity as discussed in sections 3.5 and 3.6. Fig. 11 shows that through excitation, the volume entrainment has been increased in the converging region but decreased in the merging and combined regions.

3.8 Turbulence intensities

The spatial development of x-component (u') and y-component (v') turbulence intensities for both excited and unexcited jets are depicted in Figs. 12 and 13 respectively. Regardless of whether excitation has been applied, both u' and v' distributions exhibit two peaks in the inner and outer shear layers upstream of the merging point. In the converging region, excitation enhances both u' and v' in the inner and outer shear layers. This enhancement appears to be stronger in the inner shear layer and the recirculation zone. The peaks of u' and v' in the outer shear layer persist as the flow proceeds downstream. It should be noted that in addition to the u' peak in the inner shear layer, another peak in u' has been detected at x/w=2.5 close to the vortex centre in the recirculation zone. By x/w=3, the u' peak in the inner shear layer has merged with that in the recirculation zone. In the merging region, turbulence intensities (u' and v') have been reduced by excitation and approach that of the unexcited jet downstream of the combined point.

3.9 Reynolds shear stress

The effect of excitation on the spatial development of the Reynolds shear stress $\overline{u'v'}/U_o$) can be observed in Fig. 14. Reynolds shear stress in the converging region appears to be enhanced by excitation in both the inner and outer shear layers, thus indicating higher momentum transfer through acoustic excitation. In the recirculation zone, Reynolds shear stress for the excited jet is considerably increased around the vortex centre and merging point where the turbulent momentum transfer is high. In the merging region, Reynolds shear stress for the excited jet is lower than that of the unexcited jet. Downstream of the combined point, the distribution of the Reynolds shear stress resembles that of a single free jet and by x/w=14, there is virtually no difference between the excited and unexcited jets.

4. CONCLUSIONS

Acoustic excitation at the fundamental vortex roll up frequency in the outer shear layer has been applied to unventilated two parallel plane jets with nozzle aspect ratio of 24 and nondimensional nozzle spacing (s/w) of 4.25 . The effect of the excitation on the velocity field of the parallel jets at a nozzle exit Reynolds number of 11,000 has been studied using LDA. Results indicate that excitation enhances jet spreading and volume entrainment and reduces the maximum velocity and the size of the potential core in the converging region. The merging length and combined length has also been reduced through excitation.

ACKNOWLEDGEMENT

A. Nasr acknowledges receipt of a scholarship from Scholarship Department of Iran's Ministry of Culture and Higher Education to undertake this study.

REFERENCES

1. Nasr, A. and Lai, J.C.S. (1994) Mean Flow Characteristics of Two Parallel Plane Jets. 2nd Int. Conf. on Experimental Fluid Mechanics, 4-8 July Torino, Italy.
2. Lai, J.C.S. (1989) Some Instability Characteristics in Jets. *Tenth Australian Fluid Mechanics Conference*, University of Melbourne, 1.13-1.16.
3. Lai, J.C.S. (1984) Unsteady Effects in Mechanically - Excited Turbulent Plane Jets. *Int. J. Heat and Fluid Flow*, **15**(4) 215-221.
4. Lai, J.C.S. and Simmons, J.M. (1980) Instantaneous Velocity Measurements in a Periodically Pulsed Plane Turbulent jet. *AIAA J.*, **18**, 1532-1534.
5. Fiedler, H. and Mensing, P. (1985) The Plane Turbulent Shear Layer with Periodic Excitation. *J. Fluid Mech.* **150**, 281-309.
6. Zaman, K.M.B.Q. and Hussain, A. K. M. F. (1981) Turbulence Suppression in Free Shear Flows by Controlled Excitation. *J. Fluid Mech.* **103**, 133-159.
7. Thomas, F.O. (1990) An Experimental Investigation into the Role of Simultaneous Amplitude and Phase Modulation in the Transition of Plane Jet. Phys. Fluids A, **2**(4), 553-573.
8. Hussain, F. (1986) Coherent Structures and Turbulence. *J. Fluid Mech.* **173**, 303-35.
9. Ko, N.W.M. and Lau, K.K. (1989) Flow Structures in Initial Region of Two Interacting Parallel plane Jets. *Experimental and Fluid Science*, **2**, 431-449.

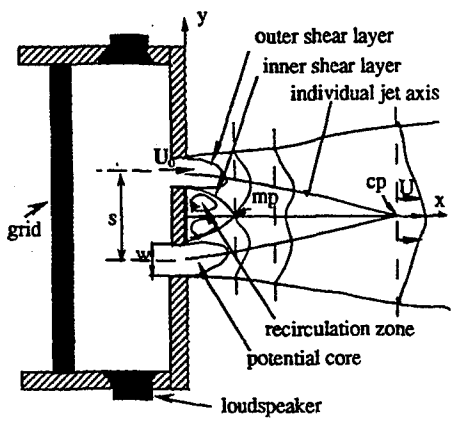

Fig.1 Schematic diagram of set-up for excited parallel jets.

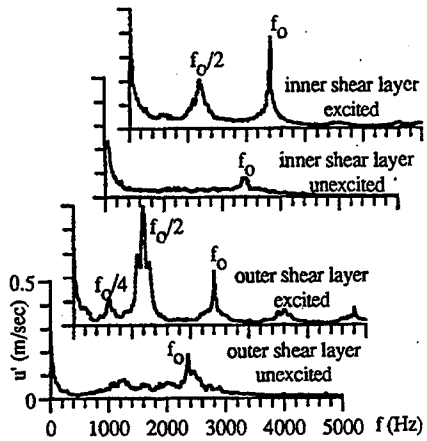

Fig.2 Spectra of u' in the inner and outer shear layers.

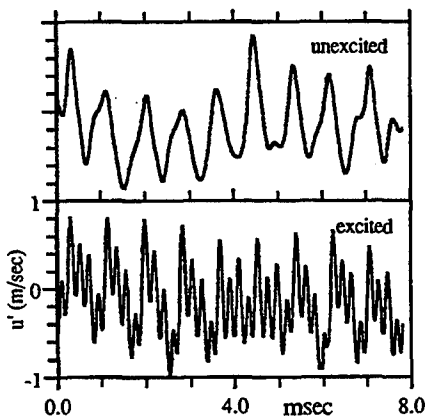

Fig.3 Hot-wire signal in the inner shear layer.

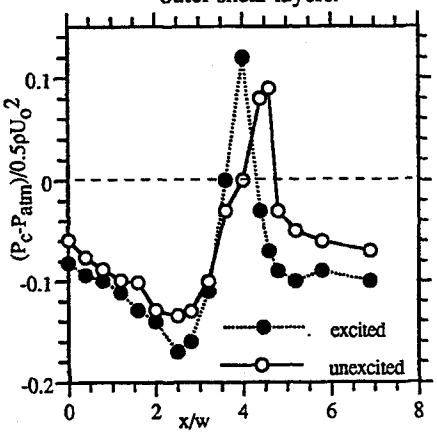

Fig.4 Variation of static pressure on x-axis with downstream distances.

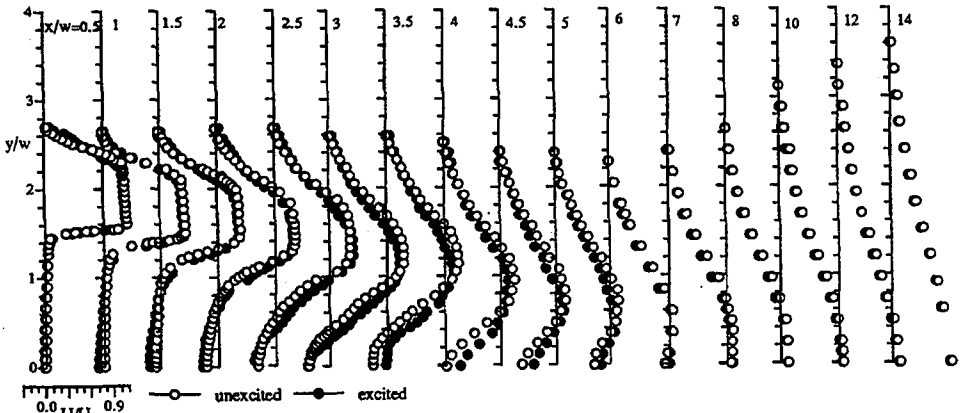

Fig.5 Spatial distribution of x-component velocity (U/U_o).

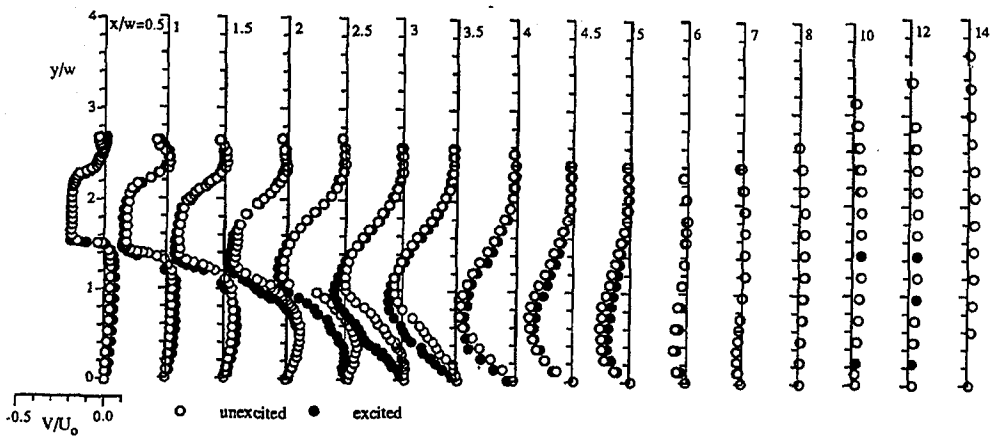

Fig. 6 Spatial distribution of y-component velocity (V/U_o).

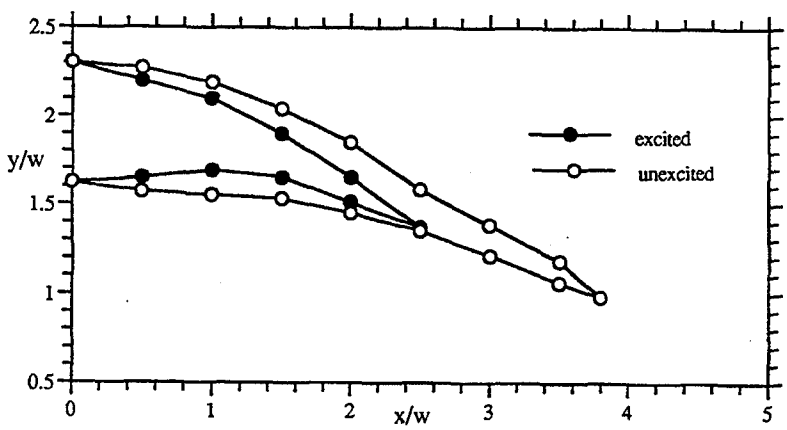

Fig.7 Potential core of the unexcited and excited jets.

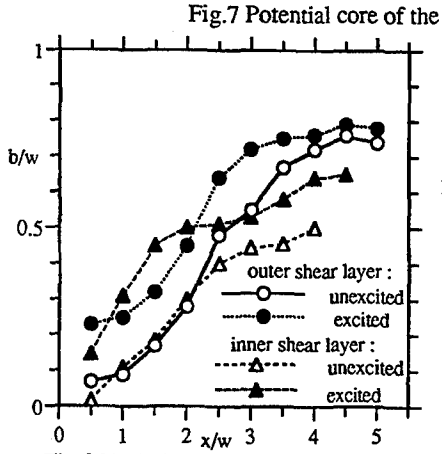

Fig.8 Variation of half-widths in inner and outer shear layers with downstream distances.

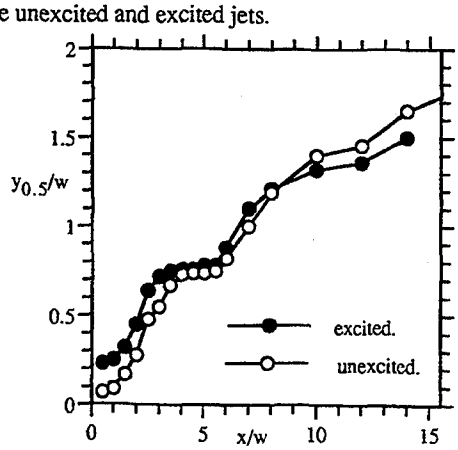

Fig.9 Location of half-width in the outer shear layer.

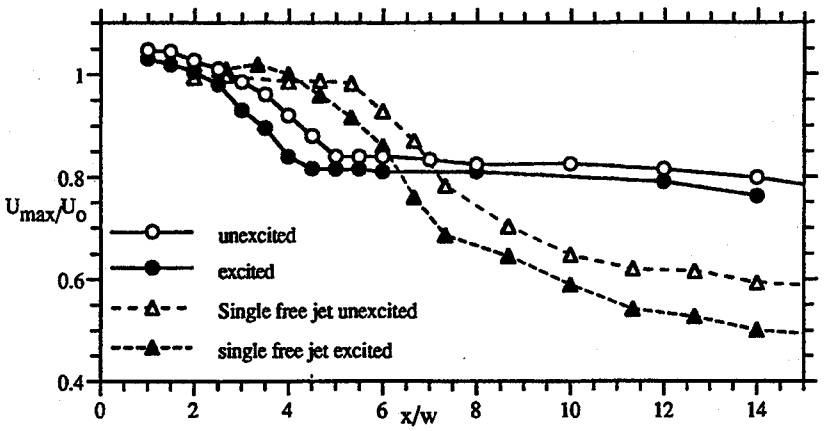

Fig.10 Variation of decay of maximum velocity with downstream distances.

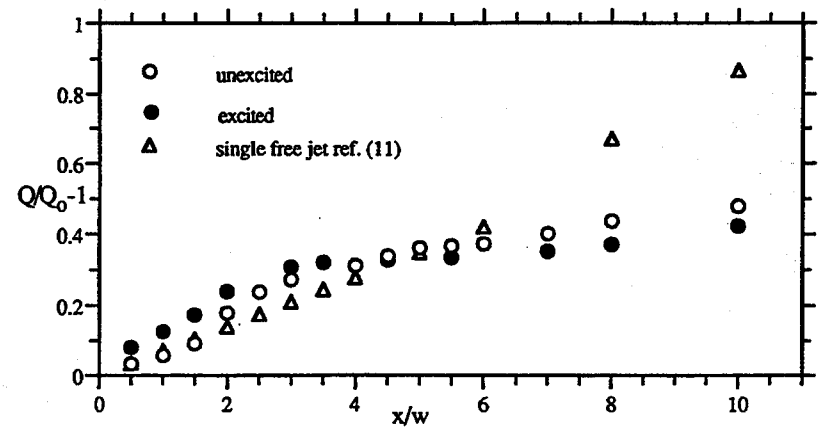

Fig.11 Variation of volume entrainment with downstream distances.

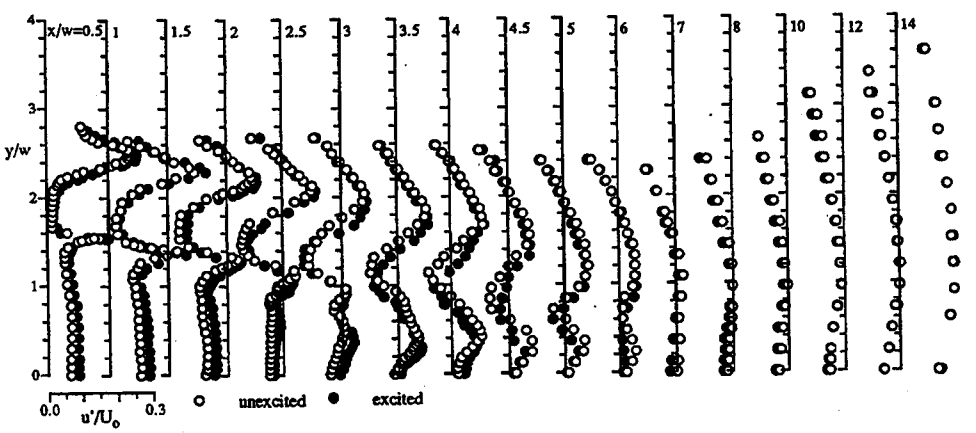

Fig.12 Spatial distribution of x-component turbulence intensity.

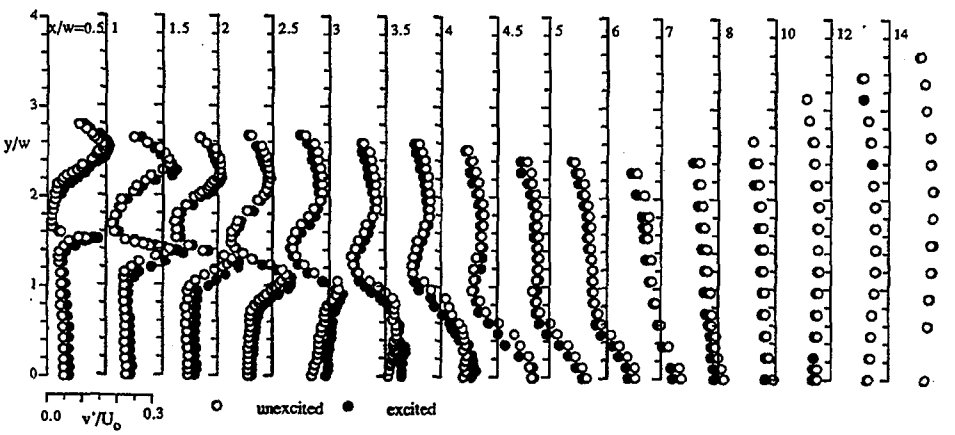

Fig. 13 Spatial distribution of y-component velocity (v'/U_o).

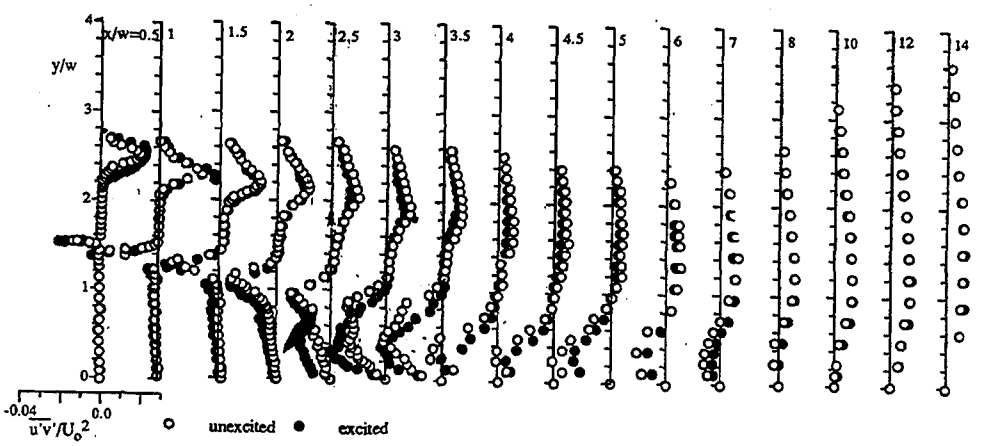

Fig. 14 Spatial distribution of Reynolds shear stress ($\overline{u'v'}/U_o$).

EXPERIMENTAL INVESTIGATION OF TURBULENT FLOW FIELD IN THE INTERACTION ZONE OF TWO OPPOSED JETS

M.MOUQALLID - P.PARANTHOEN - J.C.LECORDIER - R.BORGHI

URA 230 CNRS / CORIA - Université de Rouen
76821 Mont Saint Aignan Cedex - France

Abstract

This paper presents an experimental study in the interaction zone of two opposed turbulent jets. Velocity statistics have been measured using a two components laser Doppler velocimetry. The analysis of the dynamic field shows an increase of the turbulence and of the anisotropy in the interaction zone. Dynamic thicknesses of the interaction zone have been determined. The essential feature of the axial velocity probability density functions is its bimodal aspect in the interaction zone.

Introduction

The system consisting of two intersecting jets appears in various technological applications including chemical reactors, burners, rocket engine, internal combustion engine,....
During the past years, there has been a large number of investigations carried out on the interaction of jets with different configurations, such as parallel, coaxial and inclined jets. On the other hand experiments and information on opposed jets have been very limited, although the impingement of two opposed jets is often used in study of counterflow flames. In this area of combustion research, there have been many experimental and theoretical investigations in this configuration and most of the published work deals with visualization and studying extinction. However recently very few studies have been performed on nonreacting turbulent counterflow (1),(2),(3),(4).
The objective of the present communication is to present and discuss some results of the velocity field in the interaction zone of two circular opposed turbulent jets. This experimental study is concerned with symmetrical jets (jets with equal exit momentum rate).

Experimental facilities

Fig. 1 shows a schematic of the impingement region in two axisymmetrical jets flow field together with the definition of the coordinate system.
The two jets are issued from two circular tubes with the same diameter D (D=5 or D=10mm) and (34D or 17D) long, separated with a distance H. This distance could be adjusted to investigate the influence of velocity gradient along the centerline of this configuration. In this facility, a compressor supplies the air. The air is divided and follows through two pipes. The air follows into a stilling chamber fitted with grids and contractions for generating uniform mean flow with low turbulence.
An important feature to the understanding of the fundamentals of interaction of opposed jets is the axisymmetry structure of the resultant flow field. In our experimental configuration, this condition was difficult to realize due to the small dimensions of the jets. Our guide to the final alignment was obtained by the visualization of the flow field with tomography laser and by using a traverse mechanism which moved the two pipes with an accuracy of $\pm 1/10^{e}$ mm in the three directions.
Flow velocities were measured by a four beams two colors laser Doppler velocimeter (LDV) with a 3W Argon laser. Seeding is provided by silicon oil particles of 1µm generated by an atomizer. With this system, it was possible to measure simultaneously the axial component U (in the z-direction) and the radial component V (in the x-direction) of the velocity. The measurements volume of LDV consisted of 0.9 mm length of the focused laser beams, of approximately 0.08 mm diameter.

The LDV signals were analyzed by two counters wnich were interfaced with a PDP 11/34 computer.
In order to detect and reduce bias due to non uniform seeding of the two jets, statistics were obtained by two averaging procedures : classical ensemble averaging and time averaging. Time averaging was selected for the results presented here.
The Reynolds number based on the diameter of the nozzle was in the range of (4000-15000) and the ratio H/D ranged from 5 up to 40.
The origin of the coordinates was located on the axis at the inlet of the lower jet.
Velocity component U was taken to be positive in the z-direction and the velocity component V was to be positive in the x-direction.
Some of the results were presented using the parameter M defined as M=2z/H and corresponding to nondimensional locations on the axis of jets.(M=0 at exit of the lower jet, M=1 at the location of the stagnant plane).

Results and discussions

In this configuration, the two jets have the same initial momentum and the stagnation plane where the mean velocity U is zero, was found experimentally at equal distance H/2 from the inlets of the jets.

Flow visualization

Laser tomography is used for flow visualization by means of a laser sheet produced by a 3W Argon laser. The two jets were marked with smoke. Fig. 2 shows an example of flow visualization for the impingement of jets of equal exit velocity.
These visualizations provided an indication that the impingement of the two jets on each other led the complex resultant flow to oscillate around the stagnant plane location. These irregular oscillations have been also observed on the signals of the axial velocity component near the stagnation point (not shown). These signals showed clearly an alternation on the sign of this velocity about the value zero which corresponds to the location of the stagnation plane on the centerline of the jets.

Velocity field

Axial profiles

Axial evolutions of axial mean and fluctuating velocity are shown in Fig. 3 and Fig. 4 respectively. The evolution of the centerline velocity of the free jet is also presented for comparison. The characteristics of the free jet used in the present experiment were studied and compared (not shown) with available work published in the literature [5],[6] and were in a reasonable agreement with these results.
For the counterflowing jets, the axial evolution of the mean velocity is found symmetrical with respect to the stagnation plane. We can distinguish two zones. In the first zone, the mean velocity was found to have exactly the same behavior as the free jet. Then a second zone named the "interaction zone" where the first jet intercepts the other opposed jet. This interaction induces rapid decreasing of the mean velocity and a rapid increasing of the amplitude of the axial velocity fluctuation. The maximum value of the root mean square of the axial velocity fluctuations $\sqrt{\overline{u'^2}}$ was found at the stagnation point. It can be observed that the level of the amplitude of the axial fluctuating velocity increases more rapidly when H/D is reduced.
The limit of the interaction zone is defined in an arbitrary manner by the position where the curve of axial velocity was observed to diverge from that of the free jet. The total thickness of this zone measured for different Reynolds number and different values of H/D appeared to be approximately independent of D and with a mean value of about 0.2H:

$$0.15 < \frac{\Delta Z_u}{H} < 0.25 \text{ for } \frac{H}{D} > 10.$$

Where ΔZ_u denotes the thickness of the interaction zone.

Fig. 5 illustrates some probability density function (pdf) of the axial velocity at different locations downstream along the jets centerline. In the first zone corresponding approximately to $0<M<0.8$ and $1.2<M<2$, the pdf in the opposed jets was found similar to the pdf observed with a single free jet. Now in the interaction zone where M was about between 0.8 and 1.2, the shape of the pdf was modified. It appears in the Fig.5 that when M increase, a small portion of negative velocity appears, which indicates the alternating presence of the upper jet. This intermittency effect increases steadily. At the stagnation plane (M~1), both peaks of the pdf are of about the same magnitude. This bimodal distribution consists of contributions from both the flow coming from the lower jet and flow coming from the upper jet.

In order to evaluate the stretch rate, axial velocity profiles for different Reynolds number are plotted together in Fig 6 with U/U_c as a function of $(Z-Z_p)/(0.5\Delta Z_u)$. Here U_c is the velocity at the beginning of the interaction zone, Z_p is the position of the stagnant plane. The profiles are similar and can approximately be described by one single curve. The stretch rate estimated from the local velocity gradient in this zone, is of about $kU_c/\Delta Z_u$ where k is found to vary between 3 and 5.
These velocity results presented above are consistent with the analysis given by Mastorakos (3) and Kostiuk (4) concerning the interaction of two opposed jets. They can be explained by considering that the thin interface separating the two jets is moved by the velocity fluctuations and induces the intermittent character observed in the results.

Radial profiles

In the Fig. 7 the velocity vectors are plotted in the x,z plane. This figure shows the strong divergence of the flow near the stagnation region and the good axisymmetry of the velocity field.

Evolutions of axial and radial mean velocity , U and V with x/D at different M stations are shown in Fig. 8 and Fig. 9 respectively. In these figures,the mean velocities have been normalized by the jet exit velocity U_j.
As the flow approaches the stagnation plane, profiles of the axial velocity are found to be flat and the amplitude of this velocity decreases to zero. In parallel, the radial velocity profiles reach a maximum value at x/D ~1 on the stagnation plane.

Measurements of the axial and radial turbulent intensities, where the root mean square of the velocity fluctuations have been normalized by the exit velocity U_j and presented in Fig. 10 and 11. It appears that the values of the axial velocity increases strongly in the "interaction zone". The maximum value of 40% is observed on the centerline at the stagnant plane location while the value of this intensity was about 10% at the beginning of the "interaction zone"

The intensity of radial turbulence is also found to be increase as the stagnation plane is reached. But the level of $\sqrt{\overline{v'^2}}/U_j$ is always lower than $\sqrt{\overline{u'^2}}/U_j$. The maximum value of $\sqrt{\overline{v'^2}}/U_j$ about 20% is observed at x/D = 2 on the stagnation plane.
These results put in evidence that the structure of turbulence in the interaction zone is anisotropic and inhomogeneous.

In Fig. 12, some profiles of the Reynolds stress $\overline{u'v'}$ are presented. As M is significantly lower or larger than 1, we can observe the usual behaviour of the Reynolds stresses existing in turbulent jets. As the stagnant plane is approached these Reynolds stresses are found to be zero. In this plane, for each x/D, the probability density function presented in Fig. 13 are characterized by a single peak pdf around the zero value. The fact that a bimodal shape of the pdf is not observed indicates that a simple interface model is only valid close to the jet axis.

Conclusions

This paper presents an experimental study in the interaction zone of two opposed circular jets. The main results are summarized as follows:

- flow visualization and axial velocity signals indicates that strong oscillation of the stagnation point occurs;
- turbulence intensities in the axial direction are more higher substantial than the radial ones;
- pdf of axial velocity puts in evidence a clear bimodal behavior due to the intermittency in the interaction zone;
- the interaction zone has been characterized as a function of the distance between the two jets H and has been found to be about 0.2H;
- the Reynolds stresses $\overline{u'v'}$ are about zero at the stagnation plane;

References

1. Ogawa, N. and Maki, H. "*Studies on opposed turbulent jets*", Bulletin of JSME vol 29 , N 255, paper n° 85-0078, September 1986.

2. Rolon, J.C, Veynante, D.,and Martin, J.P "*Counter jet stagnation flows*" Experiments in Fluids 11, 313-324 (1991).

3. Mastorakos, E. Taylor, A. M. K. P. and Whitelaw, J. H. " *Mixing in turbulent opposed jet flows"* Ninth symposium on "turbulent shear flows" Kyoto, Japan,august 16-18,1993.

4. Kostiuk, L. W, Bray, K. N. C, and Cheng, R.K., "*Experimental study of premixed turbulent combustion in opposed streams. Part I - Nonreacting flow field*" Combustion and Flame. 92: 377-395.(1993).

5. Chua, L.P and Antonia, R.A "*The turbulent interaction region of a circular jet*". Int. Comm. Heat. Mass. Transfer 13, 545, (1986).

6. Corrsin, S. and Uberoi, M. "*Further experiments on the flow and heat transfer in a heated air jet*". NACA Rep 998. (1950).

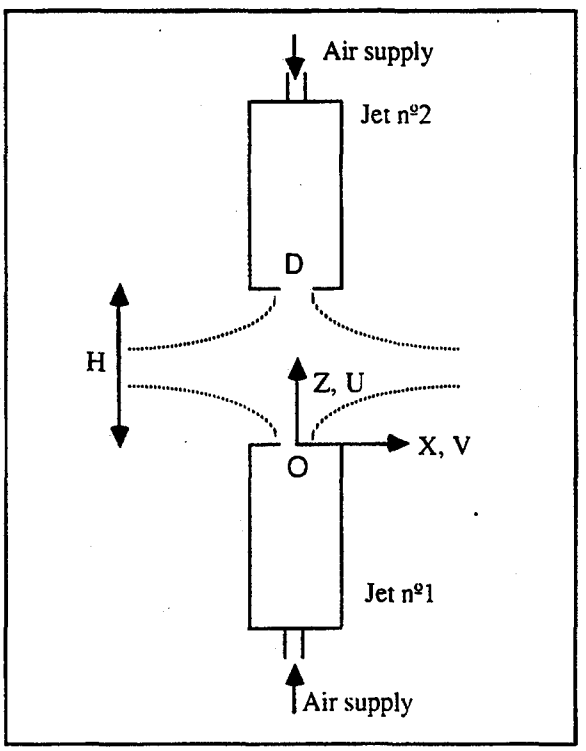

Fig.1 Schematic of impingement region in two axisymmetrical jets flow field

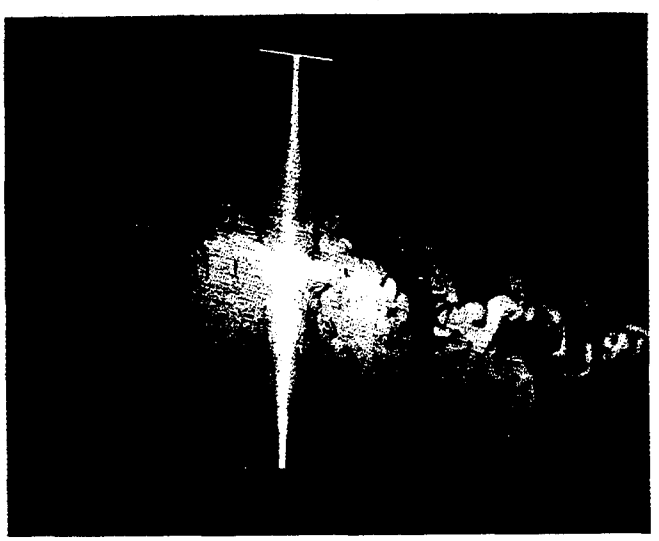

Fig. 2 Laser sheet visualization of the flow field

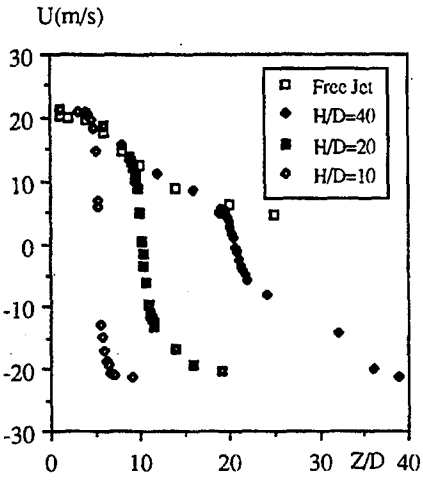

Fig. 3 - Evolution of mean axial velocity on the axis of jets, Re=6600, H/D=20

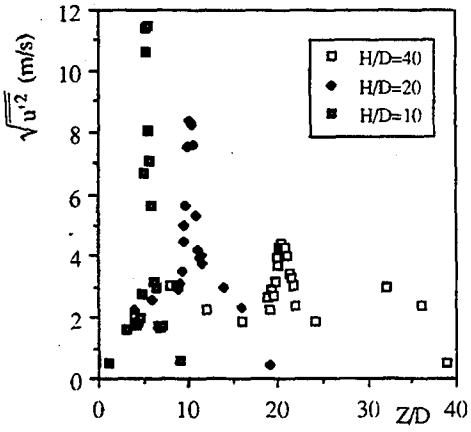

Fig. 4 - Evolution of axial velocity fluctuations on the axis of jets, Re=6600, H/D=20

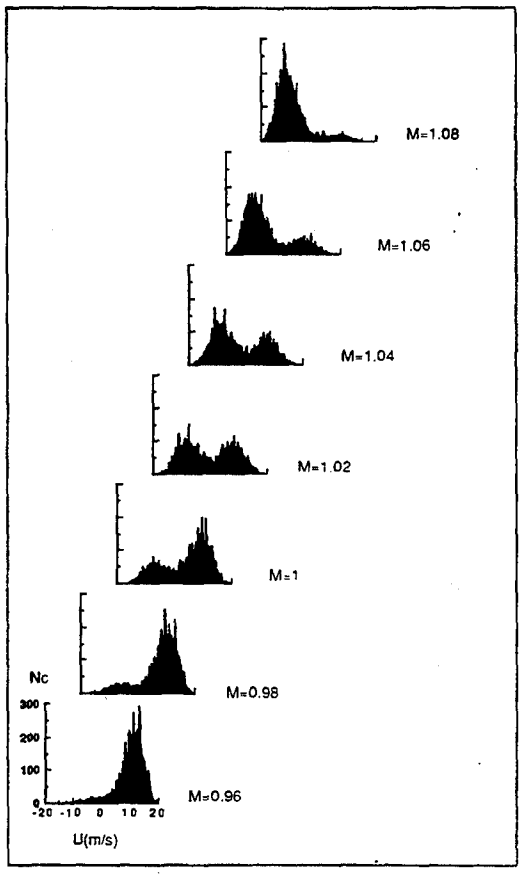

Fig. 5 - Probability density function of axial velocity on the axis of jets, Re=6600, H/D=20, X/D=0.

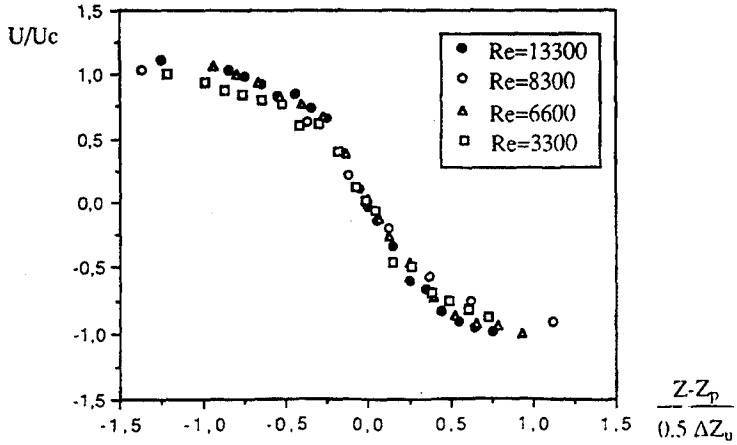

Fig. 6 - Normalized mean axial velocity along the centerline of the jets, H/D=20

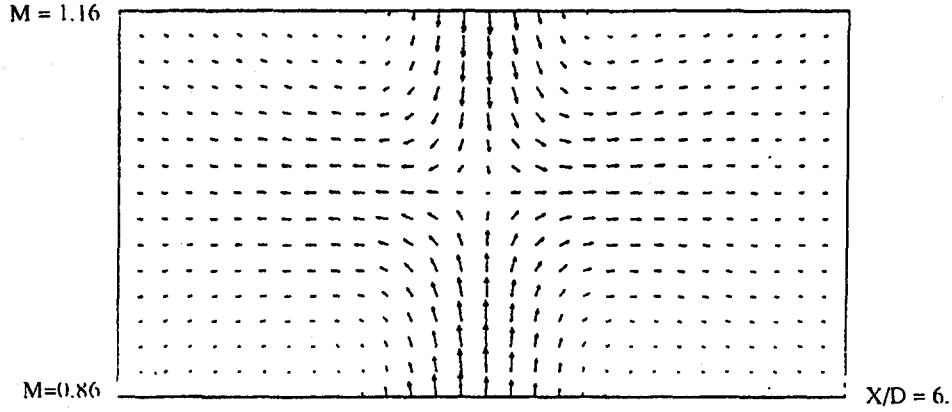

Fig. 7 - Mean velocity vector field, Max vector = 14.1m/s, Re = 6600, H/D = 20.

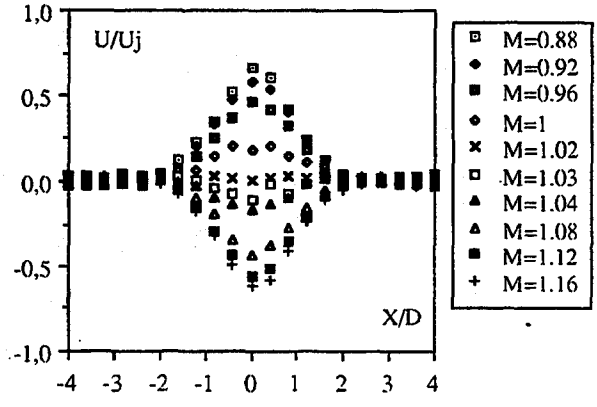

Fig. 8 - Radial evolution of axial component of the velocity.

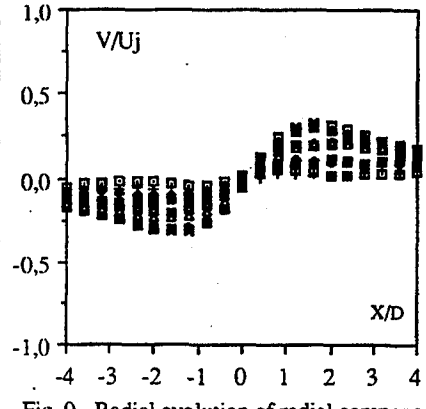

Fig. 9 - Radial evolution of radial component of the velocity.

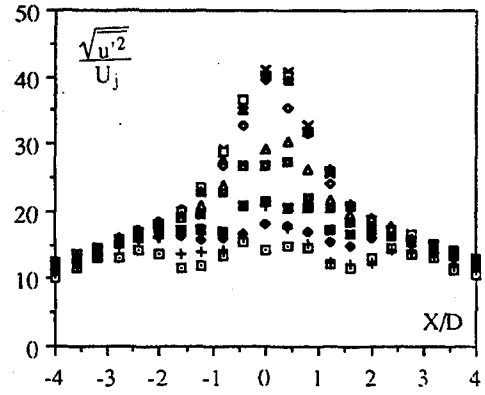

Fig. 10 - Axial turbulence intensity profiles

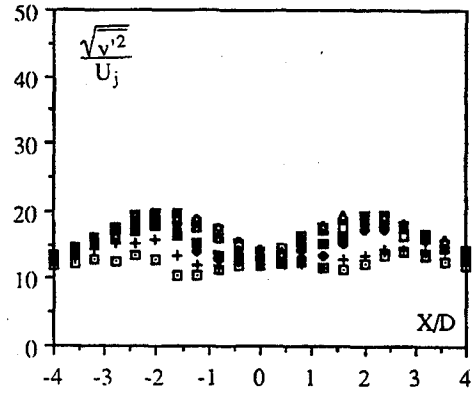

Fig. 11 - Radial turbulence intensity profiles.

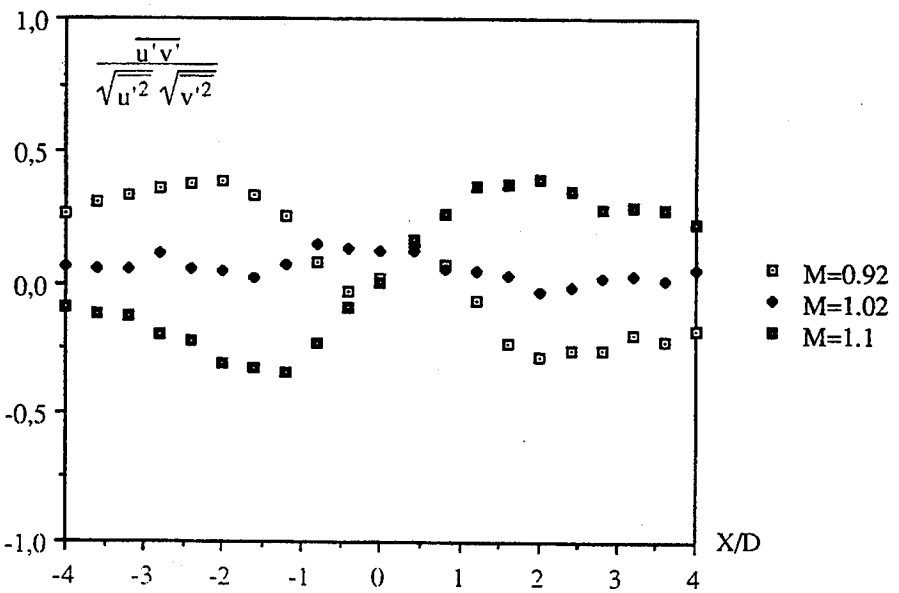

Fig. 12 - Evolution of Reynolds stress profiles

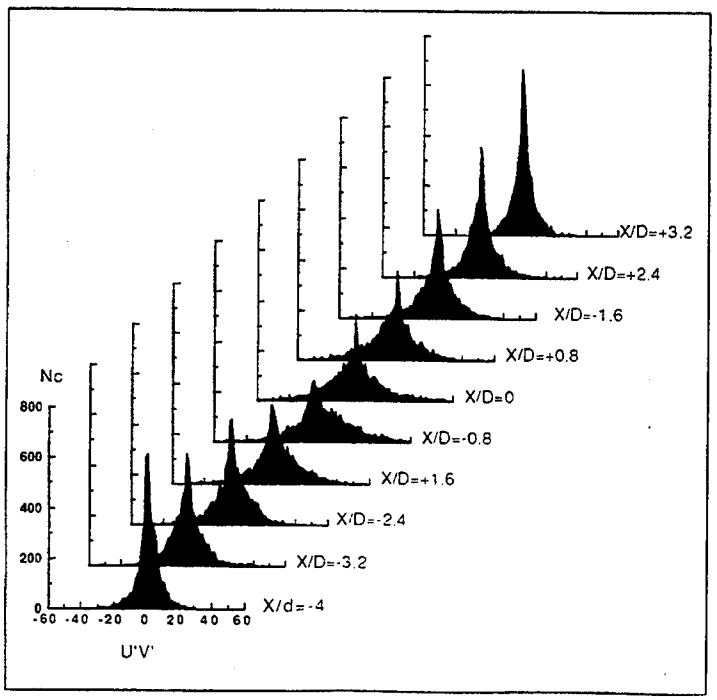

Fig. 13 - Probability density function of u'v' along the stagnation plane, M=1, Re=6600, H/D=20.

A COMPARATIVE STUDY OF THE SPECTRA OF TURBULENT JETS AND BOUNDARY LAYERS AT HIGH WAVENUMBERS

I. MARUŠIĆ, T.B. NICKELS AND A.E. PERRY

Department of Mechanical and Manufacturing Engineering
University of Melbourne, Parkville, Vic. 3052, Australia

This paper describes measurements of spectra taken in a coflowing jet and in a boundary layer with zero streamwise pressure gradient. The spectra are compared to examine universality of the small scales and to examine the scaling laws of Kolmogorov. Comparisons are also used to examine differences in the distribution of the Reynolds shear-stress spectra in wavenumber space between the two flows and these experimental observations are explained in terms of models for the turbulence structure which have been developed by the authors for each of these flows.

1. INTRODUCTION

The measurement of spectra in turbulent shear flows has long been a useful tool in examining its underlying structure. However, comprehensive measurements in a range of different shear flows are still scarce. Work in the past has often concentrated on a single shear flow and this has limited the range of parameter space which can be investigated. One of the long-standing questions in the study of turbulence is whether the small scales are universal in different flows as suggested by the Kolmogorov universal equilibrium theory. This theory suggests that the smallest scales are locally isotropic in wavenumber space and depend only on viscosity (ν) and the dissipation of turbulent kinetic energy (ϵ). This leads to the definition of a length scale and a velocity scale

$$\eta = (\nu^3/\epsilon)^{1/4} \text{ and } v = (\nu\epsilon)^{1/4} \tag{1}$$

respectively. Therefore if these scales are used correctly to non-dimensionalise the normal components of the spectra, each of these components should collapse onto a single curve in the high wavenumber range where the Kolmogorov arguments should apply. A good test of these ideas requires the comparison of different flows with as wide a range of η and v as possible. Another consequence of the Kolmogorov theory is that if the Reynolds number is high enough it may be possible to have a range of wavenumbers which are locally isotropic but the eddies are large enough such that viscosity is not important (called the *equilibrium range*). This leads to a -5/3 power-law form for the normal spectra in this range.

If carefully interpreted, spectra can also give much insight into the underlying large scale structure of turbulent shear-flows. In particular a comparison of the spectra from two very different turbulent flows may be used to elucidate the fundamental differences in their structure. Recently the authors have had some success in physically modelling both jets and boundary layers using inviscid coherent structures. While the approach used in both cases is similar, the appropriate underlying structure used is quite different. Briefly, the major difference between the two is that the boundary layer model consists of a range of scales of eddies which are *attached*[1] to the wall, whereas the jet model consists of a single scale of eddies which scale with the local jet width (Δ) and which are randomly jittered about a mean position.

In this paper, first the applicability of Kolmogorov scaling is examined for the two different flows and the existence of a -5/3 law examined. Then comparisons are made of the large scale structure of the two flows in the light of the existing coherent eddy models.

[1]Here *attached* is used in the sense of Townsend's[1] attached eddy hypothesis i.e. the size of the eddies scales with their distance from the wall.

2. EXPERIMENTAL APPARATUS AND TECHNIQUES

The apparatus used for the jet flow and the boundary layer measurements are described fully in the respective theses of Nickels[2] and Marušić[3]. Only a brief description will be given here.

In the case of the jet: the wind-tunnel has a cross-section of 1220x890 mm with a maximum velocity of 3.5 m/s and a turbulence intensity of less than 0.6%. The jet issues from a 25.4 mm nozzle aligned with the wind-tunnel centre-line. The nozzle has a contraction ratio of 9:1 which gives a turbulence intensity of less than 0.5% at the outlet. The exterior of the nozzle has perforations which allow for boundary layer suction to avoid separation of the flow on the outer surface and allow control of initial conditions. Flow in the jet is produced by a centrifugal blower through honeycomb and a series of screens. The jet flow could be varied from 0-35 m/s.

In the case of the boundary layer: the wind tunnel is of a open-return blower type. It consists of a contraction with area-ratio 8.9:1 leading to the inlet of a 4.3 m long working section with a cross-section measuring 940x388 mm. The free-stream velocity at the inlet of the working section can be varied between 2-35 m/s, while the free-stream turbulence intensity is of the order of about 0.3%. The working section consists of a smooth wall made from a polished acrylic laminate and a series of louvres (or bleeding vanes) which make up the roof. The working section is operated above atmospheric pressure and thence the streamwise pressure gradient is adjusted by controlling the location and amount of air leaving the working section through the louvres. For the data to be presented in this paper the streamwise pressure gradient was set to be nominally zero. Spanwise X-wire surveys of the spanwise velocity component confirmed the flow to be nominally two-dimensional in the mean. All details are given by Marušić[3].

All turbulence measurements were made with 90° X-wires constructed with 5 μm diameter 90% Pt-10% Rh Wollaston wire, etched approximately to 1.0 mm. Constant temperature hot-wire anemometers were used and operated at a resistance ratio of 2.0.

Power spectral densities were calculated from dynamically matched but uncalibrated X-wire signals by using a FFT-algorithm. The signals were sampled at three different sampling rates to improve the frequency bandwidth of the spectrum at low frequencies and were low-pass filtered at less than half the digital sampling rate to avoid aliasing of the measured spectrum. The three resulting spectral files were matched and joined to form a single spectral file which was then smoothed. To transform the spectral argument from frequency, f, to streamwise wavenumber, k_1, Taylor's hypothesis of frozen turbulence was used, i.e. $k_1 = 2\pi f/U_c$, where U_c is some local convection velocity assumed to be equal to the local mean velocity of the flow at the point of interest. The spectra were normalised so that

$$\int_0^\infty \phi_{ij}(k_1)\, dk_1 = \overline{u_i u_j} \tag{2}$$

where $\overline{u_i u_j}$ is the appropriate component of the Reynolds stress tensor and ϕ_{ij} is the corresponding one-dimensional power spectral density. It should be noted that with this convention repeated subscripts do not denote a summation. In addition, it is important to note that by definition $\phi_{ij}(k_1 l)$ represents the power spectral density per unit non-dimensional wavenumber $k_1 l$; which implies

$$\phi_{ij}(k_1 l) = \frac{\phi_{ij}(k_1)}{l} \tag{3}$$

where l is some length scale of interest[2]. In this paper the co-ordinate convention is such that the streamwise (x) fluctuating velocity is u_1 and the cross-stream (wall-normal z for boundary layers and radial r for jets) is u_3.

In order to determine the Kolmogorov length and velocity scales an estimate of the

[2]Here it is understood that the functional form of ϕ_{ij} is different on both sides of the equation. Rather than defining a new function for each scaling, the difference is assumed to be understood

dissipation is required. Here the isotropic assumption is used giving

$$\epsilon = 15\nu \int_0^\infty k_1^2 \phi_{11}(k_1)\, dk_1. \tag{4}$$

for want of a better method.

3. RESULTS AND DISCUSSION

3.1 Local isotropy and Kolmogorov scaling

In order to examine the universality of the fine-scales in the two flows, spectra were measured and compared. If the high wavenumbers are universal then it would be expected that the spectra from all flows should collapse when non-dimensionalised with the Kolmogorov length and velocity scales. Figure 1 shows a range of typical streamwise spectra from the two different flows scaled with this Kolmogorov scaling. It may be seen that all profiles shown from both flows seem to collapse onto a single curve in the high-wavenumber region. There is however some peel-off from this universal form at the highest wavenumbers which is probably due to the limit of the spatial resolution of the hot-wire sensor. This explanation for the peel-off is supported by the fact that the spectra peel-off at values of $k_1\eta$ that correspond to $k_1\ell = 1$ where ℓ is the length of the hot-wire sensor. The limited length of the sensor acts as a spatial filter which attenuates all scales smaller than ℓ (i.e. $k_1\ell > 1$).

The lower diagram in figure 1 shows the same streamwise spectra premultiplied by $(k_1\eta)^{5/3}$. On this plot a -5/3 power-law in the spectrum appears as a plateau. The diagram shows a short region which appears to be of -5/3 power law form. It is also possible from this plot to estimate the Kolmogorov constant for the one-dimensional spectrum (K_o where $\phi_{11}(k_1\eta)/v^2 = K_o(k_1\eta)^{-5/3}$). Here it appears to be approximately $0.5 < K_o < 0.6$ which is close to the value found in various other flows (Townsend[1] gives the value of K_o as 0.5 ± 0.03 but the data he presents varies more than this).

The arguments of Kolmogorov also suggest that the universal form for the spectra should correspond to a region of local isotropy. Since we have shown that the streamwise spectra appear to be universal it is worthwhile examining the existence of local isotropy in the flows. There is no definitive way to check for local isotropy experimentally but there are a number of options. Here we have chosen one of the simplest. We will examine the Reynolds shear-stress correlation coefficient defined as

$$R_{13}(k_1\eta) = -\frac{\phi_{13}(k_1\eta)}{\sqrt{\phi_{11}(k_1\eta)\phi_{33}(k_1\eta)}}. \tag{5}$$

Since there can be no shear-stress component in isotropic turbulence then R_{13} should go to zero if the flow becomes locally isotropic. Figure 2 shows the premultiplied spectra and the corresponding plot of R_{13} taken at a single value of R_λ (Taylor microscale Reynolds number) for both flows. Two points are worth noting. Firstly the plateaus occur, not where R_{13} is zero, but in the region where it is dropping to zero. This is consistent with the findings of Saddoughi & Veeravalli[4] who examined a very high Reynolds number boundary layer flow. It should be pointed out that strictly it is possible that the fine scales may be locally isotropic even in a region where R_{13} is non-zero since large scales may contribute something to the shear-stress spectrum at the high wavenumber end. This is due to the fact that if the velocity signature of an eddy is not simply sinusoidal it will contribute some energy to the spectra at all frequencies. Hence the flow may in fact be locally isotropic in the region of the -5/3-law behaviour. More work would be needed to resolve this issue.

It is also worth noting that, the jet profile in figure 2 shows R_{13} falling to negative values. The authors believe this to be a consequence of correlated high-frequency noise which becomes significant where the signal-to-noise ratio is very small, rather than being the consequence of any physical flow process.

The other point of interest is the difference in behaviour of the jet and the boundary layer flow. It would seem that R_{13} in the jet drops off much more quickly *at the same Taylor microscale Reynolds number* than the boundary layer which indicates a difference in the

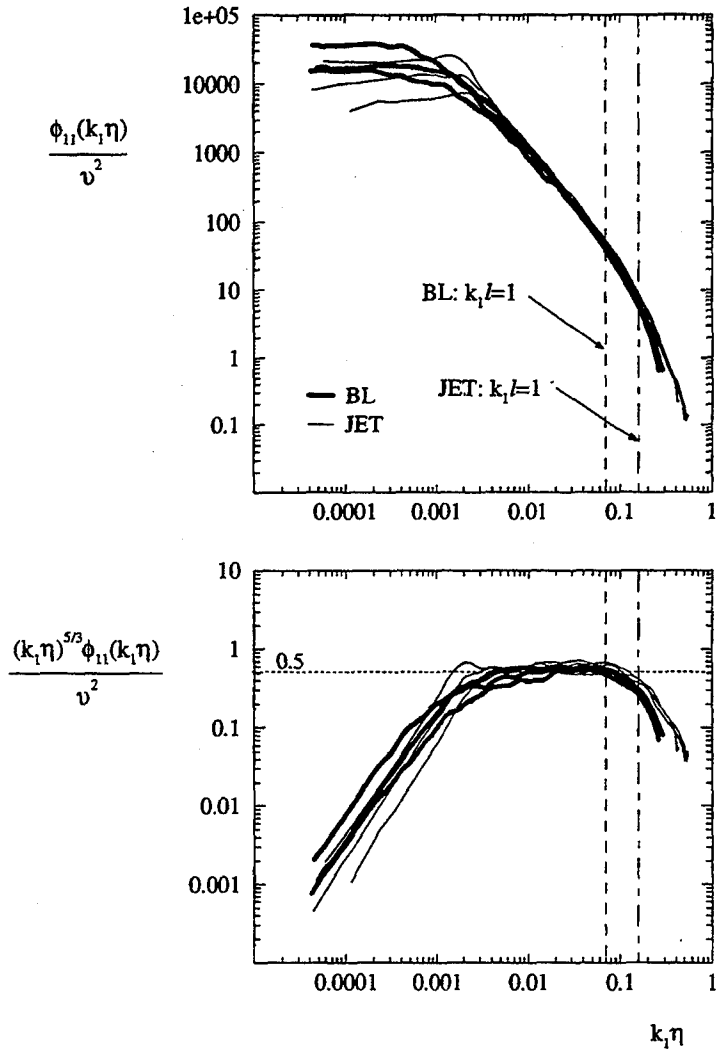

Figure 1: Collapse of data for jet and boundary layer with Kolmogorov scaling showing effect of limited spatial resolution. Dashed lines show median value of $k_1\eta$ for which $k_1\ell = 1$ where ℓ is length of hot-wire sensor. Lower diagram shows the extent of the -5/3-law for the different cases.

underlying structure of the flows. This point is taken up in the next section.

3.2 Structure

Before discussing the differences in structure of the two flows it is important to have a basis for comparison. It is necessary to define an appropriate Reynolds number and also to define an appropriate shear layer thickness so different levels through the layer may be compared. In boundary layer work a useful Reynolds number is the Kármán number $K_\tau = \delta_c U_\tau/\nu$ where δ_c is the boundary layer thickness (see Perry & Li[5] for details) and U_τ

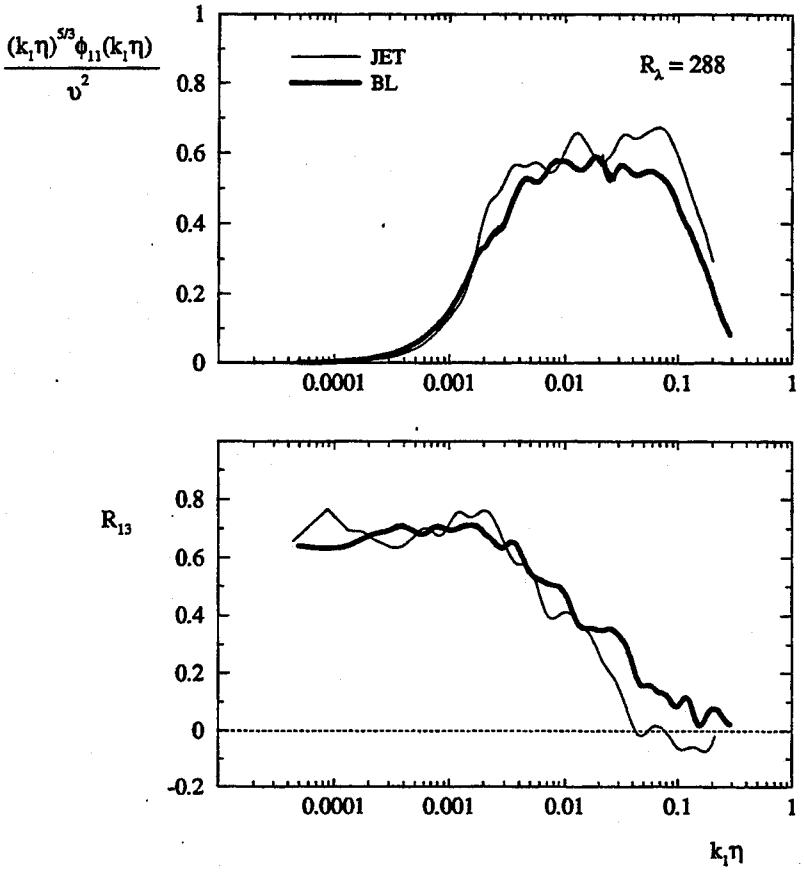

Figure 2: R_{13} profiles together with corresponding streamwise spectra premultiplied by $(k_1\eta)^{5/3}$ for $R_\lambda = 288$.

is wall shear velocity. For jets an equivalent Reynolds number based on local conditions can be defined as $R_\Delta = \Delta U_o/\nu$ where U_o is the local velocity excess (i.e. velocity on centre-line minus external velocity) and Δ is the standard deviation of the mean velocity profile. These definitions are based on measurements of the mean flow. In order to compare different cross-stream levels, a relationship between δ_c and Δ needs to be established. If we consider the edge of the turbulent zone to be the point where the Reynolds shear-stress has fallen to zero (or some small value) and call this δ_{SS} then $\delta_c/\delta_{SS} \approx 1$ and $\delta_{SS}/\Delta \approx 3$. Wherever possible, levels with similar z/δ_{SS} and r/δ_{SS} have been shown (although legends give r/Δ and z/δ_c values in all cases). Unfortunately, an equivalent factor relating U_o and U_τ is unknown and hence, in the absence of a better criterion, similar values of K_τ and R_Δ have been chosen for comparison. It should be noted that this choice does not seriously affect any of the conclusions to be presented.

Figure 3 shows profiles of R_{13} for the two flow cases for similar Reynolds numbers and similar cross-stream levels. It can be seen that the behaviour is quite different. In particular it would seem that R_{13} goes to zero much earlier in the jet case than in the boundary layer case. This suggests that the eddies which contribute to the Reynolds shear stress extend to much higher wavenumber in the boundary layer.

In order to examine the effect of changes of Reynolds number on the wavenumber extent of the Reynolds shear-stress spectra (ϕ_{13}), figure 4 shows the premultiplied Reynolds shear-

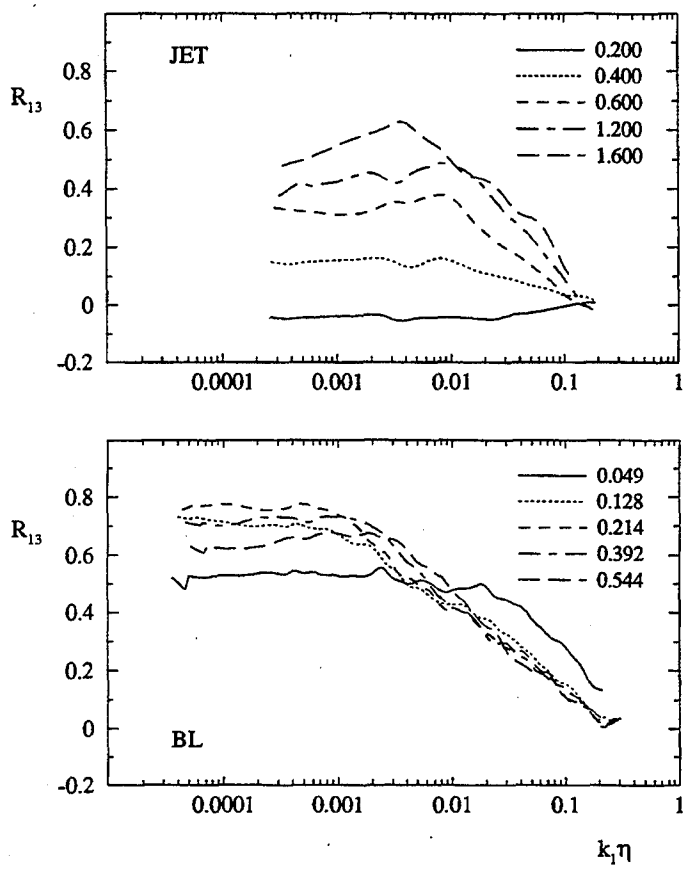

Figure 3: Comparison of variation of R_{13} through shear-layer for jet and boundary layer. Non-dimensional cross-stream co-ordinates (r/Δ for jet, z/δ_c for boundary layer) for each profile are given in the legends. $K_\tau = 4412$ for BL; $R_\Delta = 2384$ for Jet.

stress spectra for several Reynolds number cases for each flow at a fixed cross-stream level. Since we are only interested in the wavenumber extent, or bandwidth of the spectra they have been divided by their maximum values. Hence we can see the change of shape without regard to the actual magnitudes.

It can be seen that the bandwidth does not seem to change significantly for either the jet or the boundary layer flow. A possible physical explanation for the result will be considered shortly.

Figure 5(a) shows the change in the bandwidth of the Reynolds shear-stress spectra at a fixed Reynolds number for varying cross-stream levels. It may be seen that as the wall is approached the bandwidth increases for the boundary layer flow but remains substantially unchanged for the jet flow. This suggests that, as the wall is approached, the range of scales which contribute to the Reynolds shear-stress increases for the boundary layer. In particular the contribution from high-wavenumbers and hence smaller eddies increases.

Based on these (and other observations) it is possible to suggest physical models which mimic this behaviour. In the case of the boundary layer, the appropriate model is based on the attached eddy hypothesis of Townsend[1] as developed by Perry & Chong[6]. Briefly, this model consists of random arrays of attached eddies of different scales which extend from the wall and scale with their distance from the wall and are distributed with an inverse power-

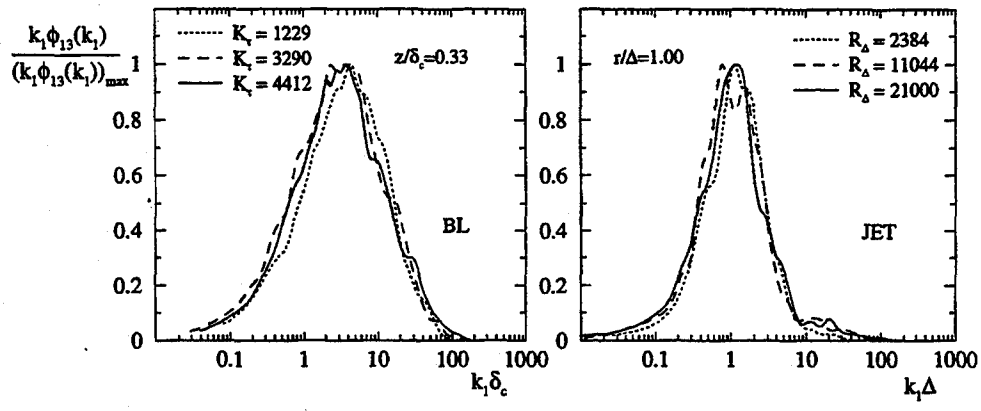

Figure 4: Comparison of effect of Reynolds number on form of premultiplied Reynolds shear-stress spectra at a fixed cross-stream position.

law p.d.f. in eddy scale. The range of scales in this model would increase with Reynolds number (K_τ) since the smallest eddy scales with ν/U_τ and the large eddies scale with δ_c. Therefore, considering a probe at a given fixed level of z/δ_c (above the smallest attached eddy), an increase in K_τ results in a decrease in size of the smallest eddies relative to δ_c. The fixed probe cannot "see" these additional eddies which will be below the probe, and thus the contribution to ϕ_{13} recorded by the probe remains unchanged. This then explains the behaviour observed in figure 4. It is only when the probe position (i.e. z/δ_c) is changed that a change in the range of scales and therefore a change in the bandwidth of $k_1\phi_{13}(k_1)$ is detected (see Perry, Henbest & Chong[7] for further explanation).

In the case of the jet, the model consists of one scale of eddies which scale with the local jet width (Δ) and which span the jet width. Hence at all positions the extent in wavenumber space is constant. Similarly with a change in Reynolds number there will be no increase in bandwidth since there is only one scale of eddies.

The results for the Reynolds shear-stress spectra from the models are shown in figure 5(b). It may be seen that they seem to agree very well at least qualitatively with the experimental behaviour shown in figure 5(a). Quantitative agreement depends on the eddy shapes assumed in the model. These results give further support to the basis for the structure of the models, namely: with an decrease in z/δ_c in the boundary layer, the bandwidth in $k_1\phi_{13}(k_1)$ increases whereas for the jet, the bandwidth remains essentially constant as r/Δ is decreased. It should be stressed that these models also predict other trends and quantities not shown in this paper (for example all components of Reynolds stresses, mean flow and other components of spectra). Further details of these models may be found in Nickels[2] (for the jet) and Perry & Marušić[8] (for the boundary layer).

It is also worth noting that the ϕ_{13} component is not the strongest indicator to show the differences in structure between the two flows. However, it is the only component which is not affected by additional locally isotropic Kolmogorov contributions which will affect the bandwidths of the other components. A feasible way of subtracting off the Kolmogorov contribution is not known at this stage and therefore only ϕ_{13} has been considered here.

4. CONCLUSIONS

Comparisons of spectra in a jet and a boundary layer suggest that the fine-scales may be universal and scale with the Kolmogorov scaling. There is also some evidence of the existence of -5/3 law in the streamwise spectra. Measurements of Reynolds shear-stress correlation coefficient spectra suggest that the finest scales are locally isotropic, however, the region where the -5/3 law seems to apply may not be locally isotropic except at the highest of wavenumbers. More work needs to be done to resolve this issue.

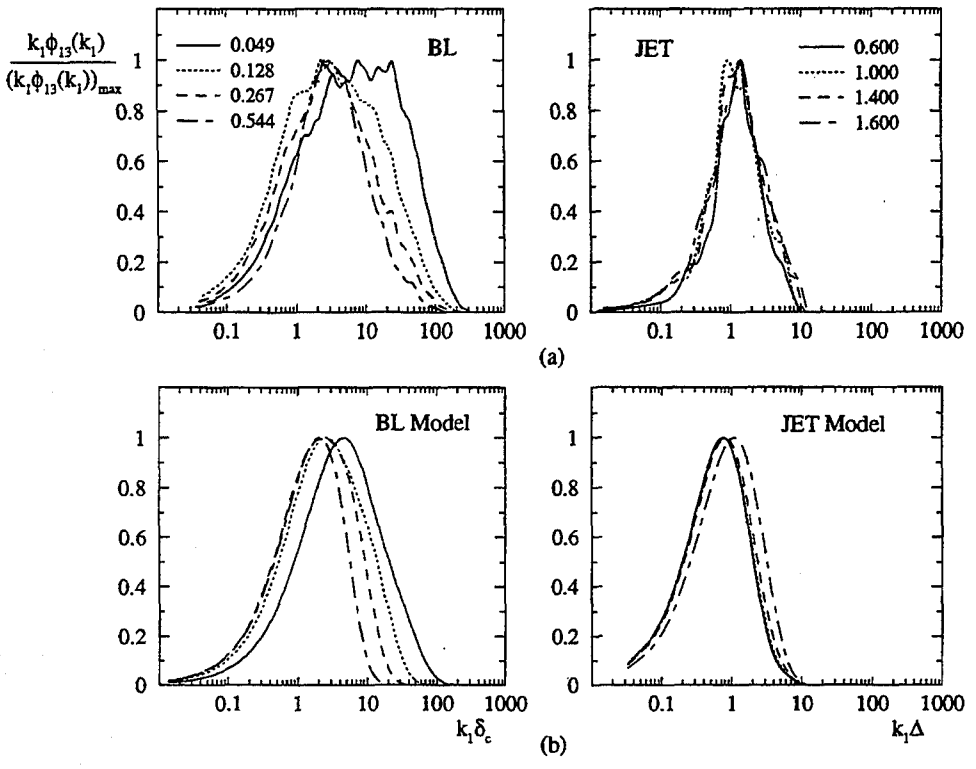

Figure 5: Comparison of variation of bandwidth of premultiplied Reynolds shear-stress spectra at a fixed Reynolds number with cross-stream position. Note increase in bandwidth for boundary layer as wall is approached. (a) Experimental results, $K_\tau = 4412$ for BL; $R_\Delta = 2384$ for Jet, (b) Results from coherent structure models developed by the authors for same levels as in (a).

Further comparisons have illustrated the difference in structure between boundary layers and jets and suggest that the boundary layer has a much wider range of scales which contribute to the Reynolds shear-stress. This is in line with models for both flows which have been developed by the authors.

The authors wish to thank the Australian Research Council for the financial support of this project.

4. REFERENCES

[1] Townsend, A.A. (1976) *The structure of turbulent shear flow.* Cambridge Uni. Press.
[2] Nickels, T.B. (1993) Turbulent coflowing jets and vortex ring collisions. Ph.D. thesis, University of Melbourne, Australia.
[3] Marušić, I. (1991) The structure of zero and adverse pressure gradient turbulent boundary layers. Ph.D. thesis, University of Melbourne, Australia.
[4] Saddoughi, S.G. & Veeravalli, V. (1994) *J. Fluid Mech.*, **268**.
[5] Perry, A.E. & Li, J.D. (1990) *J. Fluid Mech.*, **218**, 405-438.
[6] Perry, A.E. & Chong, M.S. (1982) *J. Fluid Mech.*, **119**, 173-217.
[7] Perry, A.E., Henbest S.M. & Chong, M.S. (1986) *J. Fluid Mech.* **165**, 163-199.
[8] Perry, A.E. & Marušić, I. (1993) *Rep.* FM-21. Dept. of Mech. Eng., University of Melbourne.

INVESTIGATION OF EFFECT OF DENSITY ON MIXING AND TURBULENT STRUCTURE OF A ROUND JET

OLIVARI D., TROUPAKI E.

Von Karman Institute for Fluid Dynamics,

Rhodes St. Genese (Belgium)

1. INTRODUCTION.

Turbulent buoyant jets are an integral part of many waste disposal systems including cooling towers, smoke stacks and fires. An understanding of the entrainment and mixing processes in such jets is necessary to permit optimal design of such systems. At present no simple theory exists to describe the evolution of turbulent no-isodensity jets: a number of methods have been proposed for calculating the practically important cases ranging from simple empirical formulas to complex models involving partial differential equations. Experimental data are required by all methods either as a direct basis for the empirical formulas or to determine empirical constants and functions appearing in the equations. Despite the large number of investigations reported in the literature so far [1][2][3][4], many uncertainties still remain concerning both qualitative and quantitative behaviour of these flows. Furthermore very little is known about the turbulence properties and especially its spatial structure.
In this paper results are reported of concentration measurements at different cross sections of a series of five jets of different density, obtained by a mixture of Air and Helium ejected in a quiescent environment. A non intrusive light scattering technique combined with Digital Image Analysis was used as diagnostic tool to record both mean and instantaneous properties of the resulting turbulent field. The influence of the global density ratio on the jet spread and the concentration decay and of the structure of the turbulence are investigated and the first results reported here.

2. THE EXPERIMENT.

2.1 General Considerations.

Any non isodensity jet released in a environment at rest is to be considered as a buoyant flow. When, as in the case of the present work, the jet is released vertically upwards, the buoyancy force acts in the direction of the jet velocity, and adds-up to the mechanical momentum. However if the discharge velocity at exit is sufficiently large in the region close to the nozzle momentum forces dominate the flow [1]. There follows an intermediate region where the dominance of the initial momentum forces decrease and finally a region where the buoyancy forces dominate the flow which then behaves more like a plume.This research is interested on the behaviour of mechanical turbulence, to connect it with previous work by one of the authors [11], so the region of interest has to be clearly identified and delimited.

The local character of the jet at each point is determined by the relative magnitude of the inertial, buoyant and viscous forces. Of interest here are the conditions under which the jet may be considered as non-buoyant. These can be defined in terms of initial momentum flux and weight deficit ,in the Densimetric Froude Number. It has been found experimentally [6][8] that the downstream distance, z, for which the buoyancy term is negligible is given by the expression :

$$z \leq 0.5 DF^{2/3} \left(\frac{\rho_o}{\rho_a} \right)^{1/3}$$

However, it is important to recall that the Froude Number value may play an important role in so far as it

may influence the laminar to turbulent transition, and hence be determinant, together with the Reynolds Number, in defining the position of the virtual origin of the flow.

2.2 The Experimental Set-Up.

The measurement technique used to evaluate the concentration field consisted in illuminating a cross section of the jet, perpendicular to its axis, with a plane sheet of laser light. The section was recorded by a video camera into an array of 512*512 pixels having 256 possible grey levels of intensity each. It should be recalled here that the rectangular shape of pixels resulted in scales for one line of the image 1cm=30 pixels and that for a column 1cm=40 pixels. From light scattering theory, there is a linear relationship between the concentration of smoke particles contained in a jet section and the total intensity of the light scattered by this section since this concentration is low enough so that secondary reflections and absorption by the particles can be considered as negligible.

The experimental set-up is sketched in figure 1. The axisymmetrical turbulent jets were made of mixture of Air and Helium gases and letting the mixtures flow through a circular nozzle into a box of Plexiglas containing still air. The inner diameter of the nozzle was equal to 1 cm The box was slightly elevated (1 cm) from its basis and a small suction was provided at the top edge in order to allow fresh air in and avoid recirculation phenomena.

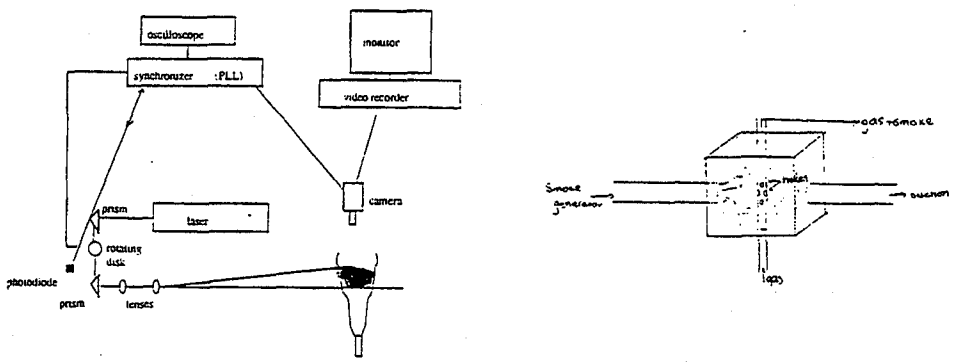

Fig.1. test Set-Up.

Flowrates were measured using two rotameters. A digital thermometer was used to measure the temperature of the mixture filled with smoke upstream of the nozzle. The laser used to illuminate the different cross sections of the jet was a Spectra Physics Argon Laser of 4W maximum power. Two lenses were also used; a converging one to reduce the width of the laser beam and a semi-cylindrical one to spread the beam into a plane sheet.

The illuminated plane was seen by a IEC800BL type CCD camera placed above it at a distance of around 90 cm and recorded using a U-matic video recorder.The exposure time of a standard video frame is 40 ms , to long to obtain a sharp image at the actual flow velocities. A rotating disk with two slots was used to reduce the exposure time to 2 ms. This disk rotation and the camera were synchronised using a Phase Locked Loop (PLL) system designed for the purpose [7][8].

The tracer used was oil vapour produced by an smoke generator . It was fed into a small box and there seeded the jet flow which was passing into an ejector-like device.

To instantaneous pictures were analysed using the digital image processing system PCscope. and also the biggest part of the image processing was done using purpose made external programs .

3. EXPERIMENTAL RESULTS.

For this type of experimental study two approaches were considered: One was to keep the same value of Re at the source for all of jets, a condition requiring very high initial velocities for the lighter gases. The other to keep the same initial velocity for all the jets during the experiments, as in [3]. Uo was set to a value equal to 25 m/s. so Re values varied from 2300 for the pure Helium jet to

16500 for the 100% Air jet. The values of Fr varied from 1000 to 56600 and thus the height of the momentum dominated region was found to be smaller for the lighter gases. This value Zm was calculated to be in the range .26 to 7 m..

3.1. Mean Flow Results.

The results concerning the mean flow parameters were obtained by averaging between 20 and 60 instantaneous images, pixel by pixel. As it will appear later such values are not sufficient to always obtain statistically correct averages and further analysis is being carried on [7].

From these images radial profiles of the mean concentration were obtained and typical examples are shown in fig.2 for different downstream distances. Widths r are normalised with the downstream distance z. Mean concentration, C, is also nondimensionalised with the local maximum value, Cmax, at each cross section. These mean flow profiles, collapse for each mixture, so the jets were found to be self-preserving to the accuracy of the analysis and the number of instantaneous images used for the derivation of the mean values.

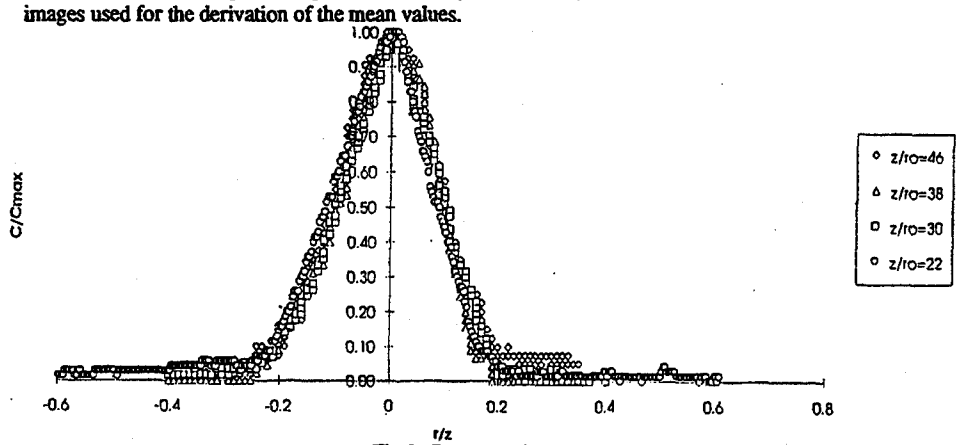

Fig.2. Concentration Profiles.

In figure 3 the radial evolution of the absolute pixel intensity is shown for two different jets at different downstream distances.

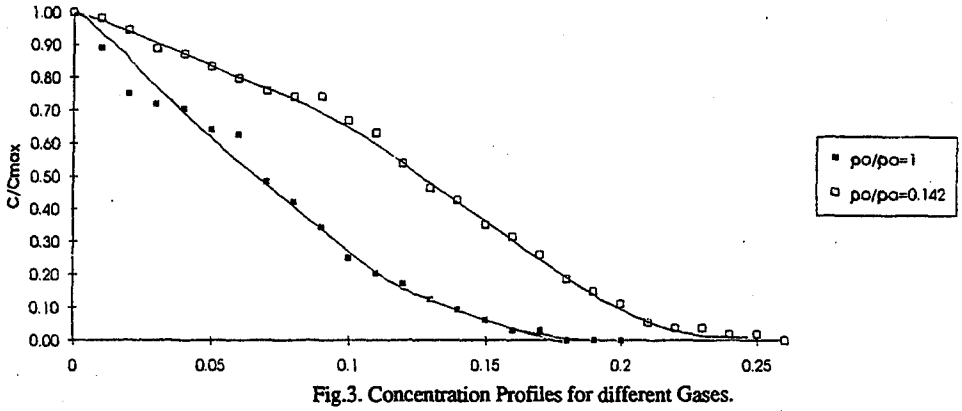

Fig.3. Concentration Profiles for different Gases.

In figure 4 the values of the jet thickness re at concentration value equal to 1/e Cmax, obtained by computing the average radius of the points located at distance Cmax/e from the jet centroid are plotted as a function of the downstream distance z. In agreement with the requirements for self-preserving behaviour, all jets spread linearly downstream. More surprisingly, the values of the spreading rate, K, appears to be constant while the position of the extrapolated Virtual Origin, Zo,

appear to be strongly influenced by the value of the density ratio.

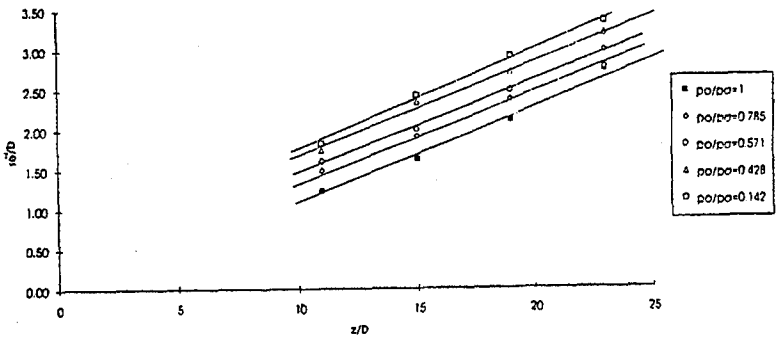

Fig.4. Jets Spreads.

The average value of the spreading rate was found to be equal to Ke=0.122 with an average deviation of 7%., very close to the ones published [7], as shown in the table.

ρo/ρa	Ke	Zo,e cm
1.000	0.13	1.82
0.785	0.11	-2.79
0.571	0.12	-2.65
0.428	0.12	-3.91
0.142	0.13	-3.79
Papanicolaou & List(1988)	0.139	-
Fischer *et al.*(1979)	0.127	-

The evolution of the centerline value of concentration **Cmax** (average value for 20-60 images) is plotted in figure 5 as a function of the downstream distance **z**. Since no absolute value for the concentration of smoke at the jet source was available, the normalisation of the graph has been made using as reference the maximum concentration, Co, at the first section (z/ro=22) . The concentration decay has been found to very sensitive to the density ratio and to be higher for the lighter gases.

3.2. Fluctuating Values.

From the analysis of the instantaneous images it was possible to determine the statistical properties of the concentration fluctuations, a work is still being completed and only some preliminary results will be shown to illustrate the potentiality of the technique.

In figure 6 are shown the instantaneous values of **r1/2** (obtained from the instantaneous images in the same way as **re** for the average ones) around its mean value and it is apparent that the deviations are more intense for the lighter mixtures.

Evaluating the values of the difference of the instantaneous value of the intensity for each pixel from the average one, it is then possible to reconstruct a two-dimensional map of the RMS value of the concentration fluctuations at each jet section were measurement were made. An example is presented in fig.7. The "picture" so obtained can the be compared with the average one to easily asses the basic properties of the concentration at each cross-section for the different initial jet density. In the same way as for mean concentration it is then possible to determine the equivalent radii for different ISO-RMS values and relate them to the jet properties.

More simply, here are presented the RMS values measured along one diameter for a full Air and a full Helium jet. The diameter chosen is defined as one passing on the centroid of the average image, and the plotted RMS is obtained by averaging the MS values on that diameter an on two lines of pixels adjacent to it. The result so obtained are plotted as Turbulence Levels in fig.8

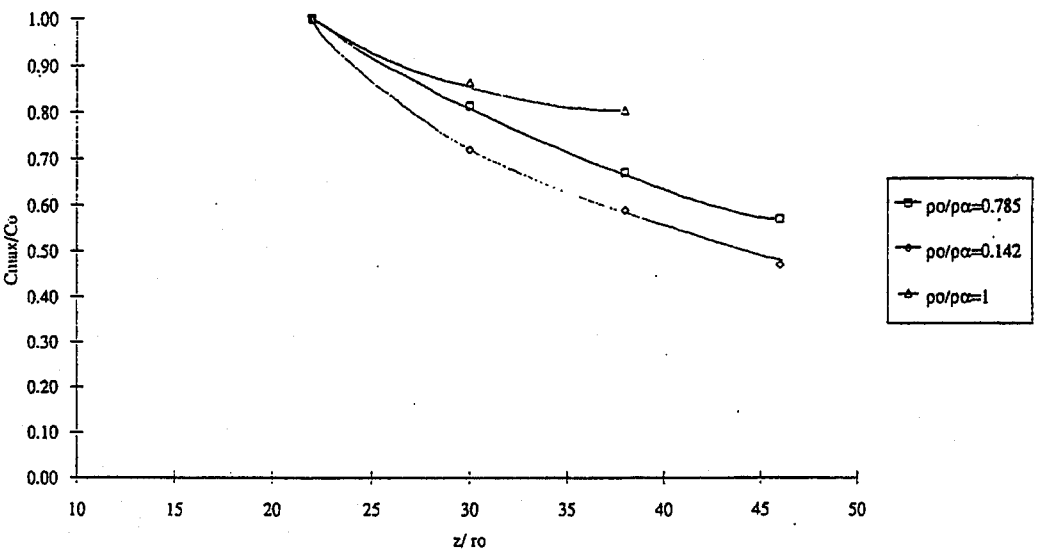

Figure 5. Centerline Decay of Cmax.

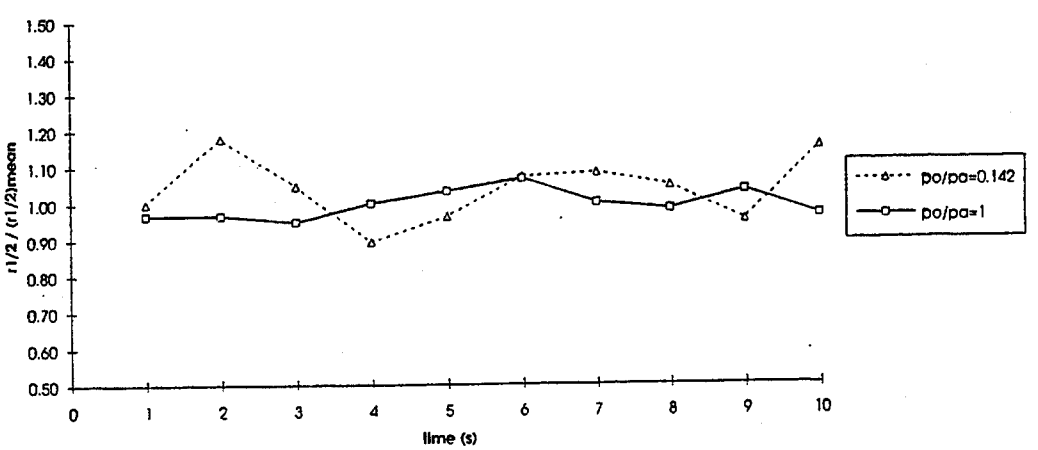

Figure 6. Variability of instantaneous Plume Radius r1/2.

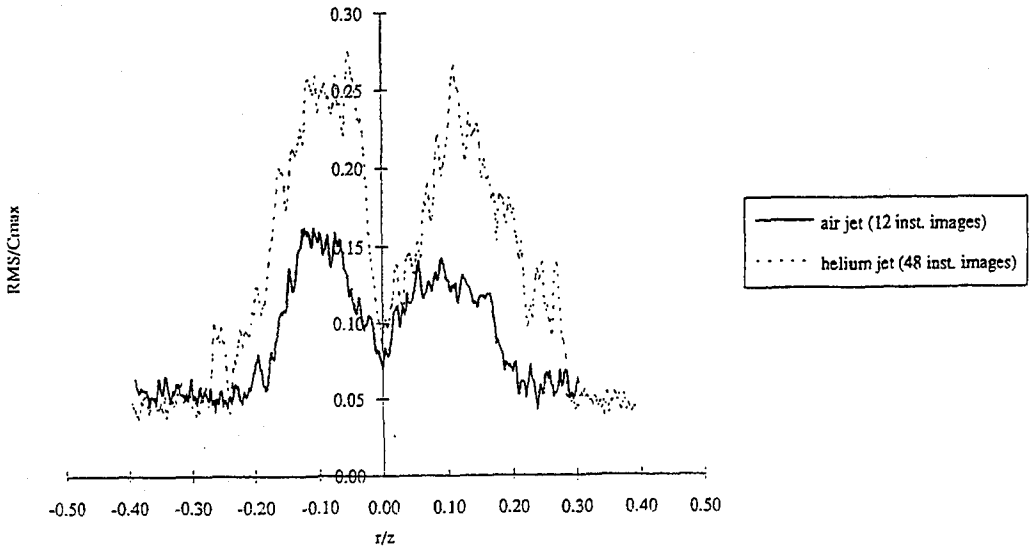

Fig. 8. Normalised Concentration RMS for Air and Helium.

3.4. Some Comments.

Noise, and in particular electronic noise was present during the experiments. For higher distances downstream its value was relevant in comparison to maximum pixel intensity. Attempts were made of subtracting it (by recording an image of the empty box before each experiment and measuring the mean pixel intensity without jet and also directly while plotting the graphs), a procedure not without danger since the edge values of the concentration in the jet were somewhat affected and, at the limit, possibly not taken into account for the calculations especially for the higher values of z.

The synchronisation between the camera and the laser light using the PLL did not perform correctly during some of the tests, resulting in a "twin exposure frame", i.e. having on the same image the even lines and the odd one recorded at different time. While this effect is often exploited by the author to achieve faster time response at lower resolution, in this context it was a nuisance for the study of the instantaneous profiles since in the instantaneous image the resolution of turbulent scales is decreasing by a factor of two.

4. THE "GEOMETRY" OF TURBULENCE.

It has been shown in a number of papers that there are good theoretical and practical reason to assume that the structure of turbulence could be described using fractal geometry, or that the turbulent properties scale with power laws, as a consequence of an internal statistical auto-similarity. Although this analysis is based on, and will be used for the study of, theoretical aspects [10][11], this point will not be discussed here and only some preliminary, an limited, findings are reported here.

The first results isthe determination of the measure of the lines of iso-concentration levels of instantaneous images. This is done using the Minkovsky approach, that is covering each point (pixel in this case) of the line with a box of dimension l and then measuring the surface S of the "sausage" like form obtained. Evaluating the limit of S the dimension **Dm** of the line defined above, is obtained as:

$$Dm = \lim (S / l^2) / (1 / l)$$

which results in the value Dm=1 for a Euclidean line.

Typical results for the jets of pure Air and pure Helium are presented in the figures below, together with a comparison of the two and the corresponding average best fit for Dm, which clearly indicates a value larger than 1.

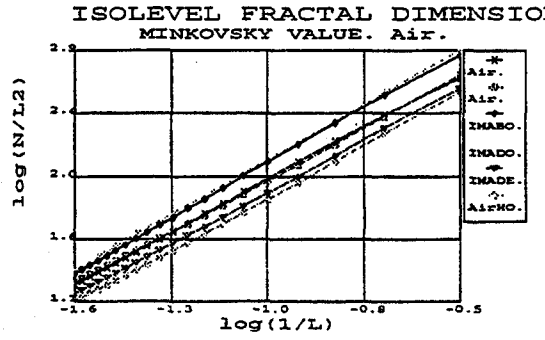

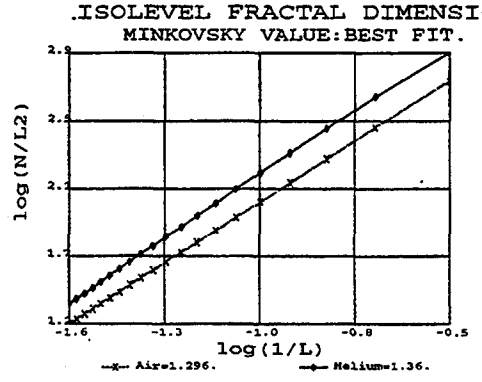

The next step is to evaluate the dimension Ds associated to the Moments of the Structure Function of the Concentration defined as:

$$< | C(x) - C(x + l) |^n > = l^{Ds}$$

and obtained by evaluating the average value of the required power of the difference, as a function of the distance l, over a large number of points, again on a number of instantaneous images. The results obtained, and plotted below, also indicate a fractal behaviour for Ds, and a small, but consistent difference between the Air and Helium jets.

Finally an investigation was made to see if was possible to associate a fractal (or eventually integer) dimension to the two-dimensional repartition of the Concentration Dissipation on the plane associated to individual instantaneous images. Information on the third dimension not being available the Dissipation was approximated by the sum of the square of the two space derivatives **d / dx** and **d / dz** in the plane of the picture. The dimension was then determined using still another approach [8], that is evaluating the limit of the RMS value of average taken of surface of decreasing dimension l, as:

$$Dd = \lim (RMS(\text{mean} (C < \text{over } l^2 >))) \; / (1 / l)$$

This analysis is even more speculative, at the moment, than the previous ones. However as the results seems to indicate there is a definite trend to put into evidence. Since a visual observation of the images representing the Dissipation look like a White Noise picture, in the plot are also reported the results obtained from the same approach applied to pure noise with uniform probability distribution, and the difference is significant.

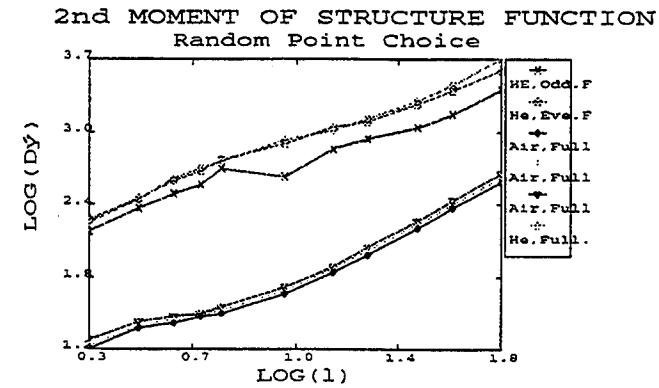

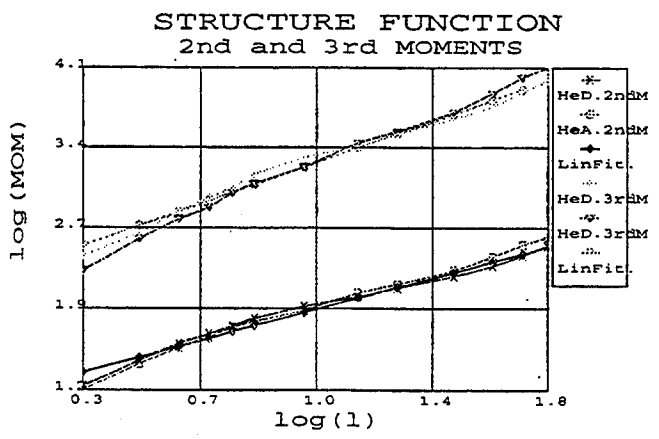

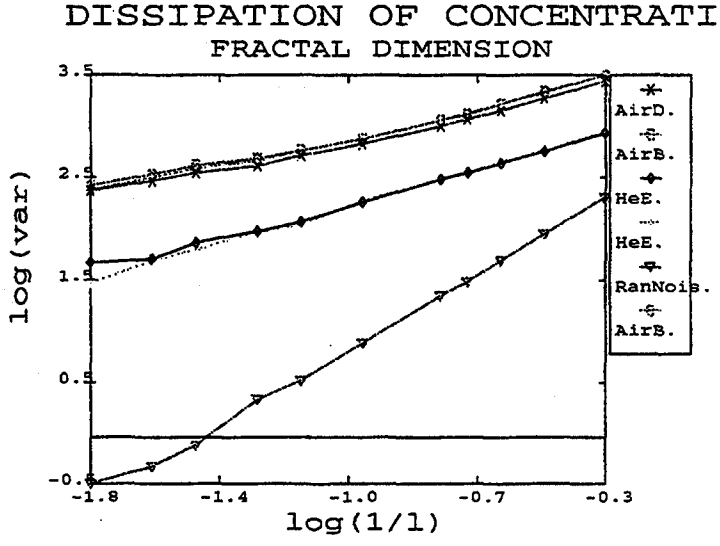

5. CONCLUSIONS.

The major conclusions concerning the concentration field in the momentum-dominated region of axisymmetrical turbulent jets with initial density difference are:

1. Regardless the initial conditions, axisymmetrical turbulent jets decay at the same rate. This is supported by the very good agreement with values found in the literature.
2. Mean concentration values collapse in a form consistent with full preservation.
3. The virtual origin obtained from the spreading data has embodied apparently the memory of the jet. The dependence of this value on system parameters such as Re and Fr requires additional investigation.
4. The technique was proved to be useful for this type of investigations since it is non intrusive, fast and allows a direct visualisation of the concentration field. However, there are some points where an improvement should be made.
5. Initial concentration measurements should also be made, at the jet source for a more complete study of the density effects on the concentration evolution and for comparison with the existing published results.

References

[1]. CHEN, C. J. & RODI, W., A Review of Experimental Data of Vertical Turbulent Buoyant Jets, IIHM Report No 193, Iowa Inst. of Hydraulic Research, October 1976.

[2] PAPANICOLAOU, P. N. & LIST, E. J., Investigations of Round Vertical Turbulent Buoyant Jets, J. Fluid Mech. (1988), vol. 195, pp. 341-391.

[3] PITTS, W. M., Effects of Global Density Ratio on the Centerline Mixing Behaviour of Axisymmetric Turbulent Jets, Experiments in Fluids, 11, pp. 125-134.

[4] RICHARDS, C. D. & PITTS, W. M., Global Density Effect on the Self Preservation of Turbulent Free Jets, J. Fluid Mech. (1993), vol. 254, pp. 417-435.

[5] DOWLING, D. R. & DIMOTAKIS, P. E., Similarity of the Concentration Field of Gas Phase Turbulent Jets, J. Fluid Mech. (1990), vol. 218, pp. 109-141.

[6] GAMEIRO - LOPEZ, A. M., Investigation of Mean and Instantaneous Concentration Properties of Neutral and Buoyant Plumes in a Turbulent Boundary Layer, VKI Project Report 1989-26
[7] OLIVARI, D., PALLI, E., Investigation of Fluctuating properties of a Neutral Plume using Digital Image Analysis Techniques. Atmospheric Environment, Vol. 25A, No.8, 1991.
[8] FLOHR, P., Fractal Characteristics of a Turbulent Jet, VKI Stagiaire Report 1993-16.
[9] OLIVARI, D., Thin Shear Flows: An Introduction to jets and Plumes, VKI Course Note 116, December 1980.
[10] SREENIVANASAN, K.R., RAMSANKAR, R., MENEVAU, C.., Mixing Entrainment and Fractal dimensions of Surfaces in Turbulenr Flows. Proc.R. Soc. London. A 421, 79-108, 1989.
[11] FLOHR, P., OLIVARI, D. , Fractal and Multifractal characteristics of ascalar dispersed in a turbulent jet. PHYSICA D. To be published.

ON THE REYNOLDS NUMBER DEPENDENCE OF A PLANE TWO-DIMENSIONAL WALL-JET

L. Löfdahl, H. Abrahamsson, B. Johansson and T. Hadzianagnostakis

Department of Thermo- and Fluid Dynamics
Chalmers University of Technology
S-41269 Göteborg
Sweden

ABSTRACT

Measurements in a plane two-dimensional turbulent wall-jet has been conducted at different slot Reynolds numbers using hot-wire techniques. The wall-jet was shown to be two-dimensional and self-preserving. Using momentum scaling, based on viscosity and inlet momentum flux, the growth of the half-width and the decay of the maximum mean velocity were showed to be independent of the slot Reynolds number. It was also found that as compared to an ordinary wall boundary layer, the strong interaction between the inner and outer regions limited the extension of the logarithmic part of the mean velocity profile, and enhanced the turbulence level close to the wall.

1. INTRODUCTION

Many experimental investigations have been conducted on the turbulent wall-jet due to its important applications in engineering flows, e.g. the film-cooling of combustion chambers and gas turbine blades. The first reported experiment considering the isothermal plane two-dimensional wall-jet in a quiescent surrounding was conducted by Förthmann[1], and later followed by e.g. the skin friction measurements of Sigalla[2] and turbulence measurements of Bradshaw & Gee[3]. Tailland & Mathieu[4] made the observation that the streamwise evolution of the half-width and maximum mean velocity was dependent on the slot Reynolds number. Narasimha et al.[5] investigated the influence of different scaling parameters. Most of these early investigations have been reviewed in Launder & Rodi[6],[7], who stated a lack of fundamental, simple and well-defined experiments on wall-jets. Quite recently, Wygnanski et al.[8] found a Reynolds number dependence of the mean velocity profile outside the half-width as well as close to the wall in the viscous region. Wygnanski et al.[8] also pointed out a non self-preserving behaviour in the streamwise turbulence intensity.

The objective of the present work was to investigate the Reynolds number dependence and the scaling laws of a plane two-dimensional wall-jet in a quiescent surrounding. The interaction between the inner and outer layer was studied by looking at the mean velocity profile, the streamwise turbulence intensity and the streamwise component of the Reynolds stress transport equations. A special attention was put on the boundary conditions, i.e. the geometry of the experimental set up and the flow conditions.

2. EXPERIMENTAL ARRANGEMENTS

The used wall-jet facility is showed in Figure 1, and consists of a fan, a settling chamber, an inlet device and a flat horizontal plate, which has a length of 6.0 m and a width of 2.0 m. To obtain a two-dimensional flow, and to shield the wall-jet from outer disturbances, the plate is surrounded by high vertical side-walls. A vertical back wall above the slot creates a well defined boundary condition at the inlet, and the wall-jet facility is located in a large laboratory hall in order to obtain a flow where the influence of the outer disturbances and boundaries are negligible. The importance of large scale experimental facilities has recently been pointed out by Hussein et al.[9]

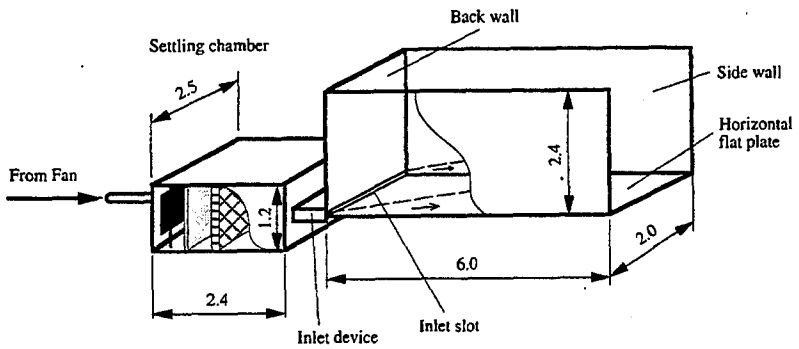

Figure 1. The wall-jet facility. All dimensions in [m].

The high velocity fluid is injected through a slot (of 10 mm height) with an aspect ratio of 200:1. To create a uniform "top-hat" mean velocity profile with a low turbulence level, the inlet device was designed with a contraction ratio of 10:1 according to Morel[10].

All measurements were carried out using a constant temperature anemometer system, Dantec 5600, with miniature probes. The anemometer output was digitized, and a computerized evaluation procedure was employed. The hot-wire probes were calibrated in a low speed wind tunnel against a Prandtl tube, and the anemometer voltages were transferred into velocities using the function suggested by Siddal & Davies[11]. Long integration times, of the order of 5 to 10 minutes, were utilized to obtain a good statistical accuracy, and the wall shear stress was determined using Preston tubes (with different diameters in the interval of 50 to 80 wall units) together with the calibration of Patel[12].

3. RESULTS AND DISCUSSION

The measurements were conducted at slot Reynolds numbers in the range 7.5 10^3 to 2.0 10^4, focusing the region 30 to 250 x/b, which has been shown to be self-preserving in Abrahamsson et al.[13].

Measurements in the inlet slot were carried out and revealed a uniform "top-hat" mean velocity profile within 1%, and a turbulence level of order of 0.4%[13]. The two-dimensionallity of the wall-jet was assessed by the momentum integral equation and the momentum losses were found to be comparable to the wall-friction[6],[13].

A. Self-preservation

The mean velocity profiles at different streamwise positions and slot Reynolds numbers are shown in Figure 2. Noticeable is that the mean velocity profiles are self-preserving, when scaled with the local maximum velocity and the local half-width, which is in contradiction to Wygnanski et al.[8] who found the profile shape outside the half-width to be dependent on the slot Reynolds number. In

comparison to the LDA experiment of Karlsson et al.[14] the present measurements indicate slightly higher velocities, which might be due to the influence of the boundary conditions, i.e. a slow circulation in the water tank.

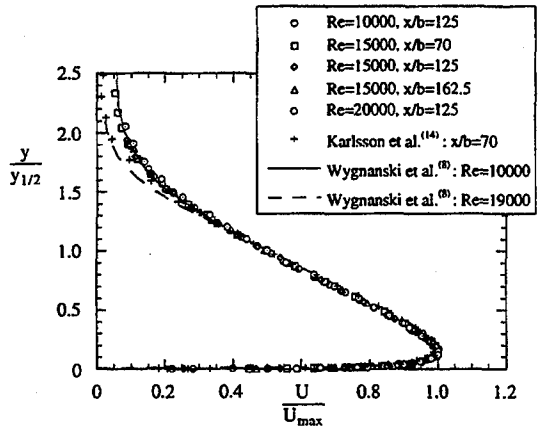

Figure 2. The mean velocity profile.

In Figure 3 the streamwise turbulence intensity distributions are displayed, and reveal a clear self-preserving behaviour for the different streamwise positions as well as for the studied Reynolds numbers. Two clear maxima may be noticed, one close to the wall and another one in the free shear region. These findings are in good agreement with the experiment by Kobayashi & Fujisawa[15], and a comparison to the work of Karlsson et al.[14] shows that the correspondence is good up to about 60 % of the half-width, however, further out, the LDA measurements yield a higher turbulence level. The data of Wygnanski et al.[8] show a dependence on the streamwise position and of the slot Reynolds number.

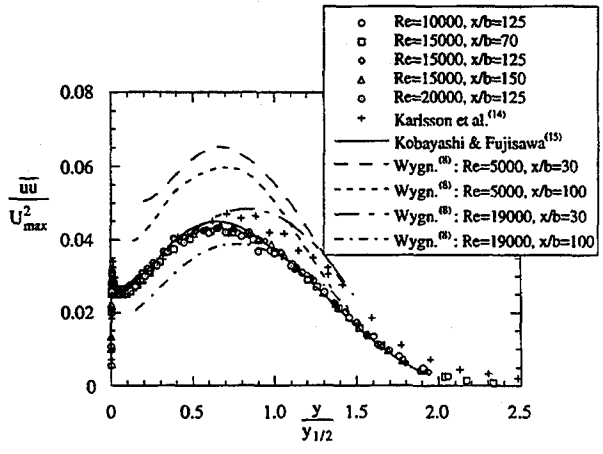

Figure 3. Streamwise turbulence intensity.

B. Scaling of the streamwise development

The streamwise development of the half-width and the maximum mean velocity are presented in Figure 4 and Figure 5. In these figures the scaling parameters are the slot height and inlet mean velocity. It is clear that the half-width as well as the maximum mean velocity reveal a slot Reynolds number dependence, fully in agreement with observations made by e.g. Tailland & Mathieu[4], Narasimha et al.[5] and Wygnanski et al.[8]. Noticeable is also that the growth rate of the half-width decreases slightly with an increasing Reynolds number, in accordance with Tailland & Mathieu[4].

Other parameters for the scaling of the streamwise development of the half-width and the maximum mean velocity were proposed by Narasimha et al.[5], who claimed, using dimensional analysis, that the inlet momentum and the kinematic viscosity were more suitable. This scaling of the half-width is shown in Figure 6, and as compared to Figure 4 no Reynolds number dependence may be noticed. A result in correspondence with what was found by Narasimha et al.[5] and Wygnanski et al.[8]. The power law curve fit shows an exponent which deviates from unity, in agreement with Narasimha et al.[5] as well as Wygnanski et al.[8], and this indicates a slightly non linear development of the half width.

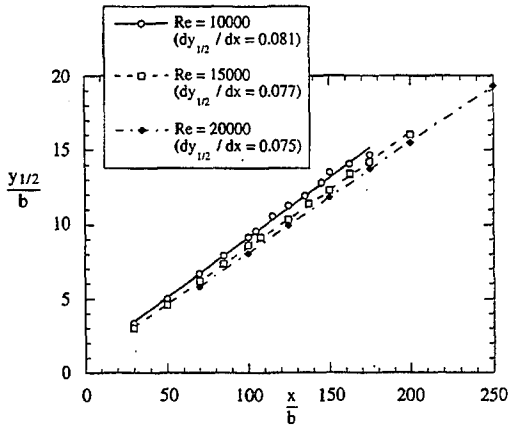

Figure 4. Streamwise development of the half-width in slot scaling.

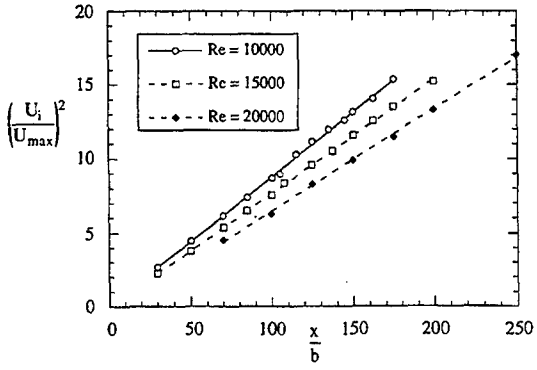

Figure 5. Streamwise development of the maximum mean velocity in slot scaling.

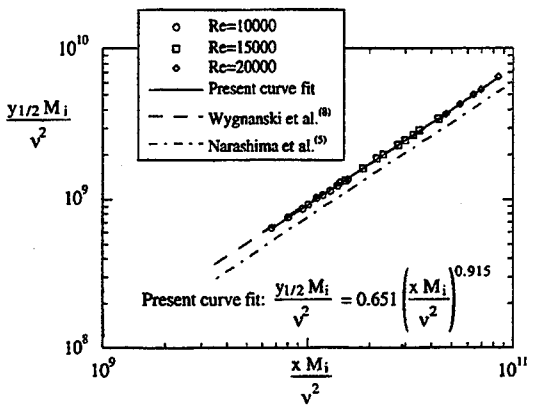

Figure 6. Development of the half-width in momentum scaling.

Figure 7 display the momentum scaling of the maximum mean velocity development. A weak Reynolds number dependence may be noticed if the distance is measured directly from the slot, however, introducing a virtual origin, as suggested by Wygnanski et al.(8), the streamwise velocity distribution of the three Reynolds numbers merge into one single curve.

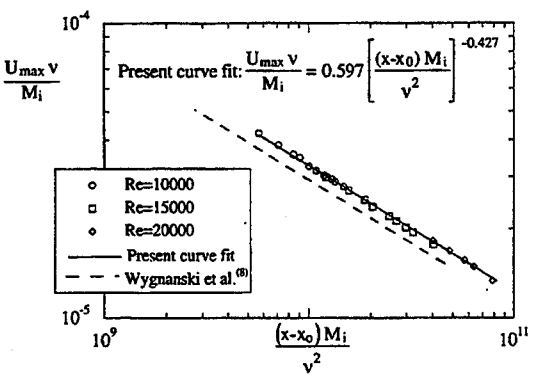

Figure 7. Development of the maximum velocity in momentum scaling.

C. Near wall region

A result of the strong interaction between the inner and outer layer of a wall-jet is the short logarithmic mean velocity profile, which has been debated in the literature(3),(16),(6),(13). It has been argued that the extension decreases in the streamwise direction and sufficiently far downstream no sign of a logarithmic mean velocity profile may be found. However, using an assymptotic scale matching, Abrahamsson et al.(13) point out that a weak logarithmic region existed, and increased slightly in the downstream direction.

The present mean velocity distributions, in inner scaling, for different downstream positions and slot Reynolds numbers are shown in Figure 8, and it can be seen that the same logarithmic line

with the universal constants, 2.44 and 5.0, is valid for the different slot Reynolds numbers. This finding is in contradiction to the results of Wygnanski et al.[8].

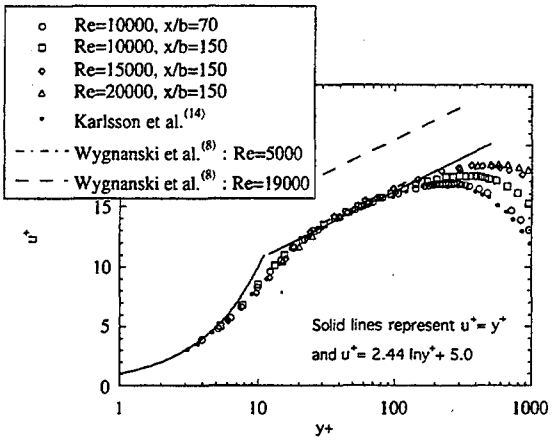

Figure 8. The mean velocity close to the wall.

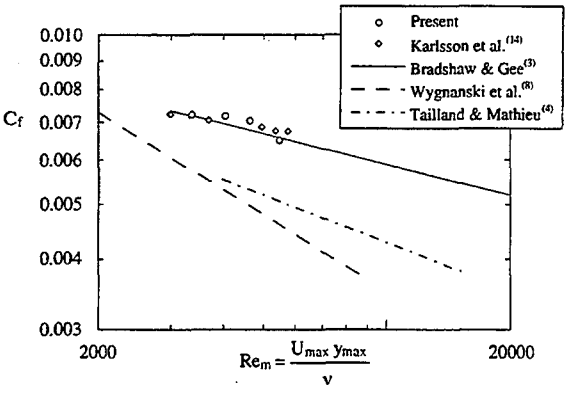

Figure 9. The local skin friction.

An uncertainty of Figure 8 is the accuracy in the skin friction measurements. Launder & Rodi[6] draw the attention to this problem, and compared different methods to determine the skin friction factor, C_f. They found that C_f obtained by calibrated surface impact tubes was comparable to the factors determined by the direct force balance measurement, in turn well represented by the formula of Bradshaw & Gee[3]. It was also found that the C_f determined from the velocity gradient measurements in the viscous sublayer using hot-wires, e.g. Tailland & Mathieu[4] and Wygnanski et al.[8], indicated values of the order of 20 to 35 % below those of Bradshaw & Gee[3].

In Figure 9, the measured C_f is plotted as a function of the local Reynolds number, Re_m. These results were obtained employing Preston tubes and agree well with Bradshaw & Gee[3] as well as with gradient LDA measurements of Karlsson et al.[14]. There is a good correspondence between these surface impact tube measurements and the gradient measurements, since the here

employed Preston tube was larger than the buffer layer and smaller than the outer limit of the logarithmic layer[13], underlining the aforementioned discussion of the universality of the mean velocity profile close to the wall.

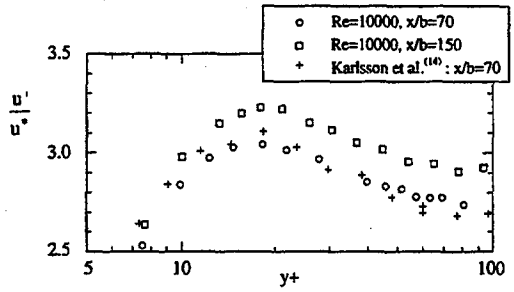

Figure 10. Turbulence intensity close to the wall in inner scaling.

To further elucidate the interaction between the inner and outer layers, the turbulence intensity is showed in Figure 10. In the figure reference data of Karlsson et al.[14] are included, and noticeable is the good agreement between the hot-wire and LDA measurements. Compared to an ordinary wall boundary layer, the levels of the near wall peaks are high, and tend to increase slightly in the streamwise direction[13],[17]. Figure 11 shows the production, the advection and the turbulent diffusion terms of the streamwise component of the Reynolds stress transport equations[18]. The magnitude of the production and diffusion terms are the dominating ones, while the advection seems to be smaller. The enhanced turbulence intensity close to the wall might be explained by the loss of the diffusion term, at approximately $y/y_{1/2}$=0.5, which yields a transport towards the wall, since the production is almost zero in the region around the point of maximum mean velocity.

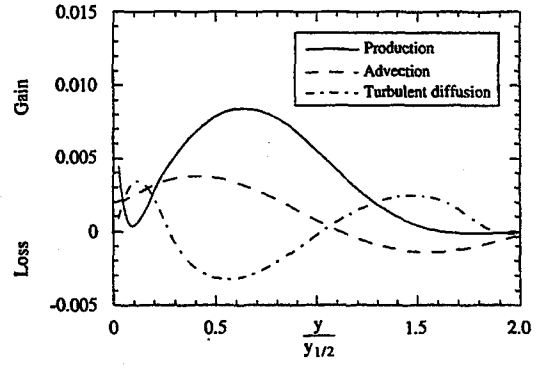

Figure 11. Some terms in the energy budget for the streamwise normal stress. Normalized by the half-width and maximum mean velocity

4. CONCLUSIONS

An investigation of the turbulence field of a plane two-dimensional wall-jet in a quiescent surrounding has been carried out. From the measurements the following main conclusions may be drawn:

* The wall-jet was found to be self-preserving, and the mean velocity as well as the streamwise turbulence intensity profiles were independent of the Reynolds number.
* Using momentum scaling, and a virtual origo, the streamwise development of the half width and the maximum mean velocity were Reynolds number independent.
* As compared to an ordinary wall boundary layer, the strong interaction between the inner and outer regions limited the extension of the logarithmic part of the mean velocity profile, and enhanced the turbulence level close to the wall.

5. ACKNOWLEDGEMENT

Financial support from the Swedish Board for Industrial and Technical development (NUTEK) is gratefully acknowledged.

6. REFERENCES

(1) Förthmann, E., 1934: Über Turbulente Strahlausbreitung, Ing. Arch., Vol. 5, pp. 42-54.; 1936, Turbulent Jet Expansion, N.A.C.A. T.M. 789.
(2) Sigalla, 1958: Measurements of Skin Friction in a Plane Turbulent Wall-Jet", J. Royal Aero. Soc., Vol. 62, pp. 873-877.
(3) Bradshaw, P. and Gee, M.T., 1960: Turbulent Wall-Jets with and without an External Stream, Aero. Res. Council, R&M 3252.
(4) Tailland, A. and Mathieu, J., 1967: Jet pariétal, J. Mech., Vol. 6, pp. 103-131.
(5) Narasimha, R., Narayan, K.Y. and Parthasarathy, S.P., 1973: Parametric Analysis of Turbulent Wall-Jets in Still Air, Aero. J., Vol. 77, pp. 355-359.
(6) Launder, B. and Rodi, W., 1981: The Turbulent Wall-Jet, Prog. Aerospace Sci., Vol. 19, pp. 81-128.
(7) Launder, B. and Rodi, W., 1983: The Turbulent Wall-Jet, Measurements and Modelling, Ann. Rev. Fluid Mech., pp. 429-459.
(8) Wygnanski, I., Katz, Y. and Horev, E., 1992: On the Applicability of Various Scaling Laws to the Turbulent Wall-Jet, J. Fluid Mech., Vol. 234, pp. 669-690.
(9) Hussein, J.H., Capp, S.P. and George, W.K., 1994: Velocity Measurements in a High-Reynolds-Number, Momentum-Conserving, Axisymmetric, Turbulent Jet, J. Fluid Mech., Vol 258, pp. 31-75.
(10) Morel, T. 1975: Comprehensive Design of Axisymmetric Wind Tunnel Contractions, J. Fluids Eng., Vol. 97, pp. 225-233.
(11) Siddal, R.G. and Davies, T.W., 1972: An Improved Response Equation for Hot-Wire Anemometry, Int. J. of Heat and Mass Transf., Vol. 15, pp. 367-368.
(12) Patel, V.C., 1965: Calibration of Preston Tubes and Limitations on Its Use in Pressure Gradients, J. Fluid Mech., Vol.18, pp. 185.
(13) Abrahamsson, H., Johansson, B. and Löfdahl, L., 1994: A Turbulent Plane Two-Dimensional Wall-Jet in a Quiescent Surrounding, European Journal of Mechanics B/Fluids, To appear.
(14) Karlsson, R.I., Eriksson, J. and Persson, J., 1992: LDA Measurements in a Plane Wall-Jet in a Large Enclosure, 6th International Symposium on Applications of Laser Techniques to Fluid Mechanics, Lisbon.
(15) Kobayashi, R. and Fujisawa, N., 1982: Turbulence Characteristics of Plane Wall-Jets, Rep. Inst. High Speed Mech., Tohoku Univ., Vol. 45, pp. 95-114.
(16) Guitton, D.E., 1970: Some Contributions to the Study of Equilibrium and Non-Equilibrium Wall-Jets over Curved Surfaces, Ph.D. thesis, Mech. Eng. Dept., McGill University.
(17) Karlsson, R.I., Eriksson, J. and Persson, J., 1993: An Experimental Study of a Two-Dimensional Plane Turbulent Wall-jet, Vattenfall Utveckling AB-Nuclear Power & Industrial Fluid Mechanics, VU-S93:B36.
(18) Vicari, K. and Abrahamsson, H., 1994: An investigation of the Production, Advection and Turbulent Diffusion in a Plane Two-Dimensional Wall-Jet, Report 94/8, Dept. of Thermo- and Fluid Dynamics, Chalmers University of Technology, Göteborg, Sweden

THE STABILITY OF A LAMINAR WALL-JET SUBJECTED TO BLOWING OR SUCTION

M. Amitay and J. Cohen
Faculty of Aerospace Engineering, Technion - Israel Institute of Technology

The effects of wall blowing or suction on the mean flow and the stability characteristics of an incompressible laminar two-dimensional air wall-jet are investigated experimentally. Hot-wire measurements of the streamwise mean velocity confirm previous theoretical self-similar solutions in which the vertical velocity at the wall varies as a power of the downstream distance. Phase-locked experimental data obtained when the wall-jet is subjected to two-dimensional excitation confirm linear stability calculations, according to which the relative dominance of the viscous and inviscid modes coexisting in the flow can be controlled by subjecting the wall-jet to small amounts of blowing or suction.

Introduction

An incompressible wall-jet is a thin jet of fluid tangential to a wall. It consists of an inner wall boundary layer and an outer free shear layer. Since the wall-jet possesses a point of inflection in the outer region of the mean velocity profile[1], the flow is unstable when the local Reynolds number exceeds 57[2]. At higher Reynolds numbers a second mode of instability, associated with the viscous layer, develops, causing the amplification of relatively small-scale oscillations. Linear stability calculations[3,4] have indicated that the highest amplitudes of the inviscid mode (large scale disturbances) are at the outer region of the wall-jet, while the highest amplitudes of the viscous mode occur close to the wall. The coexistence of the two instability modes has been confirmed experimentally[4].

The purpose of the present work is to find ways of controlling the stability characteristics of the 2-D wall-jet. Furthermore, controlling the relative dominance of each one of the modes can help in understanding similar physical phenomena where both types of instability coexist simultaneously, e.g., separated flows. To achieve these goals, Cohen *et al.*[4] investigated theoretically the effects of subjecting the wall-jet to small amounts of blowing or suction of fluid through the wall. A new family of laminar self-similar solutions was found in which the streamwise velocity U, and the vertical velocity at the wall V_w, are $U(x,\eta)=(1-b)x^{1-2b}f'(\eta)$ and $V_w(x)=-(1-b)f(0)x^{-b}$, respectively, where the function f depends solely on the similarity variable $\eta=(1-b)y/x^b$. According to the values of b, or the more convenient parameter γ=(2b-1)/(1-b), the solutions can be divided into three cases: suction with $V_w<0$ for $\gamma>2$, Glauert[1] with $V_w=0$ for $\gamma=2$ and blowing with $V_w>0$ for $1<\gamma<2$. Linear stability computations, using the above self-similar solutions as the base laminar flow[4], showed that blowing stabilizes the inviscid mode while destabilizing the viscous one. The effect of suction was found to be just the opposite.

Experimental setup

The experiments were carried out in an open circuit air jet facility. In order to control the amount of blowing or suction to which the wall-jet was subjected, a new apparatus consisting of a porous plate (a 200 mesh size screen) and a supporting box was built (Fig. 1). Since the amount of injection (or suction) is a non-uniform function of the streamwise direction[4], the box was divided into 2-D cells. Each one could be subjected to a different and controlled pressured air flow or low vacuum for blowing or suction, respectively.

To observe the behavior of small wavy disturbances under well-defined conditions, the wall-jet was artificially excited by vibrating a 2-D flap. The flap was placed 10mm above the jet exit upper side and extended 8mm downstream the jet exit plane. The excitation signals were

generated by D/A converters. The measurements of the streamwise velocity were conducted using a standard Disa Model 55P11 single hot-wire probe. A right-handed coordinate system is defined with $\hat{X}$ and $\hat{Y}$ as the downstream and vertical (wall normal) coordinates, respectively, with $\hat{U}$ and $\hat{V}$ being the corresponding velocity components. Note that quantities with hats are not dimensionless.

Three sets of experiments were carried out, corresponding to three jet exit Reynolds numbers R_j, based on the jet exit velocity U_j and the jet exit width H. The Reynolds numbers in the three sets of experiments were R_j=125 (U_j=2.5m/s, H=0.75mm), R_j=270 (U_j=5.8m/s, H=0.7mm) and R_j=466 (U_j=7m/s, H=1mm), respectively. Each set of measurements consists of two levels of wall suction (γ=2.3 and 3), two levels of wall blowing (γ=1.5 and 1.7) and a case in which no blowing or suction was applied (γ=2).

Measuring the vertical velocity of the flow entering each cell is difficult because it is so small. For example, in the three sets of measurements reported here, the predicted normal velocity at the wall surface in the first cell is less than 2cm/s, two orders of magnitude smaller than the jet exit velocity. Therefore, to obtain the exact amount of blowing or suction through each cell a unique method[5] was used.

Results

The mean profiles of $\hat{U}$ measured at R_j=466 and $\hat{X}/H$=30 are plotted in dimensional coordinates in Fig. 2. The various symbols represent the measurements obtained at different wall conditions and the solid lines are the corresponding theoretical solutions[4].

The downstream development of the local maximum velocities U_m and the local boundary layer thicknesses δ, where $\hat{U}=0.5U_m$ in the outer region, at R_j=466 are shown in Figs. 3a and 3b, respectively. The good agreement between the measurements and the theoretical solutions indicates that the correct streamwise distributions of the vertical velocity at the wall were obtained.

To assess the effects of blowing or suction on the stability of a wall-jet, the Orr-Sommerfeld equation for small wavy disturbances was solved numerically, where U_m and δ were used to render all variables dimensionless. The neutral stability curves for three cases in which suction (γ=3), Glauert (γ=2) and blowing (γ=1.5) are applied, are plotted in Fig. 4a. Three regions of instability can be distinguished: region I, where only a single mode is unstable; region II, where two unstable modes correspond to two different bands of frequencies and region III, where two bands of unstable modes have an overlapping region in which two waves have the same frequency, but different eigen-values.

Representative amplification curves for γ=2 and for each one of the stability regions are plotted in Figs. 4b-d against the non-dimensional frequency $\tilde{\beta}=2\pi F\delta/U_m$, where F is the dimensional excitation frequency. When blowing or suction are applied, region III begins at a lower or a higher local Reynolds number, respectively (Fig. 4a). Furthermore, the instability regions above and below region III are increased and decreased, respectively, when blowing is applied. The effect of suction is just the opposite. This is related to the fact that blowing tends to destabilize the high frequency waves and to stabilize the lower ones. The effect of blowing and suction on the instability waves can be appreciated when the exponential growth rate $\tilde{\alpha}_i$ (Fig. 5a) and phase velocity $\tilde{C}_{ph}$ (Fig. 5b) are plotted against $\tilde{\beta}$. At this relatively high local Reynolds number of $R_\delta=U_m\delta/\nu=800$, the instability mode is clearly separated into two modes having two different dispersion relations. Blowing tends to destabilize the small scale disturbances but stabilizes the larger scales. The effect of suction is just the opposite.

The normalized modulus of the fundamental component of the fluctuating streamwise velocity $|\tilde{u}|$ at R_δ=469, corresponding to the three cases mentioned above, are plotted in Fig. 6. For large scale inviscid disturbances ($\tilde{\beta}$=0.431) the amplitude reaches a maximum at the outer region (Fig. 6a), while for small scale viscous disturbances ($\tilde{\beta}$=0.972) the amplitude has

a maximum within the region close to the wall (Fig. 6b). The non-dimensional frequencies of the excited waves were chosen to be above and below region III so that for each one of the forced waves only a single mode could be amplified, according to linear stability theory. The amplitudes were normalized by the values of the outer and inner maxima in Figs. 6a and 6b, respectively. The dashed, solid and dotted lines are the theoretical eigen-functions for γ=1.5, 2 and 3, respectively, and the symbols are the corresponding phase-locked data obtained when the wall-jet was subjected to 2-D excitations. Blowing and suction tend to increase and decrease (respectively), the ratio between the outer and inner amplitude maxima. This is related to the increase and decrease of the slope of the mean velocity profile at the wall when suction and blowing are applied. It should be noted that the experimental results for the three cases presented here were obtained at different jet exit conditions so that the local Reynolds number and the non-dimensional frequency at $\hat{X}/H$=30 were the same.

In order to characterize the stability of the wall-jet, the streamwise evolution of the disturbances throughout the following three regions: region I, across region II and region III, were examined. In region I only the inviscid mode exists. The measured (symbols) cross-stream distributions of $|\tilde{u}|$ at $\hat{X}/H$=50, 70 and 90, are shown in Figs. 7a, 7b and 7c and compared with theoretical computations (lines) for γ=1.7, 2 and 3, respectively. For all cases the experimental data follows the trends predicted by the linear stability theory, according to which the ratio between the inner and outer maxima of the streamwise eigen-functions increases with downstream distance, while the ratio between the width of the disturbed region and the local boundary layer thickness decreases. These are not surprising results since as the downstream distance increases, $\tilde{\beta}$ increases as well and consequently smaller scales, governed by the near wall region, become more and more dominant.

The overall amplification of the disturbance in the downstream direction measured at two vertical locations where $\hat{U}=0.55U_\infty$ in the inner region, $\hat{Y}=\hat{Y}_{55}$ (circles), and where $\hat{U}=0.8U_\infty$ in the outer region, $\hat{Y}=\hat{Y}_{80}$ (squares), are plotted in Fig. 7 for γ=1.7, 2 and 3. For each value of γ the amplification of the disturbance in the inner region is greater than that in the outer region. This is related to the explanation mentioned in the previous paragraph, in conjunction with the ratio between the inner and outer maxima of the eigen-function. As is predicted by the theoretical amplification curves and confirmed experimentally, the initial amplification of the disturbance when suction or blowing are applied is larger or smaller, respectively, than that corresponding to γ=2, whereas the opposite trend is observed at distances further downstream.

Next, the evolution of the excited instabilities across region II is investigated. The distributions of the measured amplitude $|\tilde{u}|$ at three downstream locations and for γ=1.5 are shown in Fig. 9 and compared with the theoretical computations. The corresponding distributions of the viscous and inviscid modes are shown on the same figures by the dotted and dashed lines, respectively. The experimental data fits the theoretical distribution of the inviscid mode at $\hat{X}/H$=30 (below region II) and the theoretical eigen-function of the viscous mode at $\hat{X}/H$=70 (way above region II). However, the experimental results do not fit the theoretical distribution of either one of the modes in the downstream range between these two stations (see Fig. 9b). In this domain, where the inviscid and viscous modes coexist simultaneously, we had to decompose the experimental signals into their respective contributions. In order to do so we followed the method proposed recently by Tumin[6], who used the orthogonality property of the Orr-Sommerfeld operator with respect to various modes having the same frequency but different eigen-values and eigen-functions. In Fig. 9b the theoretical distribution based on the weighted contributions of both modes is shown by the solid line. Indeed, the experimental results are well described by the combination distributions.

In region III, the inviscid and viscous modes co-exist simultaneously. Thus, the fundamental component of the measured phase locked data contained a combination of both modes. Therefore, the decomposition procedure mentioned above had to be used. The measured and theoretical distributions of $|\tilde{u}|$ for γ=2 are shown in Fig. 10, which follows the

same structure as in Fig. 9b. As in region II, the experimental amplitude of $|\tilde{u}|$ do not fit either one of the two theoretical modes while it is well described by the combined theoretical distribution.

Acknowledgment

This research was supported by grant no. 88-00228 from the United States-Israel Binational Science Foundation (BSF), Jerusalem, Israel and by Technion V.P.R.Fund J. and J. Gringorten Aeronautical Research Fund. The authors would also like to express their thanks to Mr. Amos Beer for designing and building the apparatus.

References

1. M.B. Glauert, 1956, The wall jet, J. Fluid Mech. **1**, 625.
2. D.H. Chun & W.H. Schwarz, 1967, Stability of the plane incompressible viscous wall jet subjected to small disturbances, Phys. Fluids **10**, 911.
3. P. Mele, M. Morganti, M.F. Scibilia & A. Lasek, 1986, Behavior of wall jet in laminar-to-turbulent transition, AIAA **24**, 938.
4. J. Cohen, M. Amitay & B.J. Bayly, 1992, Laminar-turbulent transition of wall jet flows subjected to blowing and suction, Phys. Fluids. **4**, (2), 283.
5. M. Amitay & J. Cohen, 1993, The mean flow of a laminar wall jet subjected to blowing or suction, Phys. Fluids. **5** (8), 2053.
6. A. Tumin,1994, Decomposition of complex signals as a sum of a few eigen modes, submitted to AIAA 25th Fluid Dynamics conference.

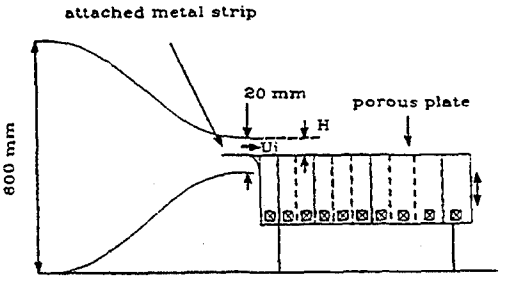

Fig. 1: A schematic side view of the blowing and suction apparatus.

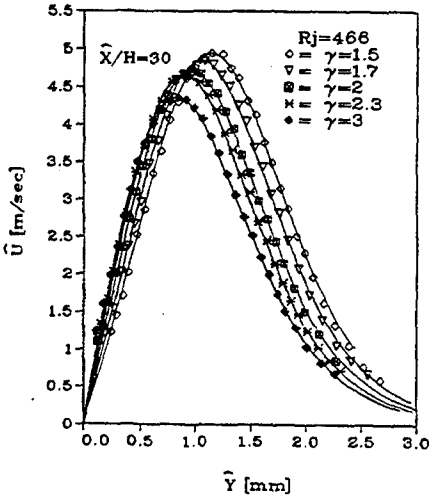

Fig. 2: Comparison between the theoretical and measured velocity profiles for various values of γ.

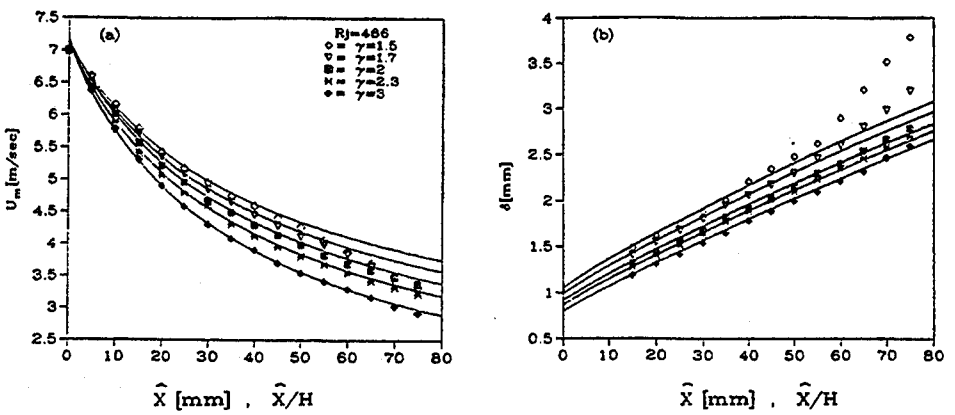

Fig. 3: The streamwise variation of (a) U_m and (b) δ for various values of γ.

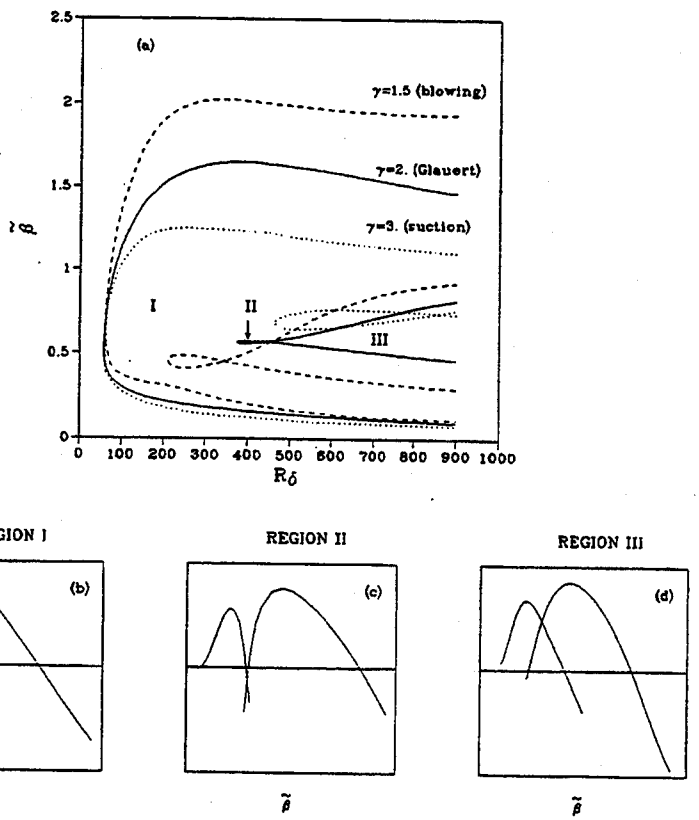

Fig. 4: (a) Neutral stability curves for γ=1.5, 2 and 3; (b), (c) and (d) representative amplification curves for regions I, II and III, respectively.

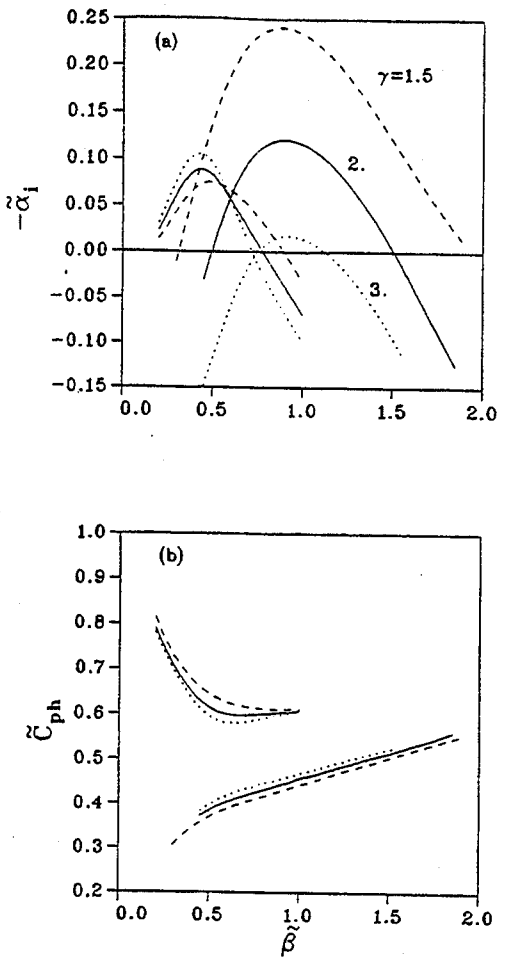

Fig. 5: (a) Spatial amplification rate $\tilde{\alpha}$ and (b) phase velocity $\tilde{C}_{ph}$ versus $\tilde{\beta}$ at R_δ=800 and various values of γ.

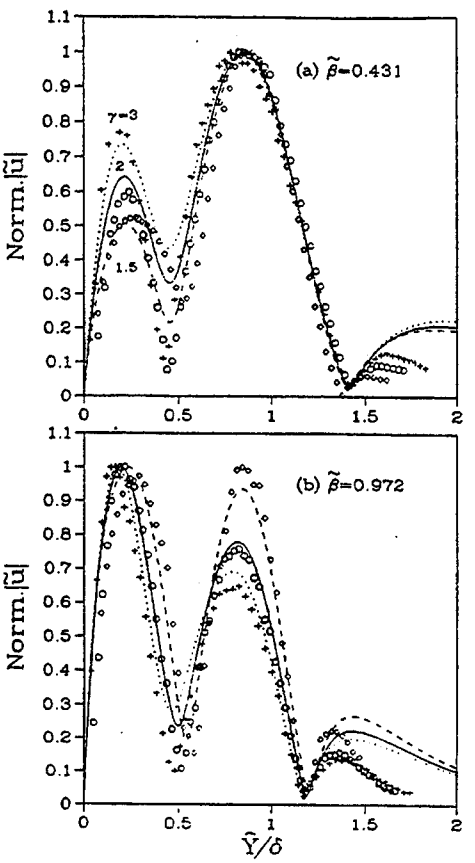

Fig. 6: The normalized modulus $|\tilde{u}|$ at R_δ=469 and γ=1.5, 2 and 3. (a) $\tilde{\beta}$=0.431 and (b) $\tilde{\beta}$=0.972. The symbols represent the experimental data while the solid lines are the corresponding theoretical solutions.

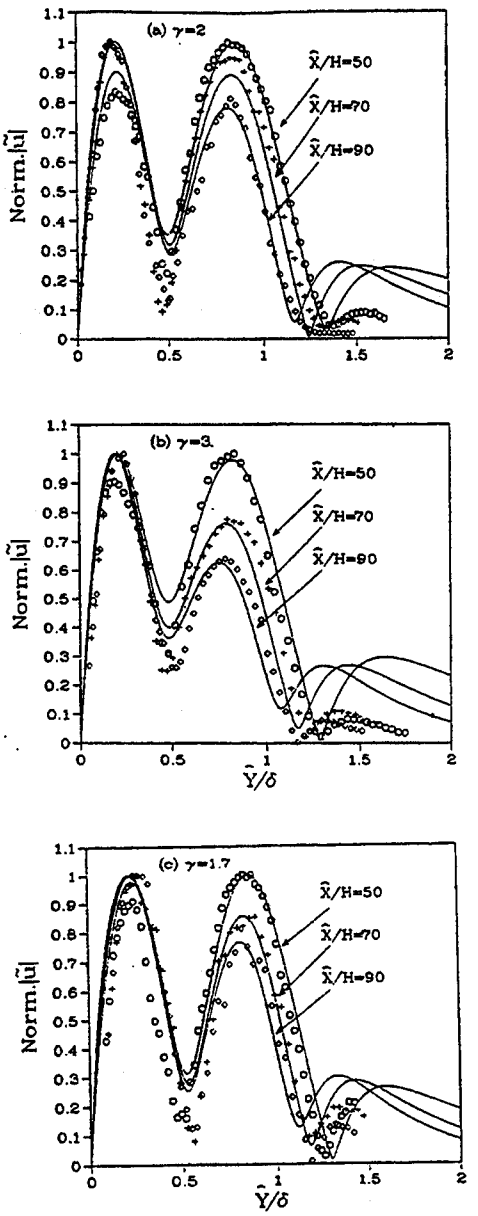

Fig. 7: Measured (symbols) and theoretical (lines) cross-stream distributions of $|\tilde{u}|$ at R_j=125 and for (a) γ=1.7, (b) 2 and (c) 3.

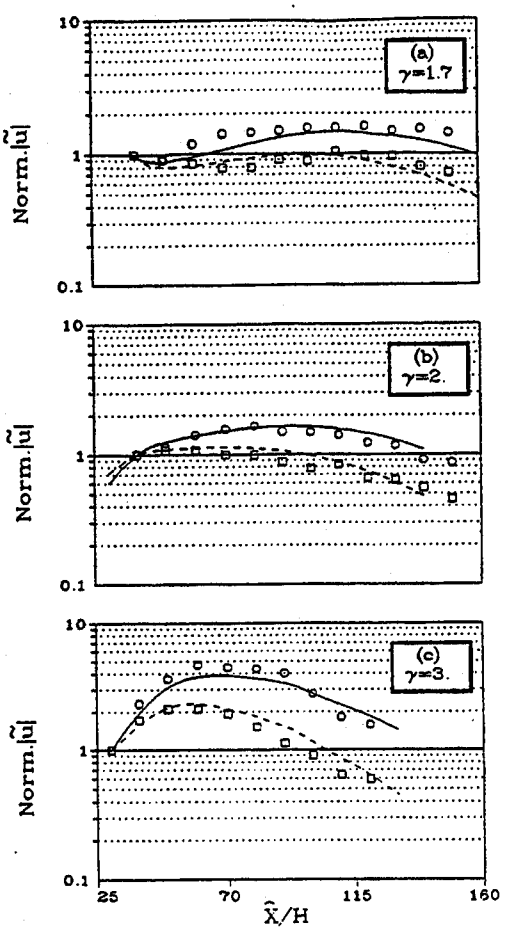

Fig. 8: The downstream development of $|\tilde{u}|$ measured at $\hat{Y} = \hat{Y}_{55}$ (circles) and $\hat{Y}_{80}$ (squares), R_j=125 and γ=1.7, 2 and 3. The solid and dashed lines are the corresponding theoretical predictions.

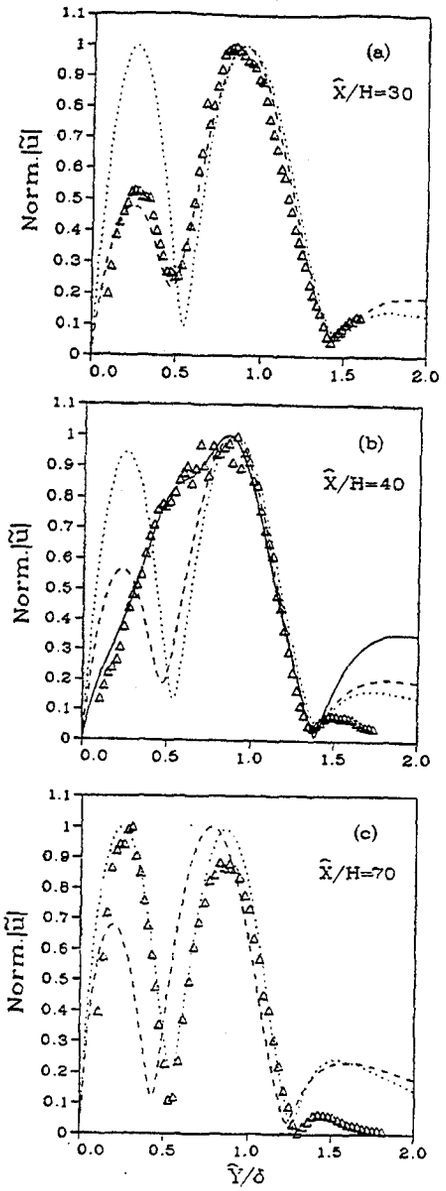

Fig. 9: The amplitude distribution of $|\tilde{u}|$ at R_i=180 and for γ=1.5. The symbols represent the experimental data while the lines are the corresponding theoretical distributions of the inviscid mode (dashed). viscous mode (dotted) and the weighted contribution of both modes (solid).

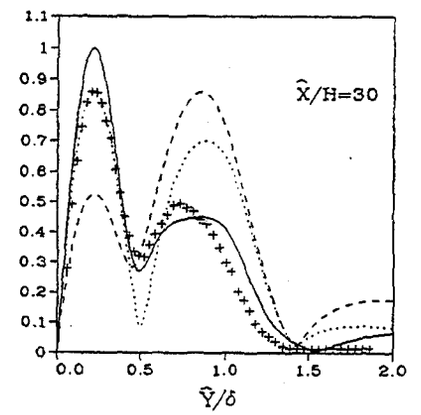

Fig. 10: The amplitude distribution $|\tilde{u}|$ at R_i=466 and for γ=2. The symbols represent the experimental data while the lines are the corresponding theoretical distributions of the inviscid mode (dashed). viscous mode (dotted) and the weighted contribution of both modes (solid).

MEAN FLOW CHARACTERISTICS OF TWO PARALLEL PLANE JETS

A. Nasr and J. C. S. Lai

Department of Aerospace and Mechanical Engineering, University College
The University of New South Wales, Canberra, ACT 2600, AUSTRALIA

ABSTRACT

The flow field generated by unventilated two parallel jets has been investigated using LDA. The two nozzles each with an aspect ratio of 24 were separated by 4.25 nozzle widths. Results show that a recirculation zone with sub-atmospheric static pressure was bounded by the inner layers of the individual jets and the nozzles plate. The effects of Reynolds number and side plates on the development of two parallel jets are discussed. Comparisons of LDA and hot-wire measurements are also made.

1. INTRODUCTION

Parallel turbulent jets have numerous technological applications such as entrainment and mixing processes in boiler and gas turbine combustion chambers, injection and carburetter systems, waste disposal plumes from stacks; all of which require an optimum nozzles' spacing to achieve desirable conditions. Parallel jets may be classified as ventilated or unventilated, depending on whether the surrounding air is entrained between them. The flow pattern of two unventilated plane jets is schematically shown in Fig. 1. Due to the mutual entrainment of the two jets, a sub-atmospheric region between the nozzle plate and inner shear layers is formed, thus resulting in the individual jet's axis being defected towards the axis of symmetry (x-axis). In general, the flow field of the two parallel jets can be classified into three distinct regions: converging region, merging region and the combined region. The merging region includes a recirculation zone which is bounded by the common wall of the two nozzles and the inner layers of the individual jets. The recirculation zone terminates at the merging point (mp) and the two individual jets continue to merge until at the combined point (cp) where the x-component velocity on the axis of symmetry becomes maximum. Downstream of the combined point, the two individual jets have combined to resemble a single jet. There have been several experimental studies on unventilated two parallel plane jets[(1)-(7)]. Table 1 shows the nozzle configurations, experimental conditions, measurement techniques and various parameters of unventilated jets reported in the literature. The following comments can be made on various studies listed in Table 1.

• In ref. (6), while the nozzle spacing (s/w) is small, the nozzle aspect ratio is low. Since side plates (for the ceiling and floor of the nozzles) were not used, there was essentially no flow convergence. Other studies, as listed in the Table 1, were mainly focussed on large nozzle spacings (s/w) with slow flow convergence rate. Quantitative measurements of the whole flow field are generally incomplete and there is a lack of documentation of nozzle exit conditions. Consequently, it is rather difficult to make comparisons between measurements obtained under different experimental conditions. For example, the following empirical results are reported by Tanaka[(2)] for $8.5 < s/w < 16$:

$$x_{mp}/w = 5.06(s/w)^{0.27} \qquad x_{cp}/w = 7.08(s/w)^{0.27}$$
$$x_p/w = 5.82(s/w)^{0.27} \qquad U_{max}/U_o = 1.96\,(s/w)^{-0.5} \qquad (1)$$

Here, U_{max} and x_p refer to the maximum x-component velocity and the location of the maximum pressure on the axis of symmetry (x-axis) respectively. These results may not be generalized to small s/w. As shown in Table 2, the agreement between parameters such as x_{mp}(merging length), x_{cp}(combined length), x_p and U_{max}/U_o determined from measurements and those obtained by equation (1) is quite reasonable for s/w=6 but there are substantial discrepancies for s/w<6. Such discrepancies indicate the need for studies of parallel jets with small nozzle spacing which produces faster flow convergence.

• As pressure and hot-wire measurements are subject to severe errors in the converging and merging regions, a non-intrusive measurement technique which can discriminate against reversed flow such as laser Doppler anemometry (LDA) should be used in these regions.

The objectives of this paper are, therefore, to document LDA measurements of the flow field formed by two parallel plane jets with a small nozzle spacing (namely, s/w=4.25). The effects of using side plates to enhance two-dimensionality of the flow and Reynolds number on the spatial development of the two parallel jets will be examined. Comparisons are also made between some LDA and hot-wire measurements.

2. EXPERIMENTAL METHOD

2.1 Apparatus

Two identical two-dimensional nozzles each of width w=10 mm and length l =240 mm (and hence an aspect ratio of 24 were made in stainless steel plates. The non-dimensional spacing (s/w) between the nozzles is 4.25. The nozzle plate thickness is 7.5 mm and the nozzle profile consists of a relatively short inner smooth section with a straight conduit of 6 mm. Side plates were placed horizontally at the top (ceiling) and bottom (floor) sides of the nozzles in order to enhance the two-dimensional behaviour of the flow by eliminating air entrainment between the jets through the top and bottom sides of the jets. Air from a blower was passed through a series of grids which reduced turbulence intensity. The nozzle exit Reynolds number is 11,000 with a x-component turbulence intensity u'/U_o of 0.01 on the jet axis at the exit of each nozzle. The ambient temperature variation was within 1°C.

2.2 Instrumentation

The laser light source for a two colour laser Doppler anemometer (LDA) was a Coherent INNOVA-70 Series Argon-ion laser with a maximum power of 10 W. Two DANTEC model 57N10 Burst Spectrum analyzers (BSA) were used to extract the Doppler frequencies. The BSA units were controlled by an NEC 386 computer through an IEEE interface for data acquisition using DANTEC BURSTware application program. A two channel TSI IFA 100 constant temperature hot-wire anemometer (HWA) was also used. Both single and X-wire sensors were gold-plated tungsten wires with a diameter of 0.005 mm and an active length of 2 mm. The hot-wire signal was digitized using a TSI IFA 200 A/D 12 bit converter. Both IFA 100 and IFA 200 were controlled by a PDP 11/23 computer for data acquisition and processing. Frequency spectra of the x-component velocity fluctuations u'(f) were determined by an Onosokki CF-350 FFT analyzer from the signal of a single hot-wire linearized using a DISA 55D10 linearizer. Both LDA and HWA probes were traversed by stepping motors controlled by an NEC 286 computer.

2.3 Experimental procedure

For LDA measurements, the flow was seeded using Rosco Fog Fluid. The particle concentration was optimized to achieve optimum visibility factor. In the BSAs, amplitude discriminations such as oversize rejection, quality factor, envelope and pedestal, can be applied to the captured Doppler signals. This capability and the possibility of applying different acquisition modes such as continuous, burst, controlled dead time and external modes were tested to reject large particles and to reduce bias errors. All results reported here were acquired in burst mode based on both pedestal and envelope. Electronic noise was minimised and the laser beam intensity was set at about 200 mW to reduce shot noise. Noise from the surroundings was negligible. The number of bursts used for each measurement was at least 2000. All velocity data were weighted with a transit time weighting function. For hot-wire measurements, the sampling rate was set at 5 kHz. All frequency spectra were obtained using a single hot-wire. As the flow field is symmetric, only half of the flow field in the positive y direction was measured and presented.

3 RESULTS

3.1 Effect of side plates

The variation of the normalised mean x-component velocity on the x-axis (U_c/U_o) with downstream distances, in the presence of side plates, is shown in Fig. 2. It can be seen that U_c/U_o is negative in the merging region, thus indicating reversed flow. At the merging point, U_c/U_o is zero and owing to the merging process, it continues to increase up to the combined point. Downstream of the combined point, the two individual jets have combined to resemble a single jet and U_c/U_o decreases as the jet spreads. For unventilated parallel jets with low nozzle's aspect ratio, there could be significant entrainment of the surrounding air through the top and

bottom sides of the jets if side plates were not installed. In the absence of side plates, the magnitude of U_c/U_o is lower in the merging region than that with side plates installed, because of the entrainment of air between the jets through the top and bottom sides of the jets. Consequently, the rate of convergence of the individual jets is smaller, resulting in less curving of the individual jet axis towards x axis. This interpretation is supported by Fig. 3 which shows higher turbulence intensities (u_c'/U_o,v_c'/U_o) on the x-axis in the merging region when side plates were installed.

3.2 Effect of Reynolds number

The distributions of mean x-velocity components (U/U_o) at x/w=2 in Fig. 4 indicate that they are virtually independent of the nozzle exit Reynolds number in the range of 11,000 to 19,300. This is also supported by the variation of U_c/U_o with x/w as shown in Fig. 5. Similar results were reported by Tanaka[2] who examined the effect of Reynolds number on the location of maximum pressure and the magnitude of the maximum velocity on the axis of symmetry.

3.3 Variation of static pressure on x-axis

The static pressure distribution plays a significant role in determining the flow characteristics of parallel jets. Fig. 6 displays the static pressure distribution, $(P_c - P_{atm})/0.5\rho U_o^2$, on the x-axis for various Reynolds numbers. The static pressure decreases to a minimum around the vortex centre (x/w=3), increases near the merging point to a maximum above atmospheric, and decreases to below atmospheric as the individual jets merge and spread. This trend of pressure distribution is in agreement with those of refs.(1), (3)-(5). The locations of minimum and maximum pressure as shown in Fig.6 are virtually independent of Reynolds numbers. These locations occur further downstream when side plates were not used, which are consistent with observations in Figs. 2-3.

3.4 Spectral measurements

The dynamic behaviour of the free shear layers is governed by the formation and evolution of the flow instabilities. The development of instabilities in the outer shear layer of the parallel jets and of a single free jet at various downstream distances can be illustrated by the frequency spectra of the x-component fluctuation u'(f) at the edge of the potential core, as shown in Figs. 8 and 9 respectively. Similar behaviour of instability waves, though not presented here, were observed in the inner shear layer of the parallel jets. As expected, since the nozzle conditions are identical, the parallel jets and single free jet have the same fundamental frequency of 2400 Hz. However, in a single free jet, the structures appear to be stronger and their development is more distinct than in parallel jets.

3.5 Mean velocity distributions

The spatial development of the mean x- velocity components U/U_o is plotted in Fig. 9. Unlike single free jets, the interacting parallel jets have inclined velocity profiles in the potential core region due to the deflection of the individual jet's axis towards the axis of symmetry (x-axis). Reversed flow in the recirculation zone can be seen from Fig. 9 up to x/w=4 where the two jets merge. Downstream of the combined point, at x/w=8, the two jets combine to spread like a single free jet. Fig. 10 shows the x-component velocity profiles in the combined region. Here, the x-component velocity and the y-axis have been normalized by local maximum velocity (U_m) and jet half width ($y_{0.5}$) respectively. While the velocity profiles are still developing for x/w<20, the flow appears to be approaching fully-developed 'state' by x/w=20 since the measured velocity profile there agrees with the theoretical curve of Gortler[8].

3.6 Turbulence intensity distributions

Fig. 11 displays the spatial distributions of normalized x-component turbulence intensities u'/U_o. Two peaks for turbulence intensities are observed in the inner and outer shear layers near the nozzle exit. The u' peak has a higher magnitude in the outer shear layer than that in the inner shear layer and is dominant in the whole flow field, indicating that u' in the outer shear layer is less constrained by the recirculation flow and the merging process. The u' peak in the inner shear layer disappears at x/w=6 just upstream of the combined point. It should be noted that another

peak in u' has been detected at x/w=2.5 close to the vortex centre. By x/w=3, the u' peak in the inner shear layer has merged with that in the recirculation zone.

3.7 Reynolds shear stresses distributions

The spatial development of the Reynolds shear stress is presented in Fig. 12. It can be seen that the Reynolds shear stress in the inner and outer shear layers are similar in magnitude close to the nozzle exit for x/w<2.5. A local maximum in Reynolds shear stress in the recirculation zone starts to appear at x/w=2. Just upstream of the merging point (x_{mp}/w=4), Reynolds shear stress in the neighbourhood of the axis of symmetry has increased substantially, thus indicating high momentum transfer between the flow near the axis of symmetry and the outer shear layer. The behaviour of the Reynolds shear stress resembles that of a free single jet beyond x/w=10.

4. COMPARISONS BETWEEN LDA AND HWA MEASUREMENTS

Traditional hot-wire techniques are subjected to measurement errors in the converging region. Attempt was made to identify the extent to which hot-wires could be used for measurements of parallel jets. Both LDA and HWA measurements were first validated in a single free jet. For comparisons, measurements were then made by LDA and HWA at three different cross sections x/w=1, 4 and 7 in the converging and merging regions. Results for mean x-component velocity, turbulence intensity and Reynolds shear stress are shown in Figs. 13 to 15 respectively. The agreement between LDA and HWA results is good in the outer shear layer for x/w=1 to 7. However, there are significant differences between the LDA and HWA results in the inner shear layer, in the converging region and in the vicinity of the merging point. These differences are being attributed to the presence of recirculation flow in the converging region and the flow angle in the initial merging region that may exceed the calibration angle of X-wires. However for x/w=7, near the combined point, the LDA and HWA results agree very well with each other.

5. CONCLUSIONS

The velocity field of two parallel plane jets with nozzle aspect ratio of 24 and nozzle spacing (s/w) of 4.25 has been measured using LDA. It has been shown for nozzles with aspect ratio less than 30 that side plates should be used to enhance the two-dimensionality of the flow. For the Reynolds number range between 11,000 and 19,300, the flow is virtually independent of Reynolds number. The spatial distributions of x-component velocity and turbulence intensities clearly reveal the recirculation zone, the merging point and the combined point. Comparisons between HWA and LDA measurements indicate good agreement in the outer shear layer for all x/w but substantial discrepancies exist in the recirculation zone and near the merging point.

ACKNOWLEDGEMENT

A. Nasr would like to acknowledge the receipt of a scholarship from Scholarship Department of Iran's Ministry of Culture and Higher Education to undertake this research.

REFERENCES

1. Miller, D.R. and Comings, E.W. (1960) Force - Momentum fields in a dual - jet flow. *J. Fluid Mech.* **7**, 237-256.
2. Tanaka, E. (1970) The Interference of Two - Dimensional Parallel Jets. (1st Report, Experiments on Dual Jet) *Bulletin JSME*, **13**, 272-280.
3. Tanaka E. (1974) The Interference of Two - Dimensional Parallel Jets. (2rd Report, Experiments on the combined flow of dual jets), *Bulletin JSME* , **17**, 920-927.
4. Murai, K. et. al. (1976) An Experimental Study on Confluence of Two-Dimensional Jets. *Bulletin JSME*, **19**, 956 - 964.
5. Militzer, J. (1977) Dual plane parallel turbulent jets. *PhD thesis*, University of Waterloo.
6. Ko, N.W.M. and Lau, K.K. (1989) Flow Structures in Initial Region of Two Interacting Parallel Plane Jets. *Experimental and Fluid Science*, **2**, 431-449.
7. Lin, Y.F. and Shev, M.J. (1991) Interaction of Parallel Jets. *AIAA J.*, **29**, 1372-1373.
8. Gortler, H. (1942) Berechnung Von Aufgaben Der freien Turbulenz Auf Grund Eines Neuen Naherungsansansatze. *Z. Angew, Math. Mech.* **22**, 244.

Table 1 Summary of experimental studies of unventilated parallel plane jets.

Author	Aspect ratio	s/w	Re	Measurement technique	x_{mp}/w	x_{cp}/w	Main regions and quantities considered
Miller & Commings ref. (1)	40	6	17,800	Disk type static pressure probes and hot-wire	6.8	12.4	Pressure, velocity and turbulence intensity in the merging and combined regions.
Tanaka refs. (2)-(3)	60–80	8.5–26.3	4,290 – 8,750	Single hot-wire and Disk type prssure probe	Eq. (1)	Eq. (1)	Streamwise velocity, turbulence intensity and pressure distributions in merging and converging regions and velocity in combined region.
Murai ref. (4)	20.6	4.1 17.5 20.6 23.7 31	3,350 – 18,600	Static and total pressure probes single hot-wire	—	9.8 21 23.7 26 31	Pressure and streamwise velocity in the converging and combined regions considering the effect of nozzle converging angle.
Militzer ref. (5)	13.32	6	55,600	Pressure probe and hot-wire	7.1	12	Pressure and velocity in the converging and merging regions.
Ko & Lau ref. (6)	5.6	2.5	40,000	Single and x-wires	—	10.5	Streamwise velocity, turbulence intensities, Reynolds shear stress, and time and frequency domain instability measurements in the merging region.
Lin & Sheu ref. (7)	90	30 40	7,600	Split-film	21.6 27.6	30.5 40	Streamwise mean velocity, turbulenc intensities and Reynolds stress in the combined region.

Table 2 Comparison between various parameters determined by measurements and calculations (in parentheses) from equation (1).

refs. / parameters	present study s/w=4.25	ref. (6) s/w=2.5	ref. (1) s/w=6	ref. (5) s/w=6
x_{mp}/w	4 (7.5)	1.5 (6.48)	6.8 (8.2)	7.1 (8.2)
x_{cp}/w	8 (10.4)	10.5 (9.06)	12.4 (11.48)	12 (11.48)
x_p/w	4.7 (8.6)	—	7.4 (9.44)	8.1 (9.44)
U_{max}/U_o	0.81(0.95)	—	0.76 (0.8)	8 (8)

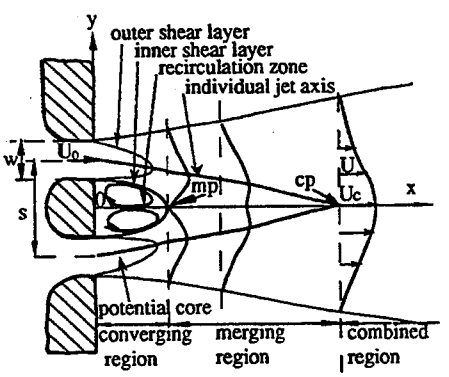

Fig. 1 Schematic diagram of two parallel plane jets.

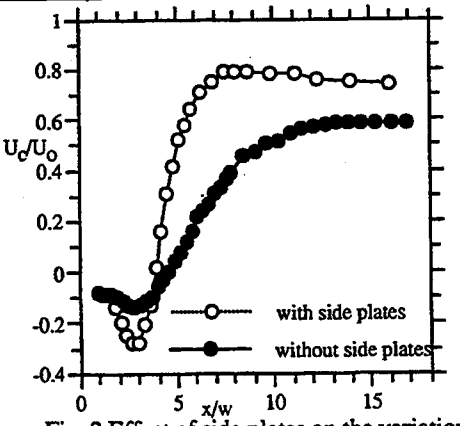

Fig. 2 Effect of side plates on the variation of U_c/U_o with downstream distances

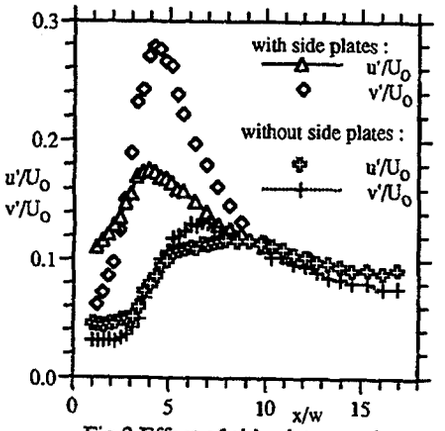

Fig.3 Effect of side plates on the variation of turbulence intensities.

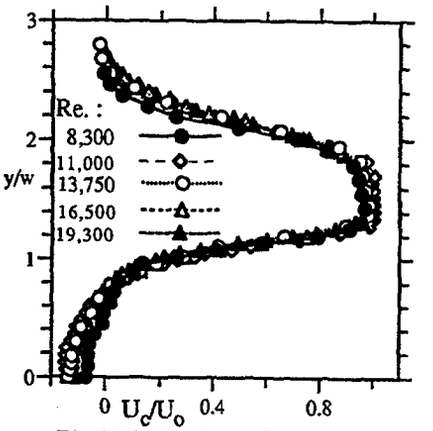

Fig.4 Distributions of x-component velocities at x/w=2.

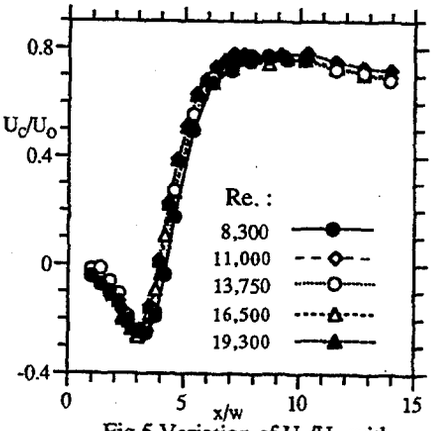

Fig.5 Variation of U_c/U_o with downstream distances.

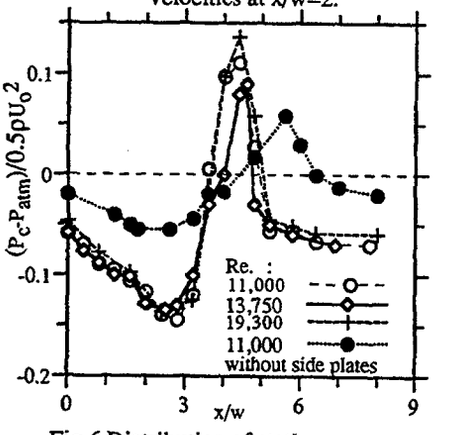

Fig.6 Distribution of static pressure.

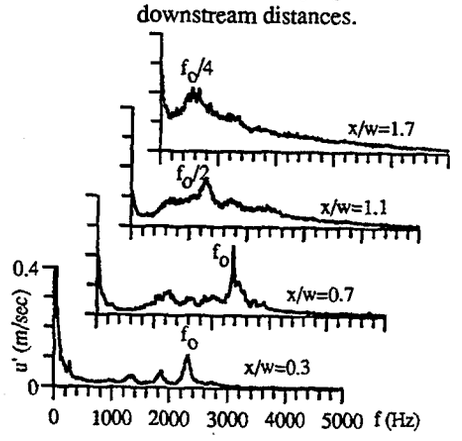

Fig.7 Evolution of instabilities in the outer shear layer of parallel jets.

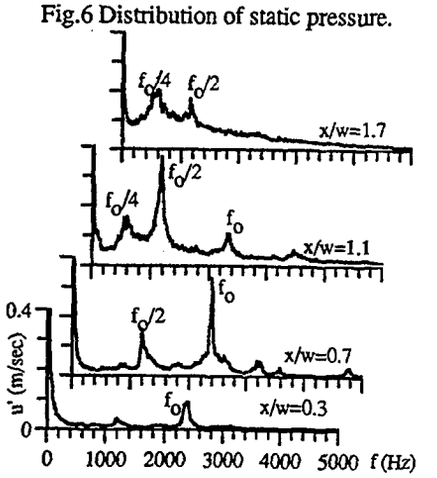

Fig. 8 Evolution of instabilities in the shear layer of a single free jet.

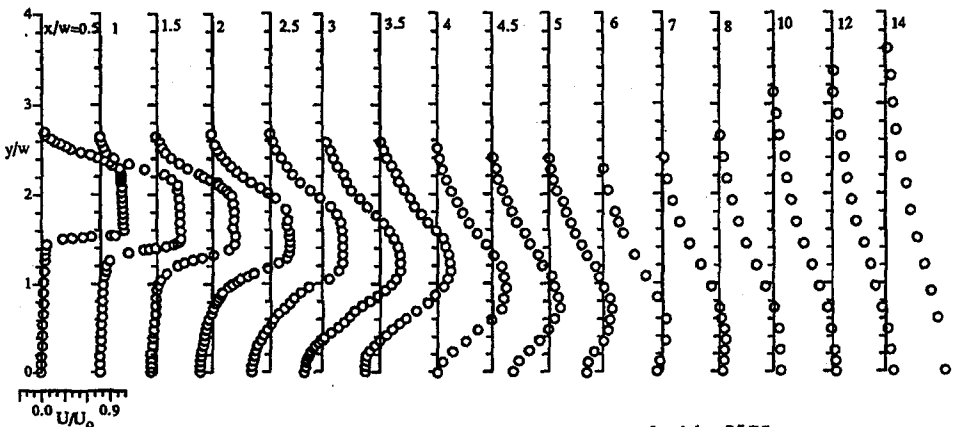

Fig. 9 Spatial distributions of x-component velocities U/U_o.

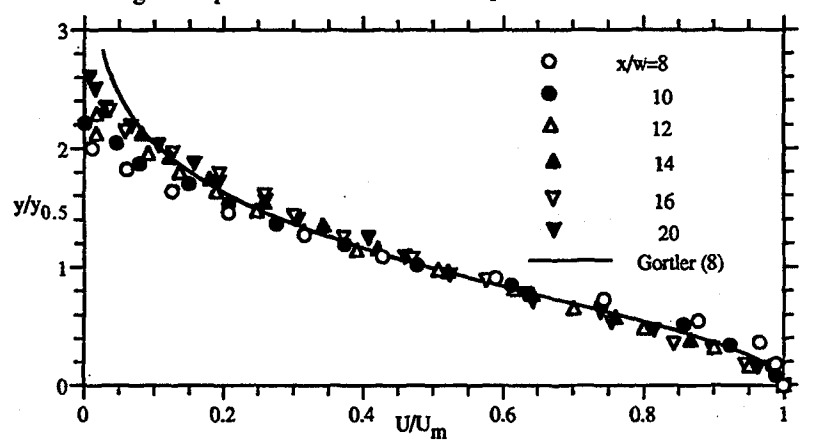

Fig. 10 x-component velocity profiles U/U_o in the combined region.

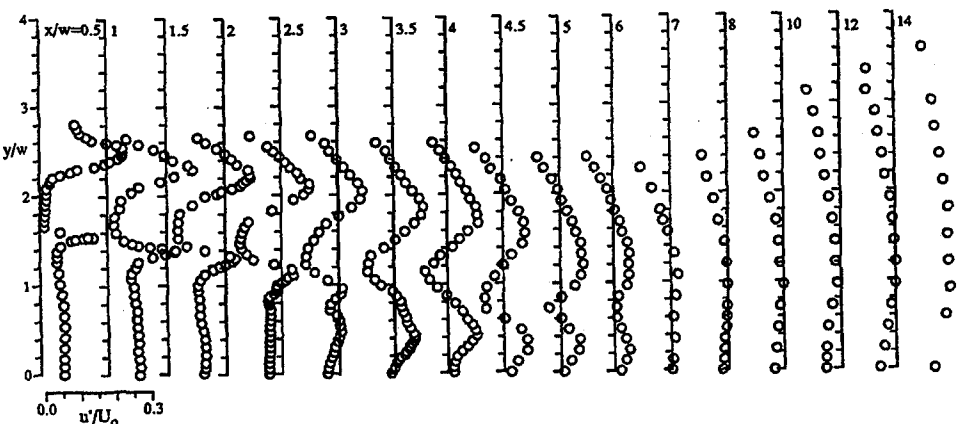

Fig. 11 Spatial distributions of x-component turbulence intensities u'/U_o.

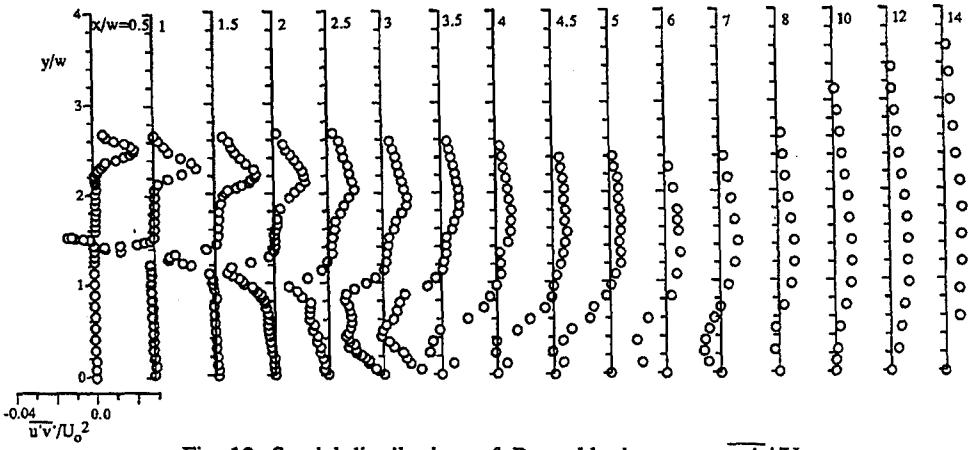

Fig. 12 Spatial distributions of Reynolds shear stress $\overline{u'v'}/U_o$.

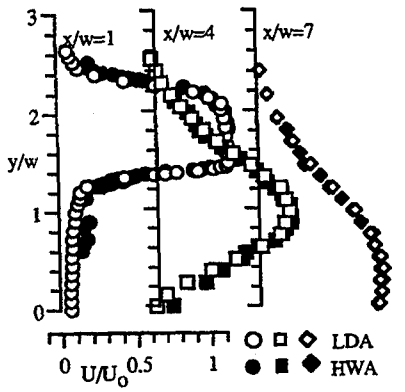

Fig. 13 Comparisons between LDA and HWA for x-component velocity profiles.

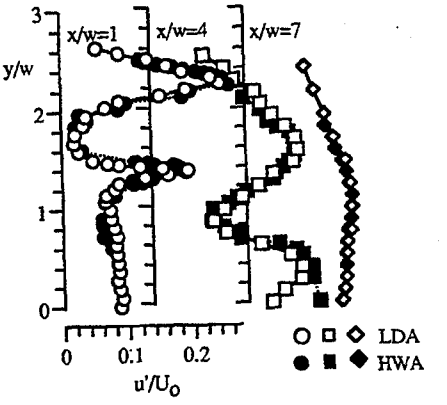

Fig. 14 Comparisons between LDA and HWA for x-component turbulence intensity profiles.

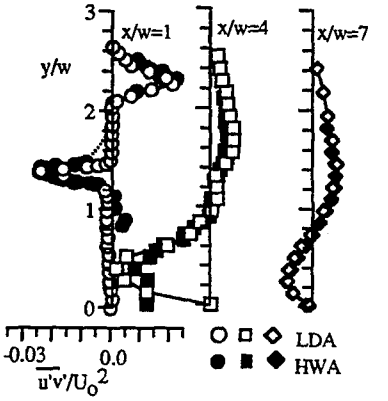

Fig. 15 Comparisons between LDA and HWA for Reynolds shear stress profiles.

INTERACTION OF A PERPENDICULAR WALL JET WITH A CROSS FLOW

J.-M. Charbonnier[+] R.L. Leblanc[*]
Laboratoire d' Etudes Aérodynamiques (URA 191)
Université de Poitiers
Centre d' Etudes Aérodynamiques et Thermiques
Poitiers, (France)

Abstract

An experimental investigation of a jet in cross flow for low injection ratio is reported. The emphasis is put on the detection and analysis of the unsteady phenomena present in the jet's wake. For this case of low injection ratio (R=0.56), vortex shedding in the jet's wake, already observed for high injection ratio, is coupled with the jet deformation into the injection duct and it leads to a transverse flapping of the jet. This study clearly shows than any attempt to simulate a jet in cross flow in such a case will require to account for the unsteady effects which are governing the jet development.

Nomenclature

D	Jet diameter [mm]	R	Mass flux injection ratio $\rho_j V_j/\rho_{ref} U_{ref}$ [-]
U, V, W	Mean velocity components [m/s]	Re	Reynolds number $\rho_{ref} U_{ref} D/\mu_{ref}$ [-]
$R_{uu, vv, ww}$	Non dimensional Reynolds stresses [-]	St	Strouhal number $f D/U_{ref}$ [-]
Pd	Dynamic pressure [N/m^2]	**Subscripts**	
Cpt	Total pressure coefficient $(Pt_{ref}-Pt)/Pd_{ref}$ [-]	ref	reference conditions measured at X/D=-3
Cps	Static pressure coefficient $(Ps-Pw_{ref})/Pd_{ref}$ [-]	t	stagnation value
V_j	Velocity in the potential core of the jet at -1.5D inside the injection duct [m/s]	s	static value
		w	wall value
		j	jet value

Introduction

In many applications, the configuration of a jet introduced in a main flow is encountered : VSTOL aircraft, pollutant dispersion, aerodynamic control, fuel injection, turbine blade cooling. In a recent publication, Margason[1] made a review of the research conducted in this field during the

[+] presently Assistant Professor at von Karman Institute for Fluid Dynamics
Rhode-Saint-Genèse, Belgium

[*] Research Engineer

last fifty years where he concluded that more appropriate turbulence models in and near the jet exit are needed to improve the numerical simulation of jets in cross flow. Of course these improvements require that an important effort is made to provide both steady and unsteady detailed measurements.

The study presented in this paper is dedicated to the application of turbine blade film cooling by discrete injection of cold air in the boundary layer. In order to have a better understanding of the flow interactions between the jet and the cross flow which control the efficiency of the cooling, a fundamental experimental study was initiated at the Centre d'Etudes Aérodynamiques et Thermiques (CEAT) in Poitiers.

A large scale model (jet diameter D=100mm) is used to conduct a detailed investigation of the jet development in the vicinity of the injection exit in the incompressible regime. Figure 1 shows the experimental arrangement used. The jet duct is perpendicular to a flat plate installed in a subsonic Eiffel wind tunnel of 1.7 m diameter. The cross flow velocity equals 16 m/s and the jet velocity equals 9m/s. Both the cross flow and the jet fluids are air at the same temperature, and the injection ratio defined as the mass flux ratio R is equal to 0.56. At the jet location, the boundary layer on the flat plate without jet is fully turbulent and the thickness at 99% equals 0.1D. The velocity profile at the jet exit without cross flow shows that the duct flow is not fully developed (fig. 1).

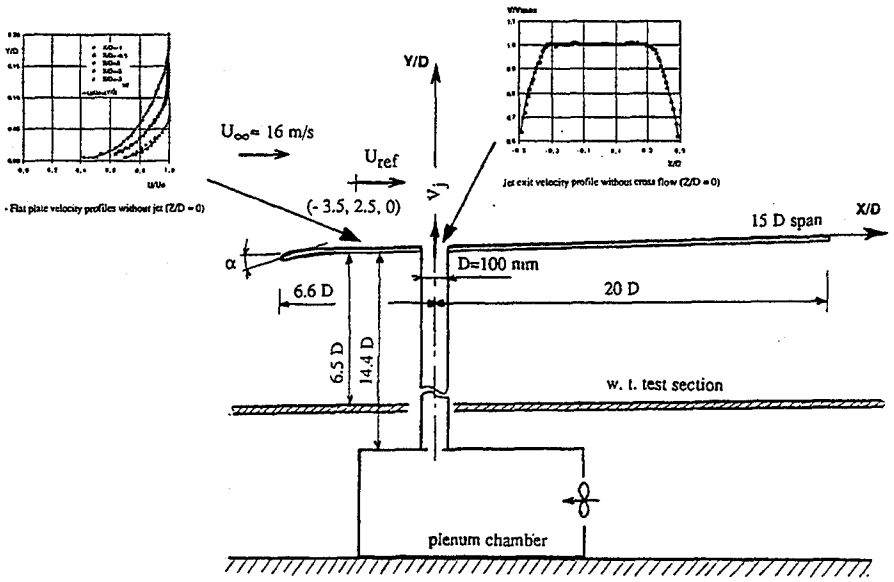

Fig. 1 : Experimental set-up

Mean velocity and pressure measurements are made with a five hole directional probe which is iteratively aligned with the mean flow direction in order to increase the accuracy of the measurements. Cross slanted hot wires are used to characterize the velocity fluctuations and in order to improve the accuracy, the hot wire probe axis is aligned with the mean flow direction deduced from the five hole probe measurements. Flow visualizations including oil flow and laser sheet techniques are used to provide a detailed picture of the flow interaction.

Global description of the interaction

Figure 2 presents a schematic picture of the interaction when the injection ratio is sufficiently high so that the jet penetration into the cross flow is significant [2,3]. The jet behaves as an obstacle for the cross flow and it creates a pressure difference which bends the jet. The streamlines passing around the jet contribute to the strength of two counter rotating vortices in the lee side of the jet. In such configuration, integral modelization of the jet development were made using singularities to simulate the entrainement and the vortices [4,5]. The models were improved recently to provide a better description of the jet potential core, the jet shape and the decrease of the vortex intensities [6,7]. These modelisations give an adequate simulation of the interaction provided the injection ratio is greater than 1. In the case of low injection ratio, the interaction is much more complex and already takes place within the injection duct [8,9].

In this experimental study, the region of interest is located around the jet exit and in the jet duct. Figure 3 shows the total pressure coefficient Cpt measured with the five hole probe in two vertical planes. In this low injection case (R=0.56), the jet remains close to the flat plate and a strong interaction takes place between the jet and the flat plate boundary layer [10].

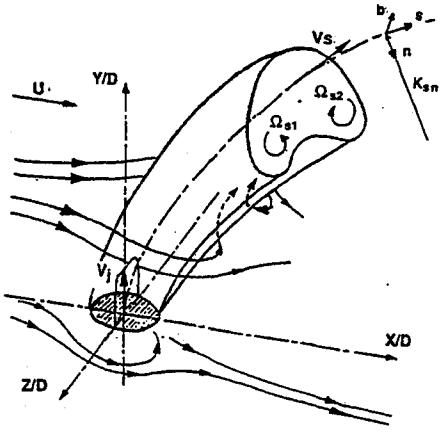

Fig. 2 : Schematic of a jet in cross flow

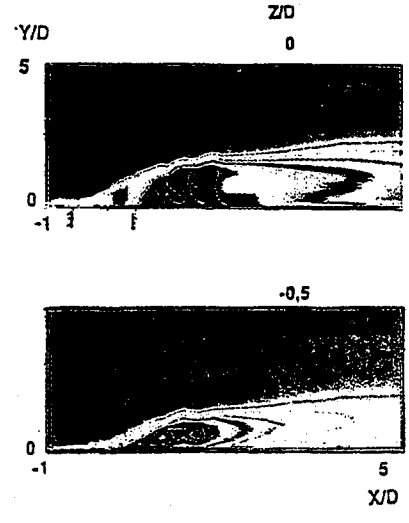

Fig. 3: Total pressure coefficient in vertical planes

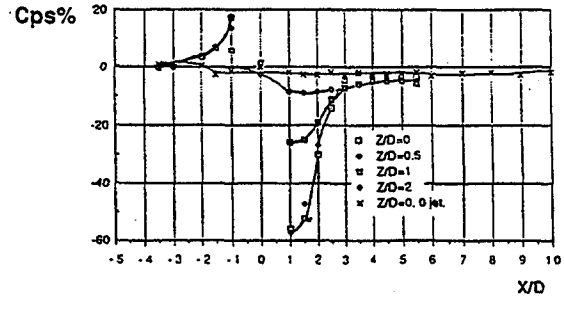

Fig. 4 : Wall pressure coefficient around the jet exit (R=0.56)

Figure 4 displays the wall static pressure coefficient measured around the jet exit and compared to the pressure distribution for the smooth flat plate without injection. The large expansion observed immediately downstream of the exit is responsible for the jet bending. In the case of low injection ratio, the jet pressure field is distorted within the injection duct (fig. 5). It is clearly seen that the perturbation extends as far as 1.5D inside the duct. Static pressure coefficient in the exit section of the jet shows the distortion of the potential core of the jet with the flow acceleration on the downstream side and the deceleration on the upstream side of the duct.

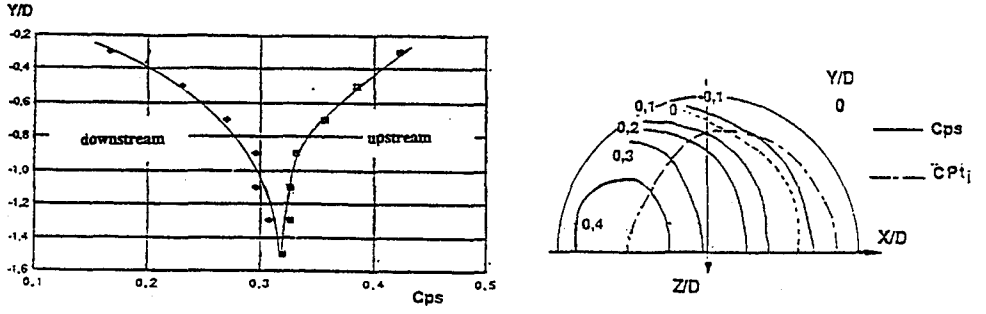

Static pressure coefficient on two generatrix of the injection pipe Static pressure coefficient in the exit section of the injection pipe

Fig 5 : Static pressure coefficient in the injection duct

The oil flow visualization in figure 6 describes the flow pattern around the exit. Using the topological rules[11,12] and information collected in this study[10], a schematic of the flow pattern is proposed.

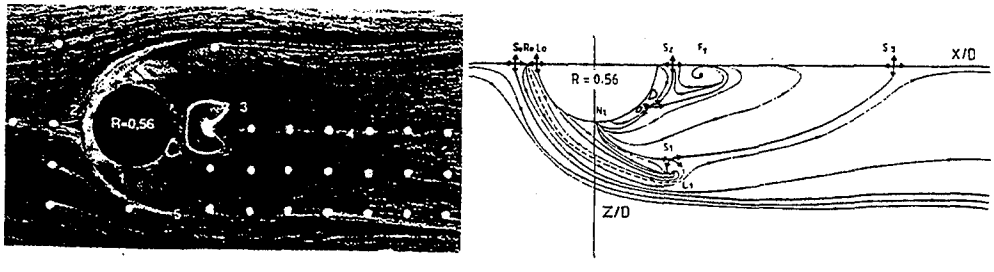

1 : separation line
2: three dimensional separation point
3 : reverse flow region
4 : saddle point ending the reverse flow region
5: horseshoe vortex system

Fig. 6 : Wall streamline visualization around the jet exit

A horseshoe vortex structure appears around the exit and the two branches of the vortex remains separated in their downstream development. Downstream of the exit in the jet wake, complex vortical structures are present. A region of reverse flow is ended by a saddle point (S_0) in the

centerline at 2.5D downstream of the jet exit. Inside the reverse region, two counter rotating foci (F_1) are found close to the jet exit and they allow to evacuate the reverse flow into the jet vortices. A separation line is also hardly visible between the horse shoe vortex and the upstream side of the exit (L_0L_1). The separation line ends near the horseshoe vortex at X/D=1 and Z/D=-1. The combination of saddle point (S_1) and focus (L_1) placed at this location is linked to the vortex shedding phenomenon in the jet wake which will be described in the next section.

Characterization of the unsteady phenomena

Vortex shedding in the jet wake was discovered very early by spectral analysis of the velocity measurements[13,14,15] but it was not explained correctly. The first correct analysis of the phenomenon was given by Fric and Roshko[16] using both visualizations and spectral analysis in the case of injection ratio larger than 2. Vortex shedding occurs in the flat plate boundary layer on each side of the jet when it faces an adverse pressure gradient. This vortex shedding develops in "spin up vortices" in the jet wake that go up under the action of the jet main vortices. The flow visualizations by Fric and Roshko[16] show a mushroom pattern in a plane parallel to the wall instead of a classical von Karman vortex arrangement. Recently, flow visualisations conducted in a water tunnel[17,18] for injection ratios from 2 to 4 have shown that these vortices undergo a pairing which may explain this mushroom pattern. So far, all study mentioning these wake vortices were conducted for injection ratio higher than 1. In such a case, the jet remains far from the wall and the jet's wake vortices are not likely to play a significant role in the development of the jet at least close to the exit. Very few investigations were conducted for injection ratio lower than 1[9,15], and it is not clear if these vortices are still present and if they play a role in the jet development. In the present study, the dimension of the experimental set-up allow for a detailed investigation of the vicinity of the jet exit. The results presented hereafter put the emphasis on the detection of the wake vortices and the evaluation of their effect on the jet development.

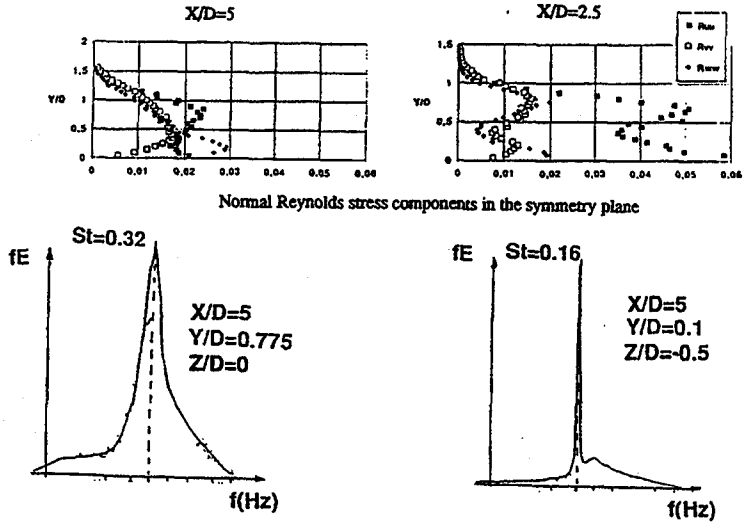

Fig. 7 : Measurement of velocity fluctuations

Based on an extensive survey of the mean flow quantities with a five hole probe[10], velocity fluctuations are measured using a hot wire probe which axis is aligned with the mean velocity direction. Figure 7 shows the normal Reynolds stresses normalized by the infinite upstream velocity in the symmetry plane Z/D=0 for two streamwise positions X/D=2.5 and X/D=5. Very high level of turbulence are measured and the transverse component Rww increases near the wall when the distance to the exit increases. Such a variation was already measured by Crabb et al[13] but not explained. On the contrary, Andreopoulos et al[9] mentioned that the transverse component of the normal stress is negligible.

A spectral analysis of the velocity fluctuations for positions respectively in the symmetry plane Z/D=0 and at Z/D=-0.5 (fig. 7) shows well defined frequencies corresponding to Strouhal numbers respectively equal to 0.32 and 0.16. These values of Strouhal numbers are likely to be related the vortices shed in the jet wake, and the frequency doubling may attributed to the fact that the probe placed in the symmetry plane "feels" the vortices shed on both side of the jet. In order to verify these assumptions, flow visualizations using smoke as a tracer and a laser sheet are performed. Images taken with a video camera with an exposure time of 1/4000s show the jet frontier in the symmetry plane by injecting smoke in the cross flow (fig. 8).

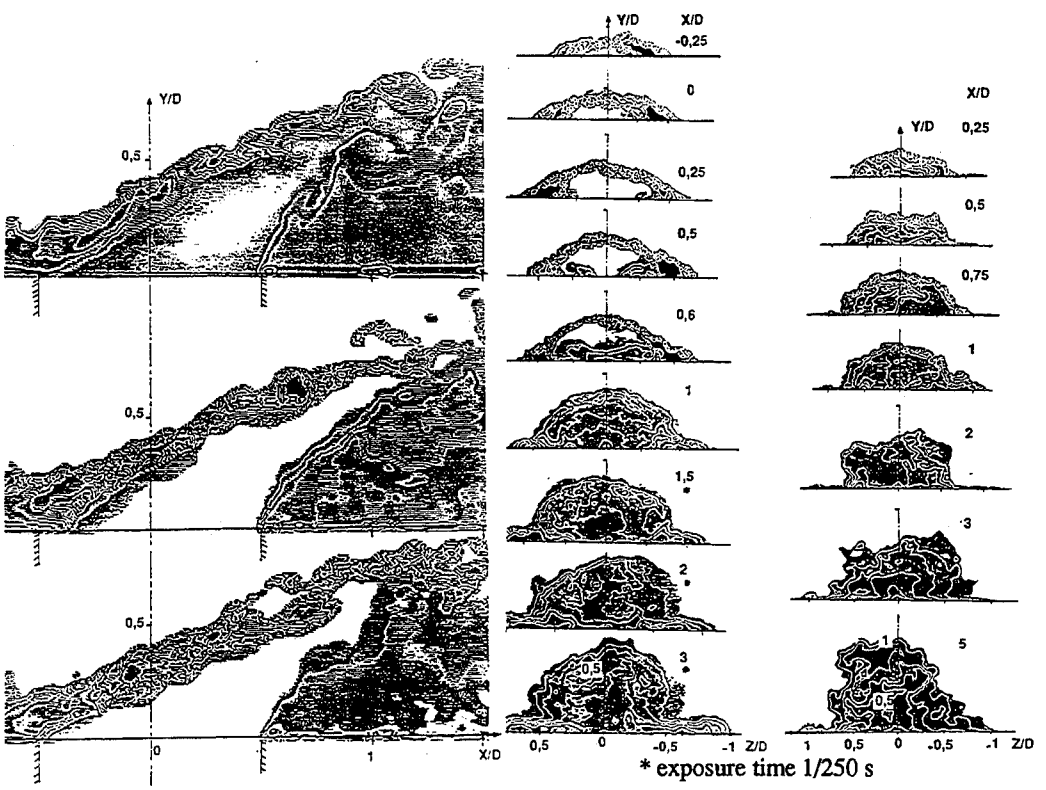

Fig. 8 : Flow visualisations in the symmetry plane

Fig. 9 : Flow visualisation in cross sections

An unsteady behavior of the jet frontier is clearly visible and for the central image, fluid coming from the cross flow is entering into the jet duct[10]. Figure 9 shows similar visualizations done in

An unsteady behavior of the jet frontier is clearly visible and for the central image, fluid coming from the cross flow is entering into the jet duct[10]. Figure 9 shows similar visualizations done in cross sections where the smoke is injected in the cross flow (left in fig. 9) or in the jet flow (right in fig. 9). Smoke injected in the cross flow allows to visualize the formation of the two counter rotating vortices over the jet exit (X/D=0.25, 0.5). It gives an evidence that the jet boundary layer is actually the source of these vortices. Further downstream, the jet cross section becomes non symmetric and small exposure times allow to visualize a large deformation of the jet (X/D=3, 5 in the right of fig. 9). The higher part of the jet is swept away from the symmetry plane alternatively on the right and on the left side whereas the lower region close to the wall moves in the opposite direction. When the images are taken with an exposure time of 1/250s, this effect is averaged and the cross section becomes symmetric as found with the pressure probe.
This periodic transverse flapping of the jet results from the interaction of the jet with vortices shed in the jet wake. In this low injection ratio case, there is strong interaction between the jet and the vortices shed alternatively on each side of the jet. Figure 10 focuses on the region where the vortex shedding takes place.

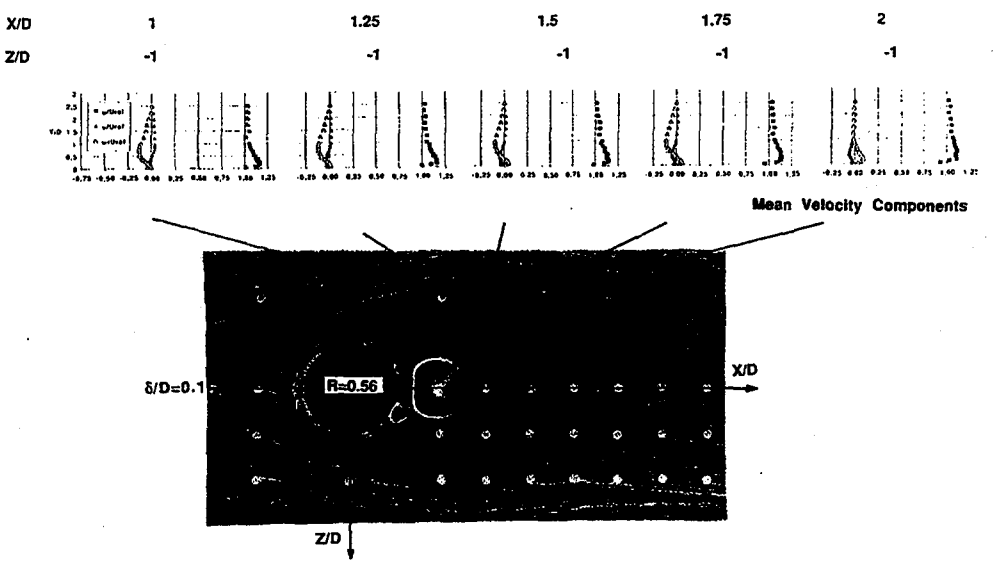

Fig. 10 : Mean velocity profiles in the vicinity of the vortex shedding

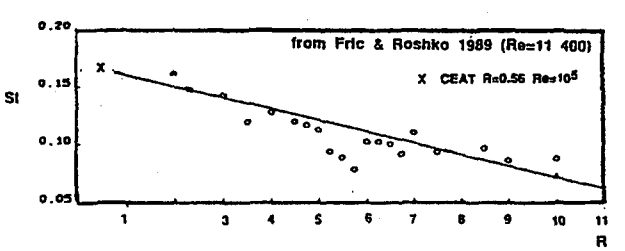

Fig. 11 : Strouhal numbers in the jet's wake

Actually, it corresponds to the location where the separation line ends and where a focus was placed in the schematic of the wall streamlines in figure 6. Using the mean velocity component profiles, it can be seen that this location corresponds to the first streamwise position at which the external cross flow starts to enter the jet wake ($w/U_{ref}>0$). The Strouhal number based on the vortex shedding frequency is in good agreement with the trend found by Fric and Roshko[16] for higher injection rates (fig. 11).

A schematic of the interaction studied is proposed in figure 12 where the main phenomena identified are represented; namely the jet counter rotating vortices, the separation surface in front of the jet exit, the reverse flow with two additional foci and the vortex shedding process. In this configuration of injection, the vortex shedding in the flat plate boundary layer on each side of the jet is strongly coupled with the deformation of the jet into the injection duct. This interaction, leading to the transverse flapping of the jet, is likely to enhance the mixing of the jet with the cross flow. For the particular application of turbine blade film cooling, it may explain the extension of the cooled region in spanwise direction observed in experiments and not reproduced by the numerical simulation[10].

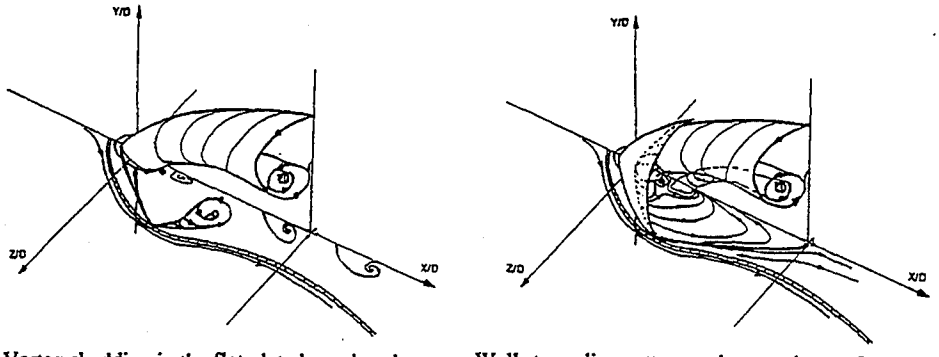

Vortex shedding in the flat plate boundary layer Wall streamline pattern and separation surface

Fig. 12 : Schematic of the interaction process

Concluding remarks

In this study devoted to jet in cross flow for low injection ratio, it is shown that unsteady phenomena are essential to understand the interaction. Actually in case of injection ratio larger than 1, vortex shedding was identified in the jet wake but since the jet is strong enough, the influence of these wake vortices remained very limited. On the contrary, in this case with an injection ratio lower than 1 (R=0.56), vortex shedding in the jet wake is coupled with the jet deformation into the injection pipe and it leads to a transverse flapping of the jet. The region of vortex shedding is located at X/D=1, Z/D=±1 close to the horseshoe vortex where the separation line corresponding to the separation surface in front of the jet ends. This study clearly shows than any attempt to simulate the jet in cross flow in such a case will require to account for the unsteady effects which are governing the jet development.

Acknowledgements

The authors are grateful for the support of the technical staff of the Centre d'Etudes Aerodynamiques et Thermiques of Poitiers and to the Printing Services of the von Karman Institute.

References

1 R.J. Margason : Fifty years of jet in cross flow research. AGARD CP 534 on "Computational and Experimental Assessment of Jets in Cross Flow", Winchester, UK April 1993.
2 Y. Kamotani; I. Greber : Experiments on turbulent jet in a cross flow. AIAA J., Vol. 10, 1972, pp. 1425-1429.
3 E. Le Grives : Champ aérodynamique induit par un jet pénétrant dans un écoulement transversal en régime subsonique. Journal de Mécanique, Vol. 17, 1, 1978, pp. 23-52.
4 E. Le Grives; A. Benoit : Nouveau modèle théorique d'analyse de la pénétration d'un jet dans un écoulement subsonique. La Recherche Aérospatiale, Vol. 3, 1972, pp. 133-142.
5 R.L. Fearn; R.P. Weston : Vorticity associated with a jet in a cross flow. AIAA J., Vol. 12, 1974, pp. 1666-1671.
6 A.R. Karagozian : An analytical model for the vorticity associated with a transverse jet. AIAA J. Vol. 24, 3, 1986, pp. 429-436.
7 G.P. Huang : Modélisation et calcul des jets tridimensionnels en présence d'un écoulement transversal. Thèse de Doctorat, Ecole Centrale de Lyon, 1989.
8 J. Andreopoulos : Measurements in a jet pipe flow issuing perpendiculary into a cross stream. Trans. ASME I: J. Fluid Eng. 104, 1982, pp. 493-499.
9 J. Andreopoulos; W. Rodi : Experimental investigation of jet in cross flow. J. Fluid Mech., Vol. 138, 1984, pp. 93-127.
10 J.-M. Charbonnier : Analyse et modélisation de l'interaction d'un jet perpendiculaire de paroi avec un écoulement principal. Thèse de Doctorat, Université de Poitiers, France, CEAT, 1992.
11 M.J. Lighthill : Attachment and separation in three dimensional flows. Laminar Boundary Layers, Oxford U. Press, 1963
12 A.E. Perry; M.S. Chong : A description of eddying motions and flow patterns using critical point concepts, Annual Review of Fluid Mech., Vol. 19, 1986, pp. 125-155.
13 D. Crabb; D.F.G. Durao; J.H. Withelaw : A round jet normal to a cross flow. Trans. ASME I: J. Fluid Eng., 103, 1981, pp. 142-152
14 H.M. Mac Mahon; D.D. Hester; S. Palfery : Vortex shedding from a turbulent jet in cross wind. J. Fluid Mech., Vol. 48, 1971, pp. 73-80
15 J.M. Wu; A.D. Valkili; F.M. Yu : Investigation of the interacting flow of non symmetric jets in a cross flow. AIAA J., Vol. 26, 8, 1988, pp. 940-947.
16 T.F. Fric; A. Roshko : Structure in the near field of the transverse jet. 7th Symp. on Turbulent Shear Flow, Stanford Univ., 1989.
17 A.E. Perry; R.M. Kelso; T.T. Lim : Topological structure of a jet in a cross flow. AGARD CP 534 on "Computational and Experimental Assessment of Jets in Cross Flow", Winchester, UK April 1993.
18 R.M. Kelso; C. Delo; A.J. Smits : Unsteady wake structures in transverse jets. AGARD CP 534 on "Computational and Experimental Assessment of Jets in Cross Flow", Winchester, UK April 1993.

VELOCITY AND REYNOLDS STRESSES IN A PRECESSING, DEFLECTED JET

SCHNEIDER G.M., NATHAN G.J., LUXTON R.E.
Department of Mechanical Engineering, University of Adelaide, SA 5005 (Australia)
HOOPER J.D., MUSGROVE A.R.
CSIRO Division of Mineral and Process Engineering, Menai, NSW 2234 (Australia)

ABSTRACT

A precessing jet flow occurs downstream from a large abrupt axisymmetric expansion into a short cavity. When a lip is placed at the exit of the cavity, the jet is deflected at an angle of about 45° from the nozzle axis and precesses around that axis. This fluid mechanical instability is used in the precessing jet gas burner nozzle to create large scale mixing between the fuel and the air resulting in a highly luminous flame, which reduces NO_x significantly while maintaining low CO emissions.

The paper presents experimental data obtained from measurements with a miniature, rapid response four-hole "Cobra" pitot probe in the cold, non-reacting field of the precessing jet. To facilitate measurements in the extremely complicated time varying flow field a mechanically rotated nozzle is used to provide a clearly defined origin for the flow on the axis of rotation. Phase-averaged three dimensional velocity vectors identify the large scale motions and primary and secondary flow patterns. The measured Reynolds stresses are compatible with the higher entrainment rates of the jet found in earlier investigations.

1.0 INTRODUCTION

The precessing jet burner, which is now commercialised as the "GYRO-THERM" burner, has been under development at the University of Adelaide since 1984 [11],[13]. It has been applied succesfully in various large scale industrial trials in collaboration with Australian and overseas industries. In the burner the precessing jet flow is generated by a fluid mechanical instability in an axi-symmetric duct following a sudden large expansion [10]. Experiments with the GYRO-THERM have shown that the combustion is dominated by turbulent structures of a scale many times that of the nozzle dimensions. Measurements in the precessing jet flame have also shown that the peak flame temperature is typically 150°C lower than that of a comparable swirl burner, which leads to a reduction of NO_x emission by about 50% while maintaining low CO emissions [13].

The aim of the present investgation is to be able to explain the fluid mechanics involved in the above characteristics of the burner. Therefore only the cold, non-reacting flow field is investigated and the precessing jet is created by mechanical means. The mechanically rotated nozzle (3.1 and Fig. 1), unlike the fluid mechanical burner nozzle, enables the Reynolds number to be decoupled from the Strouhal number of precession.

Previous measurements of basic flow parameters in the precessing jet have shown

significant differences from coventional turbulent jets. A large scale recirculation, in which strong entrainment of fluid occurs, was revealed by a conditional flow visualisation technique [16]. Also Nathan et al have shown an increased entrainment rate and wider initial spreading for the precessing jet flow [9],[11]. This has been confirmed by measurements of the velocity and pressure contours respectively [17],[18].

Bremhorst et al stated in their investigation of a pulsed jet that the cause of the enhanced entrainment rate was a markedly increased Reynolds stress field [2]. It can be anticipated that measurements of three dimensional velocity vectors will reveal both the large scale flow patterns and an enhanced level of Reynolds stresses which together could explain the greatly enhanced initial entrainment rates of the precessing jet.

2.0 NOTATION

d_e	= exit diameter of the spinning nozzle
α_e	= exit angle of the spinning nozzle
f_p	= frequency of precession
Re	= Reynolds Number = $\frac{u_e \times d_e}{\nu}$
St_p	= $\frac{\text{Strouhal Number}}{\text{of precession}} = \frac{f_p \times d_e}{u_e}$
r,x,Φ	= cylindrical coordinates (Fig.1)
u_e	= exit velocity of the precessing jet
$\overline{u_m}$	= local mean velocity
u'_r	= fluctuating radial velocity component
u'_x	= fluctuating axial velocity component
u'_Φ	= fluctuating azimuthal velocity component
φ	= pitch angle of the Cobra probe
Θ	= yaw angle of the Cobra probe

Table 1: Definition of Variables and Parameters

3.0 EXPERIMENTAL TECHNIQUE

3.1 The Mechanical Nozzle

The mechanical nozzle (Fig. 1) creates a well defined precessing jet flow by mechanical means. The inlet conditions of this mechanical nozzle were tested for the stationary case ($f_p = 0$) and was found to create the desired simple turbulent jet [16]. The exit diameter and the exit angle relative to the spinning axis of the nozzle can be adjusted by interchangeable nozzle tips. The results presented in this paper are for an exit diameter d_e=10mm and an exit angle $\alpha_e = 45°$ located with the exit of the jet centred on the spinning axis.

The nozzle also enables the exit velocity to be varied independently of the frequency of precession, and hence the Reynolds number can be decoupled from the precessional Strouhal number (Fig. 1). An exit velocity of u_e=30m/s and a frequency of f_p=15Hz have been chosen corresponding to a Reynolds number of Re=20,000 and the Strouhal number of $St_p = 5 \times 10^{-3}$. The exit velocity is adjustable by a flow rate meter with high accuracy and a 300W variable frequency electric motor is controlled by a TASC Speedstar II unit which allows the frequency of precession to be varied with an accuracy of $\pm$ 0.25Hz at the maximum frequency of 60Hz.

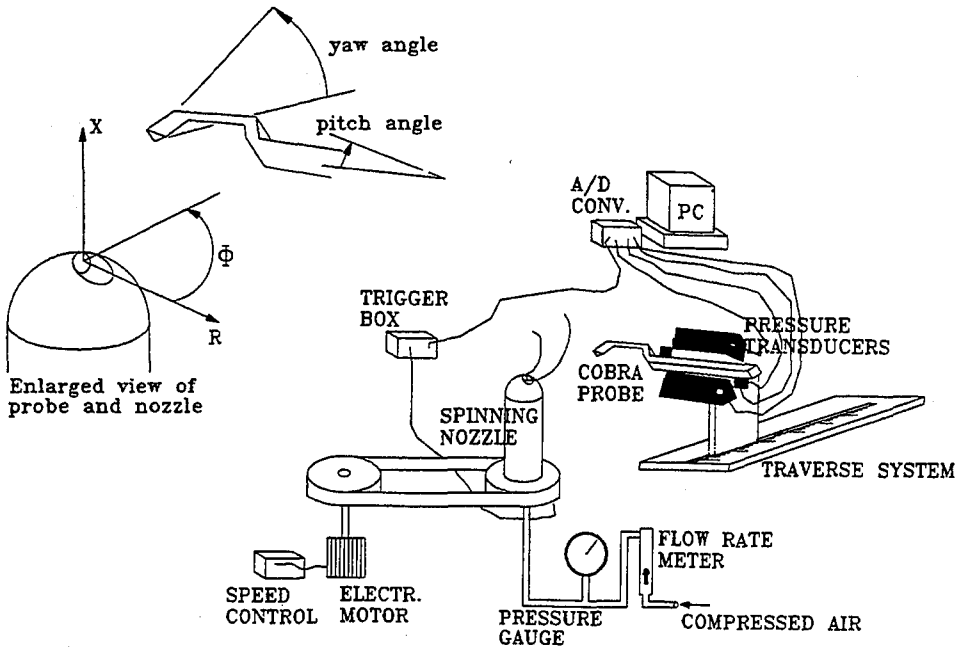

Fig. 1: Cylindrical Coordinate System and Apparatus

3.2 Cobra Probe

Measurements of phase-averaged three dimensional velocity vectors and the Reynolds stresses were conducted using a four-hole Cobra probe, delevoped at the CSIRO Division of Mineral and Process Engineering, Menai, Australia. The probe has been used successfully in various highly turbulent flow fields [4],[5],[8]. Measurements of the flow parameters within a 90° included cone angle with a frequency response up to 3000Hz are possible with the Cobra probe. An instantaneous picture of the main flow variables at any point in the turbulent field can be obtained easily. The four-hole Cobra probe used for the measurements has a spatial resolution of approximately $5mm^3$. The four Sensym detectors have a pressure range from 0 to ± 1.0kPa and have been specifically modified to give a high frequency response. To enable the results to be phase-averaged over multiple cycles of precession, four channels of the pressure signal from the probe were collected simultaneously with a fifth channel containing a trigger signal to reference the angular position of the spinning nozzle. The sampling rate of 5kHz with 22,500 points recorded on each of the 5 channels allows 67 cycles of the precessing jet to be recorded and phase-averaged for each probe position. The probe was radially traversed in 5mm increments. At each of the radial positions it was orientated at 6 different yaw and pitch angles to detect the full 3-dimensional flow field.

The Cobra probe with the four pressure transducers was calibrated in a known flow of 30m/s. The geometry of the probe head ensures a response which is relatively independent of the Reynolds Number. From a comparison of the frequency response of the probe and a B&K microphone an experimental transfer function can be obtained to correct the signal in the frequency domain [1],[6].

4.0 RESULTS

4.1. Velocity Vectors

Figure 2 shows the three dimensional velocity vectors at the plane $x/d_e=3$. The size of the vectors represent the magnitude of the velocity. The results show an initial radial spreading angle of the jet of $\approx 24°$ which is similar to a simple turbulent jet. In the azimuthal direction the precessing jet shows a higher spreading angle ($> 35°$) (Fig. 2) which is consistent with the higher entrainment rates [9]. It can also be seen that at this distance from the nozzle a swirling flow is created between the jet and the spinning axis. This swirl has the direction of the precession and is compatible with a low pressure field found between the precessing jet and the x-axis [17].

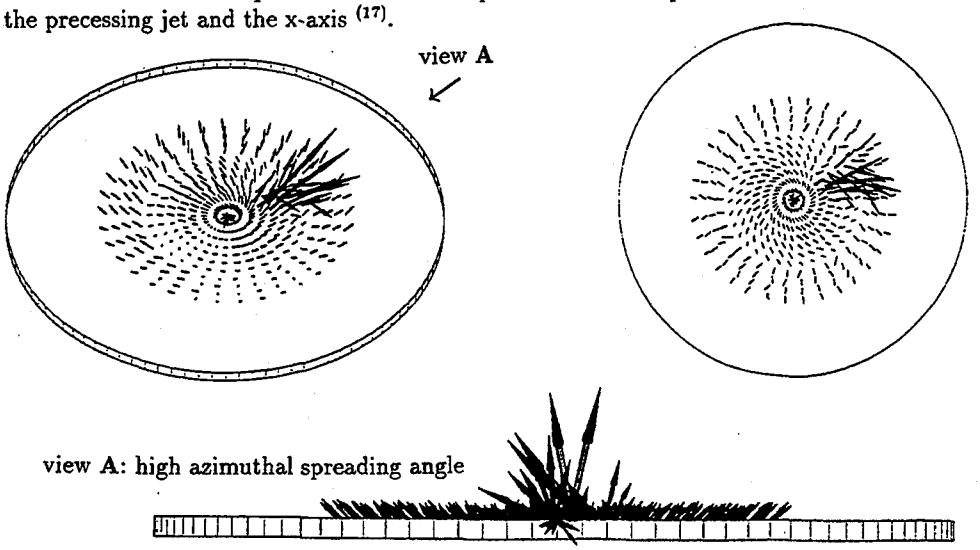

Fig.2: Three-dimensional velocity vectors at $x/d_e=3$

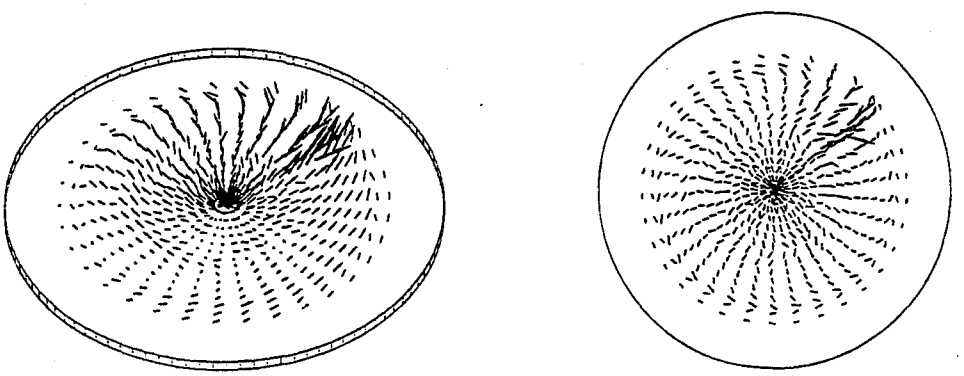

Fig.3: Three-dimensional velocity vectors at $x/d_e=6$

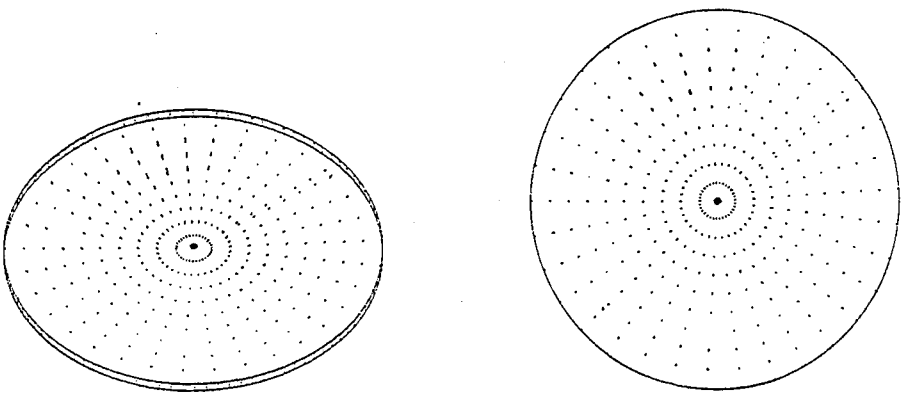

Fig.4: Three-dimensional velocity vectors at x/d_e=11

At x/d_e=6 (Fig.3) it can be seen that the jet velocity has decayed rapidly. The swirling motion between the jet and the x-axis has also decayed. At x/d_e=11 (Fig.4) the energy of the jet is almost totally dissipated. Only a secondary flow pattern, a slight reverse flow, can be detected. This reverse flow seems to explain the recirculation found with flow visualisation techniques in earlier investigations [16].

4.2. Reynolds stresses

The Reynolds shear stresses, which are a measure of the turbulent transport, are larger than in either a simple turbulent jet or a pulsed jet [2]. Bremorst et al found in a pulsed jet at x/d_e=10 values of up to 0.08, compared with a simple turbulent jet with maxima up to 0.02.

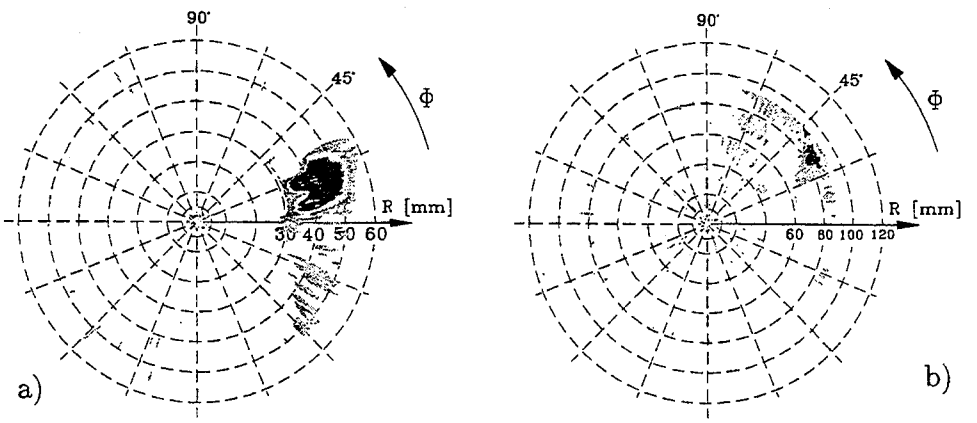

Fig.5: Negative Reynolds stresses $\frac{\overline{u'_r \cdot u'_\Phi}}{\overline{u_m}^2}$ at a) x/d_e=3 and b) x/d_e=6

The precessing jet shows, at a distance x/d_e=3, maximum absolute values of 0.3–0.4 in all three stress components (Fig. 5a–7a). At the distances x/d_e=6 the values are still 0.2–0.3 (Fig. 5b–7b). At x/d_e=11 the Reynolds stresses show values of 0.12–0.2 over the whole plane of measurement.

The shape of the stress contours is initially (x/d_e=3) similar to that of a round jet, but in the precessing jet high values of shear stress are maintained over a wide region of the jet. These high levels of Reynolds stress are the reason for the higher entrainment rate measured previously and the higher initial spreading of the jet, as described in Section 4.1.

The shear stresses in the low velocity regions in the flow in Figures 5 to 7 probably result from electrical noise as the number of averages is relatively low (67) and any noise peak will be registered as a high fluctuating component.

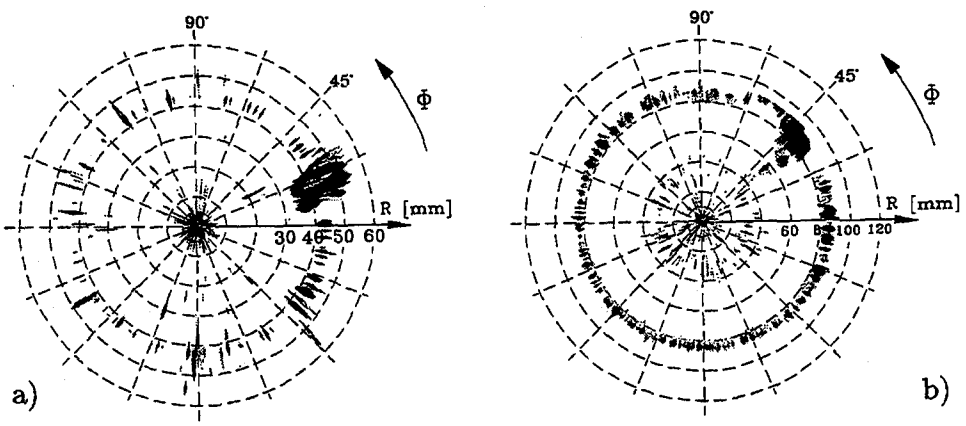

Fig.6: Positive Reynolds stresses $\frac{\overline{u'_x \cdot u'_r}}{\overline{u_m}^2}$ at a) x/d_e=3 and b) x/d_e=6

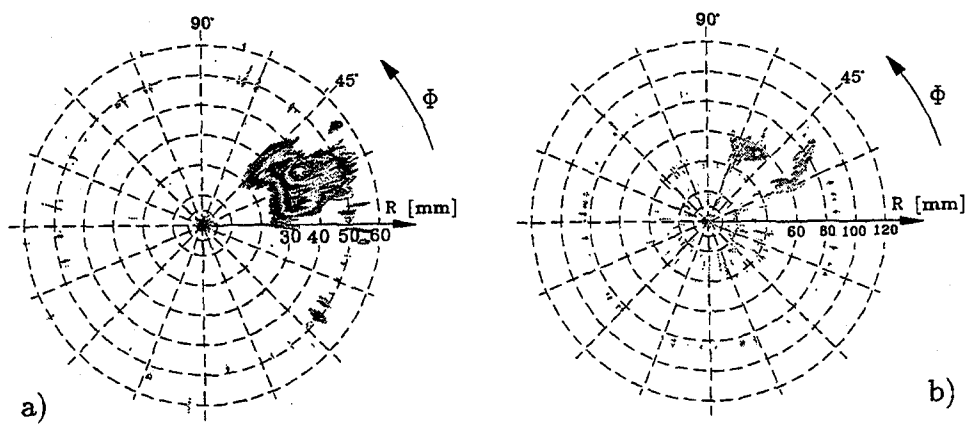

Fig.7: Negative Reynolds stresses $\frac{\overline{u'_\Phi \cdot u'_x}}{\overline{u_m}^2}$ at a) x/d_e=3 and b) x/d_e=6

5.0 CONCLUSIONS

Phase-averaged measurements of the velocity vectors within a precessing jet have shown distinctive flow characteristics. A high spreading angle in the azimuthal direction and a high rate of decay of jet velocity were found in the primary flow field. The secondary flow showed a slight reverse flow at $x/d_e = 11$ and an initial swirl, induced by the pressure field between the jet and its spinning axis.

Measurements of Reynolds stresses, which are an indicator of entrainment rate, confirm the results of the entrainment experiments of Nathan et al which showed the precessing jet to have higher initial entrainment than a simple turbulent jet [9].

Further measurements with a series of Cobra probes and with rakes of hot-wires are planned to obtain not only phase-averaged results but also simultaneous measurements of instantaneous pressures and velocities. From these the dependence of the local structures in the precessing jet on the Strouhal number and Reynolds number will be identified.

6.0 REFERENCES

[1] Bergh,H. and Tijdeman,H. (1965). *Theoretical and experimental results for the dynamic response of pressure measuring systems.* National Aero and Astronautical Research Institute, Amsterdam, Report NLR–TRF.238, 1965

[2] Bremhorst,K. and Hollis,P.G. (1990). *Velocity Field of an Axisymmetric Pulsed, Subsonic Air Jet.* AIAA-Journal. v 28, pp 2043-2049.

[3] De Guzman,M.M., Fletcher,C.A.J. and Hooper,J.D. (1993). *Computational Investigation of Cobra Probe Operation.* Subm. Journal of Methods for Heat and Fluid Flow.

[4] Hooper,J.D. and Musgrove,A.R. (1991). *Multi-Hole Pressure Probes for the Determination of the Total Velocity Vector in Turbulent Single-Phase Flow.* 4th Int.Symposium on Transport Phenomena. Sydney, July 1991.

[5] Hooper,J.D., Musgrove,A.R. and Smith,B. (1992). *Pressure Probe Measurements of the Mean and Turbulent Structure of a Swirling Jet.* 11th Australasian Fluid Mechanics Conf. Hobart, Dec.14-18 1992.

[6] Irwin,A.P.A.H., Cooper,K.R. and Girard,R. (1979). *Correction of Distortion Effects Caused by Tubing Systems in Measurements of Fluctuating Pressures.* Journal of Industrial Aerodynamics. v 5 (1979), pp 93–107.

[7] Ligrani,P.M., Singer,B.A. and Baun,L.R. (1989). *Miniature five-hole pressure probe for measurement of three mean velocity components in low-speed flow.* Journal of Physics E: Sci.Instrum. v 22, pp 868-876.

[8] Musgrove,A.R. and Hooper,J.D. (1993). *Pressure Probe Measurements of the the Turbulent Stress Distribution in a Swirling Jet.* 3rd World Conf. on Experimental Heat Transfer, Fluid Mechanics and Thermodynamics. Hawaii/USA, Oct.31-Nov.5 1993.

[9] Nathan,G.J. and Luxton,R.E. (1991). *The Entrainment and Combustion Characteristics of an Axi-Symmetric, Self Exciting, Enhanced Mixing Nozzle.* ASME/JSME Thermal Engineering Proceedings. v 5, Reno/Nevada, March 17-22, 1991.

[10] Nathan,G.J. and Luxton,R.E. (1991). *The Flow Field within an Axi-Symmetric Nozzle Utilising a Large Abrupt Expansion.* The International Conference on Experimental Fluid Mechanics. Chengdu, China June 17-21, 1991.

[11] Nathan,G.J. and Luxton,R.E. (1991). *Mixing Enhancement by a Self-Exciting, Asymmetric Precessing Flow-Field.* Fourth International Symposium of Transport Phenomena, Sydney, July 14-18, 1991.

[12] Nathan,G.J. and Smart,J.P. (1991). *An Investigation of the Combustion Characteristics of the Enhanced Mixing Burner firing Natural Gas at 2MW.* Research Digest, International Flame Research Foundation. IFRF Document–No.F90/y/9, Ijmuiden December 1991.

[13] Nathan,G.J., Luxton,R.E. and Smart,J.P. (1992). *Reduced NO_x Emissions and Enhanced Large Scale Turbulence from a Precessing Jet Burner.* 24th International Symposium on Combustion,The Combustion Institute. Sydney, July 14-18, 1992.

[14] Proctor,D., Nathan,G.J., Luxton,R.E., Pearson,I.G., Brumale,S.A., Mann,B.A., Schneider,G.M. and Newbold,G.J.R. (1993). *The Efficient Low NO_x Burning of Gas for Large Scale Industrial Applications.* 2nd International Conference on Combustion Technologies for a Clean Environment. v II, paper 26.1, pp 1-8. Lisbon, Portugal, Sep. 19-22 1993.

[15] Proctor,D., Nathan,G.J., Pearson,I.G., Mann,B.A., Schneider,G.M. and Luxton,R.E. (1993). *The Turbulence and Combustion Interaction in a Free Precessing Jet Flame.* The Australian Symposium on Combustion incl. The Third Australian Flame Days. Newcastle, Nov. 1-2, 1993.

[16] Schneider,G.M., Nathan,G.J. and Luxton,R.E. (1992). *An Experimental Study of a Precessing, Deflected Jet.* 11th Australasian Fluid Mechanics Conference Hobart, December 14-18 1992.

[17] Schneider,G.M., Vidakovic,S.S., Hooper,J.D., Musgrove,A.R., Nathan,G.J. and Luxton,R.E. (1993). *Theoretical and Experimental Pressure Field Evaluation Downstream of a Mechanically Precessing Jet.* 4th Heat and Mass Transfer Conference. Brisbane, Dec. 1992.

[18] Schneider,G.M., Nathan,G.J. and Luxton,R.E. (1994). *Velocity Contours in a Precessing, Deflected Jet.* 1st International Conference on Flow Interaction. Hong Kong, Sep.5-9 1994.

[19] Shepherd,I.C. (1981). *A Four Hole Pressure Probe for Fluid Flow Measurements in Three Dimensions.* Journal of Fluids Engineering. v 103, pp 590-594.

[20] Wright,M.A. (1970). *The evaluation of a simplified form of presentation for five-hole spherical and hemispherical pitometer calibration data.* Journal of Physics E: Sci.Instrum. **3**,p.356-362.

TURBULENT MIXING BETWEEN A HIGH PRESSURE JET AND A CO-FLOWING OUTER STREAM

by

S.C. Favaloro

Aeronautical and Maritime Research Laboratory
Defence Science & Technology Organisation
Melbourne, Australia

ABSTRACT

Two-component laser Doppler velocimetry has been used to study the mixing between a non-reacting compressible central jet and a co-flowing incompressible outer flow in an axisymmetric model of a ramrocket combustor. Experiments were performed with a range of underexpanded central jets, which were formed from a conical convergent nozzle operating at different blowing pressure ratios while the outer co-flowing stream was held constant. An indication of the shock structure in the core of the jets was able to be determined from the mean flow measurements. Over the range of nozzle blowing pressure ratios tested, the mean flow results also showed the size and strength of the toroidal recirculation region set up between the two flows was not heavily influenced by the level of underexpansion of the central jet. High Reynolds shear stresses were measured at the boundaries of the jet up to 15 nozzle diameters from the nozzle exit for all pressure ratios tested. Very high turbulence levels were also recorded at the jet boundaries and in the core of the jets.

NOTATION

D	=	Parallel test section and centrebody diameters
d	=	Nozzle exit diameter
M1	=	Primary flow Mach number
M2	=	Secondary flow Mach number
P1	=	Nozzle blowing pressure
r	=	Radial co-ordinate
R	=	Test section radius
U,V	=	Axial and radial mean velocities
U2	=	Outer flow inlet velocity
u,v	=	Axial and radial fluctuating rms velocities
$\overline{uv}$	=	Reynolds shear stress
x	=	Axial co-ordinate
y	=	Radial co-ordinate (vertical direction)

INTRODUCTION

Recent developments in propulsion systems for tactical missiles have concentrated on variants of integral rocket/ramjets. The ramrocket is one such variant wherein a high stagnation pressure, high temperature, fuel rich efflux from a solid propellant gas generator expands through a nozzle into a combustion chamber (ramburner) and mixes with air ingested from the atmosphere through an intake system for further combustion. The mixing processes between these two streams have features which are unique to ramrockets. These features, which include recirculating regions, overexpanded and underexpanded jets with accompanying shock and expansion waves, and free shear layers with very high velocity gradients, effectively

control the combustion performance of the system. To gain an understanding of the fluid mechanics of ramburner flows and some insight into the geometric parameters which impact on the mixing processes, experiments have been performed, and are continuing, in an idealised, axisymmetric, cold flow representation of a ramburner. In this paper, results from laser Doppler velocimeter (LDV) measurements are presented for one ramburner geometry consisting of a conical, convergent nozzle operating at varying degrees of underexpansion and with a constant velocity co-flowing outer stream.

BACKGROUND

The advantages of applying LDV for fluid flow measurement have been well documented over the last twenty years (eg, reference [1]). Since the LDV is non-intrusive, calibration free, and possesses high temporal and spatial resolution, its range of application has been diverse, covering low velocity to hypersonic flowfields, laminar to highly turbulent flow regimes, and combusting flows in gas turbines, furnaces, and internal combustion engines. The practical problems associated with applying LDV include the requirement for aberration free optical access with minimum flow disruption, and in most cases, the need to seed the flowfield with particles which will follow the flow with high fidelity.

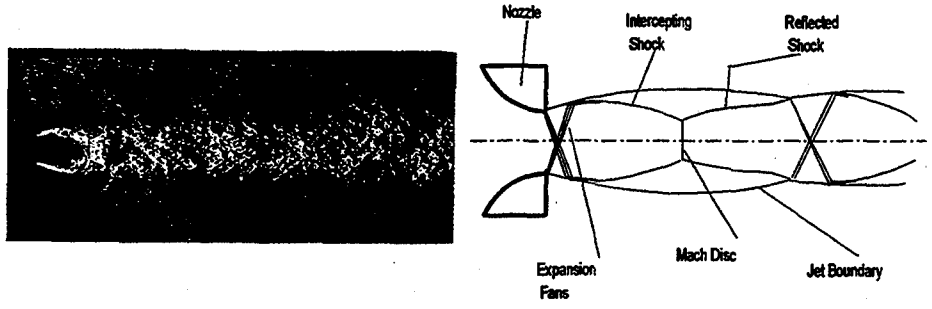

(a) Ejector flow pattern (A.M. Abdel-Fattah) *(b) Underexpanded Jet Structure*

Figure 1

The ability of a particle to track the flow is most difficult in flow regimes with high frequency turbulent fluctuations, high accelerations and shock waves, all of which can be found in ramburner flowfields. For example, figure 1(a) shows a schlieren photograph of an underexpanded nozzle flow into an ejector duct of square cross section - the pressure ratio across the axisymmetric sonic nozzle was approximately 8 to 1. The photograph, supplied by Dr. A. M. Abdel-Fattah of the Aeronautical and Maritime Research Laboratory, is from unpublished work on ejector mixing. Although the ejector and ramburner geometries are not identical, it is expected that the flow pattern depicted in figure 1(a) will be similar, at least in a qualitative sense, to ramburner flows with the nozzle operating at similar pressure ratios. Figure 1(b) shows a sketch of typical highly underexpanded nozzle flows with the important features noted. As the flow emerges from the nozzle exit, it passes through an expansion fan, expanding to ambient pressure at the jet boundary. The requirement for constant pressure at the boundary causes the boundary to be bent back towards the axis; the change in flow direction along the boundary causes the weak compression waves, which are reflected from the boundary, to coalesce and form the intercepting shock as shown. In highly underexpanded flows, the intercepting shocks are connected by a Mach disc (normal shock) as shown above. As the distance from the nozzle exit increases, the structure is no longer apparent and large scale turbulent structures become predominant, as depicted in figure 1(a). Reducing the level of underexpansion, by lowering the nozzle blowing pressure ratio, causes the intercepting

shocks to approach each other and the size of the Mach disc to decrease. With sufficient decrease in nozzle blowing pressure the intercepting shocks meet on the axis and form the familiar diamond pattern.

Problems associated with particle lag through shock systems and particle frequency response to turbulent fluctuations have been well documented (eg, references [2], [3] [4]). Mostly, these relate to flowfields which are either shock free or contain only a single oblique shock, and are much simpler than those studied here. Other difficulties with LDV measurements in compressible turbulent flows include a number of biasing problems which arise directly from the fact that the instantaneous velocities are measured discretely, as opposed to the continuous signal from analogue systems such as hot wire anemometers. The errors that can arise from velocity, density, fringe, and clock biases have been extensively documented in the literature (eg, [1],[2], [5]) - discussion of these items in this paper will be limited to the methods adopted for their correction.

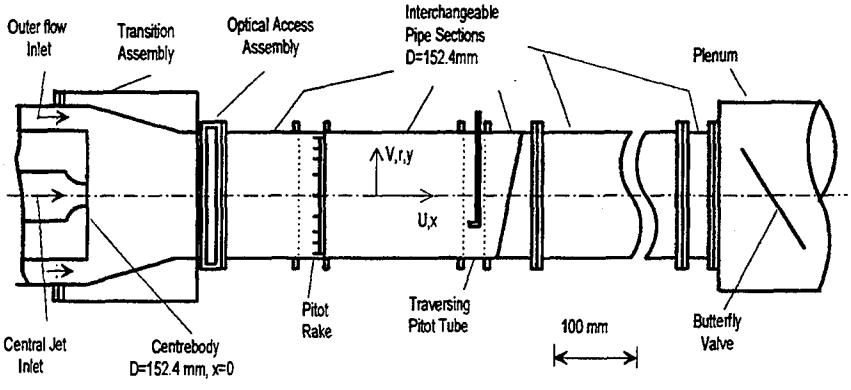

(a) Schematic of Experimental Rig

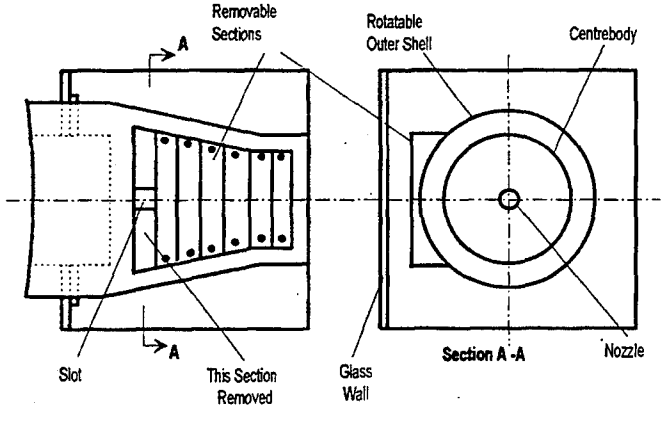

(b) Schematic of Transition Section

Figure 2

EXPERIMENT

Figure 2(a) shows a schematic of the experimental rig. The rig was designed to provide two independently controlled, co-flowing, axisymmetric air streams which mix with each other in a 1600mm long test section. The test section consisted of a 100mm conical transition section and a parallel section fabricated from a number of different pipe lengths of internal

diameter 152.4mm. Optical access for LDV measurements in the parallel section was achieved through a flat strip of 3.2mm float glass, mounted vertically in an assembly which could be translated axially along the length of the test section at 40mm intervals. Figure 2(b) shows the arrangement for gaining optical access to the flow in the conical transition section. The combination of a flat glass wall, a 15mm slot (which was cut along the length of the rotatable outer flow shell), and a number of removable plugs enabled aberration free optical access with minimum disruption to the flowfield. The central jet (primary flow) was formed from air issuing from a conical convergent nozzle, of exit diameter 14.7mm, which was centrally located in an axisymmetric centre body of diameter 152.4mm. The outer co-flowing stream (secondary flow) came from a settling chamber via an annular passage, 250mm in length and 25mm in width, before passing over the centre body at the start of the test section. The total pressure in the secondary flow was set to provide a nominal axial velocity of 52 m/s (U2) in the annular section. Three different nozzle blowing pressure ratios, namely 1.9, 4.5, and 8.5, were tested with fixed secondary flow conditions. The secondary flow was held constant by adjusting the butterfly valve in the rig plenum chamber (figure 2a) so the pressure at the nozzle exit plane was approximately atmospheric.

The secondary flow was seeded with polydisperse sugar particles, which were generated by the atomisation of a 5 per cent sugar and water solution in a Thermo Systems Incorporated (TSI) model 9306 six jet atomiser. The seed was introduced to the flow in a settling chamber, well upstream of the test section, through a six-point manifold to provide a uniform particle distribution in the test section. Data published in reference [6] for the model 9306 atomiser suggest that atomisation of a 5 per cent sugar/water solution will produce particles ranging in size from 0.6 to 3 micron, with a mean around 0.9 micron. A high pressure version of the TSI seeder was constructed to seed the primary flow. A 50 cP Dow Corning fluid was used as the seed base rather than a sugar/water solution - the possibility of water condensing out of the primary airstream and forming ice particles or condensation shocks after expansion through the nozzle was considered undesirable. Secondary/primary mass flow ratios varied between 2.8 and 13; to ensure equal concentrations of particles in both streams, the seeders were controlled so their output was in the same ratio as the volume flow ratio of the two streams.

LDV SYSTEM

The LDV used in the experiments was a TSI 9100-7 two channel, two colour system which was optimised for high speed flow measurement in the range -300 to +1100 m/s. The system operated in backscatter mode with frequency shifting on both channels. The combination of 13 mm beam spacing, 2.75 beam expansion and a 750 mm focussing lens gave ellipsoidal measuring volume dimensions of approximately 0.13 mm diameter and 4 mm length. The frequency/velocity conversions for both channels were usually around 8 m/s/MHz, but depended upon the final beam half angles that were measured once the crossing point was established. A 0.1 mm aperture in the field stop system reduced the measurement volume diameter seen by the photomultipliers, but the on-axis collection forced velocity realisations to be made over the full length of the measurement volume. Both channels had Bragg cells in one beam which provided a frequency shift of 40 MHz. The combination of 40 MHz frequency shifting against the mean flow direction and 45 degree beam orientation effectively eliminated any fringe bias, and allowed the maximum expected Doppler frequencies to be well within the detectable range of the photomultipliers.

The whole system was mounted on a milling machine base which, in combination with a TSI model 9400 traverse table controlled by a TSI model 9430 positioner, enabled the measurement volume to be located inside the test section with an accuracy of 0.05 mm. Radial and axial velocity components were obtained by locating the measurement volume on the rig centreline and traversing the milling machine along a vertical radius (y direction, figure 1b).

When measurements were performed in the transition section, figure 2(b), the secondary flow outer shell was rotated to allow access for the laser beams through the slot.

Two TSI 1990 counter processors, a TSI 1998 interface and a PDP-11 computer constituted the data acquisition and processing system. The 1998 interface was set in 'non-priority' mode and provided coincident velocity measurements from both channels within a time interval of 1ms. The data transfer to the computer, via DMA, proceeded at a much faster rate than the velocity realisation rates (typically 100 to 2000 Hz) in the two counters; hence, the data in most sections of the flowfield was fully velocity biased. Corrections for velocity bias were made by particle interarrival time weighting, [4], with the time between velocity realisations transferred to the computer along with the velocity data. This was the preferred correction method, since the possibility of low data rates inhibited the use of constant time interval sampling, while the likelihood of zero velocity components in both channels (and the lack of simultaneous 3D velocity measurements) prevented the use of velocity magnitude weighting.

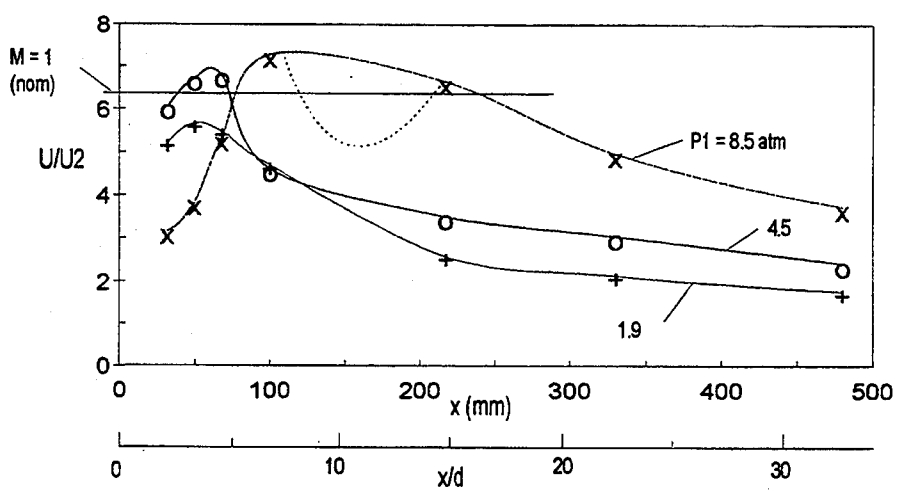

Figure 3 - Axial Centreline Velocities

RESULTS & DISCUSSION

Figure 3 shows axial centreline velocities determined from LDV measurements in the test section (figure 1) for the three primary blowing pressures with the secondary inlet flow held constant at U2 ≈ 52 m/s (M2 ≈ 0.15). The data have been normalised with respect to U2. Comparison of the distributions reveals the effect of the level of underexpansion, especially in the flow region up to 100mm (7 nozzle diameters) from the nozzle exit. Figure 2(a) showed the first Mach disc (normal shock) at approximately 1.8 nozzle diameters from the exit with a nozzle blowing pressure of around 8 atm. In the current work, at a nozzle blowing pressure of 8.5 atm, the centreline flow accelerates from subsonic at approximately 2 nozzle diameters to supersonic at around 6 diameters. Evidently, the flow passed through the first normal shock prior to the first measurement location, and accelerated through the expansion fans in the next 'shock cell'. Further downstream, the flow apparently decayed back to subsonic levels, but although there are no data points between x/d = 6 and x/d = 15, it is likely that the flow passed through another shock system as indicated by the dotted line in figure 3. Similar arguments apply to the case where the nozzle blowing pressure was 4.5 atm. However, in this instance, the first measured transition to supersonic flow occurred closer to the nozzle exit at

approximately 2.5 nozzle diameters. The inference is the normal shock was also closer to the nozzle exit which is consistent with the flow undergoing a lesser degree of underexpansion as discussed earlier. The rapid transition of the 4.5 atm flow back to subsonic suggests that a second normal shock was located between 4.5 and 5 nozzle diameters, after which large scale turbulent mixing promoted a gradual decay of the flow. In the 1.9 atm flow, which was very close to correctly expanded flow, no supersonic velocities were detected, and the flow decayed slowly in the streamwise direction.

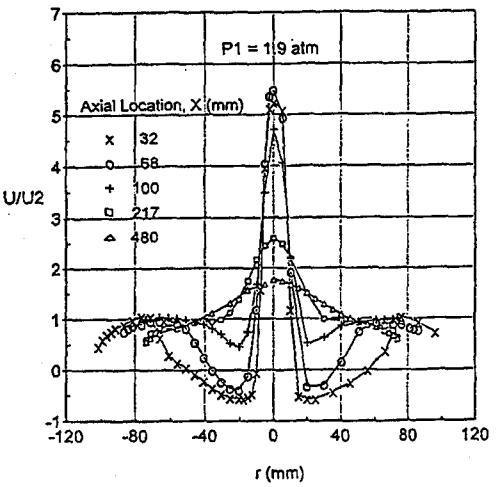

Figure 4 - Axial Mean Velocities

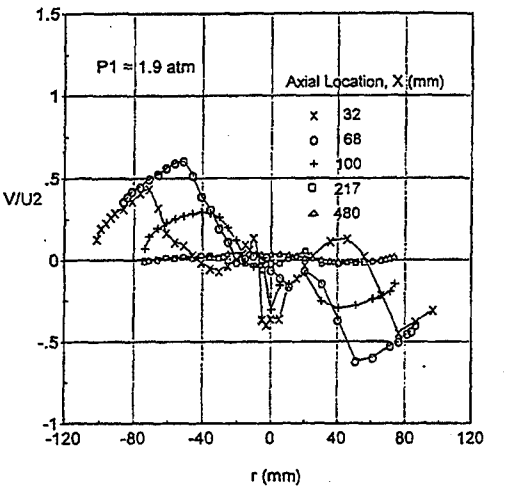

Figure 5 - Radial Mean Velocities

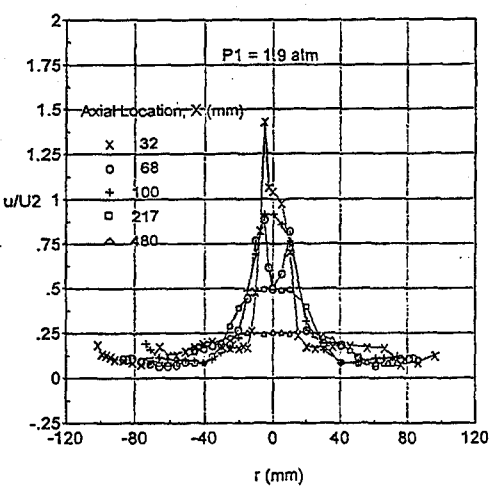

Figure 6 - Axial Turbulent Velocities

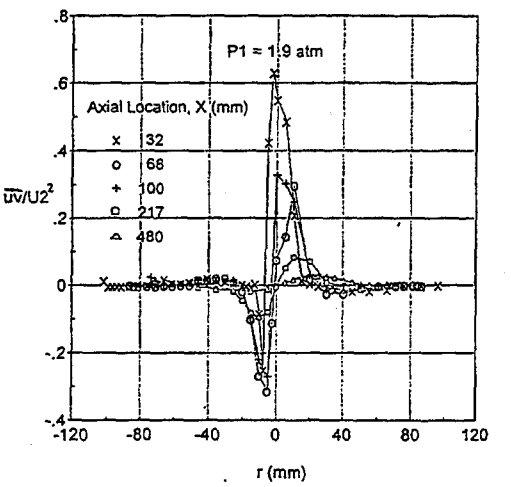

Figure 7 - Reynolds Shear Stress

Figures 4 to 7 show the development of the flowfield up to 480mm (x/D ≈ 3.2, x/d ≈ 33) from the nozzle exit plane for a nozzle blowing pressure of 1.9 atm. The results were obtained from radial traverses of the LDV in the vertical direction at selected streamwise locations, and are shown normalised with respect to U2. The axial mean velocity profiles (figure 4) illustrate the overall symmetry of the mixing flowfield except for minor differences in the core of the central jet. Notable features include a reversed flow region downstream of the bluff centre body extending for approximately 0.55D, and a fairly slow decay of the central core flow. In

combination with the axial mean velocities, the radial mean velocity profiles (figure 5) correctly depict the outer secondary flow and recirculating flow patterns. Significant negative values are evident in the core of the central jet, especially in the region close to the nozzle exit. There is no immediate explanation for this anomaly since near zero radial velocities were recorded on the centreline with the other two blowing pressures (not shown). The axial turbulent velocity field (figure 6) shows high values in the core flow, which decay in the downstream direction, and also indicates the rapid growth of the jet boundaries. Expected peaks in the profiles at the boundary of the core and outer flows are only evident at x = 68mm. It is believed that the peaks at the other axial locations occurred between the data points. Radial turbulent profiles (not shown) are similar with peak values occurring on the centreline. Profiles of Reynolds shear stress (figure 7) show very high values at the boundary of the core and outer flow up to 217 mm (x/D ≈ 1.4, x/d ≈ 15) from the nozzle exit. These high values indicate high momentum transfer rates in the radial direction, which is consistent with the radial expansion observed in these regions in the previous results.

Figure 8 compares axial mean velocities, normalised with respect to U2, for the three nozzle blowing pressure ratios at selected streamwise locations. Mean velocity profiles at 32mm (x/D ≈ .2, x/d ≈ 2) show that increasing nozzle blowing pressure had virtually no impact on the axial velocities in the recirculation region. In addition, the outer half of the flowfield (r > 40mm) remained relatively unaffected by the level of blowing pressure up to 217mm (x/D ≈ 1.4, x/d ≈ 15) from the nozzle exit plane, even though the initial width (figure 8a) and spreading rate of the jets (figures 8b and 8c) increased with increased blowing pressure. At 32mm from the nozzle exit plane, the measured velocities at the jet boundaries were higher than the velocities recorded near and on the centreline for the two higher nozzle blowing pressures. This is consistent with the flow passing through one or more oblique shocks near the jet boundary, compared with the flow crossing a normal shock close to and on the centreline. It is also clear that for the 1.9 atm case, maximum axial velocities occurred on the centreline - this is also consistent with a flow which is nominally shock-free.

Figure 9 shows comparisons of axial turbulent velocities normalised with respect to U2, at the same locations and nozzle blowing pressures as figure 8. It is apparent that while the outer half of the mixing flowfield remained relatively unaffected by variations in the blowing pressure ratio, there were significant differences in fluctuating velocities between the core flows. Generally, the fluctuations decreased in magnitude with decreasing blowing pressure and increasing distance from the nozzle exit. However, at x = 100mm (x/d ≈ 7), extremely high fluctuating velocities were recorded close to and on the centreline with the 4.5 atm flow. It is postulated that these high values are a consequence of large scale eddies and/or instabilities which cause the jet to oscillate around the centreline - counter-based LDV systems are incapable of discriminating large scale oscillations from conventional turbulence. Another cause of very high turbulence readings can be attributed to the poor resolution of the LDV measurement volume. The on-axis collection system allowed velocity realisations to be achieved over the full length of the measurement volume (≈ 4mm) which, in some parts of the flowfield, spanned regions of very high velocity gradient (eg, along the jet boundaries).

CONCLUSIONS

Initial examination of the flowfield in an idealised model of a ramrocket combustor has shown that:

(1) estimates of the shock structure and expansion regions in highly underexpanded supersonic jets can be made from LDV measurements of the mean flow;

(2) changing the mass flow ratio of the outer co-flowing stream and the central jet from 3 to 13 has minimal effect on the mean flow pattern in the base recirculation region; and

(3) Off-axis collection in LDV systems would enable finer resolution of fluctuating velocity components in shear layers with very high velocity gradients such as those found along the boundaries of supersonic jets.

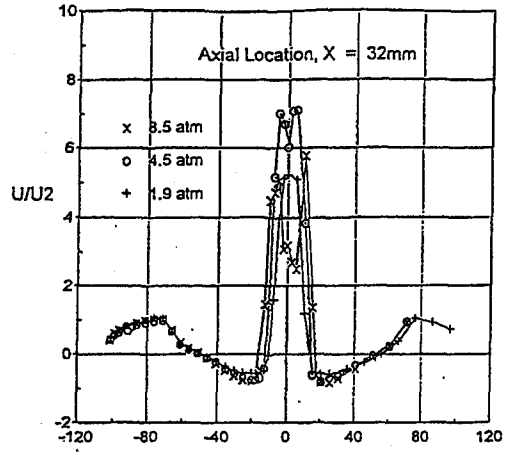

(a)

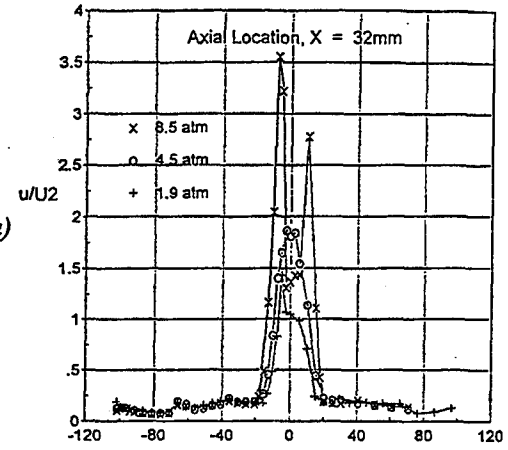

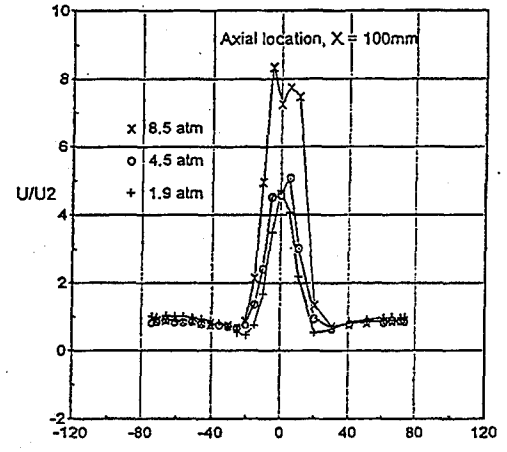

(b)

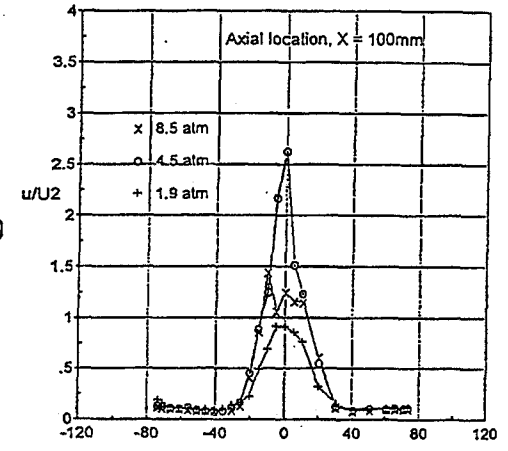

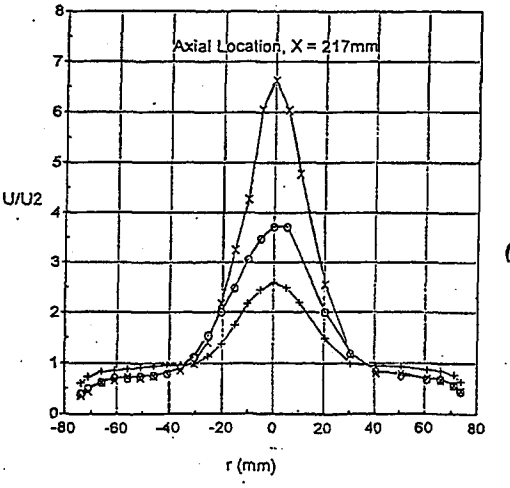

(c)

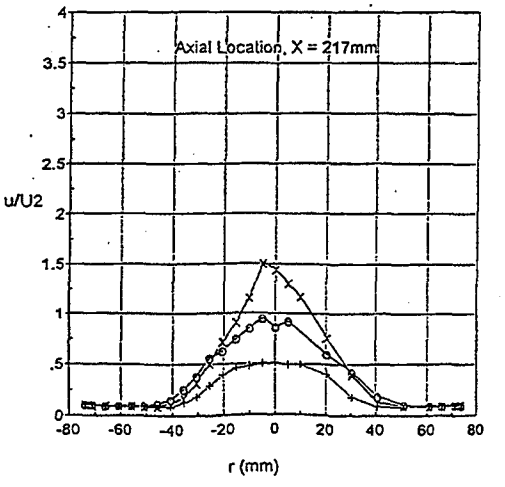

Figure 8 - Axial Mean Velocities

Figure 9 - Axial Turbulent Velocities

ACKNOWLEDGEMENTS

The author wishes to thank Mr. G. Wells, Mr. D.Dyett, Mr.M.Fisher and Mr.R. Maier for their assistance in configuring the rig and gathering the experimental data.

REFERENCES

1. Thompson, H.D. and Stevenson, W.H., "Laser Velocimetry and Particle Sizing", Proceedings of the third international Workshop on Laser Velocimetry, Hemisphere Publishing Corporation, 1979.

2. Petrie, H.L., " A Study of Compressible Turbulent Free Shear Layers Using Laser Doppler Velocimetry ", PhD Thesis, University of Illinois,1984 .

3. Favaloro, S.C. " Laser Doppler Velocimeter Measurements in Compressible Flow ", Proceedings from the Workshop on Laser Diagnostics in Fluid Mechanics and Combustion, DSTO, Australia, AR-008-93, pp 11.1-11.5, Oct., 1993.

4. Haghgooie, M., Kent, J.C., and Tabaczynski, R.J. " Verification of LDA and Seed Generator Performance ", Experiments in Fluids, Vol 4, pp 27-32, 1986.

5. Nejad, A.S., Vanka, S.P., Favaloro, S.C., Samimy, M., and Langenfeld, C., "Application of Laser Velocimetry for Characterisation of Confined Swirling Flow", Journal of Engineering for Gas Turbines and Power, Vol 111, No.1, pp 36-46, Jan., 1989.

6. Agarwal, J.K. and Johnson, E.M., "Generating Aerosol for Laser Velocimeter Seeding", TSI Quarterly, Volume VII, Issue 3, pp 5 -12, July-Sept 1981.

EVOLUTION OF TWO-SCALE, SHEARLESS GRID TURBULENCE

A.F. Heenan - J. F. Morrison
(Imperial College - Dept. of Aeronautics)
G. Iuso - M. Onorato
(Dept. of Aerospace - Politecnico di Torino)

ABSTRACT

The interaction of two streams of nominally homogeneous turbulence with velocity- and length-scale ratios of about two is studied experimentally. Two homogeneous streams separated by a mixing layer are formed downstream of a monoplanar two-scale grid of uniform solidity so there is a nominally-zero mean-velocity gradient. The turbulent diffusion processes are examined and the applicability of several transport models is assessed. A non-linear diffusion model, based on the turbulent kinetic energy, appears to provide the best representation of the turbulent diffusion.

INTRODUCTION

Many turbulent flows are characterized by the nonlinear interaction of different imposed scales. Often, this interaction is complicated by the effects of the production of turbulent shear stress or kinetic energy that occurs in shear layers. An example might be the interaction between the two halves of an asymetric wake at the trailing edge of an aerofoil where the boundary-layer thickness and Reynolds number of the separating boundary layer could be much larger on the suction surface.

The object of this work is to study the interaction of two scales of turbulence in isolation, without the complicating effects of turbulent production or upstream history effects. It involves the generation of grid turbulence by two set of horizontal bars, each having the same solidity and geometric shape but with different dimensions. For a given bar geometry, the pressure drop depends only on the grid solidity (Baines and Peterson[1]). Therefore there is no mean velocity gradient and the shear stress and production of turbulent kinetic energy are nominally zero. The flow downstream of the grid is therefore dominated by turbulent transport between two adjacent streams of (nearly) homogeneous turbulence with scales determined by the two grid sizes.

Physically, this lateral transport can be accomplished by two mechanisms: gradient diffusion of the quantity down its gradient in a manner not unlike but not analogous to molecular diffusion, and bulk convection which is related to the levels of turbulent kinetic energy present and occurs due to the convection of small eddies by larger ones. The gradient-diffusion approximation for turbulent transport (whether by velocity fluctuations or pressure fluctuations) has been used almost exclusively in second-moment models; and the same assumption is, of course, inherent in eddy-viscosity models, but the physical basis for such a model is lacking. The present flow has been studied previously by Gilbert[2] and Veeravalli and Warhaft[3],[4] (hereinafter referred to as VW1 and VW2, respectively), although in each case the exact geometries are different (as is our own), so that the relative importance of these two processes may also be different. We attempt to clarify the nature of the interaction by a detailed examination of the turbulent transport processes, as outlined above, as well as re-examining the penetration model put forward by VW2, where it is assumed that the p.d.f. of the velocity fluctuations in the mixing region is given by a linear

combination of those from each of the homogeneous limits of the flow, and which, although a valid model, will never occur in isolation. Owing to the direct measurement of the dissipation rate, ε, the pressure diffusion term has been deduced by differences in the energy balance. In principle this means that the pressure and turbulent diffusion processes can be assessed independently, although the relatively poor accuracy of the dissipation measurements meant that the estimates of pressure diffusion were also poor so that no firm conclusions regarding its nature could be drawn.

EXPERIMENTAL APPARATUS AND PROCEDURE

The wind tunnel

The experiments were conducted in the 'Arancione' wind tunnel of the Politecnico di Torino. It is an open-return wind tunnel powered by twin 13 HP fans 0.95 m in diameter. They are aligned with the flow direction and rotate in the same sense. A maximum operating speed of around 15 ms^{-1} is possible. Between the contraction and the test chamber there is a short duct, 50 cm long with the same cross-section of the test section, where flow manipulators such as the grids can be placed. The working section is in three parts with a total length of 6.34 m with cross section 90 cm x 130 cm. The walls are perspex supported by a steel framework. Supports for sensors enter the tunnel through a slot cut in the floor with longitudinal and vertical traverses providing probe mobility. The flow uniformity in the test section is less 0.75% in terms of dynamic pressure and turbulence intensity is less than 0.1%. Figure 1 is a dimensioned schematic diagram of the experimental layout.

The parallel-bar grids

The grid is made up of two sets of geometrically similar aluminium bars supported by an aluminium frame. The ratio between their dimensions was 3.3 and the geometric centre of the grid was 430mm above the tunnel floor. Table 1 details the grid's geometry, after the tuning operation to obtain a uniform mean velocity profile.

PARAMETER	LARGE	SMALL
Bar Dimensions	20mm x 18 mm	6mm x 6mm
Bar Separations	M_1 = 60mm	M_2 = 18mm
Aspect Ratios	65	217
Solidity	0.33	0.33

Table 1. Grid geometry

Two main problems had to be solved before obtaining acceptable flow conditions, namely: the transverse oscillations of the small scale bar and the large mean velocity gradients.

Oscillations were not surprising considering that the bars were of hollow aluminium and had an aspect ratio greater than 200. To attenuate these oscillations the vertical rigidity of the bars was improved by supporting them with lengths of studding 250 mm from the grid frame. The bars were fixed to the studding with fencing wire. Furthermore, two more wire supports were fixed to the bars 130 mm from the tunnel walls, in this way the oscillations were suppressed up to a flow speed of around 9 ms^{-1}, which was above the operating flow speed for the experiments.

The initially large mean velocity gradients were reduced by slightly repositioning bars where velocity gradients were present. This movement of individual bars often had non-local effects and the velocity gradient reduction was basically a trial-and-error process which lasted several weeks. The final result was a configuration that produced a maximum local velocity gradient below 4 sec^{-1} and an average gradient of $0.0024s^{-1}$.

Measurement equipment and techniques

A standard pitot-static tube with a Betz manometer was used to measure mean velocity. The turbulence measurements were made using single and X-hot wire coupled with Dantec 55M constant-temperature anemometer bridges; an overheat ratio of 1.7 was fixed. A National Instruments SCXI-1140 'sample and hold' board, with 12-bit resolution was used to sample the amplified signals simultaneously. For the correlations of second and higher order, a sample rate of 10 kHz was used, sampling forty data blocks, each containing 4096 samples. The repeatability of the results was within 1-2% for second order products, with a slightly greater spread for the higher orders.

After conversion of the signal to a cooling velocity using a look-up table, the cosine law was applied to evaluate the velocity components, allowing the calculation of the second and higher order correlations. The energy dissipation rate was calculated from the derivative time histories of the u, v and w components, applying Taylor's hypothesis. Measurements (with both single and X-wire probes), were taken at 2 cm intervals from 20 cm to 70 cm above the tunnel floor. The way in which the dissipation measurements were made required careful consideration: oversampling could produce spurious overestimates of ε simply by differentiation of signal noise; on the other hand, too-low-a sampling rate would certainly produce underestimates. The time resolution was therefore set to be the same as the spatial resolution of the hot-wire probe, using Taylor's hypothesis. The Kolmogoroff length scale was estimated to be between 0.24 and 0.35mm for this flow and, taking the wavelengths of the dissipating eddies to be between 6η to 60η these are likely to be about one to ten times the wire length (1.5mm). Thus some spatial averaging will undoubtedly occur so that estimates of ε will inevitably be low.

RESULTS and COMMENTS

The optimized mean-velocity profile (at the nominal mean velocity of 7.5 ms^{-1}, $Re_{M_1} \approx 30500$). The turbulence intensity components (Figure 2), as well as higher order products and correlations, were measured at five x locations downstream of the grid: $x/M_1 = 17.5$, 20.0, 21.7, 23.3 and 29.2, the three central locations were grouped relatively close together to allow reasonable accuracy in the estimation of the streamwise derivatives appearing in the advection terms. The distances downstream are sufficently large for the turbulence to be approximately self-similar, although this proved difficult to establish at the homogeneous limits to the flow because of the effect of the tunnel wall boundary layers. In general, the ratio of the length- and velocity-scales of the energy-containing turbulence in the large-scale region to those in the small-scale region was about two.

The decay of the two homogeneous regions is shown in Table 2, which shows the constants appearing in the power law equation $\overline{u^2} = AU^2(x/M)^{-n}$. The constants are similar to those of VW2 and also to those obtained in bi-planar grid turbulence (n =1.4, Batchelor[5], n=1.24, Comte-Bellot and Corrsin[6] and n = 10/7 from Kolmogoroff 's[7] theoretical analysis).

component	A	n	component	A	n
u_2	0.151	1.19	u_1	0.322	1.42
v_2	0.155	1.19	v_1	0.262	1.44
w_2	0.099	1.18	w_1	0.216	1.34

Table 2. Coefficients of the power law decay equation

VW1 have discussed the degree of inhomogeneity produced by a monoplanar grid as opposed to that of a traditional biplanar one. This appeared to be worse on the large-scale side and is therefore likely to be due to the persistence of the large eddies, the maximum change in any one component of the turbulence intensity was about 5% (about the same as that of VW2, for their modified grid) and appeared to be in the u component at the first x station, but in the v component at the last. The relative ease at which reasonably homogeneous flow could be obtained for the two grids in the present work is probably due to their large aspect ratios (tunnel width/bar thickness), which were about twice those of VW2. Figure 3, which contains profiles of the ratios between the u and v r.m.s. values, shows the variation of u-v anisotropy across the flow. This should, of course, decrease downstream (Lumley and Newman[8]), but it is possible that effects from the wall boundary layers could increase the anisotropy at the homogeneous limits, with downstream distance. Nevertheless, in general the anisotropy at the homogeneous limits is slightly less (by 1%) for the traverse furthest downstream. $\overline{v^2}$ Generally the u-component normal stress is the largest, but in the lower parts of the mixing region, $\overline{v^2}$ increases due to the vertical transport of momentum, which obviously will always appear in correlations where the powers of v are the largest. In agreement with VW2, all of the present results show that the centre of the mixing region lies below the position of the geometric centre, that is, on the small-scale side of the mixing layer.

Figure 4 shows the evolution of the shear correlation coefficient, R_{uv}, which shows an oscillatory behaviour, and Figure 5 shows the mean velocity gradient. The sign of the velocity gradient appears to be in antiphase to $\overline{uv}$, as the production term for $-\overline{uv}$ would suggest. Therefore there does appear to be some shear stress and energy production. However the turbulence production terms were small compared to the other transport terms. VW2 show that shear stress can also be produced by the anisotropy between $\overline{u^2}$ and $\overline{v^2}$.

$$\frac{\partial}{\partial y}\frac{\partial}{\partial x}(\overline{u^2}-\overline{v^2}) = \frac{\partial^2}{\partial x^2}(\overline{uv}) - \frac{\partial^2}{\partial y^2}(\overline{uv}) \qquad (1).$$

The dynamics of this process linking anisotropy, shear stress and mean velocity gradients is not clear but equation (1) suggests that variations in the shear stress contribute to the observed variations in anisotropy in the nominally homogeneous regions. The shear correlation coefficient was always low at around 0.05.

Figures 6 and 7 show the normalised profiles of $\overline{u^2v}$ and $\overline{uv^2}$ respectively at the three central x locations. The former represents the transport of the $\overline{u^2}$ normal stress by v-component velocity fluctuations. Since these are strongly skewed in the negative y direction, the correlation has a strong negative peak, and is an indication of the propagation of the large scale turbulence into the small-scale region, where the minimum is below the geometric centre of the grid. The $\overline{uv^2}$ coefficient is a measure of the transport of $\overline{uv}$ by the v-component velocity fluctuations. Therefore it can be expected to show the same behaviour as $\overline{uv}$, but again in antiphase due to the

dominance of downward transport. Unlike $\overline{u^2v}$, $\overline{uv^2}$ is finite at the homogeneous edges, presumably because of the anisotropy of the turbulence there.

Figures 8, 9 and 10 show the skewness factors S_u, S_v and S_w respectively: at the homogeneous limits, S_v should be zero; S_w should be identically equal to zero everywhere because of spanwise homogeneity; S_u should be approximately zero everywhere as the turbulence is approximately homogeneous in the x direction. S_v reaches a minimum of -0.95 (compared with VW2's value of -1.2), again below the geometric centre of the grid. The S_u profile is similar to the inverted $\overline{uv}$ distribution and the minimum is considerably smaller than that of VW2, as is the minimum of S_w. The non-Gaussian values of skewness at the outer edges of the mixing region, particularly on the large-scale side, can be attributed to both the anisotropy of the normal stresses producing shear stresses via equation (1) as well as, to a lesser extent, the influence of the wall boundary layers. The value of S_u here remains at 0.1, more than twice the value for homogenous biplanar grid turbulence reported by Maxey[9].

Figures 11, 12 and 13 show the equivalent Kurtosis factors, K_u, K_v and K_w, respectively. Again, in the mixing layer, these show large departures from Gaussian values implying significant transport mechanisms are operating in addition to diffusion. Equation (2) defines the kurtosis value supposing that the mixing process is basically one of linear superposition of the p.d.f.'s of the two velocity fluctuation fields:

$$K_u(r) \equiv \frac{\overline{u^4(r)}}{\left(\overline{u^2(r)}\right)^2} = \frac{\overline{u_2^4}r + \overline{u_1^4}(1-r)}{\left(\overline{u_2^2}r + \overline{u_1^2}(1-r)\right)^2} = \frac{3\left(\overline{u_2^2}\right)^2 r + 3\left(\overline{u_1^2}\right)^2 (1-r)}{\left(\overline{u_2^2}r + \overline{u_1^2}(1-r)\right)^2} \qquad (2).$$

where r is the intermittency of the large-scale side (as per the definition in VW2). This "penetration" model has been suggested by VW2 and the theoretical data for all three components are plotted with the experimental data. Equation (2) assumes that the p.d.f.'s of the velocity fluctuations transported from the homogeneous limits to the mixing region are Gaussian. Table 3 shows the maximum 'kurtosis excess factors' (KEF), that is the difference between the kurtosis value and the gaussian value of three, together with those of VW2. KEF therefore is a measure of the relative importance of penetration over diffusion. For the u and w components, the ratios of theoretical and experimental KEF's are similar, and are all substantially less than unity showing that turbulent transport is accomplished not only by penetration but also by diffusion. The downward transport of v momentum is not well represented by the linear superposition of two Gaussian p.d.f.'s because the v-component penetrations which effect the lateral transport are present in the v component p.d.f. in the mixing region resulting in a very 'spikey' signal and large values of kurtosis.

	u	$u_{(VW2)1}$	$u_{(VW2)2}$	v	$v_{(VW2)1}$	$v_{(VW2)2}$	w	$w_{(VW2)1}$	$w_{(VW2)2}$
KEF_{exp}	0.7	1.36	6.1	2.2	-	-	0.7	1.1	5.7
KEF_{theo}	1.7	3.56	18.78	2.2	-	-	2.4	3.05	15.11
$\frac{KEF_{exp}}{KEF_{theo}}$	0.41	0.38	0.32	1.0	-	-	0.29	0.36	0.38

Table 3. Experimental and Theoretical KEF

DISCUSSION OF DIFFUSION MODELS

Opinions vary as to the relative importance of the various mechanisms of the lateral transport process. Gilbert[2], using a two-scale monoplanar grid (similar to the one used in the present experiments, but with a much lower scale ratio), found little evidence of large-scale transport mechanisms and was able to model transport in the mixing region solely as a diffusion process. However, there is evidence in the present work and VW2 that both mechanisms are significant. The KEF ratios for the monoplanar grid experiments of VW2 and the present work are similar (≈ 0.3) for those components for which the model is valid (i.e. u and w), suggesting that the relative importance of each mechanism may not be specific to each configuration. VW2 also suggest that, as the scale ratios in Gilbert's experiments were low, it would have been difficult to observe significant bulk convection. This and gradient-diffusion transport are generally defined as respectively:

$$\frac{\overline{pv}}{\rho}+\frac{1}{2}\overline{q^2v}=V_q\left(\frac{1}{2}\overline{q^2}\right) \qquad (3).$$

$$\frac{\overline{pv}}{\rho}+\frac{1}{2}\overline{q^2v}=C_q\frac{\partial}{\partial y}\left(\frac{1}{2}\overline{q^2}\right) \qquad (4).$$

where V_q is the convection velocity, and C_q is the gradient diffusivity. Figure 14 shows the transport terms $1/2\overline{q^2v}$ and $\overline{pv}/\rho$; and Figure 15 shows the turbulent transport term with the gradient of the turbulent kinetic energy. Clearly equation (4) is a better model on the large-scale side than on the small-scale side. Moreover, a simple bulk convection model will be inadequate because the energy profile (a monotonic positive gradient between two plateaux) is completely different in shape to that of $1/2\overline{q^2v}$. Such a mismatch would also prevent a linear combination of equations (3) and (4) (as Keffer[10] has done) from being an effective model if this particular definition of V_q is used. It is also likely that the pressure diffusion term in Figure 14 should tend approximately to zero on the large-scale side: this does not happen because the resolution errors in the dissipation measurements are worst here where the Kolmogorov scales are smaller. Therefore we have not pursued the modelling of this term, although the results do at least indicate that the pressure term is small in the mixing region. Another possible definition of the gradient diffusion is:

$$\frac{\overline{pv}}{\rho}+\frac{1}{2}\overline{q^2v}=\frac{1}{2}\overline{q^2}\,C_q\frac{\partial}{\partial y}\left(\frac{1}{2}\overline{q^2}\right) \qquad (5).$$

where the diffusion coefficient is made a function of the turbulent kinetic energy with one free constant, a 'time-constant' of energy-containing eddies. This is done to reflect the nonlinearity of the mixing process exemplified by the large values of K_V and suggested by the failure of the linear models to represent the vertical diffusion adequately. Figure 16 shows the agreement of the model with the data is better than in the case of the linear diffusion model. It is likely that any model which prescribes the eddy diffusivity, C_q, as a constant times the product of appropriate velocity and length scales will fare better than a constant diffusivity.

A simple profile for $V_q(y)$ across the mixing region may be estimated by using similarity arguments to assume Uy/x as an estimation of the convection velocity to transport an eddy from the homogeneous large-scale boundary to a position y (U being the mean velocity and x the

distance downstream from the mixing layer origin). Therefore, in the mean, eddies will be convected to y at an effective velocity of rUy/x where r is the (experimentally determined) intermittency factor. Figure 17 compares the product of V_q (as defined above) and $1/2\overline{q^2v}$ with $1/2\overline{q^2v}$. There is a reasonable match with the experimental results over the lower half of the mixing region but this deteriorates closer to the high intensity region as the definition of V_q requires that lateral transport goes to zero at the boundary between the large- and small-scale regions. This is not physically true as there are penetrations from the small-scale side into the large-scale side. A more sophisticated definition of V_q, describing penetrations from both high and low intensity regions may produce better results.

CONCLUSIONS

Several simple models of turbulent diffusion in the mixing layer between two nominally-homogeneous streams, of different scales, have been assessed. For velocity- and length- scale ratios of about two, a simple diffusion model for turbulent kinetic energy is not particularly good, a better representation being obtained by using a nonlinear model which, in effect, uses the turbulent kinetic energy as the square of the velocity scale. A simple bulk convection model with a constant convection velocity is wholly inappropriate, although a simple expression allowing for the variation of the convection velocity across the mixing layer did improve agreement considerably.

This work was carried out with financial support from the Ministero dell'Università e della Ricerca Scientifica e Tecnologica and the CSDF (CNR).

REFERENCES

1. Baines, W.D.; Peterson, E.G. *An investigation of flow through screens* Trans. Amer. Soc. Mech. Engr. 73, p.467, 1951.
2. Gilbert, B. *Diffusion mixing in grid turbulence without mean shear* J. Fluid Mech. Vol.100, p.349, 1980.
3. Veeravalli, S.; Warhaft, Z. *The interaction of two distinct turbulent velocity scales in absence of mean shear* Turbulent Shear Flows 5 (ed. L.T.S. Bradbury et al.) p.31, 1989, Springer.
4. Veeravalli, S.; Warhaft, Z. *The shearless turbulence mixing layer* J. Fluid Mech. Vol.207, p.191, 1989.
5. Batchelor, G.K. *The theory of homogeneous turbulence* Cambridge University Press.
6. Comte-Bellot, G.; Corrsin, S. *The use of a contraction to improve the isotropy of grid generated turbulence* J. Fluid Mech. Vol.25, p.657, 1980.
7. Kolmogoroff, A.N. *On the degeneration of istropic turbulence in an incompressible viscous liquid* C.R. Akad. Sci. SSSR (Dokl.), Vol.31, p.538, 1941.
8. Lumley, J.L.; Newman, G.R. *The return to isotropy of homogeneous turbulence* J. Fluid Mech. Vol.82, p.161, 1977
9. Maxey, M.R. *The velocity skewness measured in grid turbulence* Phys. Fluids Vol.30, p.935, 1987.
10. Keffer, J. F. *The uniform distortion of a turbulent wake.* J. Fluid Mech. Vol.22, p.135, 1965.

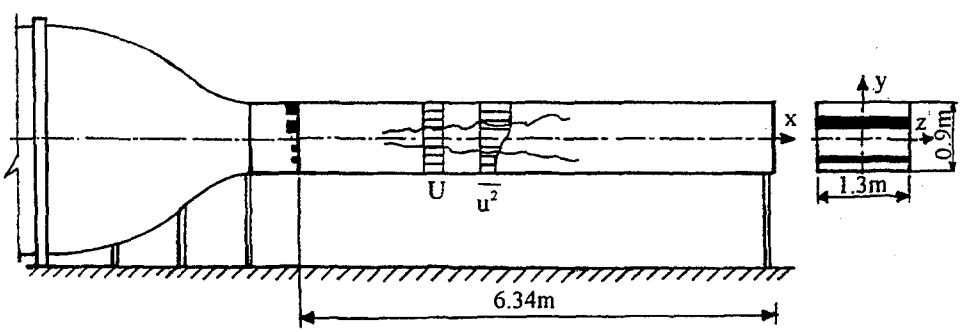

Fig. 1: Experimental Layout

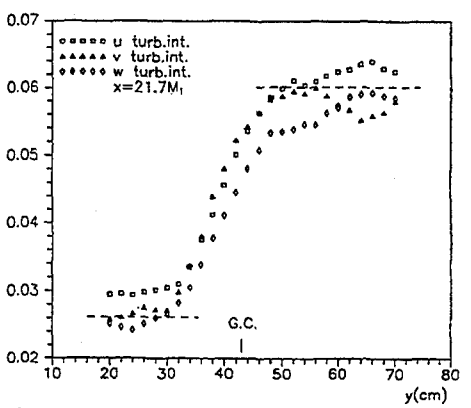

Fig.2 Component Turbulence Intensity Profiles

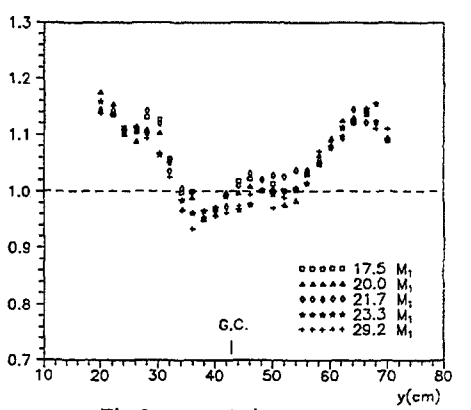

Fig.3 u - v Anisotropy

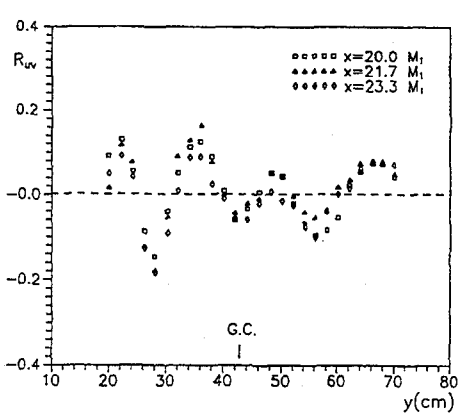

Fig.4 $\overline{uv}$ Reynolds Stress Coefficients

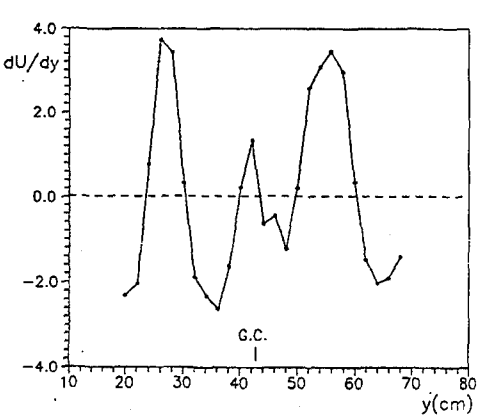

Fig.5 Mean Velocity Gradient

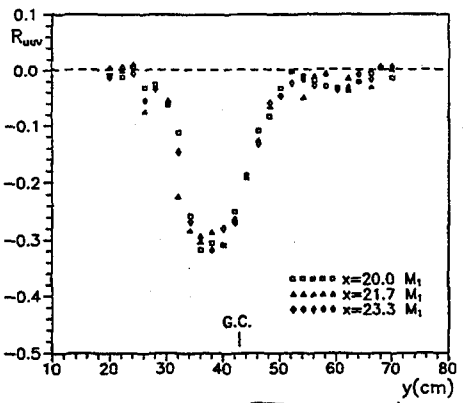

Fig.6 Normalised $\overline{u^2v}$ Triple Product

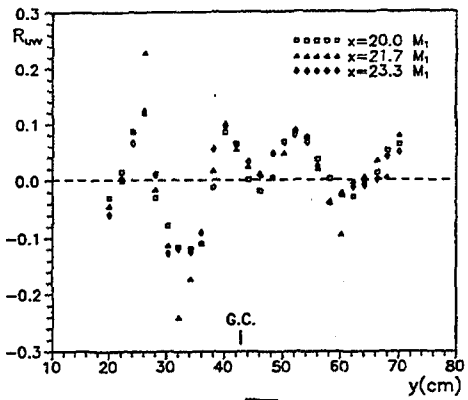

Fig.7 Normalised $\overline{uv^2}$ Triple Product

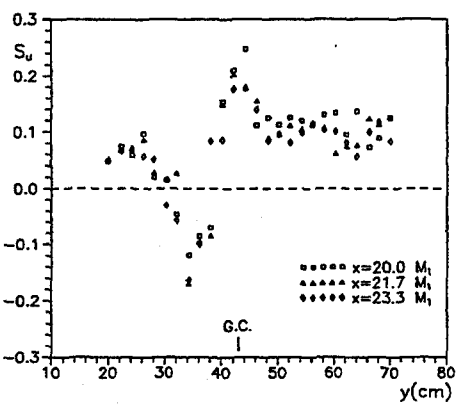

Fig.8 u Component Skewness

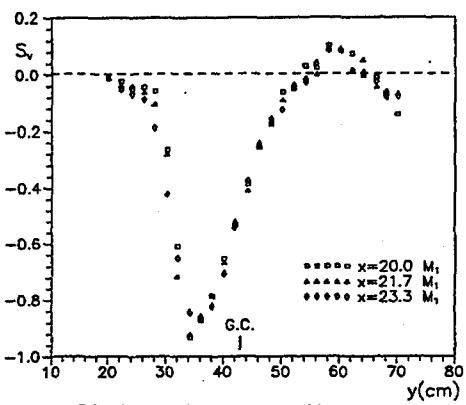

Fig.9 v Component Skewness

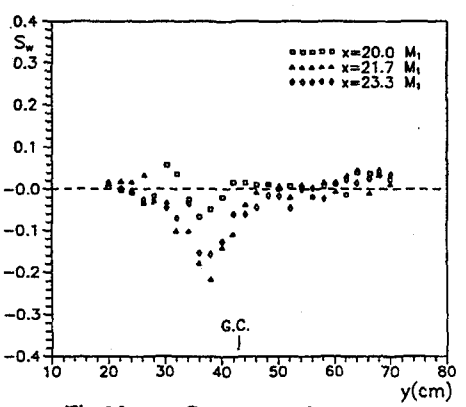

Fig.10 w Component Skewness

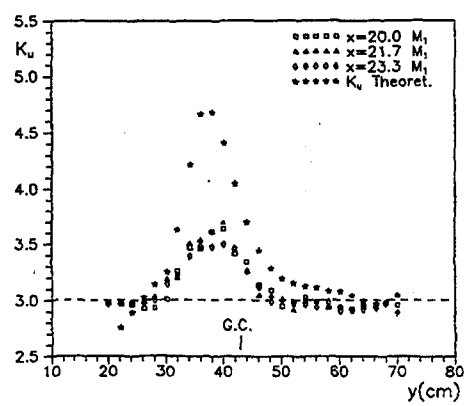

Fig.11 u Component Kurtosis

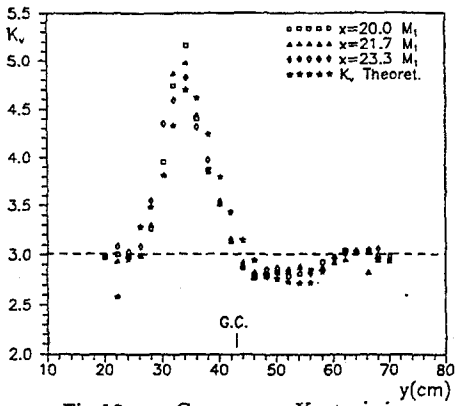

Fig.12 v Component Kurtosis

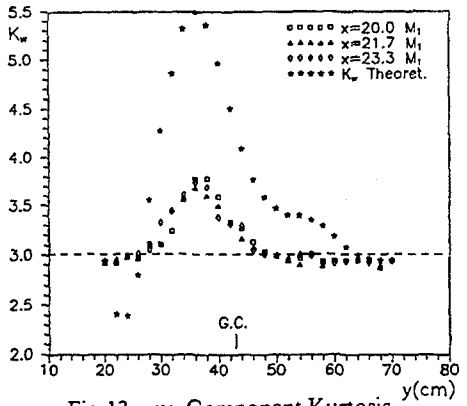

Fig.13 w Component Kurtosis

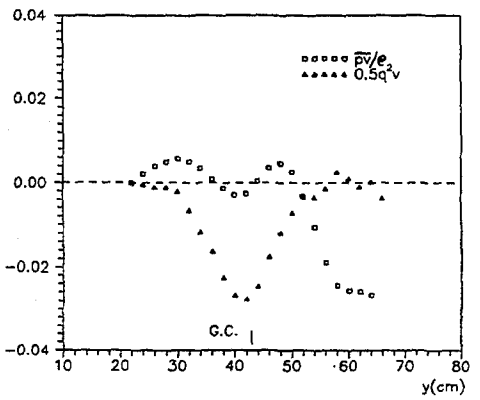

Fig.14 Triple product and pressure term

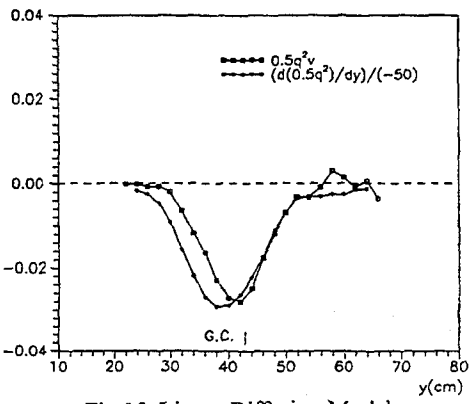

Fig.15 Linear Diffusion Model

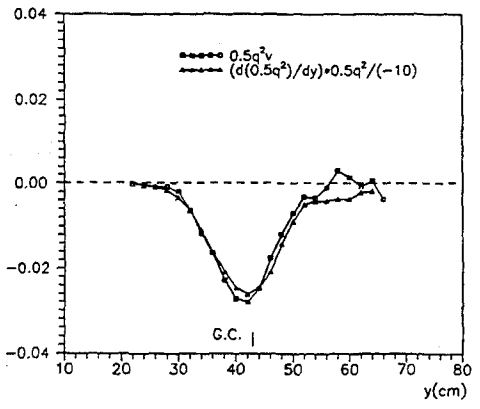

Fig.16 Nonlinear Diffusion Model

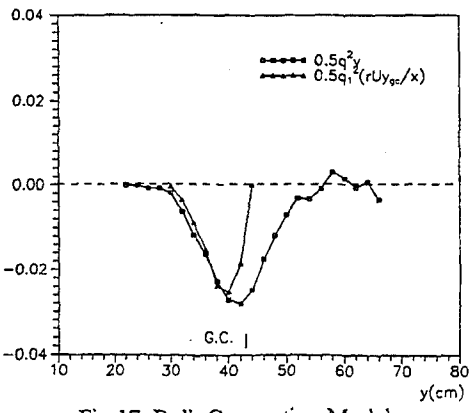

Fig.17 Bulk Convection Model

ADVANCED METHODS FOR STRUCTURE IDENTIFICATION IN TURBULENT FLOWS

L. Bergamini, A. Cenedese, G. Querzoli, G.P. Romano

Department of Mechanics and Aeronautics
Universita' "La Sapienza" - Roma
Via Eudossiana 18 - 00184 Roma - ITALY

Abstract

Velocity measurements in a convective flow are performed using Particle Image Velocimetry (PIV): two velocity components are simultaneously detected. A linear heating element is placed on the bottom wall of a rectangular vessel, the temperature of such element is maintained higher than that of the other isothermal or adiabatic walls. Images are acquired by a videocamera and stored on a videorecorder for further processing. Each particle is tracked along its trajectory with a frame by frame scanning procedure. The investigated flow shows periodic oscillations of the main configuration consisting of two counter-rotating vortices: their size is of the same order of that of the vessel. The oscillations take place on a vertical plane. To describe the flow pattern as well as to investigate the dynamical behaviour of such physical system, Proper Orthogonal Decomposition (POD) is used: main modes are computed to characterize both space and time evolutions without using Taylor hypothesis. Tests are performed to verify the effectiveness of the decomposition. Two main results are obtained: 1) the mechanism responsible for the instability in the basic flow configuration derives from instantaneous coupling between different modes; 2) the detected number of degrees of freedom is about 1/25 of the total grid variables.

Introduction

The eduction of simple patterns from an apparently complicated flow field is a fundamental task for basic fluid-dynamic investigations. A wide variety of methods have been proposed in recent years: VITA[1], Quadrant Analysis[2], Linear Stochastic Estimation[3] and Wavelets[4] to cite only the main ones. All these methods allow to obtain subsets of the whole data base. They have advantages and disadvantages one over the other, depending on the set of variables that have been detected, therefore their usefulness is connected to different flow conditions. However, it is not possible to prove the decomposition in subsets to be optimal, that is to have the maximum convergence rate and the maximum amount of energy in each element of the decomposition. This is the case for orthogonal eigenfunctions of the Karhunen-Loève decomposition. Lumley[5] introduced such decomposition in fluid-dynamics: in order to obtain modes, he proposed to extract the candidate structure which is the best statistically correlated with the background velocity field. Whenever the decomposition is performed in homogeneous directions, standard Fourier components are reproduced. Such modes are used to investigate the evolution of the flow in terms of basic energetic patterns; the next step is to insert such modes in basic equations and eventually to describe properties of solutions[6].

In fluid-dynamics POD is used to decompose one or two-dimension velocity fields. Usually Taylor hypothesis is employed: signals from rake of sensors along non-homogeneous directions are acquired in time and the evolution is assumed to be representative of that in space. However Taylor hypothesis is strictly valid only at high Reynolds number and in isotropic conditions[7],[8].

Multipoint simultaneous measurements allow to obtain velocity fields without using Taylor hypothesis: PIV satisfies the requirements of high spatial and time resolutions in low speed flow fields.

Convective flows have been extensively studied in the past: examples are simulations of atmospheric boundary layer or in Rayleigh-Benard convection. In the present paper, however, interest is focused on the external forcing to investigate departure from equilibrium. The basic geometrical configuration consists of a rectangular vessel (adiabatic side walls and isothermal top and bottom walls) heated from below by a linear element. Similar geometrical configurations were already studied both numerically[9] and experimentally[10],[11]: two main counter-rotating vortices originating from the heating element and filling the whole vessel are observed. However when simulations and experiments last over several characteristic times (time for a particle to cross all over the vessel) such basic configuration starts to oscillate in a vertical plane[9]. For small values of the temperature difference between heating element and walls, that is for small Rayleigh numbers, these oscillations are almost regular in time. The velocity power spectrum depicts one sharp line at the frequency of the oscillations. For increasing Rayleigh numbers regular oscillations are limited to definite time intervals suddenly followed by irregular intervals where the power spectrum shows several lines. The critical Rayleigh number for such transition is connected not only to the temperature difference but also to the physical properties of the fluid and to the geometry of the vessel. The origin of the observed behaviour is not completely understood.

The analysis of this flow using POD could give new insight on the mechanisms for such transition to take place. However, the present analysis is not intended to investigate the dynamic behaviour as a function of Rayleigh number, but it is presented here to show the potential of PIV experimental procedure associated to POD analysis.

Experimental set-up and data analysis

The experimental set-up is designed for the investigation of two-dimensional unsteady buoyancy-induced flow inside a rectangular vessel: in figure 1 the overall optical and geometrical configuration is shown. The linear heat source is placed in a small region (L/10, where L is the width of the vessel) in the middle of the bottom wall. The walls are made of plexiglas. Bottom and top walls are isothermal, whereas side walls are adiabatic.

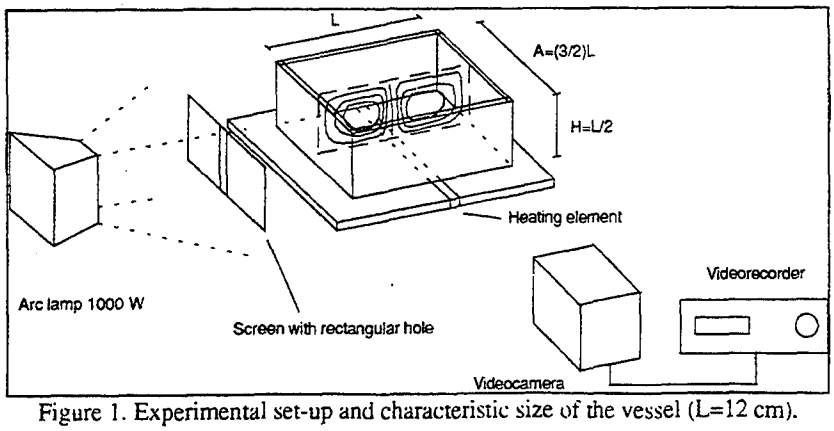

Figure 1. Experimental set-up and characteristic size of the vessel (L=12 cm).

Hot fronts ("plumes") rise from the heat source exhibiting swaying motion in the measurement vertical plane. This motion is the object of PIV and POD analyses. A mixture of water and 7.5% (vol.) of glycerine is employed. A temperature difference of 12.5°C between the heat source and the top wall corresponds to $Ra=4.27\times10^7$. The critical Rayleigh number, Ra_c, was not exactly determined, but the present case lies in the range $10<Ra/Ra_c<10^2$ where instabilities of the flow are well established (naturally swaying motion of the plume) and the flow motion is still dominated by large scale organized structures (non chaotic or weakly chaotic flow).

Pollen particles are used to seed the flow (mean size equal to 80 μm). The images are acquired by a videocamera on tape in S-VHS format (25 images/s). The image processing is performed by acquisition on a frame grabber (512x512 pixels, 256 grey levels) and by a Particle Tracking (PTV) algorithm to detect particle displacements and the corresponding velocities (detail on the procedure are described elsewhere[12]). Only one out of four images are used to evaluate trajectories and velocity vectors. As a consequence, the sampling rate is lowered to 6.25 images/s in order to maintain enough accuracy for the determination of the lowest speed. The density of seeding particles allowed the recognition of about 200 trajectories per image and roughly the same number of velocity vectors. POD analysis requires the knowledge of the complete velocity field discretized on a grid. For the present measurements a regular grid is employed with 23 cells along the horizontal direction and 15 cells along the vertical one. With this space discretization almost all cells are filled with data averaged in the selected time interval. This interval is about 5 s, which is small enough compared to the integral time scale of the phenomenon, about 100 s, resulting from separated LDA measurements. Sometimes cells have no data, such limitation is partially overcome by interpolating the missing data. Numerical tests are performed to verify the independence of the shape of computed eigenfunctions by using coarser and finer space discretizations.

POD is applied to PIV data on a regular grid by solving the Fredholm integral equation of the first kind whose symmetric kernel is the two point correlation matrix: in this way the magnitude of the projection of the eigenfunctions over correlation matrix is maximized in a mean square sense. Computational steps are the following:

- evaluate of the velocity correlation matrix: $R(\bar{x},\bar{x}')=<u(\bar{x})u^*(\bar{x}')>$
  where the averaging is performed on all images;
- solve the integral equation $\int_\Omega R(\bar{x},\bar{x}')\Phi(\bar{x}')d\bar{x}'=\lambda\Phi(\bar{x})$
  to determine eigenvalues, λ, and eigenfunctions, Φ, over the investigated region Ω;
- reproduce every member of the ensemble by modal superimposition $u(\bar{x},t)=\sum_k a_k(t)\Phi_k(\bar{x})$.

Tests are finally performed to verify the goodness of the decomposition: comparison between the first mode and the mean field, cumulative energy contribution of the modes, and the eigenvalue spectrum.

PIV and POD results

In the following, some result of the PIV acquisition and POD analysis will be presented.

Figure 2 shows the average velocity field over the whole acquisition time which is 1800 s long and includes 359 flow realizations. The flow field is not exactly symmetric mostly because the two side walls are not completely adiabatic. The wall to the right is slightly heated by the incident light of the arc lamp whereas the wall to the left has the thermal insulation interrupted by a window.

The velocity vectors in the figures are represented with a scale proportional to the length of the vector with the maximum magnitude, therefore these plots can be used only to qualitatively examine the flow field.

Figures 3 and 4 show two opposite oscillations of the plume. The first corresponds to t=1300 s and the second represents the flow 30 s after the first one.

Figures 5 through 8 show the first four POD eigenfunctions. As mentioned before, the first eigenfunction corresponds to the average field and it captures most of the kinetic energy of the flow (72%). The eigenfunctions tend to be either symmetric or antisymmetric.

In figure 9 it is plotted the cumulative energy contribution of the eigenfunctions. According to the criterion proposed by Sirovich and Deane[14], the Karhunen-Loève dimension of the system, d_{KL}, is 14. This dimension is defined as the number of modes required so that the captured energy is at least 90% of the total and that no neglected mode contains more then 1% of the energy contained in the first mode. In this case d_{KL} is roughly 1/25 of the number of variables involved (degrees of freedom) 23x15x1 = 345. The factor 1 takes into account the continuity relation between the two components of the velocity. Though, a more rigorous analysis should include an additional variable: the temperature.

Figure 10 shows a bilogarithmic plot of the spectrum of the eigenvalues. This plot is used to test the convergence of the POD decomposition. The POD decomposition requires the minimum number of modes to capture a given percentage of the total energy.

The time series (400 s $\leq$ t $\leq$ 700 s) of the first four modal coefficients are plotted in figure 11. The coefficient relative to the first mode has the highest mean value, all the others oscillate around zero with negligible mean values. The second coefficient shows oscillations with the highest amplitude. It is worth noting the presence of interactions between modes and the importance of the relative phases. According to POD theory, these time series are uncorrelated.

The normalized power spectra of the first four modal coefficients are plotted in figures 12 through 15. It is apparent the peak in the spectrum of the second and fourth mode that corresponds to the main frequency of the swaying motion of the plume (0.017 Hz).

Concluding remarks

This paper gives a quick view on what a POD analysis can produce from complex spatio-temporal data acquired by PIV. The concept of K.L. dimension and the statistics of the time series of the modal coefficients are some of the tools that can be very useful to understand the system from the dynamic point of view.

A limitation to the present analysis is the lack of data about the temperature field. The dynamics of the velocity field can be strongly influenced by the behaviour of the heat exchange on the upper wall. Further efforts should be made to include the temperature in the POD analysis. The major obstacle to be overcome is the difficulty of measuring the instantaneous temperature field with the same accuracy and resolution of the velocity one. For this particular experimental set-up a possible solution could be the measure of the temperature on the boundary only and the numerical computation on the rest of the field once the velocity has been acquired experimentally.

Acknowledgments

The authors are grateful to Prof. J.P. Bonnet and J. Delville for introducing them to POD in connection to the European ERASMUS program. Special thanks are due to M. Miozzi for the realization of the experimental set-up.

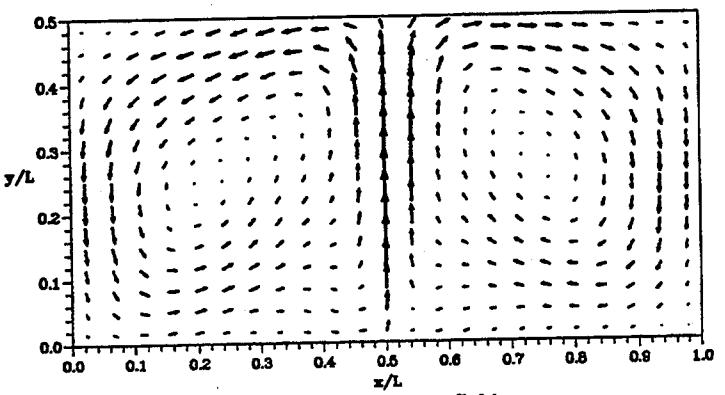

Fig.2. Average velocity field.

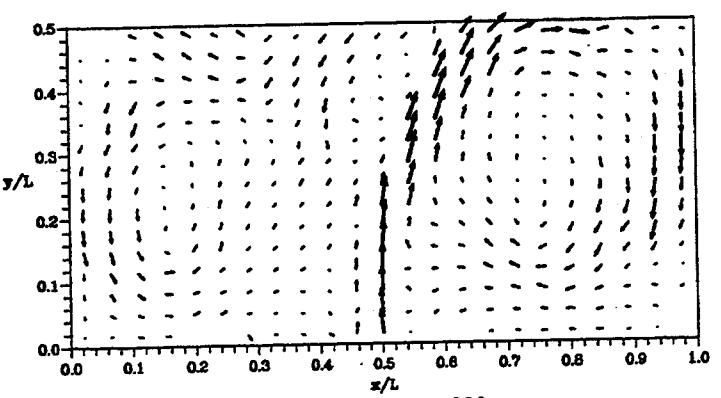

Fig.3. Velocity field, t=1300 s.

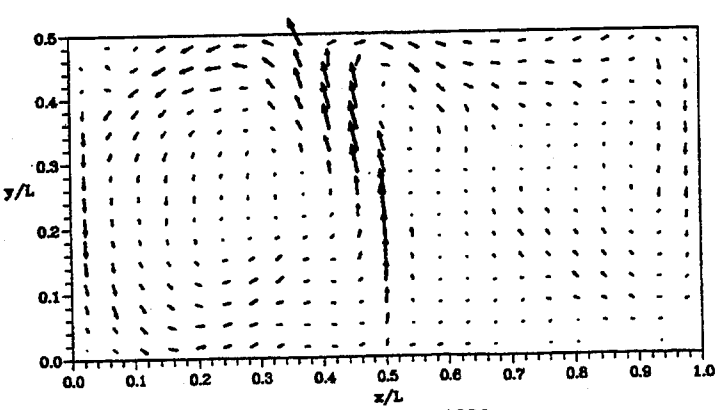

Fig.4. Velocity field, t=1330 s.

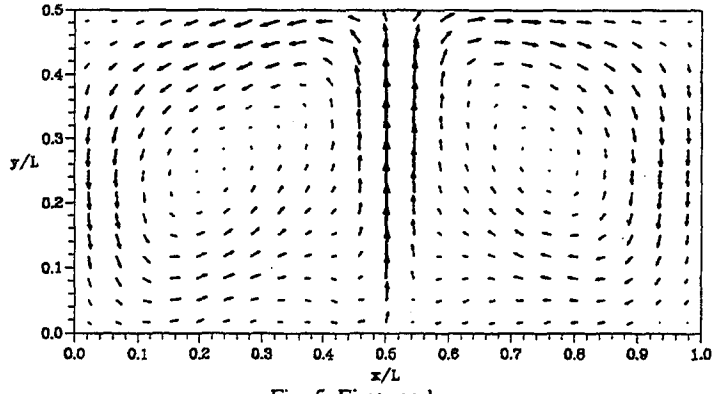

Fig. 5. First mode.

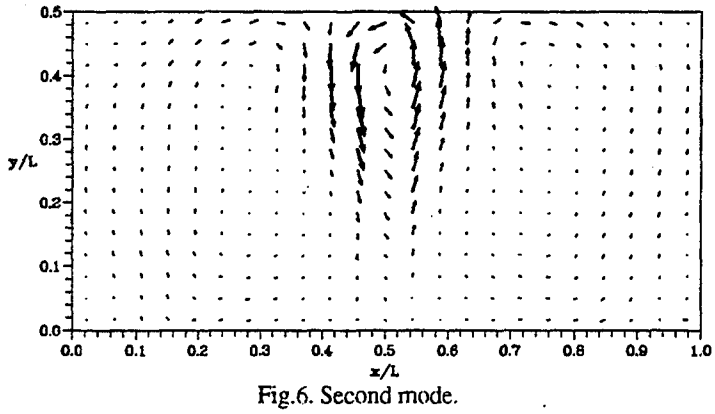

Fig.6. Second mode.

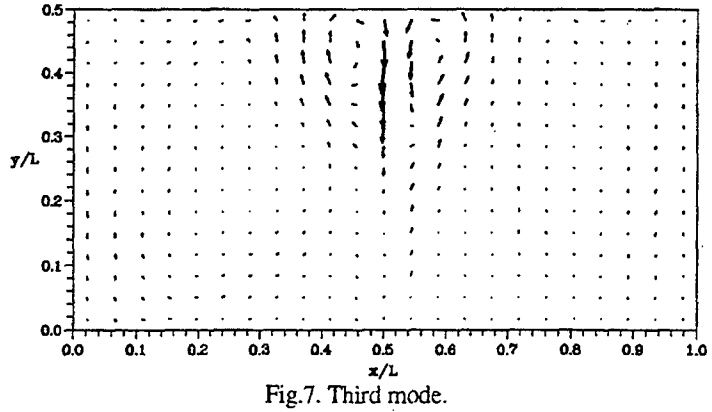

Fig.7. Third mode.

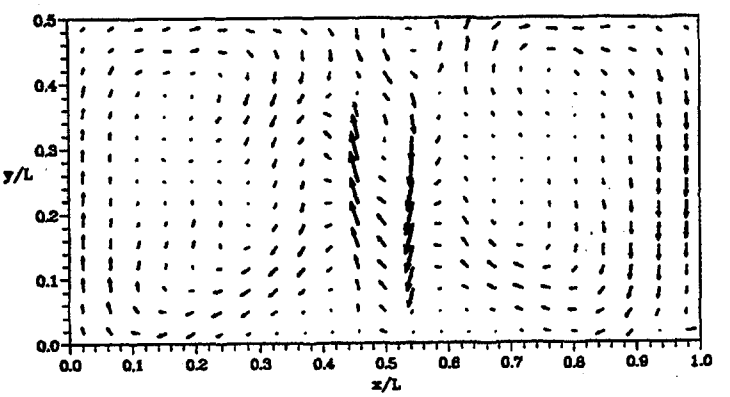

Fig.8. Fourth mode.

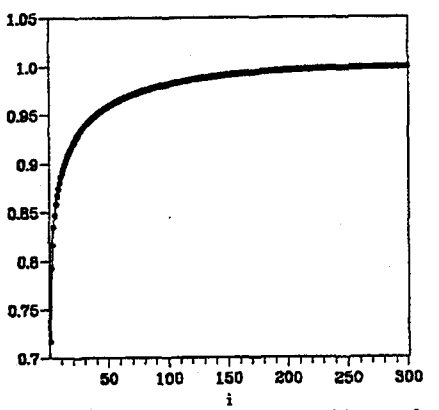

Fig.9. Cumulative energy captured by modes.

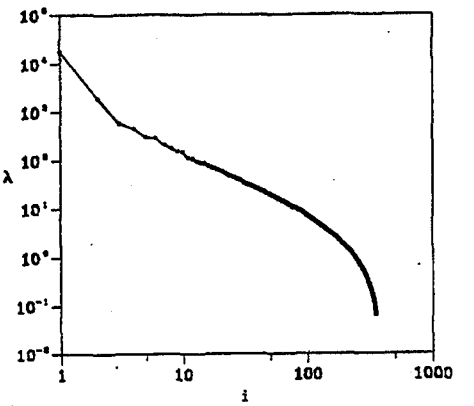

Fig.10. Eigenvalue spectrum.

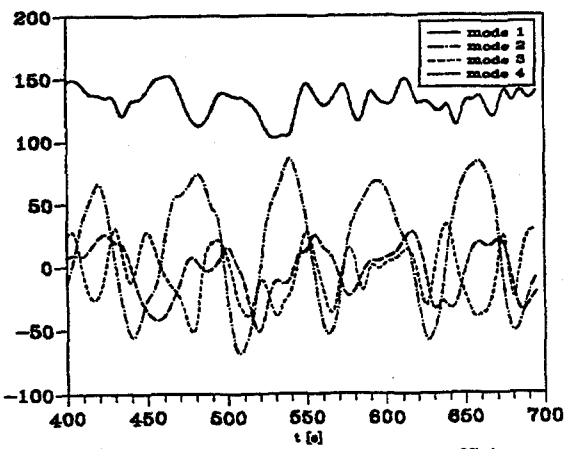

Fig.11. Time history of the first 4 modal coefficients.

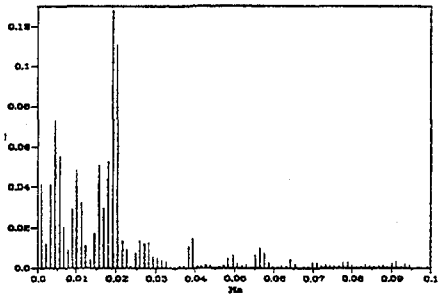

Fig.12.Power spectrum of the 1st modal coeff.

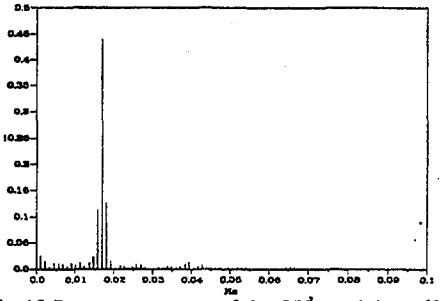

Fig.13.Power spectrum of the 2nd modal coeff.

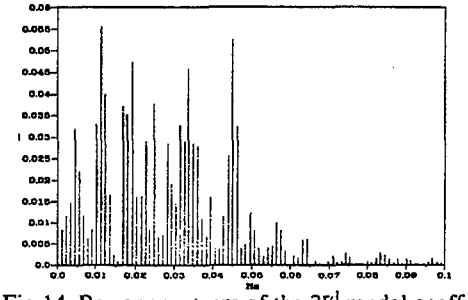

Fig.14. Power spectrum of the 3rd modal coeff.

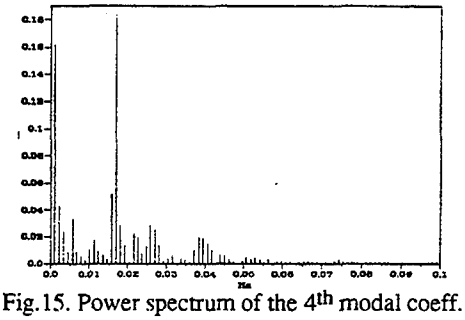

Fig.15. Power spectrum of the 4th modal coeff.

References

(1) BLACKWELSER R.G. & HARITODINIS J.H. 1983 Scaling of the bursting frequency in turbulent boundary layers. *J. Fluid Mech.* **132**, 87

(2) LU S.S. & WILLMARTH W.W. 1973 Measurements of the structure of the Reynolds stress in a turbulent boundary layer. *J. Fluid Mech.* **60**, 481

(3) ADRIAN R.J. 1988 Linking correlations and structure: stochastic estimation and conditional averaging. In *Near Wall Turbulence-Zoran Zaric Memorial Conf.* pp.420-436, Hemisphere Publishing Corporation

(4) FARGE M. 1992 Wavelet transforms and their applications to turbulence. *Annu. Rev. Fluid Mech.* **24**, 395-457

(5) LUMLEY J.L. 1967 The structure of inhomogeneous turbulent flows. In Atmosferic Turbulence and Radio Wave Propagation /ed. A.M. Yaglom and V.I. Tatarski), pp.166-178, Nauka, Moscow

(6) BERKOOZ G., HOLMES P. & LUMLEY J.L. 1993 The proper orthogonal decomposition in the analysis of turbulent flows. *Annu. Rev. Fluid Mech.* **25**, 539-575

(7) BALINT J.L., PIOMELLI U. & WALLACE J.M. 1989 On the validity of Taylor hypothesis for wall-bounded flows. *Phys. Fluids* **A1**(3), 609-611

(8) CENEDESE A., DI FELICE F. & ROMANO G.P. 1991 Experimental testing of Taylor's hypothesis by LDA in highly turbulent flow. *Experiments in Fluids* **11**,351-358

(9) DESRAYAUD G. & LAURIAT G. 1993 Unsteady confined buoyant plumes. esrayaud. *J. Fluid Mech.* **252**, 617

(10) MERZKIRCH W., MROSEWSKI T. & WINTRICH H. 1994 Digital particle image velocimetry applied to a natural convective flow. *Acta Mechanica* **4**,19

(11) MOSES E., ZOCCHI G. & LIBCHABER A. 1993 An experimental study of laminar plumes. *J. Fluid Mech.* **251**, 581

(12) CENEDESE A., QUERZOLI G. & ROMANO G.P. 1993 Comparison between PIV and LDV Velocity Measurements in a Convective Boundary Layer. In *Imaging in Transport Processes* (eds S. Sideman and K. Hijikata) chap.26, Begell House Inc. Publishers

(13) DEANE A.E. & SIROVICH L. 1991 A computational study of Rayleigh-Benard convection. Part 1. Rayleigh number scaling. *J. Fluid Mech.* **222**, 231

(14) SIROVICH L. & DEANE A.E. 1991 A computational study of Rayleigh-Benard convection. Part 2. Dimension considerations. *J. Fluid Mech.* **222**, 251

AUTOCORRELATION AND RELATED QUANTITIES OF THE LONGITUDINAL TURBULENCE VELOCITY COMPONENT. AN EXPERIMENTAL INVESTIGATION IN A WATER FLOW IN A SMOOTH PIPE

Luigi Butera - Amilcare Porporato - Luca Ridolfi - Sebastiano Sordo

Dipartimento di Idraulica, Trasporti e Infrastrutture Civili - Politecnico di Torino

ABSTRACT

The present work studies how, in a water flow, the autocorrelation of the longitudinal turbulence velocity component and the quantities related to it perform for varying Reynolds numbers at different points along the radius of a smooth circular pipe. The measurements were taken at fixed points using a laser-Doppler anemometer (LDA) and presented a high data rate and large data sets, allowing adequate precision in evaluating the quantities studied. It was observed that there was a maximum of the integral length scale occurred in the core region, and that this moved along the radius as the Reynolds number varied.

1. INTRODUCTION

When examining turbulent quantities, studying the behaviour of the statistical moments, of the autocorrelation functions, of the integral scales, of the spectra, in function of the Reynolds number (Re) and of the transversal position in the flow can be useful for localising the greater or lesser degree of organisation of motion and for observing how the different areas of the flow interact.

This study, carried out in uniform water flows in a smooth circular pipe, investigated the behaviour of the longitudinal turbulence velocity component along the radial direction, measured at fixed points. It is part of a larger research project on these flows. Previous studies have dealt with the problems of measuring the mean velocity and with the possibility of incomplete self-similarity for its profile. Here we can only limit ourselves to a brief outline description of the experimental equipment and of how the measurements were obtained, but a fuller description can be found in our previous works (1), (2).

The experiments were carried out using an LDA; this is highly suitable for measuring turbulent quantities in water, as it gives a high data rate and above all does not affect the flow. In order to achieve suitable resolution at the smallest scales of motion and at the same time to reduce the inevitable instrumental disturbance, great care was taken in carrying out measurements and in elaborating data, especially with regard to the problem of reconstructing the signal and appraising the field of validity of the results.

Where possible, we confirmed the validity of our measurements and elaborations by comparing the results with those of some of the well-known results already published(3), (4), even though these were not obtained with an LDA but with a hot-wire anemometer in air-flows.

2. APPARATUS AND TESTING

The hydraulic system consisted of a horizontal rectilinear pipe with a diameter of D=0.15m, fed by a tank whose level was kept constant. The final portion of the assembly is shown in fig.1.. In order to obtain the smooth pipe flow, the measurement section was set at 43 diameters from the end of the steel pipe and at 103 from the final curve. The discharge was measured with a suitably calibrated electromagnetic flowmeter which does not affect the flow. To check that the pipe was hydraulically smooth, 3 piezometric taps were fixed to each of 7 sections of the plexiglass pipe, set at 120° and connected to a single piezometer. The velocity measurements were taken using an LDA system fitted with a Burst Spectrum Analyser.

For the purposes of the experiment 4 discharges were considered. The values of these are given in table I together with the corresponding values of the kinematic viscosity ν, of the Reynolds number of the flow, $Re=U_m D/\nu$ (with U_m= mean global velocity) and the friction velocity u_*.

Having verified that the mean and standard deviation of the velocity were symmetrical, the

measurements were effectuated only along the horizontal radius placed towards the laser source, assuming the hypothesis of complete axial symmetry.

For every discharge we took measurements at 23 points along the radius at intervals of $1 \cdot 10^{-3}$m in the central part of the section up to $10 \cdot 10^{-3}$m from the wall and of $1 \cdot 10^{-3}$m in the remaining part.

$10^3 \cdot Q$ [m^3/s]	$10^6 \cdot \nu$ [m^2/s]	$10^{-3} \cdot Re$	$u*$ [m/s]
1.73	1.037	14.2	0.0058
6.18	1.029	51.0	0.0177
23.17	0.998	197	0.0575
55.12	1.058	442	0.1292

table I. Characteristics of the flows observed.

In the experiments, attention was paid to reducing instrumental noise as much as possible, to obtaining a high sampling rate, and to effecting a high number of data which, being statistically independent, would allow an adequate evaluation of the mean values.

After several preliminary tests, the anemometer was used in forwardscatter mode, with a record length of 32 and with the data acquisition in continuous mode. This gave an excellent signal to noise ratio and a high data rate (averaging between 2500 and 3800 Hz) with the upper values corresponding to the higher Re numbers. Fairly high noise levels were registered only in the lower discharge at some points near the wall. On the other hand the data rate did not prove sufficient to resolve the smallest scales of motion for either the highest Re (where the turbulence becomes finer grained) or for the point nearest the wall (where the number of particles transiting the measurement volume is reduced).

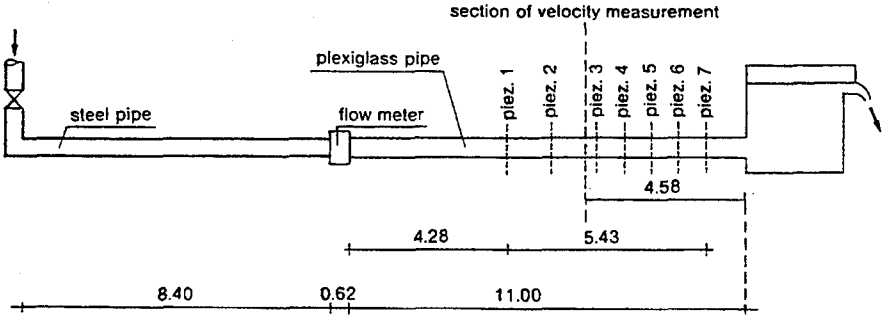

Fig.1. Diagram of the final portion of the assembly

At every point the measurement was extended for 600s; on the basis of a previous work by the present writers [1], this duration was deemed sufficient for obtaining the various mean quantities being studied with adequate precision. It is only near the wall, where the integral time scale is larger, that the smaller number of statistically independent samples might reduce precision of the time averaging, especially for statistical moments of a higher order.

3. DATA ANALYSIS

Because the moment of sampling the velocity is tied to the discontinuous and random transit of the particles in the measurement volume, the LDA provides a discrete and non-equispaced time series for every measurement point. This means that the first problem is how to evaluate the various statistical quantities, starting with the discontinuous, non-equispaced series provided by the data acquisition.

There are two possible solutions: to elaborate the non-equispaced data directly, or to reconstruct the continuous signal by interpolating data, to resample it at equispaced intervals and then to

elaborate the resulting data. The advantage of the first approach[6], [7], [8] is that it is immediate and does not introduce the disturbances which interpolating data inevitably causes; whilst the second approach allows the use of fairly efficient algorithms which are available for the series of equispaced data, including of course FFT. The solution presented in most publications is sampling and holding interpolation[9], [10], [11] because it is simple and reliable, even though mention is often made[9], [10], [12] of the fact that disturbances caused by interpolation can be reduced by reconstructing the data with more refined interpolators, such as linear or spline; however not many studies have been done either on this or, more particularly, on its experimental application. Two of the present authors have carried out such tests[13] on a signal generated with a given spectrum and on measured signals (at a point placed on the axis for $Re=51.0\cdot10^3$), using various techniques both on the non-equispaced and equispaced data. These tests showed that the cubic spline interpolation and the direct elaboration of the data using the short-block method algorithm (proposed by Gaster and Roberts[6], [7]) were inadequate for dealing with the problem being studied, and that, in the case of a high data rate and large number sets, good results were obtained by using other techniques (sampling and holding interpolation, linear interpolation and direct equispacing without interpolation). This last one in particular proved to be the best for high frequencies. Fig.2 gives the spectra for the measured signal[*].

As these techniques still await more detailed research, it was decided to carry out the present elaborations using the well-tried technique of sampling and holding, followed by resampling with frequencies identical to the mean data rate; in addition, Adrian and Yao [9] have deduced an expression for the series interpolated by sampling and holding which permits the evaluation of the distortion in the computation of the spectra, thus allowing a correct interpretation of the same.

Having thus obtained the equispaced series, the autocorrelation, the integral length scale and the one-dimensional spectrum of the longitudinal turbulence velocity component were calculated for each one. We also calculated the standard deviation, the skewness and the kurtosis of the fluctuating turbulence velocity component u'.

In order to reduce the variance in the estimate, the autocorrelation function $\rho(\tau)$ was obtained with FFT, breaking the series into blocks and averaging the results. The numeric integration of the autocorrelation gave the integral time scale $\Im$, defined thus[14]:

$$\Im = \int_0^\infty \rho(\tau)d\tau \quad , \qquad \text{with} \quad \rho(\tau) = \frac{\overline{u'(t)\cdot u'(t+\tau)}}{\overline{u'^2}} \tag{1}$$

where u' is the longitudinal turbulence velocity component.

The integral length scale $_u$ was evaluated using Taylor's hypothesis[14] with the relation

$$\Lambda_u = \Im \cdot U \tag{2}$$

where U is the mean local velocity.

In order to obtain the one-dimensional spectrum E_{u^2}, it was first necessary to evaluate the temporal spectrum S(f), defined by the relation

$$S(f) = \frac{1}{2\pi}\int_0^\infty \rho(\tau)\cdot e^{-j2\pi f\tau}\,d\tau, \tag{3}$$

[*] Whilst greater detail will be found in the aforementioned work [13], we wish to briefly explain why the spline interpolator and the direct elaboration of non-equispaced data are inadequate. On the one hand, although the spline interpolator sometimes produces sound results, in this situation it produces peaks in the signal reconstruction which alter both the statistical quantities and (even more so) the spectrum. This happens when there are abrupt variations in the series followed by large time intervals between samples. On the other hand, the direct technique is inadequate because the proposed algorithms are valid in theory only for signals with Poisson distribution in the arrival times. In reality it emerged that, when there is a slight shift away from Poisson distribution (as in the case of data acquisition using the LDA set to continuous mode), the spectrum calculated with Gaster and Roberts' algorithm presents severe distortion at the higher frequencies.

This was calculated by averaging the spectra obtained on the blocks of 2^{12} data. For each one, the spectrum was calculated with FFT, using the Hanning window.

From this, keeping to Taylor's hypothesis, the one-dimensional spectrum

$$E_{u^2}(k_u) = 2 \cdot S(f) \cdot U \tag{4}$$

was obtained with E defined so as to be normalised according to

$$\int_0^\infty E_{u^2}(k_u) dk_u = 1 \tag{5}$$

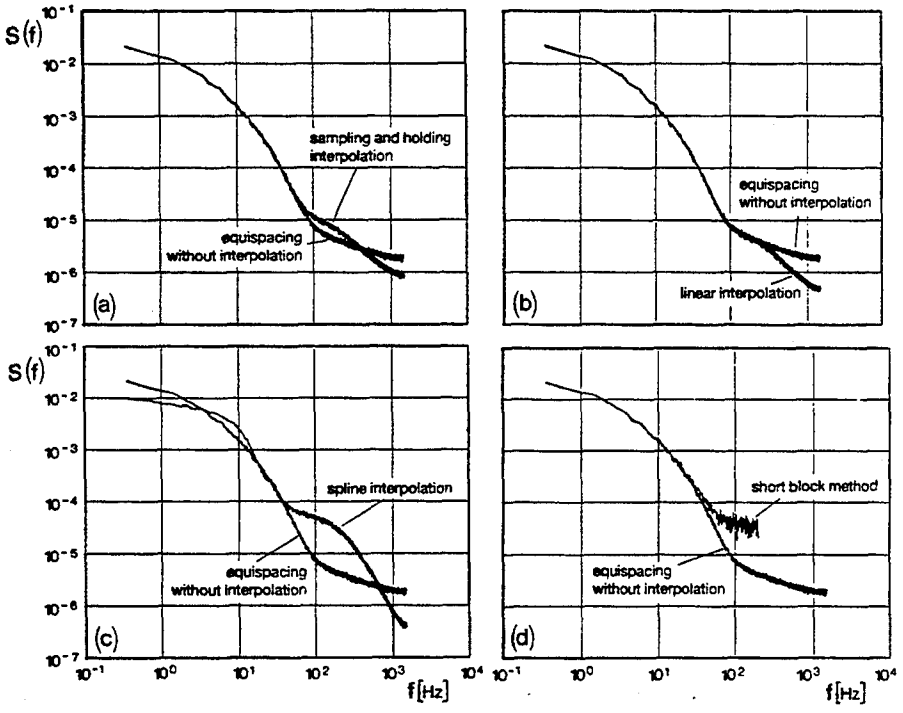

Fig. 2. Comparison of spectra obtained using different methods on the point on the axis Re=51.0·10^3: (a) sampling and holding; (b) linear interpolation; (c) cubic spline interpolation; (d) short-block method. The spectrum used as a reference is that of equispaced data without interpolation.

4. RESULTS

The most interesting results concern the autocorrelation and the way the behaviour of the integral length scale changed according to variations in the position of the measurement point along the radius.

Fig.3 shows how the autocorrelations depend on Re when the position along the radius remains the same. From this it can be seen that the autocorrelation decreases increasingly rapidly as the intensity of the turbulence increases, showing how the "memory" of the measured signal diminishes.

Figures 4a÷d take the various Re tested and show the autocorrelations corresponding to the most significant points along the radius of the integral length scale Λ_u, given in fig.5.

From fig.5 it emerges that Λ_u/R for given y/R increases through the first three Reynolds

numbers and then decreases. For example, for y/R=0.4, Λ_u/Rpasses from a value of 0.55 in the lower discharge, to about 1.95 for $Re=197\cdot10^3$, subsequently dropping again to values of about 1.46 for $Re=442\cdot10^3$. This pattern can be easily explained by looking at the equation (2) introducing both the relation U=U(Re) and the monotonic decrease of the integral time scale versus the Reynolds number, which can be inferred from fig.3. In fig.5 it is also possible to see that the degree of organisation of the signal reaches a maximum in the core region. The zone where this occurs does not have a set position, and for the first three Re it moves from the boundary with the logarithmic zone to the centre of the pipe, only to return again to near the wall for the higher Reynolds number.

Towards the wall, the integral length scale drops sharply. Then, as it moves towards the axis of the pipe, this decrease becomes gradually less pronounced; close to the axis itself it almost disappears completely.

The decrease towards the wall can be attributed to the presence of the zone of greatest turbulence production. The fact that the maximum is reached before the axis with a subsequent decrease up to the centre would seem to be due to the effect of the opposite wall of the pipe. That the maximum zone moves as Re changes might be explained by the reciprocal interaction of the effects of both walls.

In order to confirm our results, we calculated the behaviour of Λ_u using Laufer's data on the kinetic energy and dissipation in pipe flow. The calculation, which used Hinze's indications as given on p. 740 of his book[14], gave results which nicely confirm those we obtained.

Analysis of the signal in the frequency domain gave further pointers. On the basis of Adrian and Yao[9], the upper limit of validity for the time spectra S(f) is around a frequency of 150÷200 Hz, depending on whether the data rate was higher or lower. Figures 6a-b refer to the spectra at the point on the axis of the pipe for $Re=14.2\cdot10^3$ and $Re=51.0\cdot10^3$ respectively. They clearly show the shoulder at about 450 Hz caused by the low pass filtering of the interpolator on the both the step and instrumental noise. This means that , for these flows, there are no problems of resolution at the higher frequencies, since the turbulence spectrum is not altered by the reconstruction of the signal. It is only near the wall that, in the lowest discharge, the instrumental noise causes a peak at the origin of the autocorrelation; fig.4a clearly shows, for y/R=0.040, the resulting lowering for small τ.

For the two higher Re (figures 6c-d) the alterations caused by the interpolation also affect the turbulence spectrum. In fact, above 500 Hz the spectrum is changed by the low pass filtering with a slope proportional to f^{-2} . The effect of this is already felt between 200 and 500 Hz, where the spectrum therefore has a purely qualitative validity. This could be corrected by looking for more sophisticated interpolators or algorithms which would give spectra even at higher frequencies.

Having evaluated the field of validity for temporal spectra, the one-dimensional spectra which are derived from the latter can only be given for that part which is not distorted by instrumental noise or by interpolation.

Fig.7 shows the behaviour of E_{u^2} (adimensionalised with respect to the radius of the pipe) versus the Reynolds number. As with autocorrelation (fig.3) it is clearly visible that, as Re increases, the turbulence becomes increasingly finer grained, and the inertial subrange zone with its typical slope of -5/3 gradually extends.

For the dependence on y/R, figures 8a1÷d2 show the spectra at the most significant points. The diagrams on the left show, for each Re, the comparison between the spectra in the central point and in the zone of maximum Λ_u. The diagrams on the right compare the spectra corresponding to the wall zone with those of the point on the axis of the pipe.

The behaviour of the low wave numbers mirrors that of the integral length scale and the closer it gets to the wall, the more it shows the presence of a zone with slope -1, due to the effect of the anisotropy. This defines a double intersection between the spectrum at the point near the wall and that of the central zone.

At the highest frequencies obtained, the presence of increasing smaller scales of motion, as we move from the centre of the pipe towards the wall, results in a progressive increase of the spectrum.

Figs.9a÷c give the values of the statistical moments of u'. These are consistent with other well-known published data[3], [4]. The standard deviation does in fact show a maximum in the area of greatest turbulent production, and the skewness becomes positive as it moves towards the wall. The inversion of the antisymmetry of the velocity probability density function confirms the transversal interaction between the central zones and those of the wall, due to the intermittent input of fluid at a speed considerably different from the mean. The kurtosis, which increases rapidly near the wall, also displays the bursting phenomenon which happens near the wall.

We have not reported the behaviour of the statistical moments of the velocity derivative and of the Taylor microscale, whose quantities are highly sensitive to the disturbances present at the higher frequencies. However they show trends consistent with other findings published [15], [16].

5. CONCLUSIONS

This experiment, which was carried out in a uniform hydraulic flow in a smooth pipe, has highlighted the fact that the integral length scale shows a maximum in the core region. It has also shown that the position of the maximum changes as the Reynolds number varies, getting progressively closer to the centre of the pipe for the first three Re examined, to return to the wall for the maximum Re.

In the light of this behaviour, comparing the spectra at the most significant points allowed us to observe the characteristics of the energy distribution at the various scales of motion in relation to different positions along the radius.

In order to improve the resolution at the highest wave numbers, we intend to refine the elaboration of the data by filtering the instrumental noise which is more sensitive at low Re and by testing better techniques of interpolation or more efficient algorithms on non-equispaced data for higher Re.

BIBLIOGRAPHY

(1) Butera L., Ridolfi L. and Sordo S. *Valutazione sperimentale della velocità media locale per un moto stazionaro turbolento. Problema di precisione.* XXIII Convegno di Idraulica e C.I.. Firenze, 1992.

(2) Butera L., Ridolfi L. and Sordo S. *On the hypothesis of self-similarity for the velocity distribution in turbulent flows.* Excerpta, 1994.

(3) Laufer J. *The structure of turbulence in fully developed pipe flow.* Nat. Adv. Ctee. Aer.. Washington, rep. no. 1174.

(4) Lawn, C. J. *The determination of the rate of dissipation in turbulent pipe pipe flow.* J. Fluid Mech., 48, pp. 477-505, 1977.

(5) Buchhave P., George W. K. Jr. and Lumley J. L. *The measurements of turbulence with the laser-Doppler anemometer.* Ann. Rev. Fluid Mech. 11, 443-504. 1979.

(6) Gaster M, and Roberts J. B. *The spectral analysis of randomly sampled records by direct transform.* Proc. R. Soc. Lond. Ser. A 354, 27-58. 1977.

(7) Gaster M. and Roberts J. B. *On the estimation of spectra from randomly sampled signals: a method of reducing variability.* Proc. R. Soc. Lond. Scr. A 371, 235-258. 1980.

(8) Mayo W. T. Jr. *Spectrum measurements with laser velocimeters. Proc of the Dynamic Flow Conferece 1978.* Skovlunde, Denmark, 851 868. 1979.

(9) Adrian R. J. and Yao C. S. *Power specta of fluid velocities measured by laser Doppler velocimetry.* Experiments in Fluids 5, 17-28, 1987.

(10) Leneman O.A.Z. and Lewis J.B. *Ramdom sampling of random processes: mean square comparison of various interpolators.* IEEE Trans. on Automatic Control, 396-403, 1966.

(11) Cenedese A., Paulucci F. and Romano G.P. *Dynaical behaviours of turbolent boundary layers.* 9th Symposium on "Turbolent Shear Flows". Kyoto (Japan) 1993.

(12) Benak M., Sturm M. and Tropea C. *Correlation estimators for two-point laser-Doppler anemometry.* SPIE Vol. 252, Laser Anemometry Advances and Applications, 1993.

(13) Porporato A. and Ridolfi L. *Confronto tra stime spettrali per segnali turbolenti misurati con LDA.* XXIV Convegno di Idraulica e I.C.. Napoli, 1994.

(14) Hinze J.O. *Turbulence.* McGraw-Hill, 1975.

(15) Hinze J.O. and Ueda H. *Fine-structure turbulence in the wall region of a turbulent boundary layer.* J. Fluid Mech., 67, 125-143, 1975.

(17) Van Hatta C. W. and Antonia R. A. *Reynolds number dependence of skewness and flatness factors of turbulent velocity derivatives.* Phys. Fluids, 23(2), pp. 252-257, 1980.

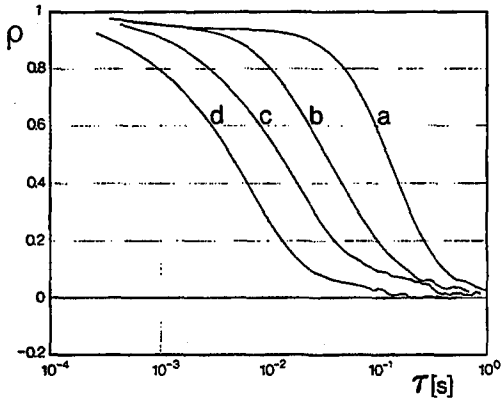

Fig. 3. Autocorrelations for the four Reynolds numbers examined, for $\frac{y}{R}$ =1. Re = 14.2•10^3 (a); Re = 51.0•10^3 (b); Re = 197•10^3 (c); Re = 442•10^3 (d).

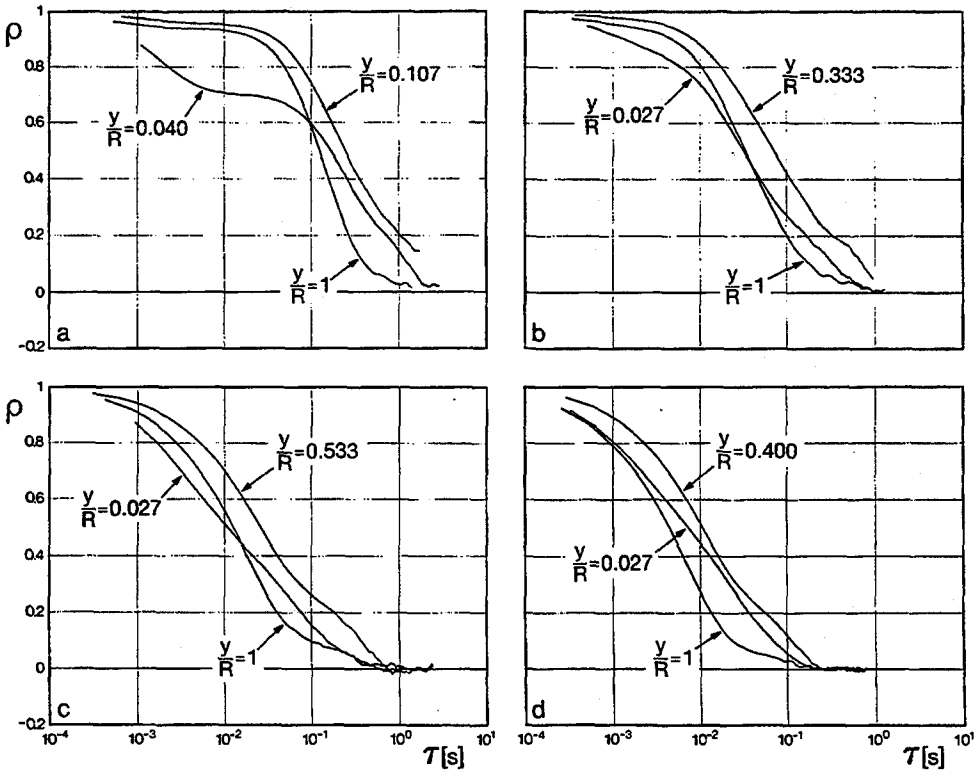

Fig. 4. Comparison of the autocorrelations for the most significant points. Re = 14.2•10^3 (a); Re = 51.0•10^3 (b); Re = 197•10^3 (c); Re = 442•10^3 (d).

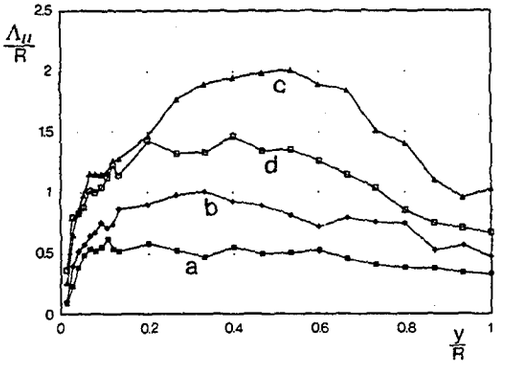

Fig. 5. Space integral scale Λ_u versus $\frac{y}{R}$. Re =14.2•10^3 (a) ; Re = 51.0•10^3 (b); Re = 197•10^3 (c); Re = 442•10^3 (d).

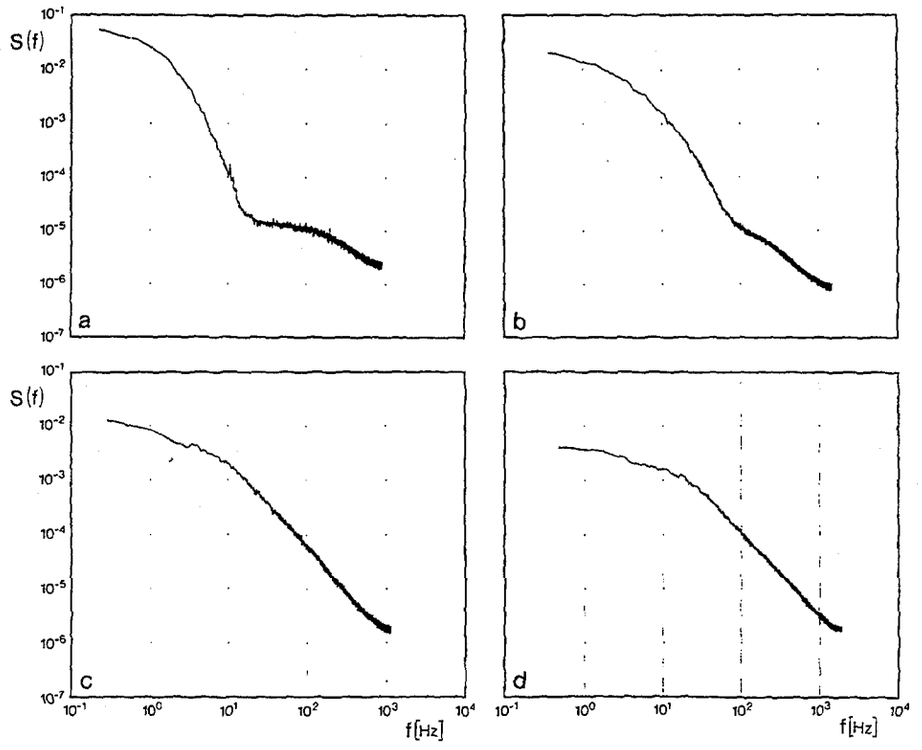

Fig. 6. Time spectra for the four Reynolds numbers examined, for $\frac{y}{R}$ =1. Re =14.2•10^3 (a); Re = 51.0•10^3 (b); Re = 197•10^3 (c); Re = 442•10^3 (d).

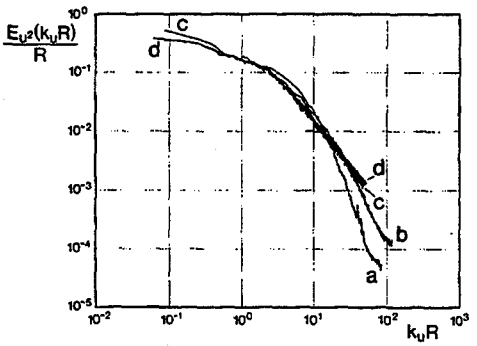

Fig. 7. One-dimensional spectra for the four Reynolds numbers examined, for $\frac{y}{R}$ =1. Re = 14.2•10^3 (a) ; Re = 51.0•10^3 (b); Re = 197•10^3 (c); Re = 442•10^3 (d).

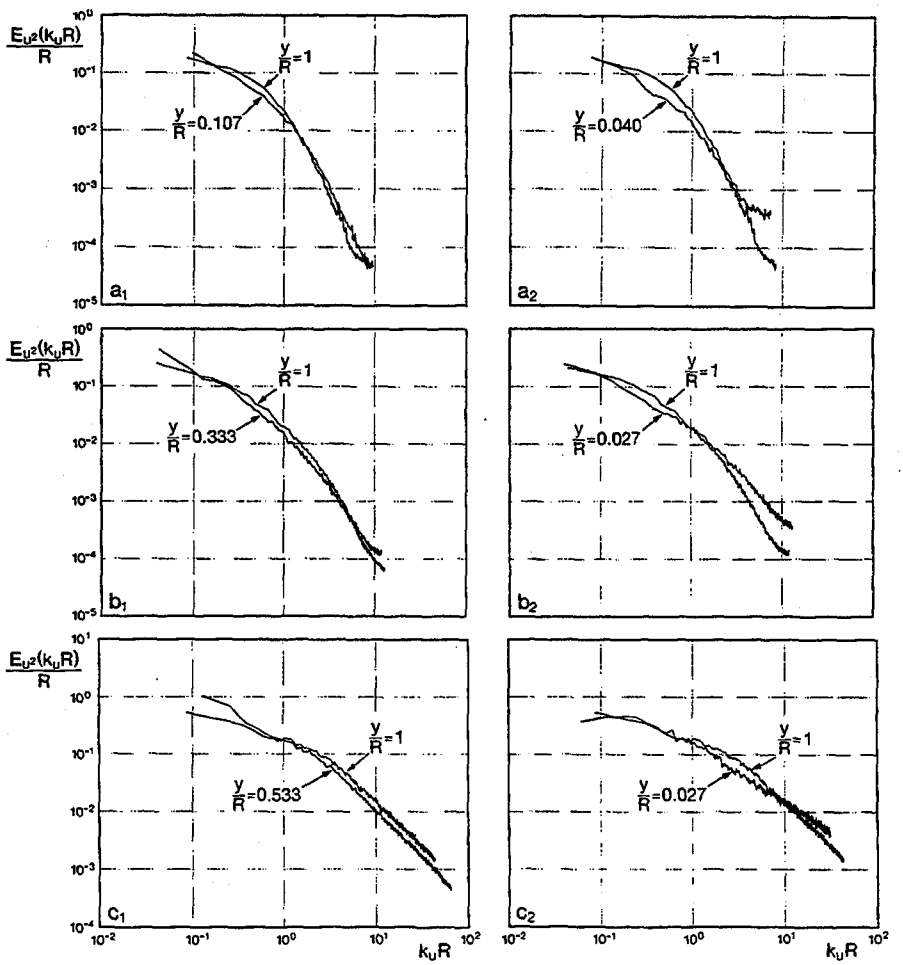

Fig. 8. Comparison of the spectra corresponding to the points on the axis, in the Λ_u maximum zone and near the wall. Re=14.2•10^3 (a) ; Re = 51.0•10^3 (b); Re = 197•10^3 (c).

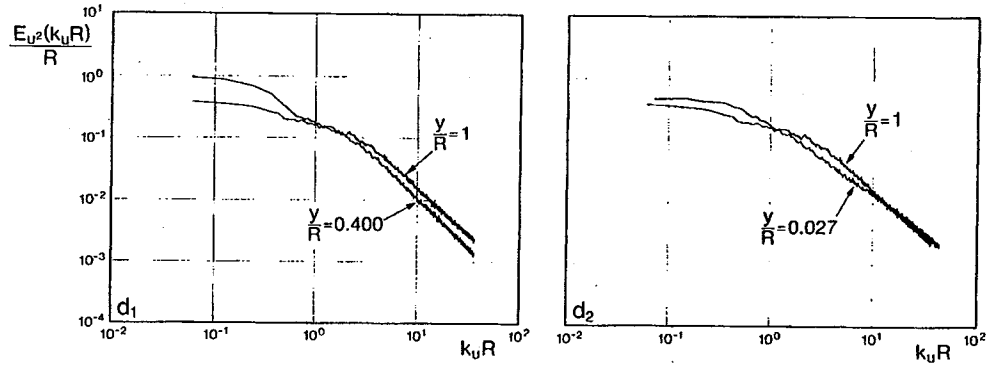

Fig. 8 d_1-d_2. Comparison of the spectra corresponding to the points on the axis, in the Λ_u maximum zone and near the wall for Re=442•10^3.

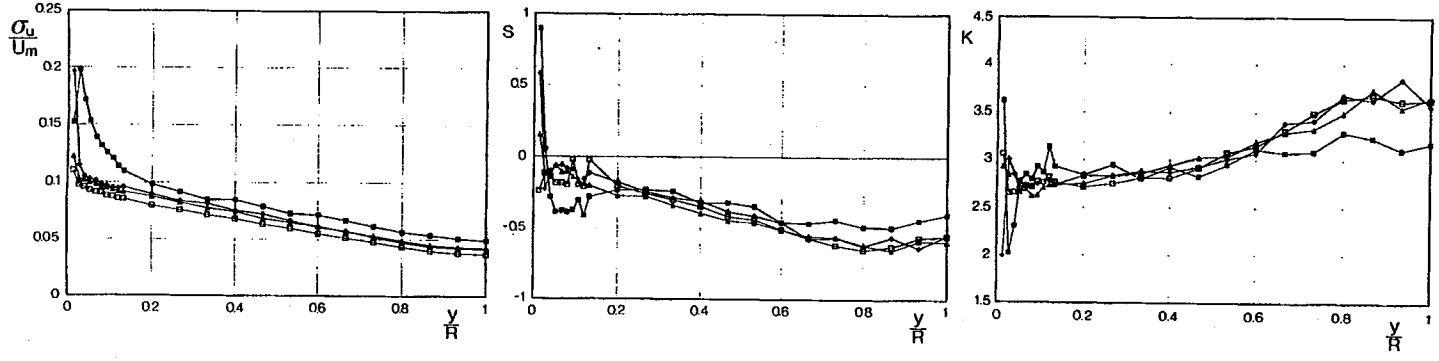

Fig. 9. Behaviour of the standard deviation, skewness and kurtosis of u' versus $\frac{y}{R}$. ■ Re = 14.2•10^3; ◆ Re = 51.0•10^3; ▲ Re = 197•10^3; ⊟ Re = 442•10^3.

June 15,1994

MEASURING SECOND-ORDER MOMENTS OF VELOCITY DIFFERENCE BY DYNAMIC LIGHT SCATTERING AND LASER DOPPLER VELOCIMETRY IN MODERATE REYNOLDS NUMBER TURBULENCE

A. Sirivat

National Metal & Materials Technology Center,

National Science and Technology Development Agency,

Ministry of Science, Technology and Environment

Rama VI Road, Bangkok 10400, Thailand

Tel: (662) 247 1336, Fax: (662) 247 1455,

E-mail: fluidyna@nwg.nectec.or.th

A novel technique namely the homodyne photon correlation spectroscopy was used to measure the spatial dependence of a characteristic velocity difference of the form $< \Delta u^2 > \propto r^{\alpha}$, where r is the spatial separation. As the Reynolds number is increased, the scaling exponent α increases from a value close to zero to some value close to 2/3, a value which is commonly known as the classical Kolmogorov value. However, when the conventional laser Doppler velocimetry is applied, the same exponent decreases from the onset value of 1.5 to 2/3. This conflicting result seems to suggest a failure of the Taylor's hypothesis which was necessary to convert the measured temporal structure function to a spatial one. To explain the dependence

of the scaling exponent on the Reynolds number and the discrepency, a theory based on the viscoinertial subrange is proposed. In this finite Reynolds number theory, effects of molecular flux is taken into account in addition to the customary inertial cascade. The discrepency can be explained in terms of the differing features between the tails of the spatial and the temporal correlation functions. The calculated scaling exponents can be calculated with no adjustable parameter and fair agreements with experimental data are obtained.

I. INTRODUCTION

In 1941, Kolmogorov [1] originally proposed the scaling law of the form $< \Delta u^2(r) > \propto r^{2/3}$ in the inertial subrange at high Reynolds number, based on a dimensional analysis of the exact theory for the third-order moment of the velocity difference. Here Δu is some characteristic velocity difference associated with an eddy of size r. This '2/3 law' has been remarkedly confirmed by several experiments [2, 3].

In those measurements, conventional techniques such as the laser Doppler velocimetry (LDV) or the hot-wire anemometry were employed and the spatial correlation function or the spatial structure functions are constructed via the Taylor's hypothesis from the temporal functions [2, 4, 3]. In this article, we present some recent experimental results [5–7] using a novel technique called the homodyne photon correlation spectroscopy (PCS).

Both methods (PCS and LDV) were applied to study the scaling law of $< \Delta u^2(\vec{r}) >$ under the same flow conditions. The longitudinal structure function $D_{LL}(r) =< \Delta u^2(r) >$ depends on r as r^{α}, where $\Delta u(r)$ refers to the fluctuating velocity difference component along $\vec{r}$ and α is some scaling exponent. The scaling exponents α_{PCS} and α_{LDV} were extracted from the structure functions measured by the two schemes and are found to differ at

low Reynolds numbers under identical experimental conditions. As Re increases, the scaling exponents approach the asymptotic value of 2/3 from below and from above respectively. The discrepancies of the measured scaling exponents at low Re are quite significant; it is conjectured that they cannot be accounted for by neither technical differences between the two schemes nor by a failure of the frozen or the Taylor's hypothesis.

A mechanism, which contains intrinsic features of turbulence, is proposed to account for the differing dependences of α_{PCS} and α_{LDV} on Re. The theory proposed introduces a key feature, namely the transition from the *viscoinertial* subrange to the *inertial* subrange which drives both exponents toward the asymptotic value of 2/3. The two exponents α_{PCS} and α_{LDV} differ at low and moderate Re since they are extracted from basically two different structure functions. In the PCS experiments, α_{PCS} is extracted from the spatial structure function $D_{LL}(r)$ whose spatial correlation function $f(r)$ is exponential-like at moderate Re. The function $f(r)$ becomes a featureless one in the transition process as Re increases and becomes large. In the LDV experiments, α_{LDV} is extracted from the temporal structure function $D_{LL}(t)$ whose temporal Eulerian function $f(t)$ is cosine-like at moderate Re and changes to the featureless one asymptotically.

II. EXPERIMENTAL DETAILS

A. The Water Tunnel

The water tunnel was built specifically for the experiment. The water is circulated by a variable speed pump (P). Background disturbances generated by the pump or the piping system are damped out by a honeycomb, screens and a 25:1 contraction. The turbulence-generating grid (G) is placed between the contraction and a square test section (T) (10 cm $\times$ 10 cm). It is a bi-plane type, with round rods of diameter 0.016 mm and a mesh size M of 0.85 cm. Polished plexiglas windows are furnished on four sides of the water tunnel to admit the incident laser beam and to observe the scattering.

B. Homodyne Photon Correlation Spectroscopy (PCS)

The theory of the homodyne photon correlation spectroscopy or dynamic light scattering can be simply understood by considering a diagram in Fig.1. Plane waves are in the direction of $\vec{k}_o$ impinging on a pair of particles which are suspended in a turbulent medium. The scattered electric field from each particle is Doppler-shifted from the frequency of the incident electric field, due to the movement of particle caused by the random medium motion and by the Brownian motion.

A photomultiplier (PM) is located at an angle θ or in the direction of $\vec{k}_s$. It detects the scattered light intensity or the square of the sum of all scattered electric fields with Doppler frequencies of $\vec{q}\cdot\vec{v}_i$ and $\vec{q}\cdot\vec{v}_j$. $\vec{q}=\vec{k}_s-\vec{k}_o$ is the scattering vector with $q=2k_o\sin(\theta/2)$, where $\vec{v}_i$ and $\vec{v}_j$ are the instant velocities of i and j particles respectively.

The intensity correlation function can be calculated as

$$\begin{aligned} g(t) &= < I(t'+t)I(t') > /(I(t')^2 >= 1+G(t) \\ &= 1+(1/N^2)\sum_{m\neq n}^{N} < \cos[t\vec{q}\cdot\Delta\vec{v}(\vec{r}_{mn})] > . \end{aligned} \tag{1}$$

The bracket implies an ensemble averaging. $I(t')$ is the scattered light intensity detected by the photomultiplier. N is the number of particles in the measuring volume, which is assumed to be very large. $\Delta\vec{v}(\vec{r}_{mn})$ is the velocity difference of a particle pair (m and n) separated by a distance $\vec{r}_{mn}$. The second term in Eq.(1) concerns only with contributions from particle pairs; contributions from other omitted terms cancel on the ensemble average [5–7].

The measuring volume assumes a cylindrical shape with its length determined by a variable slit width which can be changed continuously from 0.01 cm to 0.2 cm. The water was seeded with polystyrene spheres, 0.106 μm in diameter. The laser was an argon-ion type ($\lambda_o=514.5nm$) and $q=(4\pi n/\lambda_o)\sin[45°]$ where n is the refractive index of water.

C. Laser Doppler Velocimetry (LDV)

Figure 2 shows the setup for the LDV measurements. It is of a differential mode with dual beams and of a forward-scattering type. The LDV or *heterodyne* technique is based on mixing of scattered lights from a single particle in the measuring volume. The scattering vectors are $\vec{q}_1 = \vec{k}_s - \vec{k}_{i1}$ and $\vec{q}_2 = \vec{k}_s - \vec{k}_{i2}$ where $\vec{k}_{i1}$ and $\vec{k}_{i2}$ are incident wave vectors for the two beams respectively and $\vec{k}_s$ is the scattered wave vector. It can be shown that the ac component of the instantaneous intensity is

$$I \sim \cos[\frac{4\pi n}{\lambda_o} \sin[\frac{\theta}{2}](\vec{e}_{\Delta\vec{q}} \cdot \vec{v}t) + \phi] \tag{2}$$

$\vec{e}_{\Delta\vec{q}}$ is a unit vector along $\vec{q}_1 - \vec{q}_2$. θ is the intersection angle between the two beams, $\vec{v}$ is the particle velocity in the measuring volume and ϕ is an irrelevant phase constant. In Eq.(2), the intensity fluctuates at a Doppler frequency $f_D = (2n/\lambda_o)\sin[\theta/2]v_{\Delta\vec{q}}$, where $v_{\Delta\vec{q}}$ is the component of an instantaneous velocity along $\Delta\vec{q}$.

The fringe spacing was $d_f = \lambda_o/(2n\sin[\theta/2]) = 4.4$ μm. The probe spatial resolution is limited by the measuring volume size of 0.283 mm. Polystyrene spheres with a diameter size of 1.0 μm were added to make a very dilute solution.

III. RESULTS

A. The PCS Experiments

Figure 3 shows a plot of the correlation time scale $T(L)$ vs. the slit width L at three different Reynolds numbers. It can be seen that $T(L)$ indeed obeys the scaling power law of the form $T(L) \propto L^{-h}$; h is some exponent dependent only on Re and can be directly determined from the plot. From Eq. (1), since the characteristic time scale T is proportional to $1/(\vec{q} \cdot \Delta\vec{u}(L))$, therefore $\Delta u(L) \propto L^h$. $\Delta u(L)$ is some characteristic velocity scale associated with the measuring volume of size L or the eddies of size $r = L$.

Figure 4 shows a plot of $\alpha_{PCS}(\equiv 2h)$ vs. Re. The onset Re for the power law of $\Delta u(L)$

is 8.35. The scaling exponent α_{PCS} increases monotonically to 2/3 at $Re \simeq 20$. This asymptotic value of 2/3 appears to be in agreement with the classical Kolmogorov value [8].

B. The LDV Experiments

The spatial structure function $D_{LL}(r) =< \Delta u^2(r) >$ was obtained from the measured the measured temporal second-order moment$< \Delta u^2(t) >$ by invoking the Taylor's hypothesis $r = -Ut$. The scaling behavior of $D_{LL}(r)$ at the intermediate scales is seen at all Reynolds number, provided that $Re > Re_c = 10$. The scaling exponent was then extracted from the log-log plot by measuring the slope of the solid line. Figure 5 shows the dependence of the scaling exponent on Re for the LDV experiments. Contrary to the PCS results mentioned earlier, α_{LDV} decreases monotonically from its onset value of 1.5 to an asymptotic value of about 0.74 as Re increases. When Re is large, the scaling exponents, as determined by the two techniques, agree within experimental error.

IV. VISCOINERTIAL SUBRANGE THEORY

For finite Re, the *inertial* subrange does not exist nor is it well defined in the strict sense; the dissipation range and the energy-containing range overlap to a certain extent due to a limited range of length scales available. This range of length scale $r_{cr} < r < l$ is called the *viscoinertial* subrange where $D_{LL}(r) \propto r^{\alpha}$ and the scaling exponent is expected to vary with Re.

When Re is finite, $\lim_{r \to l} f = \lim_{r \to l} e^{-r/l}$, where f is the normalized correlation function of u_L, the longitudinal velocity fluctuation. It can be shown that

$$\alpha = \frac{2}{3} + \frac{I}{\ln Re}, \tag{3}$$

where $I = (e-1)/e$. The expression of α in terms of Re in Eq.(3) contains no adjustable parameter. Moreover, it approaches the Kolmogorov value of 2/3 as $Re \to \infty$. Returning to Fig.4, α in Eq.(3) is shown as the solid line. The symbols are the PCS data whose l in

Re was determined from using $r_{cr}/\eta = 8$.

For the LDV data, since α decreases with Re the suitable large-scale feature transition would be from $f \propto \cos[2\pi r/l]$ to the featureless f at moderate Re and it can be shown that

$$\alpha = \frac{\frac{2}{3}\ln Re + \ln 2}{\ln Re - \ln 2}. \tag{4}$$

The analytically derived expression for α contains no adjustable parameter and its asymptotic value is the classical Kolmogorov value of 2/3. Figure 5 shows the plot of α vs. Re obtained from Eq. (4) as the solid line. The experimental LDV data are plotted for comparison, using $r_{cr}/\eta = 8.0$.

In summary, it is shown that the dependence of the scaling exponent on Re is a manifestation of the transition from the *viscoinertial* regime to the *inertial* regime when Re increases and becomes very large. Moreover, it is shown by the PCS data that the spatial correlation is exponential-like at large scales, when Re is moderate. This feature is not observed in the LDV data since the measurements are not spatial but a temporal one. The measured Eulerian temporal correlation function is periodic-like at large scales when Re is small. The findings also suggest that a temporal periodicity does not necessarily imply a spatial periodicity and that the Taylor's hypothesis at moderate Re is an inappropriate transformation, even though the turbulent intensity is low. The shortcoming of the frozen pattern at moderate Re has been observed and reported recently with a single moving probe [9].

REFERENCES

[1] A.N. Kolmogorov. Local structure of turbulence in an incompressible fluid at very high reynolds numbers. *Dokl. Akad. Nauk. SSSR*, 30(4):299–303, 1941.

[2] C.W. van Atta and J Park. Structure function. In *Statistical Model and Turbulence*, pages 402–426, Lectures Notes in Physics, Springer-Verlag, 1972.

[3] F. Anselmet, Y. Gagne, E.J. Hopfinger, and R.A. Antonia. High-order velocity structure function in turbulent shear flows. *J. Fluid Mech.*, 140:63–89, 1984.

[4] P. Mestayer. Local isotropy and anisotropy in a high-reynolds-number turbulent boundary layer. *J. Fluid Mech.*, 125:475–503, 1982.

[5] P. Tong, W.I. Goldburg, C.K. Chan, and A. Sirivat. Turbulent transition by photon-correlation spectroscopy. *Physical Review A*, 37:2125–2133, 1988.

[6] P. Tong and W.I. Goldburg. Relative velocity fluctuations in turbulent flows at moderate reynolds numbers. i. experimental. *Phys. Fluids*, 31:2841–2848, 1988.

[7] H.K. Pak, W.I. Goldburg, and A. Sirivat. An experimental study of weak turbulence. *Fluid Dynamics Research*, 8:19–31, 1991.

[8] A.N. Kolmogorov. Energy dissipation in locally isotropic turbulence. *Dokl. Akad. Nauk. SSSR*, 32(1):19–21, 1941.

[9] A. Sirivat. Measurement and interpretation of space-time correlation functions and derivative statistics from a rotating hot wire in a grid turbulence. *Experiments in Fluids*, 7:361–370, 1989.

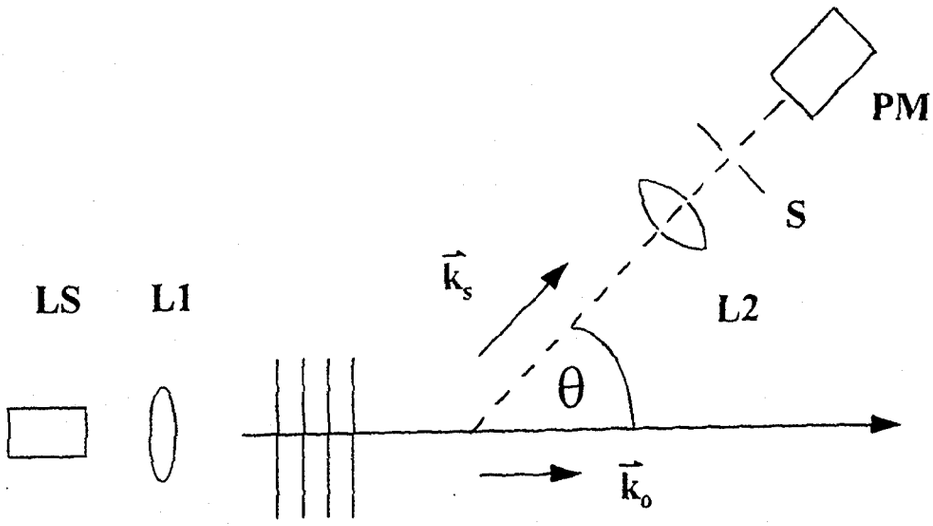

Fig. 1 The PCS setup

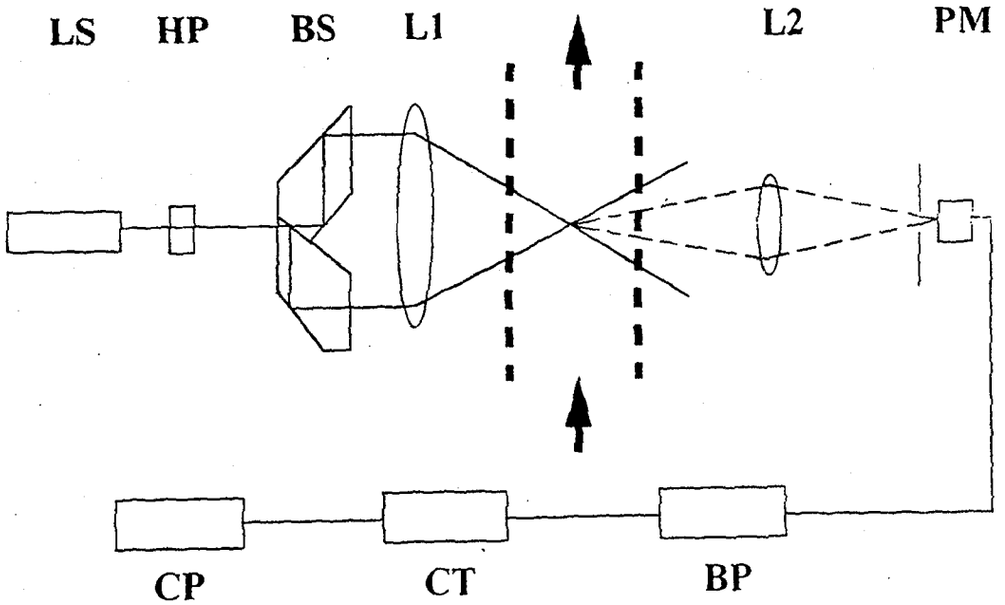

Fig. 2 The LDV setup

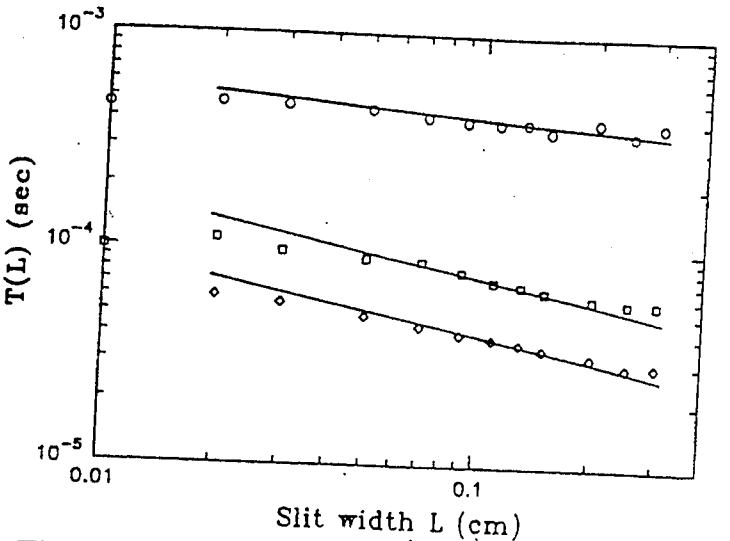

Fig. 3 The characteristic time scale $T(L)$ vs. the slit width

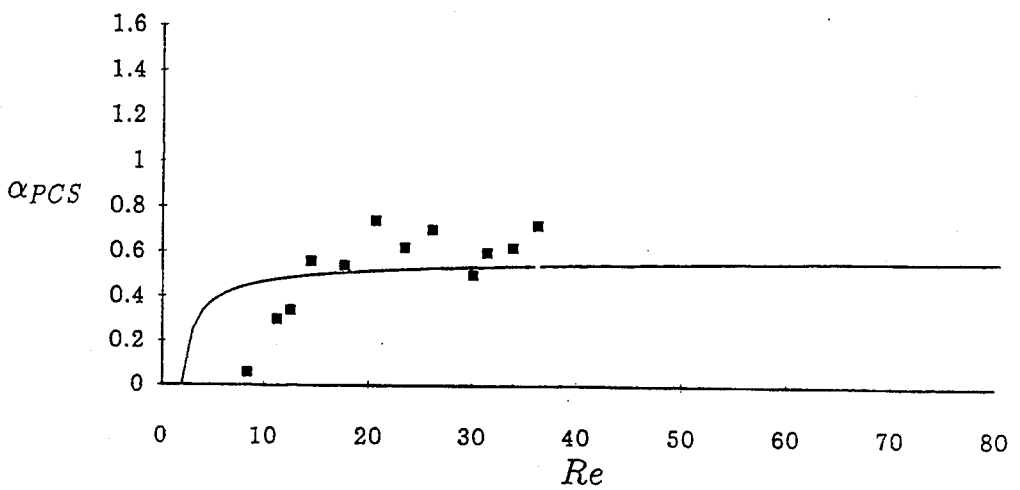

Fig. 4 The scaling exponent α_{PCS} vs. Reynolds number

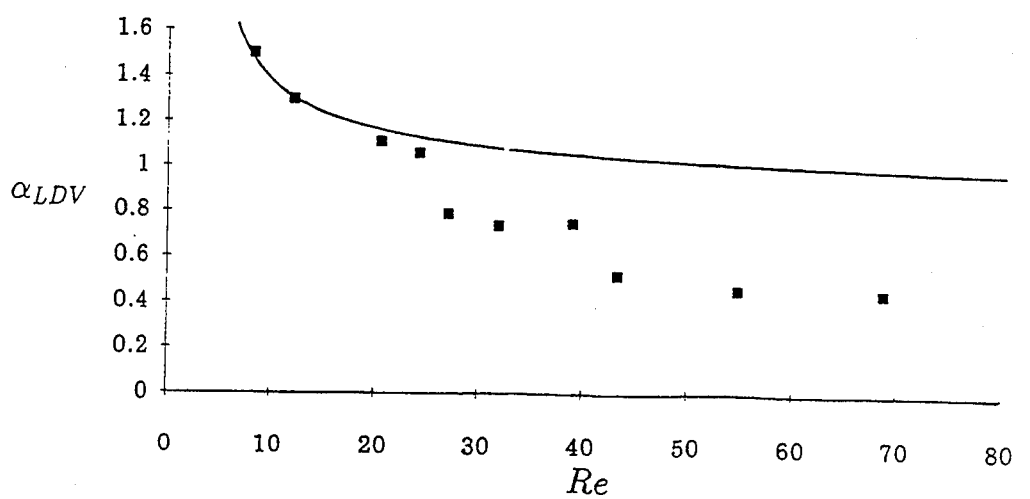

Fig. 5 The scaling exponent α_{LDV} vs. Reynolds number

PIV MEASUREMENTS OF THE VELOCITY DISTRIBUTION CAUSED BY FLOW STRAIGHTENERS

Th. Schlüter, W. Merzkirch
Lehrstuhl für Strömungslehre
Universität Essen
D-45117 Essen, Germany

ABSTRACT

PIV measurements are performed in the air flow through a pipe line with internal diameter of 100 mm. The development of the velocity profile downstream of a 90°-bend and two 90°-out-of-plane bends is observed at various axial positions. These measurements are also conducted using different types of flow straighteners, e.g., a tube bundle[5] and a perforated plate[4]. The air flow is seeded with 20 µm tracer particles, flow velocities range up to 50 m/s. A double-pulsed ruby laser is used to produce the double exposed PIV records. After being digitized and filtered, the double exposures are evaluated by an autocorrelation algorithm. The velocity distribution is presented in form of vector plots and velocity profiles.

INTRODUCTION

Accurate flow rate measurement is essential in many industrial processes. For this purpose it is nessecary to set the velocity profile upstream of the measuring device to the normal (fully developed) flow profile. Often straight pipe lengths are not sufficient to reduce swirl or non-uniformities, and flow straighteners are placed in front of a flowmeter to promote the formation of a normal profile.
In this paper we report on the measurement of disturbed velocity profiles generated, e.g., by one or two successive 90°-bends. The disturbances comprise non-symmetric deformation of the developed profile, secondary flow, and swirl. The development and the decay of these disturbances with increasing distance from the 90°-bends are measured by means of Particle-Image-Velocimetry (PIV)[1]. Also measured are the velocity profiles at various axial positions downstream of a flow straightener in order to investigate the effectiveness of such a device in dissipating the disturbances.

EXPERIMENTAL PROCEDURE

The experiments are performed with air flow in a pipe line with 100 mm internal diameter. The setup allows a maximum straight pipe length of 51.5 D in front of the test section. Reynolds numbers can be up to $3*10^5$. A vortex flowmeter is installed to control the flow rate. The setup is shown schematically in Fig. 1.

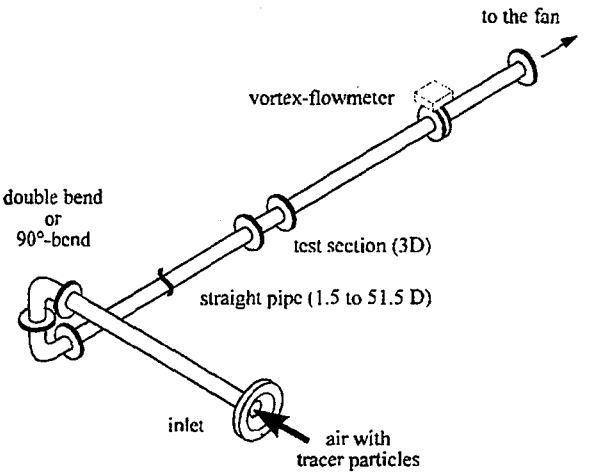

Fig. 1: Schematic setup of the pipe line

The test section with a total length of 300 mm is made of glass to minimize optical distortion. To avoid reflections the inner background is frosted black. Two different setups are required to measure the streamwise/radial and the radial/circumferential velocity components: A "conventional" optical PIV-setup with a light sheet parallel to the pipe axis is used to measure the streamwise and radial velocity components (Fig. 2a). For measuring the radial and circumferential velocity components the light sheet is orientated perpendicular to the pipe axis, and the velocity is measured by means of an endoscope, which is placed downstream of the light plane (Fig. 2b).
A double-pulsed ruby laser with 1 J output is used as the light source. The time separation is adjustable between 1 and 800 µs with a pulse width of 30 ns. The parallel light sheet is generated by different cylinder lenses. In the case of the "conventional" setup the light sheet is very thin (< 1mm) to reduce background noise, while the perpendicular setup with the endoscope needs a relatively thick (~ 3mm) light plane to ensure, that the particles form image pairs with a suitable separation. This can become a problem, when the ratio of the circumferential to the axial velocity is very small. Then two parallel, separated light sheets provide a technical solution[2].

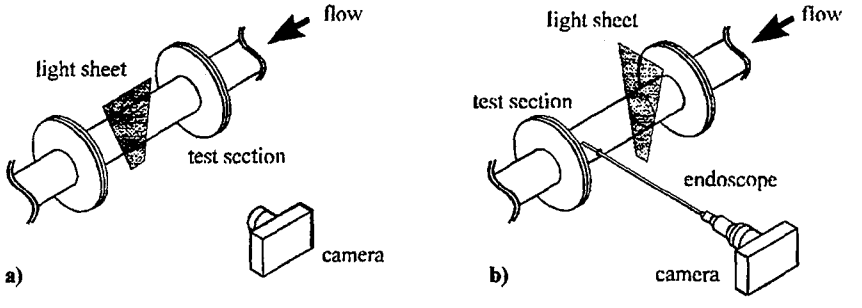

Fig. 2: Optical setup to measure a) mean axial and b) circumferential velocity component

The flow is seeded with 20 µm tracer particles (Vestosint, Hüls AG). The particles are injected by a continuously operating particle generateor designed especially for this application. It allows an adjustment of the particle rate to the chosen volume flow rate.
The PIV-double exposures are recorded on photographic film. After being digitized with a resolution of 5000 x 7000 pixels and high-pass filtered the PIV-records are evaluated by an autocorrelation algorithm. The algorithm determines the amount and the direction of the velocity in a window of 128 x 128 pixels[3]. The results are displayed as velocity vector plots and, since it is of interest for this application, as velocity profiles.

MEASUREMENTS AND RESULTS

PIV velocity profile measurements are performed in different planes and at different distances from the characteristic disturbances. These are the 90°-bend, which produces a non-uniform flow profile, and two 90°-out-of-plane bends, producing swirl. In another set of experiments these two characteristic flow disturbances are rectified by a flow straightener.
The PIV data are taken at Reynolds numbers of 100000, 150000 and 200000 and compared with the results of hot-wire measurements. Fig. 3a gives a comparison of PIV and hot-wire measurements of the axial velocity component u in the horizontal plane at a position 1.5 D downstream of two 90°-bends and at a Reynolds number of 100000, Fig. 3b shows the velocity profile at a position of 6.5 D. Apparent is the good agreement of the results obtained by the two different measuring techniques. The hot-wire data are taken by scanning the cross-section during a certain period of time, while the PIV data are recorded simultaneously at one instant of time and at a much higher signal rate.

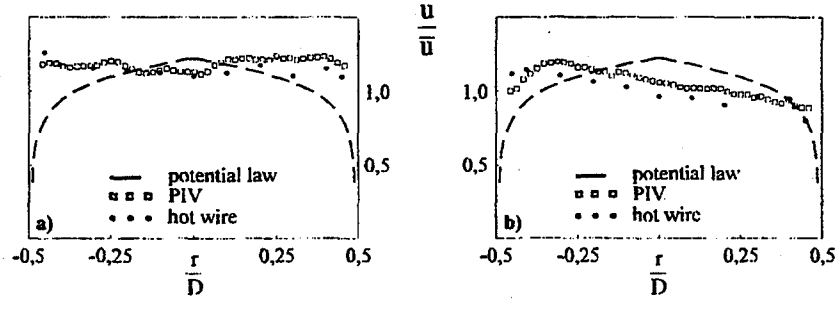

Fig. 3: Comparison of PIV and hot-wire measurements downstream of two 90°-bends at Re = 100000 at an axial position of a): 1.5 D b): 6.5 D

Also shown in Fig. 3 is the fully developed axial velocity profile of u calculated by applying the power law with n as a function of the Reynolds number formed with the mean velocity $\bar{u}$,y is the wall coordinate, and R is the radius of the pipe:

$$\frac{u}{\bar{u}} = \left(\frac{y}{R}\right)^{\frac{1}{n}}$$

To indicate how the decay of the disturbances is affected by the use of a commercial flow straightener, different types of flow straighteners are placed at positions 2 D and 5 D downstream

of the two elbow configurations. These two positions are chosen in order to investigate the influence of the axial position of the straighteners. Again velocity profiles are measured at various locations downstream of the device. In Fig. 4a the results for a tube bundle flow straightener, in Fig. 4b for a perforated plate (Mitsubishi-flow straightener[4]) are presented. The devices are placed 5 D downstream of two 90°-bends. The velocity profiles are measured 1.5 D downstream of the straighteners.

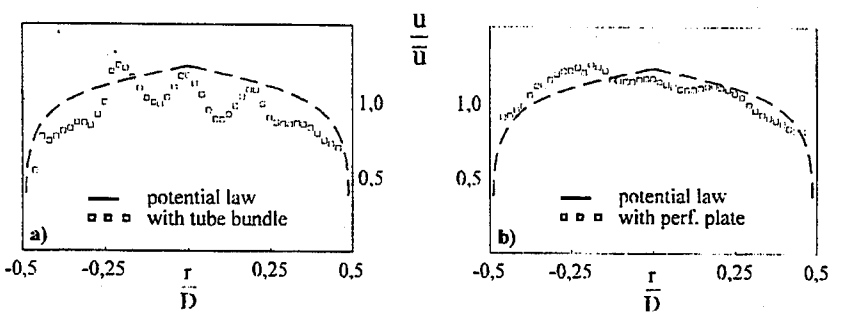

Fig. 4: PIV-measurements downstream of two 90°-bends at Re = 100000 1.5 D behind a a): tube bundle flow straightener b): perforated plate

Clearly visible in Fig. 4a are the velocity peaks caused by three free jets issuing from single tubes of the straightener. The position of the light sheet is such that these three jets in the center of the pipe become visible. The profile of the axial velocity at 1.5 D downstream of the tube bundle is to a high degree undeveloped; the deviation from the normal profile is significant. In Fig. 4b the profile 1.5 D downstream of the perforated plate is shown. With the present position of the light sheet the flow from five holes of the perforated plate is illuminated. The free jet effect as seen in Fig. 4a is barely visible here. The mixing between the free jets has progressed very fast within a distance of 1.5 D, the velocity profile still exhibits a certain deformation, but the deviation from the normal profile is considerably smaller than in Fig. 4a. This profile appears to develop faster into a normal state than the respective profile downstream of the tube bundle. It is interesting to note, that the tube bundle flow straightener causes twice the pressure loss of that generated by the perforated plate. Further work that aims at clarifying the dependencies of rectifying effects and pressure loss is in progress.

REFERENCES

1. Adrian, R.J.: Particle-imaging techniques for experimental fluid mechanics, Annu. Rev. Fluid Mech. 23 (1991), pp. 261-304
2. Schoppen, W.: Messung der Umfangsgeschwindigkeit einer drallbehafteten Rohrströmung mit PIV unter Anwendung eines Endoskops, Diplomarbeit, Universität Essen (1994)
3. Heckmann, W., Hilgers, S., Merzkirch, W., Schlüter, Th.: Automatic Evaluation of Double-Exposed PIV Records by an Autocorrelation Method, In: Optical Methods and Data Processing in Heat and Fluid Flow,Inst. Mech. Eng's., London (1994), pp. 5-8
4. Akashi, K., Watanabe, H., Koga, K.: Flow rate measurement in pipeline with many bends. Mitsubishi Heavy Industries 15 (1978), pp. 87-96
5. International Standard ISO 5167 (1980) (E)

RECOGNITION OF PARTIALLY OVERLAPPED PARTICLE IMAGES USING THE KOHONEN NEURAL NETWORK.

F. Carosone, A. Cenedese, G. Querzoli

Mechanics and Aeronautics Department
University of Rome "La Sapienza"
V. Eudossiana 18
Rome, Italy.

Abstract.

A neural network is proposed for the recognition of partially overlapped particle images ("*spots*") in the analysis of Particle Tracking Velocimetry (PTV) frames. The neural network is shown a set of synthetic images ("*training set*"), containing single and overlapped particle images, of various shape and size. It learns the correct recognition from these examples. Once trained, the network is able to perform recognition on different PTV frames. The neural particle recognizer extracts the barycenter co-ordinates of every particle image; for instance, when two particle images overlap partially, both barycenters are detected. The management of overlapped spots allows the seeding density in PTV images to be increased. The practical consequence is that the spatial resolution in the velocity field calculation can be increased as well.

1. The overlapping particle problem.

In PTV images, particles usually look like bright rounded spots on a dark background. Yet, not every spot is rounded. Sometimes, more complex shapes appear (fig. 1), produced by the partial overlap of two or more particle images.

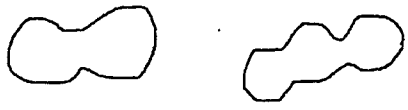

Fig. 1. Shapes of some overlapping particle images.

The partial overlap of particle images constitutes a problem for a particle recognition software, since more than one centroid has to be looked for in the spot (i.e. two centroids for a "double overlap", three centroids for a "triple" overlap). This is the so called 'overlapping particle problem'. Producing one centroid in these cases would not only find the right centroids, but also introduce a

false result. A previous solution consisted in discarding all spots having area larger than a threshold. This had two drawbacks: first, a different threshold value for area had to be set for every experiment, depending on the average spot area in the image. Second, in case of many overlaps, it produced a loss of information, that affected spatial resolution and increased the interpolation errors in the velocity field calculation. The practical result was that all experimental settings (e.g. actual particle size, seeding density, camera magnification and so on) were chosen to avoid overlaps as much as possible.

An improved particle recognition software, based on a neural network, was developed. It is able to:

1. tell the rounded spots from the overlaps;
2. work independently on spot size;
3. output the right number of centroid locations for each case.

2. A neural particle recognizer.

A particle recognizer can be regarded as an interface between the experimental equipment and the numerical treatment device that performs trajectory recognition. The interface accepts raw images as inputs, and returns the positions of the particles with which the fluid in study is seeded.

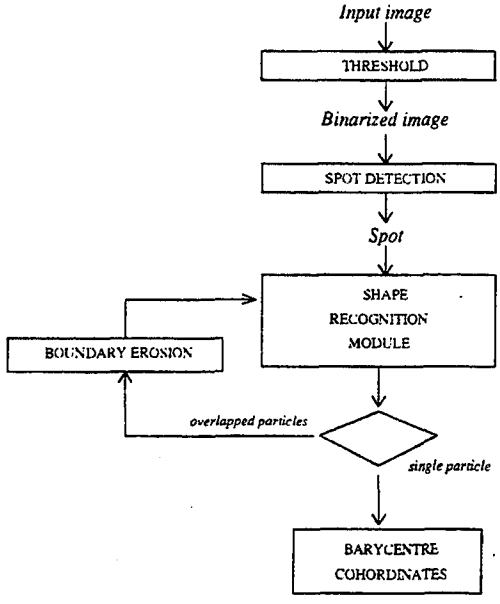

Fig. 2 . Flow chart of the neural particle recognizer.

In our case, the input was a 512×512 pixel image, where each pixel had a grey level in the range 0-255. The output was a two column matrix, where each row contained the co-ordinates of a particle barycenter, including those of partially overlapped particle images (named '*overlaps*' hereafter). The input image is first thresholded (fig. 2). The binarized image shows a number of white spots on a

black background. Every spot, defined as a connected domain of lighted pixels, is detected and sent to a neural shape recognition module.

The basic idea is that a spot may represent either a particle or an overlap. If it is recognized to be a particle image, its barycenter co-ordinates are calculated and produced as outputs. If it is recognized to be an overlap, the spot is eroded until it splits in the component particles: the barycenter calculations are then reduced to the previous case.

A Kohonen neural network is used in the shape recognition module, that distinguishes the rounded spots (single-particle images) from differently shaped spots (overlaps). For each spot, a couple of geometrical features is calculated, which describes its shape. The measured values of these features constitute a two-dimensional vector, that is the actual input to the neural network [1]. Shape similarity is thus reduced to euclidean distance [2] in a plane: two spots are said to have similar shape if the corresponding feature vectors are close in this plane. Two vector classes are defined: "particles" and "overlaps". Hence, recognition is a classification: a particle (*overlap*) is said to be recognized when the corresponding feature vector matches the "particle" (*overlap*) class. The network performs a vector classification.

2.1. Feature selection.

Shape features must be invariant on translation, rotation and scaling [3]. Besides, for convenience, features were defined in the range [0, 1].Ten candidate couples of features were tested. The best couple was retained: it consisted of a circularity measure (S_1), and a convexity measure (S_2). In a circumference, the ratio between squared perimeter p^2 and area is 4π. This value is smaller than any other plane figure, hence

$$S_1 = \frac{4\pi \cdot Area}{p^2} \qquad (1)$$

is a circularity measure in [0, 1], and $S_1 = 1$ for a circumference.

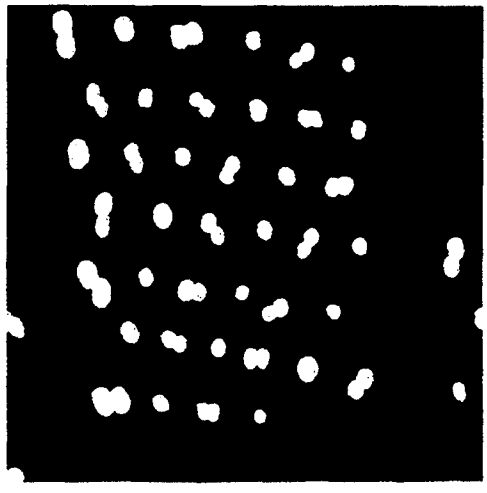

Fig. 3. Training image.

A convexity measure stems from the following procedure: the smallest convex region enclosing the spot is first found. Then S_2 is defined as the ratio between the two perimeters:

$$S_2 = \frac{smallest\ enclosing\ convex\ perimeter}{spot\ perimeter} \tag{2}$$

Also S_2 is in [0, 1], and $S_2 = 1$ for any convex region, e.g. a circumference.
Joint use of three features was also tried, with no better results than this couple.

2.2. The Kohonen neural network learning classification.

Six synthetic images were prepared to constitute the examples for the neural network. They contained single particles and overlaps in equal number. One of these is reported in fig. 3. The total number of spots in all test images was 228: these spots constituted the training set.

A Kohonen network with the Desieno correction was used: a detailed explanation and discussion may be found in many texts on artificial neural networks [4] [5] [6] [7].

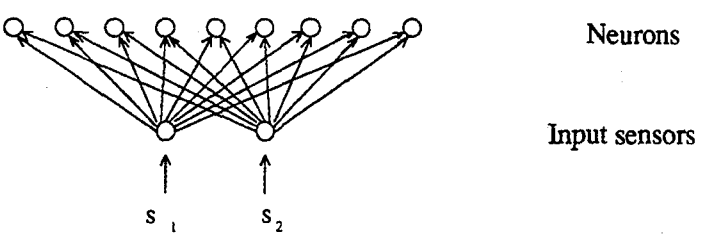

Fig. 4. Network architecture.

The network architecture is shown in fig. 4. The two circles below represent the sensory nodes through which the two-dimensional shape vector **S** (S_1, S_2) feeds the network. The sensors constitute an 'input layer', that receives information in parallel and distributes it to the neurons above. Everytime a spot is detected, one neuron in the second layer puts itself into a state of activation. A sixteen neuron Kohonen network was trained to activate one of the first eight neurons in response to a single particle, and one of the remaining eight in response to an overlap.

The mathematical properties of the Kohonen network were demonstrated and discussed by Kohonen [8], LaVigna [9], Desieno [10] and others. In particular, it was shown that the net is able to calculate the multivariate probability density function of the shape vectors **S** over the training set, and produce an approximation to the classification rule given by the Bayes' decision theory [11]. The Bayes' classification rule is optimal, in that it minimizes the average mistake probability E

$$E = \int_S p(S_1, S_2 | mistake) \cdot p(S_1, S_2) dS_1 dS_2 \tag{3}$$

where $p(S_1, S_2 \mid \text{mistake})$ is the mistake probability density:

$$p(S_1,S_2|mistake) = \begin{cases} p(S_1,S_2|particle) \text{ if } (S_1,S_2) \in overlap\ class \\ p(S_1,S_2|overlap) \text{ if } (S_1,S_2) \in particle\ class \end{cases} \quad (4)$$

The probability densities on the right hand of (4) are joint posterior densities [12].

After presentation of the examples, the network was aked to perform classification on the same spots that has been used for the training. The 99.13% of the spots in the training set was recognized correctly (2 mistakes over 228). In fact, classificating the same spots that were used for the training is a relatively easy job: lower accuracies are to be expected when recognition is requested on new spots, that the net never "saw". Yet, the test result is the only basis upon which different neural networks can compare their performances in learning a new task.

Doubts may arise about the network capability to manage triple overlaps (i.e. composed of three partially overlapped particle images) or more, since it was trained by means of images that presented double overlaps only (as in fig. 3). When a triple overlap is presented to the net, the two chosen features give values that make it classified as an overlap anyway (because it is still more different from a circular and convex shape than a double overlap is). Then erosion takes place until disjunction in two spots occurs(fig. 2): the only difference with the double overlap case is that, after separation, only one component spot represents a single particle, while the other is still an overlap and is therefore subdued to further erosion.

3. Results and limits of the neural particle recognizer.

A set of synthetic PTV multi-exposed images was produced, representing a vortex. Synthetic images are necessary to test and compare different particle recognition softwares, since barycenters are known in advance, and their position can be used as an exact reference. The recognition performance of the neural particle recognizer is compared to that of a previous non neural version. Fig. 5 shows one of these images after thresholding: three consequent instants of time were superimposed.

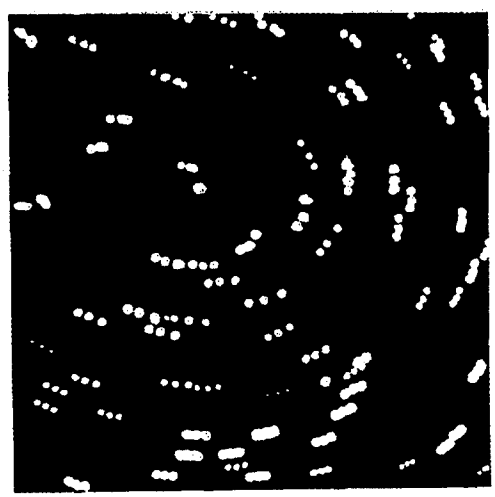

Fig. 5. Binarized PTV image.

Figg. 6-7 offer a visualization of the particle recognition process. A cross is put on the barycenter of every recognized particle. Fig. 6 shows the behavior of the previous non neural recognizer. All spots with area larger than a threshold were discarded from barycenter calculation, since it might have been misleading. The new neural result is illustrated in fig. 7. A first qualitative comparison is possible form these visualizations: in fact, all triple overlaps in the lower part were correctly identified.

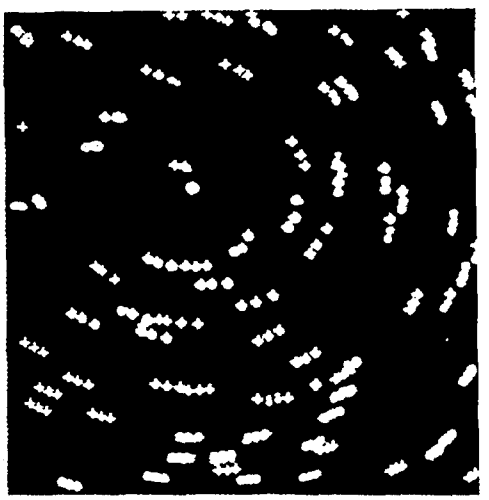

Fig. 6. Previous non neural particle recognition.

Fig. 8 enables a quantitative comparison. Recognition accuracy is plotted versus average particle area: as the last increases, the number of overlaps is expected to grow as well. Recognition accuracy is expressed in percent of identified barycenters. The non neural recognizer falls down, while the neural one proves to be far more robust.

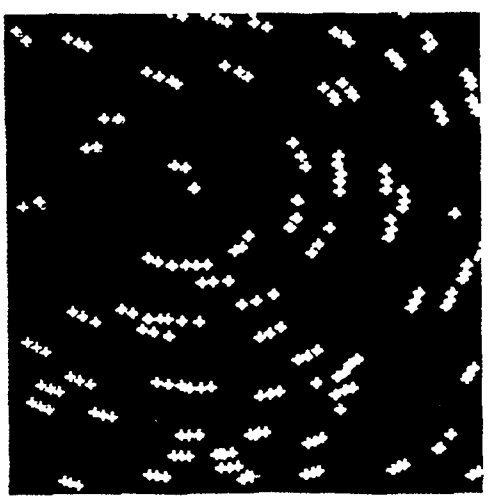

Fig. 7. Neural particle recognition.

Application of the neural particle recognizer should be limited to the following cases:

1. Images containing a large number of overlaps. In fact, even if the neural network is computationally extremely light, the feature calculations for every spot slow down the neural recognizer. Hence, this is more cumbersome than the previous non neural software, and its use on images with few overlaps would not be worthwhile.
2. Images with no electronic noise. In fact, the feature calculations in the shape recognition module is not accurate for very small spots (i.e. less than 3 pixels): the practical effect is that these spots are always considered as particle images. An inequality on spot area can solve the problem.

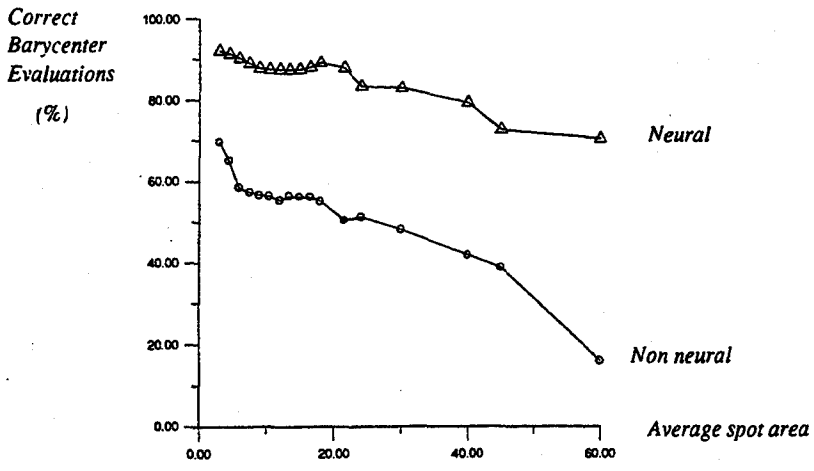

Fig. 8. Recognition accuracy (%) v. average area for two particle recognition softwares.

Conclusions

The neural-based particle recognizer is able to manage partial overlaps of particle images in the PTV technique. The software produces a sharp increase in the number of identified barycenters in PTV images with many overlaps.

The practical significance of a more robust image analysis software is that also rather 'dirty' images can be correctly analyzed: hence, the experimental set-up parameters become less critical. This property may be of great help in the analysis of both multi-exposed and stereoscopic PTV images. For instance, the time interval between two consequent shots in the multi-exposed technique can be made shorter, and thus increase the dynamic range. In the stereoscopic technique, seeding density can be increased, and thus spatial resolution is improved.

Acknowledgements

Marcello Sallusti produced the synthetic PTV multi-exposed images that were used in this project. Gianni Leuzzi and Paolo Monti helped clearing the statistic properties of the neural network through infinite discussions. We would thank them all, since we are aware that they all gave a decisive contribute to the project.

References

[1] Lippmann R.P. (1989), "Pattern Classification using neural networks", IEEE Comm. Magazine, November.
[2] Cotterill R., Oja E. (1990),"Neural Computing and Pattern Recognition", Courses in Advanced Technology, CEI-Europe/Elsevier.
[3] Parker J. (1994), "Practical computer vision using C", Wiley & Sons.
[4] Lippmann R.P. (1987), "An introduction to Computing with Neural Nets", IEEE ASSP Magazine, April.
[5] Wassermann P.D. (1989), "Neural Computing", Van Nostrand-Reinhold.
[6] Hecht-Nielsen R. (1990) "Neurocomputing", Addison-Wesley.
[7] Kabrisky M., Rogers S. (1991), "An introduction to neural networks for pattern recognition", SPIE Press.
[8] Kohonen T. (1990), "The Self-Organizing Map", Proc. IEEE on Neural Networks, September.
[9] LaVigna A. (1989), "Nonparametric classification using learning vector quantization", Ph. D. Maryland.
[10] Desieno D. (1988), "Adding a conscience to competitive learning", Proc. Int. Conf. on Neural Networks, IEEE Press, July.
[11] Papoulis A. (1965), "Probability, random variables, and stochastic processes", McGraw-Hill.
[12] Kosko B. (1992), "Neural networks for signal processing", Prentice Hall.

Digital-Particle-Image-Velocimety (DPIV) in a scanning light-sheet: Experimental study of the 3D flow around a short circular cylinder

BRÜCKER, CH.
Aerodynamisches Institut, RWTH Aachen (Germany)

Abstract

An experimental technique is presented, which offers the quantitative investigation of three-dimensional unsteady flows. The technique, introduced and applied by Brücker[1] and Brücker & Althaus[2] to the phenomenon of vortex breakdown, combines classical Particle-Image-Velocimetry (PIV) with volume scanning by means of the scanning of the light-sheet. The flow is continuously sampled in depth by the scanning light-sheet and in each plane PIV is applied to obtain the 2D velocity field. The technique was applied here to the 3D starting flow around a short cylinder. Because the scanning frequency is high in comparison with the characteristic time-scale of the flow a complete time-record of the evolution of the 3D flow during the starting process is obtained. In principle, the out-of plane velocity is determined by the continuity concept which allows the construction of the three-dimensional vorticity field and streamlines. This is demonstrated through the evaluation of the spanwise velocity which shows the suction effect of the starting vortices as observed in qualitative experiments.

1 Introduction

The major aim of recent development in experimental flow measurement techniques is to offer a quantitative whole-field study for three-dimensional unsteady flows. The increasing effort gives the chance for experimentalists to investigate those flow configurations by means of their three-dimensional structure and its time-dependent development as well as, e.g., the distribution of quantities like the vorticity or shear-rate. Single probe techniques like LDA (Laser-Doppler-Anemometry) cannot tackle those flow problems. Nowadays, the increasing availability of modern computers and image-processing-techniques have allowed the wide-spread application of more-dimensional methods like the Particle-Imaging-Techniques PIV (Particle-Image-Velocimetry) or PTV (Particle-Tracking-Velocimetry) in experimental flow studies (see the reviews [3],[4]). These techniques are pushing forward the experimental investigations of complex flows and their understanding.

In classical 2-D PIV, the flow, seeded with small tracer particles, is illuminated in a small light-sheet in direction of the prevailing velocity. By multiexposure- or multiframe-technique, the approximate instantaneous 2-D component of the velocity field within the light-sheet can be obtained from the projection of the displacement of the particles' images or the patterns of their local clusters. Using a high particle density one yields a dense velocity distribution from which the spatial derivatives of velocity can be obtained within a certain accuracy. This, for the first time, allowed the experimentalists the evaluation of the instantaneous in-plane distribution of vorticity or shear-rate. For those reasons this technique was very welcome. However, it yields the information only in one slice in the flow (the slice of the light-sheet) and the evaluation of vorticity or shear-reate is restricted only to the component directed out of the light-sheet plane.

This is one of the reasons why many approaches were made to extend the classical PIV-technique to more dimensions. One of those is the concept of conventional PIV combined with volume scanning by means of a scanning light-sheet which was introduced by Brücker[1] and Brücker & Althaus[2] and will be demonstrated in this article on the unsteady 3D flow around a circular cylinder.

Our primary intent of improving classical PIV was less to achieve the 3rd component of the velocity in the light-sheet plane than rather to resolve the volumic nature of the flow and its driving quantities as for example the vorticity. The most common methods offering the extension of PIV in space are the well-known holography and stereoscopy, see the recent review of 3D-PIV by Hinsch[5]. However, their application with the primary intent to extend the measurements on the 3-D space reveal some disadvantages in comparison with the light-sheet technique. Recent results of 3-D stereoscopic PIV using two or more cameras from different directions of view demonstrated, that the volumic distribution of vorticity cannot be obtained without remarkable errors (see [6]). A usual number of vectors achieved by stereoscopic 3D DPIV in the flow volume of interest is of the order of 1000 which is the same as in DPIV within a light-sheet (limited by the resolution of the recording devices). Therefore the spatial resolution of the volumic evaluated velocity vectors is always lower compared to the resolution of vectors in a light-sheet plane. Thus the profit of these methods is questionable in flow configurations, where the vorticity is one quantity of main interest. Similar problems arise in the holographic approach of whole-volume PIV. Furthermore, a large effort is necessary for the evaluation of the velocity and only a small amount of the today existing powerful processing steps of classical PIV can be adopted. Additionally, the light sheet has to be expanded to illuminate the whole flow volume, which often leads to the limit of the laser power to still obtain appropriate exposure.

2 Whole-volume PIV by conventional PIV and a scanning light-sheet

The disadvantages of the stereoscopic and holographic methods, also with regard to the achieve of the volumic distribution of vorticity, can be circumvented using conventional PIV in combination with volume scanning by means of a scanning light-sheet as applied by [1] and [2]. The flow is repeatedly sampled in depth by the successive positioning of the scanning light-sheet. In each "cut" the velocity field is evaluated by conventional PIV. Since the high achievable spatial vector distribution is conserved due to the applied light-sheet technique the vorticity can be evaluated, too. Especially in such flows, where the vorticity vector has a more or less preferred orientation, its mean component can be obtained quasi-instantaneously in successive cuts through the flow field which enables the volumic reconstruction of the instantaneous vorticity distribution, demonstrated by [1],[2] on the phenomenon of vortex breakdown.

A similar concept was presented later by Hinsch [5] termed as "multiple light sheet holography". A stationary set of 4 staggered parallel light-sheets is optically arranged in which the double-exposed flow was holographically recorded. Although this technique yields the instantaneous flow field indeed simultaneously in several parallel cuts through the flow field, until yet the technique is limited to only few light-sheets (in their experiment 4 planes could be arranged) which additionally had to be separated to a certain amount (see [5]). Furthermore solely photographic recording is yet possible. In contrast, the combined technique of PIV and the scanning light-sheet (the scanning light-sheet is in qualitative studies sometimes called "volume scanning") allows even conventional video-recording and, depending on the optical scanning

system, a close spacing of the successive light-sheets. Therefore a continuous time-record of 3D unsteady flows can be easily obtained and evaluated. In this article, the technique was applied to the 3D unsteady starting flow around a circular cylinder using Digital-Particle-Image-Velocimetry (DPTV) and conventional video recording in combination with a rapid scanning light-sheet. It is demonstrated, that this technique yields the velocity throughout a complete volume as a function of time.

The same arguments as noted by Hinsch for the multiple light sheet-technique serves for PIV in a scanning light-sheet. This technique will be of maximum use when 3-D problems can be decomposed into 2-D subtasks. If the spacing between the successive planes of the scanning light-sheet is adjusted to the depth scale of the flow structures, much valuable information about the three-dimensionality of the flow can be obtained with a certain number of planes. As shown by [7] in a numerical simulation of PIV and demonstrated in our experiments, it is also possible to evaluate the missing third velocity component with good accuracy. In incompressible flows one can take advantage from the equation of conservation of mass, which is integrated over the measured volume to obtain the third component.

Two independent time-scales should be regarded when the scanning technique is applied. On one hand the PIV-specific time-span ΔT_{PIV} between two exposures usually has to be adapted to the range of the in-plane velocity and the spatial resolution of the recording device to obtain an optimum result by DPIV. On the other hand it is to demand that the light-sheet scans two times faster than the characteristic time-scale of the flow (following the Nyquist-criterion). Thereby a compromise has to be found between the number of samples in depth and the duration of a complete scan. There are several possible ways to scan the flow volume and to obtain the frame sequences for DPIV. Here, we only consider the multiframe-technique for DPIV using continuos recording because it allows also a complete time-record of the flow. The scanning technique will be explaned here by means of the scanning system used in the present experiments. A simple optical system for a scanning light-sheet is shown in Figure 1.

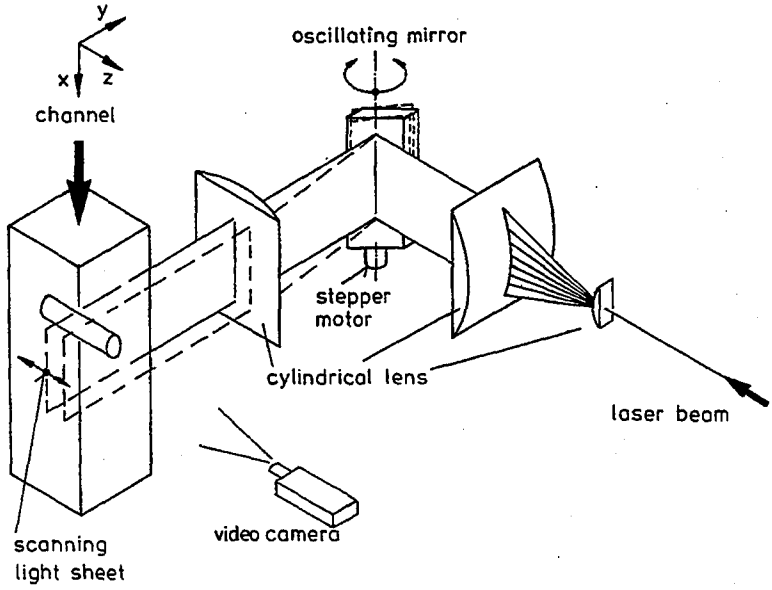

Fig. 1: Optical arrangement for the light-sheet scanning method

The scanning is realized by an oscillating mirror, whose motion is electrically controlled by a stepper motor. The slit-like expanded laser beam is deflected by this mirror and then passes a cylindrical lens whose focal line is placed in the oscillating axis. This ensures that the scanning light-sheet remains parallel to itself. This way one obtaines a set of approximately equally spaced, discrete light-sheets successive in time. Figure 2 shows schematically the time-course of the depth position of the light-sheet during the scanning.

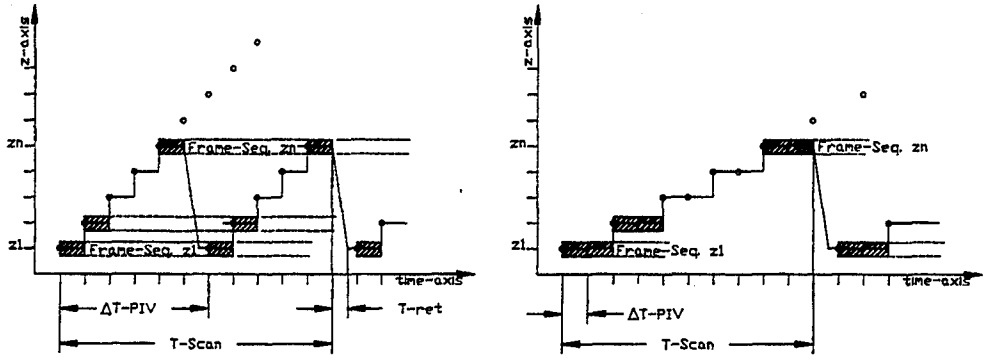

Fig. 2: Two different methods of light-sheet scanning and their characteristic time-scales for evaluation with DPIV

The time-axis displays the synchronization signal of the recording device (recording frequency f) with which the stepper motor is triggered. The z-axis shows the depth coordinate of the actual light-sheet. The first way to obtain multiframe sequences with n frames in every plane evaluable by DPIV is to perform a step every frame and to collect the frames in each plane to frame-sequences. Then the characteristic time-spans in a scan with n_S planes are the following

$$\Delta T_{PIV} = \frac{(n_S + n_{ret})}{f}, \quad T_{Scan} = n * \Delta T_{PIV} - \frac{n_{ret}}{f}, \quad f_{Scan} = \frac{1}{n * \Delta T_{PIV}} \tag{1}$$

$$\textit{with:} \quad n_{ret} = ceil\,(T_{ret} * f)$$

where T_{ret} means the retrace time of the mirror and n_{ret} the corresponding number of frames during retrace (ceil means the smallest integer value greater or equal to the argument). T_{Scan} is the duration of one depth-sampled set of frame sequences. Another way is to stay a certain number n of frames in every plane and then to move the light-sheet to the next position. Then the characteristic time-spans are:

$$\Delta T_{PIV} = \frac{1}{f}, \quad T_{Scan} = n * n_S * \Delta T_{PIV}, \quad f_{Scan} = \frac{1}{(n * n_S + n_{ret}) * \Delta T_{PIV}} \tag{2}$$

As noted before, ΔT_{PIV} is coupled with the main velocity and cannot be adjusted independently. One sees easily, that the first method should be preferred because of its smaller T_{Scan}. However, the device-limited frame rate f may not be high enough to keep the same ΔT_{PIV} at a greater desired number n of samples in depth. In addition, the retrace-time T_{ret}, which is higher in oscillating mirror devices compared to rotating polygonal mirror systems (see [8]), affects more disadvantegous in this scanning method. Therefore, the best system will be a high-speed

recording device with a rotating polygonal mirror scanning in the way of the first method. But as shown in the present experiments, also the second method is applicable if the characteristic time-scale of the flow is relatively low.

One problem is the restricted depth of focus using ordinary imaging system. With application of intense laser light it is however possible to increase the aperture and thus obtain a sufficient depth of focus. [1],[2] generated the light-sheet in their experiments by a rotating polygonal mirror in the path of the laser beam. This virtual light-sheet was then deflected by the second oscillating mirror to obtain the scanning. The use of a rotating mirror yields a more efficient utilization of ligh intensity in comparison with a cylindrical lens.

3 Application to the starting flow around a circular cylinder

Recent investigations have shown the high sensitivity of the flow around a cylinder with regard to the cylinder end-wall effects, especially for low Reynolds numbers, see for example [9]. By means of an isolated vortex and flow visualization [10] investigated the wall-induced effects during the starting process. Spanwise flow results due to the interaction of the vortex core and the boundary layer at the wall, which yields a spanwise variation of circulation and pressure. However no detailed information about the instantaneous distribution of vorticity in spanwise direction in the cylinder wake or the starting vortex was available from experiment. Recent experimental investigations of the flow around a short cylinder by [11] provided the time-evolution of the flow field in different cross sections, however, only from different runs of the experiment which diminshes the reliability of the results. Here, the above described technique offers to obtain the time-dependent flow structure in the whole-volume.

3.1 *Experimental procedure*

The flow around a short cylinder (D=2cm) of aspect ratio L/D=5 was investigated in a vertical low speed water channel, when the volume flux is impulsively increased from rest to a Reynolds number of Re=300 (based on the mean axial velocity U and the diameter of the cylinder D). Thereby, the onset of three-dimensionality in the cylinder wake induced by the endwall effects is of special concern. The experimental apparatus is as follows: the circular cylinder is placed in a squared transparent channel (area of 10cm x 10cm) 15D downstream from the entrance. Water is supported from a tank upstream whereby the volume flux is controlled by a valve at the downstream end of the channel. We used Vestamid particles (Firma Hüls GmbH) which were suspended in the fluid and illuminated with a 5 Watt Argon-Ion laser. Using a commercial S-VHS video system (frame rate f=25Hz) the flow was recorded and post-processed with the aid of a special frame coding system allowing access of each desired frame. The electrically controlled stepper motor of the scanning system was triggered by the vertical VSYNC frame signal of the video camera, whereby one step is performed every second video-frame, see the 2nd method in Figure 2. Thereby it is guaranteed that the motion of the mirror stops in the early *black-burst* part of the video signal before the frame information begins. The light-sheet plane is continuously scanned in z-direction between a plane close the the sidewall of the channel (z/D=2.25) and the middle cross section (z/D=0) in an oscillating manner with 10 successive cross-sections (n_S=10) and a mirror retrace with n_{rct}=5. The allignment of the successive

illuminated planes in relation to the channel and the cylinder is displayed in Figure 3.

Previously made qualitative investigations showed, that the flow is in spanwise direction approximately symmetrical to the centerplane over the investigated time-span of flow development and therefore we left out the other planes The spacing between the successive planes is z/D=0.25 and the dimensionless time span amounts to $T=T_{Scan}*U/D$=0.6 with a dimensionless scanning repetition rate of $f_{Scan}*D/U$=1.33 (ΔT=0.75). Therefore, the volumic measurements can be considered as quasi-instantaneous with regard to the characteristic time-scale of the flow and the repetition is high enough to resolve the unsteadiness. The two video frames in each plane were digitized and processed by digital correlation (see [12] and [13]) to obtain the 2-D velocity field in the sheets.

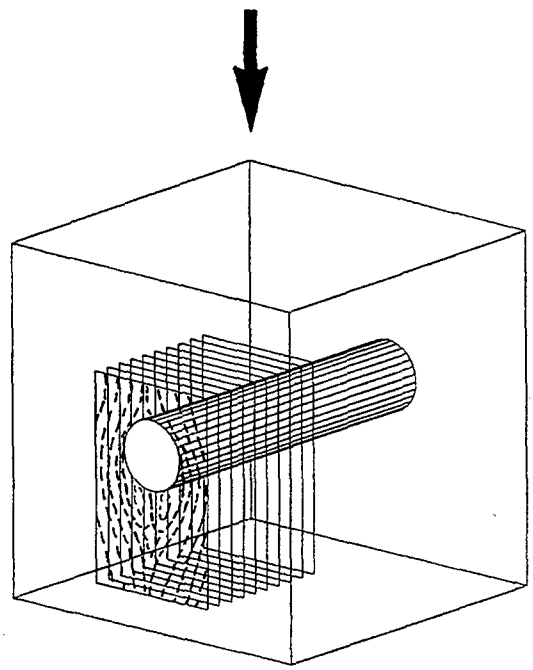

Fig. 3: Scetch of the channel configuration and the positions of the light-sheet planes

3.2 Results

Figure 4. shows the development of the flow after abrupt increase of the volume flux

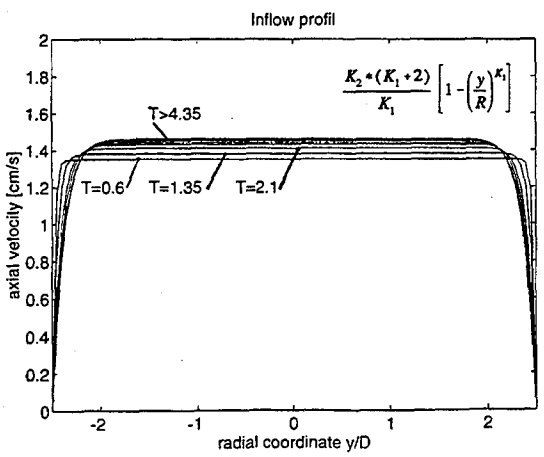

Fig. 4: Inflow profiles of axial velocity after abrupt increase of volume flux from rest to Re=300

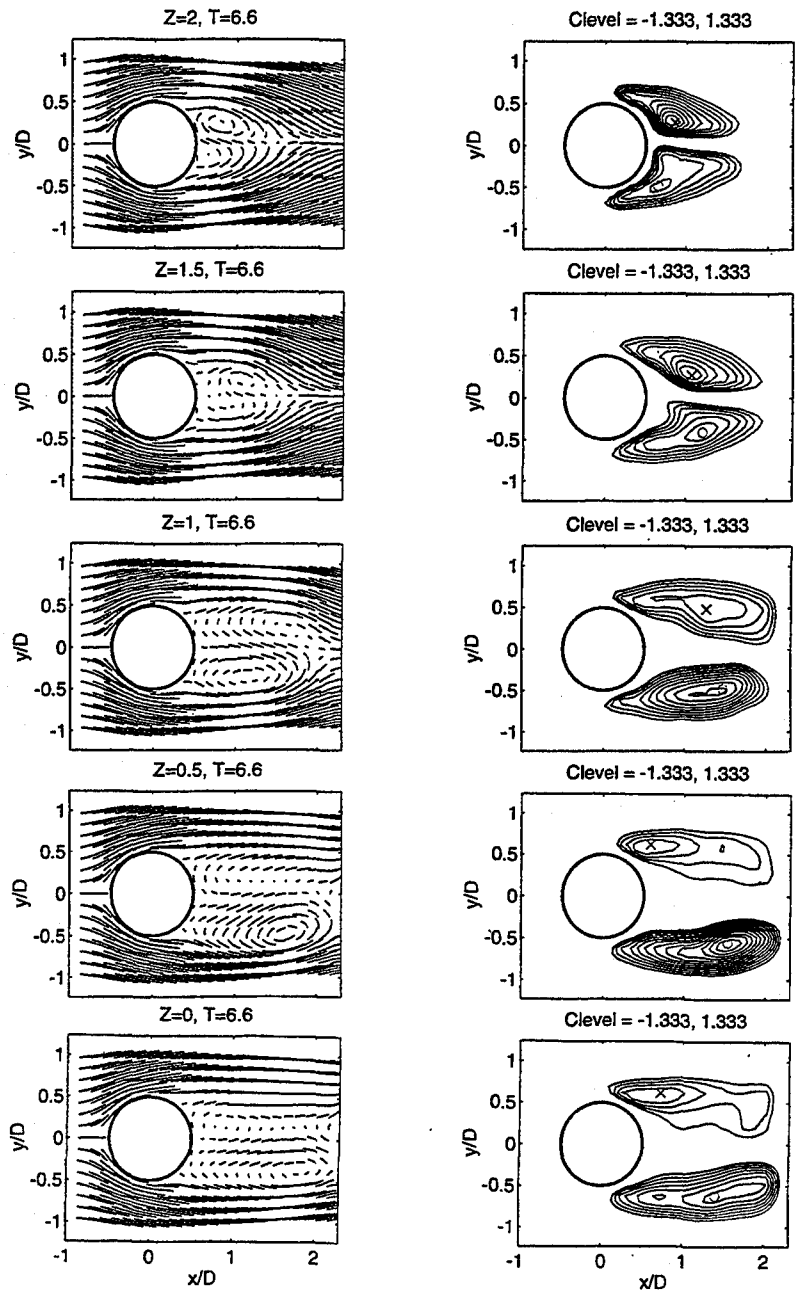

Fig. 5. Instantaneous flow structure around a circular cylinder at T=6.6 after abrupt increase from rest to Re=300 in five different cross-section ranging from z/D=2 (near endwall) to z/D=0 (middle cross section); left: short sectional streamlines; right: lines of constant dimensionless vorticity component ω_z*D/U (clevel means the level of the first contour line displayed= ±1.33, distance between successive contour lines =±0.15)

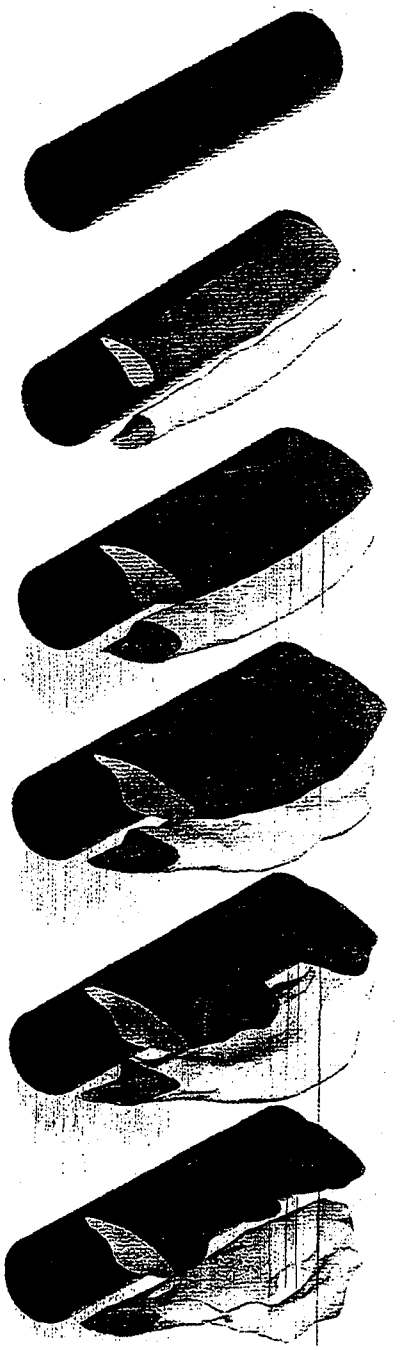

Fig. 6: Evolution of the 3D spanwise vorticity downstream of a cylinder after abrupt increase from rest to Re=300 (T_0=0.6, ΔT=1.5, level=±2.3)

from rest to a Reynolds-number of Re=300 by means of the axial velocity profiles measured with DPIV in the midplane 5*D* upstream of the cylinder. The 1st profile belongs to T=0.6 and the following have a constant increment in time of ΔT=0.75. The measurements were fitted with the given equation, usual for channel flows.

As seen in Figure 4, the profiles develop to a near stationary state which is reached at T=4.35 with a mean axial velocity of U=1.5cm/s. At the endwalls boundary layers have developed and the mean inflow velocity is approximately constant only in the range from z/D=-1.8 up to z/D=1.8. The flow structure is exemplary given for one scan at T=6.6 in Figure 5 (T means here the moment of the last plane of a scan), which displays short sectional streamlines and the vorticity distribution in 5 different cross-sections (x-y planes) with a spanwise position ranging from z/D=2 to z/D=0 (every second plane in the scan). Here, we feel the short streamlines as a good method of presentation of the flow field. The streamlines were reconstructed from the measured velocity field by following paths along the velocity vectors, while their length is proportional to the local velocity.

Near the endwall the upper and lower vorticity distribution is approximately symmetric while moving to the midplane the regions of concentrated spanwise vorticity elongate and shift against each other. One obtaines a good impression of the time-dependent behaviour if one looks the reconstruction of the three-dimensional time-dependent distribution of the spanwise vorticity in the wake of the cylinder, displayed by means of isosurfaces of spanwise vorticity (dimensionless level ω_z*D/U=±2.3) in Figure 6 for six moments ranging from T=0.6 to T=8.1 (T means here the moment of the latest plane within a scan). Because of the spanwise symmetry we displayed the whole span of the cylinder by simple flipping the measured planes around the midplane.

In the early phase one sees the approximately symmetrical formation of the two corresponding vortex cores behind the cylinder. Later in time the vortex cores elongate in the region around the midplane. Separation can then be observed, first in the upper region at T=6.6 followed by the separation of the vortex in the lower region at T=8.1. This indicates the transition to the well known von Kàrmàn vortex street. However, the vortex shedding is observed only in the region $-1.5<z/D<1.5$ while the vortices still remain connected to the cylinder in the outer planes. A problem of presentation is, that regions of concentrated vorticity after vortex shedding disappear in the isosurfaces because they have lost a certain amount of vorticity due to diffusion. In addition, only the spanwise component of vorticity is displayed. However, the results indicate, that the vortex cores develop from a parallel straight form to an Ω-shape with its elongated part in the midplane and parallel endings near the walls.

Also the spanwise flow during starting process can be obtained from the measurements. The out-of-plane velocity field can be determined using the continuity concept. This approach, in principle, can lead to construction of the instantaneous three-dimensional streamline patterns and vorticity field. The essential uncertainties associated with this procedure were numerically accessed by [7] with the aid of known theoretical solutions for generic three-dimensional flows. Their results predicted that with a high particle image density and without an interpolation procedure, which is usually necessary in Particle-Tracking-Velocimetry (PTV) but not in PIV, the out-of-plane velocity field is reproduced with good fidelity. Applying the continuity concept we obtained the missing third velocity component with the integration condition, that in the midplane z/D=0 the third component is zero everywhere.

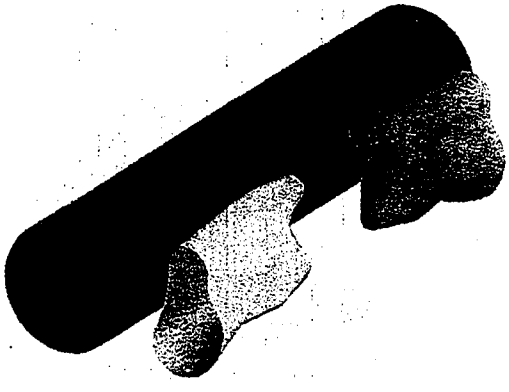

Fig. 7. Isosurface of spanwise velocity in direction to the midplane (T=2.1)

One results of the spanwise velocity is shown in Figure 7 exemplary for the moment T=2.1 by means of an isosurface, which shows the region of spanwise flow in direction to the midplane. It is well seen, that during the starting process the generated intense spanwise vortices suck mass from the near wall region into the midplane as allready seen in the qualitative experiments by [10] and [11]. The reason is the through the vortices generated radial pressure gradient, which induces in the boundary layer a radial inflow and suction of mass near the walls into the vortex cores. The results demonstrate that the reproduction of out-of-plane velocity by the continuity conept is reliable in our experiment.

4 Conclusion

The 3D starting flow around a short cylinder was investigated with an experimental technique which simultaneously combines Digital-Particle-Image-Velocimetry (DPIV) and volume scanning by means of a scanning light-sheet. Due to the continuous scanning of the illuminated light-sheet through the interesting flow region a time-record of the flow within a depth-sampled set of parallel planes with the 2D velocity field and vorticity distribution is available. Using the

concept of continuity, the out-of plane velocity is determined which allows the construction of the three-dimensional vorticity field and streamlines. To test the evaluation of the out-of-plane velocity in experiment we plan in future to apply stereoscopic DPIV in combination with a scanning light-sheet [14].

5 References

[1] Brücker, Ch. 1992: *Dreidimensionale quantitative Vermessung des Wirbelaufplatzens mit der Particle-Tracking-Velocimetry (PTV) kombiniert mit Lichtschnitt-Scanning.* DGLR-report **92-07**, pp. 445-454

[2] Brücker, Ch.; Althaus, W. , W. 1992: *Study of vortex breakdown by particle tracking velocimetry (PTV). Part 1: Bubble-type vortex breakdown.* Exp. in Fluids **13**, 339-349

[3] Adrian, R.J. 1991: *Particle-Imaging Techniques for experimental fluid mechanics.* Ann. Rev. Fluid Mech. **23**, 261-304

[4] Gad el Hak, M. 1988: *Visualization techniques for unsteady flows: An overview.* J. Fluid Eng. **110**, pp. 231-243

[5] Hinsch, K.D. 1993: *The many dimensions of optical flow diagnostics.* SPIE **2052**, pp. 63-78

[6] Sinha, S.K.; Kuhlman, P.S. 1992: *Investigating the use of stereoscopic particle streak velocimetry for estimating the three-dimensional vorticity field.* Exp. in Fluids **12**, pp.337-384

[7] Robinson, O.; Rockwell, D. 1993: *Construction of three-dimensional images of flow structure via particle tracking techniques.* Exp. Fluids **14**, pp. 257-270

[8] Rockwell, D.; Magness, C.; Towfighi, J.; Akin, O.; Corcoran, T. 1993: *High image-density particle image velocimetry using laser scanning techniques.* Exp. Fluids **14**, pp. 181-192

[9] Williamson, C.H.K. 1989: *Oblique and parallel models of the vortex shedding in the wake of a circular cylinder at low Reynolds numbers.* JFM **206**, 579-627

[10] Leweke, T.; Sawada, T. 1992: *Structure of a starting-vortex.* In Flow Visualization VI (eds. Y. Tanida, H. Miyashiro), 196-200, Springer Verlag Berlin Heidelberg

[11] Pineau, G.; Texier, A.; Coutanceau, M.; Ta Phuoc Loc 1992: *Experimental and numerical visualization of the 3D flow around a short circular cylinder fitted with endplates.* In Flow Visualization VI (eds. Y. Tanida, H. Miyashiro), 343-347, Springer Verlag Berlin Heidelberg

[12] Willert, C.; Gharib, M. 1991: *Digital Particle Image Velocimetry.* Exp. in Fluids **10**, pp. 181-193

[13] Cenedese, A.; Monti, P.;Sallusti, M. 1993: *PIV: a numerical simulation.* SPIE **2052**, pp. 493-500

[14] Brücker, Ch. 1994: *Stereoscopic DPIV in a scanning light-sheet: Technique and application to the transient wake phenomena behind a sphere.* In preparation

A PROPOSAL OF AN AUTOMATIC CORRECTION METHOD OF BAD PATH-LINES IN PTV

KATSUHIKO HOJO & MAKOTO SANO
Department of Mechanical Engineering, Osaka Institute of Technology (Japan)

Abstract

When a flow field of two dimensions is treated by PTV, bad path-lines of which shapes are not ideal are often observed in the most of binary picture. They harmfully affect the velocity vectors of which value are calculated from them. In this study, we treat two kinds of bad path-lines which occur most frequently in all of them. We propose the method to restore one kind of the bad path-lines or to separate the other kind of them.

By an automation of the processing of the restoration or the separation, the reduction in processing time will be accomplished and such the differences between individuals as happened in the manual processing will also be solved.

1. Introduction

When a flow field of two dimensions is treated by PTV, bad path-lines of which shapes are not ideal are often observed in the most of binary pictures. The probability that the bad path-lines will take place becomes more as the spatial density of tracers becomes larger, and the bad path-lines harmfully affect the velocity vectors of which values are calculated from them. Generally the bad path-lines are excepted from the object of image processing. Consequently the amount of information for the flow field decrease and it is difficult to clarify the phenomena taking place in the flow field. Therefore the shapes of path-lines must be ideal in order that one path-line corresponds to one velocity vector in the flow field.

Then it is the purpose of this study to investigate the method that the meaningful information for the flow field is derived from the bad path-lines. In this paper, we treat two kinds of bad path-lines which occurs most frequently in all of them and propose the method to restore one kind of the bad path-lines or to separate the other kind of them.

2. Image processing system and selection of data

In our image processing system, the animated images are recorded in the image processing apparatus which has the frame memory with the capacity of 512 pixel × 512 pixel × 8 bit. They are also represented in the monitors having the resolution which is 512 pixel × 480 pixel according to the aspect ratio of monitors. The recorded images are mainly processed through the host computer. All of the images were obtained under the following experimental conditions. The flows around a cylinder in two-dimensional plane were illuminated by a LLS method. The working fluid is a water. The tracer for the flow visualization are polystyrene particles which are less than 210 μm in diameter and are 1.03 in specific weight. A series of the experiments were carried out on condition that the product of frame count f_c and Reynolds number Re is 6000 (f_c•Re = 6000). The four variables (100, 300, 500 and 600) were selected for the Reynolds number. The twenty pieces of animated images were processed in consequence of selecting five pieces of the animated images per one variable of Reynolds number.

3. Kind of bad path-line

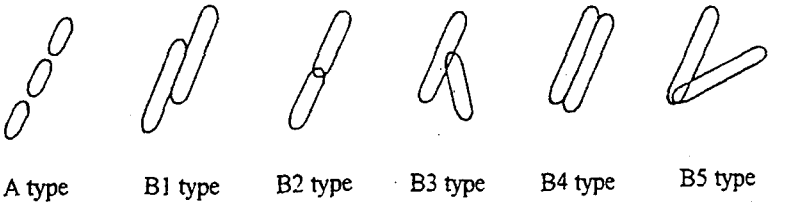

Fig.1 Kind of bad path-line

Upon thoroughly investigation of twenty pieces of the images, we could draw the conclusion that the bad path-lines could be divided into two kinds of types as shown in fig.1. One of them is separated into two or three pieces of break path-lines and is called "separating type" or "A type" for convenience in this paper. It is considered that the separation of path-line is caused by both the noise taking place in the stage of high brightness composition and the behavior of tracer in three-dimensional space. The other of them is composed of two path-lines which touch each other and is called "contacting type" or "B type" for convenience. The two path-lines in the case of B1, B2 and B4 type are parallel each other and they in the case of B3 and B5 intersect each other.

We examined the relation between types and incidences in the case of contacting type. It was clarified that the incidence of B1 type is highest in the B types and have about 50 per cent. Therefore we direct our attention to the bad path-lines of A type and those of B1 type.

4. Automatic restoration method and automatic correction method

4.1. Automatic restoration method for separating type

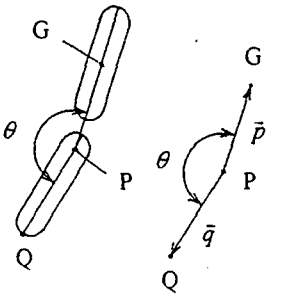

Fig.2 Two pieces of path-lines and the corresponding vectors

The bad path-line of separating type is restored by the following procedure as shown in fig.2. A path-line is approximated by an ellipse of which area is equal to that of the path-line and consequently the major axis of the ellipse is defined. A length of the major axis through the centroid of the ellipse (point G) is assumed to be equal to a displacement of the tracer. The extended line drawn from the major axis of one path-line intersects the major axis of the other path-line at a certain distance in point P. Point Q is used for the apsis of the path-line which includes point P in the major axis. The two vectors $(\vec{p},\vec{q})$ of which base point is P are composed of point G and Q. The angle θ from one vector to the other vector is regarded as the angle from one path-line to the other path-line. The relation between the angle θ and the two vectors is

$$\cos\theta = \frac{\vec{p}\cdot\vec{q}}{|\vec{p}||\vec{q}|}. \tag{1}$$

On the other hand, if the angle θ satisfies the equation which is

$$\cos\theta_b \leq \cos\theta \leq 1, \tag{2}$$

the two path-lines are classified into the bad path-lines belong the separating type and they are incorporated into one. In the above equation, the angle θ_b is a threshold level for the angle θ.

4.2 Automatic correction method for contacting type

The shape factor and the path-line length projected on the minor axis of ellipse which approximates the path-line as the both of them have the same area are introduced into the indices to distinguish the bad path-lines of contacting type from the others. The shape factor K is estimated by the equation[1]

$$K = \frac{l^2}{4\pi S}, \tag{3}$$

where S and l are the area of the path-lines composed of the two pieces of those and the perimeter of those, respectively. When the shape factor and the path-line length projected on the minor axis are greater than a certain values, the path-line is regarded as the bad one of contacting type.

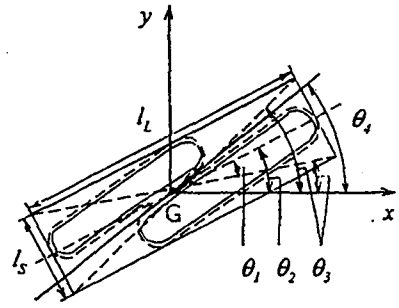

Fig.3 Bad path-line of B1 type

To correct the path-line regarded as the bad one, a straight line is defined in the position at which the two pieces of path-lines touch each other and also the brightness of images are zero. Figure 3 shows the method to define the straight line. In case of approximating the bad path-line by the ellipse, the length of major axis l_L and that of minor axis l_S are defined. Consequently the angle θ_1 as shown in fig.3 is estimated by the equation

$$\theta_1 = \tan^{-1}\left(\frac{l_S}{l_L}\right). \tag{4}$$

If θ_2 is used for the angle between the major axis and x-axis, the relations between θ_2 and the angle θ_3 as shown in fig.3 are

$$\theta_3 = \theta_2 + \theta_1 = \theta_2 + \tan^{-1}\left(\frac{l_S}{l_L}\right), \tag{5}$$

$$\theta_3 = \theta_2 - \theta_1 = \theta_2 - \tan^{-1}\left(\frac{l_S}{l_L}\right). \tag{5}'$$

The angle θ_3 is considered to be associated with the slope of the straight line which separates into the two pieces of path-lines. Now let us suppose that the bad path-line is composed of the two path-lines of which shapes are similar to those of each other. Consequently it is considered that the centroid of the ellipse which approximates the bad path-line exists in the position at which the two pieces of path-lines touch each other. Then let us consider the straight line which has the slope of $\tan\theta_3$ and intersects the centroid $G(x_G, y_G)$ of the ellipse. The equations of the straight lines are

$$y = (x - x_G)\tan\theta_3 + y_G = (x - x_G)\tan(\theta_2 + \theta_1) + y_G, \tag{6}$$

$$y = (x - x_G)\tan\theta_3 + y_G = (x - x_G)\tan(\theta_2 - \theta_1) + y_G. \tag{6}'$$

There are two kinds of the straight lines as expressed by the equation (6) and (6)'. Then to differentiate the straight line separating the one path-line from the other, the number of pixel with the highest brightness are counted in the both straight lines. The one straight line of which the number of pixel is smaller than that of the other is defined temporally for the straight line which separates into the two pieces of path-lines. To correct the straight line further, the angle θ_4 corresponding to the angle θ_3 is defined by introducing the coefficient j which varies from 0 to 1 into the equation (5) and (5)'. The angle θ_4 is expressed by the equation

$$\theta_4 = \theta_2 + j\theta_1, \tag{7}$$

$$\theta_4 = \theta_2 - j\theta_1, \tag{7}'$$

where the value of coefficient j is determined by a series of the experiments. The straight line is newly defined by using the angle θ_4 and the equation of that is

$$y = (x - x_G)\tan\theta_4 + y_G. \tag{8}$$

On the other hand, the bad path-lines of type B2, B3, B4 and B5 can be also corrected by the above mentioned method using the coefficient j of which value is variable.

5. Results and discussions

5.1 Estimation of automatic restoration method and automatic correction method

Figure 4 shows the binary images of flow behind a cylinder in two-dimensional plane. Figure (a), (b) and (c) show the image before a processing, that after a manual processing and that after the automatic processing proposed in this paper, respectively. Figure 5 shows the histograms about the frequency for the shape factor of the path-lines which are distributed over the images of

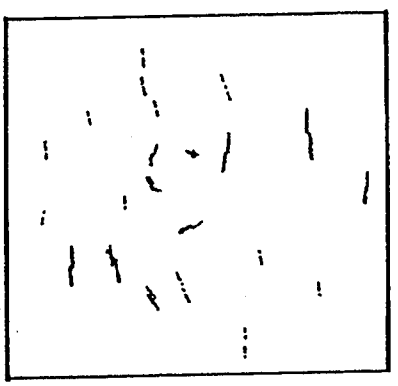

(a) image before processing

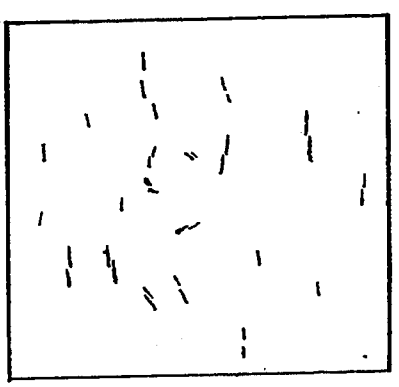

(b) image after manual processing

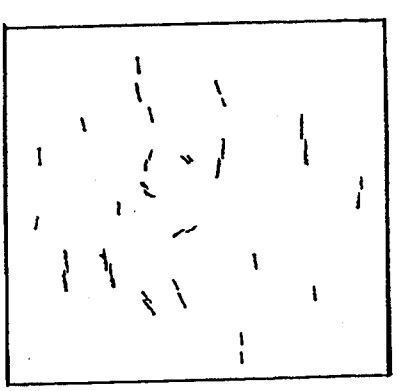

(c) image after automatic processing

Fig.4 Image of a flow behind a cylinder

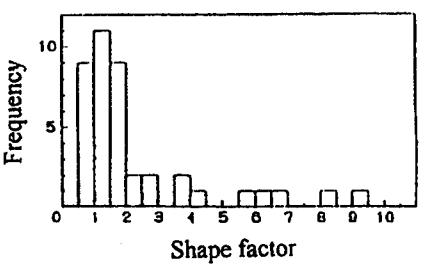

(a) image before processing

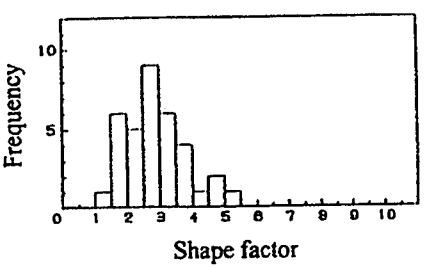

(b) image after manual processing

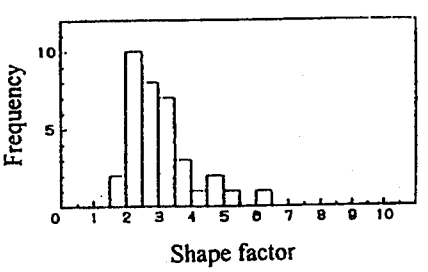

(c) image after automatic processing

Fig.5 Histograms of shape factor

fig.4. The (a), (b) and (c) in fig.5 show the histogram of (a), that of (b) and that of (c) in fig.4, respectively. The values of shape factor scatter over the range in fig.5(a), but those gather in the range from 1.5 to 4 in fig.5(b) and (c). Therefore it is clarified that the automatic processing method which is proposed in this paper to restore the bad path-lines and to correct those have similar performance to the manual processing.

5.2 Consideration of parameters

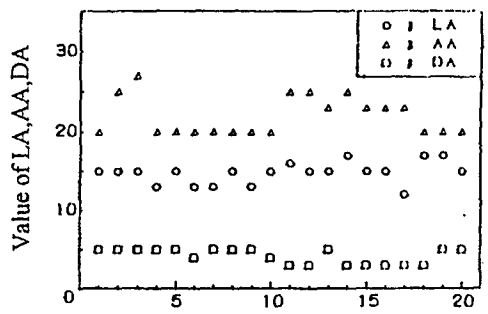

Fig.6 Distribution of parameters in the case of separating type

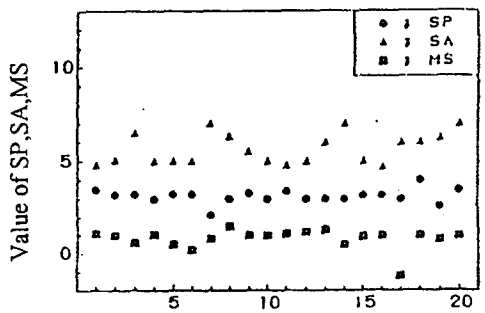

Fig.7 Distribution of parameters in the case of contacting type

There are a lot of parameters in the both methods proposed in this study. All of them are the threshold levels which are criteria for judging whether a path-line is bad or good and they are also used for the correction or the restoration. Therefore, the setting of threshold level is very important. Using twenty pieces of pictures mentioned above, we examined the values of the parameters. Figure 6 and 7 show the values of parameters given in the stage of the restoration processing and the correction processing, respectively. In the case of separating type, we adopted such parameters as a length of the major axis, LA, an angle from one vector to the other vector, AA and a distance from one vector to the other vector, DA. In the case of contacting type, we also adopted such parameters as a shape factor, SP, a length of the minor axis, SA and a slope of

the required line, MS.

In the case of separating type as shown in fig.6, we can find the fact that most of the values of LA, AA and DA gather in the range from 13 to 15, in the range from 20 to 25 and in the range from 3 to 5, respectively. In case of contacting type as shown in fig.7, we can also find the fact that most of the values of SP, SA and MA gather in the region from 2 to 4, in the region from 5 to 7 and around 1, respectively. From the results, it is considered that we can maintain those parameters at constant values.

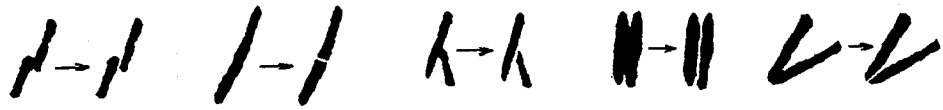

B1 type B2 type B3 type B4 type B5 type

Fig.8 the comparison of the images after processing with those before processing in the case of contacting type

Figure 8 shows the comparison of the path-lines after processing with those before processing in the case of contacting type. All of the values of j except B2 type were found to be in the range from 0 to 1. From fig.8, it is also considered that all of the path-lines are separated reasonably.

6. Conclusion

In this study, we classified bad path-lines which are often found in the stage of image processing into each of types. And, we devised the method to restore or to correct. We had the reasonable results keeping the values of the threshold level constant in the automatic processings. And, we were confident that our method proposed in this paper will be effective for real use.

By automation of the processing of the restoration or the separation, the reduction in processing time will be accomplished and such the differences between individuals as happened in the manual processing will also be solved.

Reference

(1) HASEGAWA. J., 1986, Introduction to basic technique in image processing, pp.59-64, Gijutuhyoronsha-publishing.

THE ROTATING SLANTED HOT WIRE ANEMOMETER IN PRACTICAL USE.

LÓPEZ PEÑA, F.
Escuela Politécnica Superior de Ferrol , Universidad de La Coruña (Spain)

ARTS, T.
von Karman Institute for Fluid Dynamics (Belgium)

Abstract

A single rotating slanted hot-wire is used to measure the three components of the mean velocity and the six components of the Reynolds stress tensor. This paper describes the calibration procedure, the data reduction method, the experimental set-up, and some measurements. The improvements introduced in this measurement technique, the problems encountered when using it, and some recommendations about further improvements are also discussed.

1 Introduction.

The rotating slanted hot-wire technique allows the measurement, in a given steady or periodic flow field, of the three components of the mean flow velocity and the six components of the Reynolds stress tensor. This technique was first developed by Fujita and Kovasznay (1) who used it to measure three components of the Reynolds stress tensor in a fully developed pipe flow. After this work, only a reduced number of researchers tried to implement and improve this method. The implementation of the technique differs in several aspects from case to case, but all of them are based on the directionality of the hot-wire response. The Reynolds stress tensor and mean velocity components are obtained after having measured the mean and RMS averaged values of the hot-wire output signal in at least six different orientations of the probe. The main advantage of the technique is that it uses a single hot wire, resulting in a rather inexpensive system where a single measurement chain is used. The main trouble is that the method involves the solution of a system of algebraic equations having an ill conditioned matrix of coefficients. Perdichizzi et al (2) have shown that the condition number of this matrix can be easily ranged from 10^3 to 10^6. Therefore, any error in determining the coefficients of the equations will be largely amplified in the solution. Consequently, in order to apply this technique, special care must be taken while acquiring the data at each wire orientation, this data must be averaged for a long time to assure that the mean and RMS values of the signal are correctly averaged, and the flow conditions must remain unchanged during the time the acquisitions are made at all probe orientations.
All the experiments presented in this paper were performed at the von Karman Institute for Fluid Dynamics. This work is a contribution to the effort that has been carried out at this Institute to elaborate a method allowing to diminish the errors and long data acquisition times associated with the rotating slanted hot wire technique. The technique was first implemented at the von Karman Institute by Bridgeman et al (3). The main difference with the original rotating slanted hot-wire technique is the use of more than six different orientations of the wire to take measurements, thus the six Reynolds stresses were calculated by solving a redundant system of equations with a least square procedure. In this way the error associated with data reduction is diminished. The method proved to work but some doubts about the gain on accuracy still persisted.

2 Description of the method.

2.1 Probe calibration.

For the velocity calibration of the probe the King's law is used. This law, named after King [4], is a widely accepted relation between the voltage (E) measured at the anemometer output and the effective flow velocity (Ueff) for hot wire anemometers working in a constant temperature mode. King's law is expressed as follows:

$$E^2 = A + BU_{eff}^n \tag{1}$$

where A, B and n are constants to be determined by this calibration and then set in the anemometer linearizer.

For an arbitrary probe orientation, the effective velocity (Ueff) must be determined by an angular calibration. The hot wire probe presents very low sensitivity to the velocity component parallel to the wire. The so-called cosine law was the first directional calibration law for hot-wires. It was tested in its original form by Shubauer and Klebanoff[5] and states as follows:

$$U_{eff} = U\cos\phi \tag{2}$$

where ϕ is the angle between the velocity U and a plane normal to the wire.

In this last expression the effect of the velocity component in the direction of the wire is not taken in consideration. Hinze[6] proposed the following expression to take in account this component:

$$U_{eff}^2 = U^2(\cos^2\phi + k^2\sin^2\phi) \tag{3}$$

According to Hinze, for different probe geometries, the coefficient k varies between 0.1 and 0.3.

The expressions (2) and (3) do not consider the perturbations originated in the flow by the prongs and the stem of the probe. Comte-Bellot et al(7) proved that the existence of the probe prongs and stem is responsible for a different sensitivity between the normal and binormal velocity components. Jorgensen[8] proposed to use the following expression to account for these interferences:

$$U_{eff}^2 = U_n^2 + K_b U_b^2 + K_t U_t^2 \tag{4}$$

U_n, U_b, and U_t are the normal, binormal, and tangential flow velocity components in a wire coordinate system (Fig. 1) and K_t, and K_b are the coefficients to be obtained by calibration. Note that with respect to expression (3) not only the first term has been split in two parts but now it is allowed to account for a negative coefficient of the U_t flow velocity component. The negative

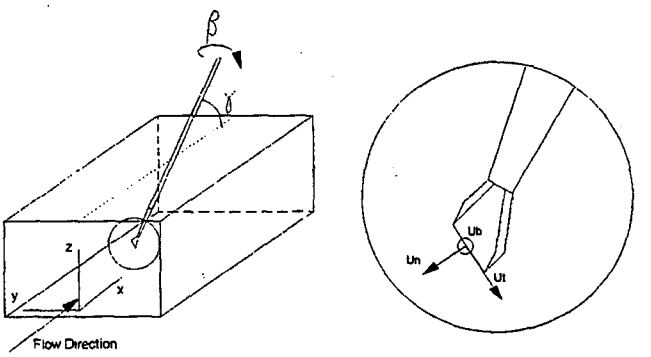

Fig. 1- The coordinate refernce systems.

influence of this velocity component could be possible because of the mentioned prongs and stem perturbations. In any case the effect of these perturbations must be small and therefore the value of Kt must be one order of magnitude lower than Kb, and this coefficient must be close to unity. If the perturbation is not small, it cannot be assured that the calibration of the probe in a uniform flow could be adequate to predict the behavior of the probe when measuring in a flow with transverse velocity gradients.

A modified version of this law by Jorgensen with the use of a third coefficient, K_n, was proposed at the VKI by Costa[9]:

$$U_{eff}^2 = K_n U_n^2 + K_b U_b^2 + K_t U_t^2 \qquad (5)$$

This K_n coefficient originally aimed to diminish the errors induced by the hot wire anemometer linearizer and by the wire imperfections when they produce a non symmetric response for the normal velocity component. Bruun and Tropea[10] have shown than the coefficients of the King's law (1) are changed with the wire orientation. In general the King's A coefficient and the n exponent do not change very much, but the B coefficient can experiment variations up to 60%. This change is partially taking into account by using a coefficient for all three velocity components and then making these three coefficients depend on the main flow direction.

In Figure 2 the two types of hot-wire probes that have been used in the present study are represented with two examples of sets of their calibration curves. A set of these calibration curves are obtained prior to any test session by angular calibration of the probe. The Jorgensen coefficients (K_n, K_b, and K_t) are calculated such as to have the best fit of the set of calibration curves from expression (5). As mentioned before, these coefficients may change with the wire orientation. This basically means that the values of the coefficients needed for the best fit differs from curve to curve of a given set. A method has been developed to account for this. After a probe has measured the flow field characteristics in a given point, the main flow direction is calculated by using the coefficients calculated as mentioned before. Once the main flow direction is

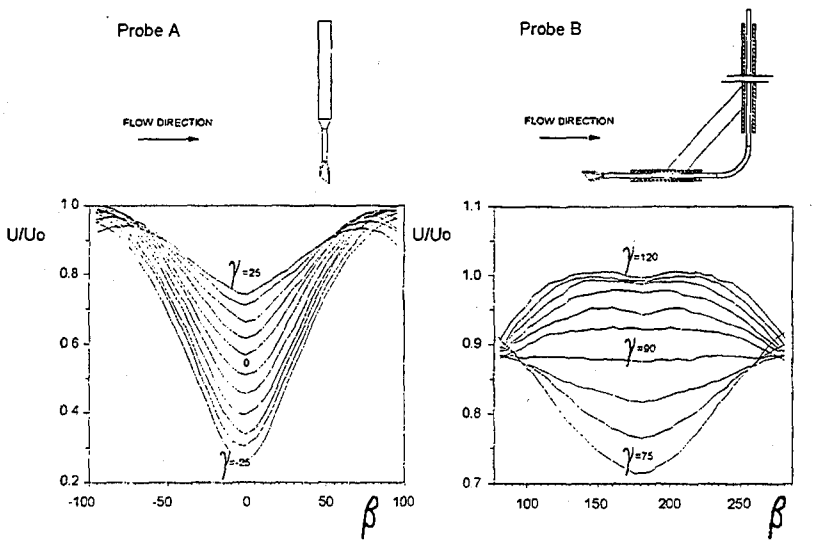

Fig.2 - The two used probes and their calibration curves.

known, the Jorgensen coefficients are calculated again but just to have the best fit of the calibration curves nearest to the calculated flow direction. In this way the Jorgensen coefficients are locally calculated. The use of these local coefficients does not significantly improve the accuracy of the calculations of the main velocity components nor the normal Reynolds stress tensor components, but, in general, it does increase the accuracy of the shear Reynolds stress measurements.

2.2 Derivation of the rotating slanted hot-wire technique governing equations.

A coordinate transformation from the frame relative to the wire to the absolute frame of reference provides the following relationship:

$$U_{eff}^2 = A_1 u^2 + A_2 v^2 + A_3 w^2 + A_4 uv + A_5 uw + A_6 vw \tag{6}$$

where the A_i are the coordinate transformation coefficients, depending upon the wire orientation. For a generic probe orientation these coefficients are:

$$A_1 = K_n(\cos\alpha\sin\gamma + \sin\alpha\cos\beta\cos\gamma)^2 + K_b \sin^2\beta\cos^2\gamma + K_t(\cos\alpha\cos\beta\cos\gamma - \sin\alpha\sin\gamma)^2$$

$$A_2 = K_n \sin^2\alpha\sin^2\beta + K_b \cos^2\beta + K_t \cos^2\alpha\sin^2\beta$$

$$A_3 = K_n(\cos\alpha\cos\gamma - \sin\alpha\cos\beta\sin\gamma)^2 + K_b \sin^2\beta\sin^2\gamma + K_t(\sin\alpha\cos\gamma + \cos\alpha\cos\beta\sin\gamma)^2$$

$$A_4 = -K_n(\sin 2\alpha\sin\beta\sin\gamma + \sin^2\alpha\sin 2\beta\cos\gamma) + K_b \sin 2\beta\cos\gamma +$$
$$+ K_t(\sin 2\alpha\sin\beta\sin\gamma - \cos^2\alpha\sin 2\beta\cos\gamma)$$

$$A_5 = K_n(\cos^2\alpha\sin 2\gamma + \sin 2\alpha\cos\beta\cos 2\gamma - \sin^2\alpha\cos^2\beta\sin 2\gamma) - K_b \sin^2\beta\sin 2\gamma +$$
$$+ K_t(\sin^2\alpha\sin 2\gamma - \sin 2\alpha\cos\beta\cos 2\gamma - \cos^2\alpha\cos^2\beta\sin 2\gamma)$$

$$A_6 = K_n(\sin^2\alpha\sin 2\beta\sin\gamma - \sin 2\alpha\sin\beta\cos\gamma) - K_b \sin 2\beta\sin\gamma +$$
$$+ K_t(\cos^2\alpha\sin 2\beta\sin\gamma + \sin 2\alpha\sin\beta\cos\gamma)$$

From the expression (6) we can see that it is possible to calculate the three components of the velocity in a given flow field by using King's law to calculate U_{eff} for different wire orientations with respect to the main flow direction.

The RMS value from the hot wire anemometer output is used to calculate the Reynolds stresses. The expression that relates this value with the Reynolds stresses can be obtained by introducing the mean and fluctuation terms in the velocity components. After substitution in the modified Jorgensen formula(5), by subtracting the mean velocity, neglecting second order perturbation terms, and averaging, the following expression is obtained:

$$\overline{u_{eff}^2} = C_1\overline{u'^2} + C_2\overline{v'^2} + C_3\overline{w'^2} + C_4\overline{u'v'} + C_5\overline{v'w'} + C_6\overline{u'w'} \tag{7}$$

where the C_i coefficients are:

$$C_1\overline{U_{eff}}^2 = D_1^2 \qquad C_2\overline{U_{eff}}^2 = D_2^2 \qquad C_3\overline{U_{eff}}^2 = D_3^2$$

$$C_4\overline{U_{eff}}^2 = 2D_1D_2 \qquad C_5\overline{U_{eff}}^2 = 2D_2D_3 \qquad C_6\overline{U_{eff}}^2 = 2D_1D_3$$

and these D_i new coefficients are function of the A_i ones in the following way:

$$D_1 = A_1\bar{u} + \frac{A_4\bar{v} + A_5\bar{w}}{2} \qquad D_2 = A_2\bar{v} + \frac{A_4\bar{u} + A_6\bar{w}}{2} \qquad D_3 = A_3\bar{w} + \frac{A_5\bar{u} + A_6\bar{v}}{2}$$

As previously mentioned for the three velocity components, it is also possible to obtain the six Reynolds stresses by taking measurements at six different wire orientations. The VKI procedure

uses up to 39 different orientations in order to minimize the acquisition errors by solving an redundant system of equations with a least square procedure.

2.3 Uncertainty analysis.

To evaluate the improvements in accuracy achieved by the above described method, a statistical error analysis has been developed in collaboration with Rau(11). This uncertainty analysis is performed by means of a computer simulation program. A simplified flow chart of this computer program is presented in Figure 3. The analysis is applied to three test cases having typical characteristics of the studied flow field. For each case the velocity components (V_i), and the components of the Reynolds stresses tensor (T_{ij}), as well as a set of calibration curves, are given as input to the error analysis program. The first step is to calculate the input data, that is, the output that the hot-wire anemometer linearizer would produce for the mean velocity (U_{lin}) and for the RMS velocity (U_{rms}). This hypothetical output is to be calculated for each of the 39 orientations at which the wire takes measurements in a given point. This is a straight calculation that does not present any difficulty. If, at this point, the calculated values are given as measured data to the data reduction program, the velocity components and the Reynolds stresses will be, obviously, correctly calculated. To simulate the data measured in a real case, a Gaussian distribution of errors is injected in the calculated exact data by means of a random number generator. The data synthesized in this way are then processed by the data reduction program, and the result is compared with the exact solution from which the calculation has started. It is worth to notice that the result will change if the process is again repeated because the random number generator will not assign exactly the same errors at the same positions, even if the overall Gaussian distribution is the same. Therefore, for a given value of the standard deviation of the Gaussian distribution, the process shall be repeated a number of times in order to have a significant number of samples for statistical analysis. In the present study the process is repeated 250 times for each standard deviation value. Variations in the standard deviation of the linearizer mean value (V_{lin}) show much less effect in the final error than variations in the standard deviation of the RMS value (V_{rms}). Therefore the standard deviation of the linearizer mean is kept equal to 2% while the one of the RMS is varied between 0 and 5%. In terms of errors, these values roughly correspond to 4% error in linearizer mean and 0 to 10% error in RMS (when a confidence level of 95% is used).

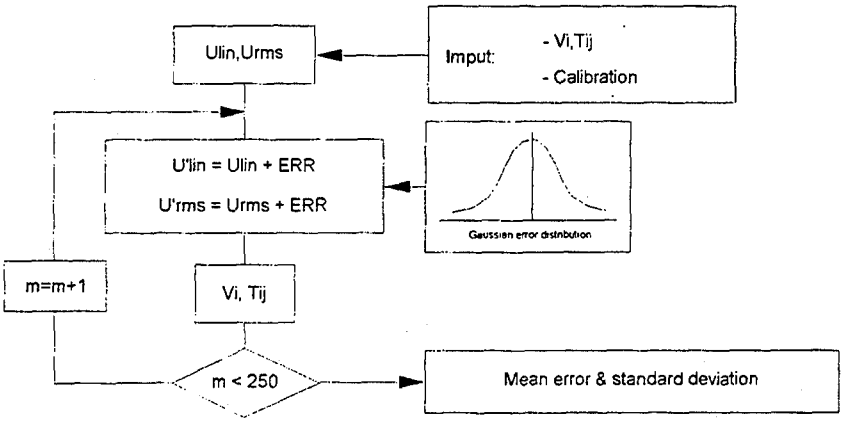

Fig. 3 - Flow chart of the uncertainty analysis procedure.

Figure 4 shows the influence of the matrix size on the uncertainty of the normal Reynolds stresses calculations. For a 5% uncertainty in the RMS of the voltage linearizer, the error in estimating normal stresses drops from 8% till 1% in the case of 8% turbulence level, and from 40% till 4% in the case of 20% turbulence level. The influence of the error in determining the Jorgensen coefficients and the angular orientation of the hot wire were also analyzed by Rau[11]. Both parameters present a weak influence on the overall uncertainty of the method, but they increase the minimum error to about 2% for the case of 8% turbulence level. In conclusion, the error analysis shows that the use of an overdetermined system of equations to reduce the data significantly improves the uncertainty of the measurements with an estimated error of about 2% if the error on the linearizer output is kept lower than 5%. Despite this result, the reader must be aware about the fact that the total error is probably higher. In fact the present analysis only evaluates the errors originated by the data reduction procedure; some other sources of error as the errors caused by the calibration procedure, or the fluctuations in flow conditions during the considerably long test sessions, are not considered. Additionally, the mathematical transformation, used to generate the data and to reduce it later, is based on the assumption of small perturbations; this assumption breaks down when the turbulence level is high. All these additional sources of error should require further studies to be evaluated.

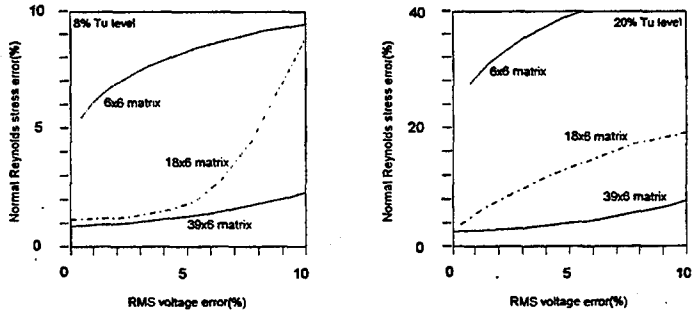

Fig. 4 - Influence of matrix size and turbulence level on the calculations.

3 Experimental apparatus.

The experiments with the rotating slanted hot wire were performed in a low turbulence wind tunnel of the von Karman Institute where measurements were taken in the boundary layer and in the meridional plane of turbulent jets emerging from inclined holes made in a model flat plate. The measurement and control system (Fig. 5) are based on an IBM AT computer equipped with a control card and a data acquisition card. The first card is used to control the rotation and the traverse probe movements. The acquisition card samples outputs from different transducers and stores the hot wire anemometer outputs.

The final goal pursued for the implementation of the method at the VKI was to use it for mapping the Reynolds stresses in between the blades of turbine stators. The idea was to introduce the probe through an orifice made on the turbine casing and perform the measurements with the hot wire stem placed transversally to the main flow direction. It was known that, placed in this way, the hot wire probe could perturb the flow field in its vicinity, but it was assumed that this perturbation was

small. In any case, due to the geometry of the machine and to the lack of space, it seems to be no other better way to place the probe there. We found that, in some conditions, the errors introduced by putting the probe were not small. To evaluate these errors, a new probe has been designed, constructed and tested during the present work. In this new probe the rotating stem is placed downstream of the hot wire. A sketch of the two probes tested altogether with their calibration curves is shown in Figure 2. In addition to the hot wire anemometers, a two component fiber optic Laser Doppler Anemometer was used to have an independent set of measurements.

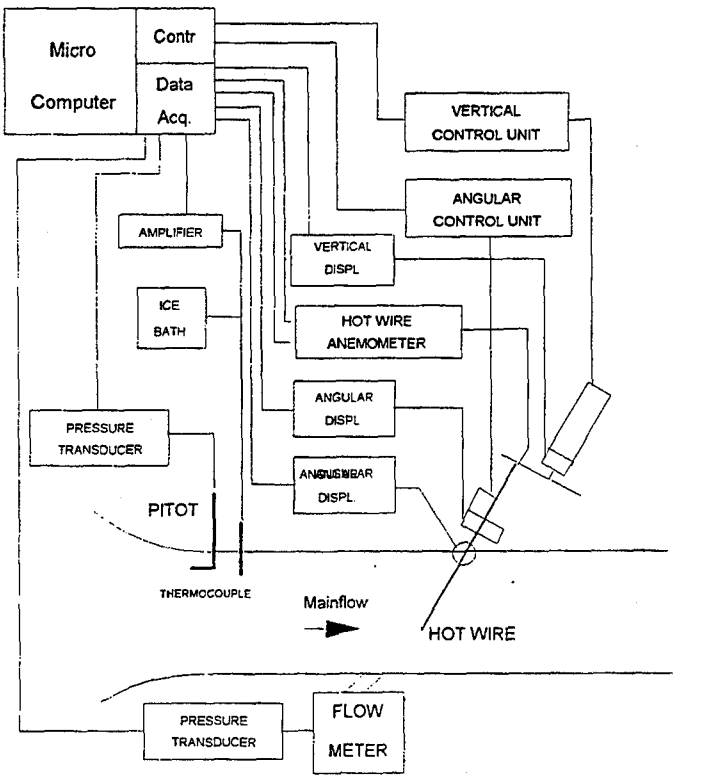

Fig. 5 - Schematic of the measurement and control chain.

4 Measurements.

As indicated earlier, measurements in a boundary layer and in the flow field along the meridional plane of a wall jet have been performed with the rotating slanted hot-wire and with a LDV anemometer. In most of the measured velocity profiles, relatively large discrepancies, up to 30%, have been observed between the data taken by the two measurement systems. As an example, some of these velocity profiles are represented in Figure 6. These curves are taken along the

meridional plane of a single jet of air with mass flux ratio equal to 1.35. The profiles are measured at positions equal to 1, 2, and 3 injection hole diameters downstream of the injection site. In light of these discrepancies it is clear that one of the experimental techniques is giving wrong results. Some of the traverses were performed upstream of the injection hole, where the boundary layer is undisturbed and laminar. Therefore these traverses can be used as a control to compare the measurements with the Blasius boundary layer profile. This comparison is shown in Figure 7. The LDV system presents a good agreement with the Blasius profile while the hot-wire does not. Looking at Figure 6 it is clear that wherever a gradient exists, the hot-wire seems to shift it downwards. Such an effect is also found to be stronger in laminar flow regions. This leads the authors to suspect that, as the hot-wire stem is transverse to the main flow direction, it perturbs the flow at the measurement site. This supposition is also supported by the analysis of the work of De Grande and Kool[12]. In their work a similar technique is used to measure a turbulent boundary layer on a curved wall. The hot-wire probe is also placed with its stem traversed to the main flow but they measure through a whole made in the same wall were the boundary layer is going to be measured, and therefore the probe stem remains inside the wall or just coming out in a region of low momentum flow. Their measurements do not show any disturbance, so it is logical to think that, in the present case, the presence of the probe stem in the main flow is causing the disturbances.

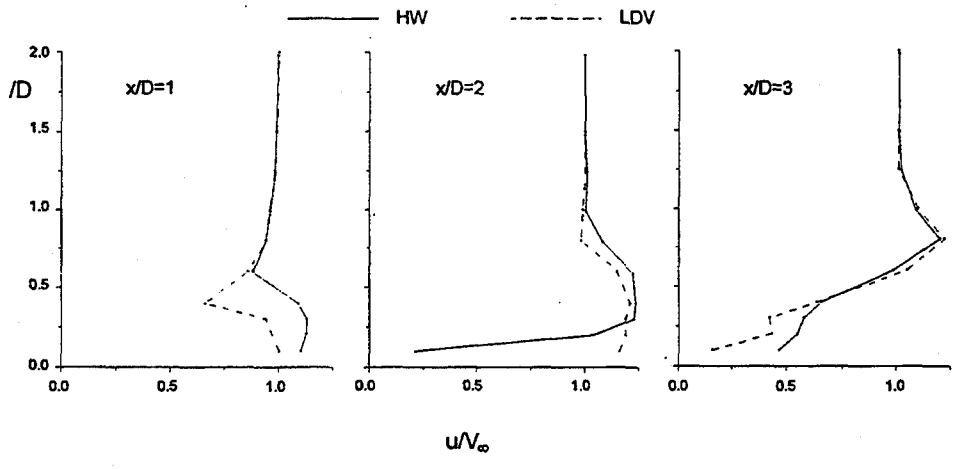

Fig. 6 - Velocity profiles along the meridional plane of a wall jet.

To confirm this hypothesis, a new set of LDV measurements was performed along the same traverse and under the same flow conditions. For this test, the hot-wire probe was positioned as if it were to measure the same traverse, but only with the purpose to produce the same perturbation as when the hot-wire measurements were made. For practical reasons the probe was not rotated during these tests but fixed at the central position of the rotation. In addition the hot-wire was broken to avoid it to interfere with the laser beams. The hot-wire and LDV probes were vertically displaced by separate traversing mechanisms. After a measurement at a given z position, both probes were displaced by the same amount, so as to have the LDV always measuring at the center

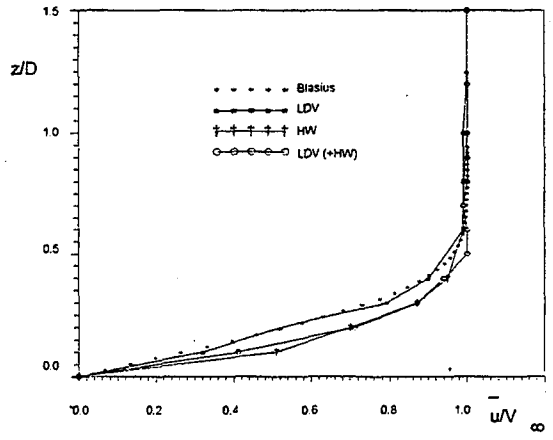

Fig. 7 - Comparison between Blasius boundary layer profile and measured data.

of the broken hot-wire. The result of this set of LDV measurements is shown in the fourth curve of Figure 7. As was expected, the new LDV measurements do not follow the Blasius profile but lie on the hot-wire data. This confirms the hypothesis that the hot-wire is correctly measuring the flow field velocity around itself, but this measured flow is perturbed by the presence of the hot-wire stem.

The mechanisms for which the hot-wire probe perturbs the flow field can be put in evidence by looking at Figure 8. This figure presents the turbulence level and the w velocity component measured in the laminar boundary layer with the LDV alone and their comparison with the LDV measurements taken in the presence of the hot-wire probe. The values of the turbulence level measured in the no perturbed flow lie in a band between 0.2% and 0.9%, while in the presence of the hot-wire this band of values increases to a range from 1.2% to 3.6%. This increase in the

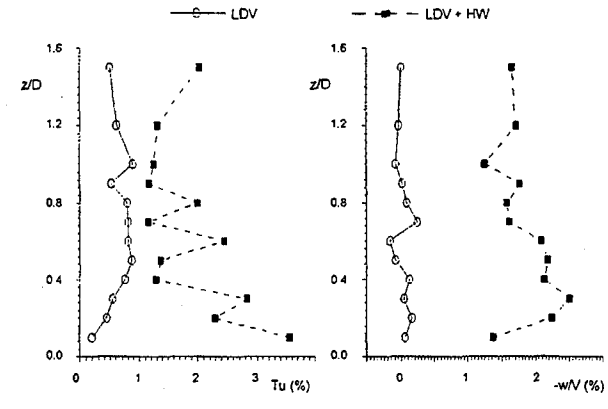

Fig. 8 - Perturbations introduced by the HW probe in the flowfield.

turbulence level must produce changes in the Blasius laminar boundary layer profile. A second mechanism for which the hot-wire probe perturbs the flow field is observed in the w velocity component distribution. While the LDV alone measures w values very close to zero (within the accuracy of the instrument), in the presence of the hot-wire these values range from -1.2% to -2.5% of the free stream velocity. This indicates that the hot-wire stem is producing a blockage effect on the flow, forcing it to go around and underneath the probe. Therefore, this blockage effect transports some flow from the high to the low z coordinate levels. These two perturbation mechanisms play a similar role when low turbulence flows (Tu<<5%) are considered. However, as the first perturbation mechanism increases the turbulence level only by about 2%, it will have less influence when measuring high turbulent flows (Tu>>10%).

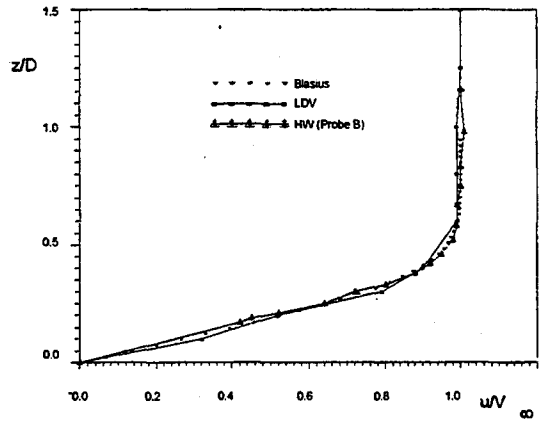

Fig. 9 - Comparison between Blasius boundary layer profile and measured data.

To evaluate the performance of the rotating slanted hot-wire, and to obtain some better data to compare with the LDV measurements, a new hot-wire probe has been designed and constructed as described in Figure 2. The laminar boundary layer has been measured with the new probe; the result is presented in Figure 9, which shows the hot-wire data to be in close agreement with the Blasius profile. Thus, this test indicates that the new hot-wire probe perturbs the flow much less than the original one, and particularly demonstrates a clear improvement of the new probe over the old one when measuring laminar flows. To obtain some additional information about the performance of the new probe in measuring turbulent flows, some traverses for the jet test case of Figure 6 were measured again. The results are shown in Figure 10. In general, they compare better with the LDV data, but some discrepancies are still present. Figure 11 shows the turbulence intensity measurements for these traverses. The discrepancies between hot-wire and LDV turbulence intensity data are even larger than for the velocities, but these results show that, in any case, the largest differences appear at positions where the turbulence intensity is large. This is in agreement with the general limitations of the rotating slanted hot-wire technique. In the light of the present results, it may be concluded that the new probe does not introduce noticeable perturbations in the measured flow field. Nevertheless, this new probe presents some inconveniences too. Firstly it cannot be used for the original purpose of measuring inside the

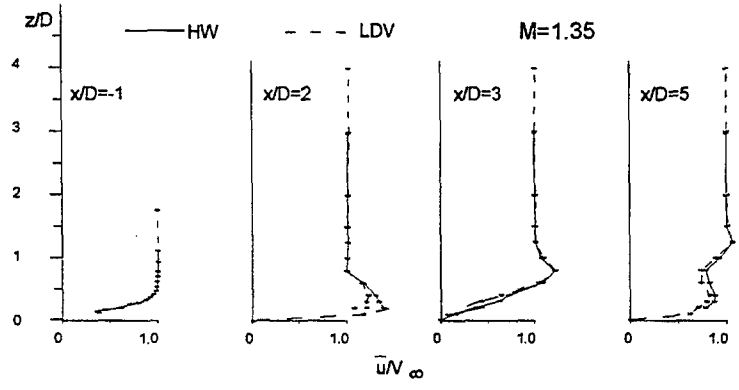

Fig. 10 - Velocity profiles measured along the meridional plane of a wall jet with the new probe.

turbine stator because of leak of space. It is less sensible than probe A to any change in orientation, as it can be seen by looking at the angular calibration curves presented in Figure 2. This reduction in angular sensibility is clearer for the upper curves of this figure that remain very close together. These upper curves present a local minimum in their middle part. This is an indication of the existence of a important flow perturbation produced by the prongs, because at this position the orientation of the wire is such that the normal velocity component reach a maximum, and, if no perturbation existed, the curve would have a maximum there too. It is also evident that when the probe stem is aligned with the main flow the binormal velocity component is always zero all along the corresponding calibration curve, thus it will be not possible to determine all three Jorgensen coefficients when only this curve is used, and therefore the technique explained at the end of paragraph 2.1 will be impossible to use here.

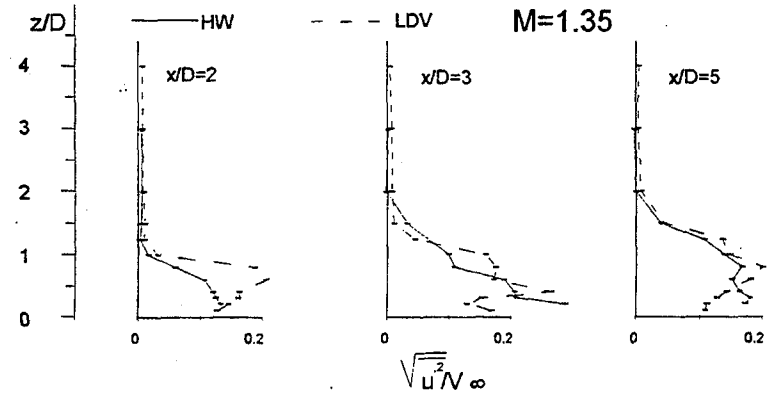

Fig. 11 - X component of the Reynolds stress tensor.

5 Conclusions.

This paper presents a method to improve the accuracy, and to reduce the data acquisition time, of the rotating slanted hot wire technique. The method uses and over determined system of algebraic equations at data reduction time and uses a modified version of the Jorgensen formula to make the angular calibration of the probe. The new formula uses a coefficient for each of the normal, binormal and tangential velocity components. The use of these three coefficients allows a better fit of the calibration curves. A statistical error analysis program used to study the method shows a clear gain in accuracy when the overdetermined system of equations is used.
In a series of experiments performed to check test the technique, some problems concerning the perturbations induced by the probe in the flow were detected. The analysis of the perturbation mechanisms shows that, if the perturbation induced by the probe in the flow at the measurement site is not very small, a great loss in accuracy appears in measuring the regions where the transverse velocity gradients are important. This behaviour is not specific of the present method and can be extended to any intrusive measurement device.

References.

(1) Fujita, H. and Kovasznay, L.S.G.; *Measurements of Reynolds Stress by a Single Rotated Hot Wire Anemometer*. The Review of Scientific Instruments. Vol. 39, N. 9, Sept. 1968.
(2) Perdichizzi, A.; Ubaldi, M. and Zunino, P.; A *Hot Wire Measuring Technique for Mean Velocity and Reynolds Stress Components in Compressible Flow*. Proceedings of the 10th Symposium on Measurement Techniques for Transonic and Supersonic Flows in Turbomachines, paper 8, held in Burssels (VKI) in September 1990
(3) Bridgeman, M.; Borsboon, M. and Sieverding, C.H.; *Development of a Method to Measure Reynolds Stress with a Rotated Slanted Hot Wire*. von Karman Institute. P.R. 1985-14. June 1985.
(4) King, L.V.; *On the Convection of Heat from Small Cylinders in a Stream of Fluid: Determination of Convective Constants of Small Platinum Wires with Application to Hot-Wire Anemometry*. Phil. Trans. R. Soc. of London, A 214. pp. 373-432. 1914.
(5) Shubauer, G.B. and Klebanoff, P.S.; *Theory and Application of Hot-Wire Instruments in the Investigation of Turbulent Boundary Layers*. NACA WR-86. 1946.
(6) Hinze, J.O.; *Turbulence, an Introduction to its Mechanism and Theory*. McGraw Hill. New-York. 1959.
(7) Comte-Bellot, G.; Strohl, A. and Alcaraz, E.; *On Aerodynamic Disturbances Caused by Single Hot-Wire Probes*. Journal of Applied Mechanics, Vol. 38 N. 4, Dec. 1971. pp. 767-774.
(8) Jorgensen, F.E.; Directional Sensitivity of Wire and Fibre Film Probes. DISA Information, N. 11. 1971. pp. 31-37.
(9) Costa, J.; *Reynolds Stress Measurements Downstream of an Annular Turbine Cascade*. von Karman Institute P.R. 1986-21, June 1986.
(10) Bruun, H.H. and Tropea, C.; *The Calibration of Inclined Hot-Wire Probes*. J. of Phys. E: Sci. Instrum. Vol. 18, 1985.
(11) Rau, G. and Arts, T.; *Aerodynamics of Jet-Crossflow Interaction*. von Karman Institute, P.R. 1991-29. June 1991.
(12) De Grande, G. and Kool, P.; *An Improved Experimental Method to Determine the Complete Reynolds Stress Tensor with a Single Rotating Hot Wire*. J. of Phys. E: Sci. Instrum., Vol 14, pp. 196-201, 1981.

PULSED HOT WIRE ANEMOMETRY IN TWO DIMENSIONS

VENÅS B., TORBERGSEN L.E., KROGSTAD P.-Å, SÆTRAN L.R.
Department of Mechanics, Thermo- and Fluid Dynamics,
University of Trondheim, NTH (Norway)

SUMMARY: A two-dimensional Pulsed Hot Wire Anemometry technique based on a "crossed wire" probe is described (analogous x-wire probes in conventional hot wire anemometry). It is shown that the technique at reasonable accuracy allows measurements of Reynolds stresses including the shear stress $\overline{uv}$ in highly turbulent flows.

INTRODUCTION:

Pulsed Hot Wire Anemometry (PHWA) is a velocity measuring technique specially suited for highly turbulent flows in which flow reversals can occur. The technique was first described by Bradbury and Castro[1] in 1971 as a means for measuring fluctuating velocity in flows where conventional hot wire anemometry (hereinafter; CTA - Constant Temperature Anemometry) fails due to high relative turbulence. Today sophisticated methods are available for measuring such flows, e.g. Laser Doppler Anemometry (LDA) and Particle Image Veliocimetry (PIV), but PHWA has several advantages making it a serious alternative or supplement to these newer techniques - seeding of the flow is unnecessary - small dimensions, and no need for optical access makes it a very mobile unit - plus the fact that the price is an order of magnitude lower.

Fig.1 shows a typical PHWA probe of the type designed by Bradbury and Castro. It consists of a hot wire in the middle and two sensor wires placed at right angles to it and one on each side. The working principle is that heat tracers are emitted from the hot wire by passing short-duration electric currents through it. Each tracer convects with the instantaneous flow and is detected by one of the sensor wires which are operated as resistance thermometers. The time passed from emission to detection ("the time of flight") and the distance separating the wires then provide a direct measure of the velocity. A conventional PHWA measures one component of the velocity vector; that is in the direction perpendicular to both pulsed- and sensor wires.

PHWA has mainly been used for measuring mean velocity U and Reynolds normal stress $\overline{u^2}$ in the dominant flow direction. These are often main parameters in quantification of industrial flows, but for turbulence modelling purposes mean lateral velocity V, the other Reynolds stresses, $\overline{v^2}$ and $\overline{uv}$, and often higher order moments are sought. These quantities can be measured by PHWA using slanted wire methods[2], but this approach has certain weaknesses - the method is laborious (Reynolds stresses require three measuring sequences at different slanting angles, while Dianat and Castro[3] found 10-12 angles necessary for third order correlations to be reliable) - the slanted wire technique can not provide time resolved information in two dimensions - imperfections in angular response may bias measurements[2],[4].

However, slanted wire methods are based on the PHWA being directionally sensitive with respect to probe orientation and this fact initiated the present work; - it is possible to use PHWA in a crossed wire arrangement analogous conventional cross hot wires in CTA. The paper concentrates on the construction, calibration and testing of this technique; 2D-PHWA based on a crossed wire PHWA-probe.

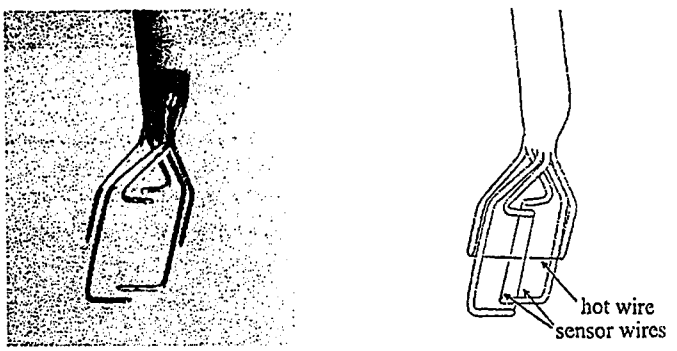

Fig.1 - One-dimensional pulsed hot wire probe (1D-PHWA)

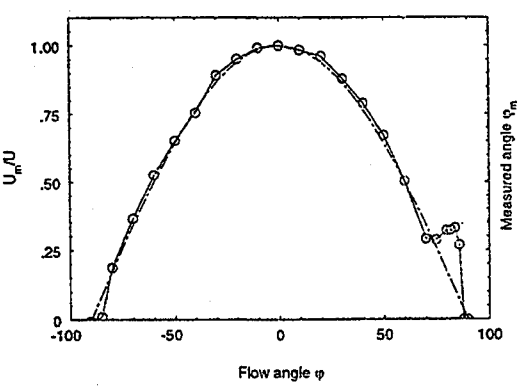

Fig.2 - Pitch response of 1D-PHWA

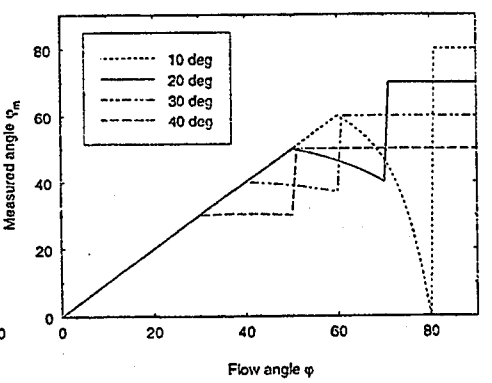

Fig.3 - Theoretical response of 2D-PHWA

ANGULAR RESPONSE OF PHWA

The wires in standard PHWA probes are made as long as the physical strength of the material allows. This is done to prevent heat tracers from escaping the probe without being detected and to move disturbing prongs as far from the measuring volume as possible. Typically used are 5µm Tungsten wires of length ~10 mm and spacing hot- to sensor wire ~1 mm. With these characteristics heat tracers leaving the probe without being detected are restricted to angles outside approximately the interval $\varphi \sim \pm 80 - 85°$ (where $\varphi = 0$ is the measuring direction). In addition there are critical regions stretching from approximately 60-70° to 80-85° where heat tracers are detected, but to some extent give erroneous results. This is due to phenomena such as flow interaction with prongs or probe stem and lateral diffusion of heat tracers. The extent and form of the critical response are heavily dependent upon choice of probe geometry and detection criteria.

Fig.2 shows the pitch response curve of the 1D-PHWA probe in fig.1. It follows the theoretical "cosine response" for most of the 180° range and escaping tracers are restricted to angles outside the interval $\pm 80 - 85°$. A serious deficiency however is the "bump" stretching from approximately +70 to +85° where instantaneous velocity vectors will be measured as considerably higher than their true physical velocities.

The impact this has got on measurements depends upon what has been termed "the structure of the turbulence field encountered"; i.e. to what extent the Probability Density Function (PDF) of instantaneous velocity vectors lies outside these intervals. In slanted wire

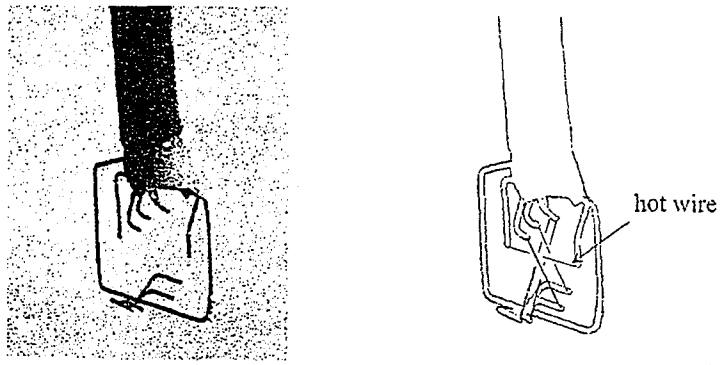

Fig.4 - The two dimensionsal pulsed hot wire probe (2D-PHWA)

measurements this may be extra critical due to that when the probe is slanted with respect to the dominant flow direction, the critical ranges will be pitched into more dominant flow angles and that their influence thus will be increased.

CHOICE OF 2D-PHWA PROBE GEOMETRY:

Fig.4 shows the prototype 2D-PHWA probe, where a single pulsed hot wire has been placed in the middle of a parallelogram formed by four detection wires. All wires have diameter 5μm and length 10 mm. The sensor wires are placed in two parallel pairs 0.5 mm from each other and 1 mm from the pulsed wire. A constructional difference from the 1D-probe is that all the detection wires have been connected to the same prong on the lower side of the probe. This simplifies the probe geometry considerably causing less flow interference than independent prongs would have done. The prong has in addition been formed as a closed frame in order to make it more rigid.

The probe measures two components of the velocity as the same heat tracer crosses two differently slanted detection wires at separate timings. The perpendiculars to the wires (and thus their slanting angle) define the directions α_ζ and α_η of the two measured velocity components u_ζ and u_η. These are then decomposed into Cartesian coordinates in the same manner as for crossed wire probes in CTA

$$u_m = c(u_\eta \sin\alpha_\zeta + u_\zeta \sin\alpha_\eta) \quad (2)$$

$$v_m = c(u_\eta \cos\alpha_\zeta - u_\zeta \cos\alpha_\eta) \quad (3)$$

where $c = (\sin\alpha_\zeta \cos\alpha_\eta + \sin\alpha_\eta \cos\alpha_\zeta)^{-1} = \sin^{-1}(\alpha_\zeta + \alpha_\eta)$ and the subscript 'm' signifies a measured value. If the probe is to be symmetrical the angles α_ζ and α_η should have the same value α. This gives the following relations for u_m, v_m and measured flow angle φ_m

$$u_m = c(u_\eta + u_\zeta)\sin\alpha \quad (4)$$

$$v_m = c(u_\eta - u_\zeta)\cos\alpha \quad (5)$$

$$\varphi_m = \arctan\left(\frac{v_m}{u_m}\right) = \arctan\left(\frac{u_\eta - u_\zeta}{u_\eta + u_\zeta} \cdot \frac{1}{\tan\alpha}\right) \quad (6)$$

To investigate the angular response we consider a high positive flow angle φ. u_η will in this case be correctly measured while u_ζ may be either too high due to the "bump" in the response (fig.2) or too low due to missing tracers. From the decomposition of eq.6 it is seen that a too high u_ζ makes φ_m become lower than the physical flow angle φ and that φ_m will equal $90^\circ - \alpha_\zeta$ when missing tracers make u_ζ become zero.

Based on this, regions of correct angular response are defined as limited by the lowest (in absolute value) erroneous measurement of $\varphi_m(\varphi)$. Limiting angles φ_l are then set by

$$\varphi_l = \min(\varphi_m|_{\varphi_m \neq \varphi}) \tag{7}$$

for each of the four extreme angles separately; i.e. when a measured instantaneous flow angle lies outside φ_l the velocity sample may be false and should be refused. Fig.3 is a response estimate based on the response of the 1D-probe; fig.2. It shows that choosing less than 30° slanting makes the probe "alias" high angle velocity vectors into lower angles and thus narrows the region of correct response, while slanting more than 30° narrows the region by moving the critical regions closer. Between 20° and 30° the angular limit is at a maximum having a value of $-40°$. The prototype probe shown in fig.4 has wire slanting angles of approximately 20° (the exact angles are found by pitch calibration).

Fig.5 shows the angular response of the probe as found by pitching the probe in a constant velocity low turbulence flow. The response is seen to be correct up to 40-45° both forwards and backwards, varying some for the different wires. The four limiting angles found by pitching the probe are used for filtering out false measurements in the data reduction routines by only accepting values inside the regions of correct response. In addition the data reduction routines count the number of refused pulses upwards $< \varphi_{lf+}, \varphi_{lb+} >$ and downwards $< \varphi_{lf-}, \varphi_{lb-} >$ separately by use of the same limiting angles.

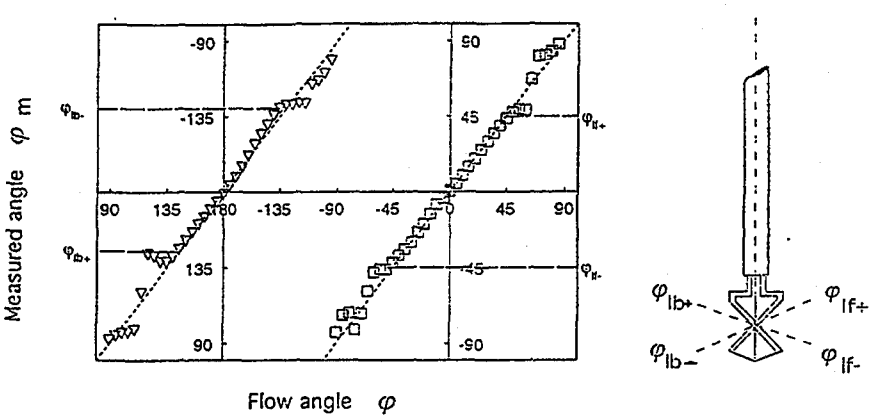

Fig.5 - Angular response of 2D-PHWA-probe (□ - forwards, ▽ - backwards)

TEST EXPERIMENT: WAKE BEHIND CYLINDER IN CROSS FLOW

The probe is basically constructed for measuring Reynolds stresses and time resolved information in separated flows. However, due to limited access to detailed experimental data in such flows we have chosen to test the probe in a flow where CTA can be used as a reference. The PHWA is designed for and performs best in highly turbulent flows. The near wake behind a circular cylinder in a cross flow was therefore chosen as a demanding test satisfying both these criteria.

The 2D-PHWA measurements were performed at a Reynolds number of 15800, and are compared against CTA crossed wire measurement at the slightly higher Reynolds number of 18400. The 2D-PHWA profile is taken at a location 8 cylinder diameters D downstream of the cylinder axis (x/D=8). It is compared with the CTA profiles at x/D = 4, 8 and 25 in order to get a physical impression of the size of any discrepancies between the two techniques. The CTA

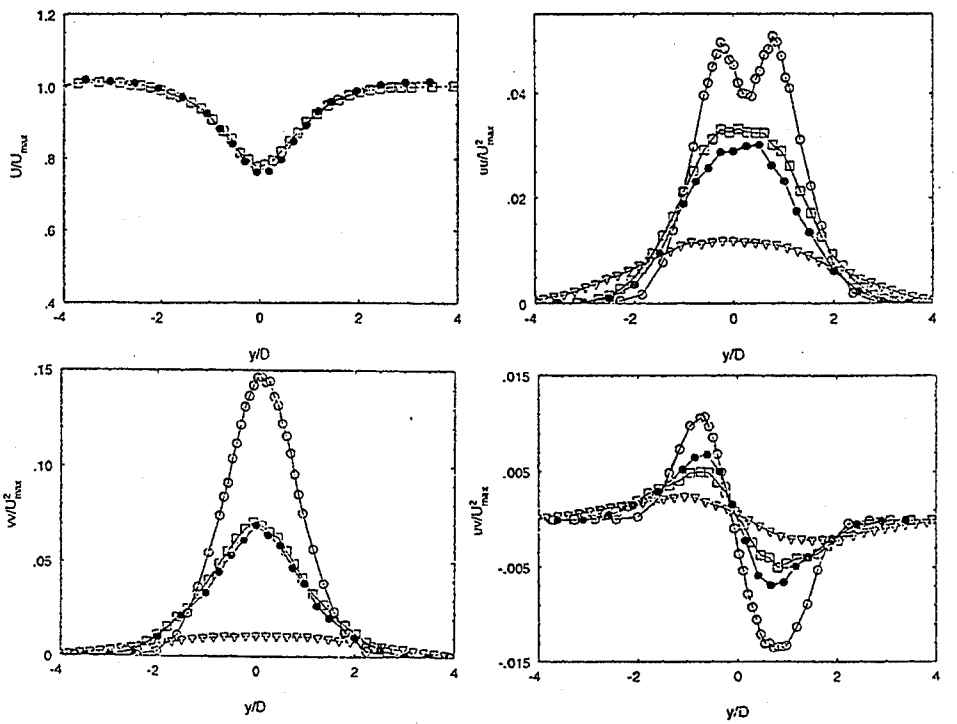

Fig.6 - The wake behind a circular cylinder. Comparison between 2D-PHWA (●) at x/D=8, and x-wire CTA at x/D=4 (○), 8 (□) and 25 (▽).

profile at x/D=25 is in good accordance with recently published results by Zhou and Antonia[5] at x/D=20 and this is taken as a good indication that the CTA results are representative for the flow tested. The results are shown in fig.6 in separate plots for U, $\overline{uu}$, $\overline{vv}$ and $\overline{uv}$; all normalised by the max. velocity U_{max} outside the wake.

The first crucial test was the similarity between the two techniques in mean velocity U. As we see in the upper left plot the differences are very small. This shows that the decomposition of velocity measured at to crossed pulsed wires is able to represent the velocity in the mean dominant flow direction. The maximum mean velocity deficit is found on the axis of symmetry and is U/U_m=0.76 with 2D-PHWA and U/U_m=0.78 with CTA. The width of the wake is found to be approximately 3D for both techniques.

The $\overline{uu}$ correlation shows a slight difference in value, but not in the distribution. The difference between the max. values are about 10%. In relative turbulence intensities based on local velocities this represents the difference between 22% and 23% and is considered as a reasonably good result. The $\overline{vv}$ results shown in the lower left plot is even better having a differences in values of the order less than 5%.

The only significant difference is found in the Reynolds shear stress $\overline{uv}$ where the difference between the max. values are approximately 30%. It is here to note that the flow has a relative turbulence intensity up to higher than 20% in U and 30% in V, and that the CTA measurements may be less accurate due to this high intensity. Comparing with the CTA measurements at x/D=4 and x/D=25 we see that the results by the two techniques at x/D=8 are relatively similar to each other compared to the results at the other locations. The conclusion

based on the experiment is that the 2D-PHWA has been shown able to measure the Reynolds stresses at a reasonable accuracy.

EXAMPLE OF USE: SEPARATED FLOW BEHIND MODEL HILL

The 2D-PHWA measurements in the wake of the cylinder showed no backflow. The turbulent fluctuations were small enough for all heat tracers to be detected forwards within the $< \varphi_{lf+}, \varphi_{lf-} >$ zone, i.e. within $\varphi = \pm 45°$ from the free stream direction. To test the probe in reversed flow we have used it in the separating and reattaching flow behind a wind tunnel model hill.

The incoming flow is a thick boundary layer 9 hill heights H thick. It separates at x/H=0.75 and reattaches at x/H=5.25. Figs.7 and 8 shows measured profiles at x/H=3; i.e. at the backward facing foot of the hill. The profile thus cross a fully separated region including mean backflow.The mean velocity profile in U as measured with 2D-PHWA shows good agreement with the 1D results except for some differences in the upper region of the recirculation zone. This is also the case for the turbulence intensity profiles in U; fig.8. The mean vertical velocity V is seen to be negative above, and in the upper part of the recirculation zone. It changes sign at the same location as the U velocity, signifying the backward flow up the hill towards the point of separation. Further, the turbulence intensity of the V velocity is seen to be smaller than that of the U velocity in the whole region measured. As expected the max. intensities of all Reynolds stresses including the shear stress are found at the height of the max. mean velocity gradient. More thoroughly documented results from this case are to be published later.

CONCLUSION:

The 2D-PHWA technique developed has been shown to give easily accessible and reasonable results in complicated and highly turbulent flows. Based on initial measurements the accuracy of the technique seems relatively good.

ACKNOWLEDGEMENT:

We would like to thank the Norwegian Civil Aviation Authority for supporting us financially and for always showing interest in our work.

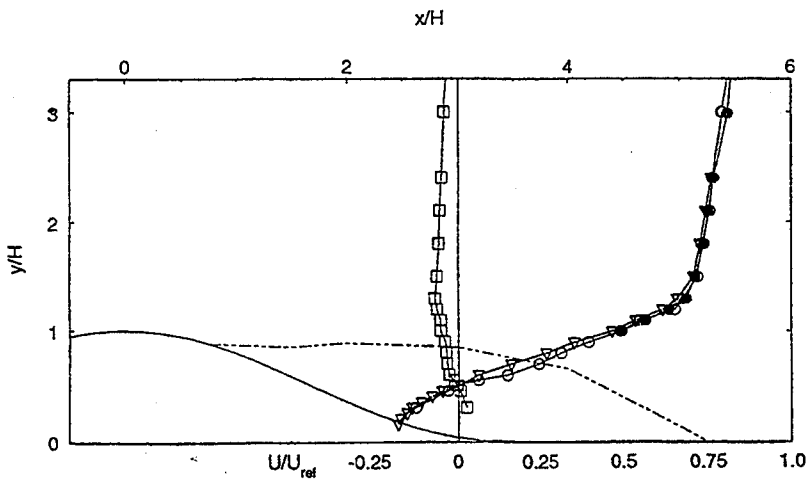

Fig.7 - Mean velocities behind model hill; 2D-PHWA: U (o), V (□); 1D-PHWA: U (▽).

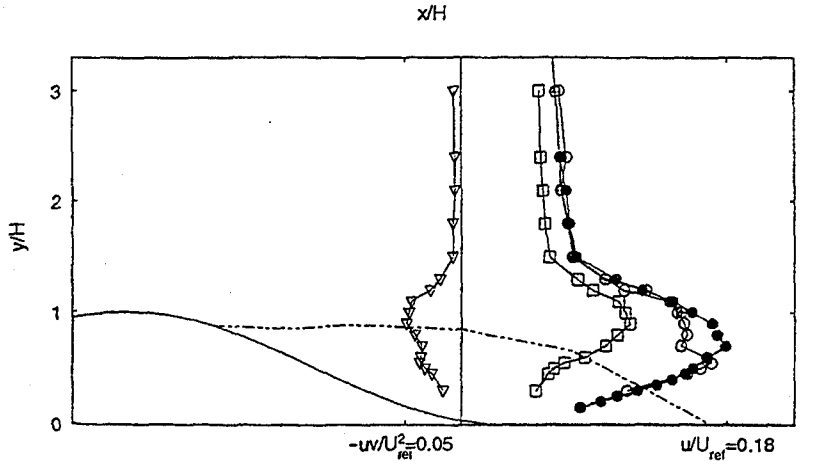

Fig.8 - Reynolds stresses behind model hill; 2D-PHWA: $\sqrt{\overline{uu}}/U_{ref}$ (○), $\sqrt{\overline{vv}}/U_{ref}$ (□), $\overline{uv}/U_{ref}^2$ (▽); 1D-PHWA: $\sqrt{\overline{uu}}/U_{ref}$ (●).

REFERENCES:

(1) Bradbury L.J.S. and Castro I.P., ' A pulsed-wire technique for measurements in highly turbulent flows', Journal of Fluid Mechanics, vol.49, 1971

(2) Castro I.P. and Cheun B.S., 'The measurements of Reynolds stresses with a pulsed wire anemometer', Journal of Fluid Mechanics, vol.118, 1982

(3) Dinat M. and Castro I.P., 'Turbulence in a separated boundary layer', Journal of Fluid Mechanics, vol.226, 1991

(4) Hanford P.M. and Bradshaw P., 'The pulsed-wire anemometer', Experiments in Fluids, vol.7, 1989

(5) Zhou Y. and Antonia R.A., 'Effect of initial conditions on vortices in a turbulent near wake', AIAA JOURNAL, vol.32, 1994

ON THE IMPORTANCE OF CORRECTIONS FOR VELOCITY COMPONENTS AND FLOW GRADIENTS NORMAL TO THE WIRE PLANE OF AN X HOT-WIRE

GOODEN J.H.M.

National Aerospace Laboratory NLR
The Netherlands

ABSTRACT

X hot-wire measurements are subjected to errors both due to velocity components in the binormal direction (being the direction normal to the plane of the wires) and due to velocity gradients in the binormal direction. The probe normally is aligned with the mean flow direction which minimises errors due to the binormal velocity component. Flow gradient errors can not be countered in this way. A correction method is described which allows a post-measurement correction of the results obtained from X hot-wire measurements for both error sources. For this purpose the concept of a 'nett effective cooling velocity fluctuation' is introduced. The method has been applied to hot-wire measurements of the mean and fluctuating flow velocities in a 3D turbulent flow and in the turbulent wake shed from a two-dimensional wing above a single trailing edge flap. Spatial gradients, not only in the mean flow velocity vector, but also in the Reynolds-stress components, are shown to be of importance.

1 INTRODUCTION

X-wires are a popular tool to measure the turbulence properties of a flow. The probe volume is small and manufacturing, repair and calibration are relatively simple. However, the X-wire is incapable of measuring the full instantaneous velocity vector, contrary to e.g. 3 or 4 wire probes. In principle, the correct processing of X-wire results requires the unknown, time-dependent, binormal velocity component to be known. It turns out that binormal velocity components can be neglected in low turbulence level flows, provided the X-wire is positioned such that the mean velocity vector is in the plane of the wires. In practice these conditions can not always be obtained. In that case a correction of the results for binormal mean and fluctuating velocity components soon becomes necessary.

Besides, due to the spatial dimensions of X-wires (or multi wire probes in general), flow gradients both in the direction normal to the wire plane as well as along the wire may affect the results. The latter generally are not taken into account because their influence on the effective cooling velocity is an order of magnitude less than the influence of the binormal gradients as can be inferred from the data given by Gessner and Moller[1]. On the contrary, binormal flow gradients may seriously affect the results obtained (Wallace[2], Bruun[3]) requiring appropriate correction methods. Although this paper specifically deals with a gradient correction procedure for X-wires, extension of the method to 4-wire probes - being a combination of 2 X-wires - is straightforward.

Gradient effects can be reduced by decreasing the distance between the wires. In order to avoid wake interference between the wires a reduction of the wire length and, to conserve wire aspect ratio, wire diameter will be necessary (Vagt[4]). This leads to very small probes as have been used by e.g. Ligrani[5]. These probes are very fragile and will give rise to operational difficulties as frequent wire breakage and recalibration. Nevertheless, when measuring in close proximity to a wall the reduced turbulent lenghtscales often leave the experimenter no choice in this respect.

Hirota et al[6] used two anti-symmetric X-wire probes. This method gives good results provided the wire distances are within a narrow margin for both probes, requiring probe production techniques of very high standard.

Another possible solution might be using a single rotating slanted wire, which eliminates the wire distance. Using this method it appears to be difficult, however, to get accurate values of the crosswise turbulence intensities (Fujita and Kovasznay[7]).

So, several ways exist to eliminate or reduce gradient effects, all of them requiring adapted instrumentation to be used already during the experiment. In

this paper a method is described which offers the possibility of performing corrections for both the binormal velocity components, as mentioned before, and binormal gradients while using a single, standard, X-wire probe. The corrections can be applied afterwards in the data processing phase.

First, mean flow and turbulence results will be obtained from the hot-wire response equations supposing binormal components and flow gradients to be given. During dataprocessing the binormal components are obtained from data measured with the X-wire rolled 90 degrees and gradients from data at surrounding traverse points. This leads to an iterative data processing scheme in which the results and corrections are improved from step to step.

The method, which requires no adapted instrumentation, can be applied in 2D and 3D flows but is limited to moderate turbulence intensity and gradient levels. Some results obtained in the 3D boundary layer above a wing and in a 2D viscous wing wake above a trailing edge flap will be shown.

2 DIRECTIONAL SENSITIVITY OF HOT-WIRE

The directional response of a hot-wire is often written in the form of a 'cooling law' giving the relation between the actual velocity magnitude and direction and the 'effective cooling velocity', being the velocity that is effectively sensed by the probe. The effective cooling velocity Q_e is determined from the measured hot-wire voltages using a velocity calibration of the wire. The directional response of a hot-wire is influenced by the angular sensitivity of the hot-wire filament itself and the probe geometry. In order to describe the directional response, first the coordinate systems connected to the hot-wire probe and hot-wires themselves are defined (figure 1). The coordinate system x'y'z' is connected to the hot-wire probe, with the x'-axis coinciding with the longitudinal axis of the probe body, the y'-axis directed parallel to the probe stem and perpendicular to the x'-axis. The wire-plane $x_w z_w$ is nominally parallel to both wires. x_w always coincides with the probe longitudinal axis x'. The related velocity components U_w, V_w and W_w are shown in figure 2.

The local mean flow velocity vector Q is decomposed into the components Q_r, Q_p and Q_n. Velocities Q_r and Q_p are in the wire plane with Q_r orthogonal to the wire and Q_p parallel to the wire. The velocity component Q_n is normal to the wire plane. The cooling law is often written in the form first proposed by Jorgensen[9], who included the binormal cooling contribution in the 2D cooling law of Hinze[10]:

$$Q_e^2 = Q_r^2 + k_p^2 Q_p^2 + k_n^2 Q_n^2$$

k_p and k_n are determined from angular calibrations. In general, k_p is in the range 0.0 to 0.2 for gold-plated and to 0.4 for unplated wires. The coefficient k_n may vary between 1 and 1.05 for gold-plated and go up to 1.1 for unplated wires, see e.g. Vagt[4] or Jorgensen[9]. Expressed in the mean flow angles δ_w and φ_w, the Jorgensen cooling law obtains the form:

$$Q_e^2 = Q^2\left[\left\{\cos^2(\gamma + \varphi_w) + k_p^2 \sin^2(\gamma + \varphi_w)\right\}\cos^2\delta_w + k_n^2 \sin^2\delta_w\right] \qquad (1)$$

The Hinze/Jorgensen law requires the wire angle γ to be known. In principal this value has to be determined under operating conditions. In practice it is often measured using a microscope. However, the coefficient k_p is very sensitive to errors in the measured geometric wire angle, resulting in a non-constant value of k_p with varying flow direction. Therefore, the best solution is to determine both k_p as well as γ from an angular calibration with the velocity vector in the wire plane. (For the examples shown later on the effective wire angle cooling law formulation as proposed by Bradshaw[11] is used, obtained by putting k_p equal to 0 and getting only γ from an angular calibration).

3 DETERMINATION OF MEAN FLOW QUANTITIES

The distance of each wire to the x_w-axis is assumed to be b/2 (figure 3).

The following first-order relations are being used to incorporate the time mean flow gradients in the relevant equations (j = wire index, *lower* sign for wire number 1):

$$Q_j = Q \pm \frac{b}{2} \frac{\partial Q}{\partial y_w} \quad ; \quad \varphi_{w_j} = \varphi_w \pm \frac{b}{2} \frac{\partial \varphi_w}{\partial y_w} \quad ; \quad \delta_{w_j} = \delta_w \pm \frac{b}{2} \frac{\partial \delta_w}{\partial y_w}$$

Q, φ_w, δ_w are the time mean values at the probe axis and the values indexed j are taken at the respective wire centers. In order to determine Q and φ_w, supposing δ_w and the gradient terms to be known, these relations are substituted in the cooling law, equation (1). Rewriting the cooling law to expose the unknowns one gets:

$$Q_{e_j}^2 = Q^2 \, C_{1_j} [C_{2_j} \cos 2\varphi_w - C_{3_j} \sin 2\varphi_w + C_{4_j}] \qquad (j=1,2) \qquad (2)$$

with:

$$C_{1_j} = \left[1 \pm \frac{b}{2} \frac{1}{Q} \frac{\partial Q}{\partial y_w}\right]^2$$

$$C_{2_j} = \frac{1}{2} (1 - k_{p_j}^2) \cos\left[2 \gamma_j \pm b \frac{\partial \varphi_w}{\partial y_w} \right] \cos^2\left[\delta_w \pm \frac{b}{2} \frac{\partial \delta_w}{\partial y_w} \right]$$

$$C_{3_j} = \frac{1}{2} (1 - k_{p_j}^2) \sin\left[2 \gamma_j \pm b \frac{\partial \varphi_w}{\partial y_w} \right] \cos^2\left[\delta_w \pm \frac{b}{2} \frac{\partial \delta_w}{\partial y_w} \right]$$

$$C_{4_j} = \frac{1}{2} \cos^2\left[\delta_w \pm \frac{b}{2} \frac{\partial \delta_w}{\partial y_w} \right] \left\{ 1 + k_{p_j}^2 + 2 k_{n_j}^2 \tan^2\left[\delta_w \pm \frac{b}{2} \frac{\partial \delta_w}{\partial y_w} \right] \right\}$$

Eliminating Q from the resulting cooling laws, eq.2, for both wire 1 and 2 gives:

$$F_1 \cos 2\varphi_w - F_2 \sin 2\varphi_w = F_3 \qquad (3)$$

with:

$$F_1 = C_{1_2} C_{2_2} Q_{e_1}^2 - C_{1_1} C_{2_1} Q_{e_2}^2$$

$$F_2 = C_{1_2} C_{3_2} Q_{e_1}^2 - C_{1_1} C_{3_1} Q_{e_2}^2$$

$$F_3 = C_{1_2} C_{4_2} Q_{e_1}^2 - C_{1_1} C_{4_1} Q_{e_2}^2$$

The solution of equation (3) can then be written as:

$$\varphi_w = \frac{1}{2} \arctan(F_1/F_2) - \frac{1}{2} s_1 \arcsin\left[F_3 \Big/ \sqrt{(F_1^2 + F_2^2)}\right] \quad ; \quad s_1 = \gamma_1/|\gamma_1|$$

(smallest angles taken, s_1 is introduced in order to correct for arcsin-sign changes).

Note that the above equations in principle only hold for the instantaneous values and that taking the time mean would formally introduce higher order terms as well. Introduction of these terms for hot-wire probes unable of measuring the full instantaneous velocity vector, like single and X-wire probes, is rather questionable. Error analysis shows that the errors introduced by deleting the higher order terms for these probes may even be counteracted by the errors occuring due to voltage averaging instead of analog (or digital!) linearization as was already shown by Hinze[10].

Substitution of this flow angle in the cooling law for one of the two wires gives the magnitude of the velocity vector Q. Again, for moderate turbulence levels, the time mean values of Q_e and φ_w are directly substituted in equation 2. In this way values of Q and φ_w are obtained that are corrected for (given) gradients and binormal flow components.

4 DETERMINATION OF TURBULENCE QUANTITIES

The cooling law describes the relation between the effective cooling velocity, the actual velocity magnitude Q and the flow angles φ_w and δ_w. Fluctuations in the probe-axes velocity components U_w, V_w and W_w are called u_w, v_w and w_w respectively. Turbulence levels are assumed low enough to allow linearization in the fluctuations (index j again indicates conditions at the centre of wire j):

$$q_{e_j} = A_j\, u_{w_j} + B_j\, v_{w_j} + C_j\, w_{w_j} \tag{4}$$

with

$$A_j = \frac{Q_j}{Q_{e_j}} \left[\cos\gamma_j \cos(\gamma_j + \varphi_{w_j}) + k_{p_j}^2 \sin\gamma_j \sin(\gamma_j + \varphi_{w_j})\right] \cos\delta_{w_j}$$

$$B_j = k_{n_j}^2 \frac{Q_j}{Q_{e_j}} \sin\delta_{w_j}$$

$$C_j = -\frac{Q_j}{Q_{e_j}} \left[\sin\gamma_j \cos(\gamma_j + \varphi_{w_j}) - k_{p_j}^2 \cos\gamma_j \sin(\gamma_j + \varphi_{w_j})\right] \cos\delta_{w_j}$$

For a standard ±45° X-wire A_j and C_j are around $1/\sqrt{2}$, whereas B_j is of order δ_w. This is the reason why the binormal fluctuation v_w may be neglected for X-wire measurements when the mean velocity vector is located in the wire plane (δ_w=0).

First, it is assumed that there are no gradients present. In case of a non-negligible wire-plane upflow angle δ_w and binormal fluctuation v_w the latter is considered as a known correction term. A 'nett effective cooling velocity fluctuation' q_{e_w} is introduced. This nett effective cooling velocity can be considered as the one the wire would generate in absence of binormal components:

$$q_{e_{w_j}} = q_{e_j} - B_j\, v_w = A_j\, u_w + C_j\, w_w \qquad (u_{w_j} = u_w, \text{ etc.}) \tag{5}$$

The velocity components forming part of the Reynolds stresses to be solved are left on the right-hand side. Combination of this relation for both wires leads to a set of 3 equations and 3 unknowns, which, after inversion, directly results in the relations between the wire plane Reynolds-stress tensor components at the probe axis and the time mean-square of the nett effective cooling velocity fluctuations:

$$\begin{bmatrix} \overline{u_w^2} \\ \overline{u_w w_w} \\ \overline{w_w^2} \end{bmatrix} = \frac{1}{4(A_2C_1 - A_1C_2)^2} \begin{bmatrix} (C_1-C_2)^2 & -2(C_1^2-C_2^2) & (C_1+C_2)^2 \\ -(A_1-A_2)(C_1-C_2) & 2(A_1C_1-A_2C_2) & -(A_1+A_2)(C_1+C_2) \\ (A_1-A_2)^2 & -2(A_1^2-A_2^2) & (A_1+A_2)^2 \end{bmatrix} \begin{bmatrix} \overline{(q_{e_1}+q_{e_2})_w^2} \\ \overline{(q_{e_1}^2-q_{e_2}^2)_w} \\ \overline{(q_{e_1}-q_{e_2})_w^2} \end{bmatrix} \qquad (6)$$

In case of a flow with gradients of the Reynolds stress components in the binormal direction both hot-wires experience slightly different turbulence properties. A first order relation between the fluctuating velocity component and y_w is taken:

$$u_{w_j} = u_w \pm \frac{b}{2}\frac{\partial u_w}{\partial y_w} = u_w \pm du_w \quad ; \quad \text{ditto: } v_{w_j}, \; w_{w_j}$$

The relation between fluctuating effective cooling velocity and velocity components for each wire, equation 4, can then be written as (j = wire index, minus sign for wire 1):

$$q_{e_j} = A_j \; (u_w \pm du_w) + B_j \; (v_w \pm dv_w) + C_j \; (w_w \pm dw_w)$$

Coefficients A_j, B_j and C_j are evaluated at the corresponding wire locations. Combining the relations of both wires and taking the time mean values, again gives a set of nett effective cooling velocity equations, which include the binormal and gradient contributions. All gradients occurring are derivable from measured tensor components. For this purpose higher order gradient terms of the type $\overline{du_i du_j}$ as well as terms of the shape $\overline{u_i du_j} - \overline{u_j du_i}$ are neglected. However, these terms give no significant contribution in general either because the term itself or because the coefficient in front of it is small, as has been shown in Gooden[8].

The resulting set of nett mean-square effective cooling velocity terms again can be considered as the ones that would be generated by the wires in absence of binormal velocity (v_w)-components and Reynolds stress gradients: So, they may be directly substituted in eq. (6) in order to obtain the Reynolds-stress components $\overline{u_w^2}$, $\overline{w_w^2}$ and $\overline{uw_w}$:

$$\begin{aligned} \overline{(q_{e_1} \pm q_{e_2})_w^2} = \; & \overline{(q_{e_1} \pm q_{e_2})^2} \\ & - (B_1 \pm B_2)^2 \overline{v_w^2} \; - \; 2(A_1 \pm A_2)(B_1 \pm B_2)\, \overline{u_w v_w} \; - \; 2(C_1 \pm C_2)(B_1 \pm B_2)\, \overline{v_w w_w} \\ & + (A_1^2 - A_2^2)\, d(\overline{u_w^2}) \; + \; (B_1^2 - B_2^2)\, d(\overline{v_w^2}) \; + \; (C_1^2 - C_2^2)\, d(\overline{w_w^2}) \\ & + 2(A_1B_1 - A_2B_2)\, d(\overline{u_w v_w}) + 2(A_1C_1 - A_2C_2)\, d(\overline{u_w w_w}) + 2(B_1C_1 - B_2C_2)\, d(\overline{v_w w_w}) \end{aligned} \qquad (7)$$

and:

$$\begin{aligned} \overline{(q_{e_1}^2 - q_{e_2}^2)_w} = \; & \overline{(q_{e_1}^2 - q_{e_2}^2)} \\ & - (B_1 - B_2)^2 \overline{v_w^2} \; - \; 2(A_1B_1 - A_2B_2)\, \overline{u_w v_w} \; - \; 2(B_1C_1 - B_2C_2)\, \overline{v_w w_w} \\ & + (A_1^2 + A_2^2)\, d(\overline{u_w^2}) \; + \; (B_1^2 + B_2^2)\, d(\overline{v_w^2}) \; + \; (C_1^2 + C_2^2)\, d(\overline{w_w^2}) \\ & + 2(A_1B_1 + A_2B_2)\, d(\overline{u_w v_w}) + 2(A_1C_1 + A_2C_2)\, d(\overline{u_w w_w}) + 2(B_1C_1 + B_2C_2)\, d(\overline{v_w w_w}) \end{aligned}$$

5 DATA ACQUISITION AND PROCESSING

In the foregoing $\overline{v_w v_w}$, $\overline{u_w v_w}$ and $\overline{v_w w_w}$ as well as the flow gradients in the binormal direction have to be known. The v_w-terms are obtained directly from X-wire measurements with a 90° rolled probe. The flow gradients are obtained from measurements at various positions along a traverse, preferably taken in the direction of the largest flowgradients. In case of boundary layers and wakes, traverses usually are performed normal to the wall or normal to the wake which suits this condition. Gradients in directions orthogonal to this one may then be assumed zero. This implies that the method requires no additional measurements to be performed. All corrections can be applied during the dataprocessing stage of the experiment, which saves tunnel time. Moreover, the correction can even be applied to previously obtained data-sets.

The hot-wire data are processed as shown schematically in figure 4. During the first iteration loop, the gradient and binormal flow component corrections are assumed to be zero, which results in uncorrected mean and turbulent flow quantities. From these, binormal contributions and gradients are determined and the hot-wire data are then processed again, giving improved results and corrections. This process is repeated until convergence of the Reynolds stress results is obtained. Generally, this is the case within a few iteration loops, depending on the level of the gradients.

6 SOME RESULTS

6.1 GARTEUR 3D SHEAR LAYER EXPERIMENT

The first example of application of the method is taken from the GARTEUR 3D shear layer experiment[13]. For the purpose of this example, flowgradients have been assumed zero, to elucidate the effect of binormal flow components. The hot wire probe used, is of NLR-design and offers the possibility to rotate the probe around its longitudinal axis in steps of 45 degrees in order to be able to measure the full Reynolds stress tensor. Measured data are composed of results obtained at 6 probe rolling angles. The tungsten sensor wires, having a wire diameter of 5 μm, were obtained from DANTEC. The wire ends were goldplated, giving an active sensor length of 1.25 mm, and the distance between the wires, measured by means of a microscope, was equal to b = 1.1 mm.

Figure 5.a shows 3 Reynolds stresses in the probe axis system with (drawn lines) and without (symbols) correction for fluctuations normal to the wire plane. Due to the large boundary layer yaw and the unusual model geometry the probe upflow angle increased to around 12 degrees over the traverse at the station shown (68% span, suction side trailing edge). The large effect, especially on u_p^2, is clear. In a subsequent angular transformation of the Reynolds stresses from probe to boundary layer axis system (index b, Zb being normal to the local surface), the errors in the normal stresses are strongly multiplied in the resulting transformed shear stress. This is seen from figure 5.b, showing the difference in the main shear stress $\overline{u_b w_b}$ using either the corrected or the uncorrected probe system Reynolds stresses from figure 5.a.

6.2 NLR 7301 WING WAKE ABOVE FLAP

The second application shown concerns measurements in the two-dimensional turbulent wing wake above a trailing edge flap (Gooden and Van Lent[14]). The elementary airfoil section is NLR 7301. The results shown are taken from station 13 (figure 6) at 13.1 degrees angle of attack. Like the measurements in the previous example these were performed in the 3 x 2.25 m^2 low-speed wind-tunnel at NLR. The hot-wire probe used was also the same but for this 2D test measurements were only done at 4 probe rolling angles.

In a 2D flow like the one shown here significant gradients only are present in the direction normal to the wall. The data have been processed, therefore, assuming gradients perpendicular to the traversing direction as well as $\overline{v_w w_w}$ in

eq.(7) to be equal to zero. As far as the mean flow components are concerned, only the gradient in the mean flow vector magnitude has a significant value, ranging to $\partial(Q/U_\infty)/\partial(Y_w/b) = 0.07$. Gradients in the Reynolds normal stresses and principal shearstress are all around $\partial(\overline{u_i u_j}/Q^2)/\partial(Y_w/b) = 0.001$, except for $\overline{u_w^2}$, which is twice as large.

The hot-wire results (figure 6) are given in the local wind axis-system with q pointing in the direction of the local mean flow velocity vector and s being perpendicular to the traversing direction. A comparison of the results for the crossflow angle β_r and the Reynolds shear stress $\overline{qs}$,which both should equal zero for a 2D flow, shows the large gradient impact on the uncorrected results. These are data measured with the wire plane parallel to the local wing surface giving the largest gradients across the wires. The effects of mean-flow gradients and Reynolds-stress gradients on the Reynolds shear-stress have been separated. From this the importance of gradients in the turbulence components is seen. From an order of magnitude consideration, given in Gooden and Van Lent[8] it can be seen that gradients in the normal stresses are mainly determining the correction on the shear stress. Reffering to the magnitude of the principal shear stress it can be seen that the Reynolds shear stress direction would be as much as 10 degrees off without correction. Despite some slight three-dimensionality in the flow, it is clear that gradient corrections substantially improve the quality of the resulting data in this case.

7 CONCLUSIONS

The influence of flow gradients on the response equations for X-wires has been determined for the case in which turbulence and gradient levels are moderate. A dataprocessing technique is proposed which enables corrections for flow gradients as well as binormal velocity components on measured data obtained from traverses with a usual X-wire probe. The corrections can be applied afterwards.

The following conclusions can be drawn:

- When performing hot-wire measurements, a critical estimation of the errors occurring due to flow gradients perpendicular to the plane of the wires should always be made in case X-wires are used. It should be determined whether these errors occur in the quantities of interest to be measured.
- The application of flow gradient corrections is demonstrated using detailed turbulence measurements that have been performed in a three-dimensional boundary layer and the heavily loaded wake above a single trailing edge flap. Both binormal components and mean flow as well as turbulence gradients have been shown to be of importance.

REFERENCES

1. Gessner, F.B., and Moller, G.L., Response behaviour of hot-wires in shear flow. J.Fluid Mech. 47, 449-468 (1971)
2. Wallace, J.M., Methods of measuring vorticity in turbulent flows. Exp. Fluids 4, 61-71 (1986)
3. Bruun, H.H., Hot wire data corrections in low and in high turbulence intensity flows. J.Phys.E: Sci.Instr. 5, 812-818 (1972)
4. Vagt, H.D., Hot-wire probes in low speed flow. Progr. Aerosp. Sci., vol. 18, pp. 271-323 (1979)
5. Ligrani, P.M., and Bradshaw, P., Subminiature hot-wire sensors: development and use. J.Phys.E: Sci. Instr. 20, 323-332 (1987)
6. Hirota, M., Fujita, H., and Yokosawa, H., Influences of velocity gradient on hot-wire anemometry with an X-wire probe. J.Phys.E: Sci.Instr. 21, 1077-1084 (1988)
7. Fujita, H., and Kovasznay, S.G., Measurement of Reynolds stress by a single rotated hot-wire anemometer, Rev. Sci. Instr. 39, 1351-1355 (1968)
8. Gooden, J.H.M., and Van Lent, M.L., Flow gradient corrections on hot-wire measurements using an X-wire probe. 12th Symposium on Turbulence, Rolla,

Missouri (1990)
9. Jorgensen, F.E., Directional Sensitivity of Wire and Fiber-film probes: An experimental Study. Disa information nr. 11 (1971)
10. Hinze, J.O., Turbulence. McGraw-Hill (1959)
11. Bradshaw, P., An introduction to Turbulence and its measurements. New York: Pergamon (1971)
12. Gooden, J.H.M., Correction of X hot-wire measurements for gradients normal to the plane of the wires. NLR TR 92311 L, (1992)
13. B.v.d. Berg: "A European collaborative investigation of the 3D turbulent shear layers of a swept wing" AGARD CP 438, 1988
14. Gooden, J.H.M., and Van Lent, M.L., Measurements in the two-dimensional turbulent wing wake above a trailing edge flap (data report). NLR CR 89274 C (1989)

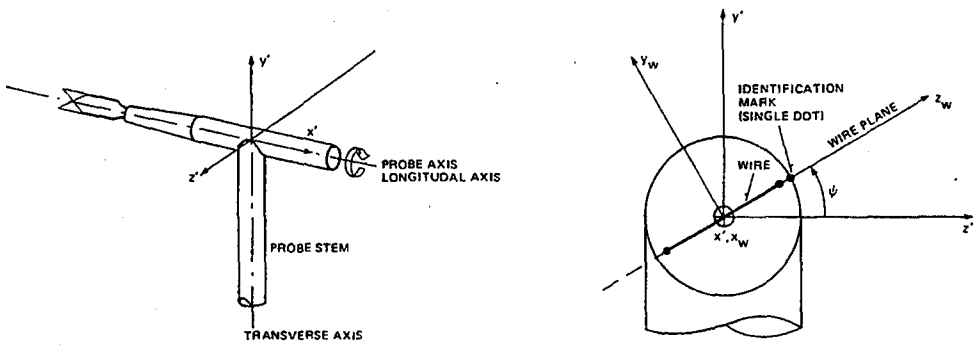

a) probe coordinate system b) wire coordinate system

Fig.1.Definition of hot-wire coordinate systems (x',y',z' and x_w, y_w and z_w)

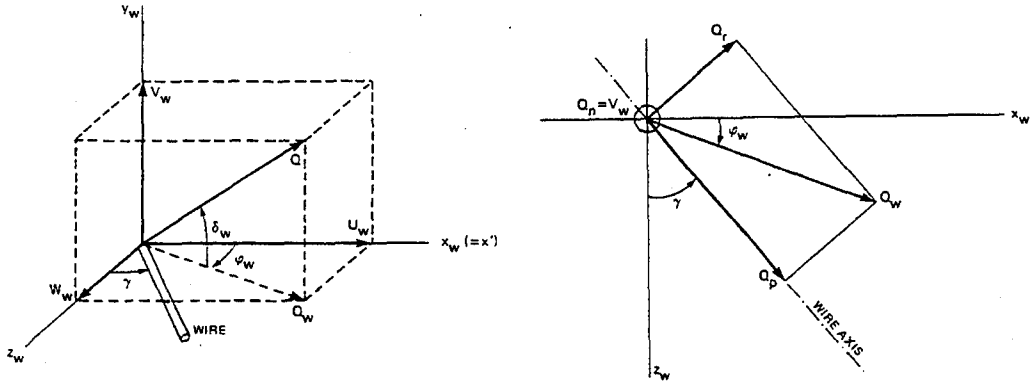

a) Velocity components in wire coordinate system b) Components of cooling velocity

Fig.2. Decomposition of velocity vector Q

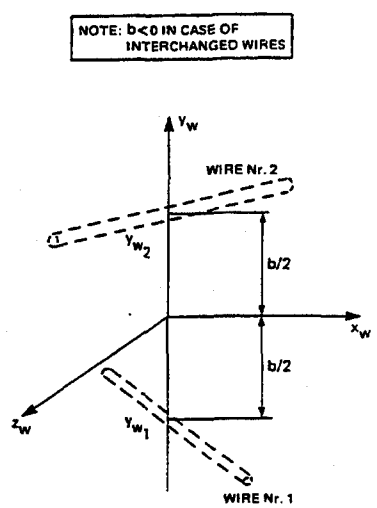

Fig.3. Definition of wire distance for gradient correction

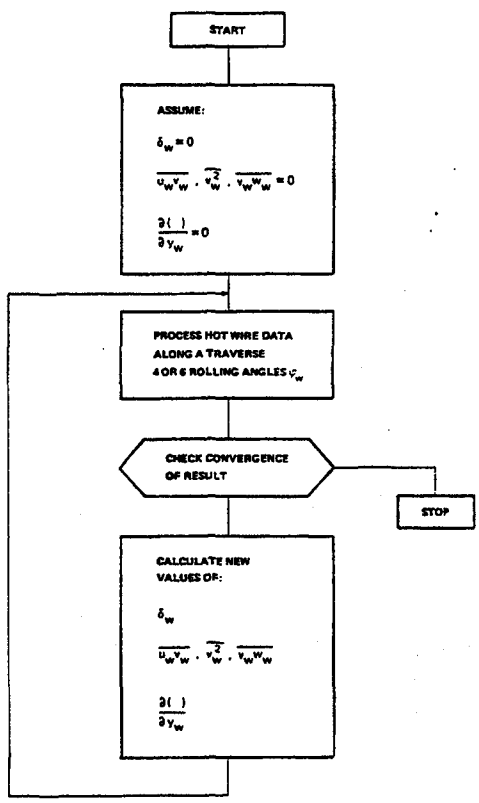

Fig.4. Hot-wire data processing scheme

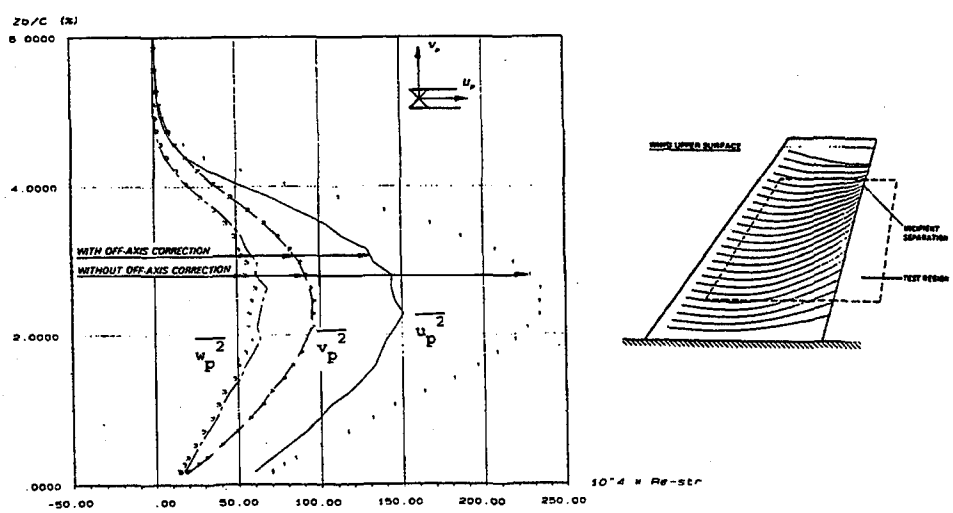

Fig.5.a Garteur 3D shear layer experiment: Influence of binormal fluctuation correction on probe frame Reynolds stresses

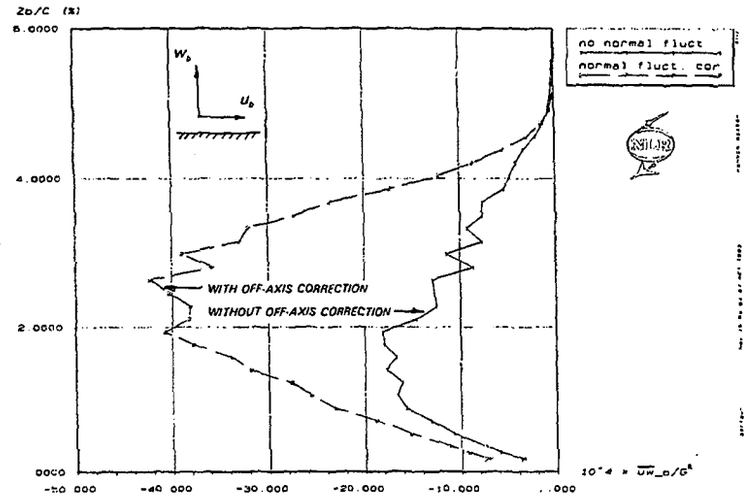

Fig.5.b Garteur 3D shear layer experiment: Shearstress in surface coordinate system, resulting after transformation of corrected/uncorrected Reynolds stresses.

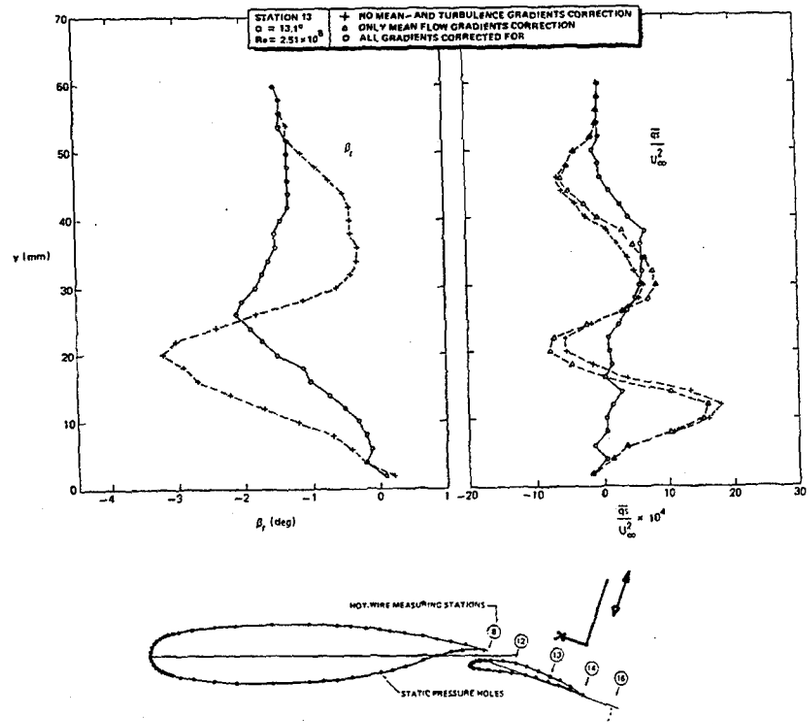

Fig.6. Wake above flap: effect of gradient corrections on crossflow angle β_r and shear stress component $\overline{qs}$

LDV Investigation Of A 90 Degree Square Duct Bifurcation

D.Lytras and D.S.Mathioulakis
National Technical University of Athens (Greece)
Dept. of Mechanical Engineering, Fluids Section

Introduction

The flow behaviour in duct branchings has attracted the early interest of fluid mechanics researchers due to the great number of engineering applications. More recently this interest has been enhanced because of the strong indications that problems associated with the human circulatory system like thrombosis and atherosclerosis initiate from arterial bifurcations.

The main features of the flowfield in the vicinity of a duct bifurcation are the recirculation zones and the secondary flows, the shape and size of which depend primarily on the Reynolds number, the Dean number, the angle of bifurcation and the volume flow rate ratio of the two branches. These quite complex flow patterns were initially investigated by experimentalists by carrying out pressure measurements or employing flow visualization techniques which however did not provide quantitative details of the flow. With the advent and progress of hot wire and Laser Doppler Velocimeters, the point by point velocity measurements provided a more comprehensive analysis of the flow as well as data for comparison with relevant analytical and numerical results.

Many works both numerical and experimental have been reported in the past concerning the flow behaviour near duct branchings for various branch angles, Reynolds numbers (Re) and flow volume rate ratios. Brech and Bellhouse[1] performed hot film velocity and shear stress measurements in a 45 degree bifurcation under steady and unsteady inlet conditions. Rodkievitz and Roussel[2] employing a hydrogen bubble flow visualization technique for various branch angles observed the characteristic separated flow regions as well as vortex shedding in the recirculating region of the main duct. One component LDA measurements were performed by Liepsh and Moravec[3] in a T-shape junction of a two dimensional duct for a Re smaller than 1200. The influence of Re and flow rate ratio on recirculation zones was numerically examined by Hayes et al[4] for a 90 degree bifurcation of a two dimensional duct. Samagaio and Vlachos[5] using a finite difference scheme compared their numerical findings with experimental ones for a two dimensional bifurcation and extended their calculations to a three dimensional configuration (a square duct) in order to study the influence of the secondary flow. Liepsh[6] in a review paper includes measurements of steady and pulsatile flow of a T-shape bifurcation of a circular duct using Newtonian and non Newtonian fluids. Secondary flow in a 60 degree symmetrical bifurcation was measured by Rieu et al[7] using a pulsed Doppler ultrasound velocimeter, whereas Yung et al[8] studied numerically a similar model, showing that helical flow was significant up to about 22 duct diameters downstream of the bifurcation.

Since the existing literature is referred only to bifurcations of two dimensional or circular ducts, the present work aimed at providing experimental evidence for the case of a 90 degree square duct bifurcation using an one component LDA system for the velocity measurements as well as flow visualization for a more global presentation of the flow field and its instabilities like shear layer movement and vortex shedding.

Experimental facilities

The experimental lay-out used is shown in Fig.1. Water flowed by gravity between two overflow tanks (having a free surface elevation difference of 2.7m) through the 90^0 bifurcation model, whereas a centrifugal pump circulated the water between the two tanks.

The model (Fig.2), positioned in an inverted T-fashion on a vertical plane, was made of 12mm thick plexiglass walls, had a $40x40mm^2$ square cross section and it was connected to three circular ducts of 40mm inner diameter. The circular duct's straight portion upstream of the model was 90 diameters long, while the square duct section, upstream of the bifurcation apex was 8 diameters long. In each of the two branches of the model a ball type vane and a volume meter were installed in order to control both the volume flow rate ratio and the inlet Reynolds number.

One component velocity measurements were performed using a Laser Doppler Velocimeter (LDV) operating in the forward scattering mode. The light beam of a 17mW Melles-Griot He-Ne Laser was split into two parallel beams, one of which passed through a bragg-cell offering the capability of detecting flow reversals. The two beams were crossed at the measuring point via a focusing lens of 120mm focal length. According to the Laser beams geometric configuration the measuring volume dimensions were estimated to be 100 by 600 μm. The scattered light (TiO_2 particles used as seeding) was collected by a Photomultiplier (RCA 8644) the output of which was analyzed by a DANTEC

counter. The output of the counter was digitized by a 12bit A/D converter (ADVANTECH PCL-818) with a rate of 20Hz. The total period for each measurement was 150s resulting in mean values which differed by an amount of less than 1% of the local mean. The LDV optics were mounted on a manual 3D traversing mechanism whereas the optical train could be rotated at any desirable angle allowing the measurement along any inclination.
Concerning flow visualization this was done by lighting the plane of interest and recording the motion of suitable particles suspended in the fluid. For this purpose a thin light sheet was produced by a 17mW He-Ne Laser beam passing through a glass rod of 6mm diameter. The particles had a mean diameter of 100μm and a density close to the water's, thus minimizing any boyancy effects. Their motion was recorded in a video tape using a CCD camera (PULNIX TM526 of 500 by 480 pixels) with a macro lens.

Discussion of Results

Velocity measurements were carried out upstream and downstream the bifurcation for a Reynolds number of 1100 and equal flow rates for the two branches. More specifically, streamwise velocity profiles were measured at 34 stations. At each measuring station two profiles were obtained along the two lines connecting the middle points of the opposite sides of the model's square cross section. Fig.3 includes the streamwise time mean velocity profiles along the midspan plane. The x and y coordinates shown in this figure correspond to the streamwise (horizontal) and vertical directions, respectively. The vertical plane x=0 constitutes the inlet plane of the model and y=0 its bottom wall. In the same figure, numbers 1 through 34 are the measuring stations, the coordinates of which are shown in Table I.
Fig.3 depicts the presence of two recirculating zones, one in the main duct and another one in the vertical branch. The separation point of the first zone was located opposite of the branch and its reattachment point 3.8 diameters downstream of the bifurcation trailing edge (point B in Fig.3), so that the total length of this zone was equal to 4.8 diameters. The negative velocities in this region were in general very low, covering at most half of the duct's height, whereas the positive ones were at most twice the inlet bulk velocity. Analogous conclusions were drawn from Ref.[3], where for a two dimensional model, Re=1062 and a flow rate ratio (vertical/inlet) 0.58, the recirculating zone in the main duct was 6 diameters long and negative velocities were observed close to the middle height of the model.
Concering the vertical branch of the model, the flow separated from the sharp bifurcation leading edge (point A in Fig.3) obtaining high values at the opposite vertical wall due to the streamlines curvature. Here, the recirculating zone was one diameter long, that is much shorter than the previous one. The velocity profiles being skewed close to the bifurcation apex, tended to become uniform 4 diameters downstream of it. The maximum streamwise positive velocity in this branch was 2.5 times the branch bulk average velocity.
The strong three dimensional character of the flow downstream of the bifurcation is depicted in Fig.4 and 5, where streamwise velocity profiles are shown at the same measuring stations as in Fig.3 but along lines perpendicular to the previous ones as explained before. In the horizontal branch (Fig.4) the flow was asymmetric up to 2.8 diameters downstream of point B, whereas further downstream the profiles obtained an M-shape (as in Ref. [6]), with the minimum value being at the center of the duct. It is also interesting to notice in the same figure flow reversal at one of the two vertical walls up to station 13. Asymmetries of the flow have been also noticed in the same region by Liepsch (6) in a circular duct bifurcation model but not so strong. The dominant asymmetries in the present work may be attributed to the fact that the inlet velocity profiles were not perfectly symmetric about the center of the duct , most probably due to the small length of the square duct for the given Reynolds number and the influence of the transition from the circular to the square cross section at the entrance of the model.
Similar asymmetries are observed in the vertical branch (Fig.5). However, 3.8 diameters downstream of the bifurcation apex, symmetry is established , the profiles being almost flat. It is also worth to notice that at station 20 (half a diameter downsream of AB) the fluid is stagnant in the middle of the duct. This, combined with the corresponding profile of Fig.3, shows that the flow separation region covers a major portion of the square cross section, allowing the fluid to pass only along the three vertical walls.
Based on flow visualization some interesting features of the flowfield were revealed. Namely, the shear layer of the horizontal duct separated zone (Fig.8)was quite stable up to a point (20mm downstream of point B), where it rolled up, producing vortices which were shed at a constant frequency of 0.4 Hz. This phenomenon has been observed both experimentaly (Ref. [2,6]) and numerically (Ref.[10]). According to Ref.(10), the shedding frequency for a two dimensional case is given by the formula $0.006U/\Theta^*$, where U is the boundary layer edge velocity and Θ^* the momentum thickness, both referred at the point of separation. Therefore, for comparison reasons, if Θ^* is computed by using the streamwise velocity profile at the midspan plane and U is the maximum velocity at the same station where shear stress becomes zero (station 9), the shedding frequency is found to be equal to 0.08Hz, namely four times smaller than that one found in the present work. This frequency (0.4Hz) was also verified by taking power

5. A.Samagaio and N.S.Vlachos, 1989"Calculation of 3-D laminar flows in T-shaped junctions"*Computer methods in applied mechanics and engineering*,75,pp.393-407.
6.D.W.Liepsch, 1986"Flow in tubes and arteries-a comparison" *Biorheology*,23,review article,pp.395-433.
7.R.Rieu, R.Pelissier, V.Deplano, 1990 "Flows in rigid and arterial graft bifurcation models" *Biomechanical Transport Processes*, edited by F.Mosore et al, Plenum Press, New York.
8.Chain-Nan Yung, Kenneth J.Dewitt, Theo G. Keith, Jr., 1990 "Three dimensional steady flow through a bifurcation"*J.Biomechanical Engineering*, Vol.112, pp.189-197.
9. B.Bara, K.Nandakumar and J.H.Masliyah, 1992 "An experimental and numerical study of the Dean problem: flow development towards two-dimensional multiple solutions" *J.Fluid.Mechanics*, Vol.244, pp.339-376.
10. Laura L.Pauley, Parviz Moin, William C. Reynolds,1990 "The structure of two dimensional separation"*J.Fluid Mechanics*, Vol.220, pp.397-411.

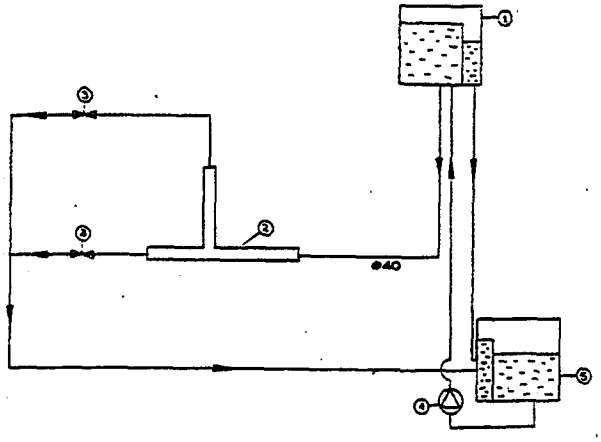

Fig.1 Experimental Lay-out

1,5: Water tanks
2: Bifurcation model
3: Vane and flow meters
4: Pump

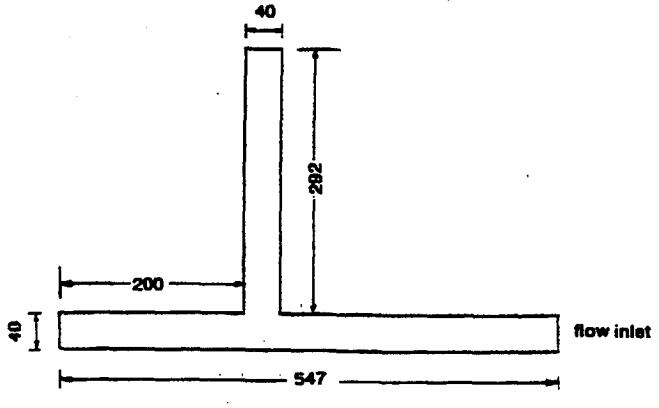

Fig.2 Bifurcation model (dimensions in mm)

spectra of the streamwise component across the shear layer at two stations, namely 15mm and 42mm downstream of point B. Two representative power spectra are shown in Fig.6 and 7 based on 4096 data points, taken with a sampling frequency of 40Hz. Further downstream the flow became quite complex, except the upper wall region, where it looked laminar.

On the midspan plane of the vertical branch, the shear layer (Fig.8) emanated from the bifurcation apex at an angle of 15 degrees with respect to the inlet flow direction without exhibiting any instabilities like those observed in the case of the horizontal branch. A close up picture of this region (Fig.9) showed that the streamline which divided the two streams, ended at a stagnation point located on the vertical wall and very close to point B . The variation of the streamwise velocity component close to the stagnation point is shown in Fig.11, measured on a vertical plane 2mm far from the wall. We notice from this figure that in almost half a diameter from the bifurcation (point B) the velocity has reached its maximum value while then it drops at a relatively low rate. If we assume that the velocity distribution is a linear function of the distance from the stagnation point, this point is located about 2mm far from the bifurcation apex, according to fig.10. Another significant aspect of the flow in this region is the secondary flow, raised by the pressure difference between the leading and trailing edge of the bifurcation (points A and B). This flow consists usually of two counter rotating vortices which superimposed on the axial component produce a two helical type of motion (more details are given in Ref[8]). In the present work both flow visualization and LDV measurements gave a good indication of such kind of motion for a region of one diameter downstream of the bifurcation. Fig.11 shows an obvious movement of the suspended particles from the higher to the lower streamline radius of curvature (from point B to point A), 5mm far from wall C, a region where pressure is the predominant factor of the fluid motion due to the low axial momentum. On the other hand, according to LDV measurements of the horizontal component , taken at various stations along the vertical branch (see Fig.12), the velocity was negative (maximum value 40% higher than the branch axial component) for a region of about 10mm far from each of the two opposite vertical walls C and D, which means that the fluid there moved from the higher radius of carvature to the lower one, whereas in the center of the duct the velocity was small becauce of the separated flow region. The shape of this region was recovered by recording particle tracks on various horizontal and vertical planes, namely normal and parallel to the main flow direction of this branch. The horizontal cross section of this zone had a triangular shape (isosceles like) with its apex at the center region of the duct as well as its vertical cross section (Fig.13) with a height of about one diameter, which practically coincided with the length of this zone. This was also verified, as mentioned before, by the streamwise velocity profiles.

Conclusions

One component velocity measurements as well as flow visualization were carried out in a square duct 90 degree bifurcation. For a Reynolds number of 1100 and a branch flow rate ratio of 1:1 the basic features of the flow were the presence of two recirculating zones, flow asymmetries close to the bifurcation and a double helical type of motion in the vertical branch. Despite the relatively stable shear layer of the vertical branch separated zone, the corresponding one of the main duct (horizontal) rolled up into discrete vortices, shed into the flow with a constant frequency. Concerning flow asymmetries although strong in a small region downstream of the bifurcation these died out moving far from it. Finally, employing mainly flow visualization the secondary flow in the vertical branch was revealed consisted of two counter rotating vortices.

Acknowledgements

This work was partly supported by the Greek Secretariat of Research and Technology in the context of the research project "Flow in arterial bifurcations".

References

1. R.Brech and B.J.Bellhouse,1973 "Flow in branching vessels," *Cardiovascular Research*, 7, pp.593-600.
2. C.M.Rodkieuikz, C.L.Roussel, 1973, "Fluid Mechanics in a Large Arterial Bifurcation", *Transactions of the ASME*, 108.
3. D.Liepsch and S.Moravec, 1982 "Measurements and Calculations of laminar flow in a 90 degree bifurcation," *J.Biomechanics*, Vol.15, No.7, pp.473-485.
4. R.E.Hayes, K.Nandakumar and H.Nasr-El-Din,1989 "Steady laminar flow in a 90 degree planar branch" *Computers and fluids*, Vol.17,No.4,pp.537-553.

Stations	Distance x (mm)
1	62
2	82
3	102
4	133
5	165
6	197
7	238
8	264
9	289
10	317
11	338
12	370
13	400
14	420
15	440
16	460
17	480
18	500
19	520

Stations	Distance y (mm)
20	59
21	73
22	84
23	96
24	109
25	129
26	149
27	169
28	189
29	209
30	229
31	249
32	269
33	289
34	309

Table I Measuring stations

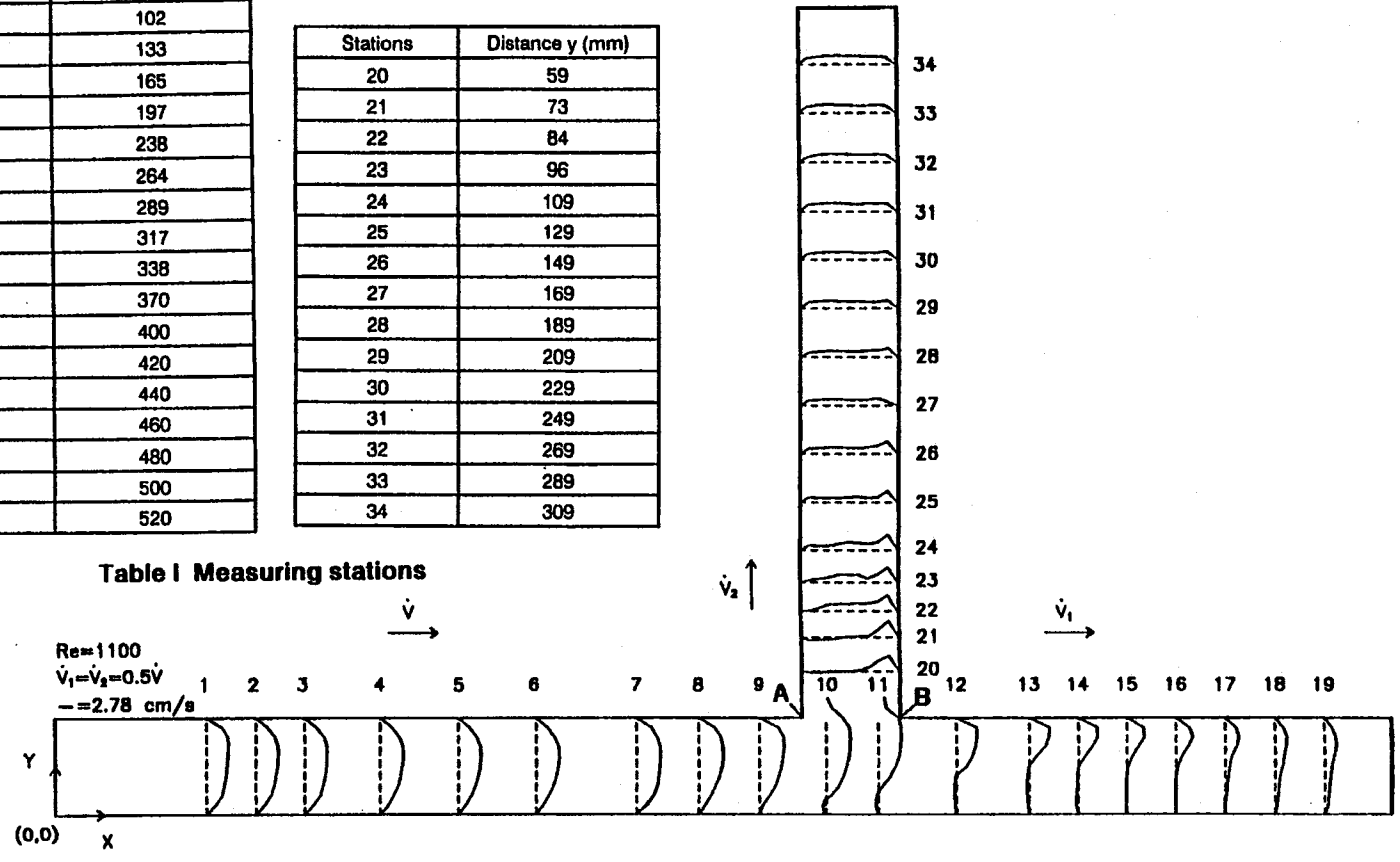

Fig.3 Streamwise velocity profiles at midspan plane

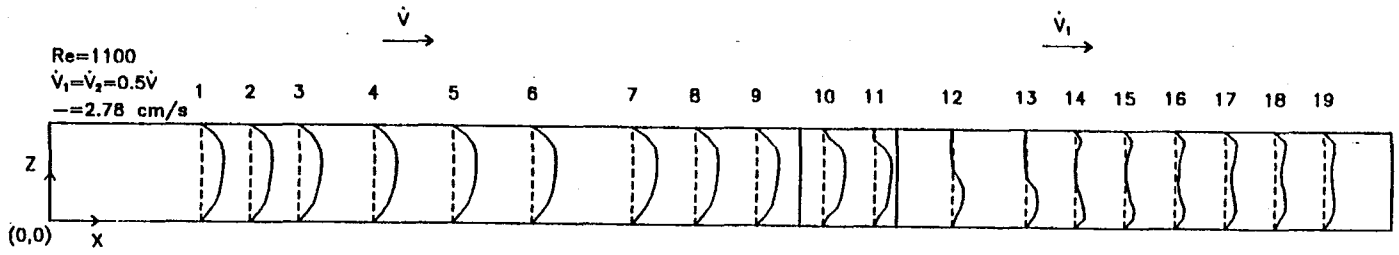

Fig.4 Streamwise velocity profiles at midheight plane (Horizontal section)

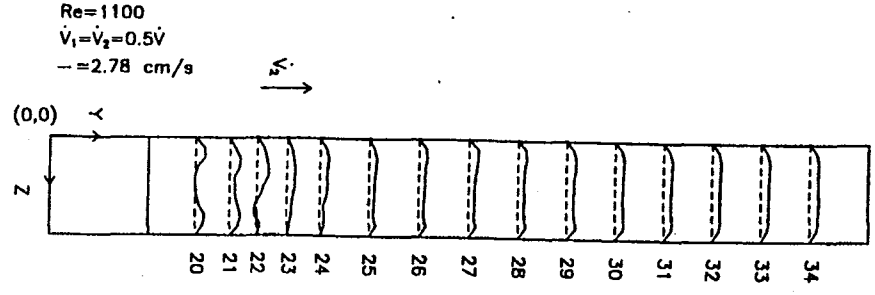

Fig.5 Streamwise velocity profiles at plane x=327 (vertical branch)

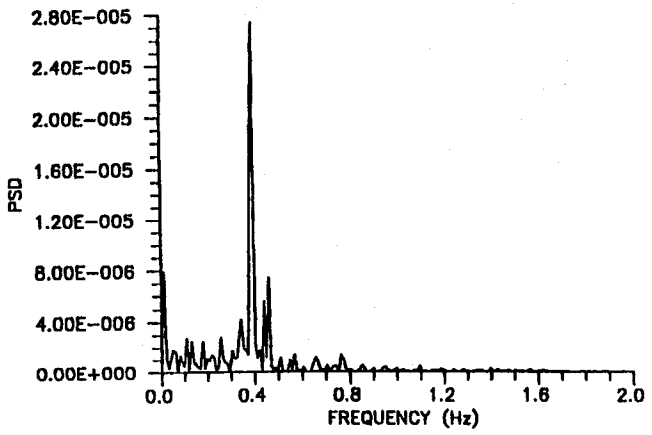

Fig.6 Power spectrum density (x=362mm, y=22mm)

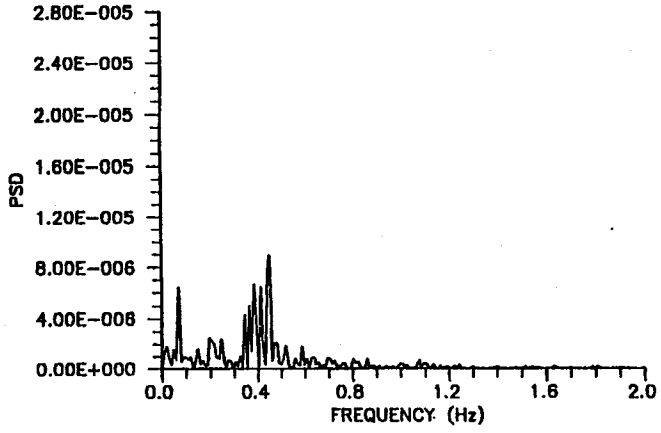

Fig.7 Power spectrum density (x=389mm, y=26mm)

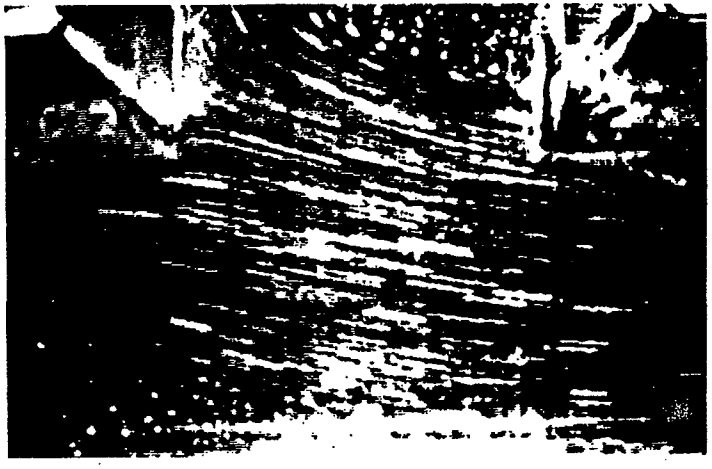

Fig.8 Horizontal and Vertical separated zones

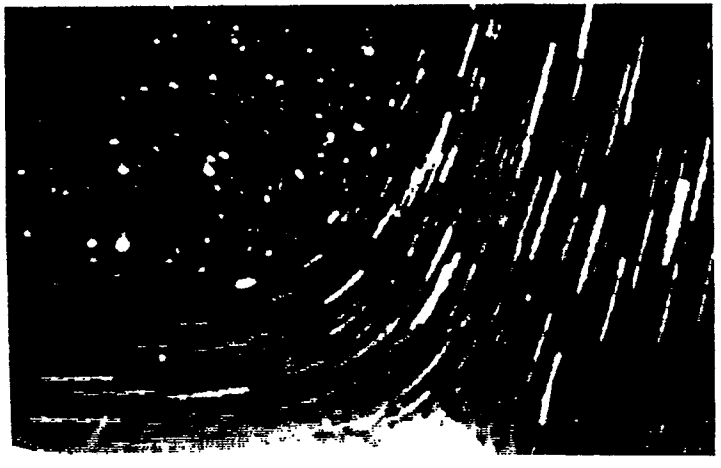

Fig.9 Close up picture of stagnation point region

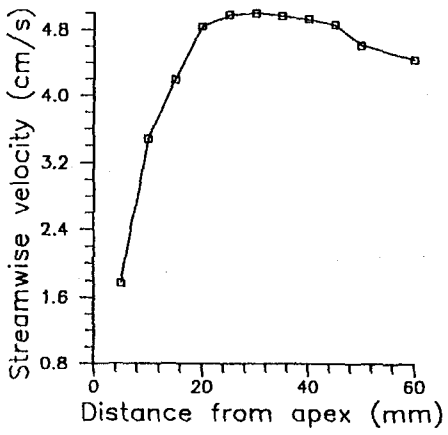

Fig.10 Velocity variation close to stagnation point

Fig.11 Picture at z=35mm (vertical branch)

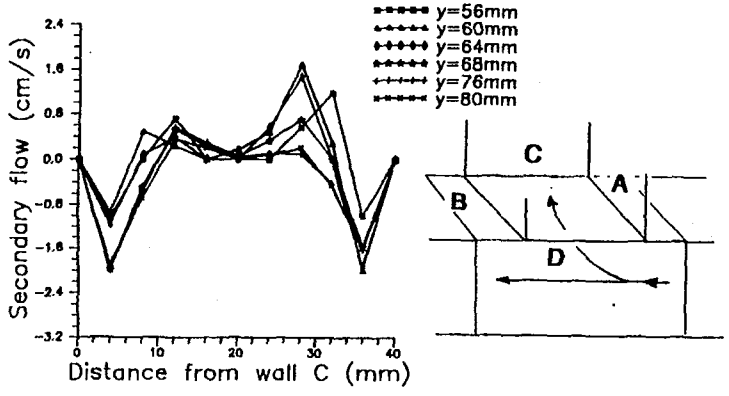

Fig.12 Secondary flow velocity profiles

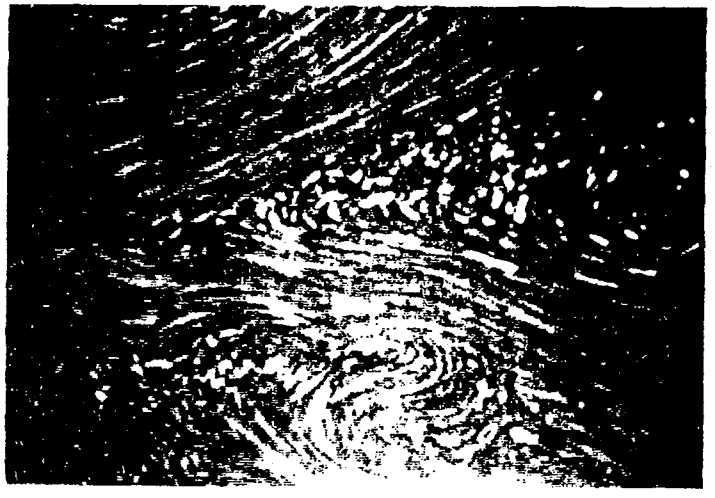

Fig13. Picture at x=327mm (vertical branch)

COMPARISON OF HOT-WIRE AND HOT-FILM SURFACE GAUGES FOR SHEAR STRESS MEASUREMENT AND EXAMINATION OF NEAR-WALL STRUCTURES

GAUDET L., SAVORY E. and TOY N.
Fluid Mechanics Research Group
Department of Civil Engineering
University of Surrey, Guildford (UK)

SUMMARY

The characteristics of a surface-mounted hot-wire have been determined and compared with a conventional stick-on hot-film gauge. The 2.5μm diameter tungsten wire was found to be robust in operation and a simple method of application has been developed to make it suitable for use on wind tunnel models. Comparative calibrations have been obtained for the measurement of the surface shear stress using Preston tube data for reference purposes. In addition, the use of twin 'V' gauges as surface yawmeters has been investigated and the wall turbulence response determined from spectral measurements. It was found that the mean hot-wire signal had a linear sensitivity to wall shear stress while the hot-film gauge signal varied as a 1/3 power law at the higher speeds. In the yawmeter mode the hot-wire gave a smooth correlation with angle in contrast to the hot-film response where irregularities occurred which were believed to be due to interference effects from the upstream edge of the substrate. At low speeds the spectra from the hot-wire and the hot-film correlated well with a Strouhal number based upon wall conditions but at higher speeds the film gauge signals were attenuated due the influence of the substrate.

INTRODUCTION

Surface hot-films are often used to investigate the near-wall flow over surfaces and there are fairly well developed techniques for their analysis[1,2]. The hot films normally consist of nickel sputtered onto a surface which may be either that of a dedicated model or a sheet of plastic foil from which individual gauges may be cut and stuck onto a surface. The films themselves are delicate and, hence, may have a coating of silica to protect them. However, this coating may dampen the high frequency response of the film. The thickness of the substrate, which is normally 25 or 50μm, may locally modify the flow and result in misleading signals. As an alternative approach there has been some recent interest in the use of hot wires[3] which rest on the surface and which, while responding in a similar manner as films, are much more robust and have the potential to produce larger signal outputs. In the present work the characteristics of the hot-wire have been investigated and compared with the stick-on type film gauge with their application to wind tunnel models in mind.

EXPERIMENTAL ARRANGEMENT

The hot-wire used in the present tests consisted of a 2.5μm diameter tungsten wire, 1mm to 1.6mm in length, spot welded to terminals which pass through an insulating plug and which have previously been made flush with the surface. The hot-wire element forms one arm of a constant temperature anemometer (CTA) bridge, the basis of which is shown in Fig 1. The resistance of the hot-wire element is of the order of 10 to 16 ohms. The performance of the hot wire has been compared with stick-on type film gauges for which the resistance of the 1mm long sensing element was between 30 and 40 ohms. The details of the film and wire configurations used are also shown in Fig 1. The power dissipated by

the film or wire gauge was determined from the feed-back voltage required to balance the bridge circuit and maintain the wire at a predetermined temperature (or resistance) by controlling the resistance R_2. The procedure consisted of determining the power being dissipated for overheat ratios of up to 20 percent for the wire and 10 percent for the film. Both steady and unsteady measurements were recorded. Three main experiments were carried out. These included: (1) Comparisons of the performance of film and wire gauges around the circumference of a large cylinder. (2) Shear stress measurements over a wide Reynolds number range in the Surrey University T2 tunnel and the DRA Boundary Layer Tunnel (Bedford). (3) Calibration in a yawmeter configuration. In all cases both steady and unsteady measurements were made.

The use of the surface heated gauge technique involves the relationship between the Nusselt number, for an element which is overheated by an amount ΔT, and a Reynolds number based on wall conditions and the length of the sensitive element in the streamwise direction. The Prandtl number is also involved but this is assumed to be constant as is normal for low speed aerodynamics. This form of relationship may be deduced by dynamic similarity considerations[1] or by theoretical analysis[1,2]. The dynamic similarity approach is adopted leading to a general relationship

$$\frac{Q\,L}{k\,\Delta T\,A} = F\left(\frac{u_\tau\,L}{\nu}\right)$$

where Q is the heat flux dissipated by the element (length L, effective surface area A) and convected away by the air, k the coefficient of conductivity for air, u_τ the friction velocity and ν the kinematic viscosity. In addition to the convection by the air, an amount of heat will be conducted into the substrate and this has to be allowed for if absolute quantities are required. The CTA involves maintaining the resistance of the element at a specific value so that ΔT can be replaced by $\Delta R/\alpha R_o$ where α is the temperature coefficient of resistance and R_o is the resistance at standard temperature. Repeatability of measurements over a period of time is often found to be difficult due changes in the ambient temperature. In order to overcome this, various overheat ratios up to the maximum were employed over a period of time, during which the ambient temperature was constant, so that for constant flow conditions the ratio $\Delta Q/\Delta R$ may be determined. Hence, allowing for the conduction of heat into the surface, which is accounted for by λ_0, the above equation may be rearranged to give

$$\lambda - \lambda_o = F\left(\frac{u_\tau\,L}{\nu}\right)$$

for which $\lambda = \Delta(V^2/R)/\Delta R$ where V is the voltage across the element and R its resistance.

It is anticipated that the response of the gauge will be affected by its protrusion from the surface into the flow. The influence of the size (h) of the element (wire) or substrate (film) is expected to depend upon the Reynolds number $u_\tau h/\nu$ so that, since h/L will be constant for a particular gauge, its calibration automatically allows for its "roughness". This may not be the case, however, if the flow over the gauge is not maintained in a constant direction such as may occur with an arbitrarily-shaped substrate for a film gauge.

Another important factor is the response times of the gauges which are illustrated in Fig 2 where the response time for the maximum step change in overheat ratio for the film and the wire are shown for a freestream velocity of 11m/s. While the film takes about 20 seconds to settle the wire settles within less than a tenth of this time.

MEASUREMENTS ON A CIRCULAR CYLINDER AND ON WIND TUNNEL WALLS

A film and a wire gauge were installed on a 159mm diameter cylinder which was mounted in the T2 low-speed tunnel at Surrey University and the tests were carried out at a speed of 11 m/s. The cylinder was mounted between the side walls and rotated via a stepper motor so that full coverage around the circumference could be obtained. The pressure distribution around the cylinder is shown in Fig 3. No corrections were made for blockage which was about 12 percent. Measurements of λ-λ_o are shown in Fig 4 together with the skin friction coefficients based upon the dynamic pressure of the flow upstream of the cylinder. It is apparent that the values for the film are larger than those for the wire. This is primarily because the conducting area of the wire is much less than that of the film. The gauges may be calibrated over the upstream region of the cylinder where the boundary layer is laminar and the surface shear may be determined by a method based upon a series expansion of the stream function[4]. At the stagnation point the shear stress is zero so that λ_o is well defined and calibration of the film and wire show a linear relationship between λ-λ_o and the shear stress τ for both the film and the wire. This linear relationship differs from the 1/3 power law which has previously been developed[1,2]. It is assumed that at the low Reynolds number of these tests the assumptions built into the theoretical solution are not fully valid. The separation point on the cylinder is well defined from the pressure distribution and the shear stress from this point onwards is assumed to be negative as the value of λ does not define the direction of the flow. Beyond the separation point the shear stress has been determined using the turbulent calibrations discussed below. The resultant skin friction distribution is similar to those obtained by Cousteix and Jullien[3] using a hot-wire and Achenbach[5] using a sublayer fence to determine the shear stress on a cylinder.

Calibrations for turbulent flows were obtained on the sidewall of the T2 tunnel with the film gauges and the wires mounted on a plug which itself was inserted in a large turntable. A similar arrangement was used in the roof of the DRA Boundary Layer Tunnel (Bedford). The results from these two tunnels are shown in Fig 5 together with data for the circular cylinder. The correction for the conduction into the substrate in these cases was determined by heating the gauges to the same overheat ratios as for the tests with no flow whilst covering the gauge with a carefully constructed cap to isolate the sensor from the ambient air. In both tunnels the surface shear stress was determined using a Preston tube.

In the case of the film gauge the three sets of data correlate very well. The cube root of the shear stress is used as this is the form which is normally assumed to correlate such data. It is clear that the low speed turbulent data correlates very well with the laminar flow results obtained from the cylinder. At higher shear stress levels the data follow roughly a 1/3 power law, with the suggestion that at the higher values of τ the data begins to fall below this line. The common laminar and turbulent flow calibration for the film is consistent with the requirement given by Liepmann and Skinner[1] and Bellhouse and Schultz[2] that

$$1 < \frac{Q\,L}{k\,\Delta T\,A} < \frac{Pr}{C_f}$$

For the wire data the calibration is close to being linear with the laminar flow data lying on a line below that for the turbulent data. The increased heat dissipation for the turbulent data is consistent with the data due to Bellhouse and Schultz as well as the experiments by Bradshaw and Gregory[6] using Stanton type surface probes, which indicated that the readings in the viscous sublayer were larger than those in the wall region of a laminar boundary layer.

Yaw calibrations for twin elements set at 90 degrees to one another and each having the same overheat ratios are shown in Fig 6. The values for λ versus α for the films indicate a slightly fluctuating correlation while those for the wires follow a fairly smooth curve. These data are shown in a reduced form in Fig 7 where

$$\Phi = \frac{\lambda - \lambda_0}{\lambda_{max} - \lambda_0}$$

for the appropriate elements of the gauge. It is apparent that there is a region of reduced sensitivity in the case of the film gauge which is assumed to be due the local interference of the flow because of the varying geometry of the substrate presented to the flow as the gauge is yawed.

Selected sets of spectra are shown in Fig 8 in the form of rms voltages plotted against a Strouhal number based on wall variables. Fig 8a shows the data for the wire gauge for three speeds in the Boundary Layer Tunnel. The data is well correlated. In Fig 8b similar data is shown for the film gauge and the graphs for the data for the three velocities shown are separated with a reduction of the signal as the velocity increases suggesting that an excrescence drag penalty is present due to the thickness of the substrate. In the case of the film the height corresponds to about 20 wall units at the highest speed and so this influence might be expected. In contrast the wire height corresponds to only 2 wall units so that little or no influence of roughness is expected. In the case of the film the influence is generated upstream of the sensor while for the wire it is actually at the sensor itself and at higher speeds would be incorporated in the calibration.

CONCLUSIONS

The hot-wire gauge which is more robust than the hot-film gauge and which has a much faster response time has the potential for use at higher speeds due to its increased sensitivity to shear, although it does produce a relatively small signal at low speeds because of its lower resistance. The hot-wire signal has been shown to have a virtually linear response to shear stress in contrast to the 1/3 power law relationship which is commonly assumed for the hot film. The hot-wire is, therefore, the more sensitive instrument and for speeds in excess of 50m/s will provide a larger and more sensitive signal than the hot-film gauge. The data for the hot-film indicates that at low values of shear the 1/3 power law relationship is not applicable, probably due to the assumptions made in the analysis upon which it is based. In both the laminar region around the cylinder (up to 10 degrees elevation) and at the lower speeds on in the turbulent tunnel sidewall flow the relationship appears to be close to linear. Well defined wall spectra are obtained in the high frequency range, where the appropriate Strouhal number is based on wall conditions, except for the hot-film at the higher speeds when roughness effects due to the thickness of the substrate appear to attenuate the high frequency signals. The hot-wire responds well in yaw in contrast to the hot-film. The drawback of the hot-film would appear to be influence of the upstream edge of substrate upon the flow over the film itself.

ACKNOWLEDGEMENTS

This work was funded by the UK Department of Trade and Industry under Agreement No 2064/145. The authors are indebted to Ms Caroline Betts of the Defence Research Agency, Bedford, for her support during the course of the research and for the use of the Boundary Layer Tunnel at DRA Bedford.

REFERENCES

1 Liepmann H.W.,Skinner G.T. 1954. Shearing-stress measurements by use of a heated element. NACA TN 3268

2 Bellhouse B.J., Schultz D.L. 1966. Determination of mean and dynamic skin friction,separation and transition in low-speed flow with a thin-film heated element. *J.Fluid Mech.*, vol.24, part 2, pp 379-400.

3 Cousteix J.,Juillen J.-C. 1982. Hot wire gauges for skin friction measurement (design, calibration, applications). Rech. Aerosp. 1982-1983

4 Modern Developments in Fluid Mechanics (1938), Chap IV, p 58, vol. 1, Oxford Univ. Press, Ed: Goldstein S.

5 Achenbach E. 1968. Distribution of local pressure and skin friction around a circular cylinder in cross flow up to Re=5×10^6. *J. Fluid Mech.*, vol 34, part 4, pp 625-639.

6 Bradshaw P.,Gregory N. 1961. The determination of local turbulent skin friction from observations in the viscous sub-layer. Aero. Res. Council, London, R & M No 1408.

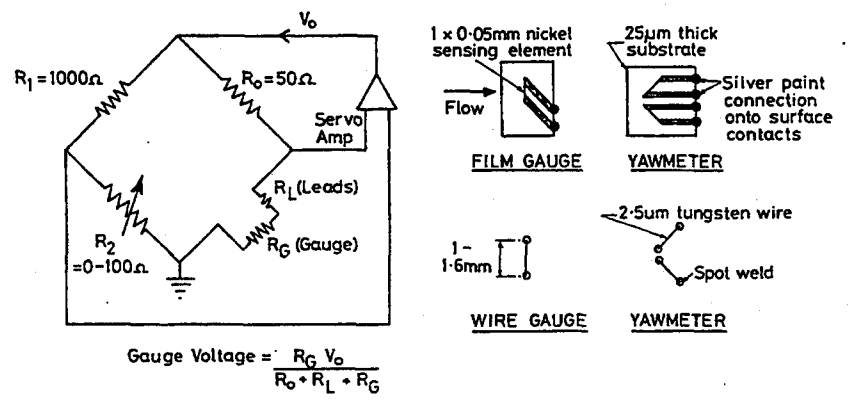

Fig. 1 Constant temperature bridge arrangement with wire and film gauges utilised

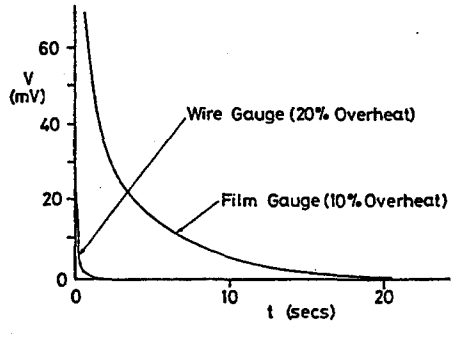

Fig. 2 Response times for the hot-wire and hot-film gauges

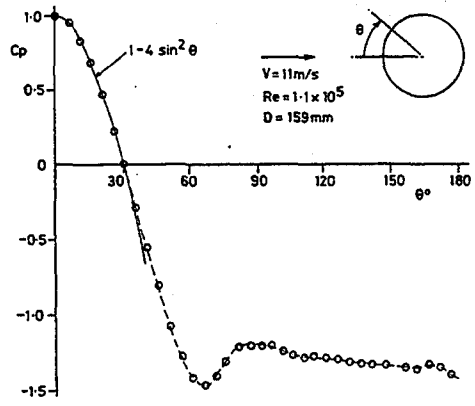

Fig.3 Pressure distribution around circular cylinder

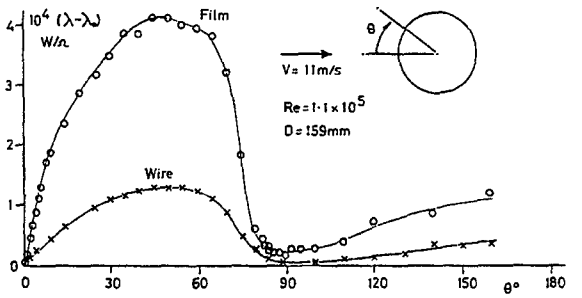

Fig. 4a Heat dissipation from a surface film and wire on the cylinder surface

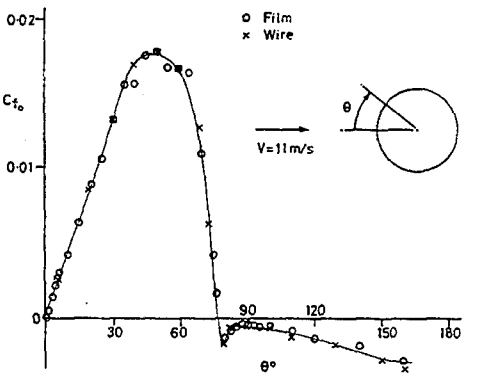

Fig. 4b Skin friction coefficient distribution around the circular cylinder

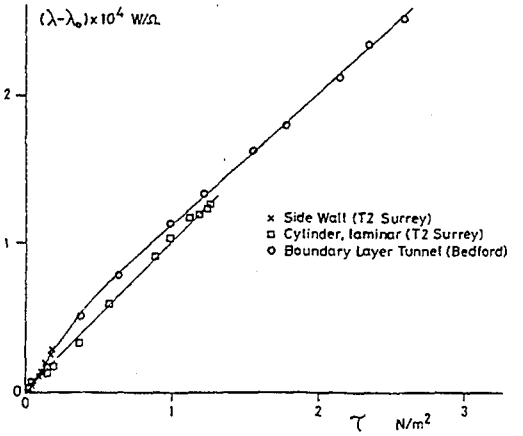

Fig. 5a Shear stress calibration for the hot-wire gauges

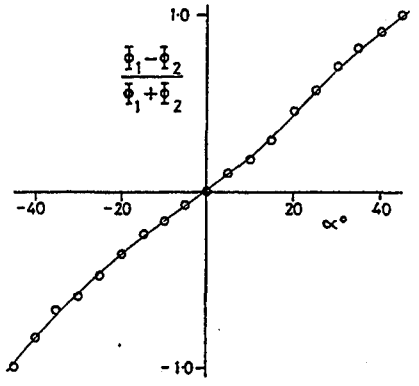

Fig. 7a Normalised yaw calibration for the hot-wire 'V' gauge

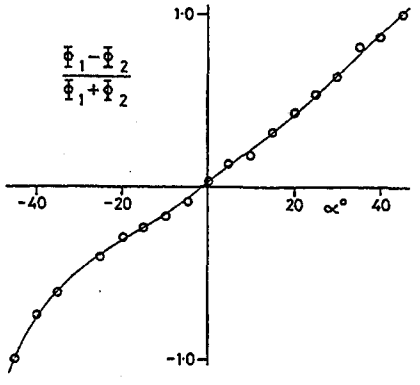

Fig. 7b Normalised yaw calibration for the twin hot-film gauge

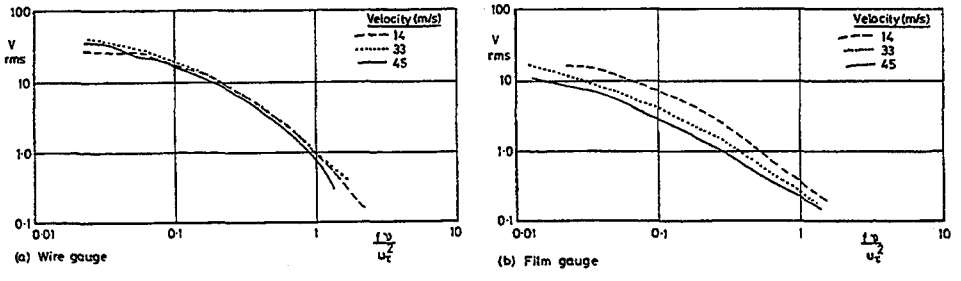

Fig. 8 Power spectra for the wire and film gauges in the Boundary Layer Tunnel

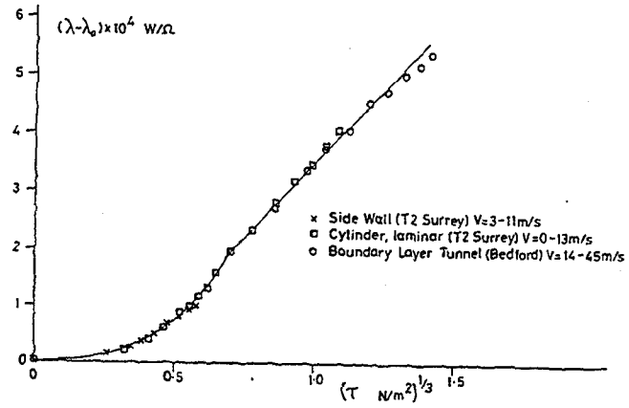

Fig. 5b Shear stress calibration for the hot-film gauges

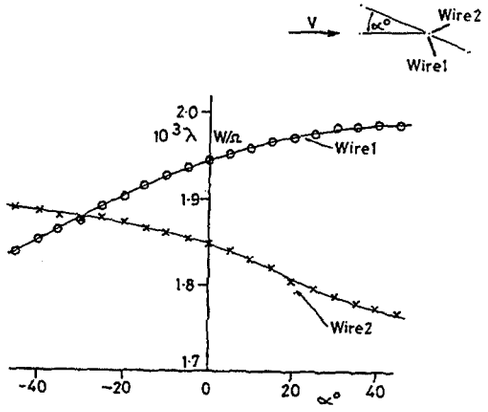

Fig. 6a Yaw response of the two hot-wires forming a 'V' gauge

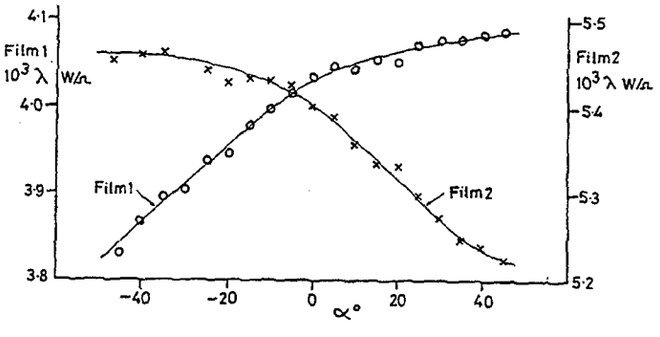

Fig. 6b Yaw response of the two sensors on a twin hot-film gauge

CALIBRATION AND USE OF A TRIANGULAR YAWMETER FOR SURFACE SHEAR STRESS AND FLOW DIRECTION MEASUREMENT

GAUDET L., SAVORY E. and TOY, N.
Fluid Mechanics Research Group
Department of Civil Engineering
University of Surrey, Guildford (UK)

SUMMARY

This paper describes the calibration of small triangular surface yawmeters and their use for measuring shear stress and flow direction in turbulent flows via local pressure measurements on the sides and upper surface of the device. The yawmeter represents an extension of existing techniques that employ razor blades, surface-mounted tubes or blocks and the results show improved performance in terms of yaw response and the incorporation of a local measurement of the static pressure as a reference. Two methods of shear stress calibration are discussed, one using a local static pressure reference and the other based on a simplified device overall "drag force" approach. Results for the mutual interference between adjacent devices are also presented, this information being of importance for the deployment of arrays of yawmeters on the surface of wind tunnel models.

INTRODUCTION AND BACKGROUND TO THE TECHNIQUE

Numerous techniques have been developed for the measurement of aerodynamic surface shear stresses. Many of these methods involve the transfer of heat from a surface wire[1], film[2] or block[3,4], often with the gauge maintained at a constant temperature, whilst other thermal gauges utilise pulsed-wires[5]. More recent advances have been the development of piezo-electric film gauges[6] and shear-sensitive liquid crystal surface coatings[7,8]. However, in principle, the simplest techniques available are those involving the relationship between one or more pressures associated with a small surface obstacle and the local shear stress. Such methods include the Preston tube[9] and associated modified versions[10], and other surface probes, such as the Stanton tube[11], and its derivatives, most notably the razor blade surface pressure method[12,13,14]. Other pressure measurement approaches have been utilised, for example the boundary layer fence[15,16] and small surface obstacles[17,18]. However, in most instances, these devices do not give any information concerning the shear stress direction and so there is clearly a need for a surface gauge which reliably provides the shear stress vector over a wide Reynolds number range. The triangular yawmeter described here has been found to be accurate, easy to install and robust in operation.

Investigations using yawed razor blades[14] showed that by using two different known angular settings of the device the local flow direction (β) could be determined through a suitable calibration. The influence of yaw on the pressure rise indicted by a blade is shown in Fig 1 where the pressure is referenced to the local surface static pressure in the absence of the blade. By measuring the relative magnitudes of two pressure readings taken at a known angular separation, for example 30^0, the direction of the skin friction may be determined from Fig 1 or, more directly, from Fig 2, with the shear stress value then being determined from a calibration obtained at zero yaw. Unfortunately, the drawback of the razor blade approach is that two accurate settings of the blade must be made in-situ, requiring two separate test runs with, possibly, a third run if a measure of the local static pressure reference is to be determined.

An advance upon the razor blade is the three-dimensional surface block[17,18] which enables all the necessary data to be obtained from a single test run. The surface block, illustrated in Fig 3, has surface "pitot" pressure orifices at the centre of each of the three vertical faces which are formed by static pressure holes aligned with semi-circular recesses. It was found[18] that an aspect ratio (L/h) of 9 was sufficient to produce a satisfactory calibration. The three side face pressures are measured and a calibration for shear stress direction (β) obtained by determining the ratio of the difference in pressure between two adjacent sides, as shown in Fig 3a. Having ascertained the flow direction, the magnitude of the pressure rise on the front face as a proportion of the pressure rise on that face at zero yaw is determined from Fig 3b. Unfortunately, the skin friction cannot be computed since a calibration for the shear stress in terms of the pressure rise on a normal face is not given in the reference. In the analysis of the data[18] the pressure rise is referenced to a value equal to the mean of the two rearward face pressures and it was indicated that this form of the pressure difference was about 30% greater than that obtained by using the undisturbed local static pressure as reference. In the present work the performance of the device has been enhanced by both changes to its geometry and improvements in the form of the yawmeter calibration.

EXPERIMENTAL DETAILS

The triangular yawmeter employed in the present work is shown in Fig 4 where it may be seen that the aspect ratio has been increased to 20, thereby removing some of the ambiguities associated with the smaller aspect ratio block used in earlier work[18] such that the device may be genuinely considered to be a two-dimensional gauge. The yawmeter is also an improvement upon a similar, but simpler, instrument developed by one of the present authors[19] which had only two pressure tappings. In the new device the pitot pressure orifices (P_1, P_2 and P_3) are much more clearly defined than those used in earlier work[18]. They are produced by milling slots into the underside of the block so that each one produces a rectangular tapping which is then connected to a surface static hole drilled into the surface upon which the yawmeter is mounted. In addition, a static pressure tap (P_4) may be incorporated in the upper surface of the block so that this pressure may be used as a local reference, if required. The installation procedure is straightforward provided that a template is made to locate the relative positions of the surface tappings for drilling and a dummy yawmeter with cylindrical legs (matching the tapping locations and diameters) used to ensure that the milled slots on the yawmeter are correctly positioned over the tappings.

The calibration of the yawmeter is based upon dynamic similarity for objects mounted in the wall region of a turbulent boundary layer such that any pressure rise experienced is a function of the appropriate wall variables, from which

$$\frac{\Delta P}{\tau} = f\left(\frac{u_\tau h}{\nu}\right) = g\left(\frac{\rho h^2 \Delta P}{\mu^2}\right)$$

where the pressure difference ΔP is referenced to the undisturbed static pressure. As any pressure difference may be expressed in a similar fashion it follows that any pressure measured by the device may be employed as the reference pressure. The pressures experienced by the device will also be dependent upon the sweep angle θ of the flow direction measured from the normal of any given face. However, it is found that for all the roughness Reynolds numbers ($u_\tau.h/\nu$) tested a unique variation of the pressure ratios exists over quite a large range of θ. Therefore, it follows that

$$\frac{\Delta P_\theta}{\Delta P_0} = m\,(\,\theta\,)$$

which is consistent with the analysis for a razor blade[14]. Consequently, in principle, the two parameters, namely the magnitude of the shear stress and its flow direction, may be determined in two separate stages.

The experiments were carried out in a low-speed wind tunnel in the Department of Civil Engineering which has working section dimensions of 1.37m (height) x 1.07m (width) x 9.0m (length) and a freestream turbulence level of 0.17%. The tests were conducted with the yawmeters mounted on a 380mm diameter turntable installed on the sidewall of the tunnel at a location 4.5m downstream from the end of the tunnel contraction. A 20mm high metal fence spanning the height of the tunnel at the entrance to the working section produced a thick turbulent boundary layer with good lateral similarity. The boundary layer parameters obtained at the reference freestream velocity of 11m/s were δ=320mm, δ_*=30.7mm, θ=23.1mm and c_f=0.00265. Three yawmeters were examined, with heights of 0.45, 0.9 and 1.8mm, respectively, but with the same overall geometry and aspect ratio L/h=20. In each experiment the four yawmeter pressures were measured, together with the pressure from a nearby wall tapping. In each case the measured pressure was referenced to the freestream static pressure. Three alternative methods of analysis were pursued. In the first case, the upper surface static pressure (P_4) was used as the reference pressure, and, in the second case, the mean of the pressures on the rearward facing surfaces ($[P_1+P_2]/2$) was utilised as the reference. The third approach was a direct calibration between the shear stress and the overall "drag force" acting on the device (treated here as a bluff body) in which it was assumed that the pressure acting on any given face (P_i) was representative of the total force (F_i) acting normally on that face. Hence, the resultant force (F) in the direction of the flow is given by

$$F = F_1 \,.\, \sin\,(\,30 + \alpha\,) + F_2 \,.\, \sin\,(\,30 - \alpha\,) - F_3 \,.\, \cos\,\alpha$$

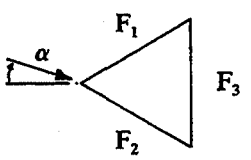

from which the device "drag coefficient" may be determined using

$$C_D = \frac{F}{q\,h\,L}$$

based upon the frontal area of the yawmeter. With this approach the drag is independent of the choice of reference pressure because

$$\sin\,(\,30 + \alpha\,) + \sin\,(\,30 - \alpha\,) - \cos\,\alpha = 0$$

The experiments were conducted over a range of freestream velocities from 3m/s to 11.5m/s, with the yawmeter pressures connected in-turn to a Furness differential pressure transducer via a Scanivalve switch mechanism. The data acquisition and analysis was carried out by an A-D converter linked to a PC. Comparative shear stress measurements were obtained using a stainless steel Preston tube, which had an outside diameter of 1.25mm, together with the standard flat plate turbulent boundary layer calibration.

DISCUSSION OF RESULTS

The basic skin friction calibration when one of the faces of the yawmeter is normal to the flow (θ=0) is shown in Fig 5 for different definitions of ΔP_0. It is evident that the use of secondary forms of reference pressure leads to values of $\Delta P_0/\tau$ that are between 10 to 30% higher than those obtained using the local wall static, depending upon the Reynolds number. It is interesting to note that the calibration using the local static pressure as the reference is virtually identical to Gaudet's analysis of a razor blade calibration[13]. Some previous data obtained at higher Reynolds numbers in the Boundary Layer Wind Tunnel at DRA Bedford are included in these plots. It is apparent that the use of the upper surface static as a reference produces only a small increase above that obtained using the mean of the pressures on the rearward facing yawmeter tappings.

The ratio of the pressure rise on a surface relative to the value when that surface is normal to the flow is shown in Fig 6, with the mean of the pressures on the rearward faces used as the reference. For the range of device heights tested it is clear that the calibration is unique over the range $0<\theta<70°$ and the data can be well-represented by the relationship

$$\frac{\Delta P_\theta}{\Delta P_0} = \cos\ (\ 1.22\ \theta\ )$$

Although not illustrated here, a similar plot for the three devices using the local wall static as the reference pressure exhibits more scatter than that shown in Fig 6. The flow direction may be determined from various different combinations of the measured pressures. However, a good correlation is obtained from the relationship shown in Fig 7. In this correlation the angle α is the deviation of the yawmeter from the angle where the two front faces are symmetrically positioned pointing into the flow. Hence, the procedure for determining the shear stress and flow direction is as follows:

(1) From the measured pressures the flow direction, θ, is read from Fig 7.
(2) The pressure ratio is then determined from Fig 6 using the value of the angle θ.
(3) The normal pressure rise, ΔP_0, is found by dividing this ratio into the measured value.
(4) Finally, the shear stress may be obtained from Fig 5 after computing $\rho.h^2.\Delta P_0/\mu^2$.

The data obtained from the three devices when the "drag force" method of analysis is used are shown in Fig 8 which illustrates the variation of the yawmeter "drag coefficient" with roughness Reynolds number. For a given orientation of the device to the flow (α=0° or 60°) there is very good agreement between the three data sets. The influence of flow incidence angle on the yawmeter drag is shown in Fig 9 for the smallest device. It may be seen that the device response is very sensitive to incidence angle and may be well-defined by the empirical curve shown in the figure. It is evident that this simplified "drag force" method is a viable form of analysis for the yawmeter data, perhaps because the large aspect ratio of the devices means that the measured pressure on any face is a good representation of the overall force on the face.

For practical wind tunnel measurements on wing or aerofoil models it is clear that a large number of yawmeters will be required, rather than the single device examined in this paper. This raises the question of measurement errors due to interference between adjacent devices. However, the results from some earlier tests, illustrated in Fig 10, show that provided the devices are spaced more than two spanwidths apart (Z/L>2) there is negligible interference between them, irrespective of the streamwise spacing of the yawmeters.

CONCLUDING REMARKS

The present work has shown how a simple triangular yawmeter may be utilised to reliably determine both the mean surface shear stress and the local flow direction. The use of a local static pressure as a reference is an improvement upon previous similar devices. Additional work is planned in order to examine the performance of the devices both favourable and adverse pressure gradients. It is also intended to provide a more definitive shear stress calibration by utilising direct force measurements from a small floating element balance using both a flush active element and one upon which a yawmeter will be mounted.

NOMENCLATURE

C_D	Yawmeter drag coefficient, F/(q.h.L)
c_f	Skin friction coefficient
Cp	Pressure coefficient, $(P_1 - P_s)/q$
F_i	Normal force acting on yawmeter face, $(P_i - P_r).h.L$
L/h	Aspect ratio (length/height) of the yawmeter
P_i	Pressure measured at yawmeter tapping i
P_r	Static pressure reference
P_∞, P_s	Local wall static pressure and freestream static pressure
ΔP_θ	Pressure on face at yaw relative to static pressure
ΔP_0	Pressure rise on face normal to flow direction relative to static pressure
q, U	Freestream dynamic pressure and velcoity
u_τ	Shear velocity
α	Incidence angle of yawmeter
θ	Sweep angle of yawmeter (=60-α)
τ	Shear stress
ρ, μ, ν	Density, dynamic viscosity and kinematic viscosity of air

REFERENCES

[1] Cousteix, J. and Juillen, J-C., 1982, "Hot wire gauges for skin friction measurements", Recherches Aerospace 1982-3

[2] Bellhouse, B. J. and Schultz, D. L., 1966, "Determination of mean and dynamic skin friction, separation and transition in low-speed flow with a thin heated film", *Journal of Fluid Mechanics*, Vol. 24, Pt. 2, pp. 379-400

[3] Ludwieg, H., 1949, "Ein Gerat zur Messung der Wanderschubspannung in turbulenten Reibungsschichten", *Ingenieur-Archiv*, Vol. 17, pp. 288-299 ("Instrument for measuring the wall shearing stress of turbulent boundary layers", N.A.C.A. Tech. Memo. 1284 (1950))

[4] Liepmann, H. W. and Skinner, G. T., 1954, "Shearing stress measurements by means of a heated element", N.A.C.A. Tech. Note 3268

[5] Castro, I. P. and Dianat, M., 1983, "Surface flow patterns on rectangular bodies in thick turbulent boundary layers", *Journal of Wind Engineering*, Vol. 11, pp. 107-119

[6] Bertelrud, A., 1987, "Use of hot film sensors and piezo electric foil for measurement of local skin friction", Proceedings 12th International Congress on Instrumentation in Aerospace Simulation Facilities, Williamsburg, Virginia, USA, June

[7] Toy, N., Savory, E., Hoang, Q. H. and Gaudet, L., 1993, "Calibration and use of shear sensitive liquid crystals in aerodynamic testing", Proceedings 15th International Congress on Instrumentation in Aerospace Simulation Facilities, ICIASF Record 93CH3199-7, St Louis, France, September, published by I.E.E.E., pp. 49.1-49.6

[8] Reda, D. C. and Muratore Jr, J. J., 1994, "A new technique for the measurement of

surface shear stress vectors using liquid crystal coatings"", AIAA 32nd Aerospace Sciences Meeting, Reno, January, Paper No. AIAA 94-0729
[9] Preston, J. H., 1954, "The determination of turbulent skin friction by means of pitot tubes", *Journal of Royal Aeronautical Society*, Vol. 58, pp. 109-121
[10] Bertelrud, A., 1977, "Total head/static measurements of skin friction and surface pressure", *A.I.A.A. Journal*, Vol. 15, Pt. 3, pp. 436-438
[11] Stanton, T. E., Marshall, D. and Bryant, C. N., 1920, "On the conditions at the boundary of a fluid in turbulent motion", *Proc. of Royal Society Series A*, Vol. 97, pp. 413-434
[12] Smith, K. G., Gaudet, L. and Winter, K. G., 1962, "The use of surface pitot tubes as skin-friction meters at supersonic speeds", Aeronautical Research Council R. & M. 3351
[13] Winter, K. G., 1977, "An outline of the techniques available for the measurement of skin friction in turbulent boundary layers", *Progress in Aerospace Science*, Vol. 18, pp. 1-57
[14] East, L. F., 1966, "Measurement of skin friction at low subsonic speeds by the razor-blade technique", Royal Aircraft Establishment Technical Report No 66277
[15] Vagt, J. D. and Fernholz, H., 1973, "Use of surface fences to measure wall shear stress in three-dimensional boundary layers",*Aeronautical Quarterly*, 14, 2, 87-91
[16] Rechenberg, I., 1963, "The measurement of turbulent wall shear stress", ZFW 11, 11, Aircraft Research Association Library Translation 11, 1965
[17] Nituch, M. J. and Rainbird, W. J., 1973, "The use of geometrically-similar obstacle blocks for the measurement of turbulent skin friction", Aero. Research Council 34423
[18] Dexter, P., 1974, "Evaluation of a skin-friction vector measuring instrument for use in 3-D turbulent incompressible flows", Project Report, University of Southampton, Dept of Astronautics and Aeronautics (see also reference [13])
[19] Gaudet, L., 1985, "A simple combined surface yaw-meter and skin-friction meter for use in 3D turbulent flows", Measurement Techniques in Low Speed Turbulent Flows, Euromech 202, The Netherlands

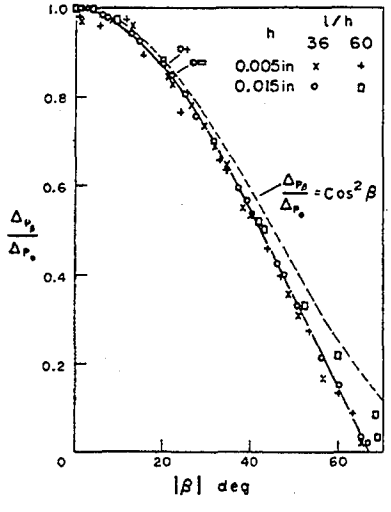

Fig 1 The effect of razor blade yaw in a two-dimensional boundary layer (East[14])

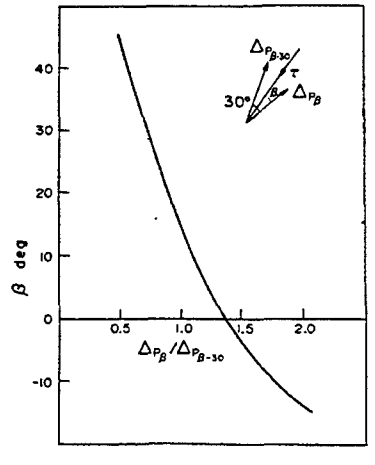

Fig 2 Empirical relationship between β and $\Delta P_\beta/\Delta P_{(\beta\text{-}30)}$ (East[14])

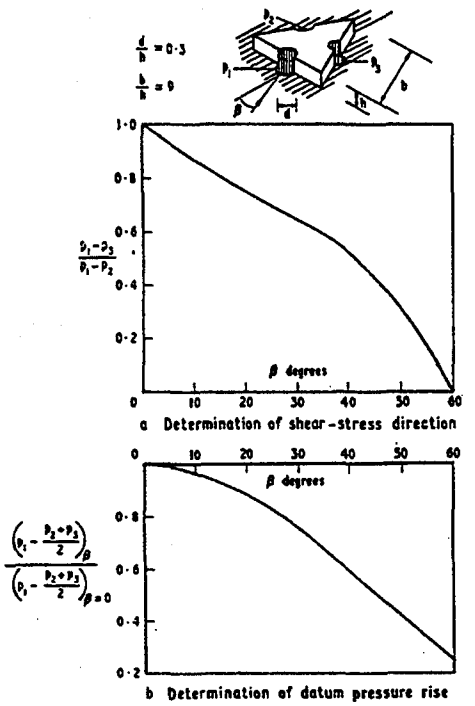

Fig 3 A surface block for three-dimensional flows (Dexter[18])

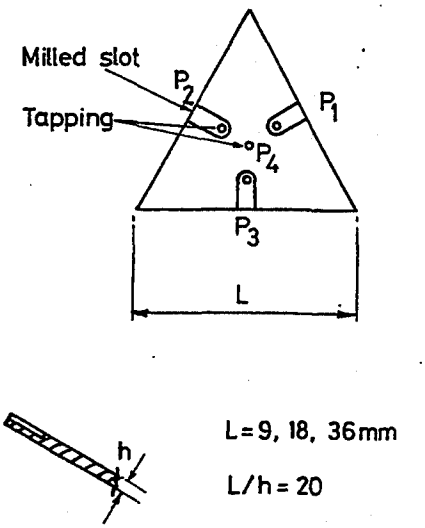

Fig 4 The triangular yawmeter block

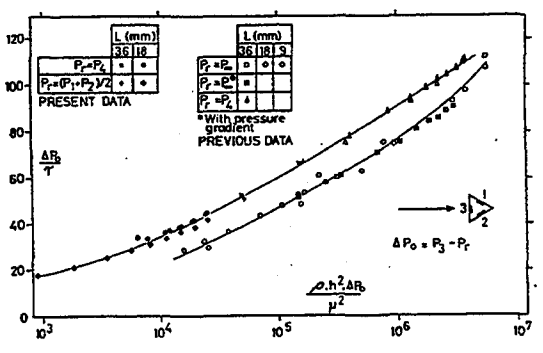

Fig 5 Basic shear stress calibration for the triangular yawmeter devices

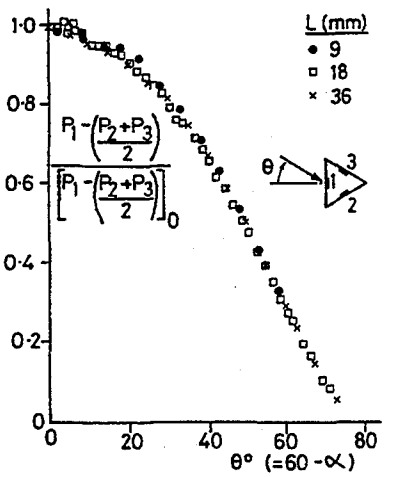

Fig 6 Pressure rise on swept front face relative to zero sweep

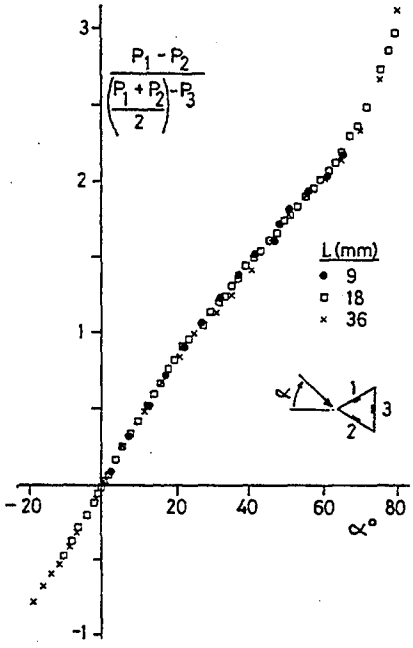

Fig 7 Determination of the flow direction from the three face pressures

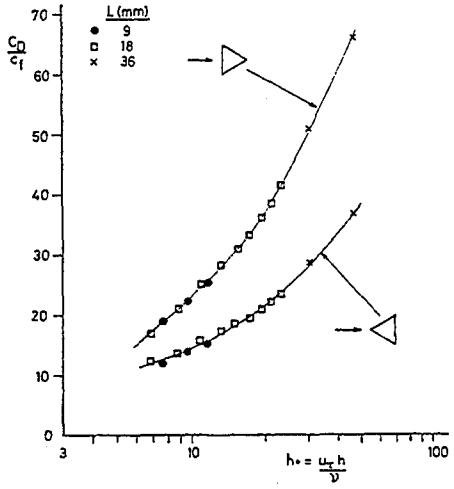

Fig 8 Variation of the drag of yawmeters with roughness Reynolds number

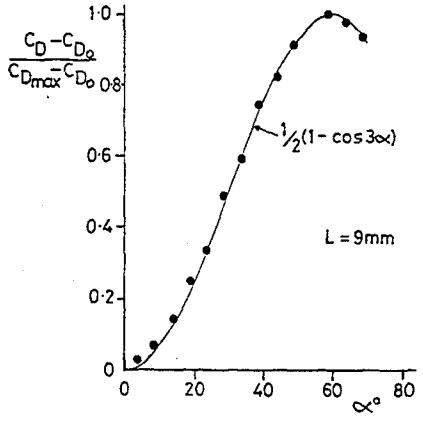

Fig 9 Influence of flow incidence angle on yawmeter drag

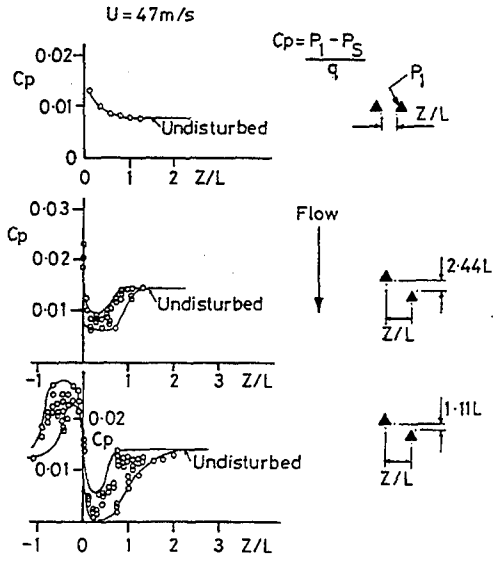

Fig 10 Mutual interference between adjacent yawmeters

SOME FEATURES OF THE TEST PROCEDURE IN THE NEW TEST SECTION #3 OF THE TSAGI WIND TUNNEL T-128

V.M. NEYLAND, A.I. IVANOV, A.V. PILIUGIN
Central Aero-Hydrodynamics Institute (Russia)

During the spring and autumn of 1993, the new test section #3 of the wind tunnel T-128 was certificated and put into operation. This facility is designed for testing airfoils at increased (up to $Re_c = 25.10^6$) Reynolds numbers with Mach numbers varying from 0.2 to 0.86. The test section #3 is equipped with the controlled side wall gas suction system intended to improve the two-dimensionality of flows over airfoils and to decrease the influence of the side wall viscosity.

The comprehensive investigations of the flow field characteristics in the "empty" wind tunnel preceded tests in the new test section. The information about the uniformity of the static pressure field and Mach numbers along the axis of the wind tunnel and near its walls, as well as the characteristics of the boundary layer for different relative mass flow rates of the gas being sucked were obtained by using a static probe, 4 Pitot rakes and closely-spaced pressure taps on the test section walls. These data were used to choose optimal suction parameters which make it possible to achieve an adequately small thickness of the side wall boundary layer without an appreciable distortion of the uniformity of the test section flow field.

The aerodynamic characteristics of airfoils were determined by measuring the static pressure in 3 sections of their surfaces and the total pressure profiles in the model wake. The Pitot tube mounted on the two-degree of freedom automatic scanning traversing gear was applied to measure the total pressure profiles. Some results of the methodical investigations of the scanning device-model interference, flow two-dimensionality, upwashes and other data are presented.

The wind tunnel T-128 is to be equipped, according to its design, with 5 removable 2.75x2.75x8m test sections. Putting into operation of each test section suggests the certification of the flow quality in terms of the flow field uniformity, the total upwash in the model zone, the flow fluctuation characteristics, and the wall boundary layer state and parameters. It is precisely these tests that were carried out to certify the flow field in the newly designed test section #3 of the wind tunnel T-128 excluding the measurements of fluctuation characteristics that would be performed later.

Fig.1 shows the schematic of the test section #3 designed to test airfoil models placed between the side walls. The model is mounted on two rotatable disks which provide, rotating in phase, the model turn by a given angle of attack.

The model drag is estimated according to the total pressure defect measured in the wake by a Pitot tube. The automatic wake scanning across the flow and along the airfoil trailing edge is executed using a two-degree of freedom computer-controlled traversing gear. Electronic scanivalves and electronic gages united in a single measuring system are used for all measurements of the pressure on the airfoil and in the wake.

The test section walls feature a longitudinal slot perforation, the open area ratio varying from 0 to 13%. The slots are segmented in the longitudinal direction so that an independent variation in the open area ratio is possible for each segment. In the model zone, only horizontal walls have the perforation, while the side walls are solid. The slot perforation behind the model is provided on all 4 walls. More than thousand static pressure taps are made along the central lines of the test section walls.

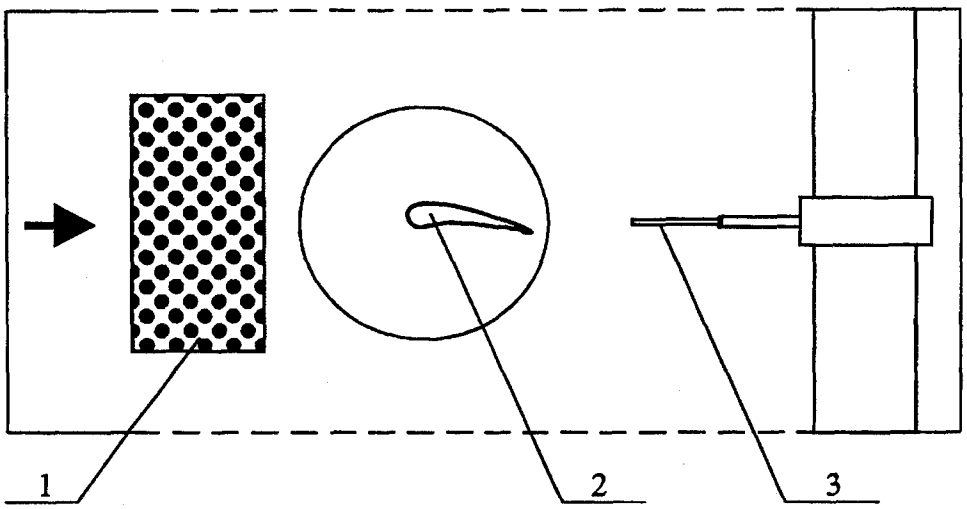

Fig.1. Test section # 3 scheme : 1- boundary layer suction; 2 - airfoil model, 3 - Pitot tube wake survey.

A valuable feature of this test section is the application of the controlled side wall boundary layer suction system ahead of the airfoil to improve the flow two-dimensionality. The suction is performed through vertical slots ending slightly ahead of the airfoil leading edge. The slots are closed by perforated plates with the open area ratio being chosen variable along the flow axis so that the best flow field uniformity is achieved within the suction zone surface.

The flow field in the "empty" test section was investigated without the airfoil model by using a static probe in the traversing gear instead of the Pitot tube. The side wall boundary layer state was analyzed by applying 4 Pitot rakes placed behind the suction windows at different heights. The tests were aimed at evaluating the flow field characteristics in the model zone depending on main flow conditions and suction factor K (ratio of the sucked air mass flow rate to the total mass flow rate in the test section). Note that the results of the tests with K=0 when the perforated suction zone surfaces were replaced by smooth impermeable plates were chosen as the baseline data to estimate the effectiveness of the suction system.

First of all, the operation of the suction system itself was analyzed, i.e., the uniformity of the static pressure field on the surface of the perforated plate through which the suction was performed. Judging by the isobars shown in Fig.2, the uniformity proved to be acceptable. The line verticality indicates the absence of the flow upwash in the vertical direction which is very important for the formation of the flow angle of attack.

Fig.3 presents typical boundary layer profiles downstream of the suction zone. A monotone and considerable decrease in the boundary layer thickness is obvious as the suction factor rises from 0 to 2.5%.

The behavior of the integral boundary layer characteristics δ^* and δ^{**} as a function of K is illustrated in Fig. 4 for two rake positions relative to the model: in front of the model (L21) and above it (L11). Below is shown that the increase in K higher than 1-1.5% deteriorates appreciably the flow field uniformity in the empty wind tunnel as a whole, while δ^* and δ^{**} decrease rather slowly; for this reason, the suction amounting to 70% of δ^* was taken as optimal.

Fig.5 illustrates the uniformity of the static pressure field in the "empty" wind tunnel: the static pressure level in the model zone along the wind tunnel axis coincides essentially with the value of

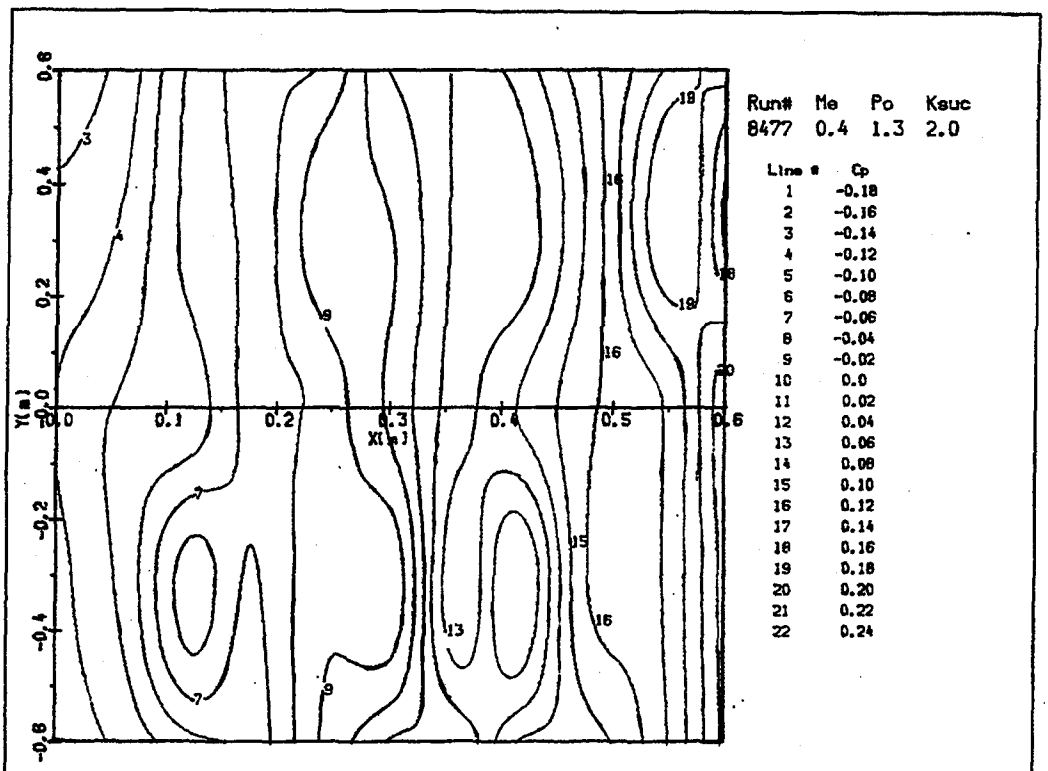

Fig.2. Wall pressure in the suction region.

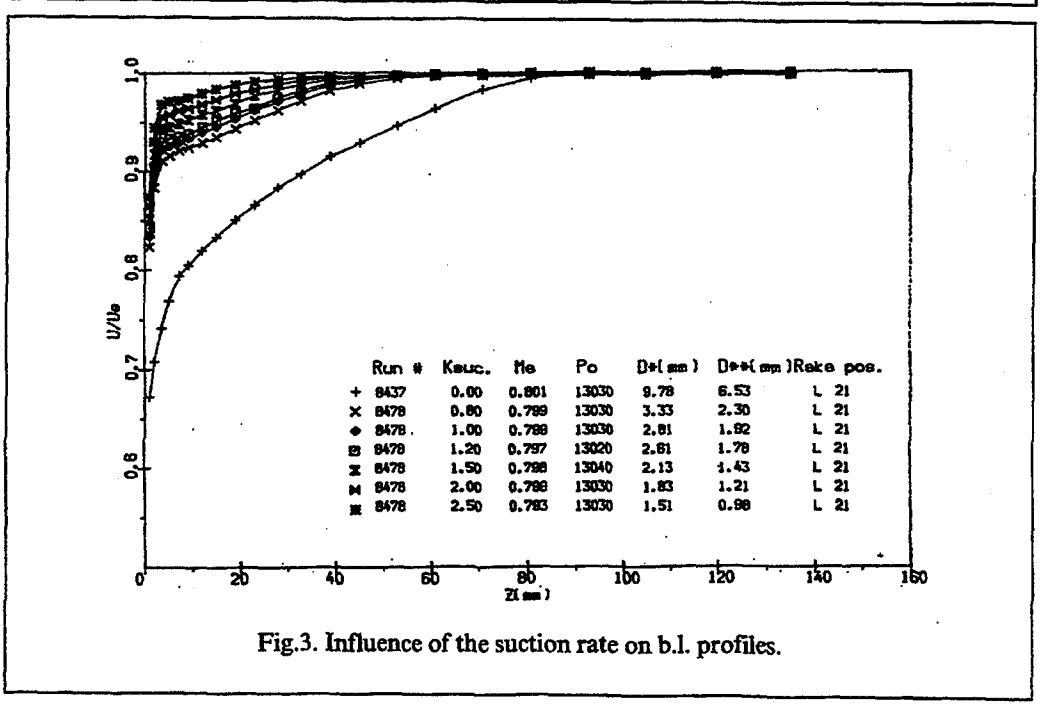

Fig.3. Influence of the suction rate on b.l. profiles.

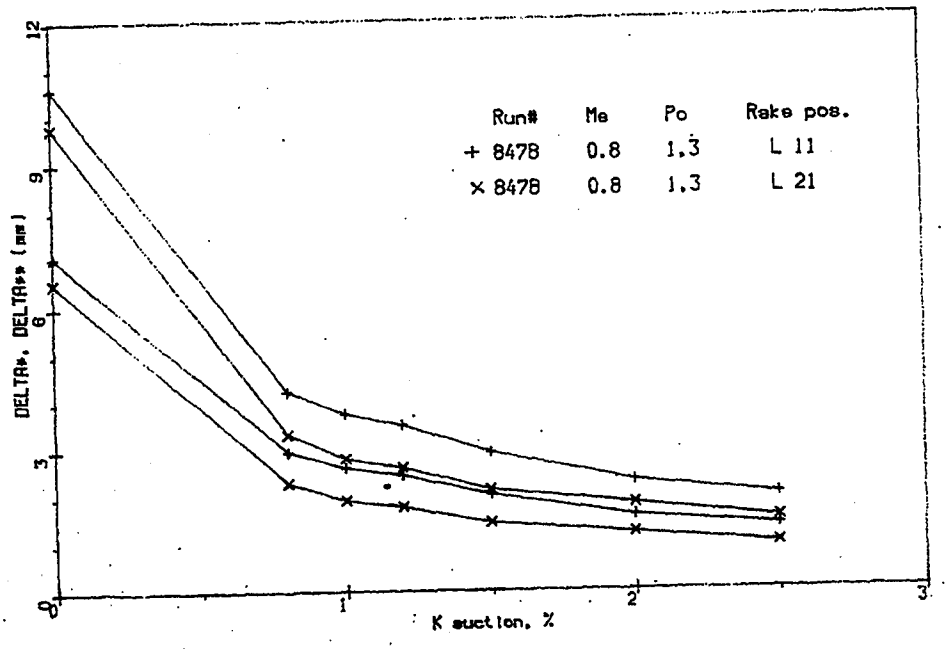

Fig.4. Influence of the suction rate on b.l. δ^*, δ^{**}.

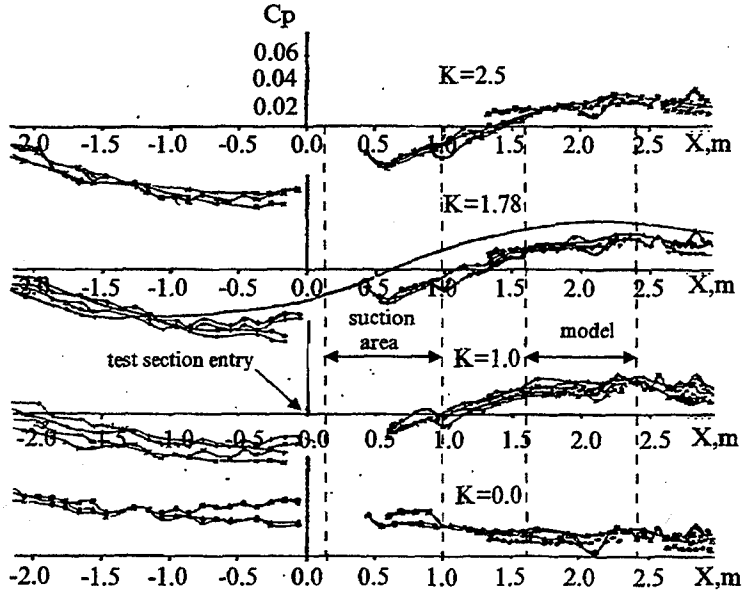

Fig.5. Pressure field in the "empty test section #3 with and without side wall boundary layer suction.

C_p near the walls at K=0, i.e., the static pressure gradient across the flow is small. The level of the longitudinal gradient of the static pressure measured by a probe along the flow axis in the model zone should also be considered insignificant.

The situation changes appreciably when the suction system is switched on resulting in the flow acceleration upstream of the system and the flow deceleration downstream of it. The pressure diagram along the test section length becomes wave-like which is easily modeled by sinks distributed over the suction zone surface. In this case, the dependence C_p assumes the following form

$$C_p(x) = -\frac{kH}{4\pi(x_1 - x)} \ln\left|\frac{(x_2 - x)^2 + \frac{H^2}{4}}{(x_1 - x)^2 + \frac{H^2}{4}}\right| \qquad (1)$$

Where H is test section width, x_1, x_2 - coordinates of suction area beginning and end.

A qualitative comparison of the above dependence with the test results (Fig.5) confirms the correctness of the modeling of this effect. From this it is inferred that the flow field distortion is inevitable as a whole when operating with the suction system. In this particular case, the situation is improved by the fact that there is a region of extremum of function (1) in the model zone, so the longitudinal pressure gradient distorting the flow over the airfoil is small, and a non zero average pressure level can be included, if necessary, in the form of corrections to the Mach number M_∞.

In the tests of the airfoil model, much attention was given to those methodical points as the influence of the boundary layer suction on the two-dimensionality of the flow over the airfoil, the interference with the traversing gear, the total flow upwash in the model zone. Some results of these tests are given below.

The influence of the traversing gear was evaluated by comparing two cases: the tests by using the traversing gear and without it (Fig.6). Only the characteristic $C_L(\alpha)$, which is natural for such an approach, proved to be accessible to the analysis which reveals a slight reduction in the airfoil lift due to a decelerating disturbance in the wake in a subcritical flow condition (M=0.7). At higher flow velocities characterized by the appearance of developed supersonic zones and by the nonlinearity in the characteristics $C_L(\alpha)$, a disturbance in the model wake leads to an increase as well as a decrease in the lift because of a complicated nature of the interference with the shocks on the upper and lower airfoil surfaces at different values of α.

In order to estimate the total upwash in the model zone, the model was tested in the direct and the overturned positions. The results of the tests are presented in Fig.7. It is seen that the average upwash does not exceed 1′ irrespective of the wall open area ratio.

Figs. 8, 9 demonstrate the increase in the flow two-dimensionality (due to the side wall boundary layer suction) in the form of the static pressure distribution along the trailing edge.

The behavior of the pressure diagrams in 3 spanwise airfoil sections in Figs.10, 11 illustrate a noticeable closure of spanwise pressure diagrams when the suction system operates.

The authors are deeply indebted to the Boeing company for the amiable permission to public the results obtained during the tests in the wind tunnel T-128 of the airfoil model ordered by this company.

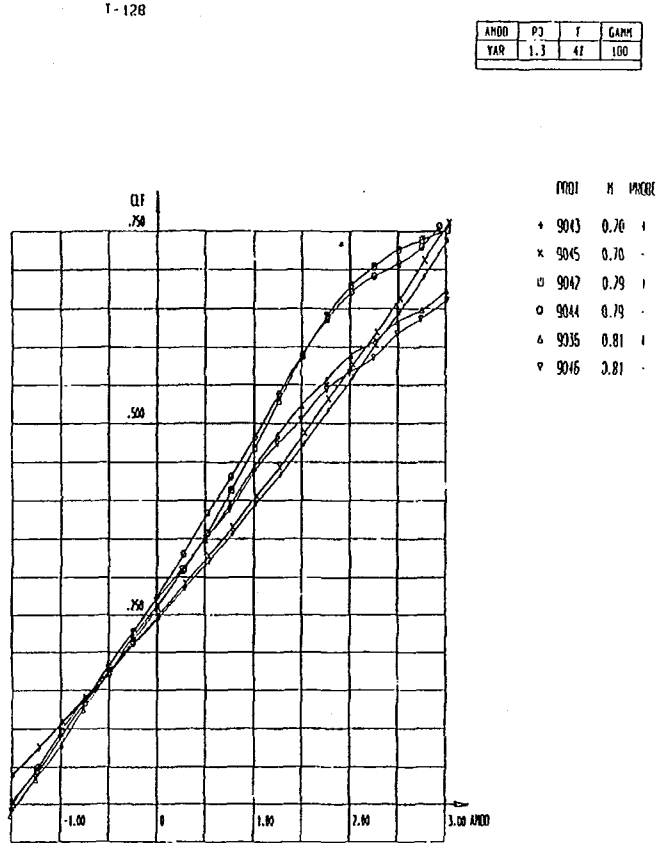

Fig.6. Wake survey mechanism ("probe") interference.

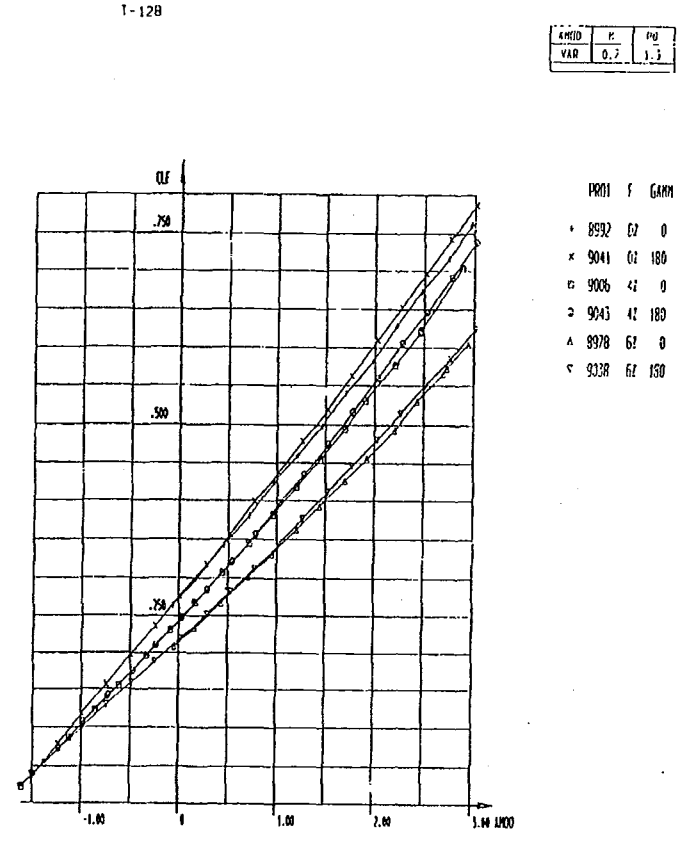

Fig.7. Model in direct ($\gamma = 0$) and inverted ($\gamma = 180°$) positions.

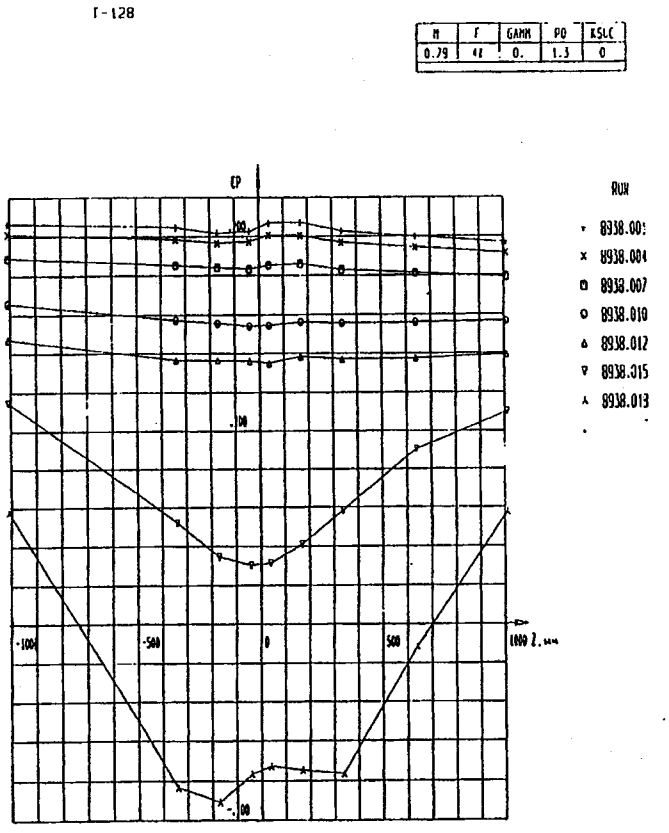

Fig.8. Pressure along trailing edge at various α (no b.l. suction).

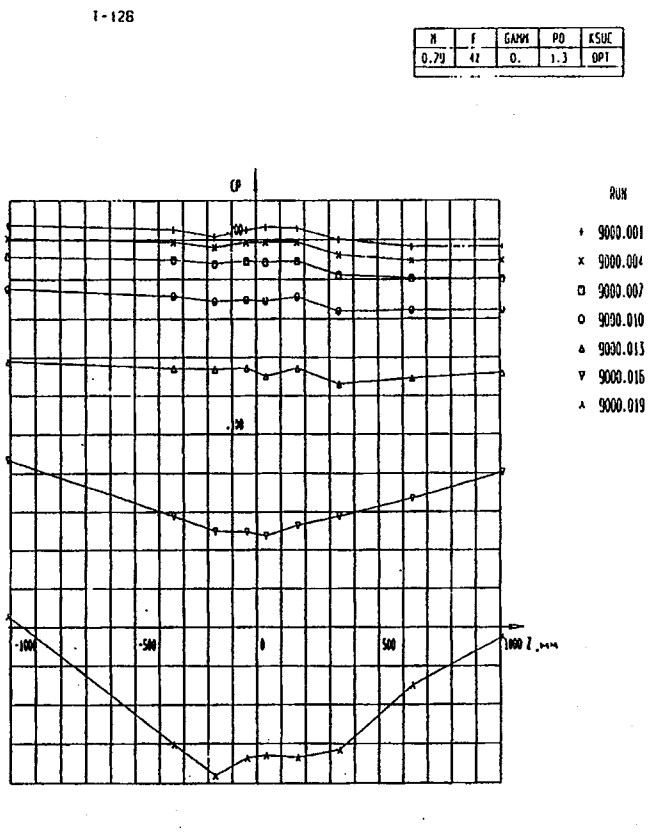

Fig.9. Pressure along trailing edge at various α (optimum b.l. suction).

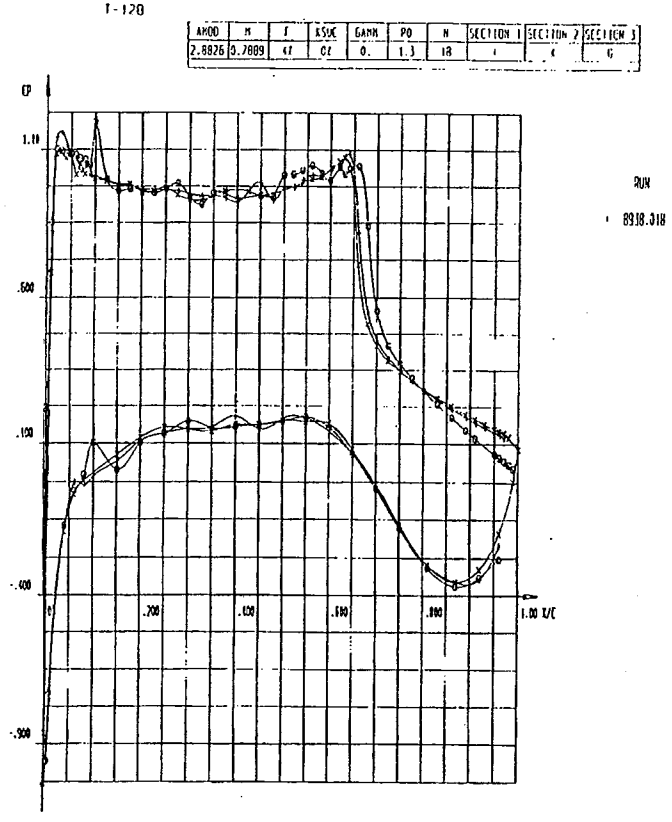

Fig.10. Pressure at three spanwise sections (no b.l. suction).

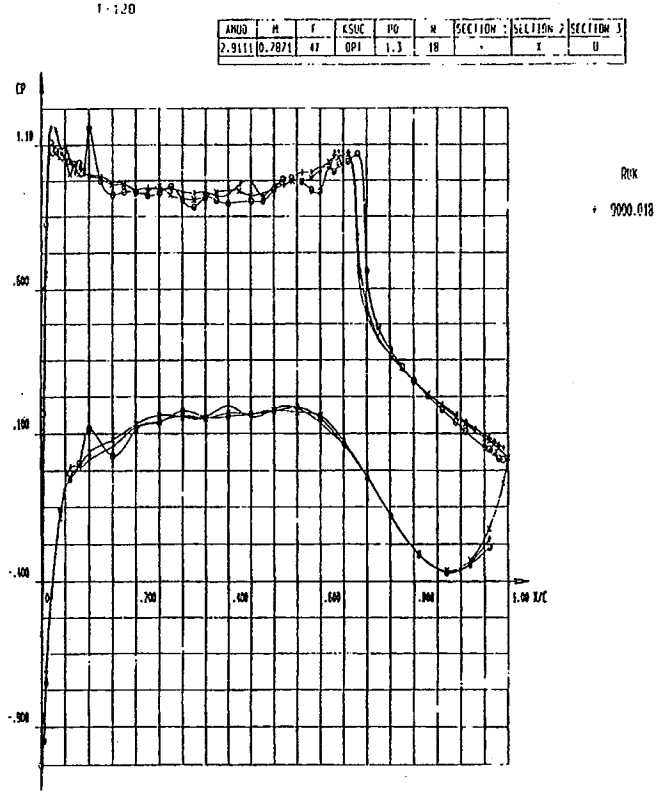

Fig.11. Pressure at three spanwise sections (optimum b.l. suction).

MODEL SUPPORT INTERFERENCE ASSESSMENT USING A METRIC REAR FUSELAGE AND A TWIN-STING AT ONERA S2MA WINDTUNNEL

M. Lyonnet, Large Test Facilities Directorate, Modane Avrieux (France)
J.F. Piat, Large Test Facilities Directorate, Modane Avrieux (France)
B. Roux, Large Test Facilities Directorate, Châtillon (France)

1 - Introduction

Testing techniques currently used in wind tunnels allow to get raw data for drag prediction of transport aircraft consistent with a repeatability of the drag coefficient around "one drag count" (1.10^{-4}) at cruise conditions.

Several corrections must be applied to such data in order to obtain measurements free from wall and support interference and from flow non-uniformity.

Model support interference is often the most critical term, typically shifting drag coefficients by 10.10^{-4}. It is usual to estimate it through CFD modelling of the stings (sources, doublets,...) reasonably accurate for far field effects but not enough to quantify the influence of supporting parts in close or direct contact with the model.

A joint effort ONERA/Aerospatiale has led, for accurate drag measurements of the AIRBUS A310 at S2MA wind tunnel, to the selection of a discreet fin sting support. The model scaled 1/38 is supported from a dorsal sting through a blade taking place of the fin. This blade penetrates the fuselage in a low pressure gradient area thus minimizing interactions in the slot. These interactions are further reduced by a sealing system between the blade and the fuselage.

In order to determine accurately the influence of this "sting + blade" support on drag, lift and pitching moment of the model and to compare it with that of the real fin, a test set-up has been developed according to the following principle : the model is supported by a twin sting fitted to its wings whilst the efforts on the rear fuselage are measured by an internal balance, first with the true shape of the fin, then with a dummy "sting + blade" support (fig. 1a and 1b).

This test procedure assumes that :

- the change from the true fin to the supporting blade only affects the rear (metric) part of the fuselage ;

- aerodynamic interference fields of the twin sting and the "blade + sting" are additional.

2 - Principle

Raw force data are first obtained through a regular model test performed with the "sting + blade" support. They are corrected from empty test section non-uniformities and from model induced wall interference. It only leaves for further correction the "sting + blade" support effect (including its own wall interference).

This effect is estimated through a sequence of two measurements made on the rear fuselage, one with a dummy "sting + blade" non metric (fig. 1a), the other one with the true shape of the fin (fig. 1b).

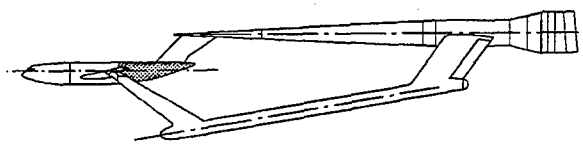

Fig 1.a Wheighing with the dummy fin-sting

Metric part

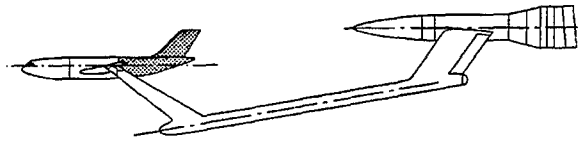

Fig 1.b - Wheighing with the real fin

These measurements provide when substracted the effect of the "sting + blade" support compared with that of the true fin. Blade effect obviously only applies to the (metric) rear fuselage. Further effects of the sting on the front part of the model are calculated.

These two tests normally allow to correct full model tests. Nevertheless several additional experiments have been made in order to validate the above procedure and to estimate the contribution of each term. Measurements were obtained on the following configurations :

- metric rear fuselage without any fin,
- same as above in the aerodynamic field of the sting alone,
- metric rear fuselage with a non metric fin,
- same as above with the blade alone instead of the fin.

3 - Test set up

The first tests were performed in the transsonic test section of the ONERA S2 tunnel in Modane, using a 1/38 scale A310 model (fig. 2).

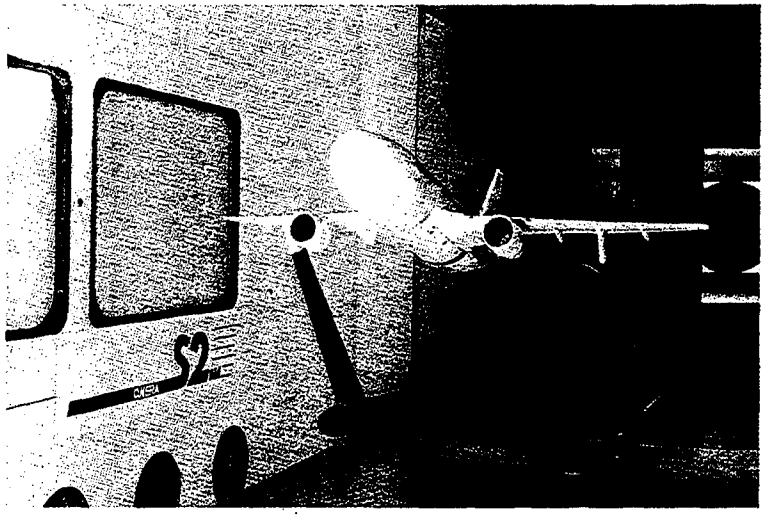

Fig.2 - A310 model on twin sting support

The model, specially designed for these tests, is supported at the wings by a twin sting rigidly connected to the sting support sector of the tunnel. The model has a split section perpendicular to the fuselage axis, just downstream of the wing/fuselage attachment, and various rear fuselage parts can be used. The split section gap is left open, with an adjustable width of about 0.3 mm.

The front (non metric) and rear (metric) parts of the model are connected with a six component balance. The balance was designed and gaged by ONERA. It has a high drag sensitivity and high stiffness in lift and moments. The high rigidity minimises distortions under loads and therefore the split gap width between the metric and non metric part can be minimised. The drag resolution is 0.02 N, i.e. 0.03 10^{-4} on the drag coefficient for the test conditions (Mach : 0.8 - Reynolds number of 3 10^{6} based on the mean aerodynamic chord).

Two long beams, which are part of the non metric model part, go around the balance through the rear metric part and are used to support additional non metric parts at the back of the model : dummy fin sting, blade of the dummy fin sting, real fin (non metric case). When the dummy fin sting is used, the blade (rigidly connected to the front fuselage through the long beams) and the sting (attached to the sector of the tunnel) have a flexible connection. This ensures that these two (non metric) parts move together when the model is being pitched.

Two types of rear model part can be used :

- The rear part # 1 is designed for tests without fin or with a metric fin. It is a single piece part ;

- The rear part # 2 is made of two half shells for tests with a dummy fin sting, the blade or a non metric real fin. The tightness between the metric rear part and non metric component is achieved with a teflon seal.

About 45 static pressure taps are located in the internal cavity of the rear part and on the downstream face of the balance support piece. Four static pressures are measured on the fuselage, on each side of the split gap. The wing is equipped with twenty taps ; four of them are on the leading edge to detect possible local incidence changes.

In order to evaluate the real sting influence areas, 45 wall pressures are measured on the rear part # 2 outer surface ; their locations are shown on fig. 3. All pressures are measured with 3 on board multisensors.

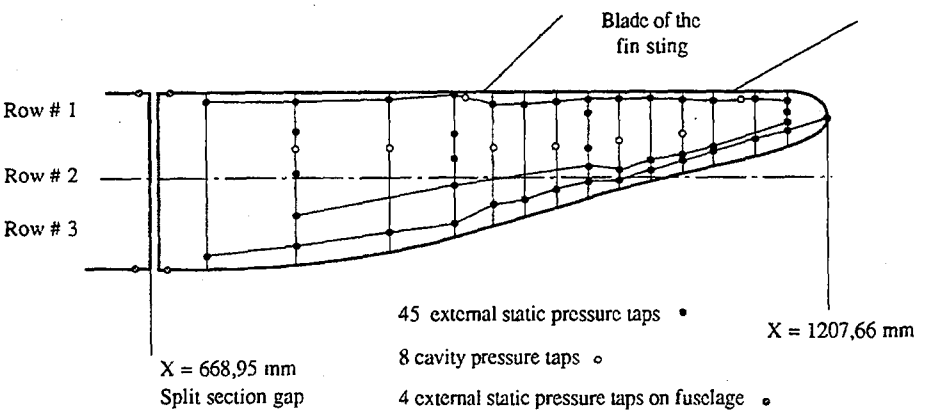

Fig. 3 - Rear Fuselage Model

4 - Test methods

In view of the required accuracy for these tests, the measurements are performed in pitch and pause mode at three Mach number values (0.78 / 0.80 / 0.82) and 3 α values (- 2° / 0° / + 2°). Each set point data is made of 8 recordings at 1 s. intervals. Before each data acquisition, the auto pilot checks the test parameter stability. The controlled parameters are the Mach number (± 0.001), the Reynolds number (± 15 000), the total temperature (± 1 K) and the model incidence (± 0.01°).

Each recording includes the acquisition of the signals of the six balance strain gage bridges, additional sensors and all pressures measured with 3 PSI multisensors.

The rear part correction is determined from the corrected coefficients measured in the two basic tests described previously (fig. 1a and 1b).

DCX = CXC2 - CXC1 is the correction to be added to the drag coefficient.

CXC2 and CXC1 are the corrected drag coefficient measured from tests 2 and 1, respectively. They are calculated as :

$$CXC = CX - \frac{(Pc - Po)\, Sc}{Qo\, Sref} \cos \alpha \qquad (1)$$

where CX is the uncorrected drag coefficient
Sref is the model reference surface
Sc is the surface of the model split gap
Po is the model point of reference pressure
Pc is the average of the 38 gap pressures
q_o is the reference dynamic pressure.

Similar corrections are performed for the lift and pitching moment coefficient.

The two tests are performed at the same Mach number at the model reference point (25 % of the mean aerodynamic chord), taking into account the far field sting effects for each test set up. Hence, the static pressure at the model reference point is the same for both tests.

As can be seen from equation (1) minor errors on the reference Mach number may result in significant errors on the final result. It is therefore very important to define carefully the reference Mach number.

Likewise, the end result accuracy is very much dependent upon the gap pressure measurement accuracy ; therefore, this pressure is the average of a large number of measurements. The multisensors used are checked for each measurement point ; zeros are measured and calibrations performed as soon as zero drifts or sensitivity changes are detected.

5 - Fuselage rear part testing

The repeatability of the measurements within a run is excellent. The measurement deviations with respect to the average corrected drag coefficient are below $0.5\ 10^{-4}$ in 80 % of the test cases, and they never exceed 10^{-4}.

With such a good repeatability, an extreme attention should be paid to the model quality. In that respect, fig. 4 shows a comparison between two test series performed with the model rear part # 2 and the dummy fin sting. The rear part has been disassembled between the two series.

The results show both the uncorrected drag coefficient measured from the balance and the net drag coefficient corrected from pressure effects in the metric / non metric gap.

For this configuration, using a rear part made of two half shells, the uncorrected drag coefficients change significantly between the two runs. There is a difference between the pressure levels within the model due to a poor repeatability of the teflon seal positioning around the fin.

However the gap pressure effect correction reduces the difference between the net coefficients down to 0.5 10^{-4} with respect to the average value. This good result is probably due to an homogeneous pressure distribution within the rear part cavity (fig. 5).

Model with dummy fin sting

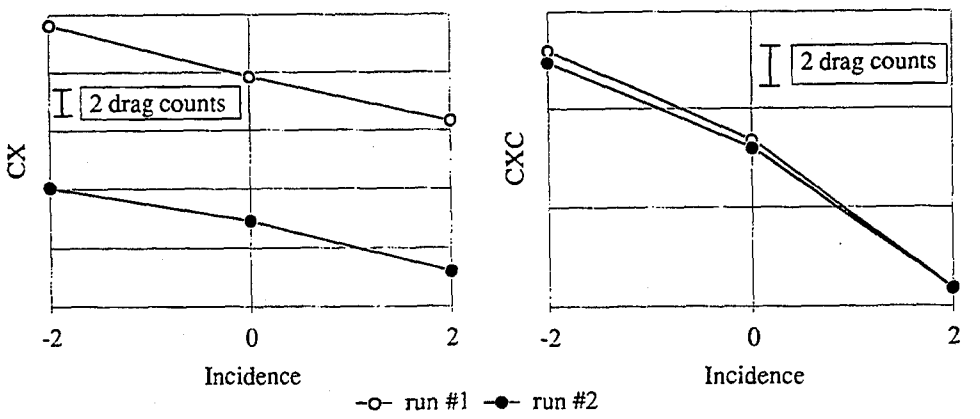

The model has been disassembled between the two runs

Fig. 4 - Repeatability of drag measurements

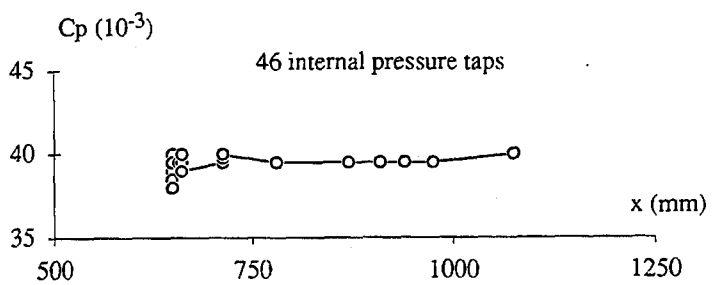

Fig. 5 - Pressure measurements in the rear part cavity

The comparison of the wall pressures measured on the rear part between the complete model configuration and the model equipped with the dummy fin sting, shows that the twin sting does not change the flow on the rear part (fig. 6). It seems reasonable to assume that the twin sting flow field effect is additional to other effects and therefore its presence does not affect the model support effect determination.

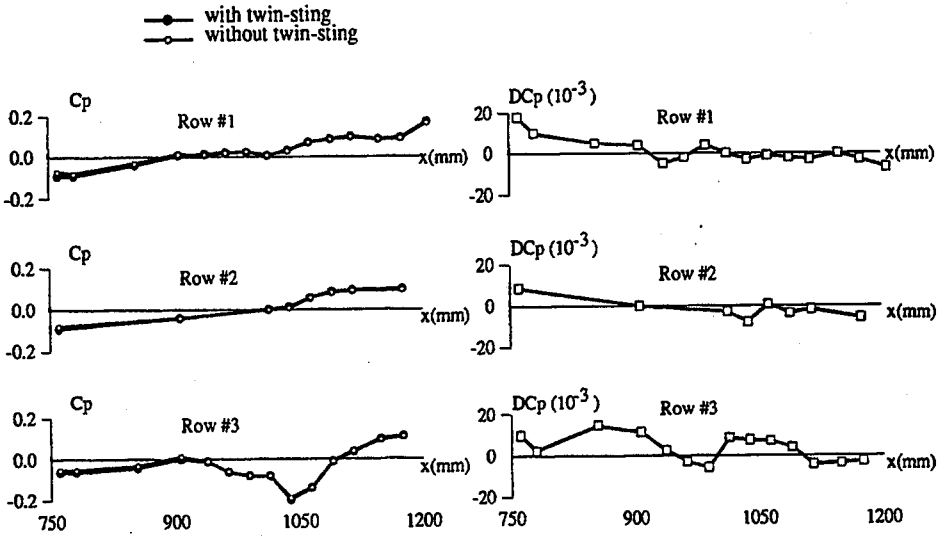

Fig. 6 - Twin-Sting Field

The gap pressure effect has also been investigated : this effect can be reduced to a pressure change within the rear cavity, with no influence on the outer flow. This effect is well accounted for by the gap pressure effect correction.

The blade effects of the fin sting on the front (non metric) part of the model have been checked by pressure measurements on the wing. These effects are negligible, below 0.001 of Cp in terms of pressure and below 0.01° in terms of local angle of attack.

The effect of the fin sting arm can be directly assessed by comparing the two rear part balance measurements shown on fig. 7. These two measurements are performed in sequence, with the rear part # 1, without any model disassembly between the two runs.

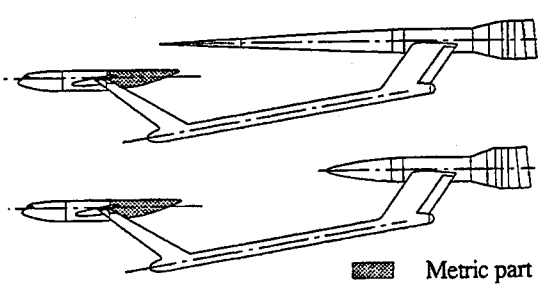

Fig. 7 - Sting arm effect

The same effect can also be determined from the comparison of the two balance measurements, shown on fig. 8, using the rear part # 2 and assuming that the blade effect is additional to the sting arm effect. However a rear part disassembly has to take place between the two runs.

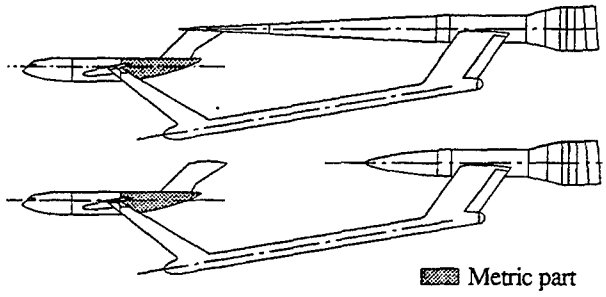

Fig. 8 - Sting arm effect (with the blade)

Finally, the sting arm flow field can be calculated using the singularity method after integration over the model rear part, taking into account the test conditions i.e. using the same static pressure at the model reference point.

The results obtained with the three above methods are shown in the following table :

	Calculated effect CXC (10^{-4})	Measured effect (without blade) CXC (10^{-4})	Measured effect (with blade) CXC (10^{-4})
$\alpha = -2°$	- 8,1	- 7,9	- 8,1
$\alpha = 0°$	- 8,6	- 8,9	- 7,1
$\alpha = 2°$	- 9	- 9,1	- 7,7

Considering the measurement errors, the three methods are in fair agreement. The combination by pairs, out of four totally independent tests with the rear part, allows the far field sting effect to be determined with a deviation less than 1.10^{-4} with respect to the average value. The difference between the measured average effect and the calculated effect is also below 1.10^{-4}. This confirms that the blade effect of the fin sting is additional and increases the confidence in the procedure in use.

These tests not only validate the method in use but also provide an estimated breakdown of the rear part correction. As far as the drag coefficient is concerned, about 50 % of the correction are due to the fin loads, while 15 % can be attributed to geometrical differences between the real fin and the blade of the fin sting and 35 % to the sting arm effects.

6 - Conclusion

The twin sting model support system, when used with extreme care, allows the support effect to be accurately assessed. The major effects are determined from balance measurements. Only the minor effects of the sting arm on the front part of the model are calculated.

This experimental set up will also be used to investigate the effects of other types of model supports (Z sting, straight sting).

In view of its slenderness, the twing sting support is also well suited for fuselage rear part optimisation.

WALL INTERFERENCE CORRECTIONS OF SWIM TESTS IN THE MODEL SUBSONIC WIND TUNNEL BRAUNSCHWEIG (MUB)

W. H. Zhang
(Nanjing Uni of Aero-& Astronautics, 210016 Nanjing, China)
A. Kupper
(DLR WT-WT, 3300 Braunschweig, Germany)

ABSTRACT

A universal wall interference correction method (UWICM) is described in this paper. A high-life model SWIM (subsonic wind tunnel interference model) of NLR was tested in MUB[1](the model subsonic wind tunnel Braunschweig) and in NWB[2](the low speed wind tunnel Braunschweig). Experimental examinations of the method gave good results for high life model.

INTRODUCTION

Owing to the finite dimensions of the test section the measured data of model in wind tunnel are not the same as those in free air. To correct measured data in wind tunnel, the different methods have been developed.

One of the oldest corrective methods is derived by Glauert[3]. Today it has been detailed in [4]and [5]. The interference factor was computed by using the image technique for closed or open rectangular test secton. The method is adequate for small angle of attack and small-blockage. It is difficult to take into account high lift, large wake region and model support.

Recognising these problems, G. Schulz[6]proposed a correction method of using the influence function, His method require a relatively limited number of static pressure measurement points at the walls. However, a model representation is not required. An experimental examination for large blockage gave good results. It doesn't know if the determined optimum measurement points for every conceivable model with high lift and large stagnant wake are optimum. The validity of his method should be checked by further experiments.

A wall pressure method is developed by Hackett[7]. By this method, the wind tunnel interference can be determined at high angle of attack. However, this method requires a model representation. If model representation in more details is required, the number of required wall static-pressure measurement points is excessive.

The developed by Holst[8] Green-method does not require model representation. The method is applicable not only for the determination of wall interference but also for the correction of rest interference concerning adaptive wall or slotted walls. The problem is,

whether the satisfactory result can be achieved at high angle of attack and large blokage. The MBC (measured boundary condition) correction method is proposed by Labrujere[9]. The method does not require model representation either. The experiment on high lift configuration gave good result. Unfortunately an experiment at high angle of attack has not been made.

In this paper is given a universal wall interference correction method(UWICM). It will be proved that the UWICM method is suitable for high lift model at higher angle of attack.

DESCRIPTION OF METHOD

The relation between the wall static-pressure (at any point of wall) and correction value at model reference point is established for the downwash correction[10]

$$\Delta\alpha_M = -\frac{1}{2f_A}\Delta C_{PW}(A) \tag{1}$$

$$f_A = \frac{\Delta V_{XW}(A)}{\Delta V_{ZM}(A)}$$

The dynamic pressure increment is given by

$$\frac{\Delta q}{q_\infty} = -\frac{1}{f_V}\Delta C_{PW}(V) \tag{2}$$

$$f_V = \frac{\Delta V_{XW}(V)}{\Delta V_{XM}(V)}$$

where $\Delta V_{XW}(V)$、$\Delta V_{ZM}(A)$ are increment of velocity due to wall interfernce, x and z direction, respectively. The influence function f_A and f_V have been calculated by using the modified vortex lattice method[11]. As a result, fv and f_A, varying along the wall circumferenc, are shown in reference 12. It will be seen that fv and f_A are a "bunching character". There are 4 small regions (nearly as the 4 points, called as optimum points) along the wall circumference, in which the influence functions are bundled up and independent of model span-tunnel width ratio. The "bunching character" of f_V、f_A is called laternal ductility. In order to obtain that longitudinal ductility, the combination influence functions $f_{V12}$and f_{A12} are employed

$$f_{V12} = K_1(V)\, f_{V1} + K_2(V)\, f_{V2}$$
$$f_{A12} = K_1(A)\, f_{A1} + K_2(A)\, f_{A2}$$

The f_{V12}、f_{A12} curves with the least undulating course are obtained, as shown in reference

12. Hence Eqs(1) and (2) become

$$\Delta\alpha_m = -\frac{1}{2f_{A12}}(K_1(A)\ \Delta C_{PW1}(A) + K_2(A)\ \Delta C_{PW2}(A) \tag{3}$$

$$\frac{\Delta q}{q_\infty} = -\frac{1}{f_{V12}}(K_1(V)\ \Delta C_{PW1}(V) + K_2(V)\ \Delta C_{PW2}(V) \tag{4}$$

The pressure coefficient increment $\Delta C_{PW}(A)$ is caused by donnwash effect and $\Delta C_{PW}(V)$ is due to the blockage effect.

Owing to the laternal ductility of f_A、f_V and the longitudinal ductility of f_{V12}、f_{A12}, the number of necessary wall pressure measurement points is kept small (=16). The wall pressure measurement systems for downwash and for blockage correction in MUB are illustrated in Fig1.

TEST APPARATUS

Wind tunnels: the small wind tunnel, referred as MUB, is a subsonic wind tunnel of the closed return type. The test section dimensions are 0.82M (breadth)×0.82M (height)×4.1M (length). The model is supported with a rear sting and vertical-shrut. There is a segmental are slot at bottom, so that the vertical strut is passed through the bottom and is connected with angle variation equipment. The large low speed wind tunnel, so called NWB, is also a subsonic wind tunnel of the return type. The test section dimensions are 3.25M(breadth) ×2.8M (height)×8M(length).

Model: The model SWIM (subsonic wall interference model) is offered by NLR for us, as indicated in Fig2, The design of the wing-flap combination turned out to be very successful. A fairly high lift ($C_{zmax}\sim 2$) can be achieved. The model span amonnt to 18% of breadth of NWB test section and 73% of breadth of MUB test section, so that the measurement in NWB is regareded as interference-free data.

Measurements equipment: The model forces and moments were sensed by means of 1.25″ 6-component balance MKXIVA, which was mounted inside of the fuselage.

The tunnel-wall static-pressure in NWB and in MUB were scanned by means of 48-port scanivalue assemblies mounted outside the test section, its measurement range is 1/3 PSI or 1 PSI, respectively for NWB or MUB.

RESULTS AND DISCUSSIONS

The wall static pressure distribution along the test section length in NWB are situated nearly in a constant level[12], not only for empty wind tunnel (without model, with rear

sting and vertical strut), but also for high lift configuration RFKH. It is seen, that the wall interference in NWB is a negligible quanitity.

The induced wall static pressure by model in MUB are obtained from difference between the wall static-pressure with model and those for empty wind tunnel. The variation curve of induced wall static-pressure displays the shape of bell[12]. The model with flap has a bigger bearing on wall static—pressure then the model without flap. The induced wall static-pressure magnitute grow on with increase of angle of attack. The conclusion is in agreement with reference 13.

Results of the measured forces, moment in MUB and corrrected results with two methods (UWICM and classical corrective method[4][5]) are shown in Fig 3. 4. 5. Simultaneously there are results of the measured forces、moment in NWB. As will be readily seen, the correction results with UWICM method for the measurement value in MUB are essential in agreement with data in NWB. But the classical corrective method is good only at small angle of attack and small lift.

CONCLUSIONS

In this paper is presented a universal wall intefernce method (UWICM) for high lift model. The experimental examinations prove, that the measurement forces、moment in MUB with helf of UMICM method can been reliably corrected to be interference-free data.

The number of the necessary wall pressure measurement points (optimum pionts) are kept low (=16). The location of the determined optimum points depend only on form of test section, indepent of model size and form.

Because of the modified vortex lattice instead of the image technique, The UWICM method is applicable for rectangular test section with corners and slotted wall.

REFERENCE

1. Muller, R., Beschreibung des Modell-Unterschallwindkanals (MUK) zum "Groβen Unterschallkanal" (GUK), DFVLR IB 151—75/14(1975)
2. Kausche, G. Otto, H. Christ, D. Siebert, R., Der Niedergeschwindigkeits-Wind kanal der DFVLR in Braunschweig, DFVLR-Mitt 88—25(1988)
3. Glauert, H., Windtunnel-interferènce on wings、bodies and airscrews, ARC R & M 1566(1933)
4. Vayssaire, J. Ch., Corrections de blockage dans les essais en soufflerie Effefs des decollements, AGARD CP-102 (1972)
5. Kramer, K., Windkanalkorrekturen fur Tragflugel ohne und mit Bodenplatte in einem rechteckigen Freistrahl, AVA Bericht 62A35, Gottingen (1962)

6. Schulz, G., Ein universelles dreidimensionales Wanddruck-Korrekturverfahren fur geschlossene rechteckige Unterschallwindkanalmeßstrecken (Verdrangung, Abwind, Krummung) DFVLR FB82—18(1982)
7. Hackett J. E. Wilsden, D. J. Stevens, W. A., A Review of the "Wall Pressure Signature" and other Tunnel Constraint Correction Methods for High Angle-of-Attack Test, Lockhead-Georgia COMPANY, Marietta, Georgian, USA (1981)
8. Holst, H., Verfahren zur Bestimmung von dreidimensionalen Windkanalinterferenzen und Wandadaptionen mit Hilfe gemessener Wanddrucke bei kompressibler Unterschallstromung DLR FB90—46(1990)
9. Labrujere, Th. E. Maarsingth, R. A. Smith, J., Evaluation of Measured-Boundary-Condition Methods for 3D Subsonic Wall Interference, NLR TR 88072U (1988)
10. Zhang, W. H. Schulz, G., A wall pressure correction method for closed subsonic wind tunnel test section. Chinese Journal of Aeronautics, Vol. 2, NO. 3(1989)
11. Holst, H., Germany Activities on Wind Tunnel Corrections, AGARD Report 692 (1981)
12. Zhang, W. H. Kupper, A., Windkanalmessungen zur Uberprufung eines dreidimensionalen Wanddruck-Korrekturverfahrens fur geschlossene Meßstrecken, DLR IB 19111—92 A11 (1992)
13. Young, A. D., Wind tunnel corrections for high angles of attack, a brief review of recent U. K. work, AD A098058 (1981)

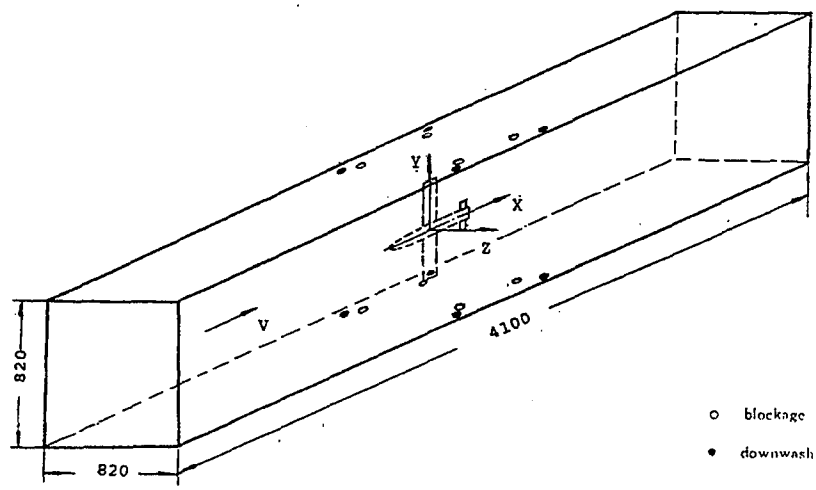

fig 1 Wall-pressure measurement systems

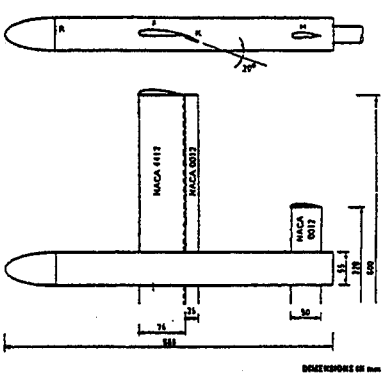

fig 2 Model SWIM

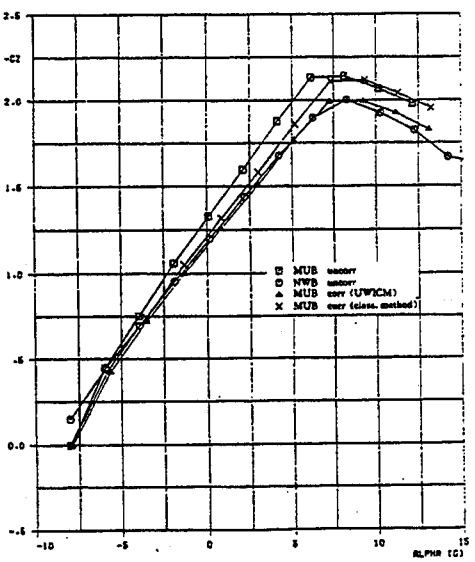

fig 3 Lift curves for MUB and NWB (RE=4.0MIO. RFKH)

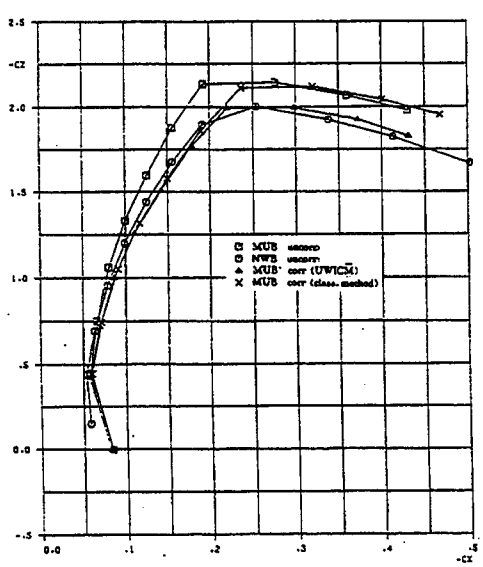

fig 4 Drag polars for MUB and NWB (RE=4.0MIO.RFKH)

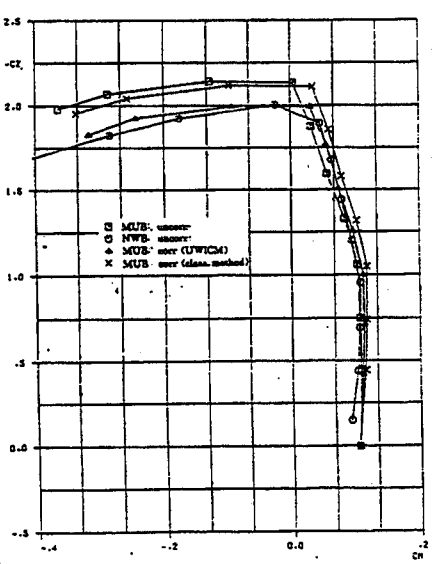

fig 5 Lift-pitching moment curve for MUB and NWB (RE=4.0MIO. RFKH)

SLOTTED WALL INTERFERENCE STUDIES IN VKI-S1 WIND TUNNEL

W. SCHRÖDER [1)]
DLR, Inst. EA, D-38108 Braunschweig, Lilienthalplatz 7 (Germany)
S. KEYE [2)]

ABSTRACT

Selected results of 2D wall interference studies in the new variable slot width and shape transonic test-section of the VKI-S1 wind tunnel are introduced. It was found that overall wall interferences could be minimized but significant gradients remained. In addition to airfoil and wall pressures, detailed plenum pressures were recorded. They indicated unfavourable wall/plenum pressure gradients in certain areas which did not support the wall cross flow direction needed for interference free flow conditions. Some active plenum pressure control is needed for a further reduction of the wall interferences. A two chamber arrangement per horizontal wall is suggested. Supporting detailed results on wall and plenum pressures, actual and needed wall cross flows, and needed suction or blowing rates are provided.

INTRODUCTION

Wall interference assessment, correction, and adaptation has been a subject of activity at VKI during the past few academic years. The research has concentrated on two aspects:

- "mechanical" solid wall adaptation in T'3, the cryogenic pilot wind tunnel of ONERA/CERT, given on loan to VKI,
- "pneumatic" adaptation by ventilated walls. For this purpose VKI's supersonic wind tunnel S1 had been equipped with a new transonic slotted wall test section which features slots of variable width and shape.

The wall interference assessment, correction, and adaptation techniques have been provided by DLR, where they had been succesfully applied to a variety of 2D experiments in several DLR and foreign wind tunnels. Based on the results obtained thus far, some are reported in this paper, the ongoing VKI activities will mainly be concentrated on a simplified active control of the plenum pressures to reduce wall interferences to the flow quality requirements[1].

WIND TUNNEL, INSTRUMENTATION AND TEST CONDITIONS

A photo and principle sketch of the new slotted wall test section is shown in Fig. 1. The slotted part of the test section is equivalent to 10 chord lengths. The side walls are parallel. The horizontal walls can be converged or diverged to control the pressure gradient in the empty test section. Each of the horizontal walls has 4 full and 2 half slots. The mechanism to adjust the slot width is drawn in Fig. 2. Each slat consists of a fixed and a moveable piece. The slot width can be manually adjusted to any value between 0 and 6 mm, being equivalent to an open area ratio σ from 0 to 6.75 %. Each moving slat is cut into two parts each of half the test-section length, so the slot widths S_1, S_2 and S_3 (see sketch of Fig. 1) can be set individually to enable piecewise linearly converging, diverging, or constant slot widths. The photo (Fig.1)

1) DLR visiting professor at VKI 91-93
2) VKI Diploma Course student 92/93

shows a plenum chamber behind each slotted wall. The total plena volume is approximately the same as the test-section volume. There are additional instrumentation cavities behind each plenum.
Two kind of plena have been considered (Fig. 2). The "open plenum chamber" is identical to that full plenum as shown in the photo of Fig. 1. The plenum pressure distribution is measured along a rail. The rail rotated by 90° closes a small, well defined "closed slot chamber". These chambers are ventilated at both ends to the overall plenum.
Static pressures along airfoil contour (47), horizontal walls (47 each), and plenum rails (23 each) have been taken by 4 transducers and 4 scanning valves on 2 shafts. To avoid any leakage, the intrumentation had been placed in the two instrumentation plena.
Tests have been performed with a DLR R4 airfoil of 150 mm chord at 0°, 1° and 2° incidence at Mach numbers between 0.4 and 0.75. At a total pressure level of 100 mm Hg, the chord Reynolds number ranged from $2 \cdot 10^5$ to $4 \cdot 10^5$.

INTERFERENCE ASSESSMENT METHOD

The DLR 2D wall interference, correction, and adaptation method is based on Cauchy's integral. For a closed wall configuration the wall pressures and wall slopes serve as boundary conditions[2],[3]. In the case of ventilated walls, the wall crossflow boundary condition is difficult to measure and therefore usually unknown. In this case, it can be calculated by a model representation technique. The iteration technique[4],[5] has been replaced by an 'inverse' Cauchy approach. The airfoil geometry and contour velocity, derived from the measured airfoil pressure, serve as input. The Cauchy integration, taking the line integral in the opposite sense, yields the model disturbance velocities along the walls. The disturbance potential of the walls is represented by vortex sheets and is determined by the difference of the measured and model induced pressures along the walls. Once the wall disturbance is known, the total cross flow component at the wall can be determined, which completes the set of boundary conditions for the wall interference assessment.

Compressibility is covered by the Prandtl-Glauert rule, which limits the method's validity range. The Cauchy code itself does not need any information about the model. As long as the flow field close to the walls is linear, the method works well. In cases such as these experiments, where the wall crossflow has to be calculated by model representation, the character of the airfoil flow really determines the validity range of the whole interference assessment. Flow cases with significant nonlinear effects on the airfoil have therefore been avoided.

EXPERIMENTAL RESULTS

Typical empty test-section pressure gradients are shown in Fig. 3 for solid and slotted walls. Airfoil tests in the solid test section have been performed at wall divergence DH for zero pressure gradient at each particular Mach number, while all slotted wall experiments have been carried out between parallel walls. The influence of the plenum configuration on the plenum pressure is illustrated in Fig. 4 for the lower wall. While the pressure in the open plenum is nearly constant, the wall pressure dominates the plenum pressure of the closed slot chamber. The difference between the two pressures is nearly constant along the whole test section length.

All airfoil tests addressed in this paper have been performed at 1° incidence. A typical test result is summerized in Fig. 5. The measured pressure distribution along airfoil and walls are shown by circles, as well as the wall cross flow as predicted by the model representation. Plenum pressures are included in the middle diagrams.

The corrected flow properties, i. e. those at interference free flow conditions, are shown as dashed lines. The wall interferences in terms of wall pressure and cross flow are indicated by the cross-hatched regions.
The corrected wall contours in the lower part of the central diagrams can be interpreted as that contour of the slotted wall (mechanical readaptation) being necessary to eliminate the wall interferences which could not be covered by the plain slotted walls (pneumatic adaptation).

WALL INTERFERENCE ASSESSMENT

All model tests with uniform slot width showed that the wall induced average blockage (Mach number correction) could be eliminated with slot widths between 3 and 4 mm, while an increase in incidence correction and some reduction of wall induced flow camber was observed. A typical example is shown in Fig. 6.
Moreover the wall induced interference gradients were hardly reduced (Fig. 7) and are still inacceptable from the standpoint of the flow quality requirements for transonic testing[1].
Additional tests with linearly varying slot widths did not show significant improvements.

WALL CROSS FLOW ASPECTS

The further considerations were concentrated on the wall cross flow mechanism. Based on the experiments (Fig. 5), Fig. 8 focuses the pressure difference between wall and plenum, as well as the necessary correction in cross flow for interference free conditions. The wall/plenum pressure gradient does not support the needed cross flow direction. While upwash (outflow) is needed in front of the model and downwash (inflow) behind, the actual pressure difference causes maximum test-section inflow at the model position where nearly no cross flow is needed. This causes an unfavourable flow direction downstream.

An active plenum pressure control is needed. According to Fig. 9, plenum suction is needed on the upstream top wall section to remove 2.75% of the test section flow which must be pumped back into the test-section through the downstream slots. In front of the bottom wall 2.25% blowing into the test-section is needed, and suction into the plenum at the rear. The compensation of the model wake blockage can be done either by diverging the horizontal walls, or by removing some amount of the rear plenum flow directly into the reentry/diffuser section downstream of the slotted test-section. Fig. 10 indicates maximum cross flow rates between 2% and 3.75% as function of the slot width.
For the particular experiment of Fig. 5, the actual slot cross flow Mach number distribution is plotted along both walls in Fig. 11. The maximum Mach number above the model is about 0.5 and the total slot velocity well below sonic speed, justifying the linear assumption of the interference assessment.
Fig. 12 compares the slot cross flow and the slot pressure difference. The pressure difference determines the cross flow direction and a nearly constant factor relates the two quantities. Such slot loss factor is mainly dependent on the geometry of the slots, i.e. shape of the lips and width/depth ratio. Only the latter one has been varied by the slot width during the experiments. Due to different slot lip shapes at the wall and plenum side, and due to plenum imperfections like back up structures etc., the loss factor may locally differ and can be dependent on the cross flow direction. Such effect seems to be responsible for the slight defect between both curves downstream of the model.

A simplified plenum control mechanism seems to be attractive for further studies. Two plena per ventilated wall with a dividing wall near the model's centre of lift should provide the appropriate pressure difference in sign and magnitude. Due to continuity, the pumping of the flow from one plenum into the other determines the flow direction. The fan rpm and the wall overall open area ratio controls the overall massflow. Local slot massflows should be adjusted by simple piecewise linear slot tailoring like in the present test-section.

CONCLUSION

The new VKI-S1 wind tunnel features slotted horizontal walls of variable slot width and shape. Tests with a DLR-R4 airfoil at different Mach numbers and with uniform slot widths show that the wall induced average blockage can be eliminated with slot widths between 3 and 4 mm, while an increase in incidence correction is observed. Moreover, the wall induced interference gradients are hardly reduced.

Detailed slot flow analysis emphasizes that the plenum pressure does not support the needed crossflow direction for interference free conditions. Some plenum pressure control is needed to reduce the wall interferences to an acceptable limit, especially for transonic testing.

A simple plenum pressure control mechanism is suggested to reduce ventilated wall interferences (especially their gradients), i.e. a two plenum layout per horizontal wall, to provide the appropriate pressure gradient for the needed wall crossflow direction. The magnitude of the local cross flow can be controlled by simple slot tailoring means, such as a linearly variable slot width in one or two flowwise segments.
A complete elimination of the wall interferences is believed to be not necessary. It is already possible to correct for small interference gradients with confidence.

REFERENCES

1. Steinle F, Stanewsky E, AGARD-AR-184 (1982).
2. Smith J, AGARD-CP-335, paper 9 (1982).
3. Schröder W, Li Huaxing, Recent Advances in Experimental Fluid Mechanics, pp. 610-616, International Academic Publisher, Beijing (1992).
4. Schröder W, Zhang Naiping, Recent Advances in Experimental Fluid Mechanics, pp. 623-628, International Academic Publisher, Beijing (1992).
5. Schröder W, Proc. of Intern. Conf. on Adaptive Wall Wind Tunnel Research and Wall Interference Correction, paper W18, CAE-NPU X'ian (June 10-14,1991).

FIGURES

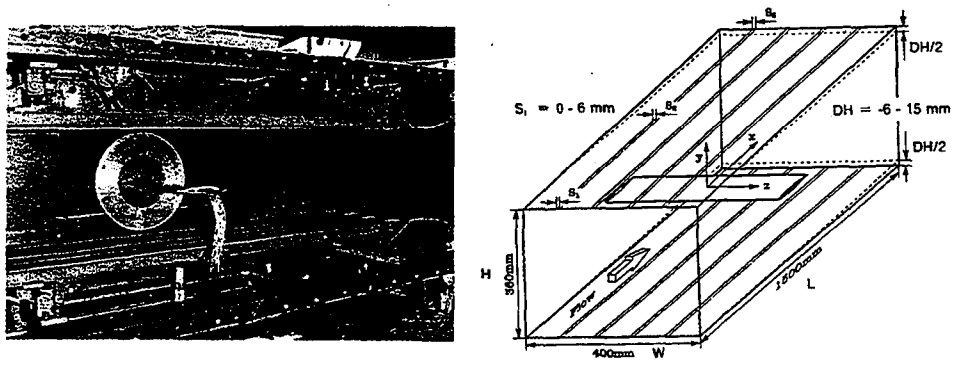

Fig. 1 The new slotted wall test section of VKI-S1 wind tunnel

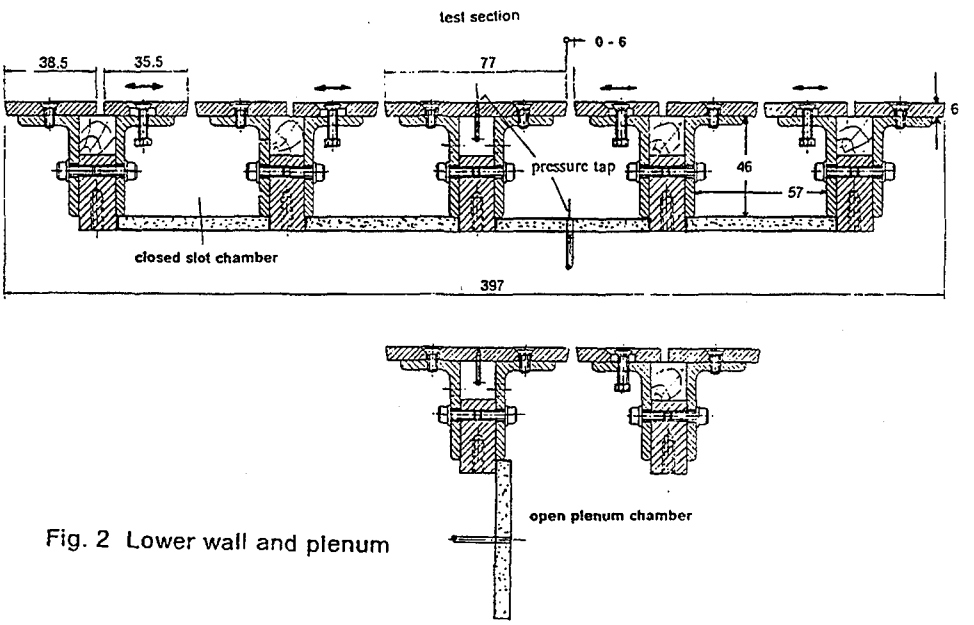

Fig. 2 Lower wall and plenum

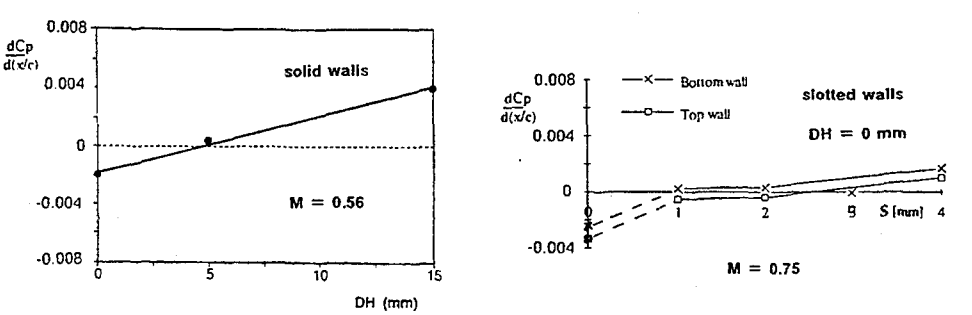

Fig. 3 Empty test section pressure gradients

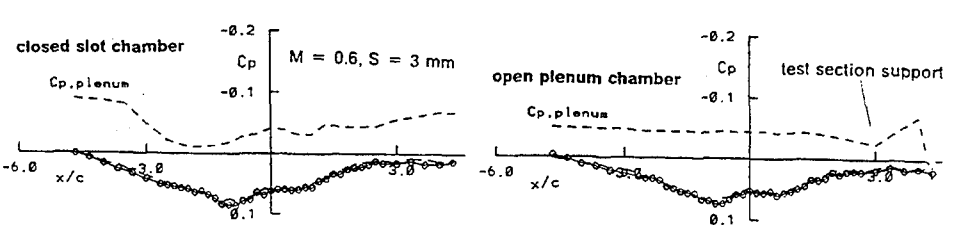

Fig. 4 Lower wall and plenum pressures

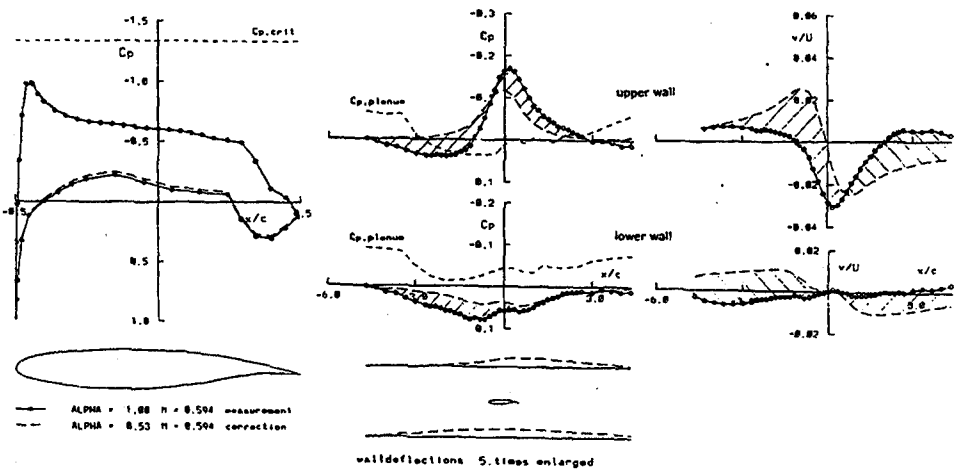

Fig. 5 Measured and corrected airfoil pressures and wall conditions

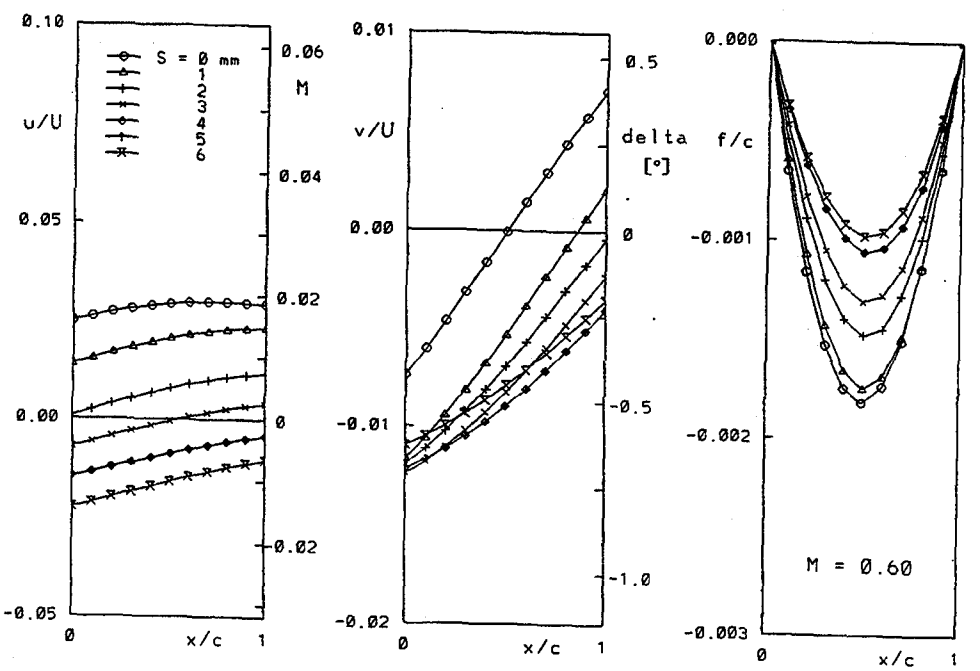

Fig. 6 Wall induced blockage, upwash and flow camber for different slot widths

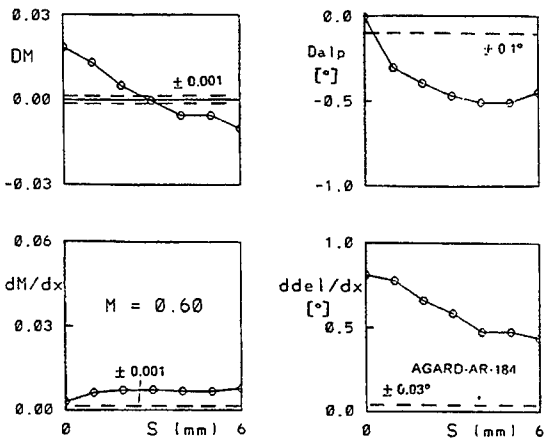

Fig. 7 Overall wall interference parameter

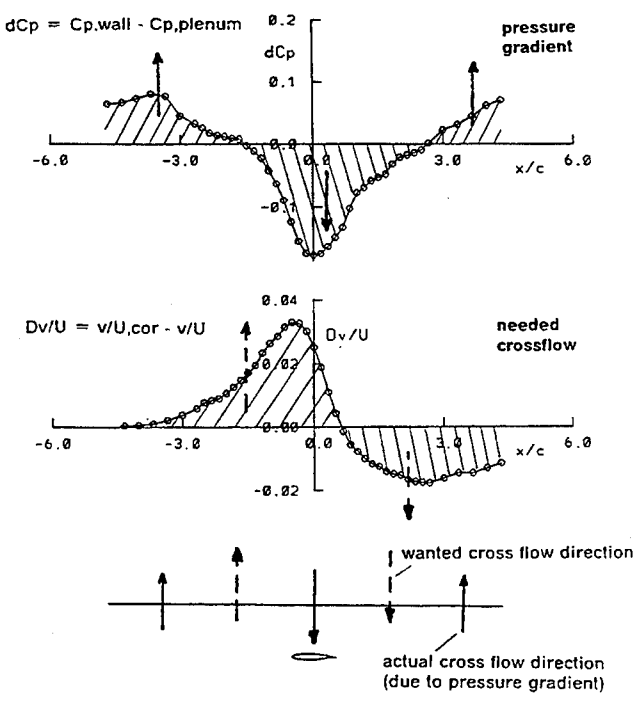

Fig. 8 Upper wall pressure gradient and needed wall cross flow

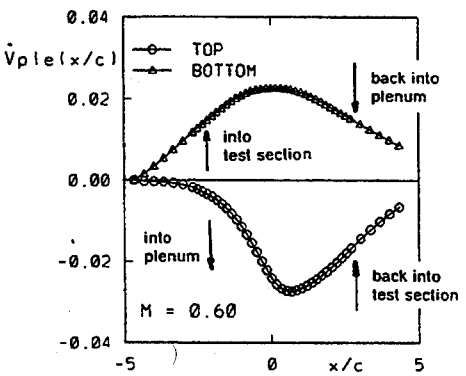

Fig. 9 Needed local plenum volume flow rates

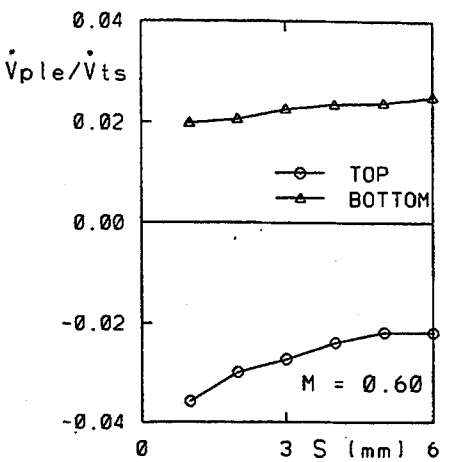

Fig. 10 Maximum plenum volume flow rates

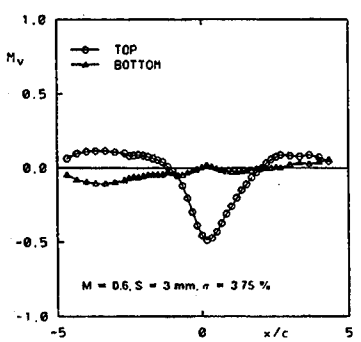

Fig. 11 Local slot cross flow Mach number

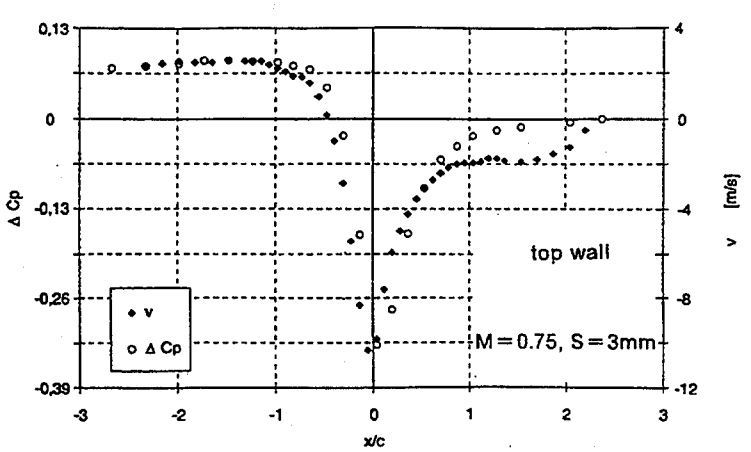

Fig. 12 Wall/plenum pressure difference and slot cross flow

2-D TESTS IN THE ADAPTIVE-WALLS WIND-TUNNEL IN NAPLES

RUSSO G. P., ZUPPARDI G., BASCIANI M.
Institute of Aerodynamics "Umberto Nobile", University of Naples "Federico II" (Italy)

Abstract

In the first part of the present work an experimental comparison is made between two adaptation strategies: the Southampton method and the Everhart's method. The two strategies show a fairly good agreement as far as global results (c_p distribution on the model and lift curve) are concerned. In the second part the idea is tested of obtaining a still good adaptation by operating on the top wall of the test chamber leaving the bottom wall flat: since a fair 90% adaptation is obtained the idea shows promising in terms of reduction of the hardware modifications needed to give adaptive wall capabilities to existing conventional wind tunnels.

Introduction

A good level of confidence has been reached in the operation of the Adaptive-Walls Wind-Tunnel in Naples since results obtained in it have shown[1] to be in good agreement with results reported in open literature and obtained in large wind tunnels at low blockage ratios. The purpose of the present work is twofold: an experimental comparison of two different strategies used to adapt the walls of the wind tunnel in 2-D tests and an experimental assessment of the possibility of reducing to a minimum both the hardware modifications (cost) and the software (time) needed to give adaptive-wall capabilities to existing conventional rigid-walls wind tunnels.

The adaptive-wall technique is based on the premise that if streamlines near the wind tunnel walls may be allowed to take their interference-free shape then the entire flow in the working section is free of wall interference and the force and pressures on the model would represent free-air data. The over-all benefit of an adaptive wind tunnel is that use of much larger models than usual is allowed (higher Reynolds number).

The adaptive-wall concept relies on the assumption of a fictitious flow existing outside the wind tunnel with the same free-stream velocity as the real flow in the wind-tunnel and undisturbed conditions at infinity. The external flow is in general not a physical continuation of the internal flow unless the fluid dynamic parameters are continuous across the wall. The measured velocity components on the walls or, equivalently, static pressure and wall slope, are compared with the computed velocity components in the external flow giving vanishingly perturbation at infinity; the wall shape is modified in order to reduce the discontinuities at the wall between the fluid dynamic parameters of the internal and of the external flow. When these discontinuities are brought to negligible values the walls can be considered adapted and the flow on the model is similar to a free-flight flow[2,3].

Flow disturbances induced by the model are assumed to be small at the entrance and exit sections and on the walls of the test chamber (and hence also in the exterior imaginary flow field). The flow in these regions is amenable therefore to the linear potential flow approxima-

tion. Excluded is the region surrounding the model where viscous flow and, in general, strong perturbations are confined. In any case an accurate description of the flow far away from the model can be obtained, although the local detailed structure of the flow may vary widely with the aerodynamic body.

It must be stressed that the wall adaptation procedure with respect to the classical wall interference correction methods:

- avoids calculating the disturbance potential induced by the model
- reduces the limitations of linear theory by applying it only to the smaller flow disturbances near the walls and outside the test chamber (imaginary flow).

Experimental set-up

The AWWT in Naples[4] is an open return, indraft, wind tunnel with a 0.2 m x 0.2 m x 1 m closed test chamber. The wind tunnel is powered by a 50 kW a.c. motor driving a centrifugal fan. Maximum Mach number in empty wind tunnel is 0.55. Maximum unit Reynolds number is about 10^7 m^{-1}. Stepless variation of speed from zero to the maximum value is achieved through inlet vane control which changes the angle at which the airstream approaches the impeller. Adaptation is obtained by modifying the shape of the flexible horizontal walls of the test chamber made with steel plates, 0.6 mm thick. On each plate 16 control stations, less spaced in the model zone, are equipped with a pressure tap, a jack and a displacement indicator.

The open return configuration has been chosen because it is free from the need of cooling the airstream (a critical problem in closed-circuit wind-tunnels); the pressure in the test chamber is therefore well below atmospheric pressure and this implies that plenum chambers vented to the airstream must be provided to alleviate pressure loads on the two horizontal flexible walls. In order to achieve a low turbulence level both a honeycomb with hexagonal elements with L/D = 10 and a low-turbulence gauze screen have been installed in the settling chamber. A high contraction ratio (= 25) has been used to minimise losses through the honeycomb and the screen and to help turbulence reduction. Two diffusers are provided, one upstream (with a 4° divergence semiangle) and one downstream (6° semiangle) of the centrifugal fan, in order to reduce to a minimum the loss of kinetic energy at the exit.

Besides the 16 pressure taps drilled on each flexible wall, one for each control station, needed to give inputs to the adaptation strategy, several static pressure holes have been drilled on the vertical Plexiglas test chamber wall in order to increase knowledge of stream quality: i.e. n.2 static holes in the two plenum chambers to monitor the effectiveness of venting to the airstream, n.3 static holes at the downstream end of the test chamber to integrate the total pressure measurements made by the wake rake used when profile drag has to be calculated. A Pitot-static tube has been inserted in the upstream end of the test chamber to measure the test Mach number. A 2 x 48 ports Scanivalve is used to measure pressures that are sent through an analog to digital converter to a control computer.

The NACA 0012 airfoil has been selected as a test model since this airfoil has been extensively tested in many wind tunnels; all the published data have been collected and critically correlated[5]: the resulting correlated data can be considered as free from wall interference being obtained at very low blockage ratios.

Three aluminium alloy NACA 0012 models with chord c = 100 mm, 150 mm and 200 mm (giving blockage ratios at $\alpha = 0$ equal to 6%, 9% and 12%) respectively, worked with a numerically controlled machine, have been used in the present tests. Each model is cut along the chord plane in two symmetrical parts to allow correct positioning of pressure tubes connecting pressure taps drilled on the model surface with the Scanivalve. With this configuration it has been possible to provide 41 pressure taps on the model surface aligned along the centreline of the model (1 on the leading edge, 20 on each surface) less spaced in the leading edge zone where pressure variations are more severe.

Only the tests made with the c = 200 mm model are reported in the present paper since they give the most significant results due to the large blockage ratio.

Experimental comparison of two different adaptation strategies

Two main different approaches to the adaptation strategy, i.e. the way chosen to calculate external flow and to modify the wall shape have been made. The first one, named WAS, was derived in Southampton by Judd, Wolf and Goodyer[6] and successfully tested also in the 0.3 m TCT at NASA LaRC. The method is based on a sound physical approach: the walls of the wind tunnel are considered as two independent straight walls and the difference in the velocity components along the wall between the internal and the external field is considered as a local vortex whose strength has to be reduced by wall deflection. The mutual influence of the two flexible walls is taken into account by a coupling factor (CF) chosen empirically for the peculiar wind tunnel, as it depends on the aspect ratio of the test chamber.

The alternative approach, named FLEXWALL by Everhart[7], is of a mainly mathematical nature. The external flow is considered as a domain extending to infinity from which the test chamber, with its real walls and virtual entrance and exit planes is excluded. In the domain, as said before, the flow can be considered as being irrotational. In 2-D fields a complex velocity can thus be defined and via the Cauchy integral formula the velocity in every point of the domain can be calculated by the knowledge of its values on the boundary. Since on the boundary extending at infinity all perturbations are vanishingly small and their contribution can be therefore neglected, the knowledge of the complex velocity components on the boundaries of the test section are sufficient to determine the velocity components in the external field and, in particular, on the wall itself (Cauchy principal value). For instance from the measured velocity components along the axis of the test chamber, u, the normal components, v, are calculated by the Cauchy principal value and compared with the measured v components; the differences are then gradually eliminated by appropriate displacements of the wall.

Although starting from a different approach the Judd's strategy has been shown[8,9] to be a particular case of the Cauchy approach for two straight independent walls. It seems appropriate therefore to test also experimentally the effectiveness of the simpler Judd's strategy, promising for further simplification of the adaptation process, against the Cauchy approach, more rigorous from a mathematical point of view.

In the present tests adaptation has been considered completed when the displacement required by the adaptation strategy in the current step is lower than 0.5 mm, the minimum displacement that can be practically obtained with the jacks at the moment still operated manually; at the same time the convergence criteria proposed in[6] are monitored to test the effectiveness of adaptation.

The results obtained with the FLEXWALL strategy are considered as a reference since it has been shown[1] that they are practically in line with the McCroskey correlation[5].

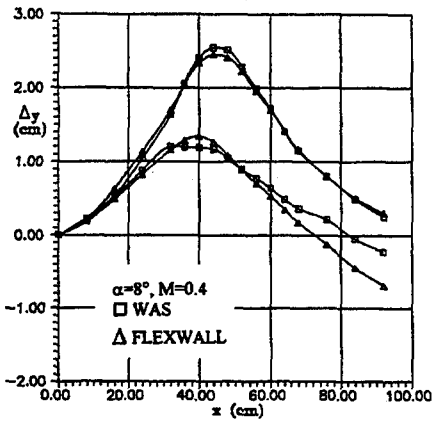

Fig.1- Displacements of the adapted walls

In Fig.1 the displacements of the two flexible walls in the adapted configurations determined both with the FLEXWALL strategy and the WAS strategy are reported for the NACA 0012 model with c = 200 mm at M = 0.4 and $\alpha = 8°$ (the vertical scale is 20 times the horizontal scale). The two strategies give practically equal displacements in the zone of the model (40 cm $\leq$ x $\leq$ 60 cm). Relevant differences result only for the bottom wall in the zone of the wake produced by the model; the WAS strategy is evidently less accurate in this zone because of lack of closure conditions at the exit section of the test chamber. Accordingly the c_p distributions on the model when adaptation is obtained (Fig.2) are practically coincident. This behaviour is regularly repeated at the various angles of attack giving very similar lift curves for the adapted walls with both strategies (Fig.3). The WAS and FLEXWALL strategies are therefore to be considered equivalent when global results on the model are considered.

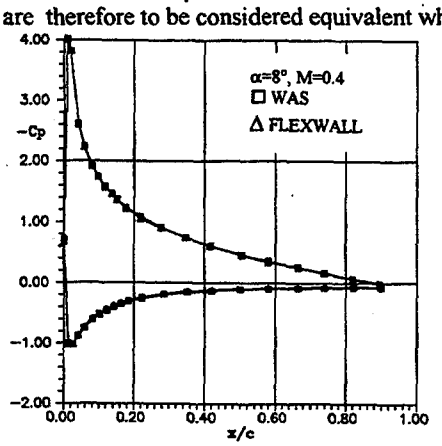

Fig.2- Distribution of the pressure coefficient c_p on the NACA-0012 model.

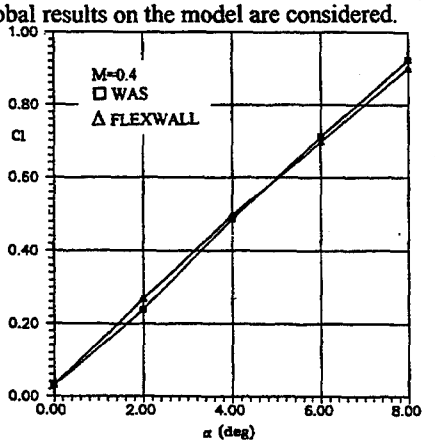

Fig.3- Comparison of the lift curves obtained with the two strategies.

It was then tried to find the optimum coupling factor for the WAS strategy. From Fig.4 it can be seen that the absolute values of the displacements increase when the CF is increased as can be expected. From the point of view of c_p distribution (Fig.5) the values of CF < 0.35 are practically not influent. Since the CF = 0.35 gives a good agreement with the displacements given by the FLEXWALL approach, in which the coupling of the two walls is implicit in the method referring to a closed circuit, it can be argued that this value selected for the wind tunnel in Southampton and NASA LaRC is also valid for the AWWT in Naples and perhaps for all wind tunnels having a square test section.

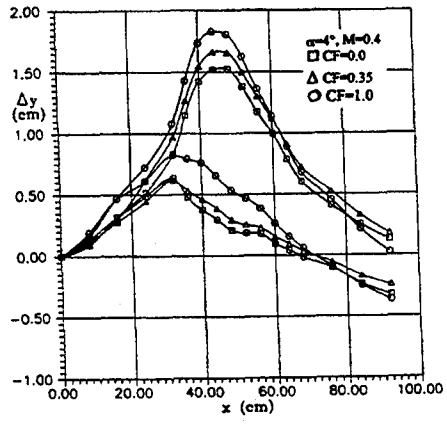

Fig.4- Influence of the coupling factor on the displacements of the adapted walls.

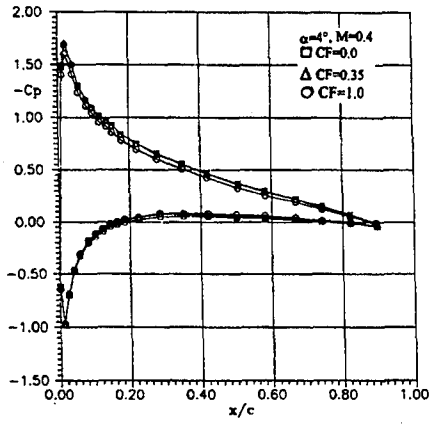

Fig. 5- Influence of the coupling factor on the distribution of c_p on the model.

One-wall adaptation

Evident difficulties are encountered when trying to give adaptation capabilities to existing full-scale industrial wind tunnels. The first objection is the time needed to adapt the wall. Typically in an industrial test a complete polar is desired for each run and is obtained by a continuous sweep through the required range of angles of attack. When adaptation has to be achieved, the sweep must be stopped for each desired angle of attack, the adaptation procedure has to be started, then when adaptation is obtained forces on the model can be measured. Since for each angle of attack the initial wall shape is that obtained in the adaptation at the immediately previous angle of attack the adaptation can be obtained very rapidly, typically in one or two steps.

A second critical feature of the adaptive concept is the amount of work (and money) needed to modify the test chamber. The major modification to be made on the test chamber is the replacement of two rigid walls by flexible walls instrumented with a row of pressure taps, pressure transducers, motorised jacks and displacement transducers. Furthermore if the test chamber is below atmospheric pressure a plenum chamber for each flexible wall must be provided in order to relief the pressure difference acting on the usually thin flexible walls. These modifications do not interfere with the model support and balance system in 2-D tests, where the model is supported through the lateral windows, nor in 3-D tests where a sting support or a magnetic suspension and balance system is used but would be a problem for wind tunnels with external balances where struts connecting the model to the balance must pass through the floor of the test chamber.

These problems in configuration, and cost, arising from the introduction of the adaptive capability in an existing wind tunnel would be obviously halved if a sufficiently good adaptation could be obtained by operating only on one wall. Tests have therefore been made to evaluate the possibility of obtaining an efficient adaptation by acting on a single flexible wall. The idea is based on the observation that the displacements are larger on the top wall.

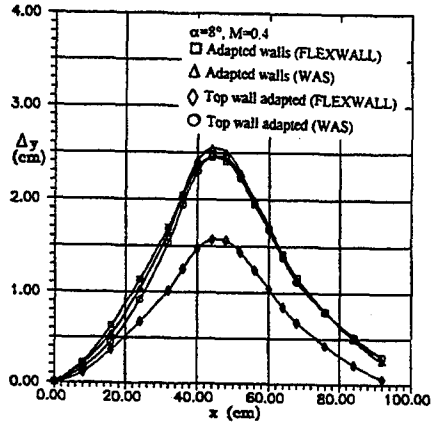

Fig.6- Comparison of the displacements of the top wall obtained with two-walls and one-wall adaptation.

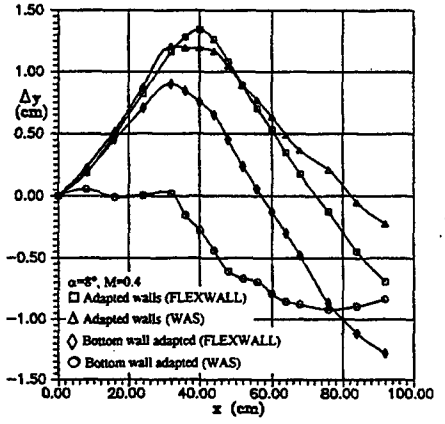

Fig.7- Comparison of the displacements of the bottom wall obtained with two-walls and one-wall adaptation.

To test the effectiveness of this approach one of the walls in turn has been left flat during the adaptation of the other wall. The displacements of the top wall are similar to the corresponding displacements obtained with the adaptation of both walls with the WAS strategy and much smaller with the FLEXWALL strategy (Fig.6). Completely different is the sensitivity of the lower plate where the displacements of the FLEXWALL strategy are not dissimilar from (although smaller than) those obtained with the two-walls adaptation, whilst the WAS strategy produces anomalous displacements (Fig.7).

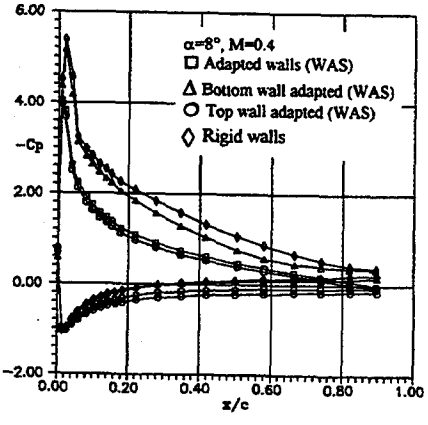

Fig.8- Comparison of c_p distribution on the model obtained by two-walls and one-wall adaptation (WAS strategy) and with rigid walls

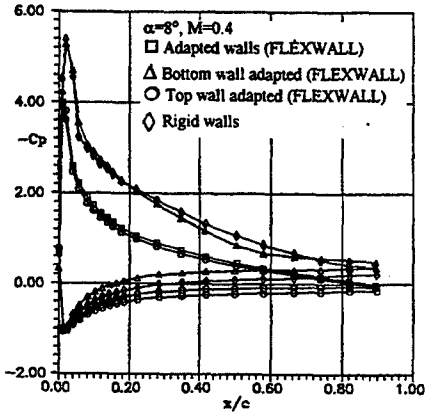

Fig.9- Comparison of c_p distribution on the model obtained by two-walls and one-wall adaptation (FLEXWALL strategy) and with rigid walls

Looking at the pressure distribution on the model (Figs.8, 9) it can be seen that adapting only the bottom wall produces only small effects, the resulting c_p distribution is much similar to that obtained with completely flat walls. The adaptation of the top wall on the contrary produces a c_p distribution similar to that obtained with two-walls adaptation.

This behaviour is confirmed by the lift curves (Figs.10, 11) both for the WAS and the FLEXWALL strategies.

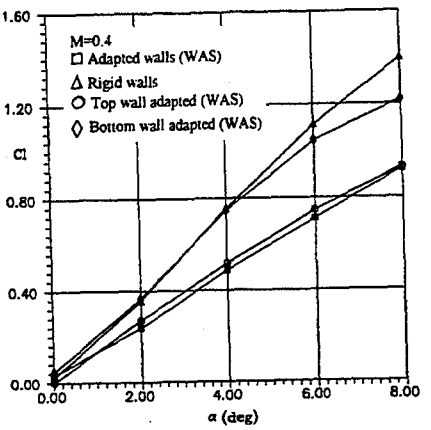

Fig.10- Comparison of lift curves obtained by two-walls and one-wall adaptation (WAS strategy) and with rigid walls

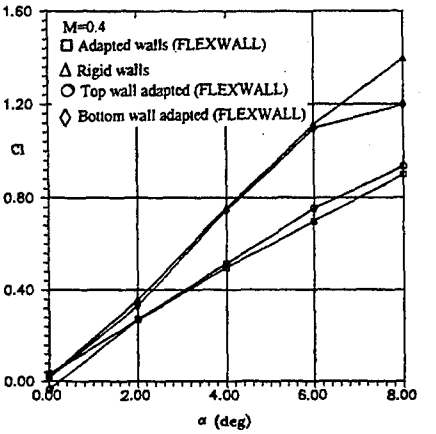

Fig.11- Comparison of lift curves obtained by two-walls and one-wall adaptation (FLEXWALL strategy) and with rigid walls

For the WAS strategy also residual interference has been computed for the various levels of adaptation (rigid walls, bottom-wall adapted, top-wall adapted and both walls adapted) in terms of distribution along the chord of the model of corrections to angle of incidence and to Mach number. As far as the correction of the angle of incidence is concerned it can be seen from Fig.12 that the corrections are reduced when the level of adaptation is increased; again the adaptation of the top wall give results similar to that obtained with complete two-walls adaptation: on the contrary bottom-wall adaptation gives results mostly similar to the results obtained with rigid walls. The same behaviour can be observed in Fig.13 where the corrections of Mach number are reported; it is interesting to note that for the two-walls adaptation the Mach number correction is less than 0.5% and that for top-wall adaptation the correction is still less than 2%.

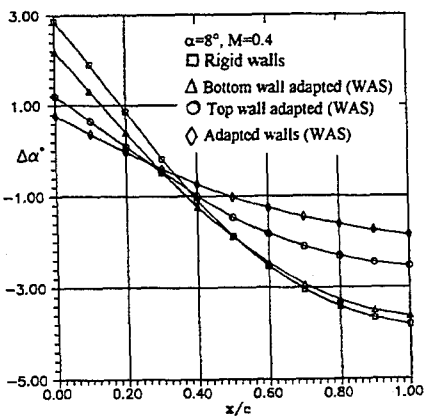

Fig.12- Residual correction of the angle of incidence at various levels of adaptation (WAS strategy)

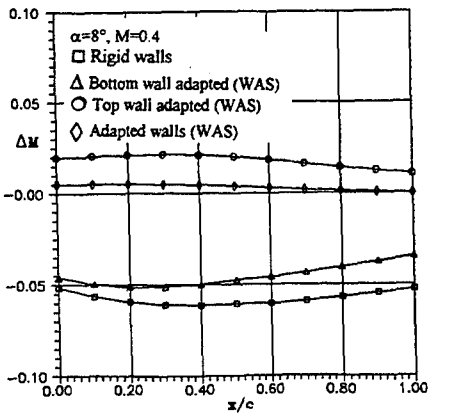

Fig.13- Residual correction of the Mach number at various levels of adaptation (WAS strategy)

References

1. Russo G.P., Zuppardi G. and Basciani M.: "Recent Developments of the Adaptive Walls Wind Tunnel in Naples", Pacific International Conference on Aerospace Science and Technology (PICAST'1 1993), Tainan, Taiwan, 6/9 December 1993.
2. Ferri A. and Baronti P.: "A Method for Transonic Wind Tunnel Corrections"- AIAA Journal, vol.11, no.1, Jan.1973, pp. 63-66.
3. Sears W.R.: "Self Correcting Wind Tunnels"- The Sixteenth Lanchester Memorial Lecture, May 3, 1973 - The Aeronautical J., vol.78, Feb./March 1974.
4. Russo G.P., Zuppardi G. and Basciani M.: "Evolution of the Adaptive Walls Wind Tunnel", Proceedings of the Sixth International Conference on Computational Methods and Experimental Measurements (CMEM93), Siena 3/5 May 1993, pp.395-410.
5. McCroskey, W.J.: "A Critical Assessment of Wind Tunnel Results for the NACA 0012 Airfoil", AGARD CP - 429 *'Aerodynamic Data Accuracy and Quality: Requirements and Capabilities in Wind Tunnel Testing'*, Naples, Italy, 28 September, 1 October, 1987, paper n.1.
6. Judd M., Wolf S.W.D. and Goodyer M.J.: "Analytical Work in Support of the Design and Operation of Two-Dimensional Self Streamlining Test Section", NASA CR-148196, March 1976.
7. Everhart J.L.: "A Method for Modifying Two-Dimensional Adaptive Wind-Tunnel Walls Including Analytical and Experimental Verification", NASA TP-2081, February 1983.
8. Russo G.P. and Zuppardi G.: "Numerical Simulation of an Adaptive Wall Wind-Tunnel: a Comparison of two Different Strategies", L' Aerotecnica, Missili e Spazio, n.4, Dicembre 1987, pp. 239-249.
9. Russo G.P.: "The Judd's Adaptation Strategy as a Peculiar Application of the Cauchy Integral Formula"- 4th Meeting of the AGARD WG-12 on "Adaptive Wind Tunnel Walls: Technology and Applications", NASA Langley, April 26/27, 1989.

Acknowledgements

This work has been sponsored by the Italian Ministry for University and Scientific and Technological Research (MURST 60%)

THE PLANNED C.I.R.A. ICING WIND TUNNEL (IWT)

A. Garrone - F. Di Felice

C.I.R.A.
(Italian Aerospace Research Center)
Via Maiorise
81043 CAPUA (CE)
ITALY

ABSTRACT

In recent years accidents as a result of icing problems, along with the introduction of anti-icing fluids and apparent uncertainties in certification of de-icing devices, have stimulated renewed research activities in this area.

Flight testing of aircraft under natural icing conditions are expensive and some what risky. However such testing has been required to demonstrate the effectiveness of de-icing devices and to certify new aircraft. To reduce the need for extensive flight testing, the icing tunnel is an important tool for developing ice shapes and evaluating anti- icing features on full scale sections of critical parts of the aircraft.

The NASA Lewis (6 x 9) foot and now the BOEING BRAIT (5 x 8) foot are the world's leading facilities. So in response to the need for an icing facility in Europe, C.I.R.A. is starting with the design of such a facility in ITALY.

This paper describes the IWT where both icing simulation phenomena and ice protection systems will be easily studied and tested.

NOMENCLATURE

A_{TS}	Test Section Area	m^2
Cd	Drag Coefficient D/qA_{TS}	—
D	Model Drag	Kg
A_M	Model Frontal Area	m^2
B	Blockage A_M/A_{TS}	%
V	Test Section Velocity	m/sec
T	Test Section Temperature	°C
q	Test Section Dynamic Pressure	Kg/m^2
ρ	Air density	$Kg\ sec^2/m^4$
K_l	Local Loss Factor	$\Delta p/q_l$
K_o	Local Loss Factor	$\Delta p/q$
ΣK_o	W.T. drag Coefficent	—
A_{loc}	Local W.T. Section Area	m^2

INTRODUCTION

Flight testing of aircraft under natural icing conditions can be extremely time consuming, costly and somewhat risky. However such testing is required to demonstrate the effectiveness of anti-icing and de-icing systems and to certify new aircraft models. The FAAs FAR, part 23 and 25 for the aeroplane and part 27 and 29 for the helicopters, require that a manufacturer demonstrates

the handling qualities of the aircraft under icing conditions. Demonstration is performed in two step:

- the ice shape under various flight condition is extracted by mean of intensive flight test
- further flight test is required to demonstrate the handling qualities with deformed leading edge and nacelle inlets extracted from the ice shape obtained from the pervious flight test.

Because of inherent difficulties of documenting icing conditions in the atmosphere and the repeatability of such test, model testing in an icing wind tunnel is an attractive alternative. Furthermore the FAA has recently issued guidelines to permit the determination of ice shapes in the wind tunnel instead of flight testing.
According to the National Aeronautical Research Program for Aeronautics (PRORA), in agreement with the European Aircraft Industry and with the certification Agencies RAI-JAA involvement and recommendations, the CIRA S.c.p.A. is proceding-with the design and construction of an icing wind tunnel (IWT).
This tunnel will be used to verify aircraft de-icing systems and to support the certification testing of production aircraft. The IWT Tunnel will also be devoted to research programmes aimed at understanding the icing physics and in support of the mathematical models which predict ice shapes and accretions.

WIND TUNNEL TESTING REQUIREMENTS AND PERFORMANCE GOAL

The CIRA IWT is a multipurpose icing test facility which allows the testing of

- full scale parts of wings equipped with de-icing system
- full scale movable parts (flaps, slats, rotors, etc.)
- air intakes
- flight instrumentation

in order to perform research activities on the following areas

- ice-accretion study
- de-icing system effectiveness
- malfunction of mechanical exposed parts
- flight instrumentation protection

The design of the IWT is focused on providing a state of the art icing test facility able to have different testing capabilities. The wind tunnel has been provided with two interchangeable test sections.
The main test section will have a crossection area of 8.75 m^2 (2.5X3.5, height by width) with a maximum speed of 129 m/sec when testing a model with a blockage of 20 % and the temperature ranging from ambient to -32°C. In fact, as the wind tunnel demonstration of full scale de-icing systems are acceptable to the FAA, instead of flight testing, high blockage is required in order to test

a) High lift systems as 2D wing modules in real scale and full scale air turbine performance during icing condition at lower speed of 150 Kn. and with temperature up to T = - 32°C.
b) Aeroplane components exposed to ice accretion during the climb and hold pattern. In this condition the aeroplane is flying at V = 250 Kn. at an altitude of about 3000 to 5000 m.
c) full scale air intakes and small engine for lighter aircraft

The secondary test section will have a crossection area of 4.5 m^2 (2.5X1.8, height by width) with a maximum speed of 214 m/sec (Mach = .7) and a static temperature of -40 °C
Test section area has been defined in order to perform the following tests:

a) Probes performance and calibrations under icing conditions
b) Probes de-icing systems effectiveness
c) Aeroplane components (clean wing, horizontal and vertical tails) in cruise configuration and descent phase. M = 0.7

Maximum model blockage foresee for this test section is 6%.
Flow Quality to met in the design has been defined for both test section and listed in the following

Turbulence Intensity		≤ 0.5% RMS
Velocity distribution	ΔV/V	≤ ± 1 %
Temperature distribution	ΔT/T	≤ ± 1°C

over a 0.64 of the test section area and with the spray bar off but installed in the settling chamber.

CLOUD SIMULATION

The cloud simulation is the most important aspect in an icing wind tunnel. In order to simulate the clouds in the test section, a spray bar system atomising water droplets is installed in the settling chamber. The cloud characteristics to be simulated are defined by the FAA Aircraft Icing Handbook (AIHB) and are summarised by the diagram shown in fig. 1. Two types of operating envelope for the liquid water content versus the mean droplet size can be seen in the previous diagrams. In order to met the FAR specifications up to 100 nozzles are foreseen in the settling chamber which should be capable to perform the following operational range:

a) Liquid water content 0.5 to 3 gr/m^3
b) Droplet size 5 to 50 μ (microns)

WIND TUNNEL AEROLINES

The drawing in fig.2 shows the aerodynamic layout of the wind tunnel with the two test sections. The two test sections have the same height. So to reduce the area the two side walls move inward from W = 3.5 to W = 1.78 m. The feasibility study of the IWT shall define the details regarding the consequent nozzles exit area reduction. The possible solution should be:

a) Nozzle built and splited in three modules. The first one is fixed and has only one contour. The second one (nozzle exit) will be movable and built into two pieces which represents the two nozzle geometry.
b) Nozzle with the second part having flexible contour
The two nozzle contours (side walls only) should be achieved either by jacks or by local variable deformation obtained by the thickness change in the material from which the side walls are made.

The rear transition from the main test section to the first diffuser entrance is convergent in order to ensure a good flow quality at the first diffuser entrance.
Two lateral and adjustable flaps will provide the test section side walls continuity and they might act as re-entry flaps if a slotted test section. walls are adopted.
In order to ensure a more favourable design for the small secondary test section, the first diffuser aerolines have been selected in order to avoid separations. (1,2,3)
The equivalent Conical Angle, Area Ratio and Length of the first diffuser, cross leg n° 1 and fan diffuser have been selected in order to avoid the flow boundary layer separations near the end of the diffuser itself.
In order to minimise the typical problems of flow separation at the nozzle entrance and the so called "overshoot" at the nozzle exit, a numerical method based on three-dimensional potential flows, integrated by a bi-dimensional boundary layer calculation, has been used(4).
A wide angle diffuser has been used in the aerodynamic design to avoid a large wind tunnel layout.
The wide angle diffuser main characteristics are:

Area Ratio A2/A1 = 1.78
Conical diffuser angle = 2 φ = 36°
Length = 4.4 m

Due to the very high pressure losses of the heat exchanger no screens are foreseen in the wide diffuser and attached flow is expected.
Based on the BRAIT and IRT experience a heat exchanger with 6 to 8 rows has been foreseen in order to dissipate the fan power of about 6 MW.The frontal area has been sized in order to achieve an approach velocity of 8.5 m/sec. as specified by the heat exchanger manufacturer.
The stilling chamber has been designed to accommodate two interchangeable modules:

a) Spray bar + honeycomb module for icing testing
b) Honeycomb + screens for aerodynamic testing.

The substitution of the spay bar system with the Honeycomb and screens module allows the wind tunnel to be used also for aerodynamic purpose, with very good flow quality because of high contraction ratio. The possibility to increase the Reynolds Number by testing at low temperature will be also considered.
The contraction ratio has been defined in function of

a) to obtain the local velocity through the heat exchanger not higher than 8.5 m/sec
b) to achieve good flow quality in the test section with the spray bar on.

and has been chosen equal to 14.5 for the main test section.

De-icing systems are foreseen in the first and second corner to prevent ice formation in the wind tunnel circuit. Special scoop systems to catch the ice debris are located in several part of the tunnel circuit.

FAN PERFORMANCE SPECIFICATIONS

The table 1 summarised the loss factor for the tunnel components with model installed in the test sections. A margin of 15% of the power has been considered in the fan specification for the

pressure losses due to the ice formation. The fan pressure rise requirement for each test section configuration at the design points are shown in table 2. Based on CIRA experience of the design of several wind tunnels both RPM and blade pitch angle should be necessary to cover the wide range of the operating conditions..

CONCLUSION

Design of the icing wind tunnel is presently being developed. Special attention is being paid to the requirements which might impact the wind tunnel geometry and performance. Cloud characterisation will be deeply considered in the spray bar design.
In table 3 the IWT is compared with the most significant USA icing wind tunnel[5]. This comparisons shows the validity of the facility in the world contest.

REFERENCES

[1] Design, manufacturing, calibration of the German - Dutch Wind Tunnel - DNW.

[2] ESDU - Introduction to design and performance data for diffusers - Rept. n° 76027.

[3] Aerodynamic design guide lines and computer program for estimation of subsonic wind tunnel performance - NASA TN D-8243.

[4] Programma numerico per il calcolo di condotti convergenti o divergenti a sezione rettangolare - G- Chiocchia - Polit. Torino - Giugno '89.

[5] Cain,Yurczyk, Belter, Chintamani: "Boeing research aerodinamic/icing tunnel capabilities and calibration",1994 Subzero Enginering Conditions Conference, ISBN 156091-457-2

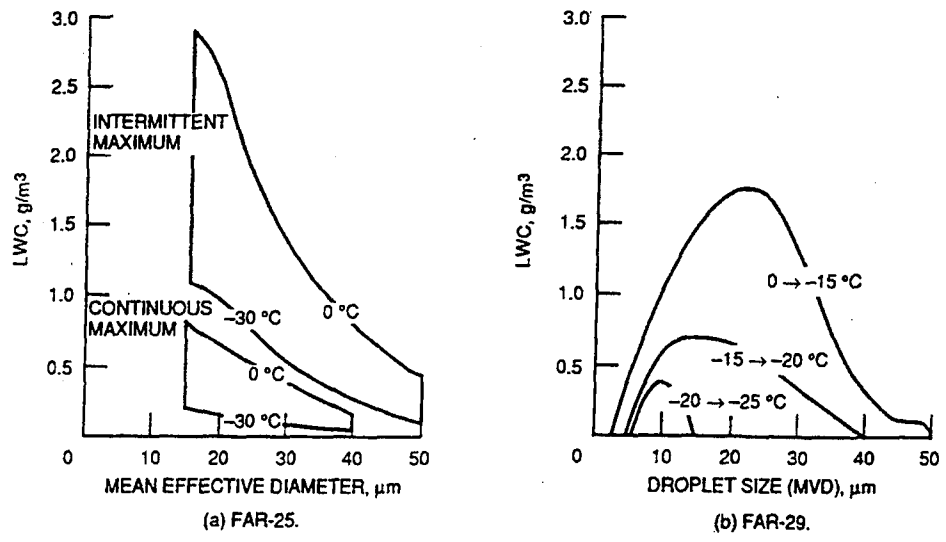

Fig.1 FAA aircraft icing certification criteria

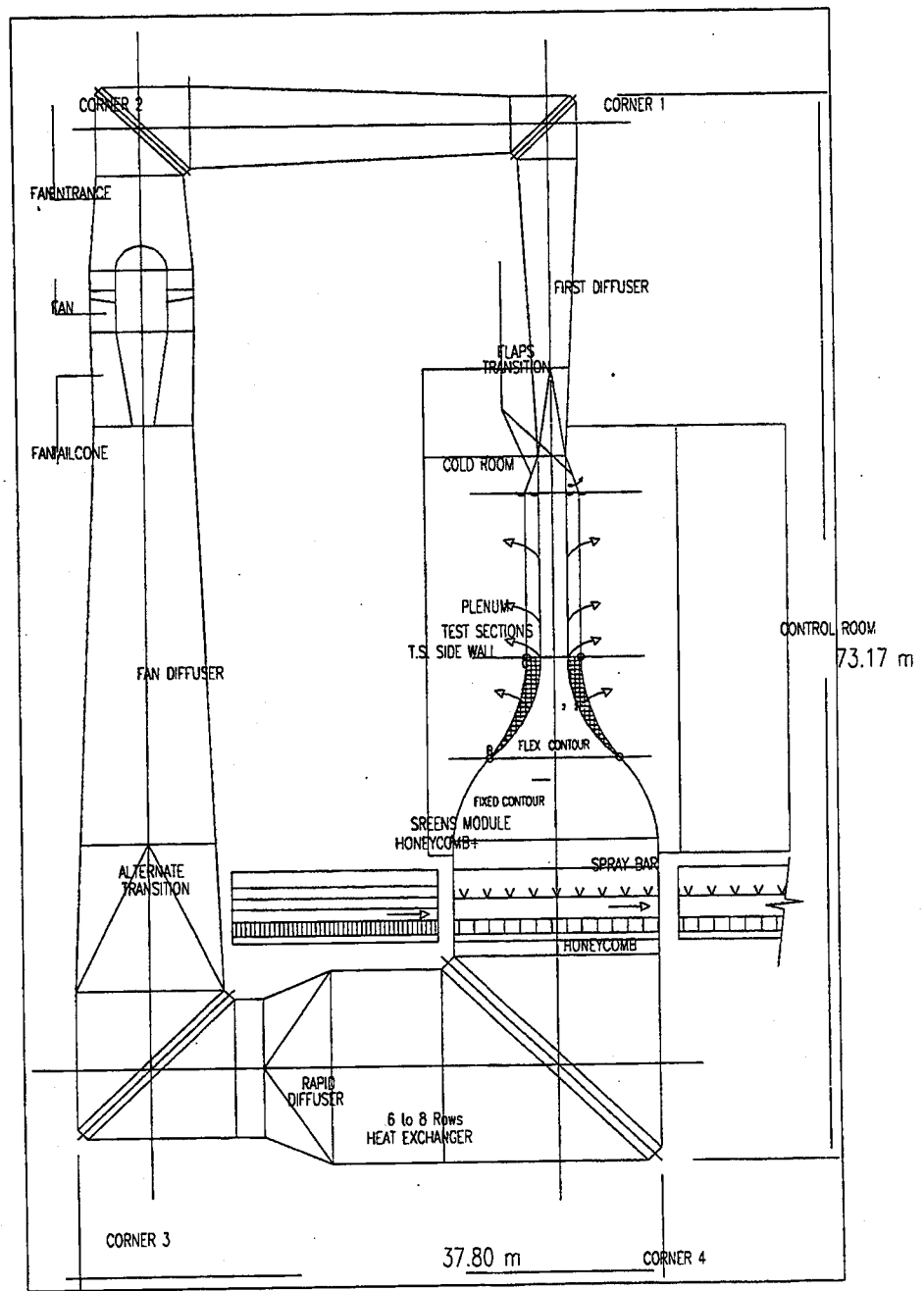

Fig.2 Icing Wind Tunnel Lay Out

ITEM	MAIN T.S. (2.5 x 3.5) m			SECONDARY T.S. (2.5 x 1.78) m		
	Ko B = 20%	Ko 6%	Ko 0	Ko B = 20%	Ko 6%	Ko 0
CONTRACT	0.0040			0.0040		
TEST SECT	0.1300	0.0542	0.040	0.1300	0.0542	0.040
FIRST DIFF.	0.0800			0.0800		
CORNER 1	0.0705			0.0182		
CR. LEG 1	0.0117			0.0030		
CORNER 2	0.0158			0.0041		
SAF. SCREEN	0.0040			0.0010		
FAN INLET	0.0012			0.0003		
FAN TAILC.	0.0033			0.0008		
FAN DIFF.	0.0047			0.0012		
CORNER 3	0.0016			0.0004		
CR. LEG 2A	0.0003			0.0001		
W/A DIFF.	0.0027			0.0007		
H/X	0.0720			0.0185		
CORNER 4	0.0006			0.0001		
HONEYC. SPRAY BAR	0.0034			0.0008		
TOTALS	**0.4058**	**0.3300**	**03158**	**0.2632**	**0.1875**	**0.1732**

Table 1 Wind Tunnel Loss factor

TEST SECTION	B %	V m/sec	z Ko	p	q mm H2O	FAN RISE mm H2O	VOL. FLOW m3/sec
MAIN	20%	129	0.4058	0.141	1173	476	1129
T = - 32°C	6%	143	0.3300		1441	475	1251
	EMPTY	146	0.3158		1502	474	1278
SEC.	20%	192	0.2632	0.146	2691	708	854
T = - 40°C	6%	214 M = 0.7	0.1875		3343	627	952
	EMPTY	219	0.1732		1502	474	1278

Table 2: Fan Operating Conditions

Table 3:IRT, BRAIT and IWT Performace Comparision

FACILITY IDENTIFIC.		TEST SECT. DIMENS m	PRIMARY USE	MAX SPEED m/sec B%	AIR TOTAL TEMP °C	ACTITUDE m	NOTE
NASA LEWIS IRT		H = 1.8 W = 2.7 L = 6.1	ICING	V = 134 Empty 20%	-40	3000 at V = max	Still chamber at ambient pressure
* BOEING BRAIT	T.S. n. 1	H = 2.62 W = 1.64	High lift - Ram air Turbine	V = 77 with model ------	- 32	Ambient	Not yet available
	n. 2	H = 1.97 W = 1.31	Aircraft in Hold pattern	V = 128 with model ------	- 32	>>	Available
	n. 3	H = 1.64 W = 0.98	Probe perform.	V = 180 with model -----	- 40	>>	Not yet available
* CIRA IWT	MAIN	H = 2.5 W = 3.5	High lift Hold pattern Ram Air Turb	V = 129 B = 20% 143 B = 6% 146 B = 0	- 32	0 - 5000	V and z can vary indipendently
	SEC.	H = 2.5 W = 1.78	Descent and Cruise Probe perf.	V = 192 B = 20% 214 B = 6% 219 B = 0	- 40	0 - 5000	>>

* BRAIT & CIRA can also perform aerodynamic testing

THE CRYOGENIC LUDWIEG-TUBE OF DLR: DESIGN FEATURES, STATUS AND FIRST RESULTS

Hefer, G.
European Transonic Wind Tunnel, Cologne, (Germany)
Rosemann, H., Stanewsky, E.
Institute of Fluid Mechanics, DLR, Göttingen (Germany)

Abstract

The Cryogenic Ludwieg-Tube of DLR (KRG) was especically designed for high Reynolds number research in transonic flow. The paper gives an overview over its design features together with a description of the new 2-D adaptive wall test section which is currently beeing put into operation. Some results of the present calibration program of the slotted test section including hot-wire measurements are presented.

Two airfoils have been tested in the KRG for validation purposes so far and the results are in good agreement with those of other wind tunnels. On a laminar-type airfoil, the Reynolds number dependence of the lift coefficient could be demonstrated.

1 Introduction

Despite the progress of computational design of transonic airfoils, wind tunnel testing still plays an important role in the design process. Numerical results have to be verified and there is a number of flow phenomena, e.g. various methods for drag reduction, like laminarization, shock control by means of passive or aktive ventilation or adaptive contours, that has to be investigated in the wind tunnel. For these techniques, the capability of performing experiments at the correct design Reynolds number is very important.

Therefore, a new transonic facility, the Cryogenic Ludwieg-Tube (KRG), has been designed and built at DLR in Göttingen during the past years. The Ludwieg-Tube concept was choosen to minimize operating costs and achieve good flow quality. Currently, a new 2-d adaptive wall test section is going into operation which will allow to test larger models with nominally no interferences from the horizontal walls.

The following chapters will give an overview over the design principles of the KRG and show some results obtained during the calibration and validation program with the slotted wall test section.

2 Design and Operational Characteristics of the KRG

2.1 The concept

A Ludwieg-Tube consists basically of a long storage tube, a converging section followed by the test section, a valve, and a dump tank. The gas dynamic process is explained in Fig. 1 by means of an x,t-diagram. The valve separates the high pressure in the tube (charge conditions) from the low pressure in the dump tank. When the valve is opened, an expansion wave moves upstream accelerating the gas in the tube to a Mach number M_1 determined

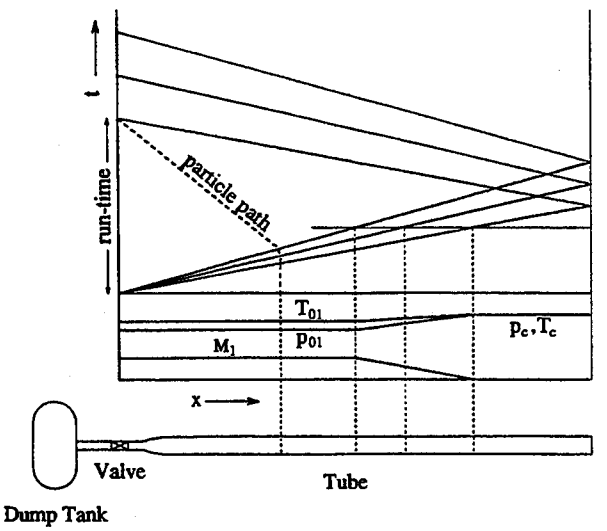

Figure 1: x,t-diagram of a Ludwieg-Tube wind tunnel

by the area ratio of the sonic throat of the valve and the tube. The flow parameters behind the wave are constant as long as viscosity effects can be neglected. The measuring time is determined by the time it takes the wave to travel to the end of the tube and back to the test section. The stagnation conditions (denoted by the subscript 0) are different from the charge conditions (denoted by c). Fig. 2 shows the ratios p_{01}/p_c, T_{01}/T_c, the Mach number in the tube, M_1, and the length $\Delta L/L$ of the gas column passing through the test section as functions of the Mach number in the test section M, for a nozzle contraction ratio of 3.6 which applies to the tunnel to be described below.

The advantages of a Ludwieg-Tube wind tunnel are

- simplicity of the system,
- low capital cost,
- high flow quality provided the running time is not too long,
- high discharge efficiency since the stagnation pressure is higher than the pressure of the gas remaining in the tube.

For cryogenic use, additional advantages are

- no temperature distortions due to LN_2–injection,
- lower stagnation temperature than charge temperature,
- extended measuring time as the expansion wave moves with the reduced speed of sound.

The operating costs are determined by the consumed nitrogen; they can be kept low compared to continuous tunnels.

2.2 Specifications

The basic requirement for the design of the wind tunnel was to obtain a Reynolds number of at least $50 \cdot 10^6$ on an airfoil model of 150mm chord at transonic speeds. For an adaptive wall

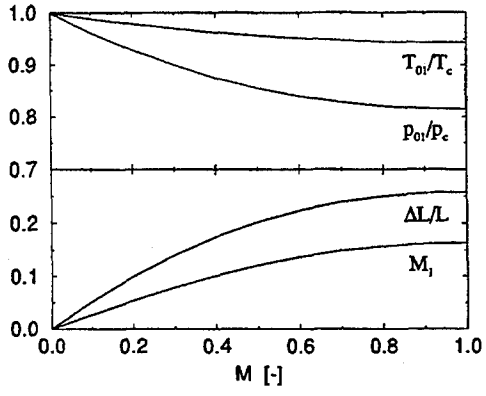

Figure 2: Characteristic flow parameters as function of the test section Mach number

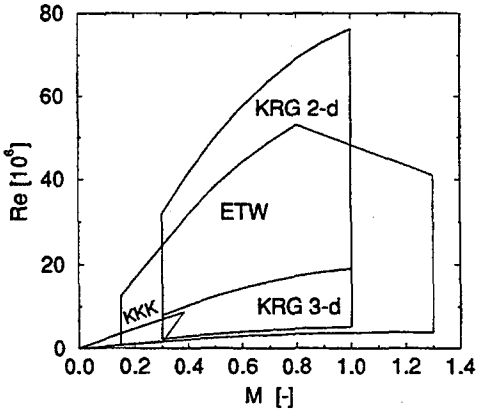

Figure 3: M,Re-diagram of the KRG

test section with flexible top and bottom walls the chord may be increased to 200 mm. From this, the main dimensions of the test section have been determined to be 400 mm width, 350 mm height and 2000 mm length. For wall mounted models a relatively high maximum stagnation pressure of 1000 kPa is possible yielding Reynolds numbers at a stagnation temperature of 120 K according to the above stated requirement. In Fig. 3 the M,Re-envelope is given for 2-D and 3-D models in comparison with the envelope of the ETW (3-D) and KKK (3-D).

Considering flow quality, which is influenced by the instationary boundary layer developing behind the expansion wave in the tube, there is a relationship between run time (i.e. tube length), tube diameter and contraction ratio of the nozzle which determines the discharge Mach number in the tube. In the present case, the basic requirement was a run time of 1 second at cryogenic temperatures resulting in a charge tube length of about 130 m. To keep the maximum discharge Mach number sufficiently low, the contraction ratio has been chosen to be 3.6, yielding a tube diameter of 0.8 m and a boundary layer displacement thickness at cryogenic temperatures of less than 4% of the tube radius.

2.3 Description of the Facility

2.3.1 Tube and Charging System

A sketch of the general tunnel arrangement is given in Fig. 4. A gate valve upstream of the nozzle separates two charging and temperature conditioning loops: Tube and test section (i.e. model) temperature can be adjusted independently offering the possibility of preconditioning the model to the correct or any other desired temperature.

The cool-down of the facility upstream of the valve is carried out by circulating cold nitrogen by means of a blower using three feeding location as indicated in Fig. 4. The gas is cooled before it enters the wind tunnel by spraying liquid nitrogen into the circulation tubings. The speed in the main tube is high enough to achieve a uniform circumferential and longitudinal temperature distribution. Hence, a vertical temperature stratification is avoided and the temperature is constant during a run. The pressure can be adjusted by an

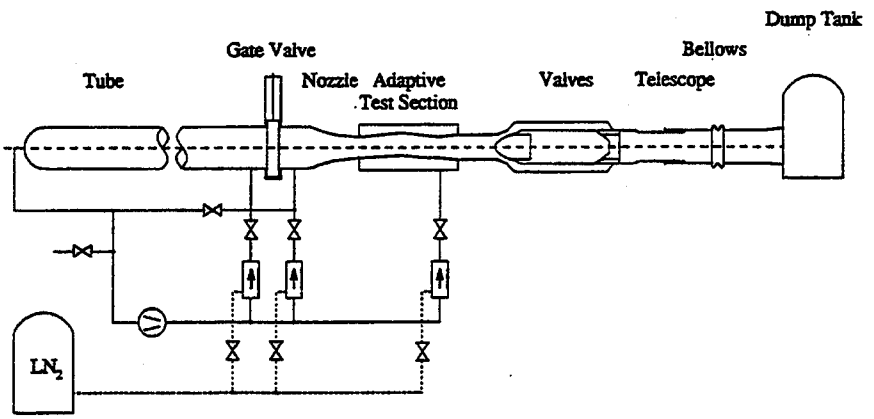

Figure 4: General arrangement of the Cryogenic Ludwieg-Tube (KRG)

exhaust valve.

The entire wind tunnel has been manufactured of stainless steel and has been externally insulated. A nitrogen purge system maintains the entire insulation at a low over-pressure to preclude entry of air or moisture.

2.3.2 Diffusor and Quick Opening Valve

The crucial components of a Ludwieg-Tube wind tunnel are the quick-opening valve which starts the flow and the sonic-throat diffusor which controls the Mach number in the test section. Both functions have been combined in the fast-acting control valve sketched in Fig. 5.

The valve consists of an enlarged tube with a centre body which contains two hydraulic actuators used to operate the control cone and the sleeve valve. The control cone can reproducibly be located with an accuracy of 0.01 mm in order to adjust the test section Mach number with an accuracy of better than 0.001. The sliding cylinder at the rear of

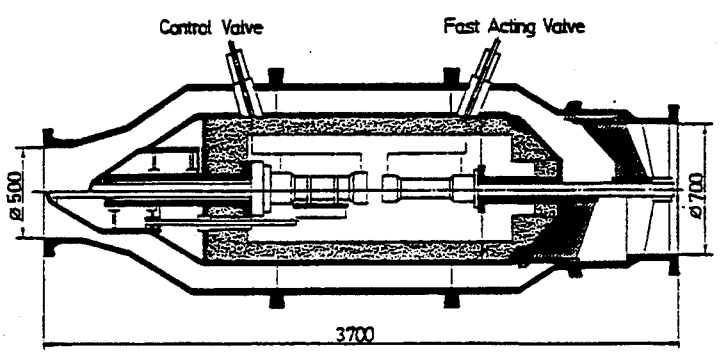

Figure 5: Fast-acting control valve

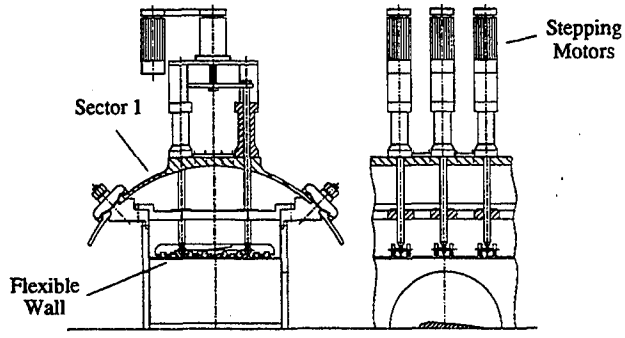

Figure 6: Scetch of the adaptive wall test section of the KRG

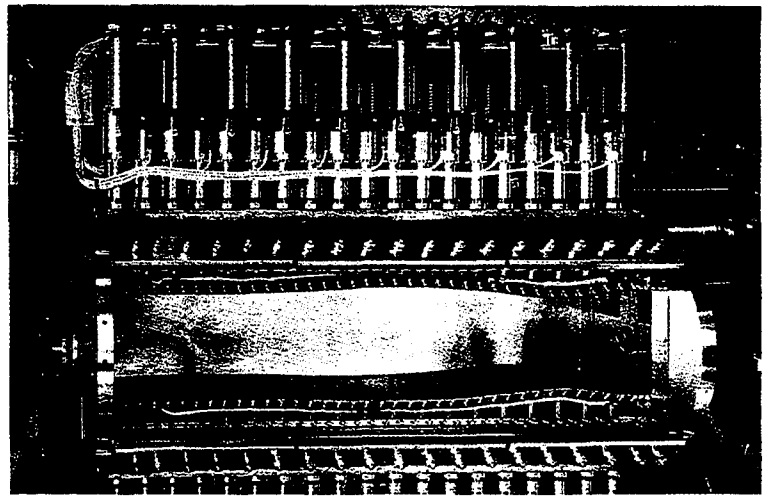

Figure 7: Adaptive wall test section

the valve starts the flow moving downstream. The opening time can be adjusted to be less than 0.1 s.

The centerbody is insulated on the inside; the temperature will be controlled by electrical heating.

2.3.3 Test Sections

A test section with slotted top and bottom walls and a test section with flexible, adaptable top and bottom walls have been designed and manufactured. The common features are a circular pressure shell with openings for the installation of the model and the windows, and solid side walls with turntables at different locations. The slotted wall test section has an open area ratio of 3% based on top and bottom wall area. Pressure distributions can be taken along the centre lines of each wall.

The pressure shell of the adaptive wall test section consists of four sectors to be clamped together, thus alleviating the assembly of the flexible walls. A cross sectional view and a

longitudinal section is sketched in Fig. 6. The flexible walls are made of glass and carbon fiber epoxy and can be adjusted by means of 19 jacks each which are operated by electrical motors outside the wind tunnel shell. Each wall has three rows of pressure taps to enable pressure measurements for the adaptation. A photograph of the interior of the test section with walls and drive system is given in Fig. 7.

3 Calibration and Flow Quality

An extensive calibration and validation program was carried out in the slotted test section. First pressure measurements revealed a streamwise pressure gradient in the empty test section. Adjusting the divergence of the upper and lower walls appropriately resulted in a constant streamwise Mach number distribution, Fig. 8. A typical airfoil model (150 mm chord length) would extend from $x/l = 0.469$ to $x/l = 0.563$. Towards the end of the straight section at $x/l = 1$ the Mach number increases somewhat due to boundary layer growth and inflow from the plenum, before the flow is decelerated in the diffusor at $x/l > 1$.

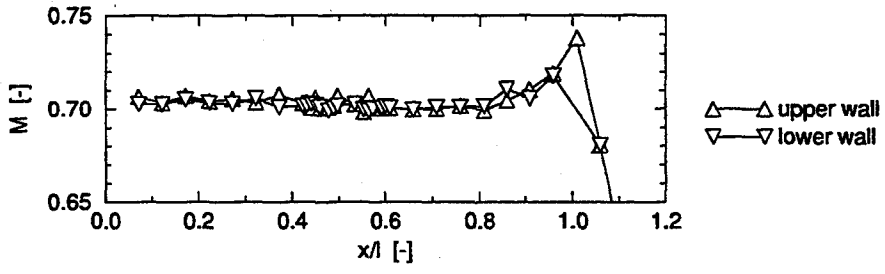

Figure 8: Streamwise Mach number distribution in the slotted test section

The influence of Mach and Reynolds number on the Mach number at the model position at $x/l \approx 0.516$ is shown in Fig. 9. There seems to be a slight decrease in Mach number with increasing reference Mach number, but the variations are not large. They can be taken into account by an appropriate calibration procedure. Some Reynolds numbers could be realized with different temperature/pressure combinations and here no systematic influence of the temperature is visible.

Especially for high Reynolds number research, the flow quality of a wind tunnel is very important. Therefore, a number of hot-wire measurements have been performed in the

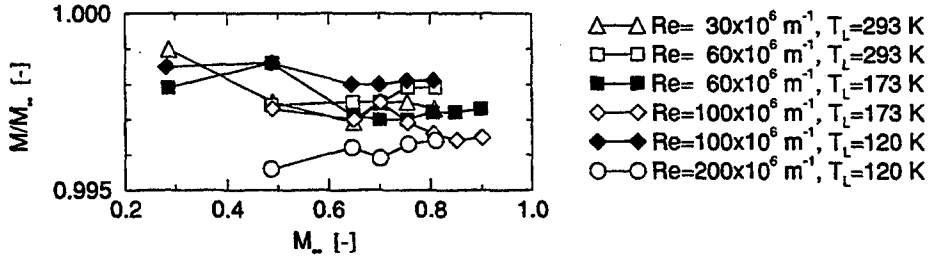

Figure 9: Mach number variation at the model position in the slotted test section

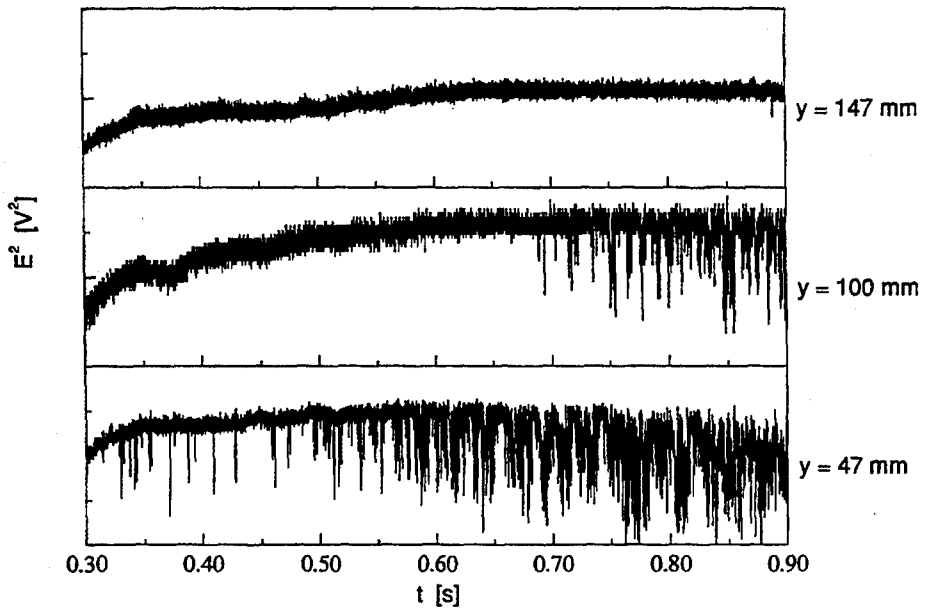

Figure 10: Hot-wire signals at different wall distances

test section of the KRG. Since a hot-wire signal depends (at least) on velocity, density and temperature of the flow, obtaining quantitative results in a transonic and cryogenic enviroment is very difficult. But already the qualitativc evaluation yielded an interesting result. Figure 10 shows time traces of hot-wire signals measured in the test section at the streamwise model position and various distances from the side wall. Depending on the wall distance, a sudden occurrence of larger fluctuations is observed at different times.

In Fig. 11 the wall distance is plotted against the time of the onset of these fluctuations measured at different Mach numbers in the range of $0.3 \leq M \leq 0.8$ and charging pressures between 300 kPa and 600 kPa. All points fall, more or less, onto a single straight line with its origin at about the time of the start of the flow. Because of the difficulties mentioned above the magnitude and structure of these fluctuations could not yet be determined. However, it seems reasonable to assume that they stem from the instationary turbulent boundary layer that developes in the storage tube behind the expansion wave.

The boundary layer thickness at the tube exit grows from zero at the start of the run to at least about 50% of the tube radius at the end of the run. Even though it decreases to virtually zero in the nozzle, as calculations and experiments show, some of the flow material now forming the inviscid region in the test section was part of the turbulent boundary layer in the tube and may still have conserved a larger turbulence level. As the interface, which represented the boundary layer edge in the tube, moves across the hot-wire probe, the increase of fluctuations is observed.

It has to be mentioned that so far an effect on surface pressure distributions has not been observed. At least in the Reynolds number investigations described in Section 4.2, no obvious effect was found.

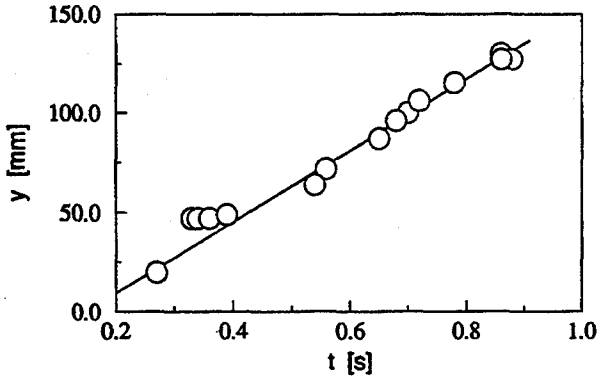

Figure 11: Wall distance over time of intermittency onset in the slotted test section

4 Comparative Airfoil Measurements

Part of the validation process of the KRG involves the investigation of airfoils over a wide range of Reynolds numbers for which, at least in part, data from other wind tunnels are available. This is to explore the performance of the tunnel under high Reynolds number/low temperature conditions and to obtain information, although in an indirect way, on the flow quality of the present type of wind tunnel as compared to conventional wind tunnels.

4.1 Pressure Distribution Measurements

For the first pressure measurement tests the CAST 7 airfoil was chosen because of its use in the GARTEur Action Group AD(AG-02)[6] for a comparative study of the performance of a number of European wind tunnels and their correction methods. Tests were performed in the KRG at a nominal Reynolds number of $Re = 6 \cdot 10^6$ with fixed transition at various Mach numbers and angles of attack.

Figure 12 shows as an example a pressure distribution obtained at $M = 0.70$ compared with interference free results from the T2 wind tunnel (ONERA). Also plotted are the values corrected for wall interference by a correction method for slotted walls based on wall pressure measurements and a model representation[4]. The corrected results come close to the values obtained in the T2. Remaining differences might be due to the relatively small ratio of model chord to tunnel height of 150 mm/350 mm in the KRG, which can result in wall interferences not correctable by the present method and due to sidewall interference, which is partially reduced by the wall adaptation process of the T2, but not taken into account by the correction method applied here.

The resulting lift versus angle of attack curve for $M = 0.70$ is given in Fig. 13 together with results from other wind tunnels. The overall agreement is relatively good and again, the correction for wall effects results in a closer agreement with the T2 curve. In the region of maximum lift, the correction method can not give accurate results, since it is based on a linear treatment of the flow close to the walls and does not account for separated flow on the model.

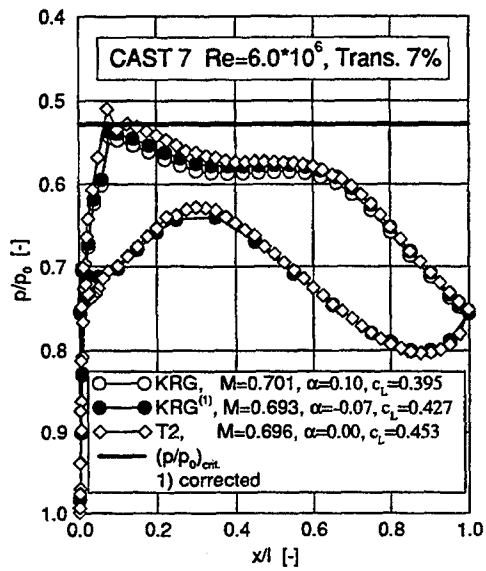

Figure 12: Pressure distribution in different wind tunnels at $M = 0.70$

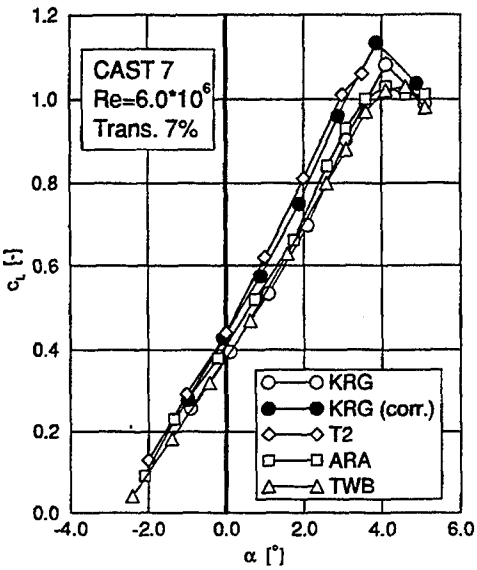

Figure 13: Lift versus angle of attack at $M = 0.70$

In Fig. 14 the shock position depending on Mach number is shown for an angle of attack that yields the design lift coefficient of $c_L = 0.52$ at a Mach number of $M = 0.76$ in the different wind tunnels. The overall agreement is good.

4.2 Reynolds Number Effects

For a first investigation of Reynolds number effects, a laminar-type airfoil (LV2F[1]) was selected due to its possibly high sensitivity to Reynolds number changes and flow quality.

The investigation was carried out over a selected Mach number and angle of attack range; however, here we will concentrate on the design Mach number of the airfoil, i.e., $M_\infty = 0.740$. Fig. 15 compares for this Mach number lift curves obtained in the KRG and the Transonic Wind Tunnel Braunschweig (TWB[3]) at a Reynolds number of $Re_c = 6.7 \cdot 10^6$ and free transition, i.e., with the transition point being allowed to move freely as a result of changes in the freestream conditions, such as changes in angle of attack and Reynolds number, and the wind tunnel environment. One observes that for both tunnels the lift curves exhibit a sudden change in slope at an incidence of about 1°, with the original slope, however, being recovered at higher angles of attack, although at a lower level in lift coefficient. It is judged that this particular lift behaviour is caused by the movement of the transition point towards the leading edge due to changes in the pressure distribution with increasing incidence. The later break in the lift curve for the KRG is probably due to a somewhat better flow quality in that wind tunnel.

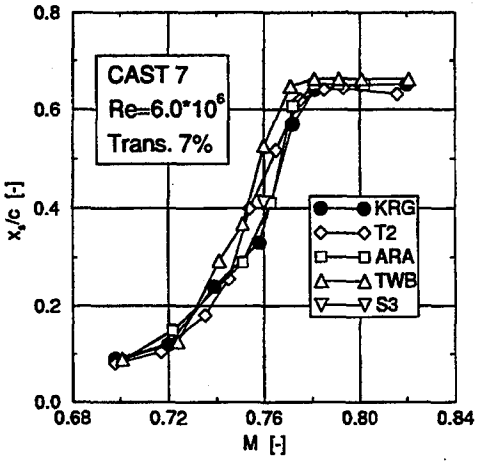

Figure 14: Shock position versus Mach number for different wind tunnels

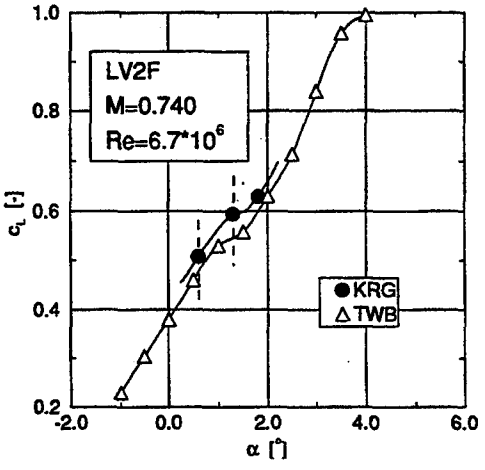

Figure 15: Comparison of lift coefficient obtained in the KRG and TWB

The corresponding flow development with Reynolds number at otherwise constant freestream conditions ($M_\infty = 0.740$ and $\alpha = 0.6°$ and $1.3°$) is demonstrated in Figs. 16 and 17: With increasing Reynolds number the lift coefficient initially increases due to improved flow conditions at the trailing edge of the airfoil and a corresponding improvement of circulation. At higher Reynolds numbers, a rapid drop in lift occurs due to the forward movement of the transition point and a corresponding deterioration of trailing edge conditions. This movement slows down as the transition point approaches the leading edge and a reversal in the Reynolds number dependence can be seen for reasons outlined above. The earlier onset of the transition point movement in the case of the TWB is also seen in the Reynolds number dependence, Fig. 17.

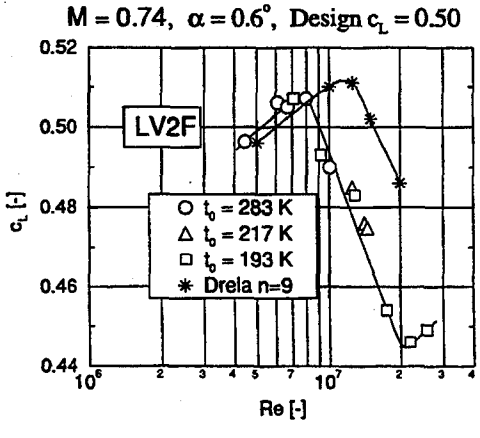

Figure 16: Reynolds number dependence of lift for $\alpha = 0.6°$

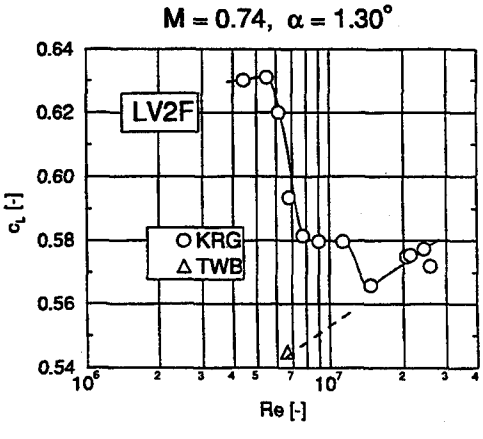

Figure 17: Reynolds number dependence of lift for $\alpha = 1.3°$

Also studied was the effect of temperature on the flow development since there was some indication that the wind tunnel flow quality might deteriorate with decreasing temperature[5]. This was accomplished by producing identical Reynolds numbers by temperature and by total pressure variation, respectively. It is shown in Fig. 16 that there is no obvious effect of temperature on the transition point location, hence flow quality, since the behaviour of the lift coefficient with Reynolds number is independent of temperature, at least in the temperature range investigated.

Also presented in Fig. 16 is a comparison with computations employing the numerical viscous-inviscid interaction method of Drela which is based on an Euler solver coupled with a boundary layer code[2]. In the computation an n-factor of 9, given by Drela as being representative of free-flight conditions, was used to determine transition locations. It can be seen that the Reynolds number dependence is well represented by the numerical results; the theoretical transition locations given explicitly by the code confirm that the drop in lift coefficient is indeed caused by the transition point movement. It should be noted that the comparison with the computational results is not intended to draw any conclusions with respect to flow quality, since the transition behaviour also depends on other factors, such as model surface finish, not modelled in the computational method.

5 Conclusions

The calibration and validation experiments carried out so far in a Reynolds number range of up to $Re_c = 25 \cdot 10^6$ have shown that the Cryogenic Ludwieg-Tube is well suited for two-dimensional experiments and that it is a valuable and relatively easy to handle tool for high Reynolds number research.

The adaptive test section will increase the quality of the experimental results by minimizing wall interferences and further push the M-Re envelope. Special effort will be undertaken to find out the nature and origin of the flow distubances in the test section in order to be able to minimize their effect on the flow quality.

References

1. Private communication.
2. M. Drela. *A User's Guide to MSES V2.1.* MIT Computational Fluid Dynamics Laboratory, Cambridge (USA), 1992.
3. W. Puffert-Meißner. The Transonic Wind Tunnel (TWB) at DFVLR in Braunschweig (Status 1987). ESA-TT-1114, 1988.
4. W. Schröder. 2D-Wall Interferences of the Transonic Wind Tunnel (TWB) of DLR Braunschweig (TWB). Interner Bericht IB 129-89/24, DLR, 1989.
5. G. Viehweger, R. Rebstock, B. Stahl, K. Wichmann, W. Becker, R. Kronen, and D. Distelrath. Der Kryo-kanal Köln (KKK) der DLR (Stand 1992). DLR-Mitt. 93-10, DLR, 1993.
6. Garteur Action Group AD(AG-02): Two-dimensional transonic testing methods. NLR TR 83086 L, GARTEur TP-011, 1981.

PHASE LOCKING OF THE FLUCTUATING VELOCITY AND VORTICITY VECTORS WITH THE KÁRMÁN VORTEX IN A CYLINDER WAKE

PHUC N. NGUYEN
Propulsor Technology Branch, David Taylor Model Basin (U.S.A.)

BARSAM MARASLI and JAMES M. WALLACE
Mechanical Engineering Department, University of Maryland (U.S.A.)

Abstract

Hot-wire measurements of the instantaneous velocity and vorticity vectors in the wake of a circular cylinder are presented. Conditional analysis is performed to characterize the coherence of the fluctuating velocity and vorticity fields with the shedding vortices. A comprehensive analysis is possible due to the availability of all velocity and vorticity components. Overall results indicate that a significant percentage of the fluctuations are phase locked to the Kármán vortices. The Reynolds normal stresses are maximum near the vortex center and minimum near the saddle region; the shear stress $-\overline{uv}$ has the reverse trend.

Introduction

Vorticity is a key parameter to understanding the dynamics of turbulent flows. Previous attempts to measure vorticity components with X-wires in a cylinder wake have been reported by Hussain & Hayakawa [1] and Antonia et al [2]. These X-wire measurements have only one component at a time due to the extreme difficulty of multi-component velocity measurement with a small probe. The present results are the first simultaneous single-point measurements of all three components of the velocity and vorticity vectors in a wake flow.

The measurements were performed at 30 diameters d downstream of a circular cylinder for $Re_d = 2000$ with a miniature 12-sensor probe. The data were reduced with an iterative error-minimization technique. The experimental equipments and data reduction technique are documented by Marasli et al [3]. The velocity and vorticity statistics such as mean values and higher moments for these measurements have been shown to have relatively high accuracy [4,5].

Conditional Analysis

Conditional analysis of the measurements with respect to the passage of the Kármán vortices is performed. This is achieved by: (1) band-pass filtering the time series of the spanwise vorticity component Ω_z in a narrow band around the shedding frequency, and (2) using a phase of this periodic time series as the phase reference for ensemble averaging all other variables considered. In this paper, the phase reference is the peak of the periodic spanwise vorticity. With the triple decomposition technique [6], the instantaneous velocity

or vorticity component, say Ω_z, is decomposed in the mean $\overline{\Omega}_z$, coherent $\tilde{\omega}_z$ and ω'_z parts. The sum of $\tilde{\omega}_z$ and ω'_z is the total fluctuating ω_z. Except for $\tilde{v}$ and $\tilde{\omega}_z$, other coherent variables are much smaller than their incoherent counterparts at $x/d = 30$. For the phase averages of the variance, it can be shown that

$$<\omega_z^2> = <\tilde{\omega}_z^2> + <\omega_z'^2> . \tag{1}$$

Fig. 1 shows a schematic vortex model for the cylinder wake. The streamwise locations of detection event can be visualized as a line approximately normal to the wake centerline, running through the vortex center in the lower wake, and the saddle region in the upper wake. The length scales in Fig. 1 are nondimensionalized by the wake half-width L_o. The streamwise and lateral dimensions of the vortices are estimated to give a rough idea where the vortex center and saddle regions are located. The coherence of the fluctuating velocity and vorticity fields is analyzed and discussed in relationship to the vortex center and saddle regions. All fluctuating velocity, vorticity components and their respective variances are analyzed, but only a few variances are presented here due to space limitation.

Discussion of Results

Fig. 2 shows the phase averages of the variance of the spanwise velocity $<w^2>$ at 6 wake locations in which negative and positive $\eta \equiv y/L_o$ values denote lower and upper wake, respectively. Velocity components are nondimensionalized by the centerline velocity deficit u_o, and time by the shedding period T. The detection event is at $t/T = 0$ and positive time corresponds to its upstream region. The phase locking of w^2 comes entirely from the incoherent w' fluctuations since $\tilde{w}$ turns out to be negligible. This phase locking is small near the wake centerline and the wake edges, and is maximum near the centers of the upper and lower vortices ($t/T = 0$ at $\eta = -0.47$ and $t/T = \pm 0.5$ at $\eta = 0.71$). The phase averages of the other velocity variances show similar behavior in this regard. Therefore, the Reynolds normal stresses have maxima near the vortex center, and minima near the saddle region.

Fig. 3 shows the phase averages of the shear stress uv and its incoherent part, $u'v'$, which are related by

$$<uv> = <\tilde{u}\tilde{v}> + <u'v'> . \tag{2}$$

Across the wake, the total is only slightly different from the incoherent contribution. The coherent contribution is very small mainly because $\tilde{u}$ is small. Fig. 3 reveals a clear pattern that at the vortex center, $<uv>$ has the lowest magnitude (≈ 0.01), and at the saddle, it has the highest (≈ 0.08). The left column is for the lower wake, and $<uv>$ has a positive sign except around $t/T = 0$ for $\eta = -0.47$; the right column is for the upper wake, and $<uv>$ has a negative sign everywhere except near the centerline ($\eta = 0.12$). The high $<uv>$ values in the saddle region (0.09 for $\eta = -0.47$ and -0.08 for $\eta = 0.71$) means that turbulence production is predominantly occuring there, and the vortex center just collects the turbulent kinetic energy produced in the saddle regions. These observations and those about the normal stresses are consistent with the findings of Cantwell & Coles [7]. Hussain & Hayakawa [1] reported a peak $<u'v'>$ value of approximately 0.006 U_∞^2 at $x/d = 30$. The peak $<u'v'>$ at $\eta = -0.47$ in Fig. 3 is about 0.0025 U_∞^2. The value from Hussain & Hayakawa is higher

probably because their accepted structures must have "large-scale vorticity concentration", whereas the structures in the current measurements are the periodic Kármán vortices.

In Fig. 4, the $<\omega_x^2>$ values show strong coherence with the passage of shed vortices. Here, the vorticity components are nondimensionalized by the ratio u_o/L_o. The incoherent part is practically the same as the total due to the extremely small $\tilde{\omega}_x$. For $\eta = -1.06$, $<\omega_x^2>$ has a peak at $t/T \approx 0.3$, i.e. in the region upstream of the vortex center, or in the diverging leg region of the saddle. This phenomenon is directly observed here for the first time due to the availability of these vorticity data. The phenomenon reaffirms the vortex model in Fig. 1 since the diverging leg of the saddle region, associated with vortex stretching, is dominant over the converging leg which is associated with compression. This phenomenon can also be seen in the upper wake, at $\eta = 1.29$, where the detected event is the saddle region. The downstream region is the diverging leg of the saddle ($t/T < 0$) and it has higher $<\omega_x^2>$ than the upstream converging leg. The schematic vortex model in Fig. 1 illustrates these flow regions as arrows in the plane of the mean shear. This diverging leg, commonly called "braid", could extend to the wake edges and join with the converging leg of the downstream saddle at a different spanwise location. This is a possible mechanism for the generation of three-dimensional flow structures. Hussain & Hayakawa [1] speculated that these braids with predominantly streamwise vorticity interact with the spanwise vortices to produce small-scale, three-dimensional vorticity fluctutations.

Fig. 5 shows the phase averages of the total variance ω_y^2 since $\tilde{\omega}_y$ is very small. Even though the rms values of the fluctuating ω_x and ω_y are approximately the same across the wake [4], $<\omega_x^2>$ shows significantly higher coherence with the passage of the shed vortices than $<\omega_y^2>$. Overall results indicate that a significant percentage of the fluctuations are phase locked to the Kármán vortices. Therefore, turbulent fluctuations in the cylinder wake are strongly affected by the large-scale coherent structures, far from being incoherent as commonly thought.

Acknowledgements

This work was sponsored by the Independent Research Program of CD/NSWC. P.N. especially wants to thank Drs. Frank Peterson and Bruce Douglas of CD/NSWC and Dr. Pat Purtell of the Office of Naval Research (USA).

References

1. A.K.M.F. Hussain and M. Hayakawa, "Eduction of Large-Scale Organized Structures in a Turbulent Plane Wake," *J. Fluid Mech.* (1987), **180**, pp. 193-229.

2. R.A. Antonia, L.W.B. Browne and D.A. Shah, "Characteristics of Vorticity Fluctuation in a Turbulent Wake," *J. Fluid Mech.* (1988), **189**, pp. 349-365.

3. B. Marasli, P.N. Nguyen and J.M. Wallace, "The Vortical Structure of the Near Wake of a Circular Cylinder," *Experiments in Fluids* (1993), **15**, pp. 209-218.

4. P.N. Nguyen, B. Marasli and J.M. Wallace, "The Vortical Structure of the Near Wake of a Circular Cylinder," IUTAM Symposium, University of Göttingen, Germany, Sept. 1992.

5. P.N. Nguyen and B. Marasli, "Velocity Measurement in a Plane Wake with a 4-Sensor Probe," 2nd International Conference on Turbulence Modelling and Measurements, Florence, Italy, June 1993.

6. W.C. Reynolds and A.K.M.F. Hussain, "The Mechanics of an Organized Wave in Turbulent Shear Flow. Part 3. Theoretical Models and Comparison with Experiments," *J. Fluid Mech.* (1972), **54**, pp. 263-288.

7. B. Cantwell and D. Coles, "An Experimental Study of Entrainment and Transport in the Turbulent Near Wake of a Circular Cylinder," *J. Fluid Mech.* (1983), **136**, pp. 321-374.

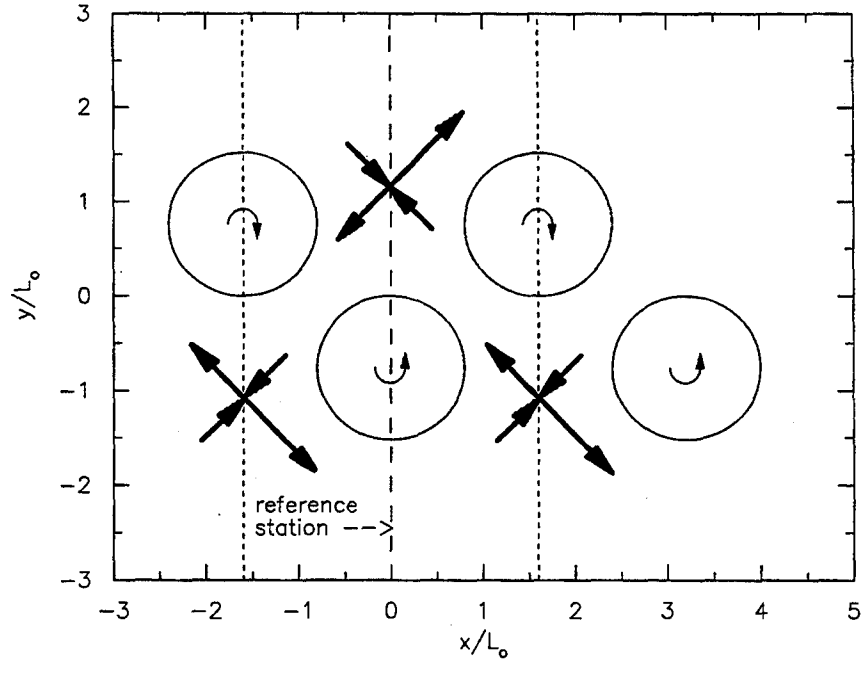

Figure 1: Schematic sketch of the vortex shedding and the saddle regions. The dimensions are estimated from current database and from Hussain & Hayakawa [1] at $x/d = 30$. The reference station at $x/L_o = 0$ indicates the detected events across the wake.

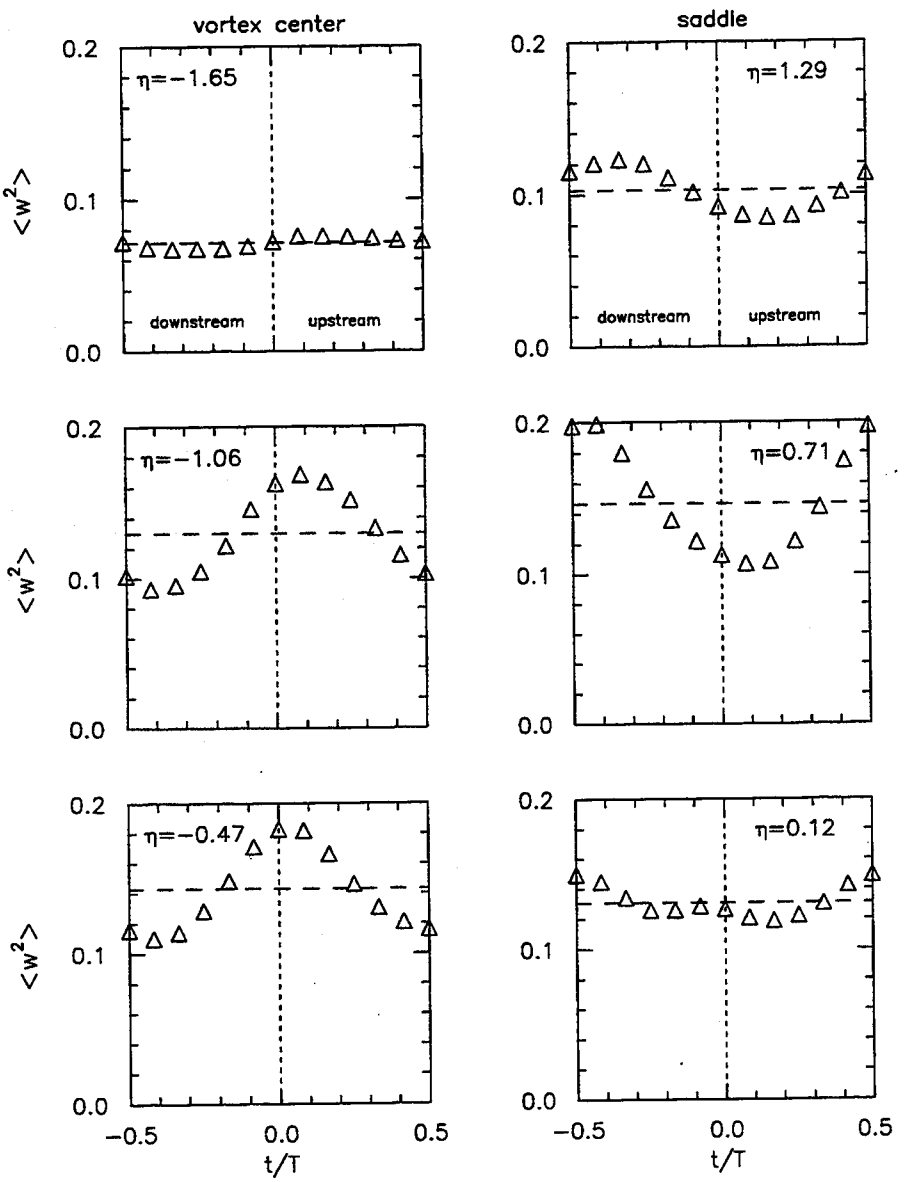

Figure 2: Conditional averages of the total w^2 fluctuations. The incoherent contribution is almost the same as the total therefore not shown. The long dashed lines indicate the time averages.

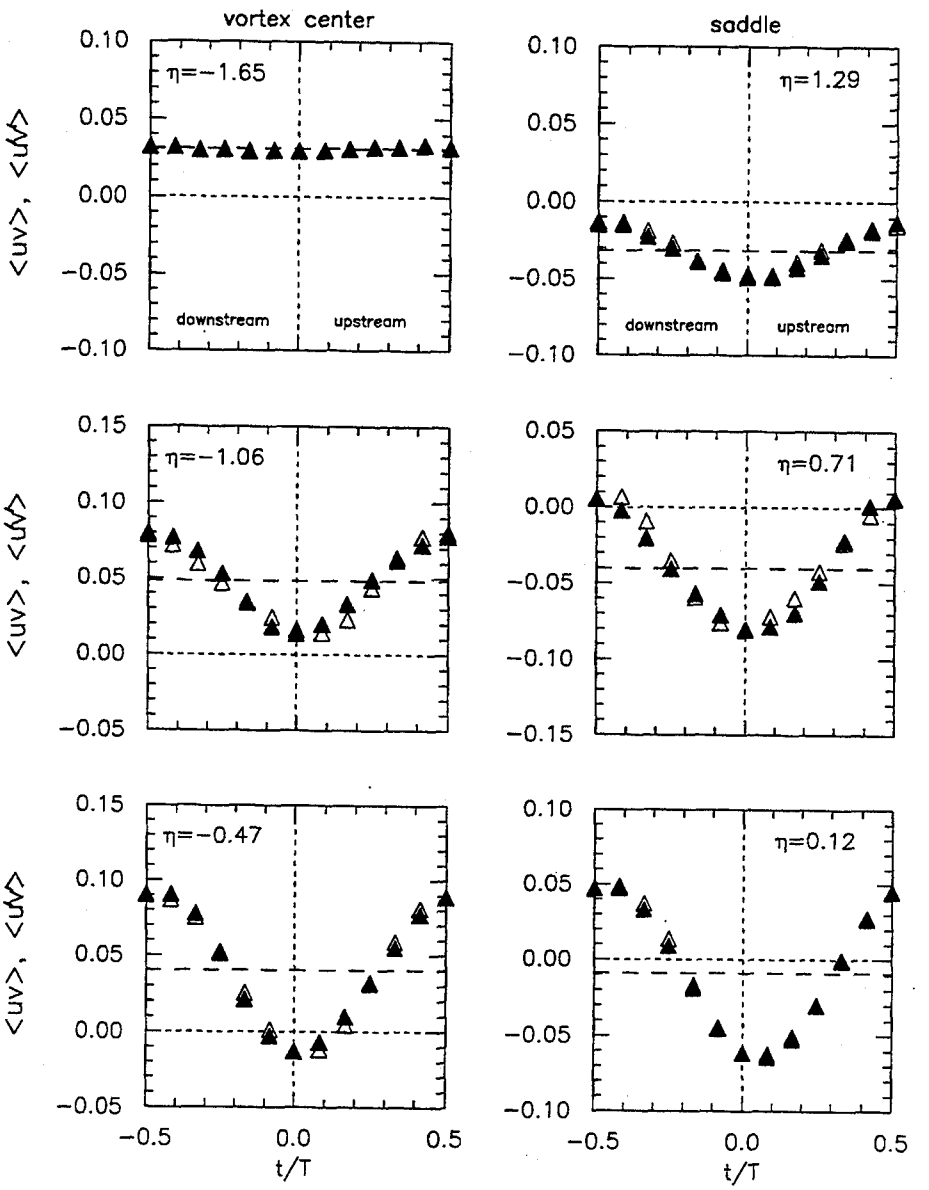

Figure 3: Conditional averages of the total and incoherent uv fluctuations. The closed symbols are for the incoherent fluctuating field. The open symbols are for the total fluctuating field. The long dashed lines indicate the time averages of the incoherent field.

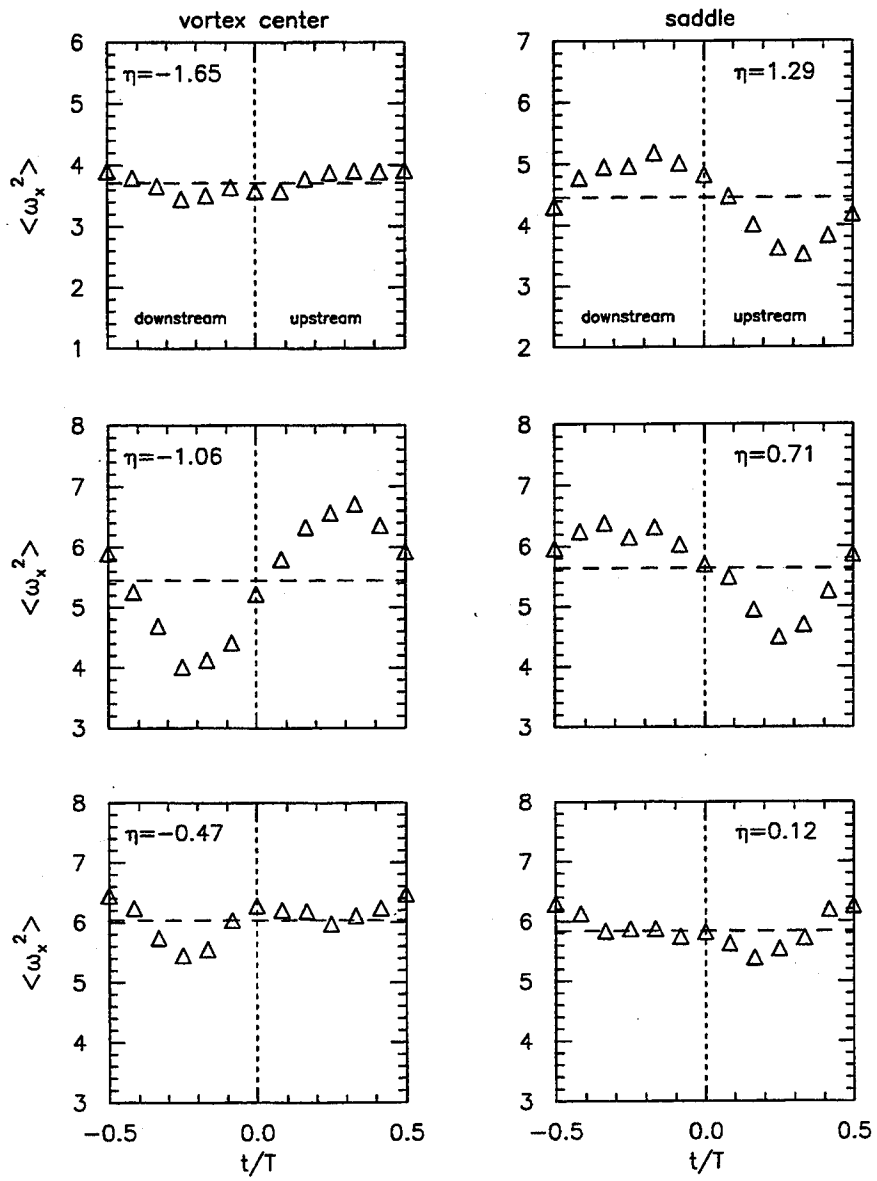

Figure 4: Conditional averages of the total ω_x^2 fluctuations. The incoherent contribution is almost the same as the total therefore not shown. The long dashed lines indicate the time averages.

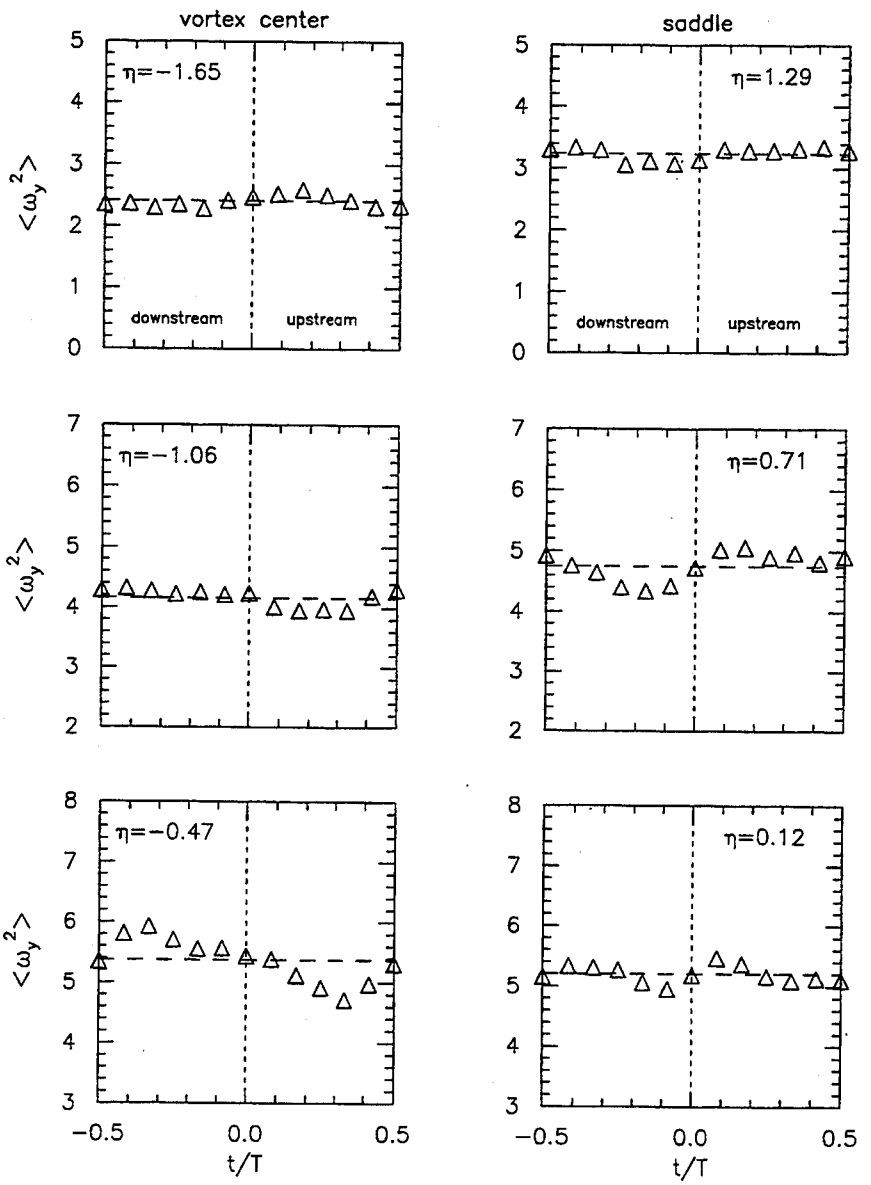

Figure 5: Conditional averages of the total ω_y^2 fluctuations. The incoherent contribution is almost the same as the total therefore not shown. The long dashed lines indicate the time averages.

AN EXPERIMENTAL STUDY OF FLUID FLOW AND HEAT TRANSFER CHARACTERISTICS BEHIND A CIRCULAR CYLINDER IN CROSSFLOW

SHUICHI TORII
Department of Mechanical Engineering, Kagoshima University,
Kagoshima 890, Japan

ABSTRACT

An experimental study is conducted to investigate fluid flow and heat transfer characteristics behind a slightly heated circular cylinder in cross flow. Emphasis is placed on the transport mechanism in laminar separated flows. By using a hot-wire anemometer, spectrum analysis of its signal is performed to examine the separated shear layer formed behind the circular cylinder. A resistance thermometer is employed to measure the time-averaged temperature behind the cylinder and the power-spectral density of the temperature fluctuations in the thermal boundary layer. It is disclosed that higher heat transfer performance from the cylinder, particularly at the rear stagnation point, is achieved in the following process: (i) with an increase in the turbulence intensity, its effect may penetrate deeper into the boundary layer formed at the front part of the cylinder and advance the laminar-to-turbulent transition, (ii) an exchange of momentum between the voltex wake and the free stream is made in an active manner, resulting in a substantial diffusion of vorticities at a relatively early stage, and (iii) the corresponding heat transfer from the cylinder is promoted due to its effect.

1. INTRODUCTION

Circular cylinders find the most widespread application in heat exchangers, power generators, and other thermal apparatus. Its instrument design depends strongly on heat transfer behavior and specific feature of fluid dynamics. It has been known for a long time that the heat transfer from a body in cross flow is induced as the free-stream turbulence intensity is increased, and many experimental results pertinent to this effect have been reported, particularly for the overall coefficients of heat transfer from a circular cylinder placed normal to an air stream.

Comings et al. [1] reported that in the higher Reynolds number region, the overall heat transfer coefficient from a circular cylinder was intensified with an increase in the turbulence intensity in the lower turbulence intensity region, tending toward a definite value at higher turbulence intensities. Kestin and Maeder [2] presented the experimental results for the effect of screen-produced turbulence on the overall coefficient of heat transfer from a cylinder in an air stream. It was found from these results that the heat transfer rate was increased substantially by a slight increase in the turbulence intensity, and that it becomes almost constant with further increases in the turbulence intensity. Giedt [3] measured local heat transfer coefficients from a circular cylinder set normal to an air stream and reported the increased rate of heat transfer to the laminar boundary layer on the front of the cylinder. Seban [4] investigated the effect of screen-produced turbulence on heat transfer performance for different sizes of cylinders, and found that an increase in turbulence intensity produced larger local heat transfer coefficients. Sato and Sage [5] measured the overall heat transfer form spheres and observed a substantial rate of heat transfer as the turbulence level rises. Throughout these results, no information, however, is available about the fluid flow and heat transfer mechanisms behind the circular cylinder, particularly the specific feature in the separated shear and thermal boundary layers formed behind the cylinder.

The purpose of this paper is to investigate the flow and heat transfer characteristics behind the circular cylinder in the Reynolds number range of laminar boundary-layer separation. Emphasis is placed on the effect of free-stream turbulence on the separated shear and thermal boundary layers. A hot-wire anemometer and a resistance thermometer are employed to measure the velocity and temperature fluctuations behind the cylinder.

2. EXPERIMENTAL APPARATUS AND PROCEDURE

Figure 1 depicts a schematic of the experimental apparatus employed in the present study. It consisted of a blower, a settling chamber containing a honeycomb and nets, and a rectangular duct 1,620 mm in length with a square cross-section 420 (=L) X 180 mm. The test cylinder was positioned normal to an air stream, at 300 mm downstream from the entrance of the rectangular duct. Upon passing an electric current from a DC generator, heat was generated in the cylinder with a uniform surface heat flux over 140 mm length in the central section. This uniform heat flux section was used for surface temperature measurements by mounting chromel-alumel thermocouples. The velocity fluctuation and the time-averaged streamwise velocity in the flow field were measured with the use of a constant-temperature hot-wire anemometer with a single-wire probe. The signal was fed into a Fourier analyzer to determine the power spectra of velocity fluctuations. The time-averaged temperature of the fluid downstream of the cylinder and the power spectrum in the thermal boundary layer were obtained by using a resistance thermometer with a sensor made of signal platinum.

The circular cylinder with the diameter of 18 mm was employed here. The corresponding blockage ratio was 0.043. This value produces no effect on the flow around the cylinder because the blockage ratio is comparable to the critical value of 0.04 [6]. The Reynolds number ranges from 7,000 to 13,000, and the turbulence intensity of the free stream from 1 % to 10 %.

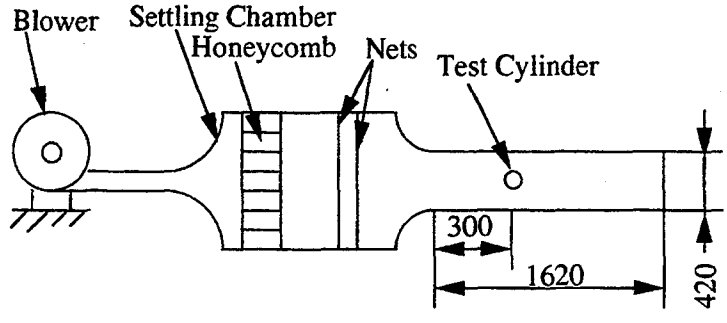

Fig. 1 Experimental apparatus

3. RESULTS AND DISCUSSION

Heat transfer performance at the rear stagnation point is represented in Fig. 2 in the form of Nusselt number (Nu) versus Reynolds number (Re) with the turbulence intensity, Tu, as the parameter. The experimental results of Petrie and Simpson [7] are superimposed with solid straight lines for comparison. The Nusselt number is increased with an increase in the Reynolds number. A higher heat transfer rate is observed in the group of a higher value of Tu. This observation suggests that the heat transfer rate at the rear stagnation point depends on the level of the turbulence intensity. This tendency agrees well with experiments by Petrie and Simpson.

An attempt is made to explore the mechanism of fluid flow and heat transfer behind the cylinder by examining the separated shear and thermal boundary layers. Adachi and Kato [8] and Arie et al. [9] evaluated the thickness of the separated shear layer from the transverse profile of the streamwise velocity obtained by a hot-wire anemometer. The same method is employed here. Figure 3 illustrates the streamwise profiles of the separated shear layer for two different levels of the turbulence intensity. (a), (b) and (c) of the figure correspond to Re=7000, 10000 and 13000, respectively. Note that the origin of the (X, Y) coordinates is fixed on the cylindrical axis. It is observed that the separated shear layer spreads in the streamwise direction as the Reynolds number is increased. This trend is amplified with an increase in the turbulence intensity. To further understanding of the flow characteristics in the separated shear layer, a spectrum analysis was performed with the aid of a Fourier analyzer.

Figure 4 shows the streamwise variation of the peak power spectrum S(f) in the separated shear layer, where f is the frequency of the velocity fluctuation. Bloor [10] reported

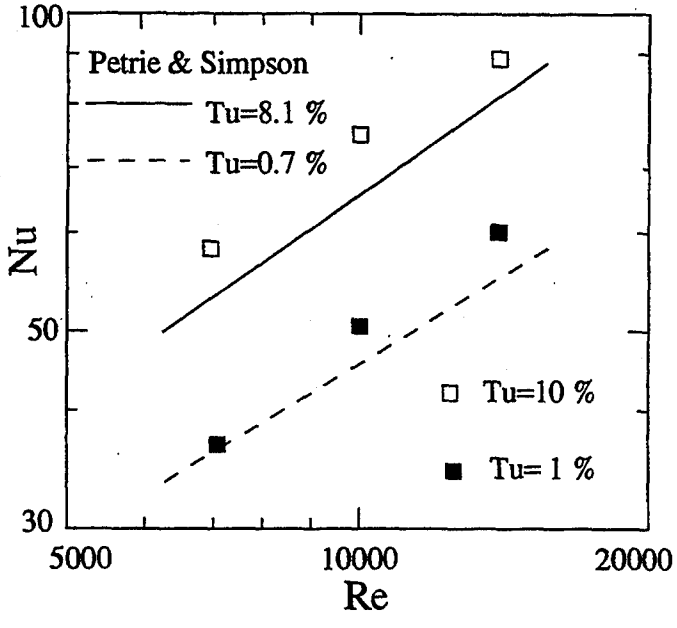

Fig. 2 Nusselt number at the rear stagnation point

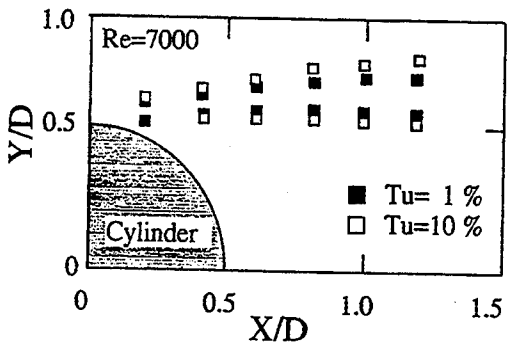

(a) Re=7000

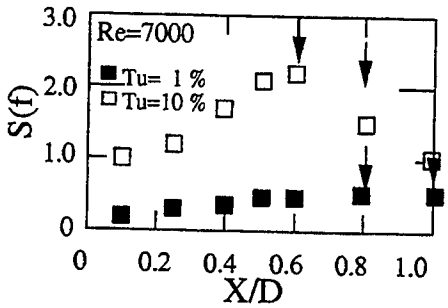

(a) Re=7000

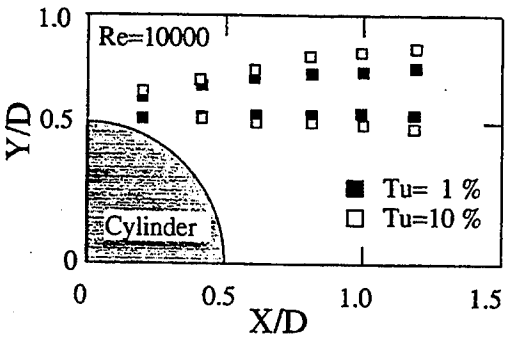

(b) Re=10000

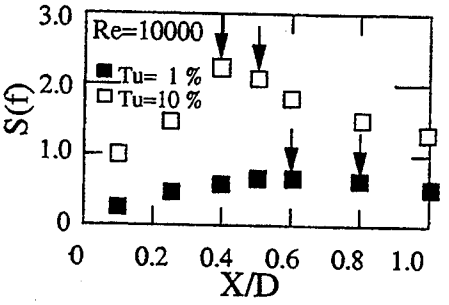

(b) Re=10000

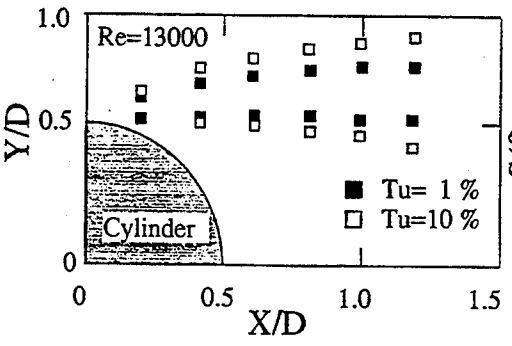

(c) Re=13000

Fig. 3 Formation of the separated shear layer

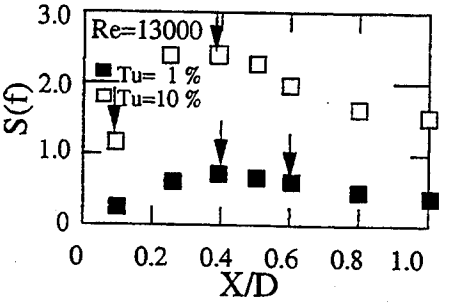

(c) Re=13000

Fig. 4 Streamwise variation of power spectrum

that the transition from laminar to turbulent flow is characterized by the appearance of a relatively high frequency in waves of vortex shedding. These waves are referred to as transition waves. Based on this phenomenon, he defined the laminar-to-turbulent transition which occurs between two locations, that is, the onset is determined by the first appearance of the waves with higher frequency and the flow degenerates perfectly to turbulence (completion of flow transition) when the fundamental frequency is almost masked. Both locations are shown in Fig. 4 with an arrow. The range of X/D between the two arrows corresponds to the transition region. One observes that for the three different Reynolds numbers, vortex shedding is substantially triggered in the higher case of the turbulence intensity, because of higher power density distributions. The transition region is seen to be shifted toward the upstream as the Reynolds number is increased. At the same Reynolds number, the laminar-to-turbulent flow transition takes place at an earlier stage with an increase in the turbulence intensity. The movement of the transition region in the separated layer is found to affect the fluid flow characteristics, i.e. flow structure, behind the circular cylinder.

To further understand the mechanism of heat transfer, an attempt is made to examine the time-averaged temperature distribution in the wake and the power spectrum of the temperature fluctuation in the thermal boundary layer. Figures 5(a) and (b), for Re=10000, depict the streamwise variations in the transverse distribution of dimensionless temperature, Tr, in the lower and higher cases of the turbulence intensity, respectively. The fluid temperature increases along the Y axis, reaching a maximum value followed by diminishing to the freestream value (a minimum value, i.e. Tr=0), except at X/D=0.1 and 0.2. This negative temperature gradient region at each X/D is regarded as the thickness of the thermal boundary layer. It is observed that the thickness is increased in the flow direction, whose trend becomes larger at the higher level of the turbulence intensity, as shown in Fig. 5(b). Thus, it is postulated that active thermal exchange between the thermal boundary layer and the freestream take places in the case of the higher turbulence intensity. The observation is supported by the results of power-spectral density of the temperature fluctuation in the thermal boundary layer. The streamwise distribution of the peak value at each downstream location is illustrated in Fig. 6 in the same form as Fig. 4. A higher temperature fluctuation is found at the higher turbulence intensity level, because its power-spectral density is larger than that at the lower level.

In summary, a higher heat transfer rate at the rear stagnation point is achieved in the following process: (i) as the turbulence intensity of the free stream is increased, its effect may penetrate deeper into the boundary layer formed at the front part of the cylinder and may induce the transition of laminar to turbulent flow; (ii) when the transition occurs at a relatively early stage, an exchange of momentum between the vortex wake and the free stream takes place actively, resulting in a substantial growth of the vorticities in the vicinity of the separation point; and (iii) the corresponding thermal diffusion is also promoted.

SUMMARY

An experimental study has been performed to investigate the heat transfer and flow characteristics behind a cylinder in the Reynolds number range of laminar boundary-layer separation. The results obtained from the study are summarized as follows:

(1) Heat transfer performance at the rear stagnation point depends on the turbulence intensity and this result agrees well with the existing experimental one.

(2) The transition from laminar to turbulent flow in the separated shear layer is promoted as the turbulence intensity is increased. Correspondingly, the velocity fluctuation in its layer is induced. It is accompanied by a substantial enhancement in thermal diffusion from the cylinder.

(3) Heat transfer from a cylinder is affected by a shift of the transition region in the separated shear layer. Accordingly, the transition phenomena in a separated shear layer play an important role in heat transfer from the cylinder.

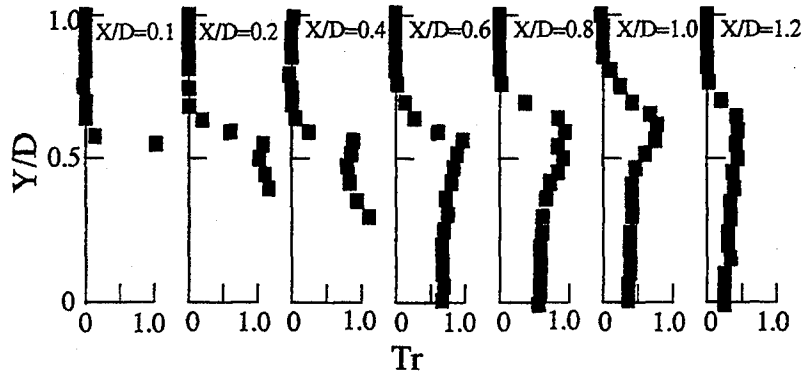

(a) Tu=1 %

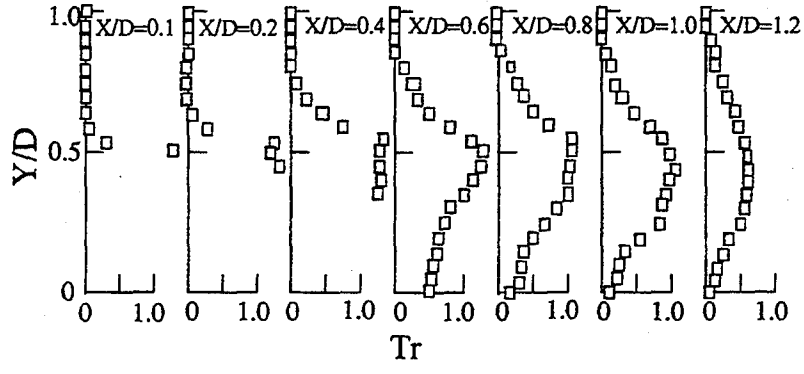

(b) Tu=10 %

Fig. 5 Temperature distributions behind a cylinder

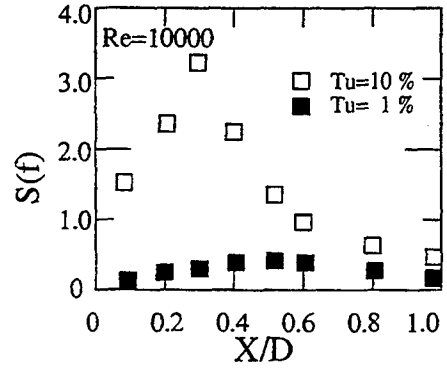

Fig. 6 Streamwise variation of power spectrum in the thermal boundary layer

NOMENCLATURE

D	diameter of circular cylinder, m
f	frequency
h	local heat transfer coefficient around cylinder, W/Km^2
L	height of rectangular duct, m
Nu	Nusselt number, =hD/λ
r	radial coordinate, m
Re	Reynolds number, =U_∞D/ν
S(f)	power spectrum
T	fluid temperature, K
T_O	surface temperature at the front stagnation point, K
Tr	temperature ratio, =(T-T_∞)/(T_O-T_∞)
Tu	turbulence intensity, =$(u'^2)^{0.5}$/U
T_∞	free-stream temperature, K
U_∞	free-stream velocity, m/s
U	time-averaged velocity in the streamwise direction, m/s
u'	longitudinal component of the velocity fluctuation, m/s
X	Cartesian coordinate in the mean flow direction, m, with the origin fixed on the cylindrical axis.
Y	Cartesian coordinate normal to free stream, m

Greek Letters

λ	thermal conductivity of fluid, W/Km
ν	kinematic viscosity of fluid, m^2/s

REFERENCES

1. Comings, E. W., Clapp, J. T. and Taylor, J. F., Air turbulence and transfer process (Flow normal to cylinders), Int. Engng. Chem., Vol. 40, 1948, pp. 1076-1082.
2. Kestin, J. and Maeder, P. F., Influence of turbulence on the transfer of heat from cylinder, NACA TN 4018, 1957.
3. Giedt, W. H., Effect of turbulence level of incident air stream on local heat transfer and skin friction on a cylinder, J. Aero. Sci. Vol. 18, 1951, pp. 726-737.
4. Seban, R. A., The influence of free stream turbulence on the local heat transfer from cylinders, J. Heat Transfer, Vol. 102, 1960, pp. 101-106.
5. Sato, K. and Sage, B. H., Thermal transfer in turbulence gas streams: (effect of turbulence on macroscopic transport from spheres, Trans. ASME, Vol. 80, 1958, pp. 1380-1394.
6. Okamoto, T. and Takeuchi, Y., Effect of wind tunnel wall on the flow past a circular cylinder and the wake, Trans. JSME, Ser. B, Vol. 41, No. 341, 1975, pp. 181-188, (in Japanese).
7. Petrie, A. M. and Simpson, H. C., An experimental study of the sensitivity to free-stream turbulence of heat transfer in wakes of cylinders in crossflow, Int. J. Heat Mass Transfer, Vol. 15, No. 8, 1972, pp. 1497-1513.
8. Adachi, T. and Kato, E., Study on the flow about a circular cylinder in shear flow, J. Jpn. Aer. Spa. Soc., Vol. 23, No. 256, 1975, pp. 45-53 (in Japanese).
9. Arie, M., Kiya, M., Suzuki, Y., Hagino, M. and Takahashi, K., Effect of the free-stream turbulence on the flow characteristics past a circular cylinder, Trans. JSME, Ser. B, Vol. 46, No. 405, 1980, pp. 1427-1436 (in Japanese).
10. Bloor, M. S., The Transition to Turbulence in the Wake of a Circular Cylinder, J.Fluid Mech., Vol. 19, No. 2, 1964, pp. 290-304.

MEASUREMENT AND SIMULATION OF STATIC WIND FORCE ON TRANSMISSION LINE CONDUCTORS AND INSULATOR STRINGS IN THE WIND TUNNEL

B.R.SRINIVASA RAO* & S.P.GOVINDA RAJU**
*Principal Research Scientist, **Professor
Dept. of Aerospace Engg, Indian Institute of Science,
Bangalore - 560 012. (India)
and
R.SUSENDRAN #, N.S.PARTHASARATHY ## & P.KRISHNAMURTHY ##.
#Joint Director, ## Engineering Officer Grade IV.
Central Power Research Institute,
Bangalore - 560 094. (India)

ABSTRACT

Wind Tunnel Tests were conducted on a section of bundled conductors in selected configurations and drag force due to wind was measured. For simulating the drag force of bundled conductors, a parachute was designed and fabricated. A 1/5th scale model of suspension insulator string was tested in the wind tunnel for measuring swing angle. The measured swing angle and calculated swing angle were found to be in good agreement.

1. Introduction

In recent times,long distance transmission of electric power using high voltage transmission lines is often adopted. The requirements for increased capacity has necessitated the use of bundled conductor configurations. The design of the transmission towers,conductors,insulator strings etc., have to necessarily take into account the large wind loads which occur during storms etc. In this context wind tunnel tests on transmission line systems are of relevance. The result of this study was useful in designing 800 KV transmission systems.

In this paper measurement of static aerodynamic force on bundled condutor configurations and its simulation for measurement of swing angle of insulator strings in the wind tunnel is described. The study was carried out in 4.25 x 2.75 metre open circuit wind tunnel in the Dept. of Aerospace Engineering,Indian Institute of Science, Bangalore (India). Static force was first measured on a short section of the actual conductor and then extrapolated to full span. This is convenient with bundled conductors since a short section of the actual bundled conductors with spacer, spacer dampers etc may be tested. The wind load on the conductor (drag force) was simulated by a parachute for measurement of swing angle of Insulator strings using a 1:5 scale model. The details of measurement, and results are presented in the subsequent sections of this paper.

2. Drag test on bundled conductors

A transmission line conductor is subjected to aerodynamic drag force depending on its diameter,length,surface roughness, etc. The drag force per unit length of the conductor is : D = q x d x drag coefficient, where q is dynamic pressure in the Wind Stream and d is diameter of the conductor.

In the case of bundled conductors both windward and leeward conductors are subjected to drag force which to some extent depend on the distance between them (due to the interference effect of windward conductors on leeward conductors).

A sectional model of quadruple bundled conductors considered for 800 kV transmission lines was tested in the wind tunnel on specific configurations. This consisted of a bundle of 1 metre length of 35mm diameter ACSR Bersimis conductors and spacers, spacer damper etc. Fig 1 shows a view of the model mounted in the test section. The entire assembly of conductors, spacers and spacerdamper had a blockage of lessthan 1% of the test section area, hence, there was no need to apply blockage corrections for the drag force measured.

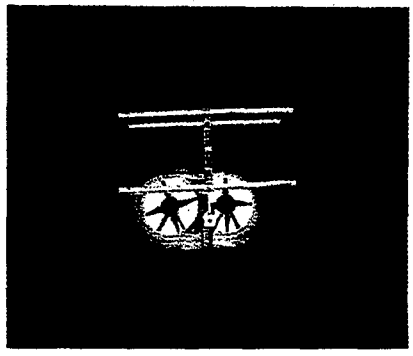

Fig. 1 Model of the Bundled Conductor

The aerodynamic drag force was measured using a six component strain gauge balance. The axial force rating of the balance was 45Kgs. The axial force component only was considered and other components ignored as they were negligible. The balance output was acquired by a data acquisition system which included precision amplifiers, PC, Plotter etc. The accuracy of measurement system was better than 0.5%.

The model was mounted on the balance which inturn mounted on the sting in the test section of the wind tunnel (Fig 1). After completing the model mounting etc and before starting the wind tunnel, initial output of the balance was acquired by the data qcuisition system. Then the tunnel was started and the wind speed raised slowly up to about 35 meters/sec. The balance output was again acquired by the data acquisition system. From the wind On and wind Off outputs of the balance, the drag force component was computed.

The measured drag force for various configurations of spacer, spacer damper, and conductor is presented in table 1. The equivalent flat plate area also is given in the same table. The equivalent flat plate area (Seq) was calculated from the measured drag force and the dynamic pressure as : Seq = D/q, where D is the measured drag force and q is dynamic pressure in the wind stream.

Since the drag force D is given by D = q X A X Cd Where A is projected area, the equivalent flat plate area divided by the

corresponding projected area gives drag coefficient Cd. The projected area of one meter length of the conductor bundle consisting of four conductors each of 35mm diameter was 35/1000 X 1 X 4 = 0.14 Sq.m and the corresponding equivalent flat plate area (Table 1) of 0.1148 giving Cd = 0.1148/0.14= 0.82. Equivalent flat plate area is convenient in designing the Parachute for simulation of conductor drag force instead of projected area which varies with wind speed. Calculation of equivalent flat plate area for full span is given in Appendix I.

Table 1:Equivalent flat plate area at 0 deg. angle of incidence

Configuration	Wind speed m/Sec	Drag force Kgs	Equivalent flat plate area Sq.m	Average Eq.flat plate area Sq.m*
1)Spacer & Conductor	35.379	9.992	0.148	
	35.379	9.8659	0.1461	0.1466
	35.4387	9.9229	0.1465	
	35.4983	9.9215	0.146	
2)3Spacers & Conductor	35.7764	12.5832	0.1812	
	36.0106	12.7004	0.1805	0.1812
	36.0398	12.7162	0.1804	
	36.098	12.9229	0.1828	
3)Spacer, Spacer damper & Conductor	33.4697	12.7831	0.2103	
	33.3753	12.7219	0.2105	0.2106
	33.2807	12.6515	0.2105	
	33.2175	12.6495	0.2113	
4)Spacer & Shortened-Conductor	33.4092	2.7957	0.0463	
	33.4408	2.7951	0.0462	0.0460
	33.4723	2.7760	0.0455	
	33.4408	2.7939	0.0462	

* Average Equivalent flat plate area of Spacer, Spacer damper and conductor are: (a) Spacer =(0.1812-0.1466)/2 = 0.0173;
(b) Spacer damper =(0.2106-0.1466)/2 = 0.032;
(c) Conductor = (0.1466-0.046)/0.876 = 0.1148

In Table 1 the equivalent flat plate area given is calculated as the difference of two lengths of conductors with similar ends. Hence, the end effect which arises due to testing of short section without simulating the complete length of the conductor cancells and true equivalent flat plate area of the bundled conductors obtained.

For studying the effect of variation of wind speed on the equivalent flat plate area, the conductor bundle was subjected to tests at different wind speeds and equivalent flat plate area obtained. The result showed that the equivalent flat plate area remained practically same. Hence, it is reasonable to assume

that the drag co-efficient has remained practically constant in the range of wind speeds tested. Tests were also conducted at different angles of attack, to find out the effect of the wake of windward conductor on the leeward conductors. It was found that there was no significant aerodynamic interference effect in the bundled conductor configuration tested. The measured drag co-efficient was found to be nearly agreeing with that given in Ref 1.

3. Simulation of Wind Load of Bundled Conductors

For measuring the swing angle of the insulator string due to steady wind on the bundled conductors in the wind tunnel, a 1:5 scale model was fabricated. The weight of the conductor in a span was calculated based on the standard method for calculation of conductor weight and this was simulated by a calibrated weight hung at the bottom of the string whose value was one fifth the calculated full scale value. The bundled conductor itself was not modelled to scale. The static force of wind on the bundle was simulated by a parachute. The design of the parachute for simulating the conductor drag force is described below.

Considering the simplicity for fabrication it was decided to design and fabricate a cruciform parachute for simulating wind load of the bundled conductors in a span. Since the parachute drag depends on several parameters such as porosity of the fabric used, method of stitching, arm ratio, rigging line length etc, it was necessary to fabricate a model parachute and test it in the wind tunnel for evaluating its drag coefficient and then designing the required parachute. Initially a 50 cm petal width and 1 meter long rigging line length cruciform parachute model was fabricated (Fig.2) and tested. The parachute model mounting arrangement in the wind tunnel consisted of a rigid metal frame which was bolted to the tunnel floor in the test section. A 2" diameter vertical support rod which was welded to this frame extended up to the centre of the test section. A hook was fixed to the support rod through a spherical bearing and a load cell (Fig. 3). The Parachute was attached to this hook so that, when deployed the parachute occupied the centre of the test section. The load cell had a 100 Kg rating and was suitable for

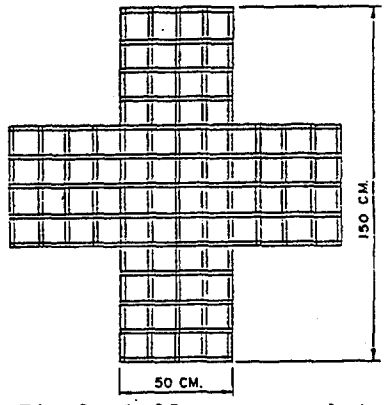

Fig.2 1.25 sqm parachute

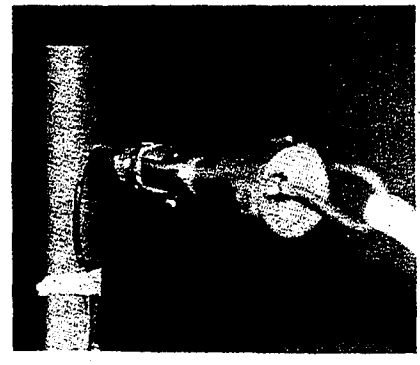

Fig. 3 Parachute mounting stand

the measurement of steady drag force. The load cell was calibrated by applying known loads in a separate calibration fixture. The load cell output was acquired by a PC based data acquisition system.

The parachute was hooked on to the hook provided on the support rod and then the wind tunnel started. The wind speed was rised slowly up to about 35m/sec. Visual observation of the dynamic behaviour of the parachute in the wind stream showed that it was quite stable without any tendency for oscillations in vertical or lateral direction. However tendency to rotate about its own axis was noticed and this did not develop into rolling instability. This is believed to be due to the rotational freedom provided by fixing the hook on bearing, which resulted in preventing rotational instability.The load cell output was acquired at different wind speeds. From this data the axial force was computed by multiplying the net load cell output and the calibration constant. The coefficient of drag was computed using the relation: $C_X = A_X/q \times S$ where A_X is Axial force (drag force) on the parachute, q is dynamic pressure and S is the constructed area of the parachute.

Constructed area of the parachute is the area obtained by multiplying the measured length and width of the petal when the parachute is streched on the ground, which is equal to 1.25 Sq. m for the initial model parachute. The measured drag coefficient was corrected for blockage (2). The calculations are given in Appendix II. The plot of dynamic pressure versus drag force is given in Fig. 4. The slope of this plot gives the average equivalent flat plate area. For the initial model parachute this was 0.845 Sq.m. The conductor bundle had an equivalent flat plate area of 46.112Sq.m as per the calculations given in Appendix I. For the model scale of 1:5, the calculated equivalent flat plate area for simulating the drag of insulator strings will be 46.112/5x5 = 1.844 Sq.m. After correcting for blockage the constructed area of the model parachute was found to be 2.44Sq.m. If we select a petal width of 0.70 meters, then the constructed area is 0.7x(0.7x3) + 2x(0.7x0.7) = 2.45Sq.m which was close to the constructed area required.

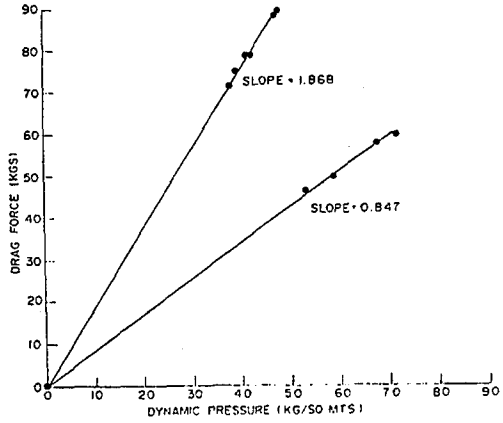

Fig. 4 Variation of drag force with dynamic pressure

The parachute of 0.7m petal width and constructed area of 2.45Sq.m was fabricated using the same fabric and stitched in similar way to 0.5 m petal width and 1.25 Sq.m constructed area initial model parachute. The parachute was tested in the wind tunnel adopting similar procedure used for 1.25 Sq.m parachute. A 200 Kg load cell was used for measurement of drag force. A plot of dynamic pressure versus drag force for 2.45Sq.m parachute is also given in fig 4. In this figure it is indicated that the parachute has an equivalent flat plate area of 1.87Sq.m, which was close to the calculated flat plate area of 1.844 Sq.m for simulation of conductor drag. It may therefore be concluded that the 2.45Sq.m parachute adequately simulates the conductor drag on 1:5 scale model of insulator strings. The 1.25Sq.m parachute represents 46% of wind load on conductors. Thus basing on the measured drag coefficient of the initial model parachute and correcting it for blockage error in the wind tunnel, the drag coefficient of the final model parachute may be calculated. This drag coefficient was corrected for blockage error again and the corrected drag coefficient obtained for finding out the constructed area of the model parachute. The parachute thus designed was tested in the wind tunnel and experimental confirmation of the drag force obtained in order to simulate the drag force of the bundled conductors.

4. Measurement of Swing Angle of Insulator Strings

The swing angle of insulator strings used on 800 kV transmission systems was measured on a 1:5 scale model consisting of two vertical I-strings. Each string contained 35 nos. of standard disc type insulators which were modelled to scale. The top end of the string was fixed to the ceiling in the test section of the wind tunnel. A pan and a rotating hook was provided at the bottom of the string. For simulating the weight of the bundled conductor in a span, a 36.7 kgs. calibrated weight was placed on the pan (Appendix III). The parachute was hooked to the rotating hook so that it simulated the drag of the bundled conductors. Fig. 5 shows a view of the model in the wind tunnel test section.

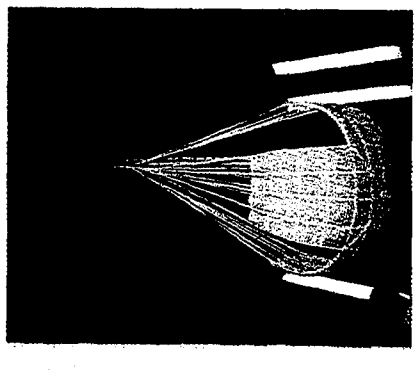

Fig. 5 Insulator string model

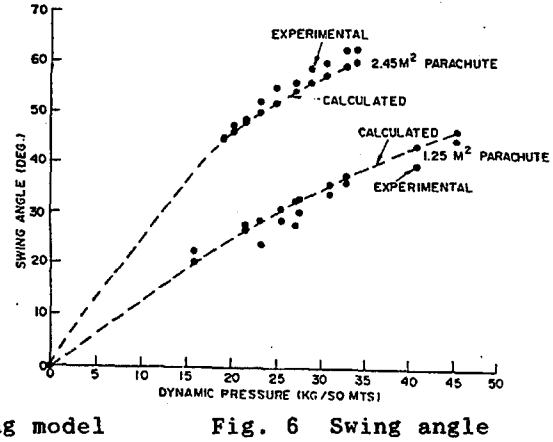

Fig. 6 Swing angle

The swing angle was measured at different dynamic pressures using both 1.25Sq.m and 2.45Sq.m parachutes, simulating 46% and 100% of wind drag of bundled conductors respectively. The result obtained is given in Fig. 6.

The suspension arrangement provided freedom for lateral and longitudinal movement of the I string in the wind tunnel similar to full scale string. This resulted in the movement of the system like a pendulum with the drag of the bundled conductor simulated as a whole. This limits the scope of the study to static swing angle of the string only. With this arrangement of simulation of drag force by parachute, it will not be possible to study the effects of bundle tilt, spacing system, effect of sagging, catenary etc. as these require to be simulated separately by suitable scale modelling. In the present study no dynamic effects were considered.

During the wind tunnel, tests it was observed that the parachute was stable in the wind speed ranges tested. The swing angle was calculated based on the horizontal and vertical displacement of the bottom clamp measured on the respective graduated scales fixed suitably. At higher wind speds some tendency for longitudinal and vertical oscillations of the string and parachute as a whole was noticed.

The swing angle of the insulator string was also calculated assuming the system as a simple pendulum acted by two forces, namely, wind drag and conductor weight. The wind drag at different dynamic pressures was obtained from the plot of Fig 4. The calculated swing angle at various dynamic pressures is also plotted in Fig 6. It is observed that the measured swing angle and calculated swing angle are in agreement with in about 5%. Thus, simple pendulum approximation for the calculation of swing angle may be taken to be adequate considering that the shape factor of insulator etc is having only a marginal influence compared to wind drag and weight of the conductor.

5. Conclusions

Based on the experimental study carried out, the following conclusions may be made:

(1) Parachute can be conveniently designed and fabricated for simulating steady aerodynamic loads on bundled conductors of transmission lines for simulating wind load on scale models of insulator strings and jumpers in the wind tunnel.

(2) Swing angle due to wind drag may be calculated accurately based on measured conductor drag. This implies that the direct effect of wind load on insulators themselves is small.

6. References

(1) Transmission line reference book, wind induced conductor motion prepared by Gilbert and Jackson, Published by Electric Power Research Institute, 3412 Hillview Avenue, Palo Alto, California, 1979.

(2) Blockage correction for large Bluff bodies near a wall in a closed jet wind tunnel by K Ramamurthy Reddy, MSc Thesis, Dept. of Aerospace Engg, IISc, Bangalore-12.

APPENDIX I : Calculation of Equivalent flat plate area of bundled conductor in a Span

From Table 1, the equivalent flat plate area of 1 metre length of bundled conductor is 0.1148 Sq.m. and one spacer damper is 0.032. For a Span of 400 metre long, the equivalent flat plate area of conductors = 0.1148 x 400 = 45.92 Sq.m.
There are 6 spacer dampers in a Span. For a Span, the equivalent flat plate area of spacer damper = 0.032 x 6 = 0.192Sq.m.
Therefore, total equivalent flat plate area = 45.92 Sq.m + 0.192 Sq.m = 46.112 Sq.m.

APPENDIX II : Design calculations for the Parachute

The Blockage correction was made as indicated in Ref.2.
Wind Tunnel Test Section Area = 10.55Sq.m. Parachute model constructed area = 1.25Sq.m.
Projected area of the cruciform parachute can be approximately taken as 50% of the constructed area = 1.25 X 0.5 = 0.625Sq.m.
Blockage = 0.625/10.55 X 100 = 5.924%
For this blockage, the flat plate area drag Co-efficient measured by experiment is 1.44. The flat plate drag Co-efficient corrected is 1.16.
Therefore the correction factor is 1.16/1.44 = 0.8
The measured drag Co-efficient of the Parachute model was 0.6692. To obtain blockage corrected drag Co-efficient we have to multiply this by the correction factor.
Therefore, corrected drag Co-efficient= 0.6692 X 0.8 = 0.53.
From appendix I, equivalent flat plate area of full span is 46.112Sq.m.
Model scale was 1:5. Hence, the equivalent flat plate area for simulating the conductor drag on the model of Insulator string is 46.112 / 5 X 5 = 1.844Sq.m.
Blockage = 1.844/10.55 X 100 = 17.47%
For 17.47% blockage, the flat plate drag coefficient = 1.88
Therefore, The blockage correction factor = 1.16/1.88 = 0.617 The model Parachute had a corrected drag Co-efficient = 0.53.
The effective drag Co-efficient of the Parachute to simulate full scale drag is 0.53/0.617 = 0.86
The constructed area of the parachute required for simulating the drag force = 1.844/0.8745 X 1.16 = 2.44Sq.m.
A petal width of 70 Cm was selected. The constructed area of this Parachute = 0.70 X 0.70 X 5 = 2.45Sq.m.
This is close to the calculated value.

APPENDIX III : Calculation of Conductor Weight for model.

Total weight of the conductors in a Span of 400m long with a bundle of 4 conductors is 4 X 400 X 2.004 = 3206.4 kgs.
(2.004 is the weight density of ACSR conductor in kgf/m).

The actual weight of the conductor is taken as 1.5 times the above value as per standard practice. Hence, the weight of the conductors is 3206.4 X 1.5 = 4809.6 kgs.

Model scale is 1:5. The weight of conductors for the model = 4809.6/5 X 5 X 5 = 38.47 kgs.

In the experiment a 36.7 kgs weight was used.

EXTERNAL FLOW FIELD AROUND AN INTERCITY BUS

SILVA, M.C.G. and VIEGAS, D.X.
Grupo de Mecânica dos Fluidos
Universidade de Coimbra (Portugal)

ABSTRACT

The external flow around an intercity bus was studied experimentally. Wind-tunnel tests, using a 1:8 scale model, were carried out in order to analyse the flow around the vehicle and in its wake. Pressure distribution on the external surface of the model was measured for symmetrical and for yawed flow situations (0°, 5°, 10°, 15° and 20°).

A seven-hole pressure probe was used to determine the three-dimensional velocity field in various transversal and longitudinal planes, for the symmetrical flow condition. For the considered planes, vectorial representations of the velocity field as well as lines of constant total pressure and vorticity are depicted.

The drag coefficient of the model was determined by three different methods: (i) using an aerodynamic balance, (ii) using the stream-tube method based on the transverse planes measurements with the seven-hole probe, and (iii) integrating the pressure distribution on the external surface.

Road tests with a vehicle driven at constant velocities were performed in order to assess the goodness of the wind-tunnel simulation. Pressure measurements on the external surface of the vehicle, as well as other overall aerodynamic characteristics provided a reasonable agreement with the scale-model measurements.

INTRODUCTION

The bus represents a good solution, as a transportation mean, because it has a low cost and a low emission rate per transported passenger and per unity of distance covered.

During the project of a bus, the external shape aerodynamic characteristics, in conjunction with aesthetics, functionality, safety and the manufacturing processes are the main aspects to be taken into account.

The aerodynamic shape has a strong influence, for instances, on the performances level, on the fuel economy, on the active safety and on the passenger's comfort.

The studies conducted by different authors [1], [2], [3], related with bus aerodynamics, had, as a main scope, the improvement of the flow quality around vehicle's body in order to get a better drag coefficient.

Being already known, from the former studies, that the most important parameter influencing the drag coefficient of a brick shaped body is the front edges' radio, the present work was conducted with the objective of getting a better understanding of the flow around a typical bus shape.

RESULTS

Two kinds of tests were done: wind tunnel tests with a 1/8 scale model and road tests with a bus prototype. The wind tunnel tests consisted on surface pressure measurements, on the mapping of the flow around the model and on drag force measurements with an aerodynamic balance.

Surface Pressure Measurements

The pressure distribution on the external surface of the bus model was measured, for different yaw conditions (0, 5, 10, 15° and 20°), during tests carried out in an open chamber wind tunnel (section 4×1 m^2), for a Reynolds number R_e based on the length model of 8×10^5. The experimental set-up used is represented on the figure 1, as well as, the pressure holes grid on the model's surface. Around two hundred and fifty pressure holes were drilled on the model. The pressure tubes were connected to Scanivalve rings and the pressure was measured with a Setra capacitive transducer. All the process was computer controlled. In each pressure tap were acquired 100 samples during a period of 1 second, being saved the average value of them.

The pressure coefficient values ($Cp=\Delta p/0.5\ \rho\ U^2$) measured in the longitudinal vertical symmetry plane are presented in fig. 2 , being established a comparison between wind tunnel and road tests. As it can be seen, a good agreement, between the two sets of results, was achieved. The main features, related with the pressure distribution along the considered contour line, can be resumed as: – In a large part of the frontal surface, the pressure values are positive, with the stagnation point located at 1/3 of the height of the model. – In the region of the frontal leading edge, strongly negative values are obtained. – After the recirculation bubble, in the frontal part of the roof, the pressure comes to values very close to the atmospheric pressure. – In the rear part the pressure coefficient is always slightly negative.

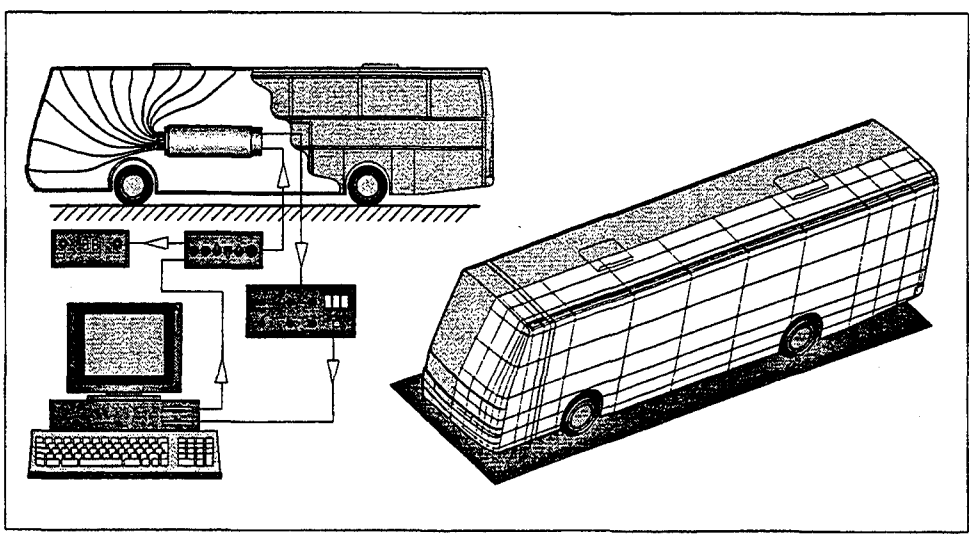

Fig. 1 - Scheme of measuring system used in surface pressure measurements and pressure holes grid.

The pressure coefficient values, obtained in wind tunnel tests, for three differente yaw conditions, in a mean height contour line, are depicted in the figure 3. As it was expected, there is a strong influence of the yaw angle on the results, with the displacement of the frontal surface stagnation point towards the windward side, and the increasing of the assymetry of the lateral panels' pressure distribution.

A more global view can be obtained with the analysis of the planar representations of the isopressure lines on the external surface of the model, presented in figure 4, also for three yaw conditions.

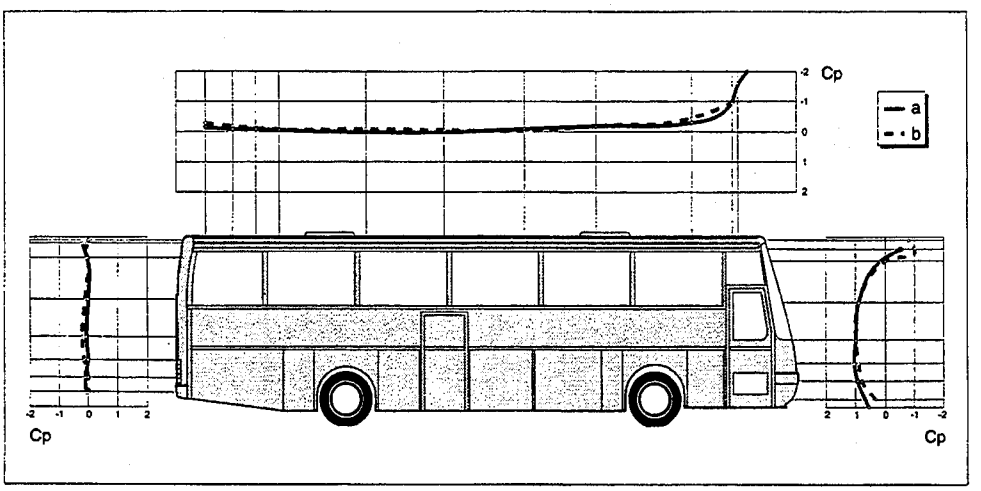

Fig. 2 - Comparison between the pressure values measured in road tests (a) and wind tunnel tests (b).

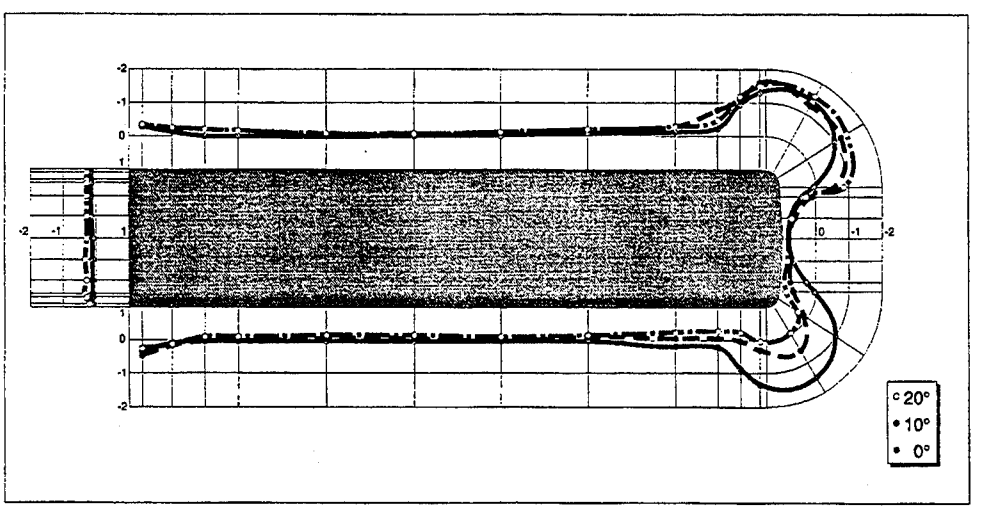

Fig. 3 - Pressure evolution in a mean height contour line, for different yaw angles. Wind tunnel results.

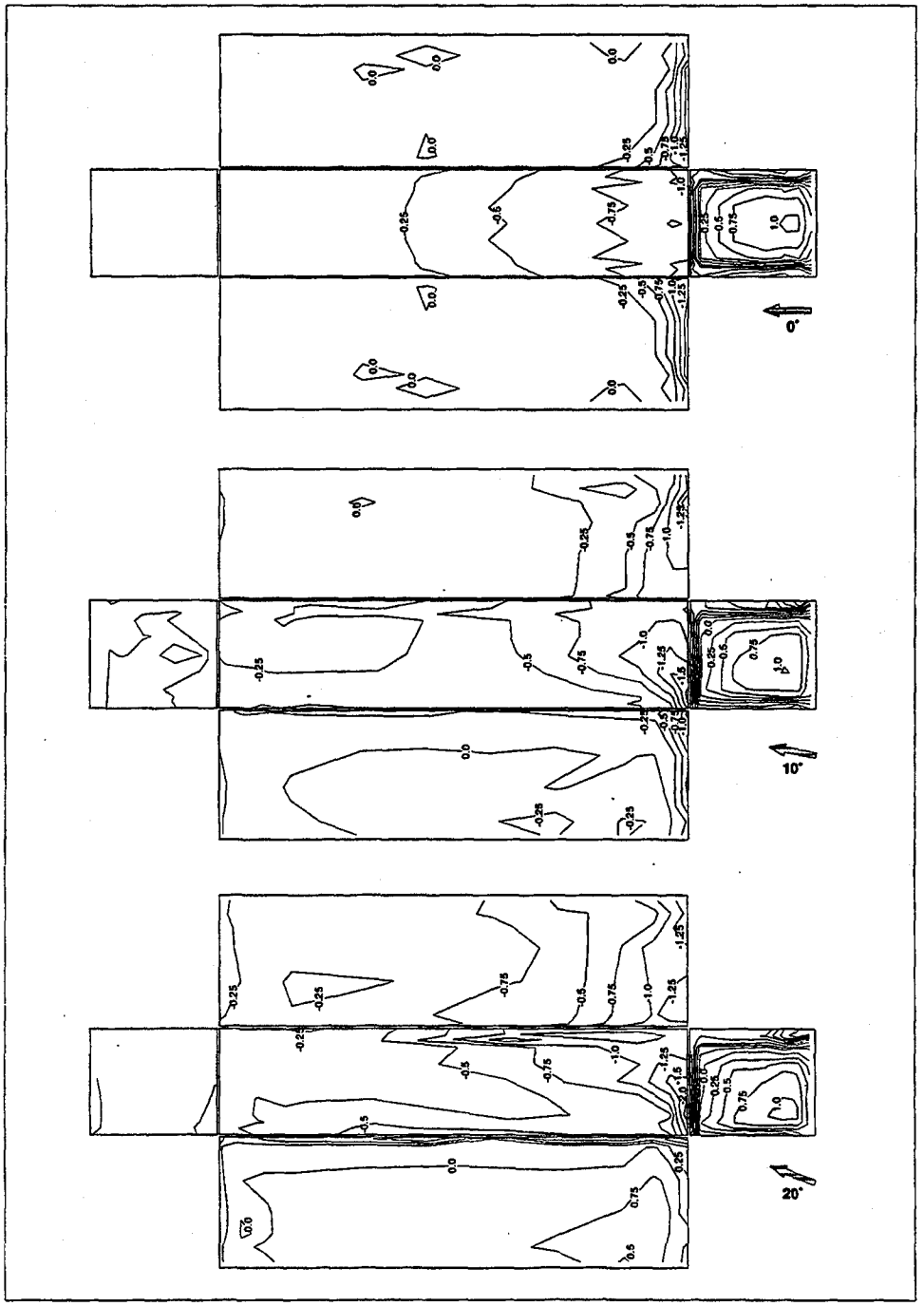

Fig. 4 - Planar representation of the isopressure lines on the external surface of the model. (0°, 10°, 20° yaw angle).

Flow Mapping

The flow field around the bus model was studied, using a 5 mm diameter seven-hole pressure probe. The calibration and measuring methods of the probe are described in Silva and Viegas [4]. The experimental set-up used in the measurements with the seven-hole probe was very similar to that one used in the surface pressure measurements with the seven pressure tubes connected to the Scanivalve. A traversing mechanism controled by the computer and used to position the probe was added. The surfaces where the measurements were done are represented in figure 5. The three components of the velocity vector as well as the static and total pressures were obtained in each measuring point. For the vertical transversal surfaces was, yet, calculated the vorticity function.

Some typical results are presented in figures 6 and 7, concerning, respectively, the velocity vectors in two longitudinal planes (one vertical and one horizontal) and the vorticity function in two vertical transversal surfaces (vt 1 and vt 2).

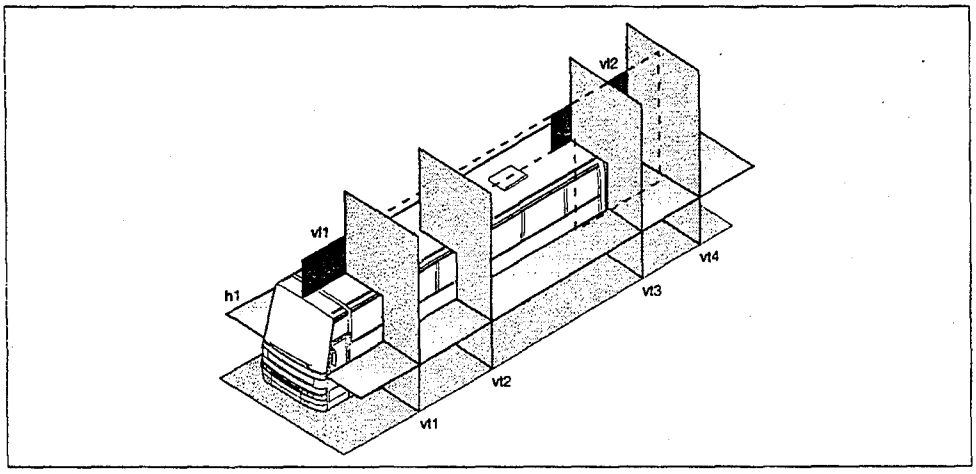

Fig. 5 - Studied surfaces in flow maping measurements.

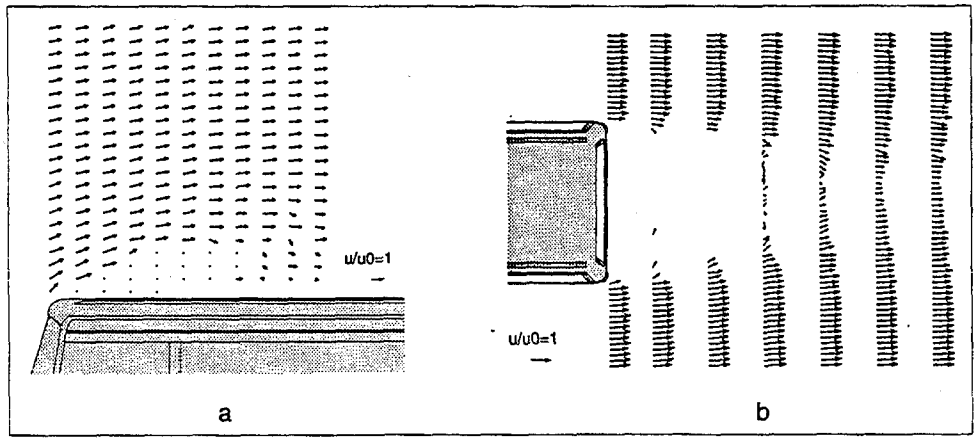

Fig. 6 - Vectorial representation of velocity fields. (a) vl1, (b) rear wake.

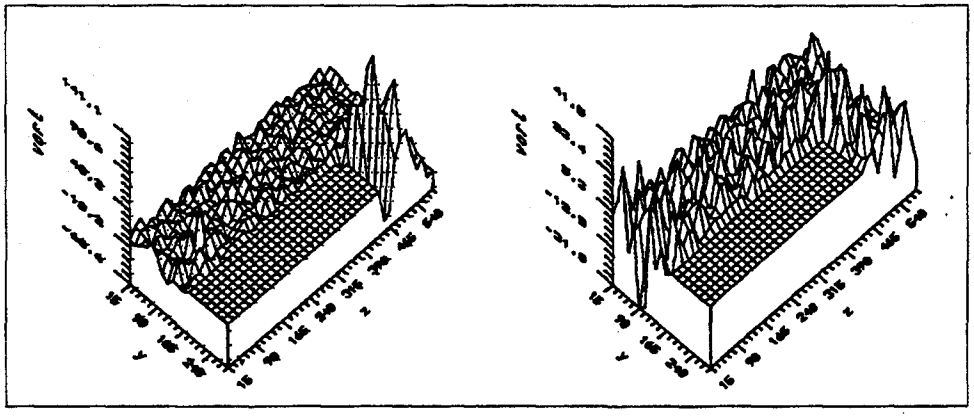

Fig. 7 - Vorticity function distribution in two vertical planes (vt1 and vt2); back side view.

Drag Coefficient

The drag coefficient was evaluated by three different methods, based on wind tunnel tests: (i) using an aerodynamic balance, (ii) using the stream-tube method, according to the method exposed by Onorato [5], (iii) integrating the pressure distribution on the external surface. A comparison between the obtained values is established in Table I.

Table I

Measuring Method	Aerodynamic Balance	Flow Tube	Surface Pressure Integration
Drag Coeficient	0.45	0.47	0.32

It should be notted that the pressure integration value doesn't integrates the effect of the shear stress forces. So, the frictional drag estimated value of the tested bus model should be around 0.13 – 0.15. Therefore, the ratio between the pressure drag and the frictional drag is in a very good agreement with that one proposed by Gilhaus [1], for buses with a total drag coefficient of the same magnitude.

Deceleration Tests

That kind of tests has been used by various authors [6], [7], as a way to evaluate the total resistances of a given vehicle.

It is obtained a record of the velocity decay during the deceleration of the vehicle, with the gear box in neutral position. The motion of the vehicle during that phase, in the absence of wind, is governed by the following equation:

$$\left(M+\frac{I}{R^2}\right)\frac{dV}{dt}=\frac{1}{2}\rho V^2 SC_x+\left(K_0+K_d V^2\right)+\left(Mg\,sen\alpha\right) \quad (1)$$

where the different terms represent, respectivelly, the inertial forces, the aerodynamic resistance, the rolling resistance and the gravitic forces.

In windy conditions, a correction of the wind effect can be considered [8], changing the aerodynamic force term in the former equation:

$$\left(M+\frac{I}{R^2}\right)\frac{dV}{dt}=\frac{1}{2}\rho SC_x\left(V-V_{wp}\right)^2\left(1+r\,arctg\left(\frac{V_{wn}}{V-V_{wp}}\right)\right)+\left(K_0+K_d V^2\right)+\left(Mg\,sen\alpha\right) \quad (2)$$

where V_{wp} represents the component of the wind velocity parallel to the vehicle motion direction and V_{wn} the normal component of the wind velocity.

A method based on the last equations has been developped, allowing the separation of the total resistance drag in the aerodynamic and rolling resistance components. Two tests with different weighting conditions are done, being recorded the vehicle velocity, the wind velocity and the wind direction.

In Table II, the aerodynamic and rolling resistance coefficients for both weighting conditions (numbered with indices 1 and 2), obtained during two sets of tests (North-South and South-North directions) in an airfield track, are presented.

The mean value for the drag coefficient, as it can be seen, is in very good agreement with that one resulting from the wind tunnel balance measurements.

Table II

	C_x	R_{01}	R_{02}	K_{d1}	K_{d2}
N - S	0.467	610	813	0.202	0.269
S - N	0.441	628	835	0.215	0.286

CONCLUSION

The interaction between the flow and a bus model has been profoundly studied using different methods.

A good understanding of the flow topology was achieved, from the surface pressure measurements and from the flow field mapping techniques. An improvement to the usually deceleration method was tested with sucess, allowing the separation of the resistances to the vehicle's motion.

A relative good agreement was obtained in the evaluation of the drag coefficient by different techniques, based, either on wind tunnel tests, either on road tests.

ACKNOWLEDGEMENT

The present work was included in a research project named "Design of a new type of intercity bus", supported by the EC Programme PEDIP and by the bus factory Salvador Caetano IMVT, SA.

REFERENCES

(1) Gilhaus – "The main parameters determining the aerodynamic drag of buses" – Proceedings of the Colloque "Construire avec le vent", Nantes, June 1981.

(2) Götz – "Bus design features and their aerodynamic effects" – Int. J. of Vehicle Design, SP3, Impact of Aerodynamics on Vehicle Design, pp. 229-255, 1983.

(3) Lajos, T.; Preszler, L.; Finta, L. – "Styling and aerodynamic of buses" – Int. J. of Vehicle Design, vol. 9, nº1, pp. 1-15, 1988.

(4) Silva, M.C.; Viegas, D.X. – "Calibration and use of a non-nulling seven-hole pressure probe" - Symposium on Wall Interference, Support Interference and Flow Field Measurements, AGARD, Brussels, Oct 1993

(5) Onorato, M.; Costelli, A.F.; Garrone, A. – "Drag measurements through wake analysis" – SAE 840302, Detroit, 1984.

(6) Roussillon, G. – "Contribution to an accurate measurement of aerodynamic drag from coast down tests and determination of actual rolling resistance" – in 4th Colloquim on Industrial Aerodynamics, Aachen, 1980.

(7) Hamabe, K.; Kitoh, K.; Ogata, H.; Kobayashi, T. – "An estimation of aerodynamic drag coefficient of a passenger car by coast-down tests in windy environments" – JSAE Review, pp. 114-119.

(8) Phillips, A.W.; Assanis, D. – "A PC-based vehicle powertrain simulation for fuel economy and performances studies" – Int. Journal of Vehicle Design, vol. 10, nº6, pp. 639-658, 1989.

EXPERIMENTAL TECHNIQUE AND RESEARCH ON THREE DIMENSIONAL YACHT SAILS

F. Inzani, M. Modotti, M. Onorato
Department of Aeronautical and Spatial Engineering, Politecnico of Torino

G. Lombardi
Department of Aerospace Engineering, University of Pisa

ABSTRACT

Specific force measurements and flow visualisation studies on three dimensional interfering sails were performed. The model reproduces the combination of two sails, mainsail and genoa. Force measurements on a single surface (under interference conditions), are performed, by means of a wire suspension. The experimental procedure developed, starting from the aeronautical typical methodologies, showed good capability to highlight the flow characteristics around three-dimensional sails. Interesting results, particularly when measuring the forces acting on one sail under interference conditions, are obtained.

INTRODUCTION

The study of the flow around sail surfaces is a very interesting field in aerodynamic research, because of the complexity of the configurations, characterised by two lifting surfaces with a strong aerodynamic interaction.

A specific research activity on the sail aerodynamic characteristics has been in progress for a few years, both at the Department of Aerospace (DIA) Engineering of the University of Pisa, [1], and at Department of Aeronautical and Spatial Engineering.(DIASP).of Torino, [2], and some preliminary results are also reported in [3].

Three main aspects of the research are involved: real flow experiments, wind tunnel experiments and numerical simulation. The above aspects are both reciprocally independent and correlated. Given the scarce data on experimental results for complex sail configurations,

specific force measurements and flow visualisation studies were performed, and this aspect of the research is described in this paper.

The model reproduces the combination of two sails, mainsail and genoa; one mainsail was used, with two different genoa sails, of equal surface but different geometry. Fog machine and tuft visualisations were also performed, to better investigate the flow around the sails.

EXPERIMENTAL SET-UP

The tests were carried out in the laboratories of the DIASP (Politecnico of Torino). The force measurements were performed in the Φ3 wind tunnel; it is a subsonic, closed-return tunnel, with circular close test section 3.1 m in diameter, turbulence level 0.3% and maximum speed of 80 m/sec.

The geometries of the tested configurations are shown in fig. 1; the surfaces of the mainsail (S) and of the genoa are 0.372 m^2 each, therefore the total sail surface of each configuration was 0.744 m^2. One of the configurations (named A) was characterised by a foreward sail (genoa) as high as the afterward sail (mainsail) -, classically named "mast-head sloop"- while the other one (named B) was characterised by a genoa lower (3/4) than the mainsail- classically named "3/4 sloop". The mast height (h_m) was 1.50 m; it was a steel cylinder, 20 mm in diameter, while the boom was a steel cylinder, 10 mm in diameter. The connection with the six-component balance, the step by step motors and the other mechanisms necessary for the regulation of the sails were placed under a plane, inserted in the test section at 0.68 m from the test section base (see fig. 2); the sails were positioned at a distance of 0.1 m from this plane, to avoid any interference effect with the plane boundary layer (20 mm tickness). No simulation of the boat shape, and no conditions with heel angle were considered, because of the basic nature of the research, independent of a specific boat geometry or condition.

To study the flow around the sails, and particularly the interference effects, force measurements on a single surface (under interference conditions), are particularly useful, but data of this type are very difficult to find in the literature. To perform this type of measurements, a wire suspension was used; in this test configuration the genoa head was constrained not to the mast, but to the test section

wall, by means of very thin harmonic steel wires (1 mm in diameter), and the genoa was disconnected, at the base, from the balance.

The sail models were made in mylar-kevlar sail-cloth. The tests for the force measurements were performed at Reynolds≈10^6, referring to the maximum chord length (see fig. 1).

The flow visualisations were carried out in the "smoke wind tunnel" of the DIASP (Politecnico of Torino); it is a subsonic, open-return tunnel, with rectangular (0.9 x 0.8 m) close test section, turbulence level 1%. The models used in this case are were smaller, with a mast height of 0.7 m (1:2.18 scale with respect to the force measurement models).

The smoke was produced by means of a Rosko2000 smoke generator. The light plane (≈10 mm thickness) was set at the sail section positioned at 1/3 of the mast height (see fig. 1), and was obtained from a 150 Watt quartz lamp. The visualisations were performed at Reynolds≈6.5×10^5, referring to the maximum chord length (see fig. 1).

CONVENTIONS AND TEST CONDITIONS

The total force acting on an aerodynamic surface is usually broken down into lift (L) and drag (D), (fig. 3). For a sailboat a more useful decomposition is in the motion direction (the thrust, T) and normal to it (the lateral force, F_{lat}). The motion of the boat is, to satisfy the lateral equilibrium, along a direction inclined by an angle, λ, with respect to its symmetry plane; defining as β the angle between the direction of the relative wind and the boat speed V_b, $(\beta-\lambda)$ is the angle defined by the apparent wind direction and the boat axis of symmetry (fig. 3). Because the angle λ is dependent on the particular boat hydrodynamic and inertial characteristics, as wall as upon the specific sea and wind conditions, and, in any case, it is quite smaller than β, forces are conventionally referred not to the direction of the boat speed but to its axis of symmetry. Thus, force decomposition is usually made in a component along the axis of symmetry (F_x) and a component normal to it (F_y), and their variation is analysed with respect to the angle $(\beta-\lambda)$. The forces F_x and F_y are then related to the lift and the drag by the relations:

$$F_x = L \sin(\beta-\lambda) - D \cos(\beta-\lambda)$$

$$F_y = L \cos(\beta-\lambda) + D \sin(\beta-\lambda) .$$

In the following sections the moment around the x axis, M_r, will be also analysed; this expresses the heeling effect caused by the sails.

In the present tests the boom direction was kept fixed, aligned with the axis of symmetry; the position of the genoa with respect to the mainsail is defined by the "sheet" angle δ_g (see fig. 3), measured at the base of the sail.

It should be noted that maximum thrust is not necessarily the optimum condition, because when sailing windward, the goal is to have the maximum windward component of the velocity, (fig. 3); this might be achieved with a lower thrust coupled with a lower β angle.

The force coefficients were non-dimensionalised with the dynamic pressure, the mainsail planform surface (S) and the mean geometric chord ($c=S/h_m$).

Tests were performed for ($\beta-\lambda$) angles from 23° to 40°; given the reduced step (1°), an accurate analysis of the aerodynamic behaviour was possible. The other parameter investigated was the sheet angle δ_g, set to the following values: 5°, 6°, 7°, 8°, 9°, 11°, 13°, 15°.

Since surfaces were of the non-rigid type, preliminary tests were performed to study the dependence on flow velocity; the force coefficients were not found to be significantly different in the analysed velocity range. Histeresis phenomena, also studied in preliminary tests, were not present; repeatibility of the results was very good, showing that the shape of the sails did not change whit use.

Tufts positioned near the leading edge of the genoa gave information on the "optimum" sail trim condition; a discussion on the aerodynamics of this condition can be found in [3].

ANALYSIS OF THE RESULTS

As an example, in fig. 4 C_{fx} values for the configuration A, as a function of the angle of attack, are reported for the isolated sails and the complete configurations, with $\delta g=8°$, which can be considered a standard value. We can see that the thrust produced by the coupled sails is normally higher than the sum of the thrusts due to the isolated sails; this is particularly true for conditions close to the optimum one.

Fig. 4 also shows that, when isolated, the two sails produce a comparable thrust; when they are interfering the situation is quite different (fig. 5), the force on the mainsail (the afterward surface) falling close to zero, while it markedly increases on the genoa. From

the aerodynamic point of view the situation can be explained by analysing figg. 6 and 7, which are the classical aerodynamic representation. It is clear that, under interfering conditions, the lift on the genoa surface increases significantly, with a strong reduction in its drag, while the mainsail shows a reduction in lift with not significant variations of the drag values.

From fig. 8 it can be seen that in the B configuration the effect on the genoa is qualitatively the same, but quantitatively different; in the mast-head configuration the mainsail (logically) contributes less to the total thrust.

There is an optimum setting of the sheet angle (δ_g) resulting in the maximum thrust (which is not, however, the condition of maximum windward speed); in fig. 9 these values, for both the configurations, are shown, while in fig. 10 an estimated values of the thrust point of application are shown. From figg. 9 and 10 it is clear that the "mast-head sloop" configuration presents higher thrust values (the aspect ratio is much higher) but with significantly higher heel moments .

Smoke visualization allowed better understand physical behaviour. When the genoa is isolated, the flow remains attached until a certain angle of attack; when it is coupled with the mainsail, the flow near the genoa trailing edge is "attracted" by the underpression present on the mainsail "lower" surface (see, e.g., fig. 11), and, in this way, it remains attached until very higher angles of attack.

CONCLUSIONS

The experimental procedure developed, starting from the aeronautical typical methodologies, showed good capability to highlight the flow characteristics around three-dimensional sails.

The application, both to isolated and to interfering sails, yielded interesting results, particularly when measuring the forces acting on one sail under interference conditions. In sail configurations typical for windward sailing, the propulsion is given mainly by the forward sail, while the afterward sail has a strong effect to increase the lift acting on the foreward sail, keeping the flow completely attached to it until very high angles of attack.

REFERENCES

[1] Tonelli A., "Studi Numerici e Sperimentali sul Comportamento Aerodinamico delle Vele", Tesi di Laurea, Università degli Studi di Pisa, 1993.

[2] Inzani F., Modotti M., " Aerodinamica delle Vele: Studi Sperimentali e Applicazioni Numeriche", Tesi di Laurea, Politecnico di Pisa, 1994.

[3] Lombardi G., Tonelli A., "Experimental Pressure Evaluation near a Sail Leading-edge under Real Conditions", The Aeronautical Journal, in printing.

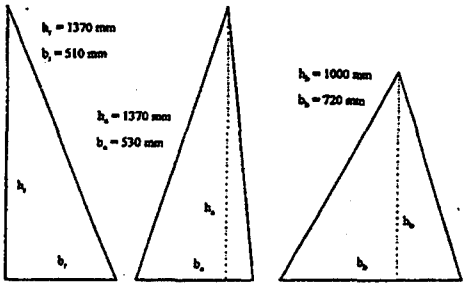

Fig.1a

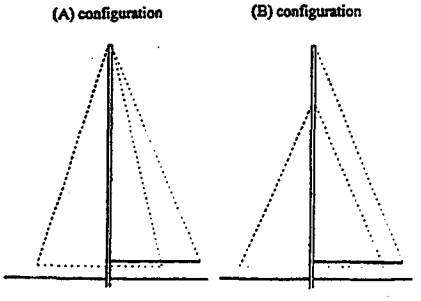

Fig.1b

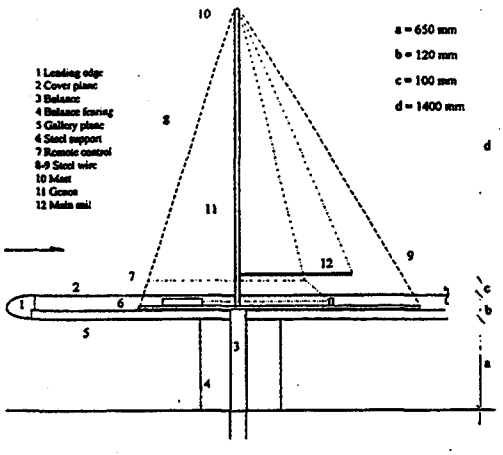

Fig.2

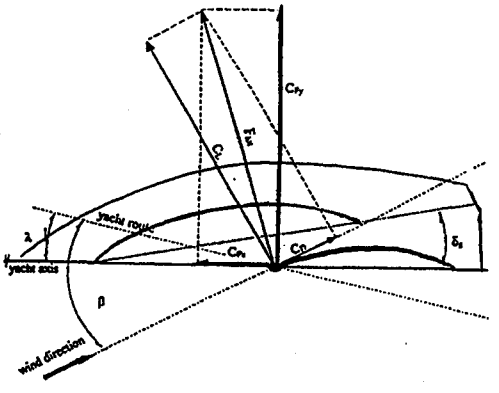

Fig.3 Gallery conventions

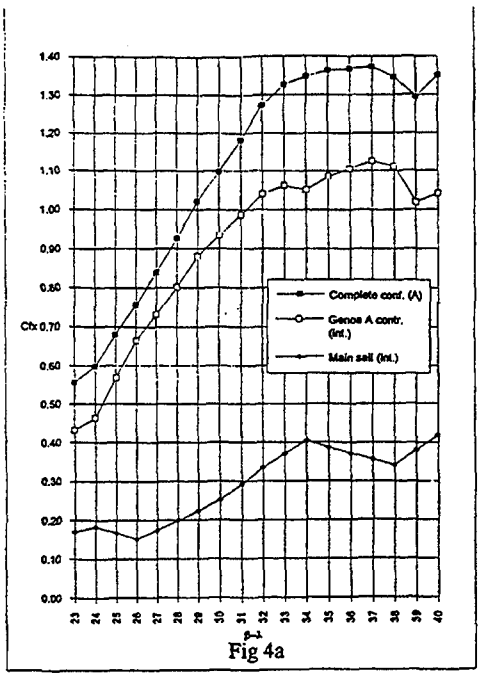

Fig 4a

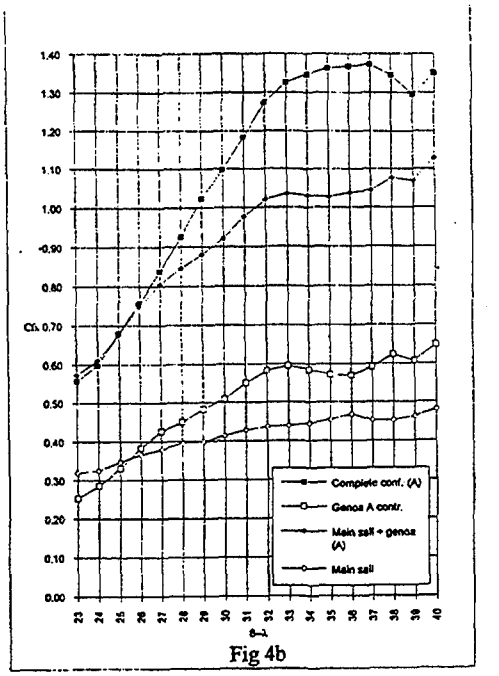

Fig 4b

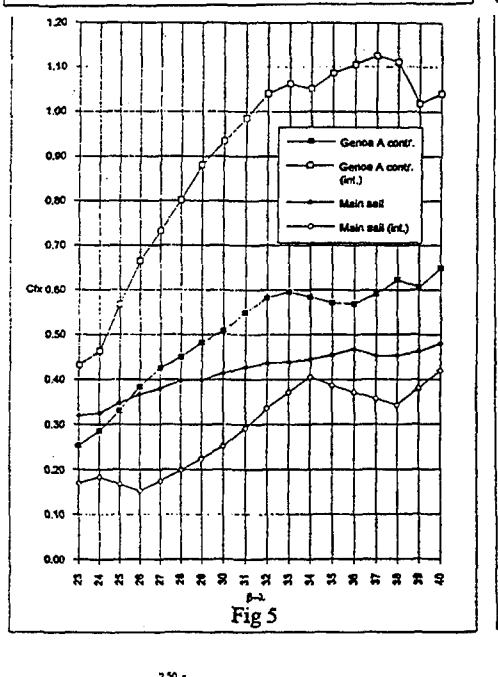

Fig 5

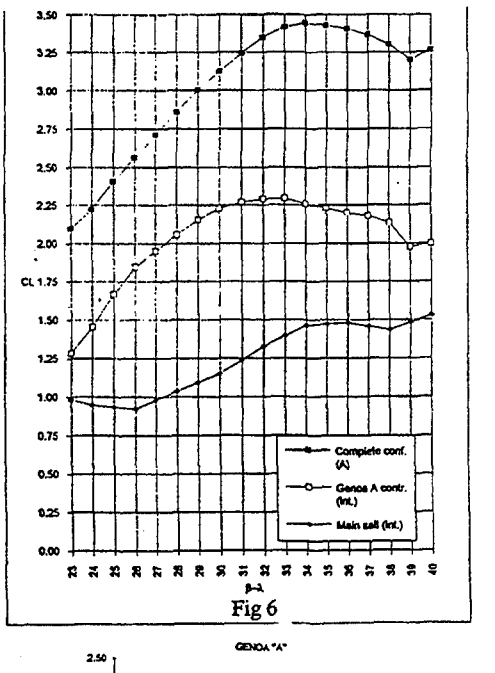

Fig 6

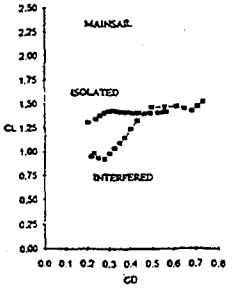

Fig 7a

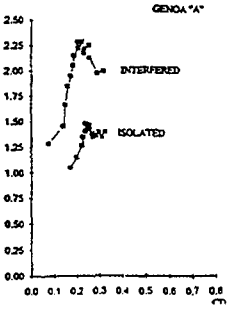

Fig 7b

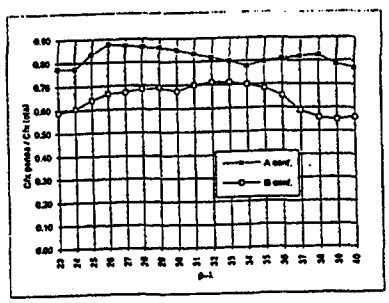

Fig 8a

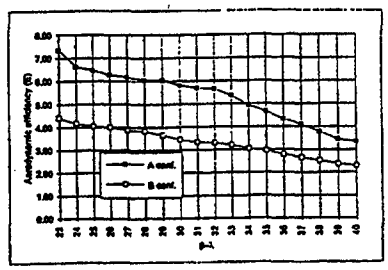

Fig 8 b

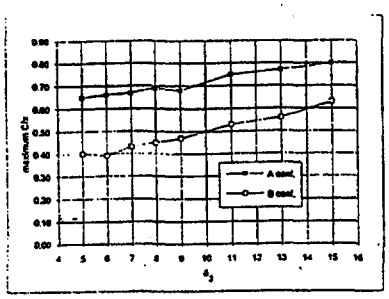

Fig 9

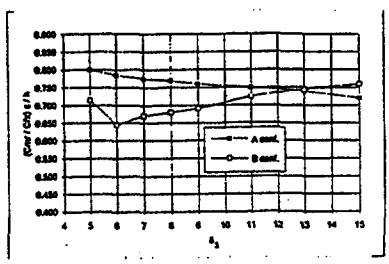

Fig 10

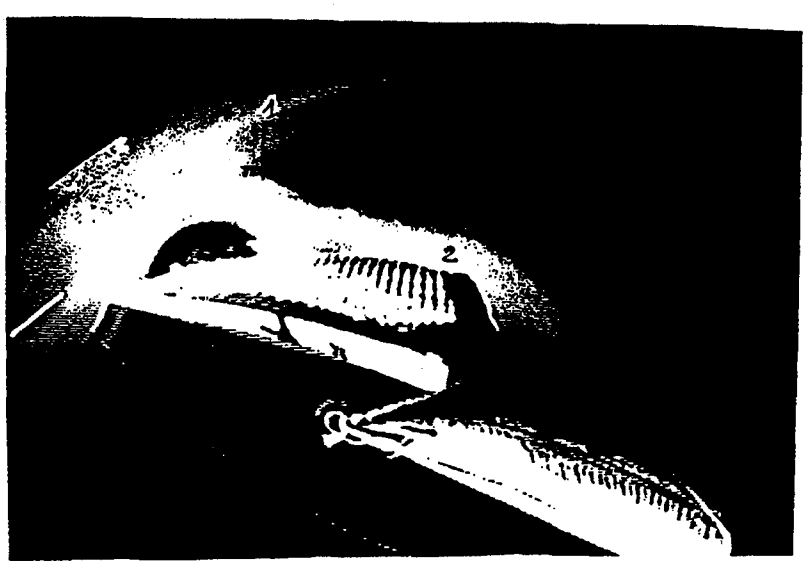

Fig 11 Smoke visualization:canal effect

THE EFFICACIOUS PGU MULTICASCADE COMPRESSION (MCC) METHOD FOR AEROTHERMODYNAMIC TESTING OF A NEW GENERATION OF AEROSPACE SYSTEMS

V.V.Kislykh
Department of Piston Gasdynamic Unit, TSNIIMASH (Russia)

Development of a new generation of aerospace systems (Sanger, Hotol, NASP and others) requires creation of new gasdynamic facilities to provide simultaneous simulation of some basic parameters or criteria. The subject of the discussion is the advantage of the efficacious simultaneous simulation of the group of parameters:

- M, Re, ($5 \cdot 10^5$ - $5 \cdot 10^8$), T_w - temperature factor (0.2 - 1) for the mode M (6 - 15);
- the rarefied gas mode where $M \cdot Re^{-0.5}$ ($H < 90$km) is the major parameter using the MCC method in the large-scale piston gasdynamic unit (PGU) U-11 of TSNIIMASN. (The nozzle diameters are up-to 0.8m.)

Fig.1 depicting the Re=f(M) dependence graph shows planned and implemented trajectories of a number of new vehicles. The most characteristic of them cover the following regions:

- M=6, $Re_1 = 10^8$,
- M=10 - 15; $Re_1 = 10^6$ - 10^7;
- M=18 - 25; $Re_1 = 10^5$.

To implement the above-mentioned modes it was necessary to achieve in the prechamber in front of the nozzle with the diameter of 0.8m the following parameters for large-scale models of a length of approximately 0.3 - 1m:

M	Po,atm	To,K
6	250	500 - 800
10 - 15	1000 - 2000	1000 - 1700
18 - 25	500 - 1000	2000 - 4000

Application of the known methods of the unit operation with a free piston did not ensure so wide variation of parameters in a single unit.

The objective set was to develop an operation technology of the piston gasdynamic unit permitting free variation of gas parameters in the prechamber, and by means of replacing some of its modules (elements) to adapt it rather quickly for the assigned mode of operation.

In the 70ies - 80ies TSNIIMASH specialists designed the so-called multicascade compression method (1) which applies a "heavy" piston for isentropical gas compression in the PGU tube, then for non-isentropical gas compression in a number of in series-placed chambers separated by specially-controlled valves and diaphragms (2).

Fig. 2 demonstrates the layouts of the known facilities where energy to the test gas is delivered mechanically, when the reservoir driver gas compresses the unit tube test gas.

Fig.3 demonstrates a conceptual sketch of the PGU, where you can see all its main elements. The working process in PGU combines firstly isentropic compression by a "heavy" piston, p.2, of test gas up to maximum pressure in the compression tube, p.3, separated from the chamber, p.5, by a control valve, p.6, and secondly nonisentropic gas compression while inflating successive forchamber vessels, p.7, joined by means of before-closed control valves, p.8, or diaphragms. These valves are fine high-speed locks, which are tuned beforehand by remote control and operate independently during experiment, opening the throats according a program needed. As it is known from classical thermodynamics, a gas accelerates the "heavy" piston with maximum efficiency, because the gas expansion process in this case is quasistatic (isentropic).

Fig. 4 demonstrates probable ranges of regulating temperature, and gas density for the types of units mentioned above. As follows from the stated relationships the PGU is capable of ensuring different gas parameter combinations in the prechamber in front of the nozzle by changing within a rather wide range the gas entropy in the course of multicascade compression.

In this case special attention should be paid to the fact that the gas is compressed in the unit tube in the instances under consideration with the maximum efficiency of using the driver gas energy.

It allows:

- first, to limit the driver gas pressure level by the value of 100 - 300atm. Air or nitrogen are used in the current facilities.

- secondly, to generate the amount of test gas 100 or 1000 times higher with the given unit dimensions providing the run time of 0.1 to 1 - 3 seconds having the same prechamber gas parameters and the same driver gas pressure level as compared with other classes of facilities.

Fig.5 gives the major geometric parameters of the TSNIIMASH U-II and U-7 PGUs, as well as the facility complex general layout.

Under real conditions in order to realize different compression modes it would be necessary to fit the unit with adequate elements and devices.

As an example Fig. 6 and 7 show the U-11 PGU configurations designed for solving a wide range of problems including the problems of simulating hypersonic flows.

Special regulating valves the unit passage is fitted with control the gas efflux from the unit nozzle ensuring different temporal pressure change laws P(t).

However, in most cases, the standard mode of gas quasi-stationary efflux from the permanent volume chamber placed in front of the nozzle assures the solution of hypersonic flow simulation problems with a high accuracy and greater volume of data.

Fig.8 illustrates the P,T parameters of gas in the three chambers and in the gun(barrel) PGU U-11 were calculated according to quasistatic method (2).

As an example, Fig. 9 - 14 demonstrate the character of gas entropy change during its efflux from the nozzle, Re number change for different compression modes of the U-II and U-7 PGUs at $Re_1 \sim 10^5$ and $Re_1 \sim 10^7$ - 10^8. The compression mode changes due to change of the regulated check valve operation mode, these valves permitting to regulate the level of multicascade compression non-isoentropy in the PGU gas chambers, and to shape the assigned distribution of the gas parameters along forchamber PGU and its temporal variation magnitude during the outflow process.

All types of aerogasdynamic tests can be conducted using the PGU. Here the object is to show that the current PGUs are the real industrial facilities and using a single unit we can simulate in a sense mentioned above all modes of hypervelocity leg trajectory.

The following experimental results were obtained by a large group of TSNIIMASH and Aerodynamic Center specialists in cooperation with PGU department ones. There is only a part of known type experimental PGU results. "Acoustic" and "jet" type experiments are lacking.

The typical for aerodynamic centers is to investigate the aerodynamic by balances method. You can see at Fig.15 - 17the examples of experimental investigation aerodynamic hypervelocity vehicles and its elements by six-component balances method in nitrogen and carbon dioxide gas flow in the PGU.

All known methods of the investigation of distributed parameters by different pressure gauges are wide used in the PGU. At the following Figures, Fig.18 - 21 you can see some examples such investigations.

Of special interest is the availability of the PGU facilities for the heat flux investigations. There are unique set of conditions in the PGU included, very high level of gas parameters and quality of flow in the nozzles, duration and the temporal variation of gas parameters very suitable for such kind of the investigation. Fig.22- 25shows, as an example, some experimental data of testing different vehicles using the U-II and U-7 PGUs.As can be seen from the pictures, there are two methods of measuring of heat flux in the PGU: the contact and thermovision methods. You can see some results of measuring heat flux on hypersonic flight vehicles including "Buran", "Hermes" and a cone.

Finally, there are some results of so named "dynamic" experiments in the PGU. This type of experiments has been used very often in the PGU for the investigation into the complex problems, for example, the hysteresis flow around the vehicle "Sojuz" type. You can see at the next pictures, Fig.26-27some of such results.

Practically all known super- and hypersonic flight vehicles including "Buran" have been tested on their models using the universal PGU U-11 and hypersonic U-7 at numbers $6 < M < 15$.

In conclusion I would like to note that the designed and implemented research methods using the PGU provide:

- maximum degree of natural condition simulation by the governing parameter set for the whole flight trajectory of a flight vehicle;
- minimum demands for buildings and structures (a single unit);
- minimum labour expenditure;
- minimum energy consumption.

References

1. Kislykh V.V., Petrova O.V., Puchkov V.V.
"Method of adiabatic compression in aerodynamic unit.
Patent N 972931 of 7.7.82, Bulletin of State Inventions Committee. Vol.29(1989)(in Russian)

2. Anfimov,N.A. and Kislykh,V.V.
"Multi-Cascade Comperion-Effective Means to Obtain High Temperature Dense Gas in Piston Gasdynamic Units (PGU)," Current Topics in Shock Waves, Proceedings of the 17th International symposium on Shock Waves and Shock Tubes.American Inst. of Physics, New York, 1990,p.p.588-593.

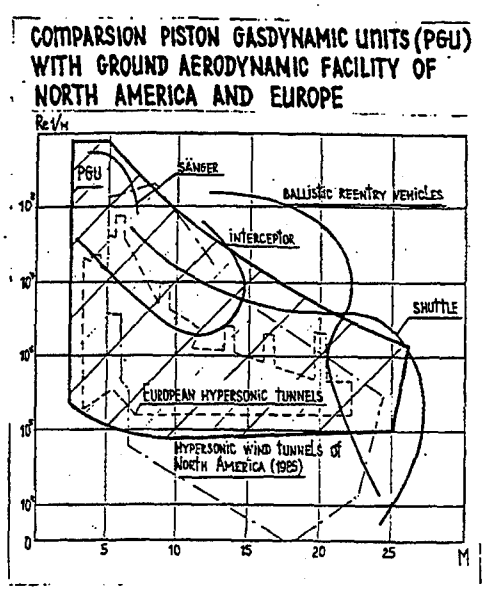

Fig. 1

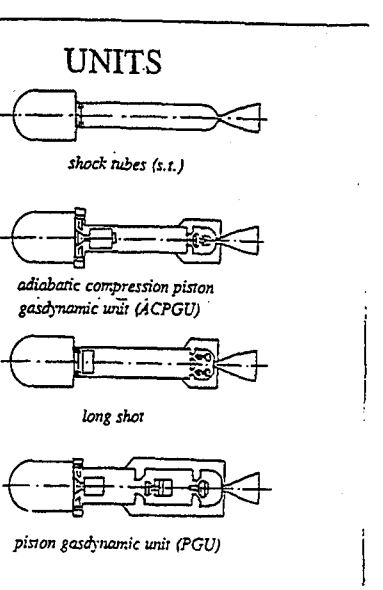

Fig. 2

PISTON GAS DYNAMIC UNIT (PGU)

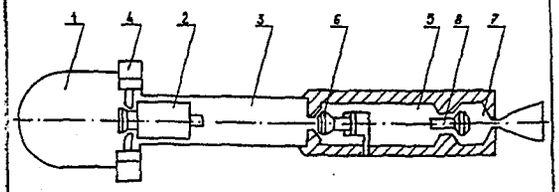

1. Bottle
2. "Heavy" Piston
3. Duck
4. Piston Keeping Junction
5. Chamber I
6. Regulated "Heavy" Check Valve
7. Chamber II
8. Regulated Throttle

Fig. 3

GAS TEMPERATURES REALIZED IN DIFFERENT TYPES OF UNITS

$$\frac{T}{T_0} = \frac{\varepsilon}{\tau_0}\left(\frac{k-1}{k+1}\right)^{k-1} \exp\left(\frac{\varepsilon^2}{2\tau_0}\right)$$

UNIT	$\frac{\varepsilon}{\tau_0}$	$\exp\left(\frac{\varepsilon^2}{2\tau_0}\right)$
SHOCK TUBE (S.T.)	$\frac{k-1}{k+1}$	$M^2 >> 1$
ACPGU	$>> 1$	1
Laval nozzle	> 1	1,5-3,0
PGU	$>> 1$	$\exp > 1$
	> 1	$>> 1$

Fig. 4

SCHEMATIC OF THE SET OF TSNIIMASH's PISTON GASDYNAMIC UNITS

I - PGU U-7; II - PGU U-11; III - HPJG U-11;
1 - barrel; 2 - nozzle;
3 - test section; 4 - exhaust channel;
5 - vacuum volume; 6 - exhaust tube;
7 - vacuum pump; 8 - air supply to FTT U-11.

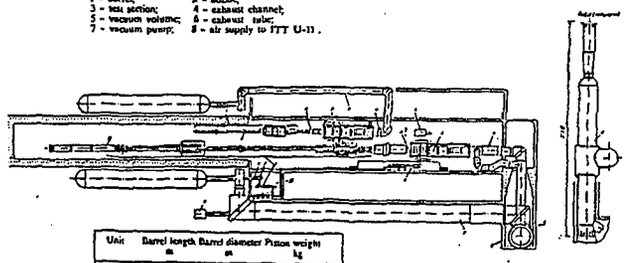

Unit	Barrel length m	Barrel diameter m	Piston weight kg
PGU U-11	45	0,46	1500
PGU U-7	12	0,2	270

Fig. 5

SCHEMATICS OF THE MULTIPURPOSE PGU U-11

1 - "Heavy" Piston
2 - Barrel
3,5* - Regulated Check Valve
4 - Forchamber
5 - Nozzle
6,7,8 - Test section

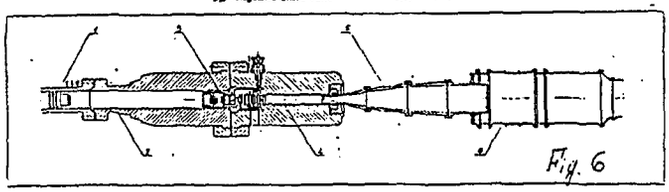

Fig. 6

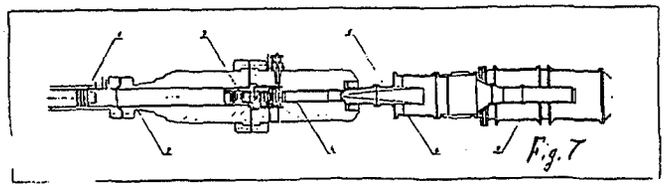

Fig. 7

CALCULATED TEMPORAL VARIATION OF THE PRESSURE AND TEMPERATURE IN THE CHAMBERS. PGU U-11, M=20 Re(1/m)·3·10⁵

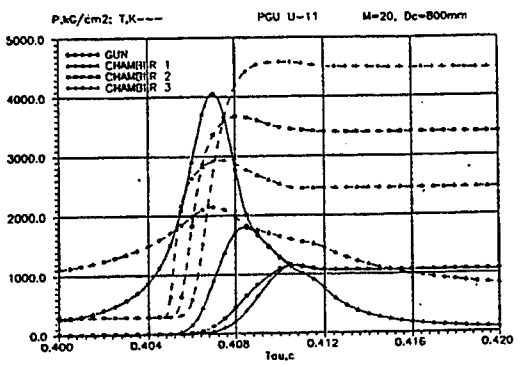

Fig. 8

TEMPORAL VARIATION OF THE P_o',atm,T_o',K,P_o,atm, PGU U-11, M=6

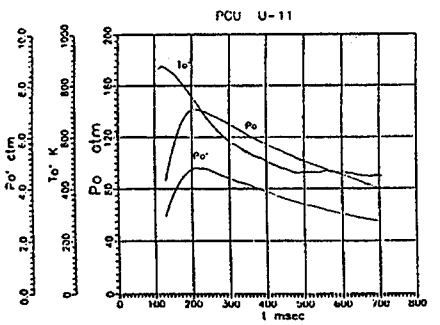

Fig. 9

TEMPORAL VARIATION OF THE $\Delta S/C_v$ PGU U-7, M=10,14

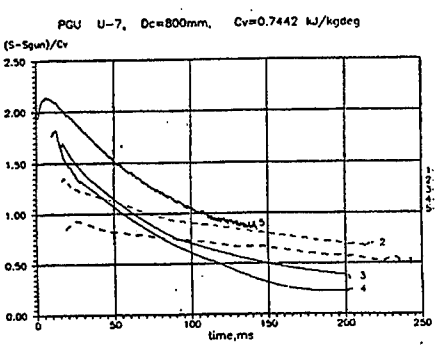

Fig. 10

DEPENDENCE OF THE PITOT PRESSURE Po',atm, ON THE STAGNATION PRESSURE Po,atm, PGU U-11, M=6

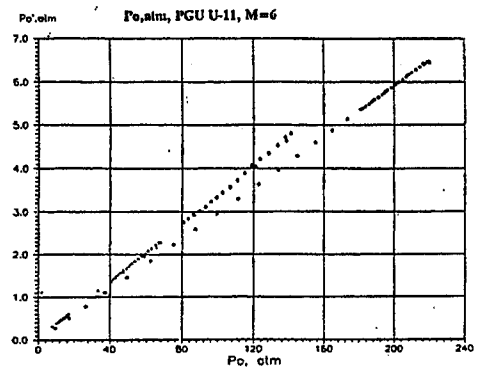

Fig. 11

TEMPORAL VARIATION OF THE Re(1/m), PGU U-7, M=10

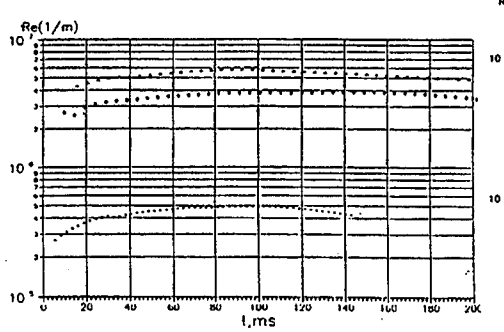

Fig 13

TEMPORAL VARIATION OF THE Re(1/m) PGU U-11, M=6

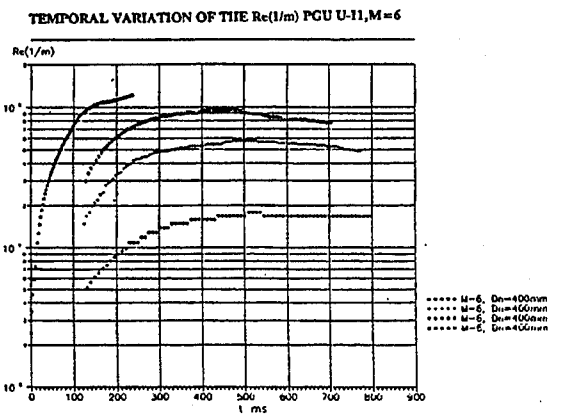

Fig 14

EXPERIMENTAL INVESTIGATION AERODYNAMIC HYPERVELOCITY VEHICLES AND ITS ELEMENTS BY SIX-COMPONENT BALANCES METHOD

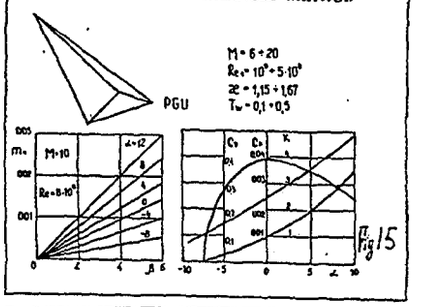

Fig 15

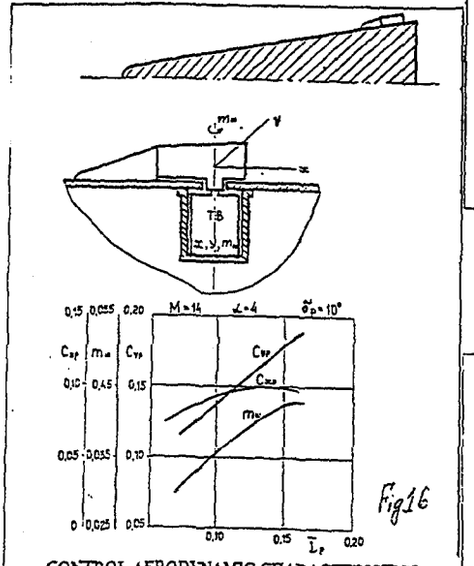

Fig 16

CONTROL AERODYNAMIC CHARACTERISTICS

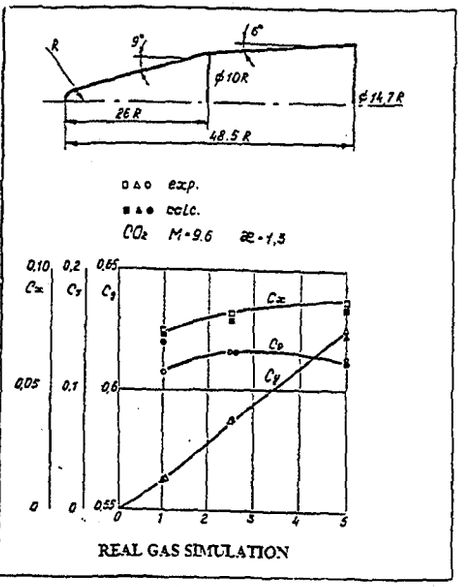

REAL GAS SIMULATION

Fig 17

DISTRIBUTION OF PRESSURE IN SEPARATED-FLOW REGIONS

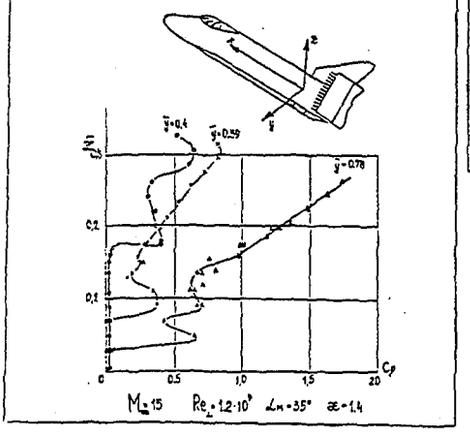

Fig 18

DISTRIBUTION OF PRESSURE IN SEPARATED-FLOW REGIONS

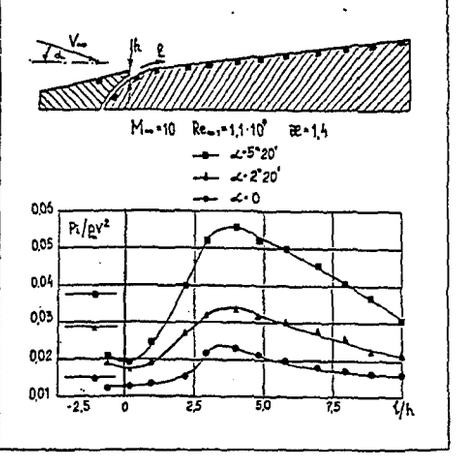

Fig 19

545

BASE DRAG OF CONICAL MODEL

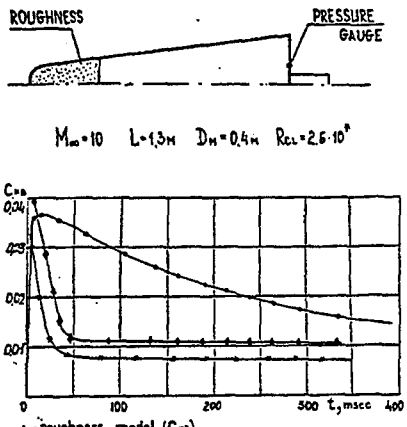

Fig 20

INVESTIGATION OF BOUNDARY-LAYER TRANSITION BY CONTACT METHODS

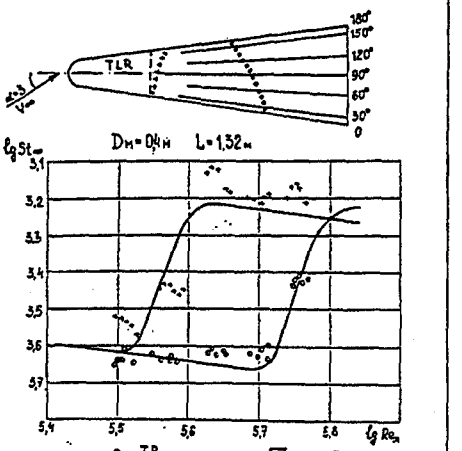

Fig 22

SHOCK AND BOUNDARY LAYER PRESSURE DISTRIBUTION

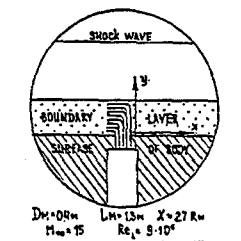

Fig 21

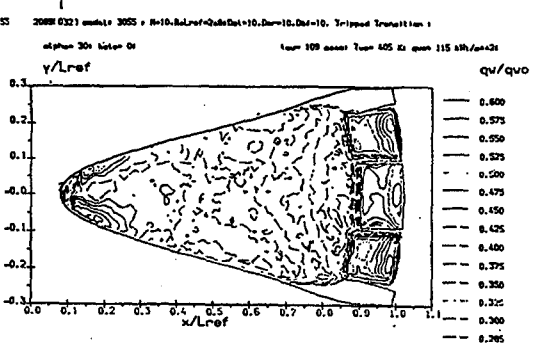

Fig 23

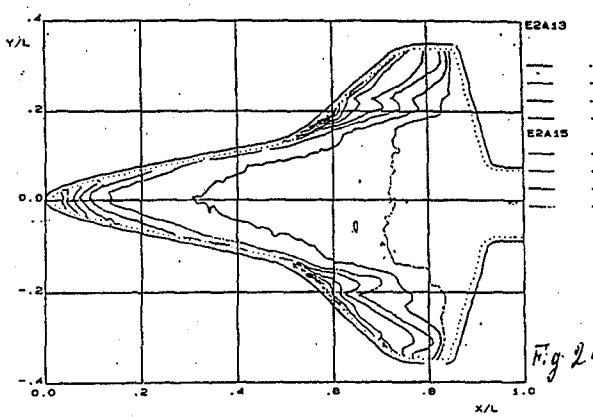

Fig 24

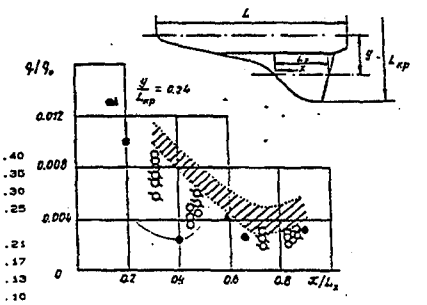

o $M_\infty = 10$, $Re_{\infty_L} = 4 \cdot 10^6$, $\alpha = 34°$
□ $M_\infty = 15$, $Re_{\infty_L} = 2{,}1 \cdot 10^6$, $\alpha = 34°$
//// $M_\infty = 15$, $Re_{\infty_L} = 2{,}1 \cdot 10^6$, $\alpha = 34°$
▲ $M_\infty = 11$, $\alpha = 39°$ STS-1
• $M_\infty = 17$, $Re_{\infty_L} = 2{,}1 \cdot 10^6$, $\alpha = 40°$ STS-3

I - II

Fig 25

PRESSURE DISTRIBUTION MEASURING BY FREE OSCILLATION METHOD

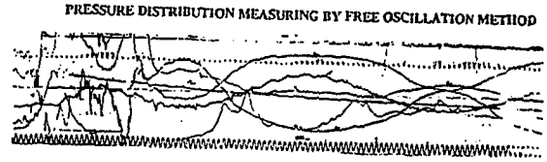

Free oscilation(two degrees of freedom) test
α - pitch angle
β - side slip angle

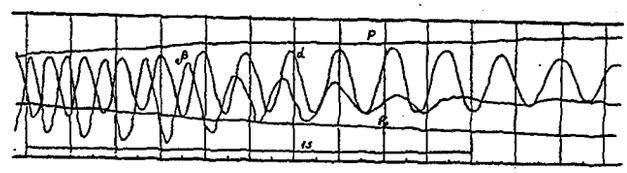

Fig 26

PRESSURE DISTRIBUTION MEASURING BY
FREE OSCILLATION METHOD

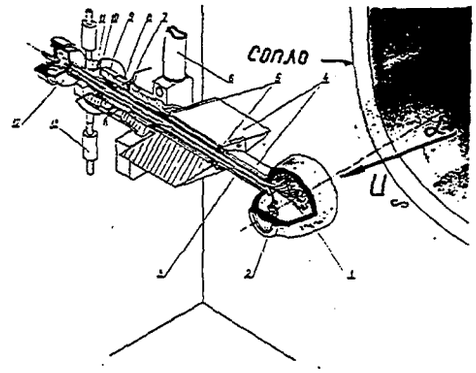

Peculiarities hysteresis of pressure local angle of attack dependence

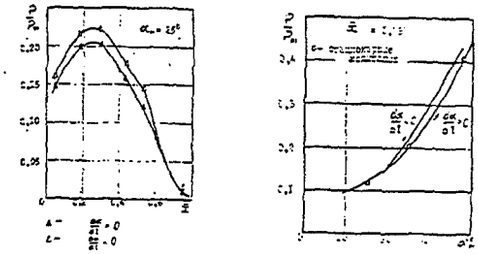

Fig 27

STATUS AND OUTLOOK OF LARGE HYPERSONIC WIND TUNNEL (HWT U 306-3) OF AEROGASDYNAMIC CENTER, TSNIIMASH

A.S.Boiko, M.G.Volikov, V.V.Kudrjavtsev, V.I.Lapygin, Yu.M.Lipnistky
(Central Research Institute of Machine Building, Aerogasdynamic Center,Kaliningrad,Moscow region,Russia)

The development of various hypersonic vehicles with main engines,control surfaces and control jets has required the use of hypersonic wind tunnels with wide ranges of Reynolds number and Mach number variation. Such wind tunnel, created recently in Russia, is supersonic and hypersonic wind tunnel U 306-3 with working flow cross section 1.2 m. The wind tunnel is intended to carry out investigations on large-scale models (full-scale in some cases) at Mach numbers Moo = 2.0; 3.0; 4.0; 6.0; 8.0; 10.0 and Reynolds numbers (based on 1 meter) Re = 10^5-10^8 (Fig. 1).

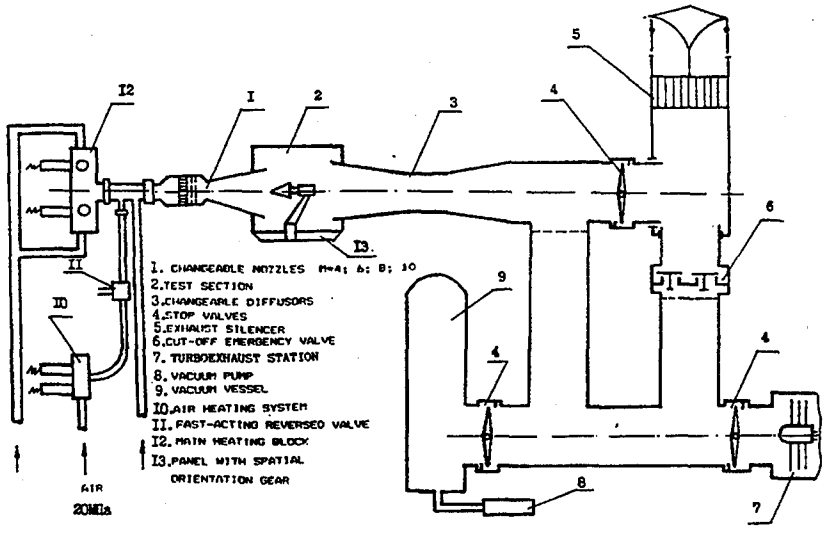

Fig. 1. Scheme of the HWT U 306-3

Tests are conducted with simulation of engine operation using jets of cold or heated air, argon, and helium with pressure in model chamber up to 30 MPa. It is possible to use also gas generators to produce high temperature jets.

To provide a wide range of Reynolds number and also to conduct special tests the wind tunnel operates with exhaust into atmosphere,or into vacuum vessel, or into turboexhaust system. The range of Mach number and Reynolds number variation along with typical trajectories of vehicles is shown in Fig. 2.

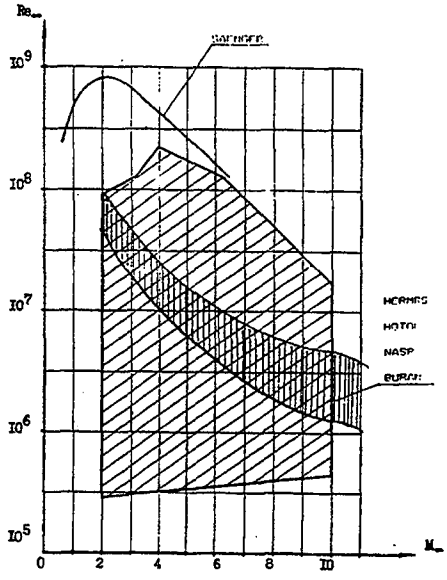

Fig.2. U 306-3 range of Mach number and Reynolds number variation

The creation of U-306-3 wind tunnel was preceded by the 1:4 scaled pilot wind tunnel. In the pilot wind tunnel there had been developed technology and techniques realized later in the large wind tunnel.

The wind tunnel is equipped by a set of axisymmetric contoured NOZZLES with equal exit diameter 1.2 m for Mach numbers Moo = 2.0; 4.0; 6.0; 8.0; 10.0.

A study of flow in nozzles with Reynolds number varied within a wide range allowed to select nozzle contour providing uniformity of working flow. All six axisymmetric nozzles of the large wind tunnel are manufactured with shortened profile (with "angular point" a nozzle throat). Evaluation tests of these nozzles in pilot tunnel verified high quality of a flow generated by them in comparison with nozzles manufactured using techniques based on the method of characteristics.

Each contoured nozzle for Moo = 4.0; 6.0; 8.0; 10.0 is manufactured as unified element in combination with settling chamber which has dimensions and equipment (honeycomb, turbulence reducing screens, probes for measuring total pressure and temperature) to provide flow of high quality (nozzle unit). shows flow field test data in the test section of the large wind tunnel. Average ununiformity for all nozzles in model position region is $\Delta Moo/Moo < 0.8\%$. Tests were carried out in 2 -3 cross sections of working flow at three values of Reynolds number.

Nozzles for Moo = 8.0 and 10.0 are connected with heating system by shielded pipe, and the nozzle for Moo = 6.0 with flow rate 110-330kg/s has a system for mixing with cold air.

The length of each nozzle unit is 6.2 m and it has the special flange for fast-demountable device of interfacing with

heating system, and the cylindrical part with a packing seal for interfacing with test section.

Nozzle units for Moo = 8.0 and 10.0 have load relief and temperature compensation devices. Nozzles for Moo = 2.0 and 3.0 have the same settling chamber (diameter 1.8 m, length 3.6 m) where equalizing perforated grid (diameter 0.8 m), honeycomb and two turbulence reducing screens are set.

HEATING SYSTEM is intended to exclude air components condensation at Mach numbers Moo = 6.0; 8.0; 10.0 and to provide heated gases for engine jets simulation.

For flow heating it was designed and tested in the pilot wind tunnel a resistance type heater of continuous action. The heater includes four-starf corrugated coil which in combination with ceramic insulators and shield screens allows with electrical power 7.5 Mw to heat gas up to 1073 K at flow rates 0.3-11kg/sec. The heater has very high efficiency (up to 96%) but possesses large hydraulic resistance, and it is used as basic one in the heating system of the large wind tunnel.

To realize flow rates of heated gas from 0.3 to 336 kg/sec and temperature of heating from 373 to 1073 K provision is made to vary number of resistance heaters. Heating system includes two stand-alone assembly of heaters.

The four heaters assembly is mounted under the test section and it is used for heating air or gases during engine jet simulation, and also for heating of a main flow through the wind tunnel when it exhaust into vacuum vessel. At the exit of the assembly there is a two-position fast-acting valve which provides start and cut of air supply within less than 0.1 s through the wind tunnel nozzle unit or through the model. Using shutoff valves,the assembly design allows to put in operation a necessary (from 1 to 4) number of heaters.

The ten heaters assembly is mounted before the nozzle unit. The assembly is extremely compact due to the heaters' arrangement in two tiers on rays intersecting in axis of the collector,which is coaxial to nozzle unit.The design provides equal hydraulic losses at inlets of each heater and allow to minimize heat losses.

TEST SECTION of the wind tunnel is designed as "Euffel" chamber with diameter 2.5 m and length 6 m, it has plane side walls with inflatable sealing.

Optical windows (diameter 0.8 m) are placed on panels which can move along working section. This allows to visualize a flow pattern around a model within the limits of 2-meters viewing port. Special hatch in the ceiling of test section and light system allows along with Schlieren pictures to obtain direct flow patterns around a model in vertical plane.

Cylindrical test section has in its lower part a pocket in with dimensions 1.7*2.1*6 m where tested model is positioned before startup and shutoff of the wind tunnel. The pocket is shielded from working flow by special blinds to protect a model from the effect of shock waves and hot air; provision is also made to thermostat a model by cold air, water or liquid nitrogen. The special panel with model spatial orientation gear is mounted on the lower rectangular flange of the pocket using 32 pneumolocks.

MODEL SPATIAL ORIENTATION GEAR has following parameters: angle of attack - $\pm 20^{\circ}$, angle of sideslip - $\pm 15^{\circ}$; linear

displacement along longitudinal axis - 0 - 670 mm, linear displacement along vertical axis - 0 - 300mm. Special support devices is used to set initial angles to provide large angles of spatial orientation.Computer control device allows to set simultaneously model displacement in three coordinates with high accuracy: error of angular setting - ±3′, error of linear setting - ±0.1 mm.

The panel with the gear can move (using automotive bogie) to special room where model and measuring instrumentation are prepared for tests. Equipped model with the gear and the bogie joins test section by hydraulic lift, load rating 47 tons.

CHANGEABLE DIFFUSERS. Models testsin the pilot tunnel have allowed to select properly shape of changeable diffusers. The use of a diffuser with relative cut diameters Fr = $F_д/F_т$=1.0; 1.5; 1.75 allows to realize optimum energy efficiency of the wind tunnel.

So the usage of diffuser with Fr = 1.0 is advantageous in tests with exhaust into atmosphere for minimizing of losses of total pressure along tunnel circuit, herewith conical part of diffuser is placed inside test section.

Overexpanded diffusers with Fr=1.5 and 1.75 are used in test with turboexhauster system and when it is necessary to increase a size of tested model.

Usual model dimensions are: diameter 0.4-0.6 m, length up to 3m.

When models are tested the ratio of the pressure in "Euffel" chamber to the static pressure in the flow was chosen for control of flow in the test section. Reference values of this parameter have been determined in pilot wind tunnel tests.

RUNNING TIME of the wind tunnel depends on a mode of operation and is equal to:

5 - 12 sec with exhaust into vacuum vessel,
10 - 30 sec with exhaust into atmosphere,
600 - 1800 sec with exhaust into exhaust system.

THE MAIN TESTING ITEMS are the following:

- aerodynamic forces and moments (hinge moment as well);
- pressure distribution;
- pressure fluctuation characteristics and buffeting;
- dynamic stability characteristics;
- large angles of attack tests;
- supersonic and hypersonic air inlet tests with operating control systems;
- free flight tests;
- aerodynamic characteristics of vehicle elements during separation(including engine jets simulation);
- engine jets simulation and their effects on aerodynamics characteristics;
- heat flux and temperature distributions on model surface;
- flow visualization;
- determination of large-scale and full-scale ramjets characteristics with simulation of engine jets; tests are conducted with simulation of the conditions at the inlet of air intake, while at the outlet of the nozzle it is provided required value of jet pressure ratio with use of exhaust system.

The wind tunnel is equipped with DATA ACQUISITION AND PROCESSING system which allow to measure up to 320 parameters in one run.Hardware and software allow to automatize measurements in all types of tests. Herewith it may be used up to 7 in-model 6-component strain-gauge balances, 100 in-model or remote pressure transducers or 200 thermocouples.

Pressure measurements on model surface is provided using pneumatic modul commutator of pyramidal scheme with single-membrane pneumatic relay. Commutator module has 16 input channels; set of parallel modules or modules in series allow to assembly commutator with required number of points and transducers.

The wind tunnel U 306-3 is equipped by optical device with diameter of viewing field 0.8 m. The device is intended for quantitative and qualitative investigations of various ununiformities in transparent mediums. Investigations of steady and unsteady processes are conducted with the help of Schlieren and shadowgraph techniques and interference methods using laser sources of light (holograms, flow patterns, density measurements) with high resolution and availability of chromatic analysis of pictures.

OUTLOOK of the large wind tunnel development is connected with the extending of Mach number range(Moo = 12.0, 15.0) and the increasing of flow stagnation parameters - pressure to 200 MPa, temperature to 2000 K. This will allow more complete simulation of real flight conditions for modern reusable aerospace systems, air intakes, ramjet engines, etc.

As a base of the wind tunnel modernization it is accepted a scheme of isochoric heating of nitrogen "working charge" in closed volume of special storage between input fast-acting valve and output fast-acting control valve and subsequent gas exhaust through settling chamber and nozzles into the test section with pushing action of precompressed cold nitrogen from high-pressure system of pressing-out (Fig. 3).

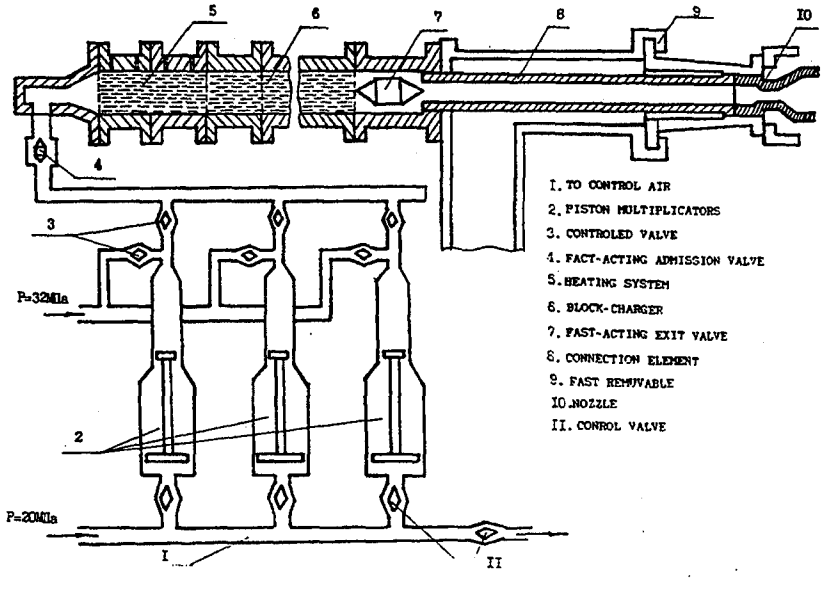

Fig.3. Scheme of the high-energy supply system

The wind tunnel possesses unique feasibility to conduct such modernization because:

- there is adjustable electric power supplying system (up to 75 Mw);
- there is 3 piston multiplicators, each of them can supply up to 30 litre of cold compressed gas;
- there is a prototype of gas heater made from SiC with heating temperature up to 2000 K at power consumption 500 kw.

Structurally high-energy supply system presents a storage with volume of 160 litre where there are placed 5 heating elements with separate adjustable power supply. Wind tunnel systems feeds this storage by nitrogen with pressure 32MPa, gas will have pressure 200 MPa and temperature 2000K after isochoric heating during 40 s. System of pressing-out using 3 piston multiplicators provides initial gas pressure up to 250 MPa, and this allows to have stationary flow through nozzles (Moo = 10.0, 12.0, 15.0) with exit diameter 1.2 m during approximately 1sec.Extended range of Mach number and Reynolds number variation is shown in Fig.4.

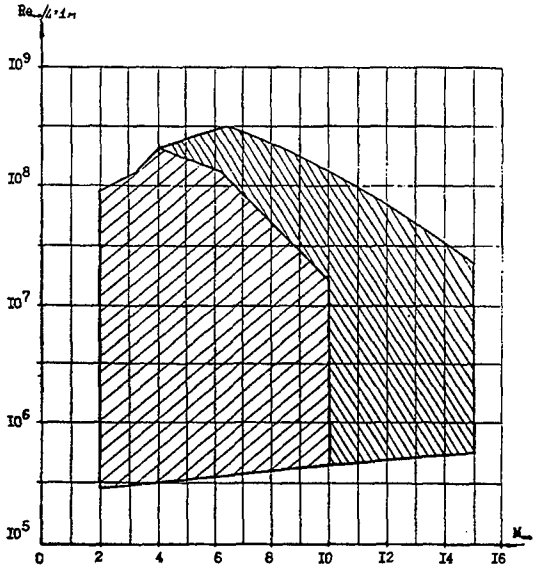

Fig.4. Extended range of Mach number and Reynolds number variation

First Experimental Results from the High Enthalpy Blow-Down Arc Facility in Naples

Rodolfo Monti - Antonio Esposito - Michelangelo Serpico
Institute of Aerodynamics "Umberto Nobile"
University of Naples
ITALY

Abstract

The High Enthalpy Blow-Down Arc Facility (HEBDAF) of the Institute of Aerodynamics "Umberto Nobile" (IAUN) in Naples, already employed for experimental/theoretical studies in the plasma diagnostic field, has been recently adapted for the simulation of the hypersonic conditions in the reentry phase of space vehicles.
This report presents the results of some preliminary calibration tests, performed to asses the simulation capabilities of this facility.
In the first part the technical characteristics of the HEBDAF, and improvements made to satisfy the new simulation requirements are described.
In the second part the measurement techniques and the numerical methods used to obtain overall thermofluidynamics free-stream properties are described.
Finally, the results of calibration tests are reported, in which total enthalpy, pressures and heat fluxes are measured at different electrical power and gas flow rates (pure nitrogen or nitrogen-oxygen mixture). These data, together with the properties numerically computed, allowed to evaluate a preliminary operating envelope for the HEBDAF, needed to evaluate its performances.

1. Introduction

One of the major problems in the ground simulation of hypersonic flows is that it is not possible to simulate all the parameters simultaneously (such a Reynolds number, Mach number, stagnation temperature etc.) which prevail during the reentry phase of the flight. Therefore it is only possible to perform partial tests, in which some relevant aerodynamic or aerothermal parameters (or non dimensional numbers) are duplicated.
The heat flux is one of most important reentry parameters, and a correct simulation can be performed by electric arc-heated facilities. Such is the case of the high enthalpy facility of the Institute of Aerodynamics in Naples. This facility consists essentially of an arc heater, a supersonic nozzle and a vacuum test chamber, in which the high-enthalpy flow exausts as a free-jet. The facility has been equipped with basic instrumentation, for measurements of total enthalpy, inlet and outlet nozzle pressures, test chamber pressure, stagnation pressure.
In a high enthalpy flow, it is very difficult to measure all thermofluidynamics parameters of the freestream; for this reason a computer code has been implemented. This code allows the evaluation of the free-stream properties (velocity, density, temperature, chemical composition) from the experimental data taken by diagnostic systems.
To obtain a freestream characterized by a composition very close to the real air, and because the arc heater can operates only with inert gases (i.e. nitrogen), it is necessary to add oxygen to the hot nitrogen flow; several mixing devices have been realized and tested. An innovative system to improve the performances of the facility, based on the use of a Radio-Frequency (RF) electrical generator, has been implemented. The nitrogen-oxygen mixture, before entering the nozzle, is inductively heated by means of RF energy. In such mode: i) the profiles of the thermofuidynamic properties would be uniformized by the "skin" effect of the RF energy, and ii) the total enthalpy of the flow would be enhanced.

2. Experimental Apparatus

2.1. Facility

A functional scheme of the HEBDAF is shown in figure 1; it consists of :
1) an electric arc heater, 80 [kW] maximum power, operating with pure inert gases (argon, nitrogen, etc.). It is powered by an electronic D.C. rectifier, which provides three open circuit voltages (80, 160 or 320 [V]), depending on the plasma-gas type to be used. Because the D.C. voltage from the rectifier is not sufficient to ionize the plasma gas, a high-frequency starter (2000 [V] at 1 [MHz]) is used to start the ionization process.
2) a supersonic De Laval nozzle, with an area ratio of 4. This nozzle is equipped with two pressure taps to measure inlet and outlet pressures.
3) a device to mix the cold oxygen with hot nitrogen, located between the arc heater and supersonic nozzle.

4) a cylindrical test chamber, equipped with windows, in which the high enthalpy flow exausts as a free jet. The test chamber walls are cooled together with the pipe connecting the test chamber to the vacuum system (two mechanical pumps), which mantains a pressure level of about 5 [Torr] in the test chamber.
5) two cooling systems. One, with distilled water, cools the arc heater, the nozzle and the gas heat-exchanger. Another system, with normal water, cools the test chamber, the vacuum pumps and the distilled water of the first cooling system.
6) a control panel, equipped with control and measurement instruments (voltmeter, ammeter, flow-meters, pressure and vacuum gauges, etc.).
7) an electronic data management device, that allows to execute the starting procedure from a personal computer. Work is in progress to manage the overall test from the P.C.
The proposed R.F. mixing system is schematically shown in fig. 2.a. The oxygen-nitrogen mixture exhausts into a water cooled cylindrical quartz channel, where the R.F. field is applied. After the R.F. reheating, the gas mixture expands in the supersonic nozzle. The R.F. field is created by a 3 1/2 turns, water cooled copper coil. The R.F. power is obtained from a Philips 22 [kW] induction heater, with three selectable radiofrequency ranges (2.4-6.5, 3.2-8.3 and 4-10.4 MHz). The coupling of an R.F. field to an arc heated flow makes it possible to use the R.F. "skin effect" (whereby most of the power in the R.F. field in a conductor tends to be concentrated close to the surface) to heat prevalently the outer regions of the stream, and to obtain a flow of more uniform temperature distribution (fig. 2.b) and hence of other properties.

2.2. Instrumentation

A mass-type calorimeter was used to measure the heat flux of the free-stream. The calorimeter, 15 [mm] O.D. and 8 [mm] thick, is made of oxygen-free copper and is supported in a shroud by a thermal insulator of low thermal conductivity. The temperature of the calorimetric mass is measured as function of time by a chromel-alumel thermocouple.
The following pressures are measured: the pressure at the downstream end of the plenum chamber; the static pressure at the nozzle exit; the static pressure in the test chamber. The freestream stagnation pressure is measured by a water-cooled pitot probe, 4 [mm] O.D., located on the centerline, 20 [mm] downstream the nozzle exit.
All gas and coolant flow rates are measured by flowmeters. Electrical parameters of the arc heater (voltage, current, voltage drop along leads, etc) are measured with analog-type gauges. A dedicated, electronic system allows to measure and store up to eight temperatures from thermocouples (arc heater and nozzle coolant temperature rises, slug calorimeter temperature, etc.).

3. Analysis

3.1 Flow Chemistry

To analyze the flow process properly it is necessary to determine the thermodynamic and chemical state of the gas at several locations through the arc-heater, the plenum chamber and the supersonic nozzle.
The kinetics in free-burning arc columns are well-documented[1]. For pressures larger than about 0.03 [atm], the various species of the flow in the arc column are in equilibrium. The pressure in the arc column of the HEBDAF is greater than 0.2 [atm] and therefore at the arc-heater exit thermodynamic and chemical equilibrium are assumed to prevail. To better understand the flow process in the plenum chamber, both the atom lifetime and the flow time of the gas species through it were estimated. The recombination times were calculated using the reaction rate constants from Evans et alii[2]. The continuity equation was used to estimate the velocity of the gas through the plenum chamber assuming one-dimensional flow. The flow time was then calculated from the known length of the plenum chamber. For the HEBDAF operating conditions, using nitrogen only, the recombination times range from 4×10^{-1} to 1.1×10^{-2} [sec], whereas the flow times are in the order of 10^{-4} [sec]. Because the time required for atom recombination is so much greater than the flow time, the chemical composition of the gas is assumed to freeze and to remain frozen during the travel through the plenum chamber and the nozzle.
The chemical state of the gas in the plenum chamber and nozzle was evaluated with the assumptions that the enthalpy of the flow at the arc-heater exit is given by the measured average enthalpy H_h (see below), and that the flow is uniform at the arc-heater exit, (i.e.ρu=const). The enthalpy and the measured pressure were then used to determine the chemical composition at the freezing point by a computer code, based on a thermodynamic model of pure nitrogen or nitrogen-oxygen mixtures in chemical equilibrium[3].

To duplicate air composition, the heated nitrogen was mixed with cold oxygen at the plenum chamber entrance. Because the flow times are very short compared to the oxygen dissociation time, oxygen was assumed to remain undissociated until the heated nitrogen is not ionized. When nitrogen ionization occurs, the oxygen is assumed to dissociate by ion-electron-molecule collisions, as the rates for these reactions are 7 orders of magnitude greater than those for atomic species[4] . With these assumptions, for the HEBDAF operating conditions (maximum enthalpy achieved was 20 [MJ/Kg]), it was found that the oxygen remain undissociated.

4. Measurement Techniques

4.1 Enthalpy measurements

4.1.1 Energy balance method

The primary method to evaluate the total enthalpy of the flow is the energy balance method[5]. The average or bulk enthalpy of the gas was evaluated at two different streamwise positions from measurements of power input to the gas, gas and coolant flow rates, and coolant temperature increases.The two measurements give an average of total enthalpy.
The average total enthalpy of the arc-heated portion of the gas leaving the arc heater and entering the nozzle is given by (for symbols see related list):

$$H_h = \frac{VI - \dot{m}_{wh} c_w \Delta T_h}{\dot{m}_{gh}} \qquad (1)$$

The average enthalpy of the flow at the nozzle exit is :

$$H_n = H_h - \frac{\dot{m}_{wn}\, c_w\, \Delta T_n}{\dot{m}_{gn}} \qquad (2)$$

After the calibration of all instruments, the overall uncertainty on the measured enthalpy was estimated (following the procedure outlined in Coleman and Steel[6]) from 9% to 20%, depending on power levels to the arc.

4.1.2 Frozen sonic flow method

It has been shown that presumably, for the HEBDAF operating condition, the flow in the plenum chamber and nozzle was chemically frozen. The nozzle thermal efficiency, (as determined from the energy balance method) was found to be about 0.75, thus a "near" isentropic expansion can be assumed. For these reasons, the so-called frozen sonic flow method[7] can be adapted to determine the total enthalpy of the isentropic core of freestream. In this method it is assumed that the flow up to the sonic throat of a nozzle can be represented by a one-dimensional, isentropic expansion under frozen conditions. The gas total temperature in the plenum chamber located upstream the sonic throat, is calculated as a function of a simple parameter which includes gas mass-flow rate, throat area and plenum chamber pressure.

The governing equation is:

$$\frac{\dot{m}_g}{p_t A^*} = \frac{CF(\gamma)}{(ZT_t)^{1/2}} \qquad (3)$$

where: $F(\gamma)= \left[\gamma(2/(\gamma+1))^{(\gamma+1)/(2(\gamma-1))}\right]$, and $C = (m_o / R)^{1/2}$.
For frozen flow, with no vibrational excitation, the value of γ is given as[7]:

$$\gamma = (4+3Z)/(4+Z) \qquad (4)$$

where $Z=1+\Sigma_i \alpha_i$. To calculate Z the gas composition must be known. As suggested by Pope[8], this can be calculated from the enthalpy and pressure measured at the arc-heater exit. The quantities $\dot{m}$, p_t and A* are

measured, and eq. (3) is then utilized to determine the total temperature at the beginning of the expansion. With the total temperature and chemical composition known, the total enthalpy is evaluated as:

$$H = h_s(T) + \sum_i \Delta h_i \alpha_i$$

where $h_s(T)$ is the enthalpy related to the temperature, and Δh_i is the heat of formation of the species "i".

4.2 Heat flux measurements

Precise,accurate heat flux measurement is a major objective in the research of thermal protection systems for reentry vehicles.
To evaluate heat fluxes on a specimen located in the center of the freestream, a mass calorimeter, made of oxygen-free copper, was realized and tested. The principle of operation of this sensor is based on storing all of the heat incident upon the surface of the sensor in a calorimetric mass in a short time period. Transient heat flux is determined by measuring the slope of the calorimeter temperature time profile, and by physical and thermal properties of the calorimetric mass as follows:

$$q(t) = \rho c l \frac{dT}{dt} \qquad (5)$$

where q(t) is the transient indicated heat flux, ρ the density of the calorimetric mass, l the thickness of the slug, c the specific heat of the copper, dT/dt the slope of back surface temperature history, and t the time.
Measured heat fluxes are compared with ones obtained by a finite-difference computer code for thermal analysis[9]. Input for this code is the time evolution of the back surface temperature of the calorimetric mass, as measured during the test.

5. Numerical computations

A numerical-experimental methodology, that allows to calculate all the thermofluidynamics free-stream properties from the experimental data (total enthalpy, pressures and gas flow rates), has been implemented. A basic assumption is that of correct nozzle expansion ($A_\infty = A_{ne}$). The equations involved are:

$$H_\infty = h(T_\infty) + \frac{U_\infty^2}{2} + \sum_i \alpha_i \Delta h_i \qquad (6)$$

$$\dot{m} = \rho_\infty U_\infty A_\infty \qquad (7)$$

$$p_\infty = \rho_\infty R_\infty T_\infty \qquad (8)$$

In these equations the gas flow rate $\dot{m}$, static pressure of the freestream p_∞, and total enthalpy H_∞ are experimentally measured. The temperature T_∞ is evaluated from tabulated thermodynamic data[2]. The gas constant R_∞ is calculated, from a frozen mixture as R_0/m, where R_0 is the universal gas constant and m the molecular weigth of the gas mixture.
For pure nitrogen, equation (6) can be written:

$$H_\infty = h(T_\infty) + \frac{U_\infty^2}{2} + \alpha_N \Delta h_N \qquad (9)$$

where the subscript "N" refers to nitrogen atomic species.
Starting from an initial value for α_N, the system (7), (8), (9) can be solved. Calculated value for T_∞, U_∞, ρ_∞ are used as input to a N-S code[10], that yields the complete flow field between the stagnation pressure probe and the bow-shock ahead the probe. The difference between calculated and measured stagnation pressures is used to upgrade α_N.
For a nitrogen-oxygen mixture, because it was assumed that oxygen does not dissociate, the system (7), (8), (9) still holds. Therefore the same methodology can be used to calculate the free-stream properties.

To validate the results of the numerical code, we have compared:
1) calculated chemical compositions of the pure nitrogen flow with the ones evaluated at the arc-heater exit in equilibrium conditions.
2) calculated Mach numbers, in frozen conditions, with the ones obtained from the isentropic expansion equations relating p_t/p_∞ and p_0/p_∞ to the specific heat ratio γ and the freestream Mach number.

6. Results

Total enthalpies vs.electrical power to the arc, as evaluated by the energy balance method and the frozen sonic flow method, are shown in fig. 3.a for nitrogen only, and in fig. 3.b for a mixture of 80% nitrogen - 20% oxygen. It can be seen a good agreement between the two methods. It is espected that the sonic flow method gives total enthalpies greater than ones obtained by the energy balance method, because it does not account for the heat losses along the nozzle. The disagreement observed for a nitrogen flow rate of 1.3 [g/s] may be due to a recirculating flow, that involves an increasing mistake on the measured pressure in the plenum chamber. When the oxygen is added, this recirculating flow is reduced, the flow fills the plenum chamber and then the pressure is correctly measured.
From the same graphs it can be seen that, as the electrical power increases, the enthalpy values from the two methods disagree. This fact can be explained noting that, as power increases, the difference between the enthalpy of the core of the freestream (measured by the frozen sonic flow method) and the average total enthalpy (measured by the energy balance) becomes larger.
To what concerns the numerical methodology above described, comparisons between computed Mach numbers, and the ones obtained from pressure measurements are shown in fig. 4. It can be seen a good agreement, that improves at high gas flow rates. It would be noted that the stagnation pressure and the total enthalpy used in the calculations are not measured at the same point in the freestream (stagnation pressure is measured at the centerline of the freestream, whereas the total enthalpy is the average over the nozzle exit section). Another comparison between the calculated atomic nitrogen mass fractions, and the ones evaluated at the arc-heater exit in equilibrium conditions, is shown in fig. 5.
After these validation tests, the freestream properties of the high enthalpy flow were calculated for the operative range of the HEBDAF, and the results are presented in the density-velocity and stagnation pressure-total enthalpy planes, fig. 6 and fig. 7. Also in this graphs the corresponding values for the reentry path of the CARINA national space vehicle, in its critical altitude range (40-60 [km]) are shown.
To what concerns heat flux measurements in fig.8 we show heat fluxes on the copper calorimeter for nitrogen and nitrogen-oxygen mixture, as determined from eq. (5) and from the numerical code[9]. The results compare favourably.
To estimate the heat flux simulation capabilities of the HEBDAF, in fig. 9 stagnation point heat fluxes, as evaluated from the Fay-Riddel expression (with fully catalytic surface) using the experimental data (total enthalpy and stagnation pressure), are compared with the ones for the CARINA space vehicle.

7. Conclusions

The High Enthalpy Blow-Down Arc Facility in Naples is an arc-heated facility for the simulation of the aerothermochemical environment experienced by space vehicles during the reentry phase.
In this report the results of preliminary calibration tests were presented, in terms of total enthalpy, plenum chamber and stagnation pressures, and heat fluxes attainable.
Also, using the available experimental data and a computer code, an operating envelope for the HEBDAF was constructed.
Finally, to evaluate the simulation capabilities of the HEBDAF, measured stagnation region heat fluxes and pressures were compared with the ones for the CARINA space vehicle during the critical phase of his reentry trajectory (40-70 [km]).
Future planned developments for this facility will be:
1) an in-depth diagnostics of the high-enthalpy flow, based on local measurements of total enthalpy (using a calorimetric probe) and another theoretical methodology to compute the free-stream properties.
2) accurate, precise heat flux measurements on blunt-shaped models, using both mass- type calorimeters and Computerized Infrared Thermography.

3) an experimental-numerical activity, to determine the performances of the radio-frequency system proposed. This activity will consist in the experimental determination of the enthalpy and oxygen mass fraction profiles at the nozzle exit. These profiles will be compared with the ones obtained from a numerical code to be implemented.

ACKNOWLEDGEMENTS

Special tanks are due to Mr. A.R. Russo, A. Loquace and A. Rolfi of the Laboratory of the Institute of the Aerodynamics for their technical support.

References

(1) Brown, S.C. "Basic data of plasma physics" M.I.T. and J.Wiley and Sons Press, N.Y.1959, pp.318-321
(2) Evans, Schexnayder, Huber "Boundary Layer electron profiles for entry of a blunt body at high altitude" NASA TN D-7332, July 1973
(3) D. Giordano and L.Marraffa "Thermodynamic model of air in chemical equilibrium" AGARD CP 514, Avril 1993,pp.26.1-26.15
(4) Massey H.S.W. "Recombination of gaseous ions" Advan.Physics 1, 1952, pp. 395-426
(5) P.Murino, R. Monti "Determinazione sperimentale della caratteristiche di correnti gassose ad elevate temperature" La Termotecnica, Settembre 1965, pp. 416-437
(6) Coleman, Steel "Experimentation and uncertainty analysis for engineers" J. Wiley ed., pp. 40-42
(7) L.H. Jorgensen "The total enthalpy of a one-dimensional nozzle with various gases" NASA TN D-2233, 1964
(8) R. Pope "Measurements of enthalpy in low-density arc-heated flows" AIAA Journal, vol. 6, n. 1, pp.103-109, January 1968
(9) System Improvement Numerical Difference Analysis (SINDA) User's Manual
(10) E.W.Miner, C.H.Lewis "Hypersonic ionizing air viscous shock layer flows over non analytic blunt bodies" NASA CR-2550, may 1975

List of symbols

A = cross sectional area of nozzle
V = arc voltage
c = specific heat
H = total enthalpy
I = arc current
m = flow rate
P = pressure
q = heat-transfer rate to surface
R = universal gas constant
T = temperature
ΔT = coolant temperature rise
U = velocity
Z = compressibility factor
α = total mass fraction of dissociated species
γ = isentropic exponent
ρ = density
m_0 = molecular weight of undissociated gas

Subscripts

e = exit
g = gas
h = arc-heater
i = ith component of mixture
n = nozzle
* = nozzle throat condition
0 = stagnation point value
t = plenum chamber condition
w = water
∞ = stream condition

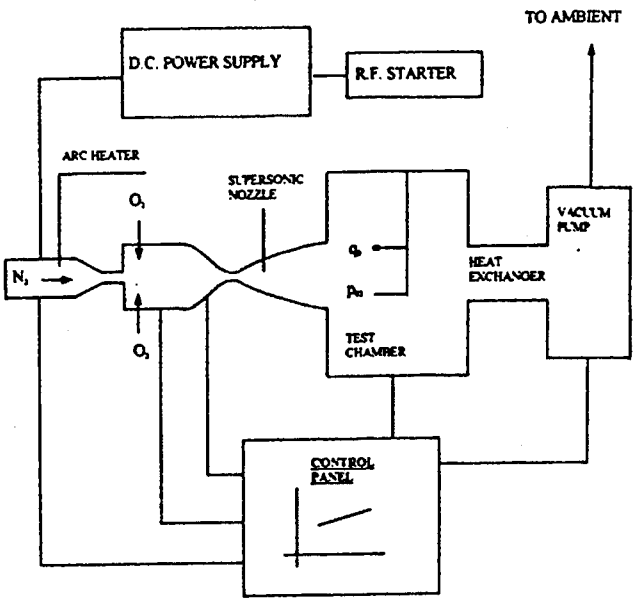

Fig. 1 - HEBDAF FUNCTIONAL SCHEME

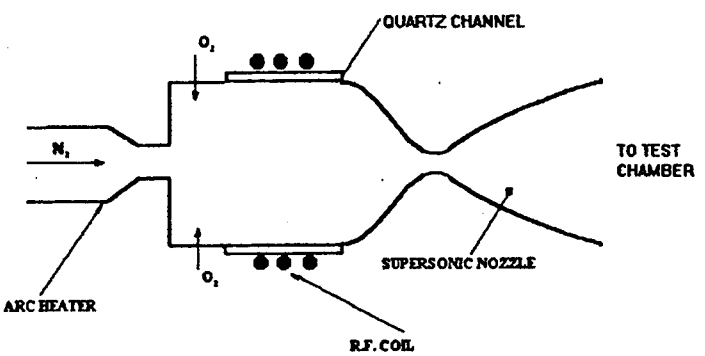

Fig. 2.a - FUNCTIONAL SCHEME OF THE R.F. MIXING SYSTEM

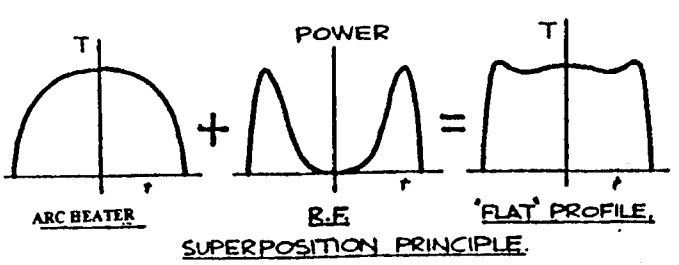

Fig. 2.b - EFFECT OF THE R.F. ENERGY ON THE TEMPERATURE DISTRIBUTION

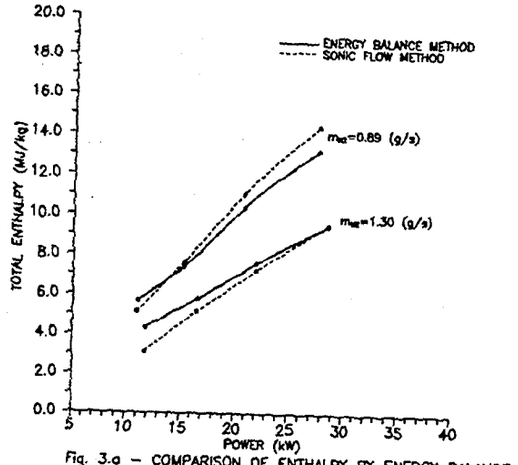

Fig. 3.a – COMPARISON OF ENTHALPY BY ENERGY BALANCE AND SONIC FLOW METHODS – PURE N_2

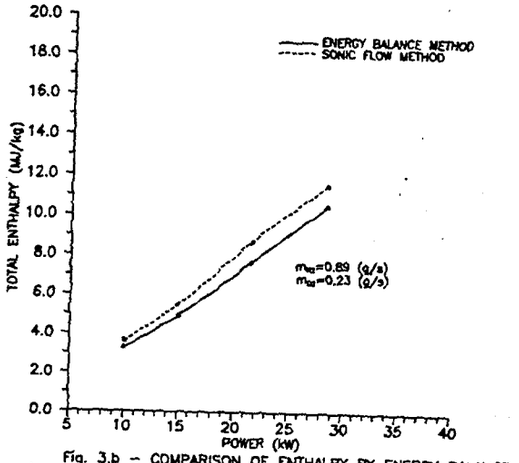

Fig. 3.b – COMPARISON OF ENTHALPY BY ENERGY BALANCE AND SONIC FLOW METHODS – N_2 + O_2 MIXTURE

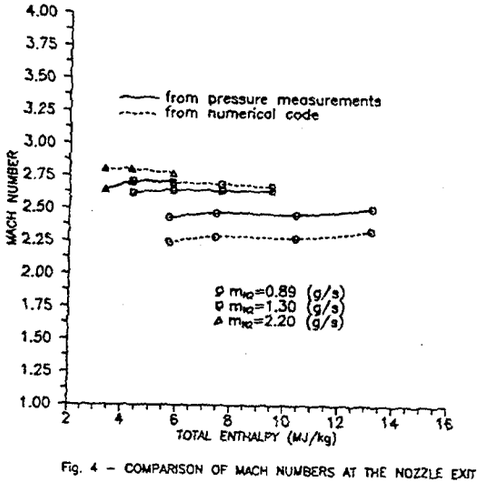

Fig. 4 – COMPARISON OF MACH NUMBERS AT THE NOZZLE EXIT

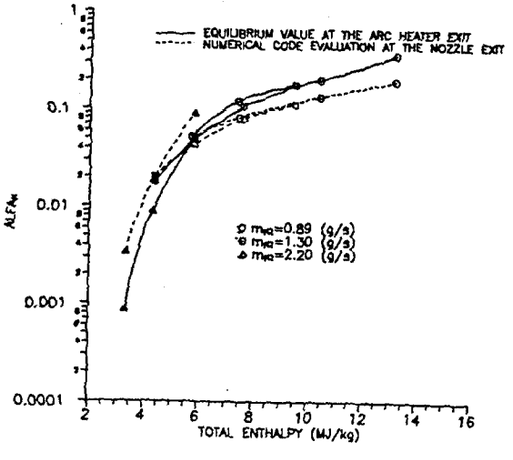

Fig. 5 – COMPARISON OF ATOMIC MASS FRACTIONS FOR PURE NITROGEN FLOW

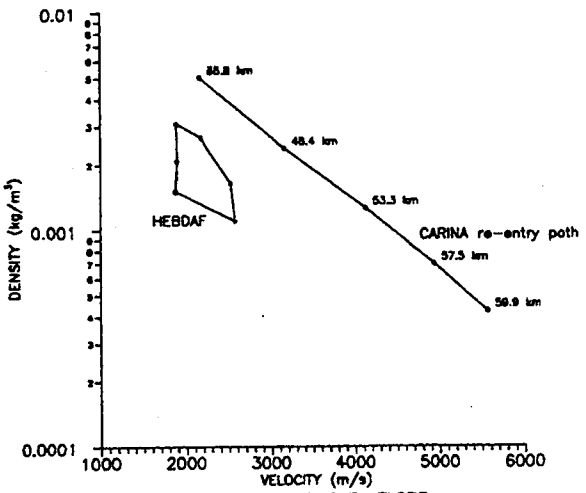

Fig. 6 – HEBDAF OPERATING ENVELOPE
DENSITY–VELOCITY PLANE

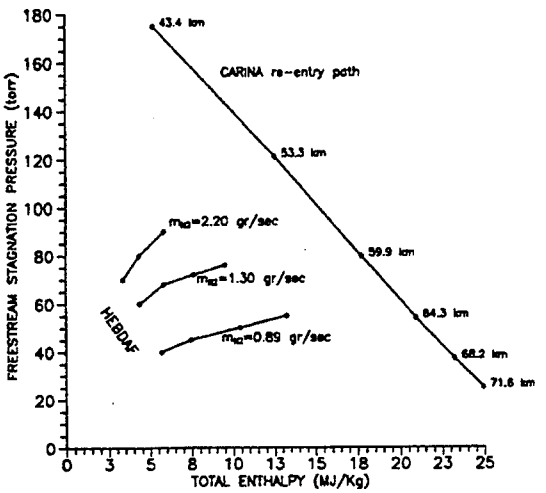

Fig. 7 – FREESTREAM STAGNATION PRESSURE–TOTAL ENTHALPY

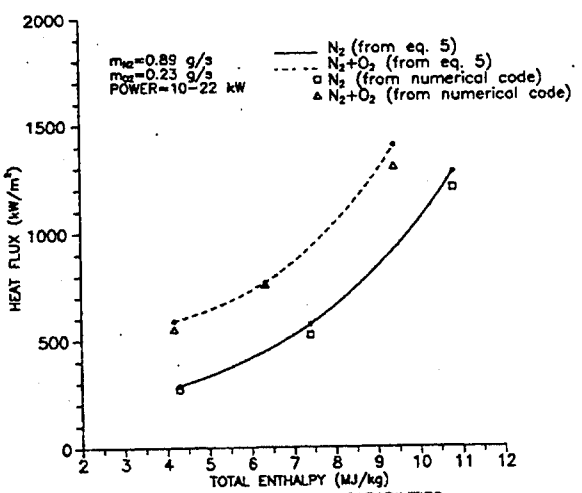

Fig. 8 – HEBDAF SIMULATION CAPABILITIES
FREE STREAM HEATING RATES

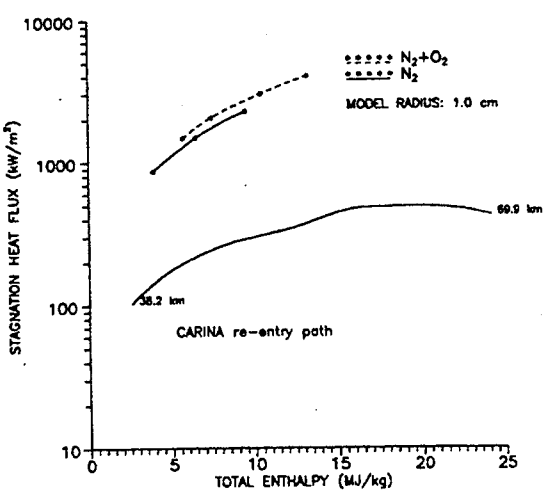

Fig. 9 – HEBDAF HEAT FLUX SIMULATION CAPABILITIES
STAGNATION POINT HEAT FLUXES

INVESTIGATION OF THE PRESSURE FIELD ON A WING EXPERIENCING FLOW SEPARATION

B.H.K. LEE
Institute for Aerospace Research
National Research Council, Ottawa, Ontario (Canada)

S. MARINEAU-MES
Dept. of Mechanical Engineering
University of Ottawa, Ottawa, Ontario (Canada)

Abstract

The pressure field on the wing upper surface of a rigid 6% scale model of the F/A-18 aircraft at high angles of attack was investigated in the Institute for Aerospace Research (IAR) 1.5m trisonic blowdown wind tunnel. The starboard wing was instrumented with 138 transducers for unsteady pressure measurements. The investigation was conducted for various Mach numbers and angles of attack. Spectral analyses of the pressures on the wing surface were carried out. Broadband space-time correlation of the pressure transducer signals was performed and the convection pattern of the pressure field and peak correlation delay contours were mapped.

Nomenclature

c	local chord
$\bar{c}$	wing mean aerodynamic chord (8.29 in.)
C_p	time-averaged pressure coefficient
f	frequency
k	non-dimensional frequency, $f\bar{c}/U_\infty$
L	distance from aircraft plane of symmetry to missile launcher (13.53 in.)
M	free stream Mach number
q	free stream dynamic pressure
U_∞	free stream velocity
x	distance measured from the wing-LEX junction in the flow direction
x'	distance measured from the leading edge along a chord line
y	distance measured from the aircraft plane of symmetry
α	angle of attack
τ	time delay

1. Introduction

The high angle of attack manoeuvring capability of the F/A-18 made it a suitable test vehicle for research in flow separation on the upper wing surface of fighter type aircraft. At the Institute for Aerospace Research, a rigid 6% scale model of the F/A-18 was manufactured and instrumented with unsteady pressure transuducers on the starboard wing and leading-edge extension (LEX) for studying flow separation on the wing surface.

It was demonstrated from flight tests[1] that the flow on the upper

surface of the F/A-18 wing flown at high angles of attack was very complex. Regions of separation and reattachment were observed on the inboard leading-edge flap and near the missile launcher. Using the oil dots flow visualization technique[2], the topology of the flow on the wing upper surface indicated that strong outflow dominated a major portion of the wing at M = 0.6 and α = 30°. It was also found that flow separation occurred on a large portion of the inboard leading-edge flap. The flow separated close to the LEX and reattached on the flap. Separation also occurred along the hinge line with the flow reattaching a short distance behind it. Flow reversal on the inboard leading-edge flap was observed. A saddle point was deduced close to the hinge line slightly inboard of the inboard and outboard leading-edge flaps junction. A focus was observed from the spiralling pattern of the streak lines. The surface flow visualization technique was not successful in revealing the flow pattern on the outboard leading-edge flap.

A second saddle point was found on the aileron. The streak lines near the wing tip in the vicinity of the missile launcher indicated the presence of a vortex which was also observed from flight tests.

Steady pressure contours on the wing upper surface[2] showed a low pressure region on the inboard leading-edge flap that corresponded to the separated flow region detected from the oil dots visualization experiment. The pressures on a large portion of the wing surface were fairly uniform, rising gradually aft the hinge line towards the trailing edge. Near the two saddle points, there were no detectable changes in the steady state pressures.

The rms values of the pressure fluctuations showed a region of relatively large pressure fluctuations originating from the hinge line at the leading-edge inboard flap where the flow separated. This region extended diagonally across the wing and terminated at the tip missile launcher. The largest fluctuations were observed near the trailing-edge of the aileron.

Complementing the surface pressure studies of the flow structure, this paper presents results from spectral and space-time correlation analyses under the same test conditions as Ref.2.

2. Facility, Model and Instrumentation

2.1 Facility

The tests were conducted in the transonic test section of the IAR 1.5m trisonic blowdown wind tunnel. This facility has a Mach number range from M = 0.1 to 4.2. The walls of the test section are perforated with 0.5 in. diameter holes inclined at 30° to the flow direction, thus allowing pressure and flow communication between the test section and a 12 ft. diameter, 16 ft. long plenum chamber. The wall porosity is adjustable and it was set at 4% for the present measurements. The model was mounted on a cranked sting that forms part of the model support system. The strut can be programmed to move vertically and with the pitch linkage mechanism, the model angle of attack can vary from 0° to 33°. Under aerodynamic loading, sting bending has to be taken into consideration and this can result in an increment in the angle of attack of up to 2°.

2.2 Model

The model used in this study was a rigid 6% scale of the F/A-18. The design is described in details in Ref.3. For the present investigation, the leading- and trailing-edge flap angles were set at 34° and 0° respectively. The horizontal stabilators were set at -9°. These angles corresponded to the flap settings taken from the F/A-18 auto flaps-up mode schedule at high angles of attack. Boundary layer transition trips were installed on the wings, LEX, fins, stabilators and forebody of the model.

Figure 1 shows the locations of the pressure transducers on the starboard wing and LEX. The transducers were mounted directly opposite to each other on the upper and lower surfaces. Thirty of them were installed on the LEX and 138 were spaced on eight rows along the wing span. The transducers were flush-mounted piezo-resistive sensors (chips from Kulite XCQ-062-50A transducers) with an active area of diameter 0.035 in. and a frequency response above 50 kHz. In preparation for the installation of the transducers, pockets with dimensions of 0.06 in. by 0.10 in. and 0.015 in. deep were machined on the wing and LEX surfaces to accommodate the chips. Trenches were also machined on the wing surfaces for the electrical wirings that were gathered in a cavity inside the fuselage and connected via cables housed in the interior of the sting support to the wind tunnel control room. A silastomer was used to fill the holes after the chips were mounted and, at the same time, served to protect the transducers. The trenches were covered with an epoxy compound and hand-finished to give a wing profile practically the same as the original wing. Details of the layout of the trenches on the wing surfaces are described in Ref.2.

The transducers were calibrated by mounting the F/A-18 model in a steel chamber with accurate temperature and pressure control. The transducers were sensitive to strain effects due to deformation of the wing under aerodynamic loadings. The effects of strain and the procedure of calibrating the transducers are described in more details in Ref.2.

2.3 Data Acquisition System

Wind tunnel run conditions, model angle of attack and other parameters were recorded at 100 Hz using a PDP 11/73 computer based wind tunnel data system. This computer system also controlled the wind tunnel operation and model positions. A microVax based data acquisition system was used to collect data at a much higher sampling rate for unsteady pressure measurements. This data system consisted of a front end, a digital concentrator and a parallel disk. The front end comprised of blocks of instrumentation amplifiers, A/D converters and filter/RMS modules. The digital concentrator provided the link between the front end and the parallel disk. It accepted serial data from all the A/D converters and transformed them to parallel data. The data could bypass the host computer and be written directly onto the disk through an interface port on the disk drive system. The sampling frequency was set at 38.4 kHz and the data system was capable of collecting up to 10 million samples per second. The parallel disk has a capacity of 6.5 gigabytes that was sufficient to hold data acquired

from an average day's wind tunnel runs. A typical wind tunnel run generated approximately 400 to 600 Mbytes of data. The data was transferred onto 8mm data cartridge overnight and the parallel disk was ready to accept data again the next day. Offline data processing was performed using an HP RISC 9000/750 workstation.

3. Results and Discussion

The flap settings used in the experiments corresponded to the operation of the aircraft at high angles of attack. The investigations were, therefore, conducted at incidence angles above 25° to be compatible with the auto flaps-up schedule. For discussion purposes, only the case for M = 0.6 and α = 30° are described in this paper. The Reynolds number based on the model mean aerodynamic chord and the dynamic pressure corresponding to this Mach number were 3.38×10^6 and 3.95 psia respectively. Within the operational range of the F/A-18 tested at this flap setting, the flowfield varied with Mach number and angle of attack, but the overall characteristics were similar.

3.1 Spectral Analysis

The power spectral density (PSD) was computed using the method given in Ref.4. The FFT block size used was 8192 and a Hamming window was applied to the data. Ten seconds of data were analyzed, and using an overlap of 50%, the number of averages was approximately 190. Only results on the wing upper surface are presented since it is on this surface that important characteristics of the flowfield occur. Because of the large number of PSD plots that were generated, it was found that the most convenient manner to present the results would be in the form of contour plots.

Surface flow visualization[2] indicated that a strong outflow dominated a major portion of main wing and trailing-edge flap. Aside from certain regions at the aileron and near the missile launcher, the flow was attached. A PSD plot along the spanwise direction starting from the seventh chordwise transducer is shown in Fig.2. It is seen that near the wing-fuselage junction, a broad peak centred at a reduced frequency k of approximately 1 is observed. This value of k corresponds to a linear frequency of about 1 kHz. Moving away from this transducer in the outboard direction, this peak decays rapidly and vanishes bewteen the second and third rows of chordwise transducers. The low frequency content of the PSD increases towards the missile launcer.

PSD computed in the chordwise direction shows the broad peaks to occur on the first row of transducers starting approximately midchord. On the second row of transducers, the broad peak is observed only close to the trailing edge. An illustration of the variation of the PSD along the fifth chordwise row of transducers is given in Fig.3. This row of transducers is very close to the saddle point detected in Ref.2 and passes over a region of reversed flow on the leading-edge flap. This figure shows that on the leading-egde flap, the PSD has a large low frequency content that decreases approximately linearly with increasing frequency. Behind the hinge line, the PSD increases to a maximum value at k approximately 1. This increase is rather gradual and does not show a broad peak as found from the transducers near the

fuselage-wing junction. This maximum vanishes near the trailing edge.

Figures 4-6 show the PSD contours on the wing surface at three frequencies, namely, k = 0.5 , 1, and 1.5. It can be seen that at the inboard leading-edge flap where the flow separates near the wing-LEX junction, the PSD is lower than that on the rest of the wing. The figures show a similar behaviour in that the PSD increases towards the wing tip with the largest values occurring at the aileron close to the missile launcher. The large values of the PSD at k approximately 1 at the trailing-edge flap is noticeable in Fig.5. For other values of k, the PSD on chordwise transducer rows 1 and 2 near the trailing edge always show larger values than those further upstream.

3.2 Space-Time Cross-Correlation

Broadband space-time correlation of the pressures on the wing upper surface was carried out using the IEEE CCSE cross-correlation algorithm (Ref.4). Cross-correlation studies were carried out where each transducer was taken as the reference and time correlations were performed with respect to the adjacent transducers.

The correlation functions are normalized with respect to the amplitude of the reference transducer auto-correlation function at $\tau = 0$. Using various reference transducers, the results show that at M = 0.6 and $\alpha = 30°$, pressure correlation is found to be good in large regions on the main wing and trailing edge flap. Using the velocities computed from each transducer pair, an approximate indication of the convection pattern can be constructed. The direction of the convection of the broadband eddies in regions on the wing surface where cross-correlation is considered good compares well with the surface streamlines determined from oil dots flow visualization studies[2].

An example of the space-time cross correlation map for the seventh spanwise row of transducers using the seventh transducer on the third chordwise row (Fig.1)as the reference is given in Fig.7. The isocorrelation lines are slightly skewed but show that correlation extends for fairly large distances on the span. Similarly, cross-correlation along the fifth row of chordwise transducers (Fig.8) shows that the spatial correlation to extend for quite large upstream and downstream distances. In this case, the sixth transducer from the leading edge was used as the reference. The time correlation usually decays in five or six milliseconds. Correlation along the third chordwise row of transducers shows that the flow on the leading edge and slightly behind the hinge line exhibits poor correlation. Surface flow visualization[2] indicated the flow to be very complicated with separation and reattachment near the first three of four transducers in the third row.

Using one of the transducers close to the middle of the attached flow region on the main wing as reference, for example, transducer '6' on the third chordwise row, cross-correlation functions with all other transducers on the upper surface of the wing are generated. The cross-correlation plots that exhibit a clear peak are selected, and the peak correlation time delay is recorded. The data is then used to generate a map of peak correlation delay contours, as shown in Fig.9. The time delay shown is in milliseconds. A large region of correlated pressure fluctuations can be seen on the wing behind the hinge line, and this corresponds to the attached flow region from the oil dots

visualization studies[2]. From the contour lines, it is possible to deduce the convection velocities of the broadband eddies and determine the convection pattern of the pressure field.

Conclusions

The flow field on the wing upper surface of a rigid 6% scale model of an F/A-18 was investigated from analyses of the PSD and broad-band space-time correlations. At M = 0.6 and α = 30°, the PSD of the pressure field near the wing-fuselage junction exhibits a broad peak centred at a reduced frequency of approximately 1. This peak could be due to the vortex formed at the wing-body junction. Spectral analyses do not show any characteristic frequency associated with the LEX vortex burst.

Space-time correlation of the pressure transducer signals shows a fairly large region on the wing where good correlation is observed. The deduced convection pattern of the pressure field agrees with the direction of the streak lines obtained from surface flow visualization studies.

Acknowledgements

The authors wish to acknowledge the financial support from the Institute for Aerospace Research , the Department of National Defence and the Natural Sciences and Engineering Research Council Canada. They are thankful to Mr. M. Polsenski for his assistance in the data reduction.

References

1. Del Frate, J.H., Fisher, D.F. and Zuniga, F.A., "In-Flight Flow Visualization and Pressure Measurements at Low Speeds on the NASA F-18 High Alpha Research Vehicle", NASA TM101726, October 1990.

2. Lee, B.H.K., Valerio, N.R. and Tang, F.C., "A Wind Tunnel Investigation of the Pressure Distribution on an F/A-18 Wing", AIAA 93-3468, AIAA 11th Applied Aerodynamics Conference, Monterey, CA, Aug. 9-11, 1993.

3. Lee, B.H.K. and Brown, D., "Wind-Tunnel Studies of F/A-18 Tail Buffet", J. Aircraft Vol.29, No.1, 1992, pp.146-152.

4. Rabiner, L.R., Schafer, R.W. and Dlugos, D., "Chapter 2.1, Periodgram Method for Power Spectrum Estimation", " Chapter 2.3, A Coherence and Cross Spectral Estimation Program", in Programs for Digital Signal Processing, Edited by The Digital Signal Processing Committee, IEEE Acoustics, Speech and Signal Processing Society, IEEE Press, New York, 1979.

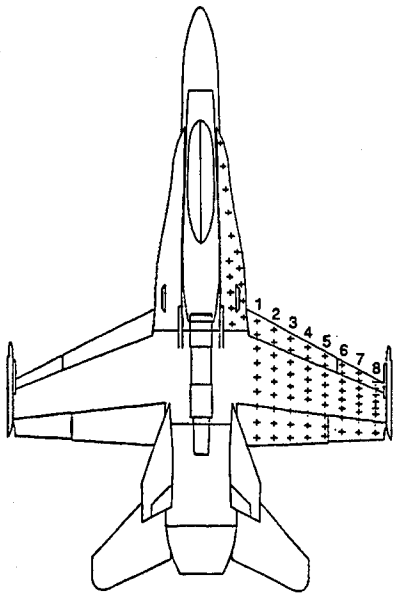

Fig.1 Location of pressure transducers

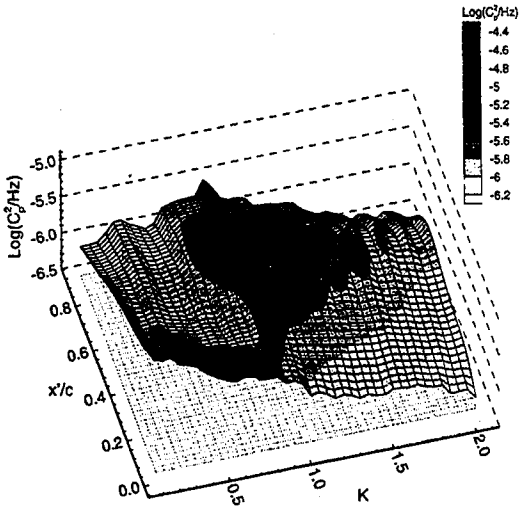

Fig.3 PSD contours along 5th chordwise row of transducers

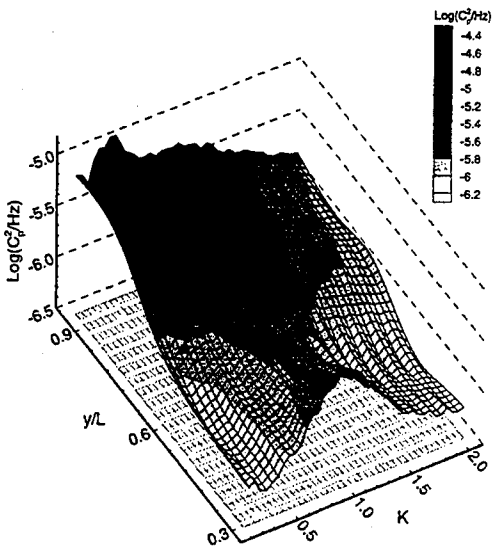

Fig.2 PSD contours along 7th spanwise row of transducers

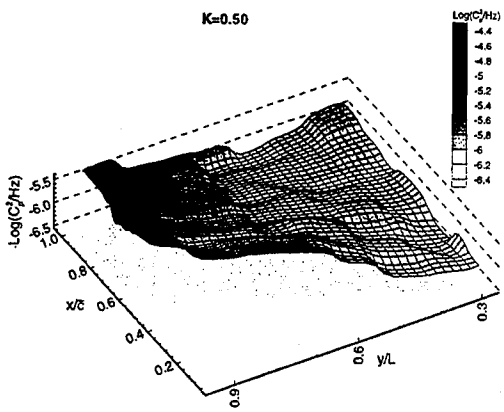

Fig.4 PSD contours at k = 0.5

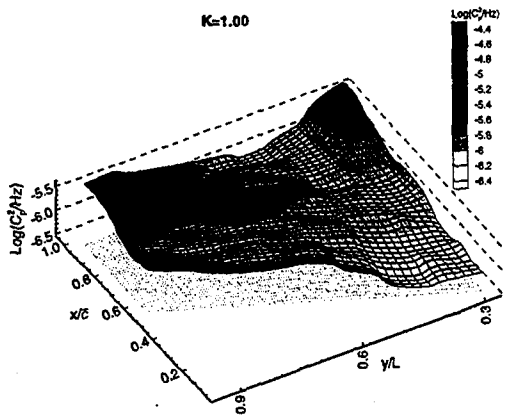

Fig.5 PSD contours at k = 1.0

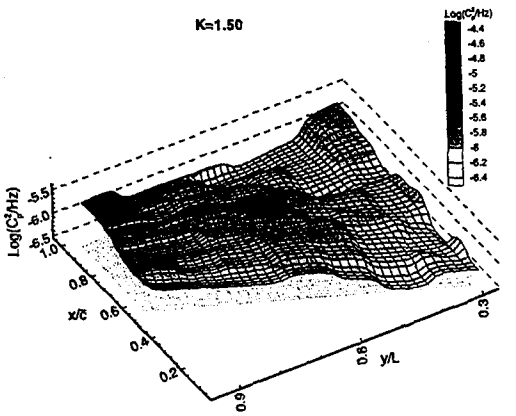

Fig.6 PSD contours at k = 1.5

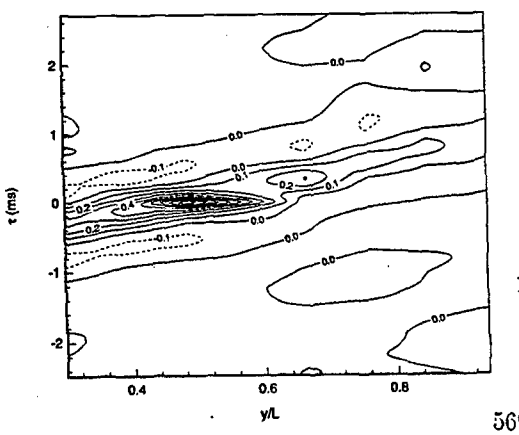

Fig.7 Cross-correlation along 7th spanwise row of transducers

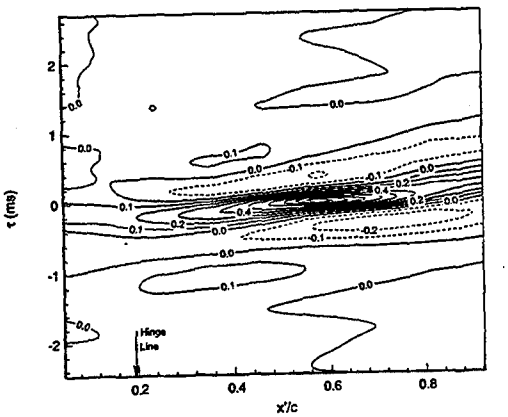

Fig.8 Cross-correlation along 5th chordwise row of transducers

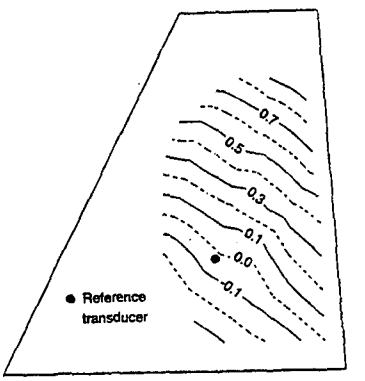

Fig.9 Peak correlation time delay contours

EXPERIMENTAL INVESTIGATION ON THE EFFECTS OF ACOUSTIC EXCITATION ON ENHANCING LIFT

LU QIZHENG HOU YUELONG YUN QILIN
(China Aerodynamics Research & Development Center, Mianyang, Sichuan, China)

ABSTRACT

This paper presents the results of the experimental investigation on the effects of internal acoustic excitation on enhancing lift and the mechanism of enhancing lift. Experiments on a two—dimensional backward—facing step model and a slotted NACA 0012 airfoil model were conducted in two low speed wind tunnels respectively. The experimental results show that significant lift enhancement by acoustic excitation is obtained by exciting at the location near the separation point so long as the exciting frequency is equal to the main frequency of the flow at the forcing location, and the kinetic energy of velocity fluctuation of excited flow is transformed into the kinetic energy of mean velocity along the flow direction.

1 INTRODUCTION

In recent years, a very strong interest appeared in the research of unsteady flow separation and vortex control. J. M. Wu thinks that the first and the second generations of aeronautical flow type[1], i. e. the attached flow and the detached vortex flow belong to steady types of flow and third generation of aeronautical flow type would be the weakly unsteady detached vortex flow, so the searching for enhanced vortex—lift by unsteady excitation constitutes precisely the first step towards the new type of flow.

Acoustic excitation is a means of weakly unsteady excitations. Parker, R. has investigated resonance effects in wake shedding from paralled plates since 1966[2-4]. Ahuja, K. K, et al, have investigated flow sepatation control by sound since 1983[5-6]. Fei—Bin Hsiao, et al, investigated the control of wall—separated flow on a NACA 63_3—018 airfoil and a circular cylinder by using the internal acoustic excitation technique in 1991[7], and the results show that as long as the emanating acoustics is "locked in "to the separated shear—layer instability frequency and forcing is applied at the separated point, the separated flow is controlled most effectively, also the lift is increased , and the drag reduced.

To study the effects of internal acoustic excitation on enhancing lift and the mechanism of enhancing lift, the experimental investigations of the above mentioned two models were conducted by CARDC in 1990 and 1992 respectively.

2 WIND TUNNELS AND MODELS

Wind Tunnels

Tests of the two—dimensional backward—facing step model were conducted in the 1. 4m×1. 4m

Wind tunnel of CARDC. This facility is a low speed(25～45m/s), closed—circuit wind tunnel. The freestream turbulence intensity is 0.14%.

Tests of the airfoil model were conducted in the 0.4m × 1m low —turbulence wind tunnel (LTWT) of NPU. The freestream speed is 5～75 m/s. The freestream turbulence intensity is 0.02%.

Models

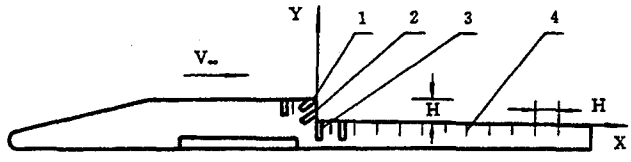

Fig. 1 Sketch of backward—facing step model

The two—dimensional backward—facing step model is shown in Fig. 1. The step height H is 35mm. The aspect ratio is slightly greater than 10 for two—dimensionality of the reattached flow. "1","2","3" showed in Fig. 1 indicate three different forcing location S=1,2,3, in each location, a row of orifices are distributed along the span direction to emit acoustic waves respectively. "4" represents 11 static pressure orifices along flow direction.

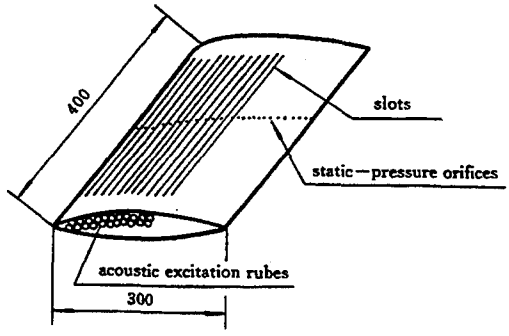

Fig. 2 Sketch of slotted NACA 0012 airfoil model

NACA 0012 airfoil model is shown in Fig. 2. Twelve 1.2mm wide slots, located at 0.73%, 4.16%, 8.83%, 16.83%, ……chord are manufactured to emit acoustic wave respectively. 64 static pressure orifices along the surfaces of the airfoil model and with 10° inclination to the mid—span plane are manufactured to measure the pressure distributions. The model was mounted on the rotary window of the test section of LTWT.

3 EXPERIMENTAL RESULTS OF THE BACKWARD—FACING STEP MODEL

Freestream speed was maintained constant in each run of the tests. Velocity fluctuations in the excited and unexcited flows were measured by a hot—wire anemometer and vortex shedding frequency was determined by power spectrum analysis of the velocity fluctuation. Also, longitudinal static pressure distributions on the upper surface behind the step were measured in the excited and unexcited cases.

Main results derived from the tests are as follows. (f is the forecing frequency, f_N is the natural vortex shedding frequency. V_∞ is the freestream speed. $K=fh/V_\infty$ is the non—dimensionalized frequency. The non—dimensionalized natural vortex shedding frequency K_N is 0.040.)

(1) Effects of Acoustic Excitation on Pressure Coefficients

Pressure distribution on the upper surface of the model at the unexcited state and the 45#,41#,42# states are shown in Fig. 3 respectively. For S=3,K=0.038, the SPL for 45#,41# and 42# state equals

to 131dB, 138dB and 142 dB respectively. It is clear that the pressure coefficients are reduced by the acoustic excitation. The mean value of the pressure coefficients along the upper surface is reduced by 68.3% for 42° state, confirming the effects of acoustic excitation on enhancing lift.

(2)Effects of SPL on Pressure Coefficients

It can be seen from Fig. 3 that, when the forcing frequency is close to the natural vortex shedding frequency ($K/K_N=0.95$), reduction of the pressure coefficients is increased with SPL. Some results also show that, when the forcing frequency is much different from the natural vortex shedding frequency, variation of the pressure coefficients with SPL is small.

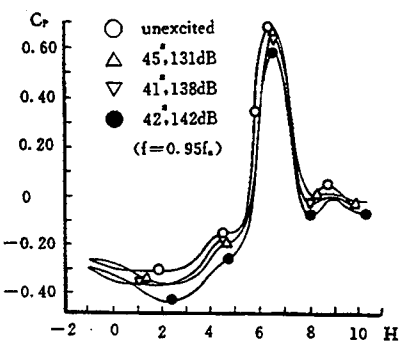

FIg. 3 Pressure distributions on the surface of model

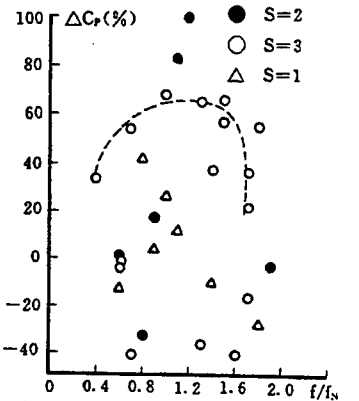

Fig. 4 Reduction of pressure coefficcients $\Delta Cp(\%)$ on the surface of model vs f/f_0

(3) Effects of Forcing Frequency on Pressure Coefficients

On the upper surface of the model, the average reduction of the pressure coefficients $\Delta C_P(\%)$ with the f/f_N is shown in Fig. 4 for the SPL=140dB and the three different forcing locations S=1,2,3. It is clear that the maximum $\Delta C_P(\%)$ occurs at $f/f_N=0.9\sim1.2$ for S=2 and at $f/f_N=0.8\sim1.2$ for S=3. when the f/f_N exceeds the above range, the $\Delta C_P(\%)$ tends to reduce, and there is some uncertainty with the data. So the results show that, when the forcing frequency is much different the natural vortex shedding frequency, the effects of acoustic excitation are reduced. But when the forcing frequency is close to the natural vortex shedding frequency, the effects of acoustic excitation are obvious.

(4) Effects of Forcing Location on Pressure Coefficients

Fig. 4 shows that, when $f/f_N\approx1$, the forcing location S=2 is the best to reduce the pressure coefficients. This is because the forcing frequency is chosen to be equal to the main frequency of the flow nearby the forcing location. The forcing location S=3 is better than the S=1.

4 EXPERIMENTAL RESULTS OF SLOTTED NACA 0012 AIRFOIL MODEL

Normal—force coefficient Cn Was obtained by the pressure distribution measurements in the tests. Time—average velocity profiles and velocity fluctuation power spectrum at different positions on the upper surface of the model were measured by the hot—wire anemometer. The effects of acoustic excitation on enhancing lift were examined at angles of attack $\alpha=16°\sim22°$. Investigation on the effects of acoustic excitation on enhancing lift and its mechanism was conducted especially at post—stall angle of attack $\alpha=18°$. The freestream speed was 30 m/s in all the tests. Main results are the following:

(1) Effects of Acoustic Excitation on Enhancing Lift

Variation of normal—force coefficient with angle of attack with and without acoustic excitation is shown in Fig. 5. It can be seen that the maximum normal—force coefficient is increased by the acoustic excitation, and the stall is delayed. It is worthy of note that because the acoustic excitation energy supplied by a tube was diffused in the long slot along the span on the surface of model, the sound—excited velocity disturbance on the surface of model was actually very weak. If we had improved the supply system of the acoustic excitation, the effects of the acoustic excitation would have been more obvious.

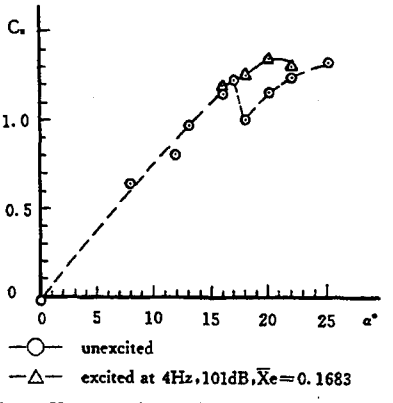

Fig. 5 Variation of normal—force coefficients Cn with α

(2) Flow Characteristics on Upper Surface of Model at α=18°

Without excitation, only small velocity fluctuation of the flow is observed at the bottom of the boundary—layer during the measurements of velocity profiles at $\bar{x}$=0.07 and $\bar{x}$=0.110. But the velocity fluctuation is large and increased with $\bar{x}$ at $\bar{x}$=0.153, $\bar{x}$=0.310 and $\bar{x}$=0.500. Also, the velocity fluctuation region along the normal direction at these locations increases. As shown in Fig. 6, the velocity near the wall at the location $\bar{x}$=0.110 or $\bar{x}$=0.153 is smaller compared with that at other locations, showing that the locations $\bar{x}$=0.110 and $\bar{x}$=0.153 are near the separation point.

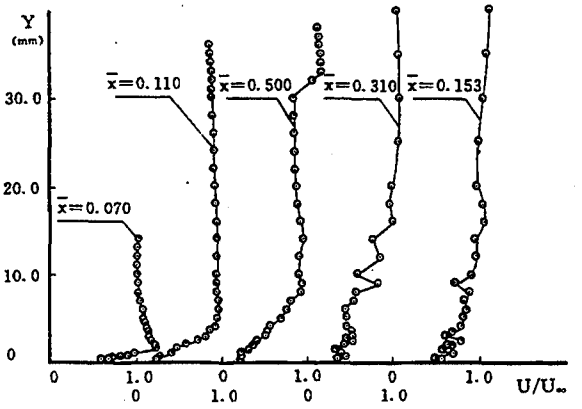

Fig. 6 Velocity profiles at different chordwise positions

In the velociy fluctuation power spectrum of the flow without excitation at $\bar{x}$=0.110 and y=0.3mm (Fig. 7), there is a peak at 11Hz, which is the shear—layer instability wave. This characteristic indicates that the flow at $\bar{x}$=0.110 has not separated. But at $\bar{x}$=0.153 and y=0.3mm, there are many peaks of different amplitudes, which shows the flow has separated at this location. So the separation point is between $\bar{x}$=0.110 and $\bar{x}$=0.153.

(3) Effects of Forcing Location and Forcing Frequency

In the airfoil model tests at α=18°, by varying the forcing frequency, a high normal—force coefficient Cn was obtained by the acoustic excitation with a frequency near the main frequency 4Hz of the flow at the forcing location $\bar{x}_e$=0.1683. Based on this, different combinations of forcing locations and frequencies were adopted in the tests. First, the forcing location is behind the separation point, $\bar{x}_e$=0.1683, the forcing frequency is 4 Hz. Second, the forcing location is $\bar{x}_e$=0.1683, the forcing frequency is 11 Hz. Third, the forcing location is before the separation point, $\bar{x}_e$=0.0883, the forcing frequency is 11Hz. The ratio of the three increments of normal—force coefficients ΔCn (compared with the Cn of unexcited flow) is 1 : 0.499 : 1.023. It can be seen that the significant increment of the normal—force coefficient is obtained by the acoustic excitation with the frequency equal to the main frequency of the

separated flow at the forcing location behind the separation point or with the frequency equal to the shear—layer instability frequency at the forcing location before the separation point.

(4) Variation of Power Spectrum by Acoustic Excitation

The velocity fluctuation power spectra of the flows at $\bar{x}=0.110$ and $y=0.3$mm with and without excitation are shown in Fig. 7. The characteristic of the power spectra indicates that the flow has not separated at this location, but the power spectrum densities at all the frequencies except the shear — layer instability frequency are reduced by the acoustic excitation. The velocity fluctuation power spectra of the flows at $\bar{x}=0.153$ and $y=0.3$mm with and without excitation are shown in Fig. 8. The spectrum of the unexcited flow has many peak, which indicates the characteristic of separated flow. At this location the main frequency of the separated flow is 4Hz. For the excited flow , the peak at the shear—layer instatility frequency is increased, but the power spectrum densities at other frequencies are reduced. This power spectrum shows the excited flow has not separated. It is clear that the kinetic energy of velocity fluctuation of excited flow is reduced and the flow which has separated at $\bar{x}=0.153$ now has reattached by the acoustic excitation.

(5) Variation of velocity profiles by Acoustic Excitation

Fig. 9 shows the velocity profiles with and without acoustic excitation at $\bar{x}=0.110$ and $\bar{x}=0.153$ respectively. It can be seen that no matter where the measurement position is (before or behind the separation point) the time—average velocities are increased by the acoustic excitation on the forcing location behind the separation point at frequency 4Hz. Similar resutls are obtained by the acoustic excitation on the forcing location before the separation point at frequency 11Hz.

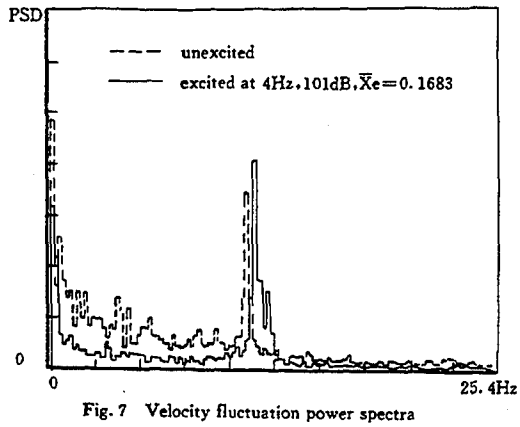

Fig. 7 Velocity fluctuation power spectra of the flow at $\bar{x}=0.110, y=0.3$mm

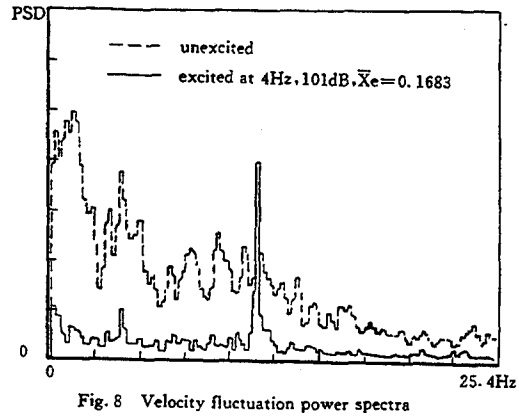

Fig. 8 Velocity fluctuation power spectra of the flow at $\bar{x}=0.153, y=0.3$mm

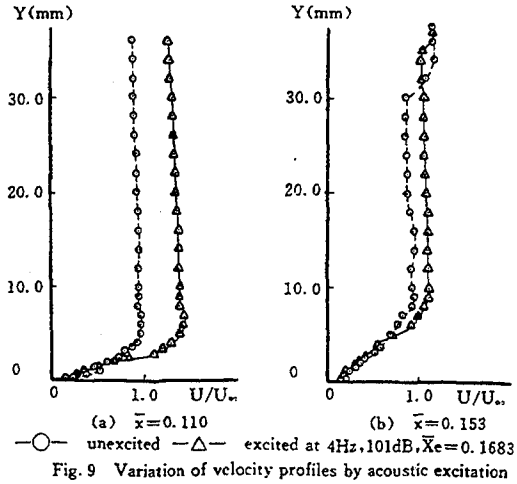

Fig. 9 Variation of velocity profiles by acoustic excitation

5 DISCUSSION ON THE MECHANISM OF ENHANCING LIFT BY ACOUSTIC EXCITATION

The mechanism of enhancing lift by acoustic excitation can be discussed as follows.

(1) Flow instability is an inherent characteristic of shear—layers and separated flows. Velocity fluctuations at the bottom of the shear—layers occur before separation. There is an obvious peak in velocity fluctuation power spectrum , indicating the instability wave of the shear—layer(T—S wave). In separated flows, the velocity fluctuations exist in the entire separated field, and many peaks at different frequencies in the velocity fluctuation power spectrum show the complicated unsteady vortex construction.

(2) As is mentioned above, unsteady excitation must be adopted in accordance to the inherent properties of the separated flows, that is to say , "receptivity " must be considered, so as to realize the sound—vortex resonance.

(3) Even if the sound—vortex resonance was achieved, the streaming effects should also be achieved to obtain significant lift enhancement effectiveness of acoustic excitation. The above—mentioned results show that the kinetic energy of velocity fluctuation of excited flow is transformed into the kinetic energy of mean veolcity. It is because this kinetic energy delays the flow separation on the upper surface of airfoil model that lift enhancement effectiveness is obtained.

6 CONCLUSIONS

(1) The effects of acoustic excitation on enhancing lift is obvious. Internal acoustic excitation is a good means of unsteady excitations for flow separation control and enhancing lift.

(2) The significant effects of acoustic excitation on enhancing lift are obtained at the forcing location near(before or behind)the separation point as long as the forcing frequency is equal to the main frequency of the flow at the forcing location. The mechanism of sound—vortex resonance is confirmed by the results.

(3) Under sound—vortex resonance, the kinetic energy of the velocity fluctuation of the excited flow is transformed into the kinetic energy of mean velocity along the flow direction. The mechanism of acoustic streaming is also confirmed by the results.

ACKNOWLEDGMENT

The authors wish to thank He kemin, senior engineer of NPU, and Zhang Weizhi, engineer of CARDC, for their help in performing the experiments.

REFERENCES

1 J. M. Wu, et al, Review on Physics of Enhancing Vortex—lift by Unsteady Excitation, 40th Ann Meeting of Division of Fluid Dynamics of American Physics Society, Nov. 22—24,1987
2 Parker. R. Journal of Sound and Vibration, Vol. 4,62
3 Welsh,M. C, et al, Journal of Sound and Vibration, Vol. 93,305
4 Stokes, A. N, et al ,Journal of Sound and Vibration,Vol. 104,55
5 Ahuja,K. K,et al, AIAA Paper 83—0726,1983
6 Ahuja, K. K,et al, AIAA Paper 84—2298,1984
7 Fei—Bin Hsiao, et al , AIAA Journal Vol. 28, No. 8,1440

EXPERIMENTAL MEASUREMENTS IN THE WAKE OF CANARD-WING CONFIGURATIONS

BURESTI G., LOMBARDI G.
Department of Aerospace Engineering, University of Pisa (Italy)
PETAGNA P.
A.R.I.A., Aerodynamic Research for Industrial Applications, Livorno (Italy)

ABSTRACT

The wake interference effects in a canard-wing configuration are characterized by measuring the axial vorticity component through a suitable pressure probe. It is shown that the canard tip vortex may be subjected to quite different evolutions if it passes above or below the wing surface. It is also ascertained that at certain angles of attack the vortex may split in two parts at the wing leading edge. Finally, the tip vortex is shown to develop through a mechanism, involving the merging of oppositely-signed cores of vorticity, which is significantly dependent on the angle of attack.

INTRODUCTION

At the Department of Aerospace Engineering of the Pisa University (DIA) experimental and numerical research on the problem of the interference between lifting surfaces has been in progress for a few years [1-4]. A comparison between computed and experimental pressure distributions acting on straight and forward swept wings in interference with a fore canard surface was presented in previous works [3-4], where it was shown that a potential non-linear vortex lattice code, in spite of its simplicity, is capable of very accurate predictions in all configurations that do not correspond to a close interference between the fore wake and the wing surface.

In the present work some experimental tests carried out to characterize the canard wake, particularly in those conditions that gave prediction problems, are described. In particular the position and intensity of the vorticity field was measured by means of a vorticity probe, in order to obtain a deeper insight on the causes of the discrepancies between numerical and experimental results, and thus to obtain indications on the possibility of modifying the computational procedure to widen its range of applicability and improve the accuracy of the predicted pressure distributions. It will be shown that the investigation, although of limited extent, and therefore still of preliminary nature, allowed some interesting physical features of the interference between canard wake and wing surface to be pointed out.

DESCRIPTION OF THE TESTS AND OF THE EXPERIMENTAL SET-UP

The tests were carried out in the DIA wind tunnel, which is a subsonic, closed-return tunnel, with circular open test section 1.1 m in diameter and 1.48 m in length. The adopted geometric conventions are shown in Fig. 1: taking also into account the tests carried out in the previous investigations [1], the relative position between wing and canard is defined longitudinally by a stagger L of 2.26 mean geometric chords of the wing, and laterally by a value T/L = 0.166, while the decalage angle γ was zero. The wing model was untwisted and had zero dihedral angle, an aspect ratio of 5.7, taper ratio of 0.4, zero sweep angle at 1/4 of the chord, and a NACA 0012 wing section. The canard model was an unswept and untwisted rectangular lifting surface, with

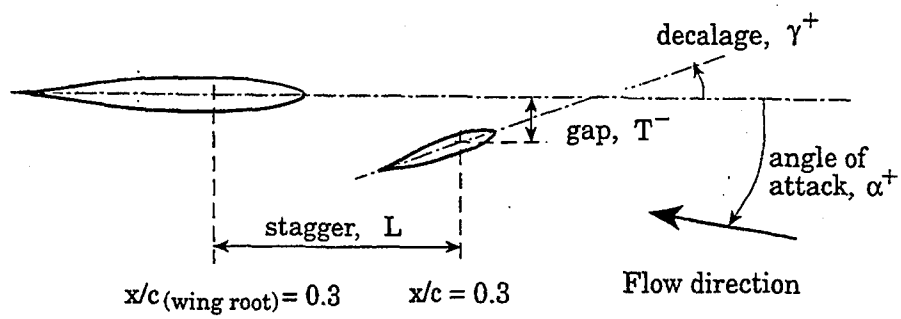

Fig. 1 - The adopted geometric conventions

zero dihedral angle, aspect ratio of 4, NACA 0012 wing section and a span equal to 0.47 that of the wing (and consequently a surface equal to 1/3 that of the wing). The studied configuration shown in Fig. 2.

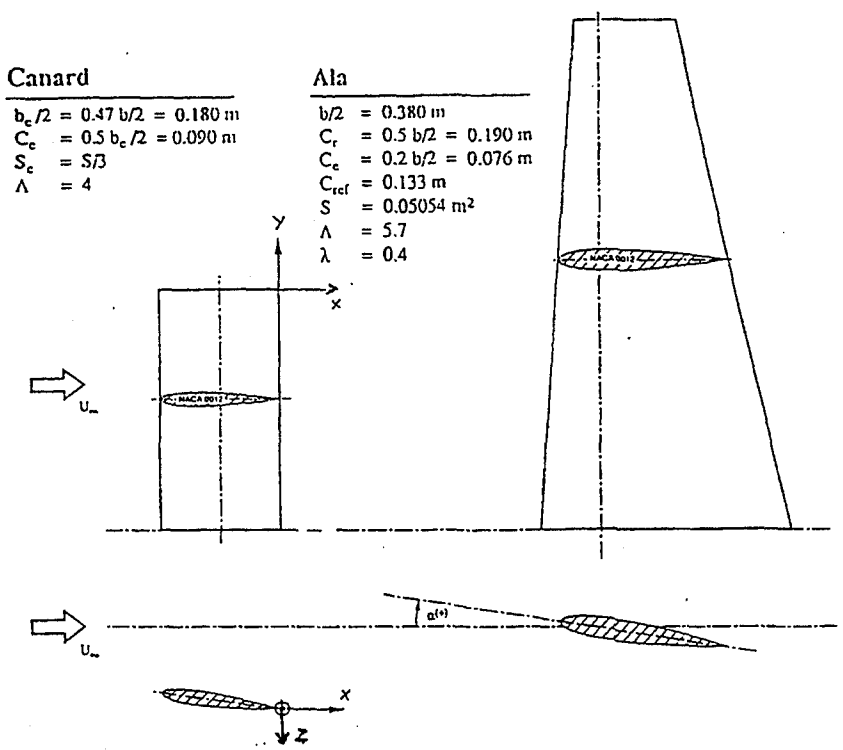

Fig. 2 - The studied configuration

In order to measure the axial component of vorticity the pressure probe shown in Fig. 3 was used; it is basically composed of four yawmeters which measure the circulation around a small circuit 5 mm in diameter. The theoretical bases of its operation are described by Freestone [5],

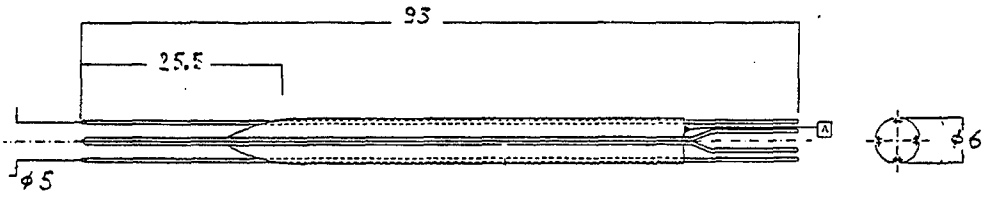

Fig. 3 - The pressure probe for the measurement of the vorticity

while the details regarding its construction and calibration are reported in [6, 7]. The response of the instrument, ΔC_{pm}, may be expressed by the relation [5, 7]:

$$\Delta C_{pm} = K \rho U \Gamma / (1/2 \rho U_\infty^2) \quad (1)$$

where U_∞ is the freestream velocity, ρ the fluid density, U the module of the velocity in the point of measurement, Γ the circulation around the circuit defined by the instrument (Fig. 3), and K is a probe constant given by

$$K = K_p / (4 \pi r) \quad (2)$$

In expression (2) r is the radius of the circuit, and K_p is the calibration constant of the yawmeters; the reading of the latter, as a pressure difference Δp, is connected to the velocity component tangential to the circuit, v_n, by

$$\Delta p = 0.5 K_p \rho U v_n \quad (3)$$

It may be observed from (1) that the probe response is proportional to the quantity $U \Gamma / U_\infty^2$; however, it should be noted that in developed axial vortices in the wake of lifting bodies the tangential velocity component is generally small compared to the axial one, which, in turn, is of the same order of the freestream velocity [8]. It may then be assumed that the response of the instrument is proportional, with good approximation, to the circulation, and may then be taken as a measure of the mean vorticity inside the measurement circuit.

By means of this instrument, a detailed analysis of the wake of the canard, both isolated and in the canard-wing configuration of Fig. 2. was carried out to characterize the interference effects. During the investigation, it appeared that the tip vorticity field immediately downstream of the canard trailing edge was actually rather different from what expected, due to the presence of a significant amount of secondary vorticity with sign opposite to the main one. Furthermore, the possibility that at certain angles of attack the canard tip vortex might be splitted at the wing leading edge in two well defined cores, which would then follow respectively the upper and lower wing surfaces, was also studied. The results of all these analyses will be briefly described in the following section.

ANALYSIS OF THE RESULTS

Description of the canard tip vortex

The detailed analysis of the vorticity field at the canard tip (that is of sharped type) revealed the presence of a secondary vorticity core, having sign opposite to the main one, and a smaller but non-negligible intensity. As an example. Fig. 4 shows the vorticity maps obtained at different distances from the trailing edge (including upstream positions), at an angle of attack of 8°. As can be seen. this secondary vorticity (having. say, negative sign) originates over the canard surface, reaches a maximum near the trailing edge. and, moving downstream, is gradually annihilated by

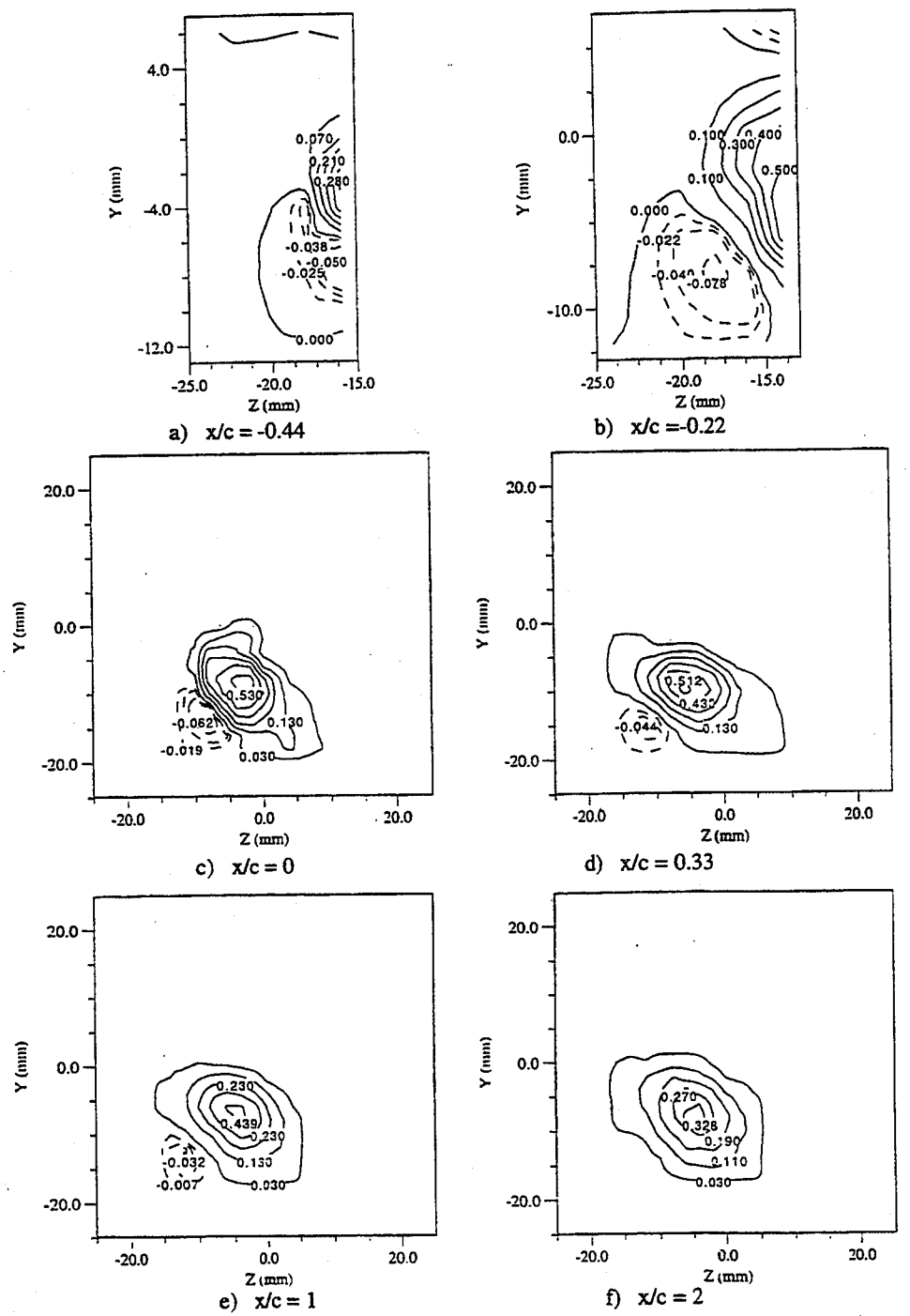

Fig. 4 - Maps of the axia component of the vorticity, isolated canard; $\alpha = 8°$

the merging with the positive main vortex, which decreases in intensity. The global vorticity is thus constant in each section downstream of the canard, but a single one-signed tip vortex may be considered to be developed only after the end of the aforesaid merging process between cores of different sign. Apparently, the secondary vortex is produced by the outward velocities induced over the upper surface of the canard by the stronger main tip vorticity, which emanates gradually along the tip chord and rapidly rolls up in a vortex core.

Fig. 5 gives an idea of the dependence of this mechanism on the angle of attack, showing the ratios between the maximum negative and positive values of the vorticity in each downstream section. As can be see, the relative intensity of the secondary negative vortex increases more than linearly with increasing angle of attack; analogously, the downstream distance for the complete merging is an increasing function of the angle of attack.

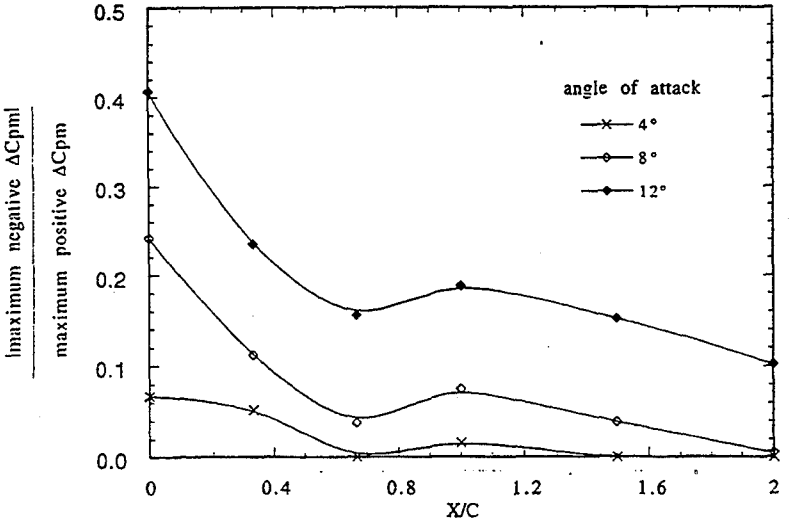

Fig. 5 - Effect of the angle of attack on the secondary vorticity core

Therefore, we can say that the detailed vorticity field at and immediately downstream the tip region of a lifting surface is somewhat more complicated than is assumed in most potential flow models including a modelling of the wake axial vorticity. This might have some relevance when configurations with close-coupled multiple lifting surfaces at relatively high angles of attack are to be analysed, in which case an uncompleted process of formation of a single vortex core might influence the load distribution on the downstream surfaces.

Interference between canard wake and wing

To study the interference effects between canard wake and wing, the axial vorticity field was measured at various cross-sections, both for the isolated canard and with the wing; in each section measurements were carried out on a grid of points with 2 mm square meshes. In Fig.6 the position of the tip vortex is shown for $\alpha = 4°$; in the figure the width of the vortex is that corresponding, in each plane, to a vorticity equal to half the maximum local value. As can be seen, at this angle of attack the presence of the wing does not modify significantly the canard vortex position, as could probably be expected, considering that for this condition the vortex remains rather far from the

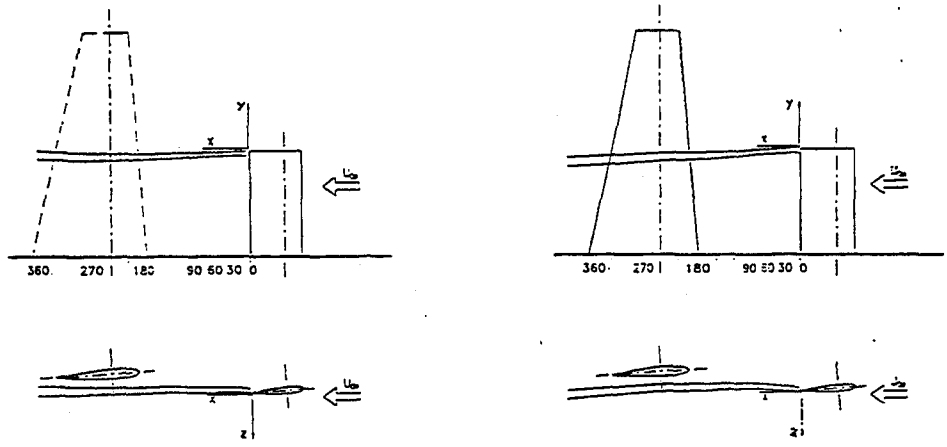

Fig. 6 - Position of the tip vortex of the canard ; $\alpha = 4°$

wing surface. The situation is quite different for $\alpha = 8°$ (Fig. 7), when the presence of the wing significantly affects the vortex, which is both displaced and diffused by the wing flow field.

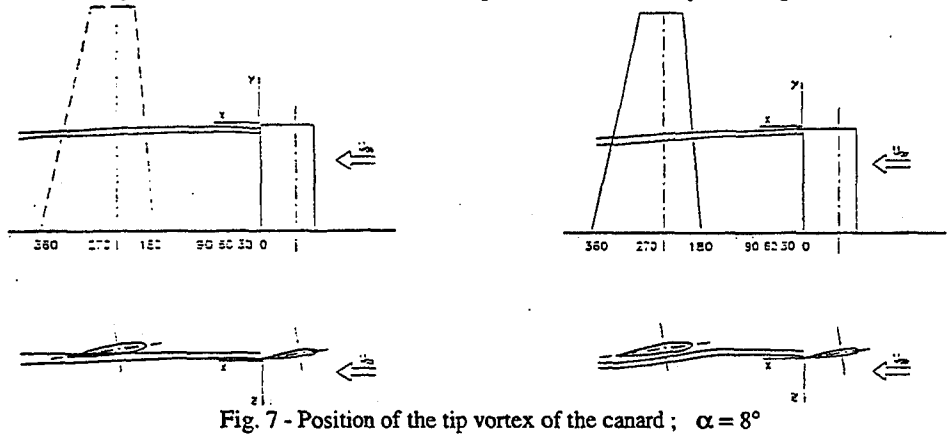

Fig. 7 - Position of the tip vortex of the canard ; $\alpha = 8°$

It should further be pointed out that in both the above cases, in which the canard vortex passes below the wing surface, the vortex core is still well concentrated downstream of the wing (Figs. 8a and 8b). Conversely, when at higher angles of attack the vortex core passes above the wing, as is the case, for instance, at $\alpha = 12°$ (Fig. 8c), its vorticity is greatly diffused, probably due to the action of the large adverse pressure gradient existing over the upper wing surface.

Splitting of the canard wake by the wing

In previous investigations [3, 4] it has been shown that certain computational potential models for the analysis of interfering lifting surfaces may, for particular configurations, predict a splitting of the fore surface tip vortex in two parts, passing over and below the rear surface; this behaviour has been also shown when Navier-Stokes codes are utilised [9]. In order to asses the physical plausibility of such a prediction, it was decided to carefully investigate the range of angles of attack in which the switching between the conditions with wake passing below or over the wing occurred.

The results showed that the splitting of the vortex in two parts can indeed be observed: in

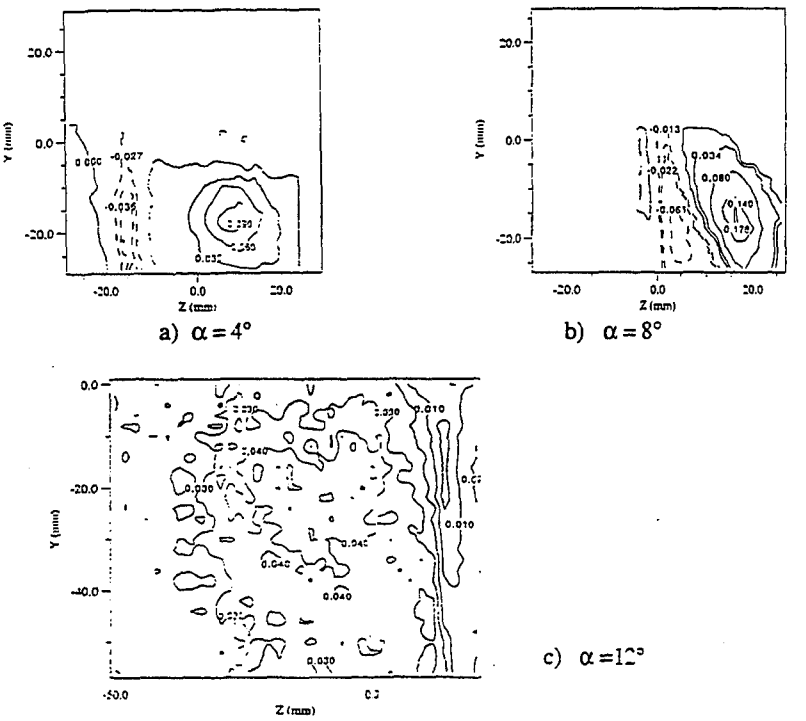

Fig. 8 - Maps of the axial component of the vorticity downstream the wing $\alpha = 4°$

particular, for the configuration analysed in the present investigation, at $\alpha = 9.5°$ the canard vortex divides in two comparable parts at the leading edge of the wing (Fig. 9a): however, it is extremely interesting to observe that downstream of the wing the two vortices are no longer similar, because while the lower one is still perfectly recognizable as a concentrated vorticity structure, the part passing over the wing has been diffused by the the gradients acting on the upper wing surface (Fig. 9b). Furthermore, the splitting occurs only in a very small interval of angles of attack (approximately 0.5° in the present case), with gradually varying ratio between the two resulting vortices. Obviously this observation is not sufficient to deduce that the computational models are capable of actually describing the real physical details and the effects of this phenomenon.

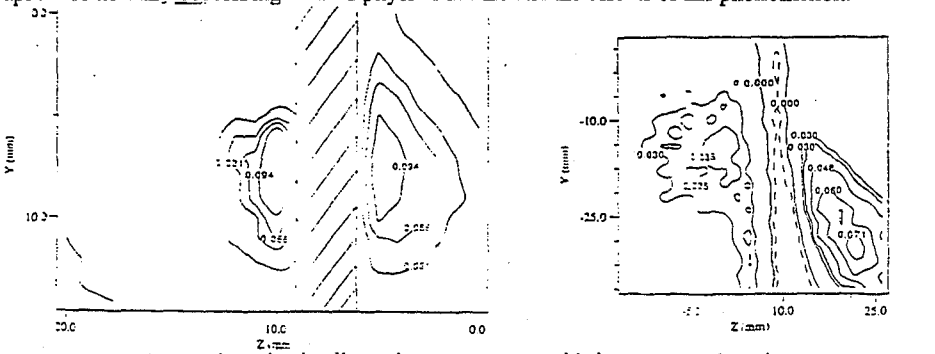

a) near the wing leading edge b) downstream the wing

Fig. 9 - Maps of the axial component of the vorticity : $\alpha = 9.5°$

CONCLUSIONS

The wake of a canard in a canard-wing configuration has been characterized through a simple pressure probe capable of detecting the axial vorticity component; this instrument proved to be extremely practical, and capable of giving in a short time a clear picture of the vorticity field and of its variation with the geometrical and flow parameters.

It was thus possible to study the effect of the interference between the canard wake and the wing, and to observe that when the canard tip vortex passes over the wing surface it is considerably diffused, probably due to the action of the adverse pressure gradients. Furthermore, it was shown that, in a small range of angles of attack, the vortex may be split in two parts at the wing leading edge, and that the one passing over the upper wing surface is again subjected to a greater diffusion and weakening than the one passing below the wing. Finally, the formation of the tip vortex downstream of a lifting surface was found to take place with a complex mechanism, involving the merging of two oppositely-signed vorticity cores, and whose details are highly dependent on the angle of attack, and, presumably, on the geometrical details of the wing tip.

All the above features should be taken into account in the development of numerical codes capable of providing detailed load distributions when close-coupled lifting surfaces are present.

Acknowledgements

The present investigation was financially supported by the Italian Ministry of University and Scientific and Technological Research. Thanks are also due to F. Cannizzo and A. Ricca for their invaluable contribution to the experimental activity.

References

[1] - Buresti G., Lombardi G. - "Indagine sperimentale sull'interferenza ala-canard", *L'Aerotecnica, Missili e Spazio*, Vol. 67, N. 1-4, pp. 47-57 (1988).

[2] - Lombardi G.; Morelli ,M. - " Pressure Measurements on a Forward-Swept Wing-Canard Configuration", *Journal of Aircraft*, Vol. 31, pp. 469-472 (1994).

[3] - Buresti G., Lombardi G., Polito L. - "Analysis of the interaction between lifting surfaces by means of a non-linear panel method", in "Boundary Integral Method Theory and Applications" (L. Morino, R. Piva Eds.) Springer-Verlag, pp. 125-134 (1991).

[4] - Buresti G., Lombardi G., Petagna P. - "Wing Pressure Loads in Canard configurations: a Comparison between Numerical Results and Experimental Data", *The Aeronautical Journal*, Vol. 96, pp. 271-279 (1992).

[5] - Freestone M. M. - "Vorticity Measurement by a Pressure Probe", *The Aeronautical Journal*, Vol. 92, pp. 29-35 (1988).

[6] - Cordova D., Manacorda G. - "Tecniche di Misura della Vorticità nella Scia di Corpi", Tesi di Laurea, Dipartimento di Ingegneria Aerospaziale di Pisa (1992).

[7] - Cannizzo F., Ricca A. - "Sviluppo ed Applicazioni di nuove Metodologie per la Caratterizzazione di Scie di Superfici Portanti", Tesi di Laurea, Dipartimento di Ingegneria Aerospaziale di Pisa (1994).

[8] - Takahashi R.K., McAlister K.W. - "Preliminary Study of a Wing-tip Vortex using Laser Velocimetry", NASA T.M. 88343 (1987).

[9] - Tu E. L. - " Vortex-Wing Interaction of a Close-Coupled Canard Configuration". *Journal of Aircraft*, Vol. 31, pp. 314-321 (1994).

THE AERODYNAMIC COEFFICIENTS AND THE FLOW FIELD AROUND A WIND TUNNEL MODEL VEHICLE

K. ROSSIS, G. BERGELES
Laboratory of Aerodynamics, National Technical University of Athens (Greece)

Abstract
Measurements for the aerodynamic coefficients of a 1:5 scale model vehicle and flow visualization with smoke and tufts are reported. The measurements were conducted in the Aerodynamics Laboratory of the National Technical University of Athens, wind tunnel with fixed ground plane, while special care was given to the shape and the size of the boundary layer in front of the model. From the results a low drag coefficient and a high lift coefficient, as well as an almost constant derivative of the side force are observed aerodynamic characteristics which seems to be in accord with the very streamlined shape of the vehicle. In addition, from the investigation of the airflow pattern, two strong vortices near the rear bumper and the leading edge of the bonnet were also observed.

Key words : Vehicle aerodynamics, aerodynamic coefficient, flow visualization, balance, wind tunnel

Introduction

The measurements of vehicle aerodynamic coefficients is of basic importance for an aerodynamic study because information for the fuel consumption, the speed and the engine power as well as the stability and passenger safety can be deduced. Due to the very strong influence of the basic shape of a vehicle as well as the details of the cooling system, the wheels and the wheel arches and the underbody, on the flow field around a vehicle, it is not possible to draw general conclusions for all types of vehicles under any operational conditions. In other words, even small differences in the shape of two similar vehicles, can lead, more or less, to different aerodynamic characteristics such as, the drag and the lift forces or the pitching moment[1][2][3]. Therefore, for any new shape of vehicle or any external modification in the shape of an existing vehicle it is essential to check its aerodynamic characteristics.

Despite the great developments of the applications of numerical methods in the field of vehicle aerodynamics, the last years, wind tunnel tests are still essential for the development and the final shaping of a vehicle. Results from wind tunnel tests are sensitive to factors such as wind tunnel flow characteristics, the size of the models[3][4], test equipment accuracy etc. However, by using semi-empirical methods, developed after many years of systematic wind tunnel testing, almost all the uncertainties related to these factors can be corrected. The use of scale models in tests, limits the accuracy of the results because of the lack of details in the geometry of the model (the cooling system, the surface finishing, the vehicle floor)[3]. In addition to this, the dynamic similarity is not valid due to the Reynolds number effect. On the other hand, scale model tests have low cost, are very easy to modify and so they are suitable for the development of a new design of vehicle.

The ground plane and the simulation of the road in the wind tunnel is also a very important factor in vehicle wind tunnel tests since the boundary layer which forms on the ground plane increases the effective angle of attack. From modelling experience, it is not possible to obtain a safe conclusion for the use or not of a moving ground plane instead of a fixed ground plane[3][5]. The comparison between wind tunnel and real condition tests for fixed and moving ground plane lead to the conclusion that the results are strongly affected by the model scale, the development of the boundary layer in front of the model and finally from the moving belt properties or the fixed ground plane surface and shape[3].

In this paper, the basic aerodynamic characteristics of a new shape of vehicle will be

investigated and the influence of the cross-wind will be examined. Moreover, the shape and the formation of the wake will be presented.

Wind Tunnel

The tests were conducted in a 2,38 m² test section of the subsonic, closed-circuit wind tunnel of Aerodynamics Laboratory of the NTUA. In this test section, a six components balance is installed while the maximum wind speed is 68m/s and the turbulence factor in the empty test section below 0,2%. The tests for the aerodynamic coefficients were performed at seven wind speeds corresponding to Reynolds numbers of $5{,}43 \times 10^5$ to $2{,}17 \times 10^6$ based on the model length. According to bibliography[3][5] these Reynolds numbers are beyond the critical Reynolds number and the flow is turbulent.

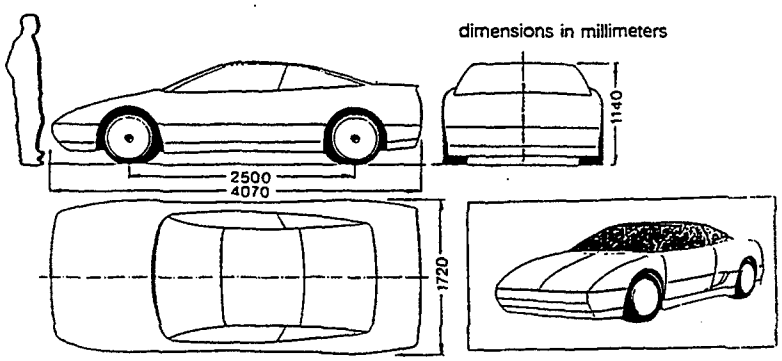

Figure 1 : Principal dimensions of the vehicle

Model

The model was a 1:5 scale sports car model whose principal dimensions are shown in Fig.1. The model was 0,814m long, 0,344m wide, 0,225m in height and had a ground clearance of 0,022m. Moreover, the model had no details for the cooling system and the mechanical parts, no wipers nor mirrors and the floor was flat. The frontal area of the model, including wheels, was 645cm² producing a low wind tunnel blockage factor of 3,6%, with respect to test section area over the ground plane.

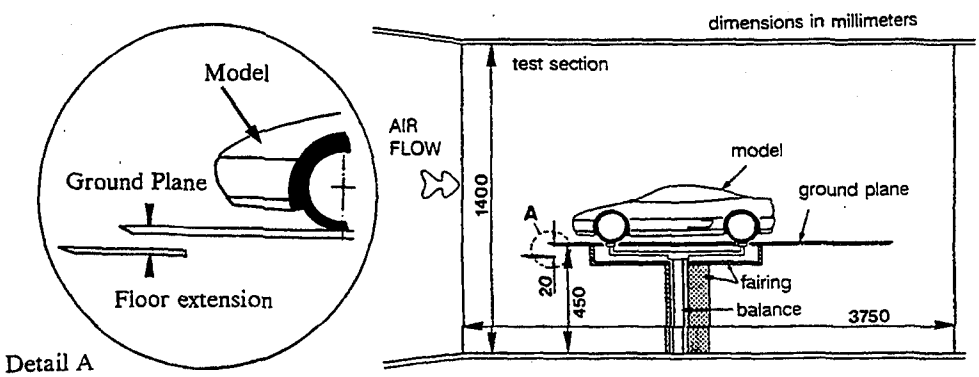

Figure 2 : The installation of the model in wind tunel

Test arrangement

The model was mounted by its wheels onto an aluminum frame which was fixed with the vertical axle of balance as shown in Fig.2, 0,45m over the test section floor. Special care was given to the front edge of the ground plane where a narrow strip (detail A on Fig.2), 0,02m under the ground plane was fixed. This structure was necessary because during the flow visualization in the front area of the ground plane, a high deflection of the flow was observed due to a strong separation in the front part. The model and the floor under it, could turn to any yaw angle, representing cross-wind conditions. Reference wind speed was determined by measuring the difference in static pressures between two cross-sections in the contraction of the wind tunnel. All six components of the aerodynamic force were recorded and were reduced to non-dimensional coefficients with the vehicle yawed at angles from 0 to 30° (in 5° increments) relative to the airstream. The reference system on which the measurements were based, the designations and the definitions of the wind force and wind moment coefficients are shown in Fig.3.

Lift: $L = C_L\ A\ \frac{1}{2}\rho U_o^2$

Drag: $D = C_D\ A\ \frac{1}{2}\rho U_o^2$

Side force: $S = C_S\ A\ \frac{1}{2}\rho U_o^2$

Rolling moment: $R = C_R\ A\ l\ \frac{1}{2}\rho U_o^2$

Yawing moment: $Y = C_Y\ A\ l\ \frac{1}{2}\rho U_o^2$

Pitching moment: $P = C_P\ A\ l\ \frac{1}{2}\rho U_o^2$

C.P. Centre of pressure
K : Forces and moments reference point
α : Yaw angle
l : Wheelbase
A : Frontal area

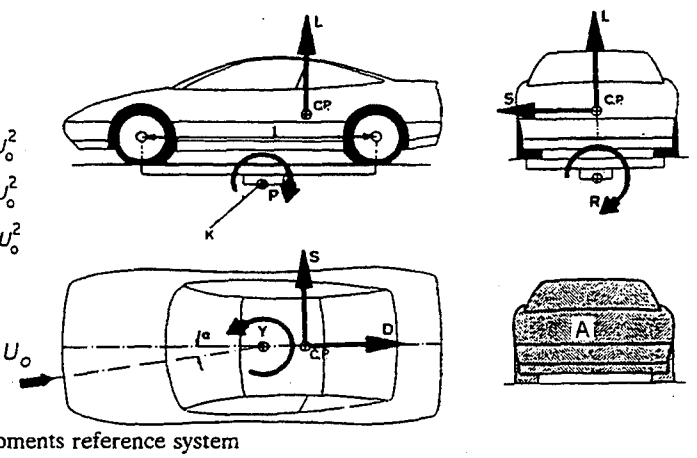

Figure 3 : Forces and moments reference system

In order to make the airflow visible and to get an overall picture of the phenomena, wool tufts fixed onto the model as well as oil smoke, coming from a smoke probe were used. During smoke visualization tests a special lighting source was used. With this arrangement a light sheet covered the model visualising the flow.

Data acquisition

The data acquisition was computerized using an analog to digital signal convertor. The signals from the load cells of the balance, as well as all corrections and calibrations were automatically taken into account. Real time processing allowed continuous monitoring of the experimental procedure while the experimental uncertainty of measurements was below 2%.

Results

Aerodynamic coefficients

The variations of the measured aerodynamic coefficients of drag, lift, side force, rolling, yawing and pitching moment as a function of the Reynolds number at seven yaw angles (b) are shown in Figure 4 (a,b,c,d,e,f respectively). Inspection of all the experimental data leads to the observation that for almost all the yaw angles the changes are small for all the velocities except the pitching moment coefficient at the 25 and 30 degree yaw angle and it is obvious that there is only a small effect of the Reynolds number. These facts can be rendered in the first place to the satisfactory modification of the front edge of the ground plane which reduces the boundary layer in front of the model and keeps the airflow steady and uniform and secondly to the low and steady

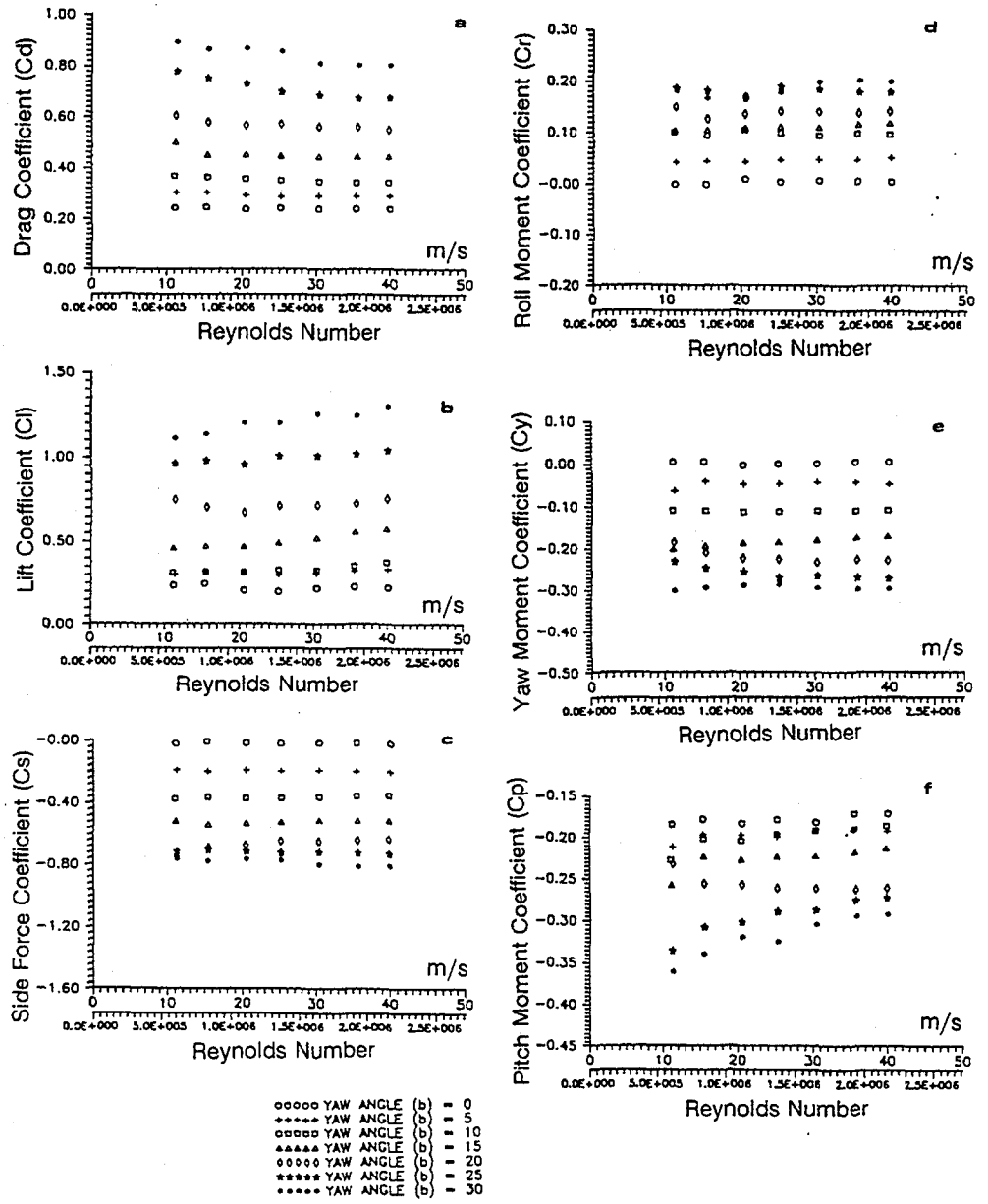

Figure 4 : Aerodynamic coefficients of drag(a), lift(b), side force(c), rolling moment(d), yawing moment(e), pitching moment(f) vs. Reynolds number

value of the blocking and turbulence factor. From the results it is deduced that the drag coefficient based on the wheelbase distance is low, equal to 0,23 at zero yaw angle. A diagram of the drag coefficient in terms of the yaw angle, Fig.5a, shows that the slope of the curve up to 10° yaw angle is small, while a much sharper increase of the coefficient in the range of 10 to 30 degrees is clearly

visible. Considering the drag components analysis (see Scibor-Rylski[14] and Carr[4] among others) it could be stated that the measured drag coefficient (0,23) refers to the form drag, the induced drag as well as the drag of the wheels and wheel wells. From the same analysis it turns out that the contribution of the interference drag (underbody roughness, drip-rails, window recesses, external mirror) as well as the internal flow drag (cooling system) to the total drag is approximately 28%. Adding that percentage to the measured drag coefficient a very approximate estimation of the total drag coefficient of 0,30 ($\pm$0.01) is deduced.

Low drag can be explained by considering the very smooth outer shape of the model, the curvature of the front part in the vicinity of the bonnet leading edge and under the bumper as well as to the high inclination of the front and rear windscreen that helps in maintaining a smooth airflow over the greater part of the upper surface. In addition to this, one has to bear in mind that the frontal area of the vehicle was only 1,61m², including the wheels and therefore the total drag force acting on the vehicle will also be small.

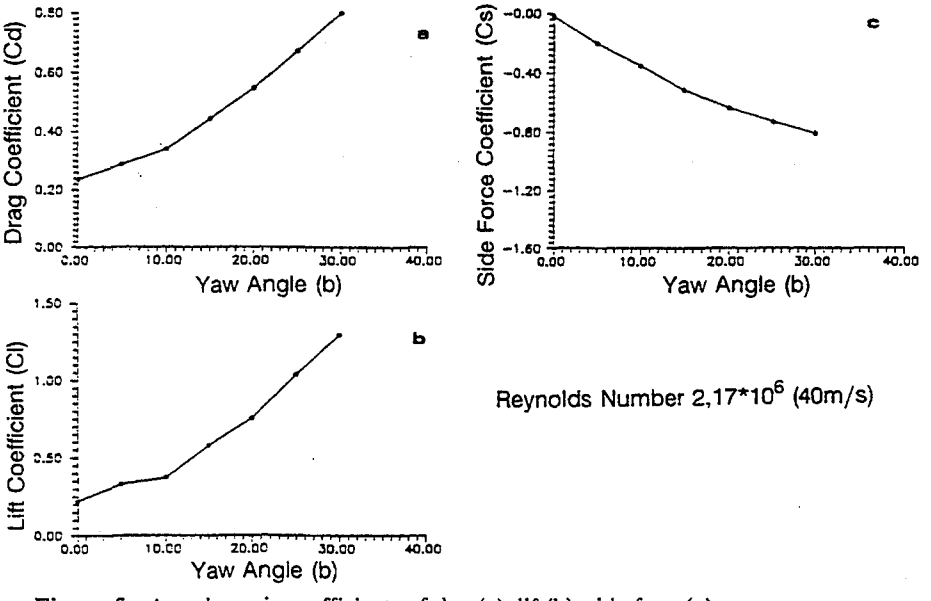

Figure 5 : Aerodynamic coefficients of drag(a), lift(b), side force(c)

Contrary to the low drag, the lift coefficient is high, nearly close to 0,22. This seems to be in accord with the very streamlined shape of the vehicle which tends to lower local pressures over the greater part of the upper surface of the model. In addition, the raised part under the front bumper of the model, the small ground clearance and the lack of significant details, mainly in the front part of the model such as the air intakes of the engine cooling system results in an increase of the total aerodynamic lift. Although the high lift coefficient seems to be an exaggeration, various studies (see Scibor-Rylski[14]) have shown that the lift coefficient range for the two seatersgroup of sports cars is usually relatively high, extending up to 0,41. As it was mentioned earlier for the drag coefficient, the variation of the lift coefficient for yaw angle up to 10° is small, while a sharp increase of the coefficient in the range of 10 to 30 degrees is observed, Fig.5b.

Concerning the pitching moment Figure 4f shows that for all the yaw angles the moment is negative (nose down) with moment centre at centre of the wheelbase distance and it is particularly well known that this characteristic gives very good driving stability and performance for almost all vehicles. Considering the negative pitching moment and the wedge shape of the front part of the model it turns out that the positive lift is mainly due to the shape of the tail of the vehicle where a rear airfoil should be installed in order to increase the local pressure and to

reduce the overall aerodynamic lift. In addition to the rear ridge installation, the flat smooth underbody can be replaced with a streamlined venturi floor with significant benefits for the lift as have been shown by Sardou[13], Barnard and Vaugham[3] for similar type of vehicles.

Figure 4c shows a diagram of the side force coefficient in terms of the Reynolds number for various yaw angles. This diagram shows that there are no significant variations of the coefficient for all the Reynolds number range. Additionally, as Fig.5c shows, the curve of the side force coefficient vs. yaw angle is almost linear, which allows us to consider the derivative of the side force as constant. This seems to be in accord with the case of a typical streamlined vehicle as Scibor-Rylski[14] has already shown although in our case the slope of the curve is much smaller. The variation of aerodynamic coefficients of rolling and yawing moment also seems to be in accord with the conclusions of Scibor-Rylski[14] and others, Figures 4d,4e. Nevertheless, the variation of the two coefficients is small, much smaller than was expected due to the streamlined shape of the vehicle. It is well known that when the vehicle shape is bad from an aerodynamic point of view the influence of the cross-wind is smaller than in a well streamlined vehicle. In conclusion, it can be stated that the shape of the tested vehicle performs like a well streamlined vehicle as far as drag and lift force are concerned, and like a less streamlined vehicle as far as side force and aerodynamic moments are concerned.

Airflow visualization

The second part of this paper summarizes the results of the flow visualization around the model and into the region of the wake. The object of the research was to localize the areas where an airflow separation occurs as well as to investigate the shape of the wake. Conclusions of the visualization are also useful for the study of the velocity field since in that way a more efficient distribution of the measurement points in the wake area is possible. The airflow at the bonnet leading edge and near the ground floor is illustrated in Figures 6a and 6b.

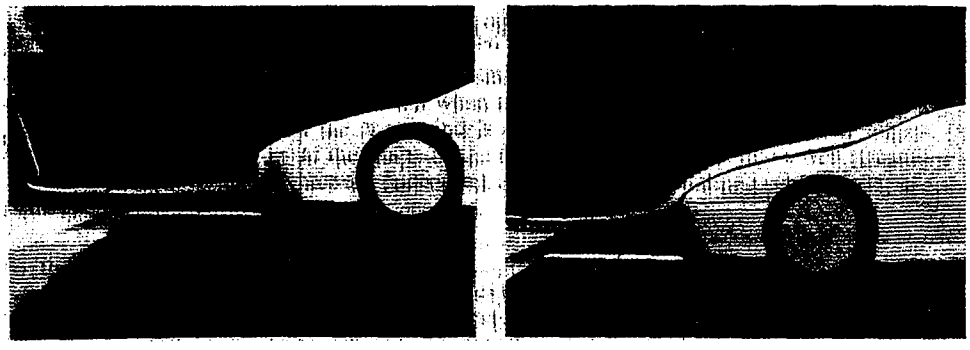

Figure 6 : The airflow at the bonnet leading edge

Without exception the flow is rather smooth over the front bumper, the bonnet and the windscreen. It is clearly visible that the smoothness at the corner of the bonnet and the windscreen and the high inclination of the A-pillar, eliminates the separation bubble which otherwise could had been formed at the bottom of the windscreen. It is also observed that the airstream in the vicinity of the ground floor by means of the modification in the region of the leading edge, is smooth, steady and parallel to the floor. Along the centre line of the model, no disturbance of the flow is observed except at a small region at the rear windscreen base, over the rear bonnet. In this area, the airflow is disturbed because of the confluence of two basic airstream lines, the oncoming flow over the model and the other in the rear side window passing over the C-pillar. As Figure 7 shows, the latter, following the side variations of the model and due to the step which is formed over the rear wheel housing as well as due to the high C-pillar radii, meets the main part of the

oncoming flow in the base of the rear windscreen. The step over the rear wheel housing is also responsible for the upward direction of the tufts in the region of the rear side window as shown in Fig.8. Despite the light turbulence in the windscreen base, the flow returns to steady over the rear hood and thus it could be deduced that due to the small height of the cabin which slopes gently backwards the formation of the wake is not affected by the cabin. This fact contributes significantly to keep drag coefficient low since flow vortices start to form only in the base area. at the rear end of the model. The formation of the trailing vortices in the wake area along the centre line is shown in Figure 9.

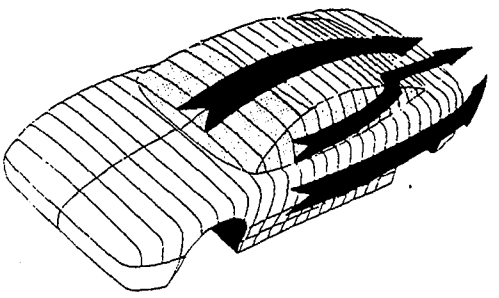

Figure 7 : The flow pattern at the rear windscreen

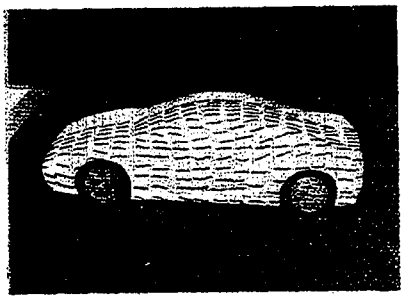

Figure 8 : The airflow in the region of the C-pillar

As the flow visualization disclosed, the vortices in this region present a similar picture to that Ahmed[2] had shown, for the case of a fast back car model. To be more specific, the flow under the floor of the model produces a strong anti-clockwise vortex moving towards the upper area of the wake. In addition to the lower vortex, in the leading edge of the rear bonnet where a sharp extension of the bonnet is formed, a narrow clockwise vortex is produced. These two regions of vortices compose the main area of the wake which is extended up to a distance of 1/5 of the total length of the body behind the rear bumper. In the vicinity of the two vortices, a small vortex rotating in a clockwise direction occurs which by means of the strong airstream under the floor of the model is moving upward, Figure 9.

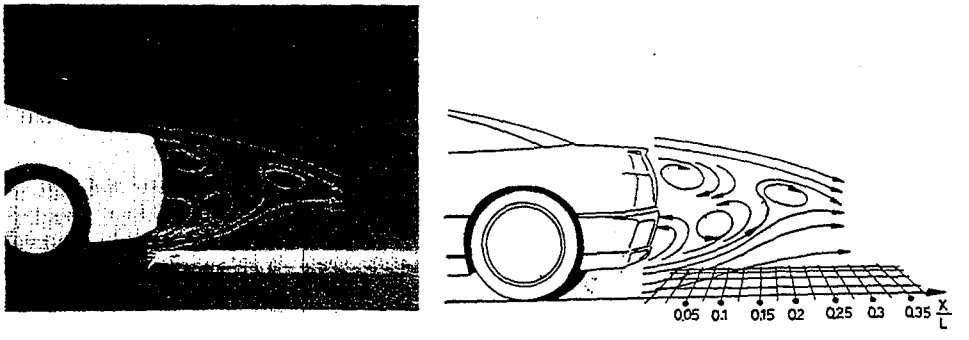

Figure 9 : The wake area

Conclusions

In this study, the six aerodynamic coefficients as a function of the airflow speed and the

yaw angle were shown. For all the yaw angles the variation is small and no significant Reynolds number effect was noticed. The drag coefficient was low while lift was high. This is probably due to the streamlined outer shape of the model, the lack of details such as air inlets in the front bumper. Due to the wedge shape and the small ground clearance, the pitching moment was negative for all the yaw angles. The behavior of the airflow pattern was investigated during the flow visualisation. The curvature of the front part in the vicinity of the bonnet leading edge and under the bumper as well as the high inclination of the front and rear windscreen helps in maintaining a smooth airflow over the greater part of the upper surface except at the base of the rear windscreen where a small separation was observed. The wake area which extends backwards up to 1/5 of the total model length, includes two strong vortices one near the rear bumper and the other at the extension of the leading edge of the bonnet. In addition to this a small vortex in the vicinity of these two vortices was also observed.

References

1. Ahmed S.R., "Influence of ground clearance on the aerodynamic characteristics and wake structure of a vehicle type body", Inter. Symposium on Vehicle Aerodynamics, Wolfsburg 1982.
2. Ahmed S.R., "An experimental study of the wake structures of typical automobile shapes", Journal of Wind Engineering and Industrial Aerodynamics, Vol.9 (1981),pp 49-62.
3. Barnard R.H., Vaughan H., "The aerodynamic tuning of a group C sports racing car", Journal of Wind Engineering and Industrial Aerodynamics, Vol.22 (1986), pp 279-289.
4. Carr G.W., "Potential for aerodynamic drag reduction in car design", International Journal of Vehicle Design, Technological Advances in Vehicle Design Series, SP3, Impact of Aerodynamics on Vehicle Design, 1983, pp 44-56.
5. Flegl, H. and Bez, U. (1983) "Aerodynamics - Conflict or Compliance in Vehicle Layout ? ", Int. Journal of Vehicle Design, Technological Advances in Vehicle Design Series, SP3, Impact of Aerodynamics on Vehicle Design, pp 9-43.
6. Hucho, W.H., "The Aerodynamic Drag of Cars. Current understanding, unresolved problems and future prospects", Sovran G., Morel T., Mason Jr W.T. (Eds.): Aerodynamic Drag Mechanisms of Bluff Bodies and Road Vehicles, Plenum Press, New York, 1978.
7. Hucho W.H., "Aerodynamics of Road Vehicles", from "Fluid mechanics to vehicle engineering", Butterworth and Co.Ltd.,1987.
8. Mason Jr W.T., Sovran G., "Ground-plane effects on the aerodynamic characteristics of automobile models - an examination of wind tunnel test technique", Advances in Road Vehicle Aerodynamics, 1973, B.H.R.A.
9. Mercker E., "A blockage correction for automotive testing in Wind Tunnel with closed test section", Journal of Wind Engineering and Industrial Aerodynamics, Vol.22 (1986) pp 149-167.
10. Mercker E., Breuer N., Berneburg H., Emmelmann H.J., "On the aerodynamic interference due to the rolling wheels", Vehicle Aerodynamics : Recent Progress, SP 855, 1991, Society of Automotive Engineers Inc., pp 63-79.
11. Morelli A., "Aerodynamic basic bodies suitable for automobile applications", International Journal of Vehicle Design, Technological Advances in Vehicle Design Series, SP3, Impact of Aerodynamics on Vehicle Design, 1983, pp 70-98.
12. Onorato M., Costelli A.F., Garrone A., Viassone L., "Experimental analysis of vehicle wakes", Journal of Wind Engineering and Industrial Aerodynamics, Vol.22 (1986), pp 317-330.
13. Sardou M., "Reynolds effect and moving ground effect tested in a quarter scale wind tunnel over a high speed moving belt", Journal of Wind Engineering and Industrial Aerodynamics, Vol.22 (1986), pp 245-270.
14. Scibor-Rylski, A.J., "Road Vehicle Aerodynamics", Pentech Press, London, 2nd Edition, 1984.
15. Takagi M., Hayashi K., Shimpo Y., Uemura S., "Flow visualization techniques in automotive engineering", International Journal of Vehicle Design, Technological Advances in Vehicle Design Series, SP3, Impact of Aerodynamics on Vehicle Design, 1983, pp 500-511.

EXPERIMENTS ON MODEL COOLING IN PERIODIC FLOW REGIME

S. RAGHUNATHAN
Department of Aeronautical Engineering
The Queen's University
Belfast, Northern Ireland,
United Kingdom

Abstract

Experiments were performed on an 18% thick biconvex aerofoil and a circular cylinder at periodic flow conditions and at (surface temperature)/(model adiabatic temperature) of 0.99 and 0.59 to study the effect of model cooling on periodic flows. Model cooling had an effect of stabilising the flow with significant reduction in periodic pressure fluctuation levels. In the case of transonic flow over the biconvex aerofoil model cooling reduced the amplitude and frequency of shock motion. In the case of flow on the circular cylinder cooling had a stable effect on the sub - critical flow. The results have implications to testing of models in wind tunnel at non adiabatic surface conditions.

Nomenclature

c	model chord length, mm
c_d	drag coefficient
c_p	pressure coefficient $(p-p_\infty)/q$
c_{pb}	back pressure
C_{pte}	pressure coefficient measured at x/c = 0.95
d	cylinder diameter
f	frequency, Hz
F(n)	contribution of p^2/q^2 in frequency band Δn.
M	freestream Mach number
M_1	Mach number just upstream of the shock
n	nondimensional frequency parameter, $2\pi fc/u$
$\sqrt{n}F(n)$	rms buffet excitation parameter $\Delta p/(q\epsilon^{1/2})$
$\overline{p}$	mean pressure N/m^2
$\overline{p}$	rms pressure fluctuations, N/m^2
p'	instantaneous pressure
q	kinetic pressure, N/m^2
Re	Reynolds number based on model chord
T_w, T_{ad}	wall and adiabatic recovery temperature, K
t	time, s
u	freestream velocity, m/s
ϵ	$\Delta f/f$
x,y	coordinates from the leading edge of model
x	co-ordinates along the tunnel centre line measured from the axis of the cylinder
y	co-ordinates normal to the tunnel centre line

Introduction

Convective heat transfer can have significant influence of aerodynamics of flow over bodies. Experiments on boundary layers with heat transfer have shown that the boundary-layer development[1], laminar or turbulent, boundary-layer transition[2,3] and separation on a model surface [4,5,6,7] are sensitive to heat transfer between the model and the flow field. It can be inferred from these experiments that cooling ($T_w/T_{ad} < 1$) postpones boundary-layer transition and for a turbulent boundary-layer produces a fuller velocity profile, increased skin friction, and decreased boundary-layer thickness and shape factor. In the case of separated flows cooling also reduces the length of separation bubble. Heating the model ($T_w/T_{ad} > 1$) has the opposite effect to that of cooling. In the case of transonic flow with shock interaction, heat transfer can have a significant effect directly on the shock wave boundary-layer interaction and indirectly through the effect on the boundary-layer approaching the shock wave[4,8,9]. It has been postulated[9] that cooling the surface will have a favourable effect on shock wave boundary-layer interaction since the increase in the surface shear stresses associated with cooling will delay the occurrence of separation. In testing a model in short duration facilities and cryogenic wind tunnels there could be significant differences between the model temperature and the free stream recovery temperature leading to spurious scale effects in measurement of both static and dynamic forces on a model. It has been estimated[10,11] that an increase in one per cent in model-to-stream temperature ratio has an effect equivalent to that of three and a half per cent reduction in the Reynolds number and some of the scale effects associated with Reynolds number can be identified by cooling or heating the model relative to adiabatic temperature of the air flow. Recent experiments[12,13] on biconvex aerofoils with cooling tend support these suggestions. The above experiments also have demonstrated that surface cooling has a large effect on dynamic measurements such as buffet.

In the case of flow around a circular cylinder both the mean and unsteady flow field is Reynolds number dependent based on which at least four distinct regions of flow have been established[14-18]. These regions of flow, although strongly dependent on Reynolds number is also sensitive to cylinder surface roughness, and freestream turbulence[14] and surface heating[6].

In order to obtain an understanding of the effect of heat transfer on periodic flows, experiments were performed on an 18% thick biconvex aerofoil and a circular cylinder at periodic flow conditions and at two ratios of model surface to adiabatic recovery temperature of 0.99 and 0.59. The results of these experiments are presented in this paper.

Experiments

Experiments were made in a 100 x 100 mm intermittent transonic wind tunnel which had a running time of 15 s. The inlet total pressure and temperature were atmospheric. The tunnel had closed side walls and perforated top and bottom walls. The porosity of the perforated walls was 9.6% (Fig. 1a).

One of the side wall of the tunnel had flush mounted Kulite pressure transducer at a position x/c=0.65 and y/c=0.17 (Fig. 1a) to sense the pressure fluctations associated with the periodic flows.

The 18% thick biconvex aerofoil was of 40 mm chord (Fig.1b) and tested transition free. It has been shown that this configuration produced periodic flows at transonic speeds with laminar or turbulent boundary layer/shock wave interactions[19]. In the present experiments the type of shock wave/boundary-layer interaction was inferred from the mean pressure distributions and high speed schlieren pictures.

The circular cylinder model was 7mm in diameter, spanning the tunnel. The model diameter chosen resulted in a blockage of 6.9% and the measured results were corrected for this blockage. Preliminary calculations indicated that for the model diameter chosen the vortex shedding frequency of the model did not coincide with the tunnel resonance frequency for this tunnel. Further it was established by spanwise pressure measurements that flow was two dimensional for 80% span.

Thermocouples were installed within the models for temperature measurements. Typical thermocouple positions for the biconvex model are shown in Fig. 1b. The thermocouples were copper-constantan (type T) which had an operating temperature range of 73-673 K. Further details of the model are given in Refs. 11 and 12.

The models were pre-cooled in a bath of liquid nitrogen at T= 77K prior to installation in the tunnel. The tunnel was started when the model temperature reached a few degrees below the required test temperature. The change in mean static pressures on the model (as observed by continuous sampling) over a period of 1 s was also found to be negligible. Further, the differences in temperatures recorded by thermocouples at various locations on the model at any instant of time were less than 4 K. Hence it was assumed that the model was at nearly uniform temperature during a sample period and the flow was a quasi-steady flow. No frost formation on the model was noticed even during runs at low temperatures.

A Scanivalve with a Druck pressure transducer (type PDCR22) and pressure storage box was used for static pressure measurements.

Surface flow visualisation at adiabatic wall temperature was performed by china clay method where the model surface was coated with a mixture of fine china clay and methyl salicylate prior to a run and the flow pattern on the model was observed subsequently. However at low temperature methyl salicylate is unsuitable as a solvent as it had a melting point of 260 K and tended to freeze. The solvent used for the china clay technique at low temperature was propane 1-OL which had a melting point of 146 K.

Experiments were coducted at a Mach number of 0.765 for the biconvex aerofoil. The experiments on the cylinder was conducted at a Mach number of 0.3 an at two levels of freestream turbulence.

Results of biconvex model tests

Fig. 2 shows the mean pressure distributions on the aerofoil for a fixed freestream Mach number of 0.765 and for temperature ratios of T_w/T_{ad}=0.99 and 0.59. The Mach number chosen is within the flow region where significant periodic oscillations occur on the aerofoil. The pressure distribution for adiabatic wall conditions is typical of laminar boundary-layer/shock wave interactions in transonic flow with an extended interaction region. It is clear from Fig. 2 that cooling the model alters the mean pressure distribution significantly in the region of shock wave boundary-layer interaction. For T_w/T_{ad} =0.59 there is an increase in the shock Mach numbers, an increase in pressure gradients in the interaction region, and a decrease in the extent of interaction. Similar effects of cooling have been observed by Inger et al[8] in a transonic turbulent boundary-layer interaction and by Frishett[6] in a supersonic turbulent boundary-layer interaction.

It is generally understood that for a laminar boundary-layer a surface heat transfer produces large changes in the velocity profile[9]. The primary effect of energy transfer from the air flow towards the surface, due to temperature gradients, is increased velocities near the surface and fuller velocity profile resulting in increased shear stresses near the surface. Reduced temperatures near the surface should decrease viscosity and increase the density of the gas. This increases the effective Reynolds number for the boundary layer. A combined

effect of increased skin friction and increased effective Reynolds number is to increase the stiffness of the boundary layer to separate.

Large changes in pressure distribution observed on the cooled model (Fig. 2) are due to the effects of cooling on the boundary layer such as reductions in boundary-layer thickness and sonic height and fuller velocity profile. In transonic flow at low Reynolds numbers, the viscous layer is of the same thickness as the sonic height, and cooling has a large effect on both. The reduction in sonic height should reduce the communication across the shock wave which is the likely reason for the increased pressure gradients in the region of shock wave/boundary layer interaction. The boundary-layer development downstream of the shock is dependent on the boundary-layer parameters at the foot of the shock, and hence cooling should have an indirect effect on the separated flow.

The divergence of mean trailing edge pressure with the increase in freestream Mach number would normally be taken as the onset of trailing edge boundary layer separation. It is observed from Fig. 2 that for a fixed freestream Mach number model cooling increases the mean pressure near the trailing edge.

The china clay flow visualisations for T_w/T_{ad} = 0.99 and 0.59 are shown in Figs. 3a and 3b respectively. In these figures the direction of airflow is shown by an arrow. The attached airflow (A) and separated airflow (S) are clearly shown in these diagrams. The line dividing the two flows is the shock position which compares favourably with that inferred from the pressure distribution. It can be observed from the pressure distributions (Fig. 2) and china clay flow visualisation (Fig. 3) that the mean shock position and length of separation is virtually unchanged with model cooling and therefore the reduced trailing edge pressure with cooling (Fig. 2) can be attributed to a reduction in the thickness of the separated layer. Similar trends, albeit of reduced magnitude have been observed for comparable tests with fixed transition[12].

Fig. 4 shows the effect of cooling on spectra of the pressure fluctuations. The empty tunnel had no discrete frequency components as mentioned earlier. The spectrum at adiabatic wall conditions has a peak at a fundamental reduced frequency n=1.1 which corresponds to a frequency of f=1125 Hz. This value compares favourably with values quoted previously[20-22]. Cooling has reduced both the levels and frequency of pressure fluctuations. As regard to the frequency both the fundamental frequency and the harmonics are reduced by cooling. The reduction in frequency of shock oscillations due to cooling is attributed to several factors. These include the reduction in the velocity of sound, increased velocities near the surface and reduced shear layer thickness.In addition the spectra clearly show a significant reduction in the amplitude of shock oscillations. It is also observed that cooling has resulted in an increase in broadband fluctuation levels. The reasons for this increase are not yet understood.

Fig. 5 shows c_p distribution for the flow around the cylinder at R = 47,000 Tu = 1.28% and 3.12% and at temperature ratios T_w/T_{ad} = 0.99 and 0.59. The effect of cooling on C_D, S, Vortex shedding are shown in Figs. 6 to 8 respectively.

It can be observed from Fig. 5 that at low Tu where the boundary layer on the surface prior to separation is laminar cooling has a large effect on C_p distribution. The effect of cooling on C_p is negligible at high Tu levels where the boundary layer is essentially turbulent. These results are similar to those observed with experiments in transonic flows. The increase in C_p values with cooling in (Fig.5) can be attributed to the increase in velocities near the surface. The postponement of boundary layer separation on the cold model can also be observed form this figures.

In the case of turbulent boundary layers the effect of heat transfer is confined essentially within the laminar sub-layer which forms only a small part of the total boundary layer. Outside the laminar sub-layer the energy exchange due to turbulence dominates over the heat transfer effects and therefore the effect of cooling on the flow field is very small.

At low Tu level model cooling has produced improved pressure recovery at the base of the cylinder (Fig. 5). A significant decrease in the values of drag coefficient (Fig. 6) and no appreciable change in Strouhal numbers (Fig. 7). Model cooling has also reduced the amplitude of periodic vortex shedding (fig. 8). It is suggested for flow around a circular cylinder in a subcritical regime model cooling stabilises the subcritical nature of the flow but with a significant reduction in unsteady pressure fluctuation levels. It has been reported that heating a cylinder in a subcritical regime can change the flow regime to supercritical[4]. It can also be observed from Fig. 5 that model cooling increases the adverse pressure gradients on the surface of the cylinder. It may be possible that the adverse pressure gradient has promoted boundary layer transition on the cylinder surface resulting in a turbulent wake. The fact that the model cooling has reduced the unsteady pressure fluctuation levels and that the Strouhal numbers have not changed significantly indicates this is not the case.

Conclusions

Experiments were conducted to study the effect of model cooling on periodic flows on a biconvex aerofoil at transonic speeds and a circular cylinder at sub critical regime. It can be concluded from these experiments that model cooling has a significant effect on both the mean and dynamic pressure levels on a model. The general effect of model cooling in periodic flow regime is to decrease the buffet levels and frequencies associated with the periodicity.

References

1. Van Duest, E.R., "Convective Heat Transfer in Gases", In: turbulent Flows and Heat Transfer in High Speed Aerodynamics and Jet Propulsion, Section F. Vol. 5, Oxford University Press, 1969.
2. Dougherty, N.S. and Fisher, D.F., "Boundary Layer Transition on a 10° Cone: Wind tunnel and Flight Test Correlation", AIAA paper 80-01544, 1980.
3. Liepmann, H.W. and Fila, G.H., "Investigations of Effect of Surface Temperature and Single Roughness Elements on Boundary Layer Transition", NACA TN 1196, 1947.
4 Macha, J.M., Norton, D.J. and Young, J.C. "Surface Temperature Effects on Subsonic Stall", AIAA paper 72-960, 1972.
5. Lynch, F.T., Faucher, M.F., Patel, D.R. and Inger, G.R., "Adiabatic Model Wall Effects on Transonic Airfoil Performance in Cryogenic Wind Tunnels", AGARD CP 348, paper 14, 1983.
6. Frishett, J.C., "Incipient Separation of a Supersonic Turbulent Boundary-layer Including Effects of Heat Transfer", PhD Thesis, University of California, 1971.
7. Elfstrom, G.M., "Turbulent Separation in Hypersonic Flow", Imperial College of Science and Technology, Aero. Report 71-16, 1971.
8. Inger, G.R., Lynch, F.T. and Faucher, M.F., "A Theoretical and Experimental Study on Non-Adiabatic Wall Effects on Transonic Shock/Boundary-layer Interaction", AIAA paper 83-1421, 1983.
9. Delery, J.M., "Shock Wave/Turbulent Boundary Layer Interaction and its Control", Prog. Aerospace Sci., Vol. 22, pp 209-280, 1985.
10. Green, J.E., Weeks, D.T. and Pugh, P.G. "Heat transfer as a source of spurious scale effects in subsonic and transonic wind tunnels", ARC 38 182, May 1985.
11. Mabey, D.G., "Effects of Heat Transfer in Aerodynamics and Possible Implications for Wind Tunnel Tests", Progress in Aerospace Sciences, Vol. 27, No. 4, pp 267-303,

1991

12. Raghunathan, S., Zarifi-Rad, F. and Mabey, D.G., " Investigations of the effect of model cooling on periodic transonic flow", AGARD conference Proc. 507, paper 26, 1992.
13. Zarifi-Rad, F., "Effect of model cooling on periodic transonic flow",PhD thesis, Aero. Eng. Dept., Queen's University of Belfast, 1991.
14. Morkovin, M.V., "Flow around circular cylinder - a kaleidoscope of challenging fluid phenomena", The Martin Company, Baltimore, Maryland, 1964.
15. Achenbach, E., "Distribution of local pressure and skin friction around a circular cylinder in cross flow up to Re = $5x10^6$", J. Fluid Mech., Vol. 34, pp 625-639, 1968.
16. Bearman, P.W., "On vortex shedding from a circular cylinder in the critical Reynolds numbers regimes", J. Fluid Mech., Vol. 37, pp 577-585, 1969.
17. Achenbach, E., "Influence of surface roughness on the cross flow around a circular cylinder", J. Fluid Mech., Vol. 46, Part 2, pp 321-335, 1971.
18. McCroskey, W.J., "Introduction to unsteady aspects of separation in subsonic and transonic flow", AGARD LS94, 1978.
19. Raghunathan, S., Hall, D.E. and Mabey, D.G., "Alleviation of Shock Oscillations in Transonic Flow by Passive Control", The Aeronautical J., Vol. 94, No. 937, pp 245-250, 1990.
20. McDevitt, J.B., "Supercritical Flow about a Thick Circular Aerofoil", NASA TM 78549, 1979.
21. Mabey, D.G., "Oscillatory flow from shock induced separation on biconvex aerofoils of varying thickness in ventilated wind tunnels", AGARD CP Paper 11, 1980.
22. Edwards, J., "Transonic shock oscillations calculated with a new interactive boundary layer coupling method". AIAA Paper 93-0777.

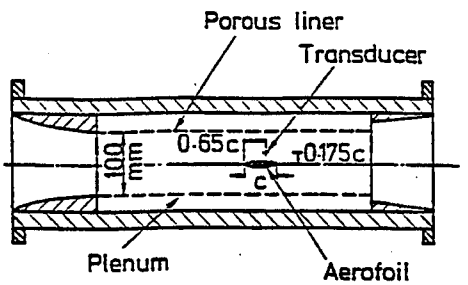

FIg. 1a. Model arrangement.

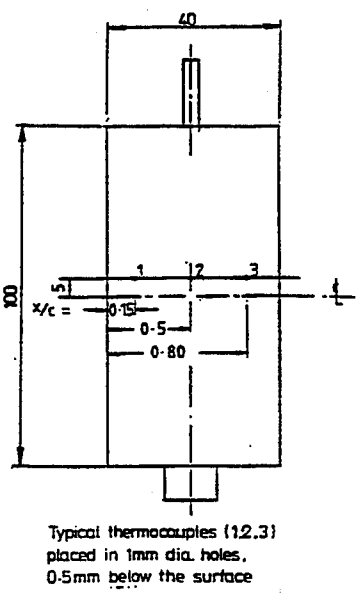

Fig. 1b. Model details - aerfoil.

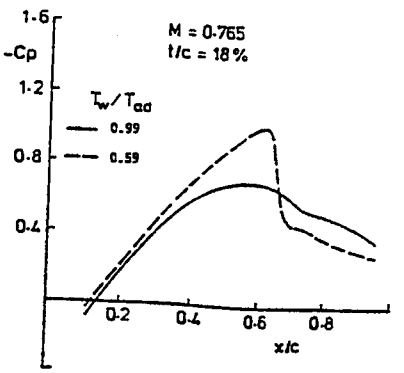

Fig 2. Mean pressure distributions - aerfoil.

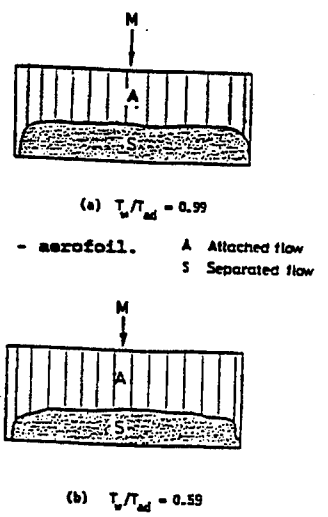

Fig. 3. Flow visualisation - aerofoil.

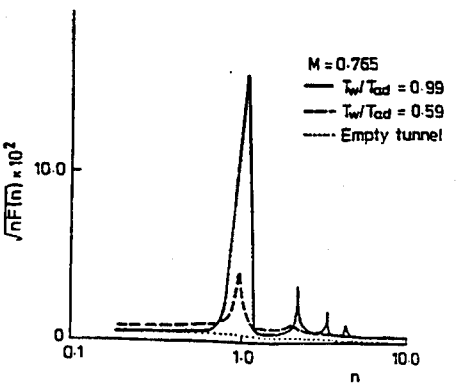

Fig. 4. Spectra of pressure fluctations - aerofoil.

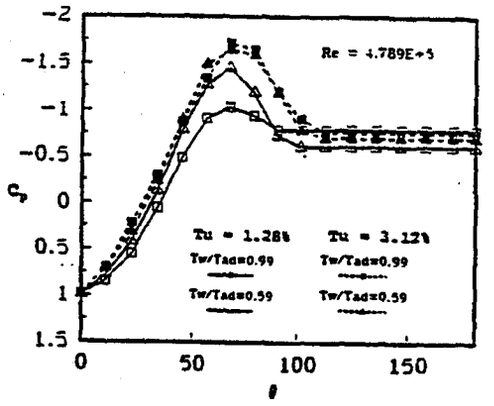

Fig. 5 Mean pressure distributions - cylinder.

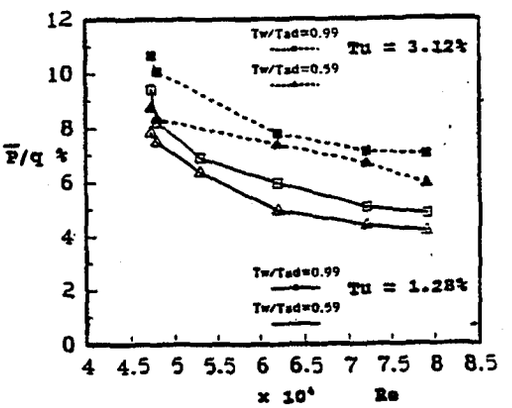

Fig. 7. Pressure fluctation levels - cylinder.

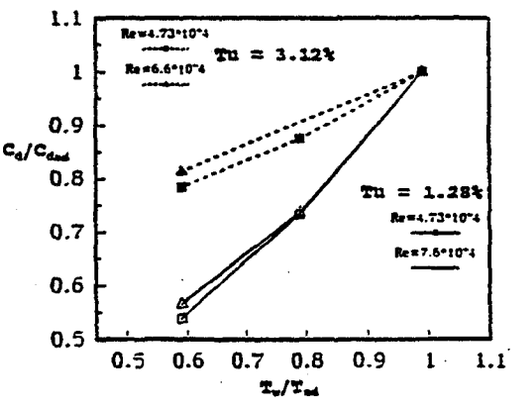

Fig. 6. Normalised drag coefficients - cylinder.

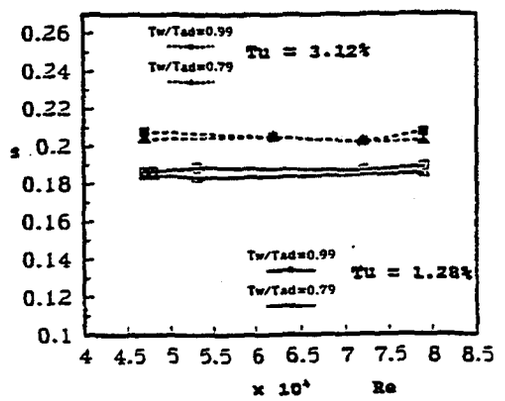

Fig. 8. Strouhal numbers - cylinder

STUDIES OF THE FLOW OVER RAPIDLY PITCHING, TWO DIMENSIONAL AEROFOILS

by

R.B. Green*, R.A.McD. Galbraith*, F.N. Coton*, J.N. Stewart†, I. Grant†

***University of Glasgow, Glasgow, Scotland**

†Heriot Watt University, Edinburgh, Scotland

SUMMARY

This paper presents data from experimental tests to assess the behaviour of the fluid flow over two-dimensional aerofoils pitching from the fully separated state to the fully attached state. Surface pressure data indicate that the bluff body behaviour is extended to much lower incidences than in static tests, and this effect has a characteristic time duration which is independent of the reduced pitch rate. Smoke flow visualisation suggests that, in addition to a delay in attachment, convection of wake fluid away from the aerofoil surface is important. Finally, particle image velocimetry used in conjunction with surface pressure measurements reveal that the bluff body behaviour ends when the wake has diminshed in size considerably.

Nomenclature

c	aerofoil chord (m)
C_N	normal force coefficient
$C_{N\,min}$	minimum normal force
f	attachment position from leading edge as fraction of chord length
r	reduced pitch rate ($\omega c/2U$)
t	time (s)
Δt	ramp-down time delay (s)
U	free stream speed (ms^{-1})
x	chordwise position from leading edge (m)
α	incidence (deg)
τ	non-dimensional ramp-down time delay ($\Delta tU/c$)
ω	pitch rate (rad s^{-1})

1. INTRODUCTION

The unsteady aerodynamics of dynamic stall have for some time received much investigation (see for example McCroskey et al. [1], Lorber & Carta[2], Green et al. [3]) However, the recovery from stall (i.e. re-attachment) has received far less attention, and this is the subject of the present paper. If an aerofoil model is "ramped-down" (i.e. pitched at a uniform rate from high to low incidence) stall recovery is free from the transient effects present during oscillatory tests. Such ramp-down tests have been performed on a large number of aerofoils at the University of Glasgow (Galbraith et al.[4]), and preliminary observations have been

discussed by Seto[5], Niven et al.[6] and Niven & Galbraith[7]. In addition to the delay in attachment, a significant result is that, at sufficiently high pitch rate, negative lift may be generated at large positive incidence (e.g. 12°). Figure 1 shows the effect of reduced pitch rate on the normal force/ incidence behaviour as a function of reduced pitch rate for the NACA 0015 at a nominal Reynolds number of 1.5 million. The salient features are indicated on the figure. The area of interest is from high incidence down to the local minimum normal force, $C_{N\,min}$. Within this zone $d(C_N)/d\alpha$ is nominally constant, and is independent of the reduced pitch rate. Thus the data indicate that, as |r| increases, the bluff body behaviour normally seen at high incidence is extended to progressively lower incidence. Consequently, at r<-0.02 $C_{N\,min}$ is negative. The attachment incidence at x/c=2.5%, which is also indicated on figure 1, was shown by Niven et al. [6] to be close to the static value and only weakly dependent upon the pitch rate. This result has been reported elsewhere by Ahmed & Chandrasekhara[8].

The present paper outlines the fundamental aspects of the flow behaviour during a ramp-down test, and concentrates upon the extension of the bluff-body behaviour to low incidence. Of great importance is the non-dimensional time delay between the first observation of leading edge attachment and $C_{N\,min}$. It is also significant that results of smoke flow visualisation show that the wake is much larger than in the static case at the same incidence. Finally, data from particle image velocimetry (PIV) experiments in the same environment as the pressure data tests reflect the observations made in the smoke flow tests, and it is suggested that convection of wake fluid, as well as attachment of the shear layer, has an important role in the flow development, and hence the recovery from stall.

2. EXPERIMENTAL DETAILS

Pressure data sampling system

Pressure data from two dimensional wind tunnel tests on a NACA 0015 profile are described in this paper. The model had a span and chord of 1.61m and 0.55m, and was constructed of a fibre glass skin filled with an epoxy foam and supported on a steel spar. It was mounted vertically in the University of Glasgow's Handley-Page wind tunnel, which is a closed return type with a 1.61mx2.13m octagonal working section. A linear hydraulic actuator and crank mechanism was used to pivot the aerofoil model about its quarter chord. Aerofoil incidence was measured using a potentiometer geared to the model's support. Thirty ultra-miniature pressure transducers (type KULITE XCS-093-PSI G) were installed below the centre span of the model. After signal conditioning the outputs of the pressure transducers were passed to a sample and hold module. Data were logged using a DEC MINC mini computer. Each ramp-down condition was repeated five times during which data sweeps containing 256 samples per channel at up to 550Hz were recorded. After sampling, the data were reduced, averaged and stored on a DEC MicroVAX for subsequent analysis.

Particle Image Velocimetry tests

The PIV tests were performed on a NACA 0015 model of 0.275m chord placed in the Handley Page wind tunnel described above. Pressure transducers were placed at strategic chordwise locations on the model to provide reference pressure data. The wind tunnel was seeded with Expancel microspheres. Illumination was provided by a pulsed ruby laser expanded into a thin sheet, shining across the centre-span of the aerofoil model. To track individual particles, three pulses were emitted by the laser at intervals of 90μs, and the flow pattern was photograped using Kodak recording

film. Each photographic negative was sub-divided into 80 frames and digitised and subjected to an individual particle tracking algorithm to determine the velocity vectors.

Smoke flow visualisation

The smoke flow visualisation tunnel used in this study is based on a design by Head (reported in Head & Bandyopadhyay[9]), and consists of a sealed room containing a 0.91m square perspex tube with one end open to the atmosphere via a 9:1 contraction. Air is sucked through the tube by a fan placed a short distance from its downstream end, and is vented out into the atmosphere through filters. Fine smoke filaments are injected in to the tunnel from a vertical tube positioned near the end of the contraction. In the series of tests described herein the NACA 0015 model was placed about 1m downstream of the end of the contraction, and was pitched about the quarter chord point using a stepper motor linked to a reduction gear box. The flow was illuminated using 500W halogen lamps shining from above and below the model at the mid-span position. Flow patterns were videotaped and digitised at 25 frames per second.

RESULTS

Pressure data

The nominal test conditions for the pressure data tests were $Re=1.5x10^6$ and M=0.12. All ramp-down tests considered herein were run from 40° to -1°. Attachment may be inferred from a characteristic response (i.e. minimum suction) on the individual pressure transducer time histories (Niven & Galbraith[7]). Figure 2 shows the 50% chord attachment incidence as a function of reduced pitch rate for the NACA 0015; attachment is delayed significantly compared to a static test, and the delay increases as the pitch rate increases. Shown in figure 3 is the time delay between attachment at 2.5% chord (which is the first sign of movement of attachment on this model) and $C_{N\ min}$. Although the scatter is large, the data in figure 3 indicate that the time delay is independent of reduced pitch rate to a first order, and the mean value of the time delay is approximately three chord lengths of travel. Further details of the time delay are described by Niven et al. [6] and Green & Galbraith [10,11]. Figure 4 shows the chordwise attachment position at the $C_{N\ min}$ condition as a function of reduced pitch rate. It can be seen that as |r| increases, $C_{N\ min}$ occurs when attachment is progressively further aft.

Smoke flow visualisation data

The nominal Reynolds number of the smoke flow visualisation tests was $1x10^4$. Figure 5 shows results from a 40° to -1° ramp-down test at r=-0.04. At 8° the flow is fully separated. Note the significant upward deviation of the streamlines above the aerofoil surface. At 4° incidence, frame 5b, the flow is still fully separated. At 0°, shown by frame 5c, it can be seen that the flow is attached in the leading edge region, although the flow is still highly separated. Figure 6 shows the static case at 4° incidence. By comparing this figure with figure 5b it is clear that in the ramp-down case, attachment is significantly delayed. Another important feature is the size of the wake; whereas in the static case the wake boundary is nominally horizontal, in the ramp-down case it is deflected upwards from leading edge to trailing edge, and the amount of fluid within the wake is significantly greater than in a static test. Figure 7 shows the amount of additional wake fluid to the static case as a function of time/ incidence. Also shown on this figure is the variation of the inclination of the streamlines above the quarter chord. It can be seen that as incidence falls the

excess wake fluid increases, and the streamline inclination increases. At about 10°, however, the excess wake fluid reaches a maximum and decreases rapidly as incidence falls further. The streamline inclination follows the same trend.

Particle image velocimetry data

Figure 8 shows a sequence of PIV pictures from a ramp-down test of the NACA 0015 at r=-0.03. The nominal Reynolds number is $1x10^6$. At 18° the flow is fully separated, and the wake is large. A large wake and fully separated flow would be expected at this incidence in a static test. At 13° incidence the wake is still very large, and it is clear from the picture that the flow is highly separated. Although a static test shows some separated flow at this incidence, the separation point is very far aft, and the wake is small. The frame at 8° incidence shows a substantial wake, and the flow is separated over approximately the last 50% of chord; a static test at 8° shows no detectable signs of separation.

DISCUSSION

A clear connection between the above pressure and flow visualisation data is the extension of the bluff body behaviour to low incidence; the fully separated portion of the C_N~α data extends to progressively lower incidence as |r| increases, and both the smoke flow and PIV data clearly show a large wake at low incidence. Although the delay in attachment observed in the above data is a fundamental feature of the flow during a ramp-down test, it may be argued that the the occurrence of $C_{N\,min}$ has no dependence on the delayed attachment; the progress of attachment along the chord is a strong function of the reduced pitch rate (figure 3), while the time delay τ is independent of r. During the bluff-body part of the C_N~α data, the presence of the wake is the significant feature of the flow-field. Therefore the end of the bluff-body behaviour ought to be associated with a change in the wake behind the aerofoil.

Further analysis of the pressure data from the ramp-down tests reveals a wave travelling from the leading edge region to the trailing edge. On the individual pressure transducer traces, the wave appears as a region of relatively high rate of decrease of suction before attachment. Figure 9 shows the effect of the pressure wave on the chordwise pressure distributions at 14° and 12°. The significance of the wave is that $C_{N\,min}$ occurs as the wave reaches the trailing edge. The wave travels at a uniform rate along the chord, and its speed is independent of the reduced pitch rate. (Further details of the pressure wave are described in Green & Galbraith [12].) The mean speed of the wave is 0.5U, so it only accounts for two-thirds of the time delay, τ. Between the beginning of the time delay, τ, and the first appearance of the pressure wave, attachment advances by only a few percent of chord. Nonetheless, with the slight aft movement of the attachment point, the curvature of the flow increases around the leading edge as it follows the surface contour. The fluid then encounters separation and begins to move away from the surface. In steady flow, the departure from the surface is such that the separated shear layer is almost tangential to the profile contour at the point of separation. As evidenced by the flow visualisation studies here, however, the wake boundary deviates upwards during ramp-down motion. This would appear to cause an acceleration of th efluid away from the wake boundary, and is the likely cause of the pressure gradients associated with the wave described above.

CONCLUSIONS

The fluid flow during a ramp-down test from the fully separated state is characterised by an extension of the bluff body behaviour to low incidence, and this phenomenon has a specific time duration. As a result, negative lift may be generated at large positive incidence. Flow visualisation data show that attachment is delayed compared to a static case, and that the wake is also much larger.

REFERENCES

[1] McCroskey, W.J., McAlister, K.W., Carr, L.W., Pucci, S.L., Lambert, O & Indergrand, R.F. 'Dynamic stall on advanced airfoil sections' Journ. A.H.S. Vol. 26, p40, (1981)

[2] Lorber, P.F. & Carta, F.O. 'Unsteady stall penetration experiments at high reynolds number' AFOSR TR-97-1202, UTRC R87-956939-3, (1987)

[3] Green, R.B., Galbraith, R.A.McD. & Niven, A.J. 'Measurements of the dynamic stall vortex convection speed' Aero. Journal, Vol. 96, p319, (1992)

[4] Galbraith, R.A.McD., Gracey, M.W. & Leitch, E. 'Summary of pressure data for thirteen aerofoils on the University of Glasgow's aerofoil database' University of Glasgow, Dept. Aero. Eng., Rept. No. 9221, (1992)

[5] Seto, L.Y. 'An experimental investigation of low speed dynamic stall an reattachment of the NACA 23012 under constant pitch motion' Ph.D. thesis, Dept. Aero. Eng., University of Glasgow, Glasgow, Scotland, (1988)

[6] Niven, A.J. Galbraith, R.A.McD. & Herring, D.G.F. 'Analysis of reattachment during ramp-down tests' Vertica, Vol. 13, p187, (1989)

[7] Niven, A.J. & Galbraith, R.A.McD. 'Experiments on the establishment of fully attached aerofoil flow from the fully stalled condition during ramp-down motions' Proc. 17th ICAS conference, Stockholm, Sweden. September, 1990

[8] Ahmed, S. & Chandrasekhara, M.S. 'Reattachment studies of an oscillating airfoil dynamic stall flowfield' A.I.A.A. 91-3225, (1991)

[9] Head, M.R. & Bandyopadhyay, P. 'New aspects of turbulent boundary layer structure' J. Fluid Mech., Vol. 107, p297, (1981)

[10] Green, R.B. & Galbraith, R.A.McD. 'A demonstration of the effect of the testing environment on unsteady aerodynamics experiments' Aero. Journal, Vol. 98, p 83, (1994)

[11] Green, R.B. & Galbraith, R.A.McD.'Phenomena observed during aerofoil ramp-down motions from the fully separated state' *To be published.*

[12] Green, R.B. & Galbraith, R.A.McD. 'Dynamic recovery to fully attached flow from deep stall' *To be published.*

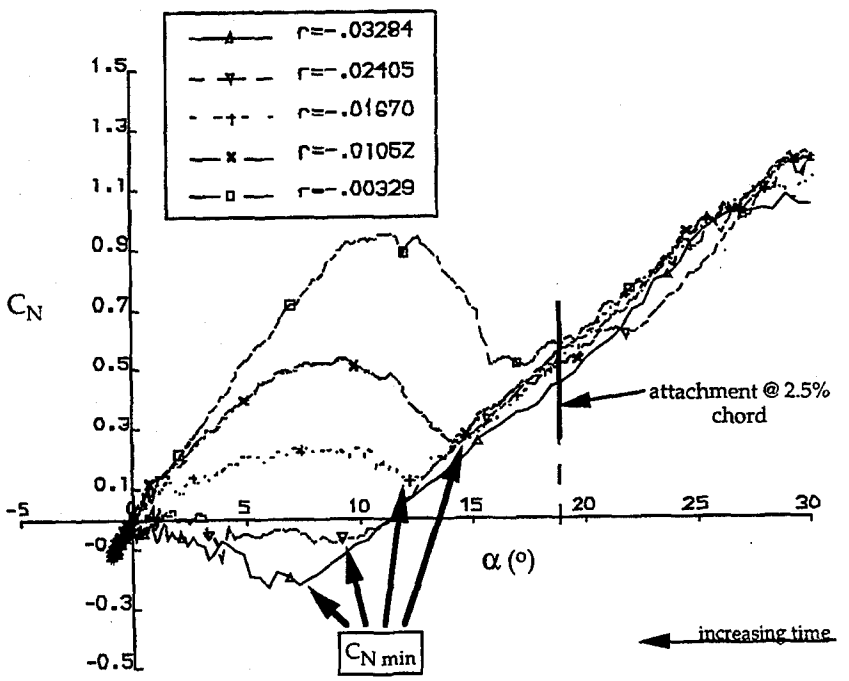

Figure 1 Plots of C_N versus α during 40° to -1° ramp-down tests of the NACA 0015. The effect of reduced pitch rate is shown. $C_{N\,min}$ and the incidence of attachment at 2.5% chord are indicated. The 'bluff response' is the behaviour down to $C_{N\,min}$.

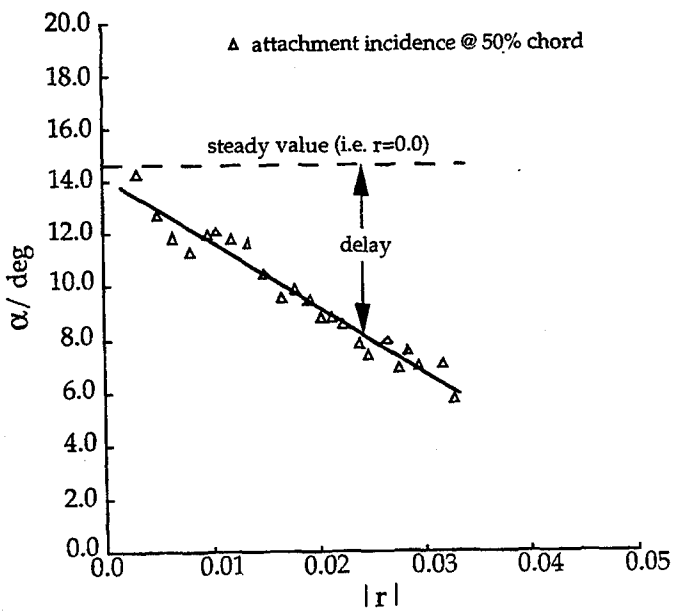

Figure 2 50% chord attachment incidence on the NACA 0015 as a function of reduced pitch rate.

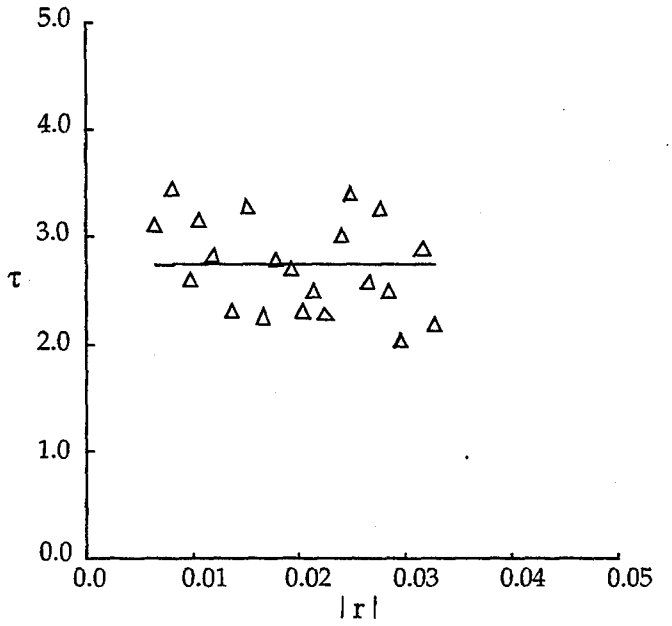

Figure 3 Time delay between attachment at 2.5% chord and $C_{N\,min}$ as a function of reduced pitch rate for the NACA 0015.

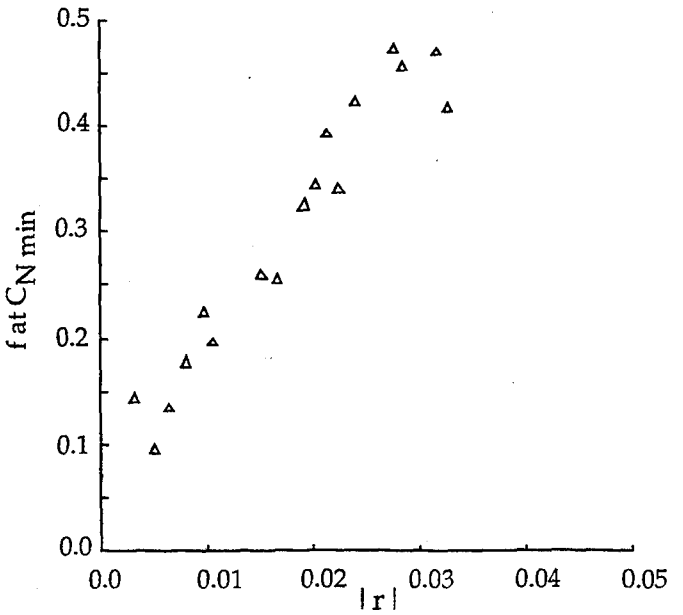

Figure 4 Attachment position, f, at the condition of $C_{N\,min}$.

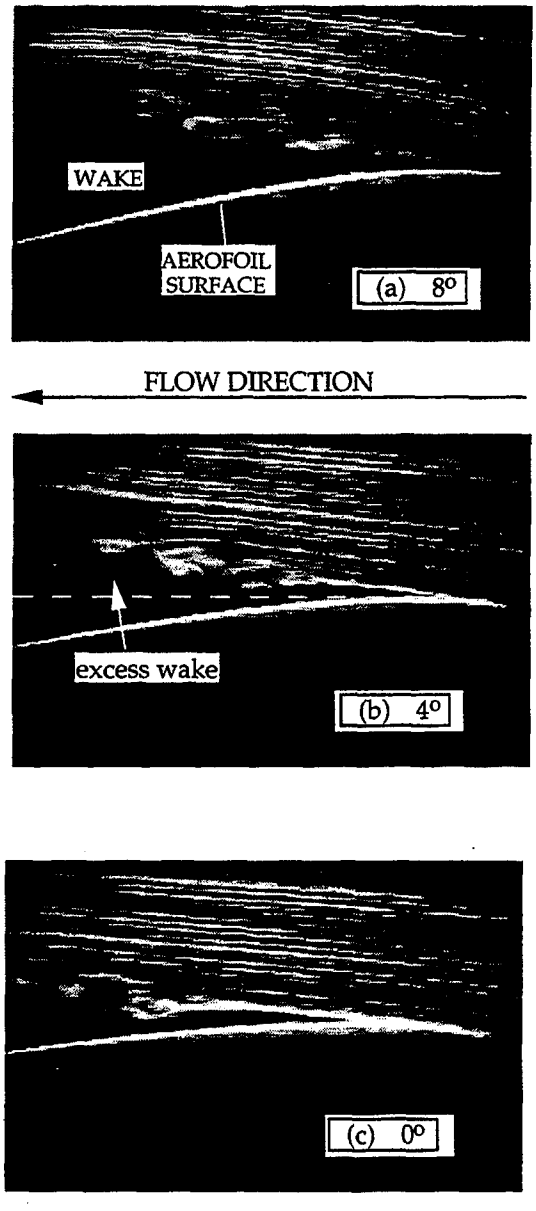

Figure 5 Smoke flow visualisation of a 40° to -1° ramp-down test of a NACA 0015 at Re=10000. r=-0.04. The wake and aerofoil surface are indicated.

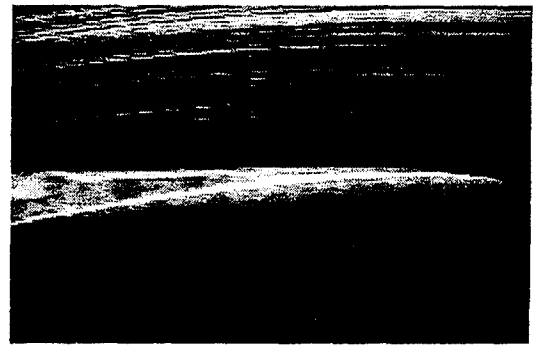

Figure 6 Smoke flow visualisation of NACA 0015 at Re=10000. Static test at 4°.

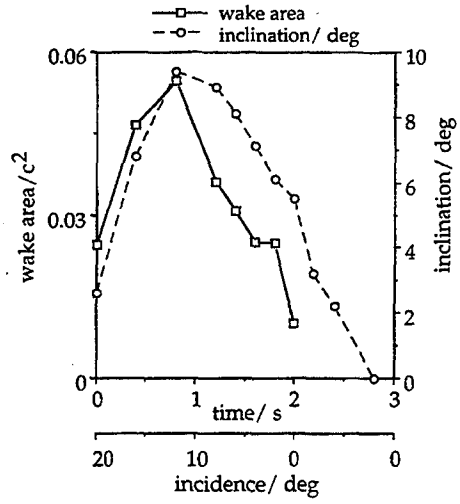

Figure 7 Variation of wake size above aerofoil 'shadow' and streamline inclination above quarter chord with time/ incidence. Test conditions as for figure 5.

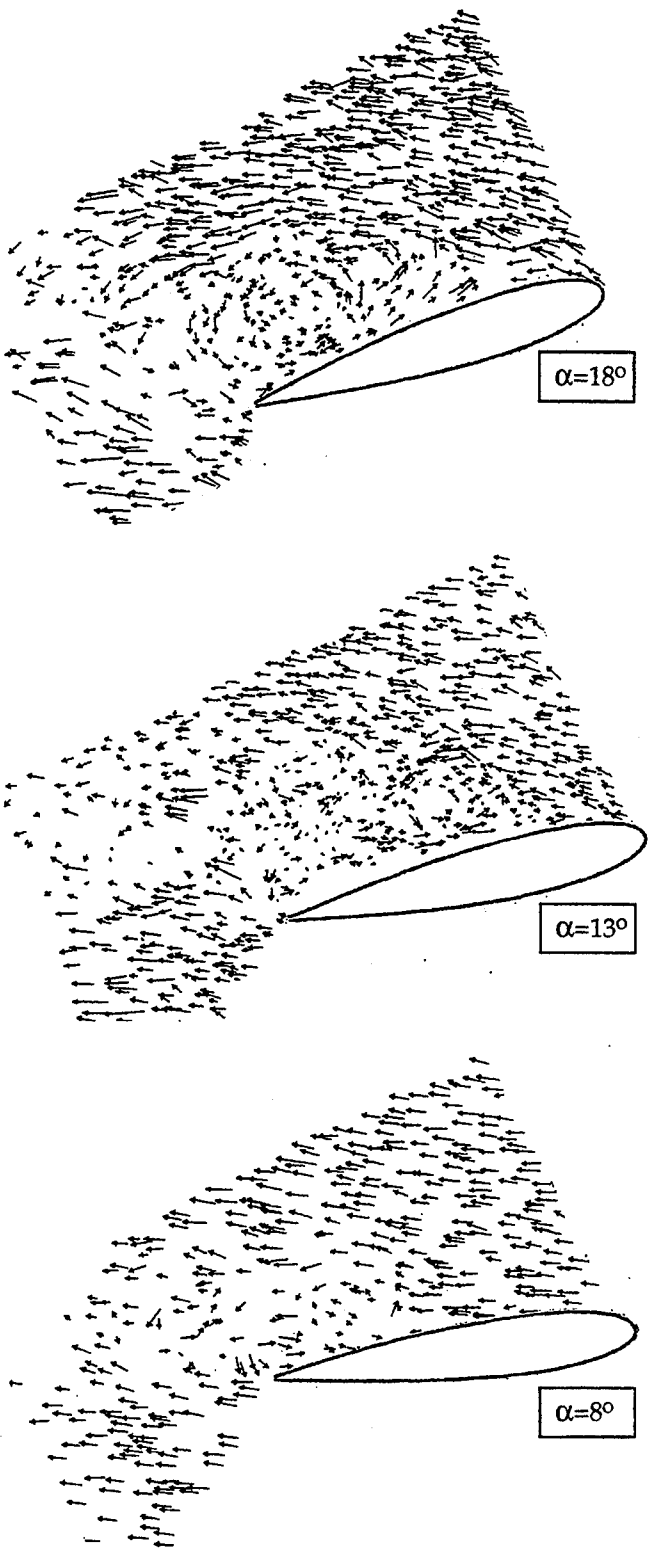

Figure 8 Velocity vectors from PIV test of the ramp-down motion of a NACA 0015 at r=-0.03. The incidence in each case is indicated.

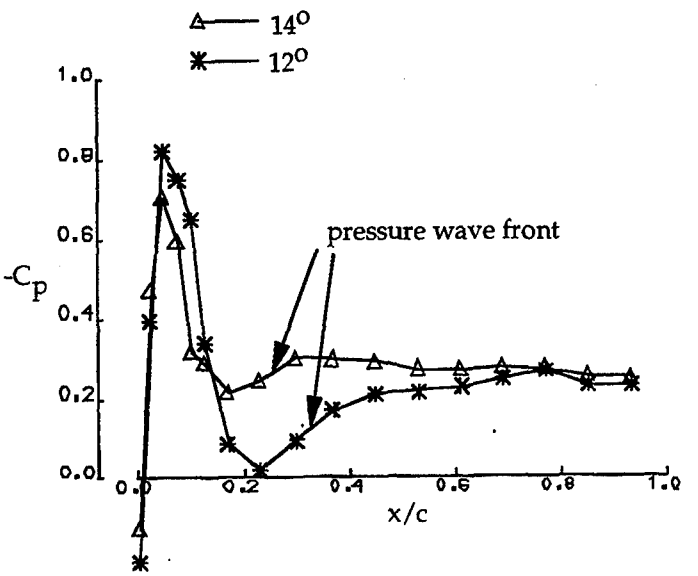

Figure 9 Lee surface chordwise pressure distributions at 14 and 12 deg incidence during a ramp-down test. r=-0.03. The pressure wave is indicated.

ASYMMETRIC WAKES OVER AN AXISYMMETRIC BODY IN CONING MOTIONS

by

Matthew D. Zeiger, Othon K. Rediniotis and Demetri P. Telionis
Department of Engineering Science and Mechanics
Virginia Polytechnic Institute and State University
Blacksburg, VA 24061-0219, USA

Abstract

An ogive-cylinder model is tested at high angles of attack. Static pressures over the surface of the model are obtained over a fixed and over a coning model. The coning motion is a ramp, initiated after steady asymmetric flow has been established. Steady, seven-hole probe measurements are obtained to give insight in the relationship of the wake asymmetry and the pressure distribution. It is found that if the model is allowed to cone in the direction of the side force, the asymmetry is initially reduced but sustained and eventually reinforced.

Introduction

The wake of axisymmetric bodies at incidence develops in the form of stationary vortical structures which emanate from two lines of primary separation. The wake over blunt-nosed bodies develop symmetrically even for very large angles of attack. A collection of references on this topic can be found in recent publications of the present group[1,2]. But for pointed bodies, it was discovered that the flow develops some very strong asymmetries[2-13]. Minute disturbances near the pointed nose like small imperfections in the machining of the model, minute physical disturbances or even dust near the tip can trigger the asymmetry[7,8,11]. It appears that the lines of separation very near the tip are affected by the presence of such disturbances. Because the downstream field is dependent on the flow near the tip, the effects of near-tip disturbances are sustained until the end of the model. The present authors have demonstrated that a disturbance placed on the nose of a hemisphere-cylinder model can also induce large asymmetric disturbances[14]. Such steady asymmetric wakes induce asymmetric pressure distributions which in turn give rise to steady side forces.

These forces can be very detrimental to the stability of the motion of rockets and missiles[7,15]. On the other hand, it is believed that side forces developed over the forebody of an aircraft at high angles of attack can be an effective control mechanism to induce a forceful rotation about the velocity axis. Sharp and efficient maneuvers could then be executed. This brings a new dimension to the problem, namely time. The flow over axisymmetric bodies at very high angles of attack tends to develop unsteadiness naturally. For angles of attack over 65°, the phenomenon of periodic vortex shedding starts to influence the flow [7,11,16]. Another class of problems involving dynamic motions has been investigated extensively. These are coning motions, whereby the model is allowed to cone under the influence of the side force[7,17,18]. Such motions develop quickly into a periodic and well organized state. But the effect of driven and controlled body motions on the fluid mechanics of the wake of such bodies have not yet been examined.

From the preceding discussion it appears that asymmetric wakes have been investigated extensively but only in steady flow conditions. Some research has been carried out with coning motions but the flow was allowed to establish a steady state. The present group examined the case of rapidly increasing the angle of attack of an axisymmetric body[19]. No effort has been directed at the problem of a transient maneuver, whereby an already developed asymmetric wake would be allowed to respond to a coning motion of the body. This is the topic of the present investigation.

The Model and Instrumentation

An ogive-cylinder model is employed in this study. The model was machined in three parts, all made of aluminum. The nose is a 3.5-to-one caliber ogive with tip radius $D/50$. The cylindrical afterbody is instrumented with pressure taps along two stations. A schematic of the model showing to location of pressure taps is shown in Fig. 1. The model is mounted at an angle of attack on a shaft. The shaft is supported on bearings and is aligned with the axis of the tunnel as shown in Fig. 2. This allows the model to perform coning motions. Rotation about the axis of the tunnel thus simulates aircraft rotation about its velocity vector when the aircraft is at a high angle of attack.

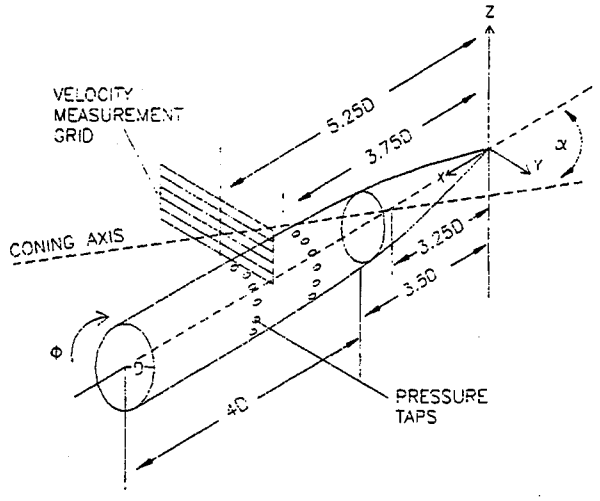

Fig. 1. Schematic of the ogive model. The model is rotated about the coning axis while at a fixed angle of attack, α.

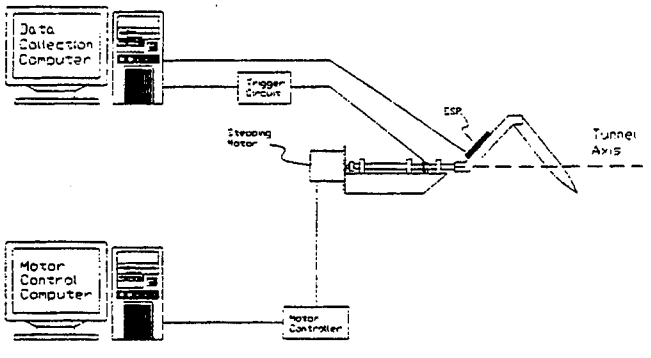

Fig. 2. Schematic of the coning mechanism and data acquisition system.

The shaft of rotation is supported by bearings and connected to a stepping motor. A computer is programmed to send pulses to the motor. The software allows the design of any schedule of coning motion. In the present experiments, a ramp schedule is executed as shown in Fig. 3. In other words, steady flow is

allowed to develop over the model. Then suddenly a nearly constant roll rate is imposed forcing the model into a coning motion.

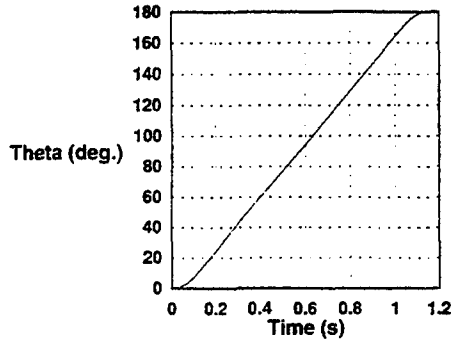

Fig. 3. Coning schedule of the model.

Tests are conducted in a wind tunnel with a test section of 20″ × 20″. A seven-hole probe with an external diameter of 0.18″ is employed. The probe was designed with a diameter small enough to reduce interference with the flow but large enough to measure temporal pressure fluctuations, so that unsteady velocities can be obtained. The probe was constructed and calibrated statically and dynamically in our laboratory. During calibration, the probe was mounted on a traversing mechanism which constrained its tip to remain at the same point in the test section. Surface pressures are obtained by a PSI pressure scanner. Short hoses are employed to connect the pressure taps with the scanner so that a reasonable frequency response can be achieved. It was estimated that for frequencies as high as 100 Hz, the delay in the response of the transducers leads to an error less than 2% of the actual value. For the temporal variations of the coning motions tested here the error is less than 0.1%.

The seven-hole probe is mounted on a traversing scale which, in both steady and unsteady cases, is supported such that it is aligned with the axis of the model. In this way, the probe is displaced together with the model. It can therefore measure velocity components with respect to a frame of reference attached to the model. Unsteady data are obtained by repeating the motion and for each realization, positioning the probe at a different location. A grid is thus constructed, fixed on the moving body as shown in Fig. 1. Seven-hole probe pressure data are obtained during many realizations, and then they are conditionally averaged. The entire operation is controlled by two computers, with data acquisition linked to the motion by an external trigger from an optical sensor.

Results and Discussion

Tests with a fixed model at an angle of attack $\alpha = 55°$ in steady flow, at a Reynolds number $Re = UD/\nu$ $= 30.8 \times 10^3$ were conducted first. These tests were carried out with different roll positions of the model in order to maximize the asymmetry in the wake. It appears that by rotating the model about its axis we rotate the mechanical imperfection which is the source of asymmetry. It should be noted that the nose of the model was machined on a computerized lathe with the utmost care and is in pristine condition. Yet, a violent asymmetry develops in the wake. In Fig. 4, we display the results of steady seven-hole probe measurements corresponding to the orientation which provides the greatest departure from a symmetric wake.

In Fig. 4, the velocity components in planes normal to the axis of the model are presented in the form of vectors, while the third component is represented by contours. The measuring grid extends above the model, as shown in Fig. 1. The asymmetric pattern is so pronounced, that the two vortices are almost one behind the other. There is a strong tendency to generate circulation in the cross plane, as evidenced by the turning of the velocity vectors adjacent to the body. As x/D increases, the vortices appear to increase their distance from the body but also tend to weaken. In fact, the vortex away from the model tends to lose its identity and can be detected only by an undulation of the streamlines. As a result, the dominant vortex tends to position itself in the center above the model, while the velocity vectors on the two sides of

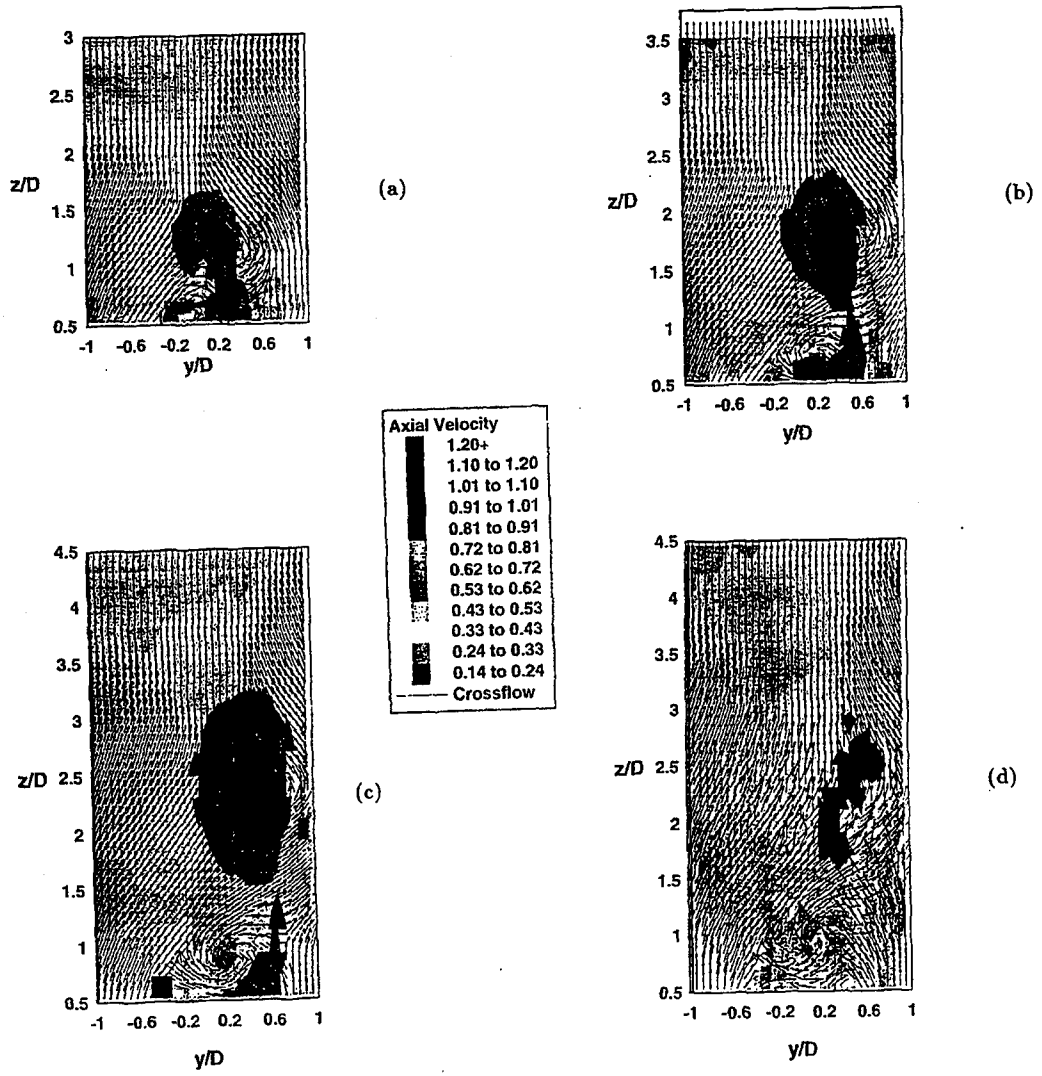

Fig. 4. Steady three-dimensional velocity in crossflow planes. (a) $x/D = 3$; (b) $x/D = 3.75$; (c) $x/D = 4.5$; (d) $x/D = 5.25$.

the model escape the model almost vertically. This implies a vanishing sectional side force, a fact which will be corroborated later by the pressure distribution.

Surface pressure data for steady flow are presented together with data obtained during coning motions in Figs. 5 and 6 for the stations $x/D = 3.75$ and 5.25 respectively. The data for unsteady flow were obtained at two reduced frequencies, namely $k = 0.0152$ and 0.0178. The asymmetry is again evident in Fig. 5. In the leeward side of the model, the pressure is lower on the left side, $\phi < 180°$ than on the right side, $\phi > 180°$. Immediately after the initiation of the motion, it then it is somewhat weakened, but then the asymmetry is reinforced.

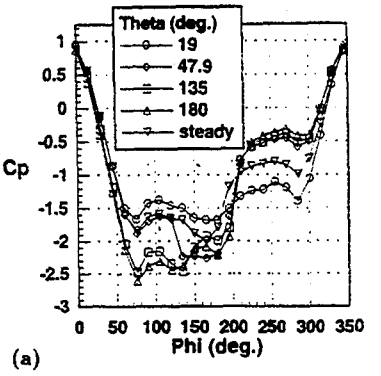

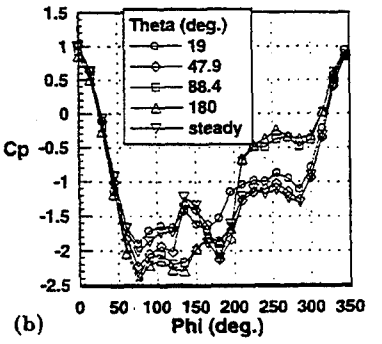

Fig. 5. Time evolution of surface pressures. (a) $x/D = 3.75$, $k = .0152$; (b) $x/D = 3.75$, $k = .0178$.

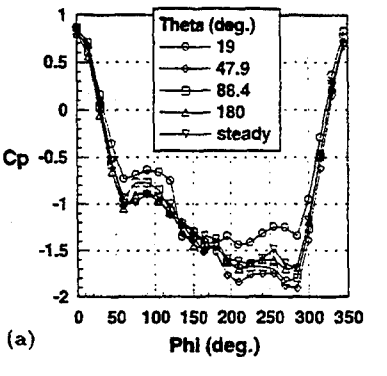

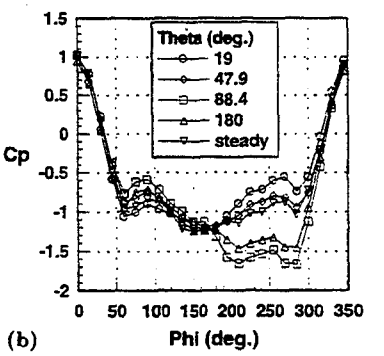

Fig. 6. Time evolution of surface pressures. (a) $x/D = 5.25$, $k = .0152$; (b) $x/D = 5.25$, $k = .0178$.

In Fig. 6 we display similar distributions, for the location $x/D = 5.25$. Now the asymmetry is reversed. This is due to the displacement of the vortices as discussed earlier. Again, once the body enters into a coning motion, the asymmetry is accentuated but the effect is less pronounced. At this point a pertinent question may be posed. Why, if the model is displaced in one direction, is the asymmetry accentuated at both x/D = 3.75 and $x/D = 5.25$, since the asymmetry reverses between the two stations? The answer lies not in the effect of the motion at the stations in question, but the effect at the nose. One would expect that if there were a change in the flow over the nose, that this change would be convected down the length of the body, and the flow at a particular point would be affected accordingly. In this case, the asymmetry is accentuated at both sections. Since the asymmetry is less pronounced at $x/D = 5.25$, the change is smaller.

The side force calculations also show that the asymmetry is enforced to different degrees at different sections. With the data obtained here, it is not possible to estimate the overall side force. Instead we estimate sectional forces by integrating pressures along the periphery of the model. The sectional force coefficient is estimated as follows:

$$C_f = \frac{1}{D}\int_0^{\pi D} p \sin\phi ds = \frac{1}{2}\int_0^{2\pi} \rho \sin\phi d\phi$$

The time evolution of the side force is shown in Fig. 7. At the beginning of the motion, the side force tends towards zero, which is expected since the impulsive flow would be symmetric. As the motion proceeds

with constant coning rate, the side force moves to a constant value, seemingly independent of the reduced frequency. At $x/D = 3.75$, the steady section coefficient is -0.125, and at $x/D = 5.25$, $C_f = 0.03$. Figure 7 shows that the side force reaches a stable state in which the original asymmetry is accentuated.

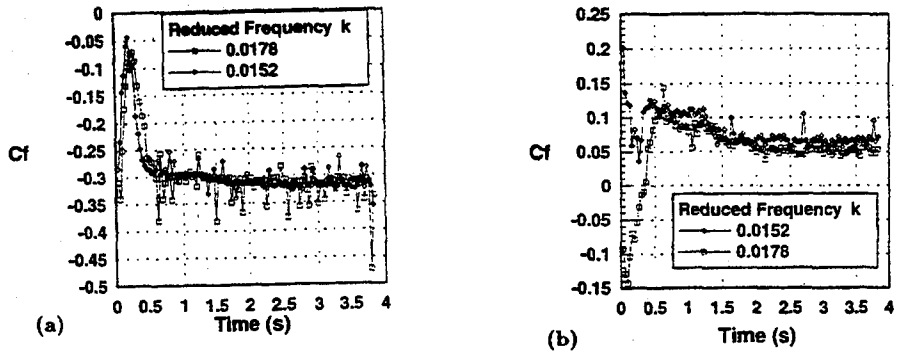

Fig. 7. Time evolution of sectional side force. (a) $x/D = 3.75$; (b) $x/D = 5.25$.

The reduced frequency is adjusted in these tests by changing the free-stream velocity. We observe that as a result, the steady-state pressure distributions do not coincide with each other. This could be due to the Reynolds number effect. For the higher frequency tested, the curves are not spread as much, but the trend is the same.

The effect of reduced frequency on the development of the wake is displayed better if data are presented with the frequency as a parameter. In Figure 8, with $x/D = 3.75$, the higher frequency results in reinforcing the asymmetry early in the motion. This can be seen in Fig. 7a which corresponds to a rotation of $\theta = 19°$ beyond the initial position. The trend is reversed at $\theta = 47.9°$ but at higher θ, the frequency effect is eliminated and the pressure distribution settles to a form which, as discussed earlier, namely it displays a more pronounced asymmetry if compared to the steady state.

Similar behavior is displayed at $x/D = 5.25$ (Fig. 8b), except that now for higher frequencies the trend is towards a symmetric distribution. The net effect should be that the overall side force should be increased with increased reduced frequency.

Conclusions

The wake vortices over ogive cylinders at large angles of attack usually display an axisymmetric but steady pattern: This asymmetry is present also in the pressure distribution which induces a side force on the model. In this paper we study the dynamic response of the flow over an ogive cylinder which is forced into a coning motion in accord with the side force due to the wake asymmetry. The basic questions we seek to answer is whether the asymmetry will be weakened or reinforced and how the flow field will be affected by the coning motion.

We discovered that at first the asymmetry is actually weakened but soon after, the asymmetric behavior is reinforced and sustained at levels higher than in the corresponding steady flow pattern. It therefore appears that this effect could be employed to turn the forebody of an aircraft about its velocity vector at high angles of attack. The reduced frequency was proven to have a strong effect on the dynamic development of the wake. A higher frequency reinforces further the asymmetry all along the model. As a result, one should expect an overall increase in the side force on the model.

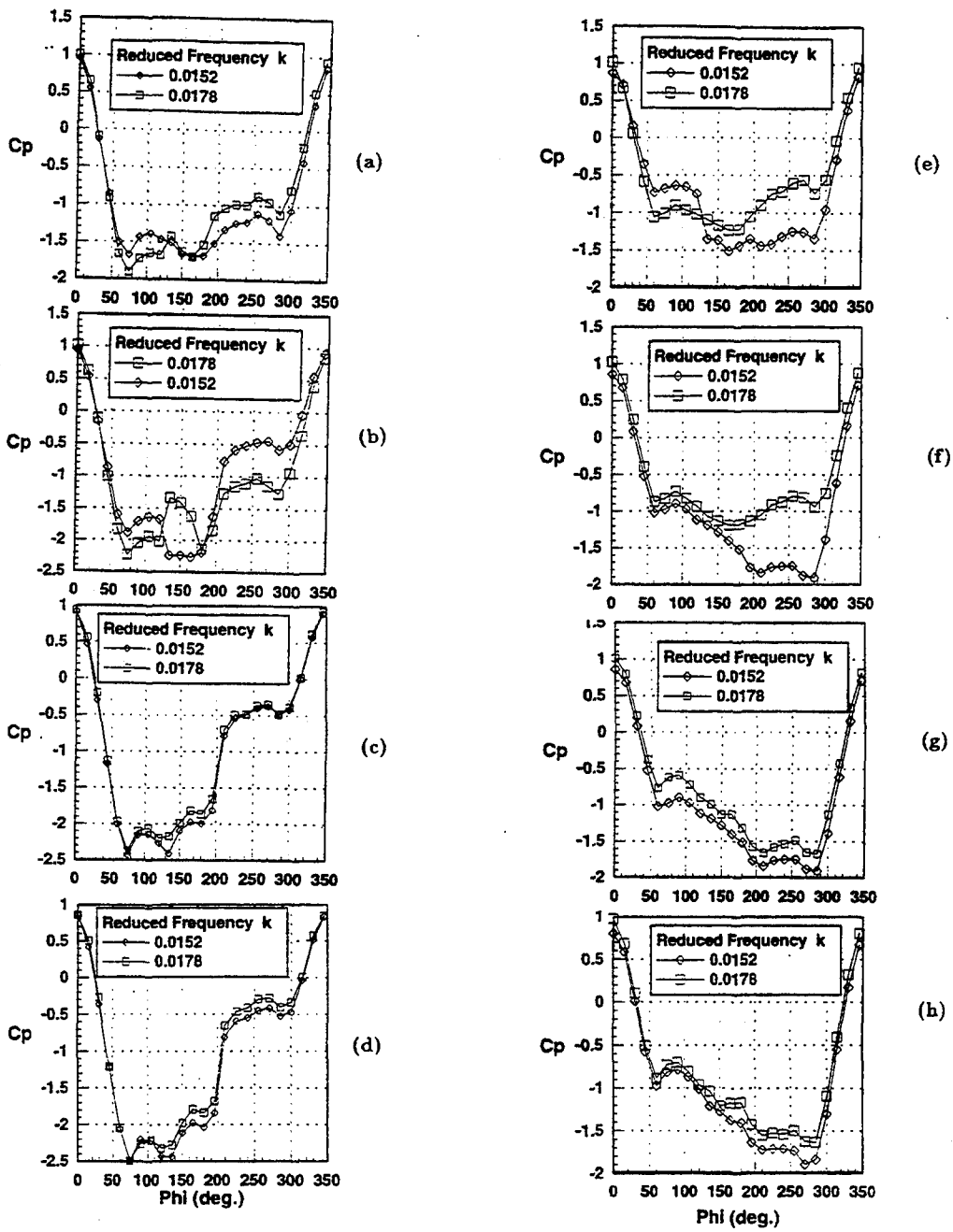

Fig. 8. Effect of Reduced Frequency. (a) $\theta = 19.0°$, $x/D = 3.75$; (b) $\theta = 47.9°$, $x/D = 3.75$; (c) $\theta = 88.4°$, $x/D = 3.75$; (d) $\theta = 180.0°$, $x/D = 3.75$; (e) $\theta = 19.0°$, $x/D = 5.25$; (f) $\theta = 47.9°$, $x/D = 5.25$; (g) $\theta = 88.4°$, $x/D = 5.25$; (h) $\theta = 180.0°$, $x/D = 5.25$.

Acknowledgement

The work of the first author is supported by the U.S. Department of Defense through an Air Force Fellowship, No 94-0328-08. The monitor of this effort was Mr. Jerry Jenkins (Wright Laboratories).

References

1. Hoang, N. T., Rediniotis, O. K., and Telionis, D. P., "Separation Over Axisymmetric Bodies at Large Angles of Attack," AIAA Paper 91-0277, January 1991.
2. Costis, C. E., Hoang, N. T., and Telionis, D. P., "Laminar Separating Flow over a Prolate Spheroid," *Journal of Aircraft*, Vol. 26, No. 9, September 1989, pp. 810-816.
3. Dexter, P. C., and Hunt, B. L., "The Effects of Roll Angle on the Flow over a Slender Body of Revolution at High Angles of Attack," AIAA Paper 81-0358, AIAA 19th Aerospace Sciences Meeting, January 1981.
4. Hunt, B. L., "Asymmetric Vortex Forces and Wakes on Slender Bodies," AIAA Paper 82-1336, AIAA 9th Atmospheric Flight Mechanics Conference, August 1982.
5. Lamont, P. J., "Pressures Around an Inclined Ogive-Cylinder with Laminar, Transitional, or Turbulent Separation," *AIAA Journal*, Vol. 20, 1982, pp. 1492-1499.
6. Lamont, P. J., "The Complex Asymmetric Flow Over a 3.5D Ogive Nose and Cylindrical Afterbody at High Angles of Attack," AIAA Paper 82-0053, AIAA 20th Aerospace Sciences Meeting, Jan. 1982.
7. Ericsson, L. E., and Reding, J. P., "Asymmetric Vortex Shedding from Bodies of Revolution" in *Tactical Missile Aerodynamics*, M. J. Hemsch and J. N. Nielsen, eds., in Progess in Astronautics and Aeronautics, published by AIAA, 1986, Vol. 104, pp. 243-296.
8. Champigny, Patrick G., "Stability of Side Forces on Bodies at High Angles of Attack," AIAA Paper 86-1776.
9. Moskovitz, C. A., Ha, R. M., and DeJarnette, F. R., "Effects of Surface Perturbations on the Asymmetric Vortex Flow Over a Slender Body," AIAA Paper 88-0483.
10. Moskovitz, C. A., Hall, R. M., and De Jarnette, F. C., "Effects of Nose Bluntness, Roughness and Surface Perturbations on the Asymmetric Flow Post Slender Bodies at Large Angles of Attack," AIAA Paper No. 89-2236.
11. Degani, D. and Zilliac, G. G., "Experimental Study of the Nonsteady Asymmetric Flow Around an Ogive-Cylinder at Incidence," *AIAA Journal*, Vol 28, 1990, pp. 642-649.
12. Zilliac, G. G., Degani, D., and Tobak, M., "Asymmetric Vortices on a Slender Body of Revolution," *AIAA Journal*, 29, 1991, pp. 667-675.
13. Ericsson, L. E., "Sources of High-Alpha Vortex Asymmetry at Zero Sideslip," AIAA Paper No. 91-1810.
14. Hoang, N. T. and Telionis, D. P., "The Dynamic Character of the Wake of an Axisymmetric Body at an Angle of Attack," AIAA Paper No. 91-3268.
15. Jackson, C. M. and W. C. Sawyer, "Bodies with Noncircular Cross Sections and Baud-to-Turn Missiles," in *Tactical Missile Aerodynamics*, M. J. Hemsch and J. N. Nielsen, ed., Progress in Astronautics and Aeronautics, Vol. 104, 1986, pp. 168-197.
16. Ramberg, S. E., "The Effects of Yaw and Finite Length Upon the Vortex Wakes of Stationary and Vibrating Circular Cylinder," *Journal of Fluid Mechanics*, Vol. 128, 1983, pp. 81-107.
17. Yoshinaga, T., Tate, A., and Inoue, R., "Coning Motion of Slender Bodies at High Angles of Attack in Low Speed Flow," AIAA Paper No. 81-1899.
18. Ericsson, L. E., "Prediction of Slender Body Coning Characteristics," *Journal of Aircraft*, Vol. 28, 1991, pp. 43-49.
19. Panzer, E. C., Rediniotis, O. K. and Telionis, D. P., "The Hemisphere-Cylinder in Dynamic Pitch-Up Motions," AIAA Paper No. 93-2963.

ESTIMATION OF STABILITY DERIVATIVES OF AN AIRCRAFT MODEL USING A DYNAMIC FLIGHT TECHNIQUE IN A WIND TUNNEL

Govinda Raju.S.P, Vageesh.K.P & V.Surendra Nath
Department of Aerospace Engineering
Indian Institute of Science, BANGALORE.

1.0. INTRODUCTION :

An airplane in flight is supported and steered by the dynamic reactions of air in the three dimensional space. The aerodynamic reactions on the airplane are described by the "stability derivatives" which represent the rate of change of aerodynamic forces or moments with respect to any one of the flow variables or control variables. It is obvious that the estimation of these derivatives is an essential part of understanding the stability of airplanes. In designing modern military aircraft having high maneuverability, an accurate knowledge of stability derivatives is required for design and optimisation of their control systems. The design of flight simulators,used for training purposes,are also based on a detailed knowledge of these stability derivatives.

These aerodynamic stability derivatives are calculated at the design stage based on the aerodynamic theories. These calculated values are refined at this stage by using wind tunnel tests. Wind tunnel tests to estimate these derivatives have largely used traditional methods like the methods of free and forced oscillations. These tests are model specific and hardware has to be designed specifically for each job. One can now replace these traditional methods by sophisticated dynamic tests in a wind tunnel. The dynamic test mehods are derived from techniques used till recently only for inflight evaluation of real aircraft. These tests are made possible by recent advances in computer based instrumentation systems of relatively low cost. The instrumentation for these tests is less model specific and hence simplify the test hardware considerably. It is expected that further developments of these test methods will lead to wind tunnel techniques of estimating all the important stability derivatives quickly and accurately. It is the development of these test methods that concerns us here.

In a typical dynamic flight experiment in a wind tunnel, one uses a model of a flight vehicle which is free to move in a windstream in a limited number of degrees of freedom. Some of the control surfaces of the model are provided with servo actuators which are commanded by a remote operator or a computer. When commanded, the control surfaces of the model move and the model responds in an appropriate manner. This model response as well as the control surface movements are sensed by suitable motion sensors which could include those for displacement (potentiometers), angular veocities (miniature rate gyros) and accelerations (accelerometers). These motion parameters as well as the wind speed in the tunnel are sampled and recorded remotely on a computer provided with suitable data acquisition interfaces. By using the technique of parameter estimation on this recorded time

series of motion history, the aerodynamic stability parameters of interest are estimated.

We have been developing the above experimental method. We have fabricated an aircraft model with only two degrees of freedom (in pitch and heave). The model is provided with servo actuation of its all moving tailplane. Provision is made for sensing the pitch orientation and tailplane incidence of the model by using suitable potentiometers. Using this model, experiments have been conducted for determinig aerodynamic stiffness and damping derivatives in pitch. The following sections describe the details of the experiments and the results obtained till now.

2.0 NOTATION :

b Reference Span-m

$\bar{c}$ Mean Aerodynamic Chord

h, h_o, h_n Reference distance of cg,aerodynamic centre and neutral point-m

I_y Moment of inertia about y-axis $Kg - m^2$

$\bar{q}$ Dynamic pressure Nm^{-2}

S_t Area of tailplane -m^2

t Time-secs

V_t Effective tail volume ratio

W weight of airplane-N

α Angle of attack-degrees

β Angle of sideslip-degrees

Δ Incremental value

δ_t Tailplane incidence-degrees

$C_{L\alpha trim}$ Lift curve slope at trim

$C_{L\delta_{t(trim)}}$ Tail plane lift effectiveness slope

$C_{L\alpha}$ Variation of lift coefficient with angle of attack

$C_{m\alpha}$ Variation of pitching moment coefficient with angle of attack

$C_{m_{\delta_t}}$ Variation of pitching moment coefficient with tail plane incidence

C_{m_q} Variation of pitching moment coefficient with pitch rate

$C_{m\dot{\alpha}}$ Variation of pitching moment coefficient with rate of angle of attack

3.0. EXPERIMENTAL SETUP AND INSTRUMENTATION :

The experiments were conducted in a low speed wind tunnel of 2.75m × 4.25m rectangular test section at the Dept. of Aerospace Engineering, IISc, in the wind speed range of about 20 to 50 m/s. Further details of this facility are reported in Krishnaswamy et al[1]

A model of a jet trainer aircraft with an all moving tailplane was chosen for this study. Photographs 1 and 2 show the details of the model. Table.1 gives the geometric data for this model. The model is of laminated wood with a hollow fuselage, split along a horizontal plane through the reference axis. The top half of the fuselage, which includes the vertical fin and the all moving horizontal tail, also houses the servomotor and angle sensing potentiometer for respectively actuating and recording the motion of the tail plane. The tailplane is hinged about its aerodynamic centre so that the force required for its actuation is small and is well within the capacity of the servomotor. The lower half of the model incorporates a guide cum hinge block at a position near the aerodynamic centre of the wing. This block contains a linear bearing and is supported on a pair of ball bearings. This arrangement provides for two degrees of freedom to the model when a guide rod is inserted through the block.

Photo.1: Model in the test section

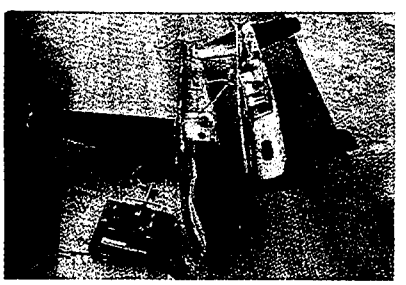

Photo.2: Model with instrumentation

The model can thus have free motion in heave and pitch without any restraint. However, due to the weight of the model, the block rests on a cushioning spring. The model with the block lifts off the spring when there is adequate aerodynamic lift. The angle between the guide block axis which is vertical and the normal to the model reference line (which corresponds to model incidence under steady conditions) is sensed by a potentiometer by using a parallelogram linkage. The forward part of the model incorporates a weight block which can move along the fuselage axis so that the centre of gravity of the model can be altered by as much as 20% of the wing mean aerodynamic chord. It is thus possible to conduct the flight experiments over a wide range of C.G positions.

The instrumentation system consists of a computer (IBM 386 personal computer) with suitable interfaces to drive the tailplane servomotor and sense the fuselage and tailplane potentiometers. A schematic diagram of this system is shown in Fig.1. It will be noted that the tailplane incidence of the model can be controlled by the computer or optionally by a joy stick. Manual control by joy stick is required for steady flight experiments as the computer cannot perform this task without autostabilization which is not available on the current setup.

TABLE 1 : AIRPLANE MODEL PARAMETERS

S.No	Model parameter	value
1	Wing span	0.89 m
2	Wing Aspect ratio	6
3	Overall length	0.88 m
4	Tail arm (l_t)	0.41 m
5	Wing area	$0.132m^2$
6	Vertical tail surface area	$0.0146m^2$
7	Horizontal tail surface area	$0.026m^2$
8	Total weigth without moving block	9.45 kg.
9	Total movement of weight block	0.12 m
10	Total C.G travel by movement of block	0.021 m

Software has been written for the computer so that the computer can actuate the servomotor, set the tailplane at any chosen angle and impart a preplanned oscillation over it. The computer also acquires data about the model orientation and tailplane incidence for a duration including the time of oscillation of the tailplane. Typically, data is acquired for about 10 seconds at the rate of about 400 samples per channel per second. This rate of data acquisition is more than necessary for the present study where the natural frequency of pitch oscillation of the model in the wind stream is around 1 Hz. The extra data acquisition capacity will be useful for more complex experiments which will be considered in the future. The acquired data is processed off-line by using parameter estimation software to be described later.

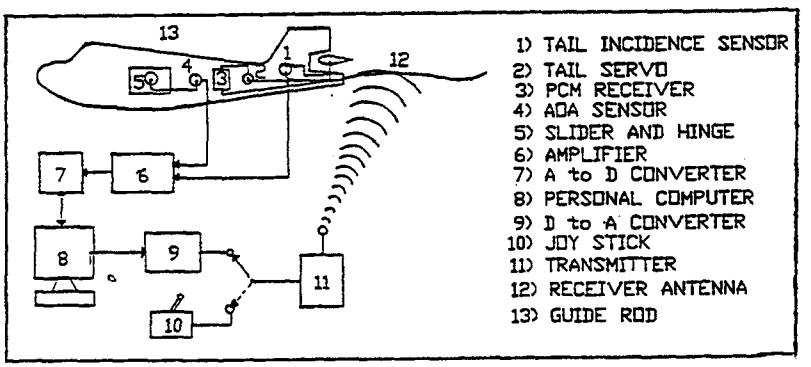

Fig.1: Schematic diagram of the experimental setup

4.0. EXPERIMENTS:

4.1. Steady State experiments :

With the setup described earlier, two sets of experiments have been conducted. The first set of experiments involving only steady conditions of the model will be described first. In these experiments, the model is held in equilibrium fully supportted by the airstream at various wind speeds above stall. This condition closely corresponds to free flight of an aircraft at a constant speed.

To conduct a typical experiment, the model is installed on the guide rod fixed vertically in the test section of the wind tunnel. The model is held with the fuselage reference line level and initial reading of the sensors are recorded on the computer. The wind tunnel is turned on and the wind speed is set at a suitable steady value above the stall speed for the model. The incidence of the tailplane is progressively made more negative by commanding the tailplane using the joy stick located outside the tunnel. The model responds with an increase of the angle of incidence and this results in an increase of lift on the model. At some point the model weight is just overcome by lift and the model floats up on the guide rod fully supported by the airstream. A skilled operator is required at the joy stick to maintain this delicate equilibrium condition long enough for all the sensor readings to be recorded. Typically one thousand values of each sensor reading are taken and averaged to get a mean value. With practice, it has been possible to consistently achieve and maintain this condition. The results presented below were obtained from such experiments.

The sensor readings recorded during a steady state test correspond to measurements of model incidence, tailplane setting and wind speeds for the configuration. Such tests can be repeated for various positions of the model centre of gravity position (by fixing the weight block inside the model at different positions) and from these one may plot C_{Ltrim} Vs α and δ_{tail} Vs C_{Ltrim} as indicated in the Fig.2 and Fig. 3 respectively.

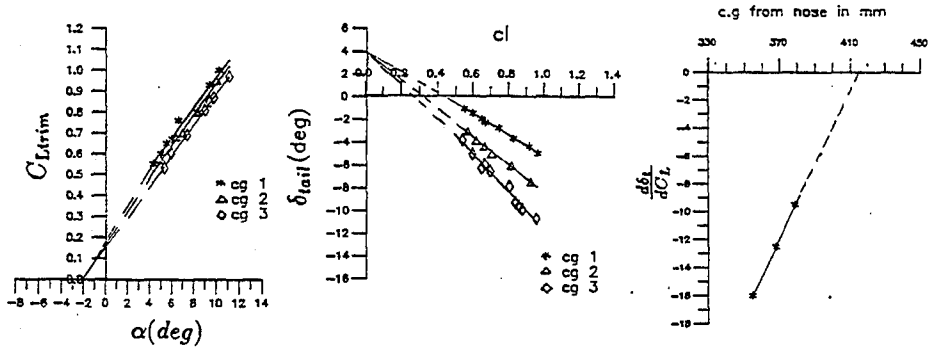

Fig.2,3,4 Curves of trim condition from steady state expriments

4.2 Dynamic Experiments :

These experiments are conducted with the model having a single degree of freedom in pitch. The heaving degree of freedom is eliminated by locking the linear bearing to the guide rod.

The model is installed in the wind tunnel as in steady experiments and the tunnel speed is held constant. The tailplane of the model is actuated by the servo under computer control. Provision exists in the software for trimming the model at any initial incidence. Over the initial setting, different tailplane motion wave forms can be easily generated by the computer and transmitted to the tailplane servo. The experiment can be repeated any number of times almost exactly.

Following servo input, the model responds in the pitch degree of freedom and the com-

puter records this motion through its analogue interface. Both the tailplane incidence and the model orientation in the pitch are sampled at regular intervals and recorded. Typically during an experiment about 8000 samples of data are recorded in about ten seconds. It is also to be noted that the tailpalne motion is recorded by sensing it independently of the input to the servo motor so that any error in the servo in tracking the command does not corrupt the experimental data. It is also to be noted that the same computer commands the servo as well as record the data by switching to command and record modes sequentially in a time extremely small compared with the time scale of model motion.

The wave forms of tailplane motion could be selected such that the model is excited over a band of frequencies including the natural frequency of its pitching motion. Accuracy of the estimated parameters depends on the input wave form and studies have been conducted with several different waveforms (like impulse, doublet, triplet and so on). Some of the input wave forms and the corresponding model pitch response are shown in Figs.5,6,7. Analysis of this data will be taken up in section 5.

4.3 Determination of Model Inertia Properties:

For analysing the data from the above experiments one needs the knowledge of model inertia properties. The relevent inertia properties are the mass, the position of model centre of gravity and the moment of inertia about the pitch axis. These are easily determined by seperate experiments. We have determined the mass and position of of the model centre of gravity by supporting the model on three calibrated load cells by pivots having known position relative to the model and using equilibrium considerations on the load cell data. The moment of inertia about a pitch axis is determined by suspendig the model about a point close to its nose and finding the period of oscillations as compound pendulum. Details of calculations involved are straigt forward and are not presented here.

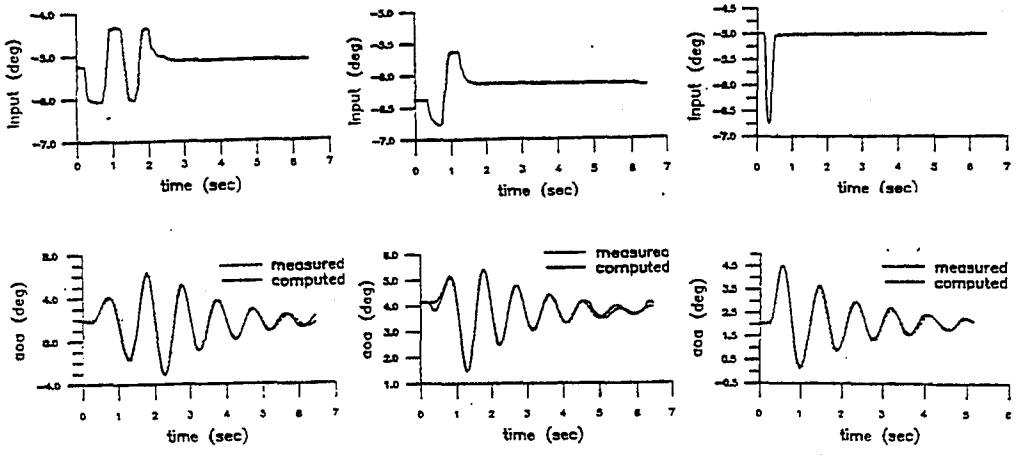

Fig.5,6,7: Typical examples of input waveforms and model response in pitch

5.0 ANALYSIS OF DATA

5.1 Steady Experiments:

We shall consider the steady experiments first. The aerodynamic forces on the model configuration,assumed to be in a linear range, can be expressed non-dimensionally as

$$C_{Lo} + C_{L\alpha}\alpha + C_{L\delta_t}\delta_t = C_L \tag{1}$$

$$C_{mo} + C_{m\alpha}\alpha + C_{m\delta_t}\delta_t = C_m \tag{2}$$

where the four quantities $C_{L\alpha}$, $C_{L\delta}$,$C_{m\alpha}$ and $C_{m\delta_t}$ are the aerodynamic force/moment coefficents which are characterstic of the configuration under study for given position of the moment reference point (ie., centre of gravity in steady experiments). For determining these by analysis of the data from steady expriments,additional information about the aerodynamics of an airplane configuration as in Klein[2] is required, as Eqn.(1) and (2) do not contain any information as to how the aerodynamic parameters depend on the moment reference point. This aerodynamic model assumes that an airplane effectively consists of a wing body and a tailplane situated in the downwash of the wing body, both having linear aerodynamic properties. Using equilibrium considerations one may derive to the following equation.

$$C_m = C_{m_o} + \frac{(h - h_n)}{\bar{c}} C_L - V_T a_1 (\delta_t - \delta_w \epsilon_o) \tag{3}$$

Here h and h represents the distance of C.G and the neutral point of the configuration from a reference point along the reference line on the model. For steady condition $C_m = 0$ and C_L is such as to balance the model weight and is denoted by C_{Ltrim}.

On the basis of Eqns. 1,2,3 we proceed to analyse the experimental data as follows. First we determine the quantity V_T a_1 of Eqn.(3) as

$$V_T a_1 = \frac{\Delta h}{\Delta \delta_t} C_{Ltrim} \tag{4}$$

where $\Delta h/\Delta\delta_t$ is the rate of change of tailplane incidence with C.G position at a constant C_L and is obtained from Fig.4 for a given C.G position. Next the neutral point of the configuration is determined by plotting $\Delta\delta_t/\Delta C_L$ with C.G position and extrapolating linearly corresponding to $\Delta\delta_t/\Delta C_L = 0$ at $h = h_n$ as in Fig. 4. Using these one calculates the four aerodynamic quantities of interest in Eqns 1 and 2 for any given C.G position h as

$$C_{m\delta_t} = \frac{-(V_T a_1)}{1 - \left(\frac{h_n - h}{l_t}\right)} \tag{5}$$

$$C_{L\delta_t} = -\frac{\bar{c}}{l_t} C_{m\delta_t} \tag{6}$$

$$C_{m\alpha} = -\left(\frac{h_n - h}{\bar{c}}\right) C_{L\alpha} \tag{7}$$

$$C_{L\alpha} = \frac{C_{L\alpha trim}}{1 - \frac{h_n - h}{l_t}} \tag{8}$$

5.2 Dynamic experiments :

The dynamics of the pitching motion is modelled as a second order system with damping and is represented by the equation.

$$I_y\ddot{\theta} - M_{\dot{\theta}}\dot{\theta} - M_\theta\theta = M_{\delta_t}\delta_t \tag{9}$$

In this equation $M_{\dot{\theta}}, M_\theta$ and M_δ are the aerodynamic moment derivatives to be determined using the experimental data. I_y, $\theta(t)$ and $\delta(t)$ are known.

We have used the technique of parameter estimation using output error method for determining the unknown aerodynamic parameters. The technique is fully described by Maine and Iliff[3]. Basically, the method consists in finding the values of $M_{\dot{\theta}}, M_\theta$ and $M_{\delta_t}$of eqn.(9) such that the solution of Eqn. (9), namely $\theta_s(t)$ and the experimental observations of $\theta_E(t)$ differ to the minimum extent in a least square sense over the interval considered. An appropriate software has been written for the purpose. The software starts with a given set of values for the unknown parameters. These values are progressively refined until a cost function reaches a minimum value within a small margin of error.

The quantities $M_{\dot{\theta}}, M_\theta$ and M_δ are related to the aerodynamic coefficients $C_{m\alpha}$, $C_{mq} + C_{m\dot{\alpha}}, C_{m_{\delta_t}}$ can be determined from the following relations.

$$C_{mq} + C_{m\dot{\alpha}} = \frac{4}{\rho V S\bar{c}^2} M_{\dot{\theta}} \tag{10}$$

$$C_{m\alpha} = \frac{M_\theta}{\frac{1}{2}\rho V^2 S\bar{c}} \tag{11}$$

$$C_m\delta_t = \frac{M\delta_t}{\frac{1}{2}\rho V^2 S\bar{c}} \tag{12}$$

6.0 RESULTS:

Table 2: Typical values for the Aerodynamic parameters estimated from experiments.

All parameters are refered to a common moment reference point at the hinge location.

Parameter	Static Expts.	Dynamic Expts. at $\alpha = 0$ with different Inputs			
		3-2-1-1	Doublet	Impulse	Free.osc
$C_{L\alpha}$	0.0783	-	-	-	-
$C_{L\delta}$	0.0080	-	-	-	-
$C_{m\alpha}$	-0.0198	-0.0232	-0.026	-0.0257	-0.0243
$C_{mq} + C_{m\dot{\alpha}}$	-	-0.3325	-0.28	-0.3400	-0.323
$C_{m\delta_t}$	-0.0333	-0.0356	-0.0345	-0.0340	-

6.1 Comparision of results from steady and dynamic experiments :

Data obtained from both the steady state and dynamic experiments have been analysed and the results are presented in Table 2. It is to be noted that only $C_{m\alpha}$ and $C_{m\delta t}$ can be determined from both the steady state and dynamic experiments and the agreement is good in these cases. The damping derivative $(C_{m_q} + C_{m_{\dot{\alpha}}})$ could be determined from dynamic experiments using different inputs and the estimated values are in fair agreement for all the

types of inputs considered . Analytical results based on datcom methods (not presented here) also indicate comparable values for this parameters. Further work is in progress to choose the best input wave form for the dynamic experiments.

6.2 Conclusions :

To our knowledge this is the first time that a free flying technique has been successfully used for determining the trim condition of an aircraft model in a wind tunnel.

Dynamic tests for exciting pitching motion and use of parameter estimation technique for analysis of this motion have been successfully used for determining the pitch damping of an aircraft model. Further developments of the technique are expected to lead to useful methods for determining other important stability derivatives. It is concluded that the dynamic flight technique in a wind tunnel can be conveniently applied to the estimation of stability derivatives of flight vehicle configurations with relative ease. The instrumentation is nearly universal and can be used in the estimation of many important stability derivatives.

7.0 REFERENCES :

1. T.N.Krishnaswamy.,S.M. Ramachandra.,V.Krishnamurthy., "Design charasteristics of the 14' x 9' open circuit wind tunnel".- Proceedings of Seminar on Aeroanutical Sciences, Nov 27-Dec 2, 1961.

2. V.Klein.,"Estimation of aircraft aerodynamic parameters from flight data ".- Progress in Aerospace Sciences vol-26,1989

3. R.E.Maine.,K.W.Illif., " Application of parameter estimation to aircraft stability and control ".NASA RP - 1168,1986.

4. Vageesh K.P., "Estimation of stability derivatives of an aircraft model using dynamic flight technique in a wind tunnel ". M.S.thesiss 1992,Dept. of Aerospace Engineering,I.I.Sc.,Bangalore,India.

TURBULENT STRUCTURE IN A BOUNDARY LAYER SUBMITTED TO STRONG PRESSURE GRADIENTS

PER EGIL SKÅRE and PER-ÅGE KROGSTAD
Department of Mechanics, Termo and Fluiddynamics
Kolbjørn Hejesv. 2, N-7034 Trondheim, Norway

Abstract

A comparison has been given between the turbulent structures found in a zero pressure gradient (ZPG) boundary layer and a layer subjected to a strong adverse pressure gradient (APG). The pressure gradient is shown to reverse the direction of the dominant turbulent motion. When the pressure gradient is present considerable turbulent diffusion towards the wall is found. This is verified by the quadrant analysis [10] which demonstrates that the strong events near the wall are totally dominated by motions in the first and fourth quadrants. The APG makes the inclination of the structures with respect to the wall much steeper. This is apparent both for the detected Q_2 and Q_4 events. For the present APG layer, a large reduction of the streamwise extent of the correlations was found, compared to the ZPG layer.

1 Introduction

The boundary layer developing on a smooth surface in the absence of streamwise pressure gradient has been studied in great detail with respect to time averaged quantities as well as the structure of the turbulent motions. In spite of its much higher engineering importance, considerably less effort has been put down trying to unveil the details of the structures in the boundary layers subjected to strong pressure gradients. This gradient directly influences the turbulent shear stress gradient, $\partial\overline{uv}/\partial y$, as may be seen from the streamwise momentum equation. Hence an APG may produce a $-\overline{uv}$ profile where the peak stress may be considerably higher than the wall shear. The pressure gradient also has a direct effect on the mean velocity gradient, $\partial U/\partial y$, which will increase in the outer layer with an increasing APG. Hence considerable changes in the main turbulence production term $-\overline{uv}\partial U/\partial y$ may be expected due to the strong APG. Consequently the other components entering the various turbulent budgets must be affected [3, 13, 14].

Very little is known about the effect of the streamwise pressure gradient on the coherent motion in the boundary layer. According to the findings from a study of scaling relations for turbulent structures [5], the effects of the gradient on the individual structures may be small. They found that the average streak spacing is rather insensitive to the APG, although quite strong effects were found to exist for favourable gradients. This appears to be in agreement with flow visualisations [7]. On the other hand a strong sensitivity of the mean time between bursts on the pressure gradient is found [5, 7]. The burst frequency appears to increase rapidly with increasing APG.

2 Experimental Details

Two "equilibrium" boundary layer experiments were carried out to study the effects of APG on the turbulent structures. The experiments were carried out in a closed-return wind tunnel

with an adjustable roof. To produce the APG flow [12, 13], the roof was carefully adjusted to give the free-stream velocity distribution $U_e = 23.6(x - 1.74)^{-0.22}$ m/s . Equilibrium was achieved over the range 4.0 m $\leq x \leq$ 5.0 m, where the non-dimensional pressure gradient $\beta = \delta^* \tau_w^{-1} dP_e/dx \approx 20$. The skin friction coefficient C_f was constant at 5.7×10^{-4}, while the Reynolds number, Re_θ, increased from 25400 to 51000 in this range.

The ZPG layer was measured at $Re_\theta = 12600$. It was verified that the layer behaved according to the accepted requirements for fully developed turbulent boundary layers. The boundary layer, δ, and the momentum thickness, θ, were 71.8 and 7.71 mm respectively. The measurements were obtained at $U_e = 24.9$ m/s, which produced a C_f of 2.3×10^{-3}. Single probes, as well as arrays of 8 X- wire probes were used to allow studies of the large scale turbulent motions. Array data for the ZPG layer ($Re_\theta = 6030$) were kindly made available to us by Professor R.A. Antonia [1] at the University of Newcastle, Australia.

Some of the characteristic differences between these flows need to be pointed out as a background for the next sections. Figure 1a shows the mean velocity profiles for the ZPG and APG flows in inner variables. The profile for the latter flow is dominated by an extensive wake in the outer layer ($\Pi = 6.8$). The APG also modifies the turbulent stress distributions compared to the ZPG case (Figure 1b). This large peak in $-\overline{uv}$ produces significant differences in the main production term for the turbulent kinetic energy, k. The APG flow has two distinct peaks in the production term (Figure 2a). The inner peak is found near the wall as for ZPG boundary layers. A second peak is found roughly midway through the layer ($y/\delta \approx 0.45$) which has strong implications on the turbulent diffusion and dissipation rates [13]. The turbulent diffusion velocity, defined as $v_k^+ = \overline{vk}/(u_\tau k)$, is shown in Figure 2b. v_k^+ is positive everywhere in the outer layer for the ZPG layer, causing a steady diffusion of turbulent energy away from the wall. The diffusion rate is generally much higher in the strong APG flow and considerable negative diffusion is found below the outer peak in turbulent production.

3 Quadrant Decomposition

The $u - v$ quadrant decomposition technique has been effective for assessing the importance of visually observed ejections and sweeps in the wall region of boundary layer and duct flows. More generally, it has enabled the importance of $Q2$ and $Q4$ motions, of particular strengths, to be evaluated across the whole flow. Using the concept of a hyperbolic hole of size H [10], the contribution to $\overline{uv}$ as well as the frequency of occurrence of a particular quadrant was estimated. The fractional contribution from the i-th quadrant to the long time averaged shear stress is defined as $S_i = \langle \overline{uv} \rangle_i / \overline{uv}$.

Distributions of S_i for both layers are shown in Figure 3 for all events ($H = 0$). While only minor differences in S_2 are found, S_4 is increased considerably by the APG. For the ZPG layer, the ratio $\alpha = S_2/S_4$ is close to unity in the inner half of the layer, except very close to the wall where it increases rapidly, as reported earlier [10, 11]. In the APG flow α is distinctly smaller than one for $y/\delta \lesssim 0.45$, showing the importance of sweeps or $Q4$ motions in this case. The crossover occurs at the location of the outer peak in the turbulence production. The sum of S_2 and S_4 is also distinctly larger than in the ZPG flow, increasing by approximately 50% in the vicinity of the wall. This is coupled to increases in both $Q1$ and $Q3$ motions (Figure 3b) although the contribution from $Q1$ is clearly the most important. This is at least twice as high near the wall in the presence of the APG. The $Q1$ motion,

known as the outward interaction, represents transport of high speed fluid away from the wall, while the inward interaction from $Q3$ motions tends to bring low speed fluid back towards the surface. Both types of motions will be present if one considers a $Q4$ sweep as a jet type motion which hits the wall and is then rolled up in some sort of vortical flow.

The differences are even more conspicuous when only strong events ($H = 4$) are selected (Figure 4). For $y/\delta \gtrsim 0.5$ contributions from $(\overline{uv})_2$ are clearly dominant for both flows. In the ZPG flow α goes towards unity in the inner part of the layer, but diverge again rapidly near the wall ($y/\delta \lesssim 0.05$ or $y^+ \lesssim 100$). Negligible contributions are found from $Q1$ and $Q3$ through the entire layer. For the APG boundary layer, considerable contributions from $Q1$ and $Q4$ are found in the inner part of the flow, while the contributions from the other two quadrants are virtually absent in this region.

The average time between events occurring in the i-th quadrant, T_i, has been defined as the time between consecutive upward crossings of the threshold level H. Further, the duration of the events is defined as the time between consecutive upward and downward crossings of the detection level in the quadrant considered. Outer scaling [8], i.e. $T_i^* = T_i u_\tau/\delta$, has been applied for the averaged times.

The average time between $Q2$ and $Q4$ events for $H = 0$ is shown in Figure 5a. Since T_i^* will contain all events in quadrant i, it is dominated by the large number of weak events. Near the surface the frequency of occurrence is slightly lower in the absence of the pressure gradient, but from $y/\delta \approx 0.1$ there is a distinct increase in the time between the events. For the APG flow a reduction is observed. Hence at $y/\delta \approx 0.6$ the frequency is more than three times higher in the case of the APG. For $Q4$ events the trends are seen to be the same, but the difference is larger near the wall since the time between these events is shorter than between $Q2$ events in the APG flow for most of the boundary layer.

When the detection threshold is increased to $H = 4$, restricting the observations to strong events, the differences between the two flows become even more evident (Figure 5b). Very few $Q2$ events are found near the wall in the APG boundary layer and the flow is totally dominated by $Q4$ motions. While for the ZPG flow $T_2^* \approx T_4^*$ at $y/\delta \approx 0.1$, it was found that T_2^* is at least twenty times T_4^* when the APG is present. Hence the quadrant decomposition indicates that turbulent motions directed towards the wall are enhanced considerably by the presence of an APG. This is further supported by the production term and the turbulent diffusion velocity.

Also the durations of the events show distinct differences between the two flows. The ratio between the mean duration and the time between events, $\Delta T_i^*/T_i^*$, which is independent of the method of scaling, shows that for both flows the relative duration increases for $Q4$ events with the distance from the wall in the outer layer and decreases for $Q2$ events (Figure 6). For the ZPG boundary layer this ratio is roughly the same for $Q2$ and $Q4$ events for $y/\delta < 0.3$ when $H = 0$, although $\Delta T_2^*/T_2^*$ decreases rapidly as the wall is approached.

When the APG is applied, $\Delta T_2^*/T_2^*$ increases rapidly with distance from the wall as was found for the ZPG boundary layer, but $\Delta T_4^*/T_4^*$ shows an equally rapid decrease producing a large difference between $\Delta T_2^*/T_2^*$ and $\Delta T_4^*/T_4^*$ at $y/\delta \approx 0.025$. This may indicate that the weak $Q4$ motions in the APG layer are dominated by short duration, intense activity while the $Q2$ motions contain slower, longer lasting activities in this region.

When the observations are restricted to strong events ($H = 4$) the difference between the two flows is quite evident. Although both flows tend towards increasing relative durations of the $Q2$ events in the outer part of the layer, the mean duration of $Q2$ events in the APG flow for $y/\delta < 0.3$ is negligible compared to the durations of the $Q4$ events. While $Q2$ and

$Q4$ events have comparable durations in the inner half of the boundary layer in the ZPG flow, the APG flow is completely dominated by the activity in the fourth quadrant.

In the immediate vicinity of the surface $\Delta T_4^*/T_4^*$ decreases for both flows. For the ZPG flow this is compensated by a corresponding increase in $\Delta T_2^*/T_2^*$. This has been shown [8, 10, 11] to result in an increased contribution to the shear stress in the second quadrant and a similar reduction in the fourth quadrant contribution. In the strong APG layer there appears to be no corresponding increase in $\Delta T_2^*/T_2^*$. Instead a very strong rise in $\Delta T_1^*/T_1^*$ is found (not shown). This gives further support to the assumtion that $Q4$ related events directed towards the wall are reflected as $Q1$ motions, returning high speed fluid away from the wall.

4 Large scale events

As a consequence of the large effects of the APG observed from the quadrant analysis, a study of the differences in large scale motion was undertaken, using an array of 8 X-wire probes. The signals from the probes were searched for simultaneous detections of $Q2$ or $Q4$ events. Defining a detector function, $D(t)$, which was set to 1 when an event was detected and 0 otherwise, a two-point correlation function, $\rho(\tau)$ was calulated. The reference probe was located at $y_2/\delta \approx 0.1$ for both flows. Only events for $H = 1$ will be presented, which produced approximately 5000 detections in the ZPG flow and 1500 detections in the APG layer, roughly constant throughout the layer.

For the ZPG layer, the vertical extent of the $Q2$ and $Q4$ correlations are roughly equal (Figure 7), but considerable differences in the streamwise lengths are evident. The $Q2$ detections are correlated over a much longer distance than the $Q4$ events, indicating that the $Q2$ events are inclined at a more shallow angle to the wall than the $Q4$ events. This is in accord with earlier results [6, 9] which have indicated that $Q4$ events near the wall travel at a velocity which is higher than the local mean, U, while $Q2$ events are convected at a velocity which is lower than U. (Time has been converted to distance using the Taylor hypothesis, where the mean velocity at the reference point has been used as convection velocity).

The APG strongly alters the correlations (Figure 8). The streamwise extent of the correlations is reduced by a factor of more than 10 for the $Q2$ events and more than 5 for $Q4$. This agrees well with the observed reductions in duration of the events. In contrast to the ZPG flow, the $Q4$ events are correlated over a larger streamwise distance than the $Q2$ detections. This was anticipated, since the quadrant analysis revealed strong dominance of $Q4$ events in this region. Due to the strong negative diffusion velocity in the APG layer, the $Q4$ correlations in this case are inclined at a much steeper angle to the surface than for the ZPG flow (note the difference in horizontal scales).

5 Conclusions

It has been shown that the large effect streamwise pressure gradients may have on the time averaged turbulent quantities is also reflected in the structures of the turbulent motion. When the APG is sufficiently strong, considerable turbulent diffusion towards the surface may be present. This was verified by means of a quadrant decomposition analysis. Unlike the ZPG boundary layer where $Q2$ and $Q4$ events are equally important, the APG flow was found to be strongly dominated by turbulent motions in the fourth quadrant. When the

observations were restricted to strong events, considerable contributions from the outward interaction found in the first quadrant were observed near the wall. This indicate reflections of large scale motions from the wall. In the ZPG flow this type of motion is virtually non-existent when only strong events are considered.

The APG was also shown to influence the duration and frequency of occurrence of the turbulent motions in the different quadrants. A very large increase in the frequency of $Q4$ motions was observed, while the frequency for $Q2$ events was considerably reduced, in particular for strong events. The strong $Q4$ events were also found to last much longer than in the ZPG layer, thereby increasing the contributions to the long time averaged shear stress.

The large scale turbulent structure is also affected. Two-point correlations of detections from the Quadrant method for $Q2$ and $Q4$ events confirmed the findings about the time scales. The strong negative diffusion velocity near the wall in the APG layer was shown to produce major differences to the length scales and structure inclinations in the two flows. This was especially evident in the detected $Q4$ events.

References

[1] ANTONIA, R.A., BROWNE, L.W.B. and BISSET, D.K. : 1990. Effect of Reynolds number on the organized motion in a turbulent boundary layer, in S.J. Kline and N.H. Afgan (eds.) *Near-Wall Turbulence*, Hemisphere Publishing Co., 488-506.

[2] BLACKWELDER, R. F. and KAPLAN, R.E. : 1976. On the Wall Structure of the Turbulent Boundary Layer, *J. Fluid Mech.*, **76**, 89-112.

[3] BRADSHAW, P. : 1967. The turbulent structure of equilibrium turbulent boundary layers, *J. Fluid Mech.*, **29**, 625-645.

[4] DUMAS, R. : 1990. Observations on the Boundary Layer Based on Measured Correlations with Various Improvements, in S.J. Kline and N.H. Afgan (eds.) *Near-Wall Turbulence*, Hemisphere Publishing Co., 437-452.

[5] FINNICUM,D.S. and HANRATTY, T.J. : 1988. Effect of Favorable Pressure Gradients on Turbulent Boundary Layers, *AIChE Journal*, **34**, 4, 529-540.

[6] GAN, C.L. and BOGARD, D.G. : 1991. Study of the Convections Velocities of the Burst and Sweep Structures in a Turbulent Boundary Layer, in F. Durst *et al.* (eds.) *8th Symp. on Turbulent Shear Flows*, Munich, 2.4.1-2.4.8.

[7] KLINE, S.J., REYNOLDS, W.C., SCRAUB, F.A. and RUNSTADLER, P.W. : 1967. The structure of turbulent boundary layers, *J. Fluid Mech.*, **30**, 741-773.

[8] KROGSTAD, P.-Å., ANTONIA, R. A. and BROWNE, L. W. B. : 1992. Comparison between rough- and smooth-wall turbulent boundary layers, *J. Fluid Mech.*, **245**, 599-617.

[9] KROGSTAD, P.-Å., ANTONIA, R. A. and BROWNE, L. W. B. : 1993. The use of orthogonal X-wire arrays for the structure investigation in a turbulent boundary layer, *Expts. in Fluids*, **15**, 231-239.

[10] LU, S. S. and WILLMARTH, W. W. : 1973. Measurements of the Structure of the Reynolds Stress in a Turbulent Boundary Layer, *J. Fluid Mech.*, **60**, 481-571.

[11] RAUPACH, M.R. : 1981. Conditional statistics of Reynolds stress in rough-wall and smooth-wall turbulent boundary layers, *J. Fluid Mech.*, **108**, 363-382.

[12] SKÅRE, P.E. : 1994. Experimental Investigation of an Equilibrium Boundary Layer in Strong Adverse Pressure Gradient, Ph.D. Thesis, Norwegian Institute of Technology, Trondheim, Norway.

[13] SKÅRE, P.E. and KROGSTAD, P.-Å. : 1994. A Turbulent Boundary Layer Near Separation, *J. Fluid Mech.*, **272**, 319-348.

[14] SPALART, P.R. and WATMUFF, J.H. : 1993. Experimental and numerical study of a turbulent boundary layer with pressure gradients, *J. Fluid Mech.*, **249**, 337-371.

[15] TOWNSEND, A.A. : 1961. Equilibrium layers and wall turbulence, *J. Fluid Mech.*, **11**, 97-120.

Figures

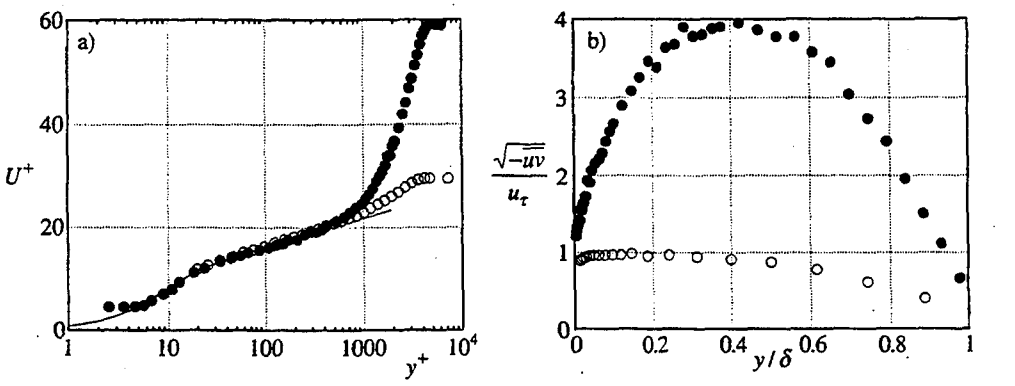

Figure 1: a) Mean velocity profiles. b) Reynolds shear stress profiles. ZPG (o), APG (•).

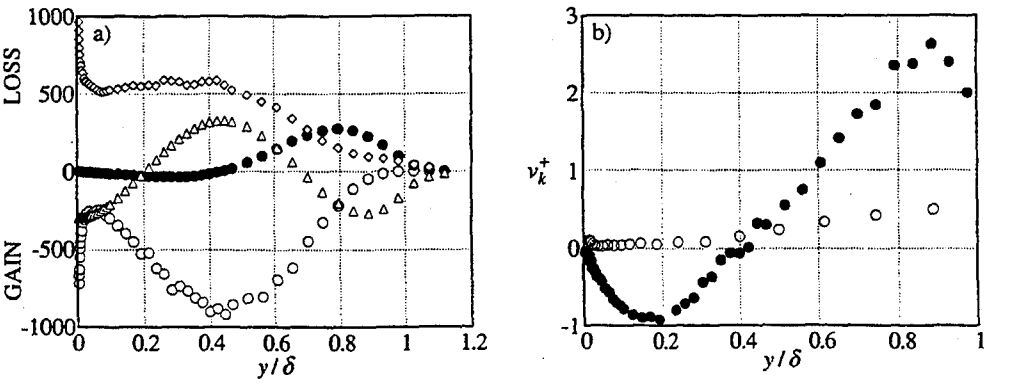

Figure 2: a) Budget for the turbulent kinetic energy. Production (o), Advection (•), Diffusion (△), Dissipation (◇). b) Turbulent diffusion velocities. ZPG (o), APG (•).

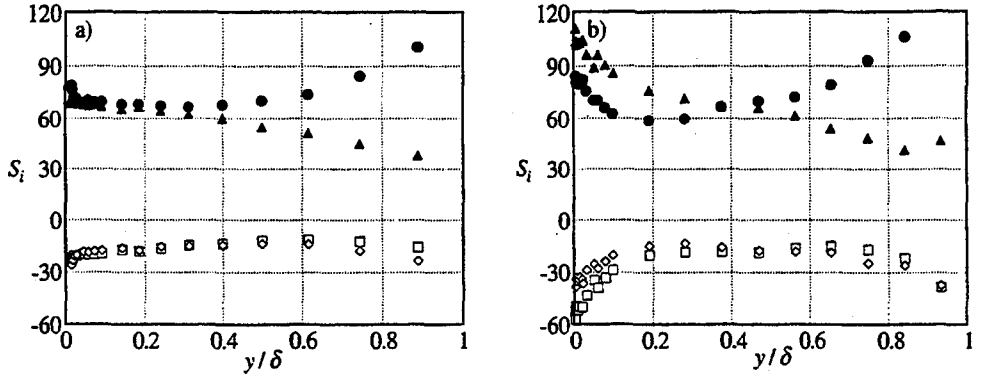

Figure 3: Fractional contribution (%) for weak events ($H = 0$) for the a) ZPG and b) APG layer. S_1 (□), S_2 (•), S_3 (◇), S_4 (▲).

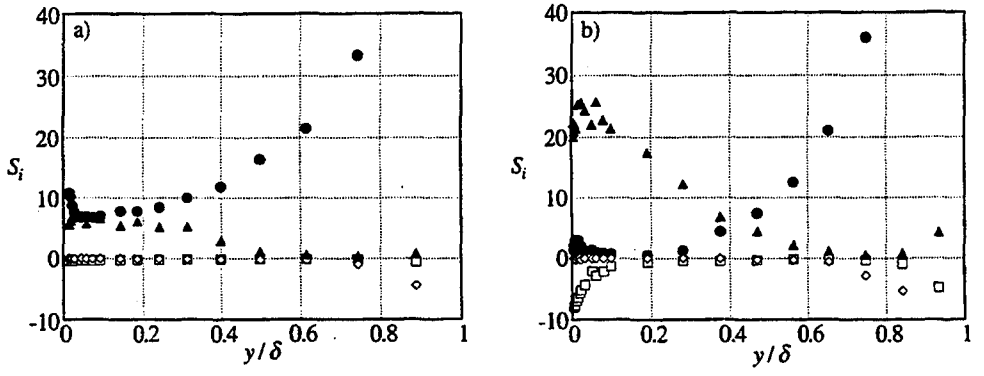

Figure 4: Fractional contribution (%) for strong events ($H = 4$) for the a) ZPG and b) APG layer. S_1 (□), S_2 (•), S_3 (◇), S_4 (▲).

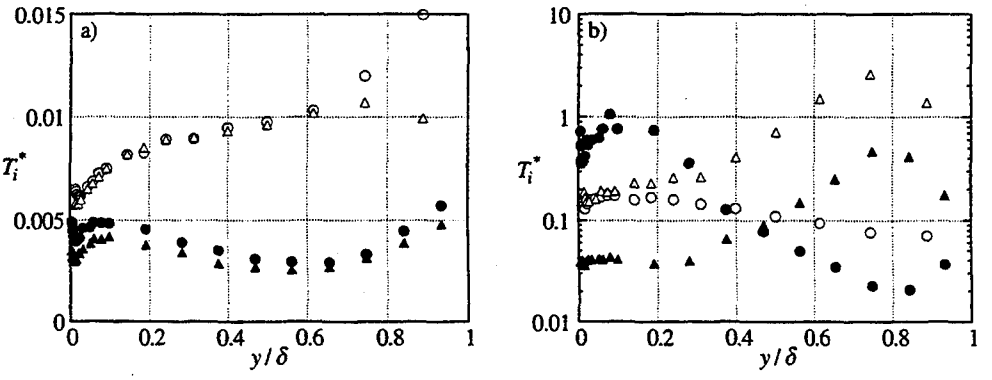

Figure 5: Mean time between Q2 and Q4 detections. a) Weak events ($H = 0$) b) Strong events ($H = 4$). ZPG : T_2^* (○), T_4^* (△), APG : T_2^* (•), T_4^* (▲).

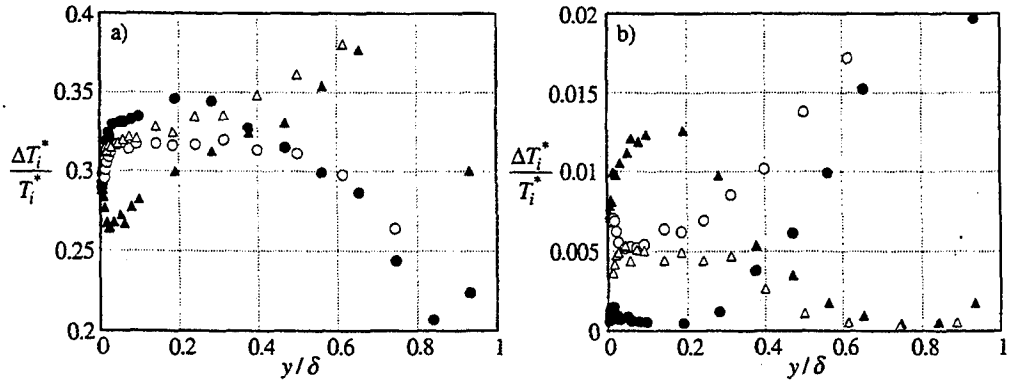

Figure 6: Ratio of mean duration to mean time between Q2 and Q4 detections. a) Weak events ($H = 0$) b) Strong events ($H = 4$). ZPG : $\Delta T_2^*/T_2^*$ (o), $\Delta T_4^*/T_4^*$ ($\triangle$), APG : $\Delta T_2^*/T_2^*$ ($\bullet$), $\Delta T_4^*/T_4^*$ ($\blacktriangle$).

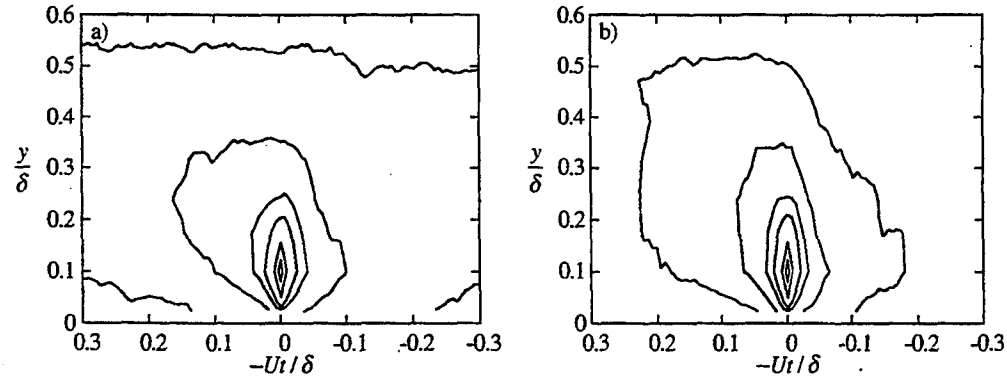

Figure 7: Two point detection correlations for a) $Q2$ and b) $Q4$ events ($H = 1$) for the ZPG layer, isolines : 0.15, 0.2, 025, 0.3, 0.5 and 0.8. Flow-direction from right to left.

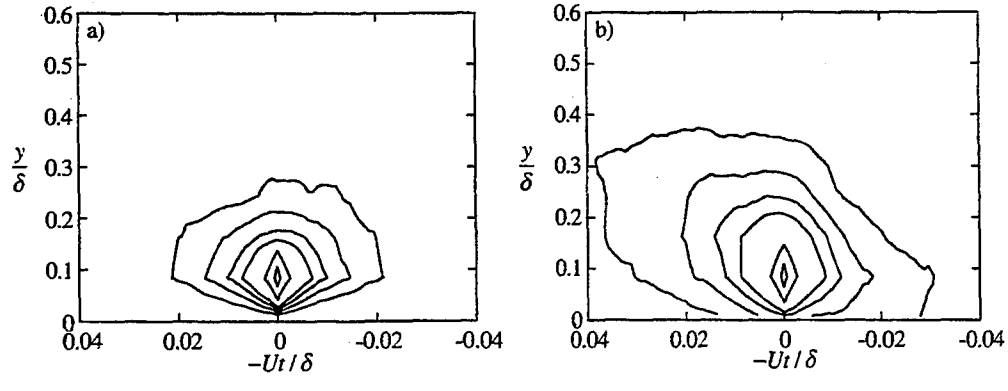

Figure 8: Two point detection correlations for a) $Q2$ and b) $Q4$ events ($H = 1$) for the APG layer, isolines : 0.15, 0.2, 025, 0.3, 0.5 and 0.8. Flow-direction from right to left.

DEVELOPMENT OF THE VORTEX-GENERATOR AND INVESTIGATION ON EFFECT OF VORTEX-GENERATOR ON BOUNDARY LAYER

Ni Yaqin
China Aerodynamics Research And Development Center
P. O. Box 211 (621000) Miangyang Sichuan, China

ABSTRACT

This paper presents the mechanism and application of vortex-generator, the development of a vortex-generator, as well as some important parameters used. The analysis and the verification of vortex-generator have been given. From the measured boundary layer thickness and distribution of Mach number along side wall of the test section of wind tunnel, it has been shown that the present vortex-generator is a successful design. With the vortex-generator, the boundary layer thickness can be decreased about 71% at M=0.4~0.85 at the place 880 mm down stream of the vortex-generator and it has no influence on the main flow while the test results of half model is improved.

INTRUDUCTION

The concept of vortex-generator was put forward by Bmynes and Taylor in 1947[1]. The vortex-generator has been used to delay boundary layer separation which may cause some departure phenomena of aircraft including airframe buffeting, pitch-up, wing dropping, rock, spin, and so on. The Vortex generator can also be used to enhance lift of aircraft. As it is not necessary to change the aircraft configuration, the vortex-generator is a kind of practical and economic means of aerodynamic technique. In recent years, A three-dimensional, multi-block, multi-zone, Euler analysis has been developed and applied to analyze the flow processes induced by a lateral array of low profile vortex generators[2].

Generally, Any thing can be regarded as a vortex-generator if it generates vortex flow. When the vortex generator mounted on the surface of a body generates vortex flow, momentum exchange occurs between the main flow with high momentum air and boundary layer with low momentum air, which results in momentum increment in the boundary layer, as well as flow disturbulence around vortex flow. The momentum exchange happens continually as that of the main flow, therefore it can be used against boundary layer separation caused by relatively high negative pressure gradient and boundary layer increment due to negative pressure gradient or surface friction. For the first point mentioned above, it has been frequently used to improve airplane aerodynamic characteristics and internal flow characteristics of air inlet. For example, Boeing 707 airplane has the vortex generator on its wing to delay flow separation. Grumman company employed vortex generator on a aircraft to delay buffeting[3]. The vortex-

generator on the wing of G91Y aircraft canceled out wing dropping within a narrow Mach number range reaching transonic flight upper limit. Many cases proved that engine stall caused by flow separation due to shock wave interference can be avoided by introducing the vortex-generators at air inlet. But it is rarely used to thin out boundary layer and it is more difficult to design. To meet the requirements of improving half-model wind tunnel test, a preliminary investigation has been made on the effect of the vortex-generator on boundary layer with the purpose of thin out boundary layer at the test section of wind tunnel without altering the uniformity of main flow. This is beneficial to the half-model test because boundary layer of the wind tunnel wall has a bad effect on the test result by decreasing lift coefficient of the model and altering focus location and drag coefficient to a certain extent.

The function of vortex-generator depends on vortex strength, vortex rotating direction and interference among vortices, which are related to some parameters of the vortex-generator including array, shape, size, orientation, number, distance between vortices, and location relative to controlled physical surface. All these parameters need to be investigated for the design of vortex-generator.

This investigation was conducted on FL-21 wind tunnel that is a half closed -circuit configuration with test section 0.6 m by 0.6 m. Tunnel operation is intermittent . It can operate over a Mach number range of 0.4 to 3.5. When it operates over Transonic. Ceiling and floor of test section is slantwise perforated wall with approximately 4.3% porosity. Unit Reynolds number range is 8.6×10^6/m～16.3×10^6/m(Fig. 1).

DESIGN AND MANUFACTURE OF THE VORTEX-GENERATOR

Design

The vortex-generator was used to thin out boundary layer at the test section of FL-21 wind tunnel, half-model can be placed down stream of the vortex-generator where boundary layer was relatively thin and the effect of boundary layer on the half model was reduced. Because the requirement of flow field uniformity is high, it was expected that the flow field uniformity be not altered once the vortex-generator was introuduced.

There are many types of vortex-generators including wedge shaped type, cascade type, wing type, wishbone-shaped[4] (Fig. 2). Cascade type was chosen after consideration. For simplicity, the blade was made of a flat plate with a thickness of 0.5 mm. The blade edge was rounded off. The plate was perpendicular to the side wall of wind tunnel. Blade incidence was determined according to the principle that vortex-strength produced was capable of decreasing the thickness of boundary layer down stream of the vortex-generator at specific region. Vortices break quickly if the incidence is too high, which are not useful for promotion of momentum exchange between main flow and boundary layer in controlled region, instead they interfere with main flow to a great extent. But the vortex strength is not large enough to be in effect if the incidence is too small. In addition, air viscous effect should be considered when the incidence is chosen. Because the effectiveness of vortex at one point is decreased as the distance

between the point to the vortex-generator is increased. The vortex may have no effect on the points far down stream of the vortex-generator. Therefore vortex strength should be increased by increasing the incidence according to the distance between the vortex-generator and the controlled region and the length of controlled region. The incidence was chosen as 12 degrees by trade-off studies.

A lot of factors determine the configuration of vortex-generator. The blade of the vortex-generator is a trapezium shaped blade (Fig. 3). The trailing edge height of the blade should be less than the thickness of boundary layer to a small extent because the vortex flow generates from side edge. If the edge height is too high, the uniformity of the main flow will be influenced. In addition, it is not beneficial to increase the flow momentum at the bottom of boundary layer because the vortex is far away from the tunnel wall. The trailing edge height was chosen as 30 mm because the boundary layer thickness of the test section of FL-21 wind tunnel is about 35 mm at test region. The angle between horizontal direction and the side edge of the trapezium shaped blade has an effect on vortex strength and vortex direction. It is expected that vortex flow around the edge of boundary layer, therefore too large angle should be avoided. Because boundary layer is grow up along the main flow, it is not adequate to set the angle to be zero. The angle was chosen as 10 degrees.

The chord of the trapezium shaped blade can not be too large, otherwise flow will be blocked up to some extent and the friction loss of flow will be increased. But the vortex strength is not large enough if the blade chord is too small. Therefore it should be considered comprehensively. The chord length of 50 mm was chosen. After all these consideration, the finial trapezium shaped blade is determined.

The last thing to be considered is the magnitude of vortices. The height of the test section of FL-21 wind tunnel is 0. 6 m and the width of controlled region is at least 0. 3 m, therefore the number of blades was chosen as six for the designed vortex-generator. Three blades was placed at upper side of the centerline of the side wall with a incidence of -12 degrees, the other three blades was placed below the center line with a incidence of 12 degrees. The distance between blades is 50 mm. As the blades are placed symmetrically with respect to the center line of the tunnel wall, vortices induced velocity will be canceled out to a large extent down stream of the vortex-generator at the center line(point A)while induced velocity perpendicular to the side wall remains(see Fig. 4). From the analysis of induced velocity at the point B, it can be seen that a induced velocity component toward the side wall exists. This is what we expect, because if the vortex flow motion is opposite to the side wall, the main flow field may be influenced to a certain extent, hence the test results of the half-model may also be influenced.

It is a very important and practical topic concerning the location of vortex-generator. If the vortex-generator was placed near model, it would influence the model. The flow around model would be very ununiform because the strength of vortex is high but the rotational diameter of vortex is small and the number of vortices is limited. If the vortex-generator was located far away from the model, the region influenced by vortex would be small. Therefore a compromise should be reached. The vortex-generator was mounted at the entrance of test section.

Manufacture

For the simplicity of manufacture and installation, to save time and to increase stiffness of the vortex-generator, the six bladed vortex-generator was made integrally by a 300(mm)×100(mm)×0.5(mm) iron plate. A 300 mm long iron plate was folded vertically to form a L shaped configration. Long side was used to made the vortex-generator by cutting metal according to the blade shape and folding it vertically while other side of the plate was mounted at the entrance of test section by bolts(Fig. 5).

The distance between the vortex-generator and the center line of second window at side wall of test section is 880 mm, which is about 25 times of the thickness of boundary layer at the center line of second window. The half model was usually mounted on the window. According to the experience of A. W Moore and K. G. Wight[5], the uniformity of flow field is not a problem. But whether the effectiveness of vortex is reached at the tail of half model can be verified by boundary layer measurement and the half-model test results. The adequacy of the vortex-generator can be verified by boundary layer measurement and model(flight)test.

THE EFFECT OF VORTEX-GENERATOR ON BOUNDARY LAYER

The total pressure recovery coefficients of boundary layer were measured at horizontal center line of side wall about 880 mm downstream of entrance section with and without vortex-generator(Fig. 6). The total pressure was measured by a mini comb pitot which has two static pressure tubes(Fig. 7). The detail of the comb pitot can be found in reference[6]. The comb pitot was mounted on the second window. The boundary layer thickness was determined on the assumption that total pressure recovery coefficient is 0.995 at edge of boundary layer. At nominal Mach number ranging from 0.4 to 0.9, the measured thickness was 35 mm without the vortex generator. When the vortex-generator was added, the boundary layer thickness reduced to about 10 mm, with a reduction of 71 percent(Fig. 8). It is obvious that large total pressure recovery value in the boundary layer exists when the vortex-generator is installed. The recovery value increases with the increasing of Mach number. For example, increment of total pressure recovery coefficient is 0.025 at a point 10 mm away from the tunnel wall when $M=0.395$, it increases to 0.125 at the same point when $M=0.89$. This phenomenon may be explained as that vortex strength increases with the increasing of Mach number. At the same point out side of boundary layer, the total pressure recovery value does not change when cases with and without the vortex-generator are comparied, which demonstrates that the vortex-generator does not have influence on the main flow.

Fig. 9 shows Mach number distribution along horizontal center line of the side wall of test section with and without the vortex-generator. It can be seen that the vortex-generator does not have obvious effect on uniformity of Mach number distribution. The average Mach number is slightly less than the reference Mach number at the chamber. This becomes obvious when Mach number exceeds 0.897. The difference of Mach numbers is about 0.01. The difference of average Mach number and reference Mach number is small without the vortex-gen-

erator. This may be explained as that kinetic energy of flow is consumed slightly when the vortex generator is added.

THE HALF-MODEL TEST

The forces measurement of the half-model was performed in the FL-21 wind tunnel with and without the vortex-generator. The model is a half-model of a complete aircraft with large aspect ratio. The length of model is 698 mm. The model was placed at the second window of test section. For the convenience of turning of model, the distance between the bottom of model and the side wall of the wind tunnel is 0. 8 mm. The distance between the model tail and the center line of second window is 360 mm.

The result of forces measurement of the half-model shows that the trend with and without the vortex-generator agrees well in principle, eventhough there are some differences. The slope of lift coefficient increases 4 percent at Mach number ranging from 0. 4 to 0. 85 on the average. The focus location is shifted back about one percent of average aerodynamic chord. The test data shows that zero lift drag without the vortex-generator is slightly less than that with the vortex-generator, the variation of zero lift drags is about 0. 001 at all Mach number of the test. The drag divergence Mach number is almost the same with and without the vortex-generator. In addition, zero lift angle approaches zero which is in agreement with the data from flight test. The zero lift moment coefficient agrees well with the flight test data. All these demonstrate that test result is improved when the vortex-generator is installed which thins out boundary layer. The increment of zero lift drag may be explained as that the flow disturbulence is increased slightly when the vortex-generator is added. The detail of the half model test can be found in reference[7].

DISCUSSION AND CONCLUSION

Discussion

- From the measured boundary layer thickness with and without the vortex-generator it can be seen that the boundary layer thickness could be further reduced by improving the design of vortex-generator.
- As the length of half-model and the distance between the tail of model and the vortex-generator are relatively long, it is estimated that the influence of the vortex-generator on the tail of model is small from the measured data of forces and focus locations. Therefore better results may be obtained by adjusting the distance between the model and the vortex-generator or increasing the incidence of blade to a certain extent.
- When the vortex-generator is installed, the flow field is relatively uniform at horizontal center line at the side wall, but the flow uniformity is not so good at the region away from horizontal center line at the side wall because the induced effect can not be canceled out. For the present test, the model is placed around the horizontal center line of the test section of

wind tunnel, therefore the effect is not so large.

● The shock wave can influence the uniformity of the flow field if the vortex-generator is used at $M \geqslant 1$.

● If the vortex-generator were designed as a coupled blades with opposite direction, the results could be better, because the induced velocities at all the other points could be canceled out approximately.

● If it is possible, it is suggested that the blade airfoil of vortex-generator be improved to increase the strength of vortex at the same platform and dimension.

CONCLUSION

● The present vortex-generator is a successful design. The boundary layer thickness can be decreased about 71% at $M=0.4 \sim 0.85$ at the place 880 mm downstream of the vortex-generator and it has no influence on the main flow.

● The present vortex-generator is easy to made and easy to mount and dismount in the test section. The low-cost vortex-generator can be used to improve the result of half model test in the wind tunnel similar to FL-21 at $M<1$. Of course it is necessary to redesign the vortex-generator if the boundary layer thickness is quite different.

● If the vortex-generator is applied to aircraft, the height of blade must be lower to reduce parasitic drag.

REFERENCE

[1] G. V. Lachmann "Boundary layer and flow control" Volume 2, 1964

[2] T. J. Barber. J. S. Mounts and D. C. Mc Cormick "Boundary layer Energization by Means of Optimized Vortex Generators". AIAA-93-0445.

[3] Walland, I. T. , Curtis, E. J. "Gulfstream Ⅱ Aerodynamic Design" SAE 670242, 1967

[4] Bruce L. Stams and Cory S. Tang "Lift Enhancement of an airfoil using a Gurnoy Flap and Vortex Generators". AIAA-93-0647

[5] A. W. Moore and K. C. Wight "On Achieving Interference-free Results From Dynamic Tests on Half-models in Transonic Wind Tunnel". ARC R&M 3636, 1970

[6] Ni Yaqin "Boundary layer measurement of the 7FD-01 wind tunne", CAE. 1965

[7] Ni Yaqin "The half model test using the vortex-generator in the wind tunnel" CARDC, 1974

Fig. 1 0.6m×0.6m trisonic wind tunnel CARDC FL-21

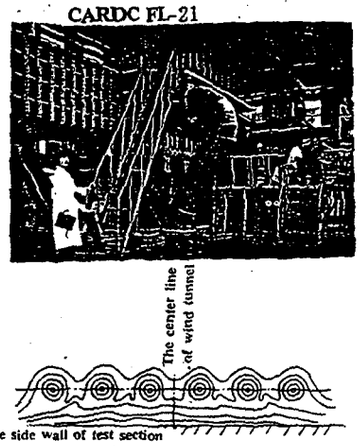

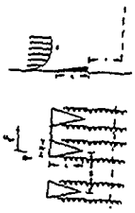

Schematic diagram of separation alleviation using vortex generation devices (triangular ramp-likeVG), AIAA 93-0115

Flow generated by submerged vortex generator of wheeler wishbone type, AIAA 93-0617

Fig. 2 Sketch of some vortex generators

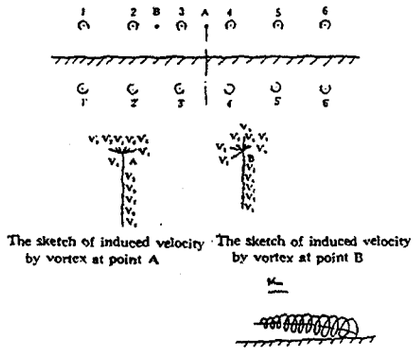

Fig4. schematic of velocity induced by vortex

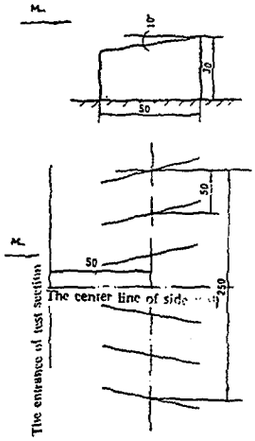

Fig3. Geometry of vortex generator and sketch of installation in wind tunnel

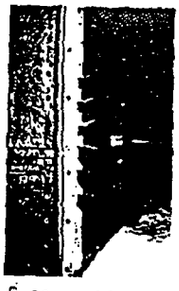

Fig. 5 Mounted Vortex-generator

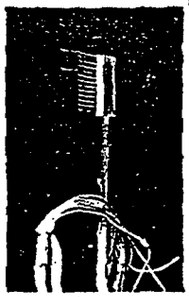

Fig. 6 Boundary layer measurement set

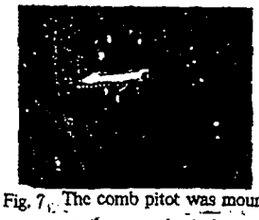

Fig. 7 The comb pitot was mounted on the second window

Fig. 8 measured boundary layer thickness of the side wall

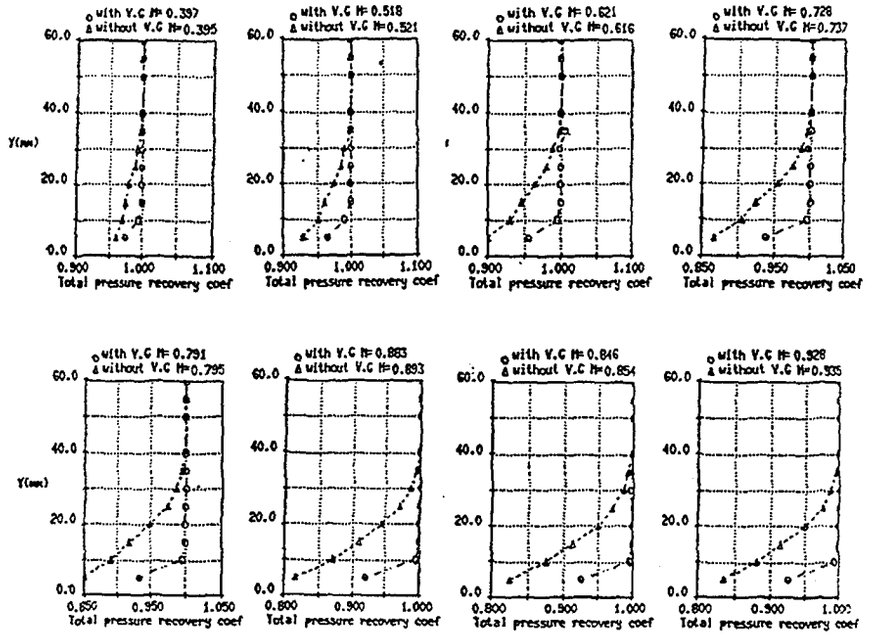

Fig9. Mach number distribution on the center line of side wall of test section

generator vortex on	M	0.4114	0.5018	0.6033	0.6983	0.7985	0.8973	0.9426	0.9[illegible]	1.0415	1.099
	M	0.4099	0.4966	0.6022	0.6903	0.7946	0.8882	0.9344	0.9752	1.0237	1.0785
generator vortex off	M	0.3867	0.5036	0.6162	0.7045	0.8108	0.9051	0.9603	0.9988	1.053	1.1070
	M	0.3878	0.5036	0.6135	0.7042	0.6090	0.9064	0.9642	0.9[illegible]	1.050	1.1013

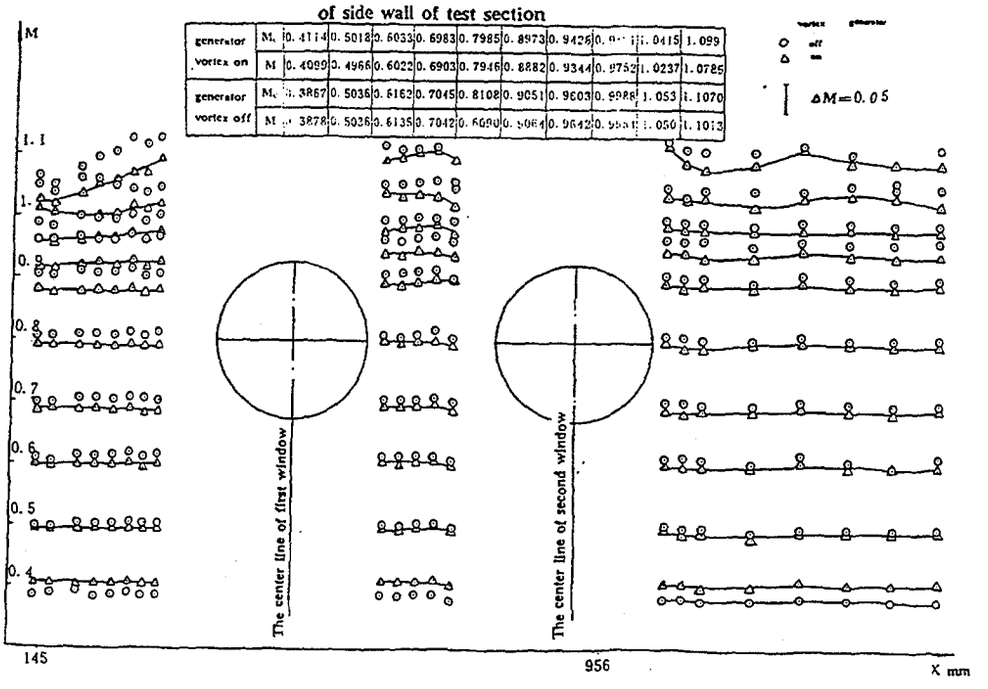

EFFECTS OF SUCTION ON VELOCITY MEASUREMENTS ON THE SURFACE OF A FLAT AND CURVED ROUGH PLATE

S. E. HÜBBE-WALKER, J. R. PINCOMBE AND A. B. TURNER

T.F.M.R.C, School of Engineering, University of Sussex, Brighton, BN1 9QT, (UK)

Abstract

The work presented in this paper originated from an industrial requirement to quantify the effects of external surface roughness (which may occur in the process of manufacturing, during operation or when ceramic thermal barrier coatings are applied) on the velocity and turbulence quantities in the boundary layer flow over turbomachinery blades.

It is well-known that surface roughness can contribute significantly to the profile loss of nozzle guide vanes and rotor blades in gas turbines as well as and compressors. Other significant influences on boundary layer development are free stream turbulence intensity and surface curvature.

This paper discusses part of the velocity and turbulence quantity measurements carried out inside the flat curved rough plate rig (FCRPR), designed and built at the University of Sussex, using a single component laser Doppler anemometer and fluid visualisation with special emphasis on the effects of reducing the boundary layer thickness by sucking off a part of the main air stream via a plenum chamber.

Measurements with and without suction were made at several stations along the wind tunnel section (set up for zero pressure gradient) on a surface where the topography was a regular array of 1 mm high trapezoidal roughness elements arranged in a square configuration.

The data obtained was used to compute and analyse various velocity and shear stress quantities. The results showed that the nature of the turbulent boundary layer flow was significantly affected by the surface topography. Sucking off part of the boundary layer had an important effect on the velocity inlet as well as Reynolds shear stress profiles. Without suction the flow separated at the leading edge and reattached to the floor 36 mm downstream. In applying suction, this separation bubble was eliminated and the optimum suction flow could be established using flow visualisation.

NOMENCLATURE

d	Beam Diameter	[mm]
H	Local Height of Tunnel	[mm]
h	Height above Base of Roughness Elements and Smooth Surface	[mm]
$\dot{Q}$	Tunnel Volume Flow Rate	[l/min]
$\dot{Q}_p$	Volume Flow Rate sucked off at Plenum	[l/min]
S_l	Distance from Leading Edge of Plenum	[mm]
S_t	Distance along the Floor of the Working Section	[mm]
U_c	Free Stream Velocity	[m/s]
$\overline{U}$	Streamwise Mean Velocity Component	[m/s]
u'	Streamwise Component of Velocity Fluctuation	[m/s]
$\overline{u'^2}$	Averaged Sum of the Squares of Streamwise Component Velocity Fluctuations	$[m^2s^2]$
$\overline{u'v'}$	Reynolds Shear Stress	$[m^2/s^2]$
$\overline{V}$	Mean Velocity Component Normal to Surface	[m/s]
v'	Normal Component of Velocity Fluctuations	[m/s]
$\overline{v'^2}$	Averaged Sum of the Squares of Normal Component Velocity Fluctuations	$[m^2/s^2]$
δ	Boundary Layer Thickness	[mm]

1. INTRODUCTION

This paper describes the turbulence quantity measurements carried out inside the FCRPR for a zero pressure gradient, using a single component laser Doppler anemometer and fluid visualisation. These measurements will be used to calibrate and validate the theoretical Reynolds stress transport model Ten developed by Tarada,[1] which solves the transport equations for turbulence quantities within the boundary layer.

Flow visualisation in the inlet section was used to establish the initial flow conditions. It revealed the presence of a separation bubble at the leading edge which decreased in size with increasing volume flow rate. A plenum chamber arrangement, integrated into the floor of the inlet section, enabled the starting conditions for the growth of the boundary layer on the floor of the working section to be controlled and optimised by sucking off part of the flow using a centrifugal blower. Fluid visualisation also showed that the developing boundary layer was affected significantly when part of the flow was sucked off at the leading edge.

LDA measurements were made at several stations along the tunnel, with and without suction, which showed that the nature of the boundary layer flow was affected by the surface topography. From the measured mean velocities and RMS levels the various velocity and shear stress quantities were computed and analysed.

2. EXPERIMENTAL APPARATUS

2.1 The Wind Tunnel

Fig.1 shows a schematic of the flow facility layout; it comprised a bellmouth intake of length 160 mm, a settling section with a length and area of 800 mm and 0.25 mm^2 respectively, a 10 to 1 area ratio contraction, an inlet section of length 160 mm, a wind tunnel working section, an outlet section and a turbo-fan operating in the suction mode up to a maximum flow rate of 40 m^3/min representing a free stream velocity of $U_c = 22$ m/s.

The geometry of the working section was as follows: A rectangular cross-section of width 300 mm and approx. height 70 mm extending for an overall length of 800 mm with a straight section for the first 402 mm followed by a curved section of radius 1.2 m over an arc of 19 degrees. The floor of the tunnel, formed from an assembly of forty alloy bars, had a rough surface. The surface topography was a regular array of 1 mm high trapezoidal roughness elements arranged in a square configuration.

In order to provide optical access for the LDA, the side walls of the tunnel were made of 10 mm thick *PERSPEX*©. To provide optical access for flow visualisation, the ceiling of the tunnel was made of 1 mm thick *PERSPEX*©. The design of the supporting side wall pillars allowed the height of the ceiling to be varied along the tunnel. A *NEOPRIM* © strip seal was used to prevent leakage between the ceiling and the side walls. This variable height, flexible ceiling arrangement enabled the streamwise pressure gradient to be varied (for future work). To facilitate measurement of the streamwise pressure distribution, the floor of the tunnel was instrumented with forty equally spaced, static pressure taps located along the mid-span line.

The inlet section served two functions. Firstly, the ceiling could be adjusted to provide a smooth transition from the height of the tunnel at the contraction (80 mm) to the height of the tunnel at the working section. Secondly, the plenum chamber arrangement in the floor of the inlet section enabled the starting conditions for the growth of the boundary layer on the floor of the working section to be controlled and optimised. This was achieved by sucking flow from the developing boundary layer via the chamber below the plenum, using a Secomak centrifugal blower. The suction flow rate was quantified using an "Annubar" differential pressure flow rate measuring device.

The outlet section provided for the smooth transition from the aperture of the downstream end of the working section of the tunnel to the intake of the turbo-fan.

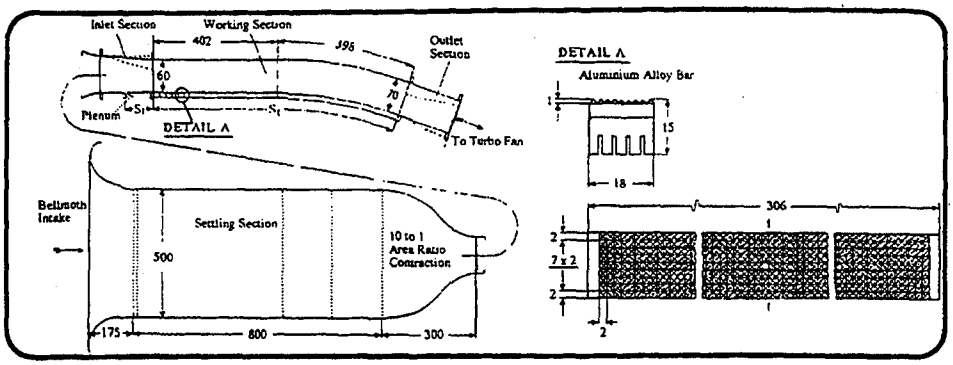

Fig.1 Schematic Of Wind Tunnel And Detail Of Aluminium Alloy Bar

2.2 The Laser Doppler Anemometer

A schematic layout of the LDA optics is shown in fig.2. The flow measurements were obtained using a single component laser Doppler anemometer arranged in the "real" fringe, forward scatter mode. The LDA comprised a 4 W Lexell Argon Ion laser (operating in the single line mode at a wavelength of $\lambda = 488$ mm and a beam diameter of, $d = 1.2$ mm), a TSI transmitting optics, a TSI receiving optics/photomultiplier assembly and a TSI 1980 Doppler frequency counter. The output signal from the photomultiplier was processed by a TSI 1980 LDA counter. The counter measured period averaged over a specified number of cycles. The high and low pass filters were maintained at 1 MHz and 10 MHz respectively. The number of cycles over which the Doppler periods were measured was set to four. This low value was chosen to minimise the dead angle for particle trajectories through the probe volume in regions of high turbulence. The comparitor tolerance was maintained at 2%. The amplifier gain was set to unity, at which the effects of noise on the RMS levels should be minimal.

The measured Doppler period (in the form of 16 bit word) was transferred, via a Zech interface card, into the memory of an IBM PS2-30 PC. After the requisite number of data samples had been acquired (typically 25000) the PC produced a velocity probability distribution and, using a statistical algorithm, calculated the mean and RMS values of the component of velocity being measured. Typically the data arrival rate was of the order of 5 kHz.

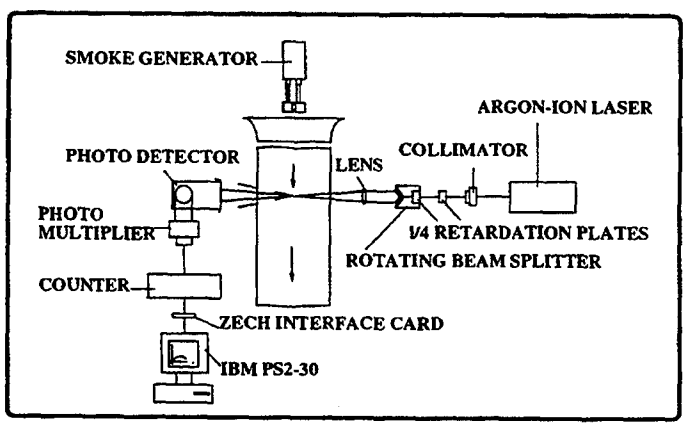

Fig.2 Schematic Of Laser Doppler Anemometer

2.3 Particle Seeding

The light scattering particles were seeded into the flow upstream of the wind tunnel intake. It was found that, the volume flow rates for which measurements were made, the atomiser type particle generators available could not generate the number of particles required to give an adequate particle arrival rate at the LDA probe volume. This problem was overcome by using commercial smoke generators. The smoke generator used to obtain the results reported in the following sections. was the Concept "Geney" which vaporised Ondina mineral oil type E. It provided vast quantities of seeds that produced good quality Doppler signals. By observing the signal from the photomultiplier, it was possible to adjust the output from the smoke generator so that in general there was never more than one particle in the probe volume.

2.4 Flow Visualisation Optics

For flow visualisation the argon-ion laser (operating at an output power of approx. 2W) was used in conjunction with cylindrical lenses to produce a sheet illumination of the vertical-streamwise plane inside the inlet section. A Canon A-1 camera (with a 50 mm objective lens operating in the aperture preferred mode at f = 1.4) was used to photograph the flow structure near the plenum, made visible by the light scattered from smoke particles seeded into the flow at the intake. The optical axis of the camera was aligned ("looking" through the side walls) to be normal to the plane of illumination. The photographs were taken using a Kodak Ektar 1000-1 ASA film.

3. FLOW MEASUREMENTS

3.1 Flow Visualisation in the Inlet Section

Flow measurements were acquired for a free stream velocity $U_c = 22.0$ m/s in a tunnel set up for a zero pressure gradient. Fig.3 shows the photographs of the smoke patterns obtained using laser sheet illumination of the vertical streamwise plane located at the mid-span position and injecting smoke into the flow at the intake of the settling section. A schematic layout of the plenum chamber is also shown in fig.3(f).

Fig.3(a) shows the smoke pattern obtained for a volume flow rate of $\dot{Q} = 4700$ l/min with no suction at the plenum. Accurate inspection of the photograph reveals that the flow downstream at the leading edge of the plenum separated from the floor of the inlet section. The separation region extended approximately 36 mm where the flow re-attached to the floor. There was also evidence of notable vortex shedding in the attachment region. Increasing the volume flow rate to $\dot{Q} = 9800$ l/min caused the separation region to reduce in size, as can be seen in fig.3(b).

It can also be seen that the streaks in the smoke upstream of the plenum appears to curve upward. It is clear that for both conditions shown in figs.3(a) and (b), the flow stream was distorted by the presence of the step in the floor and the separation region.

Fig.3(c) shows the effect of sucking away flow ($\dot{Q}_p = 115$ l/min) from the boundary layer adjacent to the floor of the inlet section. In this case the separation region has been significantly reduced. A further increase in the flow (to $\dot{Q}_p = 514$ l/min) removed at the plenum chamber is shown in fig.(d). At this suction flow rate, which was approximately 5% of the tunnel flow rate, the streaks in the smoke appeared to be parallel to the floor of the inlet section both upstream and downstream of the plenum. It would seem, that for this condition little or no flow separation occurred. The effect of increasing suction flow rate further ($\dot{Q}_p = 939$ l/min) can be seen in fig.3(e); in this case the smoke streaks upstream of the step appeared to curve downward. This distortion in the flow stream, caused by the flow being sucked into the plenum chamber, suggests that too much flow had been removed at the plenum.

This method can be used to optimise the initial flow conditions in the inlet section for future tests.

(a) $\dot{Q}$ = 4700 l/min
NO SUCTION

(b) $\dot{Q}$ = 9800 l/min
NO SUCTION

(c) $\dot{Q}$ = 9800 l/min
SUCTION
$\dot{Q}_p$ = 115 l/min

(d) $\dot{Q}$ = 9800 l/min
SUCTION
$\dot{Q}_p$ = 514 l/min

(e) $\dot{Q}$ = 9800 l/min
SUCTION
$\dot{Q}_p$ = 939 l/min

(f) Plenum Arrangement

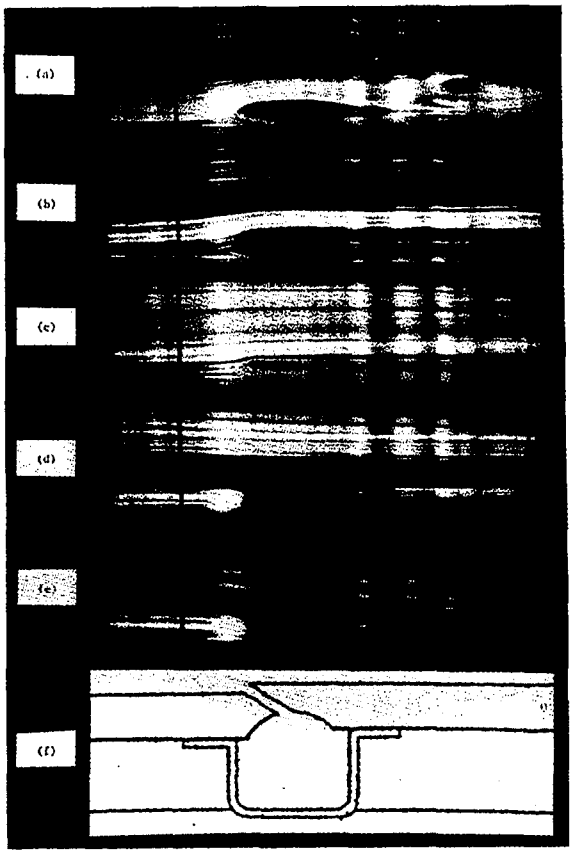

Fig.3 Fluid Visualisation In Inlet Section

3.2 Velocity Measurements

With the LDA arranged in the forward scatter mode a velocity measurement programme was undertaken in both the inlet section and the working section of the wind tunnel.

The values of the Reynolds shear stress terms, $\overline{u'v'}$ and $\overline{v'^2}$, reported below, were obtained by yawing the single component optics and measuring the mean and RMS values of velocity for three angular positions of he LDA probe. These were with the fringes aligned to be parallel to and at ± 45 ° to the surface. The values of $\overline{u'v'}$, $\overline{v'^2}$ and turbulence intensity were calculated from the equations presented by Tropea [2]. The optical axis of the transmitting optics was inclined at an angle of approx. 6 degrees to the spanwise horizontal to allow the LDA probe located at the middle of the tunnel to be lowered down to the surface when the laser beams were oriented at ±45 degrees to the surface normal.

Figs.4(a) and (b) show respectively the variation of the mean and turbulence intensity values of the streamwise component of velocity, $\overline{U}$, at a number of stations inside the inlet section. The mean velocity has been normalised to the value measured at the mid-height position, U_c, and the distance above surface, h, has been normalised to the local height, H, of the inlet section. These results were acquired for a free stream velocity of U_c = 22 m/s and with no flow being sucked off at the plenum.

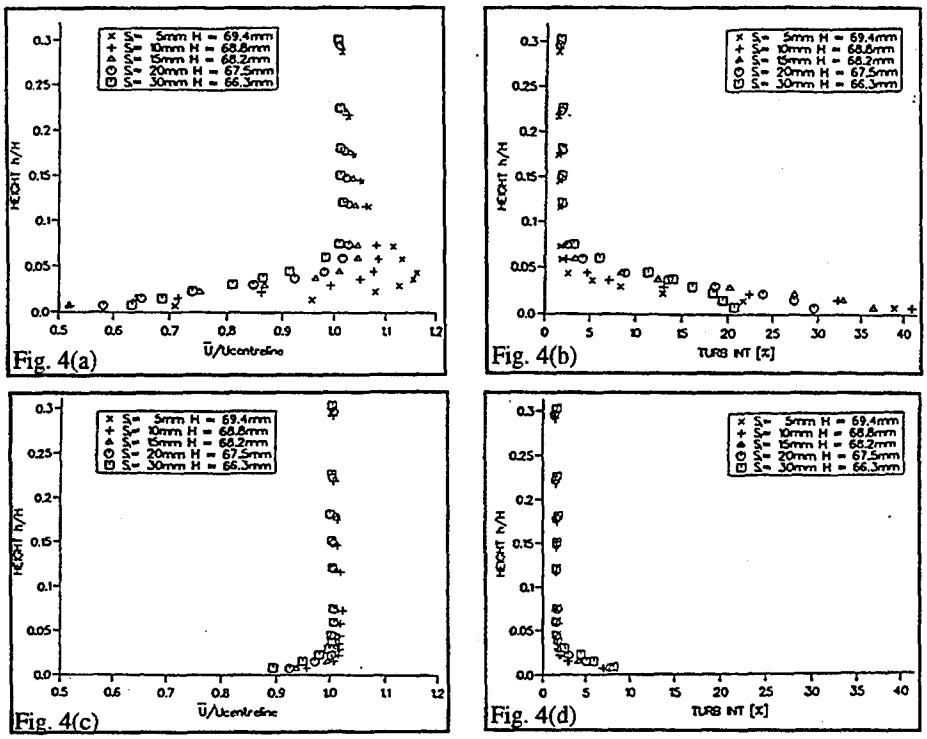

Fig.4 Velocity and turbulence intensity profiles inside the inlet section for different distances S_1 downstream of leading edge for $U_c = 22$m/s: (a) and (b) without suction (c) and (d) with suction

Referring to the results obtained at $S_1 = 5$ mm ($S_1 = 0$ mm being located at leading edge of the plenum) it can be seen that $\overline{U}/U_c$ initially increased with h/H to a value greater than unity and then decreased with h/H to the free stream value. Precisely at this location the flow stream had been distorted by the step in the floor and the associated boundary layer separation was observed by flow visualisation. At $S_1 = 10$ mm this distortion effect appeared to have been significantly reduced, and at 20 mm it disappeared completely.

These measurements were repeated with flow being sucked off at the plenum, $\dot{Q}_p = 550$ l/min being approximately 3% of the tunnel flow rate. The results are shown in figs.4(c) and (d). It can be seen that the distortion effect and the turbulence intensity have been greatly reduced compared with the results shown in figs.4(a) and (b). It can also be seen, that for a given location, the boundary layer thickness was reduced when suction was applied to the plenum chamber.

The effect of suction on $\overline{U}$, turbulence intensity, $\overline{v'^2}$ and $\overline{u'v'}$, at $S_1 = 20$ mm is shown in figs.5(a), (b), (c) and (d) respectively. Inspection of these results revealed that the boundary layer thickness was reduced by approximately 35% by the application of suction. Also the turbulence intensity near the surface was reduced from 25% to 6%; however, the free stream turbulence intensity of 2% was the same for both cases. It would appear that the high turbulence intensity that occurred for the no-suction case was caused by the vortex shedding (observed by fluid visualisation) that occurred downstream of the separation region. As a consequence there are also significant differences within the boundary layer between the values of $\overline{v'^2}$ and $\overline{u'v'}$ measured for the two inlet conditions. These effects on the measured velocity profiles in the working section of the wind tunnel are discussed in the next section.

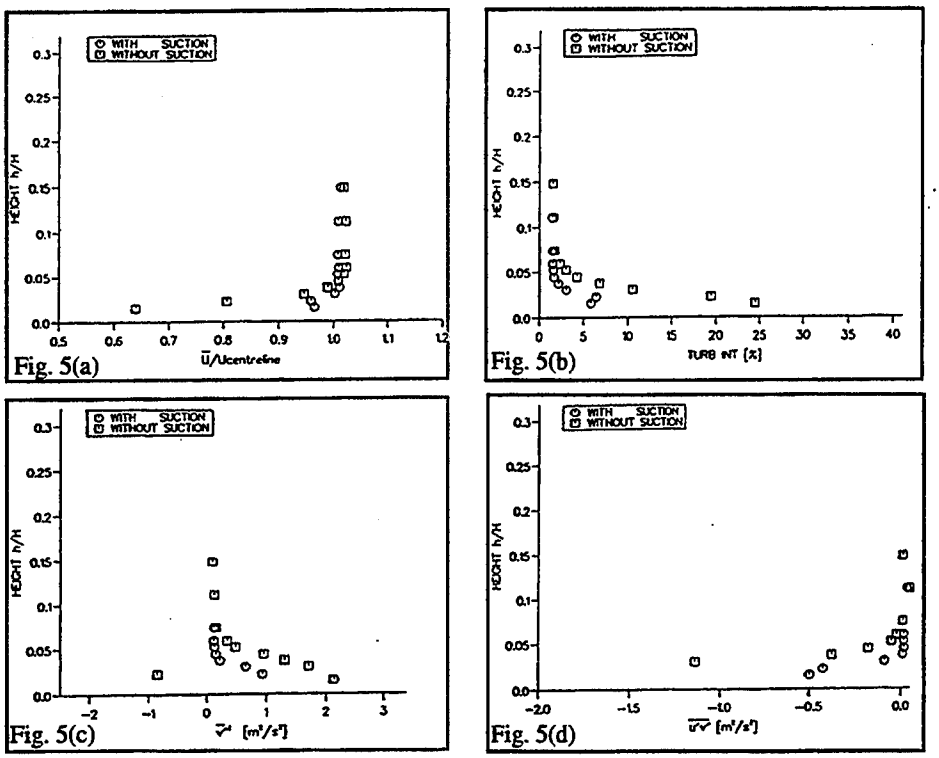

Fig.5 The effect of Sucking-off flow from the boundary layer inside the inlet section on (a) $\overline{U}$ (b) Turbulence Intensity, (c) $\overline{v'^2}$ (d) $\overline{u'v'}$ for $U_c = 22$ m/s

3.3 The Effect of Changing the Inlet Conditions on the Boundary Layer Inside the Working Section

A study of the effect of inlet conditions on boundary layer flow inside the working section of the tunnel was carried out. Velocity profiles were measured at three stations along the tunnel for both, the suction and no suction cases. Noise generated by scattered laser light prevented measurements closer than 0.5 mm above the top of the roughness elements from being obtained. For these measurements, the floor of the tunnel had the rough surface described in Section 3.1. The distance S_t corresponds to the distance along the floor of the tunnel from the beginning of the working section to the measuring station; the distance h corresponds to the height above the base of the 1 mm roughness elements.

Fig.6, 7 and 8 show respectively data obtained at $S_t = 50$ mm, 330 mm and 740 mm. Referring to fig.6, it can be seen that the measurements in the outer region of the boundary layer at $S_t = 50$ mm were significantly affected by the inlet conditions. It would appear that applying suction at the plenum caused a 100% reduction in the boundary layer thickness. Further down the tunnel, at $S_t =$ 330 mm, the effect on the boundary layer of changing the inlet conditions became less significant as can be seen in fig.7. In fact, the results presented in fig.8 show that there was almost no effect of inlet conditions on the boundary layer at $S_t = 740$ mm. It can also be seen that the nominal boundary layer thickness δ increased from 12.4 mm at $S_t = 50$ mm to 30 mm at $S_t = 740$ mm. The turbulence intensity near the tops of the roughness elements was characteristically 23%; this

progressively reduced with h to a freestream value of approximately 2%. In the Reynolds shear stress distribution a maxima occurred. The position of this maxima changed within the boundary layer as the flow developed. For fully developed flow at S_t = 740 mm it appeared at 0.25 δ.

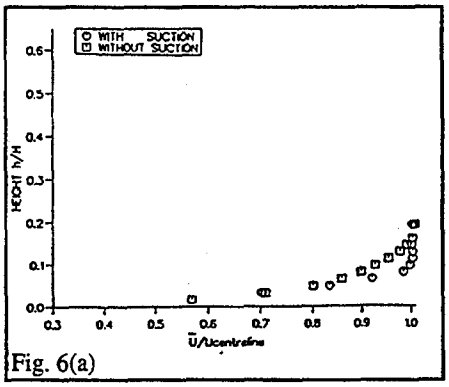

Fig. 6(a)

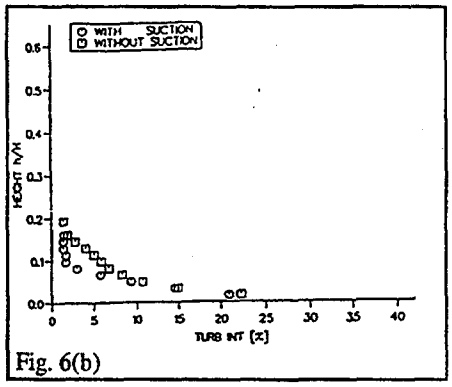

Fig. 6(b)

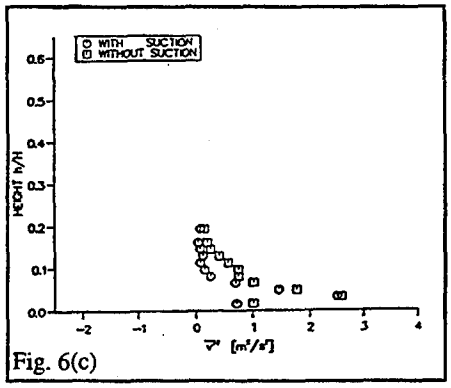

Fig. 6(c)

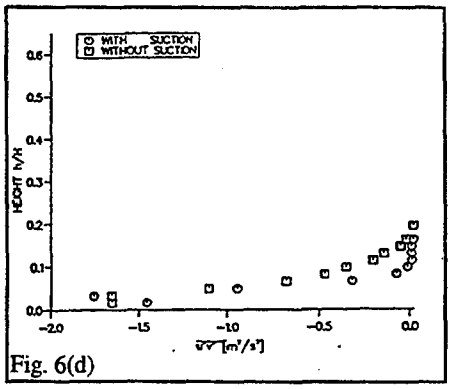

Fig. 6(d)

Fig.6 The effect of inlet conditions on the boundary layer inside the working section at S_t = 50 mm for (a) $\overline{U}$ (b) Turbulence Intensity, (c) $\overline{v'^2}$ (d) $\overline{u'v'}$; (U_c = 22 m/s)

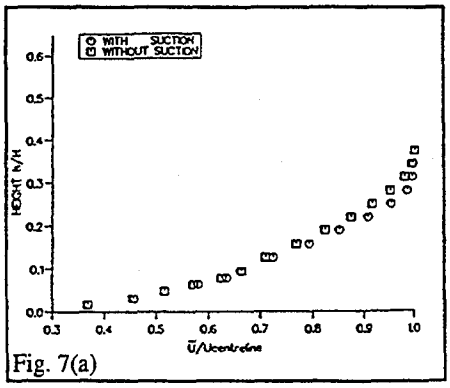

Fig. 7(a)

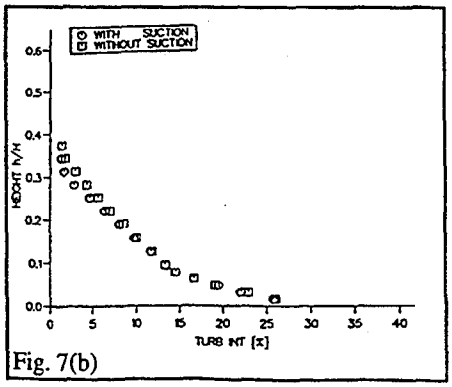

Fig. 7(b)

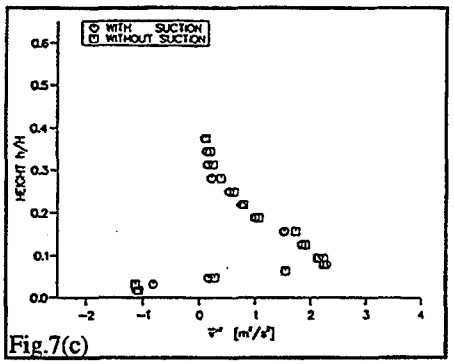

Fig.7(c)

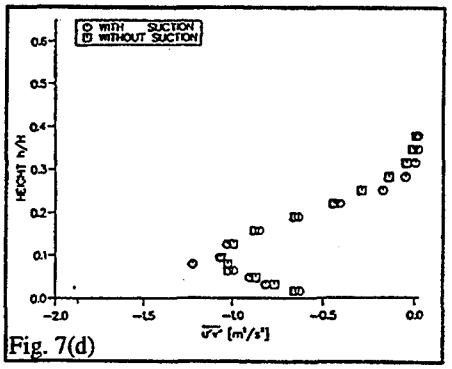

Fig. 7(d)

Fig.7 The effect of inlet conditions on the boundary layer inside the working section at S_t = 330 mm for (a) $\overline{U}$, (b) Turbulence Intensity, (c) $\overline{v'^2}$ (d) $\overline{u'v'}$; (U_c = 22 m/s)

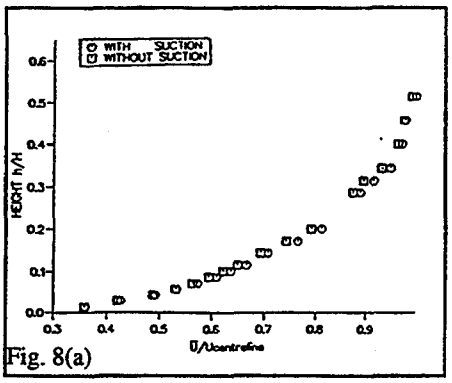

Fig. 8(a)

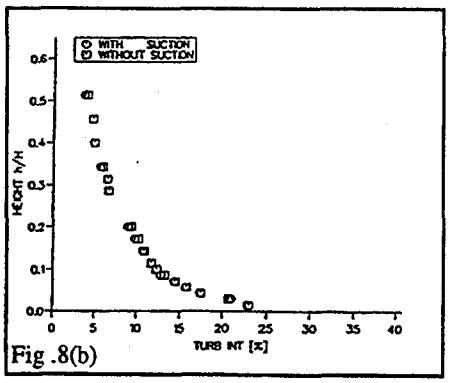

Fig .8(b)

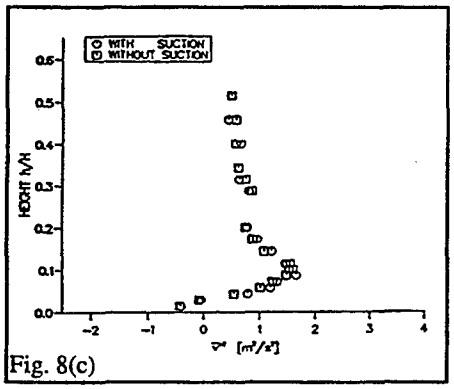

Fig. 8(c)

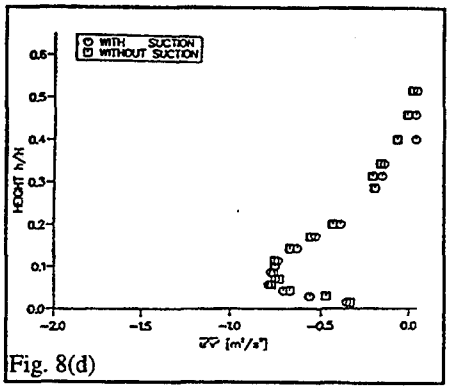

Fig. 8(d)

Fig.8 The effect of inlet conditions on the boundary layer inside the working section at S_t = 740 mm for (a) $\overline{U}$, (b) Turbulence Intensity, (c) $\overline{v'^2}$ (d) $\overline{u'v'}$; (U_c = 22 m/s)

4. SOURCES OF ERROR IN THE VELOCITY DATA

The overall accuracy of the LDA measurements should be typically of the order of ± 1%; however under certain conditions significant systematic errors may occur. The most important of these will be directional biasing and broadening of the measurements obtained in regions of high turbulence intensity (greater than 20%). Velocity gradient biasing and broadening errors may also be significant. Clearly both of these effects will be operating on the measurements made near the surface.

Detailed analysis [3] and tests such as using different modes of ensemble averaging were carried out to quantify these errors to be between 2 and 3%.

Also the measurements near the surface will be subject to noise (from surface scattered light), particularly the RMS levels.

Errors in the computed values of $\overline{u'v'}$ and $\overline{v'^2}$ caused by angular misalignment of the optics, and, in the curved section of the wind tunnel, misalignment of the traversing table from the surface normal were evaluated to be in the region of ± 1.5 %.

5. CONCLUSIONS

LDA has been used to study the effects of suction on a turbulent boundary layer over a rough surface. The measurements were made in a wind tunnel set up for a zero pressure gradient at a free stream velocity U_e = 22 m/s. the tunnel had a straight section for 402 mm followed by a curved section of radius 1.2 m over an arc of 19 degrees. The topography of the rough surface was a regular square array of 1 mm high trapezoidal roughness elements.

Flow visualisation in the inlet section showed that the developing boundary layer was significantly affected by sucking of flow at the leading edge of the plenum. It was also shown how fluid visualisation could be used to optimise the suction flow rate to give the minimum flow stream distortion in the inlet section.

The LDA measurements, made at three stations along the tunnel, showed that the nature of the turbulent boundary layer flow was significantly affected by the application of suction.

In the near future some of the above measurements will be repeated using LDA with frequency shifting. This should reduce directional biasing errors in the measurements obtained close to the surface. In the medium term a similar measurement programme will be conducted in the wind tunnel for the adverse and favourable pressure gradients cases.

6. REFERENCES

1 Tarada, F. (1987). Prediction Of Heat Transfer To Rough Turbine Blading Using A Two-Equation Model Of Turbulence University Of Sussex, Thermo-Fluid Mechanics Research Centre, 87/Tfmrc/99.

2 Tropea, C. (1983). A Note Concerning The Use Of A One-Component LDA System To Measure Shear Stress Terms, *Experiments In Fluids 1*, 209.

3 Drain, L.E. (1980) The Laser Doppler Technique, John Wiley & Sons, Chichester.

4 Hübbe-Walker, S.E. and Pincombe, J.R. (1990). Laser Measurements Inside The Flat Curved Rough Plate Rig Using A Single Component Laser Doppler Anemometer And Fluid Visualisation, University Of Sussex, Thermo-Fluid Mechanics Research Centre, 90/Tfmrc/124.

5 Hübbe-Walker, S.E. Pincombe, J.R. and Turner, A.B. (1993) Measurements And Flow Visualisation On The Surface Of A Flat And Rough Plate, Engineering and Turbulence Modelling 2, Elsevier Amsterdam.

FEEDBACK MECHANISM OF THE REATTACHING SHEAR LAYERS WITH A FIXED SEPARATION POINT.

PILIUGIN A.V.
Central Aero-Hydrodynamics Institute (TsAGI), Zhukovsky (Russia)

Currently a constantly increasing number of researchers come to recognize that a wide range of flow configurations commonly used in many engineering fields are understood by reference to unstable phenomena. In this work we shall discuss the correlation of the mean "separated bubbles" length with time-dependent bubbles behaviors.

By way of illustration let us consider three types of separated bubbles with a fixed separation point respectively generated by flow over backward-facing step (Fig.1.a), normal-plate/splitter-plate configuration (Fig.1.b) and blunt plate (Fig.1.c).

Based on study of flow downstream of a backward-facing step D. Driver, H. Seegmiller and J. Marvin[1] emerged two types of time-dependent behaviors: low-frequency irregular oscillations of shear layer and regular periodic vortex structures. By the use of gages indicating the flow direction near the wall J. Eaton and J. Johnston[2] clarified that the short-time averaged location of reattachment point can vary from mean (long-time averaged) location through wide range ± 2 step heights. The distinctive frequency of this unstable process normalized by reference velocity and step height was determined $f_t H / U_{ref} = 0.07$. In view of the fact that in this case the mean separated bubble length equals 8 step heights from the previous result we get the dimensionless frequency $f_t L / U_{ref} = 0.56$.

This unstable process was examined also by D. Driver, H. Seegmiller and J. Marvin mentioned above. They found that time-dependent behavior of a reattaching shear layer with a fixed separation point is a cyclic process. The circulating motion intensity of separated bubble is in close association with short-time averaged location of reattachment point. In the special case that the short-time averaged location of reattachment point is before the mean location X_R the intensity of circulating motion decreases, in the alternative case that the short-time averaged location of reattachment point is behind the mean location X_R the intensity of circulating motion increases.

All these facts bring up the question:

What is the mechanism controlling the mean separated bubble length?

The answer to this question may be written concisely. In the first place, stable oscillations are sustained by a feedback mechanism as in opened-end resonator with evidence condition: a mean separated bubble length L is multiple of resonance wavelength λ_r in a feedback loop

$$L = \lambda_r N \qquad (N = 1,2,3\ldots) \qquad (1)$$

where N is a resonance mode number.

Secondly, resonance tuning occurs in the neighborhood of reattachment point. That is peak energy-containing frequency of wall pressure fluctuations at the reattachment point $f_p(X_R)$, the same peak frequency of velocity fluctuations $f_u(X_R)$ and resonance frequency in a feedback loop f_r coincide very closely.

$$f_p(X_R) = f_u(X_R) = f_t \qquad (2)$$

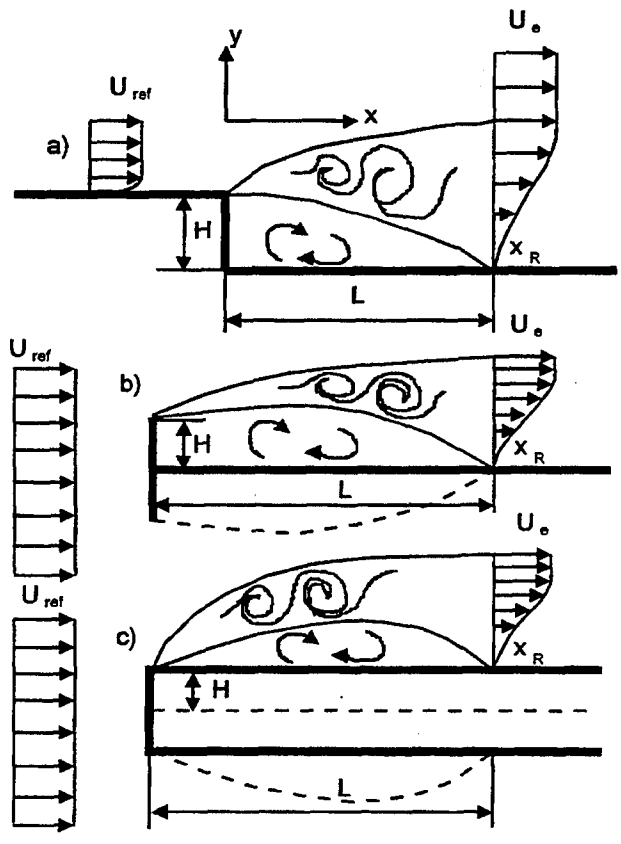

Fig.1. Bubbles types with a fixed separation point

The arguments.

G. Winant and F. Browand[3] indicated the empirical correlation of peak energy-containing frequency of velocity fluctuations f_u with vorticity thickness δ_ω and phase velocity c_{phase} fulfilled for mixing layers

$$\frac{f_u \delta_\omega}{c_{phase}} = 0.2 \qquad (3)$$

where $\delta_\omega = \dfrac{(U_2 - U_1)}{\left(\dfrac{\partial U}{\partial y}\right)_{max}}$;

U_1 - low speed limit of mixing layer;

U_2 - high speed limit of mixing layer

Recall that wavelength at the response frequency

$$\lambda_r = \frac{c_{phase}}{f_r} \qquad (4)$$

Power spectrum of wall pressure fluctuations presented by D. Driver, H. Seegmiller and J Marvin[1] (Fig.2) confirms the relation (2)

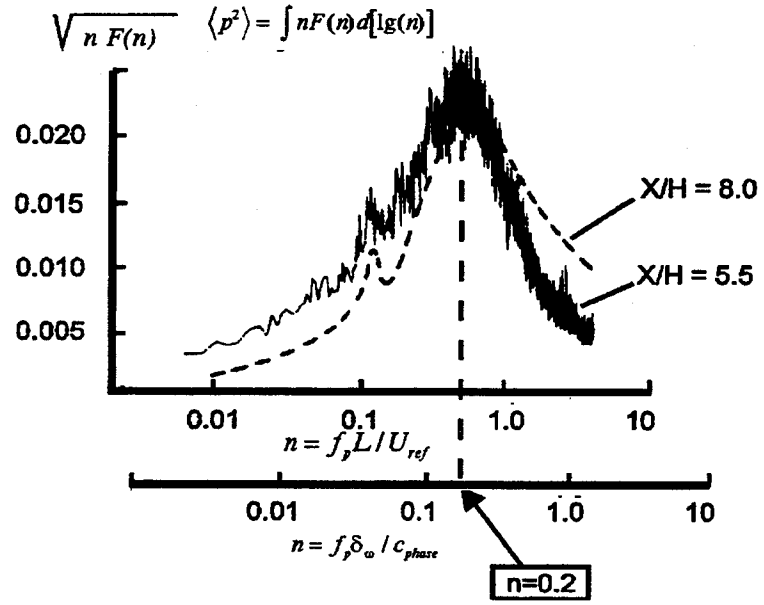

Fig.2. Power spectrum of wall pressure fluctuations.

Besides, from relations (1), (2), (3), (4) follows

$$\frac{\delta_\omega(X_R)}{L} = \frac{0.2}{N} \qquad (5)$$

Fig.3 illustrates the streamwise coordinate dependence of the vorticity thickness referred to mean separated bubbles length for three typical flow configurations mentioned above:

a) backward-facing step (solid circles, the data of D. Driver, H. Seegmiller and J. Marvin[1]);

b) normal-plate/splitter-plate configuration (open circles, the data of R. Ruderich and H. Fernholz[4]);

c) blunt plate (triangles, the data of M. Kiya and K. Sasaki[5])

Obviously, the first resonance mode is apparented for all these cases.

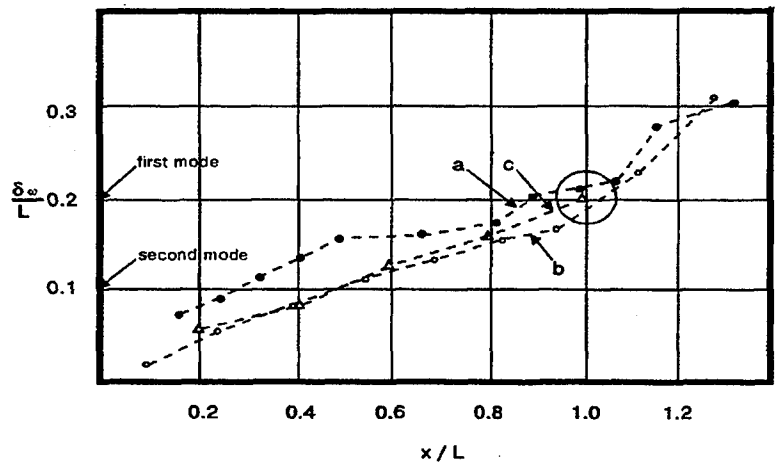

Fig.3. Resonance mode determination.

Finally the feedback mechanism of reattaching shear layers with a fixed separation point makes possible to define more exactly correlation of peak energy containing frequency of wall pressure fluctuations with separated zone length and reference (free stream) velocity by comparison the Mabey one[6]. Really from relations (1), (2), (4) follows

$$\frac{f_p L}{U_{ref}} = \left(\frac{c_{phase}}{\lambda_r}\right)\frac{L}{U_{ref}} = \left(\frac{c_{phase}}{L}N\right)\frac{L}{U_{ref}} = N\frac{c_{phase}}{U_{ref}}$$

According to Simpson measurements[7] phase velocity is determined as follows

$$c_{phase} = 0.6U_e$$

(as differentiated from mixing layer phase velocity $c_{phase} = 0.5(U_1 + U_2)$ provided that $U_1 = 0$ and $U_2 = U_e$)

Neglecting by crosswise pressure gradient and using Bernoulli Integral we get

$$\frac{f_p L}{U_{ref}} = 0.6N\sqrt{1 - C_p(X_R)} \qquad (6)$$

$$\text{where } C_p(X_R) = \frac{p(X_R) - p_{ref}}{0.5\rho U_{ref}^2}$$

Fig.4 demonstrates the streamwise coordinate dependence of wall pressure characteristics for the flow downstream of a backward-facing step.(The data of D.M. Driver, H.L. Seegmiller and J.G. Marvin[1]) Note that r.m.s. value of wall pressure fluctuations peaks at the reattachment point and varies moderately in the neighborhood of this point. This peculiarity and relation (6) allow to define more exactly separated zone length from wall pressure measurements only.

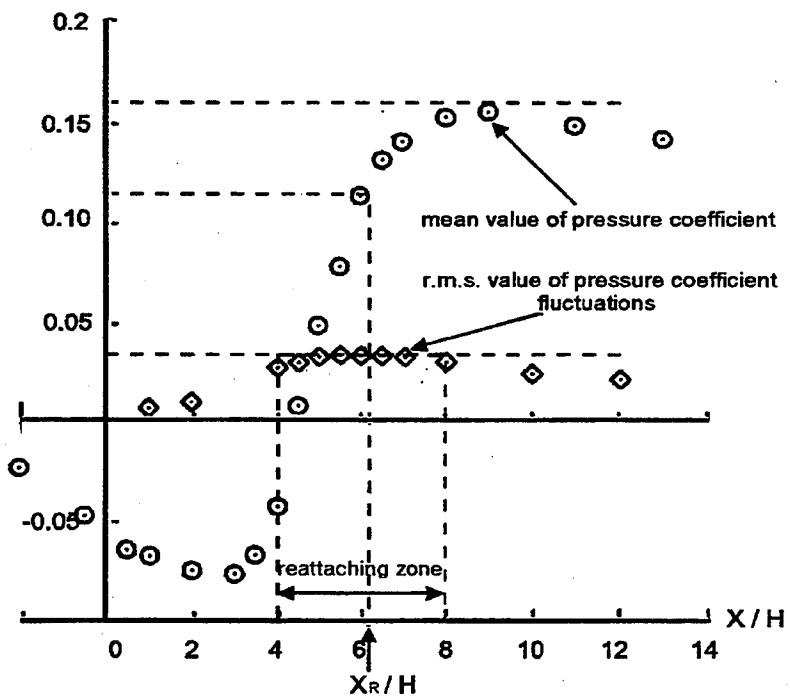

Fig.4. The pressure wall distribution for backward--facing step.

According to experimental data L = 6.1H; $C_p(X_R) = 0.12$, N = 1 and relation (6) we get

$$\frac{f_p L}{U_{ref}} = 0.56$$

Recall that the same value was obtained immediately by J. Eaton and J. Johnston[2] , while according to their measurements mean separated zone length was 8 step heights.

All these and some other experimental facts demonstrate the marked relation between mean separated bubbles length and unstable phenomena.

References

1. D.M. Driver, H.L. Seegmiller, J.G. Marvin Time-dependent behavior of a reattaching shear-layer. - AIAA Journal, 1987, vol.25, # 7.

2. J. Eaton, J. Johnston Low frequency unsteadiness of a reattaching shear-layer. Proceedings of the Third International Symposium on Turbulent Shear Flow. Davis C.A. Sept. 1981.

3. G.D. Winant, F.K. Browand Vortex pairing: the mechanism of turbulent mixing layer growth at moderate Re number. - Journal of Fluid Mechanics, 1974, vol.63, part 2.

4. R. Ruderich, H.H. Fernholz An experimental investigation of a turbulent shear flow with separation reverse flow and reattachment. - Journal of Fluid Mechanics, 1986, vol.163.

5. M. Kiya, K Sasaki Structure of a turbulent separation bubble. - Journal of Fluid Mechanics, 1983, vol.137.

6. D.G. Mabey Analysis and correlation of data on pressure fluctuations in separated flow. - Journal of Aircraft, 1972, vol.9, # 9.

7. R.L. Simpson Turbulent boundary layer separation. - Annual Review of Fluid Mechanics, 1989, vol.21.

MEASUREMENT OF TURBULENT SEPARATING FLOW IN A CURVED-WALL DIFFUSER

Yin Junfei
Department of Power Engineering
Nanjing University of Aeronautics and Astronautics
Nanjing, Jiangsu Province, P.R. China
30 October 1993

Introduction

Turbulent boundary-layer separation is one of important problem in fluid mechanics. Although many experiments were done by using well-established techniques such as hot-wires, those data were not available because of their lack of non-directional sensitivity and sensitivity to the local blockage in reversing flow. Since 80's more and more researchers have favoured to investigate such kinds of flow with laser doppler velocimeter (LDV)[1-3]. In the present experiment, A two-dimensional LDV was used to investigate a turbulent separation-reattachment flow field in a 2-D curved-wall diffuser. The turbulent boundary layer separates on a convex surface in internal flows and reattaches on the sequent parallel channel. This kind of flows provides a combined and basic situation against which many existing theories and models of turbulence can be tested.

The purpose of the present study are to measure, in detail, flow characteristics in the separating, reattaching shear layers and reversal close to the solid surface.

The emphasis is placed on LDV application and data validity. Then, the main features for mean and turbulence quantities are briefly described.

EXPERIMENTAL ARRANGEMENT

Experimental Apparatus

This experiment was conducted in a low-speed suction open-circuit wind tunnel. The test model is a two-dimensional divergent diffuser in which the upper wall is flat and the lower is curved as well as there are a constant area inlet duct and exit extended duct, which is shown in Fig.(1) . The curved-wall contour is approximate circular arc with maximum radius of 2(m). At the inlet throat, the span-to-height ratio of diffuser is about 1.73.

Measurement Means and Methods

The axes of measurement coordinates were defined that X-axis parallel to the upper wall and x = 0 is located at the start of the diffuser curved wall as well as Y-axis is vertical to the upper wall and y = 0 is located on the lower wall at the each measurement section. The streamwise stations were measured from upstream of the diffuser(X=-45mm) to X= 265mm.

The test lower turbulent boundary layer was tripped by a row of 1mm diameter wires with a screen at X = -350mm. In the constant throat(X=-100 mm), it has been developed as a typical reference shear layer.

A commercial two-colour, four-beam LDV system(TSI Model- 9100-7 shown Fig.(2) was mounted on a three-dimensional positioner to survey the whole shear-layer flow field for any selected increment of traverse from the model surface. The acquired data consisted of mean flow, Reynolds stresses and higher-order turbulence, etc.. There were total 20 sections measured from X=-45(mm) to X=265(mm). The positioning resolutions are 0.01mm in the vertical direction and 0.1mm in the horizontal direction.

Two-channel counter processor of TSI Model-1990B and PDP-11-23PLUS micro-computer were used for data acquisition, analysis and processing. Under the continue mode, the cycle number and the accuracy of comparison were respectively N = 8 and Δ = 1% . The sample size was 3840 for each point and the validation data rates varied rapidly from 100 to 500 burst per second over a distance of 3 mm away from the wall. The window width of coincidence for the both channels was set up with 30us Seeding was provided by a commerical liquid atomizer. DOP with the mean diameter of 0.54 μm was used as the scattering particles and was locally seeded at the entrance of the wind tunnel.

Error analysis and uncertainties

Overall uncertainties of the time-average velocities were carefully estimated and are shown in Tab.1.

Tab.1 The uncertainties for the mean velocities

	U(M/S)	V(M/S)
Error for light geometry	±0.077	±0.123
Error for processor	+0.355 -0.034	+0.174 -0.017
Random error	±0.12	±0.07
Overall of Uncertainty	+0.383 -0.147	+0.225 -0.143

The particle-seeding bias is not counted in. The particle seeding bias consists mainly of the individual realization bias and the Bragg bias. According to Meyer&Clommons' research[4], the effect of Bragg bias could be contrary to that of the individual bias.

Tab.2 Random error for turbulence quantities

	$\overline{u^2}$	$\overline{v^2}$	$-\overline{uv}$	r_{uv}
Error	$+0.045\overline{u^2}_{max}$	$+0.045\overline{v^2}_{max}$	$+0.035(-\overline{uv})_{max}$	$+0.08EXP(-\overline{U^2}/\overline{u^2})$

Where, it is noticed that because u and v are acquired within a short coincidence window, the actual error of $-\overline{uv}$ is larger than the estimated value.

Near-wall measurement

The optical axis was tilted forward by 5 deg. in the vertical plane to make measurement close to the surface. This means that the measured velocity components were not precisely equal to the vertical component. But the effect of inclination on vertical velocities is negligible($\delta V/V < 0.4\%$), so no correction was made.

The minimum distance from the surface for the measurement was 0.3 mm or about 0.5 percent of the detached shear-layer thickness. The data rates are gradually decreased to 20-40 bursts per second. The present results in the near-wall region only contain the fluctuating information coming from the

EXPERIMENTAL RESULTS

Test condition

The reference station was at the position of X=-100mm, the tripped shear layer has developed as a typical 1/7 exponential profile and there is a standard log law. The Reynolds number based on the height is 10400 and based on the boundary-layer momentum thickness is 4950. Those lower-wall boundary-layer parameters and free stream conditions were also shown on the Tab.3.

Tab.3 The reference parameters of the boundary layer

Ue	δ	δ^*	H	$\overline{u^2}/Ue^2$
25.2m/s	28mm	3.8mm	1.325	0.50%

Two-dimensionality

The surface tuft observation was used to judge two-dimensionality and to roughly demarcate surface-flow regimes. The intermittent transitory detachment indicated is curved line, the central ITD is located near X=95mm and 1mm upstream at 40mm to either side.

LDV was used for the further check of two-dimensionality at Z=$\pm$30mm in X=95mm(near separation). Those two-side mean velocity components are little larger than the central. The maximum differences are 0.03 and 1.8 percent of its free mean velocity in the horizontal component, as well as 0.7 and 5.6 in the vertical component.

Mean flow results

The free-stream velocity Ue and wall pressure coefficient Cpw, the surface downstream-upstream intermittency r_{puo} are shown in Figure 2. There is an acceleration before X=0, Cpw are always equal to or smaller than zero and Ue also increases along the streamwise direction. Obviously, The significant effect of streamwise curvature on the free-stream velocity and surface pressures appears some 60mm upstream of the start of wall-curvature(X=0) . Therefore, the wall-curvature plays a significant role in the present test flow.

The other significant feature in Figure 2 is that near Incipient Detachment, there is minimum difference of Cpe-Cpw. This feature is similar to the flow studied by Thompson&Whitelaw[10]. Near ID the separation produces a significant streamline curvature opposite to the wall's and causes in strong normal pressure gradient in the shear layer. In reattachment, this similar feature seems to exist.

The distribution of the surface downstream-upstream intermittency r_{puo}, at X=80mm, r_{puo}=0.99, is the Incipient Detachment(ID). At X=100mm, r_{puo}=0.80, the Intermittent Transitory Detachment(ITD), here is Y_w=0. According to r_{puo}, author gives five flow regions:

a) the attached flow before ID, X<80mm, r_{puo}=>0.99),
b)the intermittent detaching flow(80mm <=X<=120mm,0.5<=r_{puo}<=.99),
c) the recirculating flow(120mm<=X<=185mm, r_{puo}<=0.5) ,
d) the reattaching flow(180mm<=X<=245mm, 0.5<=r_{puo}<=0.99) and
e) the relaxing flow(X)=245mm, r_{puo}>0.99).

The ratio of lengths of the intermittent detaching flow, the recirculating flow and the reattaching flow is 4:7:6. The reattaching flow length is as 1.5 time as the intermittent detaching flow's.

Fig.(3) illustrates the horizontal and vertical mean velocity components at non-dimensional height of Y/δ. The maximum height is about 15 percent of the detached shear layer thickness. The height-to-length ration of the

reversal is 14.

The minimum horizontal velocity component is -0.15Ue, which occurs at X=138mm(near the corner). The vertical components are always negative constant near the boundary-layer edge. In the reversal and near surface V/Ue is close to 0 and even positive. In the reversal after the corner, V is larger than U.

Turbulence results

Fig.(4) shows profiles of Reynolds stress $\overline{u^2}$, $\overline{v^2}$ and $-\overline{uv}$. The maximum of $\overline{u^2}$, $\overline{v^2}$ and $-\overline{uv}$ have almost the same height at a section. After TD, its non-dimensional height of Y/δ is near constant(Y/δ=0.2) along the streamwise direction.

As concerns of the profile of ($\overline{T_{ij}}$), one of the most outstanding features is that there exists the second extreme of $\overline{u^2}$ near the wall after the transitory detachment. But for $\overline{v^2}$, such phenomenon is not obvious. Thompson & Whitelaw[6] and Patrick [13] also found this phenomenon. However, In Simpsom's separating flow this feature was not shown. It may be characteristic of recirculating flow in a curved wall.

Another noticeable feature is that $-\overline{uv}$ appears minus in the backflow near the wall. The minimum of $-\overline{uv}$ corresponds to the smallest value of $U/\sqrt{u^2}$ at the local section. This feature was also not obvious in Simpson's flow, but it did exist in the trailing flow of airfoil. Its mechanism is not clear. In the present flow, the negative extreme of $-\overline{uv}$ is almost as the same as its positive maximum in the magnitude.

Conclusion

In this paper, a 2-D LDV was used to survey a turbulent separation-reattachment flowfield in a 2-D curved-wall diffuser.
The uncertainty were carefully estimated by error analysis. The minimum distance from the surface is 0.3mm or about 0.5 percent of the local detached shear-layer thickness. A significant normal pressure gradient exists in the separation due to the effect of separation on the streamwise curvature. The whole flow can be divided five regions: attached, intermittent detaching, recirculating, reattaching and relaxing flow. The length ratio of reattaching to separating is 1.5. The maximum of Reynolds stresses were located at the same non-dimensional height. The second extreme of $\overline{u^2}$ and the minus of $-\overline{uv}$ near the wall after the transitory detachment are noticeable phenomena.

REFERENCE

(1) Simpson, R.L.(1981), J. Fluid Mech., Vol.113, pp.23-74, 1981
(2) Nakayama,A.(1983), AIAA 85-0181, 1985
(3) Patrick, W.P.(1987), NASA CR-4052,1987
(4) Meyer, J.F. & Clemmons, J.I.(1978), Proceedings of the 3rd International Workshop of LV, 1979
(5) Chehround, R & Simpson, R.L.(1985), J. Fluid Mech., Vol.160, pp.77-92, 1985
(6) Thompson, B.E.& Whitelaw,J.H.(1985), J. Fluid Mech., Vol.157, 1985,pp.305-326

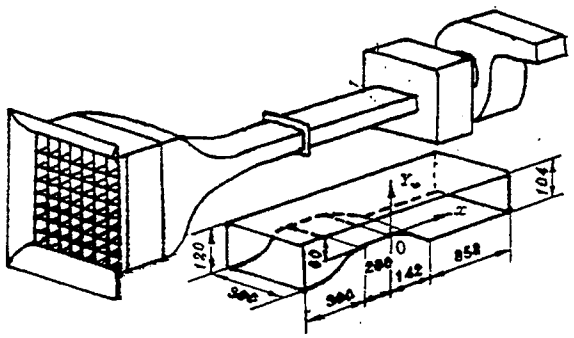

Fig.1 Test Model.

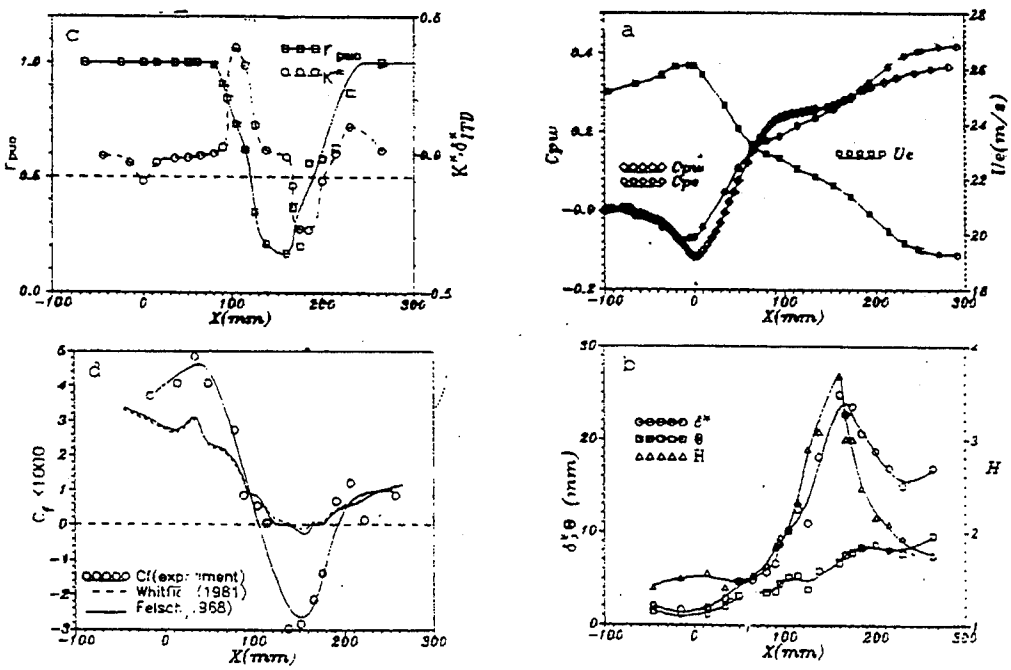

Figure 2 The distribution of flow parameters. (a) Pressure coefficient C_{pw}, C_{pe}, and free-stream velocity U_e; (b) integral parameters of H, δ^*, and θ; (c) upstream–downstream intermittency γ_{puo} and displacement–thickness curvature K^*_{max}; (d) skin friction coefficient Cf

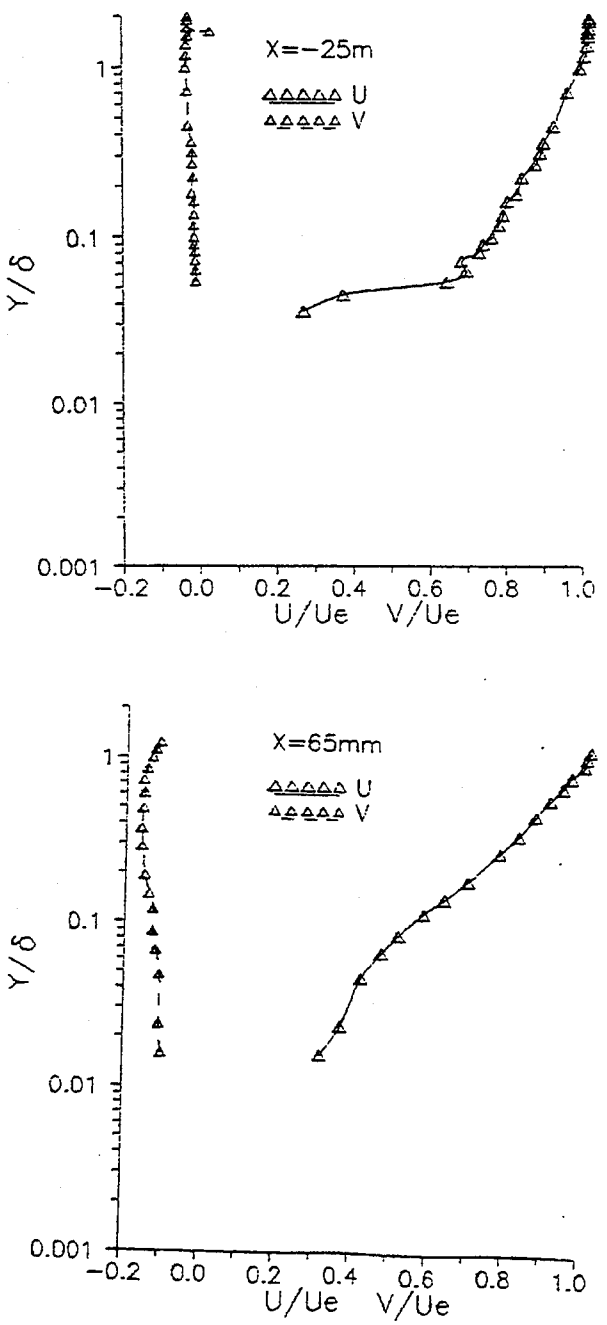

Fig.(3) Mean velocity profiles

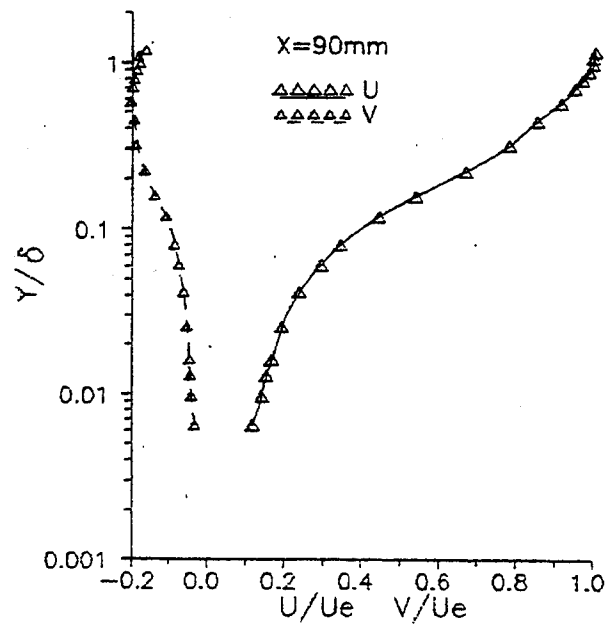
X=90mm
U
V
1
0.1
0.01
0.001
Y/δ
−0.2
0.0
0.2
0.4
0.6
0.8
1.0
U/Ue V/Ue

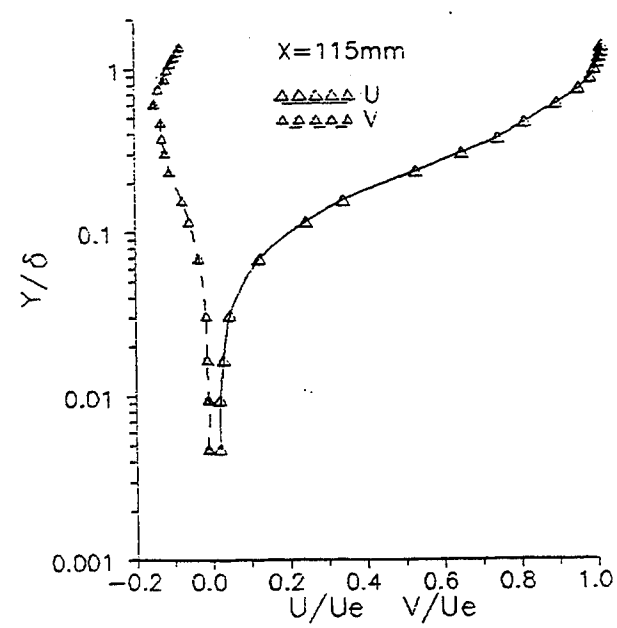
X=115mm
U
V
1
0.1
0.01
0.001
Y/δ
−0.2
0.0
0.2
0.4
0.6
0.8
1.0
U/Ue V/Ue

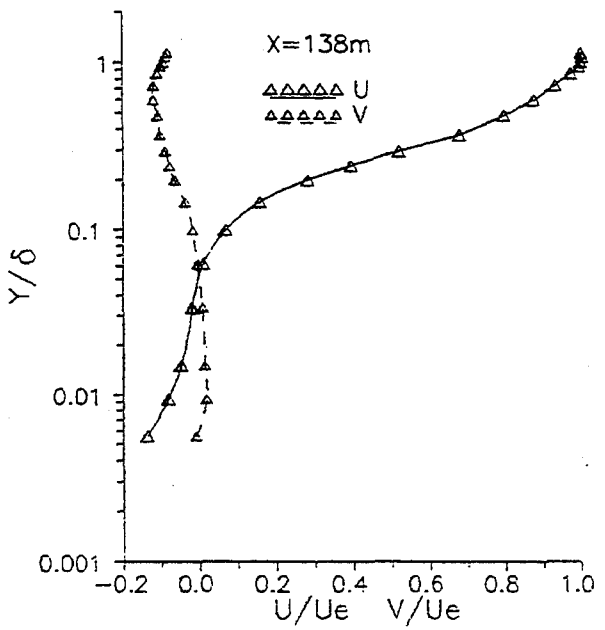
X=138m
U
V
Y/δ
1
0.1
0.01
0.001
−0.2
0.0
0.2
0.4
0.6
0.8
1.0
U/Ue V/Ue

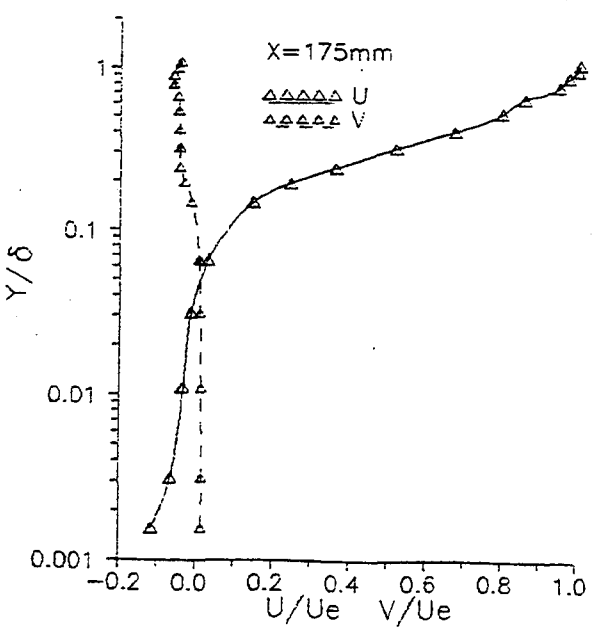
X=175mm
U
V
Y/δ
1
0.1
0.01
0.001
−0.2
0.0
0.2
0.4
0.6
0.8
1.0
U/Ue V/Ue

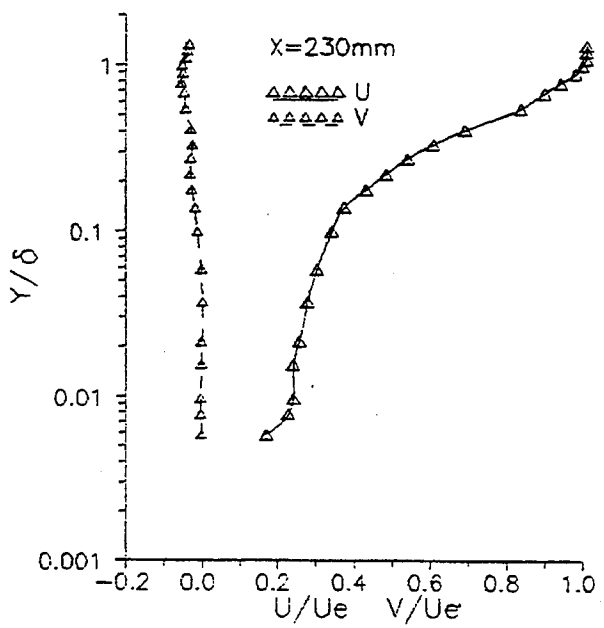
X=230mm
U
V
Y/δ
1
0.1
0.01
0.001
−0.2
0.0
0.2
0.4
0.6
0.8
1.0
U/Ue
V/Ue

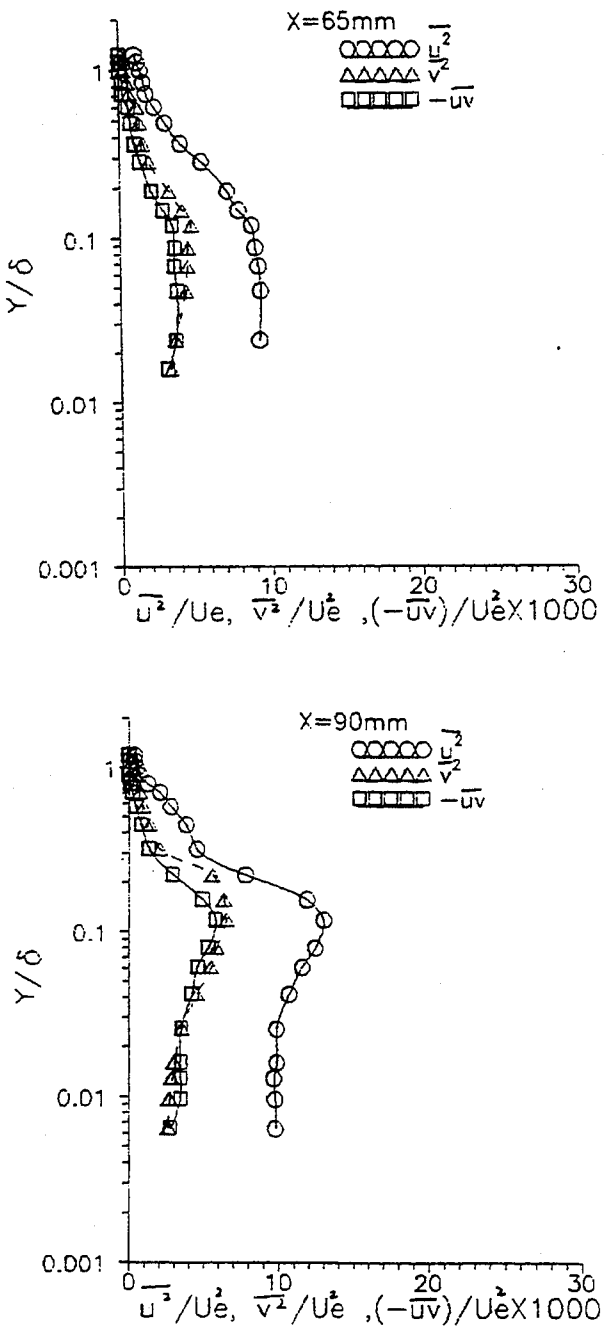

Fig.(4) Reynolds stress profile

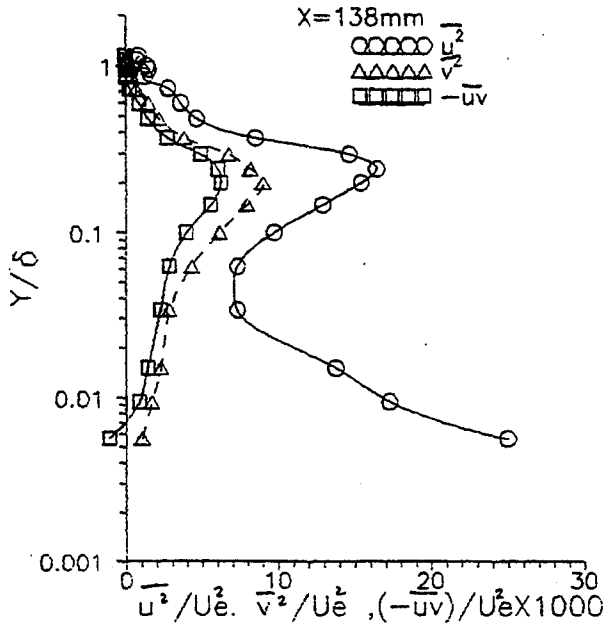
X=138mm
$\overline{u^2}$
$\overline{v^2}$
$-\overline{uv}$
1
0.1
0.01
0.001
Y/δ
0
10
20
30
$\overline{u^2}/U_e^2$, $\overline{v^2}/U_e^2$,$(-\overline{uv})/U_e^2$X1000

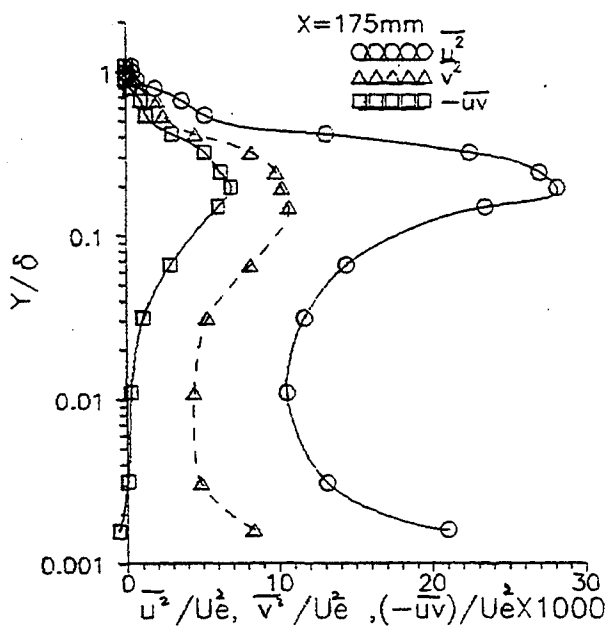
X=175mm
$\overline{u^2}$
$\overline{v^2}$
$-\overline{uv}$
1
0.1
0.01
0.001
Y/δ
0
10
20
30
$\overline{u^2}/U_e^2$, $\overline{v^2}/U_e^2$,$(-\overline{uv})/U_e^2$X1000

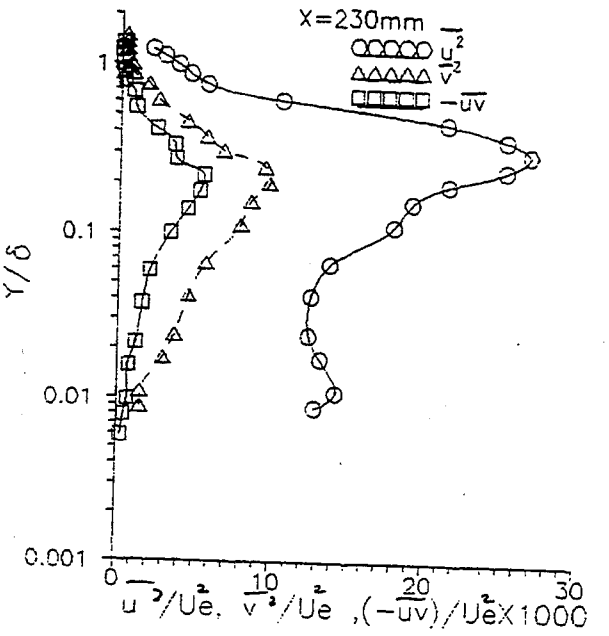
X=230mm
$\overline{u^2}$
$\overline{v^2}$
$-\overline{uv}$
1
0.1
0.01
0.001
Y/δ
0
10
20
30
$\overline{u^2}/Ue^2$, $\overline{v^2}/Ue^2$, $(-\overline{uv})/Ue^2 X1000$

Interaction of Trailing Vortices With a Nominally Two-Dimensional Turbulent Flat Plate Boundary Layer

Steiner T., Creazzo J., Hoffmann P.
Department of Aerospace Engineering, Royal Melbourne Institute of Technology, Australia

ABSTRACT

Experimental mean flow and turbulence results are presented for the strong interaction between trailing vortices generated by an upstream delta wing and a nominally two-dimensional turbulent boundary layer developing over a flat plate in a zero streamwise pressure gradient. Measurements of local total pressure and local static pressure were obtained using a five-hole pressure probe. The development of the mean flow characteristics of the interaction are compared at seven streamwise locations. The influence on the mean flow of favourable and unfavourable streamwise pressure gradients is also compared to the that of the reference zero pressure case at one of the seven stations. Anemometry with a triple-wire probe was used to obtain turbulence quantities which are related to the dominant features of the mean flow topology at one of the seven stations.

The work here is part of an ongoing program investigating this generic flow field. This work aims to improve the understanding of the behaviour of complex vortical flows and to contribute to subsequent improvements in the analysis and design of devices and vehicles which exhibit such flows. At present no detailed predictive methods are available to the design engineer for vortex/lifting surface interactions.

INTRODUCTION

The interaction between a vortex and boundary layer is categorised as a complex flow where considerable three-dimensionality and turbulence effects are present. It is well known that the interference of a streamwise vortex with a nearby lifting surface body, such as an aircraft wing, can have a strong effect on the aerodynamic characteristics of the wing. This flow interaction has been the subject of many studies.

Harvey and Perry (1971)[2] examined the behaviour of a trailing vortex interacting with a moving ground plane on which the boundary layer had been removed. Their work led to the first qualitative explanation of this kind of interaction. It is necessary to point out that the other work discussed here examined interactions involving developing boundary layers, that is the boundary conditions are quite different from those of Harvey and Perry.

In 1960 Smith and Lazzeroni[1] conducted a preliminary investigation into the influence of a vortical wake on a downstream conventional wing. Their approach was to use experimental and theoretical results to determine the aerodynamic characteristics of the wing after they had been altered by the interaction. Their theoretical analysis was based on classical inviscid concepts and this had limited success in predicting the pressure distribution over the wing surface. Patel and Hancock (1974) performed a similar experiment to that of Smith and Lazzaroni and they used a non-linear lifting line approach to predict the load distribution on a wing downstream of a trailing vortex. Overall trends of the loads induced on a wing by a streamwise vortex but again detailed behaviour of the load distributions, especially when the vortex lay near to the wing surface, was to complex for inviscid theoretical treatment. McAlister and Tung (1983)[3] extended the earlier modelling of the interaction by using the commercial panel method code VSAero which performs

boundary layer calculations iteratively with the inviscid solution to approximate the broad influence of the boundary layer. This viscous calculation is based on Thwaites' method extended to three dimensions.

It is evident that even such a relatively sophisticated approach to modelling this interaction is bound to be limited in predicting detailed behaviour of the flow field. This is largely due to the fact that not all of the important viscous dominated features of the flow may be thought of as occurring at the surface and hence amenable to modelling by Thwaites' method or similar methods. The modelling of such interactions via essentially inviscid means weakly coupled with simple viscous models may have reached close to its limit in explaining the behaviour of this flow even though the broad features may be predicted by such analyses. Mehta and Lim (1984)[4] in work on the interaction between a trailing vortex and the laminar boundary layer on a conventional wing noted that "... details of the shear layers on the main wing which must be adequately modelled if the performance of the wing is to be predicted accurately". In practice the shear layers are likely to be in a turbulent state adding to the complexity of this highly three-dimensional flow.

Cutler and Bradshaw (1986)[5] used cross-wire anemometry to investigate the interaction between strong longitudinal trailing vortices and a boundary layer. High levels of certain components of the Reynolds stresses were found in the region of separation. It was evident that the boundary layer fluid is first subjected to large cross flow and is then transported away from the surface to circulate around the vortex core. Cutler, Naaseri and Bradshaw (1989)[7] showed that the interaction between a burst vortex and boundary layer produces qualitatively similar results to those of the unburst case. This suggests that the vortex strength, unchanged through the bursting process, is the dominant parameter and that the initial stage of the interaction may be controlled by the large-scale motion providing a largely inviscid mechanism.

More systematic research needs to be directed towards understanding the effects of various parameters on the flow field. Examples of such parameters include the effects of trailing vortex structure, ground plane geometry and type of boundary layer. Approaching this study through systematic variation of key parameters should reveal the general physics of the flow and hence lead to a greater understanding of the interaction. Because of the clear importance of the turbulence it is essential to investigate the magnitude and structure of all possible turbulence quantities. Such work may at least suggest which of the turbulence quantities are of greatest importance in the interaction and this would assist in the formulation of predictive models that may be of use to the practicing engineer.

EXPERIMENTAL PROCEDURE

This work was conducted in the RMIT Aerospace Engineering department large wind tunnel which has an octagonal working section of 1370 mm × 1070 mm. The maximum flow velocity in the test section is 45m/sec and the free stream turbulence level is approximately 0.5%. The vortex generator is a 76° (unit aspect ratio) swept delta wing made of aluminium with a 0.262m span and sharp leading edges. The lower surface of the delta wing has a 10° bevel on all three sides producing very sharp edges and apex. The upper surface of the delta wing is flat. Data showed that the present vortex generator produces tight vortex cores which persist for the entire length of the working section. The Reynolds number of the flow was 720,000 based on wing chord. To produce standard turbulent boundary layer characteristics for the ground plane the EPPLER code was used as an aid for the design of the ground plane leading edge. Measurements were made of the development of the boundary layer and its characteristics were found to agree acceptably with published data. Different streamwise pressure gradients were obtained by varying the incidence of the ground plane about its leading edge. The delta wing was located at one span length upstream of the leading edge of the ground plane and its incidence was kept fixed for the zero pressure gradient case presented here.

The effects of favourable, unfavourable, and zero streamwise pressure gradients over the ground plane on the development of the interaction are compared at seven cross-stream planes using a five hole pressure

probe. In creating non zero pressure gradients using ground plane rotation caused the effective angle of attack for the delta to be changed slightly. The effective flow incidence at the delta wing position was accurately measured and adjusted so that total pressure coefficients, static pressure coefficients and vortex position at the first measurement station (ground plane leading edge) were consistent for all three cases - that is, the vortices are presented to the boundary layer in close to the same state for each case. To create constant varying pressure gradients for the non-zero pressure gradient cases required the ground plane to be extended 1500 mm into the wind tunnel diffuser. By varying the angle between the extended ground plane and working section ground plane an adjustment capability was constructed which allowed for fine adjustment of the pressure gradients. The wind tunnel arrangement is shown in figure 1.

Effective use is made of a sophisticated six degree of freedom robotic traverse. This was designed to carry pressure probes, hot wire anemometer probes or similar instruments which may need to be pitched, yawed and rolled as well as positioned accurately in space. Freedom of movement for the probe is needed to allow alignment with skewed flows typical vortex and wake flows. Probe freedom is also desired for obtaining turbulence data which can be probe orientation dependent. The traverse employs a developed algorithm to control all motions. Positional calculations are performed to ensure that the probe and other parts of the traverse will not crash into any solid surfaces that may be present in the wind tunnel. The program allows the experimenter to monitor the data effectively on-line and will permit any suspect points to be checked or re-measured at the time of the experiment. The most attractive feature of the program is the 'Auto Traverse option'. This allows the user to preset the measurement locations for the traverse to position and find the local velocity vector with periodic input for any changes in barometric pressure.

At each prescribed point the traverse will align the five-hole pressure probe in the free stream direction and data will be acquired by the computer data acquisition card. The flow speed and direction in three dimensions is inferred using four previously generated calibration charts for pitch and yaw angles in the range of -30° to +30° at 20m/sec (i.e. : coefficients of total and static pressure, pitch, and yaw) which all contribute in determining the predicted velocity vector at the point of interest. A typical calibration chart for total pressure is presented in figure 2. If the inferred angle of the velocity vector is more than, say, 5° out of alignment with the probe axis then the traverse system will automatically reorientate the probe to match the inferred velocity direction. This process may be repeated until acceptable alignment is achieved. The allowable misalignment angle is arbitrary but chosen to give reasonable accuracy based on the total pressure tube behaviour. In general one realignment is sufficient for most points, but close to a vortex core two and sometimes three iterations may be required. Points that require more than one realignment are characterised by data falling outside the calibration region for angles.

Accuracy of the five-hole pressure probe is decreased at large angular misalignment and in the presence of high shear provided by strongly vortical flows. To quantify the effects of sheared flow on the accuracy of the five hole probe is a difficult task which will be addressed at a later stage when hot wire data is available for comparison.

The hot-wire probe used to obtain turbulence measurements has three sensors in a conventional configuration. Each wire was operated with a resistance ratio of 1.8 from TSI anemometers (without lineariser). The probe was calibrated over a speed range of 5 to 30 m/s with yaw and pitch angles varying from -10° to +10° and -20° to +10° respectively. The calibration took the form of a Chebychev polynomial fit with terms up to order four in the three independent variables, including all cross-coupled terms. Analysis of the performance of the calibration scheme showed that errors in the inferred velocity increased rapidly as the range of calibration angles was widened. By aligning the probe with the mean flow the instantaneous flow angles relative to the probe could be minimised and this permitted the maximum accuracy to be obtained.
The scheme was initially developed through the use of an analytical model of the response of typical hot-wire sensors based on a modified King's Law. This generated a set of three voltages for specified flow

speed and angle. Ideal test cases were run with instantaneous velocity vectors oscillated in a sinusoidal fashion in a cone around different mean directions. Even though the calibration scheme took the voltages produced by the modelled hot-wires and gave errors in the recovered instantaneous velocity of typically a few cm/s with this "ideal" data it was found that the averaged Reynolds stresses were in good agreement with the values expected from theory.

As a diagnostic aid the probe was aligned with the mean velocity vector and a histogram was obtained of the inferred flow speeds and angles relative to the probe axis. It was found that at the locations with the highest degree of turbulence in the flow plane being measured no more than 0.2% of the samples were inferred to be outside the valid calibration window. Alignment with the mean flow was important as the flow was highly skewed and at some locations the velocity vectors could be up to 35° from the tunnel axis.

RESULTS AND DISCUSSION

A) Mean Flow Field

Experimental results showing the streamwise development of the interaction at the seven cross-flow planes are presented in the form of contours of total pressure coefficient. For the work here this coefficient is defined as local total pressure referenced to tunnel static pressure and nondimensionalised by the wind tunnel reference dynamic pressure. Contour plots of these fields for the zero pressure gradient case are presented in figures 3a-3g. The most striking features of the vortex boundary layer interaction are the well defined development of the induced boundary layer separation.

In figure 3a the primary and secondary vortices shed by the delta wing are clearly visible through the contours of total pressure coefficient and by vorticity contours (not presented here) which show concentric contours having opposite sign to that of the main vortex. This secondary vortex is generated by the same mechanism as that responsible for the later induced boundary layer separation. The secondary vortex is convected and stretched around the primary vortex which is the stronger of the two. The secondary vortex is not recognisable as an identifiable entity 600 mm downstream at X/S= 3.28 where S is the wing span.

The sequence of figures 3a through to 3g show graphically the broad characteristics of the interaction with the boundary layer thickening rapidly on the outboard side of the vortex where an adverse lateral pressure gradient exists. The boundary layer fluid is drawn up into a "tongue" which arches over the main vortex by X/S=7.86. Contours of the ratio of local flow speed to free-stream velocity at the station X/S=6.72 presented in figure 3h show that the vortex has fluid moving up to 40% faster than the free-stream.

The separated boundary layer fluid appears to slowly wrap around the main vortex. At the same time the main vortex is growing in diameter. Sectional streamlines (not presented here) show fluid to be spiraling towards the center of the main vortex in the first few cross-flow planes. This is consistent with a positive axial straining field. Sectional streamlines in subsequent cross-flow planes indicate that this straining has diminished. In the second half of the working section the sectional streamlines suggest very little straining.

The influence of an imposed constant streamwise pressure gradient on the interaction may be seen effectively in the contours of total pressure coefficient. A nearly constant favourable pressure gradient was produced by inclining the ground plane at about −5° about its leading edge. The constancy of the pressure gradient was controlled by careful adjustment of a flexible metal sheet aft of the ground plane at the end of the working section. An unfavourable pressure gradient case was generated by inclining the ground plane at +5°. The results shown in figures 4a and 4b are for respectively the favourable and unfavourable pressure gradient cases at X/S=6.72.

B) Turbulence

All the data presented in this section is far the zero pressure gradient case at the station X/S=6.72. Double correlations of velocity fluctuations are presented in figures 5a-5f. It can be seen in figures 5a-5c that in the region corresponding to the separated fluid outboard of the main vortex the peaks in the normal stresses $\overline{u'^2}$, $\overline{v'^2}$, *and* $\overline{w'^2}$ occur at different locations. The stress component $\overline{u'^2}$ occurs higher up and more inboard than the peak in $\overline{w'^2}$, and in turn the peak in $\overline{w'^2}$ occurs higher up than the peak in $\overline{v'^2}$. In other respects the three contour plots share a broadly similar topology. The peak value in $\overline{w'^2}$ is about 50% than either of the other two normal stresses.

The turbulent kinetic energy k = $\overline{u_i'u_i'}$ is presented in figure 6. There is evident a very strong similarity of the distribution of this parameter with the distribution of total pressure coefficient.

The Reynolds shear stresses in figures 5d-5f show more complex structure than the normal stresses. The contour plots of stresses $\overline{u'w'}$, $\overline{u'v'}$ and $\overline{v'w'}$ have quite different topologies. The negative peak of $\overline{v'w'}$ is found to occur where the turbulent kinetic energy is a maximum. In this region $\overline{u'w'}$ and $\overline{u'v'}$ are close to zero. The positive peak in $\overline{u'v'}$ is found outboard of the peak in turbulent kinetic energy and this corresponds with a negative peak in $\overline{u'w'}$. Conversely, the negative peak in $\overline{u'v'}$ is found inboard of the peak in turbulent kinetic energy and this corresponds with a positive peak in $\overline{u'w'}$.

These six contours of the stresses seem to be consistent with a "vortex-skeleton" (figure 7) model in which spanwise "mean" vortex filaments of the undisturbed boundary layer are swept upwards by the primary vortex into a hairpin-like vortex loop. This produces something similar to a turbulent vortex pair which is then stretched by the increased streamwise velocity away from the wall. The increased velocity in the region of the primary vortex as shown in figure 3h also contributes to the straining of this elemental hairpin vortex loop. The hairpin loop is subsequently wrapped around the primary vortex. This wrapping and stretching along the axis of the primary vortex should lead to greater values of $\overline{v'w'}$ than either of $\overline{u'v'}$ or $\overline{u'w'}$ in the region around the primary vortex. This is observed in the contour plots. It is expected that this should occur due to largely inviscid dynamics and that this process is distinct from any redistribution of turbulent energy via the various mechanisms of turbulence dynamics.

Triple correlations of velocity fluctuations are not presented due to insufficient space here to describe them in detail and to discuss their important features.

CONCLUSION

Mean-flow and turbulence results are presented for the case of a turbulent interaction between a trailing vortex and a boundary layer developing on a flat plate. The boundary layer fluid is lifted from the surface as noted by others. A secondary vortex is not observed although there is vorticity of the appropriate sense in the region outboard of the primary (trailing) vortex.

A "vortex-skeleton" model proposed here for the vortex boundary layer interaction appears to be a satisfactory first order explanation for the initial behaviour until viscous and turbulent effects start to dominate. This model is consistent with all the measured mean-flow and turbulence data presented here. The turbulence data obtained compares favourably in topology and magnitude to that of previous researchers. Differences in the relative levels of the Reynolds stresses reported by Bradshaw and others[5,7] and the present work may be significantly due to the different distances of the measurement station downstream of the wing trailing edge.

It is believed that the localised distribution of surface pressure will be modified as complicated distributions of vorticity and other parameters evolve under the influence of the complex straining fields in the region of the separation. The flow need not be turbulent to display such complexity as observed by Mehta and Lim[4] in the case of an interaction with a laminar boundary layer but turbulence may well modify the behaviour as turbulent energy is redistributed and diffused by additional mechanisms.

REFERENCES

1. Smith, W.G.; and Lazzeroni, F.A.
Experimental and Theoretical Study of a Rectangular Wing in a Vortical Wake at Low Speed.
NASA TN D-339, Oct, 1960.

2. Harvey, J.K.; and Perry, F.J.
Flow Field Produced by Trailing Vortices in the Vicinity of the Ground. AIAA J.9, 1659, 1971.

3. McAlister, K.W.; and Tung, C.
Airfoil Interaction With an Impinging Vortex.
NASA TP 2273, 1984.

4. Mehta, R.D.; and Lim, T.T.
Flow Visualization Study of a Vortex/Wing Interaction.
NASA TM 86656, Oct, 1984.

5. Cutler, A.D.; and Bradshaw, P.
The Interaction Between a Strong Longitudinal Vortex and a Turbulent Boundary Layer.
AIAA-86-1071, 1986.

6. Bryer, D.W.; Pankhurst, R.C.
Pressure-Probe Methods for Determining Wind Speed and Flow

7. Cutler,A.D.; Naaseri,M.; Bradshaw,P.
Interaction Between Strong Longitudinal Vortices And Turbulent Boundary Layers.
Presented At The 4th Symposium On Numerical and Physical Aspects of Aerodynamic Flows,
Long Beach, 16-19 Jan. 1989.

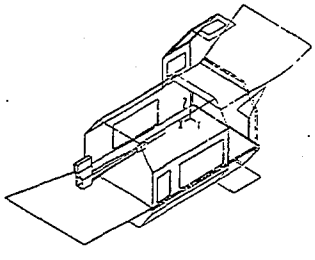

Figure 1
Wind tunnel working section arrangement

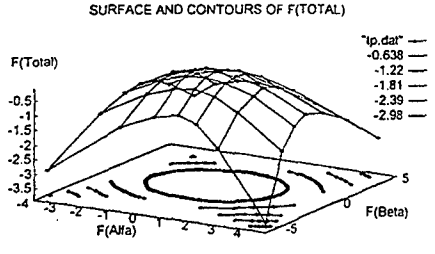

Figure 2
Example of one of the four five-hole probe calibration charts

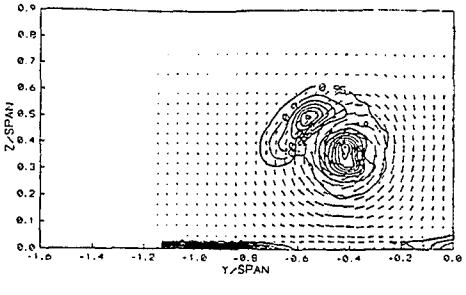

Figure 3a
Total Pressure coefficient, X/S=2.15, zero pressure gradient

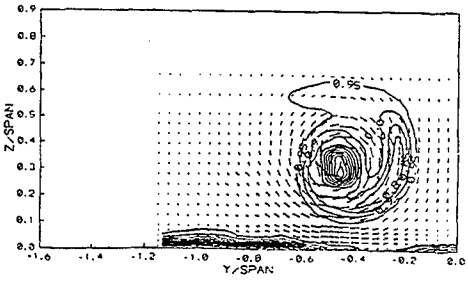

Figure 3b
Total Pressure coefficient, X/S=2.15, zero pressure gradient

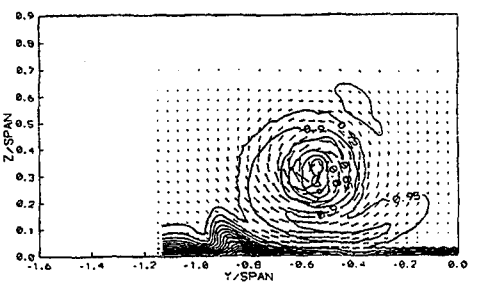

Figure 3c
Total Pressure coefficient, X/S=3.28, zero pressure gradient

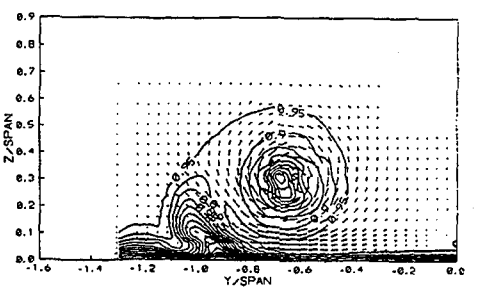

Figure 3d
Total Pressure coefficient, X/S=4.43, zero pressure gradient

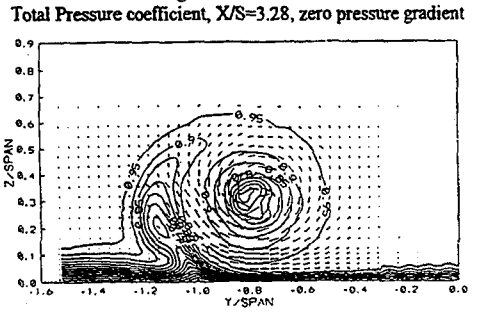

Figure 3e
Total Pressure coefficient, X/S=5.57, zero pressure gradient

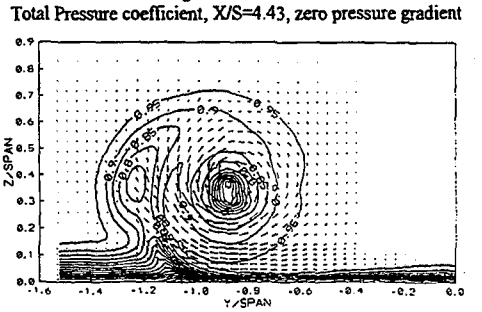

Figure 3f
Total Pressure coefficient, X/S=6.72, zero pressure gradient

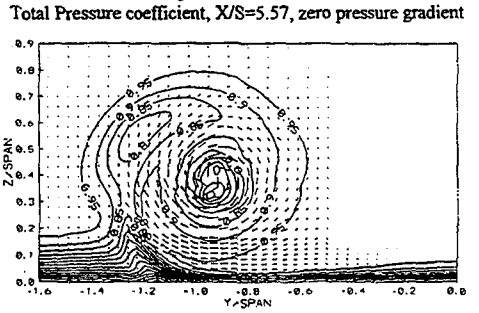

Figure 3g
Total Pressure coefficient, X/S=7.86, zero pressure gradient

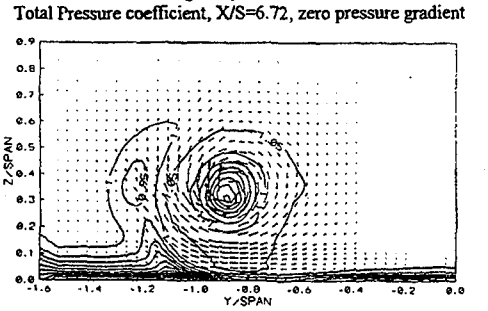

Figure 3h
Contours of Total Speed, X/S=6.72, zero pressure gradient

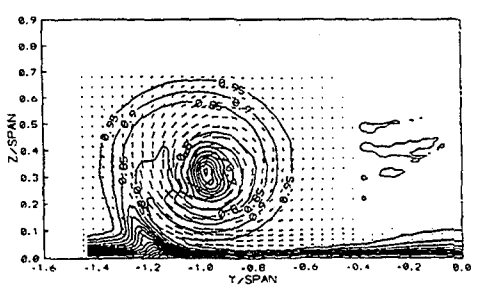

Figure 4a
Contours of Total Pressure coefficient
at X/S=6.72, favourable pressure gradient

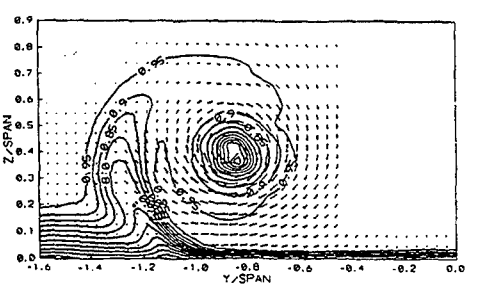

Figure 4b
Contours of Total Pressure coefficient
at X/S=6.72, unfavourable pressure gradient

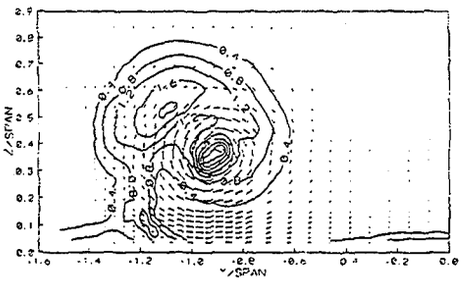

Figure 5a

Contours of $\overline{u'^2}$ at X/S=6.72, zero pressure gradient

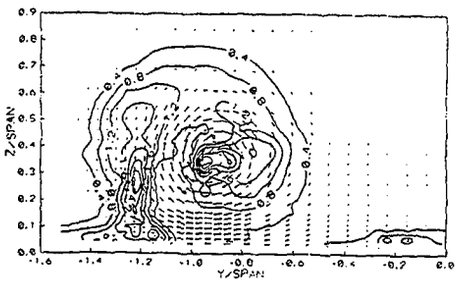

Figure 5b

Contours of $\overline{v'^2}$ at X/S=6.72, zero pressure gradient

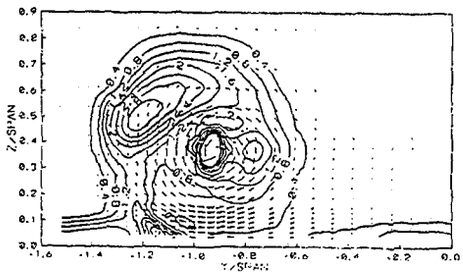

Figure 5c

Contours of $\overline{w'^2}$ at X/S=6.72, zero pressure gradient

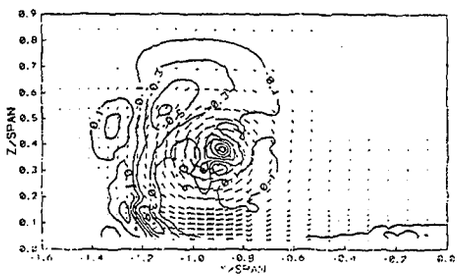

Figure 5d

Contours of $\overline{u'v'}$ at X/S=6.72, zero pressure gradient

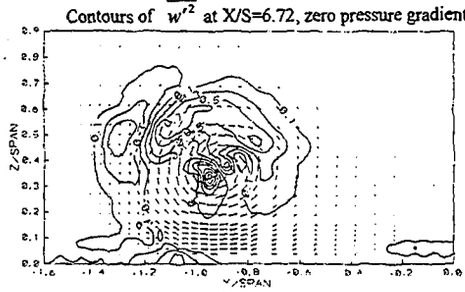

Figure 5e

Contours of $\overline{u'w'}$ at X/S=6.72, zero pressure gradient

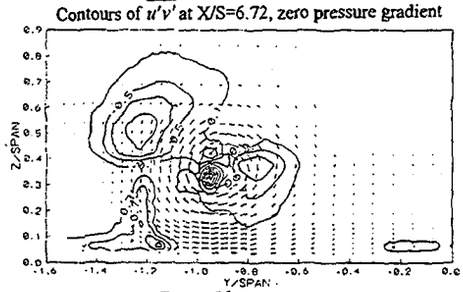

Figure 5f

Contours of $\overline{v'w'}$ at X/S=6.72, zero pressure gradient

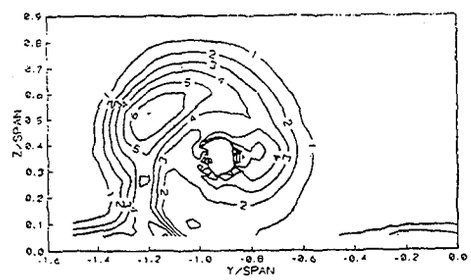

Figure 6

Contours of turbulent kinetic energy $k = \overline{u_i' u_i'}$ at X/S=6.72, zero pressure gradient

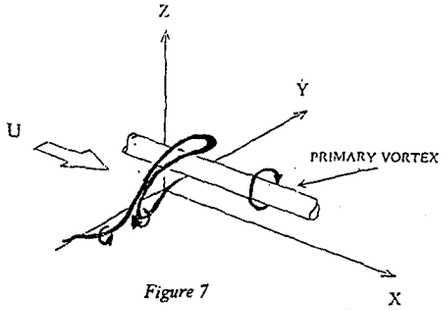

Figure 7

Conjectured vortex skeleton model of the initial stage of the interaction. Turbulent "mean boundary layer vortex filament" lifted away from surface then stretched by mean flow.

FLOW IN AN "S"-SHAPED DUCT

J. Bruns, T.V.Truong
Institut de Machines Hydrauliques et de Mécanique des Fluides
Ecole Polytechnique Fédérale de Lausanne (Switzerland)

Introduction

Three-dimensional turbulent boundary layer flows are commonly found in many industrial applications with flow around bodies and in turbomachines. They have been comparatively little investigated because of their complex nature and the large cost for measuring equipment and wind tunnel time.

There are usually two mechanisms to generate streamwise vorticity in a boundary layer, which makes it three-dimensional. In pressure-driven flows the mean flow causes the deflection of the streamlines whereas in shear-driven three-dimensional boundary layers turbulent stresses induce streamwise vorticity. In general stronger three-dimensional effects are produced in pressure-driven flows. Comprehensive overviews of three-dimensional turbulent boundary layer experiments have been given by several authors such as Fernholz and Vagt[1] and more recently Ölçmen and Simpson[2] and Schwarz and Bradshaw[3].

In the present experiment a spanwise pressure gradient is generated in an "S"-duct by the curved sidewalls thereby producing mean streamwise vorticity. Duct-flows have advantages compared to an open flow configuration. The Reynolds number and the strength of three-dimensional effects can be more easily varied and a better spatial resolution can be achieved due to thick boundary layers.

The test section of the "S"-shaped duct consists of three parts, one straight part at the inlet with a quasi two-dimensional boundary layer flow, an "S"-shaped part where the flow develops to a three-dimensional boundary layer driven by the transverse pressure gradient, and finally another straight part at the outlet where the flow recovers back to a two-dimensional flow. The boundary layer flow at the exit of the "S"-shaped part shows the interesting feature of "cross-over" profiles, a sign change of the crossflow component, due to the reversal of the spanwise pressure gradient that corresponds to an inflection point of the external streamlines in the core of the duct.

Earlier measurements in a different configuration with a smaller spanwise pressure gradient were reported by Truong and Brunet[4] and Löfdahl et al.[5].

Experimental Arrangement

The test section of the wind tunnel has an aspect ratio of 5:2 and consists of two straight parts at either end of the "S"-shaped section. Figure 1 shows the general layout of the test section with all its dimensions and the definition of the coordinate system. Internal sidewalls are installed in the "S"-part to "shave off" the sidewall boundary layers and therefore to reduce the influence of the sidewalls. In all experiments the Reynolds number at the entrance of the first straight part was set to 10^6 per meter. Approximately 1200 pressure tabs are installed in the test plate to provide detailed measurements of the static pressure. A traverse mechanism enables the probe to be moved in the two lateral and the vertical directions and to be rotated around the vertical axis as well as the probe axis. A detailed description of the traverse mechanism and the wind tunnel and its performance can be found in Truong and Brunet[4].

Six measurement positions were investigated following the centerline of the duct. Figure 2 shows the location of all the positions as well as a sketch of typical boundary layer profiles found at each measurement position. Position P1 is located in the two-dimensional part of the test section, positions P2-P4 are showing typical three-dimensional velocity profiles whereas P5 and P6 are stations where the crossflow component changes sign ("cross-over" profiles).

Flow visualization was carried using a mixture of oil and soot painted onto a foil glued to the test plate. It provides the wall streamlines over the entire "S"-part of the test section. Figure 2 shows a photograph of the visualization in the downstream part of the "S".

The skin friction was measured at all 6 measuring positions. A Preston tube was used for the two-dimensional Position P1 employing Patels[6] calibration method. The Preston tube technique presumes the existence of a log-law region within the mean velocity profile, which is not necessarily true for three-dimensional boundary layers. Therefore a surface fence with a height of 0.1 mm was used to measure the skin friction at positions P2-P6 in the three-dimensional part. The surface fence was calibrated using a Preston tube at position P1.

The velocity field of the three-dimensional boundary layer flow was investigated utilizing single hot-wire and triple hot-wire probes. The single hot-wires are miniature probes using 2.5 µm tungsten wires with a sensor length of 0.5 mm and gold plated ends. The triple wire probes employ gold plated tungsten wires of a diameter of 5 µm and an active length of 1 mm. A constant temperature anemometer TSI-IFA 100 was used for operating the hot-wires. All data acquisition and the traverse mechanism were controlled by an IBM compatible PC.

The mean velocity profiles of three-dimensional boundary layers show variations of the local streamline direction as a function of the wall distance. The local flow direction was determined by rotating a single wire probe in the plane parallel to the test plate over an angle of 80 degrees and taking 9 measurements. The maximum measured velocity, determined by a cosine fit to the data, yields the local mean flow angle. The same technique of rotating the surface fence was used to obtain the mean wall shear-stress direction.

Triple hot-wire probes were used to obtain the Reynolds stresses. The great advantage of using a triple hot-wire probe is the direct measurement of all components of the instantaneous velocity vector. The three wires are positioned orthogonally on the edges of a cube. The acceptance domain of the probe corresponds approximately to a cone with an opening angle of 50 degrees. A detailed description of the probe and the data processing procedure were given by Schön[7] and Pitteroff[8]. During the measurements the triple wire probe was always aligned with the local mean flow direction, determined by the single wire measurements, in order to keep the instantaneous velocity vector inside the acceptance domain.

Discussion of Results

The measured pressure distribution is given in Figure 3 showing a slight pressure gradient in the two straight parts of the duct. No spanwise pressure gradient was observed in the first straight part indicating a nominally two-dimensional flow configuration. A spanwise pressure gradient is generated in the "S"-part due to the curved sidewalls, which changes sign between stations P3 and P4.

The following table shows the locations of P1-P6 with respect to the tunnel coordinate system (Figure 1) and the integral parameters describing the boundary layer flow. The boundary layer thickness $\delta_{99.5}$ was defined as the height at which the magnitude of the mean velocity vector reached 99.5 percent of the free-stream velocity. The displacement thickness δ_1 and momentum thickness δ_2 were calculated using the magnitude of the velocity vector at each height.

Position	x [mm]	z [mm]	$\delta_{99.5}$ [mm]	δ_1 [mm]	δ_2 [mm]	$C_f * 1000$	Re_{δ_2}
P1	1900	-500	33.46	5.18	3.72	2.914	4010
P2	3295	-500	53.18	7.60	5.57	2.784	6010
P3	4125	-608	73.40	8.65	6.57	3.029	7440
P4	4700	-890	71.45	8.30	6.38	2.932	7840
P5	5500	-1070	82.72	11.15	8.17	2.370	9600
P6	6100	-1100	95.42	13.36	9.71	2.275	11240

Full symbols were chosen in the discussion of the following figures to exhibit the features of the different types of profiles where P1 represents the two-dimensional, P4 the typical three-dimensional (P2-P4) and P6 the "cross-over" (P5,P6) profile.

Figure 4 shows the profiles of the flow angle as a function of the wall distance with respect to the external streamline angle α. Here the angle $\beta = \tan^{-1}(W/U)$ is the absolute flow angle. The magnitude of the cross flow decreases in the streamwise direction to a minimum value of -16 degrees at P3. It increases downstream of the inflection point of the "S"-shape ($x > 4500$ mm) up to 4 degrees at P6. The wall streamline angles are given by the symbols on the abscissa and represent independent measurements with surface fence. The error of $\pm$ 2 degrees in measuring the wall streamlines (error bars on the abscissa) is due to the height of the fence of 0.1 mm. This error appears to be worst at P4.

The magnitude of the mean velocity was measured using a single hot-wire. All velocity profiles are shown in Figure 5 in wall units. Straight lines represent the linear region and the law of the wall. A slight deviation between the measured velocity profiles and the law of the wall was found. The deviation lies within the measurement uncertainty of the hot-wire and of the skin friction measurements, so that the validity of the law of the wall for three-dimensional boundary layers cannot be assessed. The magnitude of the resultant velocity in the wake region of the typical three-dimensional profile is of the same order as for the two-dimensional profile whereas the velocity increases considerably for the "cross-over" profile. A large increase of the velocity in the wake region is characteristic for two-dimensional boundary layers with adverse pressure gradients. At the "cross-over" profile positions on the centerline of the channel just a weak adverse pressure gradient was seen, but, due to the crossflow, fluid might have traveled from the sidewall where adverse pressure gradients are prevailing towards the centerline.

Profiles of twice the turbulent kinetic energy $\overline{q^2} = \overline{u^2} + \overline{v^2} + \overline{w^2}$, scaled by the friction velocity, are shown in Figure 6. The peak values of all profiles are reached close to the wall where the production of turbulent energy is largest. The typical three-dimensional profile shows $\overline{q^2}$ values of the same order as the two-dimensional profile in the log-region, but develops a plateau in the outer part of the boundary layer indicating that turbulent energy is transported outwards. The "cross-over" profile shows much higher values of $\overline{q^2}$ throughout the whole boundary layer due to increased production by the crossflow velocity gradient $\partial W/\partial y$ and a less effective transport of energy in the vertical direction.

Profiles of the $\overline{uv}$ Reynolds-stress in tunnel coordinates are presented in Figure 7 showing slopes, which are similar to the $\overline{q^2}$ profiles. The $\overline{uv}$ values of the typical three-dimensional profile are smaller than for the two-dimensional case in the law of the wall region whereas values for the "cross-over" profile are increased.

The $\overline{vw}$ Reynolds-stress is traditionally the most difficult to measure. Figure 8 shows the $\overline{vw}$ profiles, which increase from the nominally zero values of the two-dimensional case to high values of the three-dimensional profile close to the wall (50 % of the $\overline{uv}$ Reynolds-stress). The "cross-over" profile has a peak at the location where the mean crossflow velocity W changes sign and decreases towards the wall.

The ratio of the magnitude of the total shear stress to twice the turbulent kinetic energy is a parameter describing the efficiency with which turbulent shear stress is produced for a given amount of turbulent energy:

$$a_1 = \sqrt{\overline{uv}^2 + \overline{vw}^2} \; / \; \overline{q^2} .$$

The profiles of this ratio are displayed in Figure 9 showing a decrease for all locations compared to the two-dimensional position. This has been seen in other three-dimensional boundary layer experiments, see e. g. Schwarz and Bradshaw[3], as well as in two-dimensional boundary layers with adverse pressure gradients.

To investigate the response of the turbulence to changes in the mean flow it is instructive to consider the direction of the shear-stress vector γ_τ in relation to the direction of the velocity gradient vector γ_g, which are defined by

$$\gamma_\tau = \tan^{-1}\left(\frac{\overline{vw}}{\overline{uv}}\right), \quad \gamma_g = \tan^{-1}\left(\frac{\partial W / \partial y}{\partial U / \partial y}\right).$$

Figure 10 and 11 show the direction of the mean velocity, the velocity gradient vector and the shear-stress vector for position P3 (typical three-dimensional profile) and P6 ("cross-over" profile). The open symbols display the profiles for the two-dimensional case that are nominally zero for all angles. The shear-stress vector lags behind the velocity gradient vector for the typical three-dimensional as well as for the "cross-over" profile. The angle difference $\gamma_\tau - \gamma_g$ changes throughout the boundary layer, indicating that modeling of non equilibrium turbulent boundary layers by simple isotropic eddy-viscosity models poses serious problems. Note that the "cross-over" profile in Figure 11 shows maximum values of γ_τ, γ_g and $\gamma_\tau - \gamma_g$ where the crossflow velocity changes sign, i. e. where $\partial W/\partial y$ has a maximum (see also Figure 8 where $\overline{vw}$ peaks a the same wall distance).

All triple products were measured so that important parameters for the transport of the Reynolds-stresses could be calculated. The transport of turbulent kinetic energy in the y-direction can be described by the vertical transport velocity:

$$V_{q^2} = \overline{u^2 v} + \overline{v^3} + \overline{vw^2} / \overline{q^2}.$$

All profiles of V_{q2} in Figure 12 show a transport of turbulent kinetic energy from the wall towards the free-stream. Just some values outside the boundary layer are negative indicating a reverse transport. It is noted that close to the wall the vertical transport for the "cross-over" profiles at P5 and P6 is less effective than at positions P1-P4.

Conclusions

Measurements of the turbulent structure of a three-dimensional boundary layer were carried out along the centerline of an "S"-shaped duct. The three-dimensional boundary layer was generated by a spanwise pressure gradient in the "S"-part of the test section leading to typical three-dimensional velocity profiles and "cross-over" profiles.

The production of turbulent kinetic energy increased due to the contribution of the spanwise velocity gradient $\partial W/\partial y$ especially for the "cross-over" profiles at the end of the "S"-part. The $\overline{uv}$ Reynolds-stress of typical three-dimensional profiles decreased in the law of the wall region of the boundary layer whereas it increased for "cross-over" profiles. The ratio of the magnitude of the total shear stress to twice the turbulent kinetic energy was reduced compared to the two-dimensional profile especially for the "cross-over" profiles close to the wall indicating that turbulent shear-stress is less efficiently produced for a given amount of energy. Furthermore, the direction of the shear-stress vector lagged behind the direction of the mean-velocity gradient vector direction thus quantifying the time delay with which turbulence reacts to changes in the mean flow. Finally, the vertical transport of turbulent kinetic energy of the three-dimensional boundary layer studied was found to be smaller close to the wall than in the two-dimensional case.

References

1) Fernholz, H.H. and Vagt, J.D. 1981, Turbulence measurements in an adverse pressure gradient three-dimensional turbulent boundary layer along a circular cylinder. *J. Fluid Mech.* **111**, 233-269.
2) Ölçmen, M.S. and Simpson, R.L. 1992, Perspective: On the near wall similarity of three-dimensional turbulent boundary layers. *J. Fluid Eng.* **114**, 487-495.
3) Schwarz, W.R. and Bradshaw, P. 1992, Three-dimensional turbulent boundary layer in a 30 degree bend: Experiment and modelling. Report No. MD-61, Stanford University, USA.

4) Truong, T.V. and Brunet, M. 1992, Test Case T1: Boundary layer in a "S"-shaped channel, Proceedings of the Ercoftac Workshop on Numerical Simulation of Unsteady Flows and Transition to Turbulence, Cambridge University Press.
5) Löfdahl, L., Truong, T.V., Johansson, B., Bruns, J. and Olsson, C.O. 1993, Influence of different sensor configurations on the turbulent quantities in a complex three-dimensional flow field, ASME-Fluid Engineering Conference, Washington DC, USA.
6) Patel, V.C. 1965, Calibration of the Preston tube and limitations on its use in pressure gradients. *J. Fluid Mech.* **23**, 185-208.
7) Schön, T. 1990, Drei-Komponenten-Hitzdrahtmessungen im nahen Nachlauf einer quer angeströmten ebenen Platte. Dissertation at RWTH Aachen, Germany.
8) Pitteroff, R. 1991, Rechnergestützte Erprobung einer Drei-Draht-Sonde zur Messung des Reynoldschen Spannungstensors, Diploma thesis at TU Berlin, Germany.

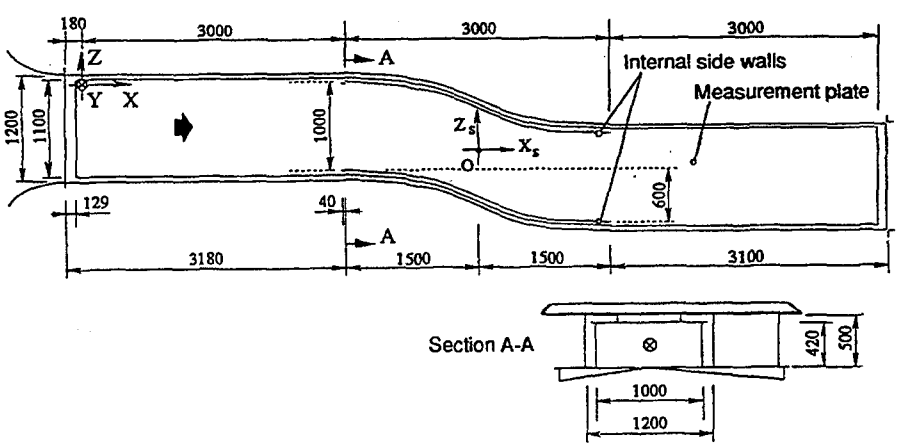

Figure 1: General layout of the "S"-shaped duct

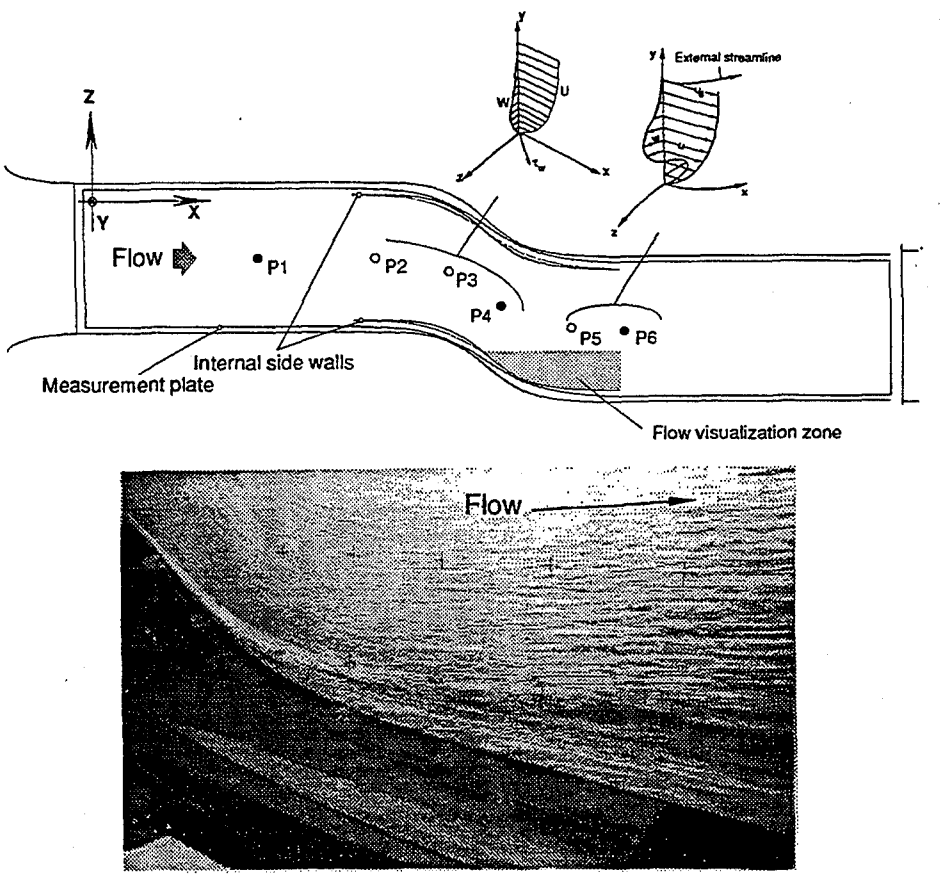

Figure 2: Measuring positions in the "S"-shaped duct; picture of the typical three-dimensional mean velocity and the "cross-over" profile; photograph of flow visualization in the downstream part of the "S" section

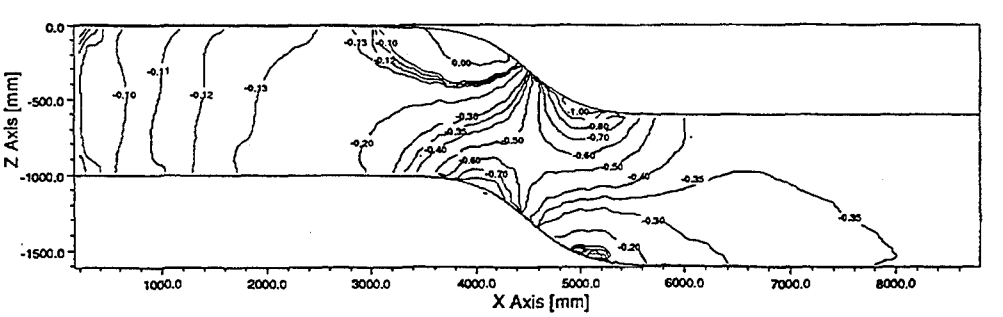

Figure 3: Contour plot of the static pressure distribution C_p on the wall of the test section

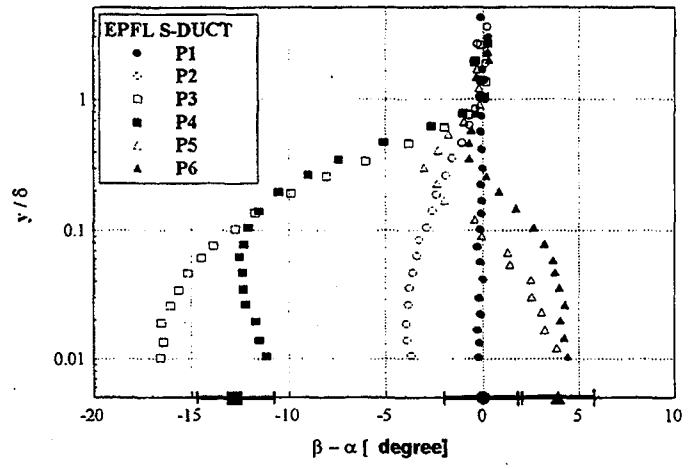

Figure 4: Local streamline direction with respect to the free-stream

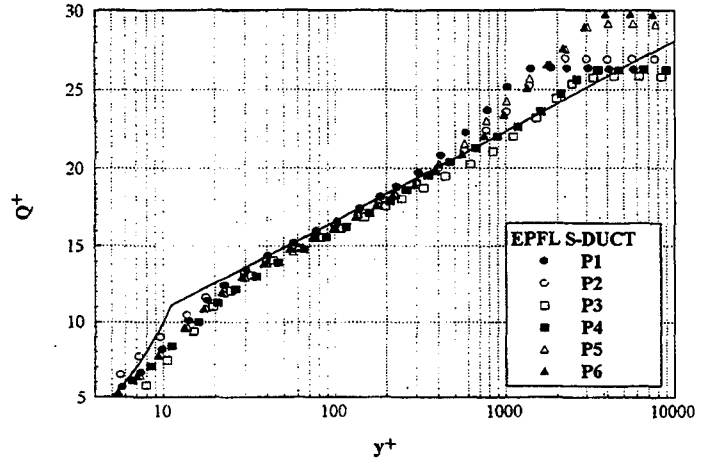

Figure 5: Magnitude of the mean velocity

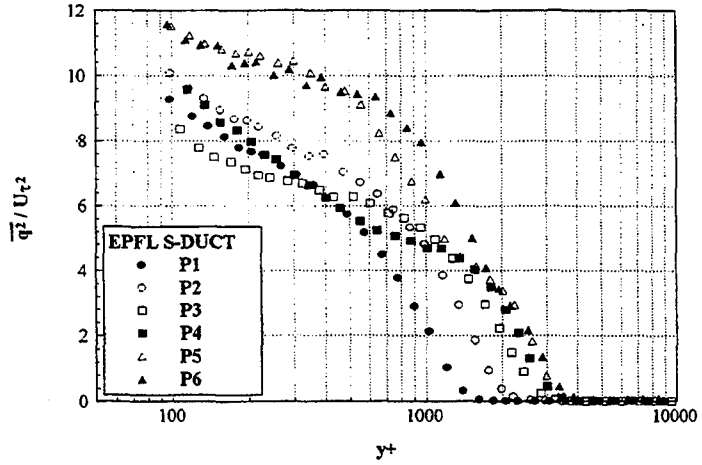

Figure 6: Twice the turbulent kinetic energy

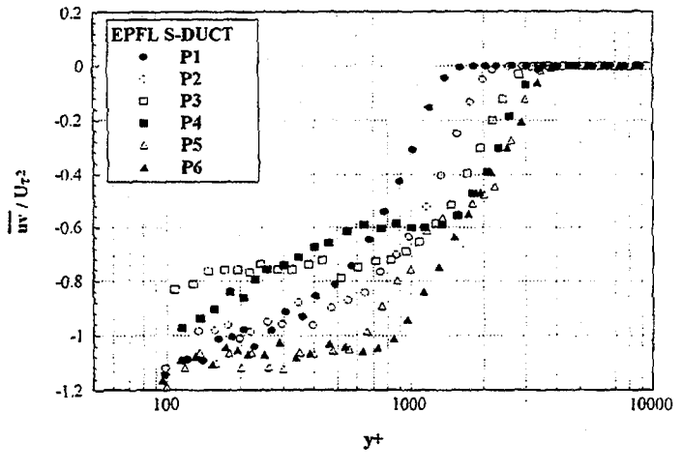

Figure 7: $\overline{uv}$ Reynolds shear-stress

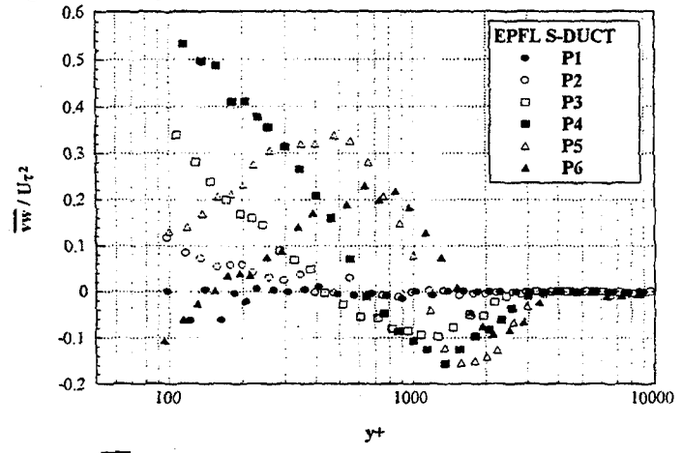

Figure 8: $\overline{vw}$ Reynolds shear-stress

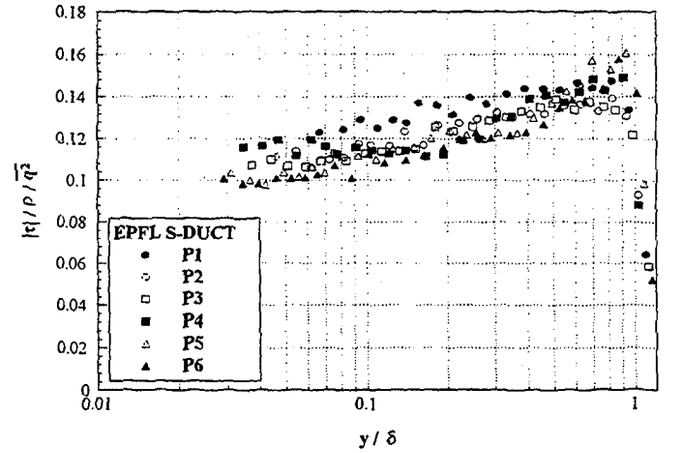

Figure 9: Ratio of total shear-stress to twice the turbulent kinetic energy

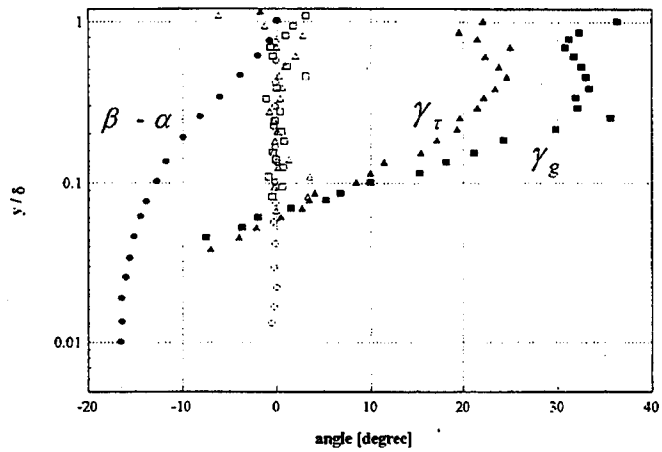

Figure 10: Direction of the velocity (β-α), velocity gradient (γ_g) and shear-stress (γ_τ) vector at P3

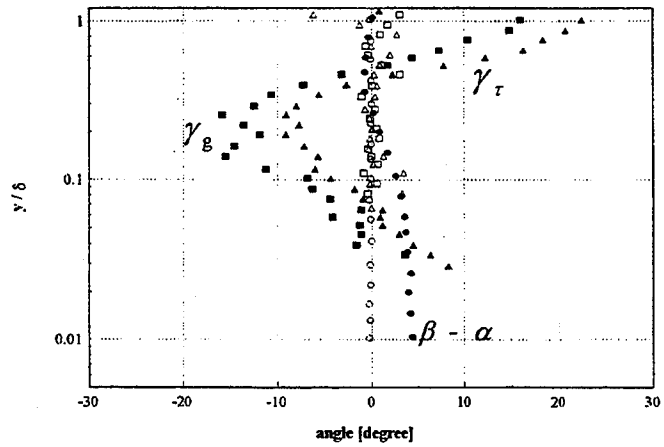

Figure 11: Direction of the velocity (β-α), velocity gradient (γ_g) and shear-stress (γ_τ) vector at P6

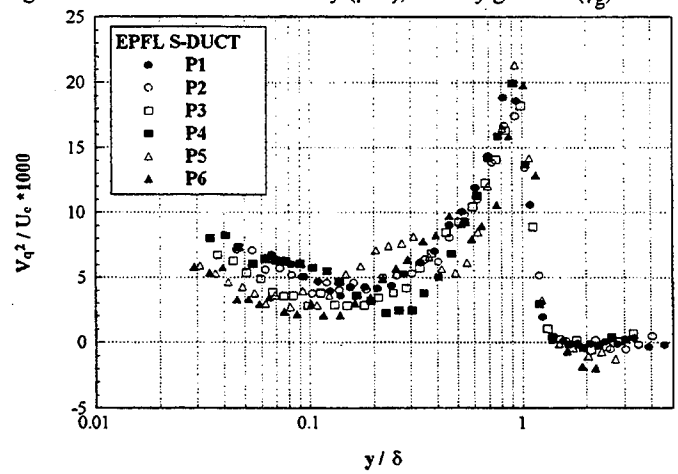

Figure 12: Vertical transport velocity of twice the turbulent kinetic energy

VORTICAL FLOW AND SKIN FRICTION IN A SURFACE-BODY INTERSECTION. AN AERONAUTICAL AND HYDRAULIC COOPERATION

S. De Ponte, , G. Gibertini, M. Cerchiari
Dipartimento di Ingegneria Aerospaziale
Politecnico di Milano, Milano, Italy

S. Franzetti, R. Monti
Dipartimento di Ingegneria Idraulica Ambientale e del Rilevamento
Politecnico di Milano, Milano, Italy.

ABSTRACT

The flow around a cylinder-surface intersection is investigated experimentally in the case of a flat surface and under various bottom geometries due to the effect of the local sediment erosion processes.
Tests and visualizations show the increase of the horseshoe vortex strength and strong skin friction close to the intersection, caused by the large shear flow induced by the main vortex.
Applications to the aeronautical problems of wing-fuselage intersection and of model, tunnell-wall interference are discussed . Also the problems connected to the water erosion are considered with particular respect to skin friction measurements-

LIST OF SYMBOLS
b cylinder diameter
G circulation
i turbulence intensity
$Re_{()}$ Reynolds number on ()
U tunnel velocity
u,v,w velocity component in the x, y, z directions
ρ radial distance from the cylinder axis
τ_w shear stress
σ rms value
<> mean value

1. INTRODUCTION

It happens sometimes that, while different field of sciences have completely different interests, common features may appear both in problems and methodologies.
In the present research, the general fluid dynamic problem is the vortical flow near the intersection of a cylinder and a plate: a fundamental problem of interest in both aeronautics and hydraulics. The hydraulic problem is the erosion around a bridge pier, or whatever cylindrical structure reaching the bottom of a water stream. The study of the final stage of erosion is the main goal on the hydraulic point of view. For this problem the flat plate case is representative of the initial stage only. Further on, the flat case is the most interestig problem in the aeronautical field, where two are the facets of the problem: the first is the simplest model of a wing-fuselage intersection while the second is the model-wall intersection flow in two-dimensional wind tunnel testing.
The complexity of the flow has many effects, beyond the problem of the local sediment transport of the hydraulic problem. In the aeronautical field in fact the horseshoe vortex leaving the wing-body intersection may induce complex flows on the tailplanes. The result is an anomalous aerodynamic derivative that causes problems in the aircraft control, up to effects on the spin and spin recovery.
In wind tunnel airfoil testing, the three-dimensional effects due to the sidewall vortices affect the reliability of experimental results.
In the hydraulic field the horseshoe vortex is the cause of the erosion and it is interesting to study which is the evolution of the vortex structure related to the bottom geometry. In fact, in the case of steady flow, the depth of the scour evolves in time reaching an asymptotic value which is directly correlated to the final stage of erosion (Franzetti et al., 1989). Of course, this evolution depends on the shear stress distribution, function of the characteristics of the vortex structure. Most of the hydraulic literature works didn't approach the problem from a fluid-dynamic point of view. The complexity of the geometry and of the kinematic field causes great difficulties both for experimental and numerical approach to the problem. In the experimental literature we know only few contributions to the study of velocity in the hole (Melville et. al., 1977; Ettema, 1980), only one contribution about the shear stress distribution (Melville & Raudkivi, 1977) and no visualizations at different steps of the scour evolution. Most of the measurements and visualizations that are possible to find about this 3D vortex flow are related to the aeronautical field and of course only in the flat plate case or in particular aircraft configurations.
The problem of local erosion was mostly approached in the past by empirical models and only some Authors (Nagakawa et al., 1975; Baker, 1980; Tsujimoto, 1988) based on some empirical-conceptual models. They recognize that a good parameter to represent the evolution of scour is the vortex strenght. With some assumption about the geometry of the vortex and supposing that the strenght remains costant (Baker, 1980) as the scour goes deeper, they correlate it to the erosion depth in every stage of the bottom evolution.
All the complex phenomena required a better insight. Some other Authors (Melville et.al., 1977) in fact disagree from the Baker's assumption. For example, Melville & Raudkivi (1977) say that the vortex circulation increases about 100 times its initial value passing from the initial to the final stage.
So in this research different kinematic and dynamic aspects have been analyzed, in order to verify Baker's conceptual model. To do this, some flow visualizations and some quantitative measurements could improve our understanding of the local erosion mechanism.
From an aeronautical point of view it is well known that sometimes the problem is to add the proper fillet in the wing-body intersection to reduce the vortex strength. In this sense, the investigation of the erosion problem, with its increase in vortex circulation, has effects in the opposite direction with respect to the fillet, is interesting because it may show larger

effects than in the case of simple cylinder plate intersection and therefore may enlarge some of the quantitative aspects.

2.EXPERIMENTAL SETUP AND MEASURING TECHNIQUE

The choice of the methodology was rather complex, due to the completely different experience of the two groups and to the many constraints on the measurements.
As in the Franzetti et al. (1982) experiment the water depth was large enough to neglect the effect of the free surface, it was decided that the Aeronautical Dep. small wind tunnel was the best choice for the present measurements, as it allowed the use of the advanced measurement techniques available in the Aeronautical Laboratory.

2.1 Flow fileld survey techniques.

LDV was rejected due to the problem of refraction. In fact the access to the erosion cavity by optical means would require the best possible matching of refraction index between the wall and the fluid, so that the channel should have filled with a specific and expensive liquid.
For the flow-field measurements a 5-holes probe seemed to be a good choice: as that the flow direction was roughly known by previous smoke visualizations, the probe axis could be properly oriented by means of a two degree of freedom support purposely designed. (with the aim of orienting the probe axis in a direction with respect to the local flow contained in the cone of monotonic response of the probe). The device allowed to tilt the probe in pitch and yaw (**photo 1**).

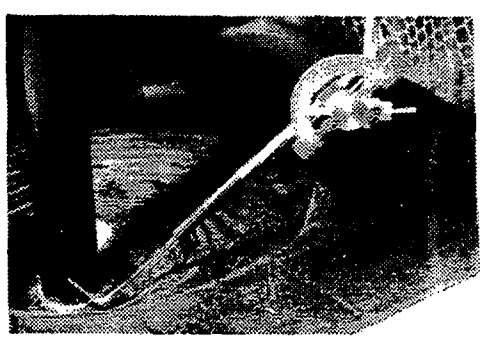

photo 1. five holes probe used for the velocity measurements.

The probe was supported by a two degree of freedom transversing gear, one of the directions being parallel to the cylinder axis and the other either along the tunnel axis or normal to free stream and cylinder axis. Pressure differences were measured by Scanivalves and pressure transducers.

2.2 Shear stresses measurements.

Hot-wires were used for turbulent measurements of the wall shear stress fluctuations, because it was the only way to have some informations on them (and then we had a rather good experience in the use of this kind of tool) (De Ponte et al., 1991). Only one component measurements was made. Before each experiment, the probes were calibrated in a wind tunnel apparatus specially designed for this purpose.The shear stresses were measured in the Reynolds numbers range 10000÷90000.
Turbulence measurements were carried out for 2 seconds recording at 257 Hz.
For the evaluation of the average wall shear stress the Preston tube was considered the most reliable instrument, provided that the local shear stress direction could be roughly estimated by surface visualizations.
Pressure measurements were carried out using a differential trasducer which could register up to 80 Hz with good accuracy. To choose the best sampling frequency, before the experiments various statistical moments were computed to evaluate the repeatibility of the mean values.
The Preston tubes and the hot-wires probes were located on the surface as indicated in **figure 1 (a and b)**

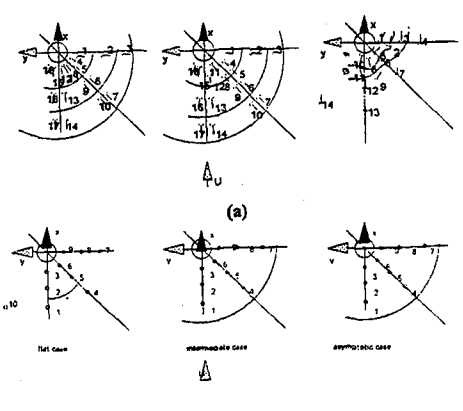

Figure 1 a) Preston tubes and b) hot-wires probes surface distribution in the three bottom configurations.

2.3 The wind tunnel and the test models.

The chosen experimental apparatus was a small open circuit wind tunnel in which an insert on the floor allowed to put the proper cavity model[1].

[1] *An attempt to simulate a thick boundary layer by means of protrudeng wanes gave so many problems due to the large turbulence that it was abandoned very soon. On the other hand, the shape of the erosion cavity was obtained in tests (Franzetti et al. 1980) where the incoming turbulence and velocity profiles were not measured and, compared to the measurement problems that arise, it was decided that a more*

The size of the test section of the aerodynamic tunnel was 0,5*0,7 m^2 with a lenght of 2,5 m. This test section (not-movable bed) was the same of the movable flume in which the hydraulic problem was formerly investigated in water (Franzetti et al., 1982). For the physical tests, three different bottom geometries have been choosen: 1) a cylinder emerging from a flat bed (initial condition); 2) the eroded bottom at an intermediate state; 3) the asymptotic erosion pattern in time (final condition). The forms of the cavities were obtained in the previous tests in water (Franzetti at al., 1982) and were reproduced in wood (**photo 2**) to get better geometric accuracy and a stiffer support to the wall shear probes. The cylinder was simply modelled by a steel tube protruding out of the lower wall and all the transversing gear was placed on the opposite, upper wall.

photo 2. Wooden cavity model in the asymptotic geometry.

The maximum tunnel speed was approximately 27 m/s, and it was adjusted to the kind of measurements: low for smoke visualizations (U=2 m/s; Re_b=7000), high for wall shear stress visualization (U=5÷27m/s; Re_b=17000- 90000) and in the best range for pressure measurements (U=6.5 m/s; Re_b=22000). Only wall shear stresses were measured in a wide range of Reynolds numbers (Re_b=10000-90000).

2.4 Accurancy and reliability

The total maximum error in differential pressure measurements was 6%. This includes the errors introduced by misalignament, wall effects, turbulence, geometry of the probes and calibration uncertainties.
The maximum error hot-wire system was estimated as 7% The error associated with bed shear stress measurements was found from the method given by Patel (1965) which amount about 3-6%.
All the measurements were repeated with good accurancy.

3. RESULTS

3.1 Flow field

The results obtained in this research, coupled with those of other flow-visualizations experiments (available only in the case of flat plane, such as: Thwaites, 1960; Hunt et al., 1978; Baker, 1979 and 1980, Langston et al, 1982; Shuz at al., 1989, Darghai ,1989; Magini, 1993)) and with other velocity measurements near bluff bodies (Abid et al., 1986; Devenport et al., 1990; Darghai, 1990; Fleming et al., 1993; etc.), is sketched for the flat case in **fig. 2**.The patterns of the mean-flow streamlines and surface-stress lines in the two eroded geometry conditions are summarized in **fig.3 and fig.4** (Monti, 1994). The experiments show clearly the connection between shear stress and stream lines patterns. These results give the dimension of the vortex in the incidence plane and characterize the overall flow structure, during the evolution of the erosion processes. Boundaries of the the vortex structure and its circulation could be obtained too.

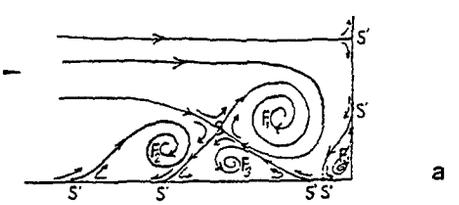

Figure 2. Sketch of the horseshoe vortex system in the plane of symmetry upstream of the cylinder at Re_b= 6800 in the flat case.

All the informations obtained by flow and surface visualizations and by velocity measurements (an example is shown in **fig. 5)** allow to describe the flow structures at different steps of the erosion process (Monti,1994).
In the flat case, the horseshoe vortex is composed by 4 permanent vortices: two steady clockwise rotating vortices and two small counter-rotating vortices (**fig.2**). The second smaller counter-rotating vortex by the cylinder (**F4 in fig.2**) is steady and clearly recognizable at Re_b less than 8000. As the velocity increases this vortex starts to oscillates and it's no more easily recognizable by the use of smoke generator, but its signature is still evident in the surface visualization (**photo 3**).
The number of attachement and separation critical lines is not affected by changes in Re_b, at least for Re_b=7000÷90000. This result is confirmed by Baker (1980) who found the same pattern at Re_b =1.1 10^5. On the contrary some Authors observed structures composed by a different number of permanent vortices (tab.1).

complex simulation of an unknown onset flow should not give a more reliable simulation

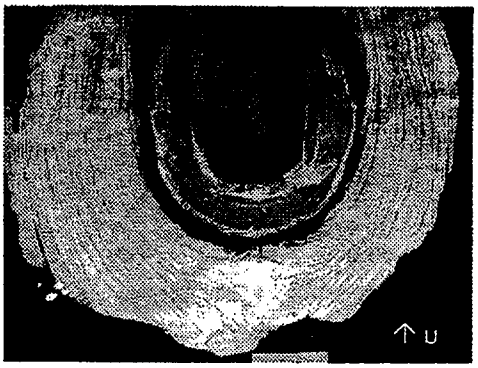

photo 3. Limiting streamlines upstream of the cylinder at Re_b=33500.

tab.1:horseshoe vortex structure in the flat geometry.

Authors	Re_b	n° permanent vortcies
Baker (1980)	$1.1\ 10^5$	4
Pierce, Kim, Harsh (1988)	$1.83\ 10^5$ *	2
Pierce and Tree (1990)	$1.83\ 10^5$	2
Eckerle and Langston (1987)	$5.5\ 10^5$	2
Abid and Schmitt (1986)	$1.05\ 10^6$	4
Ishii and Honami (1986)	very high *	4
Magini (1993)	12320	1 +
Darghai (1989)	20000	5
Monti (1994)	6830	4

* indicated in Pierce et al. (1990)
+ from velocity measurements

As the erosion increases, the vortex system enlarges and takes up all the available volume in the cavity (**fig. 3 and 4**) The system is composed by seven vortices in the asymptotic case: the main one (**F1 in fig.4**), which is the main erosive agent, is sunk in the deeper part of the hole and is a clock-wise rotating vortex; even in this configuration it is possible to find again the vortex F2 already observed in the flat case (**fig. 2**). The other vorticies are typical of this bottom configuration. Only the vortex F3 (**fig. 4**) is clearly present at the intermediate geometry (**fig.3**), with four stationary vorticies. This last configuration has the same number of vortices as in the flat case, but is completely different.

The velocity field was measured, wherever possible, by means of multi-tubes pressure probes on three different radial planes (the incidence plane θ=0°, θ=45°, θ=90°).in both bottom conditions: the flat and the asymptotic case. The main goal was to calculate the circulation of the horseshoe vortex to verify if it remains costant during the transient, as inferred by Baker (1980). Calculations doesn't substantiate the assumption! The circulation doesn't remain costant (Monti, 1994). The strenght of the main vortex F1 doubles its value evolving from the initial condition (flat case) to the final configuration: this increase is not so high as noted by Melville & Raudkivi (1977).

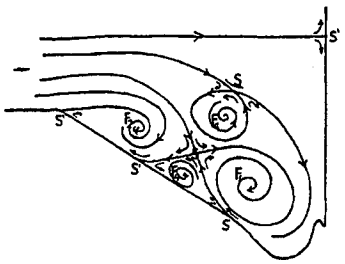

Figure 3 Sketch of the horseshoe vortex system in the plane of symmetry upstream of the cylinder at Re_b= 6800 in the intermediate hole configuration

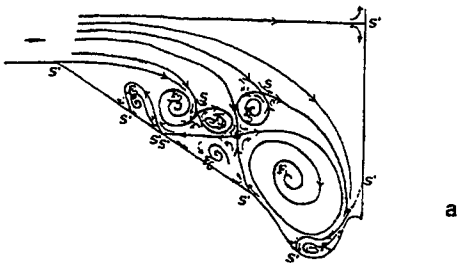

Figure 4 Sketch of the horseshoe vortex system in the plane of symmetry upstream of the cylinder at Re_b=6800 in the asymptotic hole geometry.

3.2 Shear stress field

The surface visualizations have shown in all bottom geometries strong shear stress values just ahead of the obstacle, where the main vortex induces large velocities even close to the wall (**photo 4**). Here the solid transport is related to the large shear stresses and the slope of the cavity is rather steep, because the vortex determines a backflow and the shear stresses act against gravity.

Approaching the final stage of the erosion, a part of rather small shear stresses exists from the beginning of the cavity to the proximity of the main vortex. In this part the erosion is mainly due to free falling of particles. Final transport is due to the fall of particles into the main vortex flow.

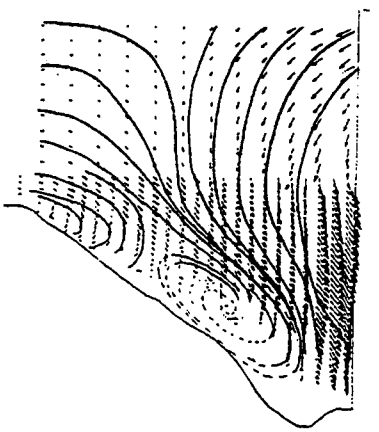

Figure 5 Velocity field in the hole at θ=90° in the asymptotic geometry. Re_b=22000.

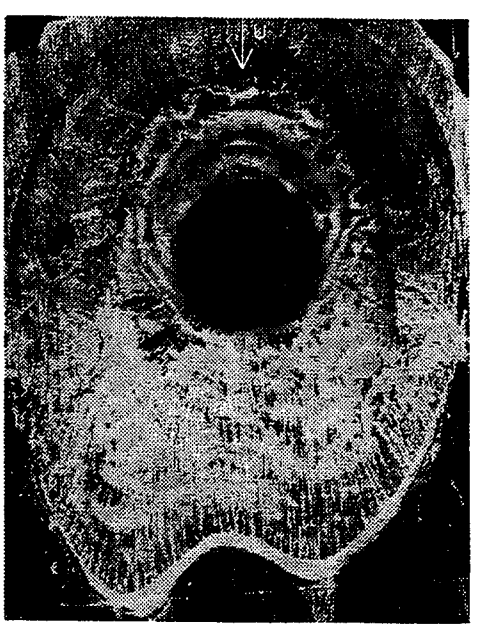

photo 4. Limiting streamlines upstream of the cylinder in the asymptotic case at Re_b=60000

The direction of the limiting streamlines was assumed to orientate the Preston tubes and the hot-wire probes within the angular tolerance required for reliable measurements.
From the Preston tubes the average value of the shear stress was obtained by standard calibration procedures (Patel, 1965).
The largest stresses, as observed from visualizations, in the flat case are located close to the obstacle and are wihitin a region at about 45°degrees from the normal flow direction.

During the erosion, shear stress measurements show a decreasing of the mean values and its surface distribution on the bottom tends to become omogeneus in all the upstream side region.
At the beginning we have rather high mean stress values (higher than the critical value for the sediment); then a second stage follows in which the mean values decrease drastically, but the instantaneus values can be still of the same order of the critical stress for sand. Approaching the "asymptotic conditions" these instantaneus stress become rare (although still present) and when the final condition is reached, the mean and instantaneus stresses are small. This gives a reason why, after a quick start, the erosion proceeds very slowly for a long time. The erosion in this second stage is reasonably connected to some instantaneous peak in shear stress and not to a continuous phenomenon. Asymptotic values are then reached only when the probability of a peak in shear stress is negligible
The analisys of the data include spectrum, which didn't give substancial information and probability density function (p.d.f.). The p.d.f. shows typical unimodal distribution in most part of the bottom surface in all the tiree investigated configurations. The distributions take an approximately Gaussian form in the region of the main vortex in the two eroded cases. In **fig. 6** is shown an example in the asymptotic case for three probes located in the symmetry plane at Re_b=11000, 20000, 35000 (Monti, 1994). The phenomenon of bimodal distribution, observed in the velocity field by Devenport et al. (1990), has no corrispondence in the stress field; it means that the shear stress component measured is always centered on the same value.

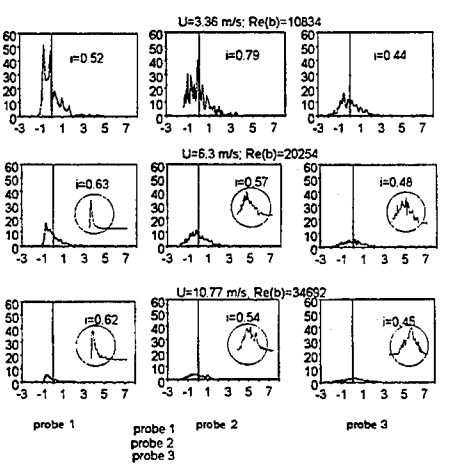

Figure 6. p.d.f. shear stress distribution versus $(\tau_\omega-<\tau_\omega>)/\sigma$ at 11000<Re_b<350000. Asymptotic bottom geometry, symmetry plane θ=0°, probe 1, 2 and 3 with rereference to fig 1 (b).

CONCLUSIONS

The first result is that the circulation increases while the scour is going on. It means, on the other hand, that a good fillet could

reduce strongly the vortex strength in the wing body intersection.

The visualizations allowed to study the overall aspect of the flowfield in the cavity and to define the vortex boundaries and the direction of the wall shear stresses.

The present investigation with single wall hot wires is only a first experimental approach to the problem, because the instantaneous shear direction is likely to be further investigated in details. Only in this way it is possible to know wheather the peaks are related only to a change of the absolute value or to the stress direction too. The double wire developed at our University (De Ponte-Parrini, 1991) is a suitable instrument for this purpouse.

As final consideration, the experimental apparatus has been working very well although the limits formerly described had limited the extension of the measurements and the results may justify the choice of the instrumentation, compared to the allowable budget for the research.

Appendix : Evaluation of the circulation

After the velocity measurement, it was possible to evaluate vorticity and circulation. Vorticity requires differentiation and it is therefore sensitive to measurement errors, while circulation may reduce errors by integration.

On a path, as shown in the figure 7, the circulation was evaluated by integration in the rough trapezoidal rule.

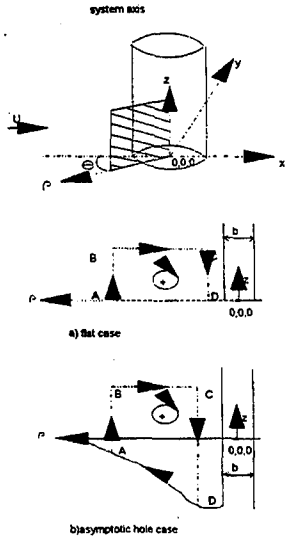

fig. 7. reference axis;. a) example of circulation contour in the flat case; b) example of circulation contour in the asymptotic case.

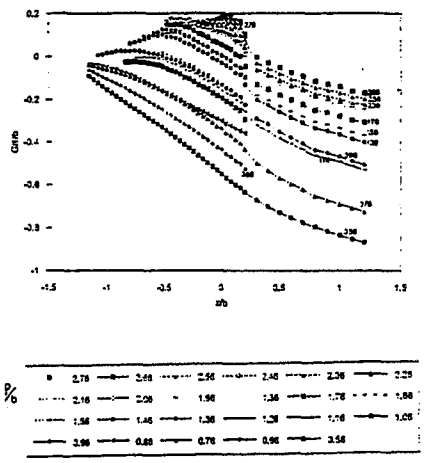

fig.8. Adimensional circulation G/Ub versus z/b varing the distance ρ/b from the cylinder axis. Section θ=90° in the case of the asymptotic hole.

It is interesting to observe that in all case (for example for the section at θ=90° in the case of the asymptotic hole, fig. 8,) the circulation has opposite sign close to the cylinder if compared to the outer part of the flow. This shows the nature of two counterotating vortical structures; one rotating in the same direction of the mean flow and the other opposite in the wall boundary layer on the cylinder.

Because of the size of the probe it was not possible to approach the bottom of the cavity to measure accurately the wall boundary layer there on. But from this simple evaluation it is clear that in the overall vorticity many important features of the flow are hidden, so that the entering vorticity as chosen by Baker (1980) as quantity characterizing the flow may not be significant and is shurely not in agreement with the vorticity measured into the main vortex. Anyway this does not mean, up to now and according to our knowledge, that a crude vortex model may not be correlated to the shear stress during the erosion process.

In the aeronautical field, two counterotating vortices may merge by either viscous or turbulent diffusion and have therefore small influence far downstream, while on short distance they may strongly interfere on some airplane component.

REFERENCEES

Abid R., Schmitt R., 1986. Experimental study of a turbulent horseshoe vortex using a trhee-component laser velocimeter. AIAA Paper 86-1069, May.

Baker C.J. 1979. The laminar horseshoe vortex. J.Fluid Mech., vol. 95, part 2, pp.347-367.

Baker C.J., 1980. The turbolent horseshoe vortex. J. of Wind Eng. and Industrial Aero., vol. 6, pp. 9-23.

Darghai B. 1990. The turbolent flow field around a circular cylinder. Experiments in Fluids 8, pp 1-12.

De Ponte S., Parrini M., 1991. A hot wire for detecting wall shear stress direction. Int. Cong. on Instrumentation in Aerosp. Simulation Facilities, Rockville, Maryland, October 27-31.

Devenport W.J., Simpson R.L. 1990. Time-dependent and time-average turbolence structure near the nose of wing-body junction. J. Fluid Mechanics, Vol. 210, pp.23-55.

Eckerle W.A., Langston L.S., 1987. Horseshoe vortex formation around a a cylinder. ASME J. of Turbomachinery, vol. 109, April, pp. 278-285.

Ettema R., 1980. Scour at bridge piers. Ph.D. thesis, dep. of Civ. Eng., Univ. of Auckland, Auckland, New Zeland, report n.216.

Franzetti S., Larcan E., Mignosa P. 1982. Influence of tests duration on the evalutation of the ultimate scour around circular piers, Prc. Int. Conf. on the Hydr. Modelling of Civ. Eng. Struct., Coventry, paper n° G2.

Franzetti S., Larcan E., Mignosa P., 1989. Erosione alla base di pile circolari di un ponte: veritica sperimentale di esistenza di una situazione finale di equilibrio. Idrotecnica, n° 3.

Hunt J.C.R., Abell C.J., Peterka J.A., Woo H. 1978. kinematical studies of the flows around free or surface-mounted obstacles: applying topology to flow visualization. J. Fluid Mechanics, Vol.86, part 1, pp. 179-200.

Langston L.S., Boyle M.T. 1982. A new surface-streamline flow-visualization technique. J. Fluid Mechanics, vol. 125, pp. 53-57.

Magini R.1993. Conf. AIVELA, Capri.

Melville B.W., Raudkivi. A.J. 1977. Flow characteristics in local scour at bridge piers. J. of Hydr. Research, 15, n° 4, pp 373-380.

Monti R., 1994. Indagine sperimentale delle caratteristiche fluidodinamiche del campo di moto intorno ad una pila circolare. Ph.D. Thesis, Politecnico di Milano, Milano, Italy.

Nakagawa H., Suzuki K. 1975. An application of stochastic model on sediment motion to local scour around bridge pier. Proc. Third Int. Workshop on Alluvial River problems, session 1.

Patel V.C. 1965. Calibration of the preston tube and limitations on its use in pressure gradients. J.Fluid Mechanics, Vol. 23:

Pierce F.J., Tree L.K., 1990. The mean flow structure on the symmetry plane of a turbolent junction vortex. VPI-E-87-6, Mechanical Eng., Virginia Polytechnic Inst. and State Univ., Blacksburg, VA, Apr.

Schuz G., Kottle V. 1989. Visualization of flow, Heat and Mass Transfert in the region of surface mounted, Noncyrcular Proc.

Tsujimoto T., 1988. Analytical approach to some practical aspects of local scour around bridge. Modelling Soli-Water-Structure Interaction, Kolkman etal. eds., Balkema Rotterdam.

Thwaites B. 1960. Incompressible Aerodynamics. Dover Pubblication Inc., New York.

INVESTIGATION OF SURFACE FLOW ON A 65° DELTA WING BY IR THERMOGRAPHY

G. Cardone, G.M. Carlomagno
Universitá degli Studi di Napoli
Facoltá di Ingegneria - DETEC
P.le Tecchio, 80 - 80125 Napoli (Italy)

L. De Luca
Politecnico di Torino
Dipartimento di Ingegneria Aeronautica e Spaziale
Corso Duca degli Abruzzi, 24 - 10129 Torino (Italy)

G. Guglieri
C.N.R. Centro di Studio per la Dinamica dei Fluidi
Corso Duca degli Abruzzi, 24 - 10129 Torino (Italy)

Abstract

IR thermography has been employed for heat transfer measurements and surface flow visualisations on a 65° delta wing model. The tests were performed in the D3M low speed wind tunnel at Politecnico di Torino.

Experimental results generally confirm the capability of the IR technique to analyse such a complex surface flow field by means of convective heat transfer coefficient measurements.

Some general conclusions were derived on the basis of the experimental results obtained at Politecnico di Torino.

In the central part of the wing, where nearly parallel flow conditions are established, a laminar core is present, followed by a transitional region after which the boundary layer becomes turbulent. Data obtained by increasing angle of attack and Reynolds number have proved that the behaviour of this portion of surface flow can be correctly explained with current boundary layer theories.

In the region influenced by crossflow a significant effect of Reynolds number is confirmed: the secondary separation line is deflected outboard in the x/c location where transition occurs.

The effectiveness of a strip in triggering transition has been found to be very relevant.

Data obtained with pressure measurements as well as oil flow visualisations generally well agree with IR thermography results. Discrepancies, if any, have been discussed.

1 Introduction

Delta wings are extensively adopted for high performance aircraft configuration design. Combat aircrafts have been historically, as well as currently, expected to be controllable within their maneuver envelopes. At the extremes of the envelope an alteration of flow characteristics may occur with the expected dual impact of lift and controllability loss [1].

As regards these particular slender wings, at moderate angles of attack the leeward flow field is dominated by highly organized vortical flow structures created by the separation of the boundary layer at the leading edge. A remarkable increase of wing lift is observed in high angle of attack subsonic flight due to the contribution of these vortices [2],[3].

In Fig. 1 the complex delta wing surface flow is presented. Notice that separation and reattachment characteristics are identified by convergent and divergent skin friction lines.
The crossflow velocity components, which increase with the angle of attack, affect the boundary layer behaviour on wing lower surface, so that the attached windward flow is deflected towards the leading edge where separation occurs (primary separation line S_1 in Fig. 1). The separated shear layer is curved inboard over the upper wing surface where, as a consequence of axial velocity effect, two symmetric stable counter-rotating vortical structures are generated. The flow in the vicinity of these primary vortices is deflected symmetrically along curved streamlines and a forced reattachment is generated on the leeward wing surface along the root chord line (primary reattachment line A_1).

The significant spanwise gradients of velocity components influence surface pressure distributions, and a sharp drop is found beneath the vortex axis. The magnitude of this suction peak, which generates a relevant percentage of total lift (vortex lift), is determined by the strength of vortices.

A second separation line S_2 is present underneath the primary vortex core, due to the strong adverse pressure gradients along the wing span. Hence, after the primary reattachment, the boundary layer separates again creating a couple of secondary vortices. Their vorticity is opposite in sign and the secondary focal points are slightly shifted outboard. The effect of the secondary vortices on the pressure distributions and the overall aerodynamic coefficients is small as a result of the little magnitude of their vorticity. However, an influence on the primary vortices position can be visualised.

The surface flow delimited by the primary reattachment A_1 and the secondary separation S_2 is typically transitional. In this region a relevant phenomenon can be observed: the boundary layer development generates a deflection of the separation line S_2 when transition occurs. This effect is the consequence of higher stability of turbulent surface flow, which delays the secondary separation in presence of the significant adverse (spanwise) pressure gradient underneath the primary vortex. Therefore, the secondary separation is related with boundary layer transition and the trace of the secondary separation line S_2 is influenced by Reynolds number and angle of attack. On the contrary, the primary separation line S_1 is marginally sensitive to these two parameters, as the generation of the main vortex is dominated by the leading edge geometry for conventional unprofiled delta wings.

At relatively high angles of attack ($\alpha > 15°$ for the tested model), the vortex breakdown phenomenon appears, consisting of an abrupt expansion of the vortex itself. It is characterized by a decrease of axial and circumferential velocity components, an increase in vortex diameter and a dissipation of turbulent energy. As α increases, the breakdown moves up the wing surface until it reaches the apex. At this point a global separation occurs, equivalent to the stall of a 2-D wing. This behaviour is evident when the delta wing primary vortices are marked by means of tracers in wind tunnel experiments [4],[5],[6],[7] : the vortex appears to break and the marked core increases in diameter, suddenly breaking into a turbulent swirling flow.

On the basis of the preceding remarks it is clear that the research on vortex phenomena over delta wings is difficult. Hence, a relevant effort towards both experiments and modelling is still required for the complete understanding of delta wing vortex dynamics.

In order to gain some new insights into this field of investigation, a 65° delta wing has been extensively tested in the D3M low speed wind tunnel of Politecnico di Torino. Part of this research program is based on measurements made by means of a computerized infrared (IR) scanning radiometer, which is employed to characterize the boundary layer development over the delta wing by measuring the temperature distribution over its heated surface.

The Infrared Scanning Radiometer (IRSR) represents an effective investigation tool in convective heat transfer, in both steady state and transient techniques [8],[9],[10]. The possibility of applying a computerized IR imaging system to measure convective heat transfer coefficients and to analyse the surface flow behaviour in a variety of physical situations, where different data re-

duction methods may be used, is discussed in Refs [11],[12],[13],[14]. The IR technique appears to be a suitable and effective diagnostic tool for aerodynamics research in wind tunnel due to its non-intrusivity, the full two-dimensionality of the measurement, and the possibility of treating the video signal output by digital image processing.

Comparisons with pressure as well as oil flow visualisation data are also presented.

2 Experimental Setup

Experimental tests were carried out in the D3M low speed wind tunnel of Politecnico di Torino, which is a closed circuit tunnel with a contraction ratio of 5.44 and a maximum airspeed of 90 m/s. The test section is circular (3 m in diameter). The turbulence level is 0.3% at $V_\infty = 50$ m/s.

The IR thermography measurements were performed in static conditions ($V_\infty = 20 \div 40$ m/s and $Re = 1.10 \times 10^6 \div 2.2 \times 10^6$) at different angles of attack ($\alpha = 5°, 10°, ..., 45°$). Note that Reynolds number is based on model root chord. Only symmetric flow conditions were considered ($\beta = 0°$).

The effect of induced transition was investigated in a limited number of tests: a strip was placed along wing span at $x/c = 0.18$.

Surface flow visualisations were also performed over the delta wing model. The adopted technique is based on a mixture of oil (kerosene), oleic acid and a UV-sensitive yellow pigment. It is applied on the model surface, so that, when the wind is running, it leaves streaks along the direction of the local flow. Therefore, the layout of skin friction lines can identify flow separations and reattachments.

The model is a 65° delta wing, with sharp leading edges. Its dimensions are: wing semi-span $s = 396.5$ mm, root chord $c = 850$ mm, wing area $S = 0.337$ m^2, bevel angle 30°, wing thickness 20 mm. It was suspended almost at the center of the test section in a 90° rotated position (Fig. 3). The C-shaped sting support was able to rotate about the vertical axis (in order to vary the angle of attack α) and the motion was driven by a servo-mechanical unit placed under the floor of the test chamber. A step motor was interfaced by a digital unit with the control computer.

The fuselage (used as a fairing for sting support connections) has a semicircular section and an ogival nose. Different upper wing surfaces can be used, one of them being provided with 64 pressure taps located at constant span and root chord percentages. A second wing surface was manufactured in polyurethane foam fixed on a layer of plywood and an iron plate used for fuselage and support connections. The top surface is made of a printed circuit board which is glued over the polyurethane foam (20 mm thickness); the circuit is used to generate, by Joule effect, a uniform heat flux on the delta wing surface, while the polyurethane layer thermally insulates the model face not exposed to the wind.

The printed circuit board, shown in Fig. 2, is designed so as to achieve a constant heat flux boundary condition over the model surface. Therefore, the thickness and width of its conducting tracks are realized with very close tolerances. Tracks are 35 μm thick and 6 mm wide. The overall thickness of the board is 0.3 mm. The viewed surface of the board is coated with a thin layer of black paint which has an emissivity coefficient equal to 0.95 in the vawelength of interest.

The IR thermographic system is based on an AGEMA Thermovision 880 scanner. The field of view (which depends on the optical focal length and on the viewing distance) is scanned by a Hg-Cd-Te detector in the $8 \div 12\,\mu$m window. Nominal sensitivity, expressed in terms of noise equivalent temperature difference, is 0.1 °C when the scanned object is at ambient temperature. The scanning spatial resolution is 175 instantaneous fields of view per line at 50 % SRF. A 20°x20° lens is used during the test at a distance of about-1.8 m.

The thermal image is digitized in a frame of 8 bits 140x140 pixels. An application software has been developed to correlate the measured temperatures to heat transfer coefficients. The IR camera takes temperature maps of the wing surface and these maps are correlated to the local heat transfer coefficient by means of the so called heated-thin-foil technique. In particular, for each

pixel, the convective heat transfer coefficient is calculated as:

$$h = \frac{q_j - q_l}{T_w - T_a} \tag{1}$$

where q_j is the Joule heating, q_l is the heat loss (including radiation and internal conduction), T_w and T_a are the wall (measured by IRSR) and the ambient temperatures respectively. The radiative thermal losses are computed from the measured T_w while the conductive ones through the back side of the circuit - i.e. towards the polyurethane foam - are neglected. Typical heat fluxes are of the order of $10^3\,W/m^2$.

3 Experimental Results

In discussing the results hereafter presented, it should be considered that when the model top surface is electrically heated in wind on conditions, regions where higher temperatures are detected are characterized by lower heat transfer coefficients (see eq. 1) - i.e. lower wall friction coefficients c_f, and viceversa.

The thermogram shown in Fig. 4 ($\alpha = 10°$ and $Re = 1.10 \times 10^6$) recovers all the features of the separated flow typical of delta wings. Freestream temperature is equal to 27.5 °C.

The central region of the wing surface is characterized by an almost two-dimensional flow. Moving from the model apex in streamwise direction along the root chord, a gradual increase in temperature is first observed, followed by a sharp drop. This kind of distribution is attributed to the laminar boundary layer development (clear arrow shaped area), so that the initial temperature increase is due to the growth of boundary layer thickness. After laminar-to-turbulent transition, the heat transfer is intensified and the temperature decreases. Finally, the thickening of turbulent boundary layer produces another slighter positive temperature gradient.

In the vicinity of the leading edge a second region characterized by a relatively high heat transfer is clearly evident. Moving along the wing span (from the root chord) a well defined decrease in temperature is found, even if a local maximum can be clearly identified close to the leading edge. Indeed, the locus of such local temperature maxima is a straight line originating from the wing apex and should be correlated with the secondary separation line S_2 of Fig. 1. By increasing Reynolds number (Fig. 5) transition is promoted and the laminar region reduces its extension. The region where secondary separation occurs is split in two parts, the second one being shifted outboard. This behaviour can be explained considering that boundary layer development in the crossflow plane influences separation and keeping in mind that transition delays separation.

In Fig. 6 ($Re = 1.65 \times 10^6$ and $\alpha = 20°$) the effect of increasing the angle of attack is presented. The laminar core becomes larger and transition is delayed as a consequence of the reduction of the axial velocity component. On the contrary, the deflection of S_2 is anticipated at lower x/c.

When transition is artificially induced (Fig. 7), the laminar region disappears and, downstream of the line marked by the strip (in the thermogram it appears as a small white hot region), the temperature drops abruptly. The secondary separation presents turbulent characteristics too.

Quantitative heat transfer distributions (in terms of Stanton number) are going to be described hereafter. Local Stanton number is defined as $h/(\rho c_p V_\infty)$, where thermophysical quantities are evaluated at film temperature.

The chordwise distribution of St as a function of Re is presented in Fig. 8. When the condition $Re = 1.65 \times 10^6$ is considered, a minimum of heat transfer coefficient is found at $x/c = 0.4$. The decrease of St moving away from the wing apex recovers the analogous trend of the heat transfer coefficient (and so the skin friction c_f) for laminar boundary layer on a flat plate. For $x/c \geq 0.4$ the sharp increase of St demonstrates that transition occurred, so that a maximum is detected when surface flow becomes completely turbulent ($x/c = 0.55$). Finally, moving towards

the trailing edge, St slowly decreases. It may be observed that the increment of Re has an evident promoting effect on transition (Fig. 8), as the minimum of St moves forward.

The influence of the angle of attack for $Re = 1.65 \times 10^6$ is shown in Fig.9: transition point is shifted back towards the trailing edge for increasing α.

Spanwise St distributions for $\alpha = 10°$ are depicted in Fig. 10 at different x/c locations. All the curves have a common local minimum at y/s = 0.66, where secondary separation is found. The alignment of such minima confirms that external flow exhibits a conical pattern.

The strong effect of Re on the secondary separation (Fig. 11) can be evaluated by comparing the position of St minima for $Re = 1.1 \times 10^6$ and $Re = 2.2 \times 10^6$, which are located at y/s = 0.66 and y/s = 0.82 respectively.

Pressure distributions confirm some of the conclusions drawn by means of IR thermography. Pressure data were previously obtained on the same model. Unfortunately the spanwise distribution of pressure taps was not sufficiently clustered and the position of the suction peak beneath the primary vortex focus could not be precisely determined. A relation between local St minimum and maximum suction must exist, as a consequence of the fact that secondary separation is induced by the adverse pressure gradient generated by the main vortex. In Fig. 12 (laminar secondary separation at $\alpha = 15°$) the singularity S_2 is almost coincident with the C_p minimum position, while in Fig. 13 separation is moved at a higher y/s location, because of the turbulent nature of the crossflow boundary layer.

The comparison of measurements made with and without transition trip (Fig. 14) demonstrates that transition, when the strip is present on the model top surface at x/c = 0.18, is immediate. The magnitude of the Stanton number peak, associated with the high skin friction coefficient, is higher when transition is induced, even if at the model apex and nearby the trailing edge the influence of strip is negligible. The outboard shift of secondary separation in presence of induced transition is evident in Fig. 15 at x/c = 0.55, while no change in the position of nodal point of separation S_2 is found at x/c = 0.78 (Fig. 16), where the boundary layer is already naturally turbulent.

Finally, data concerned with the location of S_2 obtained with oil flow visualisations and IR thermography are compared. A good agreement is detected when the surface flow is completely laminar (Fig. 17). On the contrary, for higher α and Re data seem to overlap only in the fully laminar or turbulent regions, while the transitional deflection of S_2 is not comparable (Fig. 18). This last discrepancy could be related with the boundary layer interactions with tracers used for oil flow visualisations (in other words, the smoothness of model surface was not the same).

4 Concluding Remarks

IR thermography has been employed for heat transfer measurements and surface flow visualisations on a 65° delta wing model. Experimental results generally confirm the capability of the IR technique to analyse such a complex surface flow field by means of convective heat transfer coefficient measurements.

In the central part of the wing, where nearly parallel flow conditions are established, a laminar core is present, followed by a transitional region after which the boundary layer becomes turbulent. Data obtained by increasing angle of attack and Reynolds number have proved that the behaviour of this portion of surface flow can be correctly explained with current boundary layer theories.

In the region influenced by crossflow (delimited by S_1 and A_1) a significant effect of Reynolds number is confirmed: the secondary separation line S_2 is deflected outboard in the x/c location where transition occurs.

The effectiveness of a strip in triggering transition has been found to be very relevant.

Data obtained with pressure measurements as well as oil flow visualisations generally well agree with IR thermography results. Discrepancies, if any, have been discussed.

As a final comment, it should be emphasized that, although the current state of the art concerned with the surface flow field over a delta wing is well established, the employment of IR thermography has allowed to evidence more in depth two particular aspects: the presence of the laminar central region and the secondary separation line.

References

[1] Erickson, G.E., Skow, A.M., Modern Fighter Aircraft Design for High Angle of Attack Maneuvering, AGARD-LS-121, 1982

[2] Lee, M., Ho, C.M., Lift Force of Delta Wings, Appl. Mech. Rev., vol.43, n.9, 1990.

[3] Nelson, R.C., Unsteady Aerodynamics of Slender Wings, AGARD R-776, 1991.

[4] Wedemeyer, E., Vortex Breakdown, AGARD LS-121, 1982.

[5] Guglieri, G., Quagliotti, F.B., Vortex Breakdown Study on a 65° Delta Wing Tested in Static and Dynamic Conditions, ICAS-92-4.10.2, Beijing, 1992.

[6] Guglieri, G., Quagliotti, F.B., Experimental Investigation of Vortex Dynamics on Delta Wings. AIAA-92-2731, Palo Alto, 1992.

[7] Guglieri, G., Onorato, M., Quagliotti, F.B., Breakdown Analysis on Delta Wing Vortices, Zeit. Flugwiss., n. 16/4, 1992.

[8] Gartenberg, E., Retrospective on Aerodynamic Research with Infrared Imaging, QIRT 92, Balageas D., Busse G. and Carlomagno G.M. eds, 63-85, Editions Europeennes Thermique et Industrie, Paris, 1992.

[9] Carlomagno, G.M., Infrared Thermography, in Measurement Techniques, Von Karman Institute LS 1993-05, 1-114, Rhode-Saint-Genese, 1993.

[10] Balageas, D.L., Fundamentals of Infrared Thermography, in Measurement Techniques, Von Karman Institute LS 1993-05, 1-114, Rhode-Saint-Genese, 1993.

[11] De Luca, L., Carlomagno, G.M., Buresti, G., Boundary Layer Diagnostics by Means of an Infrared Scanning Radiometer, Exp. Fluids, 9, 121-128, 1990.

[12] De Luca, L., Cardone, G., Carlomagno, G.M., Aymer de la Chevalerie, D., Alziary de Roquefort, T., Flow Visualization and Heat Transfer Measurement in Hypersonic Tunnel, Exp. Heat Transfer, 5, 65-79, 1992.

[13] De Luca, L., Cardone, G., Aymer de la Chevalerie, D., Fonteneau, A., Goertler Instability of a Hypersonic Boundary Layer, Exp. Fluids, 16, 10-16, 1993.

[14] Cardone, G., Di Leva, O.M., Carlomagno, G.M., Heat Transfer Measurements and Surface Flow Visualization of a Backward Facing Step Turbulent Flow, FED vol. 172, 35-42, ASME, New York, 1993.

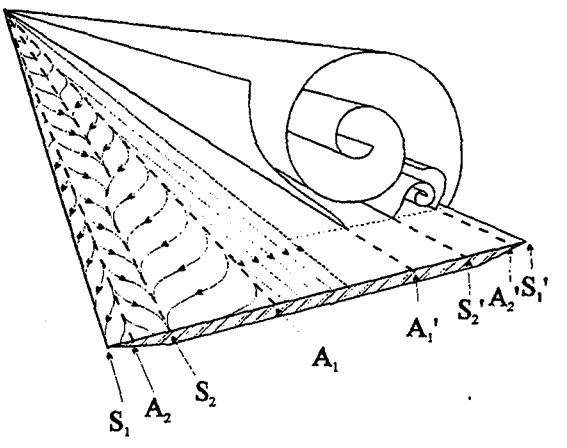

Fig. 1 - Leading edge vortices above a flat plate delta wing.

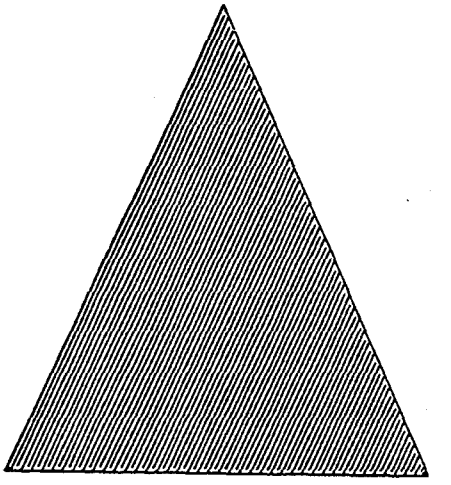

Fig. 2 - The printed circuit.

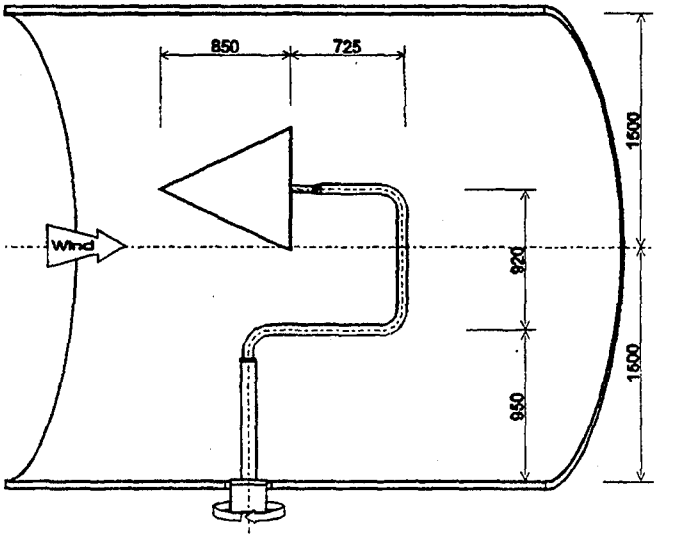

Fig. 3 - Experimental setup.

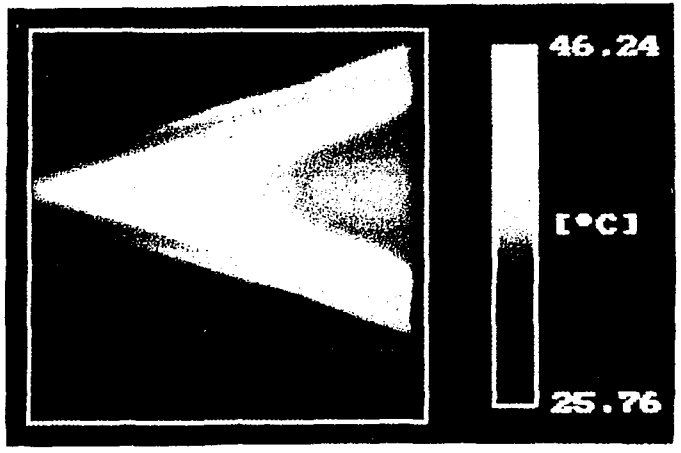

Fig. 4 - Temperature distribution on the model surface ($\alpha = 10°$ - Re = 1100000).

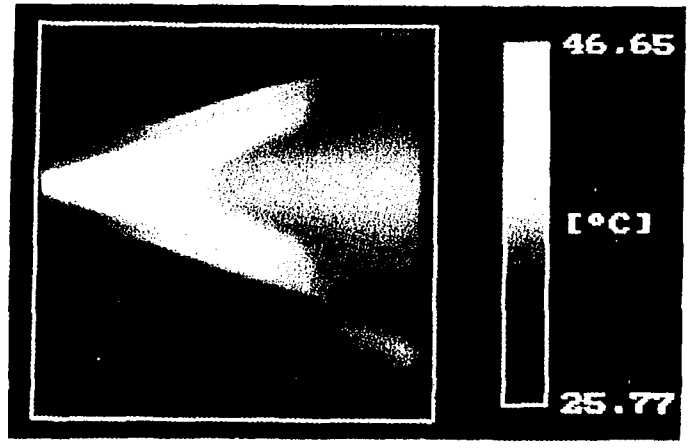

Fig. 5 - Temperature distribution on the model surface ($\alpha = 10°$ - Re = 1640000).

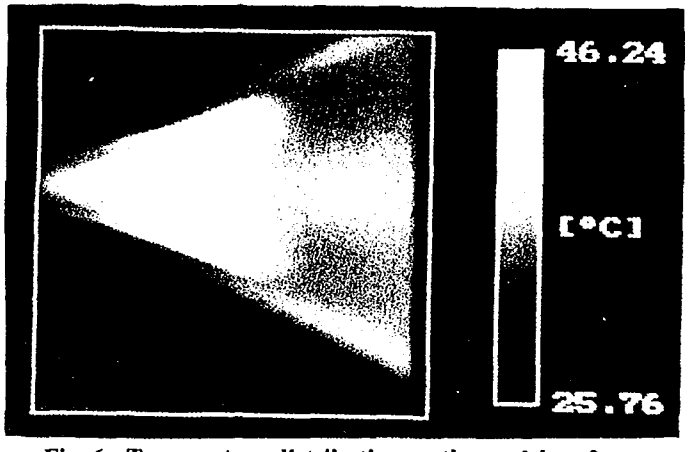

Fig. 6 - Temperature distribution on the model surface ($\alpha = 20°$ - Re = 1650000).

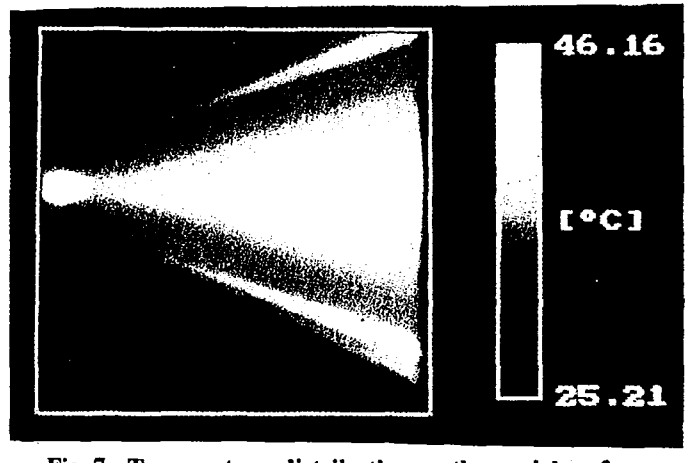

Fig. 7 - Temperature distribution on the model surface with fixed transition ($\alpha = 10°$ - Re = 1650000).

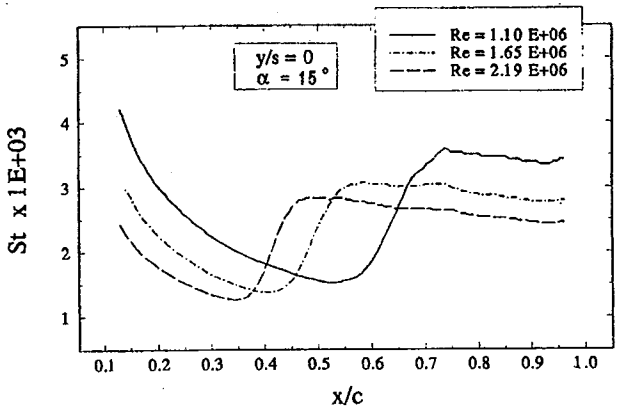

Fig. 8 - Chordwise St distribution as a function of Re ($\alpha = 15°$ - y/s = 0.0).

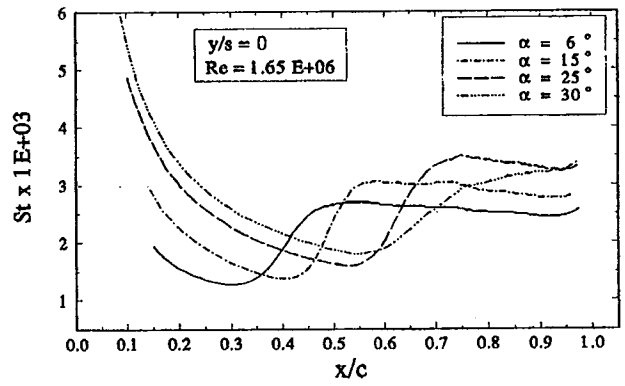

Fig. 9 - Effect of angle of attack on St distribution (Re = 1650000 - y/s = 0.0).

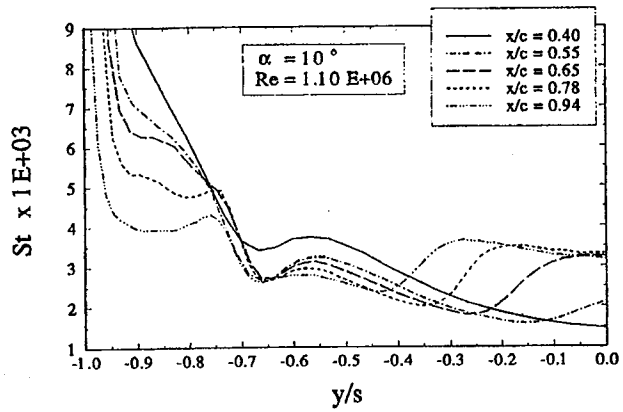

Fig. 10 - Spanwise St distribution as a function of x/c ($\alpha = 10°$ - Re = 1100000).

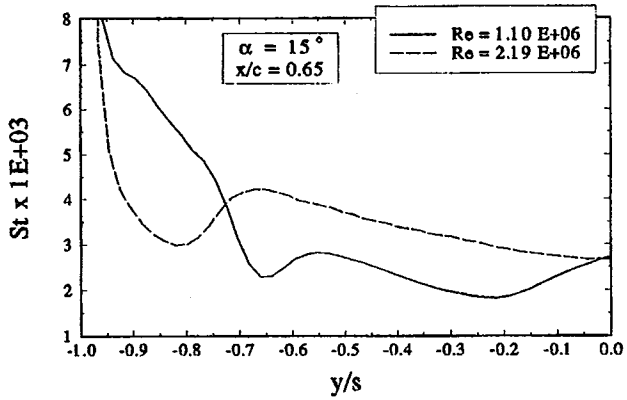

Fig. 11 - Spanwise St distribution as a function of Re ($\alpha = 15°$ - x/c = 0.65).

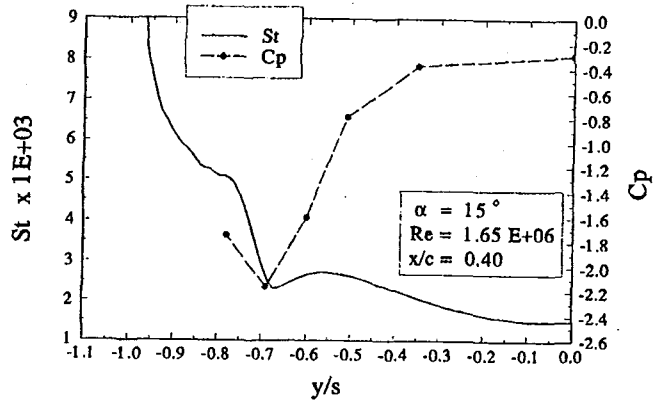

Fig. 12 - Comparison of pressure and St distributions ($\alpha = 15°$ - Re = 1650000 - x/c = 0.40).

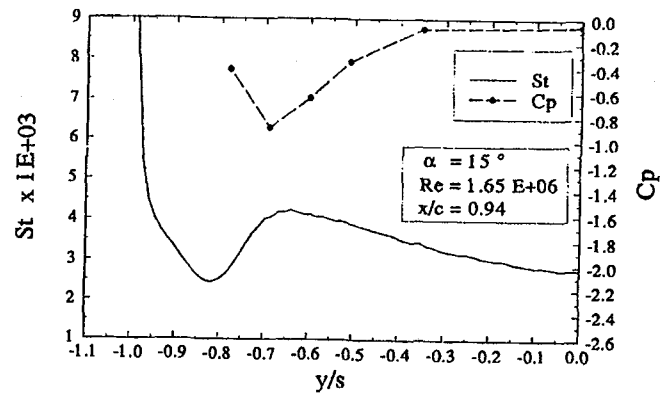

Fig. 13 - Comparison of pressure and St distributions ($\alpha = 15°$ - Re = 1650000 - x/c = 0.94).

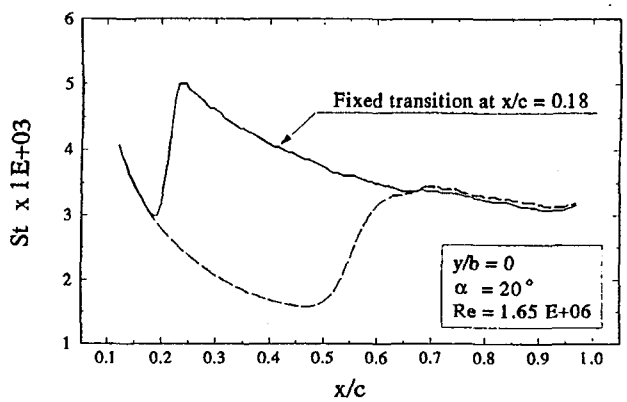

Fig. 14 - Effect of induced transition on chordwise St distribution ($\alpha = 20°$ - Re = 1650000 - y/s = 0.0).

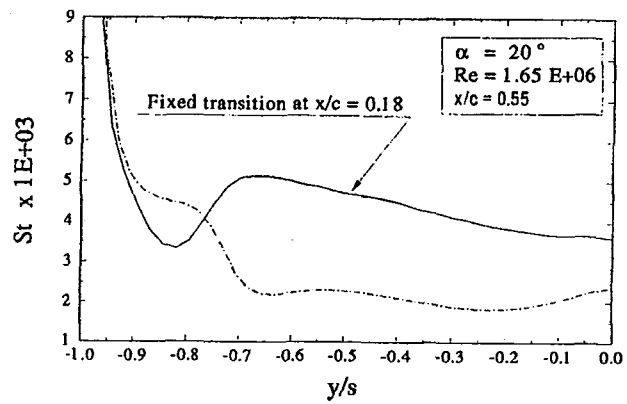

Fig. 15 - Effect of induced transition on spanwise St distribution ($\alpha = 20°$ - Re = 1650000 - x/c = 0.55).

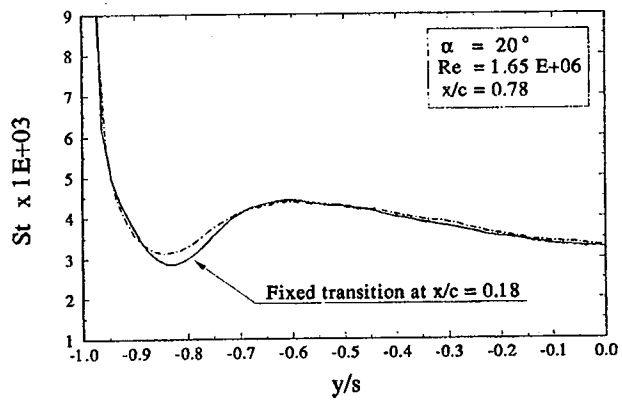

Fig. 16 - Effect of induced transition on spanwise St distribution ($\alpha = 20°$ - Re = 1650000 - x/c = 0.78).

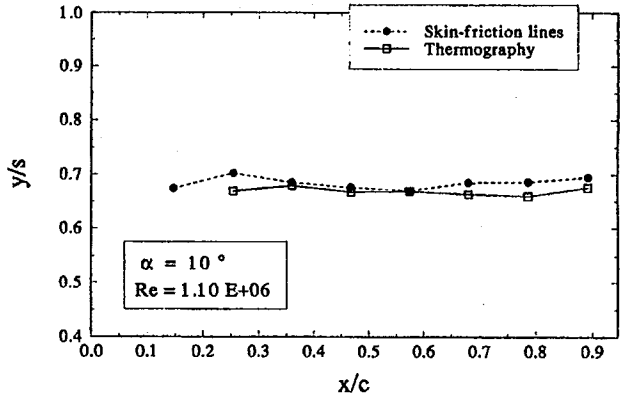

Fig. 17 - Comparison of oil flow and IR thermography measurements of secondary separation line location.

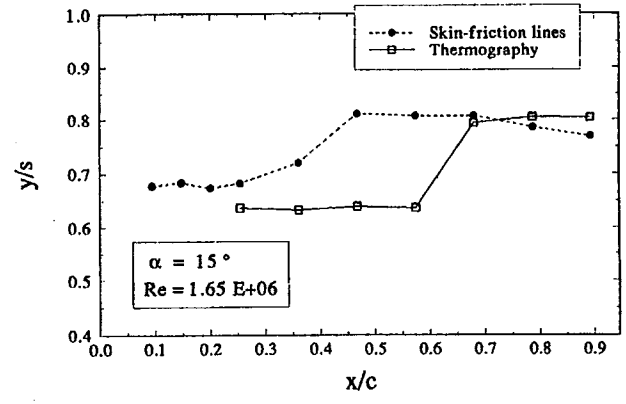

Fig. 18 - Comparison of oil flow and IR thermography measurements of secondary separation line location.

VORTICITY FIELD OF A DELTA WING IN HIGH SUBSONIC FLOW

S.R. DONOHOE, E.M. HOUTMAN and W.J. BANNINK
Faculty of Aerospace Engineering, Delft University of Technology
Kluyverweg 1, 2629 HS Delft, The Netherlands

Abstract

An investigation of the vorticity field above and behind a sharp leading edge delta wing in high subsonic flow is carried out using both experimental and numerical techniques. Experimental measurements are made with a spherical 5-hole probe utilizing a local look-up calibration algorithm. Discretizations of these data to determine the local vorticity vectors are based on conical and quasi-two-dimensional flow assumptions above and behind the wing, respectively. The numerical study is conducted using a finite volume discretization of the three-dimensional conservation law form of the Euler equations.

Both the experimental and numerical results reveal a transition of the axial velocity profile near the vortex core from a *jet-like* profile above the wing to a *wake-like* profile behind the wing. The theoretically predicted reversal of the in plane vorticity vectors associated with this transition of axial velocity profile is confirmed both experimentally and numerically.

1 Introduction

In order to achieve an attractive balance between supersonic cruise performance and maneuverability at high subsonic speeds, modern aircraft designers often utilize highly swept slender wings or delta wings. These aircraft achieve high maneuverability by exploiting the non-linear lift component generated by the powerful rotating flow existing above the lee surface of the wing when operating at angle of attack. Figure 1 illustrates the characteristic vortical flow field found above a non- cambered sharp leading edge delta wing operating at moderately high angle of attack. The location of the flow separation lines, reattachment lines and the core of the vortices is known to be a complex function of the free stream Mach number, leading edge sweep angle, leading edge shape, surface camber and the Reynolds number.

Although complex vortical flows are currently incorporated into the design of high performance aircraft, they remain an intriguing topic of fundamental aerodynamic research. At a given free stream Mach number the non-linear lift component generated by existing lee-side vortices will increase with increasing angle of attack up to the point where the vortex breaks down. Vortex breakdown is commonly described as a transition from an organized vortical flow structure to a large scale fluctuating turbulent flow. In the incompressible flow regime the breakdown position above the wing is found to move gradually forward with increasing angle of attack. In the compressible regime, however, breakdown has been noted to jump suddenly from beyond the

trailing edge to as far forward as 50% of the wing chord at a critical angle of attack [1]. The sudden presence of vortex breakdown above the wing, which is often non-symmetric with respect to the symmetry plane of the wing, can result in severe control problems for the aircraft. The vortex breakdown process is particularly complex in the high subsonic flow regime where the vortex flow is influenced by compressible flow effects.

A great deal of effort has been made over the last forty years in the investigation of vortex breakdown. In his recent survey of the last forty years of vortex breakdown research Délery [2] summarizes the most popular classes of vortex breakdown theories as "a quasi-cylindrical approach and analogy to boundary layer separation, solution of the axisymmetric Navier-Stokes equation, the concept of the critical state and hydrodynamic instabilities", yet concludes that "vortex breakdown remains a problem of major importance".

The consideration of vorticity dynamics is a relatively non-traditional approach to the investigation of vortex breakdown which was first presented in the theoretical work of Brown and Lopez [3]. Their work identified the existence of negative azimuthal vorticity ω_ϕ (see Figure 2) as an essential feature in vortex breakdown. They showed that the presence of a negative azimuthal vorticity initiated a positive feedback mechanism which led to the ultimate stagnation of the vortex core and, thus, vortex breakdown. Further investigations into the role of vorticity dynamics in vortex breakdown have been made by Nelson and Visser [4] and more recently by Darmofal [5]. Nelson and Visser conducted a low speed ($U_\infty = 10m/s$) hot-wire study of a delta wing vortex while Darmofal conducted a theoretical and computational study of an incompressible axisymmetric vortex. Darmofal concluded that the presence of an adverse pressure gradient causes a divergence of stream surfaces which tilts the axial vorticity into the azimuthal direction, leading to a further decrease of the axial velocity by amplifying the axial pressure gradient which, indeed, through continuity further increases the radial outflow.

The present investigation evaluates the changes in the velocity and vorticity field of a vortex with a positive pressure gradient along its axis. The axial velocity and in-plane vorticity components associated with a 65° sweep angle delta wing in a compressible free-stream are examined in several spanwise planes above and behind the wing using both experimental and numerical techniques.

2 Experimental Analysis

The model used for this investigation is non-cambered delta wing with a chord length of $120mm$, a leading edge sweep angle of 65° and a sharp leading edge. The model is supported by an adjustable sting in the test section which allows five-hole probe surveys to be visualized by a side-view transmission Schlieren system during the tests. The general structure of the vortex system can thus be monitored during the measurements to determine whether the probe is significantly influencing the flow field (*i.e.* initiating vortex breakdown).

Tests are made with a freestream Mach number of 0.6 ($Re = 3.5 * 10^6$) at 10° angle of attack. This angle of attack is selected because it demonstrates no vortex breakdown above or behind the wing. Both five hole probe measurements and steady Euler code numerical simulations are inappropriate tools for studying the flow field once vortex breakdown has occured. Measurements are conducted in two spanwise planes above the wing surface perpendicular to the wing upper surface on the port side of the wing and in two planes behind the wing perpendicular to the freestream flow direction (see Figure 3). The orientation of the planes is selected in order to most closely capture the vortical nature of the flow. The relevant grid spacing for each of these planes is

shown in Table 1.

The five hole probe used for this study is a spherical head probe of $1.6mm$ external diameter with pressure taps of $0.2mm$ diameter. A previously developed local look- up algorithm yields, for flow angles up to 60°, an accuracy of $\pm 3\%$ and $\pm 0.4°$ in local Mach number and flow angle, respectively [6].

3 Numerical Analysis

The computational code is based on a finite volume discretization of the three-dimensional conservation law form of the Euler equations [7]. The spatial discretization of the Euler equations makes use of the flux difference splitting approach following Roe [8], whereby physical propagation properties are taken into account to some extent. The calculation of the fluxes at the cell faces is done according to van Leer's Monotone Upstream-centered Schemes for Conservation Laws (MUSCL) approach with flux limiting, which provides second order accuracy. The system of discretized equations is solved by a nonlinear multigrid (FAS) technique, with a Collective Gauss-Seidel relaxation procedure acting as smoothing method.

The flow simulations were performed on a computational mesh representing the delta wing in the TST-27 wind tunnel, in order to get a close resemblance with the experimental investigations. The grid has a H-O topology, and covers only a half-space due to the symmetry of the flow problem. The number of grid cells is 196608, which means 96 cells in chordwise direction, 64 cells in spanwise direction and 32 cells between model surface and wind tunnel walls.

4 Results

4.1 Vortex Core Location

The location of the vortex core in each measurement plane is defined as the location of minimum total pressure. The location of minimum pressure for each of the measurement planes is presented in Table 1 for both the experimental and numerical studies. The coordinate systems used in presenting the results above and behind the wing are shown in Figures 4 and 5, respectively. The coordinate system m used to present the results above the wing is fixed on the model. The primary vortex core location is presented in terms of $(\frac{y_m}{y_{le}})$ and $(\frac{z_m}{y_{le}})$, or the conical coordinates, where y_{le} represents the local half-span. The wake coordinate system t is not rotated with respect to the tunnel, but its origin is translated to the root chord line intersection with the trailing edge of the model. The primary vortex core location is presented in terms of of $(\frac{2y_t}{b})$ and $(\frac{2z_t}{b})$, or as a percentage of the trailing edge half-span. For both the experimental and numerical studies the vortex core is noted to maintain a relatively constant location above and behind the wing in the conical and Cartesian coordinate systems, respectively. The relatively lower and more outboard location of the vortex core for the numerical results both above and behind the wing can be attributed to the absence of the secondary and tertiary vortices in the Euler solution. These vortices are inherently viscous phenomena which are not captured by the inviscid Euler equations. Contour plots of the total pressure distribution for the experimental measurements in planes relative to the rootchord c_r, $x_m/c_r = 0.7$ and $x_t/c_r = 0.5$ are shown in Figures 10 and 11, respectively. Figures 12 and 13 illustrate the total pressure distribution in these same two planes for the numerical simulation study.

4.2 Axial Velocity Distribution

Contour plots of the axial velocity component and vector field representations of the cross- flow velocity components ($v_\Sigma = v - u(y_m/x_m)$ and $w_\Sigma = w - u(z_m/x_m)$) above the wing at $x_m/c_r = 0.7$ may be found in Figures 6 and 8 for the experimental and numerical studies, respectively. The orientation of the axial velocity component u_{ax} is illustrated in Figure 4 as the component along a conical ray extending from the apex of the delta wing. The flow near the vortex center is invariably in the downstream direction and *jet-like*, that is to say that the axial velocity distribution has a maximum at the vortex center exceeding the free-stream value. The location of the primary vortex core, indicated by the labelled arrow extending into the field, coincides approximately with the local maximum of the axial velocity for both the experimental and numerical results. The agreement between experimental and computational results is quite good as far as the cross-flow velocity direction is concerned. The most significant discrepancy is found near the surface of the wing, outboard of the primary vortex core. In this region an influence of the secondary vortex is visible in the experimental results, while this phenomenon is not modelled by the Euler computations. Another discrepancy is noted near the wing surface beneath the primary vortex core where a region of low axial velocity exists in the measurements, while the computations predict high velocities. In this region the probe measurements are unreliable, however, due to the influence of high gradients and the proximity of the solid wall. The probe is not calibrated for these conditions.

In contrast, for the measurement planes located behind the wing at $x_t/c_r = 0.5$ illustrated in Figures 7 and 9, the primary vortex core location (again indicated by a labelled arrow extending into the field) coincides with a local minimum of the axial velocity component u_t in both the experimental and numerical studies. The axial velocity component in this surface, or the component most closely aligned along the core of the vortex, is the component u_t indicated in Figure 5. This type of velocity distribution is referred to as *wake-like*, implying that the axial velocity near the vortex core has a minimum value lower than that of the free-stream. The notable difference between the axial velocity distributions above and behind the wing is a very interesting phenomenon as it is indication of a transition from a *jet-like* to a *wake-like* velocity profile of the axial velocity with increasing x station. Because a characteristic feature of vortex breakdown is a stagnation of the axial velocity at the vortex core this transition from a *jet-like* to *wake-like* profile can be considered an indication of a process leading to vortex breakdown behind the delta wing. In the case of a natural dissipation of the delta wing vortex system this dramatic transition to a *wake-like* from a *jet-like* profile would not be expected. In such a case the vortex would be expected to dissipate evenly across the vortex downstream of the wing, where the vortex is no longer fed with vorticity, until the entire cross-section readjusts itself to the freestream flow conditions. It may be noted that numerical computations at increasing angle of attack (not presented here) have shown that above the wing the axial velocity in the vortex core continually increases, while the axial velocity downstream of the wing decreases. At a certain angle of attack a region of negative (upstream) axial flow occurs, which may be an indication of the onset of vortex breakdown.

4.3 Vorticity Distribution

The three vorticity components ω_i , ω_j and ω_k are calculated in each of the four measurement planes via finite difference calculations. These components are conventionally defined as:

$$\vec{\omega} = (\omega_i, \omega_j, \omega_k)^T = \left(\left(\frac{\partial w}{\partial y} - \frac{\partial v}{\partial z} \right), \left(\frac{\partial u}{\partial z} - \frac{\partial w}{\partial x} \right), \left(\frac{\partial v}{\partial x} - \frac{\partial u}{\partial y} \right) \right)^T \qquad (1)$$

The determination of the vorticity vector for the numerical simulation results requires no further assumptions above or behind the wing. The experimental measurements, on the other hand, are made at a single x station locally and require, therefore, the use of certain assumptions in order to calculate the ω_j and ω_k vorticity components. For the measurement planes above the wing a conical flow assumption is made (*i.e.* $u = u(\frac{y}{x}, \frac{z}{x})$) while for the measurement planes behind the wing a quasi-two-dimensional flow has been assumed(*i.e.* $\frac{\partial}{\partial x} \approx 0$). The accuracy of the conical assumption above the wing is examined by making additional measurements in a plane at $x_m/c_r = 0.72$ and calculating the ω_j and ω_k vorticity components for $x_m/c_r = 0.71$. The distribution of these components is then compared with the vorticity components calculated at $x_m/c_r = 0.70$ and $x_m/c_r = 0.72$ obtained via the conical flow assumption. The outcome resulting from these three different vorticity field calculations are found to agree well with each other qualitatively. The quasi-two-dimensional flow-field assumption is considered reasonable behind the wing both due to the tendency of the vortex to realign itself with the freestream direction beyond the trailing edge and also due to the lack of streamwise pressure gradients existing in the wake of the wing. The nearly constant primary vortex core location above the wing in conical coordinates and in the $y_t - z_t$ plane behind the wing indicated in Section 4.1, further supports the assumption of a conical flow above the wing and a quasi-two- dimensional flow behind the wing.

The in-plane vorticity vectors in the plane $x_m/c_r = 0.7$ are plotted as a vector field superimposed on a contour plot of the total pressure in Figures 10 and 12 for the experimental and numerical studies, respectively. The vectors represented are the components ω_η and ω_ζ illustrated in Figure 4. These components represent the two Cartesian components of the vorticity vector $\vec{\omega_\Sigma}$, which is a *non-orthogonal* projection along a line of sight parallel with the conical ray onto the cross-flow plane Σ. The in-plane vorticity vectors are noted to be oriented in the same direction as the in-plane velocity, illustrated as a vector field Figures 6 and 8 for the experimental and numerical results, respectively. The in-plane vorticity vector field is indication of a positive azimuthal velocity component surrounding the core because the in-plane vorticity vectors turn around the vortex core in the same direction as the sense of the circulation (see Figure 2).

In contrast, the in-plane vorticity vectors in the plane $x_t/c_r = 0.5$ illustrated in Figures 11 and 13 for the experimental and numerical studies, respectively, indicates a negative azimuthal vorticity. The vorticity components represented by these vectors are illustrated in Figure 5 as the Cartesian components ω_{yt} and ω_{zt} of the total vorticity vector $\vec{\omega}$. The corresponding in-plane velocity components, illustrated in Figures 7 and 9, remain oriented in the same direction as the in-plane velocity vectors above the wing seen in Figures 6 and 8. Thus, the in-plane vorticity vectors, turning about the vortex core in a direction opposite to the sense of the circulation, are indication of a negative azimuthal vorticity.

The in-plane vorticity and the axial velocity are directly related. The reversal of the azimuthal vorticity component can be anticipated, therefore, from the transition of the axial velocity distribution near the core from a *jet-like* flow above the wing to a *wake-like* flow behind the wing (see Section 4.2). Considering Equation (1) it is clear that for a vortex with its core aligned with the x-axis of the coordinate system, the azimuthal vorticity (components ω_j and ω_k) is dominated by the contribution of the $(\frac{\partial u}{\partial z})$ and $(\frac{\partial u}{\partial y})$ terms, because the gradients of the velocity along the core are very small in comparison with the gradients in a direction normal to the core (*i.e.* $\frac{\partial}{\partial x} \ll \frac{\partial}{\partial y}$ and $\frac{\partial}{\partial x} \ll \frac{\partial}{\partial z}$).

5 Conclusions

The axial velocity distribution near the core of the primary vortex is found to alter from a *jet-like* to *wake-like* distribution with increasing x station above and behind the delta wing studied. This transition in axial velocity profile is accompanied by a reversal of the orientation of the azimuthal vorticity vectors from a direction coincident with the cross-flow velocity direction above the wing to a direction opposite to the cross-flow velocity downstream of the wing. These results are found to be consistent in both the experimental and numerical studies. These results support the initial hypothesis presented by Brown and Lopez [3] regarding the function of the reversal of the azimuthal vorticity component from a positive to a negative value in the process of vortex breakdown.

Acknowledgements

The authors would like to thank M. Oledal for his work in the analysis of the 5-hole probe measurements. The technical support of E.W. de Keizer is also acknowledged.

References

[1] J.M. Muylaert, "Effect of Compressibility on Vortex Bursting on Slender Delta Wings," von Karman Institute For Fluid Dynamics, Project Report 1980-21, 1980.

[2] J.M. Délery, "Aspects of Vortex Breakdown," *Progress in Aerospace Sciences*, **30**:1–59, 1994.

[3] G.L. Brown and J.M. Lopez, "Axisymmetric Vortex Breakdown, Part 2. Physical Mechannisms," *Journal of Fluid Mechanics*, **221**:553–576, 1990.

[4] R.C. Nelson and K.D. Visser, "Breaking Down the Delta Wing Vortex, The Role of Vorticity in the Breakdown Process," Vortex Flow Aerodynamics, AGARD CP-494, 1991.

[5] D.L. Darmofal, "The Role of Vorticity Dynamics in Vortex Breakdown," AIAA Paper 93-3036, 1993.

[6] E.M. Houtman and W.J. Bannink, "The Calibration and Measuring Procedure of a Five-hole Hemispherical Head Probe in Compressible Flow," Report LR-585, Dept. of Aerospace Engineering, Delft University of Technology, 1989.

[7] E.M. Houtman and W.J. Bannink, "Experimental and Numerical Investigation of the Vortex Flow over a Delta Wing at Transonic Speed," Vortex Flow Aerodynamics, AGARD CP-494, Paper 5, 1991.

[8] P.L. Roe, "Approximate Riemann Solvers, Parameter Vectors and Difference Schemes," *Journal of Comp. Physics*, **43**:357–372, 1981.

Above wing:

$(\frac{x_m}{c_r})$	Δy_m (mm)	Δz_m (mm)	$(\frac{y_{mc}}{y_{le}})$ exp.	$(\frac{z_{mc}}{y_{le}})$ exp.	$(\frac{y_{mc}}{y_{le}})$ num.	$(\frac{z_{mc}}{y_{le}})$ num.
0.5	0.5	0.5	0.71	0.15	0.76	0.11
0.7	0.7	0.7	0.70	0.15	0.77	0.12

Behind wing:

$(\frac{x_t}{c_r})$	Δy_t (mm)	Δz_t (mm)	$(\frac{2y_{tc}}{b})$ exp.	$(\frac{2z_{tc}}{b})$ exp.	$(\frac{2y_{tc}}{b})$ num.	$(\frac{2z_{tc}}{b})$ num.
1.4	2	2	0.82	0.20	0.86	0.21
1.5	2	2	0.83	0.22	0.86	0.22

Table 1: Mesurement planes and location of primary vortex core at various x stations

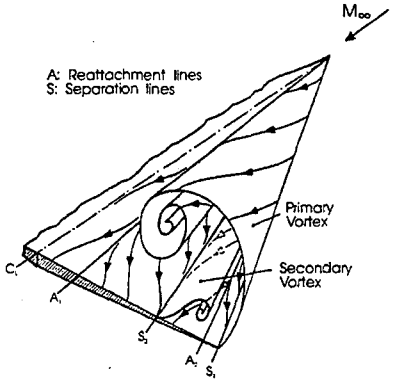

Figure 1: Characteristic Vortical Flow above lee surface of a sharp leading edge Delta Wing at angle of attack.

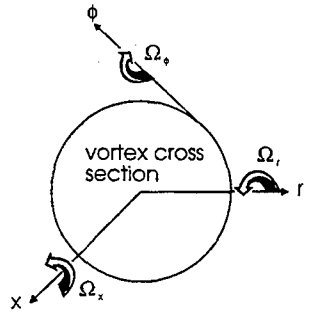

Figure 2: Radial coordinate system and vorticity components

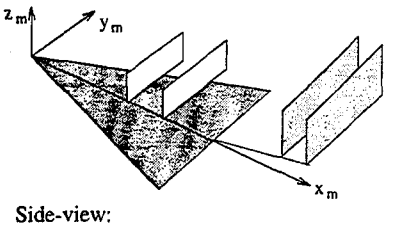

Side-view:

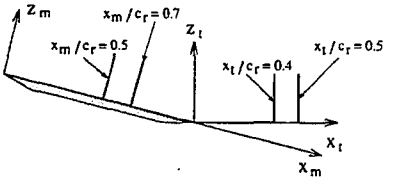

Figure 3: Illustration of body fixed Cartesian coordinate system and 5-hole probe measurement planes

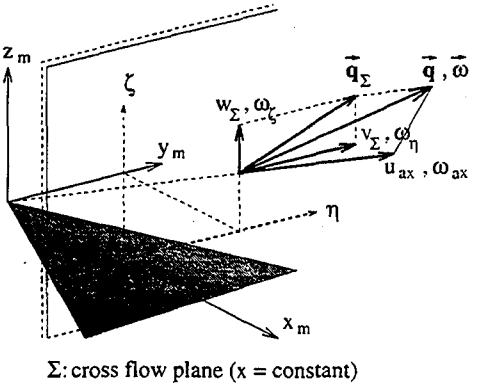

Σ: cross flow plane (x = constant)

Figure 4: Definition of velocity and vorticity components in conical coordinate system above Delta wing

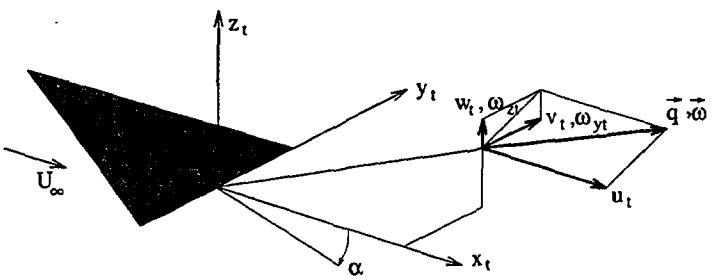

Figure 5: Definition of velocity and vorticity components in Cartesian coordinate system downstream of Delta wing

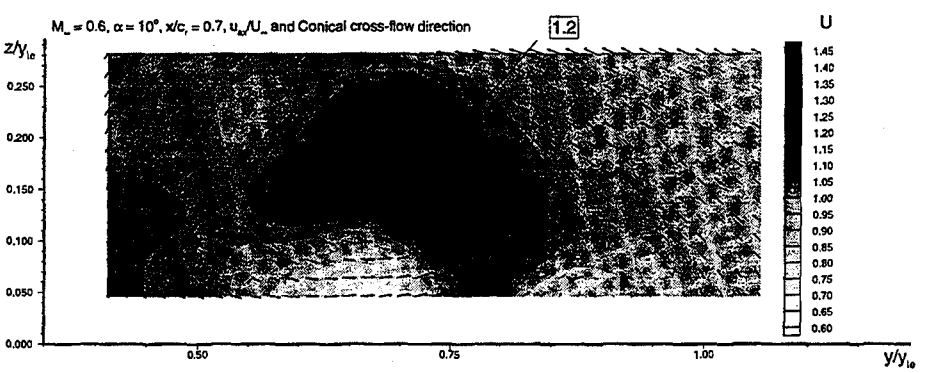

Figure 6: Experimental distribution of velocity u_{ax}/U_∞ and Cross-flow direction (v_Σ, w_Σ), $M_\infty = 0.6, \alpha = 10°, x_m/c_r = 0.7$

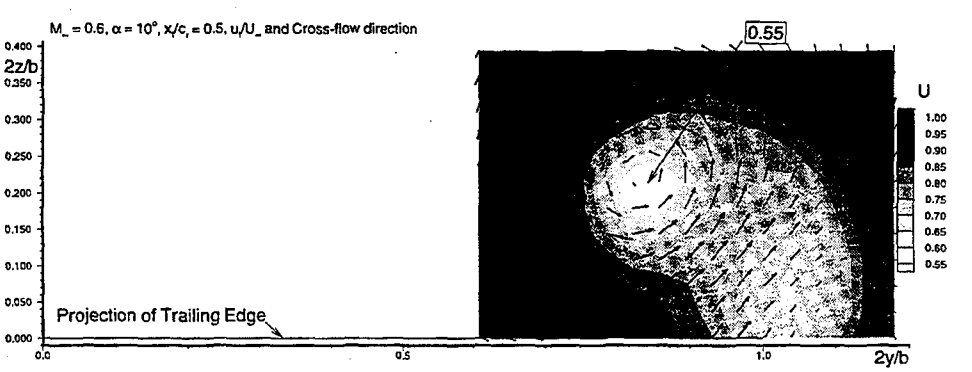

Figure 7: Experimental distribution of velocity u_t/U_∞ and Cross-flow direction (v_t, w_t), $M_\infty = 0.6, \alpha = 10°, x_t/c_r = 0.5$

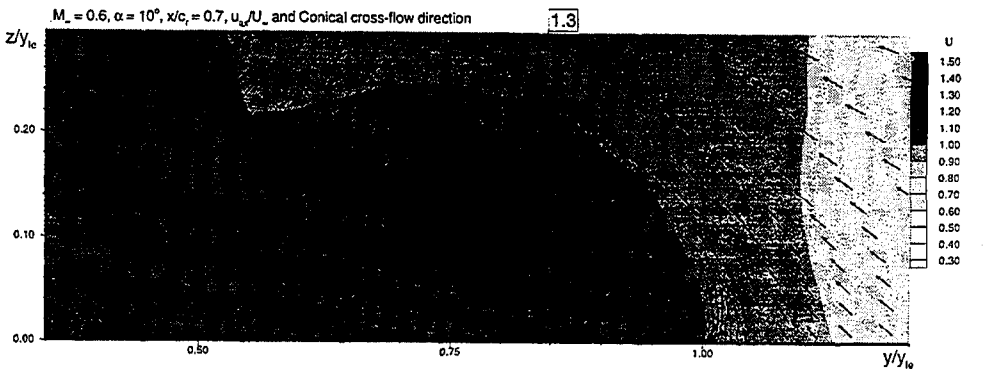

Figure 8: Numerical distribution of velocity u_{ax}/U_∞ and Cross-flow direction (v_Σ, w_Σ), $M_\infty = 0.6, \alpha = 10°, x_m/c_r = 0.7$

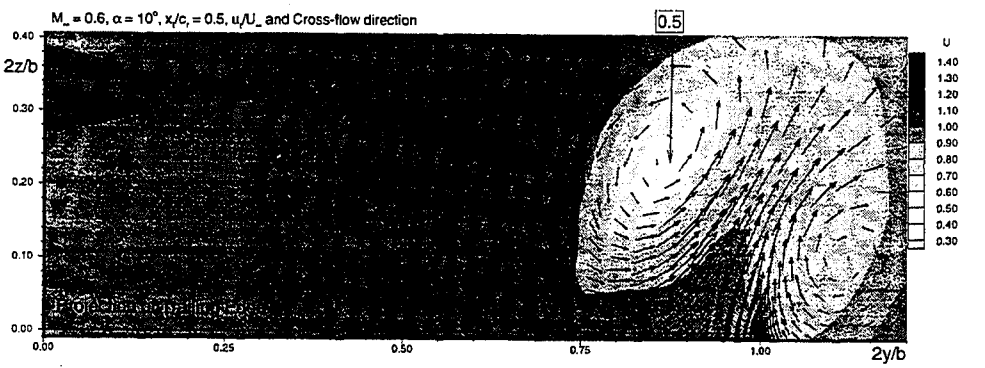

Figure 9: Numerical distribution of velocity u_t/U_∞ and Cross-flow direction (v_t, w_t), $M_\infty = 0.6$, $\alpha = 10°, x_t/c_r = 0.5$

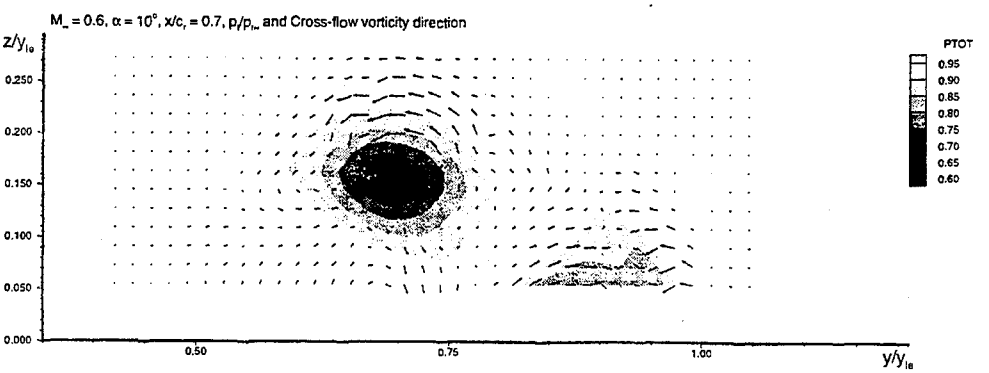

Figure 10: Experimental distribution of Total Pressure (p_t/p_{t_∞}) and Cross-flow vorticity direction $(\omega_\eta, \omega_\zeta)$, $M_\infty = 0.6, \alpha = 10°, x_m/c_r = 0.7$

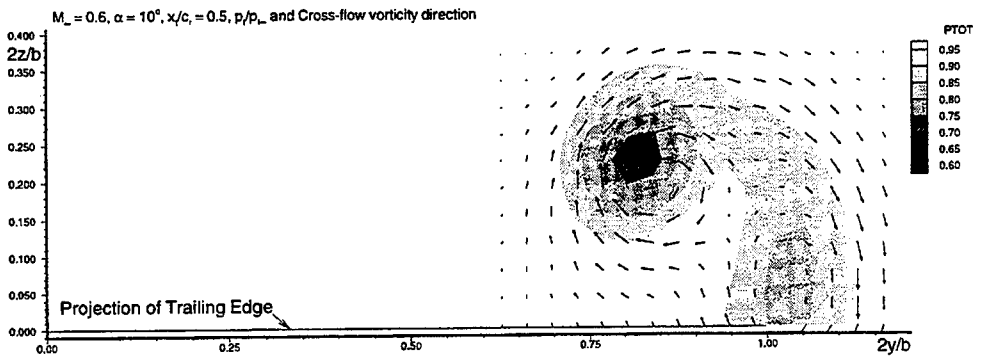

Figure 11: Experimental distribution of Total Pressure (p_t/p_{t_∞}) and Cross-flow vorticity direction $(\omega_{yt}, \omega_{zt})$, $M_\infty = 0.6, \alpha = 10°, x_t/c_r = 0.5$

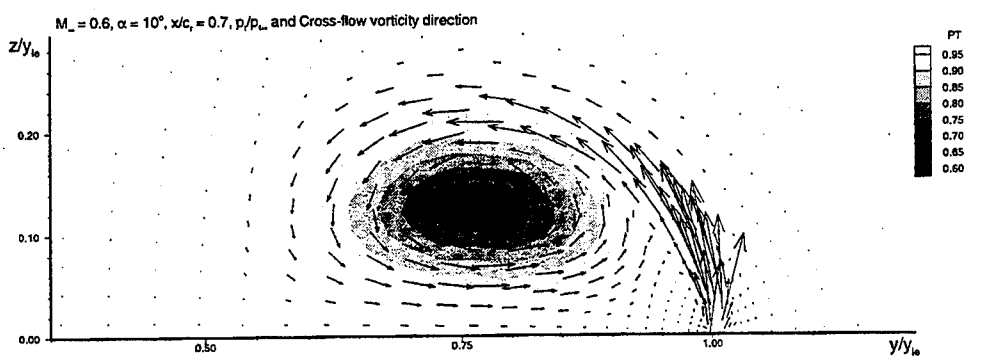

Figure 12: Numerical distribution of Total Pressure (p_t/p_{t_∞}) and Cross-flow vorticity direction $(\omega_\eta, \omega_\zeta)$, $M_\infty = 0.6, \alpha = 10°, x_m/c_r = 0.7$

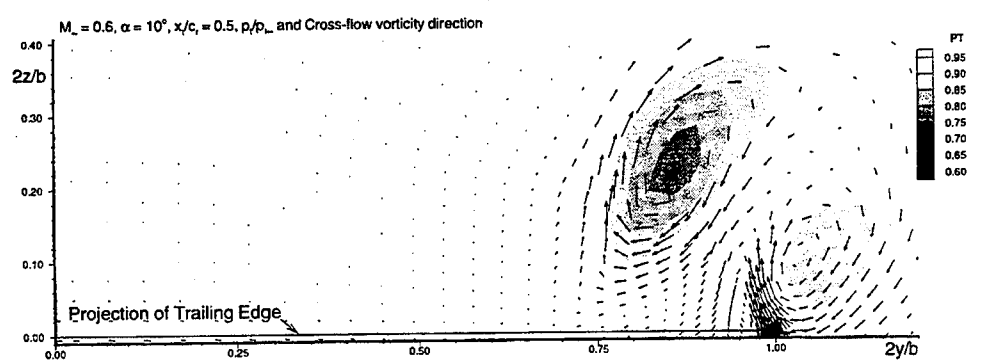

Figure 13: Numercial distribution of Total Pressure (p_t/p_{t_∞}) and Cross-flow vorticity direction $(\omega_{yt}, \omega_{zt})$, $M_\infty = 0.6, \alpha = 10°, x_t/c_r = 0.5$

APPLICATION OF LDV TECHNIQUE IN THE STUDY OF THE MECHANISM OF THE LEADING-EDGE VORTEX CONTROLLED BY SPANWISE BLOWING *

Yanhua Qin†, Tingding Hsing‡ and Fenggan Zhuang§

Beijing University of Aeronautics and Astronautics, Beijing 100083,CHINA

Abstract

To investigate interaction between spanwise jet and leading-edge vortex a flow visualization and a flow field measurement are presented in the paper. All experiments were performed in the 0.36 m by 0.6m low speed wind tunnel at Nanjing University of Aeronautics and Astronautics using a 60° delta wing with sharp leading edge at an angle of attack of 24°. The smoke technique was used to visualize the vortex core, and two-component Laser Doppler Velocimeter was used to examine the influence of the jet on the leading-edge vortex structure.The three velocity components were measured in two successive test runs. Velocity survey in the leading-edge vortex region showed that the spanwise jet alone produces a pair of additional leading-edge vortices over the delta wing with high swept and sharp leading edge of the delta wing. Together with incoming flow the entrainment of jet could be considered as introducing a velocity to the freestream, consequently, we have an increase in axial velocity but also the vorticity of the leading-edge vortex. It is concluded that the effect of SWB on the leading-edge vortex is primarily caused by the jet entrainment, rather than by the mixing. On the base of this mechanism the optimum jet position should be kept at a distance from the wing apex and leading-edge.

Nomenclature

Cr	wing root chord
C_μ	jet momentum coefficient
G	jet weight flow rate
h	distance of LDV sample volume above wing surface
Re	Reynolds number
U_∞	freestream velocity
U	velocity component parallel to freestream velocity in the vortex core(also referred as axial velocity)
V	velocity component normal to freestream velocity in the vortex core
W	spanwise velocity component in the vortex core
X	freestream direction
Y	derection normal to the freestream
Z	spanwise direction
α	angle of attack

Introduction

"Moving in the air without causing any disturbed wind" is an ideal objective but not realistic. In the early development of aeronautics the guide line for the aerodynamic design is to keep the flow attached as long as possible.Discovery of vortex lift due to leading edge separation then changed the design philosophy. Now we can think of mixed type flow in general and consider the utilization of the separated vortex and some vortex control technique to meet our specific purpose. Excellent review papers were already in existence e.g. the one given by Lamar and the other by Rao and Campbell[1-2].

At moderate to high angles of attack, the flow over wings with highly swept, sharp leading deges is dominated by large vortex structures,

*The research is supported by China National Natural Science Foundation No.9188010.

†Associate Professor

‡Professor

§Senior Professor

formed from the flow separation at the leading edge. The high vortex lift increments and vortex breakdown phenomenon depending on the particular angles of attack and geometrical configuration have been studied for many years[3~9].

The spanwise blowing (SWB) concept has been studied for almost three decades, and numerous results were obtained,which showed that it is an effective aerodynamics measure for enhancing the strength of the wing leading-edge vortex and delaying the vorex breakdown to higher angles of attack.Subsequently, the extra vortex lift and high lift drag ratio could be obtained. However the mechanism of interaction between SWB and leading-edge vortex requires further clarification.

The idea of some researchers focused on blowing as nearer the center of the core as possible to increase the axial velocity[10], but other investigations have shown that it was not an optimal choice. Campbell[11] discovered that the greatest benefit obtained from spanwise jet occurs in the region near the origin of the vortex flow rather than in the vortex core. T.T.Ng, et.al[12] revealed that the optimal jet nozzle position is not at the vortex core and suggested its location should not be too far downstream, since then there was no sufficient time for mixing. They suggested that a small distance of nozzle downstream from the apex is needed, where the mixing and entrainment are more effective. However, due to the lack of data of the vorticity flow field the machanism is still not well explained. Qin and Shen[13] found that the optimal position of nozzle should be at the conjunction with fuselage,and at a distance from the wing apex,such as 30 % – 50 % Cr,to keep the jet not to across the core of vortex.

In order to find the optimal nozzle position, it is neccessary to explore the mechanism of effect of SWB on the vortex structure. An experimental investigation has been conducted for a 60° delta wing with sharp leading-edge using smoke flow visualization and LDV technique.

Experimantal Technique

All the experimental results presented in the paper were obtained in 0.36- by 0.6m low speed wind tunnel of NUAA (Nanjing University of Aeronautics and Astronautics) on a delta wing with sweptback of 60° and sharp leading edge at angle of attack of 24° and Reynolds number of 6.6×10^4. The nozzle was placed at 0.30 Cr and aligned perellel to the leading edge, and the jet momentum coefficient C_μ was kept constant during the tests.

Three types of flow field round the wing, including incoming flow alone, spanwise blowing alone, and incoming flow with spanwise blowing were visualized and measured respectively.

The vortex core was visualized with a dense white smoke and recorded by a still photography.

A two component LDV system consisting of a argon ion laser with the power of 4 watt and TSI optics system was used for the flow measurements.The two component LDV sample volume is moved throughout the flow field by a manual-controlled, three-axis traversing system.A frequency shifting system was used, hence the velocity in opposite directions can be distinguished. A nonuniform survey grid (Fig.1)was used for measured planes. The velocities in two cross planes perpendicular to free stream were measured near the jet nozzle exit and vortex breakdown region respectively to get the cross flow velocity and vorticity distributions. Besides, the velocities in the longitudinal plane along the vortex core approximately were also measured to obtain axial velocity distribution along the vortex axis.

To obtain three components of velocity two test runs are needed, of which one was measured with the model installed normally in the wind tunnel, the other with the model turned 90 degree around the wind axis (see Fig.2).

Results and Discussion

Structure and Breakdown of Leading-Edge Vortex

In view of the previous researches the leading-edge vortex over a wing would be stable if the flow separate from leading-edge to roll up forming a free vorticity and spanwise component of freestream velocity reaches a certain value. Over the high swept and thin wing with sharp leading-edge the flow meets these two requirements and a pair of stable vortex over the wing exists at certain angles of attack.

It is found that the natural characteristics, primarily the axial velocity in the vortex core plays a critical role on stability of leading-edge vortex. When the axial velocity in the core is increased at the same circumferential velocity value the vortex breakdown point will be delayed, i.e. the vortex stability is enhanced.Fig.3(a) and (b) present axial velocity distribution at two transverse sections respectively. It is seen that the distribution of axial velocity at section 1 shows a distinct peak near leading-edge and close to the wing

surface, while at section 2 no distinctive peak of velocity distribution is observed, showing vortex burst occured. It is also noted that the region of velocity collapse is farther from leading-edge than the one at section 1, which indicates the leading edge vortex core track moves inboard and upward over the wing when the vortex grows downstream. To understand streamwise variation of vortex core structure more clearly, the axial velocity distribution at some special positions normalized was ploted as a normalized average of axial velocity based on the freestream velocity versus a distance from the wing surface (See Fig.4). It can be seen at the apex of wing the normalized velocity equals one approximately, showing the leading-edge vortex has not formed yet. Along the vortex axis the axial velocity increases rapidly downstream up to 1.6 times of freestream velocity at 10%Cr, and then increases slowly up to its maximum value, $2.3U_\infty$ at 31%Cr. And after that the axial velocity begins to decrease, but its profile still is of jet-like (see the results at x/Cr=0.4). As seen above, in the fully developed region of leading-edge vortex, the pattern of axial velocity distribution is of jet- like which is an inherence property of stable leading-edge vortex. Further downstream the axial velocity decreases rapidly and its distribution changes from jet-like to wake-like at 0.44 Cr, and finally decreases down to zero marked the vortex breakdown at 0.466 Cr , where the same phenomenon could also be seen in flow visualization. Further downstream the avarage axial velocity tends to recover to positive level.It is believed that the turbulent flow exists in the breakdown region instead of the concerntrated vortex flow. From some amplitude probability density functions it can be seen that the transient reverse flow in the core always exists and most of flow particles with reverse velocity occur near the center of vortex core rather than at the edge of vortex core.

As the measurement position comes closer to the breakdown region,the larger the instantaneous reverse velocity is and more frequently it appears. It suggests that the flow particles in the vortex core center are spiralling outward , consequently, the flow particles of downstream move towards upstream under the adverse pressure gradient, forming the transient reverse flow. As a result, the average axial velocity of vortex is decreased gradually till zero, and vortex breakdown accompanies with it finally.

In the case mentioned above, the inner core in the stable vortex rotates like a solid body and the radial distribution of circumferential velocity is almost linear at transverse section (see Fig.5), but in the outer core the radial gradient of velocity is decreased, and the velocity distribution is just like a potential flow type.

The normal and spanwise velocity component data at two sections have been used to calculate axial vorticity distribution, which are plotted in contour form in Fig.6 at flow condition without jet. In Fig.6(a) , the vorticity is highest within the vortex core region at section 1, meaning there is a fully developed vortex being consistent with the results of axial velocity distribution there. The negative vorticity near the wing leading-edge shows the existence of the secondary vortex. When Bursting of the vortex occurs abruptly the higher vorticity value in the core disapears, and the vorticity spreads throughout the entire vortex region (see Fig.6(b)).

Spanwise Jet over the Wing

It was discoveried from the smoke flow visualization with the spanwise jet alone on the wing that a small vortex with its origin at the apex of wing is formed near the leading edge, which can be considered as the result of the entrainment effects of the jet. The characteristics of the jet induced-vortex are similar to the natural leading-edge vortex over wing with high sweptback,sharp leading-edge at some angles of attack with incoming flow. It can also be seen that the jet induced-vortex is kept some distance from the spanwise jet initially without mixing between them, and then encounters with the jet downstream and vanishes finally.(see photoes in Fig.7)

It is well known that the flow field induced by a free circular jet is axisymmetrical and a jet over a infinite wall, referred as the wall jet, induces a flow field with higher axial velocity near the wall[14], while the spanwise jet over a wing induces a flow field quite different from that induced by either the free jet or the wall jet due to the leading-edge of wing, in which it not only induces a velocity along the jet axis over the wing, but also a flow around the leading-edge and if the leading-edge is sharp the induced flow would separate from the leading-edge. Consequently, the spanwise blowing over a wing provides two conditions for forming a stable concentrated vortex. The present investigation verify the concept put forward by authors, and the related test results are discussed below.

It is concerned where is the optimal chordwise position of jet such that it induces a stronger

leading-edge vortex with the same jet momentum. Fig. 8 illustrates the variation of flow pattern over the wing with jet at different chordwise position. It is obvious that the jet which is near the apex of wing, induces a vortex within a small region. This is because the vortex encounters the strong jet and is destroyed immediately by the jet , while the jet at downstream induces a weaker vortex due to the weaker inducing effects on the flow around the leading-edge near apex of wing. Accordingly, an optimal chordwise position of jet could be expected.

Fig. 9(a) and (b) indicate the axial velocity distribution with jet alone at two transverse sections respectively. At section 1, the axial velocity distribution could be divided into two regions with distinct boundary, the high speed region near the root chord having the character of jet, and the rest part of low speed region which is induced by jet. No obvious high axial velocity peak could be found near the leading-edge. But it is seen in Fig.10 that the existence of vortex could be verified by the velocity vector, which is consistent with the photo in Fig.7. At section 2 the boundary of jet becomes vague which means the jet has already expanded and covered the wing leading-edge, and no trace of vortex could be detected.

So, it seems certain that if the jet is located too close to the leading-edge, the jet with strong velocity during its expansion process would result a detrimental condition to separated flow to roll up around the leading-edge.

The Effects of SWB on the Leading -Edge Vortex and Its Mechanism

The axial velocity distribution of vortex at both of two sections obtained in the case of incoming flow with spanwise jet are shown in Fig.11(a) and (b), respectively. It is obvious that at section 1 the velocity peak, in comparison with the results without spanwise blowing, has higher value and is of great fullness, in which the flow can overcome larger adverse pressure gradient and therefore the vortex breakdown would take place at farther downstream position. It can also be seen that the velocity peak position moves closer to the wing surface and leading-edge. At section 2 the sink-like velocity distribution with incomeing flow alone shown in Fig.3(b) vanishes due to spanwise jet, instead a high velocity region spreads over a large area appears. Obviously, in the case of incoming flow with spanwise blowing the axial velocity is not only the sum of velocity induced by incoming flow and spanwise jet, but also contains the favourable interference between them , including the mixing effects to some extent.

Fig.12 indicates the axial velocity distribution at different positions along the vortex core with spanwise jet. It is seen that at all the positions, except the apex, the velocity distributions are all of jet-like and the magnitude is increased obviously, furthermore the maximum velocity is up to 2.70 U_∞, much larger then one without blowing, which means the leading-edge vortex is more stable,the breakdown point is moved farther downstream.

It can be seen in Fig.13(a) and (b) that the vorticity is increased obviously by the spanwise jet compared with the case of without blowing at both sections, especially at section 1.And it also can be seen that the jet changes the initial flow field around the wing and forms a pair of much stronger leading-edge vortex.

It is important to note here that unlike in section 1 the increment of vorticity is not very significant so as to well match with the increment of axial velocity in section 2. So, the criteria for the determination of the optimal jet position is to provide maximum possible axial velocity in the vortex core and at the same time the maximum possible concentrated vorticity over the wing surface.

Conclusion

The flow visualization and LDV technique were used to reveal the mechanism of using SWB to increase the strength of leading-edge vortex and delay the vortex breakdown point to farther downstream at given angle of attack. The spanwise jet could act on the global field around the wing by its entrainment effect rather than the direct mixing effect, changing the initial conditions of the formation of leading edge vortex, hence larger axial component of velocity and vorticity may be obtained. Accordingly, the nozzle should be located at a distance away from the apex or leading-edge of the wing to avoid early strong concentrated jet encounter with the leading-edge vortex ,thus hindering the vortex sheet to roll up.

Based on the present investigations we might draw the following conclusion: the optimal blowing position appears to correspond to where the entrainment of the jet is most efficient to the flowfield around the wing.

References

[1] Lamar,J.E., "Non-linear lift control at high

speed and high angles of attack using vortex flow technology ",AGARD R-740,1986

[2] Rao, D. M. & Campbell, J. F.,"Vortical Flow Management Techniques ", Progress in Aerospace Science (ISSN 0376-0421)Vol.24, No.3, 1987

[3] Parker, A. G.,"Aerodynamics Characteristics of Slender Wings with Sharp Leading Edges—A Review ",J. Aircraft Vol. 13, No.3, March 1976

[4] Joseph, R. C.,"High-Angle-of-attack Aerodynamics : Lessons Learned ",AIAA Paper No.86-1774-cp

[5] Rao, D. M.,"Leading-Edge 'Vortex Flaps ' for Enhanced Subsonic of Aerodynamics of Slender Wings ", ICAS-80-13.5

[6] Vakili, A. D.,"Review of Vortical Flow Utilization ", AIAA Paper 90-1429

[7] Faler, J. H.,& Leibovich, S.,"An Experimental Map of the Internal Structure of a Vortex Breakdown " J.F.M. Vol.86, Part 2, 1978

[8] Cornish ,J. J.,"High Lift Applications of Spanwise Blowing " ICAS Paper No. 70-09

[9] Zhuang, Fenggan,"Vortex Control Technology ", ICAS-92-0.1, 1992

[10] Su, Wenhan, et. al., "An Experimental Investigation of Leading-Edge Spanwise Blowing ", ICAS 82-6.6.2, 1982

[11] Campbll, J. F.," Augmentation of Vortex lift by Spanwise Blowing ", AIAA 75-993, 1975

[12] Ng, T. T., "On Leading Edge Vortex and Its Control ", AIAA Paper 89-3346-cp, 1989

[13] Qin, Yanhua & Shen, Limin, " An Investigation of Improving High Angle of Attack Performance and Flap Effectiveness of a Configuration with Delta Wing by Spanwise Blowing ", AIAA 86-1777-cp, 1986

[14] Dixon, C. J., Theisen, J. G. & Scruggs, R. M.," Theoretical and Experimental Investigaton of Vortex-Lift Control by Spanwise Blowing ", AD-771290, 1977

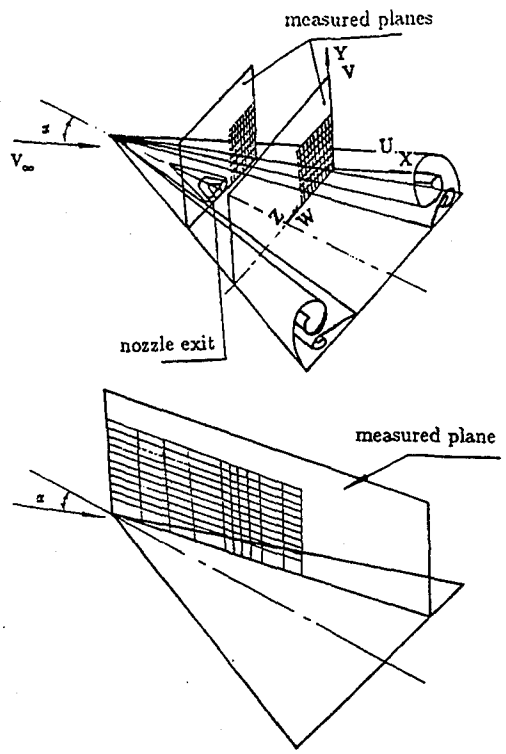

Fig.1 Schematic of LDV measured planes

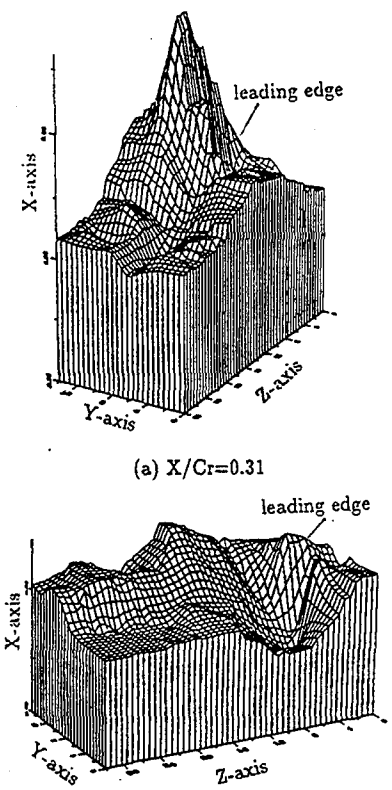

Fig.3 Axial velocity distribution at transverse sections

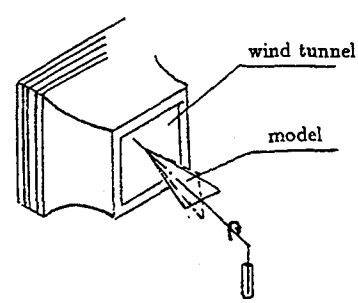

Fig.2 Model installation in wind tunnel

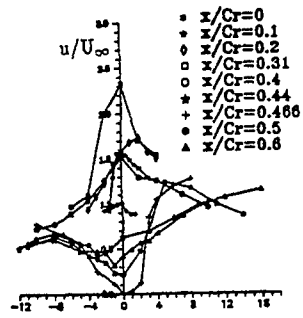

Fig.4 velocity distribution along vortex core axis

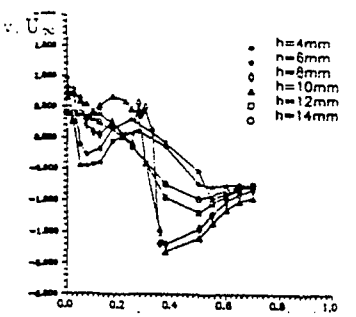

Fig.5 Normal velocity distribution at transverse sections

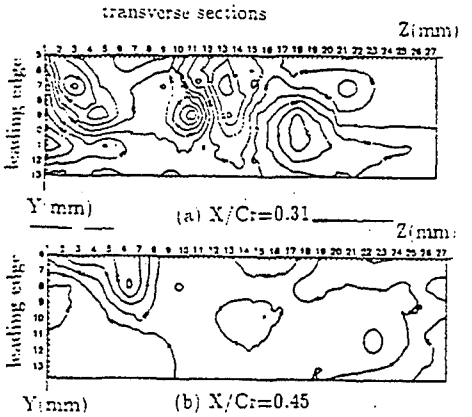

Fig.6 Vorticity contours at transverse sections

(a)

Fig.7 Jet alone induced leading-edge vortex

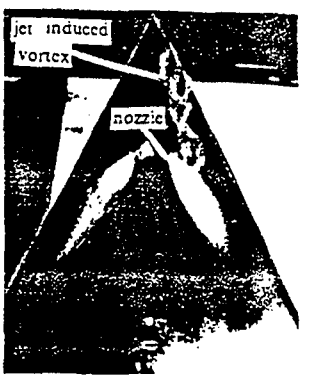

(b)

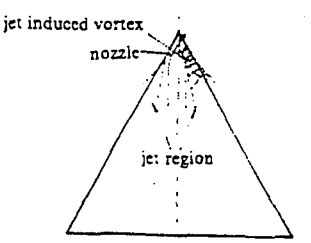

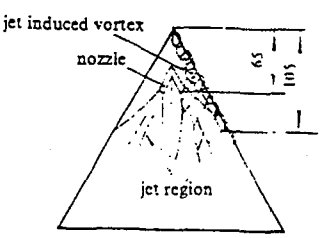

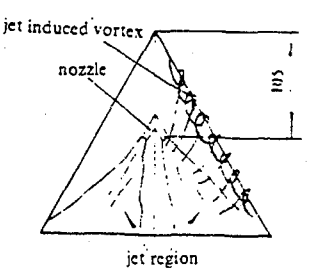

Fig.8 Effect of nozzle position on leading-edge vortex forming

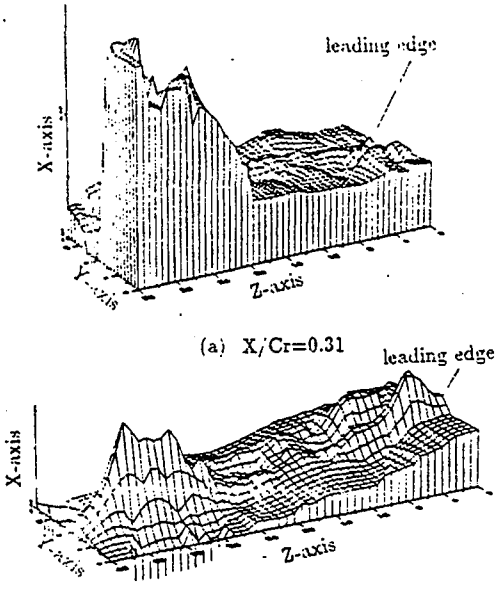

Fig.9 Axial velocity distribution at transverse sections

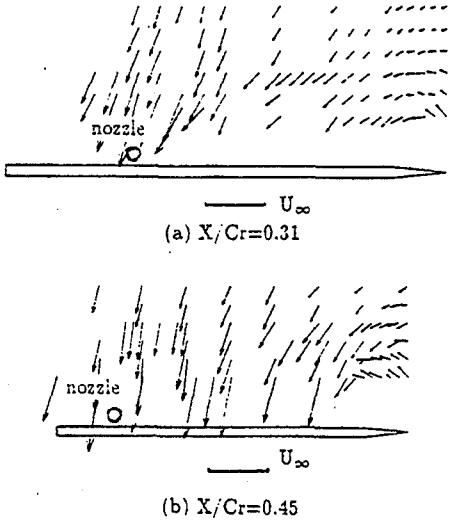

Fig.10 Velocity vector at transverse sections

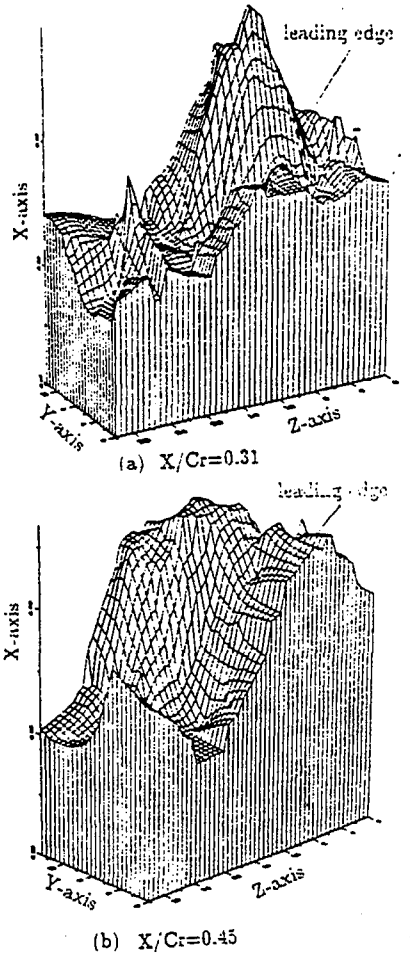

Fig.11 Axial velocity distribution at transverse sections

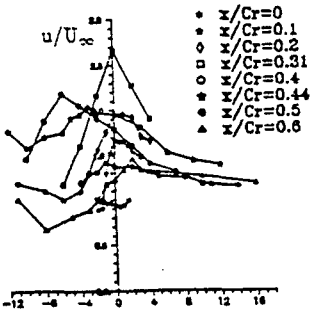

Fig.12 Velocity distribution along vortex core axis

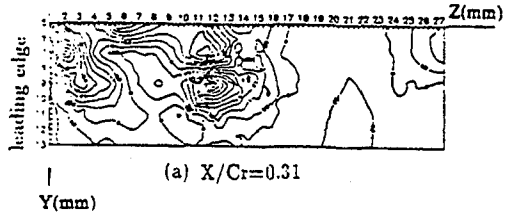

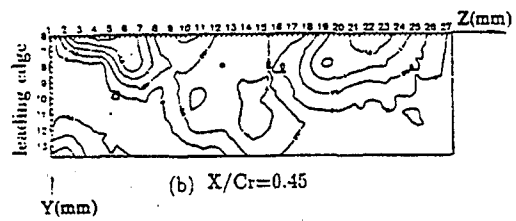

Fig.13 Vorticity contours at transverse sections

EXPERIMENTAL INVESTIGATION OF ACTIVE CONTROL OF ASYMMETRIC VORTEX FORMATION AT HIGH ANGLES OF ATTACK

LEVIN, D.
Department of Aerospace Engineering, Technion - I.I.T., Haifa (Israel)
DEGANI, D.
Department of Mechanical Engineering, Technion - I.I.T., Haifa (Israel)

ABSTRACT

An experimental investigation of the asymmetric vortex formation generated on a slender ogive-cylinder at high angles of attack was conducted in the subsonic wind-tunnel at the Technion. This study was aimed at understanding the effect of a spinning nose section as a triggering mechanism to control this formation, and obtain the ability to eliminate the large side force that is induced by this asymmetry.

Flow visualization demonstrates the effects that such triggering mechanism may have on the vortex formation, and explain the force measurements obtained. The investigation shows the potential of such a tool in eliminating the side force, and the feasibility of achieving active control to improve maneuverability in the yaw plane at high angles of attack.

INTRODUCTION

Asymmetric vortex formation appears on slender bodies of revolution at high angles of attack. This asymmetry yields strong side forces and yawing moments that are hard to counter weight, as the aerodynamic surfaces are mostly ineffective at these angles of attack due to flow separation. The onset and structure of the asymmetric vortex formation have been studied experimentally as well as computationally and analytically in numerous research efforts. Similarly, means to interfere with this formation in order to eliminate the side force or to use them as a control mechanism were studied extensively.

These studies have established the sensitivity of the vortex formation to small disturbances or manufacturing inaccuracies occurring at the tip or nose area. However, once triggered, the vortex formation maintains a stable position. Thus, in order to affect the asymmetry formation, one needs to have a triggering mechanism, as close to the tip as possible, or invest much more energy if triggering is placed further downstream.

Means to control the asymmetric formation that were applied in various configurations include blowing through various nozzle configurations and locations, suction, movable surfaces and spinning of the nose section. All these means have shown some limited effectiveness in eliminating side forces at specific angles of attack, but no method had established a comprehensive means. Moreover, some of these solutions are not practical as the energy needed in controlling the flow is high or technically hard to obtain (blowing, suction), or involve interference with the other systems located at the nose section (movable surfaces, pressure hoses etc.).

Several references (e.g., Dexter & Hunt, Lamont, Degani & Tobak, Moskovitz et al.) have provided evidence that minute changes of the tip shape could switch the direction of the asymmetry. At angles of attack above 45° these small measures induce a bistable vortex formation (i.e. either left or right hand side asymmetry).

Previous tests (Yang et al.) with a spinning nose section have shown a limited success in eliminating the side forces. The tests have not shown a possible control mechanism. For example, no correlation between the side force and the spin rate, or the spin direction were found. Moreover, since the data was restricted to force measurement only, the dynamics of the

asymmetric vortex formation was not studied, and the causes for the reduction of the side force was not explained.

The current investigation was motivated by previous works on the effect of small disturbances on the side forces at high angles of attack (Degani & Tobak), and on previous experiments of the Magnus forces acting on spinning shells, especially the phenomenon of the reverse Magnus loads that was witnessed at specific vortex formation (Seginer). Tests were conducted on a generic 3.5 D Ogive-cylinder shown in Fig. 1. Three nose sections could be attached to the body, with spinning section lengths of 3.89%, 5% and 6.39% of the nose length. The tests were conducted in the 1 m x 1 m subsonic wind-tunnel of the Aerodynamic Research Center of the Dept. of Aerospace Eng., Technion, Israel Institute of Technology. The air speed varied between 20-30 m/s, corresponding to Re/cm numbers of 1.3×10^4 to 2×10^4, and angles of attack in the range of 0° to 55°. The nose spin rate could vary between 0 to 35,000 R.P.M. The aerodynamic forces were measured by a six component sting balance. Flow visualization was obtained with an oil smoke generator and a laser light sheet and recorded on a videotape.

TEST RESULTS AND DISCUSSION

The variation of the side force with the angle of attack at different spin rates is presented in Fig. 2 for the largest nose section configuration. At low spin rates the side force is almost non-existent, at higher spin rates the side force becomes evident and grows with increasing spin rates until it achieves the no-spin values. A similar effect of the spin is presented in Fig. 3, where at angle of attack of 51°, spin is being introduced, at $t=t_0$, and increased gradually with time.

Spin of a projectile has been used in the past to average side forces induced by asymmetry. In these cases, the nonsymmetrical force would rotate with the geometrical asymmetry, and would generate a zero average in a certain direction. Previous studies, as summarized by Ericsson and Redding, show that in the case of side force generated by asymmetric vortex structure, a change in the roll position of the body might lead to a change in the direction of the side force. This behavior is typically a bistable one, with the forces being either to one side or to the other. Previous studies also showed that a 360° roll does not necessarily generate a symmetrical side force distribution that leads to a zero average. To investigate the flow patterns at different spin rates, a flow visualization study was conducted. The results show that at low spin rates a nonsteady vortex formation exists, with asymmetric vortices that switch sides, Fig. 4. The frequency of this switching varied with the spin frequency, but since standard video equipment (30 frames per second) was used, the variation recorded should be considered qualitatively only. At these low rate spin conditions the side force measurement averaged at 0.1 second time intervals, shows almost zero side force.

With the increase of the spin rate the oscillating behavior ceased and a steady asymmetrical formation appeared. However, this formation varies with the spin rate, the higher the spin rate, the stronger the asymmetry, Fig. 5. This variation is accompanied by the gradual change in the side force magnitude as shown previously (Figs. 2 and 3). This change with the spin rate continues until a maximum side force is reached. Increasing the spin rate above this point has no visible effect on the vortex formation or the measured side force.

Similar results were obtained for the smaller spinning nose sections and are not presented. For the small spinning sections tested, the length of the section had a negligible effect on the vortex formation and hence the side force measured. The spin rate was the only parameter which affected the change of the vortex formation. In previous tests (Yang et al.) a large portion of the body was spun and this may explain why spin rate effects were not found.

The realization that triggering is a feasible tool to average the side force, other triggering mechanisms that may be of more practical use for specific configurations and may be applied to introduce periodic disturbances. However, since dynamic effects are being introduced, even when

the net side force vanishes, the effects of the dynamic loading and its frequency should be further investigated.

CONCLUSIONS

The preliminary results of the controllable side force using a spinning nose section suggests that this method has a potential to become a practical low energy means for eliminating undesirable side forces for projectile performing at high angles of attack, and to supply a monotonous yaw control at a range where the traditional aerodynamic control surfaces are ineffective.

REFERENCES

Degani, D. and Tobak, M., "Effect of Upstream Disturbance on Flow Asymmetry", AIAA Paper 92-0408, January 1992.

Degani, D. and Tobak, M., "Experimental Study of Controlled Tip Disturbance Effect on Flow Asymmetry", Physics of Fluids, Vol. 4, No. 12, December 1992, pp. 2825-2832.

Dexter, P.C. and Hunt, B.L., "The Effect of Roll Angle on the Flow Over a Slender Body of Revolution at High Angles of Attack", AIAA Paper 81-0358, January 1981.

Lamont, P.J., "Pressures Around an Inclined Ogive Cylinder with Laminar, Transitional or Turbulent Separation", AIAA Journal, Vol. 20, No. 11, Nov. 1992, pp. 1492-1499.

Moskovitz, C.A., Hall, R.M. and Dejarnett, F.R., "Effects of Nose Bluntness, Roughness and Surface Perturbations on the Asymmetric Flow Past Slender Bodies at Large Angles of Attack", AIAA Paper 89-2236, Aug. 1989.

Seginer, A. Private communication.

Yang, Y., Yu, X., Wang, Z. and Li, J., "Active Control Experimental Investigation about Aerodynamic Characterisitcs at High Incidence", ICAS Conference Proceedings, Aug. 1990, pp. 292-299.

ACKNOWLEDGEMENT

The work was supported by the Israel Science Foundation administered by the Israel Academy of Science and Humanities.

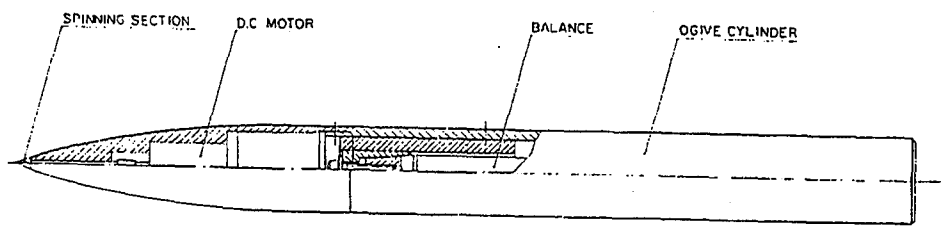

Fig. 1 Ogive-cylinder model.

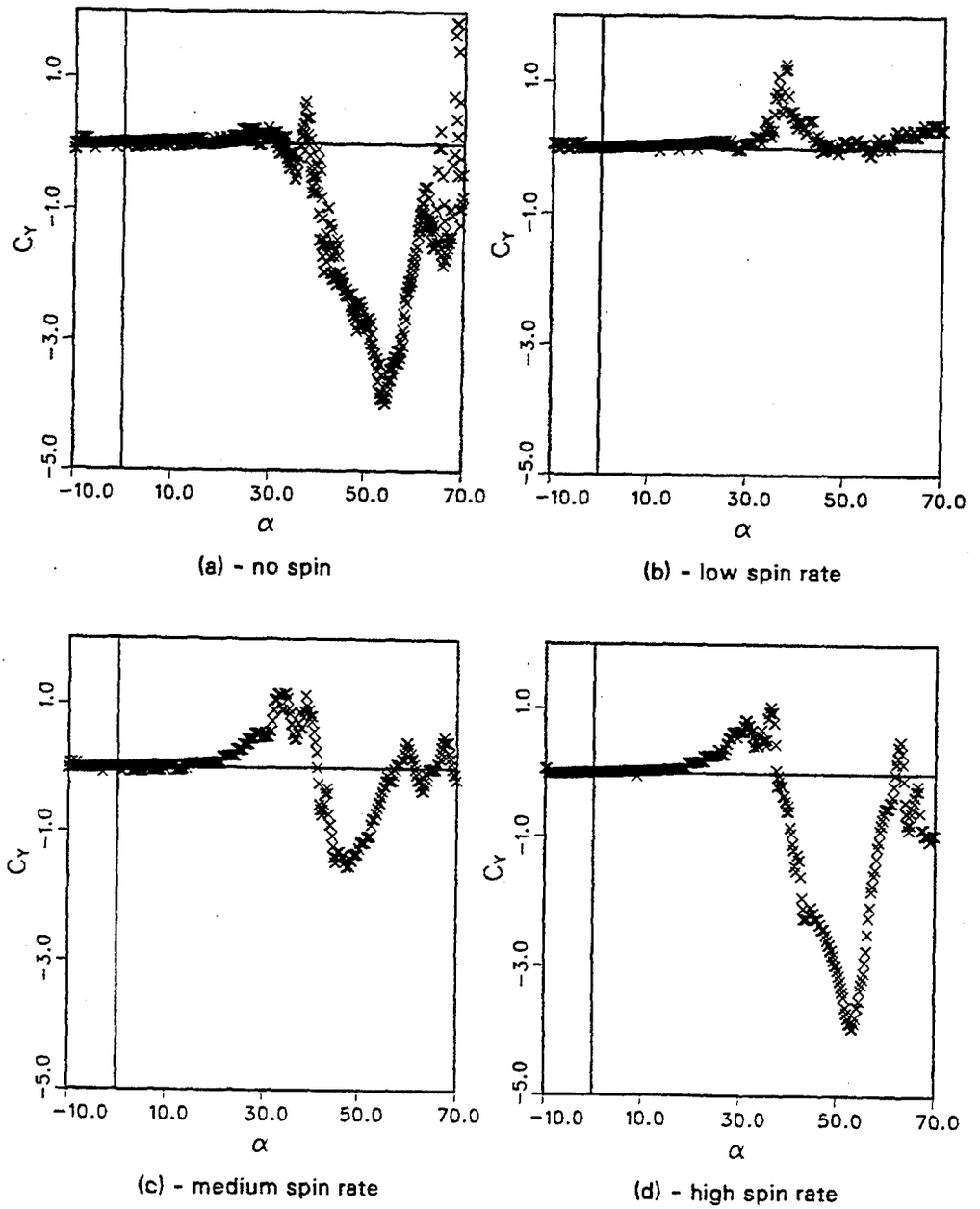

Fig. 2 Side force coefficient variation with angle of attack for different spin rates

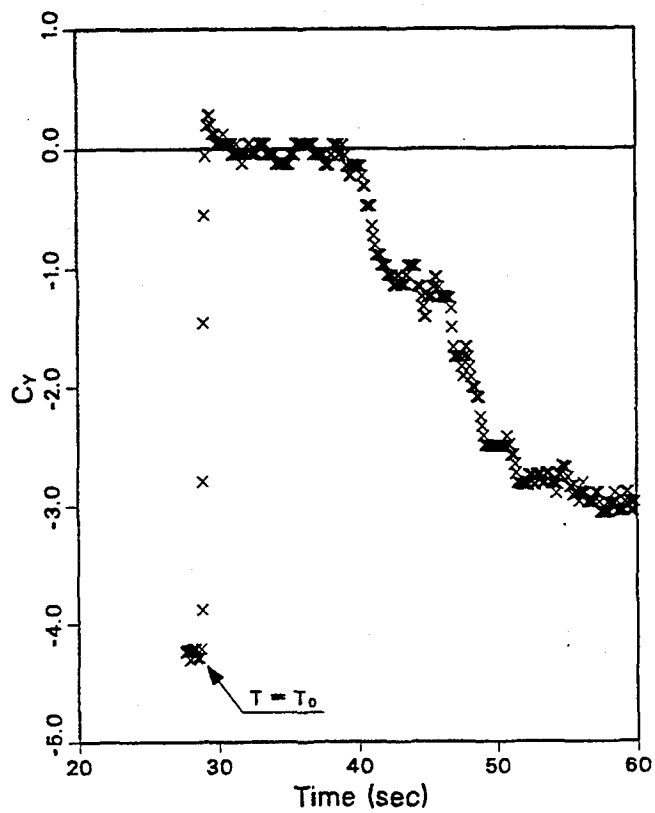

Fig. 3 Side force coefficient at 51° angle of attack with gradual increase of spin rate.

Lefthand asymmetry Symmetric formation

Righthand asymmetry

Fig. 4 Oscillating vortex formations.

Low spin rate

Medium spin rate

High spin rate

Fig. 5 Righthand asymmetry at different spin rates

EXPERIMENTAL INVESTIGATION OF THE FLOW FIELD AROUND HOVERING ROTOR BLADE TIPS

R. H. G. MULLER
F.I.B.U.S. Research Institute, (Forschunginstitut für Bildverarbeitung
Umwelttechnik und Strömungsmechanik)
Paul Klee Weg 8, D - 40489 Düsseldorf, Germany

and

E. BERTON, D. FAVIER, C. MARESCA, M. NSI MBA
Institut de Mécanique des Fluides, Université d'Aix-Marseille II, UM-34 du C.N.R.S.
Souffleries de Luminy, 163 avenue de Luminy, 13009 Marseille, France

ABSTRACT

Hover tests have been jointly conducted by I.M.F.M. and F.I.B.U.S. to investigate the detailed flowfield around rotor blade tips. The present paper presents a comparative study on the flow field around rotor blades with either rectangular or swept tip shapes. For both blade tip geometries the hover experiments include measurements of he tip vortex path, and visualisations of the vortical structures generated by the blade tip. When compared to the rectangular tip, the swept tip is shown to significantly modify the wake geometry and to generate a dual vortex structure which produces a stronger instability of the tip vortex path.

INTRODUCTION

The prediction of the flowfield and the airloads repartition in the tip region of helicopter rotor blades play a major role for providing and evaluating improved rotor designs. Since the flow tip region experiences the largest amplitudes of variations in the bound circulation and the loading repartition, the adequate tip geometry modifications can lead to significant improvements in the overall rotor performances. However, the accurate prediction of the flowfield generated by sharp evolutive tip shapes still poses some problems to available numerical schemes, and requires additional research efforts using experimental investigations. This is the motivation of the present research.

EXPERIMENTAL FACILITIES AND MEASUREMENT PROCEDURES

Rotor Model and Hover Test Conditions

The model-scale of rotor is set up on the hovering test rig installed in the testing hall of the S1-Luminy wind-tunnel. The rotor hub is mounted vertically by means of a supporting mast, so that the center of rotation is located 2.90 m above the ground. The model-rotor consists of a fully articuled rotor hub which can be equipped with interchangeable sets of blades. Rotor geometry and hovering tests conditions are given in table 1.

Table 1 : Hover Test Conditions

Test conditions	Rotor parameters
Diameter	1.50 m
Root cut out	0.22 R
Angular rotational frequency	143 rd/s
Rotational tip speed	107 m/s
Number of blades	2 to 4
Blade chord	0.05 m

As shown in Figure 1, the different sets of rotor blades tested are numbered from 4 to 7, and correspond to various combinations of blade twist, airfoil section and tip shape. All these different tip geometries are calculated so that the radii of the corresponding blade remain constant and equal to R = 0.75 m. The different tip geometries : swept, tapered, parabolic and rectangular (for rotors 4, 5, 6, 7) provide the same rotor solidity ($\sigma = 0.08403$ for $b = 4$).

Measurement Procedures

Several techniques suited for surveying the flow around the blades and the flow in the near and far wake regions, have been developed including 2D-laser velocimetry, flow visualizations with image processing and X-hot wires anemometry. More detailed informations concerning these measurement techniques are given in references [1, 2], only a short description is given here.

Overall forces measurements (averaged thrust and torque) are performed by means of a 6-components balance mounted on the rotor hub. The 3D wake velocity field is measured by means of a X-hot wires probe. The velocity field around the blade is measured by means of the 2D L.V. technique providing the axial and tangential velocity components along a close contour surrounding the blade section and as a function of the blade azimuthal position. The circulation distribution along the span is then deduced from the integration of the tangential flow velocity measurements. Tip vortex paths (r, Z, ψ) are measured by means of a hot-wires technique which allows additionally the determination of the far wake position where the vortex instability is fully developed. However, in order to determine the tip vortex structure and its development, two complementary flow visualisation methods have been used in connection with image processing techniques.

A sketch of the first visualization method [1, 2] developed at the Fluid Mechanics Institute of Marseille (I.M.F.M.) and the associated image processing system used for the present tests is given in Figure 2. The basic elements of the method are : a smoke injection in the recirculating zone outside the rotor wake ; a point light source constitued by a flash strobed at the blade rotational frequency ; and two fast cameras. As a function of time and at successive vortex locations, the trajectory of the vortex is revealed by the smoke filaments. Furthermore, by visualizing the rotor blades simultaneously, the spatial relation between the vortex and the emitting blade can be measured. The materialization of the tip vortex lines is performed by a classical smoke injection method (oil mixtures), which allows the observation and measurement of the development in space and time of the flow field in the vicinity of the blade tip. The system also incorporates two triggerable fast motion video cameras and a stroboscope light source in order to visualize a 3D-view of the tip vortex pattern as depicted in Figure 2. The azimuth of the blade is fixed using a stroboscope which produces several triggered flashes and the trace scattered by the smoke can be recorded simultaneously. All the components of the system are synchronized to the rotational speed of the rotor.

In order to extract more quantitative data from the flow visualization method, an image processing technique is used [2]. The software package (Optilab system) is incorporated within a micro-computer (Macintosh) and consists in a large set of image processing functions. Using the image processing technique, the computer can help to reveal vortex locations which are not revealed on the untreated visualization image (see Figure 3).

The second visualization method is based on the production of "time lines" within the flow at arbitrary directions [3]. These time lines can be visualized at high resolution using classical photography and high frequency stroboscopic flash sequences (see Figure 4). By measuring the local displacement of a time line within the flow at a known flash frequency, it is possible to calculate the local flow velocities. Using stereometric sets of photographs and the 3-dimensional functions of the picCOLOR 34 Image Processing System, developed by the F.I.B.U.S. research institute, the complete flow field can be investigated [4]. The system delivers velocity vector plots, which can be directly compared with data sets of the laser velocimetry. The new method, called

"Flow Visualization Gun" technique, is based on the idea to project very small burning titanium particles through the flow at a very high speed. While being projected, the particles burn to titanium dioxide smoke, which fills the wake of the particles and produces smoke traces of a width of less than 0.5 millimeters.

By shooting the particles in different directions, the smoke traces can be placed everywhere in the entire flow field, even intersecting the rotor disc. The smoke particles of the traces are extremely small (<1 μm) and can be considered as following the flow very closely. The disturbance of the flow due to the crossing titanium particle is apparently very small. When the 1/10 millimeter diameter particle has crossed the full flow field, all disturbances in its wake have decayed. With a capability of visualizing flow velocities of up to 30 m/s and more, the new method can be applied to the entire flow field of the rotor types examined in this project.

The "Flow Visualization Gun" consists of shooting elements, which are loaded into a holder (gun). By applying electrical power (200 volts, 1000 Amperes) to the wires of the shooting element, a large number of small burning titanium particles will leave the element at high speed due to a wire explosion. A screen placed into the holder selects statistically one single particle which then crosses the flow field producing the smoke trace which then can be considered as moving with the flow like a time line. If the smoke trace is placed very near to the tip of the blade, the tip vortex can be visualized by the roll up of the time line. As mentioned above, using stereometric photography and the 3-dimensional image processing technique, the complete 3-dimensional displacement of the time line can be reconstructed.The new method proved to show good results in complex flow fields containing concentrated vortices [4] and turbulence [5]. In the present investigation, the results will be used to give a better understanding of the complex vortical flow especially at the swept blade tip.

RESULTS

In the present investigation, both overall and local aerodynamic quantities of the flow field through the hovering rotor have been measured on configurations of rotors 4, 5, 6, 7, for collective pitch angles θ, and number of blades b, varying in the following ranges : $6° \leq \theta \leq 10°$; $2 \leq b \leq 4$. In each rotor configuration, the measurements have included : the overall rotor thrust coefficient, the visualisations of the vortex structure very near the blade tip region, the determination of the tip vortex path in the near and intermediate wakes, the instantaneous velocity field around the blade surface and in its wake, and the distribution of bound circulation $\Gamma = \Gamma(r)$ along the blade span. For the purpose of the present paper, the following experimental results will be only focused on the analysis of the tip shape influence as deduced from measurements of the wake geometry and from the structure and roll-up of the tip vortex, on the two rotors 4 and 7.

Wake Geometry and Vortex Instability

In Figure 5, the results concerning rotor 7 show an exponential contraction for the radial coordinate r/R, and two stages of axial convection on the axial coordinate Z/R. The change in the slope of the axial coordinate Z/R occurs at the interaction with the following blade (e.g. at $\psi = 90°$ for b = 4). This wake geometry well corroborates the classical model presented for rectangular blade tips in references [6, 7]. Except in the far wake region ($\psi \geq 180°$), the data scattering is shown to be small and conveys the fact that the tip vortex filament is stable in space and time. On the other hand, the coordinate $r/R = r/R(\psi)$, relative to rotor 4 in Figure 5, illustrates the instability of the tip vortex system even in the region close to the blade ($\psi < 90°$). The shaded zone plotted on Figure 5 corresponds to the domain of space and time where the vortex can always be localized along the consecutive revolutions of the blade, using the hot-wires technique. In this case, the scattering of data is large at the location close to the blade, and decreases as the age of the vortex increases.

The wake radial contraction relative to the swept tip (rotor 4) is no longer realized smoothly and continuously as a function of ψ (e.g. of exponential type given in the works of references [6, 7]), but occurs in two stages of linear contraction. The change in the slope of the r-coordinate also corresponds to the azimuth of interaction with the following blade ($\psi = 90°$ in Figure 5).

Structure and Roll-up of the Tip Vortex

Figure 6 gives an example of the novel technique to visualize the rolled-up tip vortex of the test rotor at the interaction with the following rotor blade (swept rotor 4). From two cameras we get the tangential view showing the trailing edge of the blade (tip in the upper right hand corner) and the axial view, showing the illuminated leading edge of the blade at the subsequent flashes (see the leading edge shape of the swept back tip). We can see on Figure 6 the images of the illuminated smoke line at different time steps. Even after a roll-up of 5 or 6 revolutions the smoke lines are still connected and distinguishable. This gives evidence that the vortices have a very clean and laminar structure. Some little irregularities in the outer core of the vortices help to determine the tangential velocities. Especially the lower side of Figure 6 gives an excellent view on the axial flow in the vortex core. It is assumed that this is the first time that the complete structure of a tip vortex of a helicopter rotor during BVI has been visualized clearly.

Figure 7 shows the tip vortex of the preceding blade during BVI, in a 3-dimensional view, which is reconstructed using stereometric set of photographs. For this sketch, the relations have been changed to a blade-fixed coordinate system, where the smoke line moves past the blade, shaped by the influence of the tip vortex.

The structure of the vortex very close to the blade tip is analyzed using the first flow visualisation technique, coupled with the image processing technique previously described. The analysis is conducted at the instant of the vortex system emission from the tip, selected as the azimutal origin $\psi_p = 0°$. At this phase $\psi_p = 0°$, the flow around the blade is revealed by the smoke injection, and illuminated by a strobe flash synchronized with the blade rotation. In such a way, the image observed in the field of the camera shows a steady flow pattern around the blade tip fixed in the vertical plane, which also corresponds to the plane of smoke injection. Moreover, in order to characterize the initial formation of the vortex system, the shooting of the flow patterns is realized perpendiculary to this vertical plane containing the tip blade and the smoke, and using a width-angle lens. So this zoomed image (factor 5) of the flow around the blade tip, provides an increase of the picture resolution and reveals detailed contours of the vortical structures. For both rotors 4 and 7, the digitized pictures in Figure 8, show the initial vortex structures associated to the swept and rectangular tips. The rotor operating parameters, as well as the shooting conditions of the flow patterns are strictly the same in both cases.

The picture relative to the swept tip (rotor 4) exhibits the presence of two vortical structures located at nearly the same altitude Z, but at different radial positions r. This reflects the fact that the roll-up of the vortex filaments shed by the blade tip into a single strong vortex, is not yet achieved at the phase $\psi_p = 0°$ of the rotation. On the other hand, the third vortical structure located more inboard the blade span in Figure 8, corresponds to the tip vortex trace shed by the preceding blade and appears to be completely formed (at $\psi_p = 90°$). Moreover, the presence of these two interacting vortical structures near the swept tip well corroborates the instability of the tip vortex system as previously deduced from hot-wire measurements. The coalescence process of the two structures into a strong single vortex at some altitude from the rotating blade tip, also explains the decrease observed on the instability of the vortex when its age increases.

On the other hand, the same image processing technique applied to the case of the rectangular tips (rotor 7), does not exhibit in Figure 8 such secondary vortices near the blade tip, and the rollup of the tip vortex is shown to be achieved at a phase of the rotation very close to $\psi_p = 0°$. Moreover, while the vortex emitted by the preceding blade ($\psi_p = 90°$) is present on the

picture of Figure 8 for rotor 4, and located close to the inboard region of the blade of rotor 4, it has been convected quicker in the case of rotor 7 and does not appear on the corresponding zoomed image of Figure 8. This amount of vorticity close to the blade and the instability of the vortical structure generated by the swept tips, also involve an interaction process with the following blade stronger on rotor 4 than on rotor 7.

CONCLUDING REMARKS

In the present study, an experimental approach based on a flow visualization technique has been used to analyze the fine structure of the flowfield around hovering rotor blades. In order to provide a focusing on the tip shape influence, data measurements have been selected on rotor 7 with rectangular blade tips, and on rotor 4 with evolutive blade tips. The major findings are as follow :

1) The two different flow visualization methods used in this study appear as a powerful tool to investigate the flowfield and the vortex formation in the vicinity of the blade tip region. Quantitative data on the vortex structure and on the roll-up altitude from the blade tip have been deduced from the present flow visualization results.

2) The flow visualization results have shown that the evolutive tip shape generates initially, a double vortical structure which coalesces into a strong single vortex at some altitude from the blade tip. This formation process has for effect to significantly increase the spatial and azimuthal instability of the tip vortex path in the flow region close to the blade. This instability is shown to decrease as the tip vortex age increases.

ACKNOWLEDGEMENTS

The authors wish to thank the support provided by the "Direction des Recherches Etudes et Techniques" under Grants 90-169 and 92-061.

REFERENCES

1. FAVIER, D., MARESCA, C., BERTON, E. and PLANTIN DE HUGUES, P., "Investigation of the Flowfield Around Rotor Blade Tips in Hover", COBEM, 11th Brazilian Congress of Mechanical Engineering, Sao Paulo, December 1991.

2. BERTON, E., "Contribution à l'Etude de l'Ecoulement Induit Autour et dans le Sillage de Surfaces Portantes en Rotation. Application au Rotor d'Hélicoptère en Vol Stationnaire.", Thèse de Doctorat, Université d'Aix-Marseille II, I.M.2., I.M.F.M., Septembre 1992.

3. MULLER, R.H.G. and STEINHOFF, J. S., "Application of a new visualization method to helicopter rotor flow", A.I.A.A., 8th Applied Aerodynamics Conference, Portland, Oregon, August 20-22, 1990.

4. MULLER, R.H.G., "Measurement of helicopter rotor tip vortices using the Flow Visualization Gun - technique", Proceedings of 18th European Rotorcraft Forum, Paper n° 82, Avignon, France, September 1992.

5. MULLER, R.H.G., HACKESCHMIDT, M., "A new method for visualization and measurement of turbulent flow patterns", 8th Symposium on Turbulent Shear Flows, Technical University of Munich, Germany, September 1991.

6. LANDGREBE, A.J., "An analytical and experimental investigation of helicopter rotor hover performance and wake geometry characteristics", USAAMRDL Technical Report 71-24, June 1971.

7. KOCUREK, J.D.,TANGLER, J.L, "A prescribed wake lifting surface hover performance analysis", Journal of American Helicopter Society, Vol. 22, n° 11, pp. 24-25, January 1977.

ROTOR NUMBER	TWIST	PLANFORM	AIRFOIL
4	-8.3°	a = 60°	OA209
5	-8.3°		OA209
6	-8.3°	0.95R	OA209
7	-8.3°		OA209

$\frac{a}{c} = 0.15$ $\frac{g}{c} = 0.25$ $\frac{d}{c} = 0.6$

Fig. 1 - Rotor blades definition.

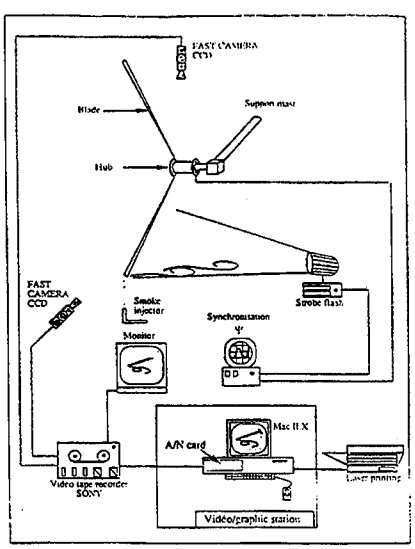

Fig. 2 - Flow visualization and image processing techniques.

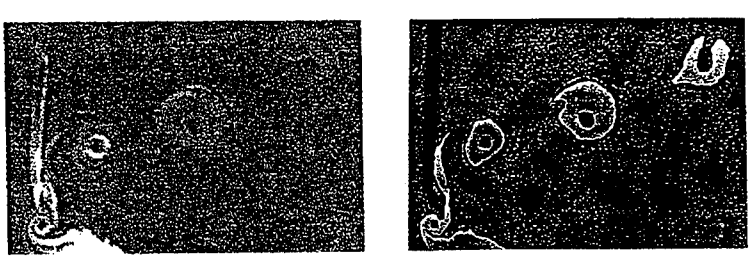

(a) Untreated flow visualization image.

(b) Treated flow visualization image.

Fig. 3 - Flowfield visualization of the rotor 6, b = 4, $\theta = 10°$, $\Psi_p = 0°$.

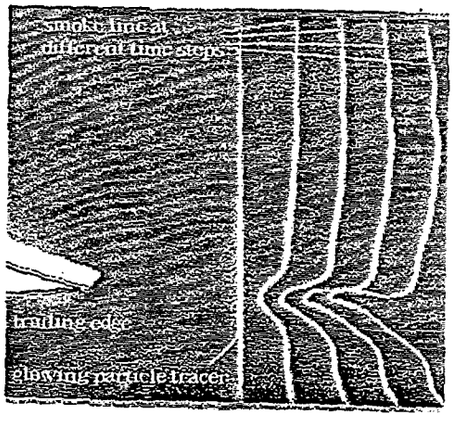

Fig. 4 - Wake of an airfoil using time line visualization.

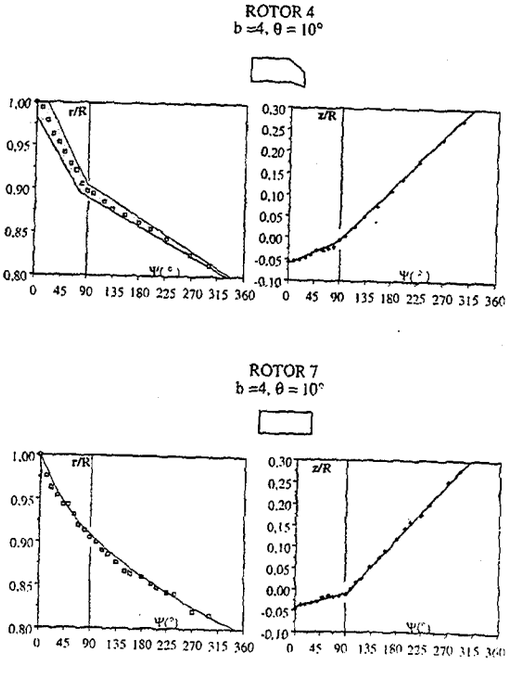

Fig. 5 - Tip shape influence on tip vortex path.

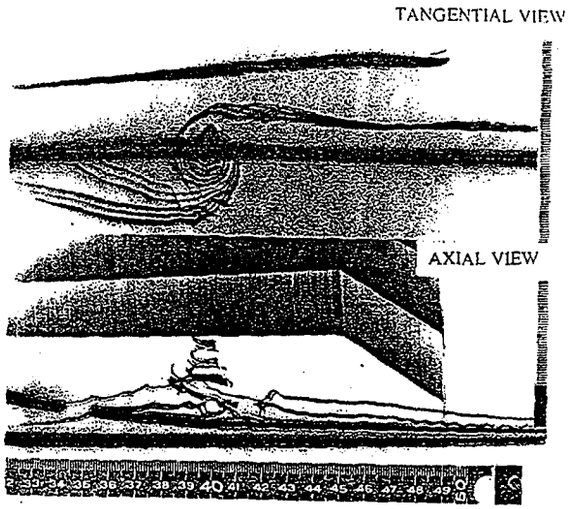

Fig. 6 - Tangential and axial views of the rotor flow, including vortex of preceding blade.

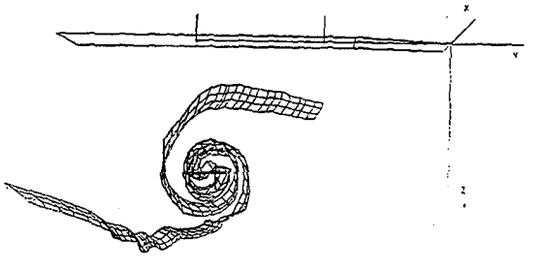

Fig. 7 - Structure of the tip vortex of the preceding blade, rotor 4, b = 2, θ = 10°.

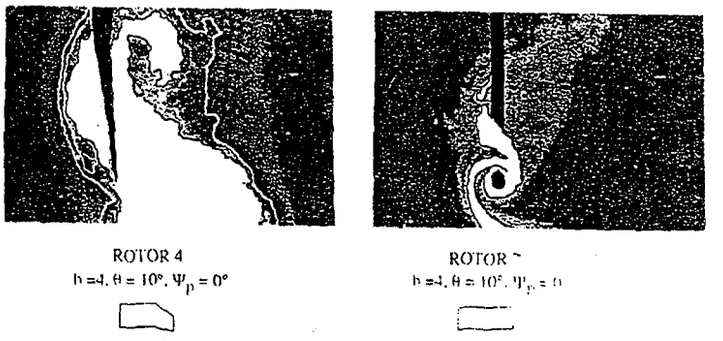

Fig. 8 - Tip shape influence on vortex system formation.

STRUCTURE OF THE TIP LEAKAGE FLOW BEHIND AN AXIAL FLOW FAN

F. Nurzia **P. Puddu**
Dept. of Mechanical Engineering, University of Cagliari, Italy

Introduction

Tip leakage flow in an axial flow compressor or fan rotor is recognized to have significant implication for efficiency, blockage, unsteady loading on subsequent blade rows, noise and instability.

Thus, because of the detrimental effect due to the presence of the tip leakage flow and vortex, a number of experimental research efforts has been directed to investigate the flow through the tip clearance of a rotor blade and the flow disturbance induced in the passage and behind the rotor, namely the tip leakage vortex [1,3,4,7-11,13,17].

On the other hand numerical studies have been performed for three-dimensional viscous flow inside a rotor including the tip clearance [2,5]. The calculated results are useful in understanding the basic phenomenon which take place in the tip region.

However critical points in the development of computational structures are the rolling-up processes of the vortices and the behaviour of the tip leakage vortex with special attention to the evolution of the size, centre position and vorticity.

The paper deals with an experimental investigation on the average structure of the tip leakage flows observed at several planes behind the rotor of an industrial axial flow fan. The relative flow was measured with fixed hot wire probes using the multisampling and phase-locked ensemble averaging techniques.

The paper provides a contribution to the understanding of the tip leakage vortex development behind the rotor, highlighting the evolution of the vorticity and the kinetic energy defect.

Experimental set up

The main geometric characteristics of the industrial axial fan are shown in the sketch of Fig. 1. The rotor rotating at the nominal speed of 1475 rpm, consists of ten aluminium alloy blades with tip diameter of 950 mm (hub/tip ratio of 0.3) and tip clearance of 5 mm. The blade profiles which are modified Gottingen 436 with tip chord of 126 mm have adjustable stagger angle. The results here reported are obtained for the blade stagger angle of 70°, estimated between the chord at the tip and the axial direction, and at high mass flow rate condition Φ_M=0.28 (fig.2).

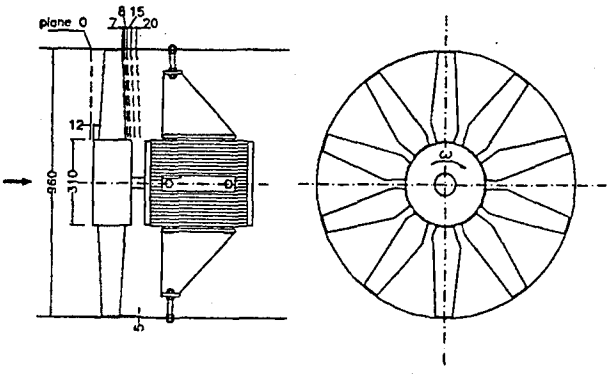

Fig.1 View of the axial fan and measuring planes

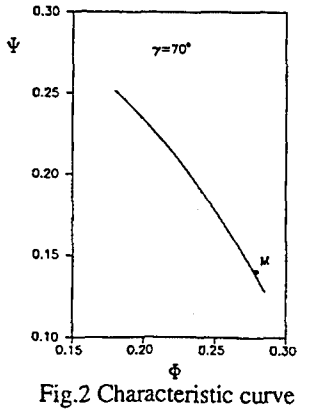

Fig.2 Characteristic curve

Instrumentation and measuring technique

The measurements of the relative flow field and the turbulence characteristics behind the rotor were made by a constant-temperature hot wire anemometer utilizing the periodic multisampling and averaging technique with a computerized data acquisition system.

The instantaneous velocity was measured using both straight and slanted hot wires sensors of 5μm in diameter (Dantec 55-P11 and 55-P12) while an aerodynamic five hole probe was used to measure the mean upstream flow characteristics.

The probes inserted through the casing were moved parallel to the blade trailing edge through different positions in the four measuring planes shown in Fig.1. At each position 9 hot-wire orientations of the slanted probe and 4 of the straight one were set by rotating the probe around its axis and for each position 300 circumferential signals along two blade pitches were acquired every rotor revolution for 512 revs. The instantaneous signals were acquired at the sampling rate of 37 kHz by means of a 12 bit A/D converter board and an optical trigger provides the starting pulse for the data acquisition. A low-pass filter and an amplifier were also included in the measuring system before acquisition to eliminate spurious signals and to improve measurement accuracy.

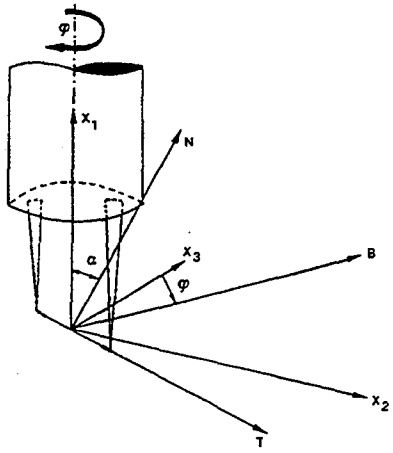

Fig.3 Hot-wire probe

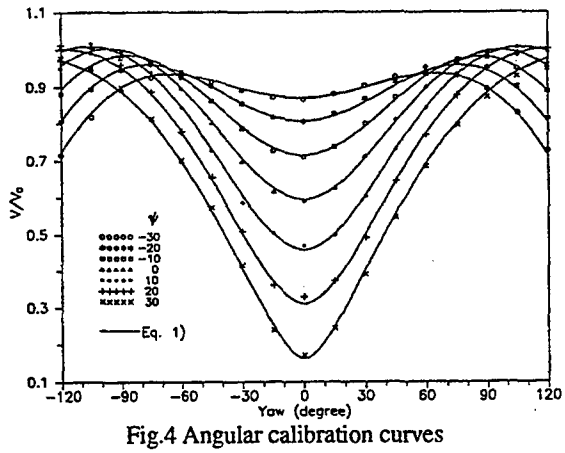

Fig.4 Angular calibration curves

The instantaneous cooling velocities, which are obtained from the instantaneous signals by analytical inversion of the King's law, are summed by the on-line computer during the 512 revolutions of the rotor to obtain the ensemble average of the cooling velocity.

In order to correctly determine the three components of the mean local velocity it is very important to know the angular response of the hot wire probe.

As reported in [16], to characterize angular behaviour, the response of the hot wire was experimentally evaluated changing its orientation with respect to a known flow (fig.3). The calibration curves thus obtained were approximated by the expression

$$V^2 = K_n C_n^2 + K_t C_t^2 + K_b C_b^2 \qquad (1)$$

where K_b, K_n, K_t are the directional sensitivity coefficients, that are calibrated as a function of pitch and yaw angles and not regarded as constants, and C_b, C_n, C_t are components of the velocity vector with respect to the intrinsic probe coordinate (n-t-b) (fig.4). The sensitivity coefficients are expressed analytically using second degree polynomials of the type:

$$K_{b,n,t} = a_0 + \sum_{i=1}^{2} a_i \varphi^i + b_i \psi^i \qquad (2)$$

whereas other workers [12,14] assume them to be constant. These coefficients are determined using the least square method, comparing experimental data with the values calculated using eq. (2). Following the same procedure described in [16], we get the expression for determining mean flow that relates non linearly the mean flow components $\overline{C_i}$ to the measured mean cooling velocities $\overline{V}$.

$$\overline{V} = \sum_{i=1}^{3} \sum_{j=i}^{3} A_{i,j} \overline{C_i}\ \overline{C_j} \qquad (3)$$

where the coefficients $A_{i,j}$ are a function of the directional sensitivity coefficients and of the probe orientations.

The mean velocity components can be calculated, from the 9 mean cooling velocities, by solving the system of non-linear equations (3).

The iterative procedure, used to solve this system, also takes into account, for each iteration, the variations of the sensitivity coefficients with probe orientation.

Using this technique, accurate mean velocity components can be obtained for a duct flow in the calibration wind tunnel [16]. Here in the mean flow field measurements the following uncertainties were estimated:

- mean velocity ±2.5%
- flow angle ±2°
- probe position ±0.1 mm

Results

The flow pattern up and downstream of the rotor has been determined along the blade span using aerodynamic probes as well as hot wire probes.

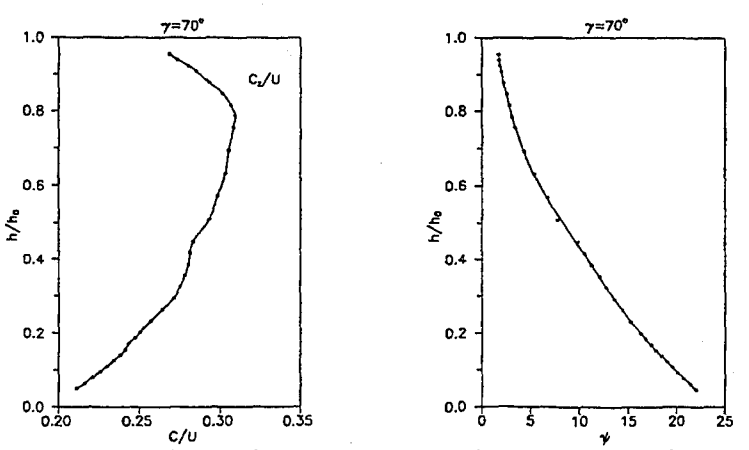

Fig.5 Mean axial velocity component and pitch angle at the rotor inlet

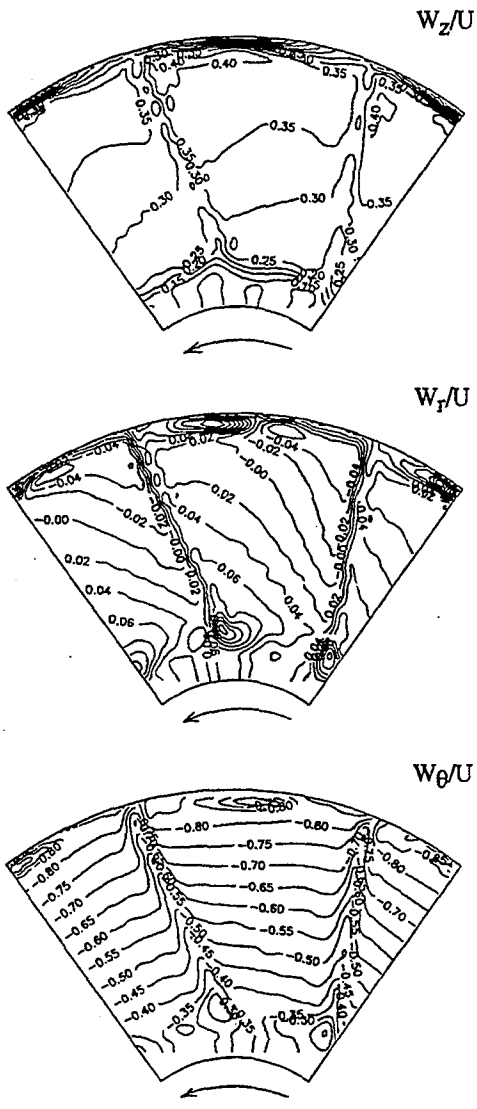

Fig.6 Contour plots of velocity components downstream the rotor z/l=0.0556

Axial velocity component and pitch angle distribution at the rotor inlet are shown in fig.5. As can be seen, significant pitch flow angle variation exists in the hub region, aided also by hub geometry, which gives rise to strongly radial inlet flow. The axial velocity distribution exhibits large variation associated to the curvature of the streamline near the hub region and to the development of the wall boundary layer along the duct at the tip.

The contour plots of radial tangential and axial velocity components in the first plane downstream from the rotor are presented in Fig.6 for the whole blade passage.

Axial velocity gradients are evident in three regions: near the hub, where an extensive separated flow region exists, in the wakes and at the casing region both in the wall boundary layer and in the leakage vortex. In the region outside the influence of viscous effects the tangential velocity component exibits a step gradient only in the radial direction whereas the radial velocity component shows a steep gradient at midspan in both the radial and tangential directions.

The reference axisymmetric flow is defined considering the flow angles and the velocity equal to those present at midpitch in the inviscid flow region and extrapolated linearly in hub and tip regions. We thus consider the secondary flows as the difference between the actual flow and this reference axisymmetric flow.

The secondary flow vectors obtained from the velocity component perpendicular to the relative reference flow direction are presented in fig.7; the behaviour of the radial component at different radii and in the pitchwise direction can be clearly seen. Radial flow towards the hub on the pressure side of the wake and towards the tip on the suction side of the wake is observed. This is consistent with the clockwise pattern of the vortex that practically fills the entire free stream region and can be interpreted recalling that, in the irrotational flow region, deviation from the free vortex law corresponds to a radial velocity gradient in the circumferential direction.

Near the hub the counter-clockwise trailing vortex can be clearly observed and it is possible also to recognize the clockwise passage vortex between the neighbouring trailing vortex.

Near the casing the flow field is strongly affected by the leakage vortex. This vortex induces significant radial flows and probably merges with the passage vortex. In fact as pointed out by Horlock [6] the direction of secondary rotation may be reversed due to the streamwise component of vorticity at the inlet. In this case the casing wall boundary layer presents a large vorticity component in the relative streamwise direction and the passage vortex could assume the same direction of the leakage vortex.

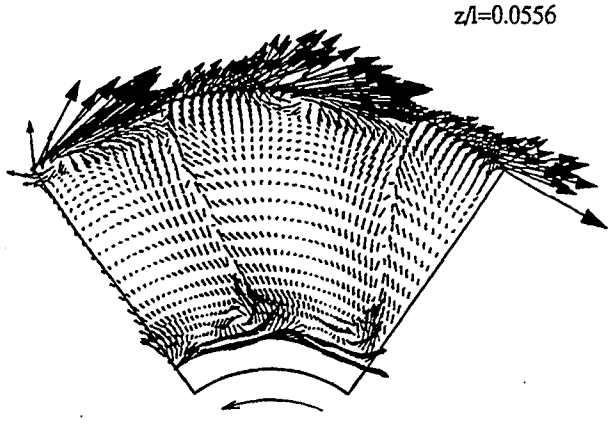

Fig.7 Secondary flow vectors

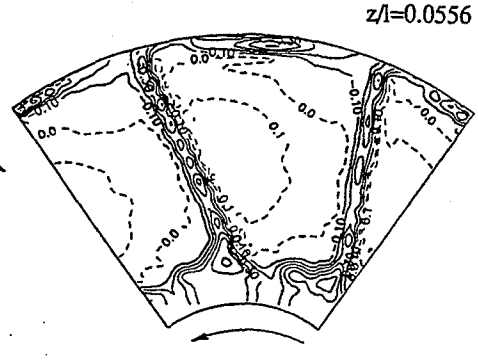

Fig.8 Kinetic energy defect

In fig.8 the energy distribution at the rotor exit (z/l=0.0556) is shown in terms of kinetic energy defect ξ_D. The contour map indicates clearly the region with low kinetic energy located in the wake, near the hub boundary layer and at the leakage and trailing edge vortex. The kinetic energy defect allows to estimate the extent of the region affected by the vortices and their position. It is worth noting that in the first plane of measurements (z/l=0.0556) the leakage vortex is located at midpitch near the casing without strong interferences with the wake. For the same plane also the streamwise and transverse vorticity components are reported in fig.9. Interestingly the high transverse vorticity in the leakage vortex region is comparable with that expected in streamwise direction. This behaviour is consistent with the turbulence characteristics of the normal components shown in fig.10. Here the streamwise and tranverse components are reported together with the intensity of turbulence showing a high value in the region of leakage vortex (more than 10%) and near the trailing vortex region (more than 6%).

The evolution of tip leakage vortex is investigated in three planes far downstream from the rotor only for 30% of the blade span from the blade tip.

Secondary flow vector plots (fig.11) clearly show the gradual displacement of the leakage vortex towards the pressure side of the wake together with an expansion of the induced flows in the free stream region. In the last plane (z/l=0.397) the leakage vortex interfere with the pressure side of the wake giving rise to a low energy region. This behaviour is confirmed by the kinetic energy defect pattern (fig.12) which allows to detect the vortex position and the gradual expansion of the low energy region (related to the leakage vortex) together with an attenuation of the gradients. Nevertheless the mixing process of the leakage vortex with the primary flow and the wake is a slow decay process as the previous diagrams show as well as the plot of the transverse vorticity component. This component of vorticity, reported in fig.13 begins to decrease slowly between the last two planes (z/l=0.199 and z/l=0.397).

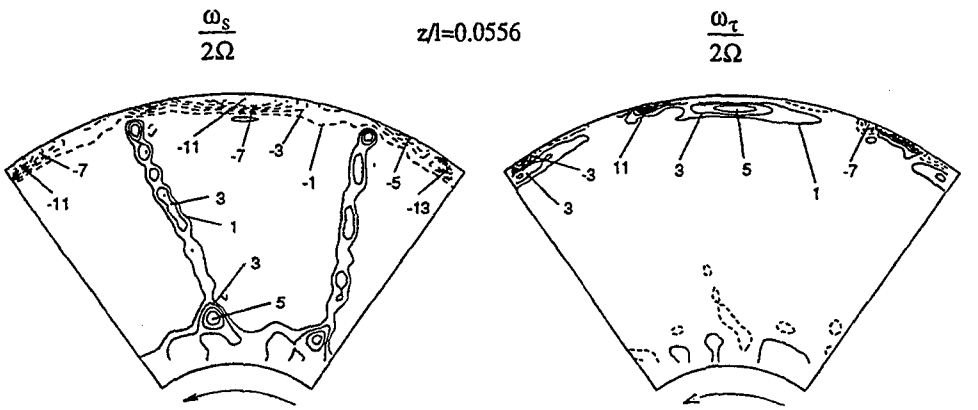

Fig.9 Total vorticity components

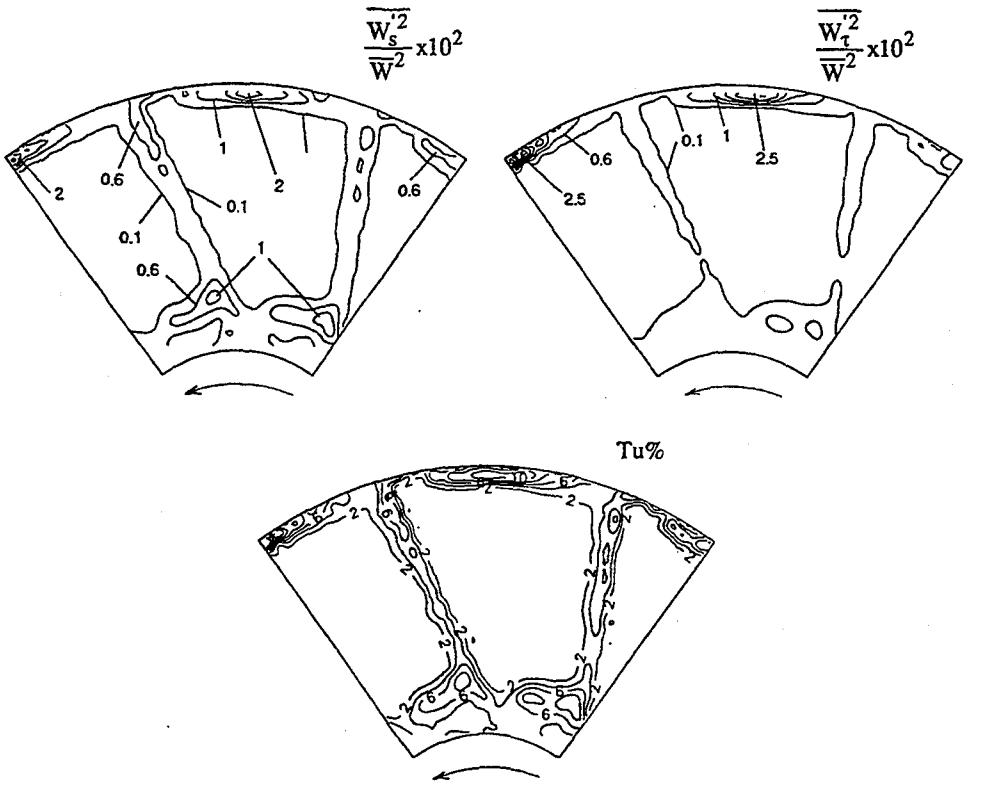

Fig.10 Turbulence characteristics in the plane at z/l=0.0556

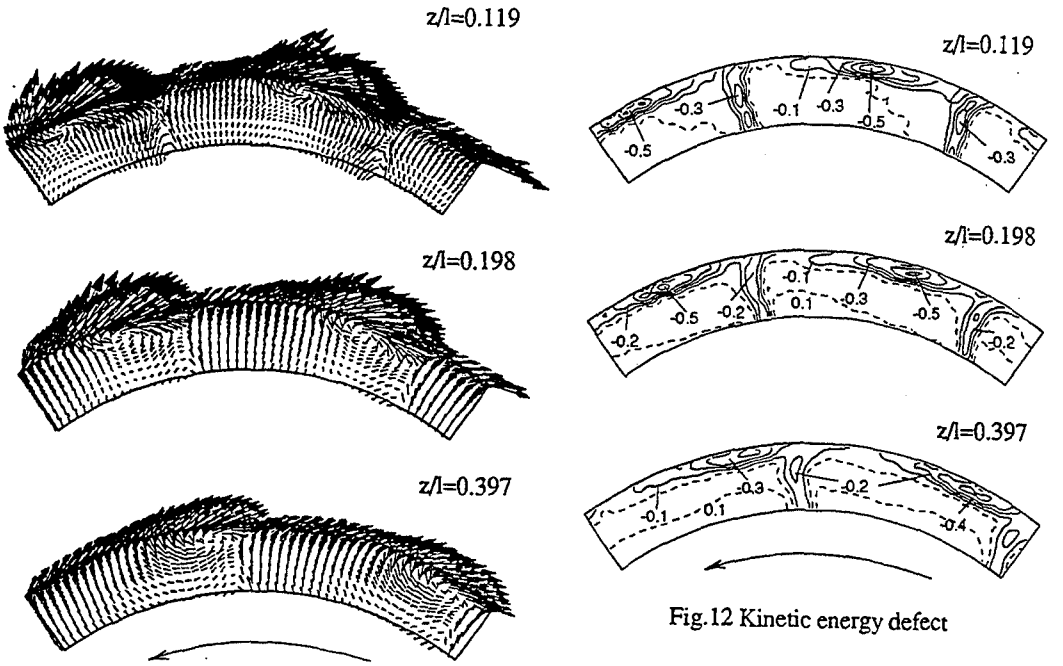

Fig.11 Secondary flow vectors

Fig.12 Kinetic energy defect

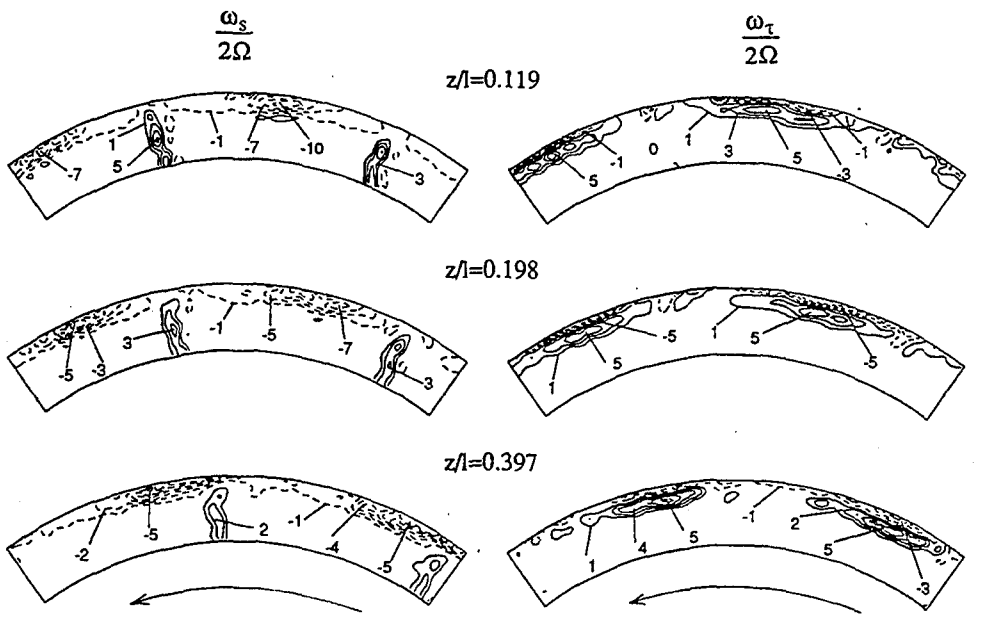

Fig.13 Total vorticity components

Conclusions

The relative flow and the evolution of the tip leakage vortex in an industrial axial fan with 0.3 hub/tip ratio has been studied using hot-wire anemometers with the well-known phase-locked ensemble averaging technique.

Flow measurements were performed at four different planes downstream from the rotor for the high flow rate condition.

The following conclusions can be drawn:

- mean flow is characterized by strong three-dimensional effects;
- secondary flows are present throughout the flow field with a vortical pattern in the free stream region, trailing edge vortex, passage vortex and leakage vortex;
- the rolling up leakage vortex is well defined and can be clearly recognized in the four different measuring planes downstream the rotor
- the leakage vortex is characterized by strong transverse vorticity component which decays slowly with a gradual extension of the related low energy region and a displacement effect toward the pressure side of the wake due to the skewed direction of the vortex respet to the mean flow direction.

List of symbols

C	absolute velocity
h	radial distance from the hub blade
ho	blade span
l	chord at the tip of the blade
$Tu = \sqrt{\overline{W_s'^2} + \overline{W_\tau'^2} + \overline{W_n'^2}} / W$	turbulence intensity
U	peripheral velocity at the rotor tip
V	hot wire cooling velocity
W	relative velocity
W*	design relative velocity
x_1, x_2, x_3	fixed cartesian coordinate system
z	axial distance from the blade trailing edge
Δp_t	total pressure rise
γ	blade stagger angle from the chord to the axial direction
ψ	pitch angle
φ	yaw angle
$\Psi = \Delta p_t / \frac{\rho U^2}{2}$	total pressure rise coefficient
$\Phi = \frac{C_a}{U}$	flow rate coefficient
ρ	air density
Ω	angular rotor speed
ω	vorticity
$\xi_D = \frac{W^2 - W_{ref}^2}{W_{ref}^2}$	kinetic energy defect

Subscript

z,r,θ	axial, radial and tangential directions
n,t,b	normal, tangential and binormal directions
s,τ,n	streamwise, transverse and normal directions

Superscript

—	ensemble average
	fluctuating conponents

Acknowledgements

This research was conducted with the financial support of the Italian Ministry for Universities and Scientific Research and National Research Council. We are also grateful to Woods for their assistance and technical collaboration.

References

[1] **Chen, G.T., Greitzer, E.M., Tan, C.S., Marble, F.E.,** 1991, "Similarity Analysis of Compressor Tip Clearance Flow Structure", Vol.113, N°2, pp.260-271.

[2] **Dawes, W.N.,** 1987, "An Numerical Analysis of the Three-Dimensional Viscous Flow in a Transonic Compressor Rotor and Comparison With Experiments", ASME Journal of Turbomachinery, Vol.109, N°1, pp.83-90.

[3] **Dring, R.P., Joslin, H.D., Hardin, L.W.,** 1982, "An investigation of Axial Flow compressors Rotor aerodynamics", Trans. ASME, Journal. of Engineering. for Power, Vol.104, N°1, pp.84-96.

[4] **Goto, A.,** 1992, "Three-Dimensional Flow and Mixing in an Axial Flow Compressor With Different Rotor Tip Clearances", ASME Journal of Turbomachinery, Vol.114, N.3, pp.675-685.

[5] **Ha, C.**, 1986, "A Numerical Modelling of Endwall and Tip-Clearance Flow of an Isolated Compressor Rotor", ASME Journal of Engineering for Gas Turbines and Power, Vol.108, N°1, pp.15-21.

[6] **Horlok, J.H.,** 1963, "Annulus Wall Boundary Layer in Axial Compressor stages", ASME, Journal of Basic Engineering, Vol.85 N°1 pp.15-21.

[7] **Hunter, I.H., Cumpsty, N.A.,** 1982, "Casing Wall Boundary-Layer Development Trough an Isolated Compressor Rotor", ASME, Journal of Engineering for Power, Vol.104 N° 4 pp.805-818.

[8] **Inoue M., Kuroumaru M.,** 1984, "Three-Dimensional Structure and Decay of Vortices Behind an Axial Flow Rotating Blade Row" Trans. ASME, Journal of Engineering for Gas Turbines and Power, Vol.106, N°3, pp.561-569.

[9] **Inoue M., Kuroumaru M.,** 1989, "Structure of Tip Clearance Flow in a Isolated Axial Compressor Rotor " Trans. ASME, Journal of Turbomachinery, Vol.111, N°3, pp.250-256.

[10] **Inoue M., Kuroumaru M., Fukuhara M.,** 1986, "Behaviour of Tip Leakage Flow Behind an Axial Compressor Rotor " Trans. ASME, Journal of Engineering for Gas Turbines and Power , Vol.108, N°1, pp.7-13.

[11] **Lakshminarayana , B., Pouagare, M., Davino, R.,** 1982, "Three-Dimensional Flow Field in the Tip Region of a Compressor Rotor - Part II Turbulence Properties" ASME, Journal of Engineering for Power, Vol.104 N°4, pp.772-781.

[12] **Lofdahl, L.**,1986, "Hot Wire Techniques for the Determination of Reynolds Stress Tensor in Three-Dimensional Flows", DANTEC Inf., N°3.

[13] **Pandya, A., Lakshminarayana , B.,** 1983, "Investigation of the Tip Clearance Flow Inside and a the Exit of a Compressor Rotor Passage. Part I: Mean Velocity Field" ASME, Journal of Engineering for Power, Vol.105 N°1, pp.1-12.

[14] **Perdichizzi, A., Ubaldi, M., Zunino, P.,** 1990, "A Hot Wire Measuring Technique for Mean and Reynolds Stress Components in Compressible Flow", Proc. 10th Symposium on Measuring Techniques for Transonic and Supersonic Flows in Cascades and Turbomachines, V.K.I., Brussels, Paper 8.

[15] **Puddu P.,** 1992, "Misure con sonde a filo caldo a valle di rotori di ventilatori assiali",. Giornata di studio su "Tecniche avanzate per lo studio fluidodinamico dei ventilatori", Cagliari, 13 Novembre 1992

[16] **Puddu P.,** 1993, "Misure di turbolenza in elementi fissi e rotanti di turbomacchine con l'impiego di sonde a filo caldo", MIS-MAC II Firenze

[17] **Stauter R.C.,** 1992, "Measurements of the Three-Dimensional Tip Region Flowfield in an Axial Compressor", ASME Paper N°92-GT-211

EXPERIMENTAL INVESTIGATION OF SUPERSONIC FLIGHT OF A SPHERE IN WEAKLY IONIZED AIR

G.I. Mishin, Yu. L. Serov, I.P. Yavor
A.F. Ioffe Physical-Technical Institute
Russian Academy of Sciences
Saint Petersburg

ABSTRACT

This report contains a short information on results of researches of flow around a sphere flying in weakly ionized air (glow-discharge low temperature nonequlibrium plasma).

These first experiments were performed by the present authors on a ballistic test range.

Experiments had shown extraordinary properties, of sphere's motion in a plasma. The observed Mach numbers of the flow pattern near the sphere are essentially less than the ratio of sphere's speed to sound velocity.

EXPERIMENTS

The experiments were performed on a ballistic facility equipped with schlieren instruments and interferometric visualization systems, which operated concurrently with laser sources at exposure times of 15 ns. An extended plasma region with uniform parameters was formed in a vertically oriented discharge with a length of approximately 500 mm in a device with a segmented anode, which made it possible to obtain a steady flow pattern near objects in a plasma. Some of the experiments were carried out in an extended plasma formation of an RF discharge with a frequency of 1 MHz.

The main series of experiments was carried out in a steadily burning discharge at a gas pressure of 40-50 torr and a discharge current density of 25÷50 mA/cm^2. The electron density was 10^{-11}- 10^{-12} cm^{-3}, the ionization coefficient was $\alpha = 10^{-5}$- 10^{-6}, and the electron temperature was Te=1-4 eV. The gaskinetic temperature T_a of the plasma was determined by several techniques: by measuring the density of the gas from

interferograms, by means of Chromel-Alumel thermocouple, by radiation pyrometry, and from the electron vibration-rotation spectra of the molecules.

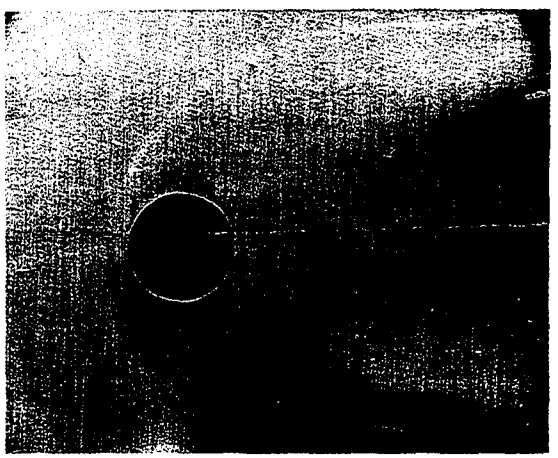

FIG. 1. Toepler shadowgraph of flow around a spherical model moving through a glow-discharge plasma (vertical orientation of the optical knife edge). Velocity of the model 2100 m/s, diameter of the model 20 mm, gaskinetic temperature on the axis of the vertical plasma column T ≲1400K, plasma pressure is 40 torr.

The principal characteristic of supersonic flow around a spherical body is the standoff distance of the bow shock from the frontal surface of the sphere on the null streamline. The dependence of the relative standoff distance of the bow shock from the sphere $\bar{\Delta} = \Delta/R$ (Δ is the standoff distance, and R is the radius of the sphere) on the Mach number $M = v/$ (is the sound velocity) of the sphere and the molecular properties of the gases has been investigated in detail both experimentally and theoretically.

An inspection of the photographs (e.g., Fig. 1) shows that the flow around the sphere in the plasma is anomalous. First, the relative standoff distance $\bar{\Delta}_p$ is much greater than the value $\bar{\Delta}_T$ of this distance for a sphere moving with the same velocity in air heated to the plasma temperature; second, the shock front is highly diffuse, vastly widen and lacking the sharp boundary normally observed in photographs obtained under such conditions in nonionized gases.

To obtain reliable data, we conducted experiments in long (~500 mm) glow-discharge plasma formations with uniform parameters (T_a = 1350 K), which enabled us to determine the values of $\bar{\Delta}_p$ corresponding to steady flow around a sphere in a plasma.

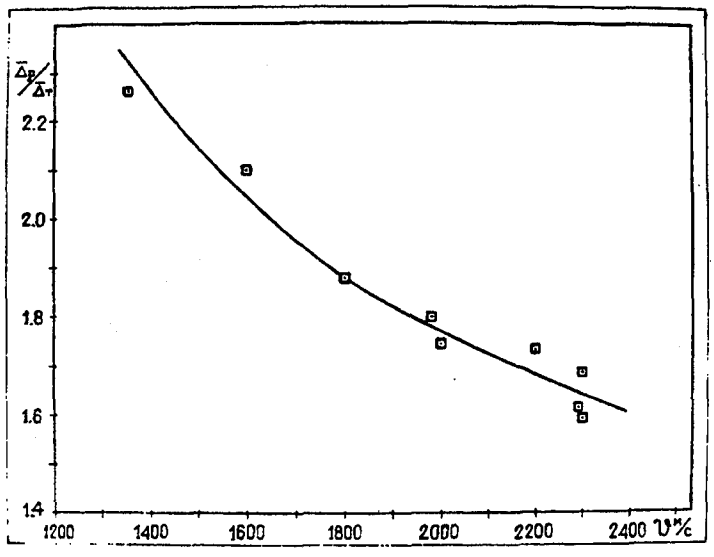

FIG. 2 Ratio experimentally determined relative standoff distance of the bow shock from a sphere moving through a glow-discharge plasma to the corresponding calculated value of the relative standoff distance in air at the same temperature as the plasma ($\bar{\Delta}_p$ is the relative standoff distance of the bow shock in the plasma, $\bar{\Delta}_T$ is the relative standoff distance in air at T=1350 K, and v is the velocity of the sphere).

Figure 2 shows the ratio of the experimentally determined relative standoff distances $\bar{\Delta}_p$ of the bow shock from a sphere in a plasma to the corresponding calculated value of $\bar{\Delta}_T$ in air at the plasma temperature as a function of the velocity of the model in the supersonic range v=1350-2300 m/s .

It is evident from the results that the standoff distance of the bow shock from a sphere with a velocity of 1400 m/s in a plasma is more than 2.2 times the classical "thermal" value for the given condition of motion. The ratio $\bar{\Delta}_p / \bar{\Delta}_T$ decreases as the velocity increases. The dependence of the specific heat of air on the temperature T_a was taken into account in the calculation of $\bar{\Delta}_T$.

In the next series of experiments we determined that the flow around bodies in an RF dicharge plasma (ν= 1 MHz) is also anomalous.

The investigations of flow around a sphere in a glow-discharge plasma in argon and xenon revealed a pattern qualitatively and quantitatively identical to the pattern observed in an air plasma. The standoff distance of the bow

shock in the inert-gas plasma was also 1,6-2.5 times the corresponding thermal value, but the density gradient at the shock front was far lower.

Measurement of the shock standoff distance from a sphere in a decaying, vertically oriented interelectrode gas-discharge plasma in air as a function of the time elapsed after termination of the discharge current confirmed the fact that $\bar{\Delta}_p$ relaxes to the value in nonionized air with a time constant $\tau = 10^{-2}$ s. The material from which the model is made does not affect the anomalous flow pattern around bodies in a plasma.

The experiments show that subsonic flow occurs when the velocity of the model is lower than ~1100 m/s. In this case the bow shock that precedes the sphere prior to entry into the plasma separates from the model and moves far forward (to a distance of several diameters), and a bow shock is no longer formed in front of the body during its subsequent flight.

Since the relative standoff distance of the bow shock from the body is a function of the number M and the specific heat ratio $\gamma = C_p/C_v$, we determined the Mach number M of a sphere in a glow-discharge plasma in air from the values measured in an air plasma, using the functional dependence $\Delta(M, \gamma)$ obtained by the interpolation of known experimental data for a gas with γ=1.33; we were then able, in turn, to determine the "effective" sound velocity a^* in the air plasma from the known velocities of the model. The affective sound velocities obtained by this procedure are plotted as a function of the model velocity in Figure 3.

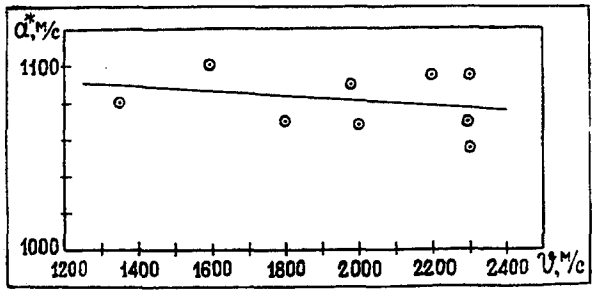

FIG. 3. "Effective" (governing the flow pattern) sound velocity in a plasma in the range of velocities of a spherical model 1350-2500 m/s (a^* is the effective sound speed, and v is the velocity of the sphere.

Under the given experimental conditions the acoustic wave velocity corresponding to the plasma temperature should be 717 m/s, but it is evident from the graph in Fig. 3 that the average sound velocity determined from the data for flow around a sphere in a plasma is equal to 1084 m/s, i.e. the effective sound velocity in the plasma is higher than the thermal velocity by a factor ~ 1.5 .

This disparity between the sound velocities cannot be attributed to error of measurement of the plasma temperature, because the occurrence of such a velocity of weak disturbances in heated air requires a temperature ~ 3000 K, which is impossible in a glow discharge.

Several alternative hypothesis have been advanced to account for the observed nontrivial dynamic properties of a thermal-nonequilibrium gas-discharge plasma.

The lack of necessary experimental data still prevents us from drawing a final conclusion as to the mechanism of the observed phenomenon.

The results of the investigations reported here are regarded from the standpoint that the sound velocity increases in the plasma, since conjecture affords the simplest and most straightforward treatment of the results.

THE EFFECT OF VORTICES IN A HYPERSONIC BOUNDARY LAYER ON THE SURFACE MASS AND HEAT FLUX DISTRIBUTION

ZEMSCH, S., DEGREZ G.
von Karman Institute for Fluid Dynamics
Rhode-Saint-Genèse (Belgium)

ABSTRACT

High speed separated and re-attaching flows including streamline curvature and cross-flow provide the necessary mechanisms for the formation of streamwise striations in a boundary layer. Such situations exist when a flat plate/conical blunt wing model is placed in a hypersonic flow. A delta-wing-type vortex forms around the wing. It was observed that for a combination of large angles of attack and leading edge sweep back angles of the wing, the flow separates from the wing leading edge and re-attaches on the flat plate part of the model to interact with the local boundary layer. Surface flow visualizations and infra-red thermography heat flux measurements revealed streamwise vortices emanating from this flow attachment line. Their formation and thus their effect on the local heat transfer coefficient was enhanced with an increase in unit Reynolds number. Observed variations due to striations reached 10 to 15% of the calculated mean in the disturbed region. The topology of the flow field under which these striations are observed is determined by conical Euler and Navier-Stokes calculations. Results were validated with experimental surface data. The good agreement between the experimental data and the computation suggests a conical flow field over a major part of the model.

INTRODUCTION

For the efficient design of the thermal-protection system of spacecraft, the local heat flux must be known which strongly depends on the conditions of the boundary layer. During early phases of the re-entry into an atmosphere large angles of attack of space craft are required. Under such conditions, streamwise striations have been observed on the side fuselage of an orbiter model[1]. The model was coated with a thermo-sensitive paint and revealed periodic striations on the side fuselage downstream of a flow attachment line. Such striations have been observed under various conditions. Their appearance was often explained by an instability mechanism due to streamline curvature. Görtler[2] theoretically predicted such instabilities, which appear when pressure and centrifugal forces due to streamline curvature do not balance. As a result, counter-rotating vortices form within in the boundary layer causing periodic variations of the surface mass and heat transfer. They were observed for the two dimensional shock wave boundary layer interaction case[3], the 2D and 3D compression corner[4,5,6] and the backward facing step[7]. All these cases are characterized by boundary layer separation and concave streamline curvature in the region of attaching flow. For the case studied herein, i.e., the fin-induced vortex/boundary layer interaction, the situation is more complicated. Although boundary layer separation ahead of the wing exists, including flow attachment leeward of the wing with concave streamline curvature, additional effects such as cross-flow exist. Cross flow instabilities occur when a transverse velocity is superimposed over a mean

flow. This causes a shear flow in the boundary layer which leads, when sufficiently strong, to co-rotating embedded vortices. Both phenomena being of vortical character, their global effect on surface mass and heat transfer are very similar.

During the early phase of this study a close correlation between changes of the topology of the flow field and the occurrence of striations was identified. Thereafter it was decided to study the vortical flow forming about the wing and interacting with the downstream boundary layer. Due to experimental difficulties to access such kinds of flows characterized by small scales and steep gradients; it was decided to compute the flow with a viscous conical flow solver and to validate the result with experimental data obtained on the same geometry. This validation was broken up into two parts: During part one, which was carried out in supersonic Mach=2 flow, flow field measurements by LDV were compared to the computation[10]. In general, good agreement between experimental data and computation could be reported.

Part two of the validation in Mach 6 conditions is discussed in this paper. The flow field topology under which striations appear is analyzed by conical computations and validated with experimental results. The vortex/boundary layer interaction is investigated in terms of the local heat flux. The effect of the striations on the heat transfer is quantified.

Experimental Techniques

VKI H3 Hypersonic Wind Tunnel

All tests described in this paper were carried out in the VKI-H3 hypersonic wind tunnel. It is a blowdown facility equipped with a 150 mm exit contoured axisymmetric nozzle. A free jet of 120 mm is produced which is swallowed by a supersonic diffuser. To avoid liquefaction, compressed air coming from a 40 bar high pressure vessel is heated. The test section is equipped with a pneumatic injection system which enables the models to be injected into the flow within about 20 msec. The tunnel conditions are known from total pressure and temperature measurements in the settling chamber. The nominal Mach number in the test chamber is known from the calibration of the tunnel to be Mach = 6±0.1. Typical conditions are listed in the table below:

p0 [bar]	T0 [Kelvin]	Re_∞ [1/m]	reference
10	550	7×10^6	Re_{low}
20	550	14×10^6	Re_{med}
30	550	21×10^6	Re_{high}

The Model Geometry

The geometry consisted of a stainless steel sharp leading edge, which ensured stiffness of the model and secured connection to the model support. On its upper surface, different flat plates could be mounted. In the case of heat transfer measurements plexiglas© was chosen to be the appropriate material. In all other cases the model was made from aluminium. A conical wing was mounted on the upper surface; it had an angle of attack α and a leading edge sweep-back angle λ. It was fixed at a distance x_{LE} from the leading edge and a distance y_{TE} from the top edge on the flat plate. A

parametric study of various α's and λ's was done but only cases where striations were observed are presented here. The various parameters are listed in the table below:

angle of incidence α	leading edge sweep λ	distance from top edge y_{TE}	distance form leading edge x_{LE}
[deg]	[deg]	[mm]	[mm]
40	75	25	0, 40 and 75

A sketch of the model is shown in figure 1:

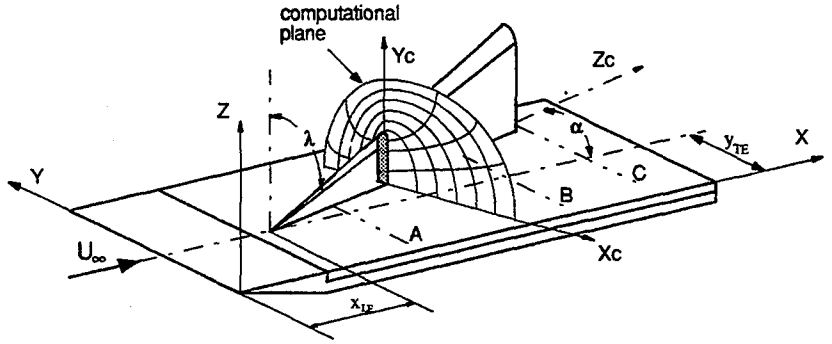

Figure 1: Schematic diagram of the conical blunt fin/flat plate model.

Measurement Techniques and Data Reduction

The foot prints of the interaction were visualized by surface oil flow and sublimation techniques. For the latter, a thin white layer of a subliming material (e.g. acenaphthene dissolved in ether) was applied to the dark model surface before being exposed to the flow. Sublimation occurs according to the diffusion mass transfer of the subliming substance in gaseous form into the boundary layer. It might be related through Reynolds analogy to the skin friction coefficient and the Stanton number.

Surface pressures have been measured using two PSI electronic pressure scanners each of which have 32 channels. They were controlled by an in-house developed electronic interface and data acquisition program[11]. The pressure model housed 48 pressure taps on three spanwise rows which were connected to the scanners. The unused channels remained open to monitor the pressure in the test chamber. A pressure model with moveable insert ensured high-resolution measurements. The scanning speed was about 250μs/channel/reading. Generally, 2 scans with 200 samples for each measurement were taken limiting the testing time to about 10 seconds. This amounts to a major reduction in tunnel running time compared to classical scanning valves (test times of about 1 minute for the same number of channels and 3 scanning valves).

Local heat flux coefficients were calculated from measurements using an Agema Thermovision 900 LW infra-red scanner. Two different optical lenses were applied providing a resolution of 0.8×0.8 mm² (standard lens) and 0.35×0.35 mm² (telescope lens). The data were acquired and directly digitally stored at a framing rate of 15 Hz. The manufacturer's non-linear camera calibration was used. A calibration was done for the emissivity of the model surface and transmissivity of the

medium between the model and the camera using a reference body. This technique was preferred to the in situ linear temperature versus intensity calibration, normally used at the VKI since it profits from the highly accurate built-in non-linear calibration done by the manufacturer. It offers the great advantage that at the same time regions of low and high surface temperature can be analyzed without a loss in accuracy due to a linear calibration. Such a calibration must be done within a small temperature range due to the non-linear function between blackbody temperature and signal output of the scanner. For data reduction the model of linear variation of the heat transfer rate with wall temperature into a semi-infinite slab was applied. The results are presented in a modified heat transfer coefficient defined as:

$$c_H = \frac{q_S}{\rho_\infty u_\infty c_p (T_{0\,perf} - T_w)}.$$

where, q_S presents the heat flux into the surface, ρ_∞, u_∞, the density and velocity evaluated at freestream conditions, $T_{0\,perf}$ the total temperature and T_w the temperature of the wall.

Numerical Techniques

Grid Generation

Conical calculations are carried out in a two dimensional plane perpendicular to the wing plane of symmetry (X_C, Y_C coordinate system). The required meshes were generated by a hyperbolic grid generation technique. Grid point distribution in the radial direction was computed by hyperbolic stretching. In the tangential direction, the surface was separated into several segments on each of which the points could be independently moved by exponential stretching. The grid is characterized by orthogonality of its grid lines. The distance from point to point on the same grid line was always smaller that 20% thus keeping the numerical error small. A typical grid as shown in figure 2 comprises 90×117 grid points.

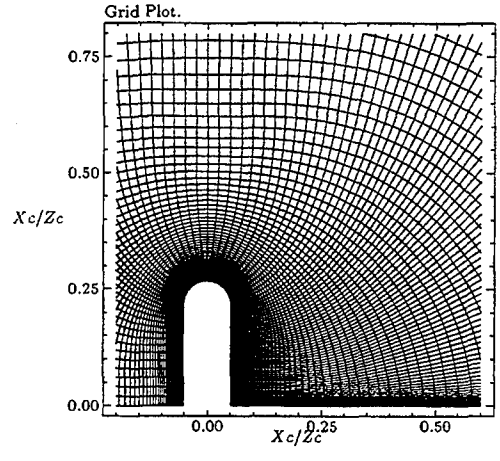

Figure 2: Numerical domain about conical blunt delta wing; 90×117 grid points.

Solution of the Conical Euler and Navier-Stokes equations

Computational results were obtained using a conical Euler and Navier-Stokes solver developed at VKI[8,9], based on upwind finite-volume discretization. All calculations were performed using van Leers flux vector or Roe's flux difference splitting scheme. Second-order computations are based on a limited MUSCL reconstruction, using the van Albada limiter. Iterative solution schemes were the single-step explicit Euler method for first-order computations and a four-step Runge-Kutta method for second-order computations. The converged first-order solution was taken as an initial guess for second-order computations. Typically, 8000 iterations were needed on an Alpha AXP3100/400 workstation to obtain a converged solution after about 12 hours of computational time.

Results and Discussion

Computations

Conical Navier-Stokes calculations were used to predict the flow field. A typical result of a Navier-Stokes calculation is a contour plot of the Mach number as shown in figure 3a. After passing through a strong bow shock, the flow expands rapidly around the wing leading edge where it separates to form the classical delta-wing-type vortex. Due to the presence of the flat plate, the flow has to turn causing a cross flow shock. Calculated particle traces in figure 3b show the flow separation at the leading edge, the delta wing vortex and the location of flow re-attachement on the flat plate portion of the model ($X_c/Z_c \approx 0.4$). Computations were also done modeling the compression side shock wave boundary layer interaction. An influence on the leeside flow, however, could not be determined.

Flow Visualizations

The footprint of the interaction was visualized by the sublimation and oil flow technique (figure 4a-d). A conical flow attachment line appears leeward of the wing under an angle of 20 deg with respect to the wing, its origin situated in the vicinity of the wing apex. Its position compares

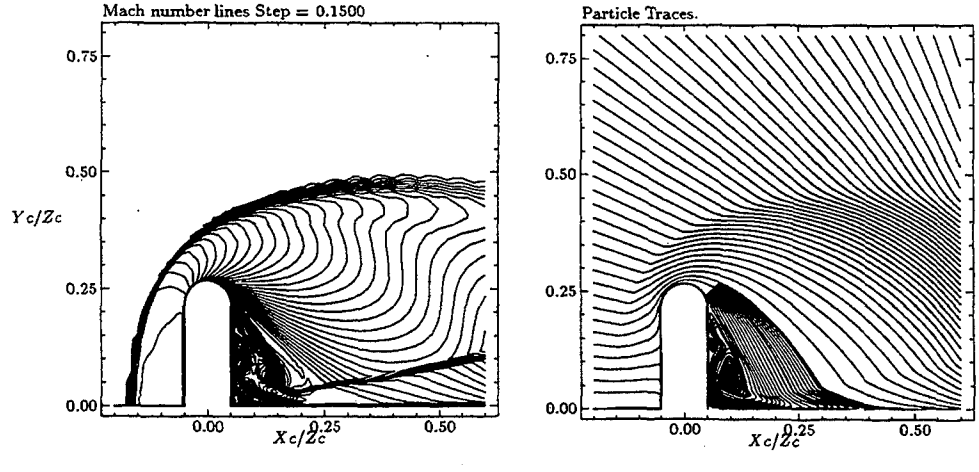

Figure 3: Conical computation, α=40deg, λ=75°: a) Mach number contours b) Particle traces.

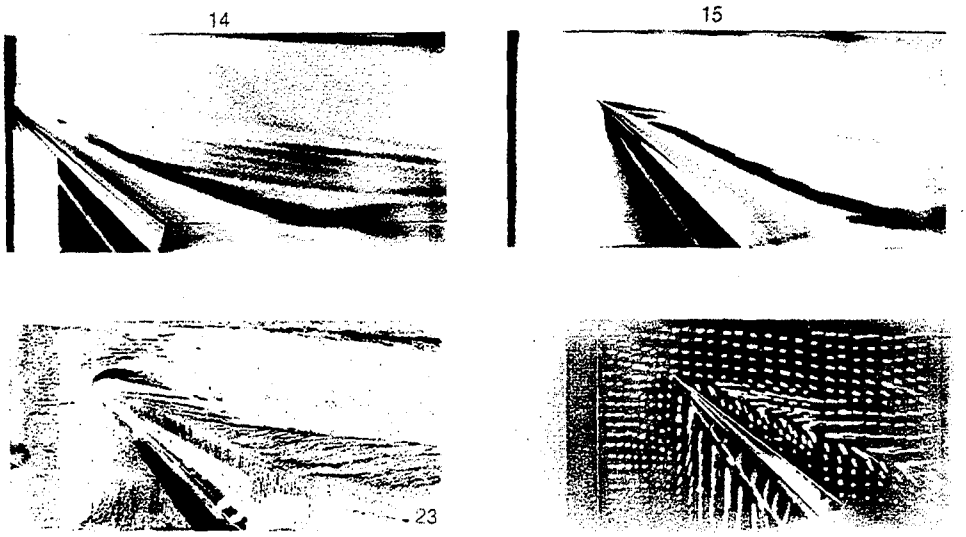

Figure 4: Visualizations, conical wing, α=40°, λ=75°. Sublimation pictures: a) x_{LE}=0 mm, b) x_{LE}=40 mm. c) oil flow picture, d) oil dot picture.

reasonably well with the numerical predictions (x_c/z_c=tan(20°)=0.36). Starting from this line and continuing downstream, a rather periodic variation of the local mass transport indicates the presence of striations. They seem not to be influenced by the incoming boundary layer since moving the wing to the leading edge of the flat plate (figure 4a, x_{LE}=0 mm) does not show any influence on this instability.

Surface Pressure Measurements

Surface pressures have been measured leeward of the wing at the three different downstream

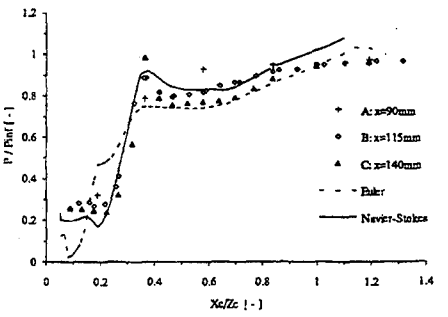

Figure 5: Leeside pressure distribution, α=40deg, λ=75deg,

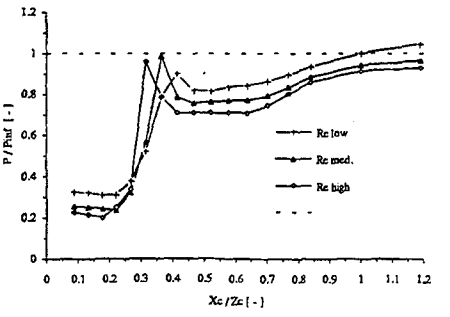

Figure 6: Reynolds number effect, position B.

positions A, B and C (see figure 1). A typical pressure distribution is shown in figure 5 where static pressure ratios are calculated as the mean values of 10 individual tests. They are normalized by the static pressure as reduced from the tunnel conditions and displayed versus the coordinate x_c/z_c. Inviscid and viscous calculations are also shown. A plateau characterized by very low absolute pressures close to the wing indicates a separated flow region. Moving further outboard, a local peak in pressure indicates the location of flow attachment ($x_c/z_c \approx 0.35$). Outboard of this attachment line the flow returns towards the undisturbed flat plate pressure ratios. A comparison of measurements taken at different streamwise positions demonstrates that, apart from the region close to the apex (position A), the flow develops conically. This is further confirmed by the good agreement between experiment and conical computation. An effect of the unit Reynolds number on the interaction is indicated in figure 6 where data at the same streamwise position C for three different unit Reynolds numbers is compared. For an increase in the unit Reynolds number the attachment line moves closer to the wing indicating a stronger expansion around the wing leading edge and higher streamline curvature at flow attachment. The general shift of data towards lower pressure values with increasing freestream Reynolds number is attributed to an increase in the freestream Mach number due to a decreasing value of the displacement thickness of the nozzle wall boundary layer with unit Reynods number.

Heat Transfer

The objective of the heat transfer measurements was to determine regions of peak heating, to confirm the conical character of the flow and to quantify the local heating due to the presence of striations. During the infra-red tests the wing was placed at a distance of x_{LE}=75mm from the flat plate leading edge. Figure 7 shows the streamwise Stanton number distribution on the center line of the model. Very good repeatability is demonstrated by the perfect agreement between the data obtained with the 20° standard and 10° telescopic lenses. Already the 20° standard lens can completely resolve peaks in heat flux coefficient. Hence, the accuracy of the measurement is not reduced by the spatial resolution of the camera. From the leading edge to a distance of x=0.055m a laminar boundary layer develops as seen by comparison to the reference temperature predictions. The following decrease in the heat transfer coefficient indicates boundary layer separation due to an adverse pressure gradient caused by the bow shock. The first peak originates from a reattaching flow and indicates the location of the most severe heating followed by a secondary separation. Since the wing is fabricated from a highly thermo-conductive material, data around x=0.11m are not valid. Downstream of the wing, low values for the heat flux coefficient give an indication for

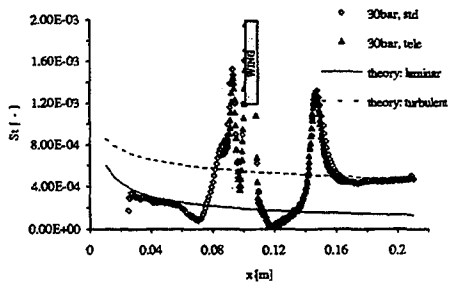

Figure 7: Streamwise Stanton number distribution on center line, α=40°, λ=75°, x_{LE}=75mm, Re_{high}.

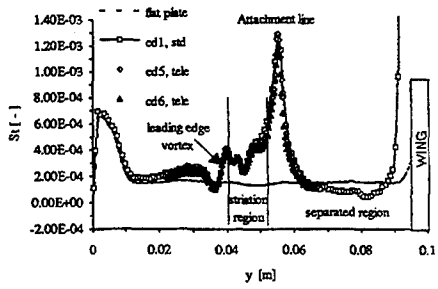

Figure 8: Spanwise Stanton number variation, Re_{high}, x=0.15m.

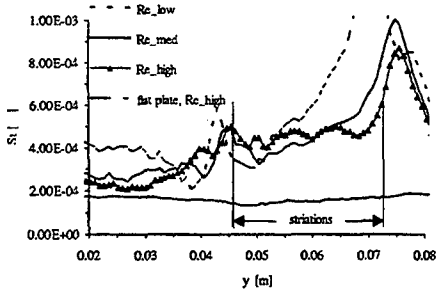

Figure 3: Spanwise Stanton number distribution, x=0.2m

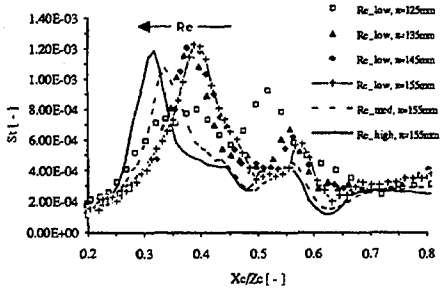

Figure 4: Effect of Reynolds number on interaction.

the severe expansion, which has taken place to near vacuum conditions. The leeward side attachment line heating gives rise to values of the same order of magnitude as observed for the compression side peak heating. Eventually, a new boundary layer originates from this attachment line. Although the level of local heating seems to have similar values as predictions for the turbulent flat plate boundary layer, the state of the boundary layer after attachment is not clear due to unknown boundary layer edge conditions.

In figure 8 Stanton number variations are shown versus the spanwise coordinate at a position of x=0.15m. The side effects seen at y=0 m are caused by the shear layer of the free jet. Stanton numbers outside of the interaction (y<0.035 m) are generally higher than the flat plate values indicating an accelerated flow. The first variation seen is a triggered disturbance coming from the apex of the wing followed by some oscillations which indicate the onset of striations. Peak Stanton numbers are obtained at the location of the flow attachment. Two tests carried out with the telescopic lens demonstrate good repeatability of the measurement. The small improvement in terms of spatial resolution (slit response) is obtained at the point of attachment.

At a position further downstream (x=0.2 m) the disturbances are more pronounced (figure 9). For the high Reynolds number case, a clear variation in the heat transfer coefficient due to the presence of striations can be noticed in the region y=0.045 m to y=0.07 m. The mean value in the disturbed region reaches up to about two times the undisturbed measured laminar flat plate value, variations in the heat flux coefficient due to the presence of striations amount to ±12% of the mean. Stanton number distributions at the same location but for different Reynolds numbers are also included. Striation heating is more pronounced for high unit Reynolds numbers.

Conicity and the effect of the free-stream Reynolds number on the interaction is addressed in figure 10, where Stanton numbers are shown in conical coordinates. For the low unit Reynolds number Stanton numbers are plotted for different streamwise positions. Apart from a region close to the wing apex (x=125 mm) where viscous effects are dominant, the location of peak heating coincides for the different x-locations confirming a conical attachment line. For an increase in the unit Reynolds number, the attachment line moves closer to the wing. This confirms the observations from the pressure measurements. Any significant trend for peak heating with the unit Reynolds number could not be established within the accuracy of the measurement.

Conclusions

An experimental and numerical investigation of the hypersonic Mach 6 flow about a conical blunt wing mounted on a flat plate was carried out. The experimental data itself and the good agreement with the computations confirm the conical character of this flow. It was found that for a combination of large incidences and leading edge sweeps of the wing a delta-wing-ype vortex forms, which separates from the wing leading edge. The flow re-attaches on the flat plate on a conical attachment line. The position of this singular line was found to be influenced by the unit Reynolds number. It moves towards the wing with increasing unit Reynolds number. The occurrence of striations correlates with the existence of this attachment line. Peak heating caused by the attaching flow on the expansion side was found to be of the same order of magnitude as the compression side peak heating. In regions with striation heating, the mean values for the local heat flux are about twice the values calculated for an undisturbed laminar boundary layer. Variations in the local heat flux due to striations are of the order of 12 % of the mean.

References

[1] Kipp, H.W. and Helms, V.T., "Some Observations on the Occurrence of Striation Heating," AIAA Paper 85-0324, 1985.

[2] Görtler, H., "Über eine dreidimensionale Instablität laminarer Grenzschichten an konkaven Wänden." Math. Phys. Klasse, Neue Folge 2, Heft 1, 1940.

[3] Kreins, A.F., "Wärmestromverteilung und Strömungsfelduntersuchung in gestörten Hyperschall-Plattengrenzschichten," Ph.D. thesis, Rheinisch-Wästfälischen Technischen Hochschule Aachen, March 1994.

[4] Cöet, M.C. and Delery, J., "Etude expérimentale de l'interaction onde de choc/couche limite en écoulement hypersonique tridimensionel au nombre de Mach 10," ONERA RT 12/4362AY, February 1990.

[5] Délery, J.M., "Shock Interference Phenomena in Hypersonic Flows," The Third Joint Europe/US Short Course in Hypersonics, Aachen, 1990.

[6] Simeonides, G., "Hypersonic Shock Wave Boundary Layer Interactions over Compression Corners," Ph.D. thesis, University of Bristol, April 1992.

[7] Ginoux, J., "On some Properties of Reattaching Laminar and Transitional High Speed Flow," VKI TN 53, 1969.

[8] Schricke, R., "Solution of the Conical Euler Equations, "VKI PR 1988-13, June 1988.

[9] Spazzini, P.G., "Improvement and Acceleration of a Conical solver and Applications to Super/Hypersonic Flows," VKI PR 1992-25, June 1992.

[10] Zemsch, S. and Degrez, G., "Wing/Fuselage Interferences in Supersonic and Hypersonic Flow," AIAA Paper 93-5140, November 1993.

[11] Zemsch, S., "An Electronic Pressure Scanning System", VKI manual ...-94, to be published.

SUPERSONIC FLOWS AROUND THIN CONES AND DELTA WINGS AT HIGH ANGLES OF ATTACK

V.I. Lapygin, Yu.M. Lipnitsky
(Aerogasdynamics Center, Central Research Institute of Machine Building, Russia)

Study of three-dimensional supersonic flow around thin cones and delta plate with subsonic edges has a long history. Still most part of investigations have been carried out at that variation range of angles of attack when flow in shock layer is supersonic. The study of hypersonic flow around delta wings [1] had shown the possibility of the existance of conical flows at $\alpha \cong \frac{\pi}{2}$. Results of numerical analysis of supersonic flow around cones [2] and wings [3] showed the existance of conical flows at $\alpha \cong \frac{\pi}{2}$.

Present experimental and theoretical investigations are devoted to the study of conical flows at high angles of attack, herewith special attention has been given to the study of conical flows at such angles of attack which are close to regimes with detached bow shock.

CALCULATION TECHNIQUE. A main problem of this investigation is the retrieval of flow parameters in the whole range of angles of attack - from zero to the destruction of conical flow, then it is used system of equations

$$\frac{\partial x}{\partial x} + B \frac{\partial x}{\partial Q} + C \frac{\partial x}{\partial t} = D ,$$

where x - vector-column of functions to be determined, x=(U,V,W, p,S); U,V,W - projections of velocity vector on unit vectors l_r,

l_α, l_ι of spherical coordinate system with centre in the point of a body , p - pressure, ρ - density, $S=p/\rho^\gamma$ - entropy function.

An introduction of time-operator $\frac{\partial x}{\partial t}$ into the system of equations for conical flow brings the system into hyperbolic form independent of Mach number, and it allows to find a solution of the problem in the whole variation range of determining parameters while shock wave is attached to cone vertex [2]. The solution of equations system was constructed by means of the methods described in [5,6].

CIRCULAR CONE. Flow around circular cones has been studied comprehensively at supersonic Mach number M_∞ and in wide variation range of semivertex angles up to the destruction of conical flow. Fig. 1, 2 show pressure distribution and radial component of velocity at windward side of a cone with $\theta_c = 10^\circ$ at $M_\infty = 5$.

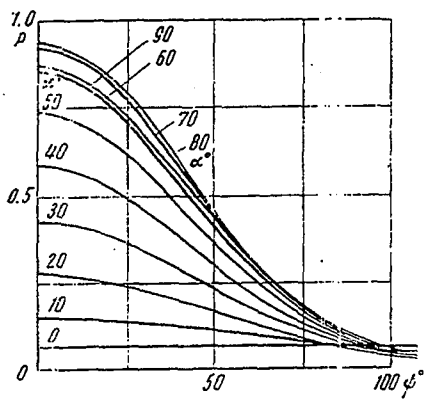

Fig. 1

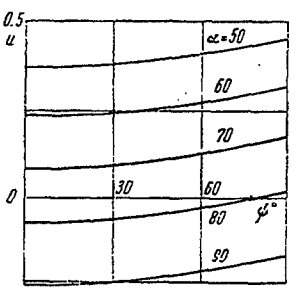

Fig. 2

At small angles of attack flow is conically subsonic everywhere in shock layer. For cones with small semivertex angles at reasonably large Mach numbers M_∞, as angle of attack α increases, local conically sypersonic zone arises at cone surface and it is closed by shock wave. On further increase of angle of attack this zone expands and reach bow shock wave. Fig. 3 (a,b) shows lines $M_{cr} = \sqrt{u^2 + w^2}/a = const$ for $\theta_c = 10^\circ$, $M_\infty = 6$, $\alpha = 13$ and 14°, a region of their convergence is indicative of the presence of inward shock wave. Herewith at $\alpha = 13^\circ$ supersonic zone is closed (Fig. 3, a), and at $\alpha = 14^\circ$ sonic line of

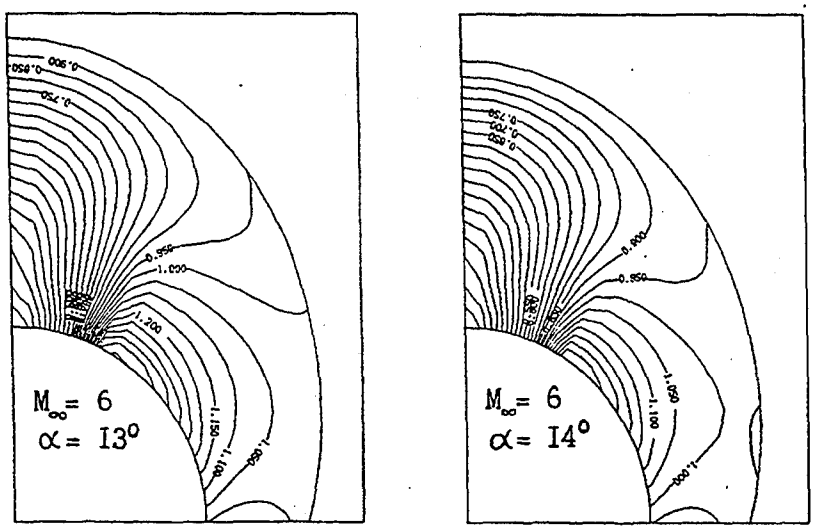

a b

Fig. 3

transverse flow impinge with bow wave. (Fig. 3, b). Pattern with lines $M_{cr}=const$ indicates that in this case inside shock wave which has maximum intensity at cone surface, does not impinge with bow shock wave. Inward shock wave keeps such behaviour also at large angles of attack.

The increase of semi-vertex angle θ_c or the decrease of M_∞ causes the appearance of local supersonic zone in vicinity of bow shock wave at first. In this case stagnation of transverse flow in the vicinity of bow shock in local supersonic zone is realized isentropically.

Let's consider flow regimes which occur with the increase of angle of attack.

Minimum Mach number M in a flow over a cone is attained on the cone surface at $\phi = 0$ and value $M^* = M$ $(\phi = 0, \theta = \theta_c)$ is set as criterion of the definition of flow regimes. Denote by α_1 an angle of attack such that $M^* = 1$. Calculations have shown that at reasonably large angles of attack $(\alpha > \alpha_1)$ it may occur a case when $M^* = 0$. Corresponding angle of attack is denoted by α_2. Third distinctive angle of attack (α_3) defines the destruction of conical flow, e.g. at $\alpha > \alpha_3$ flow with attached to nosetip shock wave does not realize. It should be noticed that for cones with small semi-vertex angles $\alpha_3 > \alpha_2$. In this case at wind ward side there is appeared a region with negative values of radial velocity which module increases monotonously with the increase of angle of attack (Fig. 2).

Distinctive angles α_1 (dash line), α_2 (solid line) and α_3 (dash-and-dot line) plotted against semi-vertex angle of cone θ_c are shown in Fig. 4. Double dash-and-dot line limits a domain of the existence of regimes α_2. It should be also noticed that at $M_\infty > 5$ Mach number does not practically influence on values α_1, α_2, α_3.

Fig.4 presents also test data on angle α_3 (solid circles) at $M_\infty = 6$ obtained from flow visualization.

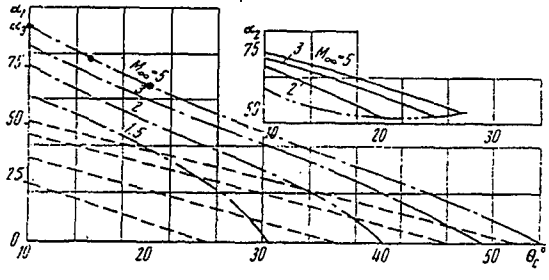

Fig. 4

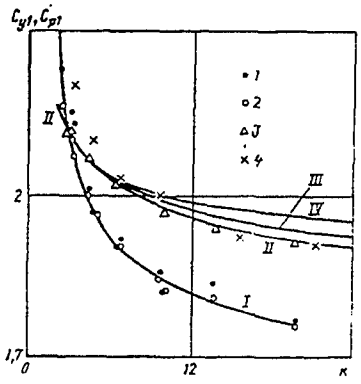

Fig. 5

Depending on a combination of parameters M_∞, θ_c, α maximum angle of shock wave inclination to axis of symmetry θ_w may be realized at $\varphi = 0$, $\psi = \pi$, and at $0 < \psi < \pi$, it is illustrated by Fig. 5 where curve 1 corresponds to $\theta_c = 20°$, $\alpha = 33°$; curve 2 - $\theta_c = 45°$, $\alpha = 15°$; curve 3 - $\theta_c = 35°$, $\alpha = 10°$. This circumstance was noticed in paper [5].

It is notable that at small and moderate angles of attack shock wave attached to cone apex is weak in the sence that theoretically it is possible to have solution with strong shock wave with higher pressure behind its front. As angle of attack increases, shock wave intensity rises and at some α a portion of its surface corresponds to strong solution. At further increase of angle of attack weak solution does not exist.

DELTA PLATE. The calculation of flow around delta plate was performed using the above mentioned equations [3]. The solution is found on a part of the surface of the unit sphere with centre at the apex of the plate bounded by the surface of the shock wave $\theta = \theta_s(\psi)$, the windward surface of the wing $\theta = \theta_p(\psi)$, the plane $\psi=\psi_1$ passing through the leading edge. It was assumed that $w(\psi_1)>a$, where a is the local speed of sound [7].

The solution of equations system was constructed by means of the method described in [5].

The analysis of calculation results demonstrates that as the angle of attack increases, the value of M on the axis of symmetry of the plate becomes equal to unity ($\alpha = \alpha_1$), and then to zero ($\alpha = \alpha_2$), and at $\alpha > \alpha_2$ the velocity vector of the flow in the shock layer is directed towards the apex of the wing - the flow regime IV described in [7] is realized. Qualitatively, the flow regimes are similar to the above ones for cones. The values of α_1 and α_2 depend weakly on χ and M_∞, and for $æ$=1.4 are as following:

M_∞	5	6	10	15	10	10
$æ$	80	80	80	80	75	70
α_1	57.4	58.2	59.6	60.3	58.3	56.7
α_2	80	80,2	81.2	81.2	78.2	74.4

As in the case of circular cones at large values of α the bow shock belongs to the strong family.

The truth of the similarity law [8] in discussed problem is illustrated by the curves in Fig. 5, where the relation $C_{y1} = C_y/\sin^2\alpha = f(k)$, $k = tg\alpha\, tg\chi$, the windward side is numbered by I and has been constructed from the data of [7]. The points 1 and 2 represent the results of calculations [7] for wings with M_∞=6 and 10 respectively, for α = 40, 50, 60°and χ = 70, 75, 80, 85°. Calculations were done for χ = 70, 75 and 80°, specific heat ratio $æ$ = 1.2, 1.3 and 1.4, and M_∞ = 5, 6, 10 and 15.

The relations $C_{p1}=C_p/\sin^2\alpha = f_1(k)$ at the surface of the plate in its plane of symmetry are numbered by II, III and IV in Fig. 5. and correspond to $æ$=1.4, 1.3 and 1.2. The differences in values of C_{p1} resulting from the variation of M_∞ and χ did not exceed 1-2%. The calculation results made in [7] for $æ$=80 and M_∞=10 (points 3) and the experimental data for χ =80° and M_∞= 5 (points 4)[9] are closely correlated with the $C_{p1}(k)$ curve for $æ$=1.4.

The value of C_{y1}at K->∞ is close to the one determined in [10]

$$C_{y1} = 2-1.8(æ-1)/(æ+1)$$

In this case the value of C_{p1} is the one at the stagnation point behind a normal shock determined with the assumption that $M_\infty \to \infty$.

EXPERIMENTAL DATA. Obviously, the existance of conical flow with subsonic velocity in the shock layer may be expected only for infinite conical bodies. At the same time, in the neihgbourhood of the apex the flow parameters may be close to corresponding values of conical flow.

In Fig.6 the calculated values of the coefficient C_p (curve 1) and the angle δ (curve 2) between shock wave and the wing surface in the plane of symmetry are compared with experimental data [8]; curve 3 corresponds to calculated $M(\alpha)$ curve. The vertical bars 4 represent variation ranges of C_p according to the data obtained in [9] up to the angle $\alpha = \alpha_2 = 80^\circ$. As it is seen, the calculated and experimental data coinside. At $\alpha > \alpha_2$ the behaviour of the calculated $C_p(\alpha)$ curve begins to deviate from the experimental observations which are associated with the detachment of the bow shock from the apex of the plate.

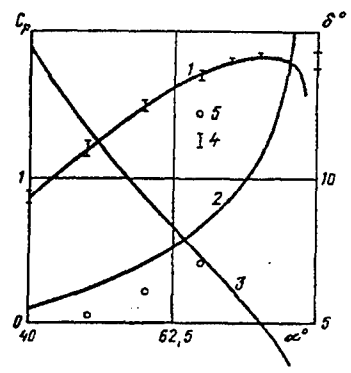

Fig. 6

Taking into consideration experimental and calculated data about the angle of bow shock at $\psi = 0$ and $M_\infty = 6$ for the cones (Fig.7) and delta plate (Fig.8) it is safe to assume that flow parameters at wing top neighbourhood are close to the ones in conical flow.

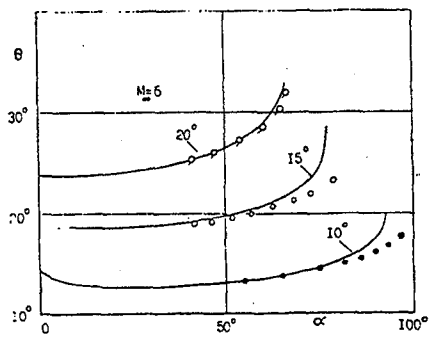

Fig. 7

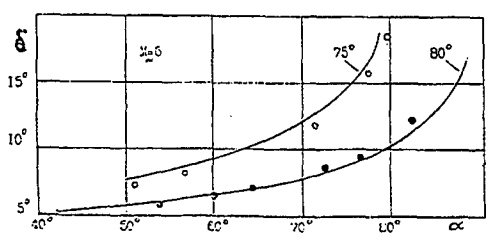

Fig. 8

Schlieren photoes of flow around the cone (θ_c=15°) and delta wing (χ=80°) at M_∞=6, presented in Fig.9, demonstrate rectilinearity of the bow shock in the vicinity of the body top, and its distortion by the apex (α=81°, θ=15° and α=86°, χ=80°) indicates on the destruction of the conical flow.

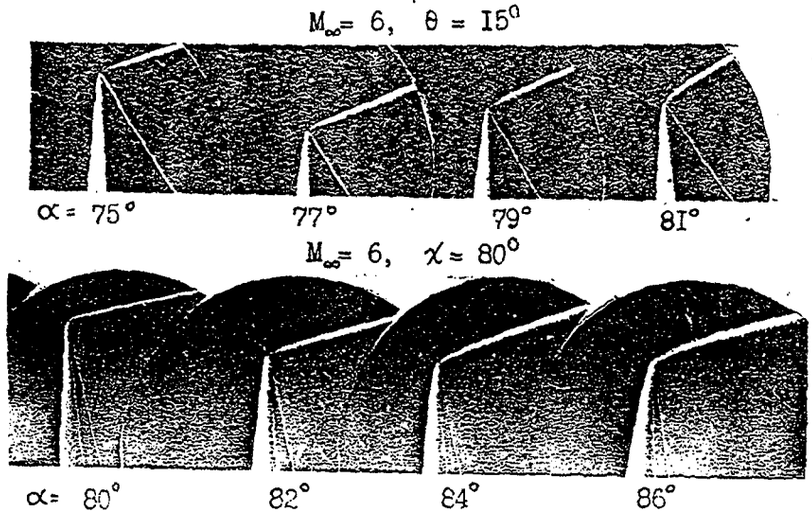

Fig. 9

The study of the streamlines on the body surface shows the complete qualitative agreement between calculation results and test data: at the angles of attack close to $\alpha=\alpha_2$ the values of velocity component u are close to zero and at $\alpha_2<\alpha<\alpha_3$ the velocity vector is directed towards the body apex.

CONCLUSION. The analysis of calculation and test data for supersonic flow around thin cones and narrow delta wings at $\alpha \approx \frac{\pi}{2}$ allows to conclude that indicated features are common for the thin conical bodies.

REFERENCES.

1. Chernyi G.G. Wings in supersonic flow. Prikl. Mat. Mech.,29, 1965.

2. Bachmanova N.S., Lapygin V.I., Lipnitsky Yu.M. Investigation of supersonic flow past circular cones at large angles of attack. Izv. Akad. Nauk SSSR, Mech. Zhidk. Gas, No6, 1973.

3. Bachmanova N.S., Lapygin V.I., Lipnitsky Yu.M. Hypersonic

flow around narrow delta plate at large angles of attack. Izv.AN SSSR, Mech. Zhidk. Gas, No5, 1992.

4. Lipnitsky Yu.M., Mikhailov Yu.Ya., Savinov K.G. Calculation of three-dimensional ideal gas flows without a plane of symmetry. Izv.Akad. Nayk SSSR, Mech. Zhidk.Gas, No3, 1972.

5. Gonor A.L. On the position of bow shock for non-symmetric gasflow around thin body at a large supersonic speed. Isv. AN USSR, OTN, Mech . and Mash., No2, 1959 .

6. Lapygin V.I. Calculation of supersonic flow over V-like wings by procedure of transition to steady state. Izv.Akad. Nayk SSSR, Mech. Zhidk.Gas, No 3, 1971

7. Bazzin A.P. Calculation of the flow over flat delta wings at large angles of attack .Izv.Akad. Nayk SSSR, Mech. Zhidk.Gas, No5, 1966.

8. Sychev V.V. Three-dimensional hypersonic gas flow around slender bodies at large angles of attack. Prikl. Mat. Mech., 24, 1960.

9. Bashkin V.A. Experimental investigation of the flow over flat wings at Mach numbers M_∞=3 and 5 on the interval of angles of attack from 0 to 90°. Tr. TSAGI, No 1175, 1970.

10.Cole J.D. and Brainerd J.J. Slender wings at high angles of attack in hypersonic flows. in: F.R.Riddell (ed.), Hypersonic Flow Research, Progress in Astronautics and Rocketry, vol.7, Academic Press, New York, 1962.

THE 1ST KIND OF UNSTABILITY OF SHOCK HEATED ARGON AND XENON IN EXPERIMENT ON SHOCK TUBE

GRIGOR'EV P.V.
Institute of Theoretical and Applied Mechanics, the Siberian Branch of the Russian Academy of Sciences, Institutskaya 4/1, Novosibirsk, 630090, Russia.

Abstract

The distribution of electron component concentrations behind the shock wave front in argon and xenon for the first kind of unstability was measured. It has been shown that in the typical of each gas interval of the Mach numbers of shock wave the periodical oscillations of electron concentration are observed in the region of electron cascade front.

1. Introduction

At the present time there exists the orderly representation about relaxation phenomena in a gas which are accompanied by ionized shock wave[1,2] . This classic theory gives the distinct dependence of the relaxation zone length l_z and maximum electron concentration value n_e^{max} in equilibrium point of the flow from the velocity of the shock wave front under the initial parameters are constant. With this, the electron concentration distribution $n_e(x)$ and the density of the plasma heavy component of the flow turn out to be monotonously increasing functions. However, at present the experimental material accumulated demonstrates that there exist the regions of initial parameters for shock wave where the relaxing gas behavior does not obey the classic description. The data on stochastic disturbances in the flow, stratifications and deformations of shock front, splashes of radiation front relaxation zone, not monotonous (oscillating) distribution of plasma parameters (for instance, $n_e(x)$) in relaxation zone, periodical pulsations of all volume of shock heated gas were obtained. For all these anomalies, at present, the term "unstability" is the most wrongly used.

Having accumulated sufficient quantity of experimental material managed to perform its classification for inert gases and to highlight 4 main kinds of unstability[3]. The truth of this classification is confirmed by all experimental data on inert gases existing in the literature at the present time. In the special case, for xenon the classification is pictorially represented in Fig.1.

Thus, in the experiment it is possible to observe several large regions of initial parameters in which relaxation phenomena while distributing shock wave are not described by classic kinetics, however, simultaneously there exist the regions of initial parameters in which the classic description is satisfactory. The I kind of unstability is characterized by strictly periodic changing of electron concentration value and radiation intensity value of shock heated plasma in the region of electron cascade front[8]. For xenon the relative depth of radiation intensity modulation achieves its own maximum 40% with the frequencies ~30 kHz[6-8] with the Mach number 8.3±0,5[7-9].

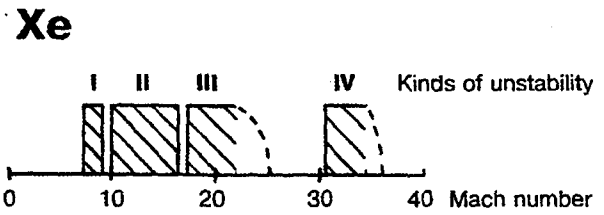

Fig. 1. The region of the Mach number of shock wave where corresponding kinds of unstability were observed. The diagram is built for xenon. Typical initial pressures are 3-20 torr.

For argon this phenomenon is observed with M≈10-10,5[6,10,14]. With this, the maximum amplitude of plasma radiation intensity modulation is probably less.

The paper is devoted to the investigation of the I kind of unstability in argon and xenon. The comparison of experimental results for these gases has been performed. In particular, the dependence of anomaly amplitude from the Mach number of shock wave is investigated.

2. Experimental arrangement.

The experiments were performed with the shock tube of the round cross section with inner diameter 76 mm. The operating surface was polished by the method of electropolish. Diagnostic schemes of two kinds were used.

a) Classic the Mach-Zehnder interferometer with reference ray. As radiation source the IR-laser with the wavelength 10600 nm which was stabilized with the help of echelette introduced as resonator element was used. It allowed to fix the IR-laser at concrete oscillating-rotating transition for the time of experiment[4], and it removed the appearing error of the measurement from change of wavelength of zonding radiation while determinating electron concentration. The random error of measurements consisted in the case ~1% n_e^{max}. However, there exists regular lowering of electron concentration in the limits 2-2,5% at the expense of decreasing effective optical path caused by the development of cold boundary layer on the walls of shock tube. The unstability in argon was investigated by this interferometer.

b) Differential laser interferometer. The optical scheme is represented in Fig,2. As radiation source He-Ne laser with the wavelength 3390 nm was used. The radiation of laser I (Fig.2) was divided on the plane-parallel plate 3 made of GaAs. On the other plane-parallel plate 4 the radiation was collected into one beam, and with the help of lense 5 it was directed into photo-detector 6. The photo-detector represented by itself photo-resistor

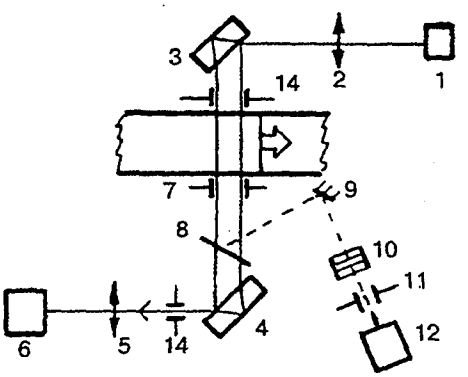

Fig. 2. Optical scheme of differential laser interferometer with electro-optical calibration of signal.

cooling by liquid nitrogen. Diaphrams 7, 14 and narrow range interference-polarization filter 8 transmitting only the radiation of probing laser served for the cutting of the own plasma IR-radiation from photo- detector. Simultaneously filter 8 served as turning mirror for the range 300-600 nm.

Then this radiation passed through filters 10 was determined for argon by photomultiplier 12. The filter combinations allowed to investigate as the radiation of only continuum as the radiation of the continuum + lines were used.

The signal of differential interferometer entered the input of integrating equipment. Then without preliminary processing (during the experiment) on the oscillograph screen the distribution of electron concentration behind the wave front was reproduced.

To the second channel of the oscillograph the signal of differential interferometer was sent directly. It allowed to compare the information about $n_e(x)$ and $n_e(x)$. In order to calibrate the interferometer (to adjust it to linear region) the linear electro-optical effect was used. On the one of crystals (3 or 4) rectangular impulse 1kV was sent. The resulting shift of the phase is distinctly seen on the oscillograph (see Fig. 3, a', b'). It allows to tune to the region of its maximum amplitude. It points out to the phase shift between rays $\Delta\psi \approx 0$. The construction of interferometer is described in detail[5]. The experiments were performed for xenon with the level of molecular admixture $2 \cdot 10^{-3}$.

For argon the experiments were conducted for two levels of relative admixture: 10^{-3} and $4 \cdot 10^{-5}$. The ranges of the Mach numbers investigated for xenon 8.5-11.5, for argon 10-12. Initial pressure for xenon 3 torr, for argon 5 torr.

3. Results and discussion.

The results of investigations of the region of shock wave velocities joined from the side of more high Mach numbers to the velocity of maximum development of the I kind unstability effect in xenon are represented in Fig.3. The curves a,b,c are the signals of differential interferometer. They show $n_e(x)$. The curves a',b',c' are corresponding signals of differential interferometer passed through integrating device. They demonstrate $n_e(x)$. The results are qualitative ones, they illustrate the measurement of unstability amplitude with various Mach numbers of shock wave. The experimental curve of the ionization velocity with the Mach number M=9.6 (Fig. 3a) shows the absence of anomalies in the view of fluctuations or distortions of the profile. Ionization profile of this signal (Fig. 3a') also is smooth. This curve qualitatively coincide with the calculated one[11]. On the ionization profile all three phases of ionization development behind the front of shock wave are distinctly seen: the region of initial ionization, electron cascade front, the region of decreasing of electron concentration. The next profile of ionization velocity (Fig. 3b) with M=9.25 is undergone to oscillating process. On the corresponding ionization profile (Fig. 3b') two bends of the curve are distinctly observed in the region of electron cascade front. With further decreasing the Mach number of shock wave up to M=9.1 clearly seen periodic oscillations of ionization velocity are developed (Fig. 3c). Corresponding ionization profile (Fig. 3c') shows usually observed the I kind unstabilities, i.e., concentration oscillations of $n_e(x)$ in the region of ionization by electron shock. From the processing of experimental material follows that the first properties of the I kind unstability in xenon (at the expense of high sensitivity of differential interferometer

to the fluctuations of $n_e(x)$) are already observed with M~9.3. While decreasing the Mach number the anomaly amplitude is gradually increased achieving its maximum value ~40% with M~8.3[8].

For argon the typical oscillogram demonstrating $n_e(x)$ in the region of unstability development is represented in Fig. 4. The signal is negative, the Mach number M=10.55. At the beginning of the curve calibration impulse is observed on the oscillogram. The back front of this impulse practically coincides with shock front. Fur-

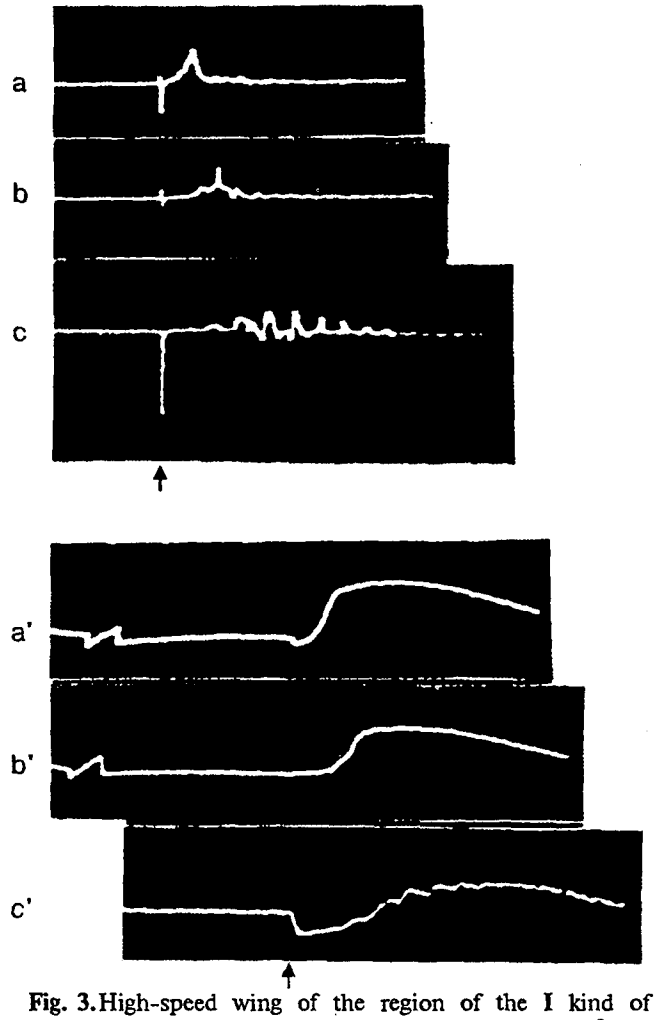

Fig. 3. High-speed wing of the region of the I kind of unstability. Xenon, p_0=3 torr, air admixture $\xi=2\cdot10^{-3}$ in per-unit, a: M=9.6, b: M=9.25, c: M=9.1; a, b, c, are the signals of differential interferometer; a', b', c' - are the same signals after integrating device. The arrow indicates the position of shock wave front.

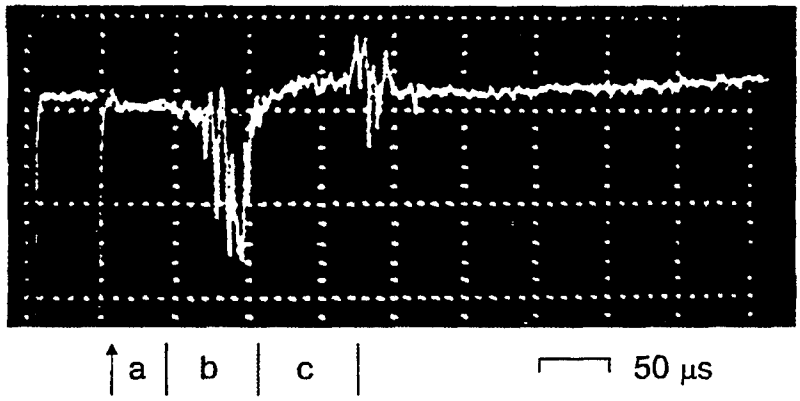

Fig. 4. Typical oscillogram of the I kind of unstability in argon. Differential interferometer, p_0=5 torr, M=10.55, air admixture $\xi=10^{-3}$ in per-unit,
a - is the zone of electron accumulation;
b - is the zone of final part of electron cascade front where the oscillations $n_e(x)$ are localized;
c - is the zone of radiation cooling.
Shock front is shown by the arrow. One scale division is 50 μs.

ther, rather elongated region ~50 μs (zone a, Fig.4) is outside the limits of device sensitivity. Then the final part of electron cascade front, i.e., zone b follows. Here relaxation oscillations are observed. Then while cooling the gas after the achieving of the point of heat equilibrium the signal becomes weakly positive (zone c), and in 70-80 μs after that chaotic changes of the signal point out to the passing of the contact surface via measuring cross section of the installation.

The comparison of the signals of differential interferometer for argon and xenon provides their complete quantitative identity: the region of maximum amplitude of the oscillations $n_e(x)$ is in the final part of electron cascade front. The interval of time between the maximums observed for each separate experiment was preserved the same. One may suppose that in all inert gases the I kind unstability develops analogously.

In Fig. 5 the distributions of $n_e(x)$ for argon determined with the help of the Mach-Zehnder IR-interferometer for three different velocities of shock wave. There one may observe the dynamics of unstability appearance in the transition zone between stable and unstable regions according to the velocities of shock wave.

On profile 1 (M=11.5) there are no any distortions, and the electron cascade front is satisfactorily described by collision model of one-level kinetics of ionization[12]. The calculations have been performed for initial parameters of the experiments in argon mentioned above. Which decreasing the Mach number up to M=11.0 (profile 2), on the curve there appear weak perturbations arranged at the same distance along the time axis. Note that the effect appears simultaneously in all region of the flow: as in the zone of relaxation as in the region of radiation cooling. With this, the amplitude of perturbations of $\Delta n_e(x)$ is the same independent of their position on the curve. On profile 3 (M=10.5) the further development of unstability effect is shown. In argon while changing relative concentration of molecular micro-admixture

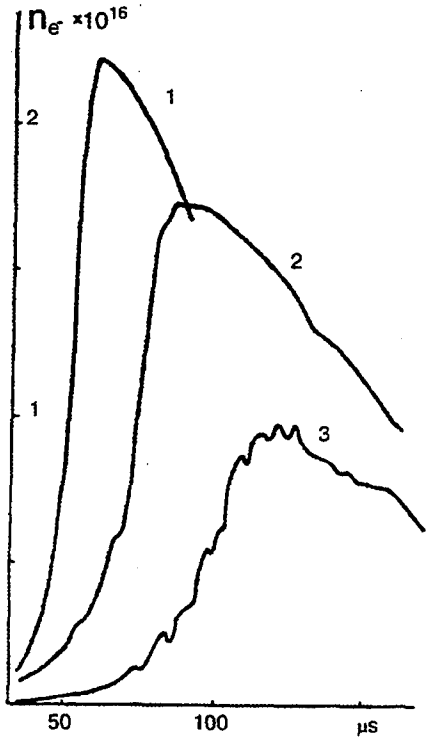

Fig. 5. Profiles of $n_e(x)$ in argon. IR-interferometer, λ=10600 nm, p_o = 5 torr, air admixture $\xi=4\cdot10^{-5}$ in per-unit: 1: M=11.5; 2: M=11.0; 3: M=10.5.

from 10^{-3} up to $4\cdot10^{-5}$ the frequency of the "peaks" following on the profiles of electron concentration with M≈10.5 is not changed. It is equal approximately 140 kHz.

The phenomenon amplitude achieving 40% of equilibrium value of ionization, the presence of limit of then effect along the velocity of shock wave and the strict periodicity of the phenomenon do not allow to explain the unstability by the influence of boundary layer on the wall behind the shock wave front. The appearance of the I kind unstability good correlates with the fulfillment of the condition of the equation of velocities of the radiation decay of 4p states in argon, and 6p states in xenon with the velocity of devastation of these exited states by the shocks of the second kind with electrons in equilibrium zone of the flow[9]. Besides that, while investigating the xenon plasma radiation intensity in two mutually perpendicular directions in one measuring cross section the identical signals were obtained[7]. At the expense of the data[8] it allows to assert that in the region there appear plane layers of electron concentration analogous to the strata in gas discharge. All this points out to the appearance of volumetric structure, changes in the flow having kinetic nature. The most likely the nature of anomalous behavior of relaxation zone of the flow is connected with self-organization of non-linear open systems. Concrete starting mechanism forming the structure may be the generation of overheat radiation of shock heated plasma. Characteristic properties of this mechanism are fixed in the ex-

periment[3]. Resent discovery[13] of the charp decrease of the coefficient absorption of the transition 5d-6p in xenon in relaxation zone of the flow counts in favour of the last thesis.

4. Conclusion.

The dynamics of the changing of the degree of I kind unstability development in argon and xenon from the Mach number of shock wave. While moving apart on the velocity scale from optimal velocity (for the effect development) the unstability amplitude smoothly decreases. The unstability stops to develop as in argon as in xenon while going over the optimal velocity in the each gas I Max. The results obtained are outside of the frames of classic representation [1,2] about kinetic ionization of one atom gases in shock wave.

I would like to thank Dr. Tumakaev G.K. for many fruitful discussions. I wish to thank the Russian Fund of Fundamental Investigations (Grand 94-01-01331-a) and the International Fund "Culture Initiative" (Soros Fund) for their financial support.

Refrences

1. Oettinger P.E., Bershader D.A. AIAA J. (1967) - V.5 - №9 - p.1625-1632.
2. Zeldovich Ya.B. and Raizer Yu.P. Physics of Shock Waves in High-Temperature Hydrodynamic Phenomena. Academic, New York (1966).
3. Tumakaev G.K. in Coll. High-Temp. gas-dynam., shock tubes and shock waves. ed. by Soloukhin R.I., (Russian), Minsk (1983). p.154-160.
4. Jacoby Yu.A., Grigor'ev P.V., Malov A.N., et all. J. Quant. Electr. (1985) - V.12 - №2 - p.351-354. (Russian)
5. Grigor'ev P.V., Krasnikov Yu.I., Rudnitsi A.L., Jakovlev V.I. in Coll. Laser beams: Distribution in medea and control for parameters. Habarovsky Polit. Inst., (1985), p.96-100. (Russian)
6. Grigor'ev P.V. in Coll. Modeling in Mechanic, ITAM SB of RAS, Novosibirsk, (1988) - V.2 - №6 - p.25-30. (Russian)
7. Tumakaev G.K., Stepanova Z.A. J.Tech. Phys. (1989) - V.59 - №6 - p.194-196. (Russian)
8. Tumakaev G.K., Stepanova Z.A., Grigor'ev P.V. J.Tech. Phys. (1991) - V.61 - №9 - p.149-152. (Russian)
9. Tumakaev G.K., Stepanova Z.A.. J.Tech. Phys. (1982) - V.52 - №11 - p.2305-2307. (Russian)
10. Jakovlev V.I. Ph.D. Thesis, ITAM SB of RAS, Novosibirsk, (1980) (Russian)
11. Kozlov G.I., Roytenburg D.I., Stupitski E.L. J.Tech. Phys. (1972) - V.42 - №9 - p.1886-1893. (Russian)
12. Zagorski A.V. in Coll. Modeling in Mechanic, ITAM SB of RAS, Novosibirsk, (1988) - V.2 - №6 - p.39-43. (Russian)
13. Tumakaev G.K., Stepanova Z.A.,D'jakov B.B. J.Tech. Phys. (1992) - V.62 - №11 - p.25-31. (Russian)
14. Grigor'ev P.V. in Coll. Kinetic and gasdynamic processes in non-equilibrium media. by ed. A.M. Prokhorov, Moskow, University (1986) - p.100-101, (Russian).

HOLOGRAPHIC INTERFEROMETRIC STUDY OF TRANSITION OF REFLECTED SHOCK WAVES IN A DIAPHRAGMLESS SHOCK TUBE

Ji-ming Yang and Kazuyoshi Takayama

Shock Wave Research Center, Institute of Fluid Science,
Tohoku University, Katahira 2-1-1, Aoba, Sendai 980, JAPAN

ABSTRACT

A holographic interferometry was applied to visualize shock reflection in a diaphragmless shock tube. This shock tube utilizes a re-usable rubber membrane to seal the high pressure and low pressure sections and can generate shock waves with much better repeatability than conventional shock tubes. The reflection of a shock wave over wedges of inclination angle ranging from 3° to 55° and incident shock Mach number between 1.02 and 1.65 were well visualized.

The visualization results of the transition between regular reflection and Mach reflection are presented. The transition of reflected shocks from von Neumann Mach reflection through simple Mach reflection to regular Mach reflection was discussed in this paper.

INTRODUCTION

When a plane shock encounters a wedge, either regular or Mach reflection occurs over the wedge surface: regular reflection where the incident and reflected shocks meet on the wedge surface; and Mach reflection in which the incident and reflected shock intersect at a point above the wedge surface. Although these phenomena have been studied for more than three decades, problems still remain unsolved. In the case of Mach reflection of weak shock waves, for example, the experiments and the von Neumann three-shock theory[2] do not agree[3]-[7]. One possible explanation for this disagreement is interpretation of the shape of triple points, yet insufficient experimental observations are available to date. In this paper, a result of experiment using high repeatability shock tube suitable for weak shock research was reported.

EXPERIMENTAL METHOD

The overall shock tube configuration is shown in Fig. 1. A 60 mm× 150 mm low pressure channel is inserted into the high pressure chamber whose diameter is 290 mm. A 0.5 mm to 1.0 mm thick rubber membrane, bulged by an auxiliary high pressure, separates the driver and driven gases. Instead of rupturing conventional diaphragms, by suddenly venting the auxiliary high pressure gas bulging the rubber membrane, the rubber membrane recedes so quickly as to allow the driver gas to flow into the low pressure channel thus creating a shock wave in relatively short formation length. The rubber membrane is operated within its elastic limit and

moves very fast, giving a good repeatability. The scatter of shock Mach number was found to be less than 0.2% from shot to shot and less than ±0.25% for several hundred runs[8].

Figure 1 shows a schematic diagram of the holographic interferometry system. The arrangement is based on a conventional shadowgraph layout with the addition of the reference beam. The path length of object and reference beam are as close as possible to equal length. Finally the image of the test section is focused onto a holographic film. A double pulse ruby laser (Apollo Lasers Inc. 22DH, 25 ns pulse duration and 2J/pulse) is used as light source. The resolution of the holographic film (100 mm×125 mm sheet films AGFA 10E75) is given as 3800 lines/mm. An Argon Ion laser (514.5 nm wave length and 1 watt) is used for the reconstruction.

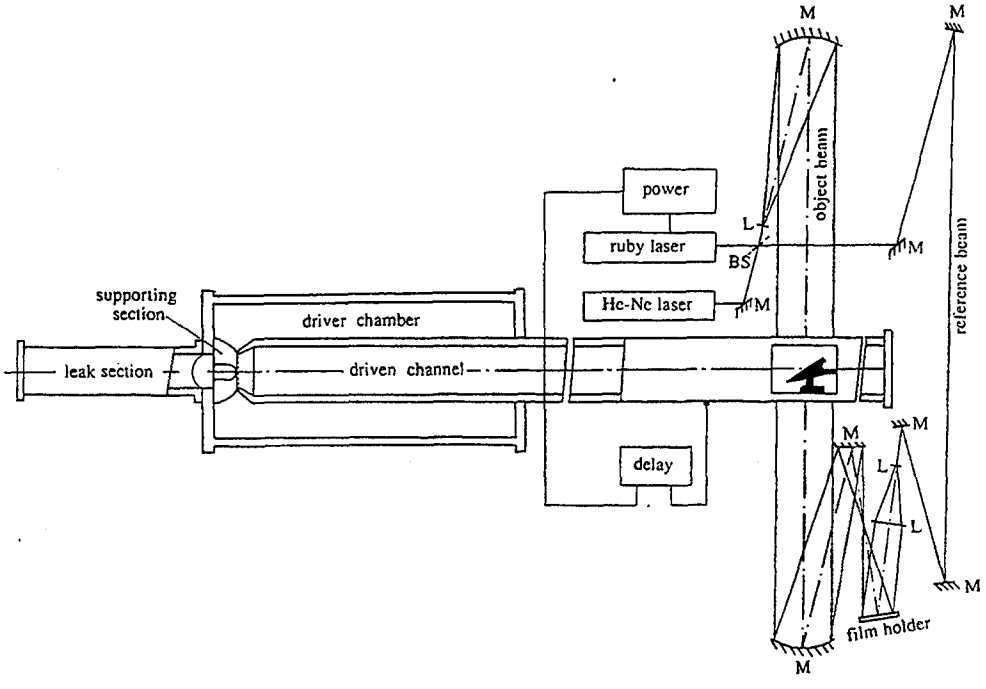

Fig.1 Experimental setup.

Nitrogen was used as driver and test gas for all cases. Mach numbers tested were Ms=1.02, 1.05, 1.10, 1.20, 1.38 and 1.65 with the scatter of shock Mach number within ± 0.002 throughout about 20 runs in each case

RESULTS AND DISCUSSIONS

The holographic interferograms for the reflection of a shock wave of Ms=1.10 are shown in Fig. 2. When the inclination angle of wedges is small, say, less than about 17° , the pattern of reflection appears to be different from the typical Mach reflection. In this case, the incident shock and Mach stem intersect with zero angle and no distinct triple point is formed as shown

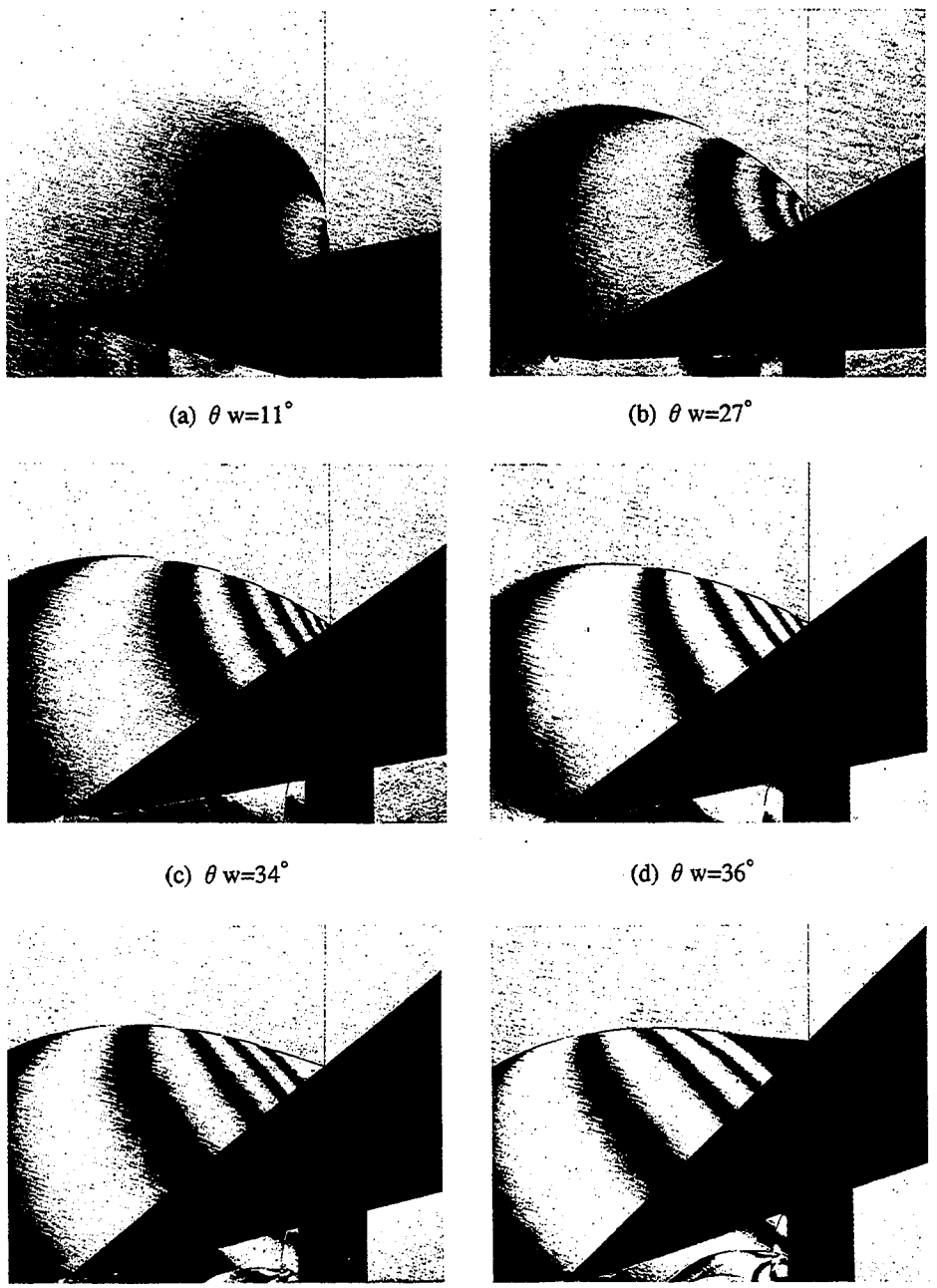

(a) θ w=11°　　(b) θ w=27°

(c) θ w=34°　　(d) θ w=36°

(e) θ w=39°　　(f) θ w=43°

Fig.2 Holographic interferogram of the reflection of shock wave at wedges. Ms=1.10, θ w: inclination angle of wedge.

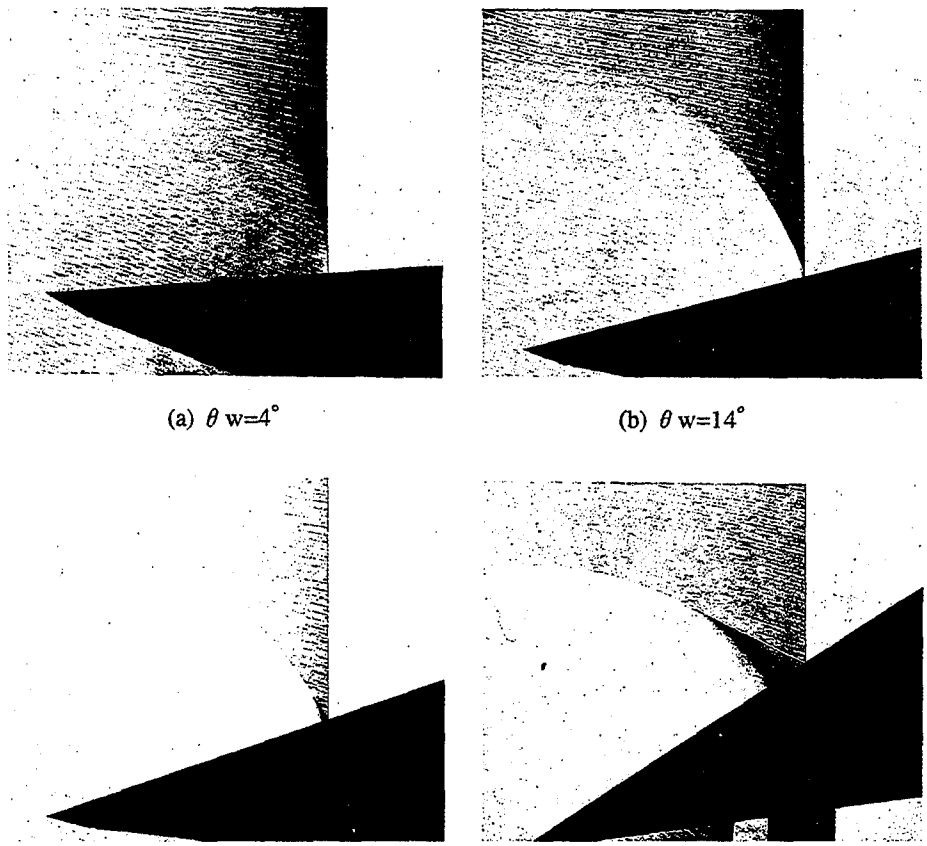

(a) θ w=4°　　(b) θ w=14°

(c) θ w=18.5°　　(d) θ w=32°

Fig. 3 Holographic interferogram of the reflection of shock wave at wedges. Ms=1.02, θ w: inclination angle of wedge.

in Fig. 2(a). Such a reflection pattern was known as von Neumann Mach reflection[9),(10)]. Sasoh et al. [11] has revealed that the local curvature along the incident shock and the Mach stem has a maximum point, and the point of maximum curvature does not coincide with that of the intersection of the incident shock and Mach stem. As the θ w increases, the maximum curvature point and the intersection point tends to coincide to form a discontinuity triple point, which is simple Mach reflection as shown in Fig. 2(b). With further increase in θ w, Mach reflection is terminated and regular reflection appears. Due to the good repeatability of the shock tube, it is possible to make a detailed examination of the reflected shock transition between regular and Mach reflection. Figs 2(c) and 2(d) show the Mach reflection and regular reflection, respectively, close to the critical transition. Figures 2(e) and 2(f) show regular reflections somewhat larger than the critical transition angle. In the vicinity of the reflecting

point, there is a local supersonic uniform flow region in both cases. The number of fringes behind the reflected shock increases as the θ w increases towards the critical transition point, but decreases with increasing θ w after the transition to the regular reflection, which means that the largest variation of density behind the reflected shock is near the critical transition angle between regular and Mach reflection. This was true for all the cases of the present work except for Ms=1.02, where the number of fringes was insufficient for examination.

Figure 3 shows the holographic interferograms of the reflection of a shock wave for Ms=1.02. For such a weak shock reflection and small θ w, the curved Mach stem, as Sasoh pointed out, tangential to the incident shock at the intersection point as shown in Figure 3(a). When simple Mach reflection is formed at larger θ w, no slipline can be observed near the intersection point between incident shock and Mach stem as shown in Figure 3(b). No appearance of the slipline was also noted in the case of Ms=1.05. Figure 3(c) shows the regular reflection on the wedge close to the θ wcrit. For larger θ w, the region just behind the reflection point is either sonic or supersonic in the frame of reference attached to the reflecting point. In the latter case, a supersonic uniform region near the reflecting point appears to which the disturbance generated by the leading edge can reach as shown in Fig. 3(d)

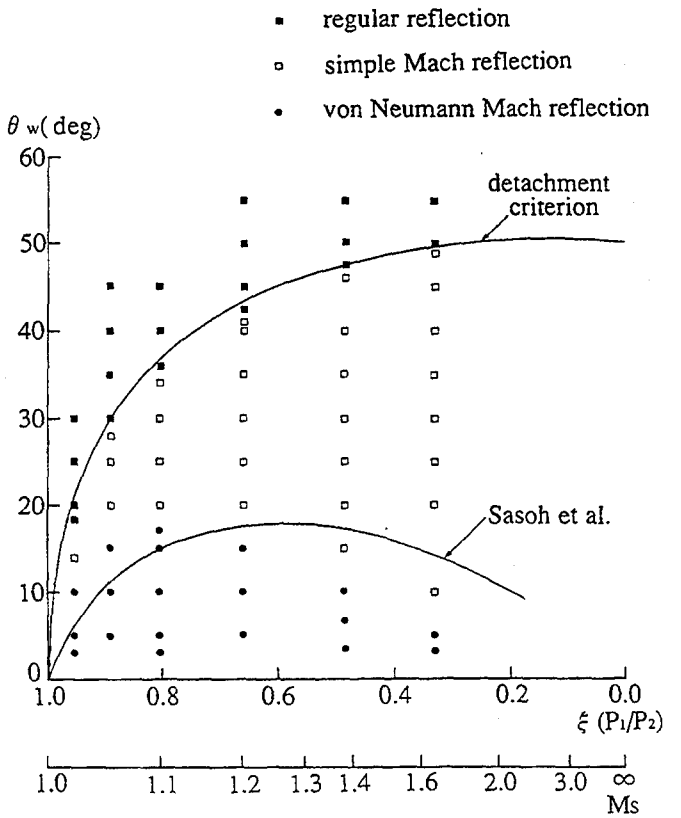

Fig.4 Comparison of the experiments and theories.

The variation of the reflection pattern which depends on the θ_w is shown in Fig. 4. An analytical prediction for the transition between regular and Mach reflection is given based on the detachment criterion. A criterion of the transition from von Neumann Mach reflection to simple Mach reflection was proposed by Sasoh et al. [11] , who tried to interpret the problem by introducing a concept of disturbance propagation. In the cases of Ms=1.38 and 1.65, the agreement between the experiments and the detachment criterion was good, while for weaker cases the experimental critical transition angles are somewhat below the theoretical results and the discrepancies between them are attributable to the existence of the boundary. As for the transition between von Neumann Mach reflection and simple Mach reflection the agreement between Sasoh's prediction and the present experiments is also reasonable.

For Ms between 1.02 and 1.65, the prediction of regular reflection based on the von Neumann two-shock theory[2] agrees fairly well with present experimental results, but three-shock theory fails to predict Mach reflections correctly for small inclination angle of wedges especially for weak shock cases. There are several possible explanations for these disagreements. The effect of the corner signal causes a partial deviation from the self-similarity assumed by the three-shock theory; the change in curvature near the triple point region causes non-uniform flow to which three-shock theory defines a discontinuous triple point. The real mechanism is not yet clear, but many evidences emphasize the importance of the careful visualization of the flow field behind the shock. By using holographic interferometry method, together with high repeatability shock tube, we hope to make further progress in the near future.

CONCLUSIONS

The shock reflection over a wedge has been examined in detail using a shock tube with a high degree of repeatability. By changing the wedge angle and maintaining a constant shock Mach number between different experiments, the variation of shock reflection configuration from von Neumann Mach reflection through simple Mach reflection to regular reflection was observed. This investigation was performed for the shock waves of Mach number Ms=1.02, 1.05, 1.10, 1.20, 1.38 and 1.65.

For the transition between regular and simple Mach reflection, the agreement of the experiments with the detachment criterion is good. For the transition from von Neumann to simple Mach reflection, the prediction given by Sasoh[11] agrees reasonably with the experiments. The largest variation of density behind the reflected shock was found to occur for wedge angles near the transition between regular and simple Mach reflection. The appearance of slipline in simple Mach reflection was observed for the cases of Mach number higher than 1.10, while no slipline were detected for the cases of Mach number lower than 1.05.

ACKNOWLEDGMENTS

The authors would like to express their thanks to Messrs. O. Onodera, H. Ojima and T. Ogawa

of the Shock Wave Research Center, Institute of Fluid Science, Tohoku University for their assistance in conducting the present experiments.

REFERENCES

(1) Mach, E, (1878) Stzungsbr. Akad. Wiss. Wien, Vol. 78, 819.

(2) von Neumann J (1943) Oblique reflection of shocks. Explosive Research Report No. 12. Navy Dept, Bureau of Ordnance, Re2C, Washington, DC

(3) Henderson LF, Siegenthaler A (1980) Experiments on the diffraction of weak blast waves: the von Neumann paradox. Proc R Soc Lond A 369:537-555

(4) Henderson LF, Gray PM (1981) Experiments on the diffraction of strong blast waves. Proc R Soc Lond A 377: 363-378

(5) Dewey JM, McMillin DJ (1985) Observation and analysis of the Mach reflection of weak uniform plane shock waves. Part 1, Observations. J Fluid Mech 152:49-66

(6) Dewey JM, McMillin DJ (1985) Observation and analysis of the Mach reflection of weak uniform plane shock waves. Part 2, Analysis. J Fluid Mech 152:67-81

(7) Olim M, Dewey JM (1992) A revised three-shock solution for the Mach reflection of weak shocks (1.1<Mi<1.5) Shock Waves. 2: 167-176

(8) Yang J, Onodera, O and Takayama, K, (1994) Design and performance of a quick opening shock tube using a rubber membrane for weak shock wave generation. JSME Journal (in Japanese) Vol. 60, 473-478

(9) Collela P, Henderson LF (1990) The von Neumann paradox for the diffraction of shock waves. J Fluid Mech 213:71-94

(10) Ben-Dor G (1991) Shock wave reflection phenomena. Springer-Verlag, New York

(11) Sasoh A, Takayama K (1992) A weak shock reflection over wedges. Shock Waves. 2: 277-281

Propagation of Shock Wave over a Wedge

Le Jialing, Li Chao
Wu Xingyan, Yang Hui, Ye Xichao
China Aerodynamics Research and Development Center
P. O. Box 211, Mianyang, Sichuan, China

ABSTRACT

This paper reports the results of experiments and computations on the unsteady diffraction process of shock wave passing through a wedge corner at incident shock wave Mach number of 1.8. The experiments were conducted in a shock tube with test section of $32 \times 32 mm^2$ using double exposure holographic interferometry. The experimental data includes holographic interferograms frame by frame and one frame with isopycnics. The flow fields were computed by using thin-layer approximated Navier-Stokes equations with second order ENO schemes. The computed results are in good agreement with the experimental results and clearly indicate the complicated shocks, slip layers, vortices and their interactions.

1. INTRODUCTION

The problem of propagation and diffraction of shock wave past solid bodies has been investigated extensively in the past, both experimentally and computationally as it is related to some important engineering problems, such as protective constructions, the design of flight vehicles. In addition, from viewpoint of fundamental flow phenomena, several aspects of this problem, such as shock diffraction, vortex formation resulted from shocks passing sharp corner, shock-vortex interactions are still rather complicated and difficult to have a profound understanding. Therefore, further investigating both experimentally and computationally will be of great value in sight to these fundamental phenomena. With regard to the shock wave reflection from wedge, H. M. Glaz and I. I. Glass[1] examined a number of shocks with various strengths, impinging on wedges of various angles, and investigated the effects of shock Mach number and wedge angle on the type of reflection. The direct comparisons were also made for fifteen basic cases of oblique shock wave reflections between interferometric and numeri-

cal results. With regard to the diffraction of shock wave passing around corners, I. I. Glass[2] conducted experiments of incident planar shock interacting with the downstream half-diamond obstacle, and offered a direct comparison between experimental and numerical results. At the same time, K. Takayama[3] briefly reported the research results from twenty six papers on a bench mark problem of 2-D planar shock wave diffration over a 90° degree sharp corner. Now the investigation on interactions of shock waves with vortex is very active, some research progresses were described by S. Silver[4]. Numerical simulations were performed by using the conservative Finite Element Method-Flux Corrected Transport (FEM-FCT) scheme and compared with previous Schrdin' s shadowgraph results. In present paper, both experimental and computational researches on more complicated flow of 2-D diffraction of shock wave (M_s=1. 8) passing over the wedge corner were considered, including the effects of shock reflected from shock tube wall and shock-vortex interactions as well as flow over the back step. Numerical simulations were carried out to solve the thin-layer approximated laminar N-S equations by using second order ENO scheme for the purpose of further confirming its capabilities of high-resolution nonoscillatory shock caputure of unsteady complex flowfields.

2. EXPERIMENTS

2. 1 Apparatus and Instrumentation

The experiments were carried out in a CARDC' s small shock tube with test section of 32mm × 32mm, which has two pairs of observation windows of 100mm × 32mm. The distance between windows is 400mm. The distance between the first window and the diaphragm is 6. 3m. The shock tube driver is a circular section with diameter of 70mm . The model (shown in Fig. 2)located in the first window is a 2-D wedge of 27° angle . The incident shock Mach number M_s can be precisely controlled by a plastic diaphragm specially made and high accuracy measurement of gas pressure in shock tube. Four transducers located at the upstream of test section are mounted on the wall of driven tube. The distances from the transducers to the model are different so as to measure the shock speed and to synchronize the ruby laser. The shock tube and the optical system of holographic interferometer are shown in Fig. 1.

For quantitatively measuring the density fields, the double exposure holographic interferometry was used. The light source is Apollo Lasers Inc. 22HT ruby laser of 694. 3nm wave length and 30 nsec pulse duration. The laser beam is divided into two

beams by a 3 : 7 beam spliter. The reflected beam passing through the test section is object beam which is changed into parallel light of 80mm diameter by lenses L3 and L4. The transparent beam, passing through the second observation window at the downstream of test section, is the reference beam which is changed into parallel light of 55mm diameter by lenses L1 and L2. Agfa 10E75 were used for recording medium and 6 inches Gong Yang film for reconstruction. Double exposures are required for the purpose of constructing a double exposure holographic interferogram. The first exposure is performed before the incident shock wave arrives and the second exposure is triggered at the moment just when the shock waves interact with the model. Consequently, the phase difference recorded on the hologram between these two exposures generate the interference fringes corresponding to the isopycnics of the flowfields in an infinite fringe interferogram. By preseting different delay time (the precison is 1μs) of the trigger, the frame by frame holographic interferograms, corresponding to the unsteady process of shock diffraction can be obtained. The density difference $\triangle\rho$ between the two adjacent fringes of same color is related to the wave length λ of the light source (694. 3nm)and the Gladstone-Dale constant K (0. 225cm^3/g) and is expressed by the relation $\triangle\rho=\lambda/KL$, where L is the width of the test section of 3. 2cm. The density corresponding to the fringe number N in an infinite fringe interferogram is $\rho_N=\rho_0+N\triangle\rho$, where ρ_0(38. 5×10^{-5}g/cm^3, in present condition)is the gas density in the test section.

2. 2 **Results and Discussion**

2. 2. 1 According to present conditions of wedge and incident shock Mach number, the flow is a typical single Mach reflection comprising the initial shock wave of Mach reflection (B), slip layer (C) and Mach stem(D) (shown in Fig4. a). In all Figues , $t=0$ is set at the moment just when the Mach stem (D) arrived the wedge corner. The Mach stem (D) has diffracted around the corner, forming an expansion fan and a diffracting shock (D). Meanwhile, the vortex layer has rolled up in a closewise manner, effectively becoming a single vortex (E). In addition , the weak slip layer(F)appeared (shown in Fig. 4b, 4c, 4d, 4e). Comparison of Fig. 4c , Fig. 4d and Fig. 4e shows that the slip layer(C)has an effect on the expansion fan. Fig. 4e shows that the shock wave (B)has reflected again off the top wall, thus reflected shock G has interactions with expansion fan and slip layer(C). It is obvious from Fig. 4f and 4g that the vortex has significant effect on the shock wave (G). At the begining , shock wave (G) is distorted a little as it approaches the vortex (E)(shown in Fig. 4f). Then the shock wave

(G)is slipted into three parts by the vortex(E)(shown in Fig. 4g). Its right half receives accelleration and its center is completely merged by the vortex(E). Fig. 4h indicates that the secondary vortex (J) has formed at the corner of back step and the shock wave (K) has been generated due to the reflection of shock wave (G) on the wedge surface. Comparison between the Fig. 4i, Fig. 4b and Fig. 4h shows that the vortex (E) is convecting downward and to the right (down stream). In the end, the vortex is disappeared (shown in Fig. 4i), which takes about 85μs from the vortex formation to its complete break.

2. 2. 2 **Quantitative measurements of density field**

In the simple diffraction of shock wave passing through the corner, quantitative measurements of density fields can be obtained directly from the holographam shown in Fig. 6, without relying on analytical considerations of three-shock theor for calculating the density of three regions near the triple point. The result of density field is shown in Fig. 6 .

3. NUMERICAL SIMULATION

3. 1 **Conservation equations and difference schemes.**

The conservation equations of 2-D thin-layer approximated Navier-Stokes equations in general coordinates (ξ, η) were applied to solve the present unsteady diffraction of shock around the wedge corner with the Strang-type dimensional splitting techniques:

$$Q_{jk}^{n+2} = L_\xi(\triangle t)L_\eta(\triangle t)L_d(\triangle t)L_d(\triangle t)L_\eta(\triangle t)L_\xi(\triangle t)Q_{jk}^n$$

The viscous terms (L_d) in conservation equations are approximated with conventional central difference. The convection terms (L_ξ and L_η) are approximated by Essentially Non-Oscillatory (ENO)schemes developed by J. Y. Yang[5]. As a class of TVD scheme can be developed into uniformly second order ENO schemes by only modifying the limiter functions, TVD can be easily reformed into ENO schemes for numerical calcuclation with higher resolution.

3. 2 **Results and discussion**

The model size and a non-uniform grid system as well as numerical domain are shown in Fig. 2. Using CFL=0. 5, the CPU time required to reach time t=89. 7μs is 72 hours on 486 personal computer. The computed results to simulate the frame by

frame holographic interferograms are shown in Fig. 3 and Fig. 5. The computed result , Fig. 3a is a simple Mach reflection. Comparison of the numerical and experimental isopycnics between Fig. 3a and Fig. 4a shows good agreement, including the location of primary shock (B) and slip layer (C) as well as Mach stem (D). Comparing the interferograms of Fig. 3 with the density contours in Fig. 4, the evolution of the diffraction of shock over the corner, including the positions of the diffraction shock (D), the vortex (E) and the reflected shock (G) as well as slip layer (C), can be quantitatively simulated in good accuracy by numerical calculation with second order ENO schemes. In addition, the weak slip layer (F) shown in fig, 3c, 3d and 3e and vortex (E)shock (G) interactions (shown in Fig. 3f, 3g) are also much clearly caputured. The density difference between region 1 and 3 shown in the Fig. 5, corresponding to the two fringes shift can be easily obtained from the computed density contour in Fig. 5.

4. CONCLUSION

4. 1 The evolution of the diffraction of shock wave passing through the wedge corner can be clearly visualized and quantitatively measured by present double expousure holographic interferometry.

4. 2 Computed density contours of the shock diffraction process at a time series demonstrate that the complicated unsteady flowfields, including shocks, slip layers, vortices and their interactions, can be simulated adequately by using the thin-layer approximated N-S equations with the second order ENO scheme.

REFERENCE

1. H. M. Glaz, P. Collella, I. I. Glass: A detailed numerical, graphical, and experimental study of oblique shock wave reflections. UTIAS Report No. 285(1986)
2. I. I. Glass, H. M. Glaz, J. P. Collins: Diffraction of planar shock waves over half-diamond and semicircular cylinders: An experimental and numerical comparison. 17th Inter. Sym. on Shock Waves. P. 240(1990)
3. K. Takayama, O. Inoue: Shock wave diffraction over a 90 degree sharp corner. Posters presented at 18th ISSW. Shock Waves. Vol. 1, Number 4, P. 301(1991)
4. S. Sivier, J. Baum: Simulations of shock wave generated vorticity. AIAA 91-1668.
5. J. Y. Yang and C. A. Hsu: High-Resolution, Nonoscillatory schemes for unsteady compressible Flows. AIAA. J. Vol. 30, No. 6, June, P. 1570(1992)

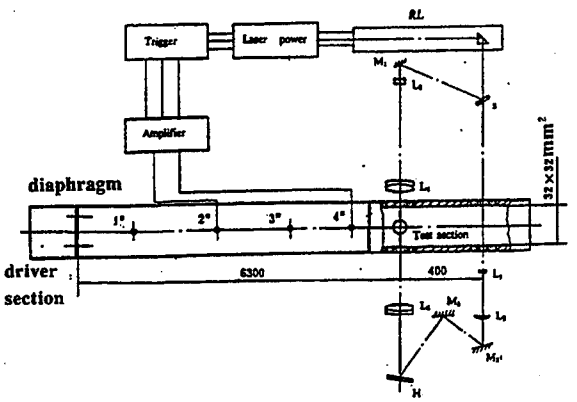

Fig. 1 Shock tube and holographic interferometer optical system

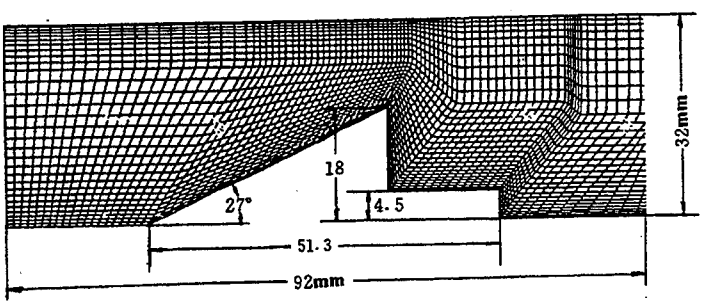

Fig. 2 Model size and grids (351×121)
M_s=1.8 Re=5.3×10^5

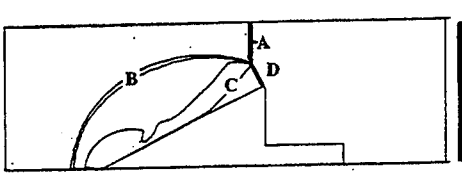

Fig. 3a Mach stem just arrives on the corner

Fig4. a △t=0μs

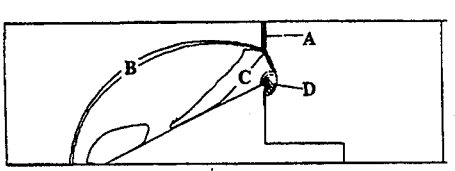

Fig3. b

Fig4. b △t=3.97μs

Fig. 3 Numerical calculation by ENO scheme

Fig. 4 Holographic interferograms

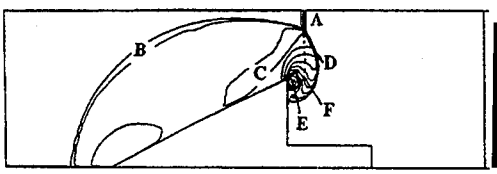

Fig3. c

Fig4. c $\triangle t = 12\mu s$

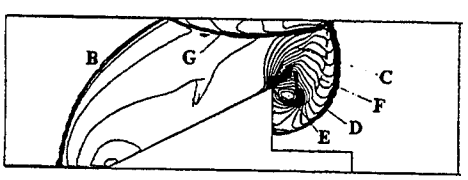

Fig3. d

Fig4. d $\triangle t = 22.1\mu s$

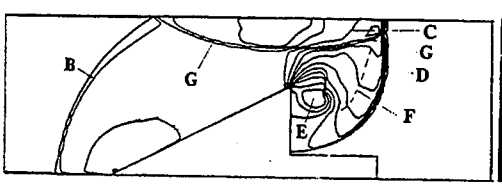

Fig3. e

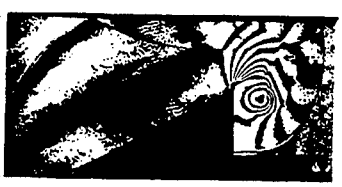

Fig4. e $\triangle t = 32\mu s$

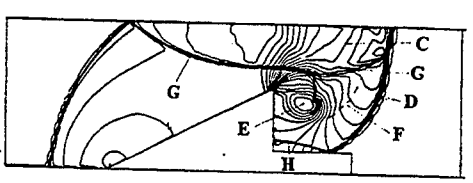

Fig3. f

Fig4. f $\triangle t = 36.90\mu s$

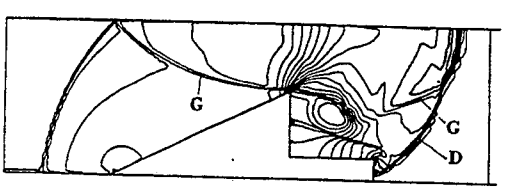

Fig3. g

Fig4. g $\triangle t = 44.88\mu s$

Fig. 3 Numerical calculation by ENO scheme

Fig. 4 Holographic interferograms

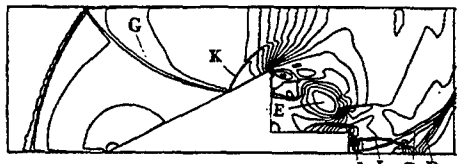

Fig3. h

Fig4. h $\triangle t=64.8\mu s$

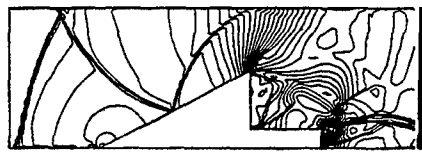

Fig3. i

Fig4. i $\triangle t=89.7\mu s$

Fig. 3 Numerical calculation by ENO scheme

Fig. 4 Holographic interferograms

A. incident sw(shock wave)
B. Initial Mach reflection sw
C. Slip layer
D. Mach stem of diffraction sw
E. Vortex
F. Weak slip layer
G. Sw reflected from upper wall
H. Sw reflected from back step
I. Sw from interaction between G and D
J. Second Vortex
L. Sw reflected from bottom wall by D.
K. Sw reflected from wedge surface by G.

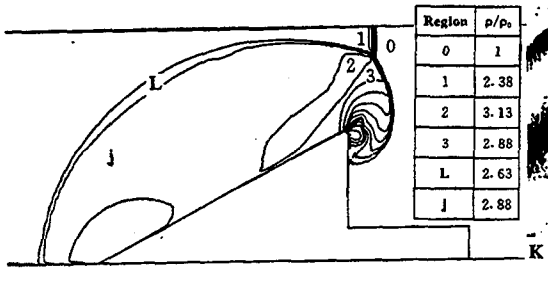

Region	ρ/ρ_0
0	1
1	2.38
2	3.13
3	2.88
L	2.63
J	2.88

Region	ρ/ρ_1
(0)	1.00
(1)	2.38
(2)	3.13
(3)	2.88
a	1.13
b	1.38
c	1.63
d	1.88
e	2.13
f	2.38
g	2.63
h	2.88
i	3.13
j	2.88
K	3.13
L	2.63

Fig. 5 Calculated density contours

Fig. 6 Holographic interferogram and measurement results
$M_s=1.80$ $T_0=285$ $P_0=32KPa$ $\gamma=1.4$ $\triangle t=12\mu s$

SIMULATED ACTIVE CONTROL OF SHOCK WAVES IN EXPERIMENTS ON AEROFOIL MODELS

P R Ashill, J L Fulker and M J Simmons
Defence Research Agency, Bedford, MK41 6AE, UK

ABSTRACT

The techniques used in wind tunnel experiments to ensure high-quality data for assessing predictions of CFD methods for aerofoils with shock-control devices are described. The experiments, performed in the 8ft x 8ft solid-wall wind tunnel at DRA Bedford, included measurements of surface static pressures and wake total and static pressures to give drag. The methods to ensure good repeatability of drag data and to determine tunnel-wall interference are described and results are presented of comparisons between the measurements and calculations by a CFD method for 'free-air' flows over aerofoils.

INTRODUCTION

The increase in strength of shock waves with Mach number or angle of incidence is a factor limiting the performance of aircraft. Increased shock strength leads to higher wave drag and, in more extreme cases, to flow separation. This problem is usually most severe on lifting surfaces such as wings. Thus the control of shock waves on wings has important implications for both military combat and civil transport aircraft.

Two main types of method have so far been developed for controlling shock waves. In the first, 'passive' technique a porous surface, beneath which there is a shallow plenum, is placed on the wing upper surface in the region where the shock wave is expected[1],[2] (Fig 1a). When a shock wave forms, the air from the region downstream of the shock flows, via the plenum, to the lower pressure region further upstream and then back downstream in the main flow. The flow displacement resulting from the surface transpiration induces compression waves which weaken the shock wave and hence reduce wave drag. However, this benefit has been found to be largely offset by increased boundary-layer drag due either to a 'roughness' effect of the holes and/or the flow through the surface[3].

This paper describes an experimental investigation in the 8ft x 8ft Wind Tunnel at the Defence Research Agency (DRA, formerly RAE) Bedford of a second, 'active' technique in which the displacement effect required to weaken the shock wave is provided (when needed) by either distorting or displacing the surface of the wing outwards into the flow (patent pending) (Fig 1b). The indications of calculations by the BVGK transonic-aerofoil CFD method[4] for aerofoils are that, with this technique, the reductions in wave drag are obtained without a significant penalty in boundary-layer drag[5]. The aim of the present study was to provide good quality experimental data for assessing the accuracy of BVGK and other CFD methods in their predictions of the effects on the flows over aerofoils of such devices.

After describing the experiment and the techniques used to ensure good quality data, the paper continues with a discussion of some comparisons between measurement and prediction by BVGK. Since BVGK is a 'free-air' method, particular emphasis is placed on the determination of wall corrections. The paper ends with some concluding remarks.

EXPERIMENT AND TECHNIQUES

Wind tunnel and models

The 8ft x 8ft Wind Tunnel is a continuous-flow, closed-circuit, tunnel with a working section having solid walls and of 8ft (2.44m) square cross section. The test Mach number range is from zero to 2.5, but excludes Mach numbers between about 0.95 and 1.3. Good control is provided of total pressure and there is adequate control of total temperature. Drying equipment is used to control the level of water vapour such that the frost point can be maintained to below 240K at all Mach numbers. The contraction ratio is 15.6:1.

Two aerofoil models with different sections (Figs 2) have been tested, one (RAE 5225, Fig 2a) with a classical 'turbulent' section, having a significant degree of rear camber, and the other a section suitable for a Natural Laminar Flow (NLF) wing (Fig 2b). Both sections were of 14% thickness/chord ratio. In each case the model spanned the working section (Fig 3) and was of 0.635m chord, giving a chord to working-section height ratio (c/H) of 0.26 and an aspect ratio A = 3.84. Model angle of incidence was adjusted by a mechanism adjacent to one side of the model, while the other end was free to rotate in a bearing, allowing the model to twist slightly under aerodynamic load. In both cases boundary-layer transition was fixed at 5% chord on both surfaces. For the first aerofoil section, this was achieved using the air-injection method[6], while, for the second, small glass spheres (ballotini) of diameter within the range 0.1mm to 0.13mm were stuck with epoxy resin to a strip of width 2.5mm.

Active control was simulated by various inserts placed in the aerofoil upper surface, as indicated in Fig 4. The geometries of these inserts are defined by the positions of their leading and trailing edges, made non dimensional by aerofoil chord, X_L and X_T, and their ordinates relative to those of the datum aerofoil, the maximum relative ordinate or amplitude as a percentage of aerofoil chord being written as h. For the 'turbulent' aerofoil (Fig 4), the inserts had fore and aft symmetry, being formed by a circular arc with leading and trailing edge positions $X_L = 0.4$ and $X_T = 0.6$. A number of amplitudes were studied, h = 0.125, 0.175 and 0.25. In order to save time, tests with the inserts were made with only the amplitude changed in the central 1.22m part of the span of the model, the amplitude being kept fixed elsewhere at h = 0.125. For the NLF aerofoil two types of inserts were tested as shown in Fig 3b, both of which are asymmetrical. The choice of asymmetrical insert was based on a previous theoretical study[5] which suggested that, for given leading and trailing edge positions, such inserts would be more tolerant of the movement of shock position with Mach number than symmetrical inserts. One of these inserts was formed from two circular arcs with zero slopes at the maximum amplitude, which was at 57.5% of its chord, and the other was triangular or of ramp form in shape, having its maximum amplitude at 75% of its chord. Both have $X_L = 0.485$ and $X_T = 0.685$ and h = 0.25. In each case, the shape of the insert was unchanged over the complete model span.

Geometric angle of incidence was measured by a digital encoder attached to the incidence-adjustment mechanism and the setting for zero incidence was determined by an electro-level meter. The accuracy of incidence measurement is estimated to be within $\pm 0.005°$. Both models were loaded in torsion to a maximum of 740Nm about their flexural axes prior to the wind-on tests to establish a calibration of the twist against applied pitching moment. For the 'turbulent' aerofoil, typical corrections to angle of incidence at mid span

for aerodynamic load are given in Ref 7. For the NLF aerofoil model, which was much stiffer than the other model, no change in angle could be detected, and no corrections have been applied to angle of incidence for aeroelastic distortion.

Measurements

Measurements included static pressures on the model as well as on the roof and floor of the working section on the tunnel centre-line, and some limited measurements were made of static pressures at two model stations either side of the centre-line (Fig 3). A wake rake, consisting mainly of total pressure tubes but also comprising some static tubes, situated about two chords downstream of the model trailing edge, was used to determine drag (Fig 3). The measurements were made using electronic scanning modules having a working range of ± 1.36 bar.

Owing mainly to the rapidity of the scanning of the pressures, good repeatability was achieved in the measurement of drag, typically within $\Delta C_D = \pm 0.0001$ at a chord Reynolds number of 19×10^6. Although good control of total pressure is achieved in the tunnel, considerable care had previously been necessary when electro-mechanical scanning was used to monitor the variation of total pressure during a scan to ensure a similar level of repeatability.

Corrections

a) Blockage

Two methods have been developed for determining blockage corrections in the 8ft x 8ft Tunnel. The first is of the type referred to as 'Wall Signature' methods[8]. The displacement effect of the model is represented by an axial distribution of sources or sinks, the distribution being taken from linear theory. The effects of the solid walls are represented by a double array of images sources[9] or a doubly-periodic Fourier series[10]. Using this method, calculations are made of velocity increments at two points on the roof at the centre-line of the tunnel and two points at the same axial and lateral positions on the floor. The axial positions of these points are chosen to coincide with pressure tappings located either side of the calculated position of the peak increment in velocity at the walls. For each test condition the value of the ratio of the blockage increment in axial velocity to the mean value of the velocity increments at the four points on the tunnel walls is determined. This ratio is then combined with measurements of pressure at the same points on the walls and referred to empty-tunnel conditions to give the blockage correction to Mach number, 'free-stream' static pressure and dynamic pressure. The corrected Mach number is then obtained by applying this correction to the measurement of the Mach number in the empty tunnel at the position normally occupied by the model, obtained from a prior calibration. It is considered that this approach is preferable to the alternative of determining Mach number directly from wall and reference static pressure tappings without reference to empty-tunnel conditions, since the present method takes account of the effect of the growth of the boundary layer in the empty tunnel and any imperfections in the wall pressure tappings.

The second method is of the 'Two-Variable' type[8],[11], which normally requires the measurement of two components of velocity at the walls. Since the walls of the wind tunnel are solid, use is made of the assumption that the normal component is zero. Strictly, this is

not correct because of the influence of the roof and floor boundary layers (in the presence of the model) on the inviscid flow in the wind tunnel. However, calculations allowing for this effect indicate that, for the test conditions of the present tests, this effect may be ignored, at least as long as wall interference is calculated using measured wall pressures as in both the methods described. To determine the streamwise velocity increment the method uses pressure measurements on the roof and floor of the working section (Fig 3), which, as before, are referred to empty-tunnel conditions.

Of the two methods, the second is expected to be more reliable since it needs no description of the flow near the model. On the other hand, the first method is the simpler to use and for this reason it is preferred, at present, for 'on-line' correction of data. Comparisons made between blockage corrections determined by the two methods for flows similar to those studied indicate that the 'Wall Signature' method gives corrections for blockage in good agreement with those of the 'Two-Variable' method[11].

b) Wall-induced upwash

Wall-induced upwash can be determined by the 'Two-Variable' method. However, it has been found that the method used for 'on-line' data reduction, which is based on linear theory and derives the sectional normal force needed in this theory from aerofoil pressure measurements, gives values of wall-induced upwash that are in good agreement with those from the 'Two-Variable' method.

Since the model is large (c/H = 0.26) and the tunnel walls are solid and straight, some consideration needs to be given to the variation of wall-induced velocities over the model. The variation of Mach number increment along the aerofoil chord has been found to be within acceptable limits[11]. Wall-induced upwash, on the other hand, can vary significantly along the chord depending primarily on lift coefficient[11]. For example, the variation of wall induced angle of incidence along the chord is as high as 0.5° when normal-force coefficient, C_N, and Mach number, M, are both equal to 0.7. This variation should be compared with the upper limit proposed in a study for AGARD[12], namely 0.03°. Consequently, a simple correction to angle of incidence is insufficient when comparing measurements with calculations made by 'free-air' CFD codes. Of course, the problem does not arise when comparing data with 'in tunnel' calculation methods. However, these methods have not yet reached as advanced a state of development as 'free-air' codes, and so an attempt has been made to allow for this effect when comparing measurement with predictions by the DRA 'free-air' CFD method BVGK[4]. The correction entails changing the camber of the aerofoil in the calculation in a way that corresponds to the calculated variation of upwash along the aerofoil chord[11]. Although raising some concerns about the validity of the comparison in absolute terms, it was considered that such a comparison would be valid for assessing the predicted differences due to active control.

c) Sidewall boundary layers

Although the effects of the boundary layers on the roof and floor are considered not to be significant for the flows studied, the effect of the interaction between the sidewall boundary layers and the model needs to be carefully assessed. Calculations by simplified methods of representing the interaction between the sidewall boundary layers and the model[13),(14)] indicate that the correction to Mach number for this effect is approximately

-0.001. However, more recent theoretical studies have shown that, while this correction is of acceptable accuracy for subcritical flows, the correction is likely to be much larger for transonic flows. Calculations have been performed by two different transonic-flow methods[15],[16] for a range of aspect ratios and for similar values of the ratio of wall boundary-layer displacement thickness, δ^*, to model semi-span, b/2, ratio to that of the present tests ($2\delta^*/b = 0.015$). It is interesting, therefore, to examine values given by these methods for the aspect ratio of the present tests A =3.84. Calculations made for the CAST 7 aerofoil[15] suggest that the Mach number correction is -0.006 at $M = 0.71$ and $\alpha = 2°$ while for RAE 5225, one of the aerofoil sections of the present study, a correction -0.005 has been calculated[16] for $M = 0.74$ and $\alpha = 2.1°$.

A correction of -0.005 to Mach number is large and, without it, poor agreement may be expected between two-dimensional aerofoil calculation and measurement. However, no explicit corrections have been made to the present data for this effect for four main reasons.

1) The roof and floor pressure tappings should sense virtually the same change in Mach number due to the sidewall effect as does the flow near the model at the tunnel centre line. Therefore the methods used for determining blockage should include some allowance for this effect. Typically, the ratio of blockage increment in Mach number to the Mach number sensed at the roof or floor is 0.4. Thus approximately 40% of the correction for Mach number due to sidewall effect is accounted for by the wall-interference correction procedure.

2) The indications of one of the transonic-flow theories for sidewall interference[16] are that improved correlation between two-dimensional theory and measurement would be obtained if a correction were made to angle of incidence as well as to Mach number. The required Mach number correction is then lower in magnitude. As shown later, the comparisons between the two-dimensional theory BVGK and experiment are made at a given normal-force coefficient, thus absorbing any correction to angle of incidence.

3) The values of Mach number corrections quoted above are for particular transonic flows using an approximate model of the sidewall boundary layer and are, therefore, only useful in providing an indication of the likely magnitude of the correction.

4) The main aim of the present study was to provide data to assess the ability of CFD methods such as BVGK to predict differences in aerodynamic performance due to active shock control. Therefore small errors in Mach number (say of the order of 0.002 to 0.003) should not be critical to the study, although there are possible exceptions as discussed later.

d) Hole-size errors

No corrections have been made to model surface static pressures for hole-size errors, but calculations based on the correlation provided by Shaw[17] indicate that a correction of $\Delta C_p \simeq -0.005$ is required over the forward 60% chord of the aerofoils for the cases to be shown in Figs 5 and 7. The corrections decrease in magnitude with chordwise distance further downstream.

TEST CONDITIONS

For both aerofoils, tests were made at the Reynolds numbers, based on chord, of 6

$x10^6$ and 19 x 10^6. The ranges of Mach number tested were 0.72 to 0.74 for the 'turbulent' aerofoil and 0.67 to 0.71 for the NLF aerofoil.

COMPARISONS BETWEEN CFD AND MEASUREMENT

Owing to space limitations, only a selection of comparisons can be shown, and so those presented are the ones which test to the full the ability of the code to predict the effects of active control. Other comparisons for the 'turbulent' aerofoil are given in Ref 18. As noted above, the calculations have been performed using BVGK, with allowance for wall-induced 'camber', and, in these calculations, ordinates obtained from detailed inspection, suitably interpolated to ensure a smooth and continuous surface, were used. All the comparisons are made for the maximum Reynolds number tested R = 19 x 10^6.

Figs 5 show pressure distributions for the 'turbulent' aerofoil RAE 5225 for M = 0.725 and $C_N \simeq 0.74$. Also shown are predicted and measured values of drag coefficient, C_D, and predicted values of wave drag coefficient, C_{Dw}. Results are shown for the datum case (Fig 5a) and for the aerofoil with the inserts h = 0.125 (Fig 5b) and 0.175 (Fig 5c). At this flow condition the insert with h = 0.175 gives a reduction in drag coefficient of about 0.0018, showing that active control is effective at this condition, while BVGK predicts a reduction of 0.0009, due entirely to a reduction in wave drag. In each case, BVGK gives broadly satisfactory predictions of the pressure distributions. However, the pressure distributions in the region of the shock wave are not represented well, BVGK underestimating shock strength both for the datum case and for h = 0.125. This may explain why BVGK underestimates the drag reduction between the datum case and the case with h = 0.175.

Comparisons between measured and predicted drag polars (ie drag coefficient versus normal-force coefficient) are shown in Figs 6, together with predictions of viscous-drag coefficient, C_{DV}. Here the experimental data have been interpolated to the common Mach number M = 0.725, the maximum difference between the test Mach number and the common Mach number being 0.002. For the datum aerofoil (Fig 6a) the agreement between prediction and measurement is generally good. However, where drag rises rapidly with lift, BVGK underestimates drag. Furthermore, for the insert aerofoils with h = 0.125 (Fig 6b) and h = 0.175 (Fig 6c), the agreement is much less satisfactory at normal-force coefficients just below that for the design value where the drag is a minimum at the drag 'bucket'. At these 'off-design' conditions the drag with the insert is larger than that of the datum aerofoil and BVGK predicts larger drag than that measured, the difference between prediction and measurement increasing as insert amplitude increases. The reason for these discrepancies is illustrated by insets in Figs 6b and c which show pressure distributions at these conditions. For the more downstream of the two shock waves on the upper surface, BVGK predicts shock strengths that, for both inserts, are of greater strength than that measured, the discrepancy being more apparent at h = 0.175 than at h = 0.125. Thus BVGK may be expected to predict larger wave drag than that measured. Reasons for these differences are not known but it is known that flows of this type are sensitive to small errors in Mach number. Thus the influence of the interaction between the model and the sidewall boundary layers may be significant for these flows. However, 'active' control would only be used when it provides drag reductions, and, at the design conditions, where control has a favourable effect on drag, BVGK predicts drag and normal-force coefficients accurately.

In Figs 7 are shown pressure distributions for the NLF aerofoil at M = 0.68 and C_N

= 0.75, without insert (the datum case) (Fig 7a), the asymmetric, circular-arc bump (referred to as the asymmetric bump) (Fig 7b) and the ramp bump (Fig 7c). The agreement between prediction and measurement is generally good except near the foremost sonic point, where it is possible that the (interpolated) representation of the ordinates obtained by inspection may not have been adequate. The predicted changes in drag between the datum and modified aerofoils are in good agreement with those of measurement, and, as with the case shown in Figs 5 for the 'turbulent' aerofoil, shock control is seen to have a favourable influence on drag.

Corresponding measured and predicted drag polars at the common Mach number 0.68 (Figs 8), are in reasonable agreement, although BVGK underestimates drag slightly at low lift. The most likely cause for this is the excess drag of the excrescence transition trip used with this model, which would not be present with the air-injection method[6] used with the other model. Nevertheless, the change in drag between the datum and ramp-insert configurations is accurately predicted over the range of normal-force coefficients, although the change in drag between the datum and asymmetric-insert cases is less well predicted. It will be noted also that, for the NLF aerofoil, there is no drag 'bucket', in contrast to the 'turbulent' aerofoil. The reason for this is that the shock wave of the NLF aerofoil moves only slightly with changes in normal force. On the other hand, the main shock wave of the 'turbulent' aerofoil moves rapidly to a position well upstream of the inserts as angle of incidence decreases below the 'design' value. Thus, for this aerofoil, the insert cannot influence the strength of this shock in these circumstances and, instead, creates a stronger second shock downstream of the main shock. For angles of incidence above the 'design' value, the main shock moves downstream of the insert.

CONCLUDING REMARKS

Wind tunnel experiments on aerofoil models, intended to provide data to assess the ability of CFD methods to predict the effects of on transonic flows of active shock-control devices, have been described. The techniques needed to ensure accurate assessment of wall interference have been discussed. No explicit allowance has been made for the effect of sidewall boundary-layer interference on free-stream Mach number, but any such effect is not expected to prejudice the assessment of predictions of favourable effects of active control. Limited results of comparisons between measurement have been presented. These comparisons indicate that BVGK gives generally accurate predictions of the effect of active control on pressure distributions and drag for flows where control is beneficial.

REFERENCES

1 Krogmann, P., and Stanewsky, E, "Transonic shock-boundary layer interaction control", Proceedings, 14th ICAS, September 1984, Toulouse, France, Paper No. 84-2.3.2 (1984).

2 Thiede, P., and Krogmann, P, "Improvement of transonic airfoil performance through passive shock/boundary layer interaction control", IUTAM Symposium Palaiseau 1985, Ed J Delery, Springer, Berlin (1986).

3 Reneaux, J., Thibert, J., and Schmitt, V, "ONERA activities on drag reduction", Proceedings 17th ICAS, September 1990, Stockholm, Sweden, Paper No. 90-3.6.2 (1990).

4 Ashill, P. R., Wood, R. F., and Weeks, D. J, "An improved semi-inverse version of the Viscous Garabedian and Korn (VGK) method" RAE Technical Report 87002 (1987).

5 Ashill, P. R., Fulker, J. L. and Shires, A. J, "A novel technique for controlling shock strength of laminar-flow aerofoil sections" Proceedings First European Forum on Laminar Flow Technology, March 1992, Hamburg, FRG, Paper No. 92-01-022 (1992).

6 Ashill, P. R., Fulker J. L., and Weeks, D. J, "The air injection method of fixing boundary-layer transition and investigating scale effects", The Aeronautical Journal, 91 pp 214-224 (1987)

7 Ashill, P. R., Weeks, D. J., and Fulker, J. L, "Wind tunnel experiments on aerofoil models for the assessment of computational flow methods" AGARD-CP-437, Vol 1 pp 4-1 - 4-14, December 1988.

8 Ashill, P. R, "Boundary-flow measurement methods for wall interference assessment and correction - classification and review", Paper 12 AGARD CP-535 October 1993.

9 Isaacs, D, "Calibration of the RAE Bedford 8ft x 8ft Wind Tunnel at Subsonic Speeds, Including a Discussion of the Corrections Applied to the Measured Pressure Distribution to Allow for the Direct and Blockage Effects Due to the Calibration Probe Shape", ARC R&M No. 3583 (1969).

10 Ashill, P. R, DRA unpublished work.

11 Ashill, P. R., and Weeks, D. J, "A method for determining wall-interference corrections in solid-wall tunnels from measurements of static pressure at the walls" AGARD-CP-335, pp 1.1 - 1.12, (1982).

12 Steinle, F., and Stanewsky, E, "Wind tunnel flow quality and data accuracy requirements", AGARD-AR-84, November 1982.

13 Murthy, A. V, "A simplified fourwall interference assessment procedure for airfoil data obtained in the Langley 0.3-Meter transonic cryogenic tunnel", NASA CR-4042, January 1987.

14 Ashill, P. R, "Effects of sidewall boundary layers on aerofoils mounted from sidewalls of wind tunnels - experimental evidence and developments of theory", RAE Technical Report 83065 (1983).

15 Archambaud, J. P., Michonnneau, J. F., and Mignosi, A, "Analysis of test section side wall effects on 2D aerofoils: Experimental and numerical investigation", Paper 26 AGARD FDP Symposium, Brussels October 1993.

16 Jones, D. J., Chan Y. Y., and Nishimura, Y, "A numerical and experimental evaluation of sidewall boundary-layer effects on aerofoils tested in wind tunnel facilities" Paper 44, Royal Aeronautical Society Conference on "Wind Tunnels and Wind Tunnel Test Techniques", Southampton September 1992.

17 Shaw, R, "The influence of hole dimensions on static pressure measurements", J. Fluid Mech. 7, 550, 1960.

18 Fulker, J. L, Ashill, P. R., and Simmons, M. J, "Study of simulated active control of shock waves on aerofoils", DRA Technical Report 93025, May 1993.

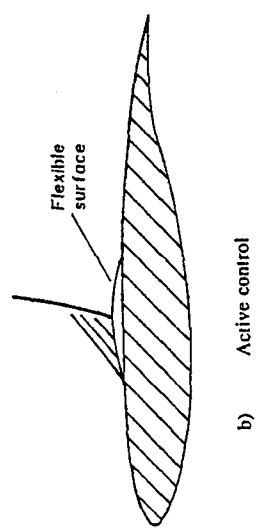

a) Passive control

b) Active control

Fig 1 Types of shock control

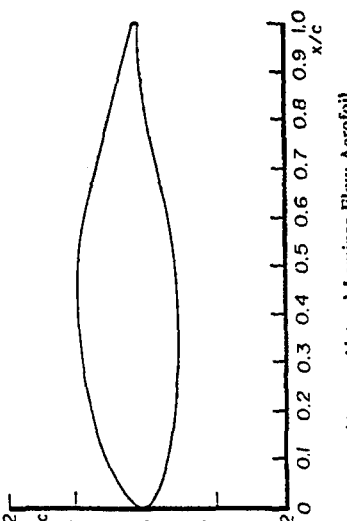

a) Classical 'Turbulent' Aerofoil RAE 5225

b) Natural Laminar Flow Aerofoil (NLF)

Fig 2 Model aerofoil sections

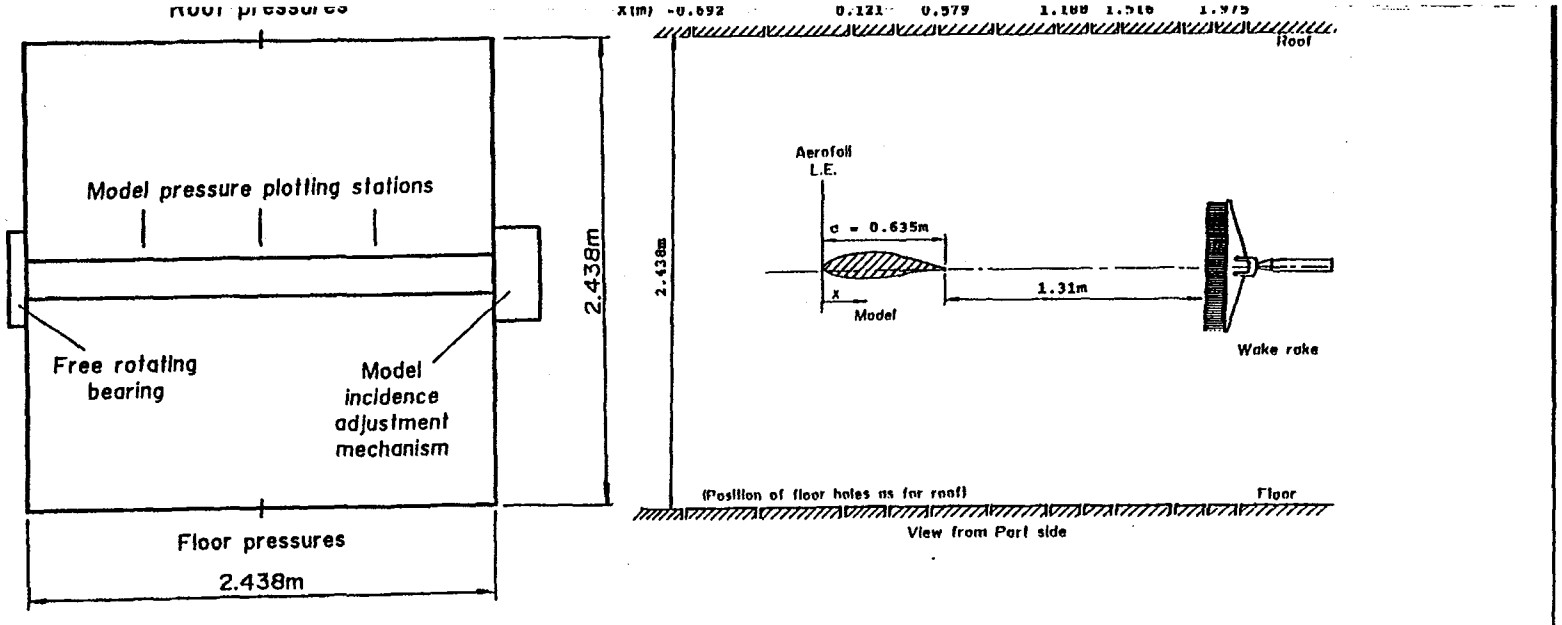

Fig 3 Layout of model in working section

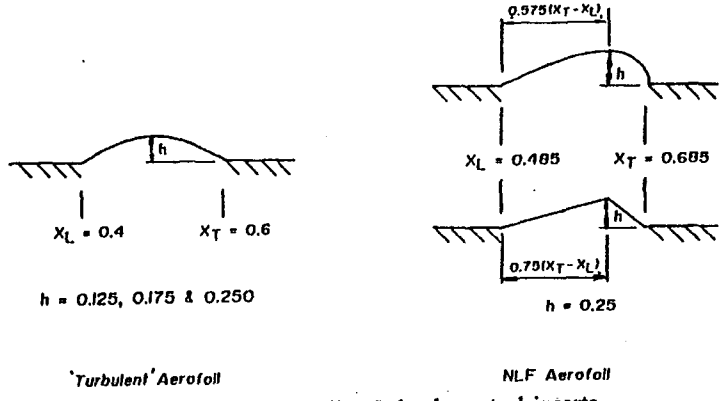

Fig 4 Details of shock control inserts

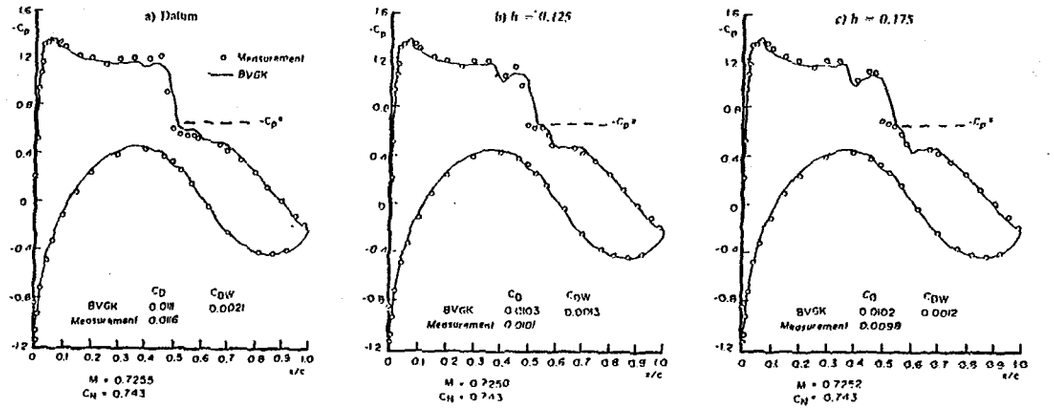

Fig 5 Pressure distribution comparisons, 'Turbulent' aerofoil
$M \approx 0.725$, $R_c = 18.75 \times 10^6$, $C_N \approx 0.74$

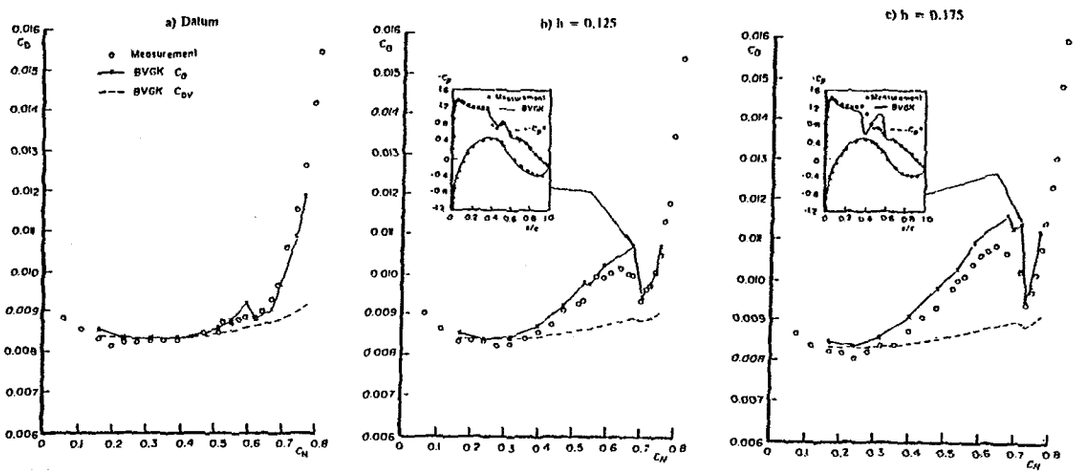

Fig 6 'Turbulent' aerofoil, drag polars
(Measurements interpolated to M = 0.725)

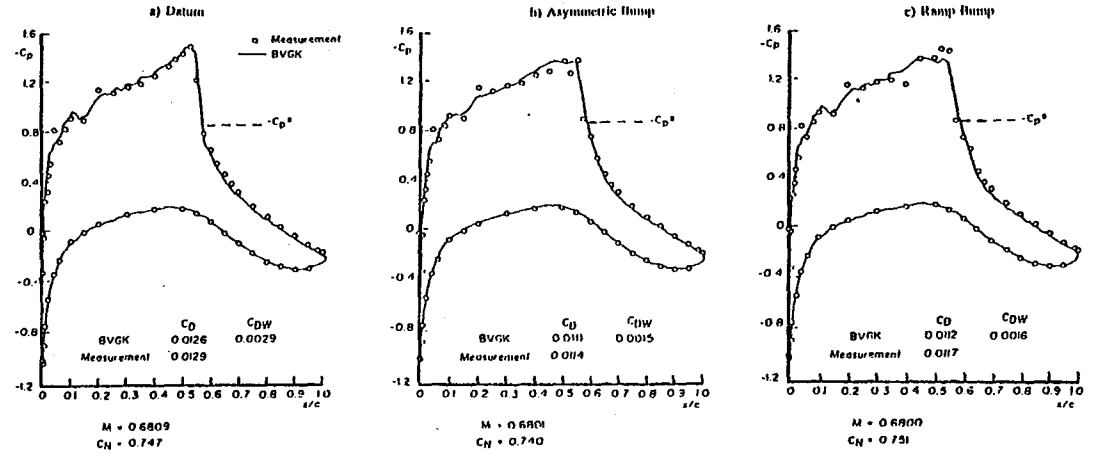

Fig 7 Pressure distribution comparisons, NLF aerofoil
$M \approx 0.68$, $R_c = 18.75 \times 10^6$, $C_N \approx 0.75$

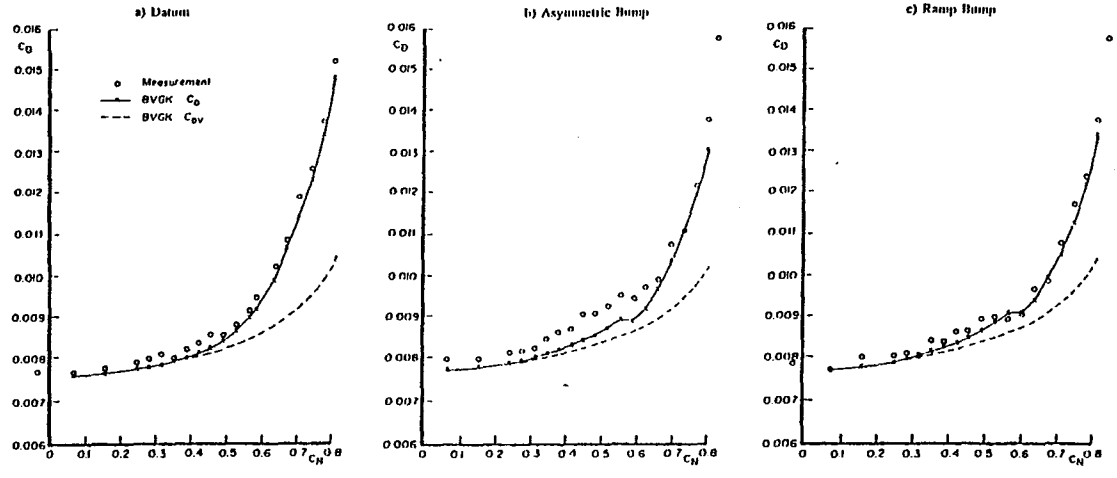

Fig 8 NLF aerofoil, drag polars
(Measurements interpolated to M = 0.68)

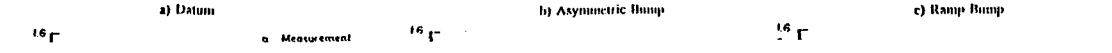

SOME FEATURES OF FLOW PAST MULTIBODY LAUNCH VEHICLES

B.N.DANJKOV,E.S.KORNIENKO,V.V.KUDRJAVTSEV,V.I.LAPYGIN
(Central Research Institute of Machine Building,
Aerogasdynamics Center,Kaliningrad,Moscow region,
Russia)

Multbody launch vehicle with parallel connection of stages (cluster configuration) are in considerable current use in rocket industry. As regards aerodynamics cluster configuration of stages arrangement is not "good". Aerodynamic characteristics of such configurations and aerodynamic loads acting on its elements are influenced significantly by interference among elements.The presence of channels between adjacent elements , variation of channels' shape along their length cause the appearance of local subsonic zones (at supersonic velocity of free stream) and supersonic zones (at subsonic velocity of free stream, and the occurence of shock waves in channels.Complex character has a flow in vicinity of nose parts of side blocks. The peculiarities of flow over multibody configurations are the most pronounced at transonic Mach number range (Moo = 0.7 - 1.3). Fig.1 presents typical flow patterns for launch vehicle "Energia" constructed with the use of oil flow visualization of surface streamlines and Schlieren flow pictures.

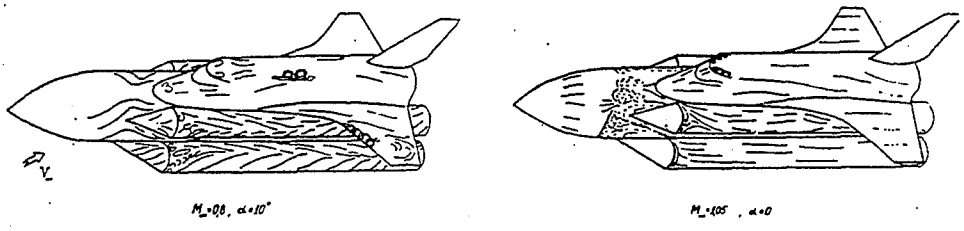

Fig.1. Typical flow patterns for "Energia" launch vehicle

Local Mach numbers Mi and local angles of attack α_i differ essentially from corresponding parameters of undisturbed flow. It was found, for instance, that local angles of incidence on the surface of the central core in region of nose parts of the strap-ons and the space vehicle reach practically 90° (Fig. 2), and the decrease of dynamic pressure in the channels - 20-50% in units of dynamic pressure of undisturbed flow. Location of numerous shock waves and boundary layer separation zones in flow field significantly depend on geometry of configuration elements (for instance, shape of nose parts of the strap-ons).

During the study of power spectral density of pressure fluctuations on the surface of multibody configurations of launch vehicle "Energia" type at Mach number range 0.7-1.2 in channels formed by the central core and strap-ons there were detected

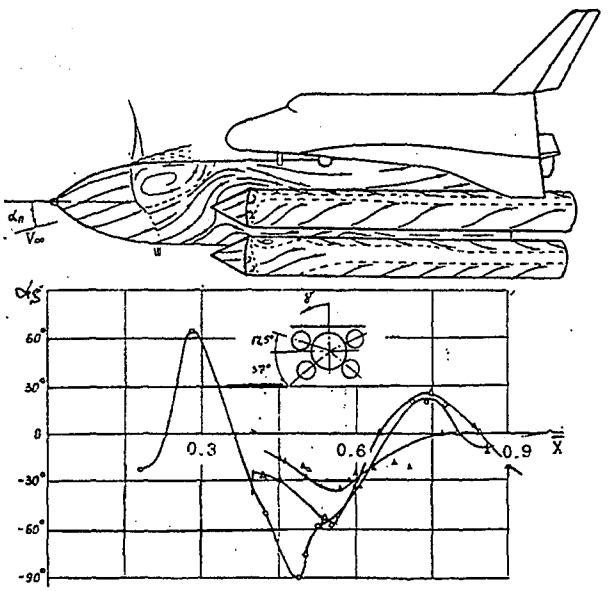

Fig.2. Variation of local flow incidence along central core generatrices with different meridian angles
○ M_∞ = 0.98, α = 10°, γ = 60°, conical strap-on noses
△ M_∞ = 1.1, α = 10°, γ = 35°, skewed strap-on noses
▲ M_∞ = 0.98, α = 10°, γ = 60°, skewed strap-on noses

narrowband maximums which exceed levels of broadband spectrum by 15-25 dB (Fig.3).Amplitude and phase distributions lengthwise had non-monotonous character, and oscillations had distinctly

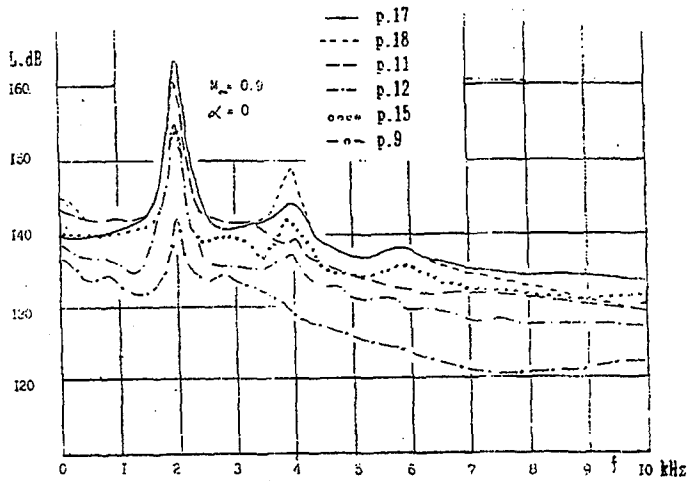

Fig.3. Power spectral density of pressure fluctuations measured at points along the channel formed by adjacent strap-ons and the central core.

resonance behaviour. This phenomenon was examined by flow visualization, measurements of distributions of averaged static and total pressures and mutual spectral characteristics of fluctuations. Fig. 4 presents a scheme of gas flow in the channel and a distribution of pressure coefficient Cp on the central core along the channel. Analysis has shown that at certain conditions (the presence of supersonic flow at the beginning of the channel.

its subsequent deceleration to subsonic speed in shock wave, and the occurence of separated zones) standing acoustic waves occur.

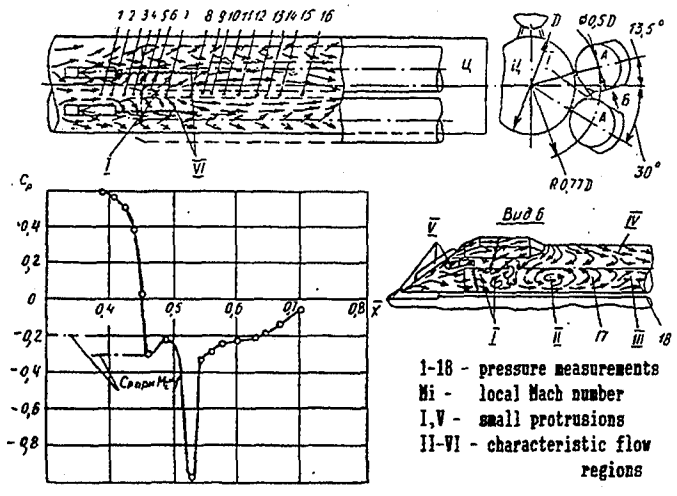

Fig.4. Flow patterns and pressure coefficient Cp distribution along the channel formed by adjacent strap-ons and the central core. $M_\infty = 0.9, \alpha = 0$

Theoretical model was developed which describes this phenomenon as a result interference of one-dimensional sound waves.

Suppose that in the channel we have

- direct wave with amplitude $P_1(x)$ and phase velocity $(c+v)$,
- reflected wave with amplitude $P_2(x)$ and phase velocity $(c-v)$,

v - flow velocity in the channel,

c - sound velocity,

f - frequency of oscillations,

L - length of the channel.

If $P_1 \approx P_2$ and there is an antinode at the beginning of the channel (source of oscillations) and a node at its end then

for direct wave

$$f_n = n \frac{c + V}{4L}, \quad n = 1, 3, 5, \ldots$$

for reflected wave

$$f_m = m \frac{c - V}{4L}, \quad m = 1, 3, 5, \ldots$$

where V - some average flow velocity; if v-const, V-v.

Frequencies f_n and f_m coincide ($f_{n,n} - f_n - f_m$) only if

$$V - V_{m,n} - c\,\frac{m - n}{m + n}\ .$$

Therefore resonance oscillations are excited at certain resonance flow velocities $V_{m,n}$; for each $V_{m,n}$ there is a spectrum of resonance frequencies: $f_{m,n}$; $f_{2m,2n}$; $f_{3m,3n}$; ...

For real conditions due to energy loss in the channel and existence of distributed disturbances resonance spikes are stretched and for V -> c discrete spectrum of resonance velocities becomes continuous. Distribution of resonance frequencies is uniform.

As tests show,an excitation of the first harmonic is the most likely

$$n - 1,\ f_1\frac{c + V}{4L}\ .$$

More higher harmonics quickly decay.

This model was used to estimate distributions of oscillation amplitudes and phases along the channel:

$$p(x,t)-P_1(x)\cos\left(\omega t - \frac{\omega x}{c + v}\right) + P_2(x)\cos\left(\omega t + \frac{\omega x}{c - v} + \Delta\right) - A(x)\cos[\omega t-\theta(x)],$$

where Δ - phase shift due to reflection conditions at ends of the channel and oscillation source location, $\omega=2\pi f$.

Amplitude of pressure oscillation

$$A(x)- \sqrt{P_1^2+P_2^2+2P_1P_2\cos\left(\frac{2c\omega x}{c - v} +\Delta\right)}$$

Phase of pressure oscillation

$$\theta(x) - \operatorname{arctg}\frac{P_1\sin\omega x/(c+v) - P_2\sin(\omega x/(c-v) + \Delta)}{P_1\cos\omega x/(c+v) - P_2\cos(\omega x/(c-v) + \Delta)}\ .$$

If P_1 and P_2 are weak functions of x then A(x) has minimums at

$$x_k = \frac{(2k+1) - \Delta}{2} \cdot \frac{c^2-v^2}{\omega c}, \quad k=0,1,2,\ldots$$

and maximums between points x_k and x_{k+1}.

There are discontinuities of phase function $\theta(x)$ near x. (if P_1-P_2 exactly at x_k). Between points of discontinuity the phase function monotonously decreases and approximately equals

$$d\theta/dx \approx -\omega v/(c^2-v^2).$$

So phase velocity Uf is negative:

$$Uf = \frac{\omega}{d\theta/dx} < 0 .$$

Above model has been used to interpret test data on distributions of phases and amplitudes of oscillations along the channel. Fig.5 shows experimental values of amplitude A, phase 0, and local Mach number Mi. Scale A is chosen in such a way that maximum value of amplitude corresponds to A-1. Using maximum measured value of A (x-0.64) as reference one, experimental values of Mi(x) and imposing that $P_1 - P_2$, dependencies A(x) and $\theta(x)$ were calculated. Then by shifting of calculated curves along x-axis through a selection of phase shift value Δ, which found to be equal 0.25 at n-4, the best agreement of calculated and test data was obtained.

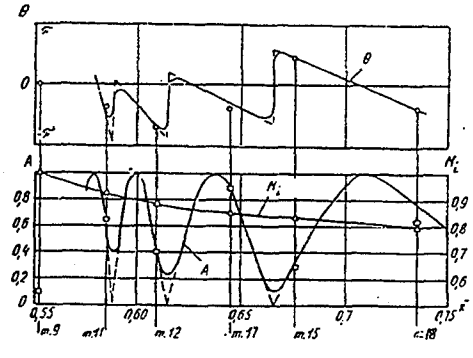

Fig.5. Distribution of local Mach numbers Mi, amplitudes A and phase θ of narrow-band pressure fluctuations along the channel. Moo = 0.9, α = 0
---- theory, o, Δ - test data, —— interpolation

It should be noticed that the calculation has used experimental values of amplitude and phase in one point only, and calculated curves have good agreement with other experimental points. Minimums of calculated curve A(x) and zones with phase $\theta(x)$ discontinuities were smoothed in order to take into account an attenuation of oscillations existing in tests(interpolation curve in Fig.5), which is expressed in the theoretical model by the distinction of amplitudes P_1 and P_2.

From the analysis of the flow in the channel and theoretical model of the phenomena it might be assumed that the key condition of the appearance of resonance oscillations is the occurence of a supersonic flow region followed by subsonic one at the beginning of the channel. Supersonic flow with shock wave behind is an ideal reflector of sound wave moving upstream.The end of the channel also reflects sound waves propogating downstream along a subsonic channel flow.The source of resonance excitation is turbulent vortex flow in the channel. A large separated zone, appearing in subsonic portion of the flow (see Fig.3), is the source of intensive fluctuations which are amplified in a resonance manner.

As free stream Mach number Moo changes,the location and the size of separated zone vary. Just non-monotonous character of the variation of the extent of separated zone explains the existence of such value of Mach number Moo when resonance oscillations are maximum. At Moo < 0.7 flow velocity in the channel is subsonic everywhere, i.e. there is no supersonic portion of flow in the channel. At Moo > 1.0 flow velocity in the channel is supersonic everywhere. In both cases there is no resonance process in the channel. Resonance process in the channel is rather responsive to the local variations of the channel geometry (curves 2 and 3 in Fig.6).

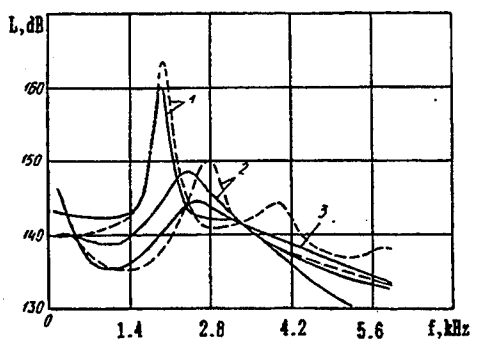

Fig.6. Influence of minor variations of the channel geometry(1,2,3) on power spectral density
——— - point 11, ----- - point 17

Apparently in this case we observed for the first time acoustic oscillations with extremely narrow resonancy peak in the resonator with such a "poor" geometry.

Insight of conditions of appearance of resonance process in the channel has allowed to derive effective means of its supression.

The presence of severe interference among elements of cluster configuration may be used for target-oriented variation of aerodynamic characteristics. One of the important parameters characterizing vehicle sophistication is an axial force coefficient which value in many respects determines payload weight. One practicable way to decrease value of axial force coefficient Cx is a selection of optimum (as regards mutual interference) position of configuration elements.

Fig.7, made from Schlieren pictures, shows position of shock wave and depression waves at Moo = 1.5 and α =0 which were observed in flows over launch vehicle "Energia" type cofigurations (1,3,5 - shock waves; 4,6 - depression waves; 2 - boundary layer separation). It is seen that the lower configuration has nose parts of space vehicle and lower strap-on located, unlike the upper configuration, in regions of depression, i.e. of reduced pressure, and coefficient Cx would be expected to decrease. So it is possible to vary to some extent the drag of a configuration by proper selection of mutual arrangement of its elements.

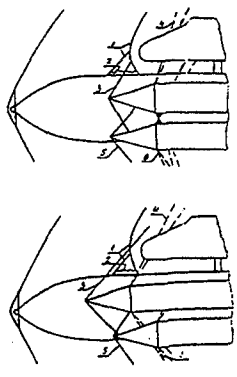

Fig.7

Test results are presented in in Fig. 9 for different modifications of configuration shown in Fig. 8 (1,2,3 - models with space vehicle; 4,5,6 - without it). Axial force coefficient Cx is plotted against free stream Mach number Moo at zero angle of attack. The increase of the length of upper strap-ons results in essential (up to 10-12%) decrease of Cx value. Investigations had shown that when nosetips of the central core and the strap-ons approach each other the configuration drag increases.

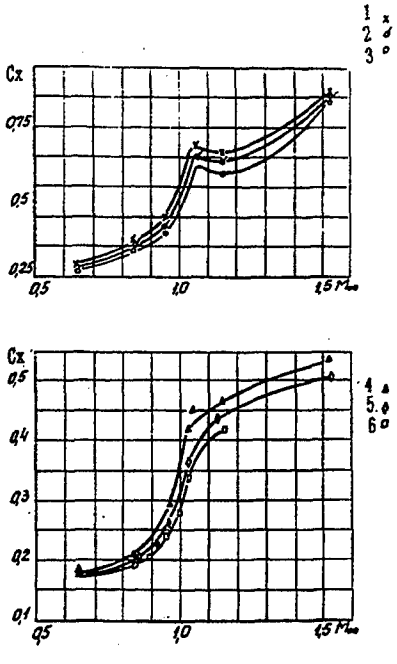

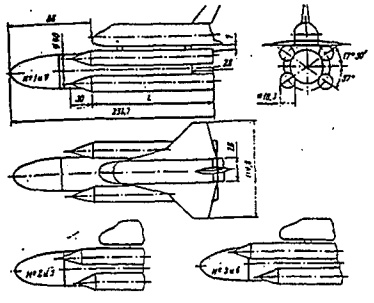

Fig.8

Fig.9

The above configuration is rather rarely packed. For more densely packed cofiguration the interference among elements of configuration and its influence on axial force coefficient may be more pronounced.

Fig. 10 shows axial force coefficient for configurations formed by the central core (diameter 2d) and eight strap-ons (diameter d) equally spaced around it. Several modifications of the configuration were tested: with conical and skewed cone noses of strap-ons, with and without (base configuration) axial displacement l of strap-on noses relative each other one by one or by pairs. For skewed cone noses a reduction of axial force coefficient with displaced one by one strap-ons may be as much as 20 - 25% with all Mach numbers. The most intensive reduction is observed for displacements up to 2d. When conical noses of strap-ons are displaced some reduction of axial force coefficient occurs only at subsonic and transonic Mach numbers.

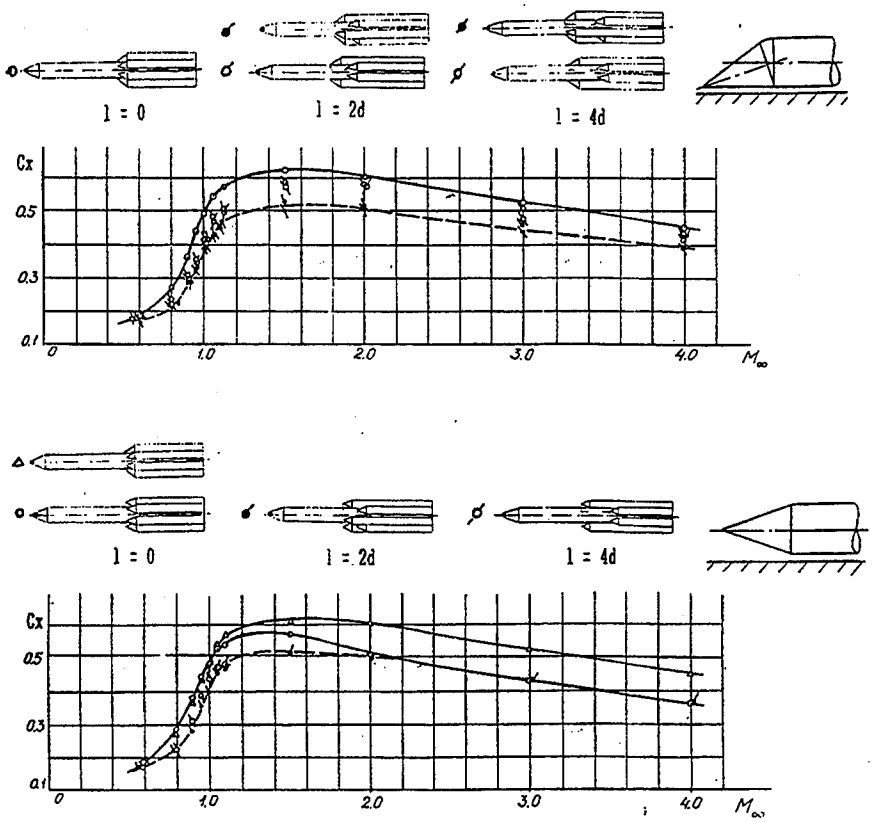

Fig.10

So investigations performed have demonstrated the possibility of noticeable drag reduction for multibody configurations.

Finito di stampare nel mese di settembre 1994
presso la Stampatre - Torino
per conto della
Editrice Levrotto & Bella - Torino